MC2023 DARMSTADT

Microscopy Conference

26 FEBRUARY–2 MARCH 2023

DARMSTADT | GERMANY

PROCEEDINGS

Organized by

DGE DEUTSCHE GESELLSCHAFT FÜR ELEKTRONENMIKROSKOPIE

DGE German Society for Electron Microscopy e. V.

conventus CONGRESSMANAGEMENT

Content

Abstracts of plenary- and invited talks are shown in the proceedings, given they were submitted.

ISBN 978-3-948023-29-4

PL.001

Integrative imaging analysis of the replication cycle of plus-strand RNA viruses

R. Bartenschlager[1]

[1]Heidelberg University, Department of Infectious Diseases, Molecular Virology, Heidelberg, Germany

Plus-strand RNA viruses such as SARS-CoV-2, hepatitis C virus (HCV), dengue virus (DENV) and Zika virus (ZIKV) comprise a large group of pathogens of high medical relevance. In spite of their divergent biological properties, they have in common the remodeling of intracellular membranes that serve as scaffold for the formation of a cytoplasmic replication organelle. To study the 3D architecture of these factories we employ an integrative imaging approach in which we combine various light and electron microscopy techniques. In this way, we found that plus-strand RNA viruses create two morphotypes of replication organelles: double-membrane vesicles (exemplified by SARS-CoV-2 and HCV) and spherules (e.g. DENV and ZIKV). By combining genetic and biochemical approaches, we study the mechanisms underlying the formation of the replication organelles while their dynamics is analyzed by means of live cell imaging. In my presentation, I will provide selected examples of plus-strand RNA viruses, focusing on the 3D structure and biogenesis of their replication organelle and the cell biology driving organelle formation. These examples shall illustrate that evolutionarily distant viruses share striking similarities in the common use of host cell factors and mechanisms with gained knowledge providing new approaches for antiviral therapy.

PL.002

From cryoEM, cryoET to ptychography – an overview

P. Zhang[1]

[1]University of Oxford, Nuffield Department of Medicine, Oxford, United Kingdom

Cryo-electron microscopy (cryoEM) is a powerful method for the high-resolution three-dimensional structural characterization of a wide range of biological samples in a close-to-native, frozen-hydrated state [1]. Such biological samples, preserved in vitrified ice, are extremely radiation sensitive, therefore images of these have low signal-to-noise ratios [2] and low contrast [3,4]. Recent development in microscope instrumentation, direct electron detector, microscope automation and high throughput imaging, and advanced software for data processing and image reconstruction, has revolutionized the field of structural biology, allowing protein structures to be determined at the atomic resolution, especially using cryoEM SPA method (Fig. 1). For studying macromolecular complexes that are intrinsically flexible and dynamic, and often function in higher-order assemblies that are difficult to purify, cryoET and subtomogram averaging (cryoET STA) has emerged as a potent tool to obtain structures of these at near-atomic resolution (Fig. 1). The study of such complexes and assemblies *in situ* using cryoET STA, coupled with cryoFIB and correlative and integrative imaging, opens a new frontier in structural cell biology [5].

While cryoEM SPA and cryoET STA rely on the use of conventional phase-contrast images that require the correction for the contrast transfer function, cryo-electron ptychography (cryoEPt) [6] (Fig. 2) is a new alternative technique that is based on dose-efficient diffractive imaging [7]. Ptychography uses a defocused probe to scan over a specimen with highly overlapping probe positions and computationally reconstructs the wavefunction of the sample. Such an approach has been widely employed in physical and material sciences, and now shows great promise for radiation-sensitive biological samples.

I will present an overview of these cryo-electron microscopy modalities, using examples of our recent studies on human viruses, including HIV-1, SARS-CoV-2, and Rotavirus [8-10], to demonstrate the power of each method to image vitrified native biological samples.

Figure legends:

Figure 1. Schematic workflow of cryoEM using three imaging modalities, cryoEM single particle analysis (cryoEM SPA), cryo-electron tomography and subtomogram averaging (cryoET STA) and cryo-electron diffraction (cryoED). The workflow involves 1) sample preparation, 2) sample vitrification, 3) data acquisition, and 4) 3D reconstruction. A representative structure from each modality is shown.

Figure 2. Schematic optical configuration diagram for cryo-ptychography (a), array of diffraction patterns as a function of probe positions (b), and reconstructed phase of rotavirus double-layered particles (c). Scale bars: 100 nm

References:

[1] R. Henderson et al., Journal of Molecular Biology 213, 899 (1990).

[2] R. Henderson, Quarterly Reviews of Biophysics 28, 171 (2009).

[3] R. Danev et al., Ultramicroscopy 88, 243 (2001).

[4] R. Danev et al., Proceedings of the National Academy of Sciences 111, 15635 (2014).

[5] P. Zhang, Curr Opin Struct Biol. doi: 10.1016/j.sbi.2019.05.021. (2019)

[6] L. Zhou, et al., Nature Communications 11, 2773 (2020).

[7] J.M. Rodenburg, Advances in Imaging and Electron Physics 150, 87-184 (2008).

[8] T. Ni et al., Sci Adv 7(47):eabj5715 (2022)

[9] L. Mendonça et al., Nat Commun. 12(1):4629 (2021)

[10] L. Zhou et al., Nat Commun 11 (1):2773 (2020)

Fig. 1

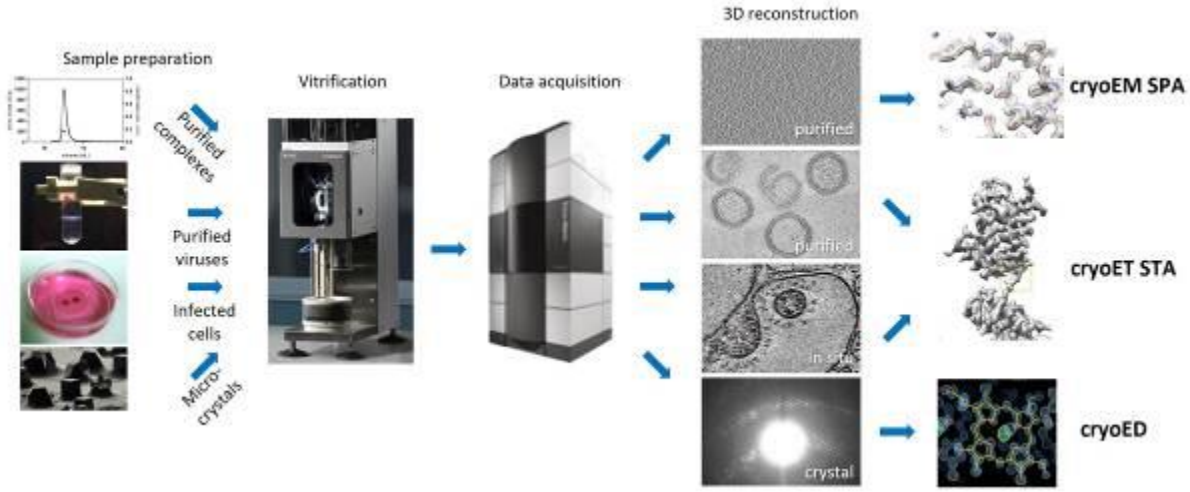

Fig. 2

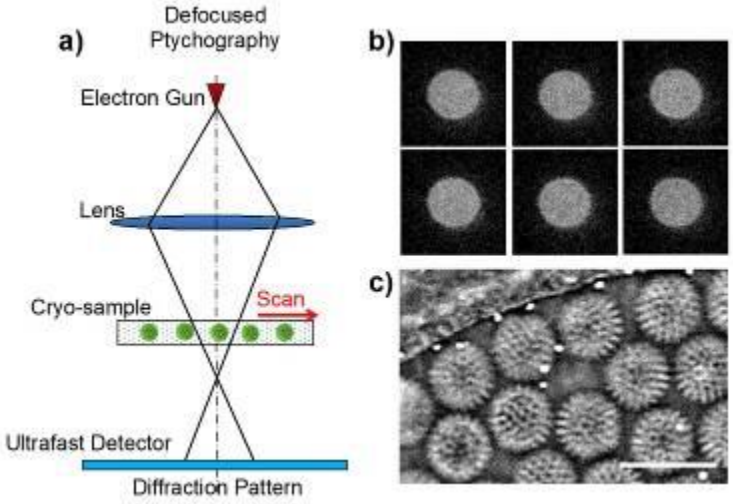

PL.003

Enhancing electron spectroscopies using light

M. Kociak[1]

[1]CNRS-CEMHTI, LPS, Orsay, France

Introduction

The wealth of information collected by electron spectroscopies, such as EELS, CL, PINEM, or EEGS, on the physical or material properties of nanobjects is now beyond dispute1.

It is pretty amazing to see how A. Howie's once-promised ability to research nanooptics with free electrons has developed into a reality that surpasses even his exhilarating predictions from almost 25 years ago.

Objectives

I wish to address two crucial questions among the new possibilities provided by cutting edge electron monochromators, light injection and detection tools, electron detectors, and lasers.

The first is technical: how can we maintain the famed spatial resolution of the electron microscope while achieving the sub-meV spectral resolution required to study excitations like excitons or photonic modes?

The second question is more conceptual: how can we comprehend an optical excitation's life cycle, from its creation as a result of interacting with a free electron to its light emission?

Materials and Methods

I'll discuss CL, EELS, and EEGS experiments that try to provide answers to these questions.

A high-precision, high-efficiency light injection and detection technology is the common factor among them all.

Although it has been utilized here in conjunction with a time-resolved EELS direct detector or a highly monochromated STEM, its design has also found utility in other techniques, such as scanning tunneling microscopes.

Results

I shall therefore demonstrate that EEGS can be several orders of magnitude better resolved than EELS, much in the vein of the work of Henke et al., but here proven on arbitrary photonic samples, despite the very high monochromaticity of modern electron microscopes beams (30 meV at 200 keV).

We will see how the combination of sub-10 meV EELS and high efficiency CL in the context of 2D semiconducting structures enables us to illustrate a direct analogy between macroscopic optical absorption and luminescence on the one hand, and EELS and CL on 2D semiconducting materials on the other.

We'll focus on remarkable differences like the direct observation of trions in CL but not in EELS.

However, at this point, it is still unclear what causes these physical distinctions.

Therefore, beyond *correlation*, we will demonstrate that the *coincidence* between an absorption event at a certain energy (as revealed by EELS) and a potential emission event at a different energy (as revealed by CL) can shed light on the various routes from absorption to emission, ultimately revealing the fate of an optical excitation.

Conclusions

It is now possible to open numerous locks in nanooptics by combining high spectral resolution EELS, CL, and EEGS. Having the appropriate light injection and detection equipment definitely helps. Although the use of electron

coincidence techniques and light (emission or absorption) techniques is still in its infancy, there is little doubt that they will be very useful in a variety of physics domains, from materials science to quantum technologies.

PL.004

Atomic resolution dynamics imaged using 2D heterostructure liquid cells

S. Haigh[1], N. Clark[1], D. Kelly[1], Y. Zou[1], A. Weston[1], R. Gorbachev[1]

[1]University of Manchester, Materials, Manchester, United Kingdom

Stacking 2D materials to build van der Waals (vdW) heterostructures can result in artificial crystals with perfect interfaces, enabling investigation and exploitation the unique electronic and optical properties of 2D crystals [1]. Transmission electron microscope (TEM) imaging has provided essential input on the nature of local defects and interface structure during the development of such vdW heterostructures [2]. For example, we have used scanning TEM (STEM) imaging to observe the atomic reconstruction that occurs when two transition metal dichalcogenide crystals are stacked with a small twist angle (Fig 1a) [3,4]. We have also used vdW heterostructures to study chemical degradation for air sensitive 2D materials such as CrBr3 TaS2 and GaSe, where mechanical exfoliation in an argon glove box and graphene encapsulation is used to protect the 2D material before TEM imaging [5-7]. VdW heterostructures also enable pioneering study of confined gases and liquids. Nanochannels with precisely controlled dimensions can be integrated in to the heterostructure by lithographic etching of specific layers but our TEM imaging is needed to ensure reliable, contamination free fabrication (Fig. 1b) [8,9].

Nanosized pockets of fluid are also highly desirable for TEM studies of atomic behavior in liquids. Commercial in-situ liquid cells enable TEM of liquid samples but the thick silicon nitride windows often prevent atomic resolution imaging and can also limit the sensitivity of spectroscopic analysis. Graphene liquid cells overcome these restrictions but the original fabrication method, suffers from poor control of the liquid dimensions and results in cells with limited stability. We have pioneered a new approach to fabrication of liquid cells based on 2D heterostructure stacking technology [10]. Our 2D heterostructure liquid cell approach also enables liquid mixing, triggered by the electron beam (Fig. 1c), allowing studies of the earliest stage of chemical synthesis at the atomic scale; something that was not previously possible by any technique [11]. Our experimental set-up contains two pockets of liquid separated by an atomically thin membrane, where mixing is induced by nanofracture of the separation membrane with the electron beam [11]. Furthermore, our platform enables the first studies of adatom dynamics at solid liquid interfaces (Fig. 1d)[12] and provides a route to understanding the enormous differences in ionic diffusion behavior for interplanar spaces as a result of changes to local crystal structure.[13]

References:

[1] Frisenda et al. Chem. Soc. Rev., (2018), 47, 53

[2] Haigh et al. Nature Mat. (2012) 11, 764

[3] Weston et al, Nature Nano. (2020), 15, 592

[4] Weston et al Nature Nano. (2022), 17, 390

[5] Hamer et al Nano Lett. (2020), 20, 6582

[6] Bekaert, et al, Nano Lett., (2020), 20, 3808

[7] Hopkinson, et al. ACS Nano, (2019), 13, 5112

[8] Q Yang et al, Nature, (2020) 588, 250

[9] A Keerthi et al, Nature (2018) 558, 420

[10] Kelly et al Nano Letters (2018) 18, 1168

[11] Kelly et al, Advanced Materials (2021) 33, 2100668

[12] Clark et al. Nature (2022) 609, 942

[13] Zou et al. Nature Mat. (2021), 20, 1677

Figure 1. ***(a)*** *Lattice reconstruction in a twisted WS2-WS2 bilayer (from [3])* ***(b)****STEM imaging of 2D nanochannels,(from [9]).* ***(c)*** *Our TEM mixing cell platform (from [11]).* ***(d)*** *STEM frame from a liquid cell movie (ref [12]).*

Fig. 1

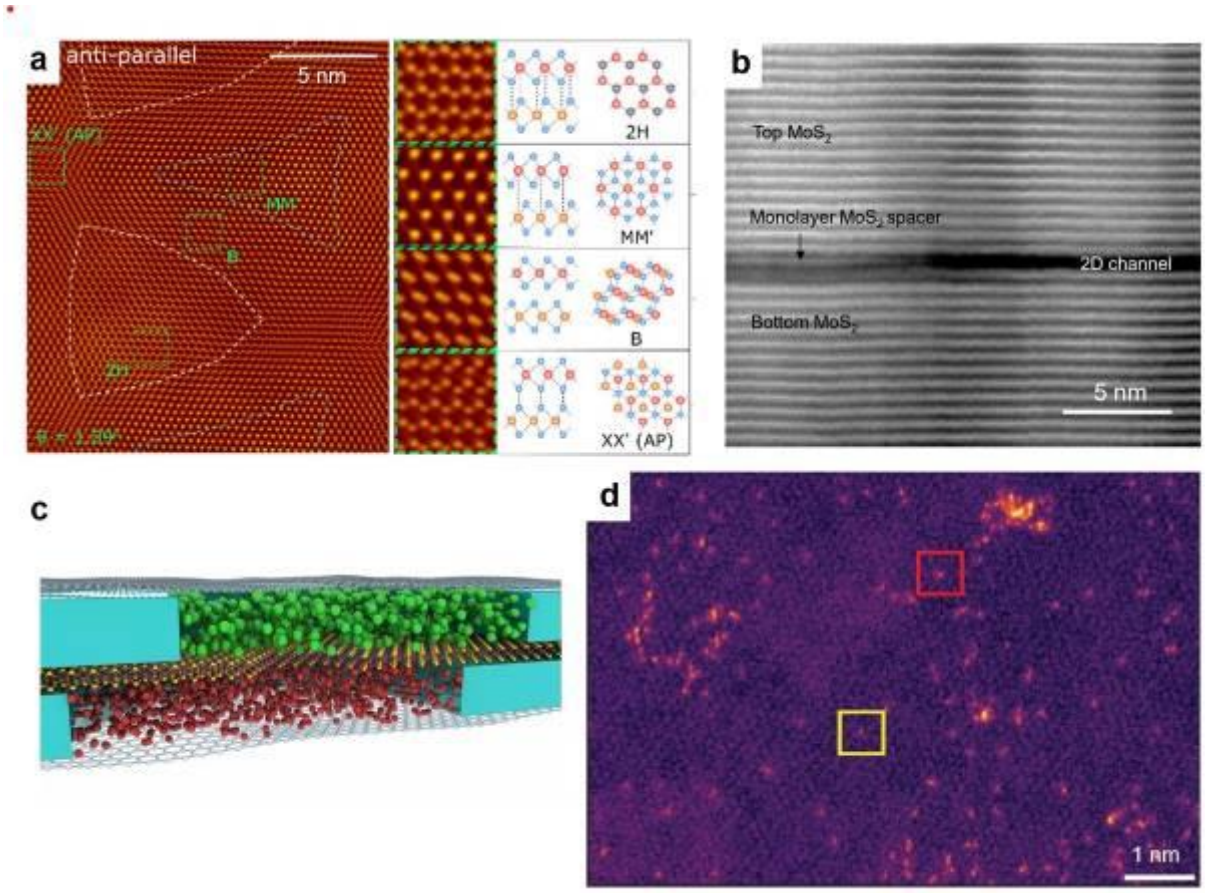

PL.005

New microscopy possibilities with electron beam shaping

V. Grillo[1]

[1]CNR, Istituto di Nanoscienze, Gattatico, Italy

While electron microscopy has reached incredible spatial and energy resolution thanks to sophisticated and bulky electron-optics, a new, somehow orthogonal, research field has emerged based on the idea of giving near-arbitrary transformation to the electron beam before or after its interaction with the sample.

By controlling the electron wavefunction we can improve the measurement sensibility, the spatial resolution, measure new quantities in microscopy, reduce the required dose in experiments, optimise the amount of information that can be extracted by a single electron.

The mathematical instruments supporting this research are the concepts like unitary wave transformation, single pixel imaging, and conformal mapping. The experimental keys are new hardware like electron holograms, miniaturised electrostatic optical elements, electron light interaction and new automatization of hardware control by the innovative use of neural networks.

I will dedicate part of the talk to describe these technical progresses: even not reaching the complexity of the largest innovation in electron optics like spherical aberration correction, they are introducing a little revolution in the way we conceive measurements.

I will conclude summarising the results on the OAM-sorter and the prospective of computational and real ghost imaging, but also a few further ideas for the future.

I acknowledge here the help of all my colleagues and co-workers in my group of CNR Istituto Nanoscienze Modena and in Università di Modena e Reggio Emilia, and all co-workers in QSORT, MINEON and SMART –ELECTRON project. A special thank is due to Prof. Rafal E.Dunin-Borkowski. This work has received funding from the European Union"s Horizon 2020 Research and Innovation Programme under grant agreements 766970 (QSORT), 964591 (SMART-electron) and 101035013 (MINEON).

Fig. 1

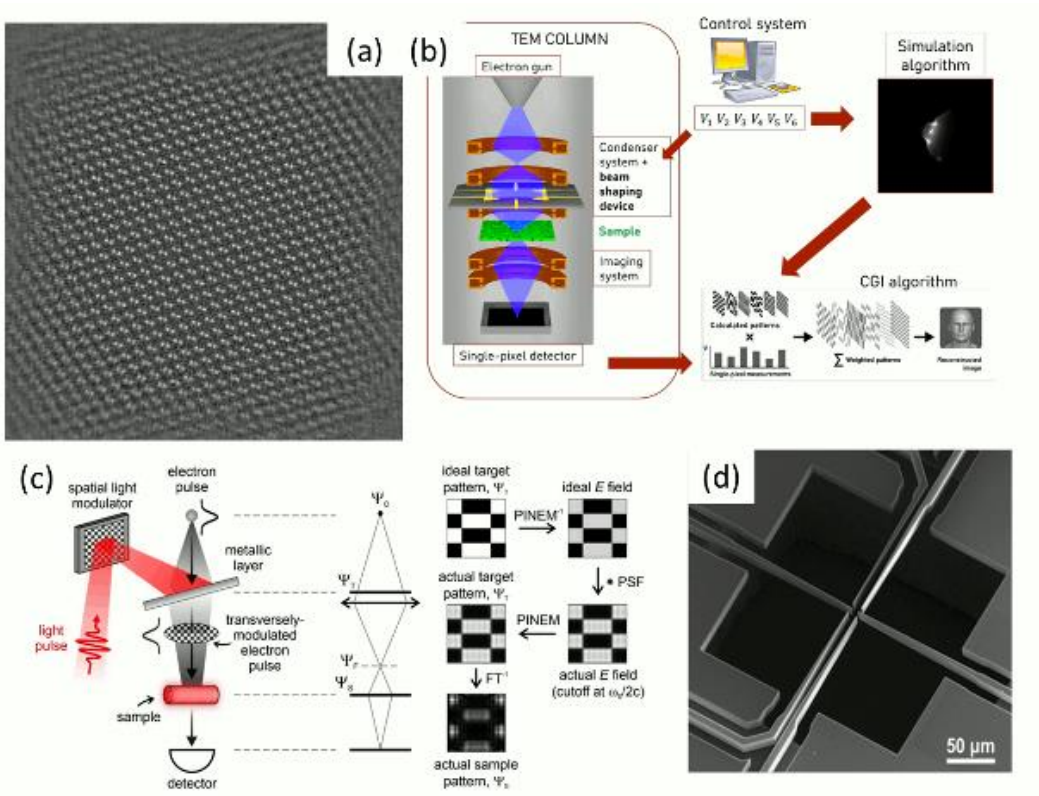
(a)
(b)
TEM COLUMN
Electron gun
Condenser system + beam shaping device
Sample
Imaging system
Single-pixel detector
Control system
Simulation algorithm
CGI algorithm
(c)
spatial light modulator
electron pulse
metallic layer
light pulse
transversely-modulated electron pulse
sample
detector
ideal target pattern, Ψ
ideal E field
PINEM⁻¹
actual target pattern, Ψ
PSF
PINEM
actual E field (cutoff at ω/2c)
FT⁻¹
actual sample pattern, Ψ
(d)
50 μm

Fig. 2


1.1 ħ

PL.006

Geometric constraints on quantum behavior revealed by spatially resolved EELS

P. E. Batson[1]

[1]Rutgers University, Physics and Astronomy, Piscataway, New Jersey, United States

For most of the 20th century, the large size of electron probes restricted our view of physical science to measurements of energy and momentum, leading to many misconceptions about the electronic behavior of nanoscale structures. Thus, measurements of Al nanoparticles using angle resolved EELS showed strong surface plasmons, but very little bulk plasmons, suggesting that small structures are dominated by a surface/bulk ratio considerations.[1] When nm probes became available, experiments showed that EELS scattering depended more on the local probe/specimen geometry, than the particle size.[2] This realization contributed to an exciting period of EELS equipment development aimed at high spatial and energy resolution that continues today.[3]

At first, simple boundary value calculations, using plane waves, were used to predict energy loss spectra as a function of transferred momentum. The energy transfer was assumed to be stochastic, carrying no phase information about the specimen excited state. In 1976, Rose proposed a Mixed Dynamical Form Factor for EELS to allow imaging of the phase of a surface plasmon.[4] His convincing argument led me to a channeling experiment in 1993 that cleanly separated the bulk plasmon from inter-band scattering in diamond, based on the transverse spatial parity of the scattered electron wavefunction.[5]

After the success of sub-Ångstrom imaging using aberration correction, observation of atomic motion became ubiquitous, and yet difficult to understand.[6] It was generally thought that an attractive, dielectric response would dominate the forces between a passing keV electron and a polarizable object. Yet for very close approaches, nanoparticles were observed to move away from the passing electron beam. Using *time-dependent* force calculations based on experimental dielectric data, we found that the magnetic field carried by the relativistic electron appeared to mediate the repulsive behavior.[7] This conclusion is tantalizing but has not yet been confirmed by other workers.

These findings of significant dependence on space and time suggest that spatially resolved EELS might soon enter the arena of relativistic space-time physics, using the geometric space-time algebra of Hestenes.[8] In addition, this kind of treatment might synergistically couple with ongoing work in quantum gravity, through the AdS-CFT correspondence that relates electromagnetism to quantum gravity.[9] In the spirit of this reasoning, I will show an EELS experiment from Vincent and Silcox, in 1973, [10] that appears to match the topology of a Penrose Diagram for entropy information exchange through an event horizon of a black hole.

References

[1] H. Petersen, Solid State Communications **23** 931-934, (1977).

[2] P.E. Batson, Solid State Communications **34** 477 - 480, (1980).

[3] M.J. Lagos, I. Bicket, S. Mousavi and G. Botton, Microscopy, **71**S i174-i199 (2022).

[4] H. Rose, Optik **45** 139 (1976), Ultramicroscopy **15** 173-192 (1984).

[5] P.E. Batson, Phys. Rev. Lett., **70** 1822-1825 (1993).

[6] P.E. Batson, N. Dellby and O.L. Krivanek, Nature, **418** 617 - 620 (2002).

[7] M.J. Lagos, A. Reyes-Coronado, A. Konečná, P.M. Echenique, J. Aizpurua and P.E.

Batson, Phys. Rev. B, **93** 205440 (2016).

[8] D. Hestenes, Oersted Medal Lecture, American Journal of Physics **71**, 104 (2003).

[9] A.V. Ramallo, https://doi.org/10.48550/arXiv.1310.4319

[10] R. Vincent, J. Silcox, Phys. Rev. Lett. **31** 1487 (1973).

MS1.001-invited

Probing local electrochemical and electrocatalytic processes in oxygen-evolving oxides in real-time

V. Tileli[1], T. H. Shen[1]

[1]EPFL, Materials, Lausanne, Switzerland

Surface and interface sensitive operando characterization methodologies are required to unlock electrochemical and electrocatalytic processes. Liquid phase electrochemical transmission electron microscopy (TEM) can provide the sensitivity and selectivity at single particle level. Herein, we investigate oxygen-evolving cobalt-based oxides in alkaline solution and we retrieve morphological, structural, chemical information during cyclic voltammetry measurements. We compare the highly active $Ba_{0.5}Sr_{0.5}Co_{0.8}Fe_{0.2}O_{3-\delta}$ (BSCF) to the spinel Co_3O_4 and rocksalt CoO. The potential-dependent variation of the local contrast is associated to the modification of the wettability from hydrophobic to hydrophilic character at the oxide surfaces through interfacial capacitance phenomena. Molecular oxygen is probed in real-time during its evolution which results to further dewetting of the surfaces. Our work on catalysts exemplifies the crucial role that surface sensitive and electrochemical microcell TEM techniques can play in detailing the mechanism of electrocatalytic processes and can provide a new characterization framework aiding development of novel design routes for targeted catalyst preparation.

MS1.002-invited

A new relativistic ultrafast electron diffraction and imaging (RUEDI) national facility for microscopic dynamics in the UK

Y. Murooka[1], W. Bryan[2], J. Clarke[3,4], M. Ellis[3,4], A. I. Kirkland[5], S. Maskell[1], J. McKenzie[3,4], B. L. Mehdi[1], R. J. D. Miller[6], T. C. Q. Noakes[3,4], I. Robinson[7], S. L. M. Schroeder[8,9,10], J. van Thor[11], C. Welsch[4,1], N. D. Browning[1]

[1]University of Liverpool, Physical Sciences & Engineering, Liverpool, United Kingdom
[2]University of Swansea, Physics, Swansea, United Kingdom
[3]STFC Daresbury Laboratory, ASTeC, Warrington, United Kingdom
[4]Sci-Tech Daresbury, Cockcroft Institute, Warrington, United Kingdom
[5]Rosalind Franklin Institute, Didcot, United Kingdom
[6]University of Toronto, Departments of Chemistry & Physics, Toronto, Canada
[7]University College, London Centre for Nanotechnology, London, United Kingdom
[8]University of Leeds, School of Chemical and Process Engineering, Leeds, United Kingdom
[9]Diamond Light Source Ltd., Didcot, United Kingdom
[10]Research Complex at Harwell (RCaH), Rutherford Appleton Laboratory, EPSRC Future Continuous Manufacturing and Advanced Crystallisation Hub, Didcot, United Kingdom
[11]Imperial College London, Department of Life Sciences, London, United Kingdom

1. Introduction

In the last two decades, there has been rapid progress in time-resolved electron diffraction and imaging using femtosecond pulsed electron beams. While light and X-ray probes are also common, electrons can probe all of lattice, charge, spin, and electromagnetic waves with high spatial resolution. Using femtosecond laser, for example, induced dynamics of lattice, charge transfer, magnetization, polaritons, have been clarified in both reciprocal space and real space.

When the acceleration voltage is about 10- a few 100 kV, dynamics is often needed to be a reversible process with a short relaxation time in a sub 0.1 um thin specimen. The number of electrons per pulse is in the single electron regime due to the space charge effect. A long experimental time and high stability are often necessary. When it is at MeV, the number can be increased by more than one million, making it possible to observe a um thick specimen in the single shot regime. The MeV approach, on the other hand, has been realized only in diffraction but not in microscopical imaging.

2. Objectives

At present, the requirements to observe dynamics have become so advanced that the conventional method often do not work. They are, for example, specimens in liquid/gas phases, complex systems as battery electrode surfaces, excitations under intense laser irradiation, and sub-100 femtosecond lattice dynamics. While attosecond phenomena have been explored in electron dynamics, it has also become important to clarify the correlation between electrons, lattices and spins. In addition, it is also urgent to improve the efficiency of experimental methods and to link them with other ultrafast techniques. RUEDI [1] has been designed and developed to enable these.

3. Materials & Methods

RUEDI utilizes accelerator technology to generate a beam at MeV with 10 fs pulse duration and high brightness, integrates electron diffraction and electron microscope imaging, and achieve high efficiency using AI technology. For the sample environment, RUEDI has not only laser and high frequency field irradiations but also liquid/gas sample holders and in-situ, operando capabilities.

Under well-controlled environments, electron diffraction plays a key role to test hypothesis and consistency as an analytical science method. Microscopic imaging becomes important in order to do observations at nm spatial resolution and, as a field science method, to obtain an overall information from a complex system where it is difficult to discover a hypothesis.

RUEDI project focuses on five research themes. They are energy materials, materials in extreme conditions, chemical dynamics, quantum materials and in vivo life science. Some examples are, interfacial dynamics in liquid phase, photocatalytic dynamics, high-pressure and temperature materials, ultrafast chemical/molecular dynamics, and observation of biological specimens under hydration.

4. Results & Conclusion:

We are developing RUEDI facility to elucidate static and dynamic structures in systems those are difficult be studied with current techniques. RUEDI will be applied to systems such as thick specimens, complex sample environments, and sub-100 femtosecond dynamics.

References:

[1] RUEDI is supported by EPSRC / UK Infrastructure Fund under grant number EP/W033852/1.

MS1.003

Unraveling (de)lithiation dynamics inside graphene sheets at atomic scale

Y. Li[1], F. Börrnert[1], S. Fecher[2], M. Ghorbani-Asl[3], Z. Li[1], J. Biskupek[1], S. Yang[2], M. Kühne[2], D. Bresser[4], A. Krasheninnikov[3], J. Smet[2], U. Kaiser[1]

[1]Ulm University, Ulm, Germany
[2]Max Planck Institute for Solid State Research, Stuttgart, Germany
[3]Helmholtz-Zentrum Dresden-Rossendorf, Institute of Ion Beam Physics and Materials Research, Dresden, Germany
[4]Helmholtz Institute Ulm, Ulm, Germany

Graphite has succeeded as a lithium-ion anode material in the last 30 years, since it enhances energy densities due to its low (de)lithiation potential and high capacity. LiC_6 had been known as the densest intercalation compound for the graphite anode. However, we observed a denser lithium phase inside graphene sheets in-situ during (de)lithiation by using spherical and chromatic aberration-corrected low-voltage high-resolution transmission electron microscopy. To meet the challenge of observing the (de)lithiation processes in-situ inside TEM, an electrochemical cell architecture including graphene sheets and polymer electrolyte was designed and placed on the Si_3N_4 membrane of a custom-made TEM sample carrier chip, as shown in Figure 1a. The lithium ions were inserted into the graphene sheets when applying a constant voltage during lithiation, while transferred back into the polymer electrolyte when the voltage was removed during delithiation (Figure 1b). Our HRTEM investigation confirms that the crystal structure of the lithium inside graphene sheets is fcc, which is denser than the LiC_6 intercalation compound. In addition, we observed that the shape of the lithium crystals is dramatically different during the (de)lithiation processes, as shown in Figure 2. During lithiation, lithium crystals nucleate at the positions of graphene defects, and grow with triangular shape further. During delithiation, the lithium crystals shrink with irregular shape. The reason for that is the introduction of oxygen atoms at different positions inside the lithium crystals. Some oxygen atoms are introduced during lithiation, and bond with lithium atoms at the octahedral interstitial positions. The distribution of the oxygen atoms is uniform. However, during delithiation, the oxygen atoms gather at the edge of the lithium crystals, and keep at the edge position while the lithium crystals are shrinking. The oxygen atoms lock part of lithium atoms, resulting in the formation of amorphous lithium oxide finally. Our work gives a detailed insight of the existence and diffusion of lithium inside graphene sheets, which may have relevance also in anode materials.

This work contributes to the research performed at CELEST (Center for Electrochemical Energy Storage Ulm-Karlsruhe) and was funded by the German Research Foundation (DFG) under Project ID 390874152 (POLiS Cluster of Excellence). We acknowledge financial support from the Baden-Württemberg Stiftung gGmbH (project CT 5) and from the Ministry of Science, Research and the Arts (MWK) of the federal state of Baden-Württemberg in the frame of the SALVE project.

Reference:

[1] Nature 564, 234-239 (2018)

[2] Nat. Nanotechnol. 12, 895–900 (2017)

Figure 1: Device layout and working principle. (a) Self-designed electrochemical cell architecture including graphene sheets and polymer electrolyte placed on the Si_3N_4 membrane of a custom-made TEM sample carrier chip. Electron beam is illustrated in blue. (b) Schematic side view of the device during the in-situ TEM investigation.

Figure 2: Overview of (de)lithiation inside graphene sheets. (a) The lithiation process. Lithium crystals nucleate and grow with triangular shape. (b) The delithiation process. The lithium crystals shrink with irregular shape.

Fig. 1

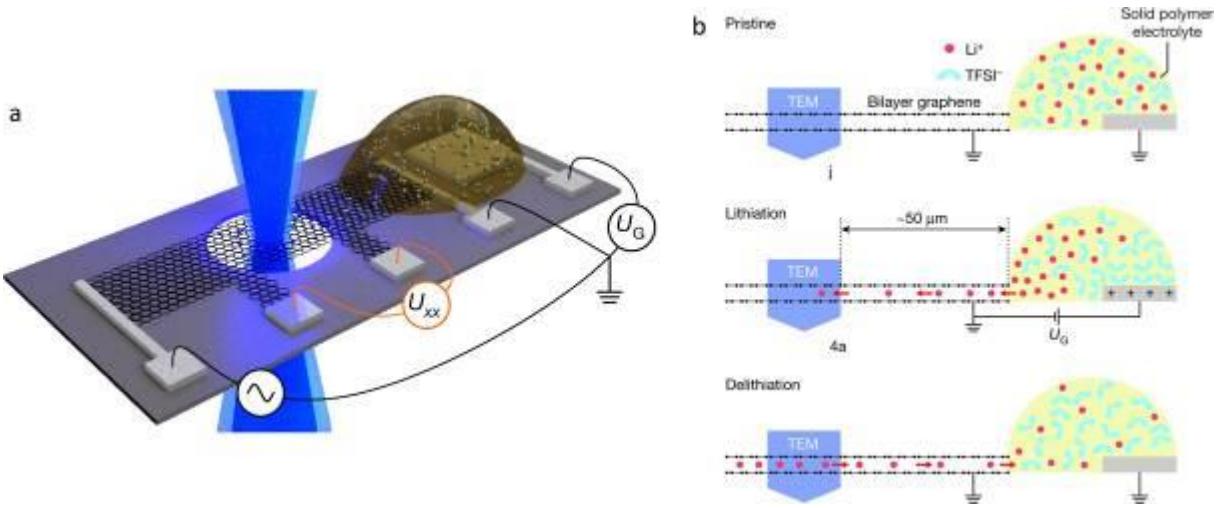
a
U_G
U_{xx}
b
Pristine
Li⁺
TFSI⁻
Solid polymer electrolyte
TEM
Bilayer graphene
i
Lithiation
~50 µm
4a
U_G
Delithiation

Fig. 2

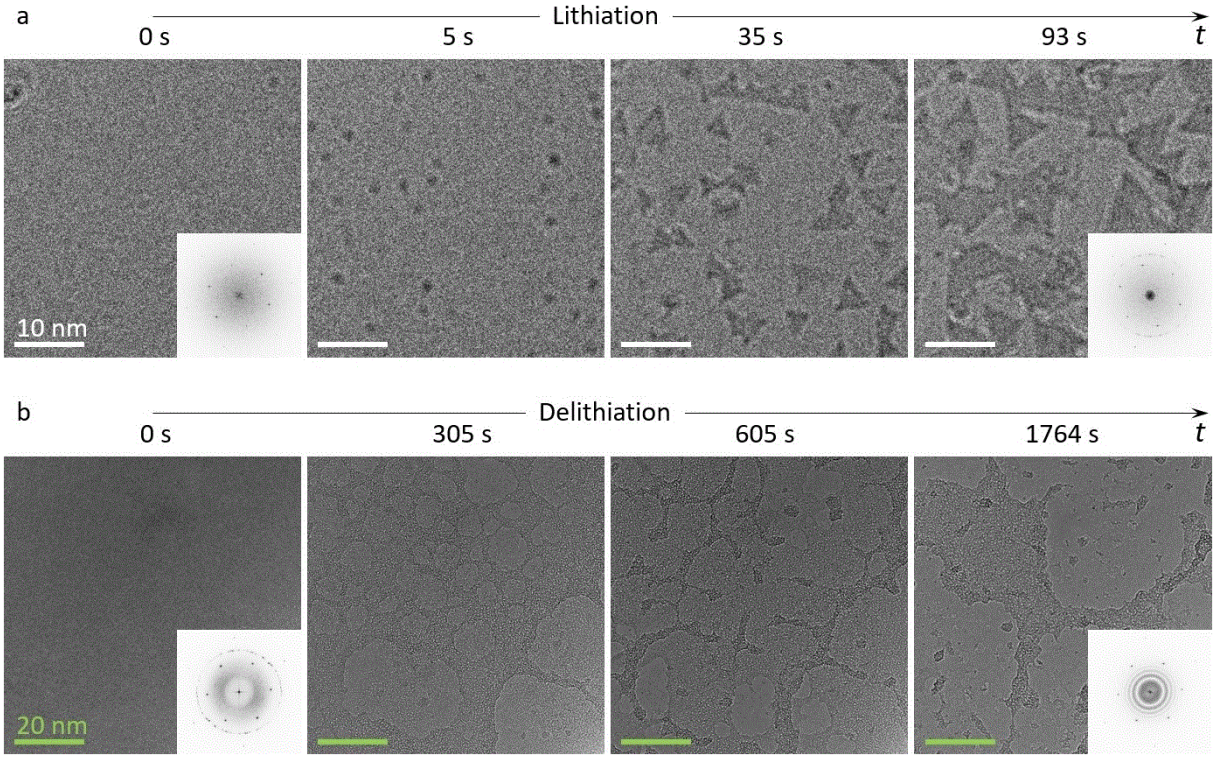
a
Lithiation
0 s
5 s
35 s
93 s
t
10 nm
b
Delithiation
0 s
305 s
605 s
1764 s
t
20 nm

MS1.004

Imaging structural defects and associated oxygen positions in Li-rich $Li_{1.2}Ni_{0.13}Mn_{0.54}Co_{0.13}O_2$

W. Song[1], P. Nellist[1]

[1]University of Oxford, Materials, Oxford, United Kingdom

Li-rich $Li_{1.2}Ni_{0.13}Mn_{0.54}Co_{0.13}O_2$ (Li-rich NMC) can deliver a high capacity over 250 mAh g-1 as a Li-ion battery cathode material compared with conventional layered metal oxides (<200 mAh g-1). Such high capacity results from the redox reaction of the lattice O2- ions and transition metals (TMs). Despite the boost in the capacities, Li-rich NMC suffers from voltage hysteresis and degradation in the voltage and capacity over cycling [1]. Synthesis efforts aim to overcome the issues but its structure is rather inhomogeneous and the role in affecting the materials performance is unclear [2]. The as-prepared material contains a number of defects, such as stacking faults, and has raised debates on whether the material is a coherent mixture of *C2/m* Li_2MnO_3 and *R-3m* $LiTMO_2$ phase or a solid solution with the monoclinic phase [2].

In this work, we performed simultaneous annular dark field (ADF) imaging and electron ptychography on Li-rich NMC. **Figure 1a** shows the ADF image containing three types of monoclinic domains projected along [100], [110] and [1-10] zone axis, respectively. The domain variants are due to the faulted stacking of the TM layers in *c* direction. The TM layers composing the three types of domains have an in-plane rotation angle of 120 degree with respect to each other and the resulting stacking faults are referred to as rotation type. In the TM layers, Li^+/Ni^{2+} and Co^{3+}/Mn^{4+} cation ordering in a honeycomb pattern leads to the dumbbell contrast in ADF that arising from the Co/Mn atom columns. The dumbbell contrast is not uniformly seen as shown in **Figure 1b**, where cation disordering contrast is seen in the transition regions between the [110] and [1-10] domains. Such transition regions possibly result from the boundaries of the two types of domains or the in-plane cation disordering. **Figure 1c** displays several types of TM layers with cation ordering (O), mixing ordering/disordering (O/D) and disordering (D) contrast in ADF imaging. In addition to the rotation-type stacking faults, **Figure 1d** shows another type resulting from out-of-plane TMs layer shift in *c* direction, namely shift type. Both types of stacking faults rely on the imaging of TMs whilst lack the understanding of oxygen stacking. To probe the oxygen lattice, we carried out focused-probe electron ptychography to reconstruct the phase image and use the ADF image to point out TMs. **Figures 2** show the ADF and ptychographic image and their composite image, respectively. Although TM layers possess a number of stacking faults, the oxygen layers are seen in an O3-type stacking. The imaging on the TMs and O layer stacking shows different structure defects in Li-rich NMC that can affect the electrochemical performance [3].

Figure 1 Stacking faults of Li-rich NMC. (a) ADF image of rotation-type stacking fault. White region is magnified in (b). The red, green and orange tetragons indicate monoclinic domains projected along [100], [110] and [1-10] zone axis, respectively. (c) ADF image of various types of TMs layers. (d) ADF image of shift-type stacking fault. Scale bar is 1 nm.

Figure 2 Imaging of faulted stacking. (a-c) Rotation type. (d-f) Shift type. (a, d) ADF image. (b, e) Ptychographic image. (c, f) Composite image. Superposed is the crystal model. Purple sphere is TM, green is Li and red is O. Scale bar is 0.5 nm.

Reference

[1] House, R.A., et. al., (2020) Nat. Energy 5, 777-785.

[2] Shukla, A.K., et. Al., (2018) Energ. Environ. Sci. 11, 830-840.

Fig. 1

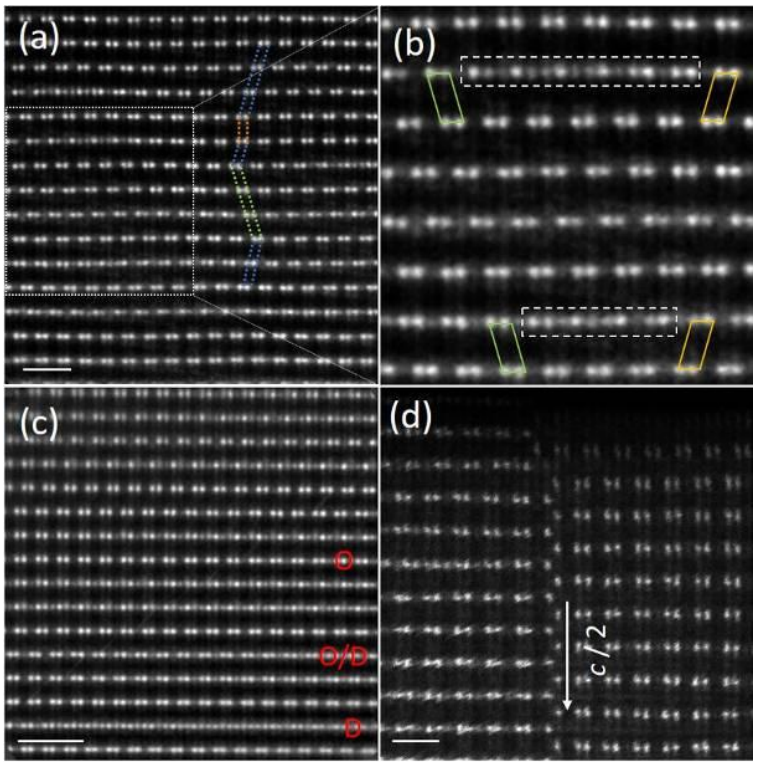

Fig. 2

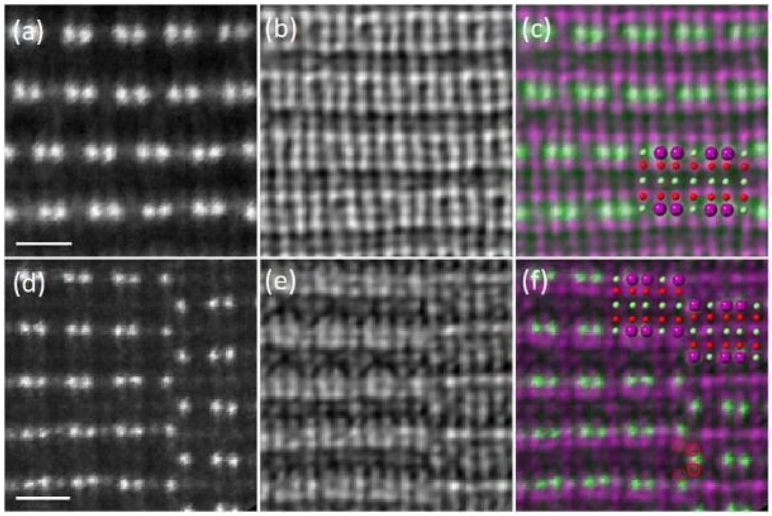

MS1.005

Establishing *in-situ* heating experiments of monolithic $LiNiO_2$ particles in O_2 atmosphere

T. Demuth[1], M. Malaki[1], S. Ahmed[1], P. Kurzhals[2], A. Beyer[1], J. Janek[2], K. Volz[1]

[1]Philipps-University Marburg, Materials Science Center (WZMW) and Department of Physics, Marburg, Germany
[2]Justus-Liebig-Universität, Institute of Physical Chemistry & Center for Materials Research, Giessen, Germany

The state-of-the-art cathode materials for lithium-ion batteries are the layered transition metal oxides $Li(Ni_{1-x-y}Co_xMn_y)O_2$ (NCM) and $Li(Ni_{1-x-y}Co_xAl_y)O_2$ (NCA). They deliver specific capacities of more than 170 mAh g-1 [1]. Manufacturers and researchers constantly try to reduce the cost as well as increase the capacity of batteries. Increasing the Ni content to 80% or higher fulfills on the one hand these goals but leads on the other hand to a reduced cycling stability of the battery, as the polycrystalline particles undergo an anisotropic volume change during (de-)lithiation [2]. By using monolithic crystals instead of polycrystalline materials, these drawbacks may be mitigated [3]. Furthermore, an annealing step at elevated temperatures can optimize the surface morphology and structure of the particles leading to an improved electrochemical performance [4]. The annealing process is executed in an oxygen atmosphere to prevent oxygen loss from the grains [5].

This study aims at gaining a thorough understanding of the influence of the annealing process on the structure of Ni-rich layered transition metal oxides. For this purpose, the model system LiNiO2 (LNO) is investigated during annealing in an oxygen atmosphere in in-situ high angle annular darkfield (HAADF) scanning transmission electron microscopy (STEM) and electron energy loss spectroscopy (EELS) experiments.

The monolithic LNO particles agglomerate to secondary particles with a diameter of approximately 4 µm. To prepare an electron transparent sample, the focused ion beam (FIB) cutting method is employed. For apposite placement of the particle on the SiN window of the heating chip, a Si lamella with a cut-out hole, in which the particle is placed before thinning, is used as support. The chip with the particle is then mounted in the enclosed gas cell TEM holder, which is connected to an oxygen bottle. Between the bottle and the holder, a flow valve controls the flow of oxygen, whereas a pressure valve downstream of the holder regulates the pressure to 1 bar in the holder tip.

We report on our experiments to heat a secondary LNO particle in an oxygen atmosphere. A heating ramp of 1 °C / s was employed up to a temperature of 700 °C. Starting at around 450 °C, structural changes of the particle begin to arise. These changes firstly appear at the grain boundaries of the monolithic crystals and later proceed to the bulk of the grains. Eventually, the whole secondary particle is severely disintegrated, as the HAADF STEM image in figure 1 shows. We propose that this disintegration occurs due to oxygen loss from the particles as EELS data in figure 2 obtained from the same region before and after heating implies.

The first experimental data has shown that our work-flow from the elaborate sample preparation to in-situ heating and the particles" investigation works fundamentally. In future experiments we will refine our set-up and parameters to try to suppress oxygen loss and disintegration of the LNO particles during heating.

Figure 1: HAADF STEM images of LNO secondary particle a) before and b) after in-situ heating to 700 °C.

Figure 2: STEM EELS signal of oxygen before (blue) and after (red) in-situ heating to 700 °C.

[1] de Biasi, L. et al. Adv. Mater. **31** (2019)

[2] Kurzhals, P. et al. J. Electrochem. Soc. **168** (2021)

[3] Langdon, J. et al. Energy Stor. Mater. **37** (2021)

[4] Huang, B. et al. Solid State Ion. **345** (2020)

[5] Karki, K. et al. ACS Appl. Mater. Interfaces **8** (2016)

Fig. 1

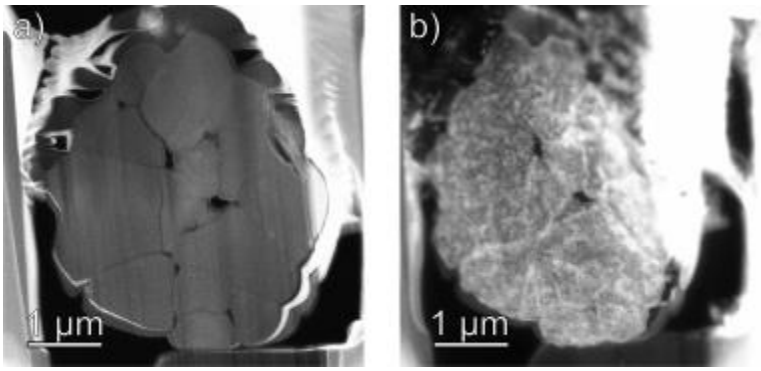
a)
1 µm
b)
1 µm

Fig. 2

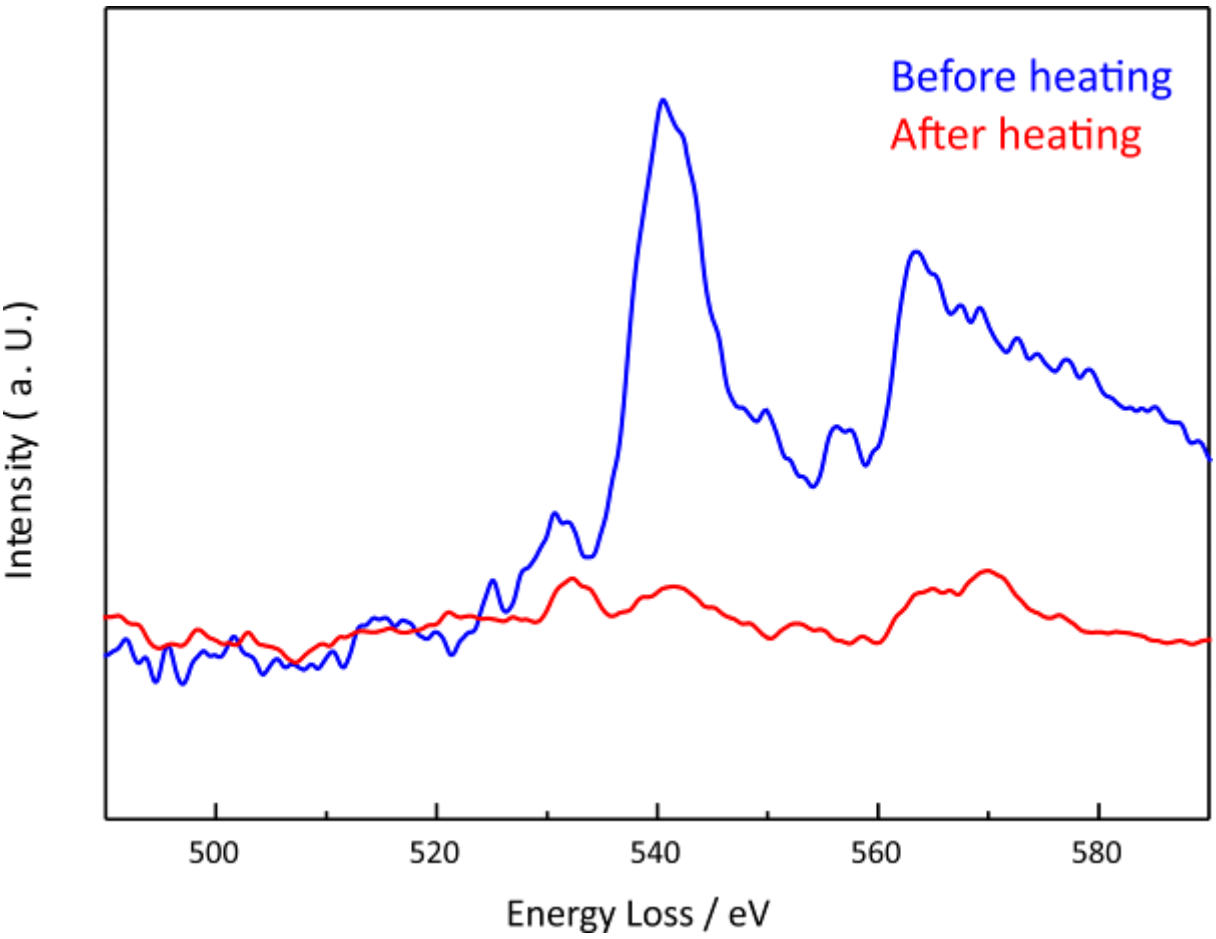
Before heating
After heating
Intensity (a. U.)
500
520
540
560
580
Energy Loss / eV

MS1.006

Low dose STEM imaging and *in situ* TEM of metal halide perovskites

N. Schrenker[1], S. Toso[2], C. P. Yu[1], B. Pradhan[3], E. Debroye[3], M. Roeffaers[3], J. Hofkens[3], L. Manna[2], J. Verbeeck[1], S. van Aert[1], S. Bals[1]

[1]University of Antwerp, EMAT, Department of Physics, Antwerp, Belgium
[2]IIT, Department of Nanochemistry, Genova, Italy
[3]KU Leuven, Leuven, Belgium

Metal halide perovskites (MHP) are promising semiconductors for the next generation of optoelectronic devices. Due to their tunable bandgap, they fulfil the requirement for various applications, including solar cells, light-emitting diodes, lasers and photodetectors. Unfortunately, MHPs still lack of long-term stability. Degradation occurs due to their phase instability and under environmental triggers, such as moisture and oxygen. In order to be able to extend the life time of MHPs a fundamental understanding of degradation mechanisms is required. To investigate these mechanisms we apply *in situ* HRSTEM under oxygen and moisture. Another challenge for TEM investigations of MHPs is their high electron beam sensitivity. Therefore, we developed low-dose protocols using integrated differential phase contrast (iDPC)1, see Fig.1b. Hence, we are able to investigate the MHP without degradation due to Pb-cluster formation or amorphization and quantitatively interpret the STEM images using statistical parameter estimation theory. For heterostructures, consisting of perovskite nano cubes and a chalcohalide, we applied the described STEM techniques to study the interface nature (Fig. 1c,d)2. Interestingly, the cationic subnetwork of Pb and Cs is maintained through the interface, which results in an epitaxial relationship. We also found that the perovskite can be used as disposable epitaxial template for the phase-selective synthesis of lead sulfochloride nanocrystals. Furthermore, in order to study perovskites with organic cations as well as the exchange of cations or halides, we utilize 4D STEM data sets to retrieve the phase information via integration center of mass (iCOM) reconstructions. This enables us to study the organic cations, which would not be possible using HAADF imaging. The developed methods provide important insights into the structure of the perovskites and enable *in situ* TEM investigations, which are essential to improve the properties and increase their chemical stability.

Figure 1. High resolution STEM imaging of metal halide perovskites. (a) HAADF image of a CsPbCl3 nanocrystal (NC). (b) Corresponding iDPC image of the NC in panel (a) revealing the Cl atomic columns. (c) High-resolution HAADF STEM image of a single Pb4S3Cl2/CsPbCl3 heterostructure. At the top is a model of the Pb4S3Cl2/CsPbCl3 epitaxial interface superimposed on a close-up view of panel (c), highlighting the continuity of the Pb2+/Cs+ cationic subnetwork. Atom color code: Cs = cyan; Pb = orange/white; S = yellow; Cl = green. (d) Column intensity map of the Pb-containing columns in the perovskite phase and of the Pb columns in the Cs2PbX4-like subnetwork of the Pb4S3Cl2 domain. The color in the intensity map correlates with the total intensity scattered from the corresponding atomic column (red = higher intensity; blue = lower intensity). (c,d) Reprinted from Ref. [2].

References

- *[1] Otero-Martinez, C., Imran, M., Schrenker, N. et al. Fast A-site cation cross-exchange at room temperature: Single-to double- and triple cation halide -perovskite nanocrystals. Angew. Chem. Int. Ed., e202205617 (2022)*
- *[2] Toso, S., Imran, M., Mugnaioli, E. et al. Halide perovskites as disposable epitaxial templates for the phase-selective synthesis of lead sulfochloride nanocrystals. Nat Commun 13, 3976 (2022)*

Fig. 1

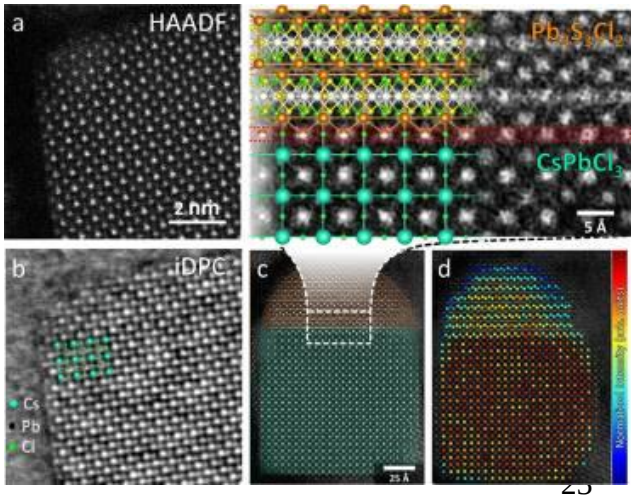

MS1.007

Operando SEM and XPS insights of self-sustained oscillatory dynamics of ethylene to syngas over nickel catalysts

C. Claudiu[1], M. G. Willinger[2], J. A. van Bokhoven[3], M. Plodinec[1], L. Artiglia[4]

[1]ScopeM, Institute for Chemical and Bioengineering, Department of Chemistry and Applied Biosciences, ETH Zurich, 8093, Zürich, Switzerland, Zurich, Switzerland
[2]TU Munich, Electron Microscopy with research focus on energy materials, Munich, Germany
[3]ETH Zurich, Department of Chemistry and Applied Biosciences, Zurich, Switzerland
[4]Paul Scherrer Institute, Laboratory for Catalysis and Sustainable Chemistry, Villigen, Switzerland

As scientists, it is our duty to pave the way for the development of a sustainable economy based on renewable energy resources and to reduce greenhouse gas emissions with an expected market value of 48Bn $ by 2027 [**1**], the catalyst—whether heterogeneous, homogeneous, or enzymatic—represents one of the pillars on which modern society is built. However, apart from the simplest model reactions, the scientific community is still unable to fully comprehend the underlying mechanism of catalysis and the atomistic details of the active state.

The objective is to obtain mechanistic insights into the role of surface species present in the catalytic process of partial oxidation of ethylene to syngas on a model polycrystalline nickel foil. Using a combination of operando scanning electron microscopy (OSEM) for real-time observation of structural dynamics and ambient pressure x-ray photoelectron spectroscopy (APXPS) we correlate the state of the catalyst with its activity. Although challenging to study, the self-sustained oscillating reaction mode enables detailed analysis of the successive elementary steps of the catalytic act (***Figure S1***). The obtained insights are envisioned to expand the research on the self-regenerating operation of real-world catalysts.

We were able to extend the functionality of a TFS Quattro S ESEM by developing a mobile in-situ that enabled the ambient pressure x-ray photoemission spectroscopy and operando scanning electron microscopy studies to be performed under identical conditions. This unit is composed of a modified sample holder that can achieve working temperatures of up to 1250C in reactive gas atmospheres, an automated heating unit and an automated gas feeding system.

By maintaining a constant gas composition in isothermal conditions, a synchronized self-sustained oscillation mode was identified, in which the reaction`s product distribution reflects the catalyst morphology and chemical state. We were able to pinpoint the catalytic behavior down to competing species that influence catalyst deactivation with excellent spatial resolution and to discriminate between local and non-local mechanisms that impact the collective dynamics usually reported using traditional approaches.

The combination of spatially resolved real-time imaging [**2**], [**3**] with integral surface-sensitive spectroscopy enables the chemical identification of surface species and simultaneous visualization of their evolution as a function of reaction conditions. We were able to provide insight into structure sensitivity and coupling phenomena between reactive gas-phase and catalyst states that are related to the emergence of catalytic activity in a synchronized self-sustained oscillatory mode. The here described structure-activity correlations are not accessible through integral characterization techniques or by studying steady-states alone, highlighting the importance of real-time, laterally resolved direct observation of active catalysts.

Figure S1: Time series of a Ni surface during ethylene to syngas conversion. HFOV is 33.5µm.

[1] Catalyst Market Size, Share & Trends Analysis Report By Raw Material 2020 – 2027

[2] Danilatos,Gerasimos D. "Environmental scanning electron microscopy and microanalysis." *Microchimica Acta* 114.1 (1994): 143-155

[3] Sandoval-Diaz, Luis, et al. "Visualizing the importance of oxide-metal phase transitions in the production of synthesis gas over Ni catalysts." *Journal of Energy Chemistry* (2020).

Fig. 1

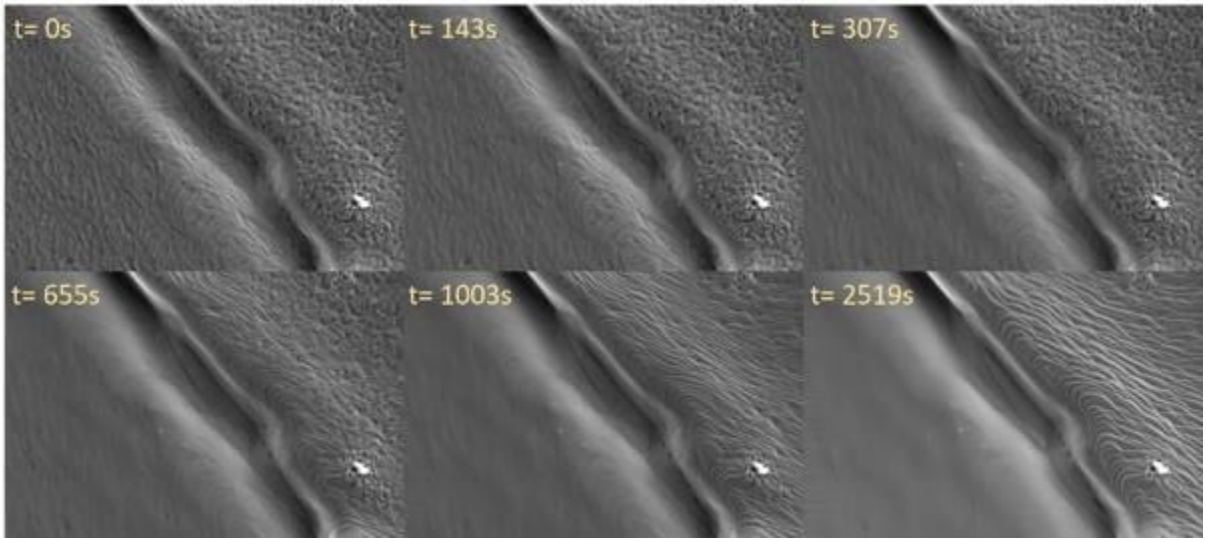

MS1.008

Evaluating charge carrier mobility of organic semiconductor using ultra-low voltage spectral SEM

W. S. Zhang[1], R. R. Schröder[1]

[1]Ruprecht-Karls University Heidelberg, Bioquant, Heidelberg, Germany

Introduction

The pivotal property of organic semiconductors (OSCs) to achieve high performance devices is a high charge carrier mobility. However, the mobility is commonly measured from a model device, most often a field-effect transistor, making the mobility value material- and device-dependent. Both, the intrinsic factors - such as energy levels of all materials involved, molecular packing of the OSC, its crystalline domain size and orientation - and the extrinsic factors - likewise device structure, morphological defect, contact defect - will influence the final result.

On the other hand, computational methods can provide intrinsic mobilities, which deviate frequently over several orders of magnitudes from the experimental data. Thus, material scientists need a reliable method to (re-)evaluate the existing and newly developed materials in order to gain a rational structure-function-relationship.

Objectives

Herein, we present an electron-spectroscopic method to evaluate the charge carrier mobility directly from thin-films or microcrystals. Such samples can easily be obtained for most materials. With the proposed method the effects of the extrinsic impact factors are reduced to only one - the contact resistance. This factor remains, as it is necessary to ground the sample for electron spectroscopic data collection. We show that the relative lateral mobilities between different OCSs can thus be directly determined.

Materials & methods

Polycrystalline thin-films of small molecules were prepared via thermal evaporation under vacuum. Microcrystals of small molecules and polymers were obtained by wet techniques. We use a demonstrator of an electron-spectroscopic SEM, i.e. Zeiss Delta-SEM, for recording the secondary electron (SE) emission spectrum. The dynamic charging map, generated from the SE spectra on each pixel, is used for the mobility evaluation (see Figure 1).

Results

First, the beam-material interaction was investigated and the electrically neutral energy points were determined under various charging conditions. Depending on n-type or p-type OSCs, suitable charging conditions that results in negative or positive charging was selected.[1] With step-wise increase of charging intensity, the OSCs turned from electrically neutral to severely charged. By comparing the stage currents among different OSCs, which exhibit the same/similar charging maps, one can evaluate OSCs in terms of lateral charge carrier mobility (example see Figure 2). The horizontal mobility is also accessible by analyzing the charging maps near and on the metal contacts. In addition, space charge, impacts from crystal orientation and molecular packing on mobility can be observed.

Conclusion

The lateral mobilities estimated with the presented method agree very well with the theoretical calculation (*eg.* transfer integral)[2]. Contact between OSC and electrode can be individually tested and thus a suitable device structure can be proposed according to the intrinsic lateral mobility.

Ref. [1] *Adv. Electron. Mater.* **2021**, 2100400. [2] *Chem. Eur. J.* **2015**, *21*, 17691-17700.

Fig. 1

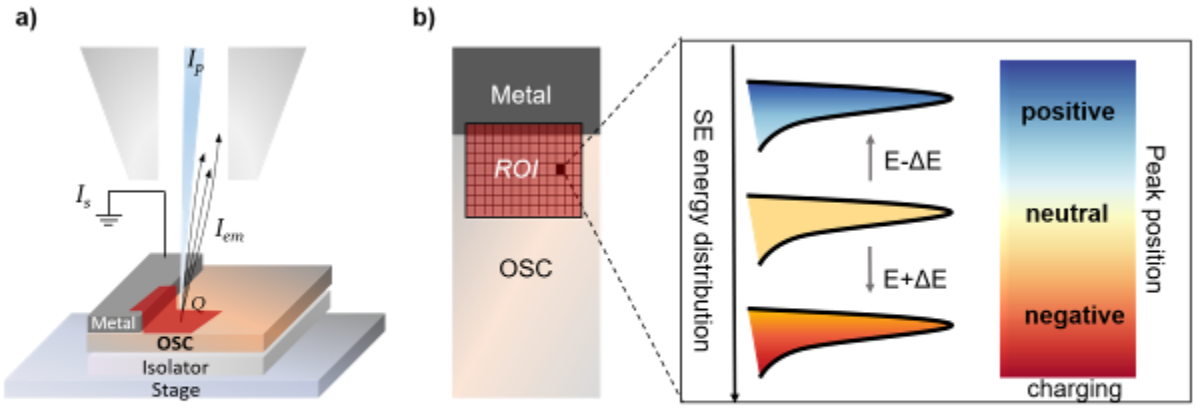

Figure 1. Conceptual illustration of the working principle: a) beam-material interaction, in which Q, I_p, I_s and I_{em} stand for accumulated charges in OSC, beam current, stage current and emission current, respectively. b) surface charging map.

Fig. 2

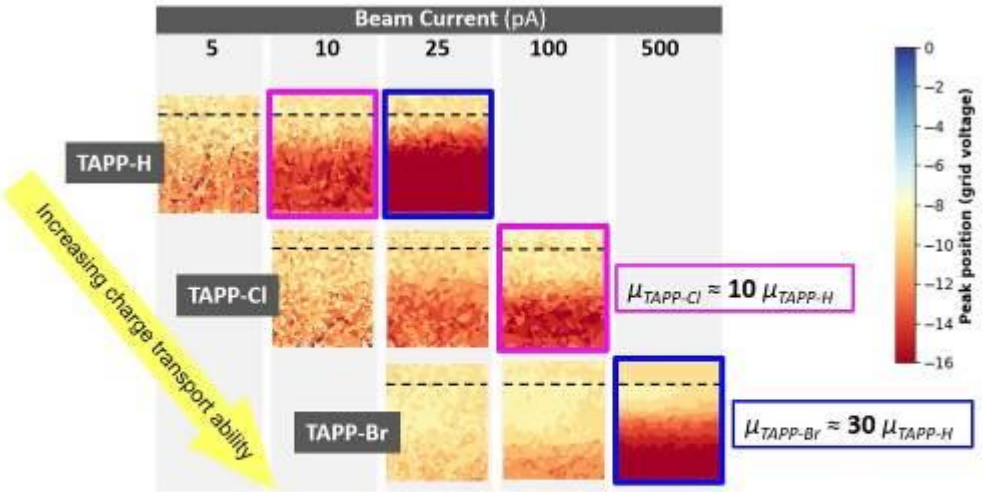

Figure 2. Lateral electron mobility comparison among three semiconducting small molecules TAPP-H, TAPP-Cl and TAPP-Br (structral analogs from tetraazaperopyrene, abbreviated as TAPP), obtained from polycrystalline thin-films. Molecular structrues and thin-film preparation see ref. [2].

MS1.009

Hydrogen uptake and phase change in Pd nanoparticles at nanometer scale with *in-situ* TEM

S. Korneychuk[1], S. Wagner[1], G. Melinte[2], R. Darius[3], P. Vana[3], A. Pundt[1]

[1]Karlsruher Institut of Technologie (KIT), IAM-WK, Karlsruhe, Germany
[2]Karlsruher Institut of Technologie (KIT), INT, Karlsruhe, Germany
[3]Georg-August-University Göttingen, Institute of Physical Chemistry, Göttingen, Germany

Introduction

Palladium-based nanomaterials play an important role in hydrogen technology. Unique properties of Pd, such as high affinity to hydrogen, good solubility of up to H/Pd = 1 atomic ratio and fast hydrogen absorption and desorption at room temperature are very attractive for various applications. Besides catalysis, Pd nanoparticles can assist in hydrogen delivery into other materials for hydrogen storage. Pd-based materials are also used as hydrogen purification membranes and hydrogen detectors.

Objectives

The hydrogenation and dehydrogenation process of Pd nanoparticles is hence of high interest in the applications mentioned above. Nanoscale systems reveal significant thermodynamic deviations from the bulk due to higher surface to volume ratio, the absence of grain boundaries, and different behavior of defects. In this work we investigate the behavior of Pd nanoparticles and the formation of PdHx in real time with *in-situ* gas TEM at room temperatures and elevated temperatures which are required by many applications.

Materials & methods

The experiment was carried out at 80 kV on the ThermoFisher Scientific Themis Z equipped with Gatan GIF Continuum. *In-situ* hydrogen loading and unloading of Pd nanoparticles was accomplished with the gas system from Protochips. The sample was tightly sealed between two chips which both have electron transparent SiN windows, and analyzed at pressures of up to half atmosphere and temperatures of up to 200°C.

Results and Conclusions

We can observe the local phase change at different temperatures and pressures by measuring the position of the Pd bulk plasmon shift in low loss EELS [1]. With this technique we can study the direction of hydrogenation and dehydrogenation, hysteresis, size and shape related effects of the nanoparticles at various temperatures and pressures. In this work we also discuss the distinction of the quasi-planar surface plasmon modes in Pd nanoparticles from the PdHx signal.

Fig.1. EELS mapping of the Pd NPs at 140 °C and 13 kPa H2 showing the separation of Pd-H phases: solid solution (blue) and palladium hydride (orange).

[1] A. Baldi, et al, Nature Materials, 2014, DOI: 10.1038/NMAT4086

Fig. 1

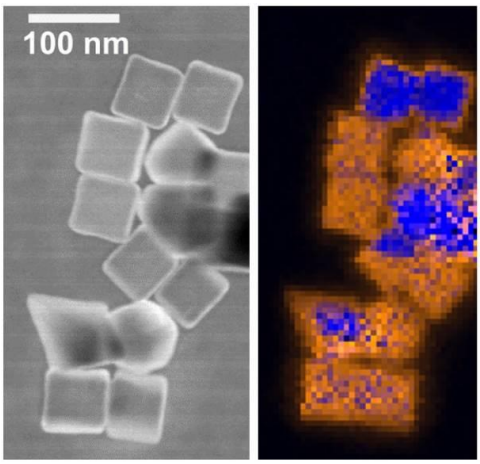

MS1.010

Structural evolution of a Cu/ZnO/Al_2O_3 catalysts revealed by operando TEM

M. Boniface[1], R. Schlögl[1,2], T. Lunkenbein[1]

[1]Fritz-Haber Institut, AC, Berlin, Germany
[2]Max-Planck-Institute for Chemical Energy Conversion, Department of Heterogeneous Reactions, Mülheim an der Ruhr, Germany

Introduction:

Cu–ZnO/Al_2O_3 catalysts have been used industrially since the mid-1960s for both the water-gas shift (WGS) reaction and methanol synthesis. Methanol produced from CO_2 and H_2 is believed to play a key role as an energy storage molecule [1]. The catalyst is activated by reduction *in situ*, which promotes the formation of a partially reduced ZnO_x overlayer over Cu NPs through the strong metal-support interaction (SMSI). The SMSI has been observed in the spent catalyst after reaction [2], but has so far scarcely been investigated *operando*.

Materials and Methods:

The catalyst (Cu–ZnO/Al_2O_3) was synthesized by calcination of a zincian malachite precursor with a Cu:Zn ratio of 70:30 and 3 mol % Al, following a protocol published previously [3]. A sample was mounted in a DENS Climate environmental TEM holder, which was connected to our homebuilt gas feed setup.

Selected area electron diffraction (SAED) temperature series were corrected for astigmatism and centered with sub-pixel accuracy[4], enabling us to track small lattice parameter changes and phase fractions from Rietveld refinement with the fast time resolution of SAED.

Results:

The calcined sample is first activated (pH_2 = 79 mbar, 10% H2, 4K.min-1) during a 2-step process involving the segregation of CuO NPs from a (Cu,Zn) carbonate phase from 110C to 200C, then reduction and sintering of these NPs from Cu^{II} to Cu^0. A Cu^I intermediate is detected as well between 200C and 250C, with all 3 oxidation states co-existing at these temperatures until only Cu^0 remains after 2h at 250C.

The SMSI ZnO_x overlayer only partially covers few particles after the reduction is complete after 2h at 250C. Cooling the sample to 50C leads to a much fuller overlayer on a much larger NPs population, indicating that the SMSI overlayer is not stable at high temperatures and forms reversibly. This is compounded by results in MeOH synthesis conditions (H_2:CO_2:He = 3:1:0.5) and reverse water gas shift conditions (H2:CO2:He = 1:1:0.5), shedding tremendous insight into how Cu wetting by ZnO_x is mediated by temperature as well as H_2 and CO_2 partial pressures (Figure 1.a) through a delicate balance of Cu-Zn alloy formation and reoxidation on Cu NPs surfaces [5]. Increasing the temperature to 400C showed a sudden increase of the Cu lattice parameter, which then leveled off to the expected Cu lattice parameter over 30 minutes, demonstrating the potential of *operando* SAED to track alloying and reoxidation in real time and revealing the time constant of these phenomena (Figure 1.b).

Figure 1. a) Evolution of the catalyst throughout activation and operating conditions. Cooling after reduction leads to a full ZnO_x coverage on the Cu NP. This overlayer is thicker and more stable as the CO_2 fraction increases disappears reversibly as the temperature increases. **b)** Evolution of the Cu lattice parameter in RWGS conditions. The increase and decrease corresponds to Cu-Zn and re-oxidation.

References

1. A. Olah, A. Goeppert, G. K. Surya Prakash, in "Beyond Oil and Gas: The Methanol Economy", Wiley-VCH, Weinheim, 2006.
2. Lunkenbein, T., Schumann, J. et al., *Angewandte Chemie*54, 15 (2015).
3. Schumann, J., Lunkenbein, T. et al. *ChemCatChem*6, 10 (2014).
4. Frisch, B., Wu, M., *Ultramicroscopy* 235 (2022)
5. Amann, P., Klötzer, B. et al., *Science* 376, 6593 (2022).

Fig. 1

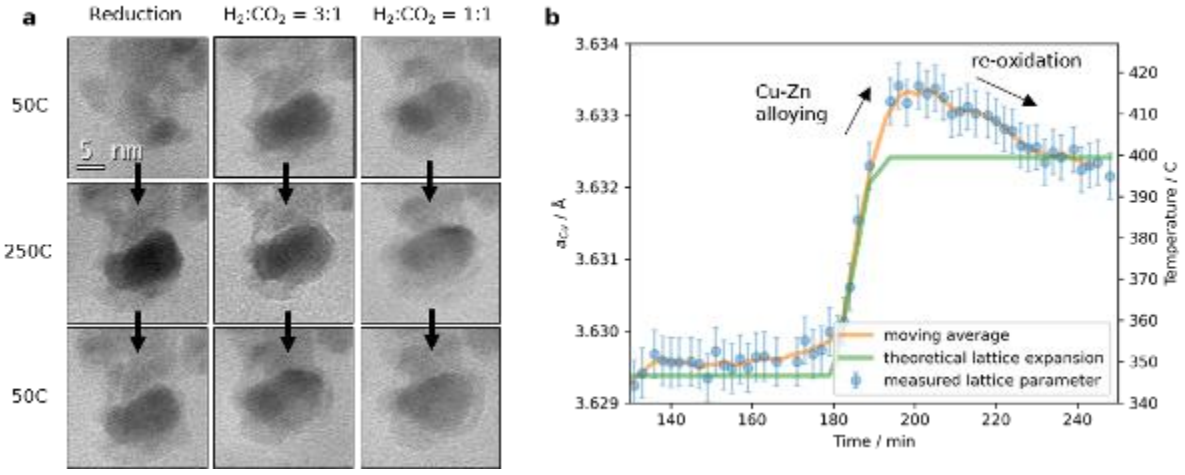
a
Reduction
H2:CO2 = 3:1
H2:CO2 = 1:1
50C
250C
50C
5 nm
b
Cu-Zn alloying
re-oxidation
moving average
theoretical lattice expansion
measured lattice parameter
Time / min
Temperature / C

MS1.P001

On the structure of small oxide-supported metal particles

H. Eliasson[1], R. Erni[1], W. Dachraoui[1]

[1]Empa, 299, Dübendorf, Switzerland

To design stable, active and selective catalyst materials, an understanding of a system's active sites is necessary. Today, many catalysts are based on materials decorated with either single metal atoms, clusters or nanoparticles, where the metal species act as reaction hubs in the catalytic process. It is known that the catalytic activity of particle based catalysts often correlates with the particle size, structure and morphology [1]. Despite this, there are not many experimental studies showing atomically resolved structural information about supported nanoparticles, and those that do are usually focused on larger particles [2, 3]. This study aims at revealing differences in the particle-support interface and particle structure of small oxide supported metal particles with diameters in the range of 1-3 nm.

Samples were prepared by dropping a dispersion of methanol with grinded catalyst powder onto regular TEM grids. Metal species were then deposited directly onto the grid by sputtering giving rise to a natural particle growth process by diffusion on the support surface. The samples are imaged with sub-Ångström spatial resolution in a probe-corrected FEI Titan Themis S/TEM microscope operated at 300 kV. High-angle annular dark-field (HAADF) STEM was chosen as imaging mode because of the incoherent nature of the signal. The inherent Z-contrast of HAADF-STEM along with the lack of Bragg diffraction contrast makes for easy image interpretation, especially useful for smaller particles with larger atomic number (Z) than the supporting material. Images were formed by aligning and summing a series of fast scans to limit the electron dose and the influence of sample drift.

We observe changes in particle shape from hemispherical to more facetted truncated octahedral-like shapes with increasing particle size, and also report the preferential orientation relations between particle and support. For particles with a favorable orientation in regards to visibility of atomic columns, the analysis was taken further and displacement and strain maps were calculated.

These results lay a foundation for further studies both in situ and ex situ. For example, to investigate electronic states in particles and interfaces by electron energy loss spectroscopy (EELS), but also to study particle behavior in situ in different gas environments and at different temperatures.

Fig. 1

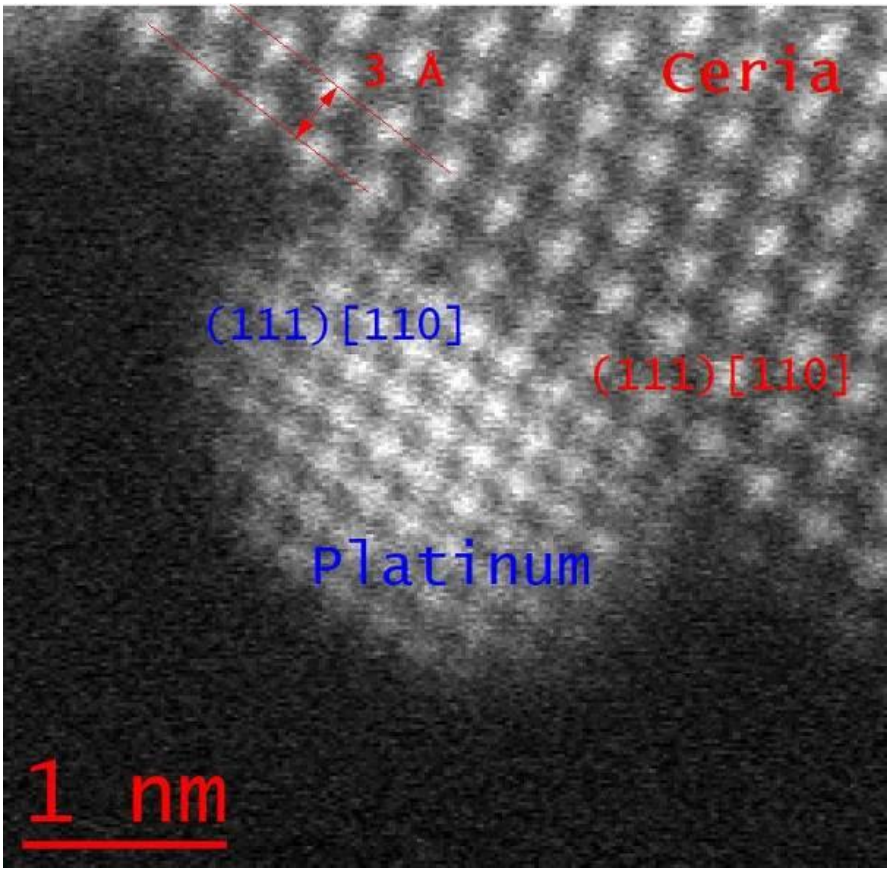

Fig. 2

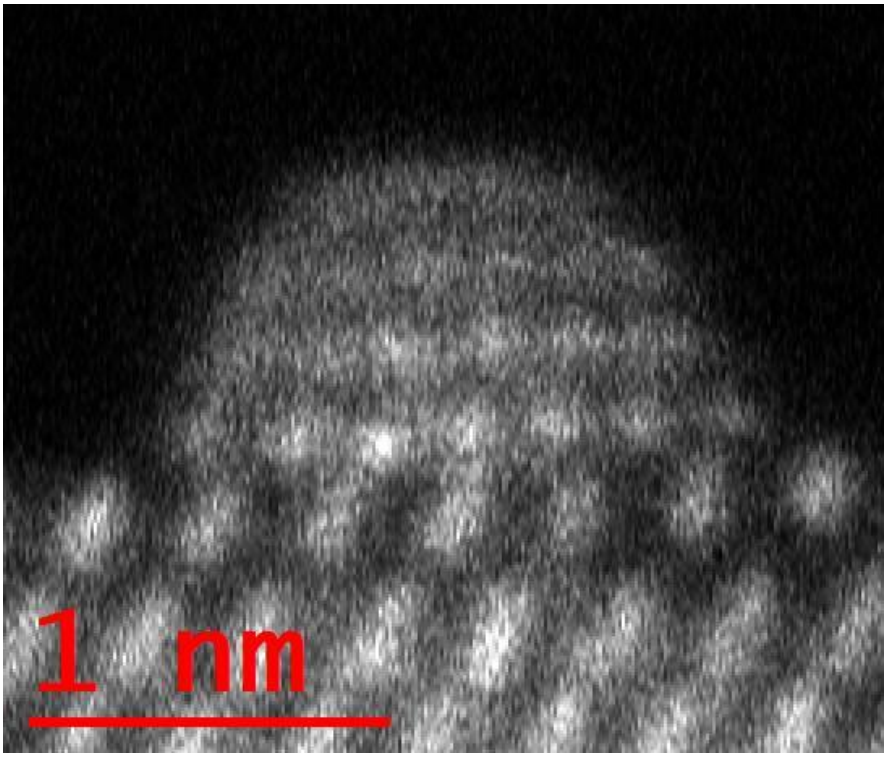

Fig. 3

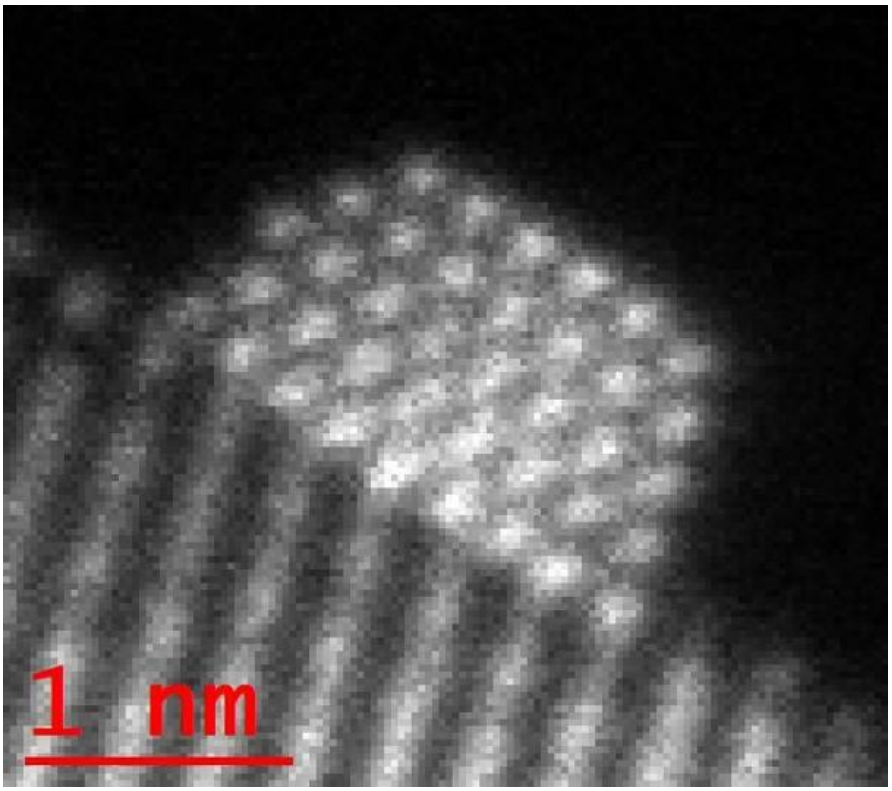

MS1.P002

Molecular mechanism of copper-based catalytic reaction of water oxidation: *in-situ* electrochemical liquid phase transmission electron microscopy study

A. Sologubenko[1], E. Balaghi[2], G. Patzke[3], M. Najafpour[4]

[1]ScopeM ETH Zurich, Zurich, Switzerland
[2]University of Freiburg, Freiburg Center for Interactive Materials and Bioinspired Technologies, Freiburg, Germany
[3]University of Zurich, Chemistry, Zurich, Switzerland
[4]Institute for Advanced Studies in Basic Sciences, Zanjan, Iran

The understanding of molecular mechanisms of water oxidation reactions is very important for development of renewable energy storage solutions. Inspired by a naturally occuring water splitting catalyst, the Mn4CaO5 particles [1], many first-row transition metal compounds are being synthesized and studied as catalysts in oxygen-evolution reactions (OER) at various conditions [2]. Copper(II) complexes are considered to be very promising, with the [Cu(TMC) (H2O)](NO3)2 (TMC = 1,4,8,11- tetramethyl-1,4,8,11-tetraazacyclotetradecane) compound (further, the **Cu(II)-complex**) reported among the most efficient copper-based catalyst for electrocatalytic OER in neutral aqueous solutions [3, 4, 5]. However, the control over the stability and catalytic activity of the compound is handicapped by a complicated reaction path, and general lack of understanding of its molecular mechanism [5].

In our study, we followed the OER in the presence of the **Cu(II)-complex** by employing the most advanced analytical and computational techniques, including *in-situ* vis-spectroelectrochemistry, *in-situ* electrochemical liquid-phase transmission electron microscopy (EC-LPTEM) and extended X-ray absorption fine structure (EXAFS) studies.

Our *in-situ* EC-LPTEM and post-reaction analytical and electron diffraction studies revealed that already in the first anodic scan, small CuO nanoparticles formed at the surface of working electrode at a significantly lower potential than required for OER (Figure). This indicates that these can be the true catalysts rather than the **Cu(II)-complex**. Further, during the OER, the small CuO particles dissolved to form larger ones. Moreover, during cyclic voltammetry (CV) runs, we observed the formation of a very thin, nearly continuous Cu-oxide film at the working electrode of the reactor cell of the TEM holder. These data accord very well with the electrochemical impedance spectroscopy (EIS) curves acquired in a separate experiment.

We show that even at the very beginning of the OER, the compound can undergo transformation. We also show that the actual OER mechanism in the presence of the **Cu(II)-complex** is more complicated than a mere molecular mechanism. All these evidences that the metal catalyst cannot be presumed to stay intact during the OER, unless the reaction path is known and fully controlled. In-depth studies of the particular reaction path using the advanced morphological and analytical methods are therefore crucially important for the catalyst design.

Figure.

(a) Degradation of Cu-complexes during anodic scan of cyclic voltammetry (Ag/AgCl reference electrode). TEM micrographs presents the snap-shots of the early stages of the nucleation of the copper oxide particles (bright yellow) at the surface of the working electrode (blue). The phase state change of the material at the electrolyte is verified by electron diffraction pattern (eDP) analyses: (b) the eDP of the Pt-working electrode. (c) Pt-electrode & CuO-phase particles. (d, e) The EDS SI elemental content analyses by of the electrode adjacent region (frame in d). The EDS SI confirms the formation of CuO phase in the electrolyte. (f) Schematic of the CuO unit cell.

[1] Y. Umena, K. Kawakami, J. R. Shen, N.Kamiya, Nature, **473** (2011).

[2] M. M. Najafpour et al., Chem. Rev. **116** (2016).

[3] X. Liu et al., Electrochem. Commun. **46** (2014).

[4] M. M. Najafpour, S. Mehrabani, Y. Mousazade, M. Holynska, Dalton Trans. **47** (2018).

[5] F. Yu et al., Chem. Commun. **52** (2016).

Fig. 1

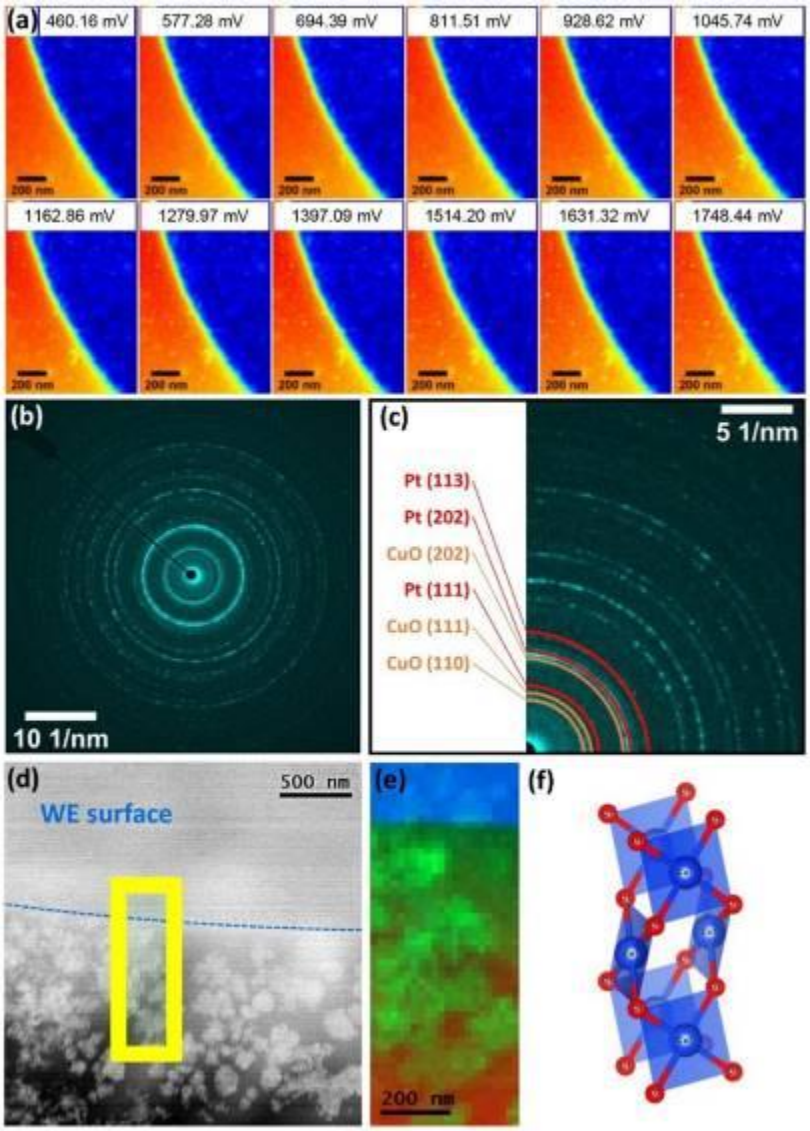
(a)
460.16 mV
577.28 mV
694.39 mV
811.51 mV
928.62 mV
1045.74 mV
1162.86 mV
1279.97 mV
1397.09 mV
1514.20 mV
1631.32 mV
1748.44 mV
200 nm
(b)
10 1/nm
(c)
5 1/nm
Pt (113)
Pt (202)
CuO (202)
Pt (111)
CuO (111)
CuO (110)
(d)
500 nm
WE surface
(e)
200 nm
(f)

MS1.P003

3D-microstructure of spindle-like $Li_1Ti_2(PO_4)_3$ particles revealed by electron microscopy

R. Schierholz[1], K. Dzieciol[1], S. Yu[1], Q. Zhang[1], H. Tempel[1], H. Kungl[1], R. Eichel[1]

[1]Forschungszentrum Jülich GmbH, Institut für Energie ud Klimaforschung Grundlagen der Elektriochemie (IEK-9), Jülich, Germany

1. Introduction

Pure $Li_1Ti_2(PO_4)_3$ (LTP) is an anode material with NASICON structure and a lithiation potential of 2.31 V.[1] This potential fits the electrochemical stability window of the promising isostructural solid state electrolyte $Li_{1+x}Al_xTi_{2-x}(PO_4)_3$ (LATP), which is obtained by trivalent substitution and application in an all-phosphate solid state battery has been demonstrated.[2] Comparison of different synthesis methods revealed an enhanced cycling performance of solvothermally prepared LTP with spindle-like particles of 2 – 5 µm size compared to the same material prepared by sol-gel based Pecchini method.[3]

2. Objectives

Scanning electron microscopy (SEM) suggests that spindle-like particles are formed by sub particles of about 300 nm size, but as only the surface is accessible by SEM the origin of the enhanced performance remains unclear. With focused ion beam (FIB) and (Scanning) Transmission Electron Microscopy the inner volume can be characterized to give a complete picture of the particles crystal- and micro-structure as well as its local chemical composition.

3. Materials and methods

The particles were synthesized by solvothermal reaction, consecutively vacuum dried and annealed at 800 °C.[3] These particles were then dispersed in ethanol and a droplet was put on a silicon wafer for FIB-SEM experiments. FIB tomography and TEM-lamella preparation were conducted with a Helios Nanolab 460F1, FEI, Netherlands.[4] TEM and STEM analysis was conducted in a Tecnai F20 and a Titan G2 Crewley.[5]

4. Results

SEM imaging shows the morphology, with sub particles forming a dumbbell like particle, and already provides hints for the presence of two secondary phases, on nanoparticles, the other a bulky phase with different surface morphology. The presence oof different phases is approved by chemical contrast in BSE-images of cross sections and STEM HAADF imaging. STEM-EDS gives an estimate of the chemical compositions which is completed by STEM-EELS for the detection of Lithium. HRTEM and HRSTEM could then identify the crystallographic structures of these secondary phases to be TiO_2 anatase for the nanoparticles and $LiTiPO_5$ (*P*nma ICSD #153522) for the bulky secondary phase. FIB-tomography revealed that the majority of the TiO_2 nanoparticles are interconnected.

5. Conclusions

The complex microstructure of the spindle-like LTP particles can only be solved by a combination of FIB-tomography and STEM-analysis. The three-dimensional network of TiO_2-nanoparticles seem to improve the cycling behavior, as it may enhance the diffusion and can also contribute to capacity and is no dead material.[6]

[1] S. Yu *et al.*, *ACS Appl. Mater. Interfaces* **(2018)** Vol. 10, No. 26 p. 22264-22277, https://doi.org/10.1021/acsami.8b05902

[2] H. Aono *et al.*, *Journal of The Electrochemical Society* , (1990) 137, 4, p. 1023-1027 https://doi.org/10.1149/1.2086597

[3] S. Yu *et al.*, *ChemElectroChem* **(2016)** Vol. 3, No. 7, p. 1157-1169 https://doi.org/10.1002/celc.201600125

[4] M. Kruth *et al.*, J*ournal of large-scale research facilities JLSRF* **(2016)** 2, A59 https://doi.org/10.17815/jlsrf-2-105

[5] A. Kovács *et al.*, J*ournal of large-scale research facilities JLSRF* **(2016)** 2, A43 https://doi.org/10.17815/jlsrf-2-68

[6] M. Madian *et al.*, *Batteries* **(2018)** 4, 7, https://doi.org/10.3390/batteries4010007

Fig. 1

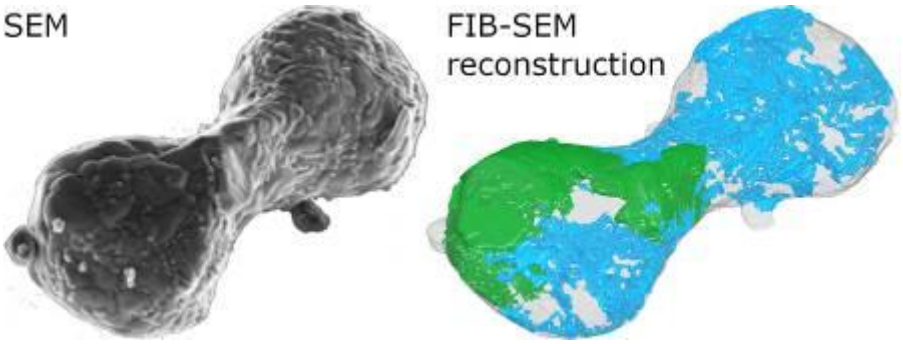

MS1.P004

Probing the microscopic properties of Cu(In,Ga)Se_2 absorbers in thin film solar cells via correlative scanning electron microscopy techniques

S. Thomas[1], W. Witte[2], D. Hariskos[2], S. Paetel[2], C. Y. Song[3], H. Kempa[3], N. El-Ganainy[4], D. Abou-Ras[5]

[1]Helmholtz Zentrum Berlin, Berlin, Germany
[2]Zentrum für Sonnenenergie- und Wasserstoff-Forschung Baden-Württemberg (ZSW), Stuttgart, Germany
[3]Martin-Luther-Universität Halle-Wittenberg, Institut für Physik, Fachgruppe Photovoltaik, Halle (Saale), Germany
[4]Competence Centre Photovoltaics Berlin (PVcomB) / Helmholtz Zentrum Berlin für Materialien und Energie (HZB), Berlin, Germany
[5]Helmholtz-Zentrum Berlin, Abteilung Struktur und Dynamik von Energiematerialien, Berlin, Germany

There are several challenges in the field of solar-cell research which cannot be solved without an in-depth investigation of the materials and devices. In the case of Cu(In,Ga)Se_2 (CIGSe) thin-film solar cells, the band-gap energy of the polycrystalline photoabsorber can be tuned by varying the [Ga]/([Ga]+[In]) (GGI) ratio. However, there are several obstacles that prevent from achieving the desired device efficiency[1]. We aim to assess the issues that deteriorate the device performance on the sub-micrometer scale. In the present work, we employ several scanning electron microscopy (SEM) techniques to examine the microscopic properties of the CIGSe photoabsorber layer of the solar cell [2]. Electron backscatter diffraction (EBSD) is used for the crystallographic characterization to determine the average grain size (d_{grain}) and identify features such as twin grain boundaries (GBs), surface texture and preferred crystallographic orientation of the grains [3]. The local radiative recombination activities are characterized via cathodoluminescence (CL) spectroscopy. We extract information of the charge carrier recombination velocity (S_{GB}) at the grain boundaries from hyperspectral CL images in combination with time-resolved photoluminescence spectroscopy. Energy-dispersive X-ray spectroscopy (EDS) is applied to determine the distribution pattern of the elements within the absorber depth. The presence of secondary phases can also be detected via EDS mapping.

As shown in the Figure below, we apply these scanning electron microscopy techniques in a correlative manner on identical sample positions. Thus, we are able to detect changes in the microscopic properties when varying the GGI ratio in the CIGSe absorber layer and to investigate the microstructure-property relationships in several CIGSe thin-film solar cells. Indeed, it is found that the changes in the microscopic properties of the CIGSe photoabsorber have a substantial effect on the macroscopic device performance.

References

[1] Stanbery BJ, Abou-ras D, Yamada A, Mansfield L. CIGS Photovoltaics : Reviewing a New Paradigm, *Phys. D: Appl. Phys*. **55** (2022) 173001.

[2] Abou-Ras D, Kirchartz T, Rau U. Advanced Characterization Techniques for Thin Film Solar Cells. Weinheim, Germany: Wiley; 2016.

[3] Abou-Ras D, Kavalakkatt J, Nichterwitz M, Schäfer N, Harndt S, Wilkinson AJ, et al. Electron backscatter diffraction: An important tool for analyses of structure-property relationships in thin-film solar cells. *Jom*. 2013;**65**(9):1222–8.

Figure 1 : A) SEM cross section of the CIGSe absorber layer. B) EBSD image showing the local grain orientation and grain sizes. C) EDS map of the Ga-L series D) CL emission energy distribution, $\sigma_{lat.CL}$ and $\sigma_{ver.CL}$ are the fluctuations in the CL emission energy in the lateral and vertical directions.

Fig. 1

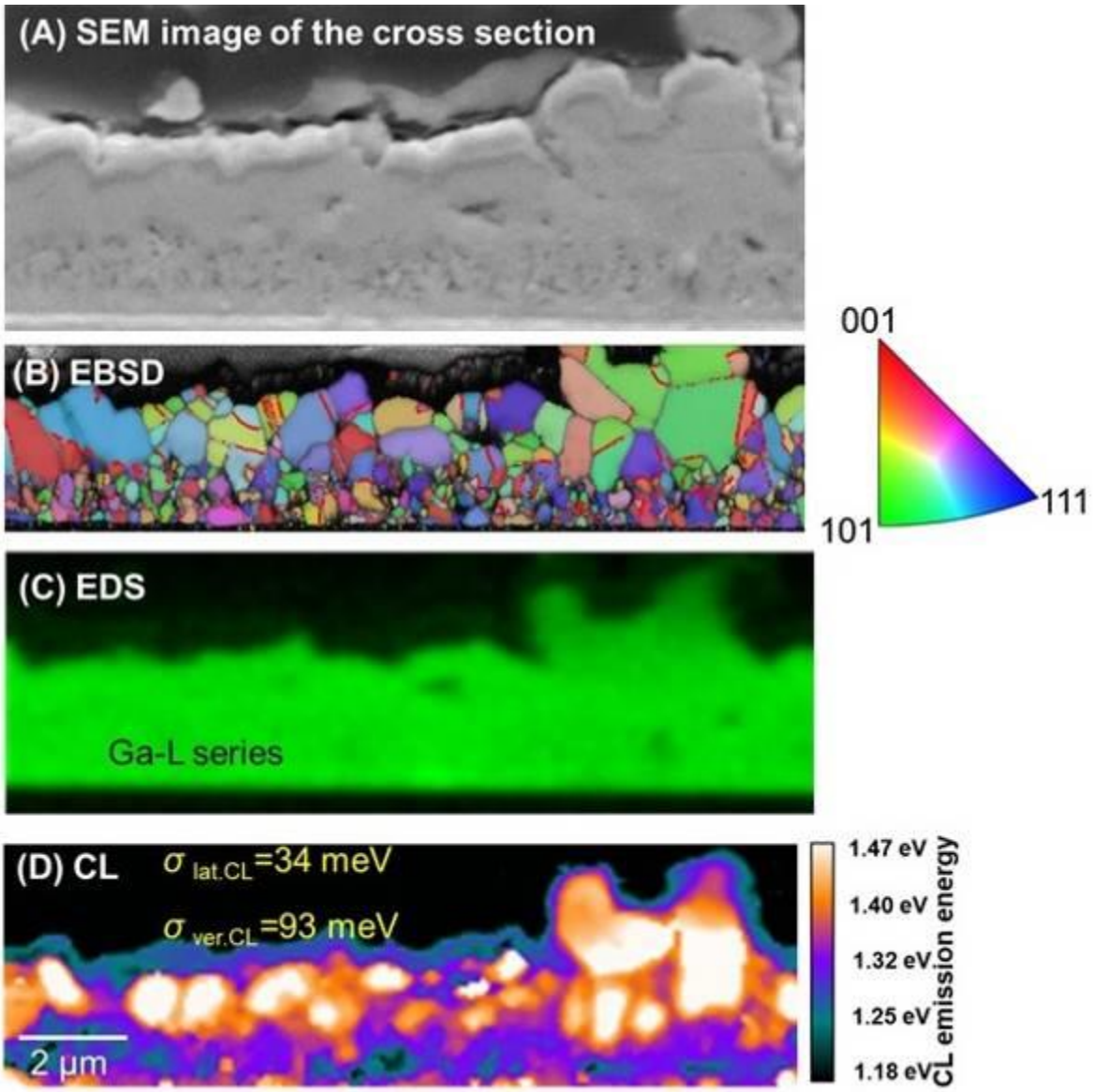
(A) SEM image of the cross section
(B) EBSD
001
101
111
(C) EDS
Ga-L series
(D) CL
σ lat.CL=34 meV
σ ver.CL=93 meV
2 μm
1.47 eV
1.40 eV
1.32 eV
1.25 eV
1.18 eV
CL emission energy

MS1.P005

Probing sodium storage mechanism in hollow carbon nanospheres anode using liquid phase transmission electron microscopy

J. Hou[1], N. V. Tarakina[1], M. Antonietti[1]

[1]Max Planck Institute of Colloids and Interfaces, Colloid Chemistry Department, Potsdam, Germany

Carbon-based electrode materials are considered promising anode materials for sodium-ion batteries. Understanding the Na transport and storage mechanism is crucial for developing more reliable anode materials. However, it has remained elusive. [1] The combination of an enclosed chamber with other stimuli in TEM brings advances in in-situ/operando detecting of dynamic phenomena in the liquid phase with high temporal and spatial resolution without risking sample modification in vacuum. Here, we synthesized hollow carbon spheres (HCSs) with tailored composition and desirable morphology for probing the Na-storage behavior in carbon-based electrode materials by means of in-situ TEM. [2]

We tracked the absorption of Na ions at the slope region of discharging nitrogen-doped porous HCSs (NPHCSs), which is followed by Na deposition at the potential plateau under the overpotential condition, by step-wise SEM-EDX experiments. NPHCSs surface remains partially covered after Na stripping (Fig. 1). We monitored the dynamic procedure of SEI formation and Na deposition within and around the NPHCSs by running micro batteries liquid phase TEM experiments (Fig. 2a-c). We observed the carbon shell expansion as a result of Na filling, SEI layer assisted NPHCSs binding, and partially reversible Na deposition (Fig. 2d-f). Na filling into carbon shells was further confirmed by energy-filtered TEM. Moreover, the electronic and ionic distribution after sodiation suggests the existence of Na0 and Na+1 within NPHCSs (Fig. 2g-h).

At the beginning of sodiation, Na absorbs on the surface of the nanospheres, accompanied by SEI formation essentially filling gaps between nanospheres within the NPHCS-based electrode. Consequently, this facilitates the Na ions' transport into the hollow spheres or through the tunnels between them until the current collector is reached. Although the curvature-induced electron density gradient in the hollow spheres can partially drive Na deposition inside the spheres at a low cycling rate, most Na deposition takes place underneath the electrode layer. Both Na storage paths contribute to improving the safety of sodium-ion batteries by preventing dendrite growth on the anode.

We gratefully acknowledge financial support of the Max Planck Society and European Research Council (ERC).

Reference:

[1] C. Vaalma, *et al. Nat. Rev. Mater. 2018 34* **2018**, *3*, 1.

[2] Z. L. Wang, *et al. J. Phys. Chem. Solids* **2000**, *61*, 1025.

Fig. 1: SEM images of NHPCSs at different stages of sodiation/disodiation and the schematic illustration of sodiation procedure with Na content detected by EDX.

Fig. 2: (a-c) In-situ STEM image of partially sodiated NPHCSs during cycling. Na is highlighted in yellow. Hollow arrows in (a) indicate the empty spheres while solid arrows in (b) indicate the Na-filled spheres. (d) STEM-HAADF image of pristine NPHCSs. STEM-BF(e) and HAADF(f) image of cycled NPHCSs. (g) Low-loss EELS comparison of pristine and cycled particles. (h) EFTEM comparison of pristine (black) and cycled particles (red). Electron density and sodium mapping are corresponding to the selected energy range between 4-7eV and 30-33 eV respectively, as highlighted in yellow in (g).

Fig. 1

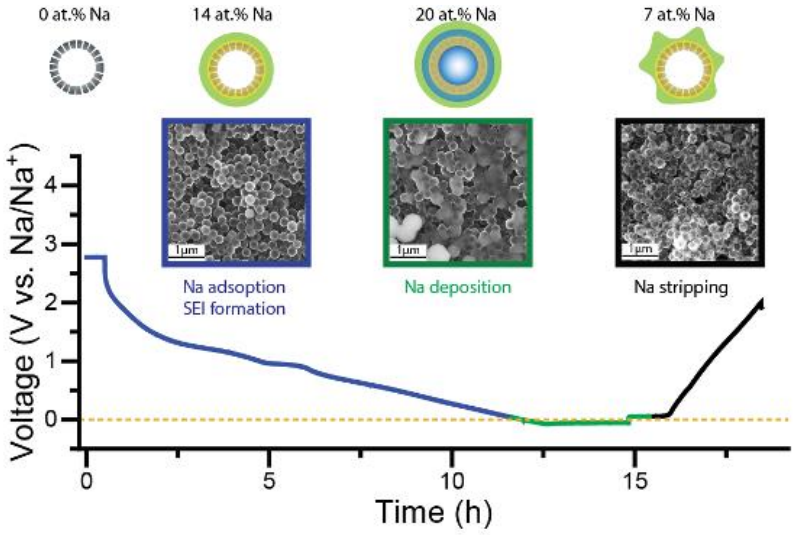
0 at.% Na
14 at.% Na
20 at.% Na
7 at.% Na
Voltage (V vs. Na/Na+)
Time (h)
Na adsoption
SEI formation
Na deposition
Na stripping

Fig. 2

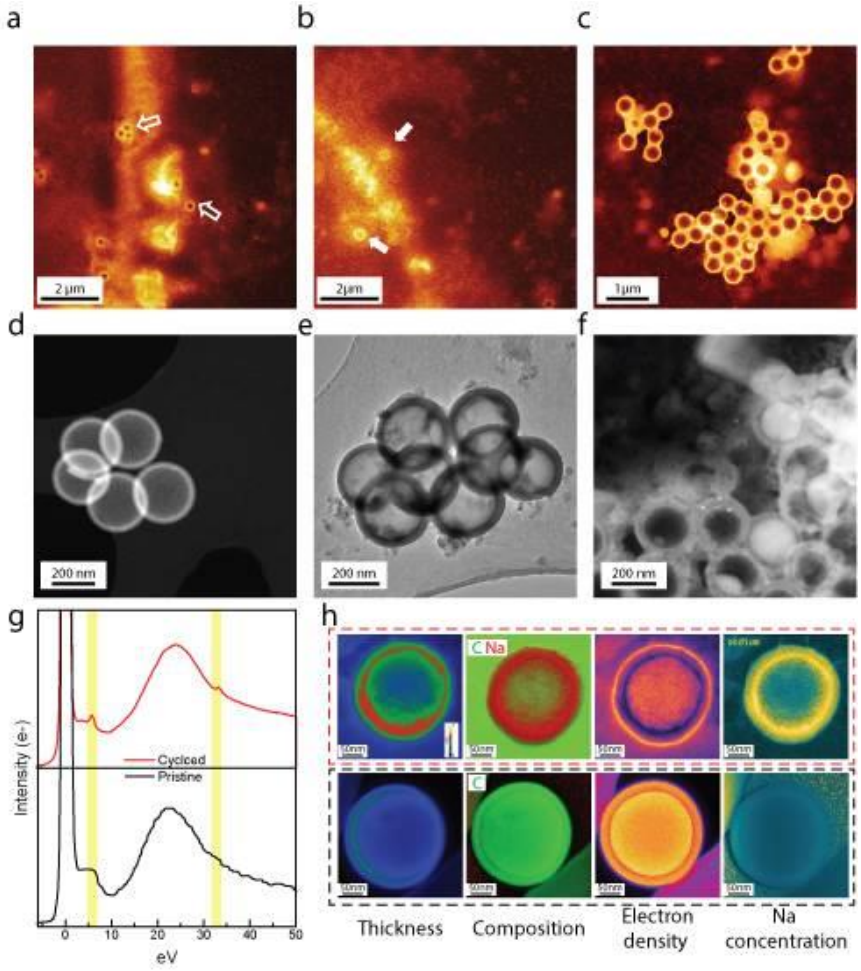
a
b
c
d
e
f
g
h
Intensity (e-)
Cycled
Pristine
eV
Thickness
Composition
Electron density
Na concentration

MS1.P006

In-situ TEM studies of phase change thermoelectric MgAgPtSb

M. O. Cichocka[1], R. He[1], D. Pohl[2], B. Rellinghaus[2], K. Nielsch[1,3], N. Perez Rodriguez[1]

[1]Leibniz IFW Dresden, Dresden, Germany
[2]Dresden Center for Nanoanalysis (DCN), Technische Universität Dresden, Dresden, Germany
[3]Institute of Material Science, Technische Universität Dresden, Dresden, Germany

The structure of thermoelectric materials largely determines their characteristics. Hence, a better understanding of the details of the structural transformation conditions can open doors for new applications. Therefore, a microscopic comprehension of the impact on the nanoscale structure dynamics is crucial, especially with the progress of intensified miniaturization. In this study, the effect of heat treatment on the structure of phase change MgAgPtSb is investigated [1,2]. The material was heated in-situ in the transmission electron microscope (TEM). Using a combination of scanning transmission electron microscopy (STEM) and energy dispersive spectroscopy (EDS) we unveil the structural and chemical state of the thermoelectric. Thus, we can correlate real-time changes during the heating process with the presence of structural distortions, impurities and compositional transformations. Additionally, the crystal structure of MgAgPtSb thermoelectric material undergoes a phase transformation when the temperature changes. The tetragonal I-centered phase transforms to the P-centered tetragonal crystal system and at approximately 400°C to a cubic Heussler structure [3]. In this work, we study the changes taking place during the phase transitions as it usually leads to increased defects and second phase precipitation [4].

Keywords: thermoelectrics, in-situ transmission electron microscopy, phase transformation

References

[1] *Chem. Mater.* **2015**, 27, 909-913.

[2] *Adv. Funct. Mater.* **2017**, 27, 1604145.

[3] *Phys. Rev. B* **2012**, 85, 144120.

[4] *Chem. Mater.* **2017**, 29, 6378-6388.

MS1.P007

Correlative microscopic analyses of PbI_2 precipitates on the surface of triple-halide perovskite films

D. R. Wargulski[1], K. Xu[1], S. Albrecht[1], H. Hempel[1], D. Abou-Ras[2]

[1]Helmholtz-Zentrum Berlin, Berlin, Germany
[2]Helmholtz-Zentrum Berlin, Abteilung Struktur und Dynamik von Energiematerialien, Berlin, Germany

Introduction

Triple-halide perovskites[1] form a promising but complex material system that offers the possibility to vary band-gap energies via compositional changes for tandem solar cell applications. Perovskite-silicon tandem solar cells already exceeded the 31% of efficiency[2] and represent today's most promising tandem solar cell technology. Main obstacles to bring this technology to the market are the upscaling to industrial cell sizes and through-puts.

Objectives

The aim of the present study is to investigate triple-halide perovskite absorber layers for solar cells by correlative electron microscopy. These layers were deposited by slot-die coating plus N2 gas quenching, a deposition technique suitable for large-area and high-throughput production. Optimal process parameters for this technique, such as substrate temperatures, have not yet been well investigated. Therefore, we analyzed absorber layers produced at various substrate temperatures by several electron microscopy methods and correlated these results with photovoltaic parameters of cells made of absorbers with identical composition.

Materials & Methods

In the present study, triple-halide perovskite thin films with the composition $(Cs_{0.22}FA_{0.78})Pb(I_{0.85}Br_{0.15})_3$ + 5 mol% $MAPbCl_3$ were analyzed. These thin films were prepared by means of slot-die coating and subsequently annealed at temperatures of 125 °C, 150 °C, 160 °C and 170 °C. We conducted secondary electron (SE) imaging, electron backscatter diffractometry (EBSD), energy-dispersive X-ray spectroscopy (EDX), and cathodoluminescence (CL) in scanning electron microscopy on these thin films and determined solar cell parameters (short-circuit current J_{SC}, open-circuit voltage V_{OC}, fill factor *FF* and photo-conversion efficiency *PCE*) under one sun illumination in a solar simulator.

Results

The SE imaging indicated and EBSD measurements confirmed an increased average grain size with increasing annealing temperature, as it had been expected. By means of EBSD, EDX and CL, PbI_2 precipitates were detected and their area fraction on the perovskite-type thin films were quantified (Fig. 1). When varying the annealing temperature from 125 to 170 °C the efficiency maximum of almost 20% was found at 125 °C, and the efficiency decreases with increasing temperature (mainly owing to decreasing V_{oc} and *FF* values). The area fraction of PbI_2 increases from 5% to more than 20% within the studied temperature range, which enhances nonradiative recombination (thus, decreasing the V_{oc}) and increases significantly the series resistance of the solar cells (thus, decreasing the *FF*).

Figure 1: Triple-halide perovskite films analyzed by SE imaging, EBSD, CL and EDX. Green colors correspond to the triple-halide perovskite phase, and blue to PbI_2.

Conclusion

We found an increasing amount of PbI_2 precipitates with increasing annealing temperatures on the surface of triple-halide perovskite films by means of various electron microscopy techniques. It was possible to correlate the presence of the PbI_2 phase on the triple-halide perovskite thin-film surface to deteriorated solar cell performances. For the further improvement of these solar cells, it is mandatory to reduce the area fraction of the PbI_2 precipitates to a minimum.

References

[1]Xu, J., et al. Triple-halide wide-band gap perovskites with suppressed phase segregation for efficient tandems. *Science* **367**, 1097–1104 (2020).

[2]NREL efficiency chart (www.nrel.gov/pv/cell-efficiency.html)

Fig. 1

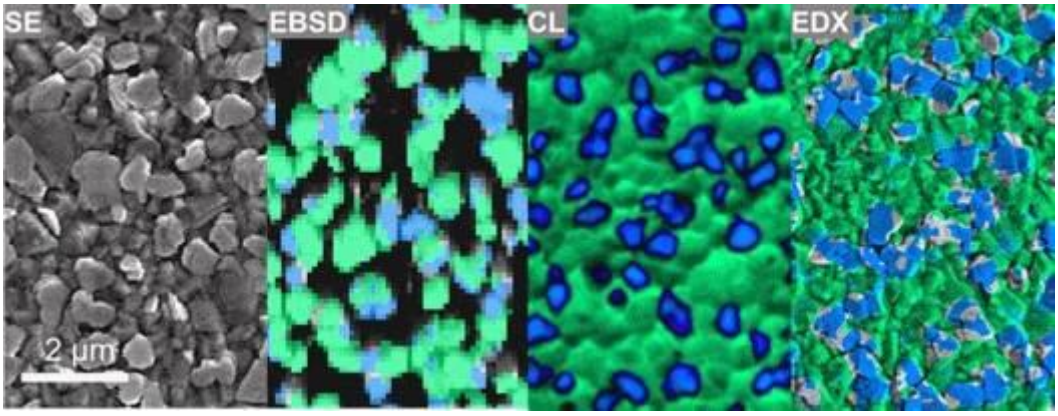

MS1.P008

Microscopic insight into the stability and activity of Pt single atom photocatalysts on TiO2

J. Will[1], N. Denisov[2], S. Qin[2], T. Yokosawa[1], J. Wirth[1], P. Schmuki[2], E. Spiecker[1]

[1]Institute of Micro- and Nanostructure Research (IMN) & Center for Nanoanalysis and Electron Microscopy (CENEM), Materials Science, Erlangen, Germany
[2]Chair for Surface Science and Corrosion, Materials Science, Erlangen, Germany

In this study, we investigate the stability and activity of Pt single atoms (SAs) deposited on TiO2 via a facile dark-deposition approach [1]. We aim to identify stable and active Pt SAs on both anatase nanosheets and ~7 nm thick polycrystalline anatase films sputtered on electron transparent SiO2 TEM grids to get an atomistic understanding on the SA anchoring as well as their stability upon photocatalytic water splitting. To identify stable species, anatase nanosheets where loaded with Pt SAs and further step-by-step leached by cyanide to reduce the SA loading while monitoring the photocatalytic activity as well as the atomistic configuration by aberration corrected high-angle annular dark field scanning transmission microscopy (STEM) [2]. In addition, we exploit the TiO2 model thin films in combination with identical location STEM investigations to visually follow the photoinduced destabilization over 24 h of operation time. Here, a machine learning-based algorithm is used to segment SAs as well as their agglomerates at various regions of interest. Within this approach we get quantitative information about the abundance and arrangement of the SAs as function of photocatalytic operation time.

We show that neither the majority of anchored Pt SAs nor metallic Pt0 species are responsible for the overall observed high photocatalytic activity. In fact, >90% of the deposited Pt can be removed by cyanide leaching without significant loss in photocatalytic activity (Fig. 1). In this way, we could identify an optimized SA loading quantity for anatase nanosheets, which is accompanied by a remarkable turnover frequency of ~4.87 x 105 h-1 for H2 evolution.

Identical location microscopy (see Fig. 2) after five different photocatalytic operation times reveals that the majority of initial deposited Pt is in a SA or multimere state. Within 1 min, ~90% of the SAs and multimeres agglomerate rapidly to 2D rafts. This agglomeration process continues, however, at a much slower speed within the next 24 h. Here, mainly the 2D rafts coarsen to nanoparticles with an average size of ~4 nm, whereas the photocatalytic activity stays unchanged and still 7% of the Pt loading maintains its SA state. In addition, the observed SA agglomeration is heavily influenced by the presence of methanol as a hole scavenger, elucidating the role of charge carriers on the stability of Pt SAs on TiO2. Moreover, identical location microscopy allows to follow various additional phenomena, like dissolution of 2D rafts, as well as morphological changes and ripening of agglomerated Pt species revealing the high dynamics in the system under photocatalytic conditions.

In conclusion, high resolution STEM on nanostructures and thin model systems is an ideal tool for studying Pt SA photocatalysts, their local arrangement as well as stability after different operation times. The correlation with photocatalytic data as well as spectroscopy (e.g. XPS, XAAS) allows to establish structure property relationships further improving the material efficient SA approach for photocatalytic applications.

[1] Cha, G., Mazare, A., Hwang, I., Denisov, N., Will, J., Yokosawa, T., ... & Schmuki, P. (2022). Electrochimica Acta, 412, 140129.

[2] Qin, S., Denisov, N., Will, J., Kolařík, J., Spiecker, E., & Schmuki, P. (2022). Solar RRL, 2101026.

Fig. 1

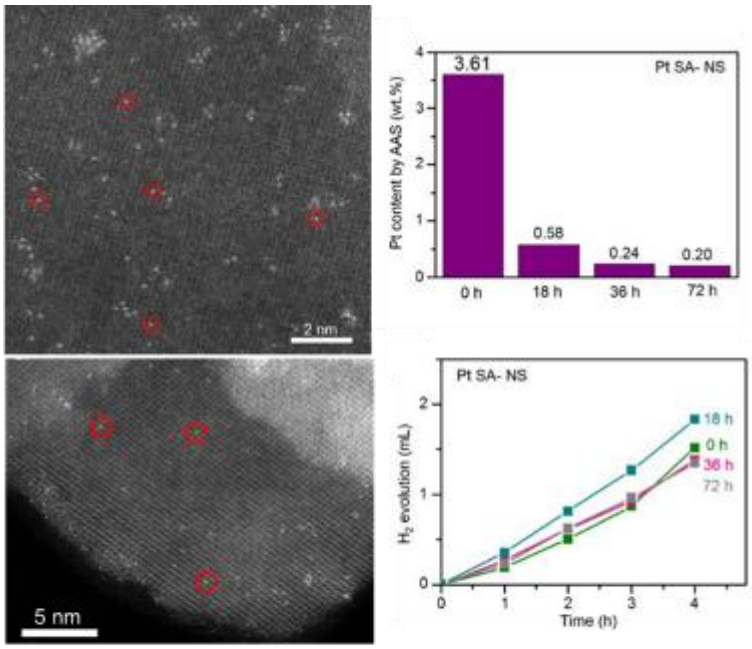

Figure 1: HRSTEM images of the as prepared sample (top, left) and after 36 h of cyanide leaching (bottom, left). Right: Pt content and photocatalytic activity after different leaching times.

Fig. 2

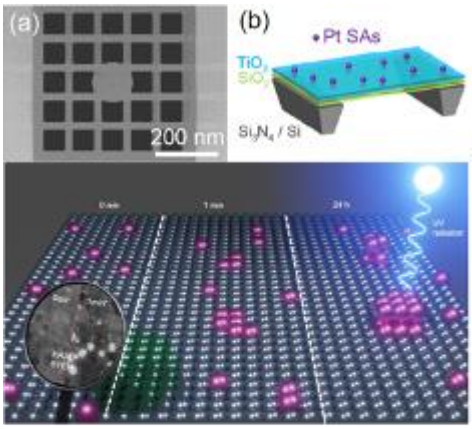

Figure 2 Top view of a TEM membrane (a) and schematic side-view of a TEM membrane including a 7 nm thick TiO2 film and Pt SAs (b). Bottom: summarizing sketch of the Pt SA agglomeration process.

MS1.P009

Surface reduction studied by *in situ* STEM on Pt-Ceria catalysts used for CO oxidation

C. B. Maliakkal[1], P. Dolcet[2], L. Braun[2], A. R. Lakshmi Nilayam[1], A. De Giacinto[3], M. Casapu[2], J. D. Grunwaldt[2], S. Gross[3], D. Wang[1], C. Kübel[1]

[1]Karlsruher Institut of Technologie (KIT), Eggenstein-Leopoldshafen, Germany
[2]Institute of Technical and Polymer Chemistry, Karlsruhe, Germany
[3]Department of Chemical Sciences, Padua, Italy

Heterogeneous catalyst systems used in exhaust gas treatment typically consist of precious metal nanoparticles (often Pt, Pd, Rh) supported on a metal oxide supports (often ceria, i.e. cerium IV oxide). The scarcity and cost of such catalysts demands careful design of more active and cost-efficient systems. Such theoretical predictions can happen only if there is a detailed understanding of the substrate-catalyst-gas interactions, the dynamic behavior of the catalyst system during catalysis and relevant gas atmospheres, and ultimately the reaction mechanism. One important parameter that should be ideally incorporated into such theoretical modelling, especially in systems such as CeO_2 where the surfaces are known to have oxygen vacancies[1], is the spatially resolved quantitative information about the oxygen vacancies on ceria and at Pt-ceria interface. However, this information at CO oxidation conditions is missing.

We measure electron energy loss spectroscopy (EELS) maps to find spatially resolved information of Ce oxidation state experimentally under vacuum, CO oxidation conditions and at other relevant gas conditions. Since the study aims at distinguishing the reduced surface layer (i.e. region containing Ce^{3+}) to that of the bulk (Ce^{4+}) it is important to study CeO_2 crystals with well-defined facets. Hence in this study we use CeO_2 cubes (with {100} crystal planes forming the surface facets). CeO_2 cubes were prepared by $Ce(NO_3)_3.6H_2O$ using an acetate-acetic acid buffer-mediated hydrothermal synthesis (similar to that of reference [2]) (Fig.1 a,b). Pt nanoparticles were prepared by microfluidic synthesis (similar to [3]) (Fig. 1 c). EELS is done in a Themis Z; while the gas experiments are conducted with Atmosphere holder from Protochips.

The EELS mapping of ceria cubes in vacuum shows that there is a surface layer containing Ce^{3+} atoms (Fig.2). When oxygen is introduced into the system we observe that this surface layer with Ce^{3+} atoms becomes narrower than in vacuum at the same temperature (Fig.3). The effect on this surface layer in N_2, H_2, CO and $CO+O_2$ mixture at different temperatures, pressures, and waiting duration after the introduction of gas, are underway. The effect of the multiple catalytic cycles on the surface layer will also be investigated. The effect of electron beam on the EELS spectrum maps is studied to find that it causes additional surface reduction, while in the bulk region no significant changes are noticed in the spectral features within the range of electron doses we studied yet. We will attempt to study the Ce and Pt oxidation state on the samples with Pt nanoparticle loaded on CeO_2 cubes. We also intend to study the structural/morphological dynamics of the Pt-CeO_2 catalyst using *in situ* STEM. Since the catalyst system is extremely dynamic during catalytic activity, *in situ* (s)TEM can provide valuable information on the active structure and its evolution in different relevant gas environments and reaction conditions. Results about Ce oxidation state mapping and catalyst dynamics will be presented.

References

[1] Goris et al. ACS Nano 2014 (8) 10878

[2] Lyu et al. Nanoscale 2016 (8) 7923

[3] Tofighi et al. Reaction Chemistry & Engineering 2017 (2) 876

Fig. captions:

1. (a, b) Ceria cubes; (c) Pt nanoparticles on ceria cubes
2. Oxidation state maps corresponding to Ce^{4+} and Ce^{3+} of a ceria cube in vacuum.
3. Normalised average EELS spectra showing the Ce core loss edge in vacuum and O_2 at both surface and interior.

Fig. 1

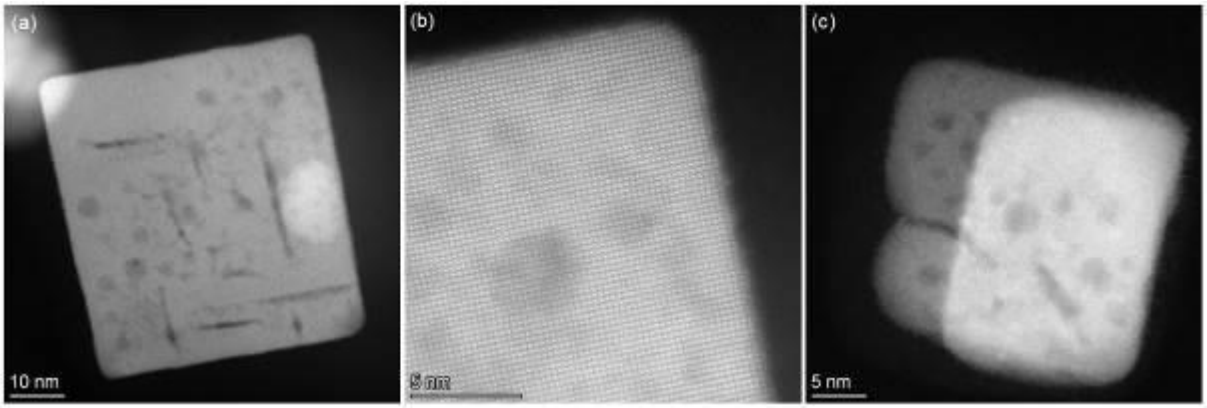

Fig. 2

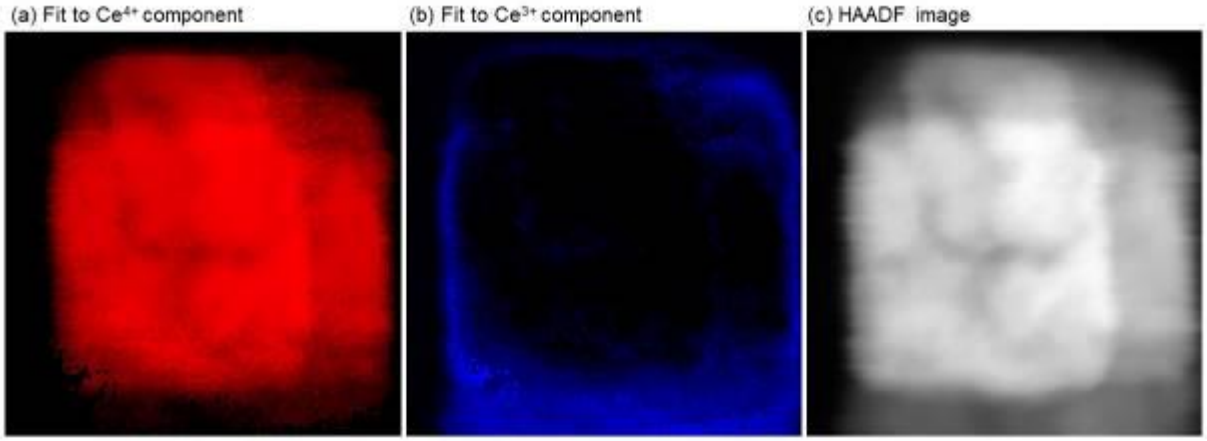

Fig. 3

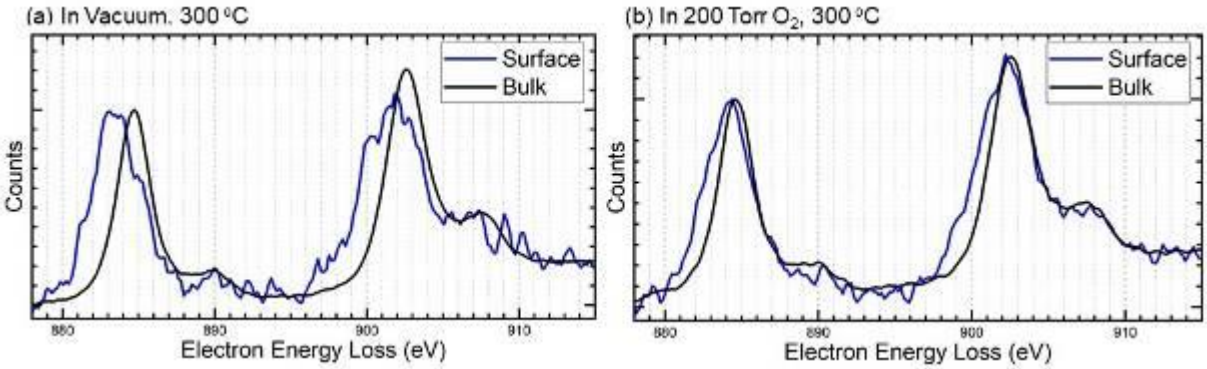

MS1.P010

Energy dispersive X-ray spectroscopy (EDS) applied on energy related materials and Li quantification as fraction of not identified element

U. Golla-Schindler[1], J. Niedermeyer[1], E. Barbosa Sa[1], C. Weisenberger[1], T. Bernthaler[1], V. Knoblauch[1], G. Schneider[1]

[1]University Aalen, Materials Research Institute, Aalen, Germany

Energy storage and conversion technologies are key technologies for the future on the way of "going green". The quantification of Li and limited spatial resolution of EDS analysis are bottlenecks to overcome. There the spectroscopy of low energy x-rays with the windowless Oxford extreme EDS detector open new prospects. This enables to reduce the accelerating voltages and/or beam currents and therefore additionally radiation damage. Fig 1a) show spectra of Li metal, where the grey spectrum is recorded directly after the transfer from the glove box to the SEM and the red spectrum after 9 days storage at air. The significant changes of the Li peak content, shape and peak position document the sensitivity and reactivity of Li, exemplary to air exposure. One sensitive part in Li-Ion batteries is the interface between the anode and the separator with the solid electrolyte interface covering the anode surface and eventually with reaction products on top. Fig. 1 b), c) show such reaction products of a Li-Ion battery with a LiFePO4 cathode and a carbon anode. The EDS spectra show significant enrichment for the dark surface coated areas on top of the massive anode encrustation spectrum16 and the round shaped particle spectrum 17. This enables to determine precipitations, which reduce the amount of Li inventory and on this way the battery performance. Starting quantification consistently upcoming questions are: How reliable are EDS studies for real life application and what are the influences of etc. sample preparation. Therefore a systematic study was performed on Li(NixMnyCoz)O2 cathode material and the first topic was the determination of the stoichiometric composition of Ni, Mn and Co, where Ni, Mn and Co share one position, therefore x+y+z=1. Fig, 2 a) shows the results for studies obtained with different sample treatment like:

1. shuttle => argon atmosphere and SEM vacuum, top view
2. air => in air, top view
3. gold => in air and coated with gold (4 nm), top view
4. carbon => in air and coated with carbon (10 nm), top view
5. cross section => in air cross section obtained with an argon ion mill

All performed studies (Fig. 2) deliver a stoichiometric relationship close to NMC (811). This shows the robustness of the performed studies. One limitation for the chemical quantification of Li-Ion battery materials is, that bonded Li cannot directly detected by EDS. We determine the Li amount as the missing element fraction of not normalized quantitative EDS analysis. Precondition is that during the measurement no dynamic processes like contamination, radiation damage, charging etc. are taking place. Additionally we solely take those spectra for the quantification into account, where the oxygen weight percent of the EDS spectra is ±3% of the expected weight percent for oxygen in Li(Ni8Mn1Co1)O2 . We obtained mean values of the Li weight percent for the analytic conditions: 1. shuttle: 6,0±0,5% ; 2. air: 6,1±0,8% ; 3. gold: 10,6±0,8% ; 4. carbon: 10,4±0,7% and 5. cross section: 6,4±0,6%. The expected value for a 100% lithiated cathode material is 7,1%, where this value overestimate the real content and will be reduced by approx. 10% formation loss after the first battery cycle. The results of the studies performed with the conditions 1, 2, 5 agree nicely with the expectation, where the gold and carbon coating lead to a significantly overestimation of the Li content. [1]

[1] The authors gratefully acknowledge the German BMBF for financial support.

Fig. 1

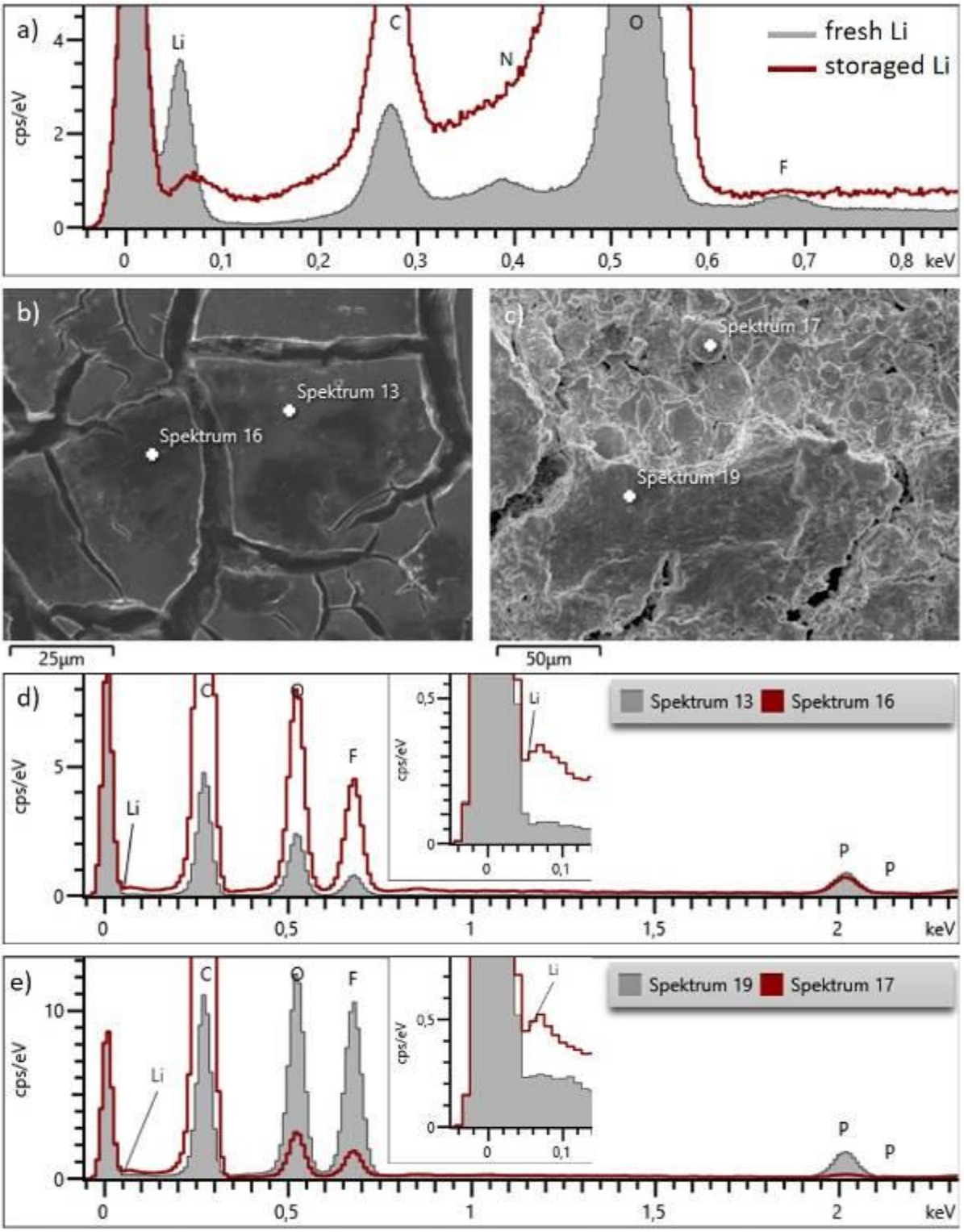

Figure 1 a) Li metal and (b-e) $LiFePO_4$ battery anode of a treated cell investigations with EDS. a) comparison of spectra taken from a fresh and storage Li metal sample. b), d) Images of surface precipitations on top of a treated anode surface with the locations of the spectra. d), e) the correlative spectra of the image in b), d) delivering significant differences in the Li content

Fig. 2

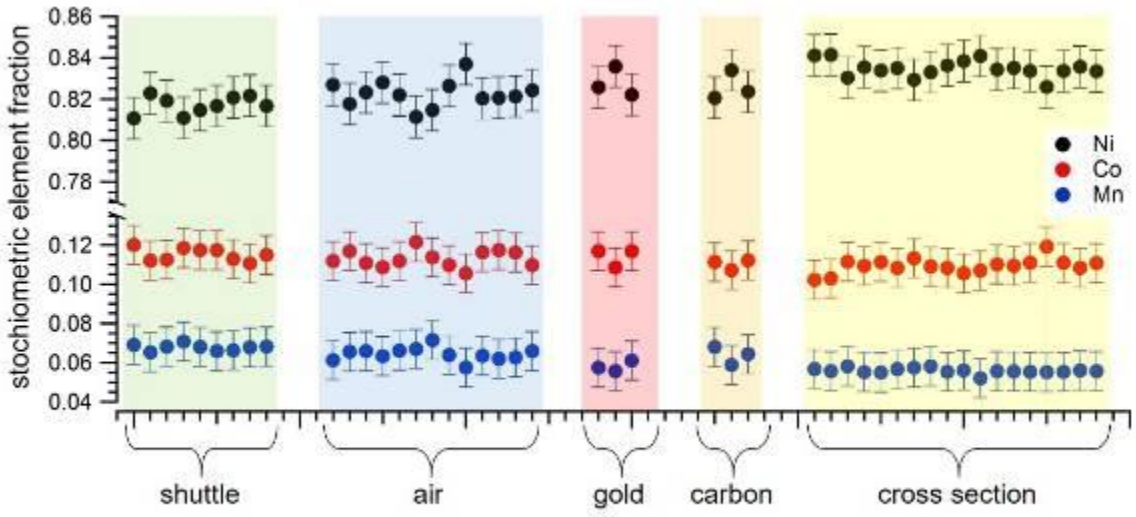

Figure 2 Stochiometric element fraction for Ni, Co, Mn and different analytic conditions

MS1.P011

Improvement of SEM-SXES analysis for beam sensitive materials by using cooling stage

Y. Yamamoto[1], T. Murano[1], S. Koshiya[1], K. Yamashita[1]

[1]JEOL Ltd., Akishima, Japan

Soft X-Ray Emission Spectrometer (SXES), which can be installed on SEM and EPMA (Electron probe microanalyzer), is a useful method for chemical state analysis by detecting the energy state of valence electrons. In particular, since it is possible to detect low-energy characteristic X-rays such as lithium (Li) K-line and analyze the chemical state, it is expected as a method for chemical state analysis of Lithium Ion secondary Battery (LIB) materials in a charged state. Field Emission-SEM equipped with SXES enables us to obtain chemical state information in the vicinity of the bulk top surface by using low-kV analysis. (1) However, it is known that the irradiation of an electron beam causes a change in the chemical state of the beam-sensitive materials such as lithium compounds during the observation. (2) This study shows the improvement of chemical state analysis for beam-sensitive materials using the SEM-SXES system with a cooling stage.

The Schottky FE-SEM, JSM-IT800(JEOL), combined with the SXES, SS-94000SXES (JEOL), and cooling stage C1003 (Gatan, Inc.), was used to examine Lithium Sulfide (Li2S) reagent for the solid electrolyte of LIB. To prevent deterioration of the samples due to atmospheric exposure, these samples were transferred to the SEM-SXES system using a transfer vessel for air isolation. The changes in the chemical state of Li2S were confirmed by time-resolved SXES analysis. (2)

SXES point analysis for Li2S at room temperature (RT), was performed at an accelerating voltage of 3 kV and a probe current of 20 nA (Fig. 1 and Fig. 2). When Li2S is continuously irradiated with an electron beam for 450 seconds, formation of deposition on the sample surface can be confirmed in the backscattered electron (BSE) image (Fig.1). And the spectrum of the precipitated Li and S are detected in the SXES analysis result at an acquisition time of 450 seconds (Fig.2 left). By contrast, in the time-resolved SXES analysis performed every 15 seconds from 0 to 450 seconds, the Li spectrum shape changes in response to the irradiation time (Fig.2 right). This demonstrates that Li is metallized as the dose of the electron beam increases. Figure 3 shows the result of SXES point analysis with -100℃ cooling at 3kV and 20 nA prove current. In the BSE image (Fig.3 left), there are no change in contrast. It can be seen that no precipitation has occurred on the surface of Li2S after performing SXES analysis with an acquisition time of 450 seconds. Even in the SXES spectrum (Fig. 3 right), which was time-resolved every 15 seconds from 0 to 450 seconds, no spectral change with the passage of time was confirmed. Comparing the SXES results obtained at room temperature and at -100 ° C, it can be seen that the Li K spectrum derived from metallic lithium was not detected and the Li K spectrum derived from Li2S was obtained by cooling at -100 ° C (Fig. 4).

This result lead to the possibility of a new technique for SEM-SXES analysis using specimen cooling system for materials whose chemical state changes due to electron beam irradiation.In this presentation, more examples of specimen cooling application for SEM-SXES analysis of materials whose chemical state changes due to electron beam irradiation, such as polymers and negative electrodes of solid-state batteries, will also be introduced.

References:

(1) Yamamoto. Y et al, Microscopy and Microanalysis 24(S1):1062-1063(2018)

(2) Yamamoto. Y et al, Microscopy and Microanalysis 26(S2):68-70(2020)

Fig. 1

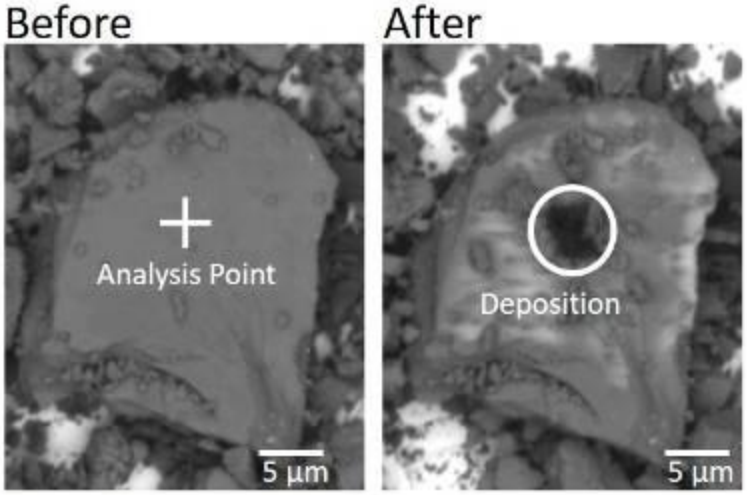

Fig.1 BSE images of Li_2S before and after analysis at RT

Fig. 2

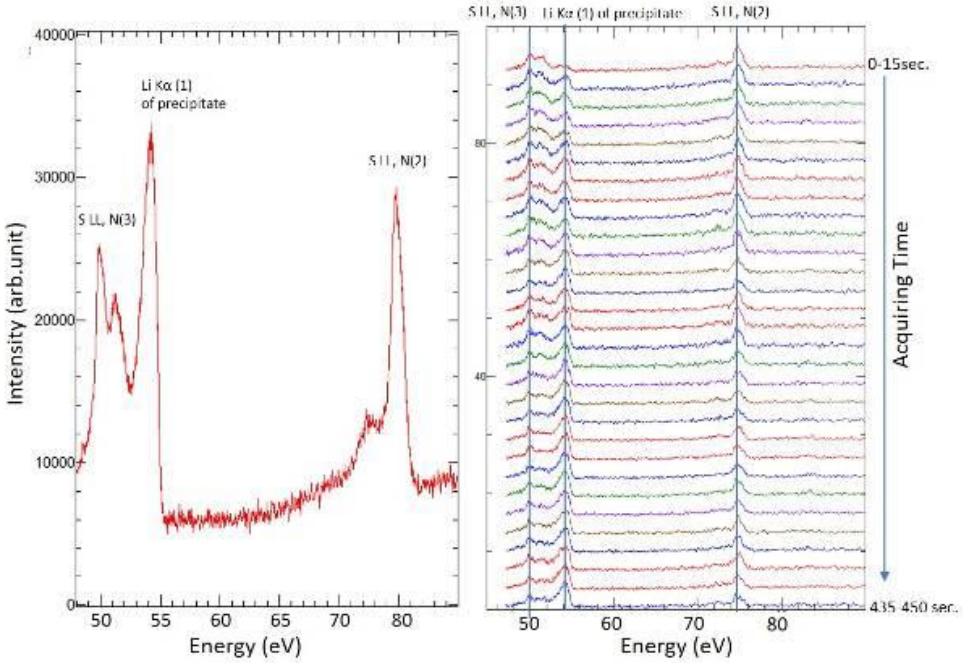

Fig.2 SXES spectra of Li_2S at RT
Left: SXES spectrum taken during 450 sec. Right: SXES spectra taken at each 15 sec.

Fig. 3

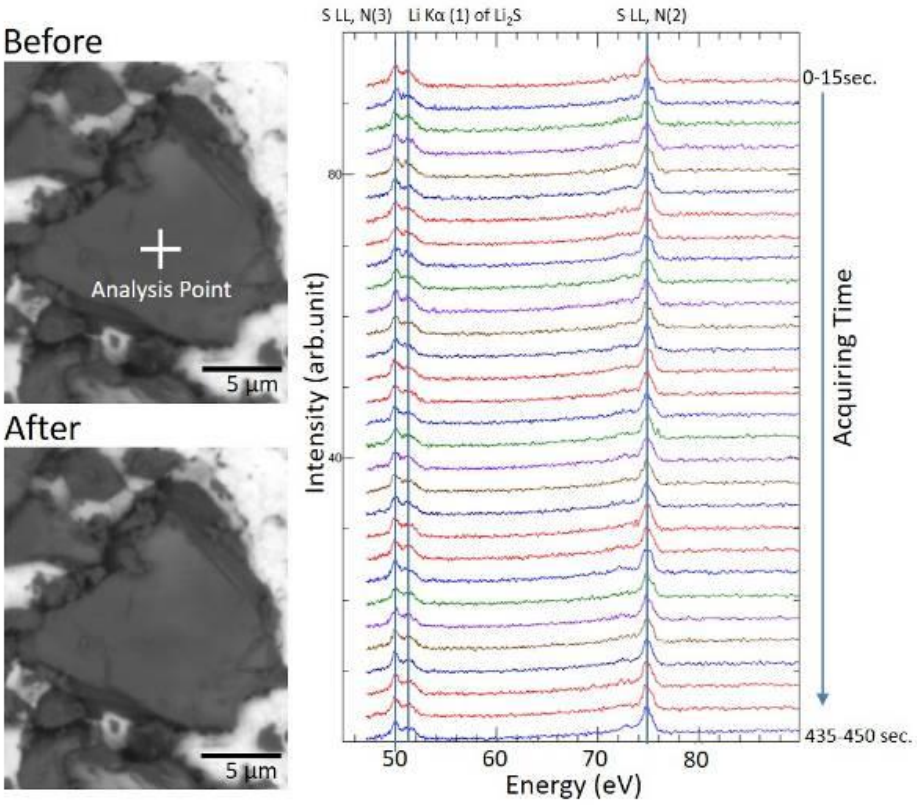

Fig.3 BSE images before and after analysis at -100°C cooling, and Time-resolved SXES spectra of Li_2S at -100°C cooling

Fig. 4

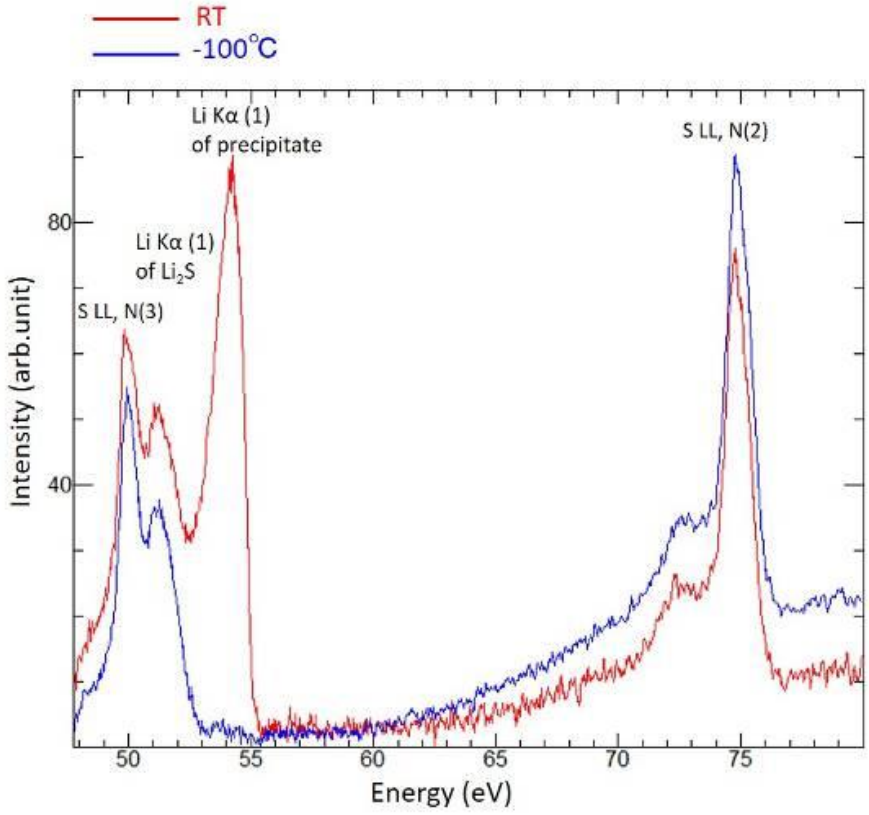

Fig.4 Comparison of SXES spectra: RT and -100°C cooling

MS1.P012

TEM analysis of the water and acid treated LNMO faceted particles

D. Geiger[1], J. Biskupek[1], T. Böhler[2,3], M. Künzel[2,3], D. Bresser[2,3], U. Kaiser[1]

[1]Universität Ulm, Ulm, Germany
[2]Helmholtz Institute Ulm (HIU), Ulm, Germany
[3]Karlsruher Institut of Technologie (KIT), Karlsruhe, Germany

Steady progress of battery performances attests the necessity of intense battery research. As promising high-voltage and high-capacity cathode material LiNi0.5Mn1.5O4 (LNMO) was investigated for Co-free next-generation Li-ion batteries. Our investigation focused on determining the structure property relationship of these materials at the microscopic and preferrably atomic level via different TEM methods to unravel the morphologic, crystallographic and chemical structure of carefully designed LNMO.

The main objectives of our research-project "H2O-LIMO" are related to the overcoming of the water sensitivity of Li transition metal oxides, especially LNMO, as Co-free cathode, which is possible only if a fundamental understanding of occurring processes is established:

-general effect of water exposure and the impact of tailored surface facets of LNMO;

-effect of adding inorganic acids (e.g., H3PO4), which have been proven [1] to stabilize the LNMO surface by forming a thin metal phosphate surface layer;

-understanding processes occurring at the LNMO/water interface.

First, the synthesis of single-crystalline LNMO particles with tailored surface facets has been carried out according to a combined precipitation/evaporation method [2]. Perfectly octahedral LNMO particles with solely {111} surface facets as well as truncated LNMO particles with a combination of {100} and {111} surface facets were obtained. Depending on the temperature and duration of the annealing, the preparation of either ordered (space group (sp): P4332) or disordered (sp: Fd-3m) LNMO is achieved. The mentioned cation ordering, the presence of Mn3+ in disordered LNMO as a result of oxygen vacancies, and that of solely Mn4+ in the ordered phase is expected. The Mn:Ni ratio, the vacancies as well as the initial oxidation state of the Mn cations is expected to play an essential role for the interaction with water. Similarly, the varying acidity of the different surface facets is expected to play a key role for the reaction with the aqueous environment.

The size morphology and crystallographic orientations were investigated by TEM bright- (fig.1a,c,d) and dark-field (fig. 1b) imaging, diffraction (fig.1e) and HRTEM (fig.1f) showing the expected octahedron faceted primary particles. Since the powder particles are disordered agglomerations of overlapping primary particles, it is difficult to find an isolated octahedron particle for the foreseen TEM analysis.Further, the effect of the (acidic) aqueous treatment on the electrochemistry of the new faceted synthesized particles has been studied by STEM-EDX. The atom concentration distributions especially at and around the particle surface (fig.2a,b) shows a change of the ratio Mn:Ni at the surface and an increased P concentration in this region. HRTEM and STEM-EDX were performed with a Thermofisher Talos 200X TEM at 200 kV and with an image Cs-corrected TEM FEI Titan 80-300 at 300kV.

The first results are promising a better understanding of the influence of the (acidic) aqueous treatment on the faceted synthesized LNMO particles and their electrochemical behaviour. The investigation will be extended to other material treatments (e.g. other acids).

[1] M. Künzel et al., ChemSusChem 11 (2018) 562

[2] M. Kuenzel et al., Materials Today 2020 (39) 127

Acknowledgement: This work was supported by DFG in the frame of the research project "H2O-LIMO" (Wechselwirkung von Wasser und wässrigen Säuren mit Lithiumübergangsmetalloxiden).

Fig. 1

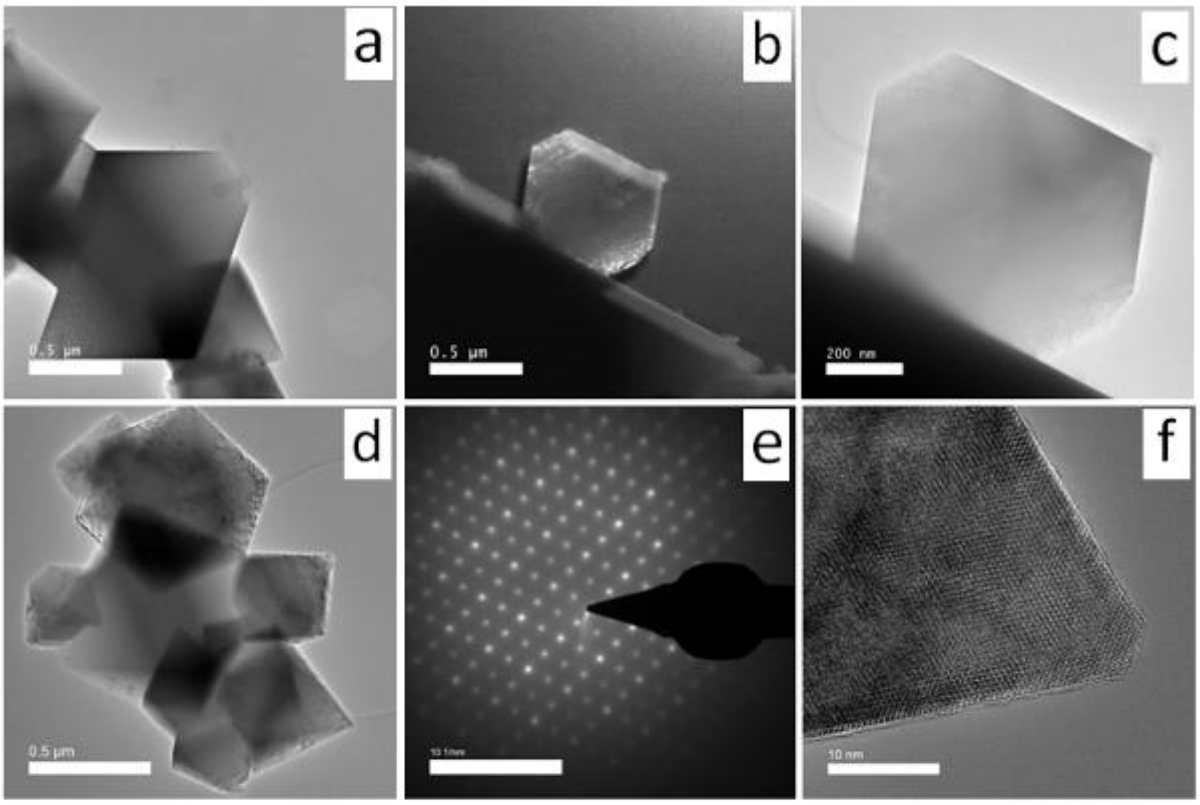

Fig.1 TEM investigations of LNMO faceted particles a),c),d), dark-field imaging b), diffraction e) and HRTEM imaging f).

Fig. 2

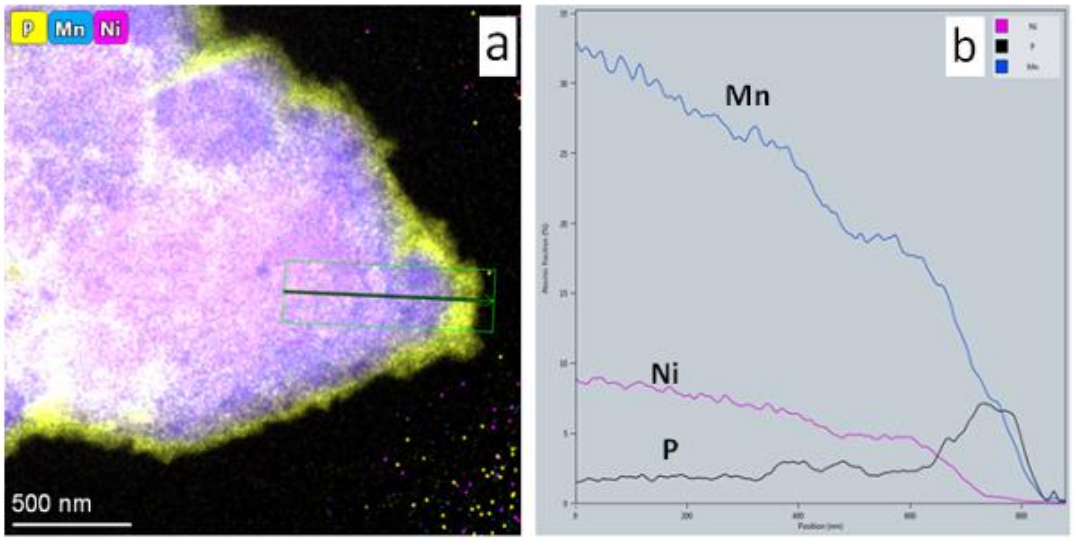

Fig.2 STEM-EDX analysis of (acidic) aqueous treated LNMO powder particles a) and the line scan (along the black line in a)) for atom (Mn,Ni,P) concentrations b).

MS1.P013

Novel enhanced particle size analysis algorithm using enhanced circular Hough transformation

J. Guckel[1,2], M. Görke[3], G. Garnweitner[2,3], H. Bosse[1,2], D. Park[1,2]

[1]Physikalische-Technische Bundesanstalt, 5, Braunschweig, Germany
[2]Laboratory of Emerging Nanometrology (LENA), Braunschweig, Germany
[3]Technische Universität Braunschweig, Institute for Particle Technology (iPAT), Braunschweig, Germany

Nanoparticles (NP) have a wide range of applications in diverse research fields, such as lithium ion batteries, catalysis, medical engineering, etc., due to their specific characteristics [1]. The surface effects become predominant as the dimension of the particles is reduced. Therefore, physical and chemical properties of NPs are closely intertwined with their particle size [2]. Due to this critical parameter of particle size, only a slight deviation from the target size is usually intended to achieve uniform characteristics for a specific application. Hence, the reliable analysis of the particle size distribution is an important task for successful implementation of advanced nanotechnological applications.

NPs size distribution can be analyzed by measuring individual particle size from a large number of images of NPs obtained by electron microscopy. The automatic analysis tools are essential, as a large number of images are required for obtaining reliable statistics for the size distribution [3]. However, currently available automatic procedures are limited to provide accurate results if the NPs are severely overlapping. In order to overcome these limitations, we developed a novel approach for the detection of spherical NPs based on the iterative particle analysis using the enhanced circular Hough transformation (CHT) algorithm. This approach solves the issue of overlapping particle clusters by iteratively detecting large particles first, removing them from the image and then find the smaller particles from the remainder of the cluster. The main loop of our iterative routine splits a singular particle size interval into multiple smaller ones and passes through them one by one. This approach keeps consistent detection quality over very large intervals. The CHT algorithm involves finding the best fit based on only contour detection of particles. However, utilizing this approach leads to critical problems, such as the halo error, void error and particle group error, as the CHT algorithm includes no local intensity analysis as explained in detail in Figure 1. In order to avoid the aforementioned problems, additional local intensity criteria are included.

We investigated synthesized FePt NPs using high angle annular dark field contrast (HAADF) imaging via a double-abberation corrected JEOL NeoARM 200F. From the single HAADF image of the FePt NPs at the magnification of roughly 2 million, 630 particles were automatically detected after manual removal of badly detected 19 particles using our algorithm (Figure 2). The measured mean particle size was 2.563 nm with a standard deviation of 0.485 nm. Although the size of NPs varies significantly with severely overlapping particles forming complex clusters in the selected system, overall our novel iterative particle analysis algorithm provided promising results in particle size distribution, showing very minor problems which can be corrected with available manual correction.

References:

[1] Görke, M. and Garnweitner, G., Crystal engineering of nanomaterials: current insights and prospects , CrystEngComm, 2021

[2] Issa, B. et al., Magnetic Nanoparticles: Surface Effects and Properties Related to Biomedicine Applications, International Journal of Molecular Science, 2009

[3] Meng, Y. et al., Automatic detection of particle size distribution by image analysis based on local adaptive canny edge detection and modified circular Hough transform, Micron, 2018

Fig. 1

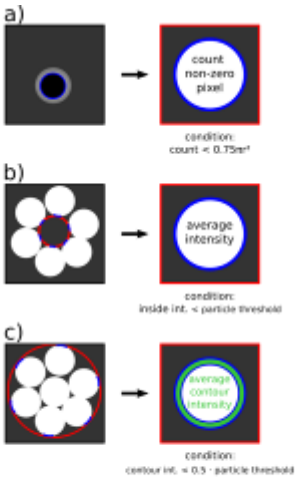

Figure 1: Problems of CHT and corresponding criteria to avoid those limitations a) Halo Error: non-zero pixel criterium prevents redetection of previous particles b) Void Error: An average intensity criterium prevents voids between particles to be detected as particles c) Particle group error: A group of particles are detected as 1 large particle.

Fig. 2

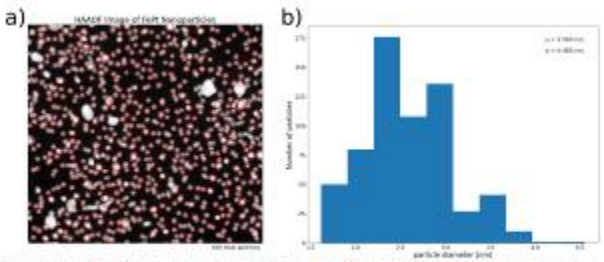

Figure 2: a) HAADF image of FePt Nanoparticles with overlapping particle position detection at 2 million magnification. b) Particle size distribution analysis. Mean particle size measured from 630 particles was 2.563 nm with a standard deviation of 0.485 nm.

MS1.P014

Unraveling the structural properties of $Bi(Fe_{1-x}Cr_x)O_3$ thin films

O. Wenzel[1], S. Petrick[1], A. Zintler[1], H. Störmer[1], M. Hoffmann[1], D. Gerthsen[1]

[1]Karlsruher Institut of Technologie (KIT), Laboratorium für Elektronenmikroskopie (LEM), Karlsruhe, Germany

This work focuses on the structural, chemical, and optoelectronic properties of $Bi(Fe_{1-x}Cr_x)O_3$ thin films synthesized by spin-coating for future ferroelectric solar-cell absorber layers. We want to use laterally polarized ferroelectric domains and their electric fields to drive the photogenerated charge carrier towards the domain walls, along which they can be extracted into the electrodes. Early results on the efficacy of this idea were achieved with methylammonium lead halide (MAPH) perovskites [1]. However, we strive for a non-toxic ceramic-based material with similar properties. A possible material system with desirable properties and suitable bandgap energy is $Bi(Fe_{1-x}Cr_x)O_3$ (BFCO), where Bi2+ occupies the A site with alternating Fe2+ and Cr2+ on the B site in the ABO3 perovskite structure. In this contribution, the material properties are investigated in detail by different electron microscopic techniques on the nanoscale to understand the bulk material's optoelectronic properties and to improve material synthesis.

BFCO films with different Fe/Cr concentrations were deposited by spin coating an Fe-, Cr- and Bi- containing sol onto fluorine-doped tin oxide (FTO) substrates followed by a calcination step at 350 °C in air. We used several analytical scanning/transmission electron microscopy (S/TEM) techniques for comprehensive characterization, such as quantitative energy-dispersive X-ray spectroscopy (STEM-EDXS), electron energy loss spectroscopy (STEM-EELS), selected area electron diffraction (SAED), and other imaging modes. Nanoscale investigations were accompanied by X-ray diffractometry (XRD) and UV-Vis spectroscopy to analyze the films.

The BFCO thin films are polycrystalline with a thickness of about 400 nm. Bright-field S/TEM images reveal a homogeneous microstructure with 30-50 nm grain sizes. The crystal structure is predominantly tetragonal BiFeO3, however, we do note that occasional metal Bi nanoparticles and amorphous Cr-Fe oxide can be seen in some synthesis batches. Quantitative analysis of STEM-EDXS maps shows that the average composition of the thin film follows the expected stoichiometry $Bi(Fe_{1-x}Cr_x)O_3$. Furthermore, core loss STEM-EELS accompanied by an analysis of the fine structure of Fe and Cr confirms the 2+ oxidation state and shows that both Fe and Cr are located at the B-site in the perovskite. Analyses of the crystal structure with SAED, HRTEM and the coordination environment revealed with STEM-EELS fits with the bulk crystal structure determined by XRD. Further, the nanoscale secondary phases which occur in individual synthesis batches help explain additional contributions to the bulk the UV-Vis signal.

Based on comprehensive electron microscopic analyses, this study demonstrates that BFCO thin films can be successfully synthesized by tuning the sol-gel synthesis conditions. Looking ahead, we are aiming to fine-tune the ferroelectric domain structure.

[1] H. Röhm et al., Adv. Mater., **2019**, *26*, 1806661]

[2] Mustonen, O. et al Chem. Commun., **2019**, 55, 1132-1135

[3] Herber, R-P and Schneider, G.A., J. Mater. Res., **2007**, 22

MS1.P015

TEM investigation of (Ag,Cu)(In,Ga)Se2 solar cells

X. Jin[1], R. Schneider[1], D. Hariskos[2], S. Paetel[2], W. Witte[2], D. Wang[3,4], C. Kübel[3,4], M. Powalla[2], D. Gerthsen[1]

[1]Karlsruher Institut of Technologie (KIT), Laboratorium für Elektronenmikroskopie (LEM), Karlsruhe, Germany
[2]Zentrum für Sonnenenergie- und Wasserstoff-Forschung Baden-Württemberg (ZSW), Stuttgart, Germany
[3]Karlsruher Institut of Technologie (KIT), Institut für Nanotechnologie (INT), Karlsruhe, Germany
[4]Karlsruher Institut of Technologie (KIT), Karlsruhe Nano Micro Facility (KNMF), Karlsruhe, Germany

The performance of Cu(In,Ga)Se2 (CIGS) thin-film solar cells can be improved by partial substitution of Cu with Ag, forming (Ag,Cu)(In,Ga)Se2 (ACIGS) [1]. However, the photovoltaic properties of ACIGS solar cells are significantly influenced by the Ag concentration and its spatial distribution. In order to determine an optimum Ag content and to identify experimental conditions for the fabrication of high-efficient ACIGS devices, ACIGS thin films in this work were prepared by supplying the Ag by two different methods. Providing Ag in both experimental campaigns, the power conversion efficiency (PCE) of the cells decreased around 2% absolute. The chemical and structural properties of the ACIGS layers were studied by (scanning) transmission electron microscopy ((S)TEM) combined with energy-dispersive X-ray spectroscopy (EDXS).

In the first experimental campaign two ACIGS layers were fabricated by in-line co-evaporation of CIGS on Mo coated glass substrates, which were pre-plated with a 40 and 80 nm Ag layer, respectively, acting as precursor. In the second experimental campaign four ACIGS films with integral Ag/(Ag+Cu) ratios (AAC) of 0, 0.05, 0.11, and 0.20, as determined by X-ray fluorescence, were fabricated by co-evaporation of all matrix elements (including Ag) on Mo substrates without a Ag precursor. Cross-sectional TEM lamellae were prepared from these samples by focused-ion-beam milling using an FEI dual beam Helios G4 FX microscope. For TEM and STEM/EDXS investigations, a 200 kV FEI Tecnai Osiris and a 300 kV Thermo Fisher Themis 300 transmission electron microscope was used, where the latter has a Cs-probe corrector.

Fig. 1 shows the depth-dependent line profiles of the Ag concentrations (Figs. 1a,c) together with the resulting Ga/(Ga+In) ratios (GGI) (Figs. 1b,d) of the ACIGS layers deposited with the Ag precursors or by Ag co-evaporation. The average Ag contents are also given in Figs. 1a,c. In general, the GGI profiles determined by STEM/EDXS are in good agreement with corresponding measurements by glow discharge optical emission spectroscopy (not shown here). Evidently, the GGI gradients are flattening with increasing Ag content (Figs. 1b,d). It is noted that the GGI gradient of the Ag-free CIGS with AAC = 0 (red line in Fig. 1d) resembles that of ACIGS with AAC = 0.05 (green line), which is likely due to the small difference in Ag content.

For the precursor-deposited ACIGS films, Ag segregation was observed in some grain-boundary regions, which is more pronounced in the sample with the higher Ag content. Fig. 2 shows elemental maps for a representative Ag-enriched grain boundary in the ACIGS sample with 80 nm Ag precursor. An In and Ag enrichment combined with Se deficiency was detected at the grain boundary with a length of several hundred nanometers. In comparison, Ag segregation was not detected at grain boundaries of the co-evaporated ACIGS films, even for the high AAC ratios.

Since the PCEs of all ACIGS devices in this work decrease with increasing Ag contents, the Ag enrichment at grain boundaries and/or the flattening of the GGI gradients are likely to contribute to the deterioration of the device performance.

[1] M. Edoff *et al*., IEEE J. Photovolt. **7** (2017) 1789.

[2] The support of the German Federal Ministry for Economic Affairs and Climate Action (BMWK) within the EFFCIS-II project under contract No. 03EE1059A (ZSW) and contract No. 03EE1059E (KIT) is acknowledged.

Fig. 1

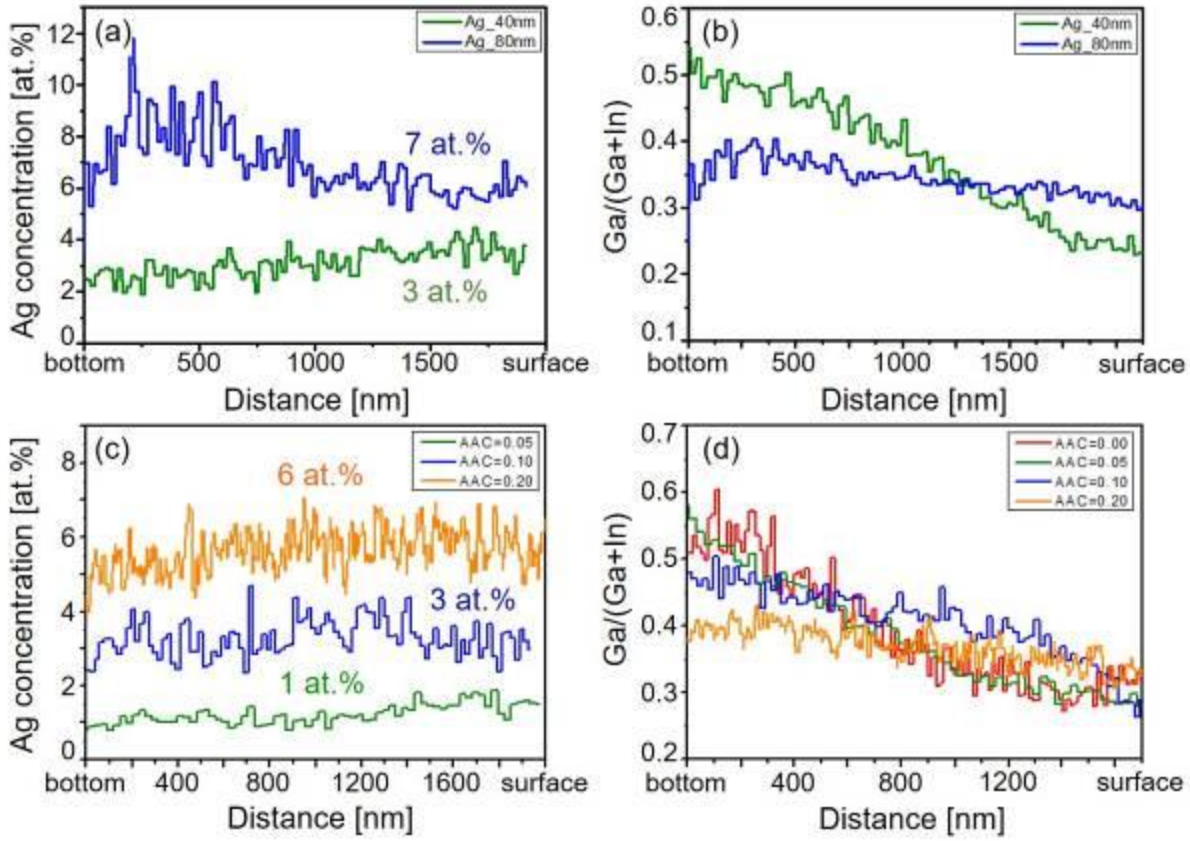

Figure 1. Depth-dependent Ag concentration and GGI values of the ACIGS thin films deposited by (a, b) Ag-precursor and (c, d) co-evaporation.

Fig. 2

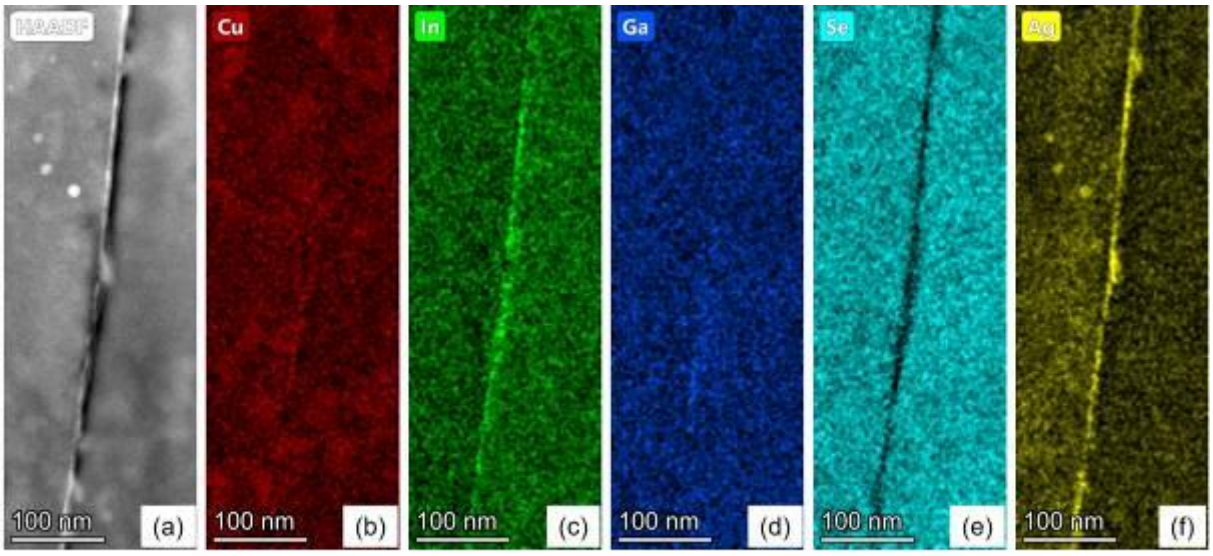

Figure 2. (a) HAADF-STEM image and the corrresponding quantitative EDXS maps of (b) Cu, (c) In, (d) Ga, (e) Se, and (f) Ag of a grain boundary in the ACIGS thin film deposited with a 80 nm Ag precursor.

MS1.P016

OsO_4 staining as a tracer for the visualization of degradation of porphyrin-based battery electrode material

G. Neusser[1], T. Philipp[1], E. Abouzari-Loft[2,3], S. Shakouri[3], F. D. H. Wilke[4], M. Fichtner[2,3], M. Ruben[3,5,6], C. Kranz[1]

[1]Institute of Analytical and Bioanalytical Chemistry, Ulm University, Ulm, Germany
[2]Helmholtz Institute Ulm (HIU), Ulm, Germany
[3]Karlsruher Institut of Technologie (KIT), Institute of Nanotechnology, Karlsruhe, Germany
[4]GFZ German Research Centre for Geosciences, Potsdam, Germany
[5]Karlsruher Institut of Technologie (KIT), Institute of Quantum Materials and Technology, Karlsruhe, Germany
[6]Centre Européen de Science Quantique (CESQ), Université de Strasbourg, Institute de Science et d'Ingénierie Supramoléculaires (ISIS), Strasbourg, Germany

Due to the growing need for sustainable, rechargeable energy storage systems, efforts are made towards the development and improvement of battery electrode components based on organic compounds. Electron donor-acceptor metalloporphyrin complexes like [5,15-bis(ethynyl)-10,20-diphenylporphinato]copper(II) (CuDEPP) are promising materials for rechargeable lithium[1], sodium[2] and magnesium batteries[3].

In this study we demonstrate that structural changes of composite CuDEPP electrode material (50 wt.% CuDEPP active material, 40 wt.% carbon black and 10 wt.% poly(vinylidene difluoride)) for Li/ $LiPF_6$/CuDEPP batteries can be visualized including the initial self-conditioning step during the first charge-discharge cycle and changes of the active material after longer charge-discharge cycles via focused ion beam/scanning electron microscopy (FIB/SEM) and energy dispersive/wavelength dispersive X-ray spectroscopy (EDX/WDX) measurements.

Pristine CuDEPP electrode and electrodes cycled for 1, 200 and 2000 times in Li half-cell with $LiPF_6$ electrolyte were treated with OsO_4 vapor and embedded in silicone resin. After staining and embedding, the samples were investigated using FIB/SEM cross-sectioning and tomography (Helios Nanolab600), EDX measurements using a Quanta 3D FEG (both Thermo Fisher) equipped with a SDD Apollo XV (EDAX) and WDX measurements obtained with a JXA-8530FPlus (JEOL).

For the pristine sample, EDX and WDX measurements show no uptake of Os, as the aromatic conjugated double and triple bonds that occur in pristine CuDEPP are not affected by OsO_4 staining. However, all cycled samples show a gradient in grey values in BSE images with highest values at the edges of each grain due to the incorporation of Os. The occurrence of Os coincides with increased P content (Fig.1) and therefore with the penetration of electrolyte ($LiPF_6$) into the CuDEPP particles during cycling. As OsO_4 does not react with the pristine material, a measurable Os content within the cycled CuDEPP directly indicates structural changes of CuDEPP (degradation) given the fact that Os enrichment is related to the formation of non-aromatic double bonds [4].

Fig.1: BSE image (a) and WDX map of P (c) and Os (d) of CuDEPP particles after 200 cycles. (b) show intensity profiles of BSE, P and Os signal along the yellow line. Two CuDEPP particle marked by red line in (a).

[1] P. Gao et al. Angew. Chemie Int. Ed. 56 (2017) 10341–10346.

[2] X. Chen et al. Nano-Micro Lett. 13 (2021) 71.

[3] E. Abouzari-Lotf et al. ChemSusChem. 14 (2021) 1840–1846.

[4] T. Philipp et al. J. Power Sources. 522 (2022) 231002.

Fig. 1

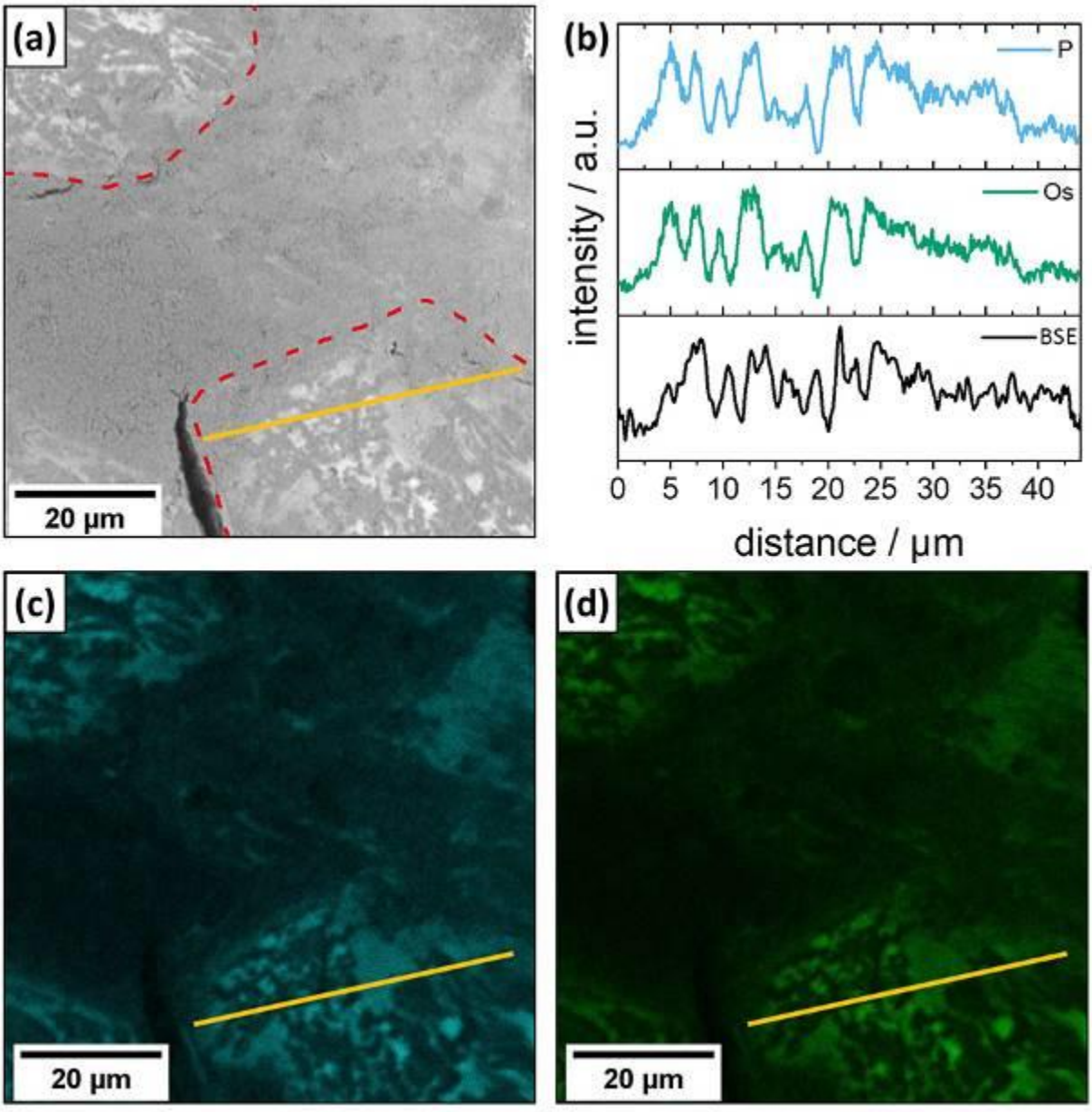
(a)
20 µm
(b)
P
Os
BSE
intensity / a.u.
0 5 10 15 20 25 30 35 40
distance / µm
(c)
20 µm
(d)
20 µm

MS1.P017

Cryo-SEM/FIB material and water contents analysis of fuel cell proton exchange membranes

J. Wissler[1], I. Lüdeking[2], F. Regnet[2], H. Baechler[2], F. Wilhelm[2], L. Joerissen[2]

[1]TESCAN, Dortmund, Germany
[2]Zentrum für Sonnenenergie- und Wasserstoff-Forschung Baden-Württemberg (ZSW), Ulm, Germany

Proton exchange membranes (PEM) are crucial to the functionality of fuel cells (FC). In those cells H_2 and O_2 is reacting to H_2O, generating electric energy and heat. Material types, composition and particle distribution within the catalyst coated membrane determine the efficiency of the hydrogen/oxygen to water chemical conversion process. The generated microscopic water distribution cannot be determined with sufficient resolution during the cell operation. Furthermore, ex-situ determination of the product water distribution within the meso-porous cell components and the membrane is neither easy nor unambiguous. The establishment of a reliable workflow for the microscopic determination of the material distribution, including water, would be very beneficial. Therefore, we elaborated a correlative workflow, using TESCANs cryo-SEM/FIB approach, for the determination of water and material distributions in PEMs. The correlative cryo-EDS approach enables the determination of the PEM layer- and material-compositions in different membrane types, whether fresh or used after operation in a FC stack. Fig.1 shows i.e., the uneven water distribution of a PEM FIB cross-section by cryo-EDS imaging. PEM-materials of different ageing states can thus reliably be tested. Generated water agglomerations can be located and imaged down to the nano-meter scale within the PEM. The relative amount can be correlated to the microporous structure. This enables to test different PEM materials which contributes to the understanding of the FC stack efficiency. (Authors 1-4 contributed equally)

(**Fig.1:** Water distribution (blue) of a fresh cryo-FIB cross-sectioned PEM)

Fig. 1

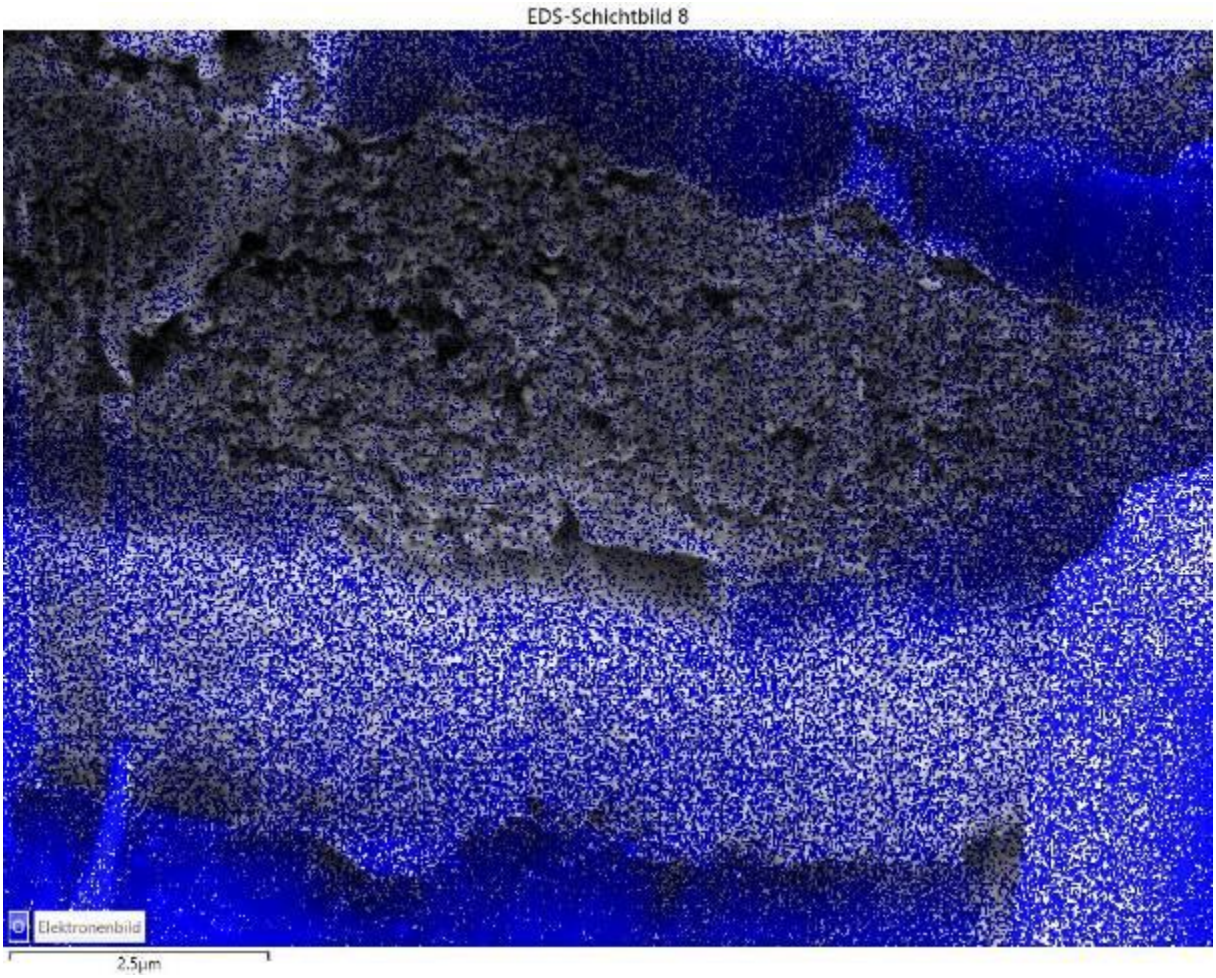

MS1.P018

Atomic scale electron microscopy characterisation of the aging processes in solid oxide cells

Q. Tran[1], H. Türk[1], F. P. Schmidt[1], T. Götsch[1], A. Hammud[1], D. Abou-Ras[2], D. Ivanov[1], E. Stotz[1], L. G. J. de Haart[3], I. C. Vinke[3], R. Eichel[3], K. Reuter[1], R. Schlögl[1], A. Knop-Gericke[1], C. Scheurer[1], T. Lunkenbein[1]

[1]Fritz Haber Institute of the Max Planck Society, Berlin, Germany
[2]Dep. Structure and Dynamics of Energy Materials, Helmholtz-Zentrum Berlin für Materialien und Energie GmbH, Hahn-Meitner-Platz 1, Berlin, 14109 Germany
[3]Fundamental Electrochemistry (IEK-9), Institute of Energy and Climate Research, Forschungszentrum Jülich GmbH, Jülich, Germany

High temperature solid oxide electrolysis cells (SOECs) are a promising technology for intermittent energy conversion and storage. However, their wider adoption for commercial applications is still limited by the rapid degradation of the cells even under steady state conditions. This calls for an in-depth understanding of their structure-performance relationship during operation, especially at the chemically and kinetically active regions between the electrolyte, electrode, and gas phase. A recent study has also confirmed the existence of a so-called complexion region at such an interface (1, 2).
In this study, we aim to elucidate the atomic scale structure and chemistry at the boundaries between the electrolyte and electrode using Cs-corrected scanning transmission electron microscopy (STEM). For this purpose, we investigated a half cell consisting of LSM (La0.8Sr0.2)0.95MnO3-δ) || LSM YSZ composite, which represents the air electrode of the electrolysers, screen printed on top of a dense 8YSZ electrolyte (ZrO2 with 8 mol% Y2O3) after thermal treatment in air at 1173 K for 150 h without any biasing operations.
Our Electron Energy Loss Spectroscopy (EELS) analysis reveals the enrichment of divalent Mn2 not only at the LSM/YSZ interface, but also at the nearby YSZ grain boundaries, which is in contrast to the dominant Mn3 /Mn(2 ,3) within the bulk LSM (Fig. 1). Such a high level of Mn2 reflects an increased concentration of oxygen vacancies and may promote electron transfer for oxygen gas evolution and transport at these interfaces. With this result, we show that thermal annealing independently plays an important role for such an elemental segregation, in contrast to another report of cathodic polarisation being the main driving factor (3).
Moreover, with atomic-resolution imaging, numerous nano-scale domains with a characteristic two-fold ordered structure can be found within the YSZ grains in contact with the LSM (Fig. 2). Their origin is likely related to the formation of a solid solution of La3 and Mn2 within the YSZ structure, assisted by the long-range diffusion of these ions along the grain boundaries. This requires further insights.
In conclusion, our study offers atomic insights into the local structures at the electrolyte/electrode interface boundaries. The result is of scientific and technological importance toward the design of more efficient and durable cells.

References

(1) Türk, H. et al., Adv. Mater. Interfaces 2021, 8, 2100967.

(2) Türk, H. et al., ChemCatChem, https://doi.org/10.1002/cctc.202200300.

(3) Backhaus-Ricoult, M., Solid State Ion. 2006, 177, 2195-2200.

Fig. 1: a) HAADF images at the YSZ/LSM interface, b), c) Sequential spectra along the line scan indicated in (a) using energy dispersive spectroscopy EDS and EELS, respectively.

Fig. 2: Colour-enhanced high angle annular dark field (HAADF) image at the YSZ grain boundaries which shows the presence of nano-scale ordered structure domains.

Fig. 1

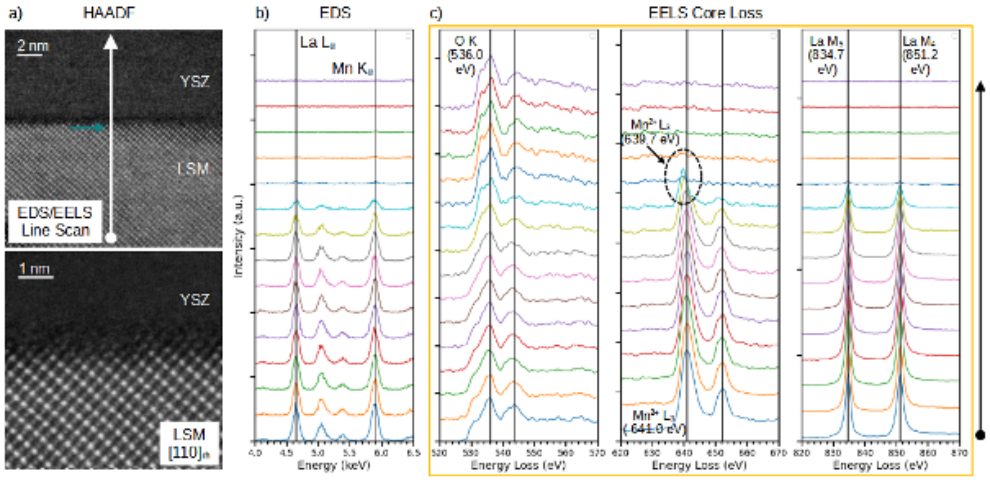
a)
HAADF
2 nm
YSZ
LSM
EDS/EELS
Line Scan
1 nm
YSZ
LSM
[110]m
b)
EDS
La Lα
Mn Kα
Intensity (a.u.)
Energy (keV)
c)
EELS Core Loss
O K
(536.0
eV)
Mn³⁺ L₃
(639.7 eV)
Mn⁴⁺ L₃
(644.0 eV)
La M₅
(834.7
eV)
La M₄
(851.2
eV)
Energy Loss (eV)
Energy Loss (eV)
Energy Loss (eV)

Fig. 2

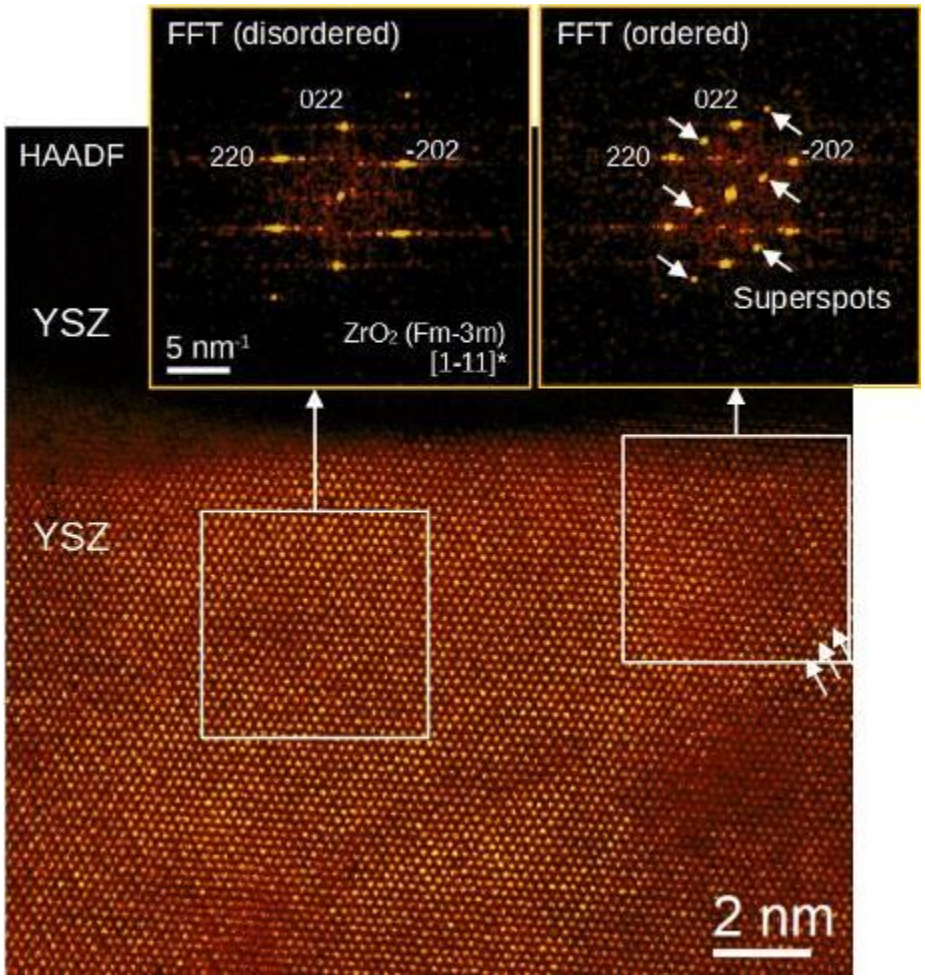
FFT (disordered)
022
220
-202
5 nm⁻¹
ZrO2 (Fm-3m)
[1-11]*
FFT (ordered)
022
220
-202
Superspots
HAADF
YSZ
YSZ
2 nm

MS1.P019

Advancing battery development with raman-SEM imaging

U. Schmidt[1], T. Meyer[1], D. Zimmer[2], T. Dieing[1]

[1]WITec GmbH, Applications, Ulm, Germany
[2]Oxford Instruments GmbH NanoAnalysis, Wiesbaden, Germany

Understanding structure-composition-property-performance relationships is essential for the development of more powerful, long-lived and affordable lithium ion batteries. Raman imaging microscopy can visualize structural and chemical information acquired from the battery"s internal components, such as details of their molecular composition, grain fractures, and electrode degradation. A confocal Raman system integrated with an SEM (RISE microscope) provides sufficient resolution to evaluate variations within single particles that can be correlated with structure. The atomic composition of a Li-ion cathode can be determined using EDS, leading to a comprehensive understanding of the cathode material. Fig. 1 shows correlative SEM, EDS and RISE images acquired from the same sample area of a Li-ion battery cathode composed of various grains. Although the particles appear as uniform in the SEM image (Fig. 1a), the EDS image shows that the particles contain a high amount of oxygen, shown in green (Fig. 1b). Red in the EDS image corresponds to the carbon matrix in which fluoride atoms could be detected. The Raman image (Fig. 1c) visualizes grains that consist of LiCoO2 in blue and LiNixCoyMnzO2 grains in green.

During electrochemical cycling of Li-ion batteries, microstructural changes can lead to a loss of energy, especially under rapid charging. Changes in performance are often nonuniform as a result of inhomogeneous degradation in which some regions in battery electrodes may experience more significant degradation than others. Such inhomogeneous deterioration can be studied using RISE microscopy. SEM images show deterioration of the large uniform lithium metal oxide-containing grains of pristine cathodes into sub-grains after rapid charging-discharging cycles. Raman images, on the other hand, reveal that not all Li-Metal-Oxide grains are affected in the same way by such rapid charging cycles and changes in the concentration of Li-Metal-Oxide composition is observed [1].

The integration of SEM with Raman imaging and EDS provides the opportunity to explore electrode inhomogeneity in a unique way. These results reveal heterogeneous deterioration of structure in Li-ion oxide cathode particles that can contribute to reduced performance and longevity in lithium-ion cells.

[1] K. Hollricher, D. Strom, and U. Schmidt, G.I.T. Imaging & Microscopy **2** (2021), 14 Wiley-VCH GmbH, Weinheim, Germany

Fig. 1: Correlative SEM (left) – EDS (middle) – RISE (right) images of a Li-ion cathode.

Fig. 1

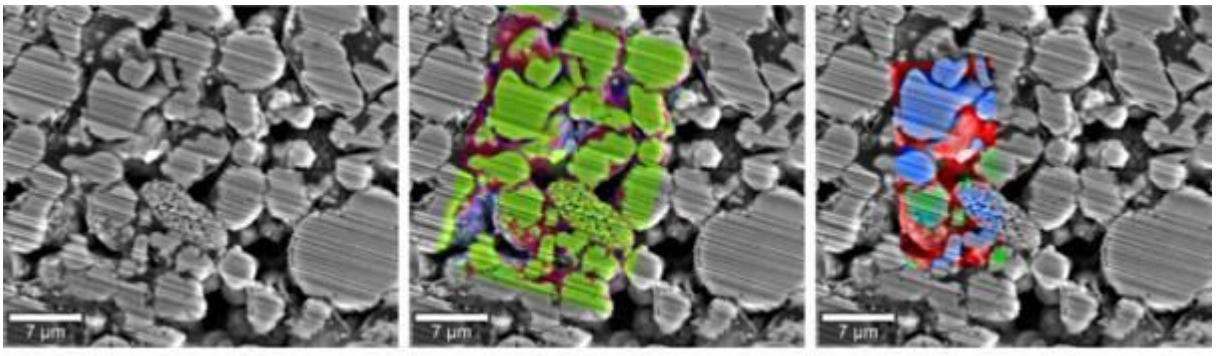

MS1.P020

Al current collector corrosion studies using liquid cell electron microscopy

M. Binggeli[1], V. Tileli[1]

[1]École Polytechnique Fédérale de Lausanne (EPFL), Institute of Materials, Lausanne, Switzerland

Lithium-ion batteries (LIBs) are the state-of-art rechargeable batteries. With the ongoing growth of the electric vehicles market, driven by the global tendency aiming toward the decrease of fossil fuel consumption [1, 2], the improvement of the current LIBs technology is required and more particularly their performance, their safety and their lifetime[1, 2]. The research in this domain has mainly been focused on electrodes and electrolyte optimization. However, the role of the current collectors (CCs) on the LIBs performance remains poorly understood [3]. The intrinsic complex and interlinked chemistry of LIBs requires a deconvolution of all effects to gain insights on the mechanisms of their degradation. In bulk devices, the cathode side CC is aluminum, which overall presents good corrosion resistance [1]. However, its corrosion is still occurring and the exact mechanism and its implication on the whole LIB cell are yet not fully understood [2, 3].

To understand the impact of the degradation of the Al CC on the performance of LIB, we use liquid cell electron microscopy (LCEM) [4]. This technique is enabled by using specific transmission or scanning EM holders that are enclosing liquid solution between two micro-electromechanical systems (MEMS) chips. On one of these chips, electrodes can be patterned and electrically biased for performing *in situ* or *operando* electrochemical experiments.

First, we developed in-house microfabricated MEMS chips that include a Al electrode and two Pt electrodes, all having a thickness of 50 nm. To determine appropriate electrochemical conditions for Al corrosion in LCEM, we performed linear sweep voltammetry (LSV) and chronopotentiometry (CP) measurement on the bench in a simplified chloride-based aqueous environment. Al corrosion was thus performed *ex situ* in 0.1 M NaCl solution (>99.5%, Carl Roth) using the Al electrode of produced chip as working electrode (WE), a Pt wire as counter electrode (CE) and a Ag/AgCl reference electrode (RE). CP was also performed *in situ* in a SEM, using on chip Al WE and Pt CE, and a bulk Ag/AgCl RE.

LSV results showed that the current increases at the pitting potential, resulting in a large part of the Al electrode being corroded within less than 10 s. This timescale is very short for properly imaging Al corrosion using LCEM. In contrast, during CP measurements, pit formation occurred between tenths of seconds and several minutes, indicated by the potential increase as a function of time. The constant potential that follows is indicative of active corrosion of the aluminum electrode. The large pits density suggests that CP measurements can be used to study the corrosion using LCEM. It is noted that gas bubble formation on the corroded region was also observed and its role on the corrosion is being investigated.

In conclusion, we report the development of a MEMS chip containing an Al electrode for use as CC on the positive electrode of the lithium-ion microbatteries. We also report that galvanostatic experiments are more appropriate than potentiodynamic for imaging Al corrosion using LCEM.

References:

[1] V. Etacheri et al., Energy Environ. Sci. **vol. 4** (2011), pp. 3243–3262, doi: 10.1039/c1ee01598b.

[2] L. Guo et al., J. Phys. Energy **vol. 3** (Jul. 2021), p. 032015, doi: 10.1088/2515-7655/ac0c04.

[3] T. Ma et al., J. Phys. Chem. Lett. **vol. 8** (2017), pp. 1072–1077, doi: 10.1021/acs.jpclett.6b02933.

[4] F. M. Ross, Science (80-.). **vol. 350** (2015), doi: 10.1126/science.aaa9886.

MS1.P021

Liquid-phase electron microscopy studies of Cu/Cu_2O nanocatalyst evolution during CO_2 electroreduction

S. Toleukhanova[1], P. Albertini[2], R. Buonsanti[2], V. Tileli[1]

[1]École Polytechnique Fédérale de Lausanne (EPFL), Institute of Materials, IMX, Lausanne, Switzerland
[2]École Polytechnique Fédérale de Lausanne (EPFL), Institute of Chemical Sciences and Engineering, Sion, Switzerland

Recent advancement in the design of novel catalysts for CO_2 reduction reaction (CO_2RR) increases demand for standardized methods for assessment of the catalyst's efficiency in CO_2 conversion to valuable hydrocarbons. Among the catalysts for CO_2RR, Cu nanocatalysts (Cu NCs) have attracted considerable attention due to copper's ability to produce a wide range of C_{2+} products and facet-dependent selectivity of Cu nanocrystals towards certain hydrocarbons[1]. However, Cu NCs undergo rapid restructuring upon CO_2RR which results in their deactivation. Therefore, a considerable amount of research is dedicated to discerning the degradation mechanisms of Cu NCs[2]. In this regard, in situ electron microscopy (in situ EM) has great potential as it allows the imaging of samples in a liquid medium under applied bias. Nevertheless, commercially available electrochemical chips with CO_2RR compatible glassy carbon (GC) working electrodes demonstrate a relatively narrow inert potential range in the cathodic region[3]. As a result, the competing hydrogen evolution reaction (HER) takes lead causing gas bubble formation, delamination, and electrical disconnection of GC electrodes within the short time of the reaction. In this work, we present correlative in situ transmission electron microscopy (TEM) and environmental scanning electron microscopy (ESEM) extended time studies of 40 nm Cu/Cu_2O NCs under CO_2RR conditions.

Samples for in situ EM experiments were prepared by drop-casting Cu/Cu_2O NCs on the membrane region of plasma-treated electrochemical chips. Thereafter, assembled in a holder the cell was filled with CO_2 saturated 0.1 M $KHCO_3$ electrolyte. Linear sweep voltammetry and chronoamperometry were utilized to drive CO_2 electroreduction. TEM images were acquired at an electron dose rate of 42 $e^{-}nm^{-2}s^{-1}$, and in ESEM experiments, a beam current was 36 pA. Energy-filtered TEM was used to enhance the contrast of catalyst particles in the liquid electrolyte.

In situ EM results indicate that in-house fabricated GC electrodes have a longer stability time as compared to values from the previous studies[4]: up to 4 min in TEM and 10 min in ESEM at a cathodic potential of -0.8 V_{RHE}. The shorter time in TEM is hypothesized to stem from an order of magnitude higher beam energy used in TEM. Nonetheless, utilizing TEM we were able to monitor the unique restructuring pathway of core-shell Cu/Cu_2O NCs inclusive of the facet selective core etching while the shell remained intact. The results were reproduced in ESEM, showing similar hollow cube particles after 10 min of CO_2RR. However, these observations diverge from bulk cell results, which points towards further studies needed to elucidate this different behavior.

In conclusion, in situ TEM and ESEM experiments are complementary for providing structural and morphological information on Cu NCs dissolution driven by CO_2RR at the nano- and meso-scale.

1. G. De Gregorio *et al. ACS catalysis* **10**, 4854-4862 (2020)
2. S. Popović *et al. Angew. Chem..* **59**, 14844-14854 (2020)
3. R. Girod *et al. Microscopy and Microanalysis* ***25***, 1304-1310 (2019)
4. J. Vavra *et al. Angew. Chem.* **60**, 1347-1354 (2021)

MS1.P022

Nanoparticle transformations retrieved by a combination of electron tomography and atomistic simulations

E. Arslan Irmak[1], W. Albrecht[2,1], A. Pedrazo-Tardajos[1], S. van Aert[1], S. Bals[1]

[1]EMAT and NANOlab Center of Excellence, University of Antwerp, Antwerp, Belgium
[2]Center for Nanophotonics, AMOLF, Amsterdam, Netherlands

The properties of metallic nanoparticles (NPs) are linked to their three-dimensional (3D) structure. However, these particles exhibit structural and morphological transformations under the conditions relevant to their applications, and subtle changes in the structure may significantly modify their performance. Hence, an atomic-scale understanding of the transformations under realistic conditions has a vital importance in preserving the functionalities of metal NPs. *In situ* transmission electron microscopy is a valuable technique to observe the dynamics of NPs. Combining the *in situ* experiments with fast electron tomography even enables 3D *in situ* measurements. [1] Despite the progress in this field, atomic-scale transformations cannot always be understood by experimental techniques alone as these measurements do not provide the necessary time or spatial resolution. In this study, we have demonstrated that such limitations can be overcome by linking 3D characterization techniques with atomistic simulations.

A first example is the *in situ* 3D investigation of the thermal stability of Au@Pt NPs, which is important to understand their behavior during catalytic reactions. However, since the heating cycles were interrupted during the experiments to acquire tomography tilt series, the ongoing transformations could not be fully monitored by experimental observations. We therefore used experimentally determined 3D reconstructions of Au@Pt NPs as realistic input models (Fig 1) for molecular dynamics (MD) simulations. In this manner, it has been possible to unravel atomic-scale dynamics at elevated temperatures, and to systematically investigate the parameters that influence the thermal stability of these NPs. [2]

This approach becomes even more important when the environmental triggers cannot be applied *in situ*. For example, in many optical and photothermal applications, Au NPs are excited by laser irradiation. However, due to the ultrafast time scales, laser-induced restructuring of NPs cannot be monitored by experiments. To do so, tomography tilt series of the same NP was acquired before and after laser excitation (*ex situ*) and the laser heating regime was modelled to mimic the experiments. By performing MD simulations based on the 3D reconstructions and the heating regime, laser-induced complex atomistic rearrangements causing shape and structural deformations have been unraveled (Fig 2). [3]

The approach presented in this study is of great potential as it enables performing simulations based on the experimentally measured surface structure. Moreover, it enables us to capture the ongoing processes at the atomic scale, as well as to understand the driving mechanisms behind the complex transformations that possibly occur during applications.

References

[1] W. Albrecht, S. Bals, *J. Phys. Chem. C* 124 (2020), 50, 27276–27286.

[2] A. Pedrazo-Tardajos, E. Arslan Irmak et al., *ACS Nano* 16 (2022), 6, 9608–9619.

[3] W. Albrecht, E. Arslan Irmak et al., *Adv. Mater.* 33 (2021), 2100972.

[4] This work was supported by the European Research Council (770887 PICOMETRICS to SVA and 815128 REALNANO to SB, 823717 ESTEEM3), Marie Sklodowska-Curie Actions (797153 SOPMEN to WA), and Research Foundation Flanders (G.0267.18N, G.0502.18N, G.0346.21N).

Fig 1. 3D reconstructions and corresponding 3D models of a Au (a,b) and Au@Pt (c,d) NP. [2]

Fig 2. 3D reconstructions of a Au NP before (a) and after (b) laser excitation. c) The results of MD simulations. [3]

Fig. 1

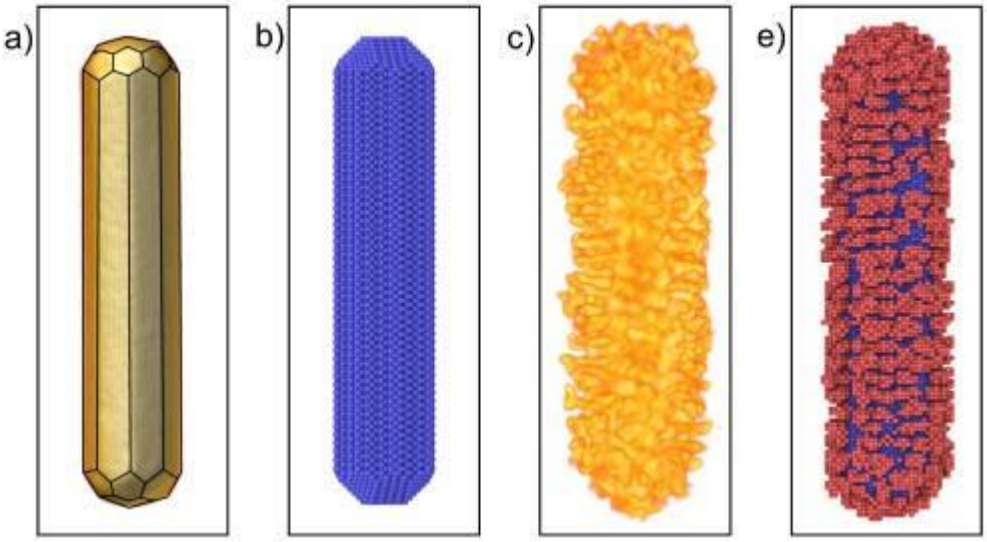
a)
b)
c)
e)

Fig. 2

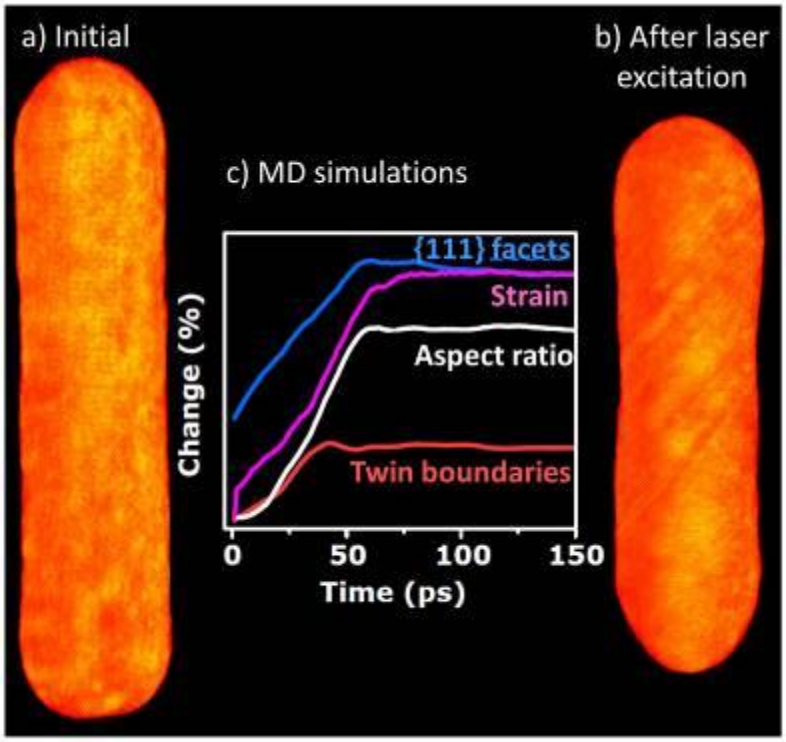
a) Initial
b) After laser excitation
c) MD simulations
{111} facets
Strain
Aspect ratio
Twin boundaries
Change (%)
0
50
100
150
Time (ps)

MS1.P023

Cryo-electron microscopy for the study of sensitive energy materials

Z. Kochovski[1], Y. Xu[1, 2], Y. Lu[1, 3]

[1]Department of Electrochemical Energy Storage (CE-AEES), Helmholtz-Zentrum Berlin für Materialien und Energie, Hahn-Meitner-Platz 1, 14109 Berlin, Germany
[2]Research Laboratory of Electronics, Massachusetts Institute of Technology, Cambridge, MA, 02139 USA
[3]Institute of Chemistry, Potsdam University, Karl-Liebknecht-Str. 24–25, 14476 Potsdam, Germany

INTRODUCTION

As current batteries are nearing their theoretical limits, future generation high-energy-density battery chemistries demand a fundamental understanding of their operation and failure pathways at the atomic level. However, most energy materials and most notably lithium (Li) are sensitive and unstable under the electron beam in conventional TEM. This problem has been addressed in recent years by the application of Cryo-EM methods, borrowed from structural biology [1].

OBJECTIVES

A major obstacle hindering the implementation of Li-metal batteries is the limited understanding of the Li nucleation and growth mechanisms. Furthermore, the solid-electrolyte interphase (SEI) is essential for the reversibility of the lithium Li-metal electrode, but the lack of in-depth understanding of its structure and unclear formation/evolution mechanisms have significantly hampered its rational design. We applied Cryo-EM and Cryo-ET to unravel the morphology and inner structure of Li deposits and to investigate the morphological evolution of Li deposition and the interface confined SEI.

MATERIALS & METHODS

We have used a JEM2100 Cryo-TEM equipped with a bottom mounted 4k TVIPS F416 camera and a Gatan 914 cryo-transfer holder. We have used a cryo-transfer procedure where the TEM grids containing the Li deposits are transferred to the TEM column without exposure to the ambient environment. Cryo-EM micrographs and tilt series have been acquired using SerialEM. Tilt series have been processed with IMOD and segmentation has been done in Amira.

RESULTS

In one work, Cryo-EM revealed two distinct types of Li deposits, depending on the current density: Li-balls, which were found to be primarily amorphous and Li-whiskers, which were found to be highly crystalline [2]. Additionally, their solid electrolyte interface (SEI) layers showed a difference in structure and composition, correlated to the underlying deposition mechanism (Fig. 1). In another work (accepted manuscript), we used Cryo-EM to reveal the morphological evolution of the SEI layer during Li plating, showing a thick (~100 nm) and wrinkled SEI layers forming in the initial stage, which progressively stretched and thinned to up to 7nm after 24 min of Li deposition (Fig 2a-c). Cryo-EM and Cryo-ET also revealed in detail the morphologies of the Li deposits (Fig2d-i).

CONCLUSION

Cryo-EM and Cryo-ET, which are methods well established in the field of structural biology, could be well adapted to the study of sensitive energy materials.

REFERENCES

[1] Y. Li et al., *Chem*, **4** (2018), pp. 2250-2252

[2] K. Dong et al., *ACS Energy Lett*. **6** (2021), pp. 1719-1728

FIGURE LEGENDS

Fig. 1 (left) Cryo-EM micrographs of Li-balls and Li-whiskers; (right) Schematic illustrations of the SEI layer structures of Li-balls and Li-whiskers. Adapted from [2].

Fig. 2 Morphological evolution of Li deposition and interface-confined SEI. (a-c) Cryo-EM images of SEI layers on 150 s, 12 min, and 24 min Li deposits; (d-f) Cryo-EM micrographs; (g-i) Cryo-ET iso-surface segmentations.

Fig. 1

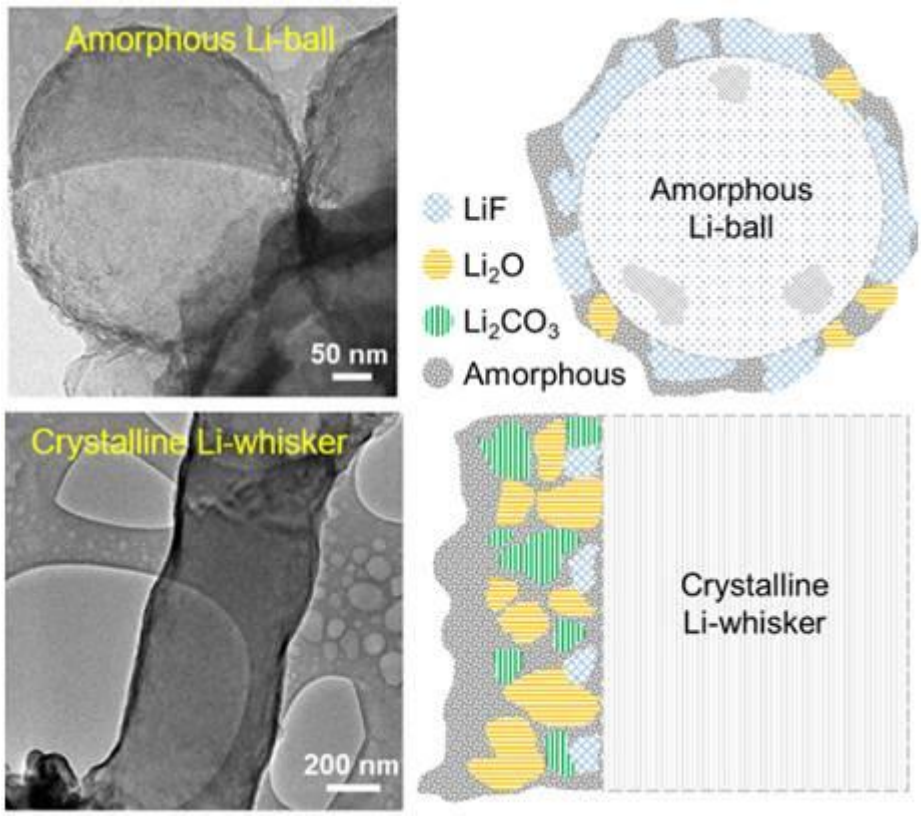

Fig. 2

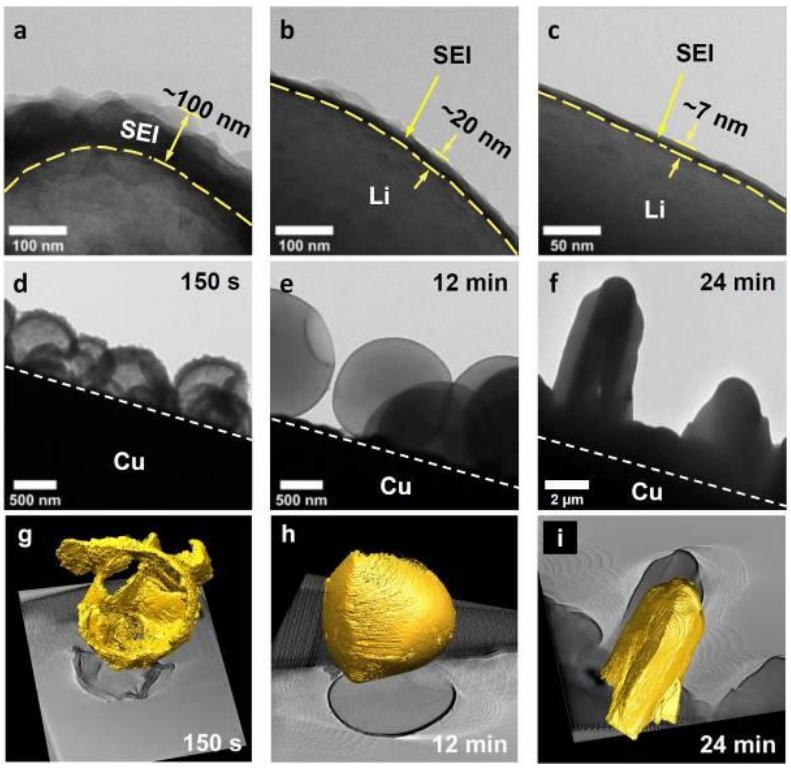

MS1.P024

Unravelling the selective oxidation of 2-propanol on Co_3O_4: *operando* TEM as a central part in a multi-modal *operando* toolset for understanding catalytic reactions

T. Götsch[1], D. Cruz[1], A. Rabe[2,3], M. Dreyer[2], M. Behrens[2,3], R. Schlögl[1,4], A. Knop-Gericke[1,4], T. Lunkenbein[1]

[1]Fritz-Haber-Institut der Max-Planck-Gesellschaft, Department of Inorganic Chemistry, Berlin, Germany
[2]Universität Duisburg-Essen, Faculty of Chemistry and Center for Nanointregration Duisburg-Essen (CENIDE), Essen, Germany
[3]Christian-Albrechts-University Kiel, Institute of Inorganic Chemistry, Kiel, Germany
[4]Max Planck Institute for Chemical Energy Conversion, Department of Heterogeneous Reactions, Mülheim an der Ruhr, Germany

Selective oxidation reactions, in many cases catalyzed by noble metals, are some of the most important industrial processes, used to synthesize base chemicals such as acetone from 2-propanol. Consequently, finding more efficient catalysts that are based on cheaper and more abundant materials is desirable. One example is Co_3O_4, which is highly active in the oxidation of 2-propanol to acetone.

On this catalyst, the reaction is split into two distinctive activity regimes: one centered around 150 °C ("low-temperature") and one up to 300 °C ("high-temperature"). While the catalyst is very selective at low temperature, it deactivates rapidly. At higher temperature, there is no deactivation, although total oxidation to CO_2 and H_2O becomes a prominent side reaction. The mechanism behind the low temperature deactivation is still unclear, with different reasons being postulated such as changes in oxidation state or simple carbon deposition.[1]

Here, we present a combined *operando* investigation of the selective 2-propanol oxidation using *operando* TEM (OTEM) together with synchrotron-based near-ambient pressure X-ray photoelectron spectroscopy (NAP-XPS) under near-identical conditions in order to unravel the origins behind the low-temperature activity region and its deactivation. OTEM was conducted using a DENSsolutions Climate holder and a self-built gas feeding and analysis setup[2] at an image-corrected ThermoFisher Scientific Titan 80–300.

After pre-sintering (600 °C, 20% O_2/He) of the nanocrystalline catalyst, hexagonal Co_3O_4 platelets derived from thermal decomposition of $Co(OH)_2$ precursors, the introduction of the reaction feed (4.5% 1:1 O_2/2-propanol in He, total pressure of 500 mbar) leads to the formation of nanoparticles beneath the {111} facets already at room temperature (see **Fig. 1**), which coincides with a slight reduction of the cobalt species as evidenced by NAP-XPS. Subsequent increases in temperature elicit an exsolution of these particles before they coalesce again to an overlayer at around 200 °C, coinciding with the transition to the high-temperature regime. At 300 °C, they roughen up significantly, accompanied by a continuous increase of Co(II) in the XPS spectra and increased conversion. According to HRTEM recorded under reaction conditions, these exsolved particles are CoO, although there is no bulk phase transition occurring. Cooling down from 300 °C back to room temperature reveals a lattice expansion, most likely due to the formation of O vacancies.

When re-oxidizing in O_2/He at 600 °C, the nanoparticles are dissolved, and the CoO signals in the SAED patterns disappear. Additionally, the original lattice parameter is recovered too.

As no carbon deposition is observed in OTEM and NAP-XPS reveals no significant build-up during the reaction either, this investigation indicates that the rapidly deactivating nature of the low-temperature regime is not simply due to carbon accumulation. Instead, because the partial reduction of Co(III) to Co(II) already occurs at room temperature, there possibly is a more complex reason for the deactivation. More experiments are currently being conducted to probe the chemical nature of the catalyst surface.

(1) Anke *et al. ACS Catal.* **2019**, *9*, 5974–5985

(2) Plodinec *et al. Microsc. Microanal.* **2020**, *26*, 220–228

Fig. 1: *Operando* bright field images during the oxidation of 2-propanol on Co_3O_4 show the restructuring of the {111} facets.

Fig. 1

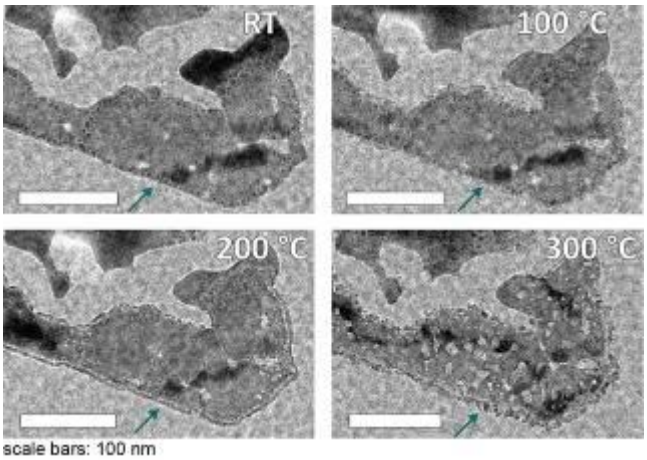

scale bars: 100 nm

MS1.P025

Bridging scales: imaging at intermediate length scales reveals the long-range effect of hydrogen spill-over

H. Frey[1], A. Beck[2,3], A. Kleibert[4], J. A. van Bokhoven[2,3], M. G. Willinger[1,5]

[1]ETH Zurich, ScopeM, Zurich, Switzerland
[2]ETH Zurich, D-CHAB, Zurich, Switzerland
[3]PSI, LSK, Villigen, Switzerland
[4]PSI, LSC, Villigen, Switzerland
[5]TU Munich, Fakultät für Chemie, Garching, Germany

In catalysis, electron microscopy is often employed to reveal atomistic information regarding the structure and composition of the fresh catalyst or to study, post-mortem or in-situ, reaction induced changes. Information is then oftentimes linked to data acquired with integral methods such as mass spectrometry or X-ray based spectroscopy methods. However, both methods fail to resolve processes that are dominant at intermediate length scales. They involve the collective transport of heat or mass and play a role in the formation and propagation of reaction fronts [1], for example. X-ray Photoelectron emission microscopy (XPEEM) enables wild field spectral imaging of planar surfaces in the micrometer range and is therefore suited to fill the information gap between local, atomic-level observation and averaging integral methods.

Hydrogen spillover concerns the surface migration of activated hydrogen atoms from a metal catalyst particle, on which molecular hydrogen dissociates, onto the catalyst support. It is of high importance for heterogeneous catalysis, hydrogen storage materials, and fuel cell technology. Its occurrence on metal oxide surfaces is established [2], yet questions remain about how far from the metal center spillover is reaching.

By employing in-situ XPEEM on a planar model catalyst [3], we were able to gather direct evidence that spillover is occurring over several microns across the oxide surface [4]. The wide filed nature of XPEEM and the tunability of the incoming X-ray beam allows for quantification of the chemical states of the oxide surface in a time resolved manner with spatial resolution. These findings and the derived understanding at which temperatures hydrogen spillover in affecting the surface will help to improve and exploit the process of hydrogen spillover for application.

Figure 1. Time and spatial resolved oxidation state of oxide film during exposure to hydrogen. Color resembles oxidation state: Red = fully oxidized, blue = reduced. Reduction is initiated at metal (indicated by lines) and propagates over the oxide support.

1] C. Barroo, Z.-J. Wang, R. Schlögl, M.-G. Willinger, R. Schlögl. **Nat. Catal.**, 2019, 3, 30–39.

[2] Prins R. ***Chem. Rev***., 2012, 112(5), 2714-2738

[3] Karim W., Spreafico C., Kleibert A., Gobrecht J., Vandevondele J, Ekinci Y., van Bokhoven J. A. **Nature**, 2017, 541(7635), 68-71.

[4] Beck A., Frey H., Willinger M-G., Kleibert A., van Bokhoven J. A. *in preparation*

Fig. 1

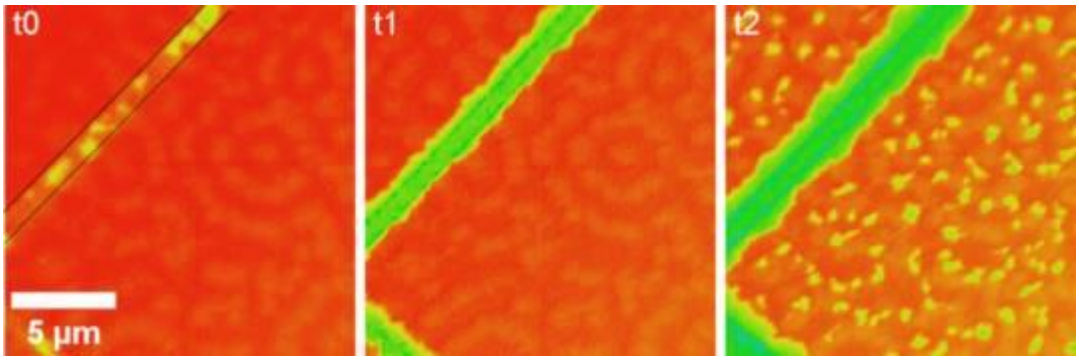

MS1.P026

*Bi*phasic layered material strengthened by tenon-and-mortise structure for robust sodium ion batteries cathode

T. Yang[1], M. Yang[2], L. Jin[1], Y. Xiao[2], R. E. Dunin-Borkowski[1]

[1]Forchungszentrum Juelich, ER-C-1, Jülich, Germany
[2]Peking University Shenzhen Graduate School, School of Advanced Material, Shenzhen, China

Layered cathode materials are commonly used in lithium and sodium ion batteries, but their structures prone to degradation during battery operation. The rigid fracture is the one of the key factors for degradation of functional materials, in particular the layered materials. Recently, the microstructure and defect engineering have broken a new ground in decreasing the rigid fracture and facilitating electrochemical performance of cathode materials. Herein, we design a buffer structure (tenon-and-mortise structure) at the biphasic boundary of Na0.67Fe0.1Cu0.1Mn0.8O2 layered oxide with a P'2/P2 biphasic structure (denoted as BP), which can inhibit the destructive evolution of layered oxides. We observe that the biphasic boundaries overlap by atomic-resolution scanning transmission electron microscopy (STEM) with spherical aberration correction. As shown in Figure 1, this phases overlap is deemed to a tenon-and-mortise structure that has been widely served as the buffer structure in traditional Chinese wooden architecture [1]. The structure Rietveld refinement combined with neutron powder diffraction (NPD) and X-ray diffraction (XRD) determine that the ration of P'2/P2 phase in BP is about 70%:30%. In addition, equipped with X-ray absorption spectroscopy (XAS), X-ray photoelectron spectroscopy (XPS), and electrochemical tests, we find that BP with low vacancy concentration is able to experience reversibly deeper desodiation/sodiation benefitted from the enhanced biphasic structure. Consequently, BP provides a competitive specific capacity of 200 mAh g-1 at 0.05C (1C = 150 mA g-1) and a superior cycling life for the retention of 84.2% after 1000 cycles at 8C. *Ex-situ* HAADF-STEM characterizations of cathode materials after different cycles illustrate that the dense tenon-and-mortise structures are stable under the operating condition. Furthermore, *in-situ* XRD demonstrates that the competition between the oxidation/reduction of transition metals and desodiation/sodiation in dense tenon-and-mortise structures buffers the interlayer spacing variation of BP, resulting in a mild snake-shaped evolution. This work provides an artful phase engineering to strengthen the original layered structure of SIBs cathodes without sacrificing the intrinsic properties.

Figure 1. (a,b) HAADF and ABF-STEM images of biphasic boundary for BP along [010] zone axis. The line scan profiles along the corresponding rectangles are shown on the right of (a). (c, d) HAADF and ABF-STEM images of biphasic boundary with clear tenon-and-mortise structure. (e) Schematic diagram of the biphasic boundary reinforced by tenon-and-mortise structure.

[1] Q. N. Liu, Z. Hu, W. J. Li, C. Zou, H. L. Jin, S. Wang, S. L. Chou, S. -X. Dou, Sodium transition metal oxides: the preferred cathode choice for future sodium-ion batteries? Energy Environ. Sci. 14, 158-179 (2021).

Fig. 1

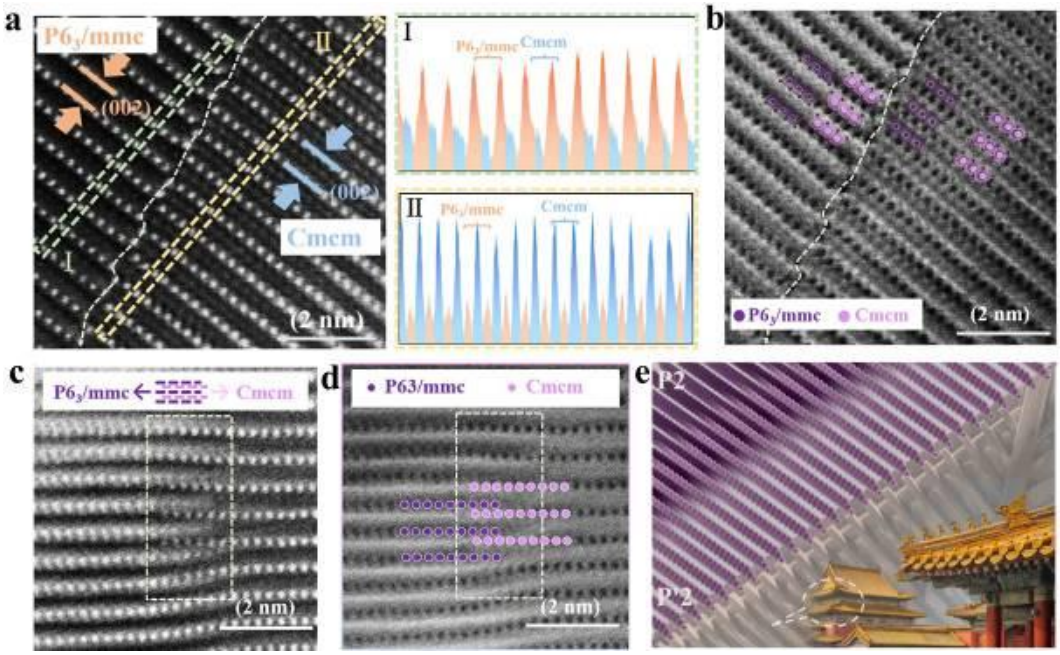

MS1.P027

Correlating electrocatalyst re-structuring with its impact on catalytic properties

S. W. Chee[1], A. Yoon[1], F. Yang[1], B. Roldan Cuenya[1]

[1]Fritz Haber Institute of the Max Planck Society, Interface Science, Berlin, Germany

1. Introduction

Establishing a direct link between the morphology of a catalyst and its associated properties is a non-trivial challenge. It is especially complicated in electrocatalytic reactions where the catalysts can re-structure and further adopt thermodynamically unfavorable motifs due to kinetic limitations. In addition, since most property measurement techniques (such as voltammetry and gas chromatography) average over the entire catalyst ensemble, a detailed accounting of the catalyst morphologies and their relative distributions at different points of the reaction is needed to establish such correlation. Electrochemical cell transmission electron microscopy (EC-TEM) is one method that can provide us with such detailed information.

2. Objectives

The aim of our research is to reveal the restructuring dynamics of catalysts during reaction and to correlate these dynamics to their impact on the catalytic properties. In particular, I will focus on my group's EC-TEM studies of Cu-based catalysts for the electrochemical reduction of carbon dioxide (CO_2RR).

3. Materials & Methods

We adopted catalyst synthesis strategies that allow us to tune the catalyst morphology, size, and loading in a controlled manner while also being applicable to different support geometries such that we have near identical electrocatalysts in different setups. The *in situ* experiments are conducted inside a 300 kV Titan TEM from Thermo Fisher in STEM mode using a Hummingbird Scientific Bulk Liquid Electrochemistry holder and with an electrolyte of CO_2-saturated 0.1 $KHCO_3$. The samples were also characterized *ex situ* after reaction. The activity and selectivity of the catalysts were measured on the benchtop using standard techniques, such as gas chromatography.

4. Results

I will discuss two examples of our work, one using electro-deposited Cu_2O cubes and the other using lithographically patterned Cu-island arrays. Our studies using Cu_2O cubes with controlled size and loading showed that drastic reconstructions occurred in the first few minutes of potential application [1]. More importantly, the catalyst ensemble is made up of two motifs, fragmented cubes, and re-deposited nanoparticles. Then, we established the impact of the observed dynamics on catalytic performance by comparing the behavior of differently sized cubes with their time-resolved changes in product selectivity.

Next, Cu-islands were used to follow how iodide species in the electrolyte cause the formation of CuI pyramids and how these pyramids restructure under reaction conditions [2]. While the CuI pyramids also restructure drastically like the Cu_2O cubes, the catalyst morphology is different, taking the form of long fragmented filaments. Furthermore, our EC-TEM observations suggest that the presence of residual iodide stabilizes Cu^+ species that have a known beneficial effect on hydrocarbon selectivity in CO_2RR.

5. Conclusions

Our results show how the re-structuring of Cu-based catalysts during CO_2RR can be very complex and how EC-TEM can provide valuable insight into the morphologies present during reaction.

References:

1. Grosse, P. *et al.* Dynamic Transformation of Cubic Copper Catalysts during CO2 Electroreduction and its Impact on Catalytic Selectivity. *Nat. Commun.* **12**, 6736 (2021).
2. Yoon, A., Poon, J., Grosse, P., Chee, S. W. & Roldan Cuenya, B. Iodide-mediated Cu catalyst restructuring during CO_2 electroreduction. *J. Mater. Chem. A* **10**, 14041–14050 (2022).

MS1.P028

Investigation of complex nanostructured particles made of Cu and Cu-oxide for catalytic applications

J. Müller[1], J. Frohne[1], C. Wiktor[1], B. Butz[1]

[1]University of Siegen, Micro- and Nanoanalytics Group, Siegen, Germany

Nanoparticles are widely used for catalytic applications. Their catalytic properties are largely defined by their size, shape, and surface chemistry. In general research is focused on small particles or, in recent years, even on single atoms. However, their synthesis is often complicated, involves toxic and expensive chemicals and the amount that can be produced is limited. Moreover, the particles themselves may pose a threat to the environment when they leak into fresh water as their size makes them difficult to filter. Instead of using single nanoparticles, an alternative way is to employ highly porous materials for catalysis. Like nanoparticles, they exhibit enormous surfaces which provide active sites for catalytic reactions. Moreover, they are bulky and are therefore much easier to handle than nanoparticles. In many cases, however, only the first few surface-near pores are available for the catalytic reaction. Deeper pores are hardly accessible to educts and products due to kinetic transport limitations.

The aim of this work is to produce larger (up to 2 µm) nanostructured metallic and metal-oxide particles that contain pores in the range of a few tens of nanometers. This way, the advantages of using particles and porous systems are combined as they are on the one hand small enough to be accessible from all sides while on the other hand are large enough to be handled easily. The pores in the materials used for this work are first produced by using a well-known controlled oxidation process called dealloying where a less noble component of a metallic solid solution is leached out in an acid bath. At the same time, the more noble component forms a bi-continuous open pore network. This process is well-established for noble elements like Au and Pt. Recently, transition metals (Cu, Ni, etc.) have come into research focus as cheaper alternatives. The Cu particles used in this work are produced by first dealloying a bulk Cu0.3Mn0.7 alloy in HCl or H2SO4 to form the porous network with pore sizes between 10-100 nm followed by sonication to break down the porous structure into smaller fragments. The resulting particles are complex in shape and highly porous (fig. 1, TEM bright field image). The size of the porous particles ranges between 200 nm and 2 µm. After fabrication, the reactive Cu particles can further be modified or functionalized. By a simple and controlled oxidation process in air, core-shell particles with a defined oxide layer can be produced, whereas fully oxidized particles form a hollow-core structure (fig. 2, HAADF-STEM image).

In order to employ such particles for catalytic applications, it is necessary to reveal the complex structure along the formation process of the Cu particles as well as their respective oxides in a three-dimensional manner. Therefore, tomography in scanning transmission electron microscopy mode has been performed at different stages of the preparation route. To prove the nature of the oxidation state of the Cu, electron energy loss spectroscopy was performed.

Moreover, small amounts of Mn below 1 at% can still be found in the fully processed particles by energy dispersive X-ray spectroscopy. It is envisioned that the remaining Mn(-oxide) can act as a dopant in the particle boosting its catalytic performance. Therefore, first tests are planned to evaluate the catalytic behavior of those particles at different oxidation conditions.

Fig. 1

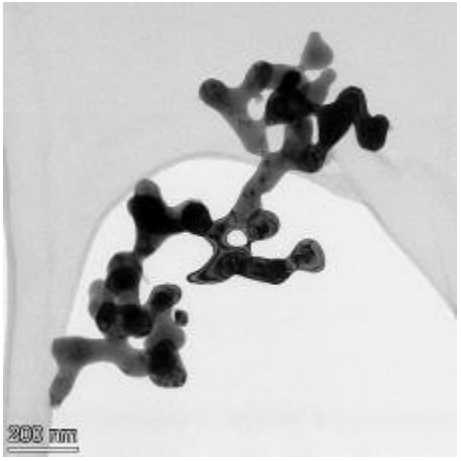

Fig. 2

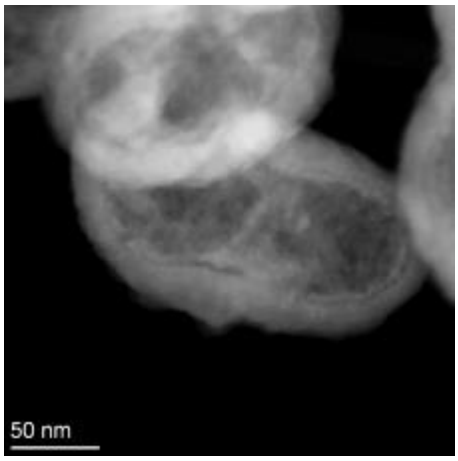

MS1.P029

STEM-EELS investigation of Cu/CeO_2-TiO_2 used in CO oxidation

N. Rockstroh[1], C. R. Kreyenschulte[1], J. Mosrati[1], T. H. Vuong[1], J. Rabeah[1], A. Brückner[1]

[1]Leibniz-Intitut für Katalyse e.V. (LIKAT Rostock), Rostock, Germany

The heterogeneous catalytic oxidation of CO is an important reaction which impacts many technical applications such as fuel cells (preferential oxidation of CO instead of H_2), air purification, exhaust-gas emission treatment, CO sensors and CO_2 lasers.[1] Therefore, research focuses on the development and investigation of active and selective catalysts, preferentially containing abundant metals. Copper is a promising and well-investigated candidate, which, upon immobilization on CeO_2, forms redox-active Cu^{2+}/Cu^{+} couples. CeO_2 itself has a high oxygen mobility and the ability to form Ce^{4+}/Ce^{3+} couples, two properties which can be even improved by incorporation of titanium.

Three Cu doped CeO_2-TiO_2 catalysts and the pure support were prepared by a sol-gel method adding 0 (**support**), 0.06 (**Cat1**), 0.26 (**Cat2**), or 0.66 wt% Cu (**Cat3**) with **Cat2** showing the best catalytic performance. To elucidate structure-activity relationships, the materials have been characterized by XRD, Raman and IR spectroscopy, STEM-EELS, NAP-XPS, and operando EPR. STEM-EELS was thereby applied to spatially resolve potential differences in the oxidation state of the containing elements.

A probe corrected JEOL JEM-ARM200F (Schottky emitter) with a Gatan Enfinium ER EELS were used for electron microscopic investigation of the catalysts. A rather high beam current was applied to keep the acquisition time low. The FWHM of the zero-loss peak (ZLP) was about 1.2 eV and the lack of de-scan was compensated by the DualEELS mode. The spectra were recalibrated at each pixel by the position of ZLP.

Cat2 (0.26 wt% Cu) shows the best catalytic performance. The relative intensity of the Raman band at 463 cm^{-1} and the appearance of separate CeO_2 entities observed by STEM increase with the Cu content. However, Cu is not visible in the STEM HAADF and BF images due to its small Z contrast and high dispersion. This high dispersion could be proven by EPR and DRIFTS. STEM-EELS enabled the determination of the oxidation state of Ce and its distribution with respect to TiO_2 (Fig. 1 and 2). It revealed that Ce is present either as Ce^{3+} in well-dispersed form or as Ce^{4+} in separate CeO^2 crystallites. It could be shown that Ce^{3+} and Ti^{4+} form a Ce-Ti oxide solid solution.

Figure 1. STEM ADF image of **Cat2** (left) with the corresponding Ce M edge electron energy loss (EEL) spectra of the highlighted areas (right). The shape and intensity of the edge signal points to Ce^{3+} in Area 1 and Ce^{4+} in Area 2.[2] Reprinted with permission from ref [1]. Copyright © 2021, American Chemical Society.

Figure 2. STEM ADF image of **Cat2** (left) with an overlaid false color elemental map. On the right, the distribution of two different cerium species (Ce-M (a) and Ce-M (b)) and titanium is shown independently as well as in a single-color elemental map. Reprinted with permission from ref [1]. Copyright © 2021, American Chemical Society.

Using STEM-EELS with this catalyst system, it was possible to benefit from this additional spectroscopic method by providing information on the Ce oxidation state distribution which is not possible with EDXS. Although EPR and XPS provide already evidence for Ce^{3+}, its exact localization is only possible with STEM-EELS.

[1] J. Mosrati, A.M. Abdel-Mageed, T.H. Vuong, R. Grauke, S. Bartling, N. Rockstroh, H. Atia, U. Armbruster, S. Wohlrab, J. Rabeah, A. Brückner, *ACS Catal.* **2021**, *11*, 10933-10949.

[2] Y. Zhang, S. Bals, G. Van Tendeloo, *Part. Part. Syst. Charact.* **2019**, *36*, 1800287.

Fig. 1

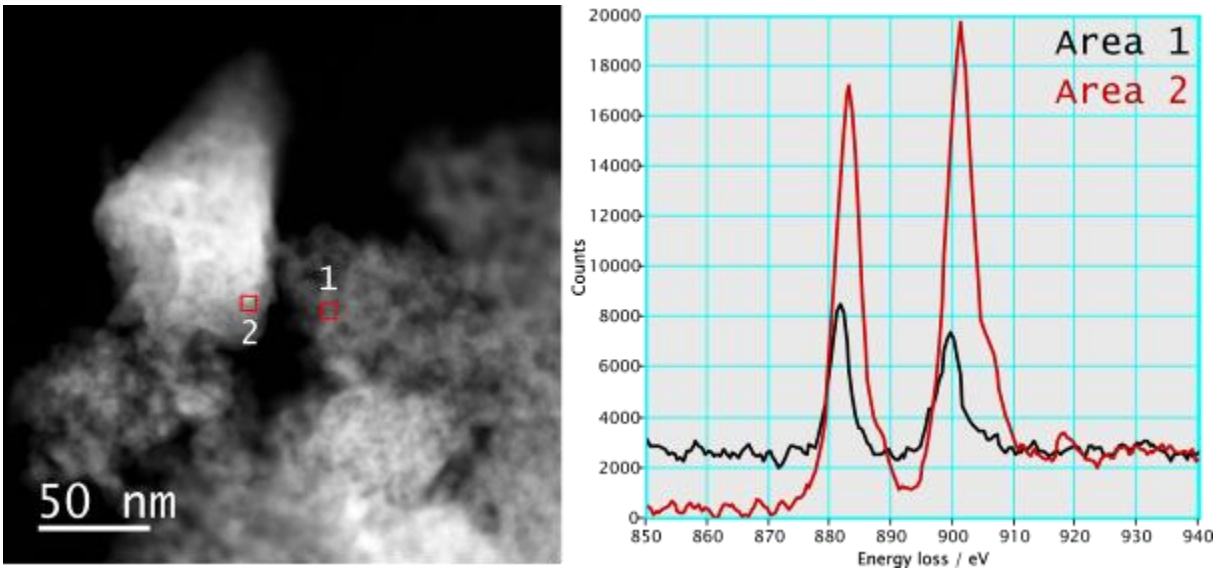
1
2
50 nm
Area 1
Area 2
Counts
Energy loss / eV
20000
18000
16000
14000
12000
10000
8000
6000
4000
2000
0
850
860
870
880
890
900
910
920
930
940

Fig. 2

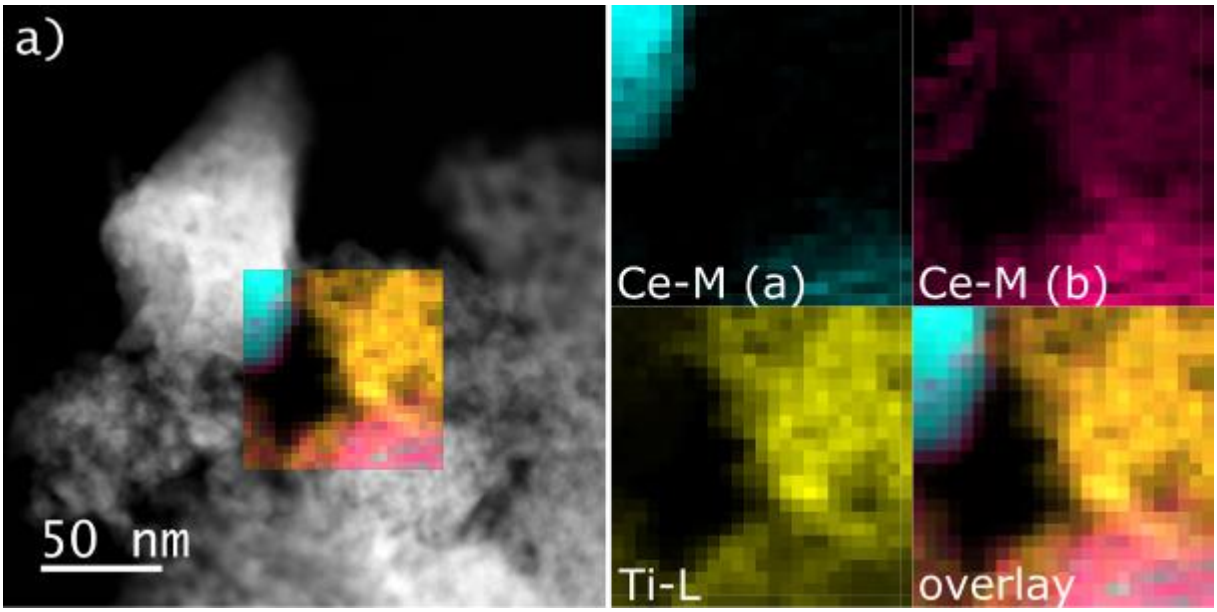
a)
50 nm
Ce-M (a)
Ce-M (b)
Ti-L
overlay

MS1.P030

Cross-sectional preparation of complex energy devices and their characterization by advanced microscopic methods

M. Hepp[1], V. Muhl[1], T. Dursun[1], B. Butz[1]

[1]University of Siegen, Micro- and Nanoanalytics Group, Siegen, Germany

Energy devices like batteries, fuel cells and solar cells are assembled from multiple functional components with different material properties. To gain a fundamental understanding of structure-property relations, to systematically contribute to performance enhancement and to unravel device degradation and failure mechanisms, high quality cross-sections of entire devices or of as large regions as possible are required. Since many devices not only consist of different classes of materials but also of liquid and/or air sensitive components, working under cryogenic and/or inert conditions is essential to conserve their pristine state.

To enable scale-bridging cross-sectional characterization of those devices all the way down to the atomic level, we utilize different preparation tools. A novel self-built cryo-cutter allows us to produce cross-sections of entire devices, e.g., pouch-cells, in a quick one-step process and to observe them in their pristine state by OM even on the centimeter scale. For smaller scales (cryo-)ultramicrotomy as well as FIB are routinely applied and capable to prepare cross-sections not only for investigations by OM and SEM but also for (atomic resolution) TEM, as high-quality thin samples below 50 nm are provided.

In this contribution we demonstrate the scale-bridging capabilities of those preparation techniques applied on various devices and their components in conjunction with advanced (electron) microscopic and spectroscopic methods. Examples include devices like batteries (Fig. 1) and complex PEM fuel cells (Fig. 2) as well as battery components (Fig. 3). The applied techniques are ideally suited to investigate the integrity of complete devices as well as the interfaces of individual layers and components in terms of their morphology and contact as well as the systematic identification of their composition and chemical bonding states.

Part of this work was performed at the Micro-and Nanoanalytics Facility (MNaF) of the University of Siegen.

Fig. 1

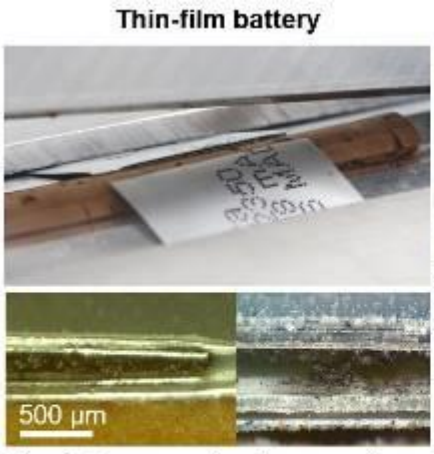

Fig. 1: Cross-sectional preparation of commerical available Li/MnO_2 thin-film battery by self-built cryo-cutter tool

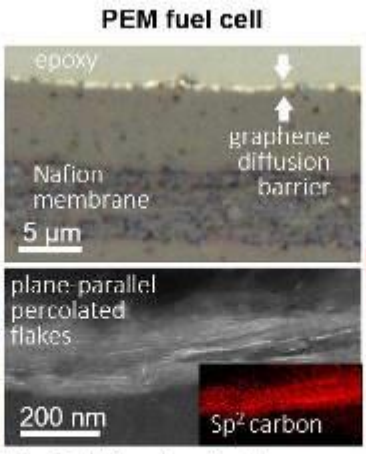

Fig. 2: Ultramicrotomic cross-section of graphene-coated nafion membrane

Ruhkopf et al, ArXiv (2022) 04509

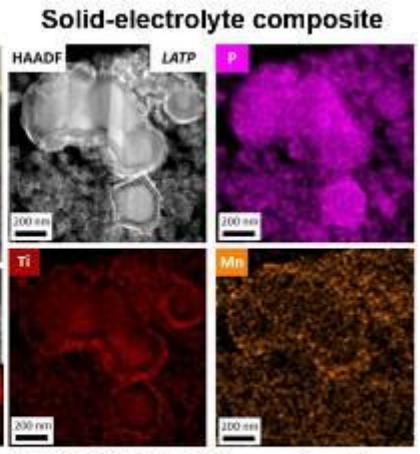

Fig. 3: STEM-EDX mapping of cross-section of solid-electrolyte composite prepared by FIB

Beaupain *et al*, Appl Mater & Interfaces 13 (2021) 47488

MS1.P031

Wetting properties of water in gas diffusion electrodes investigated with environmental scanning electron microscopy

M. Bozzetti[1], A. Berger[2], M. Fikry[3], T. J. Schmidt[3], H. A. Gasteiger[2], V. Tileli[1]

[1]École Polytechnique Fédérale de Lausanne (EPFL), Materials Science, Lausanne, Switzerland
[2]Technical University of Munich, Chemistry and Catalysis Research, Munich, Germany
[3]Paul Scherrer Institute, Villigen, Switzerland

Proton exchange membrane fuel cells (PEMFC) are promising energetic devices for automotive applications that have been widely investigated in the last decades [1]. In order to achieve their full theoretical potential, water management at the cathode side needs to be improved to avoid mass transport losses. Although water formation in the catalyst layer comes mostly from the cathodic reaction, condensation still plays an important role, as it was proven by the effect of humidifying reactants [2]. Pore size of diffusion media ranges from tenths of nanometres to few microns, and pore constrictions hindering water percolation are in the range of hundreds of nanometres [3]. Environmental scanning electron microscopy (ESEM) is therefore a suitable technique to investigate the condensation mechanism at the relevant scale for water saturation [4,5].

Previous studies have correlated the wetting behaviour of microporous layers (MPL) in the ESEM with water breakthrough from diffusion media in flooding conditions [6], while more recent studies took advantage of water condensation to compare the wettability of nanoporous carbon scaffolds to the conventional MPL [7]. However, many parameters related to the condensation mechanism are still poorly investigated experimentally, and the benefits of environmental electron microscopy have not been fully exploited yet.

Microporous layers and catalyst layers with different hydrophobicity have been observed in the ESEM at a pressure of 900 Pa varying the relative humidity. Temperature below 5°C were controlled by a cooling stage with a ramp of 0.1°C/min. Recordings of water breakthrough and droplet growth were acquired and methods to segment and analyse droplets were developed. Preliminary results suggest that larger pore size MPLs have slower droplet growth, which may be explained by the larger coalescence contribution in narrower pore size MPLs.

In this work, we report on the effects of the condensation mechanism parameters, such as droplet nucleation rate, spatial density of nucleation sites, droplet growth and coalescence rate of dissimilar gas diffusion layers. Further insights into water nucleation and growth could aid towards the optimization of the transport of reactants to the electrodes.

References

1. Majlan, E. H., Rohendi, D., Daud, W. R. W., Husaini, T. & Haque, M. A. Electrode for proton exchange membrane fuel cells: A review. *Renewable and Sustainable Energy Reviews* **89**, 117–134 (2018).
2. Sanchez, D. G. *et al.* Effect of the Inlet Gas Humidification on PEMFC Behavior and Current Density Distribution. *ECS Trans.* **64**, 603–617 (2014).
3. Bozzetti, M. *et al.* On the role of pore constrictions in gas diffusion electrodes. *Chem. Commun.* **58**, 8854–8857 (2022).
4. Lv, L., Zhang, J., Xu, J. & Yin, J. Heterogeneous condensation process observed by environmental scanning electron microscopy (ESEM): On smooth single aerosol particle. *Aerosol Science and Technology* **54**, 1515–1526 (2020).
5. Rykaczewski, K. Microdroplet Growth Mechanism during Water Condensation on Superhydrophobic Surfaces. *Langmuir* **28**, 7720–7729 (2012).
6. Nam, J. H., Lee, K.-J., Hwang, G.-S., Kim, C.-J. & Kaviany, M. Microporous layer for water morphology control in PEMFC. *International Journal of Heat and Mass Transfer* **52**, 2779–2791 (2009).
7. Islam, M. N. *et al.* Highly Ordered Nanoporous Carbon Scaffold with Controllable Wettability as the Microporous Layer for Fuel Cells. *ACS Appl. Mater. Interfaces* **12**, 39215–39226 (2020).

MS1.P032

FIB ToF-SIMS and EDS analysis of LLZO garnet electrolyte for solid-state batteries

L. Berner[1], B. Schröppel[2], R. R. Schröder[1], I. Wacker[1], Y. Sun[3], M. Nojabaee[3], A. Friedrich[3], C. Burkhardt[2]

[1]University Heidelberg, Cryo Electron Microscopy, BioQuant, Im Neuenheimer Feld 267, Heidelberg, Germany
[2]NMI Natural and Medical Sciences Institute at the University of Tübingen, Nanoanalytic, Reutlingen, Germany
[3]Deutsches Zentrum für Luft- und Raumfahrt (DLR), Institute of Engineering Thermodynamics, Pfaffenwaldring 38-40, Stuttgart, Germany

Introduction

Secondary ion mass spectroscopy (SIMS) in combination with scanning electron microscopy (SEM), focused ion beam (FIB) and energy-dispersive X-ray spectroscopy (EDS) is a powerful tool for chemical imaging of various technical devices. For the development and optimization of new Lithium batteries FIB-ToF (time of flight)-SIMS is essential as Lithium is not detectable with conventional EDS detectors and only hardly detectable with windowless EDS detectors. The solid-state electrolyte [1] family based on Lithium-Lanthanum-Zirconium-Oxide (LLZO) garnet is a promising material for next generation solid-state batteries. This electrolyte offers higher energy density and safer operation compared to standard Lithium ion batteries. To understand the internal composition and the interface of the Lithium cathode we analyzed the lateral and depth distribution of Lithium inside a LLZO pellet after processing and cycling with different parameters.

Materials & methods

LLZO pellets with a diameter of 12mm and thickness of 1mm are in development at DLR institute for technical thermodynamics. For FIB-SEM and ToF-SIMS investigation we used a ZEISS Crossbeam 540 FIB-SEM microscope equipped with a Tofwerk SIMS detector. The SIMS detector uses an orthogonal ToF system therefore no complex trigger timing for the primary gallium ion beam is necessary. A transfer optics collects the secondary ions from the sample surface and transfers the ions to the ToF detector for mass discrimination. A mass range from 1 to 500 is measured. SIMS is an optimal addition to EDS because it offers high surface sensitivity, detection of Lithium, and detection of isotopes. A lateral resolution of better than 100nm is possible. LLZO pellets were mounted on SEM sample holders. SEM, EDS and FIB- SIMS analysis was performed on the surface and on cross section of the LLZO pellets.

Results

The combination of SEM imaging with EDS and FIB-SIMS imaging gives important analytical data regarding the distribution of the elements and impurities inside the LLZO ceramic. With SIMS we could clearly resolve the distribution of Lithium inside the solid state electrolyte with high depth resolution and high lateral resolution. In the case of aluminium doped LLZO we find inhomogeneous distribution of aluminium oxide in the volume of the pellet.

Conclusion

ToF-SIMS in combination with FIB/SEM and EDS is a powerful tool in the field of Lithium ion battery research as Lithium is detectable with very high sensitivity with SIMS. It is also possible to detect the oxidation of Lithium with high depth and lateral resolution. In this way it is possible to optimize the production of LIBs and Lithium metal batteries as well as understanding degradation processes while operating the battery.

References

[1] Lei Cheng et al., J. Mater. Chem. A, 2014, 2, 172-181

[2] https://www.tofwerk.com/products/fibtof.

Fig. 1

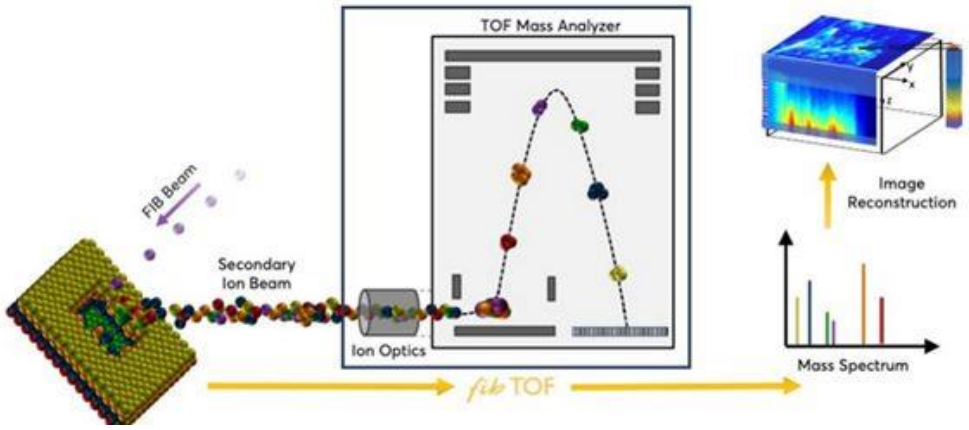

Fig. 2

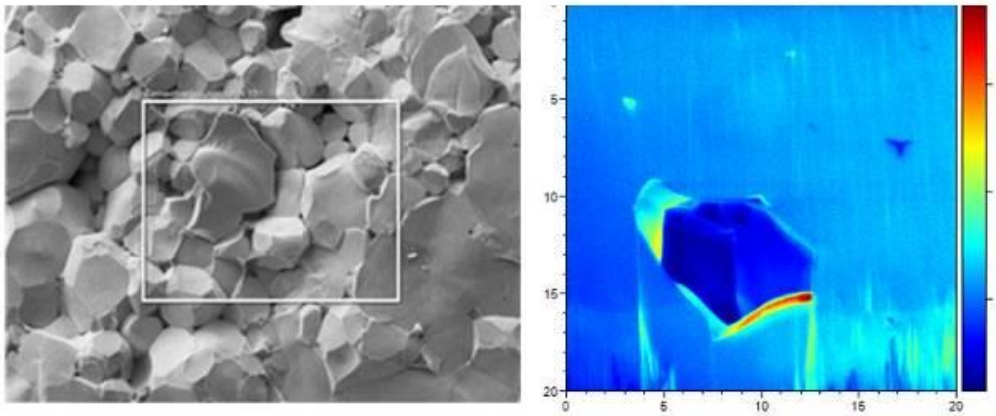

Fig. 3

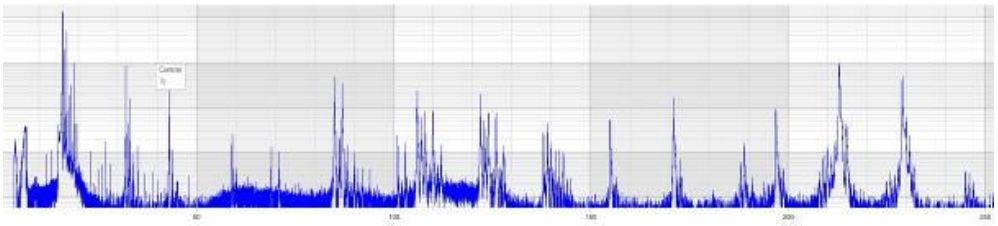

Fig. 4

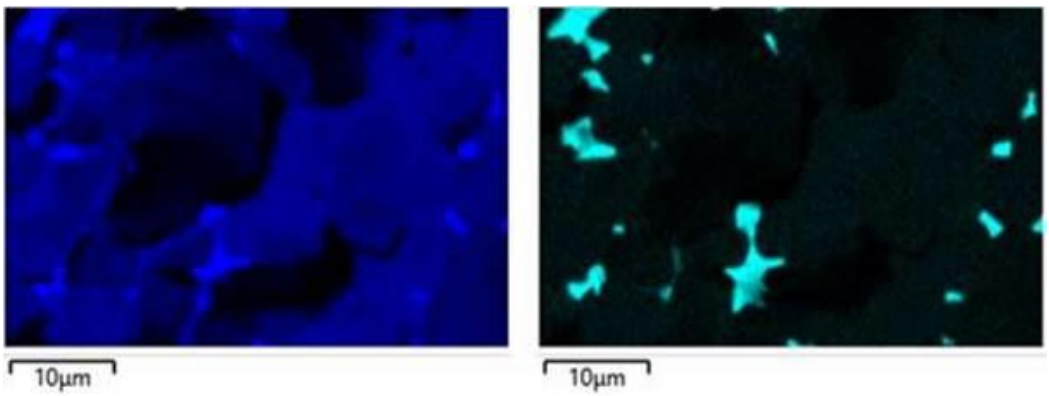

MS1.P033

Insights into the degradation of metallic core-shell nanoparticles under fuel cell conditions by 3D identical location STEM

M. Vega Paredes[1], R. Aymerich Armengol[1], N. Rivas Rivas[1], A. Garzón Manjón[1], C. Scheu[1]

[1]Max Planck Institute für Eisenforschung, Nanoanalytics and interfaces, Düsseldorf, Germany

Proton exchange membrane fuel cells (PEMFCs) are electrochemical devices capable of generating electricity by oxidizing H2, reformate (H2 rich gas with carbon monoxide (CO) impurities) or other fuels. In recent times, metallic core-shell nanoparticles (NPs) (M@Pt, M=Ru, Rh…) have attracted a big interest as anode catalysts of reformate fed PEMFCs [1]. The high catalytic activity of Pt towards the hydrogen oxidation reaction, together with the CO poisoning tolerance introduced by the accompanying metal make them ideal for heavy-duty applications. Furthermore, since in M@Pt NPs the less stable metal (Rh or Ru) is not directly exposed to the electrolyte, their stability is expected to be higher than in the corresponding alloyed NPs, which commonly suffer from dissolution and dealloying [2]. However, M@Pt can still suffer from degradation under fuel cell conditions by processes that are yet not fully understood, which hinders the design of more stable and durable catalysts.

We investigated the degradation behavior of Rh@Pt NPs by means of identical location-scanning transmission electron microscopy (IL-STEM). This quasi in-situ technique allows to overcome the limitations of the ex-situ techniques, in which only statistical general insights are possible, since in IL-STEM the changes of individual particles are tracked between potential cycles. In particular, we characterized the Rh@Pt NPs after 0, 1000, 4000 and 10000 potential cycles (0.06-0.8V, 0.1V/s). Furthermore, since many of the degradation phenomena take place in 3D (e.g., particle migration and corresponding aggregation), selected regions were reconstructed in 3D by means of electron tomography (Figure 1).

Figure 1. STEM and 3D reconstruction of Rh@Pt at 0 and 10000 cycles

We observed particle migration on the carbon support in all the stages of the potential cycling. However, no widespread particle aggregation was observed, even after 10000 potential cycles. A slight Rh dissolution (up to 5 at.%) during the cycles was detected, which decreased as the number of cycles increased. Even though some small particles dissolved during the first 1000 cycles, the main degradation mechanism responsible for the loss of electrochemically active surface area was found to be particle detachment.

Our results indicate that the investigated Rh@Pt NPs present a remarkable stability, and show how IL-STEM can be used for studying the degradation of catalyst NPs.

[1] A. Garzón Manjón, M. Vega Paredes, V. Berova, T. Gänsler, T. Schwarz, N. Rivas, K. Hengge, T. Jurzinsky, C. Scheu, Insights into the performance and degradation of Ru@Pt core-shell catalysts for fuel cells by advanced (scanning) transmission electron microscopy, [Submitted].

[2] M. Vega Paredes, A. Garzón Manjón, B. Hill, T. Schwarz, N. Rivas, T. Jurzinsky, K. Hengge, F. Mack, C. Scheu, Evaluation of functional layers thinning of high temperature polymer electrolyte membrane fuel cells after long term operation, Nanoscale. (2022). https://doi.org/10.1039/D2NR02892A.

Fig. 1

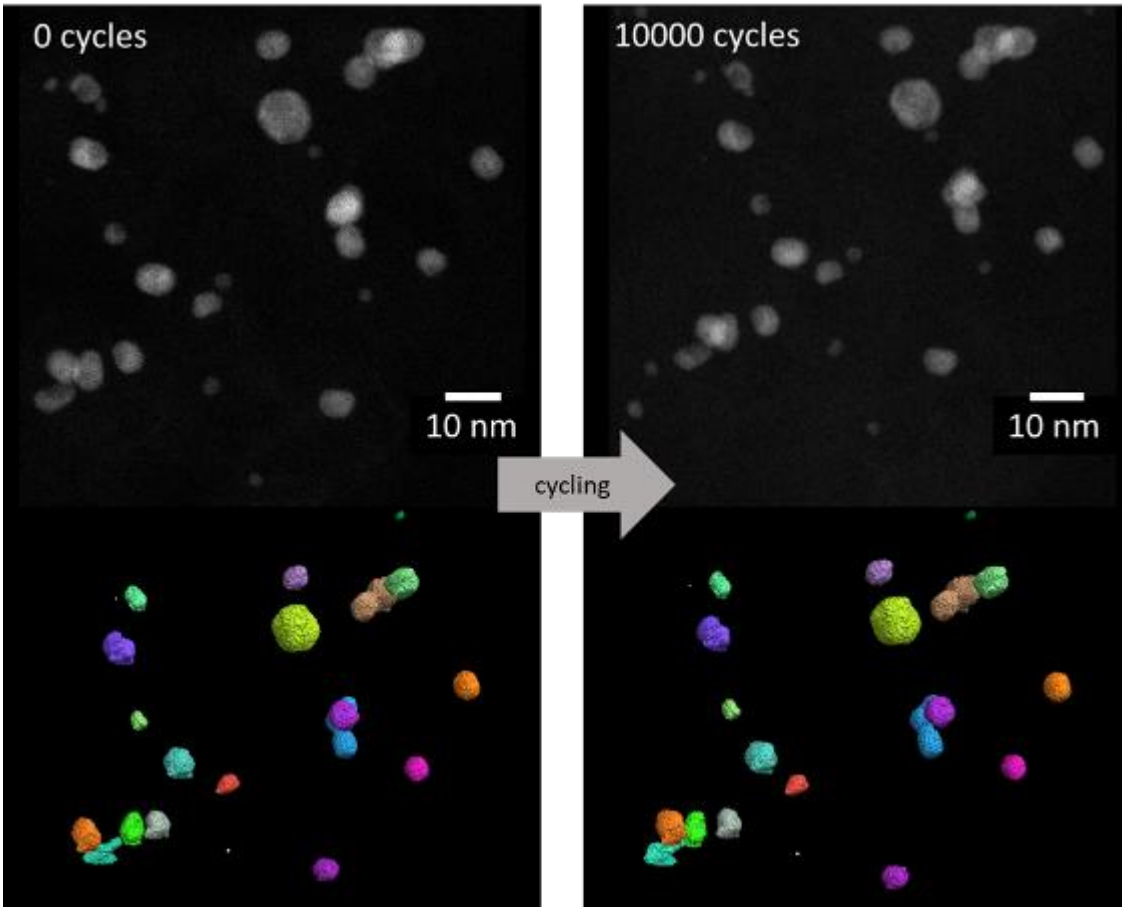

MS1.P034

Understanding of the degradation and aging mechanisms in Ni-rich NMC cathode material at the nanoscale

L. Ahrens[1,2], M. Meledina[2], S. Basak[1,3], R. Eichel[3], J. Mayer[1,2]

[1]Ernst Ruska-Centre for Microscopy and Spectroscopy with Electrons (ER-C), Jülich, Germany
[2]Central Facility for Electron Microscopy, Aachen, Germany
[3]Institute of Energy and Climate Research (IEK-9), Jülich, Germany

Ni-rich NMC ($Ni_xMn_yCo_{1-x-y}O_2$ with x > 0.8) has been a promising candidate for cathode active materials (CAMs) in Li-ion batteries (LIBs) [1,2]. Reducing the Cobalt content in NMC cathodes leads to a more environment-friendly and affordable material. Also, the specific capacity of Ni-rich NMC is significantly increased compared to conventional NMC material. However, the cycle stability is reduced. To improve the lifetime of Ni-rich NMCs, it is important to gain a deeper understanding of the degradation and aging mechanisms appearing during material synthesis and cycling. Therefore, studies of the micro- and nanostructure are key for tailoring material properties specifically, for instance through doping or coating.

Modern focused-ion-beam (FIB) preparation allows cutting of extremely thin samples, enabling high-resolution imaging. Figure 1 shows a lamella of a polycrystalline Ni-rich NMC particle, which was prepared by FIB and a corresponding HRSTEM image of a layered structure. In addition to ex-situ experiments at the atomic scale, in-situ experiments play a key role in understanding degradation and aging mechanisms in LIBs [3,4]. By applying voltage or temperature more realistic scenarios can be represented. Therefore, we focus both on ex-situ and on in-situ setups (Figure 2).

Figure 1: Polycrystalline NMC particle prepared by FIB (a) and ex-situ study of the layered structure at the atomic scale (b).

Figure 2: Setup of a biasing in-situ experiment using NMC prepared using FIB.

[1] Chao Xu et al., Adv. Energy Mater. 2021, 11, 2003404.

[2] Yu Xia et al., Nano Energy, Volume 49, 2018, 434-452.

[3] Shibabrata Basak et al., ACS Appl. Energy Mater. 2020, 3, 6, 5101-5106.

[4] Shibabrata Basak et al., Chem. Commun., 2022, 58, 3130-3133.

Fig. 1

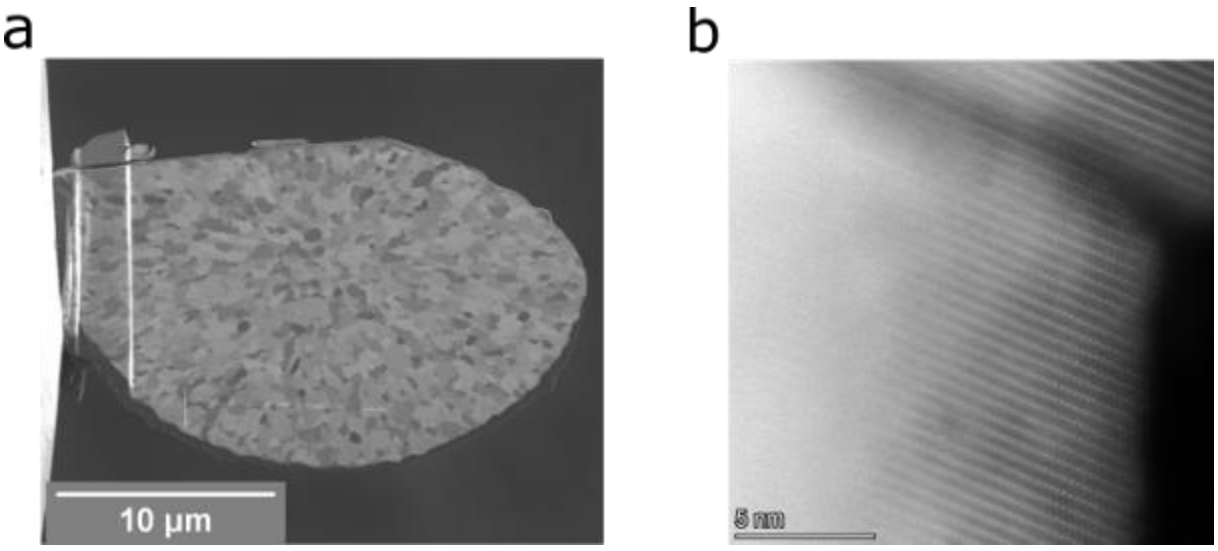

Fig. 2

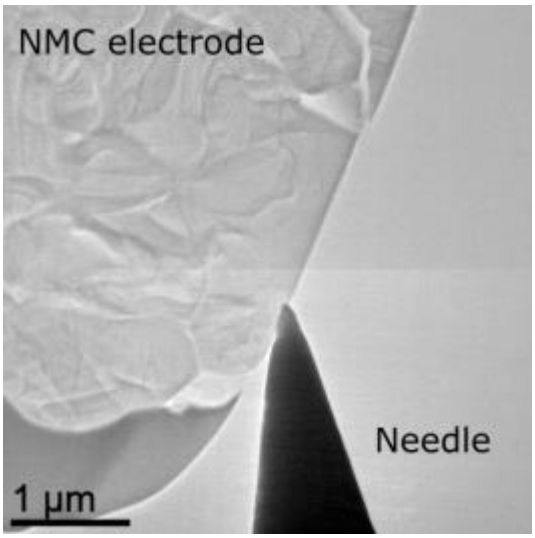

MS1.P035

A real space understanding of the short range order in disordered rocksalt cathode materials

E. Hedley[1], L. Pi[1], N. Roth[2], M. Danie[3], W. Song[1,4], P. Bruce[1,2,4,5], P. Nellist[1]

[1]University of Oxford, Materials, Oxford, United Kingdom
[2]University of Oxford, Inorganic Chemistry, Oxford, United Kingdom
[3]electron Physical Sciences Imaging Centre (ePSIC, Diamond Light Source, Didcot, United Kingdom
[4]The Faraday Institute, Didcot, United Kingdom
[5]The Henry Royce Institute, Oxford, United Kingdom

Layered cathode materials such as Li-rich NMCs (containing nickel, manganese and cobalt) show promise as new high capacity materials, as the layered structure allows the intercalation and deintercalation of lithium ions during the cycling of the battery. Many of the elements currently used in the cathode are expensive and have low natural abundance, the scope for introducing new more abundant materials is limited. Disordered rocksalt materials overcome with a much larger scope for different elements to be combined, with many examples have shown good performance using only more abundant transition metals such as manganese and titanium (1)(2).

The diffraction patterns of these materials contain clear diffuse scattering which takes many different forms depending on the composition, synthesis method and often exhibit changes on cycling of the material. This diffuse scattering is typical of materials with short range order, this type of diffuse scattering has previously been reported for many disordered rocksalt materials but to the best of our knowledge no precise understanding of the nature of this ordering has been achieved.

The disordered rocksalt Li1.2Mn0.4Ti0.4O2 (LMTO) has been studied because it is potentially commercially important material due its composition only containing relatively cheap and earth abundant elements. However, it shows poor capacity retention on cycling and poor ionic conductivity which leads to poor performance at room temperature and slow rate capability for cycling (3).

Electron diffraction has been used to study the nature of the short-range order in reciprocal space but does not give precise local information about the distribution of the ordering within a particle. In addition to TEM diffraction nanobeam electron diffraction has been used to gain real space information about the origin of the diffuse scattering.

The intensity of atomic columns scales with the atomic number in for ADF images, meaning that the Li and the transition metal in the real space images have very different intensities. While the disordered nature of these materials means that the atomic columns contain a mixture of the cations. However atomic columns with a higher number of transition metals will appear brighter than those with more lithium.

The ADF images of the particles show fluctuations in the intensity of the atomic columns, in what appears to be a random distribution. However, a Fourier transform of the ADF image reveals diffuse shapes which are like the diffuse scattering observed in the electron diffraction.

This link between the diffraction in the traditional sense and the spatial information which comes from the nanobeam diffraction with real space ADF images allows us to examine the precise nature of the local ordering in these materials and its spatial distribution.

1. Ji, H. *et al*. *Nat. Commun.* **10,** (2019).
2. Sato, T., Sato, K., Zhao, W., Kajiya, Y. & Yabuuchi, N, *J. Mater. Chem. A* **6,** 13943–13951 (2018)
3. Clement, R. J., Lun Z., Ceder, G., *Energy and Enviro. Sci,* **13,** 345 *(2020)*

Figure 1: a) ADF image of LMTO b) Fourier transform of image a. c) Electron diffraction pattern of LMTO

Figure 2: (a-c) Radial integration profiles of the a) pristine LiMnO2, b)after 1 cycle and c)8 cycles. Insets show the area where the azimuthal integration profiles are generated from. (f-g) Show virtual dark-field images which show the small crystallites

Fig. 1

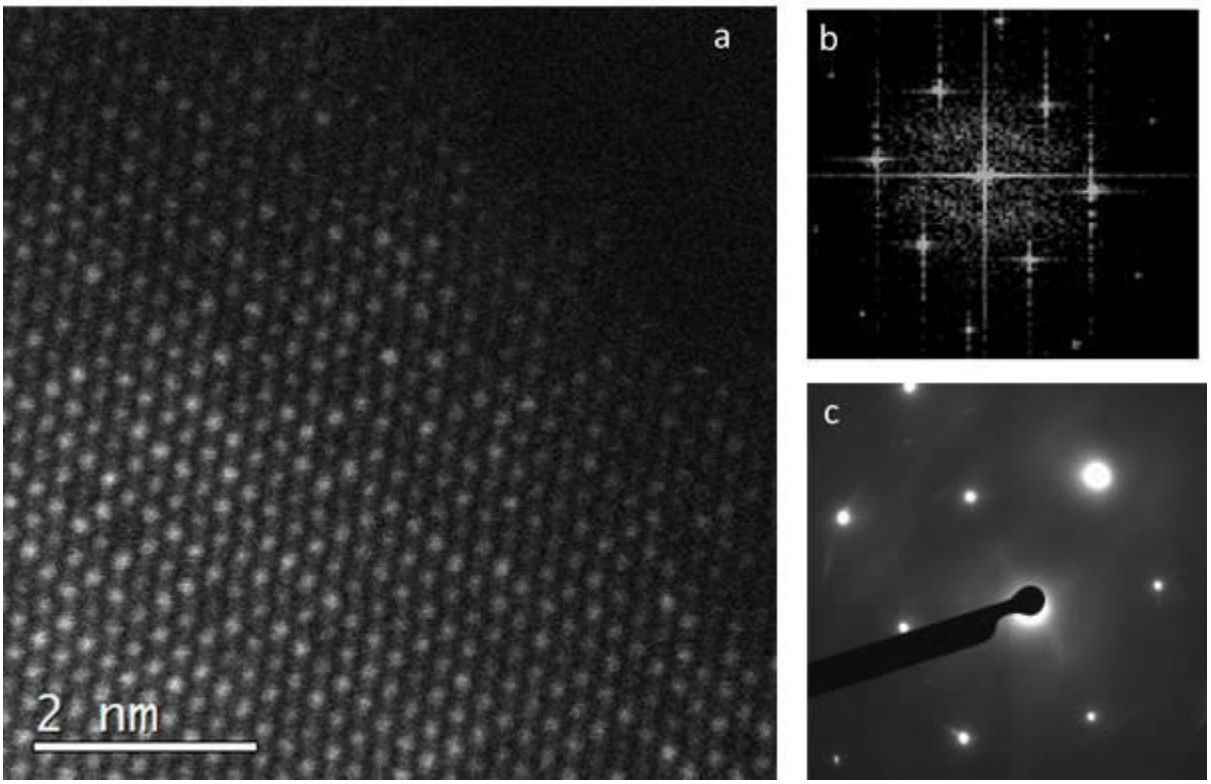
a
2 nm
b
c

Fig. 2

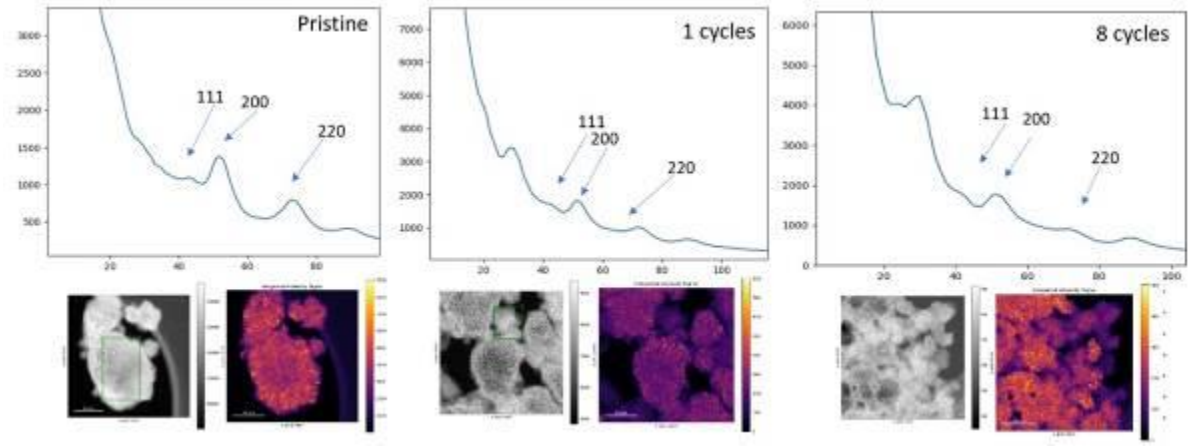
Pristine
111
200
220
1 cycles
111
200
220
8 cycles
111
200
220

MS1.P036

Phase analysis of (Li)$FePO_4$ by selected area electron diffraction and integrated differential phase contrast imaging

N. Šimić[1], D. Knez[2], I. Hanzu[3], W. Grogger[2]

[1]Graz Centre for Electron Microscopy (ZFE), Graz, Austria
[2]Institute of Electron Microscopy and Nanoanalysis, Graz University of Technology, Graz, Austria
[3]Institute for Chemistry and Technology of Materials, Graz University of Technology, Graz, Austria

Lithium iron phosphate ($LiFePO_4$) is a well-studied compound with a lot of promise as cathode material in rechargeable batteries. Due to its low cost, low toxicity, safety and the abundance of iron LFP is considered a very attractive energy storage option for the automotive industry.

$LiFePO_4$ has an orthorhombic crystal structure with Pnma space group [1]. During the discharge process lithium intercalates from a graphite anode into the $FePO_4$ cathode, where it is stored in between FeO_6 octahedra and PO_4 tetrahedra, thus slightly changing the lattice vector length of the unit cell while maintaining the same crystal structure.

Our aim is to better understand the lithium deintercalation process in (Li)$FePO_4$ battery cells on atomic and macroscopic scale. Fully delithiated, fully lithiated and partially lithiated cells are prepared using chemical- and electrochemical delithiation as well as bio templating.

We use Selected Area Electron Diffraction (SAED) and integrated Differential Phase Contrast imaging (iDPC) in the TEM in order to differentiate between lithiated and (partially) delithiated particles. FIB lamellas are prepared from electrochemically delithiated cells for this purpose.

We also aim to compare the results from our findings in the TEM with Raman microscopy measurements. Preliminary Raman experiments on bio-templated (Li)FePO4 already showed that $LiFePO_4$ and FePO4 phases are differentiable with their respective Raman-shift.

With SAED measurements we successfully managed to differentiate between $LiFePO_4$ and $FePO_4$ phases as well as partially delithiated phases for single particles as seen in figure 1. High-Resolution STEM as well as iDPC imaging have confirmed the feasibility of SAED for detection of lithium content. The lattice spacings obtained by HR-STEM FFT analysis were similar to the lattice spacings obtained by SAED. Using iDPC imaging we were able to directly show the presence of lithium in a partially delithiated particle as seen in figure 3.

We conclude that SAED analysis is feasible for differentiation between lithiated and (partially) delithiated states in Li_xFePO_4 as confirmed by HR-STEM FFT analysis and iDPC imaging. Raman microscopy may provide further insight on the delithiation process on a macroscopic scale in future work.

Figure 1: Diffraction pattern of a $LiFePO_4$ particle in 011 direction. The lattice spacing of the 001 plane indicates partial delithiation after comparison with simulated powder diffraction data from LiFePO4 and $Li_{0.6}FePO_4$.

Figure 2: Theoretical model of $LiFePO_4$ in 011 direction. The model shows Li atoms in green, Fe in orange, O in red and P in grey.

Figure 3: Integrated Differential Phase Contrast image of the same particle seen in figure 1. All corresponding columns in the image show clear contrast at the theoretical Li positions which implies Li presence, thus confirming the diffraction results. See figure 2 for better reference with the theoretical model.

[1] V.S.L. Satyavani, A. Srinivas Kumar, P.S.V. Subba Rao, et. al., Engineering Science and Technology, an International Journal, **19** (1), 178-188 (2016)

Fig. 1

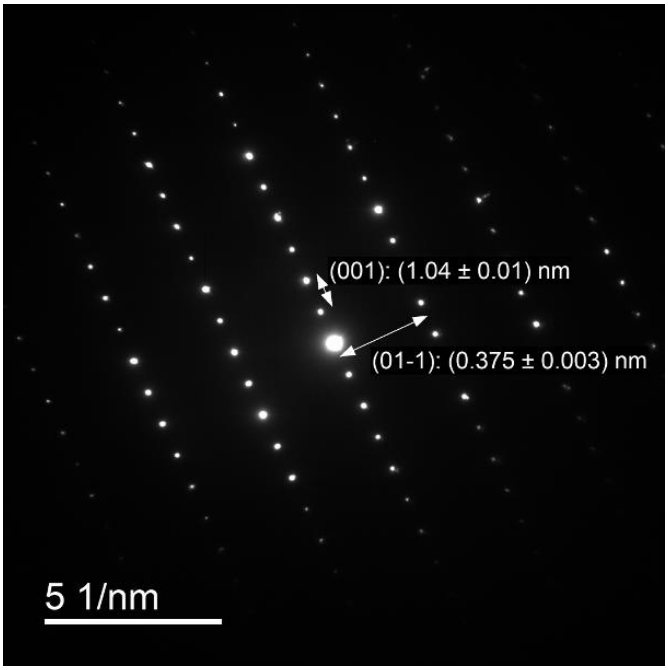

Fig. 2

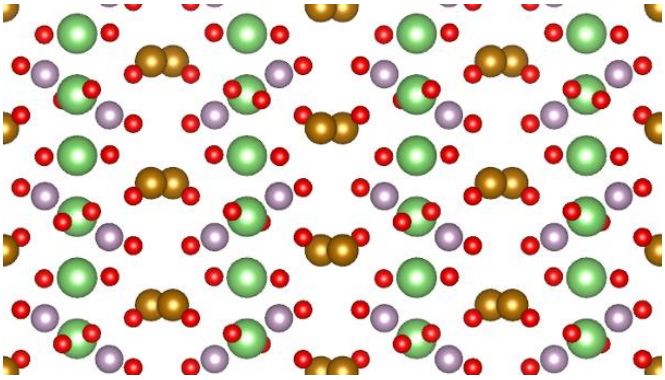

Fig. 3

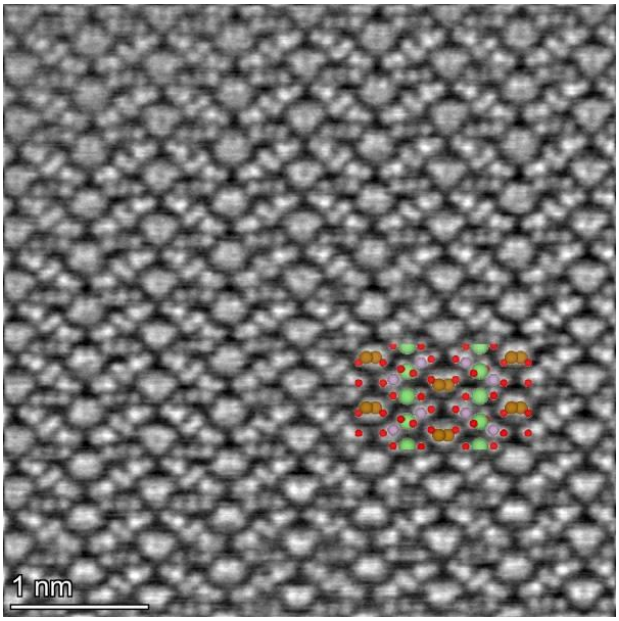

MS1.P037

Silicon microparticles for Li-ion batteries: tracking crystalline-amorphous transition

H. Valencia Naranjo[1,2], P. Rapp[3], M. Graf[3], H. A. Gasteiger[3], S. Basak[4,1], R. Eichel[4], J. Mayer[1,2]

[1]Forschungszentrum Jülich GmbH, Ernst Ruska-Centre (ER-C 2), Jülich, Germany
[2]RWTH Aachen University, Central Facility for Electron Microscopy (GFE), Aachen, Germany
[3]Technical University of Munich, Department of Chemistry, Garching, Germany
[4]Forschungszentrum Jülich GmbH, Institut für Energie- und Klimaforschung – Grundlagen der Elektrochemie (IEK-9), Jülich, Germany

The improvement of modern Li-ion batteries (LIBs) is an important step in the development of energy storage systems with regard to the growing market of electric vehicles and the realization of the European goal for climate neutrality by 2050 [1].

Silicon (Si) is one of the most promising anodes for next-generation LIBs, with its bestselling point being the theoretical capacity of 3579 mAh/g which is approximately ten-fold than that of the commonly used graphite-based materials used nowadays [2-4]. However, the ~300% volume change during (de)lithiation, which also results in crystalline-amorphous transition, limits the commercialization of Si-based anodes, particularly the Si microparticles. This transition takes place during the first lithiation cycle of the crystalline Si, which is amorphized and stays amorphous after delithiation, causing degradation. One approach to reducing the degradation is to operate the Si anode under its capacity limit, e.g., by using only ~30 % of the capacity the volume expansion is reduced to only one-third of the maximal expansion and leaving part of the crystalline Si phase unchanged during lithiation. This allows the Si anode to cycle over 200 times [5].

In order to further understand the lithiation process and the resulting capacity fading due to degradation within the Si microparticles, one needs to have an in-depth insight into the structural arrangements within the Si microparticles. Transmission electron microscopy (TEM) is the method of choice to study morphology and chemical composition of the crystalline and amorphous phases within partially lithiated polycrystalline Si microparticles. For the TEM investigation, FIB lamellas are prepared from the 5-10 µm pristine and cycled (lithiated/delithiated) particles. Bright-field (BF) imaging, selected area electron diffraction (SAED) and energy dispersive X-ray spectroscopy (EDX) revealed the presence of the crystalline phase and the complex vein-like amorphous Si phase within the cycled microparticles, the latter not being present in the pristine Si microparticles (Figure 1). This shows the complex expansion of the amorphous phase not only present at the Si microparticle shell but also along stacking faults and grain boundaries.

Figure 1*: Bright field (BF) TEM image and corresponding diffraction images of Si particles. The images in the upper row a) correspond to the pristine Si anode and in the lower row b) the cycled Si anode is visible.*

[1] European Commission Communication (COM(2019) 640) "The European Green Deal".

[2] U. Kasavajjula, C. Wang, and A. J. Appleby, J. Power Sources, 163, 1003 (2007).

[3]. M. N. Obrovac and V. L. Chevrier, Chem. Rev., 114, 11444 (2014).

[4] J.R. Dahn, T. Zheng, Y. Liu, J.S. Xue, Science 270 (1995) 590e593.

[5] Maximilian Graf et al 2022 J. Electrochem. Soc. 169 020536.

Fig. 1

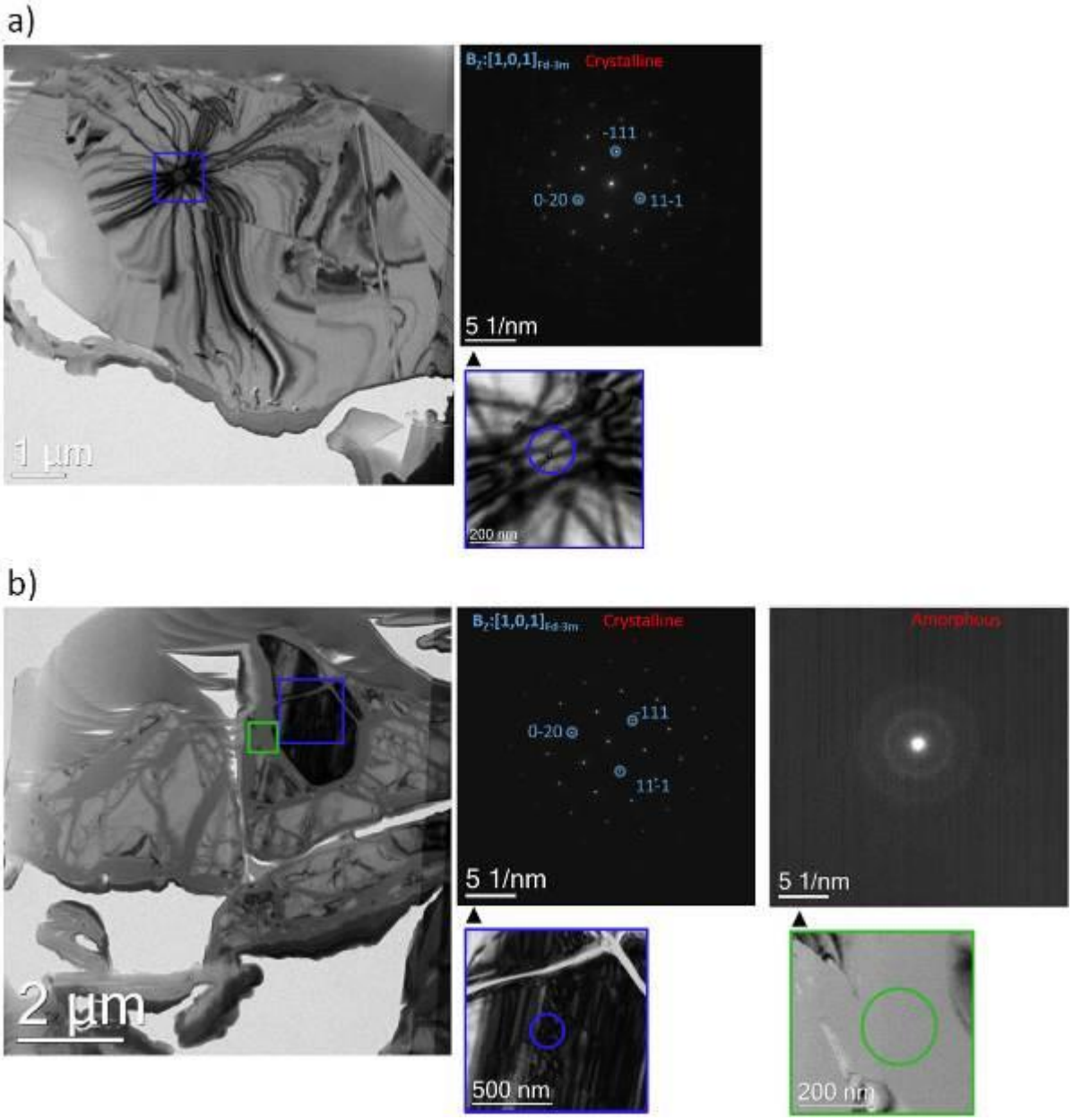
a)
1 µm
B_2:[1,0,1]$_{Fd\text{-}3m}$ Crystalline
-111
0-20
11-1
5 1/nm
200 nm
b)
2 µm
B_2:[1,0,1]$_{Fd\text{-}3m}$ Crystalline
111
0-20
11-1
5 1/nm
500 nm
Amorphous
5 1/nm
200 nm

MS1.P038

ADF/EDS/EELS characterization of spontaneous cathode/electrolyte reaction in air- and beam-sensitive solid-state Li-ion batteries

R. Zhang[1], A. Sheader[1], W. Song[1,2], E. Liberti[1,3], P. Bruce[4,1,2,5], P. Nellist[1]

[1]University of Oxford, Department of Materials, Oxford, United Kingdom
[2]The Faraday Institute, Didcot, United Kingdom
[3]Rosalind Franklin Institute, Didcot, United Kingdom
[4]University of Oxford, Department of Chemistry, Oxford, United Kingdom
[5]The Henry Royce Institute, Oxford, United Kingdom

Solid-state Li-ion batteries (SSLIBs) have potential to revolutionise the electric-vehicle industry due to their superior capacity and improved safety relative to conventional liquid cells. However, commercialisation of SSLIBs is at present hindered by the electrode-electrolyte interface side reaction which leads to voltage hysteresis and capacity fading[1].

High-resolution characterisation techniques such as STEM provides comprehensive analysis of the microstructure and chemistry of SSE/cathode interphase. However, STEM studies of SSLIBs are complicated due to the extreme air- and electron-beam sensitivity of battery materials. It is therefore important to understand the effects of such damage to the native interface structure, and operate below these thresholds during imaging and spectroscopy experiments.

In this work, we applied ADF/EDS/EELS to study the spontaneously formed interface between cathode material LiNi0.6Mn0.2Co0.2O (NMC622) and SSE Argyrodite Li6PS5Cl. We developed an anaerobic sample transfer protocol to prevent oxygen-related sample degradation. Beam damage on argyrodite was studied from the diffraction pattern revolution.

Initial observations showed that air exposure of the solid-state electrolyte argyrodite (Li6PS5Cl) is characterised by Cl inhomogeneity and O contamination, significant morphology change and also sulphur deficiency (Fig.1). Particle tilting can be observed as a result of beam damage from the Laue Zone shift in Fig.2(a)-(e). Critical dose thresholds were calculated to be 500 e Å-2 by monitoring the diffraction spots intensity decay with time (Fig.2(f)).

EELS mapping was used to reveal the extent of side reaction by tracking the Ni L2,3 white line ratio on the NMC622/argyrodite interface. We quantified Ni L2,3 white line ratio by performing model fitting (Fig.3(c)) in Hyperspy on raw data from single pixel.[3] A trend of Ni reduction in NMC622 towards the interface with argyrodite due to the spontaneous redox reaction was observed.

The ability to characterise air- and electron beam-damage is key to managing the particular experimental challenges relating to (S)TEM studies of solid-state battery materials. Such challenges are of particular importance for high-resolution characterisation, as needed to further our understanding of, for example, the argyrodite-NMC622 interface.[3]

References:

[1] J -M T., and M A., Materials for sustainable energy: a collection of peer-reviewed research and review articles from Nature Publishing Group (2011) p. 171-179.

[2] FDL P., *et al*, Microscopy and Microanalysis, **23**(S1) (2017) p.214-215.

[3] The authors acknowledge use of characterization facilities within the David Cockayne Centre for Electron Microscopy, Department of Materials, University of Oxford and in particular the Faraday Institution (FIRG007, FIRG008), the EPSRC (EP/K040375/1 "South of England Analytical Electron Microscope") and additional instrument provision from the Henry Royce Institute (Grant reference EP/R010145/1).

Figure 1 (a) EDS elemental maps on argyrodite at oxygen content of 5 at% and 65 at% (b) S: P element ratio against oxygen content

Figure 2 Diffraction pattern of argyrodite at 300kV at (a) t=0min (b) t=0.5min (c) t=1min, (d) t=2min (e) t=3min (f) integrated diffraction spots intensity over radius

Figure 3 (a) EDS map of S (yellow) in argyrodite and Ni (blue) in NMC622 (b) Ni L2,3 white line ratio map (c) Model fitting on raw data (red dots), model consists of 5 components

Fig. 1

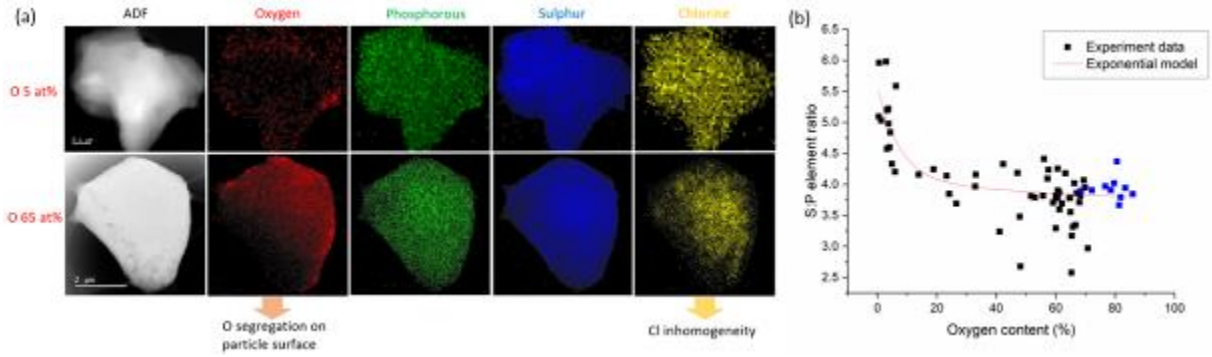

Fig. 2

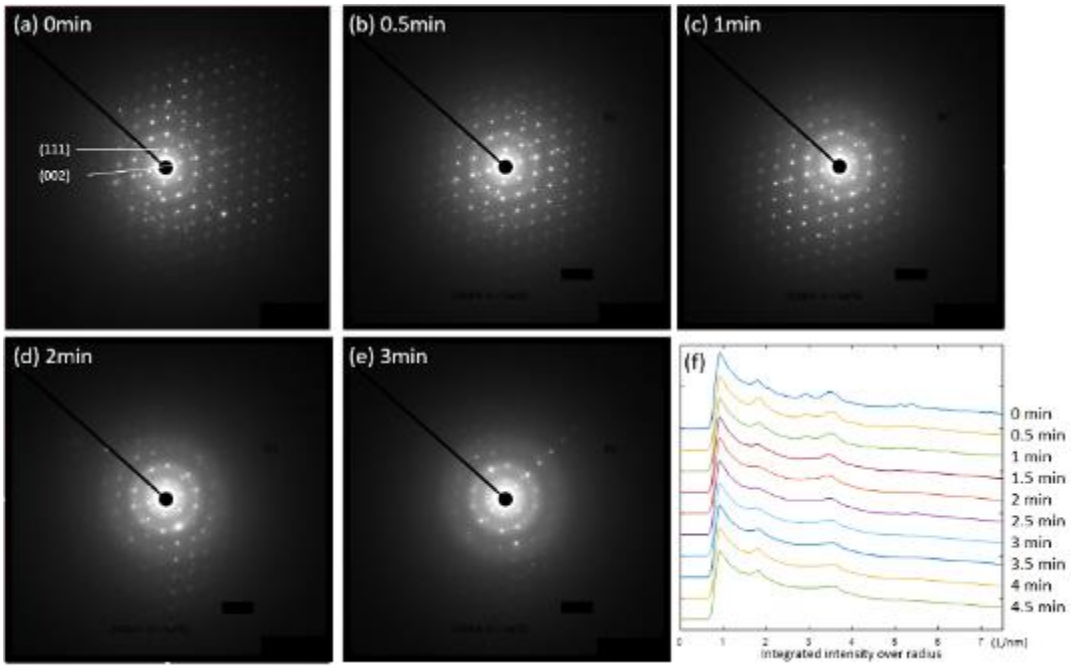

Fig. 3

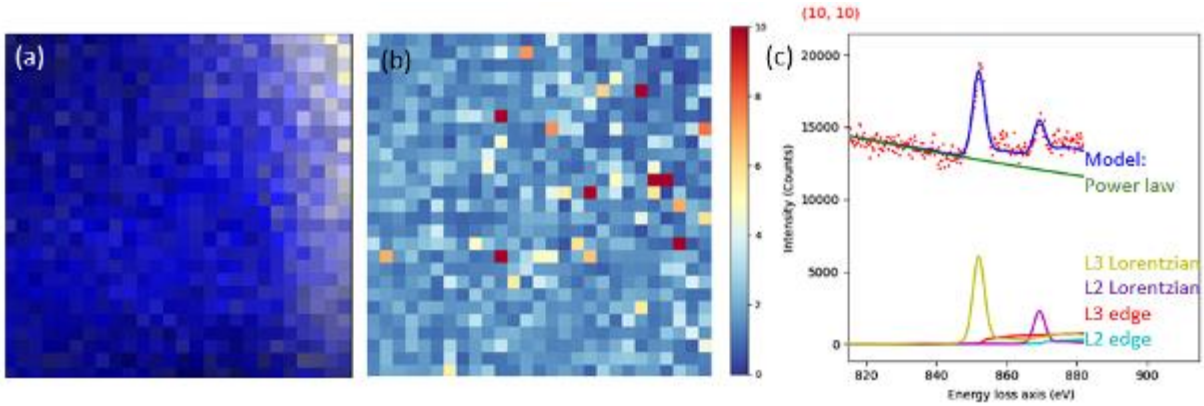

MS2.001-invited

Small scale model systems for *in situ* TEM studies: multilayered and alloyed nanowires

L. Vogl[1], P. Schweizer[1], L. Pethö[1], I. Utke[1], J. Michler[1]

[1]Laboratory of Mechanics for Materials and Nanostructures, Swiss Federal Laboratories for Materials Science and Technology (Empa), Thun, Switzerland

To understand the behavior of complex alloys and composites under mechanical and thermal loading small scale model systems are needed. Only such model systems provide the opportunity to analyze mechanisms of plastic deformation, interdiffusion and phase transformation down to the atomic scale. Tailored nanowires are ideal in this role as they can be directly studied with *in situ* TEM to elucidate the effect of compositional complexity, multilayered coatings and local ordering.

Multilayered coatings prevent the underlying core material from degradation and enhance the mechanical and wear-resistant behavior. Such a coating consists for example of alternating nm-sized layers of metals and metal-oxides. The coating life-time crucially depends on crack initialization and propagation at the interfaces. To further optimize the performance and to prevent early failure like layer delamination, the underlying **failure mechanisms on the atomic scale** have to be studied. Small scale model systems of such coatings allows characterizing application-limiting factors inside the Transmission Electron Microscope (TEM) with a view to optimize the mechanical stability of the bulk counterpart.

In this work, we use a combinatorial process based on advanced Physical Vapor Deposition (PVD) and Atomic Layer Deposition (ALD) to create complex one-dimensional nanowires (NW). These wires are ideal model-systems that enable studying the performance of different coatings. In order to analyze the **effect of multilayers on the mechanical behaviour**, we compare conventional coatings on metals (Al2O3-Cu) (Figure 1a) with nanolaminates consisting of alternating layers of Al2O3-ZnO (Figure 1b). **Defect nucleation** at the metal-metal oxide interface as well as **crack propagation** are studied via *in situ* mechanical testing inside the TEM. Figure 1c shows a cracked multi-shell NW after mechanical loading.

Figure 1: Core-shell NWs as small scale model system for bulk-coatings. Exemplary STEM images. a) Al2O3-Cu core-shell NW. The Cu NW has been subsequently coated with a conformal ALD layer. b) Nanolaminate on Cu NW. The Energy-dispersive X-ray spectroscopy (EDX) map shows the layered Al2O3-ZnO structure. c) Nanolaminate after mechanical loading.

Next to metal-metal oxide structures, intermetallic (Cu-Au) nanostructures are used to **study the effect of compositional complexity** on the material properties as well as **diffusion processes at interfaces**. By using co-sputtering at elevated temperatures alloyed NWs (Cu3Au/Au3Cu) are directly achieved. Figure 2 a shows an exemplary intermetallic Cu3Au NW with corresponding EDX mapping. The line scan across the NW is shown in figure 2c. The High-Resolution Scanning Transmission Electron Microscopy (HR-STEM) image in figure 2c emphasizes the ordering and figure 2d shows the corresponding diffraction pattern of the NW. In comparison with solid-solutions (of the same composition), such intermetallic model systems are used to characterize the effect of atomic ordering on the mechanical behavior, which is of great interest for the development of complex alloys. Beside the direct creation of the ordered phase via co-sputtering, intermetallic NWs can also be produced by heating core-shell NWs which consist of a copper core covered by a gold layer. These bimetallic nanostructures are ideal systems to study diffusion phenomena and ordering *in situ* in TEM. Figure 2e shows an EDX mapping of an initial Cu-Au NW before and after heating and figure 2f the corresponding line scans for different time intervals (initial, 50s to 2327s). Based on the Wagner equation, we calculated the interdiffusion coefficients of Cu (8.75· 10-18 m2/s) and Au (3.27·10-18 m2/s). To achieve the intermetallic phase and to observe the ordering, the NWs are annealed at 300°C (see diffraction pattern in figure 2g).

Figure 2: Intermetallic NWs as small scale model system for complex alloys. a) Exemplary Cu3Au NW directly obtained via co-sputtering. STEM image with EDX mapping. The corresponding line profile is shown in figure 2b. c) HR-STEM image with Fast Fourier Transform (FFT) and d) diffraction pattern of the NW. Cu-Au core-shell NWs as small scale model system to analyze diffusion processes. e) EDX mapping of Cu-Au NW before and after heating at 400°C. g) Diffraction pattern before and after annealing at 300°C. Reversible formation of an ordered intermetallic phase.

Fig. 1

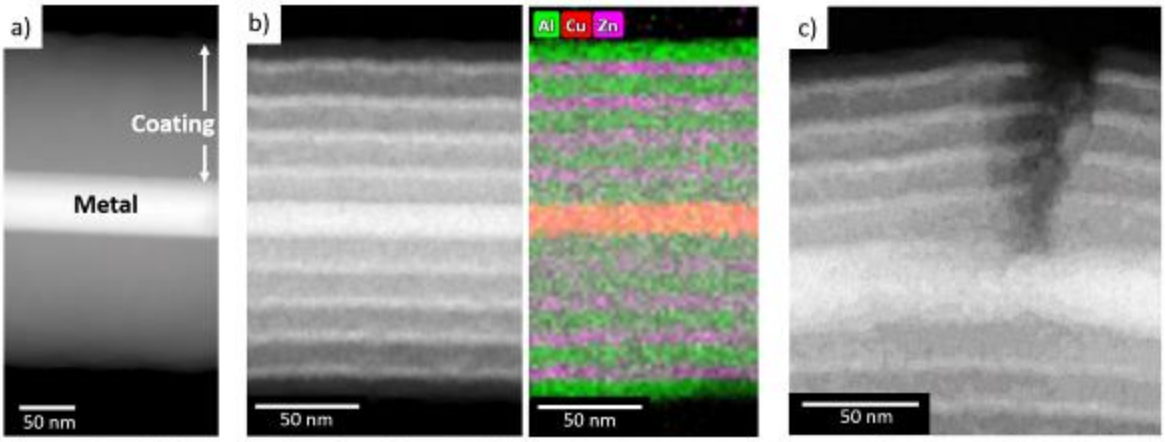

Figure 1: Core-shell NWs as small scale model system for bulk-coatings. Exemplary STEM images. a) Al_2O_3-Cu core-shell NW. The Cu NW has been subsequently coated with a conformal ALD layer. b) Nanolaminate on Cu NW. The Energy-dispersive X-ray spectroscopy (EDX) map shows the layered Al_2O_3-ZnO structure. c) Nanolaminate after mechanical loading.

Fig. 2

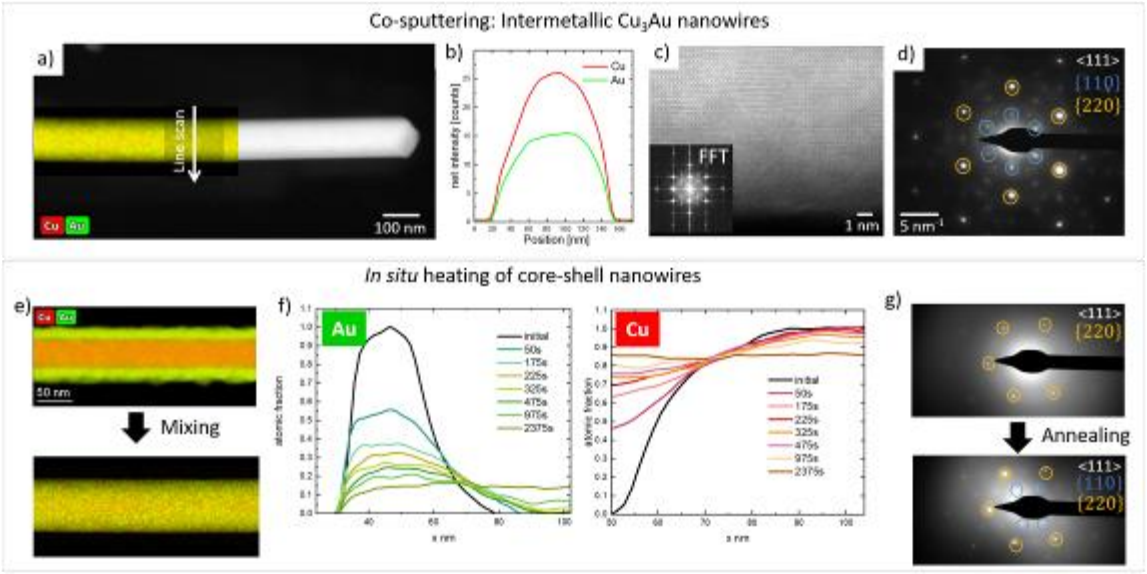

Figure 2: Intermetallic NWs as small scale model system for complex alloys. a) Exemplary Cu_3Au NW directly obtained via co-sputtering. STEM image with EDX mapping. The corresponding line profile is shown in figure 2b. c) HR-STEM image with Fast Fourier Transform (FFT) and d) diffraction pattern of the NW. Cu-Au core-shell NWs as small scale model system to analyze diffusion processes. e) EDX mapping of Cu-Au NW before and after heating at 400°C. g) Diffraction pattern before and after annealing at 300°C. Reversible formation of an ordered intermetallic phase.

MS2.002

Heat-induced alloying in individual Au@Ag core-shell nanoparticles as a function of size, shape, and presence of defects

M. Mychinko[1], A. Skorikov[1], W. Albrecht[1], X. Zhuo[2], A. Sànchez-Iglesias[2], L. M. Liz-Marzán[2], S. Bals[1]

[1]Universiteit Antwerpen, EMAT, Antwerp, Belgium
[2]Basque Research and Technology Alliance, CIC BiomaGUNE, San Sebastian, Spain

The recent and ongoing development of advanced colloidal synthetic techniques has allowed scientists to routinely produce bimetallic nanoparticles of various shapes, sizes, composition, and elemental distribution. Novel synthetic routes enable precise control of specific optical properties based on surface plasmon resonance. Thus, nanoplasmonic-based materials are of great interest for the utilization in biosensing, photocatalysts, medicine, data storage, etc. However, operation in real conditions (e.g. at elevated temperatures) may cause particle reshaping and redistribution of metals between the core and shell of the particle, which in turn gradually alter the properties of nanoplasmonics. Hence, a deeper understanding of the influence of the size, shape, and presence of defects on the nature of such processes is essential for the further development of nanoplasmonic-based technologies.

The recently developed combination of fast tomography based on High Angle Annular Dark Field Scanning Transmission Electron Microscopy with *in situ* heating holders has enabled the investigation of heat-induced processes at the single nanoparticle level with high spatial resolution in 3 dimensions (3D). Using this approach, we evaluated the influence of various parameters (size, shape, defect structure) on heat-induced elemental redistribution in Au@Ag core-shell nanoparticles qualitatively and quantitatively.

In more detail, the elemental redistribution at high temperature in single-crystalline Au@Ag nanocubes with similar size and composition, but with different shapes of the core (truncated octahedra and sphere), was shown to be uniform along all directions (Figure 1c-d, upper rows). By performing 3D simulations of diffusion based on Fick"s law, similar diffusion constants were found (Figure 1a-b and Figure 1c-d, lower rows). Additionally, our investigation indicated faster alloying kinetics for pentatwinned Au@Ag nanorods in comparison to single-crystalline nanorods of comparable sizes and composition. This may be related to the presence of twinning planes, which cause the formation of distortions and vacant sites in the crystal lattice, facilitating diffusion of atoms. Finally, the influence of the core shape was demonstrated to be negligible in the case of two pentatwinned nanorods with different Au cores (rod and bipyramid).

In conclusion, using our fast tomography approach we gained a fundamental insight into the nature of elemental diffusion at high temperature and its dependence on various factors, e.g. size, shape, and presence of twinning defects. We believe, that detailed knowledge of thermal stability and/or thermal degradation of bimetallic nanoplasmonic materials will drastically improve the application of these materials in the future.

The project has received funding from European Research Council (ERC Consolidator Grant 815128, REALNANO) and European Commission (grant 731019, EUSMI).

Figure 1. (a) – (b) Comparison of the alloying progress of single-crystalline nanocubes (with octahedral and spherical core, respectively) to diffusion simulations performed for different diffusion coefficients. (c) – (d) The upper rows show slices through the experimentally determined 3D elemental distribution at different stages of alloying of single-crystalline nanocubes (with octahedral and spherical core, respectively). The lower rows display slices through the simulated 3D elemental distribution using the optimal diffusion coefficient.

Fig. 1

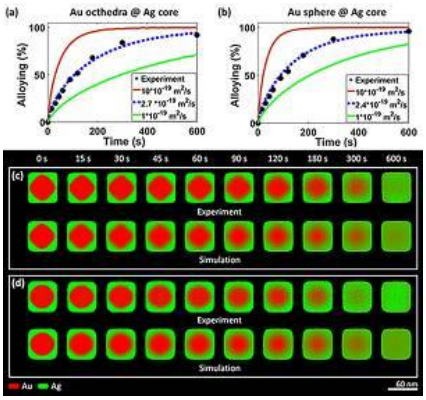
(a)
Au octhedra @ Ag core
(b)
Au sphere @ Ag core
Alloying (%)
Time (s)
Experiment
0 s
15 s
30 s
45 s
60 s
90 s
120 s
180 s
300 s
600 s
(c)
Experiment
Simulation
(d)
Experiment
Simulation
Au
Ag
60 nm

MS2.003

Utilizing gradient samples to investigate solid state dewetting of bimetallic alloys

C. Volland[1], M. Dierner[1], R. Branscheidt[1], M. Landes[1], J. Will[1], E. Spiecker[1]

[1]Friedrich-Alexander-Universität Erlangen-Nürnberg, Institute of Micro- and Nanostructure Research & Center for Nanoanalysis and Electron Microscopy (CENEM), Erlangen, Germany

Solid-state-Dewetting (SSD) is a typical degradation process of thin metallic films deposited on a substrate when annealed below the melting point. The process is driven by the minimization of total energy through surface- and interfacial energy reduction. While it used to be an undesirable effect, nowadays it is utilized as a powerful tool to fabricate bimetallic alloyed nanostructures for e.g. catalysis [1]. Here, switching from a single component film to binary systems makes the whole process more complex. A detailed understanding of this process is, however, unavoidable in order to fabricate nanostructures with targeted composition, shape and size.

In the present study, we present an elegant route for the fabrication of single-gradient (Fig.1 A) and triple gradient (Fig.1 B) samples via e-beam evaporation of Au and Ni on (0001) oriented α-Al2O3. Subsequently, rapid thermal annealing is utilized at 890°C for 120s in reducing atmosphere (Ar/5% H2). The temperature is chosen in order to anneal the samples above the miscibility gap of the Au-Ni system for the production of AuxNi1-x alloys. This type of sample preparation allows i) the preparation of AuNi alloys with fine concentration differences to study the effect of alloying on SSD and ii) to study alloying effects and film thickness effects using a single sample.

Ex-situ scanning electron microscopy (SEM) studies of the thermal annealed single-gradient sample are displayed in Fig. 2A. The homogeneous back-scatter contrast in the particles confirm a successful formation of an AuNi solid solution for all compositions ranging from 1 at% Au up to 99 at% Au. Via segmentation of the SEM images, the ratio between the exposed and unexposed are extracted to visualize the Au concentration dependent dewetting kinetics (Fig. 2B). An increased dewetting kinetic can be found in the range of 50 at% to 70 at% which is in good agreement with our recent studies [2]. Using EBSD measurement the texture of the formed particles is investigated (Fig. 2 C). The pole figures show a strong 111 out-of-plane texturing for a wide concentration range. Furthermore, the microstructure is fibre-like with tendencies towards epitaxial orientation relationships of AuNi (111)[1-10] || α-Al2O3 (0001)[10-10]. Interestingly this texture is substanial lost for the sample with 60at% Au leading to a texture free microstructure of the particles.

With the presented approach, the influence of a multitude of different factors like atomic size mismatch during alloying onto the SSD of bimetallic alloys can be investigated in just one single sample. Furthermore, we demonstrate, that the concentration can be tuned continuously over a concentration range from 1 at% to 99 at% Au, which allows a systematic investigation of the influence of the misfit between metal particles and ceramic substrate, which is currently part of further investigations.

[1] Shahvaranfard et al., CS Appl. Mater. Interfaces 2020, 12, 34, 38211–38221

[2] Dierner et al., unpublished work

Fig. 1

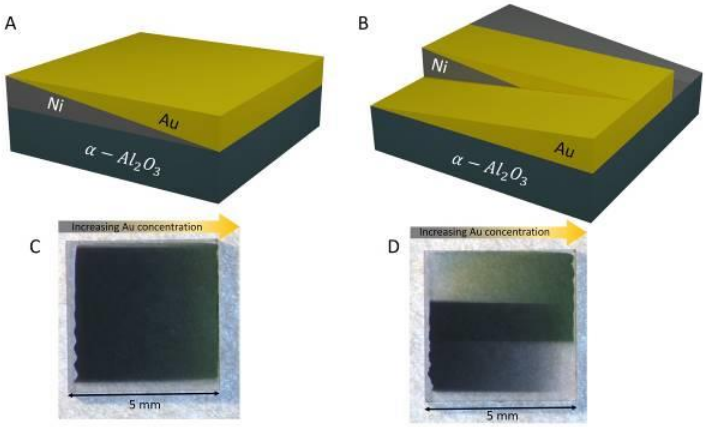

Fig. 1: Schematic illustration of the A) single gradient sample and B) triple gradient sample, as well as light microscopy images (C,D) of both samples respectively. The single gradient sample possesses a concentration gradient ranging from 1 at% Au to 99 at% Au and a constant film thickness of 40nm. The triple gradient sample has three different regions, with the inner region being identical to the single gradient film structure. The outer regions are of pure Ni or Au respectively, but possess a thickness gradient ranging from 40 to 0 nm.

Fig. 2

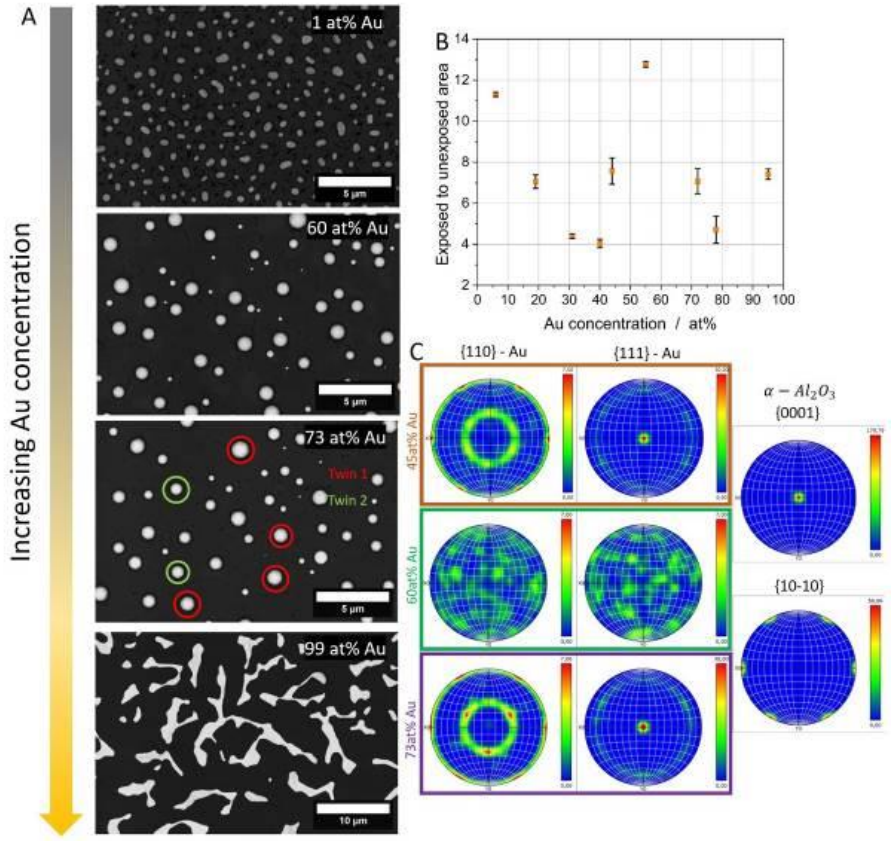

Fig. 2: A) SEM images of the single gradient sample post heating reveale, that the dewetted morphologie differes depending on the Au conetration. At a distinct Au concetration the dwetting kinetic increases and particels are formed. B) Annalizing the relation between exposed to unexposed area showed that the Au concentration further the influence of Au on the dewetting kinetic.. C) EBSD measurements show that the orientation of particles is strongly influenced by the Au concentration. At a Au concentration of arround 60 at.% the fiberlike orientation of the particles is lost and no specific plane is favoured

MS2.004-invited

Unravelling shear band formation and propagation in metallic glasses through 4D-STEM

C. Gammer[1], H. Sheng[1], S. Fellner[1], D. Sopu[1], J. Eckert[1]

[1]Erich Schmid Institute of Materials Science, Austrian Academy of Sciences, Leoben, Austria

Metallic glasses (MGs) are an exciting new class of materials due to their unique mechanical and functional properties. Still, potential applications are hindered by their limited ductility caused by the formation of shear bands leading to catastrophic failure. A fundmental understanding of the shear banding process is key for improving the mechanical properties of MGs. While progress in the understanding of deformation localization was made using colloidal solids or atomistic simulations, highlighting the importance of nanoscale structural variations and local strains for shear banding, direct experimental studies are scarce due to limited characterization techniques.

In the current work we study the deformation of metallic glasses at the nanoscale by scanning transmission electron microscopy (STEM) imaging using a JEOL 2200FS equipped with an in-column energy filter. To quantify local density and strain, a map of precession nanodiffraction patterns is recorded using 4D-STEM. Scanning and precession of the electron beam is controlled by a TVIPS universal scanning generator and the nanodiffraction patterns are recorded using a fast CMOS camera (TVIPS XF416) and a direct electron detector (Quantumdetectors MerlinEM 4R). A Cu46Zr46Al8 bulk MG plate is made by suction casting and shear bands (SB) are introduced by uniaxial compression. Cross section specimens are extracted on major SBs using a focused ion beam dual-beam workstation. Precession nanodiffraction enables to map the strain at at sufficient spatial resolution (<2 nm) to quantify atomic density and strain distribution within an individual SB.

Figure 1 shows a HAADF image and a local density map, revealing a decrease in atomic density within the SB [1]. In addition, the SB shows density alternations from the atomic scale to the submicron scale. The nanoscale density alternations show good agreement with molecular dynamic simulations indicating that they are linked to the autocatalytic generation of shear transformation zones, while the density alternation at submicron scale results from the progressive propagation of the SB front. The current results demonstrate that a direct quantitative measurement of strain in amorphous nano-volumes is important for revealing fundamental deformation processes in MGs, eventually allowing to tune their mechanical properties in a more controlled fashion.

This work was supported by the Austrian Science Fund (FWF): Y1236-N37.

[1] H. Sheng, D. Şopu, S. Fellner, J. Eckert, C. Gammer PHYSICAL REVIEW LETTERS 128, 245501 (2022)

Fig. 1

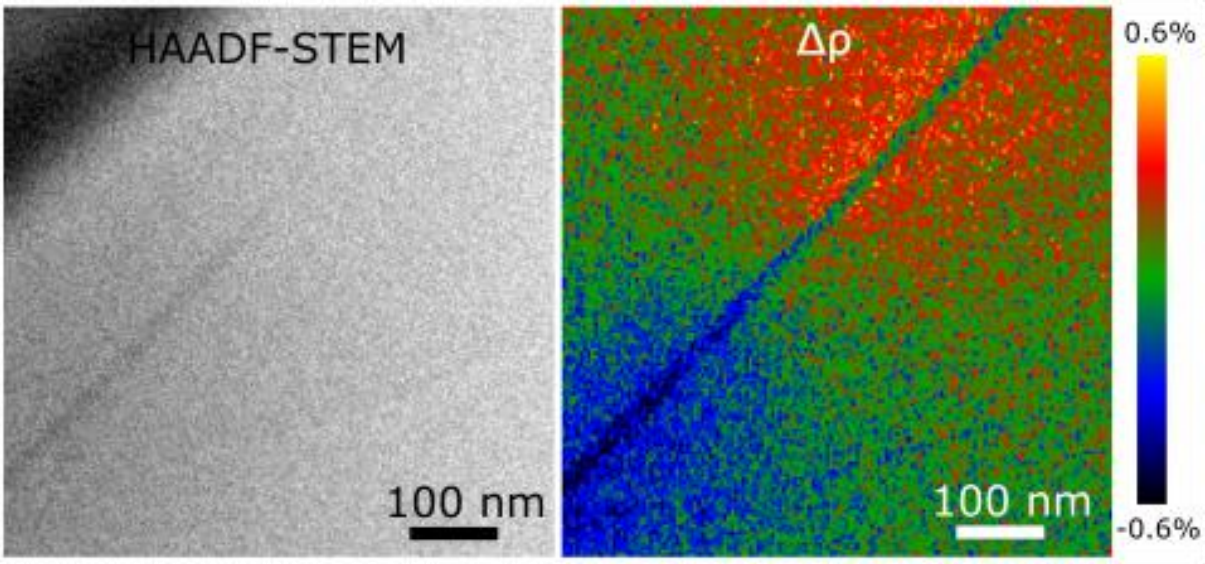

MS2.005

Electron time correlation microscopy and the stability of the numerical evaluation

M. Peterlechner[1], D. Radić[1], K. Spangenberg[1], O. Vaerst[1], M. Demming[1], G. Wilde[1]

[1]University of Münster, Institute of Materials Physics, Münster, Germany

The high spatial and temporal resolution of electron microscopy opens new ways of characterizing matter. Electron Correlation Microscopy (ECM) is a comparably new method analyzing time-intensity correlations in thermodynamic equilibrium [1,2]. For amorphous materials, transmission electron microscopy (TEM) dark-field (DF) images show speckle contrast arising by local structural arrangements. ECM measures basically a speckle lifetime. In the present work, the ECM data evaluation and the resulting accuracy are discussed. Measuring ECM out of thermodynamic equilibrium at room temperature (RT) was shown recently for a metallic glass [3,4]. ECM measurements out of thermodynamic equilibrium are here denoted Electron time Correlation Microscopy (EtCM). This brings additional evaluation criteria, visualized by calculating two-time correlation functions.

A schematic of EtCM is shown in Figure 1. An amorphous sample is imaged in TEM-DF mode to detect structural arrangements fulfilling the chosen DF condition leading to speckle contrast. Typically about 50 nm in thickness samples and a beam current density of about 105 e-/nm²s at exposure times of seconds are applied. From the image time series, a correlation function (g2(t)) is calculated, which is fitted to a stretched exponential function ($A*[1-exp(-t/\tau)\beta]$, see Figure 1 top-right). A β=1 leads overall to a single exponential function, β<1 to a stretched, and β>1 to a compressed exponential function. The β therefore reflects the energy landscape of the underlying processes. Depending on the material, the correlation time at RT can be extremely large (> 10 k seconds). Consequently, the corresponding data quality is limited due to the limited experimental accessible time. One approach is to extrapolate τ and β to infinitely long measurement times [3] by using e.g. $a*[1-exp(-x/b)]$, where a is the value of τ or β for time to infinity, b is a parameter reflecting how fast the data analysis comes to a numerical steady state and x denotes the experimentally determined τ or β for different, finite times. It should be noted, that τ and β also depend on the DF condition as the beam tilt selects the scattering vector magnitude.

In Figure 2, an example of β and τ as a function of the evaluated stack length is shown. Evaluating short measurement time leads to numerically unstable values. Evaluating longer times leads to more stable values, underestimating the real values. The dependence of β and τ on the evaluated time are different. However, the data analysis using different fractions of a DF-time series is a robust way to gain insights into the stability of the fitting parameters β and τ. Moreover, by extrapolating β and τ to timeàinfinity allows to estimate the real values (at a given beam current), or at least to estimate a proper measurement time for an EtCM experiment. Based on literature and numerical tests, the τ and β values are reviewed and discussed.

[1] L. He at al., Microsc. and Microanal. 21 (2015) 1026-1033.

[2] P. Zhang et al., Nature Communications (2018) 9:1129.

[3] K. Spangenberg et al., Adv. Funct. Mater. 31 (2021) 2103742.

[4] M. Stringe et at., J. Alloys Compd. 915 (2022) 165386.

Fig. 1: Schematic EtCM measurement: (left) data acquisition and (right) data analysis including a two-time correlation plot to confirm a quasi-equilibrium condition.

Fig. 2: Streching exponent β and correlation time τ obtained by fitting a (fraction of a) dataset.

Fig. 1

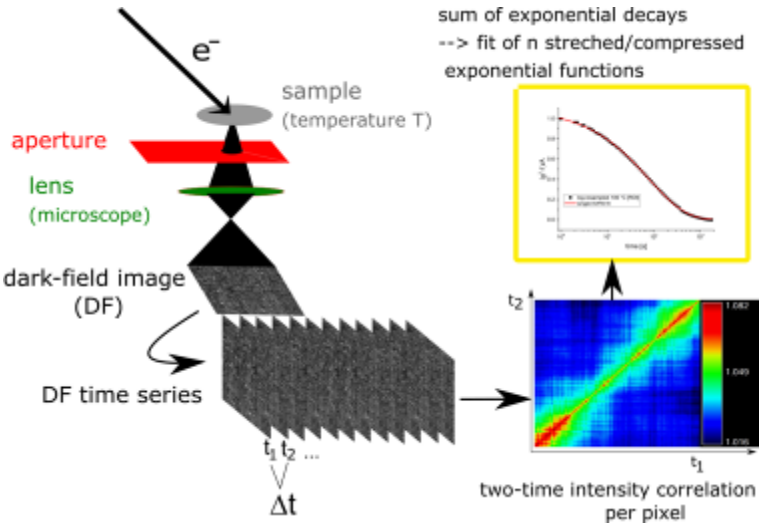
e⁻
sample
(temperature T)
aperture
lens
(microscope)
dark-field image
(DF)
DF time series
t1 t2 ...
Δt
sum of exponential decays
--> fit of n streched/compressed
exponential functions
t2
t1
two-time intensity correlation
per pixel

Fig. 2

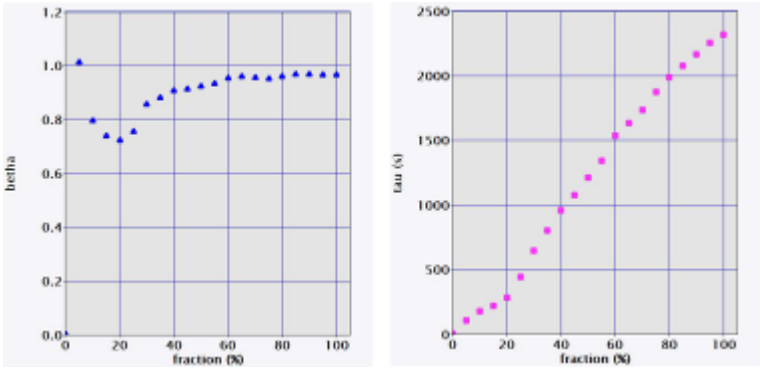
betha
fraction (%)
tau (s)
fraction (%)

MS2.006

Segregation to creep-induced planar faults in Ni-base SX superalloys

Z. Long[1], C. Dolle[1], D. Bürger[2], Y. M. Eggeler[1]

[1]Karlsruher Institut of Technologie (KIT), Laboratory for Electron Microscopy, Karlsruhe, Germany
[2]Ruhr University Bochum, Institute for Materials, Bochum, Germany

Ni-base single-crystal (SX) superalloys find application in turbine blades for gas engines due to the high-temperature and high-stress strength originating from the coherent γ/γ'' microstructure. It is well-known at sufficiently high stresses, two 1/2 dislocation families with different Burgers vector can react and dissociate into two partial dislocations in γ channels. This allows the leading 1/3[-1-12] Shockley partial dislocation continuously gliding on {111} planes to cut into γ'' precipitates where they create planar faults [1]. We study the segregation behaviours of alloying elements across the planar faults by performing the [11-2] (111) creep shear experiments, to intentionally activate the slip system [11-2] (111) with the highest Schmid factor of 1 where the resolved shear stress is exactly equal to loading stress. The creep-deformed specimens are interrupted after 1% and 2% shear strain under 250 MPa at 750°C. The resulting microstructure is investigated using conventional transmission electron microscopy (TEM), analytical scanning TEM (STEM) with energy-dispersive X-ray spectroscopy (EDXS) focussing on structural, physical, and chemical details of the local deformation.

Fig. 1 presents the specimen perpendicular to the (111) plane with the [1-10] direction parallel to the electron beam. Numerous stacking faults (SF) are observed after 1% and 2% creep strains. Fringe contrasts under two-beam conditions indicate inclined stacking faults, shown in Fig 1a and 1d, where the 2% strain sample has more planar faults within one γ'' precipitate indicating a higher density of planar faults in the 2% sample. High-resolution STEM micrographs illustrate the superlattice extrinsic nature of stacking faults (SESF) in the 1% and 2% strained samples, see Fig1b and 1e. The chemical distributions across SESF are measured by EDXS and the corresponding concentration profile of 1% and 2% samples are shown in Fig. 1c and 1f respectively. Both samples show almost similar segregation tendency, which is that γ forming elements Cr, Co and Re are enriched across the SESF while γ'' alloying elements Ni and Al are depleted, which is partly in agreement with theoretical predictions [2]. For these measurements all microscope parameters and sample thickness for EDXS analysis are kept the same to quantitatively find out how creep strain and time affect the evolution of segregation.

Figure 1.

(S)TEM micrographs of the [1-10] foil normal sample show typical planar faults in Ni-base SX superalloys crept at 750 °C/250 MPa to creep strains of 1% (upper row) and 2% (lower row). TEM bright filed images present fringe contrast of inclined stacking faults under two-beam conditions in (a) g = (00-2) and (d) g = (002) excitation condition. High resolution STEM micrographs indicate the superlattice extrinsic nature of edge-on stacking faults of (b) 1% and (e) 2% strain specimens. Alloying concentration profiles across SESF of (c) 1% and (f) 2% from corresponding EDXS mappings.

References

[1] Eggeler, Y. M. *et al. Annu. Rev. Mater. Res.*, **2021**, *51,* 209–240.

[2] Zhao, X. et al. *Comput. Mater. Sci*, **2022**, *202*, 1–8.

[3] Authors gratefully thank Christian Kübel, Di Wang and Yuting Dai (Electron Microscopy and Spectroscopy Laboratory, KIT) for HRSTEM micrographs and EDXS results, and acknowledge the DFG priority program SFB-TR 103.

Fig. 2

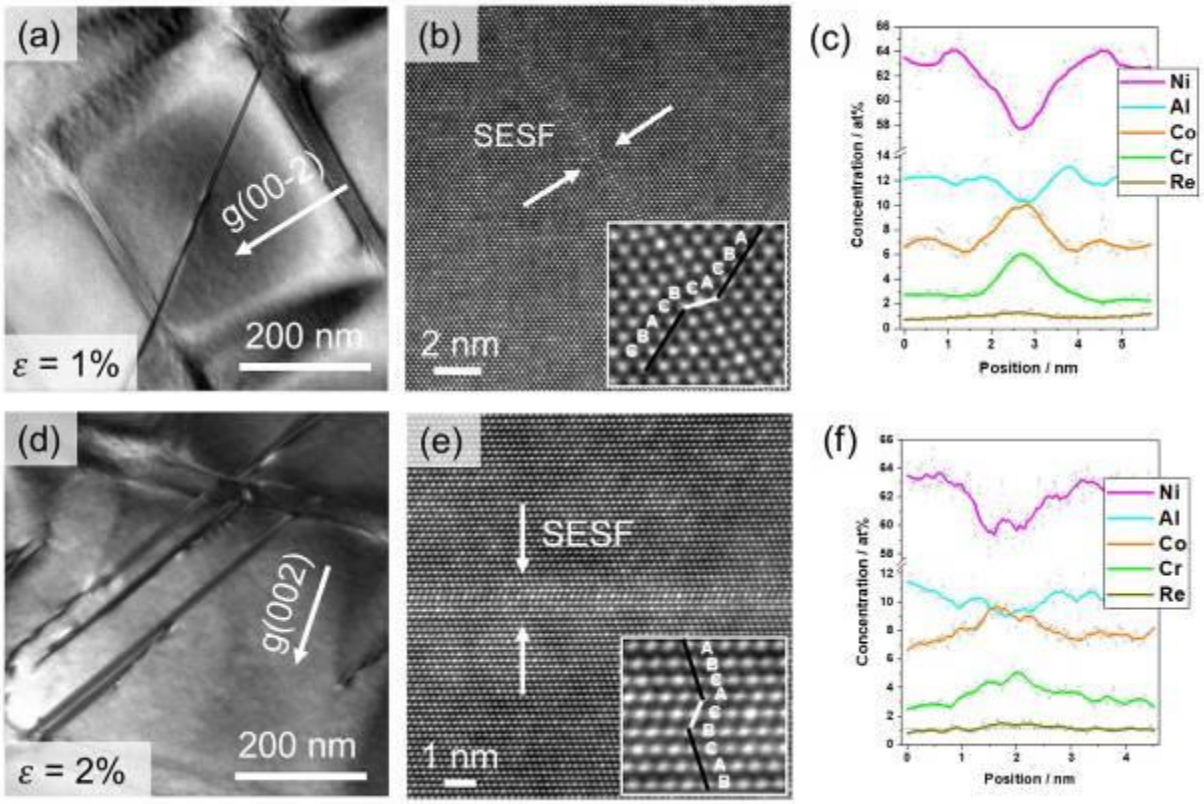
(a)
g(00-2)
200 nm
ε = 1%
(b)
SESF
2 nm
(c)
Ni
Al
Co
Cr
Re
Concentration / at%
Position / nm
(d)
g(002)
200 nm
ε = 2%
(e)
SESF
1 nm
(f)
Ni
Al
Co
Cr
Re
Concentration / at%
Position / nm

MS2.P002

In-situ observation of structural and optical properties changes in Ag-Cu plasmonic nanoparticles by using specimen heating holder

A. Yasuhara[1,2], M. Homma[2], T. Sannomiya[2]

[1]JEOL Ltd., EM Application department, Tokyo, Japan
[2]Tokyo Institute of Technology, Yokohama, Japan

[Introduction] Plasmonic nanoparticles are widely studied and used in various fields because they show unique optical properties. The optical properties, due to the surface plasmon resonances around the nanoparticles, are known to be dependent on their sizes, shapes, and dielectric functions of materials. Previously we fabricated several kinds of nanoparticles with different elemental compositions using the dewetting method[1, 2], and studied their optical properties and nanostructures by Transmission Electron Microscope (TEM). However, there are still unclear parts in the formation process of the nanoparticles during the heating procedure. In order to control and optimize the optical properties properly, the knowledge of the fabrication process of the nanoparticles becomes to be essential and important information.

[Objectives] We aim to clarify the process of nanoparticle formations and their structural changes during the dewetting procedure using a TEM and a dedicated specimen heating holder.

[Materials and Methods] The initial state of the sample was prepared by co-evaporating pure Ag and pure Cu on a thin SiO2 film for TEM observation. In order to characterize the structural changes of nanoparticles, we performed *in-situ* TEM observation by elevating the temperature from room temperature (RT) to 400 °C by a specimen heating holder. Besides, we measured the bulk optical properties of the nanoparticles during the heating process, comparing to their structural changes.

[Result] Figure 1 shows the in-situ measurement results of the optical properties of Ag-Cu nanoparticles. The peaks of the extinction spectrum were shifted to the shorter wavelength during the heating process and the double peaks were observed at higher temperatures. Figure 2 shows the elemental distributions of Ag-Cu nanoparticles by EELS at RT and 400 °C. The core-shell type nanoparticles were formed at RT. After the heating process, we found the nanoparticles changed to the Janus-type phase-separated nanoparticles.

[Conclusion] We investigated the structural changes of Ag-Cu nanoparticles by in-situ TEM observation. From the in-situ TEM results, we found that the size of the nanoparticles increased notably and in addition the Ag and Cu phases are more clearly separated at 400 °C. The red-shift of extinction spectrum is thought to be caused by the changes in the sizes and shapes of nanoparticles. The double peaks of the extinction spectrum are concluded to be related to the phase separation of the nanoparticles.

Figure 1. Extinction spectrum of Ag-Cu binary nanoparticles during the heating process

Figure 2. Elemental maps of Ag-Cu binary metal nanoparticles at room temp (a) and 400 °C (b) measured by Electron Energy Loss Spectroscopy (EELS). Green and red colors in elemental maps indicate Cu and Ag elemental distribution, respectively.

[References]

[1] C. Wadell et al., *J. Phys. Chem. C.* 121 (48), 27029-27035, 2017,

[2] A. Yasuhara et al., *J. Phys. Chem. C.* 124 (28), 15481–15488, 2020

Fig. 1

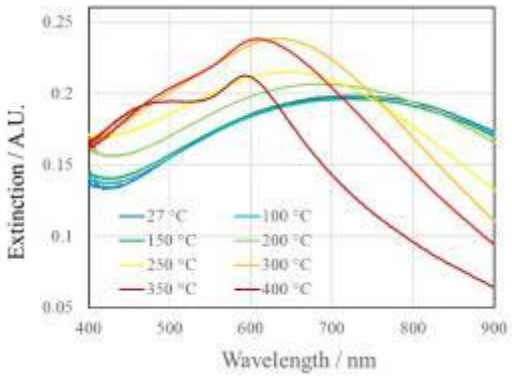
Extinction / A.U.
Wavelength / nm
0.25
0.2
0.15
0.1
0.05
400
500
600
700
800
900
27 °C
100 °C
150 °C
200 °C
250 °C
300 °C
350 °C
400 °C

Fig. 2

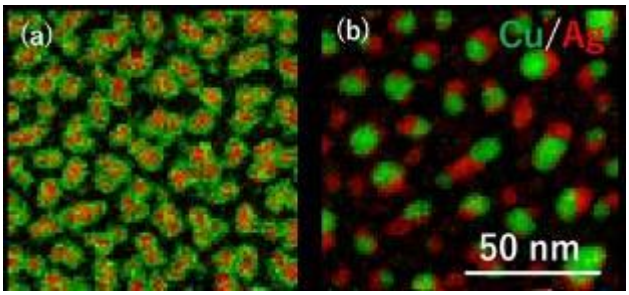
(a)
(b)
Cu/Ag
50 nm

MS2.P003

Electron correlation microscopy study of thermally pre-treated PdNiP bulk metallic glass

O. Vaerst[1], G. Wilde[1], M. Peterlechner[1]

[1]Westfälische Wilhelms-Universität Münster - Institute of Material Physics, Münster, Germany

Achieving both temporal and spatial resolution in an analysis opens new ways of investigating materials. Electron Correlation Microscopy (ECM) is a rather new method proposed by He et al. [1] yielding temporally resolved data on structural rearrangements in spatially well-resolved transmission electron microscopy (TEM). This opens up the possibility of observing atomic processes that govern basic mechanisms and the unique properties of amorphous metals.

In the present study, the focus lies on amorphous PdNiP. Pre-treatments, such as annealing and treatments of thermo-mechanical kind, significantly influence the local structure, kinetic stability, and mechanical properties of this bulk metallic glass. Thus, it is of great interest to study the dynamics in the material on the atomic scale after treatment to shed light on the origin of the property changes.

For these investigations, $Pd_{40}Ni_{40}P_{20}$ samples are produced via copper-mould casting. Basic characterizations of the material are performed, including verifying the amorphous state and the composition. Subsequently, samples are pre-treated thermally in a differential scanning calorimeter (DSC) by implementing an annealing routine below the glass transition temperature. The atomic dynamics of different thermally treated sample states are investigated at room temperature using ECM. This technique is based on investigating the speckle contrasts in dark-field images over time. By that, atomic rearrangements and local dynamics can be studied with nanometer spatial resolution [1,2]. The schematic of an ECM measurement and the corresponding analysis are shown in Fig. 1.

The obtained time series of dark-field images from ECM measurements need to be corrected for drift before speckle contrasts can be analysed. The drift-correction method that we found to work for all our data sets consists of three steps including a contrast enhancement step for more precise drift measurements. From changing speckle contrasts over time an autocorrelation function $g_2(t)$ can be calculated. By fitting a Kohlrausch-Williams-Watts function (KWW) to $g_2(t)$ the characteristic relaxation times τ are found. We analysed partial data stacks to evaluate the resilience of the obtained relaxation times and compared calculated autocorrelation functions of different sample states. The obtained relaxation times for a PdNiP as-cast state depicted in Fig. 2 are a measure of the local dynamics within the time spectrum accessible by the method.

To conclude, the effect of thermal pre-treatments on ECM evaluation parameters of amorphous PdNiP is discussed. Such investigations of atomic mobilities give further insight into the amorphous phase as well as into the local relaxation dynamics of a bulk metallic glass.

[1] L. He at al., Microsc. and Microanal. 21 (2015) 1026-1033.

[2] K. Spangenberg et al., Adv. Funct. Mater. 31 (2021) 2103742.

[3] P. Zhang et al., Nat. Commun. (2018) 9:1129.

Funding by DFG is acknowledged.

Fig. 1: Schematic setup for ECM measurement (left) and data analysis (right), adapted from [3]. Speckle contrast changes in dark-field images over time are correlated and fitted by a stretched exponential function (KWW). **Fig. 2:** Relaxation times τ for as-cast PdNiP as obtained after fitting a KWW function to the correlated speckle contrast changes over a measurement time of 20000s.

Fig. 1

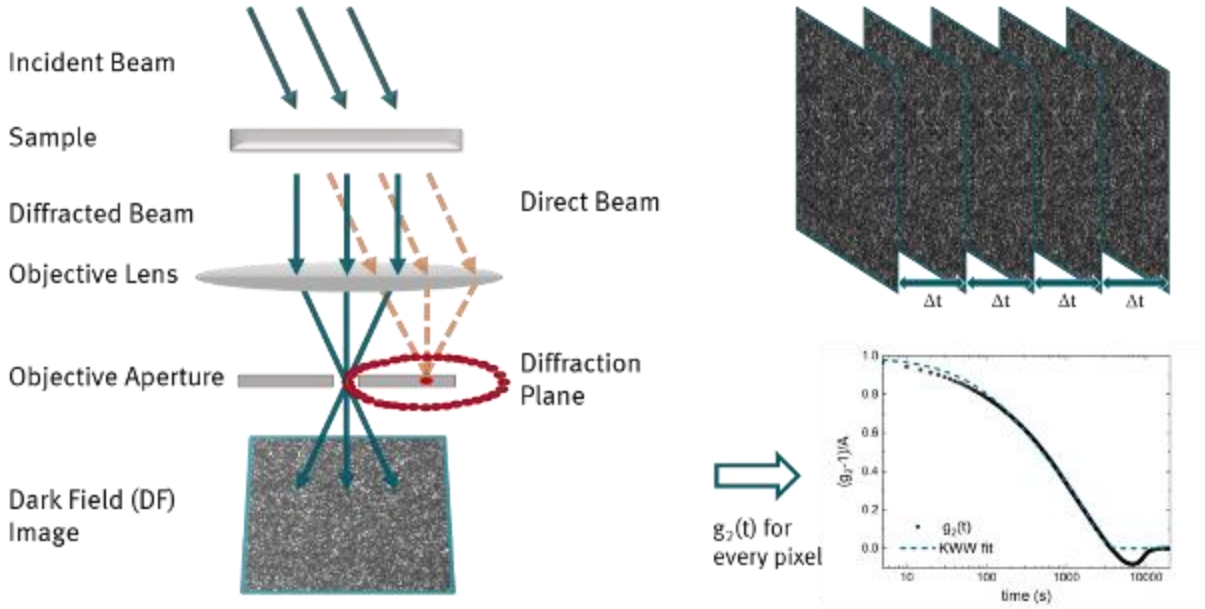
Incident Beam
Sample
Diffracted Beam
Direct Beam
Objective Lens
Objective Aperture
Diffraction Plane
Dark Field (DF) Image
Δt
Δt
Δt
Δt
g2(t) for every pixel
(g2-1)/A
g2(t)
KWW fit
time (s)

Fig. 2

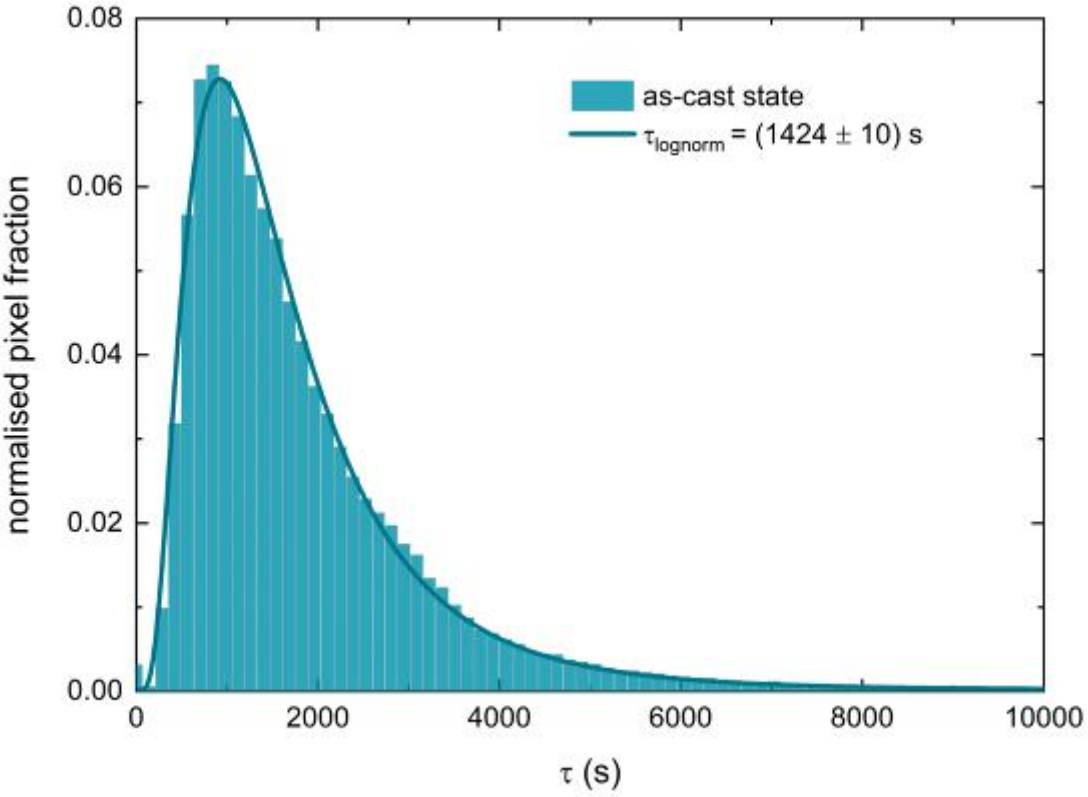
as-cast state
τlognorm = (1424 ± 10) s
normalised pixel fraction
τ (s)
0.00
0.02
0.04
0.06
0.08
0
2000
4000
6000
8000
10000

MS2.P004

Epitaxy and solid-state-dewetting of Au on polar surfaces of ZnO

M. Landes[1], M. Dierner[1], J. Will[1], E. Spiecker[1]

[1]Institue of Micro- and Nanostucture Reserach, Materials Science and Engineering, Erlangen, Germany

Metal/oxide heterointerfaces are omnipresent in functional materials and their microstructure often determines macroscopic properties. For ceramics with a wurtzit lattice like zinc oxide the surface polarity plays a major role, because it can change electronic properties [1] and influence the properties of deposited metal films [2].

In this study, the epitaxial and microstructural evolution of thin gold films on (0001)/(000-1) oriented ZnO substrates is investigated. For this, Au thin films with a thickness of 40 nm are deposited directly onto the (0001) Zn-ZnO and (000-1) O-ZnO surfaces by electron beam evaporation. Annealing of the samples at elevated temperatures was carried out with an rapid thermal annealing (RTA) furnace. During heating a constant nitrogen flow is introduced, whereas a fast cooling rate of ~200 °C/s is achieved by dropping the sample on a water-cooled steel plate. SEM imaging and EBSD measurements reveal that both epitaxial grain growth (Figure 1) and solid-state-dewetting of the film highly depend on the polarity of the ZnO surface.

From the as-deposited state up to temperatures 600°C fine grains with a predominant orientation of Au(111)[110]||ZnO(0001)[11-20] (OR2) are present on both ZnO terminations. EBSD imaging shows, that during heating at 800 °C and above large grains form in the Au film on the Zn terminated substrate. These grains have an Au(111)[110]||ZnO(0001)[10-10] orientation (OR1) and exhibit a higher thermal stability. In contrast, grain growth and solid-state dewetting of the Au film are retarded and accelerated on the oxygen terminated surface, respectively. As a result, a fiber texture with both OR1 and OR2 evolves. The different dewetting rates can be explained by a larger binding energy of Au to the zinc terminated surface [3], which lowers the Au/Zn-ZnO interface energy and makes it more resistant to dewetting than the weakly bound oxygen side. High-resolution STEM imaging was carried out to investigate the Au ZnO interface. For Au on O-ZnO a semi-coherent interface with misfit dislocations is present (Figure 2a). For the epitaxial Au/Zn-ZnO, interface reconstruction (Figure 2c) with a regular spacing is observed. This reconstruction of the Zn and Au atoms close to the interface likely reduces the interface energy of OR1, thus facilitating the transformation from OR2 to OR1.

[1] Rahman, Faiz. "Zinc oxide light-emitting diodes: a review." *Optical Engineering* 58.1 (2019)

[2] Dulub, Olga, Matthias Batzill, and Ulrike Diebold. "Growth of copper on single crystalline ZnO: surface study of a model catalyst." *Topics in Catalysis* 36.1 (2005): 65-76.

[3] Shuyi Wei, Zhiguo Wang, Zongxian Yang, "First-principles studies on the Au surfactant on polar ZnO surfaces", Physics Letters A, Volume 363, Issue 4, (2007)

Fig. 1

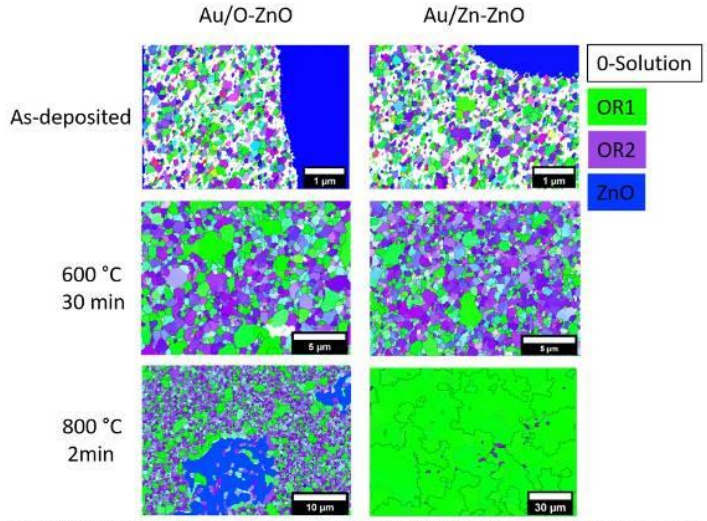

Figure 1: EBSD maps of Au on the polar surfaces of ZnO. At 800 °C large epitaxial grains appear on Zn-ZnO, on O-ZnO the grains with the same orientation relation grow slightly faster but do not dominate

Fig. 2

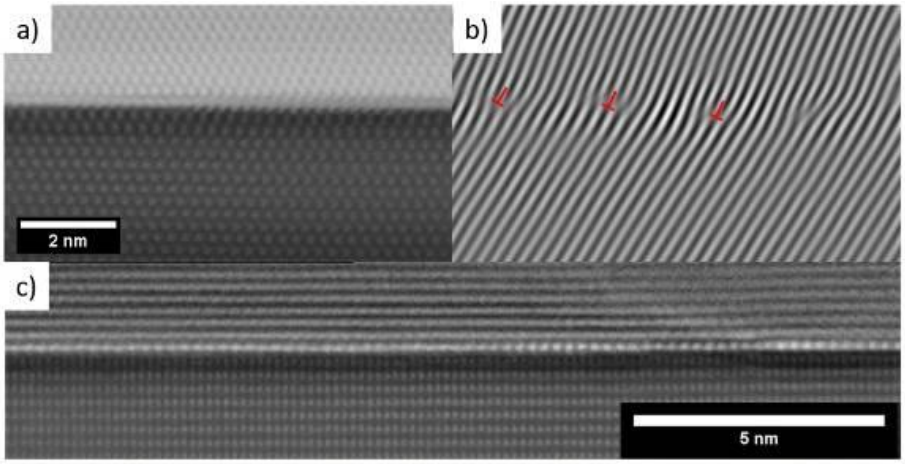

Figure 2: a) HRSTEM image of the Au/O-ZnO interface with misfit dislocations marked in the b) Fourier filtered image c) HRSTEM image with high-pass filter of the Au-ZnO interface the high and low intensity areas at the first Au layer are caused by interface reconstruction

MS2.P005

Effects of damage dose and temperature on the radiation induced formation of rhenium clusters in tungsten

M. Klimenkov[1], U. Jäntsch[1], M. Rieth[1]

[1]Karlsruher Institut of Technologie (KIT), Institute for Applied Materials - Applied Materials Physics, Eggenstein-Leopoldshafen, Germany

The development of appropriate materials for fusion reactors that can sustain high neutron fluence at elevated temperatures remains a great challenge. Tungsten is one of the promising candidate materials for plasma-facing components of future fusion reactors, due to several favorable properties as for example a high melting point, a high sputtering resistivity, and a low coefficient of thermal expansion. Pure W was neutron irradiated at 600 °C, 900 °C, 1000 °C, 1100 °C, and 1200 °C with a dose of ~1 dpa, and its microstructure was subsequently analyzed using transmission electron microscopy (TEM). The study provides the basis for a deeper understanding of the microstructural evolution of W under neutron irradiation.

Three types of defects forms in W as result of neutron irradiation: (i) voids, (ii) dislocation loops and (iii) W-Re-Os containing precipitates. The TEM study includes a detailed examination of the defect structure and, in particular, the distribution of transmutation-induced Re and Os, whose content is expected to be in the range of ~2% for Re and 0.2% for Os under the applied irradiation conditions. Analytical investigations show that the voids, precipitates and loops are surrounded by 8-15 nm Re- and Os-rich "clouds" (Fig. 01). The "clouds" do not produce any diffraction contrast in TEM images and can only be visualized by analytical methods. Grain boundaries act as sinks for all types of point defects, i.e., vacancies and interstitials, as well as Re and Os atoms, leading to the formation of a 10-20 nm wide zone adjacent to the grain boundaries that is free of voids and precipitates (the so-called depleted zone). In addition, we found that Re and Os are often inhomogeneously distributed along grain boundaries, which is due to segregation at boundary dislocations (Fig. 1).

The elemental maps in Fig.1, show the general distribution of transmutation elements on the large scale and are less useful for identifying concentration differences within individual clouds. The minor intensity variations are not well reproducible and identifiable in the color map. For this reason was used the intensity profile analysis across defects to show differences in Re and Os distribution in W irradiated at 600 °C (Fig.2). The elemental profiles in Fig. 2e shows that the Re intensity decreases slightly in the center, reflecting the position of the void. Precipitates, on the contrary, show a higher local Re and Os concentration in the center (Fig. 2e`). The intensity profiles across the marked loop are plotted in Fig. 2e``. It is notable that Re exhibits a uniform distribution in the area inside the loop, while Os tends to segregate at the dislocation line (Fig. 2e,e``).

This study presents the results of extensive microstructural analyses of W samples, which were neutron irradiated at temperatures between 600 °C and 1200 °C, up to a damage dose of ~1.0 dpa. The formation of dislocation loops, voids, and precipitates consisting of Re-Os- χ-phases was observed and characterized in detail.

Fig. 01. STEM-EDX spectrum images show the distribution of transmutation-induced Re (green) and Os (blue) inside W irradiated at 600 °C (a,a`), 900 °C (b, b`) and 1100 °C (e, e`).

Fig.02. Re, Os and combined Re/Os elemental maps obtained in W irradiated at 600 °C (a-d). The Re and Os intensity profiles of void (magenta arrow), a precipitate (yellow arrow) and a dislocation loop (white arrow) shown in parts (e-e``).

Fig. 1

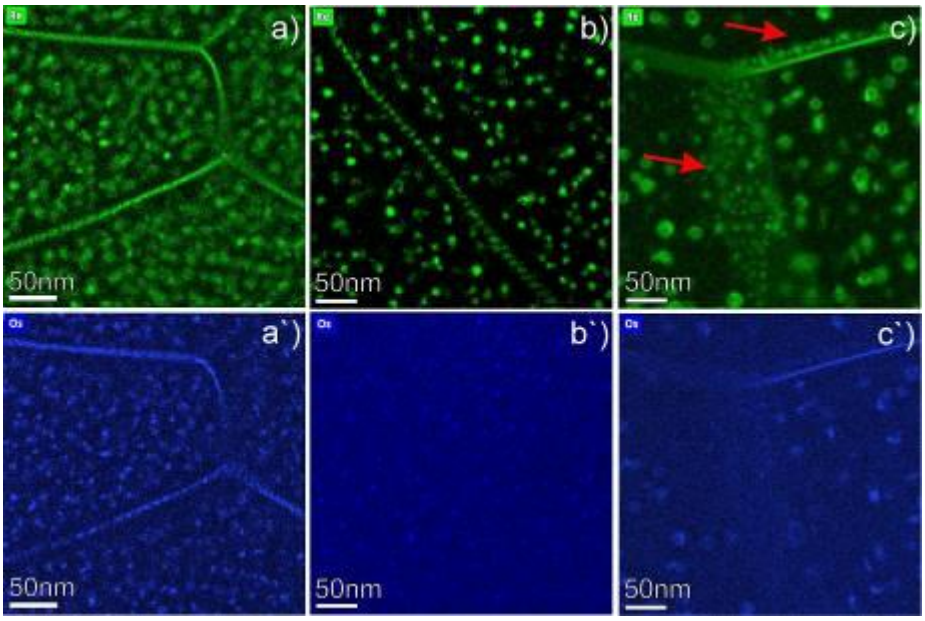
a)
b)
c)
50nm
50nm
50nm
a`)
b`)
c`)
50nm
50nm
50nm

Fig. 2

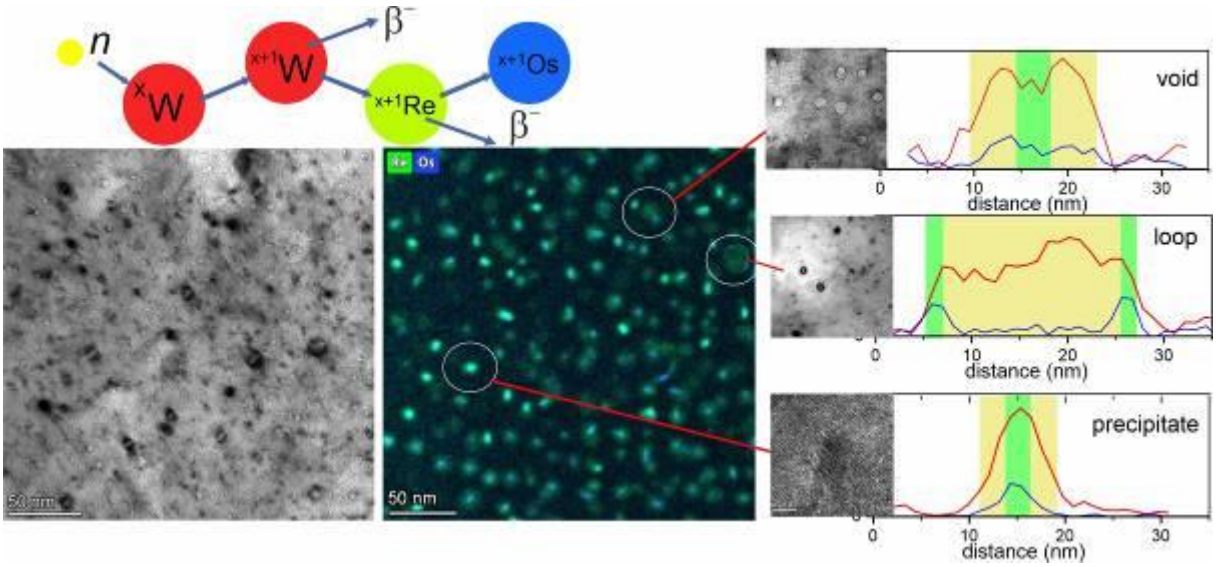
n
β⁻
β⁻
50 nm
void
loop
precipitate
0
10
20
30
distance (nm)

MS2.P006

The peculiarity of FeRh alloys: a thorough TEM investigation

E. Adabifiroozjaei[1], N. Kani[1], R. Winkler[1], T. Jiang[1], O. Recalde-Benitez[1], A. Zintler[2], A. Chirkova[3], K. Skokov[3], O. Gutfleich[3], L. Molina-Luna[1]

[1]TU Darmstadt, Advanced Electron Microscopy, Darmstadt, Germany
[2]Karlsruher Institut für Technologie (KIT), Laboratorium für Elektronenmikroskopie, Karlsruhe, Germany
[3]TU Darmstadt, Functional Materials, Darmstadt, Germany

Introduction: Fe50Rh50 alloys are known to have a B2 BCC structure with an antiferromagnetic (AFM) to ferromagnetic (FM) transition at near room temperature. The transition is isostructural with about 1% change in volume and is accompanied by giant magnetoresistive and magnetocaloric effects. Therefore, there has been a lot of interest on the Fe50Rh50 alloy as a model system [1]. Interestingly, the majority of the previously reported work do not provide extensive local atomic structure investigations (mostly thin films). Thus, the structural characteristics of the alloy at the AFM or FM states remains controversial [2]. Since this alloy is among the betta alloy series (CdAu, TiNi, Fe-C, etc…), it is expected to present a pre-martensite structure followed by a martensite structure upon cooling at cryogenic temperature[3]. The martensite was also predicted by extensive first principal calculations[2,4]. However, so far, no evidence has been given regarding the formation of either pre-martensite or martensite structures in the Fe50Rh50 alloy.

Objective: To use various TEM techniques to investigate the FeRh 50/50 alloy and demonstrate that at the AFM state, the alloy is in the pre-martensite state.

Materials and methods: Fe50Rh50 alloys were prepared at the German Electron Synchrotron (DESY) using an electromagnetic levitation facility developed and constructed at the IFW Dresden. The Fe50Rh50 material was alloyed by arc-melting of the appropriate amounts of the pure Fe (99.995%, Alfa Aesar) and Rh (99.9%, Alfa Aesar). After casting, the alloys were heat-treated at 1150°C for 9 days and quenched in water. During the heat-treatment the alloys were sealed in quartz tube with Ar atmosphere. Afterwards, the bulk alloys were cut by wire cutter and thin slices were polished to thickness of ~50 µm. Then, the slices were milled using precision ion polishing system (PIPS) with energy of 3 KeV and angles of 4 degrees. The prepared thin sections were investigated using a variety of TEM techniques including CTEM, HRTEM, STEM (HAADF), and EDS.

Results: Fig. 1 shows the HRTEM and corresponding Fast Fourier Transformed (FFT) images of the FeRh 50/50 alloy in three principal directions ([001], [-110], and [111]). As seen, although the structure of the alloy match perfectly with the B2 BCC structure, there is systematic modulation along certain reflexes (100 and 110). This was also confirmed by HAADF-STEM imaging, the results of which are given as Fig. 2. In the corresponding Z-contrast images, the modulation can only be easily seen in the [111] zone axis.

Conclusions: Our results show that the B2 BCC alloy of FeRh 50/50 at the AFM state possess a pre-martensite structure.

We acknowledge financial support by the Deutsche Forschungsgemeinschaft (DFG) within the CRC/TRR 270 (Project-ID 405553726).

Figure 1. Representative nanostructure of FeRh alloys in three principal directions: a, b and c are HRTEM images in [001], [-110], and [111] zone axes, while d, e, and f are FFT images of a, b, and c. Modulation in HRTEM images are shown as parallel pale green lines, while in FFT images related superlattice reflexes are distinguished by red circles.

Figure 2. Representation of arrangement of Fe (small) and Rh (large) atoms in three principal zone axes of alloy. Modulated structure (dashed parallelograms) is visible in [111] zone axis. For comparison, ideal arrangement of atoms exported from B2-BCC structure are imposed on nanostructures. In imposed images, green and yellow atoms stand for Fe and Rh, respectively.

Fig. 1

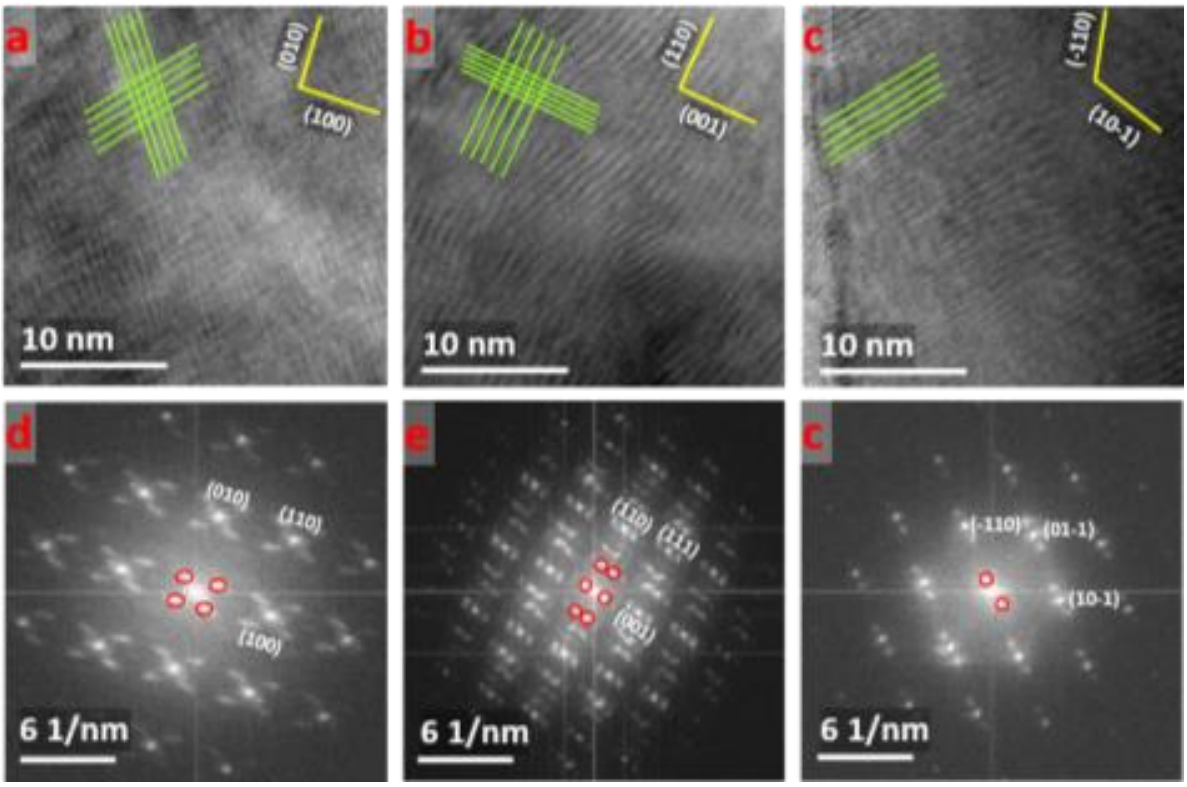
a
(010)
(100)
10 nm
b
(110)
(001)
10 nm
c
(-110)
(10-1)
10 nm
d
(010)
(110)
(100)
6 1/nm
e
(110)
(111)
(001)
6 1/nm
c
(-110)
(01-1)
(10-1)
6 1/nm

Fig. 2

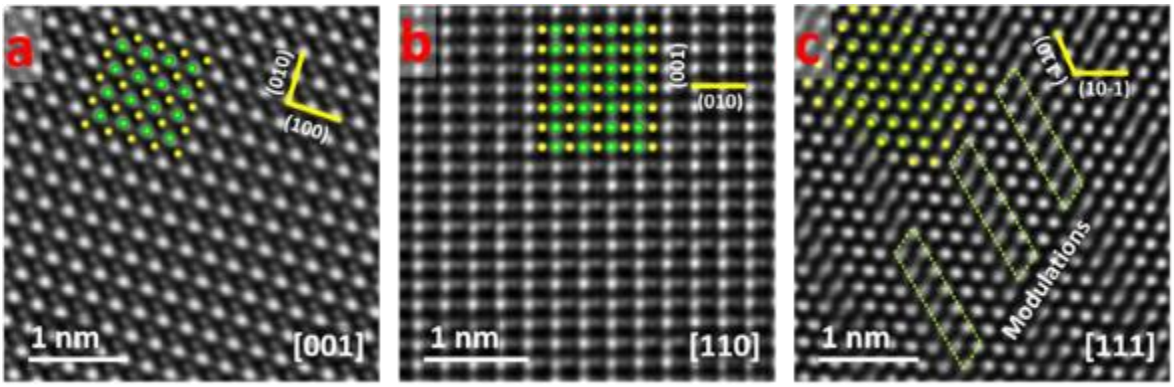
a
(010)
(100)
1 nm
[001]
b
(001)
(010)
1 nm
[110]
c
(01-1)
(10-1)
Modulations
1 nm
[111]

MS2.P007

TEM studies of the long-term high-temperature stability of TiAl electrodes for high-temperature surface acoustic wave devices

M. Seifert[1], B. Leszczynska[1], S. Menzel[1], T. Gemming[1]

[1]IFW Dresden, Dresden, Germany

There is a great need in industry for wireless sensors working at high temperatures (above 300 °C) to monitor and control high-temperature processes. Surface acoustic wave (SAW) sensors are promising candidates to realize such devices. A SAW sensor consists basically of a piezoelectric substrate on which metallic electrodes with a defined geometry are prepared. Both materials, the substrate as well as the metallic electrodes, have to be high-temperature stable to enable the application at the aimed high temperatures. Up to now, mainly noble metals, such as Pt-based materials, were reported as a high-temperature stable metallization. However, the strong tendency to agglomeration and the high costs are drawbacks. In former work, we studied the Al-based alloy TiAl as a cost-efficient alternative metallization with promising high-temperature stability up to 600 °C for 10 h by analyzing extended films [1,2].

To study the long term high-temperature stability of TiAl electrodes, TiAl-based SAW sensors were annealed at temperatures up to 600 °C for up to 192 h in air. STEM investigations in combination with EDX and EELS measurements of the electrodes were performed to study their morphology and degradation behavior. To evaluate the influence of the limited dimension of the structured electrodes, the much larger contact pads were analyzed as well.

The samples were realized by e-beam evaporation of alternating thin layers of pure Ti and Al with an individual thickness of 10 nm and a total film thickness of 200 nm on piezoelectric $Ca_3TaGa_3Si_2O_{14}$ (CTGS) substrates. To prevent a chemical reaction between the metallization and the substrate, a 20 nm thick AlNO barrier layer was deposited on top of the substrate prior to the deposition of the metallization. The structured electrodes were obtained using the lift-off technique. Finally, the whole SAW structure was covered with a 40 nm thick AlNO protection layer.

Figure 1 shows STEM images of the electrodes after the annealing in air at 400 and 500 °C for 192 h and at 600 °C for 24 and 192 h. After annealing at 400 °C, an incomplete interdiffusion of the individual metallic layers was observed. EDX analysis revealed a composition of the layers corresponding to the Ti_3Al and $TiAl_2$ phase. After annealing at 500 °C, a layered structure was still visible, corresponding to the TiAl and $TiAl_2$ phase. The annealing at 600 °C for 24 h led to a complete interdiffusion and only minor degradation was observed at the edges of the finger. In contrast to this, annealing at 600 °C for 192 h led to a strong oxidation [3].

The results demonstrated that the TiAl-based SAW sensors are promising devices for a long-term application up to at least 500 °C and allow short- and medium-term application at 600 °C in air.

[1] Seifert M, Lattner E, Menzel SB, Oswald S, Gemming T. Materials. 2020;13(9):2039.

[2] Seifert M, Lattner E, Menzel SB, Oswald S, Gemming T. JMRT 2021;12:2383-95.

[3] Seifert M, Leszczynska B, Menzel S, Gemming T. JMRT 2022;19:989-1002.

The authors gratefully acknowledge funding from German BMWI (grant number 03ET1589 A) and DFG (470028346).

Figure 1: STEM images (predominant element contrast) of the electrodes annealed in air at (a) 400 °C for 192 h, (b) 500 °C for 192 h, (c) 600 °C for 24 h, and (d) 600 °C for 192 h

Fig. 1

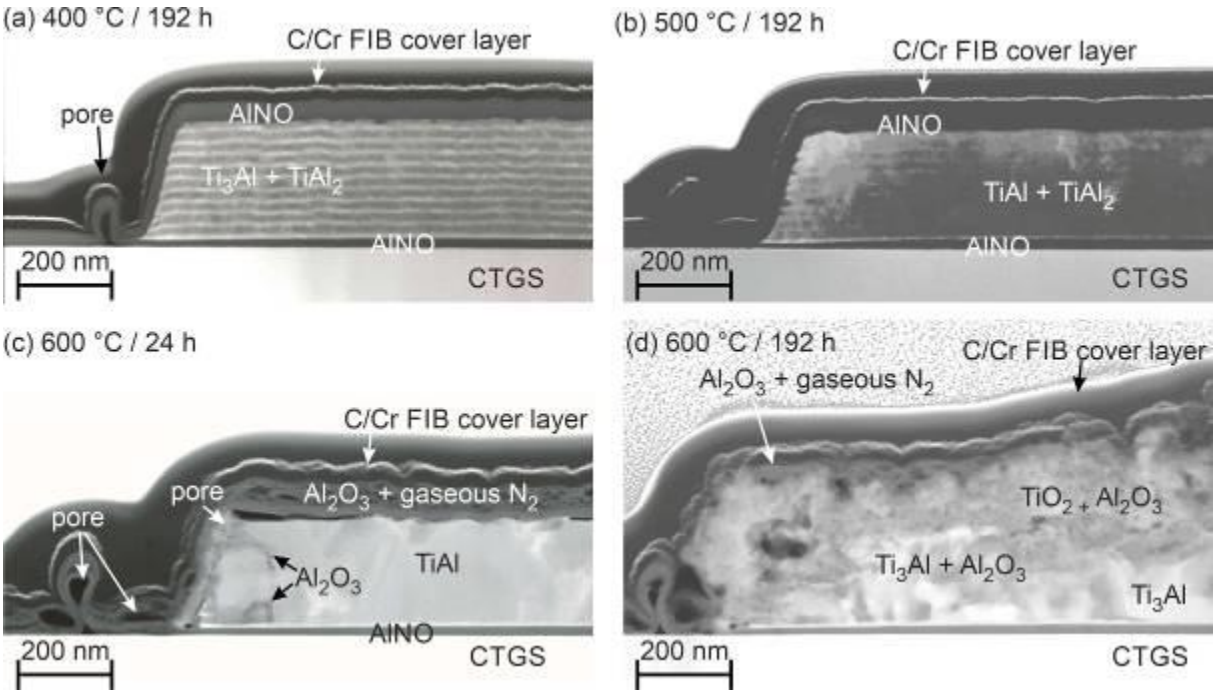
(a) 400 °C / 192 h
C/Cr FIB cover layer
pore
AlNO
$Ti_3Al + TiAl_2$
AlNO
200 nm
CTGS
(b) 500 °C / 192 h
C/Cr FIB cover layer
AlNO
$TiAl + TiAl_2$
AlNO
200 nm
CTGS
(c) 600 °C / 24 h
C/Cr FIB cover layer
pore
pore
Al_2O_3 + gaseous N_2
Al_2O_3
TiAl
AlNO
200 nm
CTGS
(d) 600 °C / 192 h
Al_2O_3 + gaseous N_2
C/Cr FIB cover layer
$TiO_2 + Al_2O_3$
$Ti_3Al + Al_2O_3$
Ti_3Al
200 nm
CTGS

MS2.P008

Helical dislocations in ion-irradiated Fe-9Cr studied by scanning transmission electron microscopy

K. Vogel[1], H. J. Engelmann[2], P. Chekhonin[1], F. Bergner[1], C. Kaden[1]

[1]Helmholtz-Zentrum Dresden-Rossendorf, Institute of Resource Ecology, Dresden, Germany
[2]Helmholtz-Zentrum Dresden-Rossendorf, Institute of Ion Beam Physics and Materials Research, Dresden, Germany

Fe-9Cr is a model alloy for studying irradiation effects relevant for potential applications of high-chromium ferritic/martensitic steels in nuclear energy devices. Ion irradiation is a tool extensively employed with the aim to emulate the neutron damage characteristic for irradiation environments in fission or fusion reactors. Here we report on STEM studies of the microstructure of ion-irradiated Fe-9Cr with special emphasis on the effects of pre-existing dislocations.

Irradiations with 8 MeV Fe3+ ions were carried out at the 3 MV tandetron accelerator at the Ion Beam Center at HZDR. Profiles of displacement damage and implanted ions were calculated using the binary collision code SRIM. Cross-sectional TEM specimens were prepared by focused ion beam lift-out technique using a Thermo Fisher Helios 5CX. The microstructure was studied in a Talos F200X.

Figs. 1a and b display STEM images of a large ferrite grain, which were acquired along the [001] zone axis, Fig. 1c contains the damage profiles calculated by SRIM. In the depth range of the highest concentration of implanted ions, a dark band is visible similar to the defect-rich bands observed in previous studies [1]. The most striking feature of the irradiated microstructure in the range of high displacement damage, but low concentration of implanted ions, is the presence of helical dislocations (examples are labelled H1 and H2). These helices are aligned at an angle of about 45° or -45° with respect to the [100] direction. No helices are present in the non-irradiated substrate. Here we observe a network of curved dislocation segments as well as nearly straight dislocation lines (S1 and S2), the latter showing the same alignment as the helices. The higher magnified image in Fig. 1b reveals a large number of small dislocation loops appearing as black dots, most of them located close to the helices.

For Burgers vector analysis, STEM images were acquired under two-beam conditions with different diffraction vectors $\boldsymbol{g}$ as displayed in Fig. 2. The helix H1 and the straight dislocation S1, both aligned at 45°, are visible with $\boldsymbol{g}$ = -110 but invisible with $\boldsymbol{g}$ = 110. To fulfill the $\boldsymbol{g} \cdot \boldsymbol{b} = 0$ invisibility criterion, the Burgers vector $\boldsymbol{b}$ must be ±½[-111] or ±½[1-11]. In contrast, H2 and S2, aligned at -45°, must have a Burgers vector of ±½[11-1] or ±½[111]. The straight dislocations as well as the helices are aligned nearly parallel to the projection of their Burgers vectors (indicated by the blue and red arrows), which means that the straight dislocations have a dominating screw component and that the helices are formed from this type of pre-existing dislocations.

The presence of helical dislocations and the accumulation of loops close to them resembles observations reported for neutron-irradiated Fe-9Cr [2]. Hence we conclude that - in the depth range of low implanted ion concentration - ion irradiation can produce similar defect configurations like neutron irradiation if the arrangement of pre-existing dislocations is comparable.

[1] K. Vogel et al., NME 27 (2021) 101007

[2] J.C. Haley et al., Acta Mater. 181 (2019) 173

[3] This work has received funding from the Euratom research and training programme 2014-2018 under grant agreement No. 755039 (M4F project).

Fig. 1: (a), (b) STEM images acquired along the [001] zone axis, (c) damage profiles calculated by SRIM.

Fig. 2: STEM images acquired with different diffraction vectors $\boldsymbol{g}$ as indicated by the white arrows.

Fig. 1

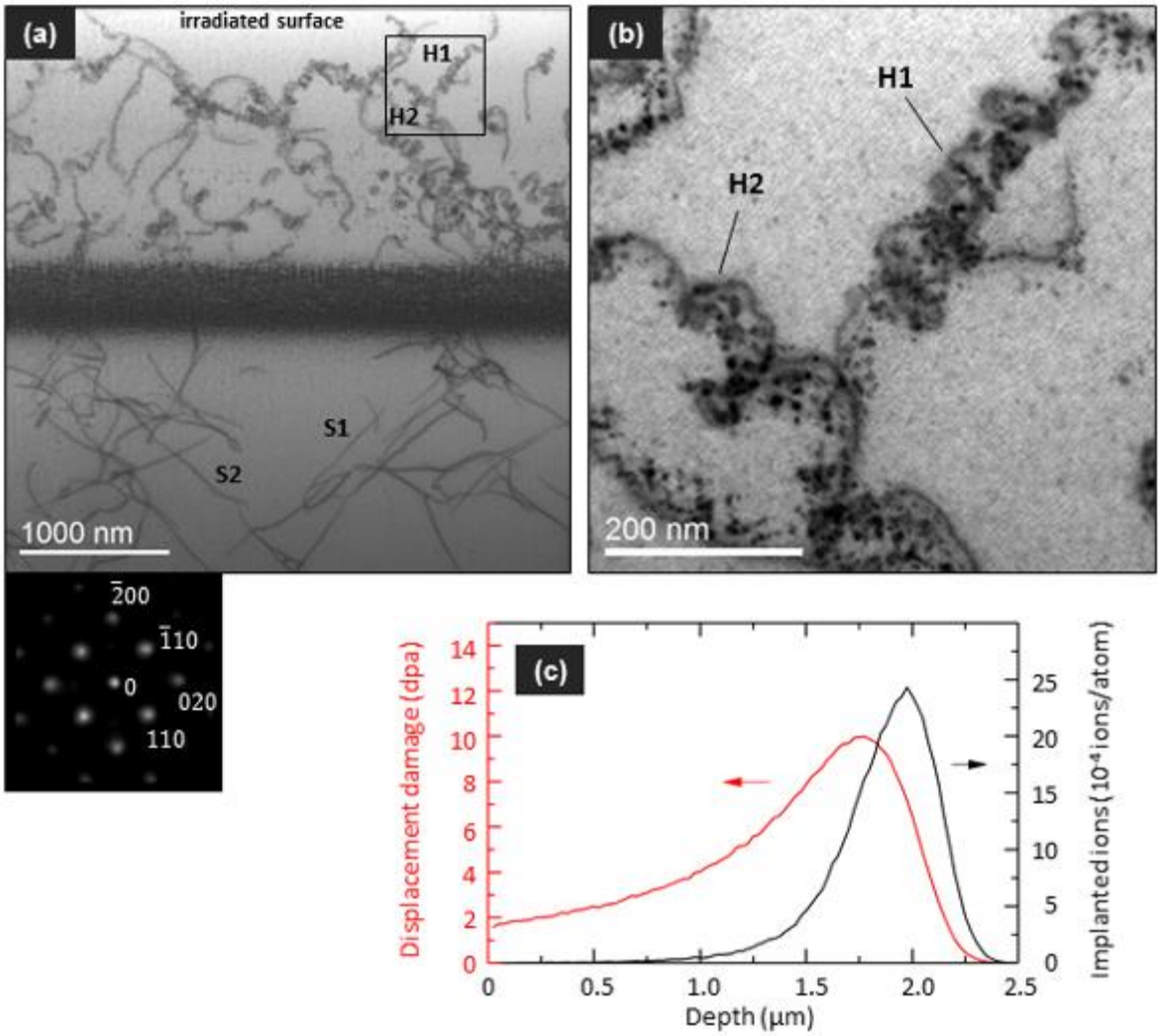
(a)
irradiated surface
H1
H2
S1
S2
1000 nm
(b)
H1
H2
200 nm
$\bar{2}00$
$\bar{1}10$
0
020
110
(c)
Displacement damage (dpa)
Implanted ions (10^{-4} ions/atom)
Depth (μm)
0
0.5
1.0
1.5
2.0
2.5
0
2
4
6
8
10
12
14
0
5
10
15
20
25

Fig. 2

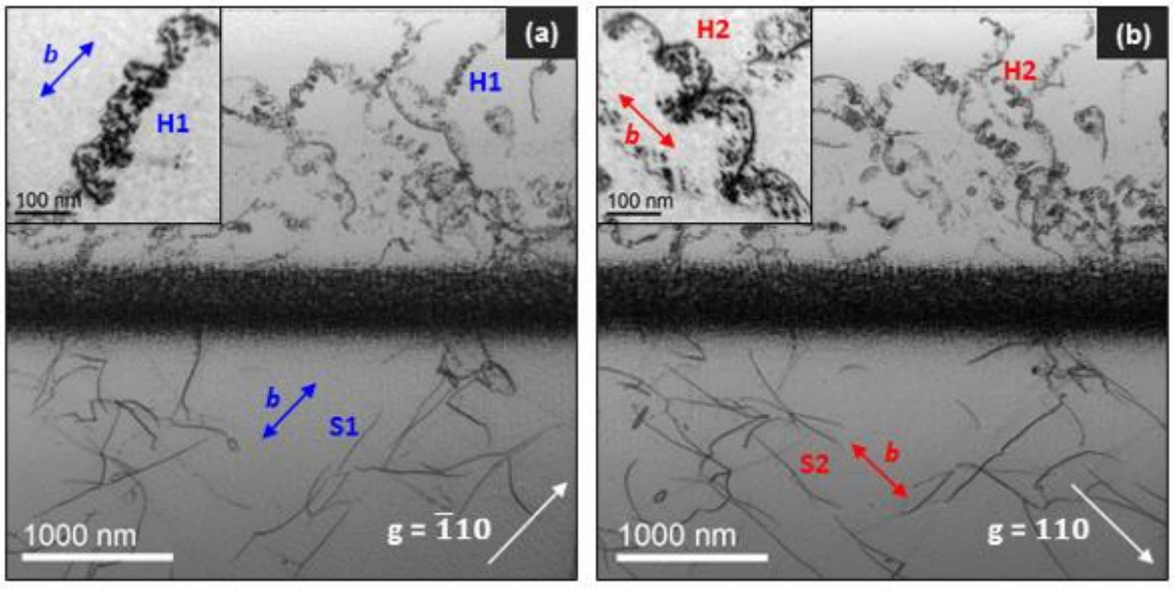
(a)
b
H1
100 nm
H1
b
S1
1000 nm
g = $\bar{1}$10
(b)
H2
b
100 nm
H2
S2
b
1000 nm
g = 110

MS2.P009

Confined chemical intermixing in Ni/Fe multilayers by He+-ion irradiation

N. Wolff[1], G. Masciocchi[2,3], A. Lotnyk[4], J. W. van der Jagt[5,6], M. A. Syskaki[2,7], A. Lamberti[8], J. Langer[7], G. Jakob[2], B. Borie[5], A. Kehlberger[3], D. Ravelosona[5,9], M. Kläui[2], L. Kienle[1]

[1]Kiel University, Department of Material Science, Kiel, Germany
[2]Johannes Gutenberg University Mainz, Institute of Physics, Mainz, Germany
[3]Sensitec GmbH, Mainz, Germany
[4]Leibniz Institute of Surface Engineering e.V. (IOM), Leipzig, Germany
[5]Spin-Ion Technologies, Palaiseau, France
[6]Université Paris-Saclay, Gif-sur-Yvette, France
[7]Singulus Technologies AG, Kahl am Main, Germany
[8]university, CNR-IMM, Agrate Brianza, Italy
[9]Université Paris-Saclay, C2N, CNRS, Palaiseau, France

The control of the magnetoelastic properties of thin films is existentially relevant for the technological development of new devices which are based on the strong interaction of the material with the surrounding magnetic field. Dependent on the application, i.e. for magnetic field sensors or magnetic actuators, the magnetoelastic coefficient λs of the thin film requires dedicated tuning. One facile approach for this optimization of magnetostriction is the material combination achieved in multilayers systems [1] and to engineer the coupling properties via modification of interfaces, e.g. controlling atomic intermixing across the interfaces [2,3].

In this contribution, the progressive intermixing at the interfaces of a (2 nm 2 nm)4 Ni/Fe multilayer caused by light-ion irradiation is characterized by spectroscopic methods of probe aberration-corrected STEM, such as energy-dispersive X-ray spectroscopy and electron energy-loss spectroscopy to identify induced changes to the film"s chemical and atomic structure. Elemental mapping revealed the introduced chemical intermixing at the Ni/Fe interfaces, suggesting the formation of NixFe1-x alloys for the ion-irradiated multilayers without introducing discernible modifications to the initial crystalline structure of the stack [3]. The local chemical analyses are congruent to averaging ToF-SIMS measurements.

In conclusion, the comparison of untreated and He+-ion irradiated Ni/Fe multilayers using dedicated chemical analysis by STEM-EDX and EELS suggest that the post-growth ion-irradiation method is able of locally modifying the degree of interfacial intermixing. Thereby the saturation magnetostriction of the magnetic stack is changed and can be tuned towards the specific needs of application.

[1] Y. Nagai, M. Senda, and T. Toshima, "Properties of ion-beam-sputtered Ni/Fe artificial lattice film," Journal of Applied Physics 63, 1136–1140 (1988).

[2] J. Fassbender, D. Ravelosona, and Y. Samson, "Tailoring magnetism by light-ion irradiation," Journal of Physics D: Applied Physics 37, R179 (2004).

[3] G. Masciocchi et al. (2022), "Control of magnetoelastic coupling in Ni/Fe multilayers using He+ irradiation," ArXiV:2207.02493

MS2.P010

Influence of repeated heat treatments on microstructure and properties of EUROFER97 (EF97)-type steels

M. Dürrschnabel[1], T. Lenoir[1], R. Gaisin[1], U. Jäntsch[1], D. Bolich[1], M. Rieth[1]

[1]Karlsruher Institut of Technologie (KIT), Institute for Applied Materials - Applied Materials Physics (IAM-AWP), Eggenstein-Leopoldshafen, Germany

1. Introduction

Current geopolitical events as well as the racing climate change demand for sustainable structural materials for CO_2-neutral energy. Future fusion reactors require large quantities (1000-ton range) of high-performance structural materials such as EF97 that can withstand elevated temperatures up to 550°C as well as a high neutron damage larger than 20 dpa.

2. Objectives

Joints of martensitic steels, specifically after liquid phase welding processes like W inert gas or laser beam welds, typically require post-welding heat treatments. The fabrication of breeding blankets for fusion reactors may involve several production steps with consecutive welding. Therefore, the structural material EF97 would be exposed to a series of heat treatments. The objective of this analysis is to study the effect of repeated heat treatments on the microstructure and mechanical properties of EF97-type steel, in the context of materials technology for nuclear fusion reactor applications.

3. Materials & methods

The samples have been heat treated (details see below) and analyzed regarding Vickers hardness. Subsequently, scanning electron microscopy with electron backscatter diffraction (SEM-EBSD in a Zeiss Merlin) scanning and transmission electron microscopy in combination with energy-dispersive X-ray analysis (STEM-EDX in a Thermofisher Talos F200X) has been performed on selected samples to determine grain sizes as well as size and composition of precipitates.

- HT1, as received: 980°C/0.45h+air quenching (AQ)+760°C 2.5h
- HT1: 980°C/0.5h+AQ
- HT2: 980°C/0.5h+AQ+750°C/2h

4. Results

Figure 1: Development of Vickers hardness with the number of heat treatments.

Figure 1 shows the development of the Vickers hardness for the different applied heat treatments compared to the as received state of the material. For HT1 a slight decrease of the Vickers hardness is observed whereas for HT2 it is quite constant compared to the as received state.

The SEM-EBSD data was evaluated regarding the martensitic lath size a well as for the prior austenitic grain (PAG) size in dependence on the applied number of heat treatments. Both quantities were found to remain constant up to 20 heat treatment repetitions, only small variations were observed in Table 1.

Table 1: Martensitic lath sizes and PAG sizes summarized for selected heat treatments.

Figure 2: STEM-EDX elemental maps after applying 20x HT1 and HT2.

Figure 2 shows two STEM-EDX elemental mappings after 20 repetitions of each heat treatment. In case of HT1 there are no $M_{23}C_6$-type precipitates observed because without tempering, C remains mainly dissolved in the Fe-Cr matrix, whereas the MX-type precipitates (TaC & VN) form. The microstructure after 20x HT2 is comparable to other EUROFER-type steels. From these elemental maps, precipitate grain sizes, number densities and compositions were extracted and compared to thermodynamic calculations.

5. Conclusion

The repetition of heat treatments did not seem to have any real influence on the evolution of the microstructural dimensions, through the grain size of the prior austenite grains and the martensitic packets. A careful TEM analysis selected samples revealed that there are some indications of ageing on the dimensions and number densities of MX- and $M_{23}C_6$-type precipitates present in the material. However, based on the currently available data a general aging trend in microstructure and mechanical properties could not be identified.

Fig. 1

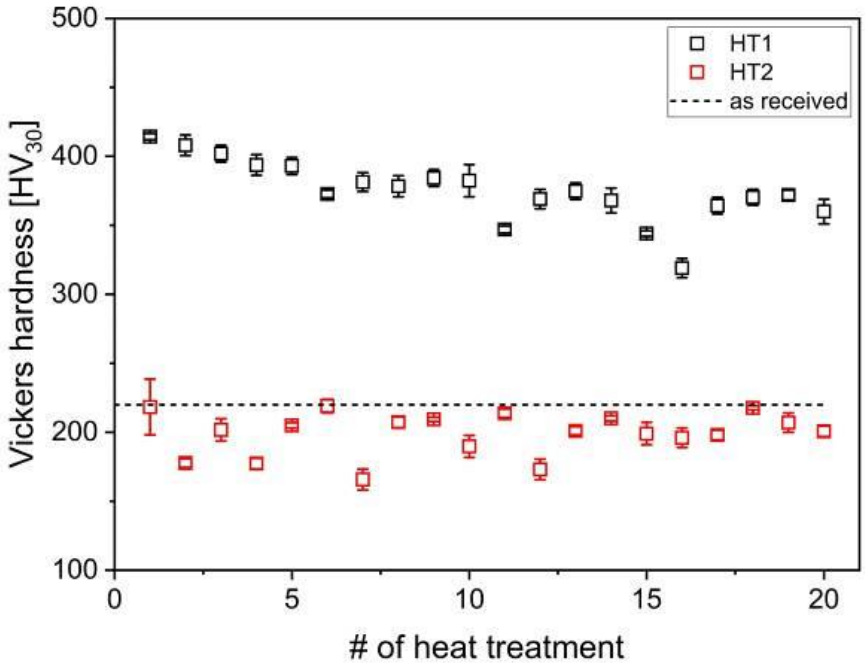

Fig. 2

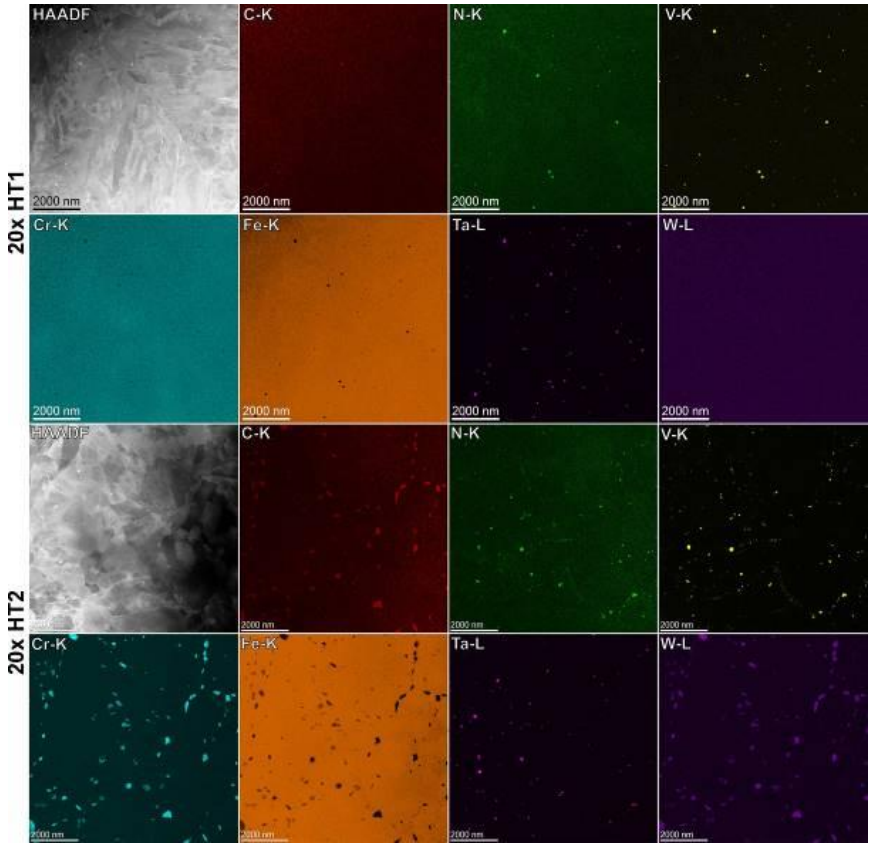

Fig. 3

HT	Martensitic lath size [µm]	Prior austenite grain size [µm]
as received	2.1 ± 2.0	14.8 ± 9.2
5x HT1	1.5 ± 1.2	11.5 ± 5.2
10x HT1	1.5 ± 1.2	10.7 ± 4.5
20x HT1	1.7 ± 1.4	11.1 ± 4.4
5x HT2	2.1 ± 1.7	12.5 ± 5.8
10x HT2	2.2 ± 2.1	13.7 ± 6.6
20x HT2	2.3 ± 2.1	12.5 ± 5.5

MS2.P011

Microstructural evolution and thermal stability of AlCrFeNiCu quinary alloy

W. Piyawit[1], K. Antanam[1], N. Chomsaeng[2], S. Kuimalee[3], P. Buahombura[1]

[1]Suranaree University of Technology, School of Metallurgical Engineering, Nakhon Ratchasima, Thailand
[2]Burapha University, Faculty of Engineering, Chonburi, Thailand
[3]Maejo University, Faculty of Science, Chiang Mai, Thailand

High temperature alloys have been remarkably known for their good mechanical behaviors at elevated temperature. Nickel-based and cobalt-based superalloys alongside with their minor alterations by adding small amount of transition elements are commercially known for their exceptional high-temperature strength, outstanding resistance to oxidizing environments up to 1150°C, premier resistance to nitriding environments, and excellent long-term thermal stability. However, the production cost effectiveness, specific strength, and high alloy homogeneity have been the major drawbacks of these superalloys. Quinary alloys with five equiatomic elemental composition have been emerged with promising properties. They can be prepared through different routes. The different processing schemes create distinct microstructures and most likely suitable for different applications. In this study, the equiatomic AlCrFeNiCu alloy was prepared by arc melting method with the expensed graphite electrodes. The fifty-gram as cast ingots were homogenized at 1,200°C with various times. To verify the stability at elevated temperature, tempering at 700°C for 2 hours was subsequently performed. Microstructures were investigated under scanning electron microscope (Zeiss, Auriga) equipped with energy dispersive spectroscopy. Phase identification was performed using X-ray diffraction (Bruker, D8). The local geometric of Fe and Ni were studied using X-ray absorption spectroscopy at SUT-NANOTEC-SLRI XAS beamline (BL5.2) facilitated by Synchrotron Light Research Institute (Nakhon Ratchasima, Thailand). The alloys were dendritically solidified. Microstructural observation suggested that the dendritic region composed of Fe-Cr and Ni-rich lamellar structures. The interdendritic regions consisted of Cu-rich phase containing nanosized precipitates alongside intermetallic compound. The modulated microstructure in dendritic regions enhanced mechanical properties. Even at high temperature tempering, the microhardness had not been sacrificed. Moreover, the phase transformation detected by X-ray diffraction measurements showed that nanoprecipitates and morphological changes occurred during heat treatments. X-ray absorption near edge spectroscopy (XANES) and extended x-ray absorption fine structure (EXAFS) spectroscopy were used to determine the local structures of Fe and Ni atoms in the alloy lattice. The spectra confirmed the formation of disordered BCC structure.

Fig. 1

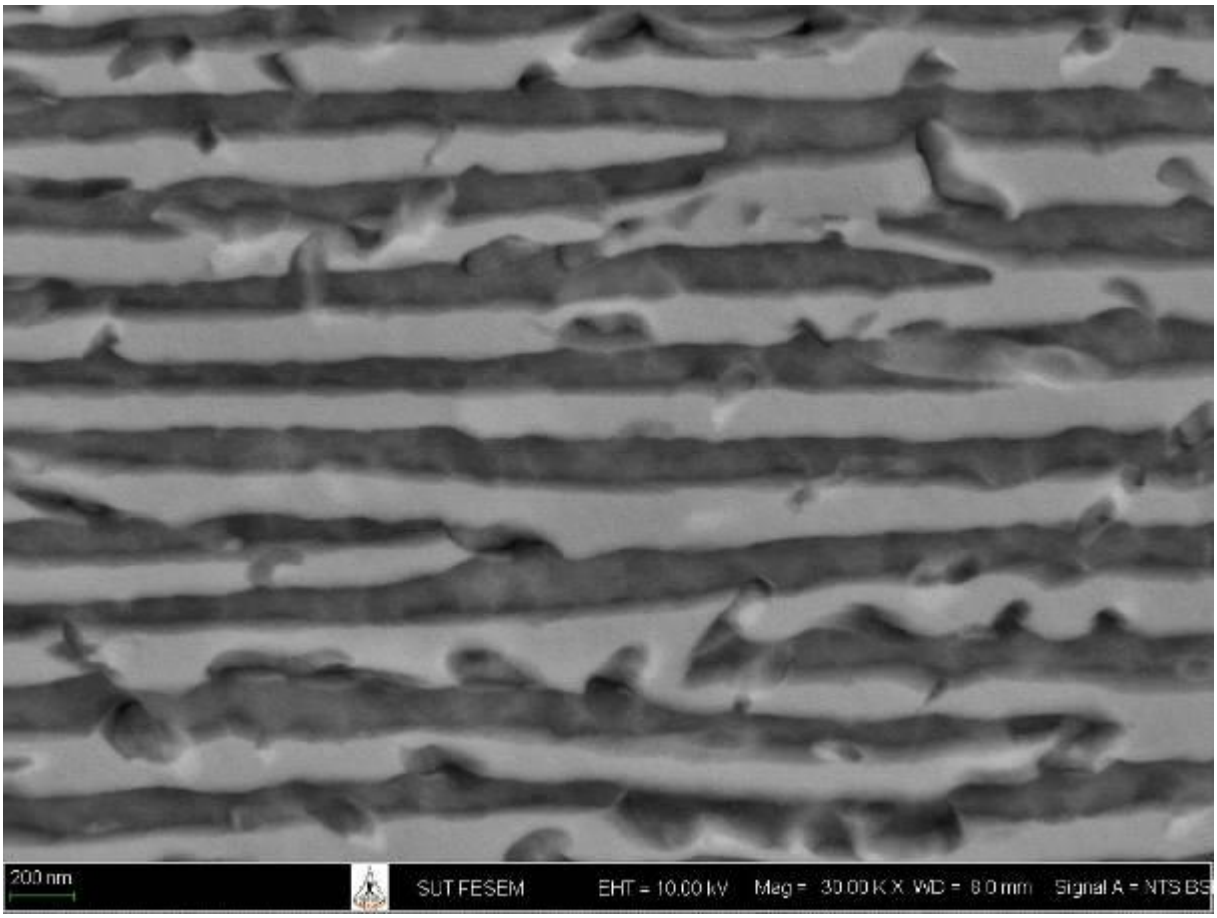
200 nm
SUT FESEM
EHT = 10.00 kV
Mag = 30.00 K X WD = 8.0 mm
Signal A = NTS BS

Fig. 2

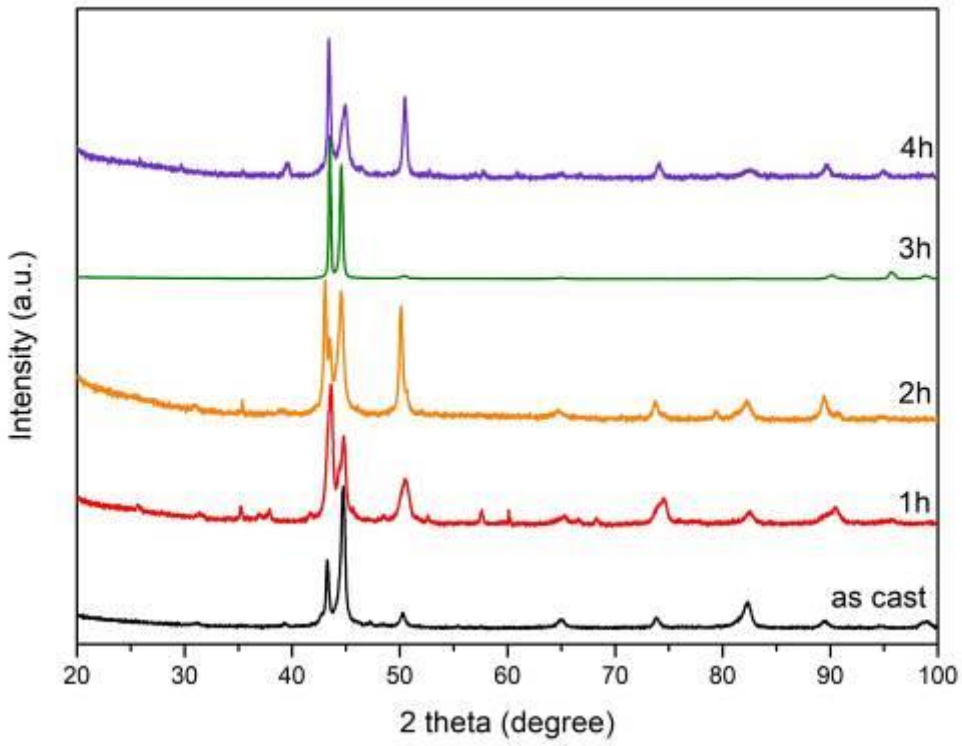
4h
3h
2h
1h
as cast
Intensity (a.u.)
20
30
40
50
60
70
80
90
100
2 theta (degree)

Fig. 3

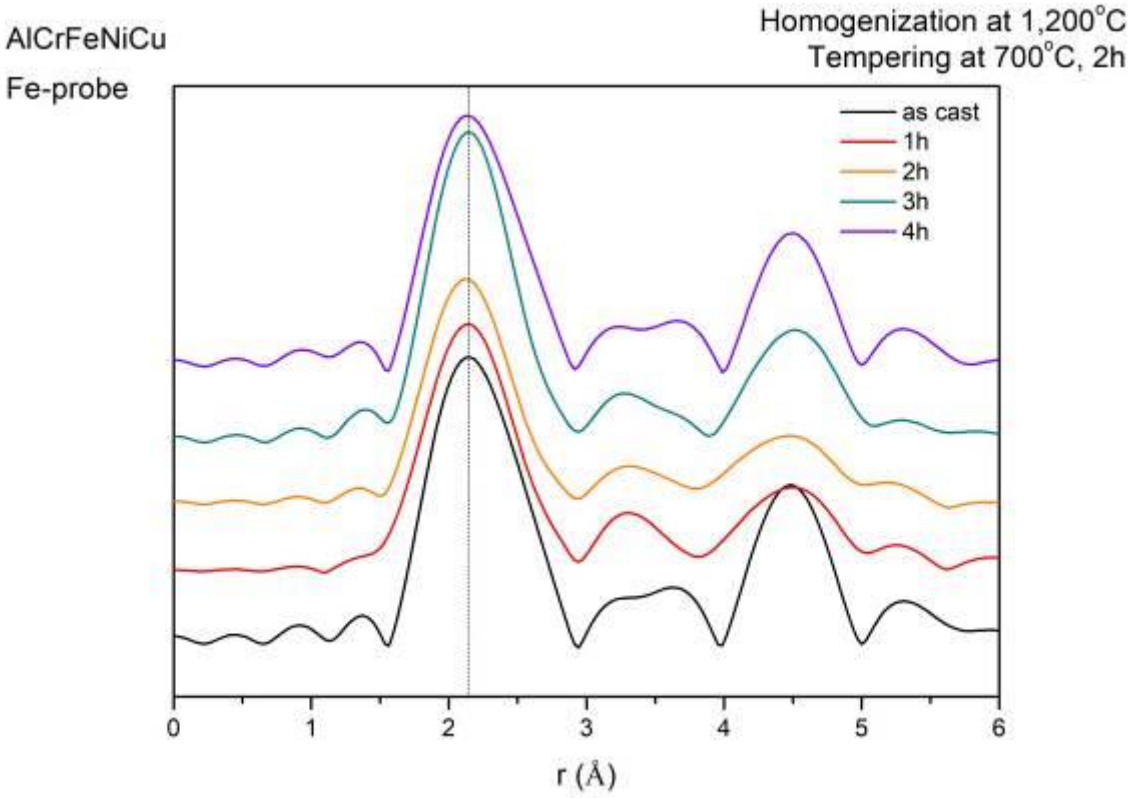
AlCrFeNiCu
Fe-probe
Homogenization at 1,200°C
Tempering at 700°C, 2h
as cast
1h
2h
3h
4h
0
1
2
3
4
5
6
r (Å)

Fig. 4

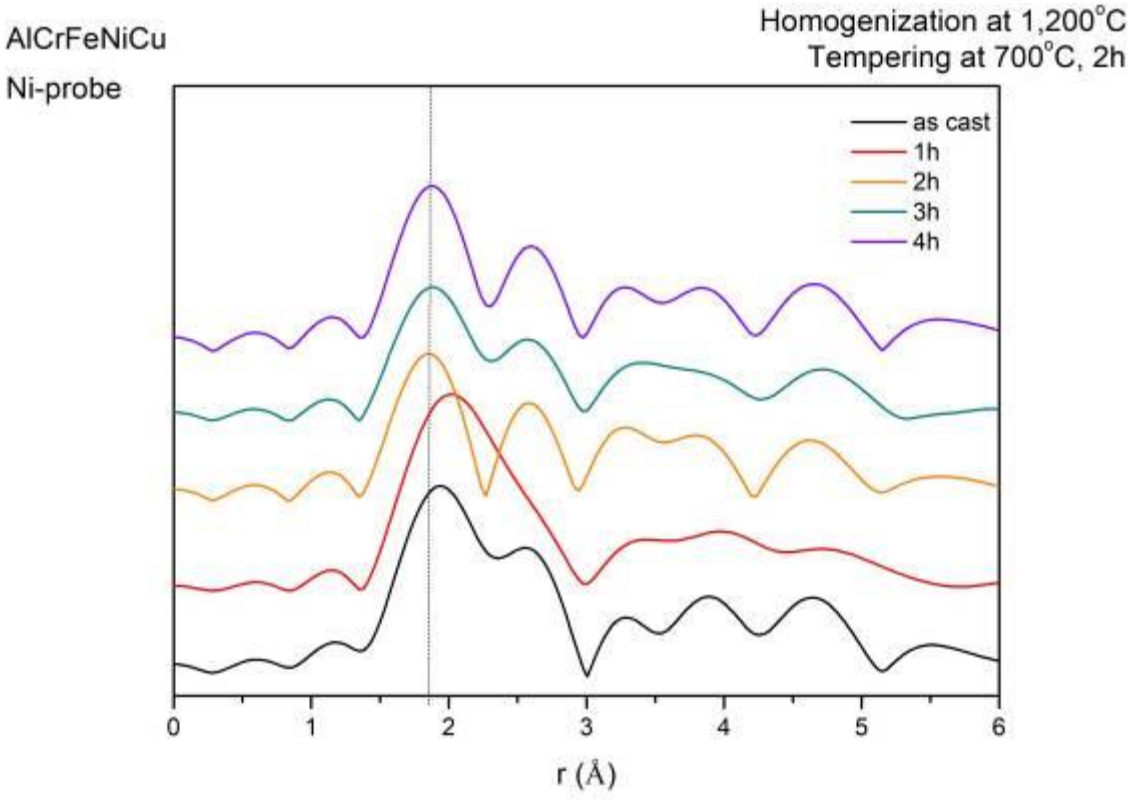
AlCrFeNiCu
Ni-probe
Homogenization at 1,200°C
Tempering at 700°C, 2h
as cast
1h
2h
3h
4h
0
1
2
3
4
5
6
r (Å)

MS2.P012

Microstructure of EUROFER97 coated with an Al2O3 layer

U. Jäntsch[1], M. Dürrschnabel[1], M. Klimenkov[1], M. Rieth[1], M. E. Angiolini[2]

[1]Karlsruher Institut of Technologie (KIT), Institute for Applied Materials - Applied Materials Physics (IAM-AWP), Eggenstein-Leopoldshafen, Germany
[2]ENEA-Brasimone Research Centre, Camugnano, Italy

1. Introduction

Reduced-activation materials that exhibit high radiation resistance are required for the design, construction, and reliable operation of environmentally friendly fusion power plants. One of the promising candidates for such an application, the reduced activation ferritic-martensitic steel (RAFM) EUROFER97 (EF97), has been systematically developed and extensively characterized in Europe for this purpose. Liquid metal corrosion is a significant problem for structural materials that needs to be avoided using a corrosion protection layer. In this case Al2O3 is used to separate the Pb-Li liquid metal from the EUROFER.

2. Objectives

A 5 µm thick Al2O3 layer was deposited by chemical vapor deposition on EF97 to evaluate the corrosion resistance of this composite in a Pb-Li liquid metal. The aim of this study is the comprehensive characterization of the oxide layer as well as the EF97/Al2O3 interface. The particular focus is on the analysis of the microstructural changes in both the Al2O3 layer and the EF97 substrate after liquid metal corrosion.

3. Materials & methods

The Al2O3 layer and its interface to the EF97 substrate have been analyzed in cross section by scanning electron microscopy (Crossbeam Auriga, ZEISS) and transmission electron microscopy (TEM) in combination with energy-dispersive X-ray analysis (STEM-EDX in a Thermo Fisher Scientific - Talos F200X). For TEM experiments a lamella was prepared using the Crossbeam FIB/SEM Auriga, ZEISS.

4. Results

Figure 1 shows a SEM cross-section of the sample structure with the 5 µm Al2O3 layer on EF97 substrate. The EF97/Al2O3 interface appears to be smooth and free of visible structural defects. Channeling contrast using a FIB scan reveals that the EF97 grain size is reduced in a 1-2 µm wide region close to interface. Furthermore, the figure shows that M23C6 and MX precipitates are located along grain or package boundaries.

Figure 1: SEM Cross-Section showing the Al2O3 layer on EF97.

TEM analysis shows that the Al2O3 layer consists of 50-300 nm grains, which are randomly oriented. The crystalline structure of the layer corresponds to the Al2O3 modification.

Figure 2 shows a STEM-EDX elemental mapping of the EF97/Al2O3 interface. In the EF97 several M23C6 and MX-type precipitates (TaC and VN) can be identified, which are comparable to bulk EF97 measurements indicating that the EF97 structure is still intact. At the EF97/Al2O3 interface a 10-15 nm thick V enrichment exists with localized Al and N rich particles having a size up to 200 nm. The presumable case of the V enrichment at the interface is related to the manufacturing of the layer or the treatment process. Close to the interface, diffusion of W, Cr and C along EF97 grain or lath boundaries was detected. This behavior is also observed in bulk EF97. The STEM bright- and dark-field images show that Al2O3 layer is not grown homogeneously, i.e., voids and Al platelets are observed.

Figure 2: STEM-EDX elemental maps after applying corrosion tests.

5. Conclusions

The microstructure of EF97 protected by a 5 µm Al2O3 layer has been examined in detail. As a result, significant changes in the EF97 substrate could not been observed. In addition, there is no evidence of oxidation in the EF97 matrix.

Fig. 1

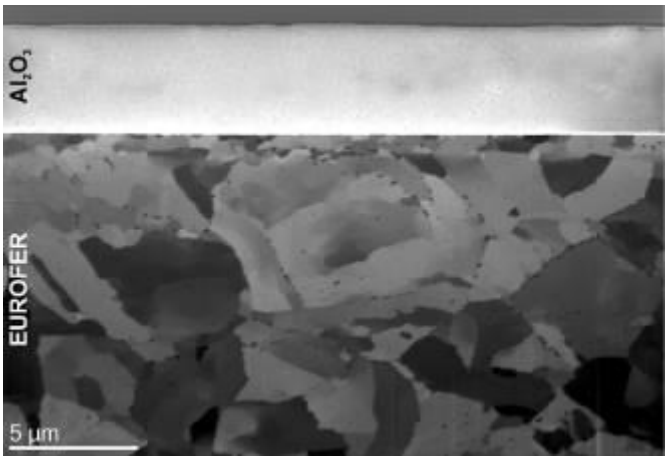

Fig. 2

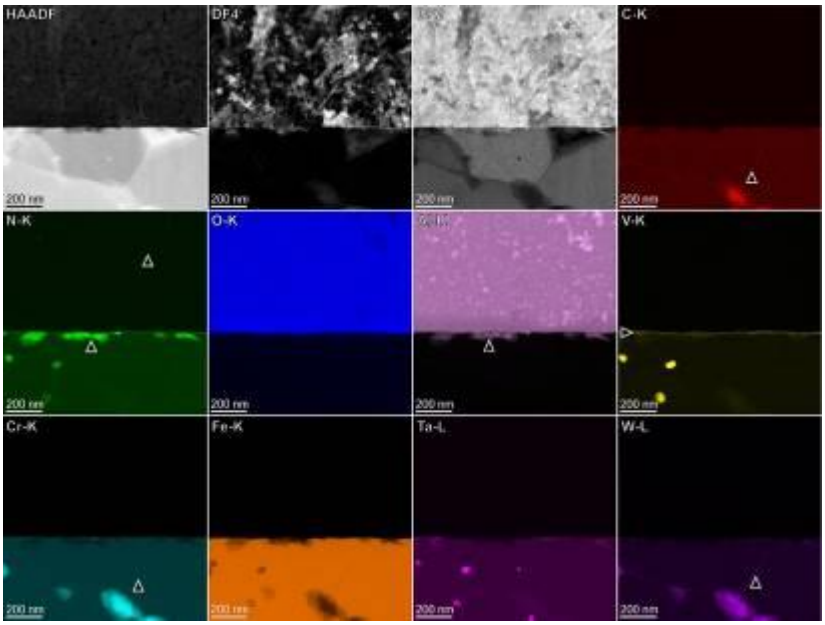

MS2.P013

TEM investigation of planar faults in Ni-base superalloy ERBO1

B. Holtermann[1], D. Bürger[2], Y. M. Eggeler[1]

[1]KIT, Laboratory for Electron Microscopy, Karlsruhe, Germany
[2]Ruhr-Universität Bochum, Institut for Materials, Bochum, Germany

Single crystal nickel-base superalloys are an important class of high-temperature materials used as blade substrate material in industrial gas turbines and jet engines. Their excellent creep properties are due to a high volume fraction of L1_2 y'-precipitates embedded in a FCC y-matrix forming a coherent y/y'-microstructure [1]. With increasing creep strain dislocations from the y-channels cut into the y'-precipitates forming complex planar faults, which show a different chemical composition than its hosting y'-phase [2]. An in-depth understanding of these diffusion-assisted microstructural deformation mechanisms is needed for further practical improvement of the next generation of nickel base superalloys [3].

In the present study TEM/STEM-methods are used to investigate the evolution of creep-induced solute segregation to planar faults and their formation in y'-precipitates in single crystal ERBO1 nickel base superalloy double shear creep specimens [4]. The specimens were creep deformed at 750°C and 250 MPa and interrupted upon 1% plastic deformation. For a detailed characterization of the planar faults, TEM thin foils were prepared with a foil normal that allows to analyze the planar faults in edge-on [1-10] and in-plane [111] configurations. First preliminary results of planar faults in edge-on configuration show planar fault traces in single or multiple y'-precipitates for 1% strain states, see Fig. 1. The planar faults are formed by partial dislocations which can be found attached to the faults within the precipitates (see arrow 1) and at the y/y'-interface (see arrow 2). Applying the g.b/R effective invisibility criterion (Fig. 1c) shows that with an excitation condition using the reciprocal space vector g(-1-1-1) the planar faults are out of contrast indicating a displacement in the [11-2] direction. With respect to the crystallographic orientations of the single crystal double shear creep specimen and the derived highest resolved shear stress and Schmid factor for the shear system [11-2](111) this displacement vector is expected.

For the in-plane configuration partial dislocations that form planar faults while cutting through the y'-precipitate can be observed, see Fig. 2. Arrow 1 marks one cutting event where dislocations have cut into a y'-precipitate leaving a planar fault in their wake, indicated by a visible change in contrast. At the same time these dislocations extend into the y-channel and seem to split up, marked by arrow 2 in the WBDF image (Fig. 2b), additional LACBED and HR-STEM analysis is needed to prove this.

To assess the evolution of solute segregation to the planar faults and gain a better understanding of the y'-precipitate cutting processes the specimens will be further evaluated. Future investigations will include a characterization of the intrinsic and extrinsic nature of planar faults and their atomic stacking sequence with HR-STEM. Furthermore, a detailed burgers vector analysis of the dislocations interacting at the y/y'-interface is planned.

The authors acknowledge the DFG priority program SFB-TR 103.

[1] R.C. Reed - Superalloys, Cambridge University Press 2006

[2] Y.M. Eggeler et al. - Acta Materialia 113. 2016. 335-349

[3] Y.M. Eggeler et al. - Annu. Rev. Mater. Res. 2021. 51:209–40

[4] D. Bürger et al. - Crystals 2020. 10. 134

Fig. 1

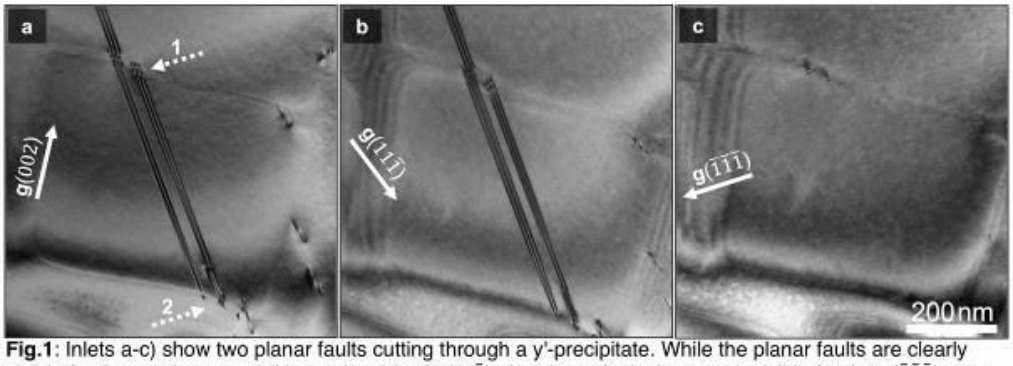

Fig.1: Inlets a-c) show two planar faults cutting through a y'-precipitate. While the planar faults are clearly visible for the two-beam conditions g(002) and g(11$\bar{1}$), the planar faults become invisible for the g($\bar{1}\bar{1}\bar{1}$) two-beam condition.

Fig. 2

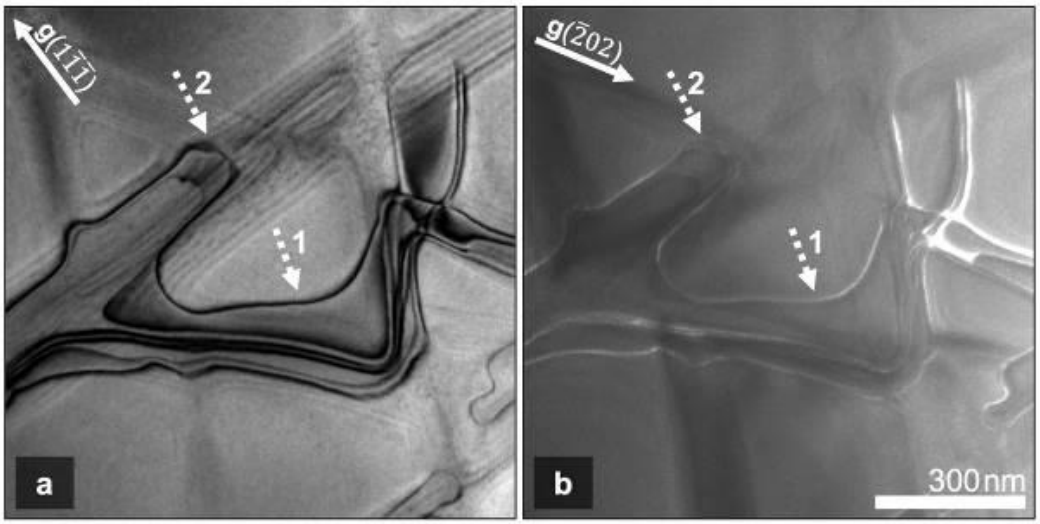

Fig.2: Inlet a) shows a bright-field image of a cutting event with partial dislocations cutting into a y'-precipitate leaving a planar fault contrast behind. Inlet b) shows a weak-beam dark-field image of the same cutting event with improved contrast for the dislocation lines.

MS2.P014

Design of lattice-matched Au_xNi_{1-x}(111)/α-Al_2O_3(0001) interfaces and their investigation by X-ray diffraction and electron microscopy

M. Dierner[1], J. Will[1], M. Landes[1], T. Yokosawa[1], T. Przybilla[1], T. Zech[2], P. Herre[3], T. Unruh[2], E. Spiecker[1]

[1]Friedrich-Alexander Universität, Lehrstuhl für Mikro- und Nanostrukturforschung (IMN) & Center for Nanoanalysis and Electron Microscopy (CENEM), Erlangen, Germany
[2]Friedrich-Alexander-Universität, Institute for Crystallography and Structural Physics (ICSP), Erlangen, Germany
[3]Institut für Nanotechnologie und korrelative Mikroskopie (INAM), Forchheim, Germany

Metal/ceramic interfaces are of great scientific and technological importance, with applications in electroceramic devices, structural composites and catalysis [1]. Due to different thermal expansion coefficients of metals and ceramics and, in many cases, a high lattice mismatch applications suffer from mechanical stresses making the metal-ceramic interfaces the weak point in the device. The usage of a binary alloy system on the metal side offers the possibility to tailor the mismatch , leading to a less strained interface with improved mechanical stability.

In the present study, this concept is elaborated for the epitaxial interface between Au_xNi_{1-x} and α-Al_2O_3. For this Au/Ni bilayers are e-beam evaporated on (0001) oriented α-Al_2O_3. Rapid thermal annealing of the bilayers above the miscibility gap at 890°C for 120s in reducing atmosphere is used to fabricate AuxNi1-x alloy nanoparticles (NPs), which are subsequently quenched into a metastable supersaturated solid solution. Here, the Au concentration (c_{Au}) is utilized to tune the {220} d-spacing of the alloyed NPs towards lattice matching with the {30-30} d-spacing of α-Al_2O_3. The influence of c_{Au} on the structure of the NP and the interface as well as the interplay of solute atoms and the substrate is monitored by complementary X-ray and electron techniques.

XRD out-of-plane scans (Fig.1A) confirmed the formation of AuNi alloy NPs. Furthermore, an influence of the lattice mismatch (e.g. at%Au) on the texturing of the NP can be seen. While all NPs show the typical <111>-OOP texture, interestingly this texture is partially lost for samples close to lattice matching (0.3%≥ δ≤ -1%). In XRD in-plane measurements (Fig. 1B), the convergence of the NP lattice parameter towards lattice matching as well as the evolution of the diffuse background can be traced. For 59at% Au the in-plane NP and substrate peak match and the diffuse background, which stems from disorder at the interface, vanishes, both revealing the (semi-)coherent nature of the interface in contrast to an incoherent or delocalized coherent [2] interface for larger lattice mismatch. Furthermore, EBSD ODFs revealed i) a pronounced AuNi (111)[1-10] || α-Al_2O_3 (0001)[10-10] orientation relationship (OR1) for NP with δ>0.3% and ii) a change in OR to AuNi (111)[1-10] || α-Al_2O_3 (0001)[11-20] (OR2) with δ<-1%.

To get a deeper understanding of the interface and the interplay of solute atoms and the substrate, cross-sectional EM-investigations on a <110> oriented lamella were carried out on a Ni-rich particle (Fig.2). The ADF image reveals a modulated contrast in the range of two interfacial layers, correlating perfectly with the disordered interface seen in IP XRD. Additionally HR HAADF imaging confirmed the semi-coherent nature of the interface with the appearance of stand-off misfit dislocations (DL). Via EDX we revealed the segregation of Au on the interface, which is driven by the minimization of strain energy by i) reducing the misfit and ii) shifting the DL to higher stand-off positions [2].

Overall, we demonstrate an elegant route to produce lattice matched alloy NPs on a ceramic substrate and provide insight into the structure and chemistry of the system by complementary scattering probes. In our contribution, the origin of the findings reported above will be discussed in light of existing literature and basic physical principles.

[1] Sinnott et al., 10.1016/j.mser.2003.09.001

[2] Herre et al., 10.1016/j.actamat.2021.117318

Fig. 1

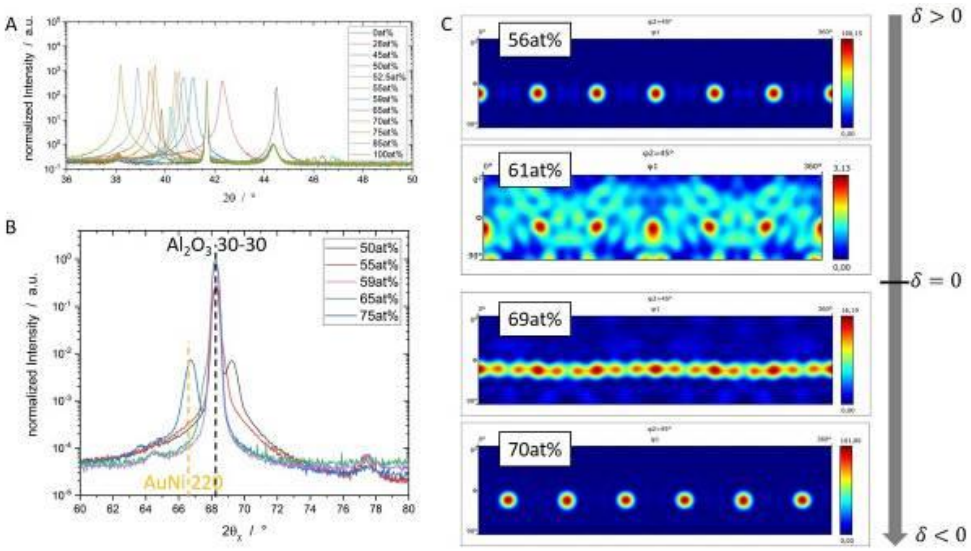

Fig. 1: (A) XRD OOP data showing a strong <111> texture. Samples close to lattice matching show a decreased <111> texture for samples close to lattice matching. (B) XRD IP scans showing the convergence of the NP lattice parameter towards lattice matching as well as the evolution of the diffuse background, stemming from disorder at the interface. (C) SEM EBSD ODF plots showing the influence of the lattice mismatch on the texture formation. For positive median misfits OR1 is present, while a transition to OR2 is visible for negative misfit of <-1%

Fig. 2

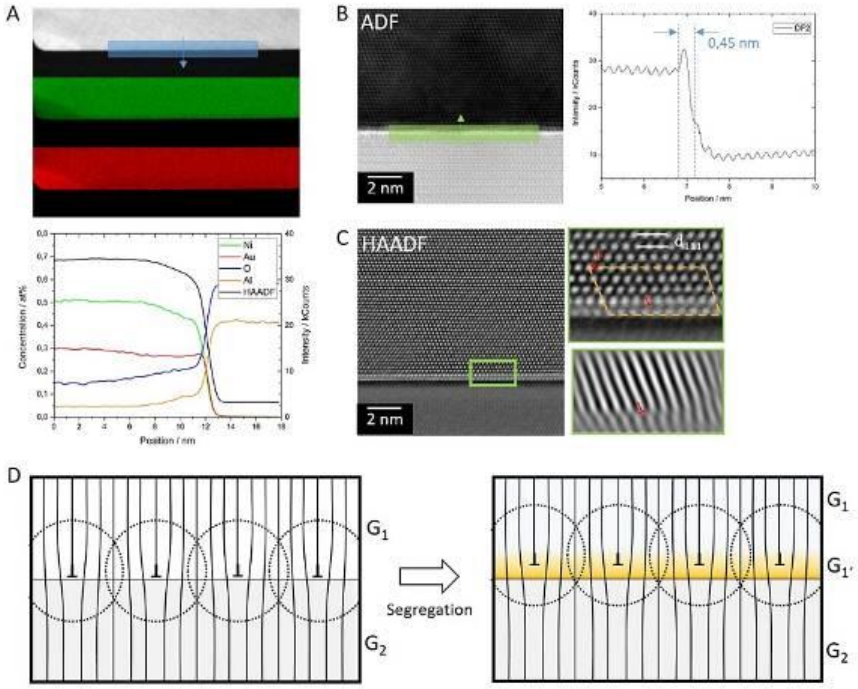

Fig. 2: STEM-EDXS mapping of a 28 at% Au particle prepared in [110] ZA clearly revealing Au segregation at the interface (A). The drop in the Au/Ni ratio profile towards the substrate cannot be interpreted since both elements are absent in the substrate. HRSTEM ADF (B) and filtered HAADF (C) images of the interface reveal a confined ~ 0.45 nm thin strained region and the presence of misfit dislocations, respectively. The Burgers circuit analysis shows a projected BV of type a/4 < 112 > , corresponding to the projection of a perfect a/2 < 110 > dislocation into the image plane. In (D) the role of Au segregation on the (out-of-plane) position of misfit dislocations and the overall reduction of the shear modulus (G 1 < G 1 < < G 2) at the interface to reduce the total strain energy is depicted.

MS2.P015

Complementary microscopy and scattering experiments on the magnetic textures in the antiskyrmion compound $Mn_{1.4}PtSn$ using LTEM and REXS

M. Winter[1,2,3,4], M. Rahn[4], D. Wolf[3], S. Schneider[2], M. Valvidares[5], C. Shekar[1], P. Vir[1], H. Popescu[6], N. Jaouen[6], G. van der Laan[7], T. Hesjedal[8], B. Rellinghaus[2], C. Felser[1]

[1]Max Planck Institute for Chemical Physics of Solids, Dresden, Germany
[2]Dresden Center for Nanoanalysis (DCN), Dresden, Germany
[3]IFW Dresden, Dresden, Germany
[4]TU Dresden, IFMP, Dresden, Germany
[5]ALBA Synchrotron, Barcelona, Spain
[6]Synchrotron SOLEIL, Saint-Aubin, France
[7]Diamond Light Source Ltd., Didcot, United Kingdom
[8]University of Oxford, Clarendon Laboratory, Oxford, United Kingdom

1. Introduction

More than a decade has passed since the first experimental evidence of magnetic Bloch-type skyrmions in MnSi [1]. Since then, driven by their high potential for applications in future magnetic memory devices, skyrmions and related magnetic nano-objects of non-trivial topology have been in the focus of intensive research in the scientific community, and many novel spin textures have been discovered. In the course of these efforts, antiskyrmions (aSks) were recently observed in the tetragonal Heusler material $Mn_{1.4}PtSn$ by Lorentz Transmission Electron Microscopy (LTEM). Beyond that, the material is known to host a wide range of other magnetic structures such as non-topological (NT) bubbles, elliptical skyrmions and spin helices [3].

2. Objectives

In order to better understand the formation of aSks we have conducted complementary experiments of resonant elastic x-ray scattering (REXS) and LTEM on an identical lamella of $Mn_{1.4}PtSn$. REXS enables us to directly measure the orientation and magnitude of the spin propagation vectors of the various magnetic phases occurring in $Mn_{1.4}PtSn$. While REXS provides for diffraction patterns, LTEM allows to directly image and identify the underlying magnetric structures and to navigate the material"s complex phase diagram, which depends not only on temperature and sample shape, but also on strength and orientation of an external magnetic field as well as on the history of its application.

3. Materials & methods

We use high quality single crystals of $Mn_{1.4}PtSn$ grown by self-flux method for our experiments. In order to realize complementary measurements on identical samples, thin lamellas were cut by FIB-Milling and placed on specifically designed molybdenum-discs (d=3 mm) fitting to commercially available TEM holders. Custom-designed sample hoilders haver been developed to ensure compatibility with the REXS setup. The REXS experiments were carried out at the I10 end station at the Diamond Lightsource (UK). The experimental setup was equipped with an octupole vector magnet, which allowed to explore the highly complex magnetic phase diagram of $Mn_{1.4}PtSn$ by offering 360° of freedom in magnetic field direction and fields of up to 600 mT.

4. Results

Our complementary approach allows us to unambiguously link the helical phase, NT bubble and aSks phase in $Mn_{1.4}PtSn$ as identified from LTEM measurements to the REXS scattering patterns we measured on the identical sample (Fig 1). In combination with the quantitative analysis of the REXS pattern the study provides new insights into the various (field-induced) magnetic phase transitions in the materials.

5. Conclusion

Along this approach, the intimate correlation of LTEM and REXS experiments conducted on identical samples has proven an ideal tool to not only doubtlessly identify individual phases but also to navigate the high-dimensional parameter space and characterize the nature of the occurring phase transition in great detail.

Acknowledgement(s):

This study was supported by the International Max Planck Research School for Chemistry and Physics of Quantum Materials (IMPRS-CPQM) and by the DFG through SPP 2137.

Reference(s):

[1] S. Mühlbauer *et al.*, *Science.* **323**, 915-919 (2009).

[2] A.K. Nayak *et al.*, *Nature.* **548**, 561 (2017).

[3] L. Peng *et al.*, *Nature Nanotechnol.* **15**, 181-186 (2020).

Fig. 1

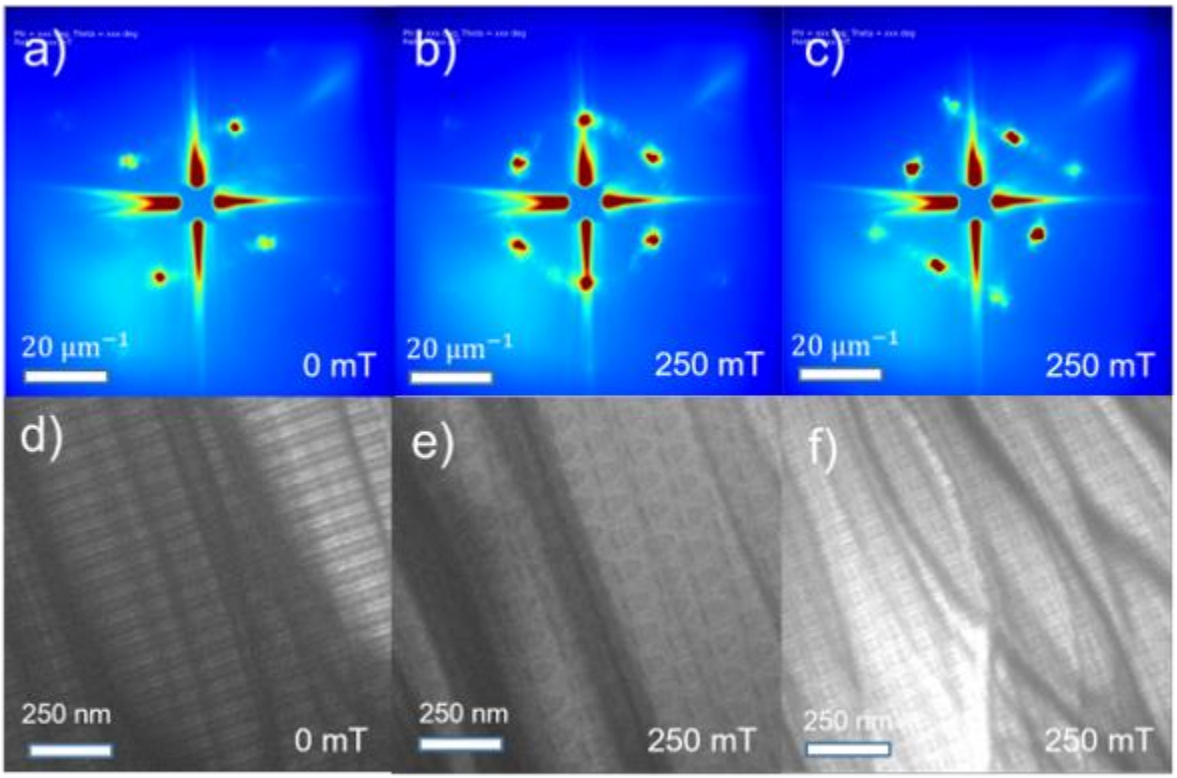

Fig. 1: Complemantary LTEM and REXS measurements on the identical lamella of $Mn_{1.4}PtSn$. REXS: a) helical phase b) NT-Bubble phase c) antiskyrmion phase LTEM: d) helical phase e) NT-Bubble phase f) antiskyrmion phase

MS2.P016

Structure of the high entropy alloy CoCrFeMnNi after low cycle fatigue

D. Litvinov[1], K. Lu[1], J. Aktaa[1]

[1]Karlsruher Institut of Technologie (KIT), Eggenstein-Leopoldshafen, Germany

Microstructural characterization of the high entropy alloy CoCrFeMnNi (HEA) after low cycle fatigue (LCF) at a temperature of 550°C was carried out by transmission electron microscopy (TEM). For the determination of the actual composition, high angle annular dark field (HAADF) scanning TEM (STEM) with an energy-dispersive X-ray (EDX) spectroscopy was used. For the crystallographic investigations, conventional TEM with selected area diffraction (SAD) was applied. The TEM samples after LCF test were prepared by electrochemical or mechanical thinning parallel to the stain direction.

We observe in the samples after LCF many additional defects in comparison to the as received sample. Fig. 1 shows inverted HAADF STEM images in large scale of the samples after LCF deformation under lowest and highest strain amplitudes of ± 0.2% (Fig. 1a) and ± 0.75% (Fig. 1b), where we can see a lot of defects. First of all, in both deformed samples, we observe thin twins (TW) and slip bands (SB). Similar twins were detected in the unreformed sample. Therefore, the kind of the twins, annealing or deforming, is not clear from these images. The broad of slip bands increases with strain amplitude. Moreover, in both samples there are two kinds of dislocations inside the grains: discrete dislocations (D1) and pileup dislocations along lines (D2). The density of dislocations D1 and D2 increases also with strain amplitude. In the sample deformed under strain amplitude ± 0.75 % (Fig. 2b), pileup of dislocations forms cells which were detected only in the sample deformed under high strain amplitudes from ± 0.5% to ± 0.75%. The density of such cells increases remarkably with strain amplitude. These cell substructures are formed because of dislocations cross slip and contribute to the near-steady state of the cyclic stress response.

The quantitative TEM EDX analysis of many grains shows an almost homogeneous distribution of alloying elements in the deformed sample with a concentration of (20 ± 3) at % for each element. However, additional secondary phases with an irregular morphology are observed close to grain boundaries with their sizes varying up to a few mm. One such case is presented in Fig. 2, where a HAADF STEM micrograph with EDX line scan (a) combined with a bright-field TEM image with SAD (b) of the same area are shown. Variation in the contrast along the inclusion in both, the STEM (Fig. 2a) and the TEM (Fig. 2b) images clearly indicate changes in chemical composition. The EDX line scan along the dashed line as well as area analysis in Fig. 2a shows that lower part of the inclusion is Mn- and Ni-rich (area 1, both elements having an atomic concentration of ca. 50 %) and the long upper part is Cr-rich (area 2). SAD from the latter part of the inclusion in Fig. 2b, which correspond to area 2, indicates a intermetalic σ phase. This phase consists of significantly more Cr and also some Mn, Fe and Co, but very little Ni.

Fig. 1. Inverted HAAD STEM images of the samples after deformation under strain amplitudes of ± 0.2% (a) and ± 0.75% (b). D1, D2 and cells indicate two kinds of dislocations. TW denotes twins, SB - slip bands. The scale bar in (b) is valid for (a).

Fig. 2. (a) HAADF STEM image with EDX line scan along the dashed arrow and elemental compositional measurements and (b) bright-field TEM image with SAD of circled areas of the same region of the sample tested under strain amplitude of ±0.3%.

Fig. 1

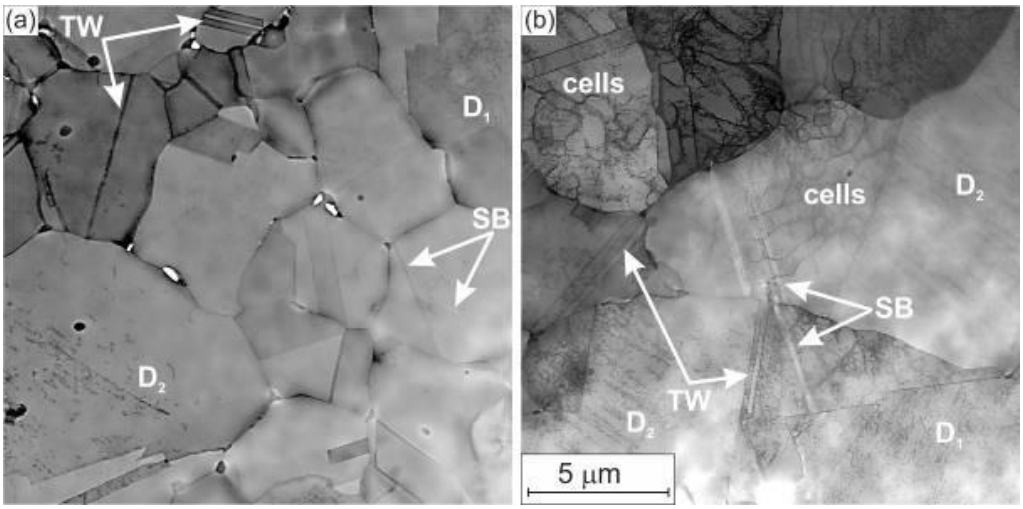

Fig. 2

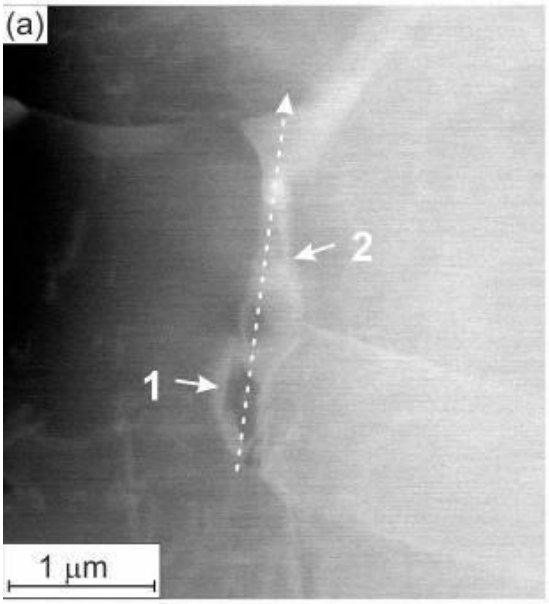

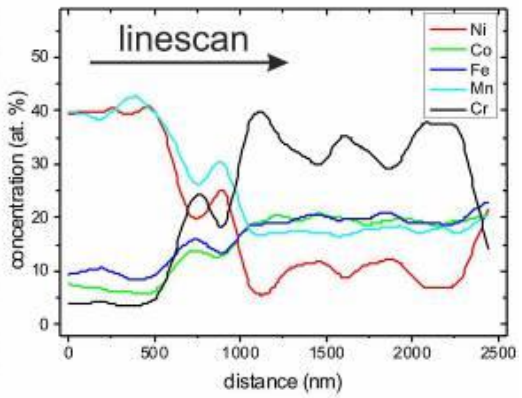

Element	Area 1, atomic %	Area 2, atomic %
Cr	1.67	40.75
Mn	46.65	14.85
Fe	2.39	18.26
Co	4.09	19.07
Ni	45.18	7.05

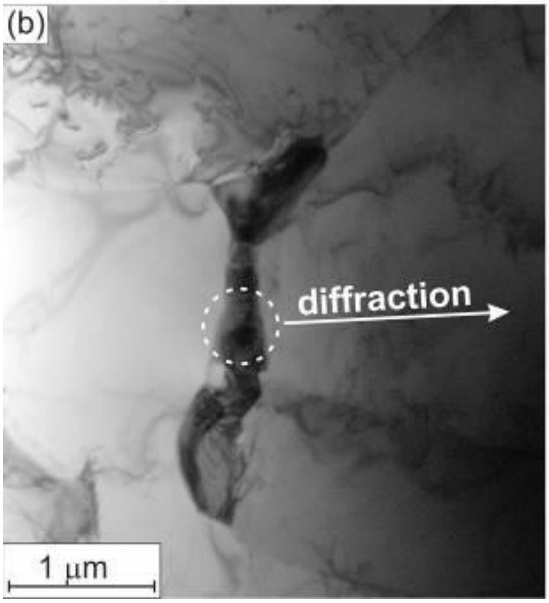

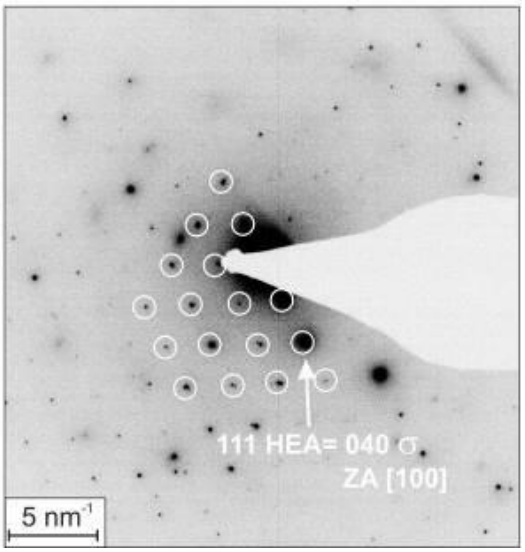

MS2.P017

Transmission electron microscopy of secondary carbides formed by annealing in high chromium cast iron

A. Wiengmoon[1], K. Ruangchai[1], H. Kurata[2], M. Haruta[2], R. Tongsri[3], S. Nusen[4], J. T. H. Pearce[4], T. Chairuangsri[4]

[1]Naresuan University, Department of Physics, Phitsanulok, Thailand
[2]Kyoto University, Division of Electron Microscopy and Crystal Chemistry, Kyoto, Japan
[3]National Science and Technology Development Agency, National Metal and Materials Technology Center, Pathum Thani, Thailand
[4]Chiang Mai University, Department of Industrial Chemistry, Chiang Mai, Thailand

Introduction

The as-cast microstructures of the 22-30wt.%Cr and 2.0-2.7wt.%C high chromium cast irons (HCCIs) consist of primary austenite dendrites and eutectic M_7C_3 carbide. The wear resistance of these irons can be improved by alloying and heat treatments. In some applications, annealing treatment is necessary for machining operations [1-2]. There are few reports on the morphology of coarse and fine secondary carbides forming during annealing.

Objectives

The purpose of this research is to use TEM for studying the secondary carbide in the annealed structure. A preliminary EELS examination of the carbides will also be presented.

Materials and methods

As-cast specimens of the 28wt.%Cr (R) and the 28wt.%Cr-1wt.%Mo (Mo1) irons were annealed at 800^{o}C for 4 h, followed by slow cooling to 500^{o}C and then furnace cooling. A JEOL JEM-2010 TEM equipped with an Oxford® Inca detector was used for conventional TEM and EDS microanalysis. A JEOL, ARM200F TEM equipped with a Gatan Quantum ERS electron energy loss spectrometer was used for EELS. Both microscopes were operated at an accelerating voltage of 200 kV.

Results

BF-TEM images in Figs. 1 (a & b) show that the microstructures after annealing of the reference (R) and the Mo1 irons, consisted of eutectic carbide with faulting contrast and precipitated coarse secondary carbides in areas close to eutectic carbides and fine secondary carbides in the centres of the dendritic matrix. The Mo1 iron contains finer and denser secondary carbides. The selected area diffraction patterns (SADPs) confirmed that the eutectic carbides are M_7C_3, the secondary carbides are $M_{23}C_6$, and the matrix is ferrite (α). The coarse secondary carbides may be nucleated along preferred directions during the early stages of annealing. The finer secondary carbide precipitation may have occurred later during longer holding time or during slow cooling. TEM-EDS in Fig. 2(a) revealed that the Fe/Cr wt.% ratio of eutectic M_7C_3 carbides was 0.4, while that of coarse and fine secondary $M_{23}C_6$ carbides were in range of 0.52-0.69. Preliminary EELS results are given in Fig. 2(b). The differences in the spectra of ELNES of the C *K-edge* of M_7C_3 and $M_{23}C_6$ were (i) the peak at 289 eV (marked by arrows) has been observed only in the case of M_7C_3, and (ii) the relative heights of peaks 1 and 2 were higher in M_7C_3.

Conclusion

TEM revealed that coarse and fine secondary carbides formed by annealing of the 28wt.%Cr without and with 1wt.%Mo addition are $M_{23}C_6$ carbides. The finger print of the C *K-edge*, including the Fe/Cr wt.% ratio can be used to distinguish M_7C_3 from $M_{23}C_6$ carbides.

References

1. K.A. Kibble and J.T.H. Pearce, Cast Metal, 1995, 8, 123-127.

2. Y.G. Song *et. al*., Metals 2021, 11, 1690.

Fig. 1

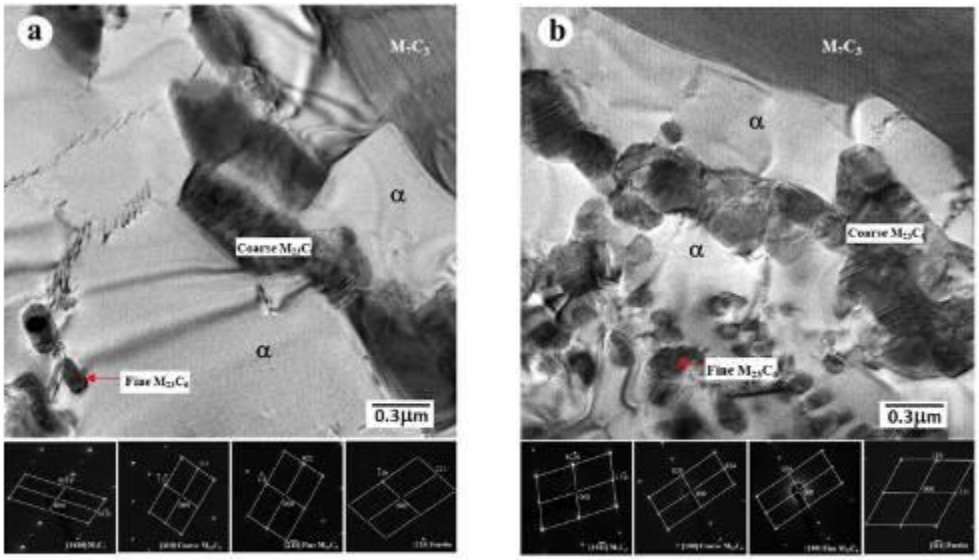

Fig. 1. BF-TEM images and corresponding SADPs from eutectic M_7C_3 carbides, coarse and fine secondary $M_{23}C_6$ carbides and ferrite (α) matrix (a) R iron (b) Mo1 iron.

Fig. 2

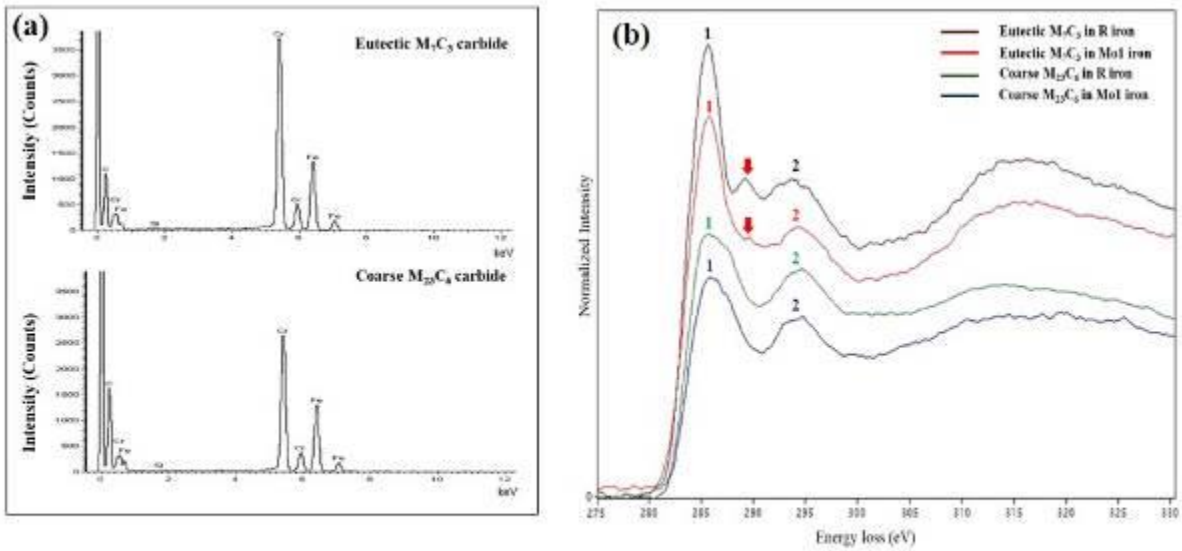

Fig. 2. (a) TEM-EDS spectra of the M_7C_3 and coarse $M_{23}C_6$ carbides of R iron (b) C *K-edge* EELS spectra from the M_7C_3 and coarse $M_{23}C_6$ carbides of R and Mo1 irons.

MS2.P018

Growth and magnetic structure of a skyrmion-hosting Co-Zn-Mn alloy

A. Kovács[1], L. Yang[1], M. Feuerbacher[1], C. Thomas[1], D. Kong[1], T. Denneulin[1], F. Zheng[1], R. E. Dunin-Borkowski[1]

[1]Forschungszentrum Jülich, Ernst Ruska Centre, Jülich, Germany

Magnetic skyrmions have attracted considerable interest over the last decade, in particular for novel information storage applications. The swirling vortex-shaped magnetic field texture of a skyrmion has topological particle-like properties and is stabilized by the Dzyaloshinskii-Moriya interaction in bulk systems and multilayers of ferromagnets and heavy metals. Co-Zn-Mn with a β-Mn-type structure is a skyrmion-hosting bulk system that has the cubic chiral space group *P*4132 (or *P*4332) and allows continuous tuning of magnetic interactions and hence control of the ferromagnetic transition temperature (*Tc*). However, only Co10-*x*/2Zn10-*x*/2Mn*x* alloys (*x* = 2-4) exhibit skyrmion lattice formation above room temperature [1]. Here, we present a reproducible growth route for Co-Zn-Mn alloys with *Tc* close to 100 ºC and microstructural, compositional and magnetic imaging studies performed using various transmission electron microscopy (TEM) methods.

A Co-Zn-Mn alloy was grown using a self-flux method in a closed, tapered quartz crucible placed on a cold finger in a buffered box furnace starting from a melt of composition Co3Zn6Mn1. Following a dedicated temperature transient with final water quenching, a conical ingot was produced, with the tip corresponding to the primarily solidified material (Fig. 1a). TEM specimens were prepared by using focused Ga ion-beam sputtering in a dual-beam scanning electron microscope (FEI Helios). Conventional TEM and electron probe aberration corrected scanning TEM (STEM) were used to study the microstructure of the alloy. Fresnel defocus imaging and off-axis electron holography [2] were carried out in magnetic field-free conditions (Lorentz mode) using aberration-corrected (FEI Titan) TEMs operated at 300 kV.

High-resolution STEM imaging along [100] is consistent with a chiral β-Mn-type structure (Fig. 1b). The chemical composition was measured to be Co8Zn10Mn2 using inductively-coupled optical emission spectroscopy. The magnetic transition temperature was determined by observing magnetic contrast elimination during *in situ* heating of a TEM specimen in magnetic field-free conditions. The helical spin texture and skyrmions disappeared in Fresnel defocus images at 98 ºC, which was assumed to correspond to *Tc*. Figure 1c shows a Fresnel defocus image illustrating skyrmion lattice formation in the Co8Zn10Mn2 specimen. Quantitative magnetic characterization of the skyrmion spin structure was carried out by combining phase shift measurements obtained using off-axis electron holography with model-based iterative reconstruction of the projected in-plane magnetization, as well as through comparisons of the recorded contrast with micromagnetic simulations.

This work was supported by the European Union"s Horizon 2020 Research and Innovation Programme (Grant No. 856538, project ""3D MAGiC"") and the Deutsche Forschungsgemeinschaft through CRC/TRR 270 (Project ID 405553726).

Figure 1. (a) Flux-grown Co8Zn10Mn2 ingot. (b) High-resolution HAADF STEM image along [100] with overlaid structure model. (c) Fresnel defocus image of a skyrmion lattice recorded at 86 ºC in the presence of an 89 mT field applied perpendicular to the surface plane.

References

[1] Y. Tokunaga, et al., Nat. Comm. 6 (2015) 7638.

[2] A. Kovács, R.E. Dunin-Borkowski, In Handbook of Magnetic Materials; Brück, E., Ed.; Elsevier: 2018; Vol. 27, pp 59-153.

Fig. 1

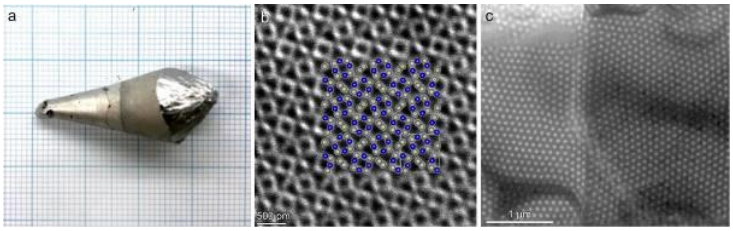

MS2.P019

Correlative imaging of the biodegradation of Mg-based alloys using *in situ* synchrotron radiation-based nano CT and (S)TEM

J. Reimers[1], M. Lipiska-Chwalek[2], L. Kibkalo[2], J. Mayer[1], R. Willumeit-Römer[3], B. Zeller-Plumhoff[4]

[1]Ernst Ruska-Centre for Microscopy and Spectroscopy/ Jülich Research Centre, ER-C-2, Jülich, Germany
[2]Ernst Ruska-Centre for Microscopy and Spectroscopy/ Jülich Research Centre, ER-C-1, Jülich, Germany
[3]Institute of Materials Research/ Helmholtz-Zentrum Hereon, Metallic Biomaterials, Geesthacht, Germany
[4]Institute of Materials Research/ Helmholtz-Zentrum, Imaging and Data Science, Hamburg, Germany

INTRODUCTION: Multi scale analysis of functional materials combining different imaging techniques for the same region of interest (ROI) is key for the development of digital twins[1]. These numerical models of the material and its behaviour accelerate the development of functional materials like biodegradable implants. Magnesium based alloys are gaining high interest for implant applications due to their biocompatibility and biodegradability.[2] Understanding the underlying degradation processes and their interdependencies during the biodegradation is necessary to control and tailor them and thus for the development of digital twins. *In situ* synchrotron radiation nano computed tomography (SRnanoCT) can be used as a non-destructive 3D imaging method to investigate dynamic degradation processes with nominal resolutions below 100nm. The investigation of the chemical compositions and morphology down to atomic-scale is possible with (scanning) transmission electron microscopy ((S)TEM). The correlation of the two techniques enable to achieve a complementary picture of the degradation process, but, at the same time, it brings a number of challenges, such as sample transfer, identification of ROI (e.g. precipitates) and image registration.

OBJECTIVES: The goal of this study is to develop a correlative workflow enabling to understand the biodegradation of Mg-based alloys at different length scales. For this purpose, a three-step workflow was developed (see Fig.1). Firstly, *in situ* SRnanoCT providing information on degradation rates, homogeneity, degradation layer (DL) formation and presence of larger precipitates within the alloy, and therewith enabling identification of degradation-relevant ROIs for further in-depth characterisation. Secondly, the transfer into a focused ion beam (FIB) and identical-location lamella preparation for the third step, i.e. correlated, in-depth (S)TEM investigation of structural defects and degradation layer.

MATERIALS & METHODS: A flow-cell setup is used for *in situ* SRnanoCT. Mg-x-wt.%Ag and Mg-y-wt.%Gd wires (80µm diameter) have been degraded in simulated body fluid (SBF) under physiological conditions (37 °C, pH 7.4, flow rate 1 ml/min) resulting in tomographic scans every 13-30 minutes. FIB lamellas for identical-location TEM characterization were prepared by a lift-out method in a dual-beam FIB FEI Helios NanoLab 400S. STEM imaging and EDX analyses were conducted with the aid of probe-corrected FEI Titan G2 80-200 at 200kV [3].

RESULTS: Figure 1 shows the correlative workflow. First results from SR tomograms (A) of Mg-4wt.%Ag yield a degradation rate of 9.4 mm/year after approx. 5 hours. A FIB lamella (B) depicts the preparation and the EDX analysis (C) shows Mg-rich bulk material , an inner and outer degradation layer, Ag-rich precipitates and FIB protection layers as well as a voids.

Figure 1: Mg-based alloy degraded in SBF: (A) SR nano tomogram (B) lamella preparation in FIB and (C) elemental map with EDX.

CONCLUSION: Preliminary results from tomograms show inhomogeneous degradation behaviours. Further studies are necessary to understand the influences on biodegradation processes, as the precipitates do not seem to act as micro galvanic elements, as no enhanced degradation can be observed in their vicinity.

REFERENCES: [1]M. Abdalla, et al., Corrs. Mater. Degrad. (2020), 219-248. [2]M. P. Staiger, et al., Biomaterials (2006), 1728–1734. [3]FEI Titan G2 80-200 CREWLEY (2016) A43.

Fig. 1

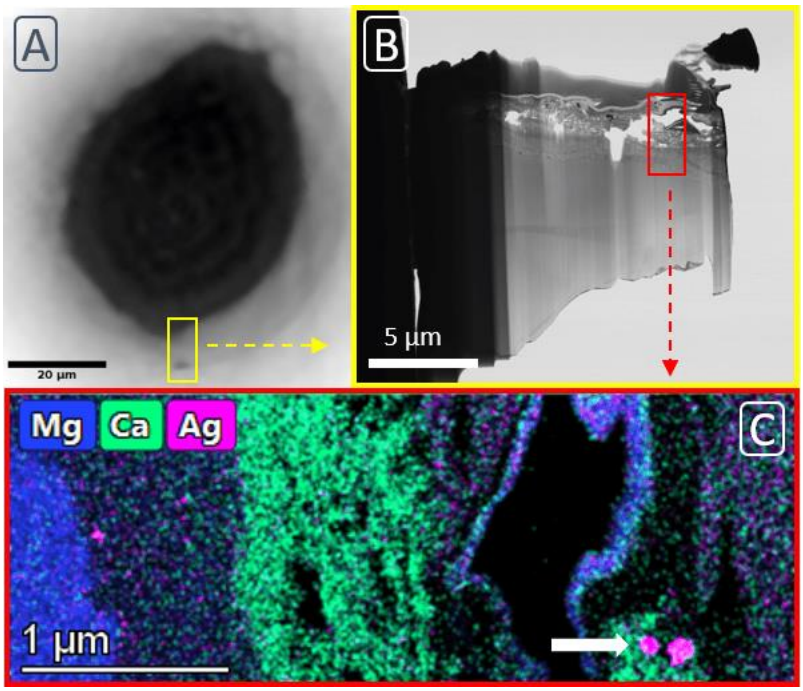

MS2.P020

Rafting in single crystal superalloys: on the influence of stress state and the transition towards topological inversion

A. Parsa[1], D. Bürger[1], L. Cao[1], G. Eggeler[1]

[1]Ruhr University Bochum, Bochum, Germany

Rafting is the directional coarsening of small cuboidal γ'-phase particles in Ni base superalloys during high temperature creep deformation. During a [001] tensile creep testing rafting occurs perpendicular to the direction of the applied stress in Ni-base superalloy single crystals with a negative misfit between the two coherent phases γ and γ' [1,2]. In the present work we take a new look at the phenomenon of rafting. Some recent results on the influence of different stress states, comparing crept microstructures after uniaxial creep, shear creep and after creep of circular notched specimens are presented. We also consider the effect of internal stresses of microstructural origin on rafting. We further look at the topological inversion within the microstructure where the initial microstructure in which small γ'-cubes are separated by thin interconnected γ-channels evolves towards a material state where the γ-phase forms isolated islands and the γ'-phase percolates through the system [3]. The changes are obvious when comparing Figure 1a (initial state after processing), 1b (material state after creep: 1223 K/200 MPa/1%) and 1c (material state after creep: 1223 K/300 MPa/26%) where after prolonged periods of creep exposure, the microstructural evolution results in the formation of isolated γ-phase regions. Our findings are interpreted on the basis of the underlying elementary deformation and coarsening mechanisms, which govern the evolution of γ/γ' microstructures. Creep testing in the high temperature low stress creep regime is combined with analytical scanning and transmission electron microscopy. Special emphasis will be placed on the microstructural transition from a rafted to a topologically inverted microstructure.

Figure 1: SEM images of ERBO1 singly crystal superalloy, (a) Initial state microstructure; (b) Rafted microstructure after uniaxial creep exposure at 1223 K, 200 MPa and 1% accumulated strain; (c) Topologically inverted microstructure after uniaxial creep exposure at 1223 K, 200 MPa and 26% accumulated strain. γ and γ′ phases shown in bright and dark contrast, respectively.

Keywords: Single crystal Ni-base superalloys, high temperature uni- and multiaxial low stress creep, scanning electron microscopy, transmission electron microscopy, rafting, topological inversion

References:

[1] R.C. Reed, The Superalloys: Fundamentals and Applications, Cambridge University Press, Cambridge, 2006.

[2] L. Agudo Jácome et al., High-temperature and low-stress creep anisotropy of single-crystal superalloys, Acta Mater., 61, 2013, 2926-2943.

[3] A. Epishin et al., Kinetics of the topological inversion of the γ/γ′-microstructure during creep of a nickel-based superalloy, Acta Mater., 49, 2001, 4017-4023.

Fig. 1

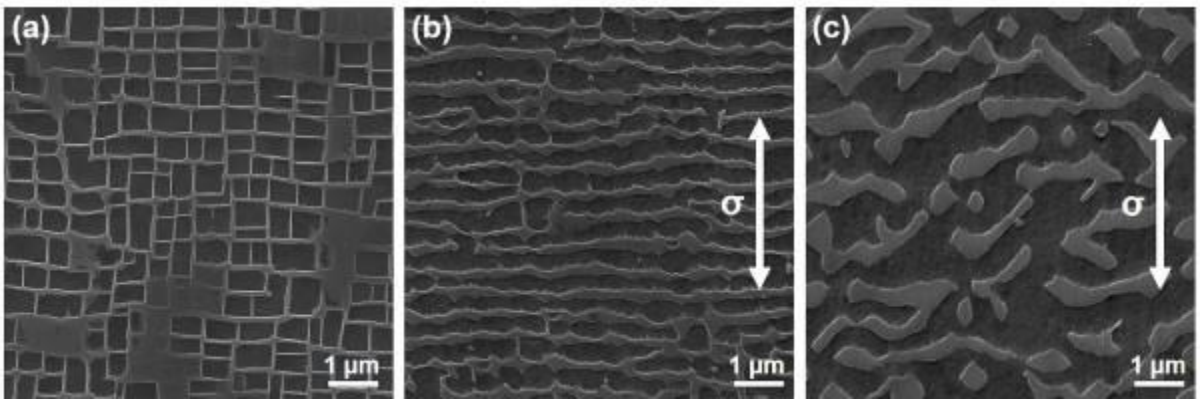

MS2.P021

Microstructural investigations of the crept eutectic MoSiTi alloy using the conventional transmission electron microscopy (CTEM)

H. Thota[1], H. Wu[1], D. Schliephake[2], C. Dolle[1], A. Kauffmann[2], M. Heilmaier[2], A. Pundt[2], Y. M. Eggeler[1]

[1]Karlsruher Institut of Technologie (KIT), Laboratory for Electron Microscopy, Karlsruhe, Germany
[2]Karlsruher Institut of Technologie (KIT), Institute for Applied Materials (IAM-WK), Karlsruhe, Germany

The current state-of-the-art, single-crystal nickel-based superalloys operate close to 80 to 90% of their melting temperatures. There is a continuous need to design newer materials that can withstand higher operating temperatures above 1100 °C, as the operation of turbine engines at higher operating temperatures leads to improved energy efficiency in the power generation and aerospace sectors [1]. On the other hand, during operation at higher temperatures, the materials undergo higher creep deformation.

The recently developed eutectic MoSiTi alloy (Mo-20Si-52.8Ti in at.%) exhibits a good combination of pesting oxidation and creep properties [2]. It consists of two phases: body centred cubic (bcc) solid solution and hexagonal Ti-rich silicide, M5Si3 (where M-Ti, Mo). The accumulation of creep strain in the two phases, particularly the deformation behavior of the two phases and lattice defects generated in response to the applied stress has to be thoroughly understood. Compressive creep tests were performed under vacuum at 1200 °C and 100 MPa stress to assess the creep behavior. The samples are tested at various true strains of 1.3, 10, 20, and 40% to understand the deformation mechanism of the alloy.

The crept samples were characterized using scanning electron microscopy (SEM)- backscattered electron (BSE) imaging to analyse the microstructure of phases, their arrangement and detect precipitation. Conventional transmission electron microscopy (CTEM) techniques such as bright field (BF), dark field (DF) and weak beam dark field (WBDF) are employed to image dislocations and analyse dislocation substructure in all crept conditions [3]. Deformation mechanisms can be drawn from the type of dislocation (edge, screw, or mixed) and the dominant slip plane in the bcc phase. In addition, dislocations in the silicide phase are imaged and the operative slip system (basal, prismatic or pyramidal) is identified. Scanning transmission electron microscopy (STEM)-energy dispersive spectroscopy (EDS) is used to determine the composition of the precipitates and analyse any segregation of the alloying elements to the dislocations in the crept samples. The high angle annular dark field (HAADF) STEM image in Fig. 1a shows the precipitation of Ti-rich silicides in the bcc matrix, that are semi-coherently embedded in the matrix. Based on diffraction analysis (Fig. 1b), the precipitates are hexagonal and dislocations are observed in the silicide phase of 10% crept samples (Fig. 1c).

Fig.1: Transmission electron microscopy (TEM) investigations of the crept eutectic MoSiTi alloy a) Scanning transmission electron microscopy (STEM)-high angle annular dark field (HAADF) image of Ti-rich silicide precipitates in body centered cubic (bcc) solid solution b) Diffraction pattern of precipitates in the bcc phase aligned to [001] zone axis in 1.3% true strain and c) Weak beam dark field (WBDF) image of dislocations in hexagonal silicide phase of 10% crept sample. The dislocations are marked with alphabets: A represents long dislocation line and B denotes dislocations inclined to the TEM foil.

[1] J.H. Perepezko, The hotter the engine, the better, Science 326 (2009) 1068–1069.

[2] Schliephake et al., Constitution, oxidation and creep of eutectic and eutectoid Mo-Si-Ti alloys, Intermetallics. 104 (2019) 133–142.

[3] D.B. Williams, C.B. Carter, Transmission Electron Microscopy, Springer US, Boston, MA, 2009.

Fig. 1

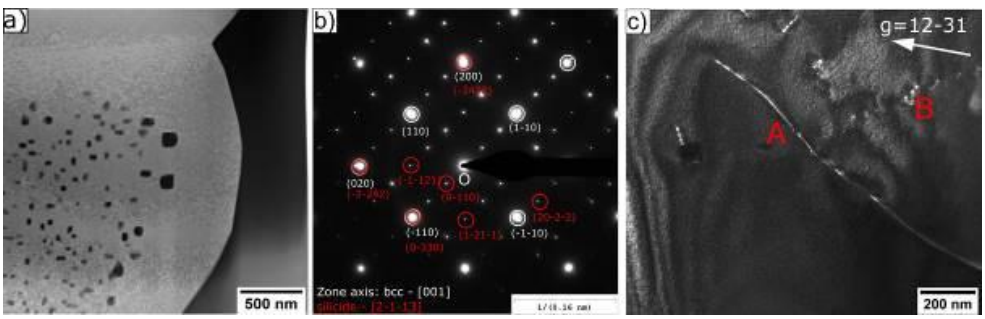

MS2.P022

An investigation of thermal stability and mechanical properties of Cu alloys by high-pressure torsion

Y. Dai[1]

[1]Karlsruher Institut of Technologie (KIT), Karlsruhe, Germany

The grain refinement can be described as a process of counterbalanced generation and annihilation (recovery, dynamic recrystallization) of dislocations during deformation. The stacking fault energy (SFE) or the solid solution hardening (SSH) contribution plays a decisive role and affects the grain refinement including the saturation grain size. [1, 2] The goal of this study is to investigate the solute effects on mechanical behavior, microstructure changes, and thermal stability in the Cu alloys after HPT processing at room temperature.

Cu and Cu alloys (CuSn5, CuZn5, CuZn30) were processed by severe plastic deformation (SPD) using a semi-constrained high-pressure torsion press under 4.5GPa. The isochronal heat treatment at different temperatures was applied to study the thermal stability of this alloy. Transmission electron microscopy (TEM) investigations indicated that dislocation wall structures are the main feature of Cu and Cu alloys after annealing treatment at different temperatures. Automated crystal orientation mapping (ACOM), which can provide full orientation maps with nanometer resolution, was used to test grain orientation, a fraction of high-angle grain boundaries, and mean grain size.

The grain growth kinetics in alloys are typically governed by the local elemental distribution e.g. the presence or absence of segregations (solute drag) or secondary phases (Zener drag). The Cu-X series remains single-phase upon annealing, indicating that the enhanced thermal stability of the alloys compared to pure Cu is related to the solute content, which provides dragging forces for grain boundary migration. A comparison of CuZn5 and CuZn30 indicates higher microstructural stability for CuZn5, as CuZn5 shows a constant hardness up to 250°C where CuZn30 has already started to soften significantly.

[1] Mohamed, F.A. and Dheda, S.S., On the minimum grain size obtainable by high-pressure torsion. Materials Science and Engineering: A, 2012. 558: p. 59-63 DOI: 10.1016/j.msea.2012.07.066.

[2] Bruder, E., Braun, P., Rehman, H.u., Marceau, R.K.W., Taylor, A.S., Pippan, R., and Durst, K., Influence of solute effects on the saturation grain size and rate sensitivity in Cu-X alloys. Scripta Materialia, 2018. 144: p. 5-8 DOI: 10.1016/j.scriptamat.2017.09.031.

Fig. 1

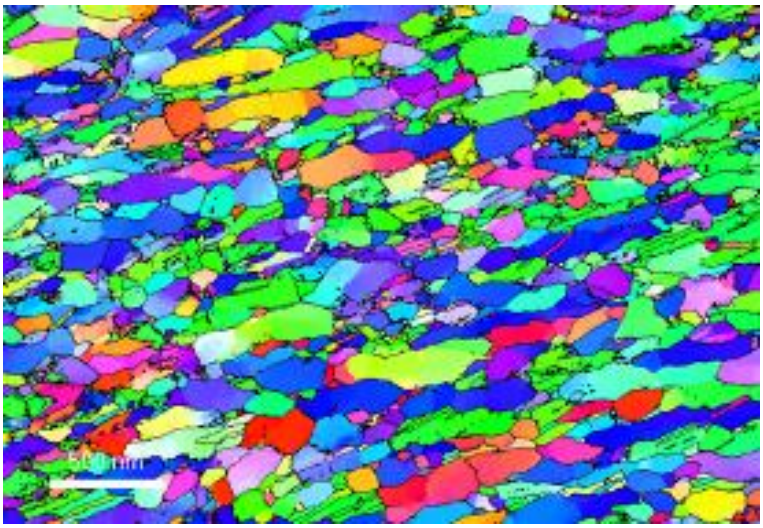

Fig. 2

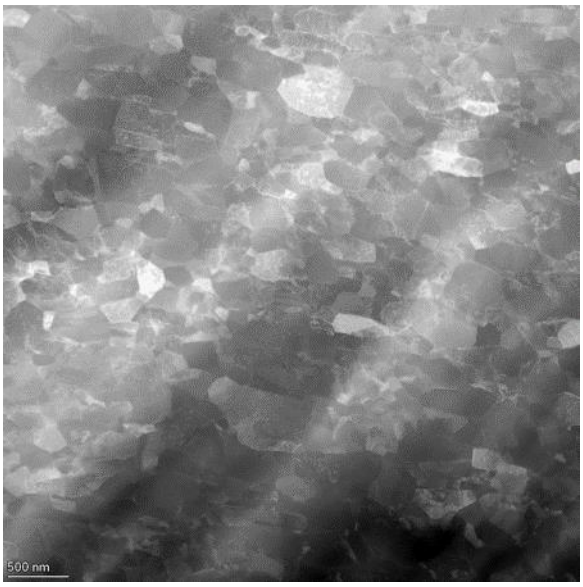
500 nm

Fig. 3

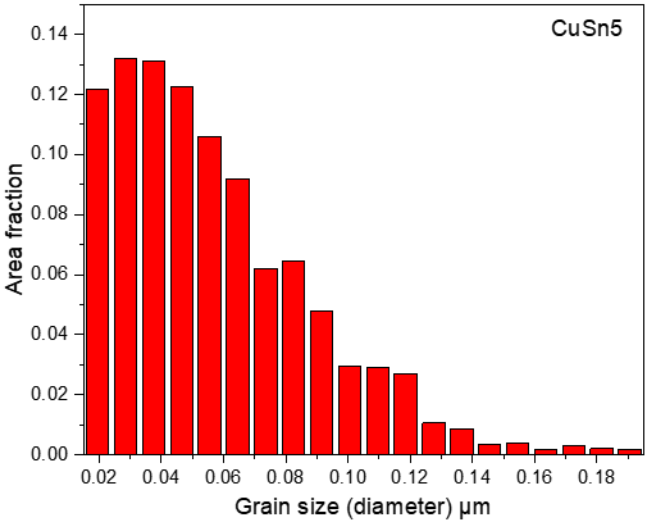
CuSn5
Area fraction
0.14
0.12
0.10
0.08
0.06
0.04
0.02
0.00
0.02
0.04
0.06
0.08
0.10
0.12
0.14
0.16
0.18
Grain size (diameter) µm

MS3.001-invited

Analyzing and assembling layered materials, atom by atom and layer by layer, in 2D and 3D

J. C. Meyer[1,2,3], C. Hofer[1,2,3], J. Haas[1,2], J. Kotakoski[3], T. Susi[3], C. Mangler[3], V. Skakalova[3], A. Mittelberger[3], G. Argentero[3], M. R. A. Monazam[3], C. Kramberger-Kaplan[3], R. S. Pennington[1,2], X. Wang[4], K. Braun[5]

[1]University of Tübingen, Institute of Applied Physics, Tübingen, Germany
[2]NMI Natural and Medical Sciences Institute at the University of Tübingen, Reutlingen, Germany
[3]University of Vienna, Faculty of Physics, Vienna, Austria
[4]Hunan University, School of Physics and Electronics, Hunan, China
[5]University of Tübingen, Institute of Physical and Theoretical Chemistry, Tübingen, Germany

Aberration-corrected electron microscopy is emerging as a versatile tool not only for analyzing, but also for manipulating materials down to the level of single atoms. I will discuss both of these aspects and present some of our recent developments in the context of layered, two-dimensional materials: On the analysis side, we developed means to identify the 3D atomic configuration of defects, grain boundaries or impurities, from only two exposures of the same structures [1,2]. The same approach, combined with the simple dependence of the intensity in annular dark field scanning transmission electron microscopy images on the atomic number provides (to some extent) chemical information about the sample, and hence allows an elemental identification in the case of light-element single-layer samples [3]. However, the intensity of individual atoms and atomic columns is affected by residual aberrations and the confidence of an identification is limited by the available signal to noise. As shown in Fig. 1, already in presence of small non-round aberrations, the histogram of intensities is significantly broadened if these aberrations are not taken into account. Here, we show that matching a simulation to an experimental image by iterative optimization provides a reliable analysis of atomic intensities even in presence of residual non-round aberrations [4]. We compare this method with other approaches demonstrating its high reliability at limited dose and with different aberrations. This is of particular relevance for analyzing moderately beam-sensitive materials, such as most 2D materials, where the limited sample stability makes it difficult to obtain spectroscopic information at atomic resolution.

Towards an atomic-level manipulation, I will present a recent development where we combine spatially controlled modifications of 2D materials, using focused electron irradiation or electron beam induced etching, with the layer-by-layer assembly of van der Waals heterostructures [5] (Fig. 2). A new transfer and assembly process makes it possible to stack the layers under observation in an electron microscope, such that pre-patterned features can be aligned to each other. The aligned stacking of individually patterned 2D materials layers can be considered as a form of 3D printing, where each layer is only one or a few atoms thick, and features within each layer can be defined with a nm-scale resolution. Moreover, as each layer can be chosen from the large zoo of 2D materials, it should be possible to directly generate a wide variety of functional devices.

***Fig. 1**. Intensity histograms from a simulated image in presence of small non-round aberrations ($C_{1,0}$ = 2 nm, $C_{1,2}$ = 1 nm, $C_{2,1}$=50 nm, $C_{2,3}$=50 nm). (a) Part of the simulated image, and (b) the simulated probe. (c) Intensity histogram using the optimization method, Gaussian fits, local maxima and the Voronoi cell integration (from left to right) [4].*

***Fig. 2**. (a-c) Schematic of cutting a pattern into individual graphene layers (a,b) followed by aligned stacking (c). (d-f) Experimental realization, (d,e) SEM images of crosshair structures cut into graphene, (f) Dark-field TEM image showing the assembled structure, set for highlighting one of the two layers. Scale bars are (d,e) 500 nm and (f) 200 nm [5].*

References
[1] 2D Materials 5, 045029 (2018)
[2] Appl. Phys. Lett. 114, 053102 (2019)
[3] Nature Commun. 10, 4570, (2019)
[4] Ultramicroscopy 227, 113292 (2021)
[5] ACS Nano 16, 1836-46 (2022)

Fig. 1

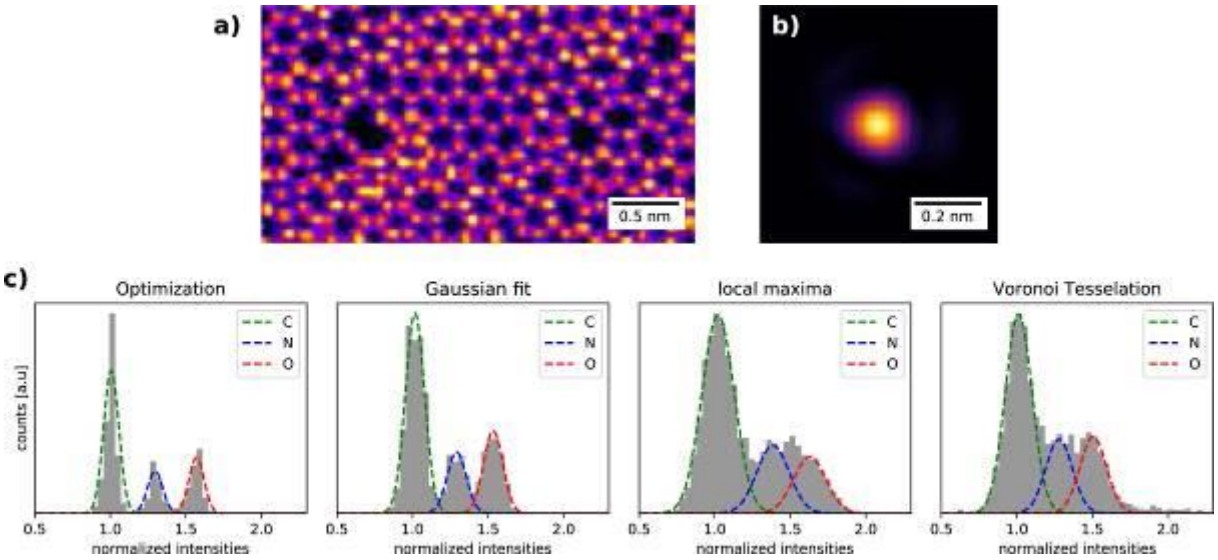
a)
0.5 nm
b)
0.2 nm
c)
Optimization
Gaussian fit
local maxima
Voronoi Tesselation
C
N
O
counts [a.u.]
0.5
1.0
1.5
2.0
normalized intensities

Fig. 2

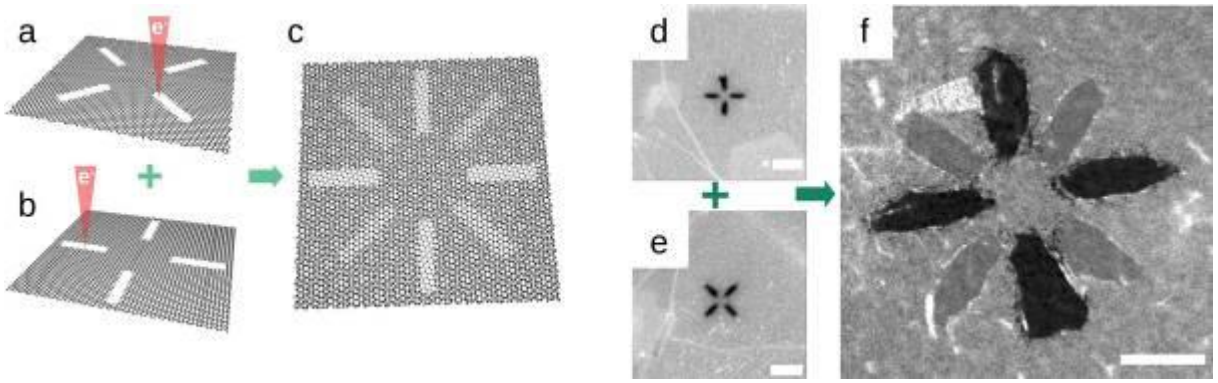
a
b
c
d
e
f

MS3.002-invited

Seeing into organic 2D materials: defects, dynamics, and resolution

H. Qi[1,2], B. Liang[1], D. Mücke[1], C. Leist[1], H. Wilson[3], C. J. Russo[3], U. Kaiser[1]

[1]Ulm University, Central Facility for Electron Microscopy, Electron Microscopy Group of Materials Science, Ulm, Germany
[2]Technische Universität Dresden, Center for Advancing Electronics Dresden (cfaed) & Faculty of Chemistry and Food Chemistry, Dresden, Germany
[3]MRC Laboratory of Molecular Biology, Cambridge, United Kingdom

Probing the structure of organic 2D materials (O2DMs), ultimately down to the atomic scale, has been a long-sought goal of materials science. AC-HRTEM is capable of direct imaging atomic structures with sub-Ångström resolution [1]. However, electron irradiation damage leads to rapid disintegration of the molecular network during the imaging process, severely limiting achievable resolution regardless of TEMs' optical performance.

Here we present various experimental efforts to extract high-resolution information from O2DMs in particular imine-based 2D polymer thin films [2,3]. Two samples were synthesized using the surfactant-monolayer-assisted interfacial synthesis (SMAIS) [4] (Fig. 1). Using low-dose methods at room temperature, we examined 2D-PI-DhTPA [2], and directly observed the grain boundaries with a resolution of 2.3 Å at 300 kV, giving insight into the formation mechanism of the 2D crystals.

Although HRTEM imaging of inorganic 2D materials can benefit substantially by restricting the electron energy below 80 keV [1], the rare TEM studies on organic 2D crystals are still usually carried out at 300 keV. We systematically evaluated the electron accelerating voltages for AC-HRTEM imaging of O2DMs [3]. We reached an image resolution of 1.9 Å at 120 kV (Fig. 2a-b). The improvement in resolution has been achieved by maximizing the efficiency of electron usage, among the acceleration voltages of 300 kV, 200 kV, 120 kV, and 80 kV. Not only could the porphyrin pores be clearly resolved, but linkers with and without hydroxyl groups could also be distinguished. We occasionally observed abnormal contrast in the vicinity of the porphyrin cores (Fig. 2c-d), conflicting with their previously reported structures. DFT calculations revealed that the additional contrast could be attributed to molecular interstitial defects (Fig. 2e) – a defect type that had not been discovered in 2D polymers before.

Recently, drawing from electron cryomicroscopy (cryoEM) in biology [5], we explored the potential of imaging our radiation-sensitive O2DMs at low temperature with direct electron detectors. This combination improved the information in a single micrograph such that reflections beyond a resolution of 1.3 Å are clearly resolved. We envisage that our results will bring new insights into the defect types and pore interfaces in O2DMS and promote a deeper understanding of structure-function correlations in this rising class of materials.

Fig. 1. Reaction scheme and atomic models of 2D-PI-BPDA and 2D-PI-DhTPA.

Fig. 2. a-d AC-HRTEM imaging of 2D-PI-BPDA at 120 kV, showing regions without and with TAPP interstitials. e, Plausible stacking modes of TAPP interstitials derived by DFTB calculations and corresponding simulated images.

References

1. Linck, M. *et al. Phys. Rev. Lett.* **117**, 76101 (2016).
2. Qi, H. *et al. Sci. Adv.* **6**, eabb5976 (2020).
3. Liang, B. *et al. Nat. Commun.* **13**, 3948 (2022).
4. Liu, K. *et al. Nat. Chem.* **11**, 994–1000 (2019).
5. Russo, C. J., & Egerton, R. *MRS Bulletin* ***44***, 935–941 (2019).

Acknowledgment

We gratefully acknowledge the funding from DFG – 492191310; 426572620; 417590517 (SFB-1415), as well as the financial support from the European Union's Horizon2020 research and innovation program under Grant Agreement No. 881603 (GrapheneCore3). This work was also supported by an Astex SIPD Fellowship (HW) and Medical Research Council grant MC_UP_120117.

Fig. 1

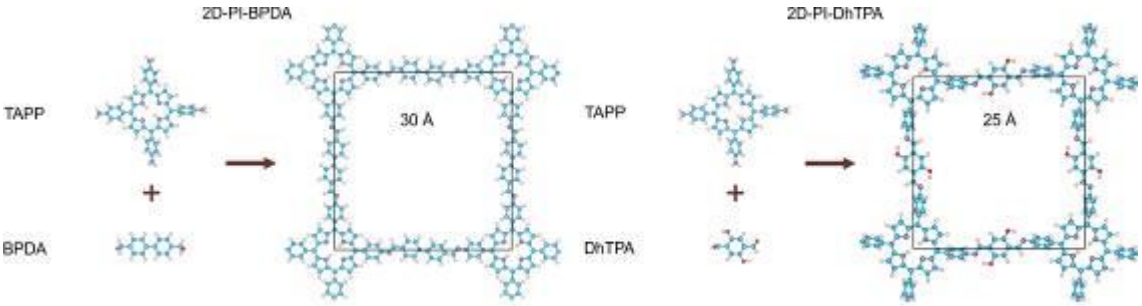

TAPP: 5,10,15,20-tetrakis(4-aminophenyl)-21H,23H-porphyrin **BPDA**: 4,4'-biphenyl-dicarboxaldehyde **DhTPA**: 2,5-dihydroxyterephthalaldehyde

Fig. 2

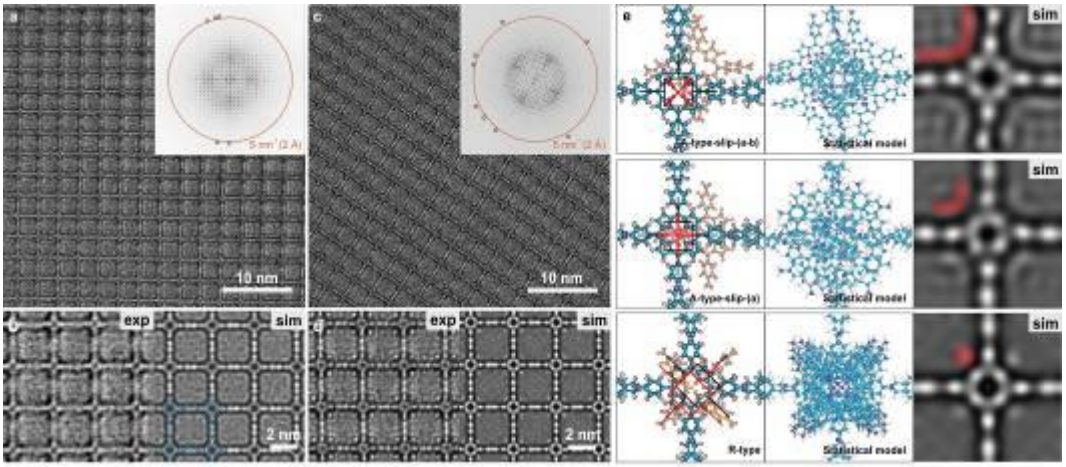

MS3.003

Tunable eccentricity of Bloch skyrmions in $Fe_{1.9}Ni_{0.9}Rh_{0.2}P$

S. Schneider[1,2], J. Masell[2,3], F. S. Yasin[2], L. Peng[2], K. Karube[2], Y. Taguchi[2], D. Pohl[1], B. Rellinghaus[1], Y. Tokura[2,4,5], X. Yu[2]

[1]TU Dresden, Dresden Center for Nanoanalysis (DCN), Dresden, Germany
[2]RIKEN, Center for Emergent Matter Science (CEMS), Wako, Japan
[3]Karlsruher Institut of Technologie (KIT), Institute of Theoretical Solid State Physics, Karlsruhe, Germany
[4]University of Tokyo, Department of Applied Physics, Tokyo, Japan
[5]University of Tokyo, Tokyo College, Tokyo, Japan

1. Introduction

The experimental discovery of antiskyrmions in $Mn_{1.4}PtSn$ [1] has opened new pathways towards using microscopically small magnetic whirls as information carriers [2]. For this purpose, a thorough understanding of the detailed three-dimensional spin texture of these magnetic solitons, including their stabilization mechanisms is essential. Quite recently, the compound $Fe_{1.9}Ni_{0.9}Pd_{0.2}P$ was found to host antiskyrmions at room temperature, which can be transformed into skyrmions, e.g., by tuning the external magnetic field [3].

2. Objectives

In this study we investigate this elliptical skyrmion phase as a function of the external magnetic field and temperature in a similar material, $Fe_{1.9}Ni_{0.9}\mathbf{Rh}_{0.2}P$, where Pd was substituted by Rh, to gain further insight into the formation mechanisms of topological spin solitons.

3. Materials & methods

The occurrence and nature of skyrmions in a $Fe_{1.9}Ni_{0.9}Rh_{0.2}P$ lamella fabricated using a focused ion beam (FIB) were studied in a JEOL Jem F-200C by means of off-axis electron holography that allows for the quantitative determination of the projected in-plane magnetic induction $\mathbf{B}_{ip}$. The sample temperature was controlled with a Mel-Build LN_2 Atmos Defend - In-situ double-tilt LN_2 cooling holder.

4. Results

In **Fig. 1** the magnitudes of $\mathbf{B}_{ip}$ in the lamella upon exposure to magnetic fields of 170 mT and 330 mT applied along [001] at room temperature are displayed. In zero field, the skyrmions initially possess an elliptical shape with the semi-major axes parallel to the ⟨110⟩ directions due to dipole–dipole interactions [5, 6]. Increasing the external out-of-plane magnetic field leads to (i) a reduction of the skyrmion size, (ii) an enhancement of $\mathbf{B}_{ip}$ and (iii) a deformation of the skyrmions. The initially elliptical skyrmions are transformed into skyrmions with circular shapes until a critical field is reached, where the system undergoes a transition into the field-polarized phase.

5. Conclusion

The current investigations provide a first insight how the balance between the symmetric and antisymmetric exchange and dipole-dipole interaction can tune the skyrmion structure in $Fe_{1.9}Ni_{0.9}Rh_{0.2}P$. By combining our experimental results with magnetostatic simulations, we can shed light on the complex interplay of these interactions in the stabilization of topological spin textures in three dimensions.

[1] A. K. Nayak et al., Nature **548** (2017), 561 – 566.

[2] B. Göbel et al., Physics Reports **895** (2021), 1 – 28.

[3] K. Karube et al., Nature Materials **20** (2021), 335 – 340.

[4] K. Karube et al., Adv. Mater. **34** (2022), 2108770.

[5] L. Peng et al., Nat. Nanotechnol. **15** (2020), 181 – 186.

[6] J. Jena et al., Nature Communications **11** (2020), 1115.

Fig. 1: Magnitude of $\mathbf{B}_{ip}$ of Bloch skyrmions in $Fe_{1.9}Ni_{0.9}Rh_{0.2}P$ in external fields of 170 mT and 330 mT, respectively.

Fig. 1

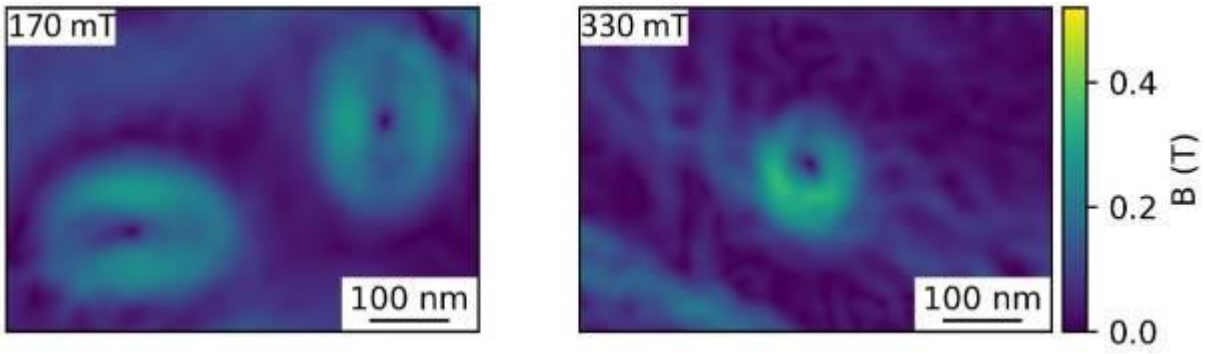

MS3.004

Synthesis and characterization of metal sulfide nanoribbons on graphene by self-assembly of inorganic ions

X. Zhang[1], K. Anggara[1], V. Srot[1], X. Wu[1], P. A. van Aken[1], K. Kern[1]

[1]Max Planck Institute for Solid State Research, Stuttgart, Germany

Bottom-up synthesis of nanostructures on surfaces depends on the self-assembly of nanoscale building blocks. The diversity of accessible nanostructures, however, have been constrained by the limited choice of atomic and molecular building blocks that can be evaporated on a surface. Here, we bypass this limitation by using complex inorganic ions generated from electrospray ionization as building blocks to synthesize nanostructures on surfaces. We deposited $HMo_nS_{3n+1}^-$ (n = 4-8) ions onto a freestanding single-layer graphene by electrospray ion-beam deposition (ESIBD), and imaged the resulting nanostructures by aberration-corrected scanning transmission electron microscopy (STEM). The molecules form anisotropic, single-layered, crystalline MoS_2 nanoflakes (< 20 nm^2), which in turn self-assemble into MoS_2 nanoribbons extending as far as 1 µm (Fig. 1). The widths of the nanoribbons were tuned by the precursors, as the $HMo_nS_{3n+1}^-$ (n = 4-8) ions formed 4 ± 1 nm wide nanoribbons, the $HMo_nS3_{n+1}^-$ (n = 5-8) ions 5 ± 2 nm wide nanoribbons, and the $HMo_nS_{3n+1}^-$ (n = 6-8) ions formed 8 ± 3 nm wide ones. This first observation of such nanostructures evidences the potential of this approach to prepare previously inaccessible nanomaterials on surfaces.

Figure 1 HMo_nS^{3n+1-} ions were deposited onto single layer graphene by ESIBD, and self-assembled into 1 µm long monolayer MoS_2 nanoribbons as observed by STEM.

Fig. 1

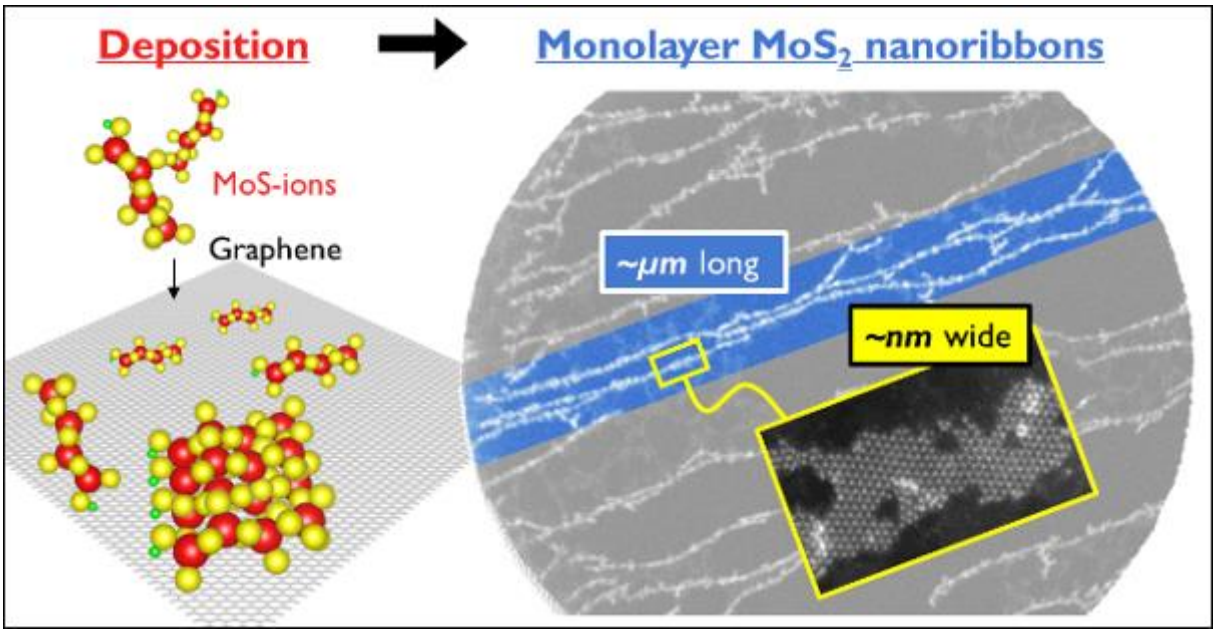

MS3.005

Hexagonal hybrid bismuthene by molecular interface engineering

C. Dolle[1,2], V. Oestreicher[2], A. M. Ruiz[2], M. Kohring[3], M. Wu[4], G. Sánchez-Santolino[5], Y. M. Eggeler[1], E. Spiecker[4], J. Canet-Ferrer[2], H. B. Weber[3], M. Varela[5], J. J. Baldoví[2], G. Abellán[2]

[1]Karlsruher Institut of Technologie (KIT), Karlsruhe, Germany
[2]Instituto de Ciencia Molecular, Valencia, Spain
[3]Lehrstuhl für Angewandte Physik, Erlangen, Germany
[4]Institute of Micro- and Nanostructure Research, Erlangen, Germany
[5]Instituto Pluridisciplinar de Física de Materiales, Madrid, Spain

Since the rise of graphene as playground for scientists in different fields, the fascination for two-dimensional materials did not cool down but rather remains at a peak interest due to the exceptional properties those ultrathin, layered structures show. While physicists are intrigued by transport properties for TMD's and material scientists praise the mechanical stabilities of even single layer thick atomic layers, chemists mainly use 2D materials as perfectly defined substrate for functionalization approaches.

In contrast to widely studied materials, we will present a chemical approach towards two-dimensional bismuth with unprecedented material quality and a surprisingly unexpected structure. In an one-pot colloidal reductive reaction, we synthesized single crystalline hexagonal platelets with diameters up to 2 µm and a thickness around 5 nm. Due to the chemical approach for the generation of these ultrathin bismuth material, we were able to introduce structurally modified bismuthene on the basal planes of the crystallites that are stabilized by a covalent functionalization.

To reveal the nature and resulting properties of this sandwiched hybrid structure we made use of a battery of characterization techniques ranging from microscopy (HRTEM, HRSTEM, EELS, EDS, SAED, AFM) to spectroscopy (XPS, Raman) and finally simulations (DFT) and single-particle transport measurements. The combination of all these techniques allowed us to describe the stabilized bismuthene capping layers as fundamentally different from pristine rhombohedral bismuth. Firstly, while bismuth shows the typical zig-zag arrangement with a lattice constant of 4.5 Å, the bismuthene layers are flat with a lattice parameter of 7.5 Å. Monochromated STEM-EELS reveals LSPR modes that are highly unexpected for a semimetal like bismuth and the calculated band structure, based on the simulated structure, shows metallic behaviour. The metallic nature of individual crystals was measured by transport experiments at room temperature.

In this contribution we show the wholistic process of an exceptional new material with a strong spin orbit coupling and postulated spin torque effects from the bottom-up synthesis to the characterization and conceivable future applications in devices.

Fig. 1 A Colloidal synthesis of the sandwich material with equivalents for the reaction. **B** PXRD pattern of synthesized material with expected diffraction peaks indicated. **C** Typical unprocessed Raman spectrum. No indication of surface oxidation. Inset optical micrograph of crystallite. **D** BF-TEM data and **E** typical indexed diffraction pattern of hybrid material with superstructural reflections indicated. **F** Colorized large area HRSTEM data with FFT as inset. Superstructure indicated in FFT. **G** AFM with height profile. **H** Experimental series of integrated EELS intensity, showing localized surface plasmon modes and **I** simulation of plasmonic modes based on model hexagon.

Fig. 2 A Integrated STEM-EDX intensity for individual crystallite with artistic representation of functionalized material. **B** Spatially integrated mean EDX spectrum with signals related to Bi. **C** Overview XPS before (red) and after (black) surface etching with Ar ions and **D** high resolution XPS of S/ Bi binding energies. A clear indication of S *2p* before the surface etching can be noticed between 165–170 eV. **E** Structurally optimized bismuth/ bismuthene hybrid with simulated ED. Bottom right cross sectional HRTEM and respective image simulation.

Fig. 1

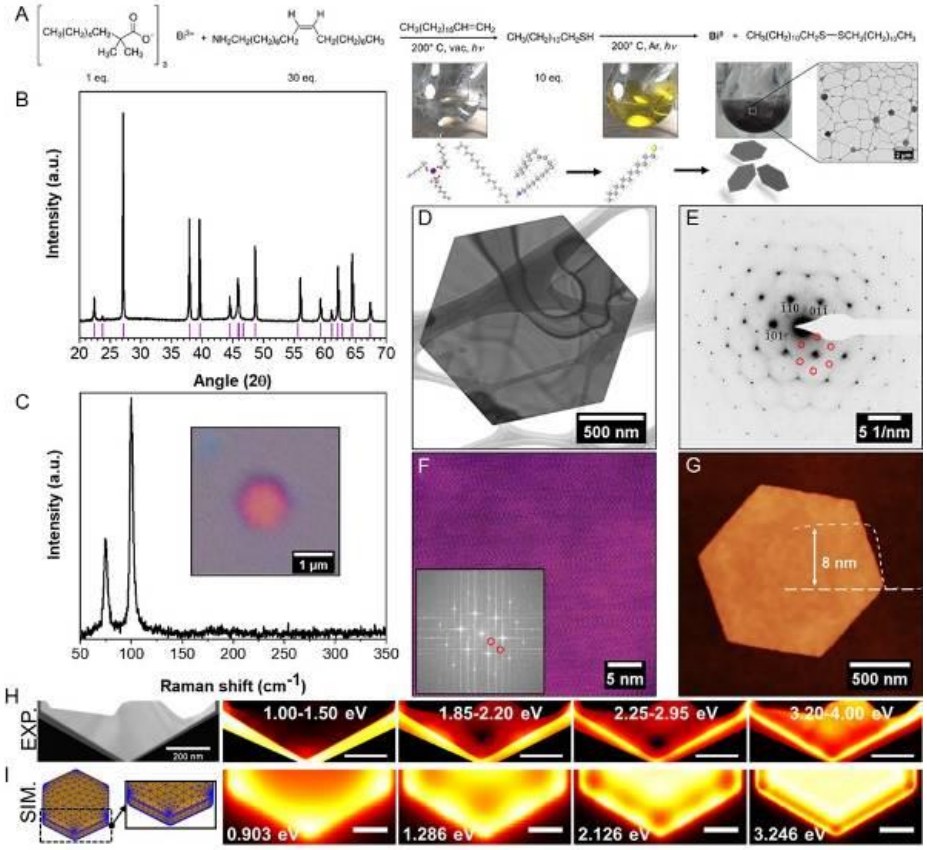
A
1 eq.
30 eq.
10 eq.
B
Intensity (a.u.)
Angle (2θ)
C
Intensity (a.u.)
1 μm
Raman shift (cm-1)
D
500 nm
E
5 1/nm
F
5 nm
G
8 nm
500 nm
H
EXP.
1.00-1.50 eV
1.85-2.20 eV
2.25-2.95 eV
3.20-4.00 eV
I
SIM.
0.903 eV
1.286 eV
2.126 eV
3.246 eV

Fig. 2

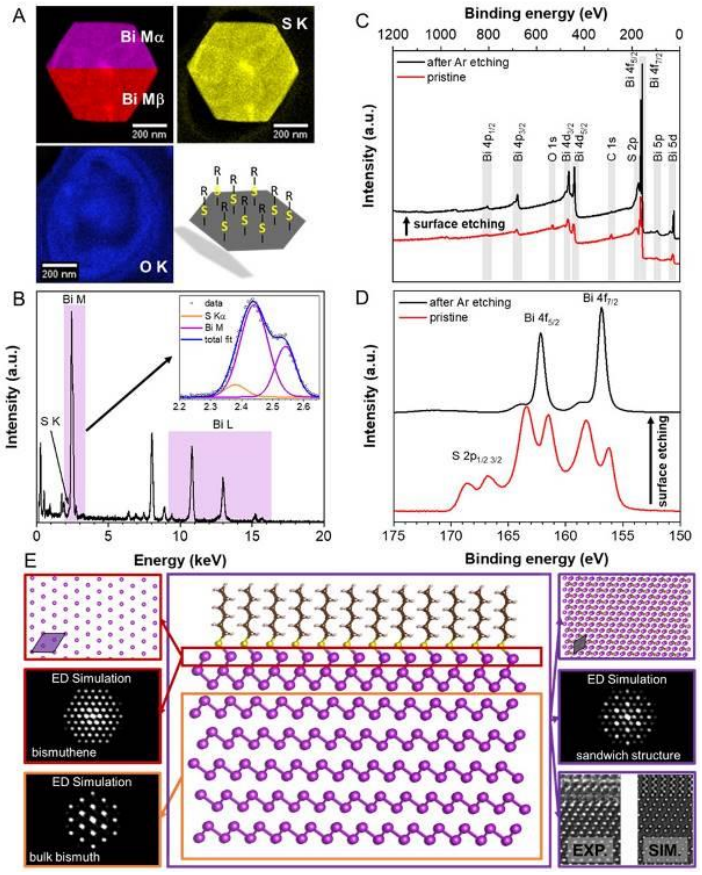
A
Bi Mα
Bi Mβ
S K
O K
200 nm
B
Bi M
S K
Bi L
Intensity (a.u.)
Energy (keV)
C
Binding energy (eV)
after Ar etching
pristine
surface etching
Bi 4p1/2
Bi 4p3/2
O 1s
Bi 4d3/2
Bi 4d5/2
C 1s
S 2p
Bi 5p
Bi 5d
Bi 4f5/2
Bi 4f7/2
D
after Ar etching
pristine
Bi 4f7/2
Bi 4f5/2
S 2p1/2 3/2
surface etching
E
ED Simulation
bismuthene
ED Simulation
bulk bismuth
ED Simulation
sandwich structure
EXP.
SIM.

MS3.006

Ordered electronic states in 2D quantum materials: imaging effects of hydrostatic pressure at the atomic scale

M. K. Kinyanjui[1], J. Ebad-Allah[2], M. Krottenmüller[2], C. A. Kuntscher[2]

[1]Ulm University, Electron Group of Materials Sciences, Ulm, Germany
[2]University of Augsburg, Experimental Physics II, Institute of Physics, Augsburg, Germany

Introduction

Charge density waves (CDW) are an ordered electronic state with periodic modulation of electron density and periodic lattice distortion (PLD) modulation of the atomic positions.[1] CDW is represented by an order parameter $\Psi = \Delta e^{i\varphi}$ characterized by a phase φ, giving position of the CDW with relation to the lattice, and amplitude,Δ, giving the value of the energy gap.[1] In some quantum materials, CDW are in competition / coexistence with the superconducting phase.[2-3] The nature of this relationship is still not well understood. Application of pressure is one experimental approach used to probe the nature of this relationship. [3] However, this also leads to the necessity to understand effects of pressure on the nature and the structure of the CDW at the atomic scale.

Objectives

Here, we have used atomic-scale transmission electron microscopy imaging to determine the influence of applied pressure on the structural properties of 1T-TaS_2 and the CDW at the atomic-scale.[4]

Materials & Methods

1T-TaS_2 samples were exposed to hydrostatic pressures of up to 2.5 GPa in a diamond anvil cell (DAC) (Fig.1 (a)). Pressurized samples were then prepared for TEM investigations through mechanical exfoliation. In high-resolution TEM (HRTEM) imaging CDW wave vectors and their respective phases are accessible and their evolution as a function of applied pressure can be mapped at the atomic scale.[4]

Results

A HRTEM image from a pressurized sample characterized by a deformation defect is shown in Fig. 1(b). Strong coupling of lattice and electronic degrees of freedom means that changes in lattice structure and ensuing deformation defects due to the applied pressure have an effect on the structure of the CDW electronic state. The modulation of CDW around the structural defect is shown in Figs 1(d)-(e). The magnitude of the CDW wave-length $|\lambda_1|$ and the respective phase φ_1 are shown as intensity maps in Figs. 1(d) and (e) respectively. The high and low intensity in the magnitude images respectively show the elongated or shortened CDW wavelength. The magnitude of the CDW wavelength and its phase are strongly modulated in the vicinity of the deformation defects. This strong modulation is characterized by (1) CDW strain which leads to local changes in the modulation wavelenght (2) Topological phase defects in the CDW order parameter in form of CDW dislocations (marked by dotted circles in Figs. 1(c)-(d)).

Conclusion

In conclusion we have mapped the atomic-scale response of the CDW order parameter in 1T-TaS_2 exposed to 2.5 GPa hydrostatic pressure. The CDW order parameter responds to the lattice defects arising from the applied pressure by showing an elastic-like strain response and topological phase defects in the electronic order.

References

[1] J. Wilson, F. D. Salvo, and S. Mahajan, Adv. Phys. 24, 117 (1975).

[2] E. Fradkin et al., Rev. Mod. Phys. 87, 457 (2015)

[3] A. F. Kusmartseva et al., Phys. Rev. Lett. 103, 236401(2009)

[4] M. K. Kinyanjui et al.Phys. Rev. B 104, 125106(2021)

FIG. 1 (a) Diamond anvil cell set-up used for pressure experiments. (b) A HRTEM image showing a deformation defect in a 1T-TaS_2 sample pressurized up to 2.5 GPa (b) FT of the HRTEM image with the Bragg spots from the atomic lattice (solid circles) and super lattice spots from the CDW (triangles). Temperature intensity maps representing (d) the magnitude (e) phase map of CDW wavelength. The dotted circles show the positions of CDW dislocations

Fig. 1

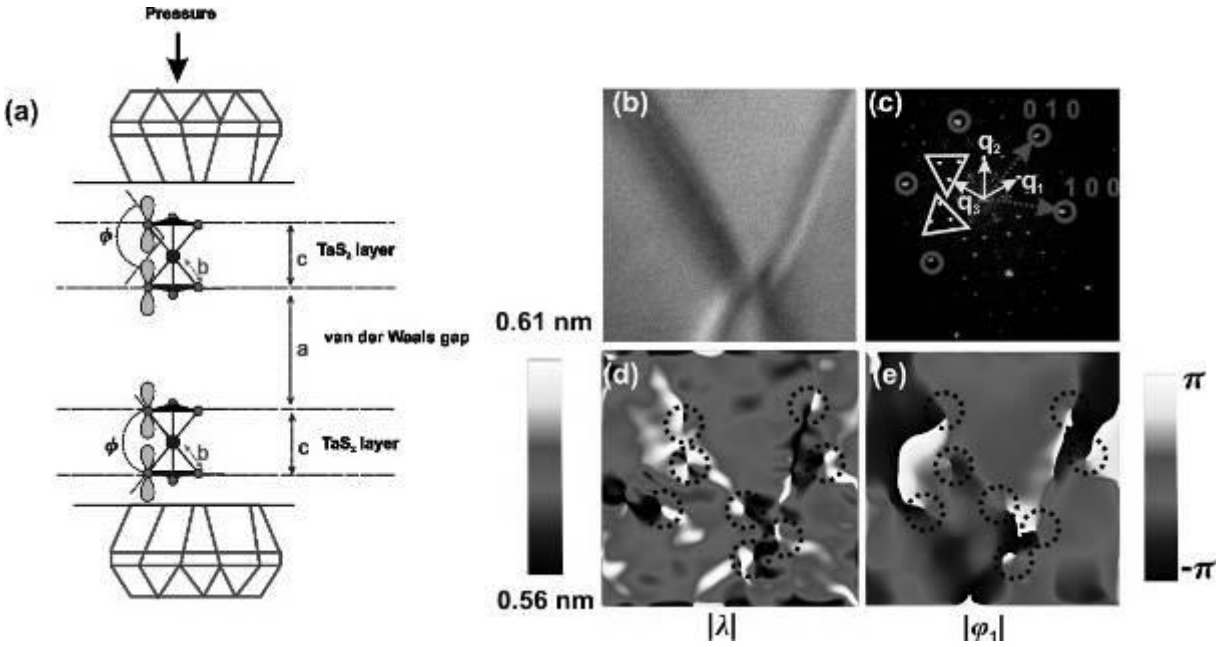

MS3.P001

Composition and strain of pseudomorphic α-(AlGa)2O3 on sapphire (0001) substrates

M. Schowalter[1], P. Vogt[1], J. A. Bich[1], A. Karg[1], C. Mahr[1], T. Grieb[1], T. Mehrtens[1], F. F. Krause[1], M. Eickhoff[1], A. Rosenauer[1]

[1]University Bremen, Institut für Festkörperphysik, Bremen, Germany

Recently, it was reported that in initial stages of Ga_2O_3 growth on (0001) sapphire substrates a thin (~3 ML) layer of α-Ga_2O_3 is forming before the formation of β-Ga_2O_3 for three growth techniques [1]. A surprising result, since the most stable polymorph of Ga_2O_3 is the beta phase, whereas the alpha phase is only the third [2]. The authors explain the stabilization of the alpha phase as being a strain effect due to the pseudomorphic character of the layer within an isotropic strain model. In this contribution a similar α-Ga_2O_3 layer was grown on a (0001) sapphire without overgrowth with β-Ga_2O_3 using molecular beam epitaxy (MBE) and investigated using TEM. Fig. 1 shows HAADF STEM image of the layer in a) together with a simulated image of an α-Ga_2O_3 layer on α-Al_2O_3 in b) for the [11-20] zone axis. The respective images for the [11-00] zone axis are depicted in c) and d). The observed contrast pattern qualitatively agrees between experiment and simulation. A close inspection of the contrast pattern for the [1-100] zone axis shows that it does not agree between substrate and layer, which can be explained by the different contributions of Ga and O to the image intensity in the layer compared to Al and O in the substrate. This was already reported in reference [1].

Fig.1: a) and c) HAADF STEM images of the layer in [11-20] and [1-100] zone axis. b) and d) Respective simulated images of Al2O3 with a Ga_2O_3 layer, for respective zone axes.

EDX mappings showed a concentration of 26% Ga. To confirm this concentration composition maps were derived from the HAADF STEM images by a quantitative comparison with simulations according to the method suggested by Rosenauer et al. [3]. A Ga concentration map and a linescan along growth direction are shown in Fig. 2 a) and b). Indeed, the EDX result of 26 % is in good agreement with the HAADF STEM measurement of about 25%. *Fig. 2: Ga composition map (a)) and linescan along growth direction (b)).* In fact, the presence of the α-Ga_2O_3 in ref. [1] was explained by stabilization of the phase due to strain within an isotropic model. Fig. 3 shows the biaxial stress as a function of the assumed bulk modulus for a Poisson ratio of 0.3 for different compositions (25%, 50%, 75% and 100% Ga). Additionally, single points are added, which correspond to critical stresses, for which the alpha phase is starting to become energetically more favourable than the beta phase. For 100%, 75% and 50 % the stress is still significantly high to be the reason for the stabilization of the alpha phase, which is not given for the measured concentration of 25 %. Nevertheless, the assumption of an isotropic strain model is certainly not correct, especially since the layer seems to be pseudomorphically grown on the substrate and therefore a tetragonal distortion of the material in the layer will take place. We will measure this tetragonal distortion and compare it with density functional theory computations in order to determine, whether α-$(AlGa)_2O_3$ can be stabilized by a distortion corresponding to a Ga concentration as low as 25 %.

Fig. 3: Biaxial stress as function of bulk modulus in isotropic approximation for different Ga concentrations.

[1] R. Schewski et al., J. Phys: Cond. Mat. **19** (2007), 346211

[3] A. Rosenauer et al., Ultramicroscopy **109** (2009), 1171

[4] H. He et al., Phys. Rev. B **74** (2006), 195123

[5] K.E. Lipinska-Kalita et al., Phys. Rev. B **77** (2008), 094123

[6] H. Wang et al., J. Appl.Phys. **107** (2010), 033520

Fig. 1

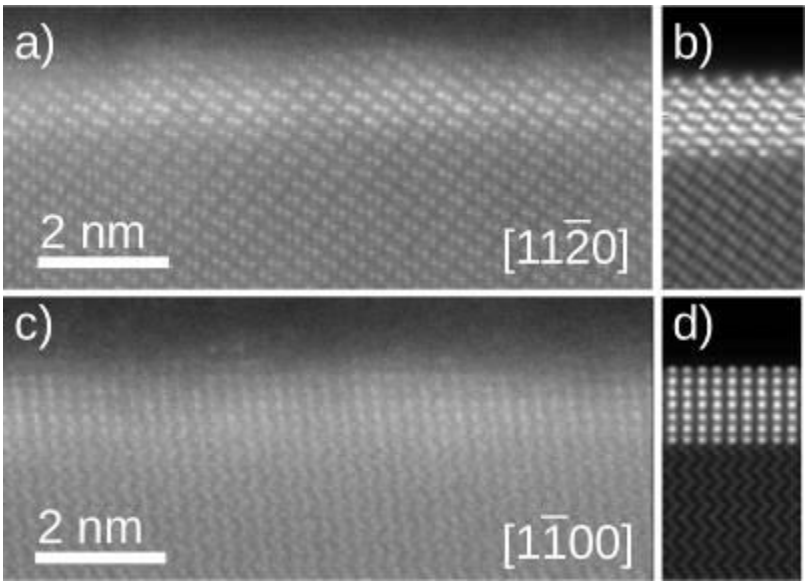

Fig. 2

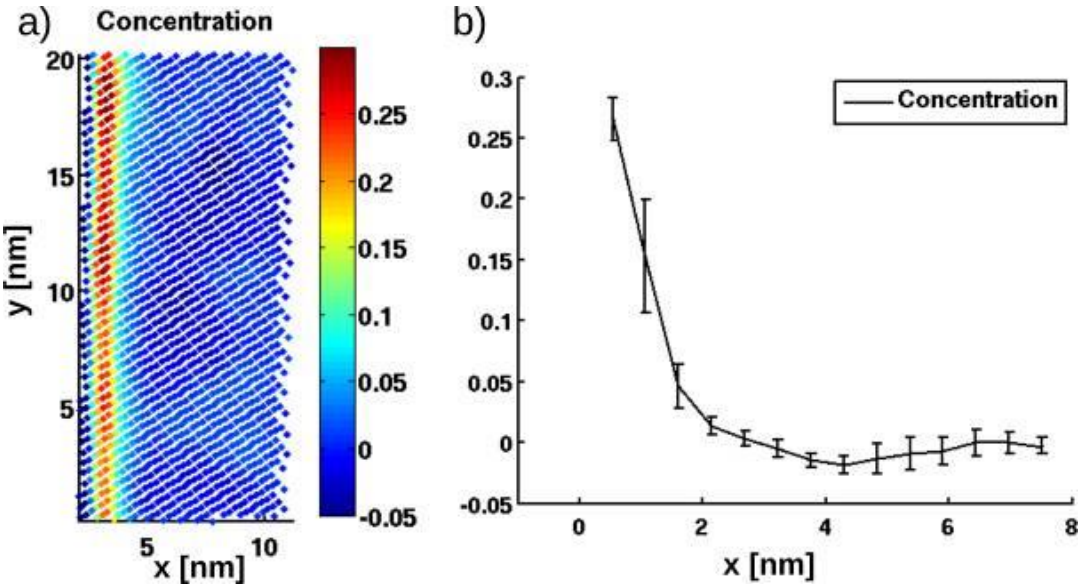

Fig. 3

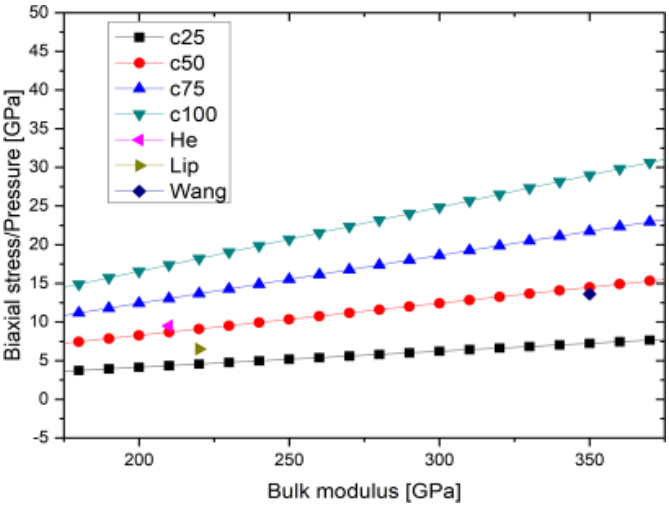

MS3.P002

In situ reflection electron microscopy for investigation of sublimation and van-der-Waals epitaxy on Bi_2Se_3(0001)

D. Rogilo[1], S. Ponomarev[1], K. Zakhozhev[1,2], N. Kurus[1], L. Basalaeva[1], K. Kokh[1], A. Milekhin[1], D. Sheglov[1], A. Latyshev[1]

[1]Rzhanov Institute of Semiconductor Physics SB RAS, Novosibirsk, Russian Federation
[2]Novosibirsk State University, Novosibirsk, Russian Federation

1. Introduction

Since the beginning of the XXI century layered two-dimensional (2D) materials have been promising candidates for use in microelectronics, photonics, and photovoltaics. To grow high-quality heterostructures and superlattices, molecular beam epitaxy is used, but various defects are generated during the growth. Therefore, the growth of wafer-scale high-quality films is a fundamental issue of van der Waals (vdW) epitaxy that requires profound investigation of growth mechanism using *in situ* experimental techniques.

2. Objectives

In this work, we aim to visualize and study surface transformations during sublimation and van-der-Waals epitaxy of 2D metal chalcogenides by *in situ* reflection electron microscopy.

3. Materials & methods

We used an *in situ* reflection electron microscope (REM, 100 kV accelerating voltage) equipped with three separate evaporators for Se and metal (Bi, In, or Sn). Samples were prepared from a Bi_2Se_3 single crystal by cleavage along (0001) plane and were heated during experiment resistively by passing direct electric current. Above 100°C, the samples were exposed to a Se molecular beam (up to ~0.1 nm/s) to avoid noncongruent Bi_2Se_3 sublimation. *Ex situ* analysis of surface morphology was carried out by atomic force microscopy (AFM, Multimode 8, Bruker). The same equipment was used for creation of 15–30-nm-deep grooves by probe lithography. The crystal phase of obtained films was analyzed by *ex situ* Raman scattering measurements (XploRa Plus, Horiba, 532 nm laser).

4. Results

When Bi_2Se_3(0001) surface is heated above 400°C, *in situ* REM images show that atomic steps move in ascending direction (towards higher terraces), which corresponds to congruent crystal sublimation. During sublimation, many 2D vacancy islands nucleate, grow, and coalesce on wide (~1–100 μm) terraces between the steps. The grooves preformed by probe lithography widen and deepen, and the center of each groove acts as a source of atomic steps that generates new steps moving in the ascending direction away from the source. We used this phenomenon to create self-organized regularly-spaced 1-nm-high atomic steps on the Bi_2Se_3(0001) surface. The onset of Bi deposition reverses the step motion direction (towards lower terraces), which corresponds to the onset of epitaxial layer-by-layer Bi_2Se_3 growth. These processes were first observed on the Bi_2Se_3 surface by *in situ* REM [J. Phys. Conf. Ser. 1984 (2021) 012016].

When In (or Sn) is deposited onto the Se-exposed sublimating Bi_2Se_3(0001) surface, In_2Se_3 (or $SnSe_2$) heteroepitaxy begins with periodic 2D island nucleation and growth. After 3–5 nm growth, this mode switches to 3D growth (mounding). *Ex situ* Raman spectra of the grown films display a set of vibrational modes typical for the β-In_2Se_3 (or 1T-$SnSe_2$) crystal phase.

5. Conclusions

Our results show that *in situ* REM technique can be applied to study real-time surface dynamics of layered 2D materials during sublimation and van-der-Waals epitaxy. Using *in situ* REM, we have first visualized motion of atomic steps, evolution of lithographically patterned grooves, and 2D island nucleation on the Bi_2Se_3(0001) surface.

Acknowledgments

This research was performed on the equipment of CKP "Nanostruktury" and financially supported by Russian Science Foundation [grant number 22-72-10124].

MS3.P003

4D-STEM on epitaxially grown vertical heterostructures of WS_2 on Graphene

O. Maßmeyer[1], J. Belz[1], S. Patil[1], R. Günkel[1], J. Glowatzki[1], S. Krotkus[2], M. Heuken[2], A. Beyer[1], K. Volz[1]

[1]Philipps-University Marburg, Physics, Marburg, Germany
[2]Aixtron SE, Herzogenrath, Germany

Introduction:

Two-dimensional (2D) materials received a lot of interest over the past decade. Especially van der Waals (vdW) 2D materials, such as transition metal dichalcogenides (TMDCs), and their heterostructures, exhibit semiconducting properties. Mixing and matching these materials with different properties and stacking them under an arbitrary in-plane angle causes structural changes as well as charge redistribution in the heterostructure, highly interesting for novel device applications.[1] For these device structures, precise control of the composition and high uniformity of the layers is desired. Therefore, bottom-up synthesis methods, like metal-organic chemical vapor deposition (MOCVD) are currently being explored.[2]

Objectives:

In this study, we aim to investigate charge redistributions occurring in 2D vertical heterostructures grown by MOCVD and to identify the epitaxial relationship of the layers within the heterostructure utilizing 4D-STEM.

Materials and Methods:

Vertical heterostructures of mono- to few-layer WS_2 on few-layer graphene were deposited by MOCVD in a 19x2 inch Close Coupled Showerhead (CCS) Aixtron reactor on c-plane sapphire substrates. These structures are then transferred onto a 3 nm carbon film TEM-Grid by the PMMA transfer method.[3] The samples are then characterized in a JEOL 3010 TEM and in an aberration-corrected JEOL 2200 FS STEM in conjunction with a fast pixelated pn-CCD detector, opening the possibility to analyze the samples by 4D-STEM.[4]

Results:

The heterostructures of WS_2 on graphene were successfully transferred by PMMA onto the TEM-Grids. The sample exhibits regions of monolayer WS_2 and multiple stacking rotations between the vertically stacked WS_2 and graphene layers. An annular bright field (ADF) image, exhibiting one of the resulting Moiré patterns is shown in fig. 1. The observed pattern aligns very well, to a rotation of about 11° between the lower and upper WS2 layer. In the FFT additional spots originating from the different lattice plane spacing of WS_2 can be observed, which to the {100} lattice spacing of the underlying graphene layers. For the graphene layers in-plane rotations of about 34° and 10° are identified. In addition to the in-plane orientation of the layers, hopping of W and S atoms induced by the electron beam was seen for imaging at 200 keV as well as 80 keV. Studying this process should allow further insights into the crystal formation process. Furthermore, the heterostructures are investigated by 4D-STEM to reveal potential charge redistributions in these structures.

Conclusion:

Our results show a successful growth of high-quality vertical heterostructures of WS_2 on graphene on sapphire and subsequent transfer to TEM-Grids. The first results are very promising to give insights into the nucleation process, the orientation relation of WS_2 on graphene and into the charge redistributions in vertical vdW heterostructures.

Figure 1. a) ABF-STEM image of 2 layers of WS_2 on top of 2-3 layers of graphene recorded at 80 keV. b) Reduced FFT calculated from the STEM image in a). c) Lattice spacings determined from the FFT spots. d) Monolayer of WS_2 on WS_2 rotated by 10.7°.[5]

References:

[1] K. S. Novoselov et al. Science 353, (2016).
[2] S. M. Eichfeld, et al. 2D Materials 3, (2016).

[3] F. Zhang et al. Nanotechnology 29, (2018).
[4] C. Ophus. Microscopy and Microanalysis 25, (2019).
[5] K. Momma et al. J. Appl. Crystallogr. 44, (2011).

Fig. 1

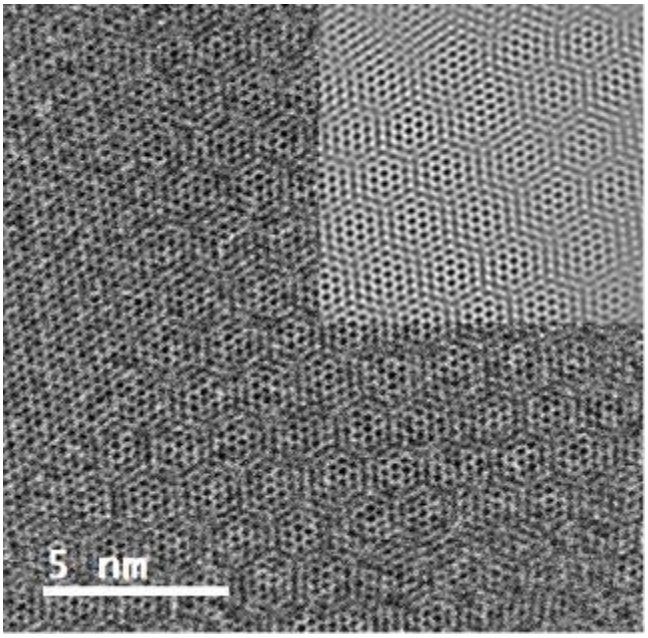

Fig. 2

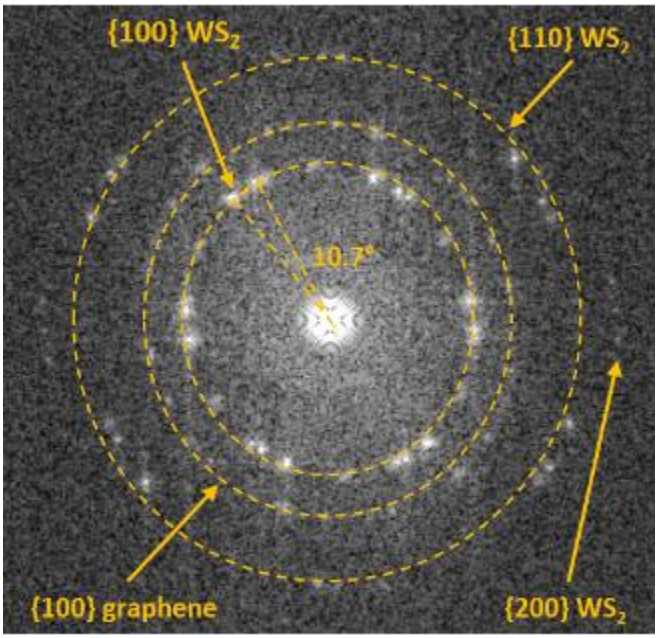

Fig. 3

Lattice Planes	Measured [Å]	Expected [Å]
{100} WS2	2.7 ± 0.1	2.76
{100} Graphene	2.1 ± 0.1	2.14
{110} WS2	1.6 ± 0.1	1.59
{200} WS2	1.4 ± 0.1	1.38

Fig. 4

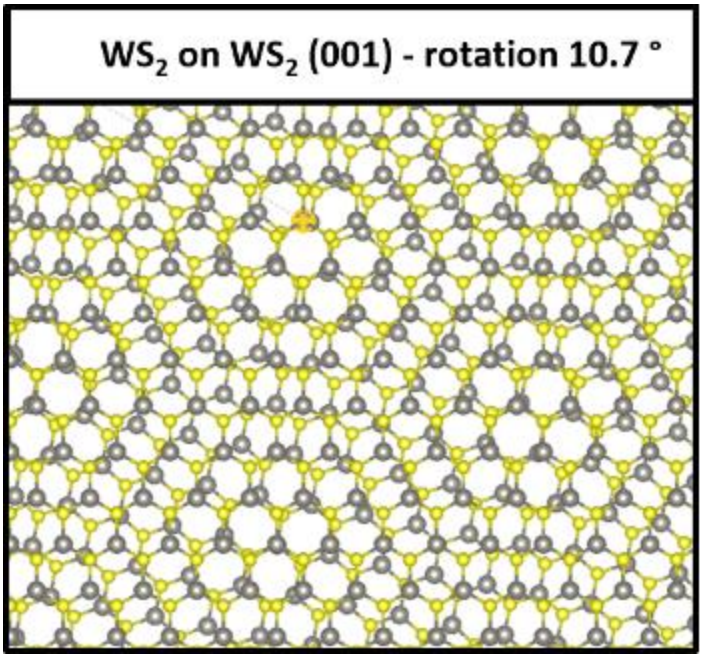

MS3.P005

Multi-core iron oxide nanoparticles: on their hierarchical architecture and coherence of their cores

S. Neumann[1], L. Kuger[2], C. R. Arlt[2], M. Franzreb[2], D. Rafaja[1]

[1]TU Bergakademie Freiberg, Institute of Materials Science, Freiberg, Germany
[2]Karlsruher Institut of Technologie (KIT), Institute of Functional Interfaces, Eggenstein-Leopoldshafen, Germany

Multi-core iron oxide nanoparticles (IONPs), usually consisting of the spinel compounds magnetite (Fe_3O_4) and maghemite (γ-Fe_2O_3), possess superparamagnetic behavior, high saturation magnetization, good biocompatibility, and interactive surface characteristics. These properties predestine IONPs for biomedical applications, for example as carrier for drug delivery in the human body, as heat mediator for hyperthermia cancer treatment, or as contrast agent for magnetic resonance imaging. However, a profound description of the hierarchical structure of multi-core IONPs, in particular the crystallographic interconnection and coherence of the individual cores which strongly influence their magnetic properties, has not been provided so far.

The aim of this study was to describe the correlations between the internal structure of the IONPs and their magnetic properties. The IONPs investigated here were commercially available, dextran-coated multi-core IONPs (synomag-D, micromod Partikeltechnologie GmbH, Rostock, Germany), which were synthesized using a polyol method [1]. Their structural characteristics and magnetic properties were investigated using transmission electron microscopy (TEM), X-ray diffraction (XRD) and alternating gradient magnetometry (AGM).

High-resolution TEM (HRTEM) showed that the IONPs consist of several cores with specific orientation relationships. HRTEM in combination with geometric phase analysis [2] disclosed that larger cores are further fragmented into small domains that have a mutual misorientation of less than 1°. The fragmentation of the cores was confirmed by XRD that revealed a dependence of the line broadening on the magnitude of the diffraction vector, which is typically observed for slightly misoriented, partially coherent nanocrystallites [3]. The particle size and the core size distributions of the IONPs were determined in a statistical manner by applying a multi-stage semi-automatic segmentation routine to several low-magnification high-angle annular dark-field scanning TEM images [4] and correlated with the microstructure characteristics. The structural properties determined in a correlative manner are related to the magnetic properties of the multi-core IONPs that were obtained from the AGM measurements.

References

[1] H. Gavilán *et al.*, Part. Part. Syst. Charact. **34** (2017) 1700094.

[2] M. Hytch *et al.*, Ultramicroscopy **74** (1998) 131-146.

[3] D. Rafaja *et al.*, J. Appl. Crystallogr. **37** (2004) 612-620.

[4] S. Neumann *et al.*, CrytEngComm **22** (2020) 3644-3655.

MS3.P006

Novel synthesis routes for nitrogen doped graphene and atomic level characterization

I. Musil[1], L. Rieger[1], J. Haas[1], K. Strobel[1], J. C. Meyer[1]

[1]Institute for Applied Physics, University of Tübingen, AG Meyer: Advanced Materials, Tübingen, Germany

Graphene has been subject of intense research and holds promising perspectives for future applications due to its unique properties. However, controlled structural modifications are desirable in order to fine-tune its properties, e.g. via the introduction of dopant atoms. In this work, we analyzed and compared nitrogen doping via ion implantation (as in [1]) with newly developed and experimentally very simple techniques of gas arc discharges in a nitrogen environment and plasma treatment with nitrogen plasma. For this purpose, several experimental setups were built, utilising (a) pure, energy-constrolled ion beams (b) gas discharge between the sample and a counter-electrode at pressures between 0.1 and 10 mbar (example in Figure 1), or (c) treatment inside a commercial plasma cleaner for TEM-holders.

HRTEM is used to examine the doped graphene, allowing to evaluate and compare different doping methods. HRTEM, combined with image simulations, allow identifying nitrogen impurities inside the treated graphene samples [2], as exemplified in Figure 2, and provides insight into the implantation processes. Several synthesis routes were established, giving the opportunity to either study the underlying processes of ion implantation or allowing straightforward production of nitrogen doped graphene that can be implemented quite easily.

[1] U. Bangert et al., Nano lett. 13:4902, 2013

[2] J. C. Meyer et al., Nat. Mat. 10:209, 2011

Fig. 1

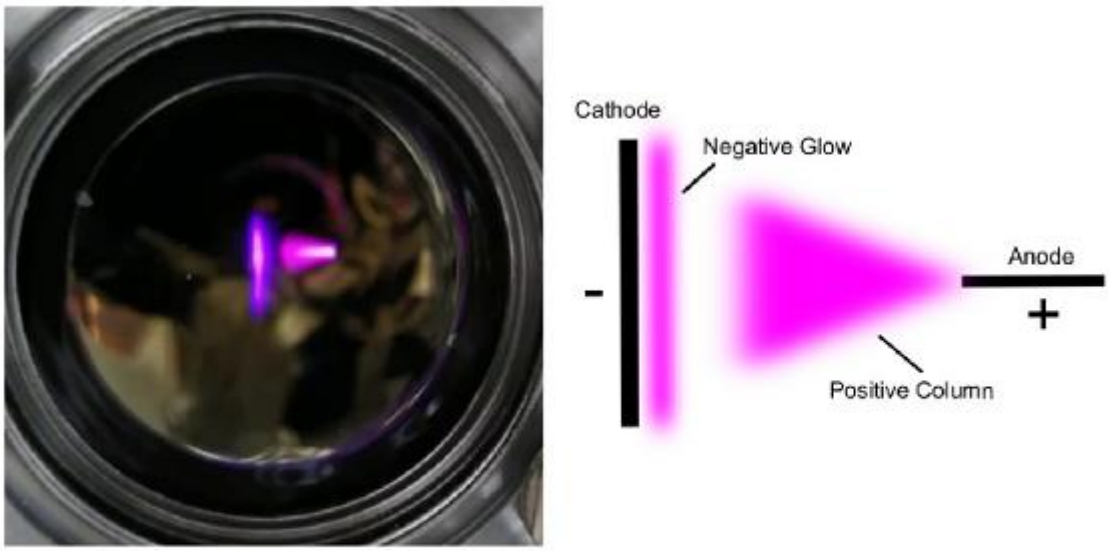

Figure 1: Left: Glow discharge at 6.5 mbar pressure and -750 V. Right: Sketch of observed light phenomena with explanations.

Fig. 2

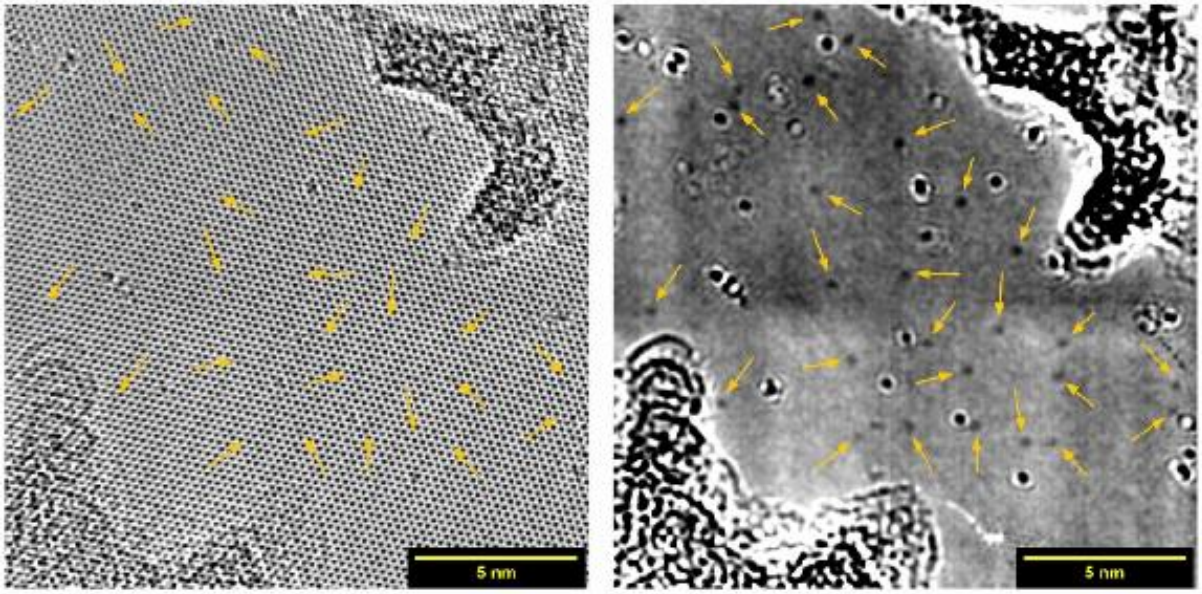

Figure 2: Example of nitrogen doped graphene prepared by a gas discharge treatment. Left: Processed image with nitrogen defects marked by arrows. Right: Applied Fourier filter and Gauss filter on the left image. Incorporated nitrogen atoms are marked with arrows.

MS3.P007

A TEM preparation technique to relate the electronic signature of defects with their atomic structure

M. Quincke[1], T. Lehnert[2], I. Keren[3], N. M. Badlyan[4], F. Port[1], M. Goncalves[1], J. Mohn[1], J. Maultzsch[4], H. Steinberg[3], U. Kaiser[1]

[1]Ulm University, Physics, Ulm, Germany
[2]Karlsruher Institut of Technologie (KIT), Laboratory for Electron Microscopy, Karlsruhe, Germany
[3]Hebrew University, Recah Institute for Physics, Jerusalem, Israel
[4]Friedrich-Alexander-Universität, Department of Physics, Erlangen, Germany

Atomic-resolution transmission electron microscopy (TEM) is the technique of choice for the structural characterization of two-dimensional (2D) materials on the atomic scale. With spherical and chromatic aberration correction (CC/CS-correction), low acceleration voltages of 20-80 kV still offer atomic resolution while allowing for good control over electron-beam-induced modifications in the sample [1]. In contrast to TEM experiments which are usually performed with the 2D materials being freely suspended on TEM-grids, many other measurement techniques such as electrical transport measurements require the 2D materials to be placed on other substrates [2]. This makes linking electron microscopy with complementary characterization techniques very challenging, as the samples may need to be transferred from a TEM grid to another substrate after TEM investigation. In our work, we aim for a controlled defect production in TEM experiments to engineer quantum dots (QDs) for subsequent electrical transport measurements. These QDs are considered as promising platforms for quantum information storage [3].

We exfoliate transition metal dichalcogenides (TMDs) on polyvinyl-alcohol coated SiO2 and transfer them to TEM grids. Following this, we use the TEM for engineering and simultaneous imaging of defects. When transferring the TMD flakes back to an arbitrary substrate, we observe that the exposure to the electron beam makes the flakes adhere more strongly to the TEM grid. This challenge is solved by the here presented "reverse transfer" preparation technique. We show proof-of-principle experiments in which we transfer electron exposed TMD flakes from a TEM grid to arbitrary substrates and measure the produced defects in photoluminescence and transport measurements.

[1] M. Linck et al., Phys. Rev. Lett. (2016)

[2] T. Dvir et al., Phys. Rev. Lett. (2019)

[3] J. M. Elzerman et al, Nature 430, 431-435 (2004)

Fig. 1

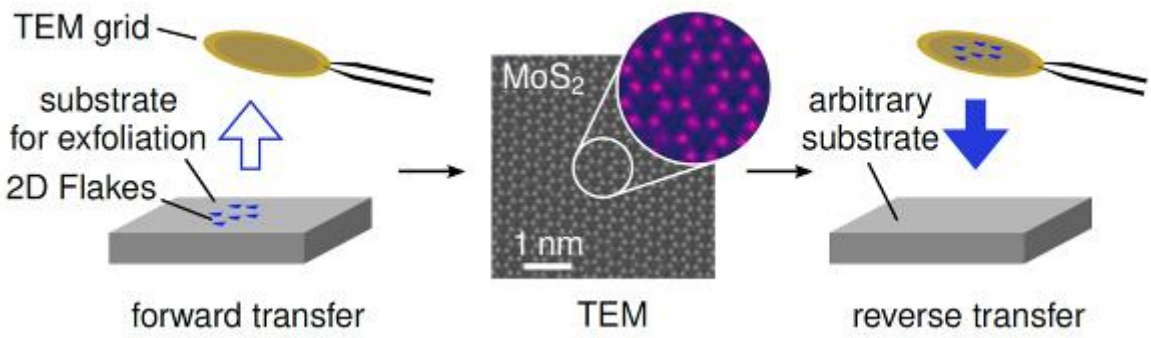

MS3.P008

In-situ formation of Mo_6Te_6 nanowire in single-layer 2H-$MoTe_2$ by annealing and electron irradiation

J. Köster[1], M. K. Kinyanjui[1], U. Kaiser[1]

[1]Ulm University, Electron Microscopy Group of Materials Science, Ulm, Germany

HRTEM, enables the investigation of electron beam-induced structural transformations, properties and single atom dynamics in two-dimensional (2D) materials. Furthermore, electron irradiation has been shown to lead to local transformations in single-layer $MoTe_2$; from the semiconducting 2H to the metallic 1T" phase [1].

Here, we report about the *in-situ* formation of Mo_6Te_6 nanowires by heating and under electron irradiation in freestanding 2H-$MoTe_2$ in TEM, as well as graphene-encapsulated samples. The transformation is specifically analysed in freestanding single- and few-layer samples.

HRTEM images were acquired at the Cc/Cs-corrected Sub-Ångström Low-Voltage Electron microscope (SALVE) at an electron accelerating voltage of 80kV [2]. 2H-$MoTe_2$ single-layers were prepared by mechanical exfoliation [3] onto Quantifoil grids and by stamping flakes with the help of a PMMA layer [4] onto a *ThermoFisher* MEMS-chip (see Fig. 1 (a-c)). Graphene-encapsulated $MoTe_2$ was prepared by transferring three separate flakes to a TEM grid by iterative mechanical exfoliation.

By increasing the annealing temperature under constant electron irradiation (Figs. 1 (d-f)), the structural evolution from layered 2H-$MoTe_2$ to one-dimensional (1D) Mo_6Te_6 chains [5] can be observed and analysed. An experimentally acquired freestanding nanowire formed within a single-layer region at a temperature of about 600°C is shown in (f). Pure electron irradiation showed in contrast to heating, nanowires are formed more slowly and at the edges of holes within the single-layer, thus the electron beam enables the precise formation of Mo_6Te_6. Figs. 2 (a-c) shows experimental images of a single-layer $MoTe_2$ bombarded by electrons forming holes and nanowires. The supreme electric and thermal conduction [6], as well as the strong intralayer covalent bonding (mechanical strength) [7] makes graphene an excellent candidate for protecting 2D materials in TEM. Fig. 2 (d) shows a schematic depiction of the solid-to-solid transformation in planar 1H-$MoTe_2$ (encapsulated between Graphene) which transforms to 1D Mo_6Te_6 nanowires under electron irradiation. A hole in one of the graphene layers, driven by the interaction with the electron beam, enables Te atoms to escape the graphene-encapsulation and form nanowires.

Our results demonstrate the controlled step by step transformation of freestanding single- and few-layers 2H-$MoTe_2$ to 1D Mo_6Te_6 nanowires and thus provide a comprehensive picture of the response of $MoTe_2$ crystals to heat and to electron irradiation. Furthermore, we compare the effect of electron irradiation and annealing on the formation of nanowires.

Fig. 1. (a-c) llustrates the sample preparation of 2H-$MoTe_2$ onto a MEMS-chip. (d-f) show the formation of freestanding Mo_6Te_6 at high temperatures.

Fig. 2. (a-c) Single-layer $MoTe_2$ under constant electron irradiation at 80kV. (d) Illustrates the formation of one-dimensional Mo_6Te_6 nanowires encapsulated between graphene under electron bombardment.

[1] J. Köster, et al., *The Journal of Physical Chemistry C*, *125*(24), 13601-13609, 2021.

[2] M. Linck, et al., Phys. Rev. Lett., 117, 076101, 2016.

[3] P. Blake, et al., *Applied physics letters* 91.6: 063124, 2007.

[4] M. Ibrahim, et al., *Sensors* 20.6: 1572, 2020.

[5] H. Kim, et al., *Small* 16.47: 2002849, 2020

[6] A. A. Balandin, *Nature materials*, *10*(8), 569-581, 2011.

[7] C. Lee, et al., *science*, *321*(5887), 385-388, 2008.

Fig. 1

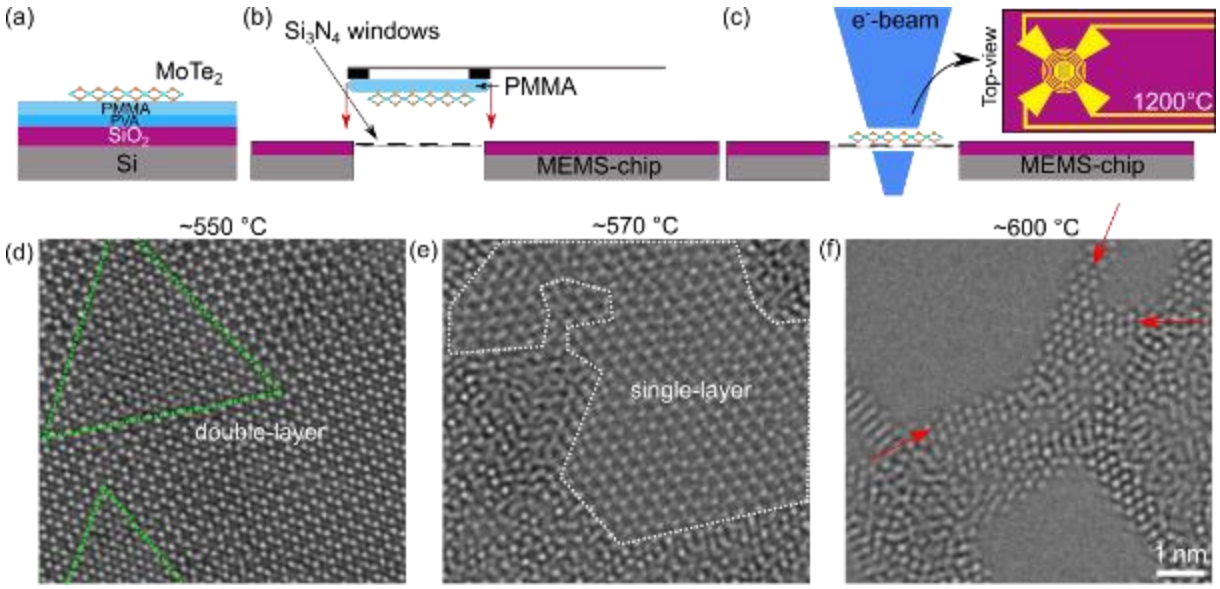
(a)
MoTe2
PMMA
PVA
SiO2
Si
(b)
Si3N4 windows
PMMA
MEMS-chip
(c)
e-beam
Top-view
1200°C
MEMS-chip
~550 °C
~570 °C
~600 °C
(d)
double-layer
(e)
single-layer
(f)
1 nm

Fig. 2

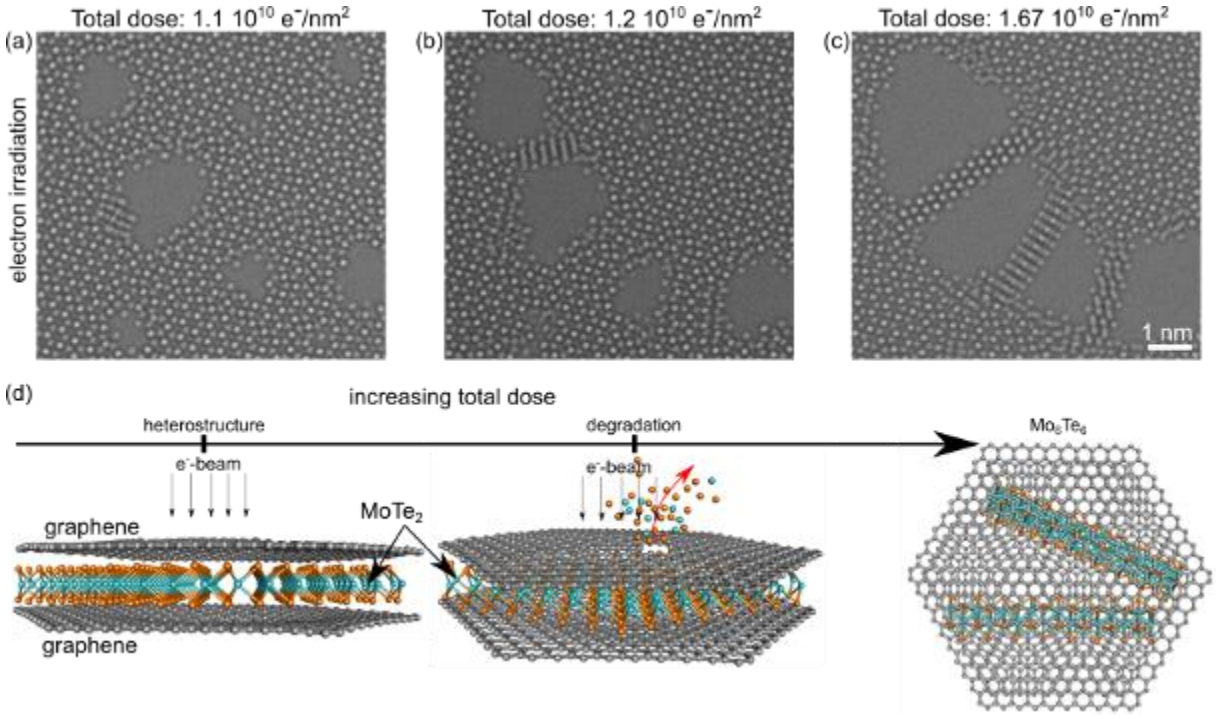
Total dose: 1.1 10^10 e-/nm2
Total dose: 1.2 10^10 e-/nm2
Total dose: 1.67 10^10 e-/nm2
(a)
(b)
(c)
electron irradiation
1 nm
(d)
increasing total dose
heterostructure
degradation
e-beam
e-beam
graphene
MoTe2
graphene
Mo6Te6

MS3.P009

Characterisation of doped graphene with focal-series reconstruction

G. Algara-Siller[1], J. Köster[2], G. Kornilov[1], M. Kühbach[1], U. Kaiser[2], C. T. Koch[1]

[1]Humboldt Universität zu Berlin, Institut für Physik, AG Strukturforschung/Elektronenmikroskopie, Berlin, Germany
[2]Ulm University, Materialwissenschaftliche Elektronenmikroskopie, Ulm, Germany

Introduction

Phase recovery techniques such as focal series reconstruction have been shown to allow characterization of materials in terms of electrostatic potential, electric and magnetic field, as well as charge density down to the atomic level. It has the advantage that, without additional physical modification to a standard microscope the exit wave"s amplitude and phase can be recovered with high spatial resolution and with relatively low noise [1,2,3]. Being very flexible regarding beam setting protocols, this technique is therefore well suited for the characterization of complex systems or materials where, for example, the contrast of different atoms in the structure is indiscernible and as such a HRTEM image is not directly interpretable or when radiation damage of a material is a limitation [4].

Objectives

The main goal of this experiment is to characterize N, O and Si doped graphene using focal series reconstruction. It is known that each of these dopant atoms occupies specific positions in the graphene structure, e. g. substitutional nitrogen, or oxygen forming an epoxy group bridging between two carbon atoms [5]. Accordingly, each dopant atom in each configuration will affect the structure and the properties of graphene differently and in a specific manner.

Materials & Methods

The fabrication of the graphene samples for TEM follows the general CVD graphene transferring method to grids [6]. The doping of graphene with nitrogen and oxygen was made by plasma generation. While silicon doping was just made with the intrinsic Si contamination on the sample, which in this case was exacerbated by removing hydrocarbon contamination on graphene [6] and the subsequently plasma generation or the electron beam irradiation. The samples were characterised in the SALVE TEM microscope [7] operated at 60 kV. The series of defocused images were taken with linear focus increments and the reconstruction was performed using the full-resolution wave-reconstruction algorithm [1]. Structure calculations and image simulations were carried out using the abTEM package [8].

Results & Conclusions

With the phase-reconstructed images it is possible to resolve the atomic position, distinguish if the doping atoms are substitutional or superficial, and ascertain the chemical composition of the dopants by phase analysis with complementary theoretical calculations and image simulations. In our experiments all three types of dopants in their most common configurations [5, 9, 10] could be characterised within the same field of view (e. g. approx. 40 nm x 40 nm). This was only possible by sequentially treating and doping the graphene. The latter experiment also highlights the robustness of graphene to external manipulation and the possible extent of graphene functionalization.

[1] C. T. Koch. Micron 63 (2014) 69

[2] S.J. Haigh, et al. Ultramicroscopy 133 (2013) 26

[3] M. Huang et al., Ultramicroscopy 231 (2021) 113264

[4] I. Biran et al. Adv. Mat. 34 (2022) 2202088

[5] X. Qi, et al. Appl. Surf. Sci. 259 (2012) 195

[6] G. Algara-Siller et al. Appl. Phys. Lett. 104 (2014) 153115

[7] https://www.salve-project.de/tools/salve3/

[8] J. Madsen et al. Open Res. Europe 1:24 (2021)

[9] W. Zhou et al. Phys. Rev. Lett. 109 (2012) 206803

[10] H. Terrones et al. Rep. Prog. Phys. 75 (2012) 062501

* Project **PReGrAM** funded by the **DFG with Project number: 451037016**

MS3.P010

Dynamics of single atoms and molecules encapsulated in carbon nanotubes

J. Biskupek[1], I. Cardillo-Zallo[2], S. T. Skowron[2], C. T. Stopiello[2], G. A. Rance[2], Q. Ramasse[3,4], E. Besley[2], A. N. Khlobystov[2], U. Kaiser[1]

[1]University of Ulm, Central Facility of Electron Microscopy, Ulm, Germany
[2]University of Nottingham, School of Chemistry, Nottingham, United Kingdom
[3]SuperSTEM Laboratory, Daresbury, United Kingdom
[4]University of Leeds, School of Chemical and Process Engineering and School of Physics, Leeds, United Kingdom

Introduction and Objectives

Molecular motion and bond dissociation are two of the most fundamental phenomena underpinning properties of molecular materials. We have entrapped single atoms such as atoms (Kr) or basic molecules (HF and H2) within the fullerene C60 cage, encapsulated within a single-walled carbon nanotube. The use of the electron beam simultaneously as a stimulus of chemical reactions in molecules and as a sub-Å resolution imaging probe allows investigations of the molecular dynamics and reactivity in real time and at the atomic scale, which are probed directly by chromatic and spherical aberration-corrected high-resolution transmission electron microscopy (CC/CS-corrected HRTEM) imaging.

Methods

Working at reduced voltages, however, decreases the obtainable resolution to about 0.2 nm at 80 kV when using standard 3rd order aberration correctors such as the hexapole-type correctors [1]. The correction of 5th order geometric aberration correction together with chromatic aberration correction is necessary to archive atomic resolution at voltages at voltages even at 20 kV. The dedicated CS/CC SALVE (sub-Ångström low voltage electron microscopy) TEM [2] operates between 20 to 80 kV and still delivers sub-Å resolution at 40 kV. EDX and monochromated EELS spectroscopy used to verify elemental composition of the tube fillings and to determine bonding information. Molecular dynamic (MD) and density functional theory (DFT) calculations are used to describe and understand the reaction processes.

Results

We present the study of single atoms and simple molecules HF and H2O embedded into C60 clusters using atomic resolved HRTEM and STEM accompanied by local electron energy loss spectroscopy (EELS) and X-Ray spectroscopy (EDX). In contrary to plain C60 clusters the embedded atoms and molecules change the behavior of dimerization and general damage behavior of the clusters. The neutral Kr atoms are trying to keep a van-der-Waals distance of 0.4 nm and this effects the dimerization behavior. For the case of H2O and HF we demonstrate the rotation of the HF@C60 resp. H2O@C60 clusters under the influence of the electron beam (Fig.1) [3]. Depending on the electron voltage and the atom species the H2O and HF molecules dissociates at different rates.

Figure captions

Figure 1. (a) Experimental time series (2 s time interval) of 30 keV Cc/Cs-corrected HRTEM images of (HF@C60)@SWNT, showing blinking of the F-atoms. The green arrows indicate examples when the F-atoms are clearly visible, these appear to be visible and invisible in the same molecules over time (see Supporting Video 1). (b) Line profile across the centre of a fullerene molecule (as shown in green and white boxes indicated in micrographs (a)) showing variation of image contrast when F-atom is visible (green plot) or invisible (black plot) within the same molecule. (c) Model and corresponding HRTEM image simulations for four different orientations of HF@C60 in SWNT (four principal projections along elements of symmetry of the C60 cage *C2*, *S6*, *C1* and *C5*). Only some orientations are able to produce a "dot" contrast at the centre of the fullerene cage due to an overlap of F-atom with two C-atoms of C60, indicated with green arrows.

References

[1] M. Haider et al. *Ultramicroscopy*, **75 (**1998) 53

[2] M. Linck et al. *Phys. Rev. Let.* **117** (2016) 076101

[3] Biskupek et al. ACS Nano 14 (2020) 11178

Fig. 1

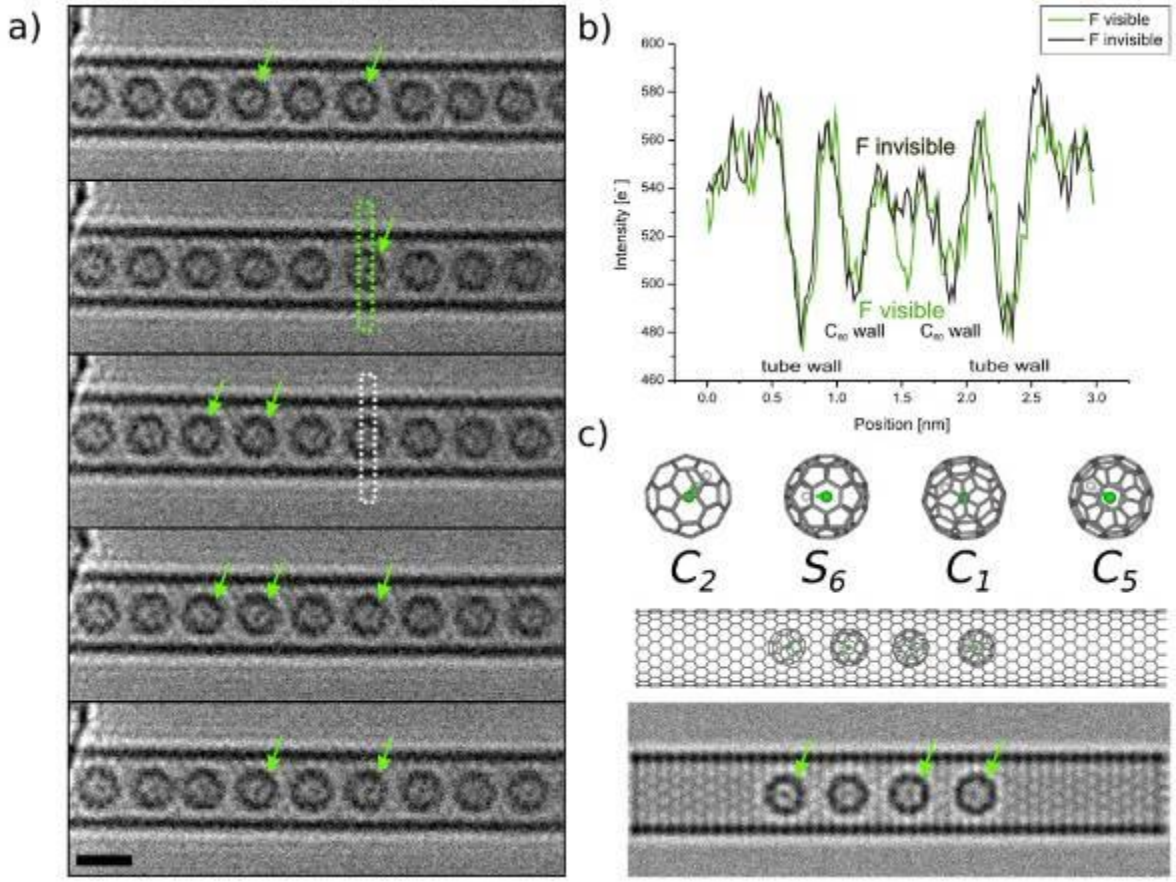

MS3.P011

Novel nanostructures and materials enabled by graphene embedding and sandwiching

K. Mustonen[1], M. Längle[1], A. Trentino[1], G. Zagler[1], C. Hofer[1,2], A. Markevich[1], H. Inani[1], C. Mangler[1], T. J. Pennycook[1,2], V. Skakalova[1,3], T. Susi[1], J. C. Meyer[1,4], J. Kotakoski[1]

[1]University of Vienna, Vienna, Austria
[2]University of Antwerp, EMAT, Antwerp, Belgium
[3]Danubia Nanotech s.r.o., Bratislava, Slovakia
[4]Eberhard Karls University of Tübingen, Tübingen, Germany

Graphene--the one-atom-thick sheet of carbon--is the most famous of 2D materials due to its unique electronic properties and mechanical strength. However, its chemical inertness makes graphene also an excellent nearly electron-transparent support for other materials and nanostructures. In this presentation, I will give an overview of our recent work, partially enabled by a unique interconnected vacuum system containing an aberration-corrected scanning transmission electron microscope (Nion UltraSTEM 100) with a unique objective area that allows sample cleaning via laser, in situ chemical experiments, and direct vacuum transfer to an atomic force microscope (AFSEM by GeTEC Microscopy), an argon glove box, a chamber for alteration and growth of materials equipped with a plasma ion source and evaporators, and long-term vacuum sample storage.

Specifically, I will show that otherwise unstable structures such as a monolayer of fullerenes [1], 2D CuI [2] and small noble gas clusters [3] can be stabilized in the van der Waals gap between two graphene sheets allowing also their atomic-resolution imaging. If time allows, I will further demonstrate that defect-engineering of graphene [4] enables its substitutional heteroatom doping [5] and growth of nanoclusters with a well-defined concentration and a narrow size distribution, as well as the direct correlation of its atomic structure and mechanical properties.

References

[1] Mirzayev et al., Sci. Adv. 3, e1700176 (2017)
[2] Mustonen et al., Adv. Mater., 202106922 (2022)
[3] Längle et al., Microsc. Microanal. 26 S2, 1086-1089 (2020)
[4] Trentino et al., Nano Lett. 21, 5179-5185 (2021)
[5] Inani et al., J. Phys. Chem. C 123, 13136-13140 (2019); Zagler et al., 2D Mater. 9, 035009 (2022); Trentino et al., 2D Mater. 9, 025011 (2022)

MS3.P012

Thickness dependent critical dose of an extremely beam-sensitive two-dimensional polymer

D. Mücke[1], U. Kaiser[1], H. Qi[1,2]

[1]Ulm University, Central Facility for electron microscopy, electron microscopy group of material science, Ulm, Germany
[2]TU Dresden, Center for Advancing Electronics Dresden (cfaed) & Faculty of Chemistry and Food Chemistry, Dresden, Germany

AC-HRTEM imaging is capable of atomically precise observation of two-dimensional materials. It has also proven itself to be a very powerful tool for probing the structures of 2D polymers, covalent and metal organic frameworks[1]. However, for these organic materials the achievable resolution is often limited by the low number of electrons the material under study can accept before it is destroyed. In extreme cases the total dose for amorphization can be as low as a single electron per square Ångström. Thus, increasing this critical dose of these sensitive materials is of highest importance. This can be achieved by various techniques developed in the past. For layer-stacked materials especially, the thickness dependency of the critical dose is a key feature, due to the easily controllable thickness. However, the effects an increase of the thickness has on the electron resilience is not completely understood[2,3]. The current assumption is, that additional layers build a cage around the inner parts, holding in produced radicals[2]. Through this recombination is made possible and the material can self-heal. Aimed at gathering a better understanding of this effect, in our study the thickness dependency of the critical dose was examined in more detail. To achieve this, the critical dose of a triazine-based 2D polymer[4] was measured for a wide thickness range. The polymer samples, obtained by mechanical exfoliation, ranged from 15 nm to 85 nm thickness. The thickness of the polymer was obtained by combining light microscopy and atomic force microscopy. In order to find the critical dose for the polymer, sequences of electron diffraction patterns with a dose of only 0.5 electrons per Å^2 were obtained and the fading of diffraction spots was monitored (Fig 1). The measurements revealed that the critical dose for amorphization of this polymer is only 1-2 e^-/Å^2 (Fig. 2), surprisingly independent of sample thickness and HRTEM imaging is made extremely challenging if not impossible. The lack of increase in critical dose with growing thickness is attributed to the porous structure of the polymer, leading to escape paths for the produced radicals. With that the caging effect is circumvented. This assumption is further strengthened by the application of graphene layers on top and bottom, preventing the escape of atoms from the polymer layers. Through that the critical dose is increased, independent of specimen thickness.

References

1. Haoyuan, Q. *et al. Sci. Adv.* **6**, eabb5976 (2020).
2. Egerton, R. F. *Ultramicroscopy* **127**, 100–108 (2013).
3. Fryer, J. R. *Ultramicroscopy* **14**, 227–236 (1984).
4. Hu, F. *et al. J. Am. Chem. Soc.* **143**, 5636–5642 (2021).

Acknowledgement

We acknowledge the funding from Deutsche Forschungsgemeinschaft (DFG) – 492191310; 426572620; 417590517 (SFB-1415), and European Union GrapheneCore3 (881603). We thank Yingjie Zhao from Qingdao University for providing the polymer.

Fig 1. a) Model of the trianzine-based polymer. b) Selected area electron diffraction pattern of the polymer. c) Series of diffraction patterns. e) With the measured intensity in every image d), the relation between intensity and accumulated dose can be obtained. The critical dose is reached, if the intensity falls below 1/e of its starting value.

Fig. 2. Diffraction patterns obtained on a) a (15.8 ± 0.9) and b) a (85 ± 4) nm thick area. c) Thickness dependent first order peak intensity of the first image of the dose series. d) Thickness dependent critical dose of the 2DP.

Fig. 1

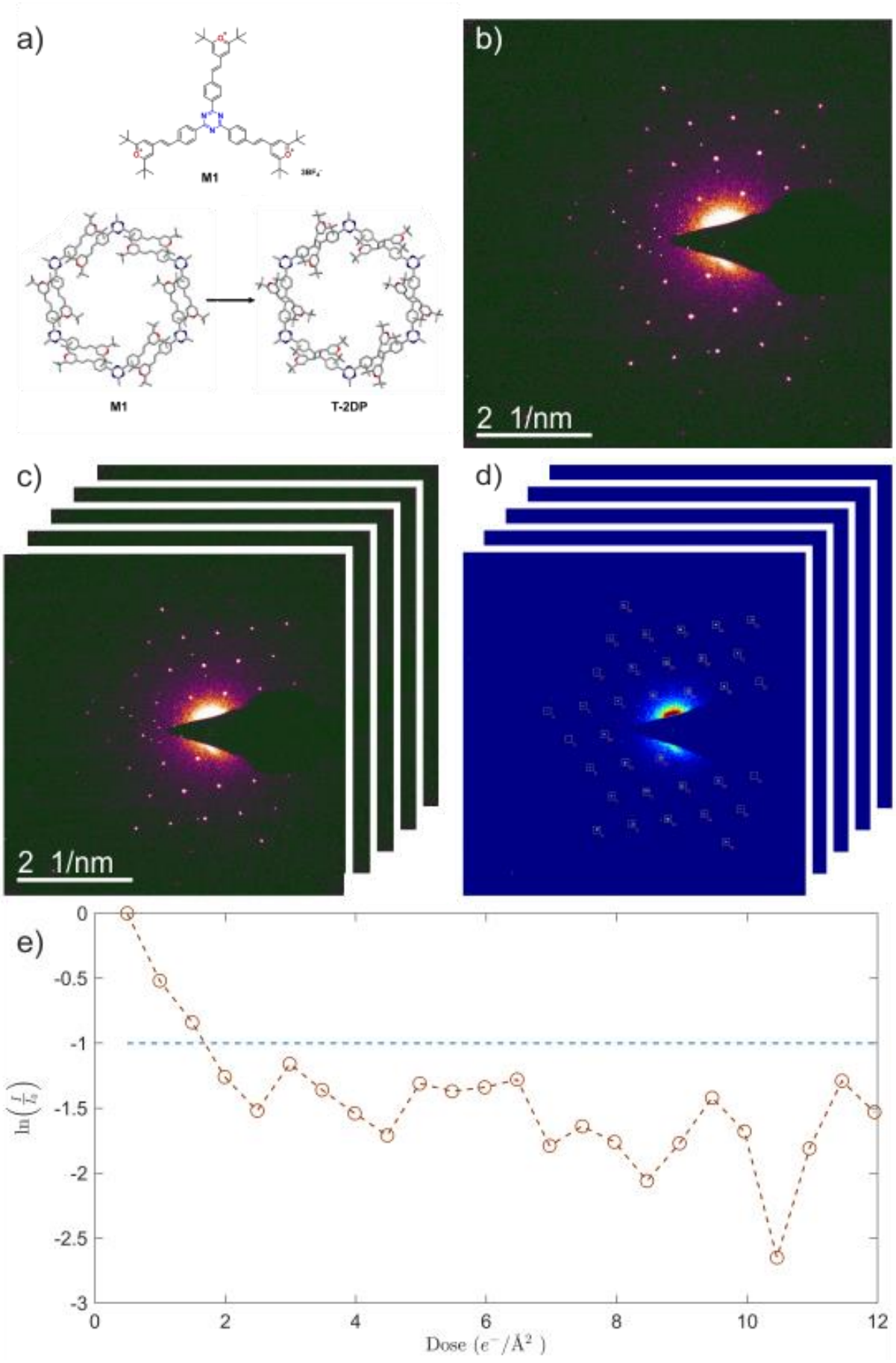

Fig. 2

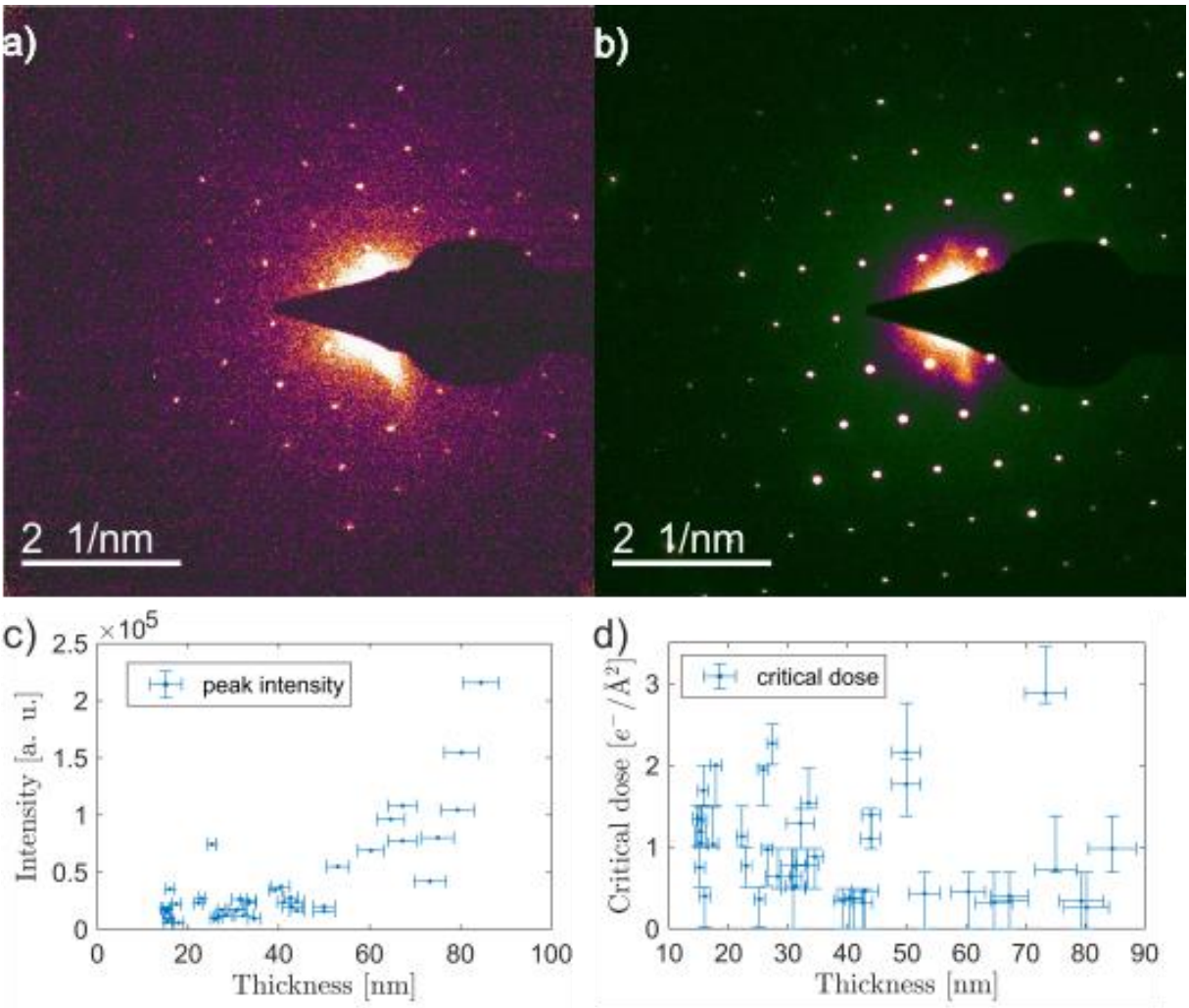
a)
2 1/nm
b)
2 1/nm
c)
×10^5
peak intensity
Intensity [a. u.]
Thickness [nm]
d)
critical dose
Critical dose [e⁻/Å²]
Thickness [nm]

MS3.P013

Design-optimized conductive 2D conjugated metal-organic frameworks allowing sub-Ångstrom resolution HRTEM imaging

B. Liang[1], D. Mücke[1], C. Leist[1], I. Cooley[2], E. Besley[2], U. Kaiser[1], H. Qi[3,1]

[1]Universität Ulm, Central Facility for Electron Microscopy, Electron Microscopy Group of Materials Science, Ulm, Germany
[2]University of Nottingham, School of Chemistry, Nottingham, United Kingdom
[3]Technische Universität Dresden, Faculty of Chemistry and Food Chemistry & Center for Advancing Electronics Dresden (cfaed), Dresden, Germany

Recent years have witnessed the rise of two-dimensional conjugated metal-organic frameworks (2D c-MOFs). 2D c-MOFs with strong in-plane π-d conjugation are particularly interesting because of their intrinsic conductivity, anisotropic charge transport, and potential (opto-) electronic applications[1]. Recently, interfacial synthesis has emerged as a new production method for highly crystalline 2D c-MOFs[1–3]. However, the AC-HRTEM structural determination of 2D c-MOFs, particularly down to the atomic scale, remains a formidable task. The electron radiation damage severely limits the achievable resolution [4,5]. Enhancing the intrinsic electron resilience of MOFs is vital to circumventing this physical limitation and improving achievable resolution. Previous researches provide insights into the empirical rules for electron radiation resilience of organic materials. For example, aromatic compounds are more electron resilient than aliphatic due to π electron delocalization and conjugation[6,7], suggesting higher stability of conductive 2D c-MOFs than conventional insulating ones. In addition, exchanging protium for chlorine on coronene molecules has increased the crosslinking dose by two orders of magnitude due to the reduced displacement cross-section of chlorine [8,9], indicating a potential negative correlation between hydrogen content and electron resilience in MOFs. Nevertheless, the effects of organometallic bonds on MOF stability remain unexplored.

In this work, we investigate the electron resilience of 2D c-MOFs with systematically altered structural attributes, including hydrogen content, framework density, and organometallic bonding, the atomic structures see Fig. 1. The critical fluence, which represents the electron resilience, is quantitatively determined at 300 kV condition for each material. The experimental results are explicated by ab initio quantum calculation. The highly conductive Cu_3(BHT) demonstrates exceptional stability, allowing information transfer to the sub-Ångstrom regime in the characterization by Cs/Cc-corrected HRTEM at 80 kV (Fig. 2), the carbon atoms in the benzene ring structure can be unambiguously distinguished.

Fig. 1. (A) Atomic models of 2D c-MOFs. (B) Intensity profile of the first-order reflections in 2D c-MOFs as a function of accumulated electron dose. The critical dose is reached when the reflection intensity drops to e^{-1} of the original value.

Fig. 2. C_S+ C_C-corrected atomic-resolved imaging of Cu_3(BHT) at 80 kV. (A) Experimental and simulated AC-HRTEM images of Cu_3(BHT). Acquisition dose: 3.2×10^3 e^- $Å^{-2}$. (B) Enlarged image of A. (C) Intensity profile from the line-scan region in (B), the peak represents the center of the carbon atom, and the distance between the two peaks is 1.4 Å.

Acknowledgment

2D c-MOF samples were synthesized by the group of Prof. Xinliang Feng and Dr. Renhao Dong.

Reference

1. Wang, M., Dong, R. & Feng, X. *Chem. Soc. Rev.* **50**, 2764–2793 (2021).
2. Yu, M., Dong, R. & Feng, X. *J. Am. Chem. Soc.* **142**, 12903–12915 (2020).
3. Liu, J., Chen, Y., Feng, X. & Dong, R. *Small Struct.* 2100210 (2022).
4. Skowron, S. T. *et al. Acc. Chem. Res. 50, 1797−1807 (2017).*
5. Russo, C. J. & Egerton, R. F. *MRS Bull.* **44**, 935–941 (2019).
6. Alexander, P. & Charlesby, A. *Nature* **173**, 578–579 (1954).
7. Fryer, J. R.*Ultramicroscopy* **23**, 321–327 (1987).
8. Stenn, K. & Bahr, G. F. *J. Ultrastructure Res.* **31**, 526–550 (1970).
9. Chamberlain, T. W. *et al. Small* **11**, 622–629 (2015).

Fig. 1

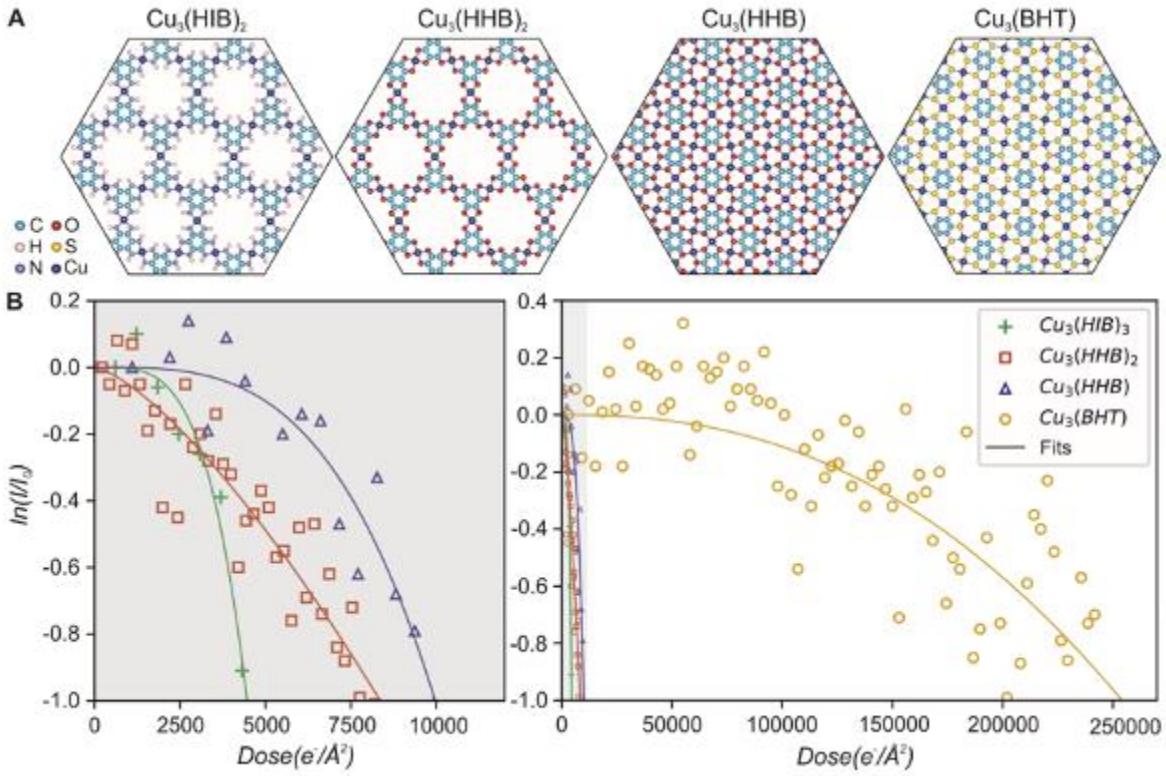
A
Cu3(HIB)2
Cu3(HHB)2
Cu3(HHB)
Cu3(BHT)
C O
H S
N Cu
B
ln(I/I0)
Dose(e/Å2)
Cu3(HIB)3
Cu3(HHB)2
Cu3(HHB)
Cu3(BHT)
Fits

Fig. 2

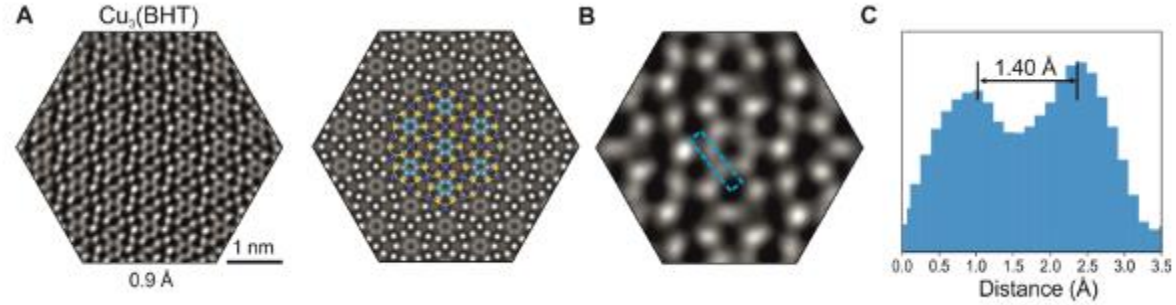
A
Cu3(BHT)
1 nm
0.9 Å
B
C
1.40 Å
Distance (Å)

MS3.P014

Aligned stacking of nanopatterned 2D materials for high-resolution 3D device fabrication

J. Haas[1,2], F. Ulrich[1,2], C. Hofer[1,2], X. Wang[3], K. Braun[4], J. C. Meyer[1,2]

[1]University of Tübingen, Institute for Applied Physics, Tübingen, Germany
[2]NMI Natural and Medical Sciences Institute at the University of Tübingen, Reutlingen, Germany
[3]Hunan University, School of Physics and Electronics, Hunan, Germany
[4]University of Tübingen, Institute of Physical and Theoretical Chemistry, Tübingen, Germany

Additive manufacturing, often referred to as 3D printing, creates structures typially by depositing material layer-by-layer. However, feature sizes in 3D printing are still not sufficient for the creation of devices on the nanometer-scale. A promising method for building smaller structures is the layer-by-layer assembly of 2D materials. The creation of these so-called van-der-Waals heterostructures can also be regarded as a type of additive manufacturing. While the feature size of each layer in the out-of plane direction is by nature in the order of a few atoms, the common techniques for building van-der-Waals heterostructures can not manipulate and control the in-plane direction on a similar scale.

In this work, we developed a method for the assembly of van-der-Waals heterostructures to overcome these limitations. Free-standing 2D materials are patterned on the nanometer-scale prior to the assembly. This is done by resist-free methods such as water-assisted electron beam etching and by sputtering with high-energy electrons in a scanning transmission electron microscope.

Stacking is performed under observation in a scanning electron microscope and with the help of nanomanipulators, allowing a precise in-plane alignment (Fig. 1).

The assembled structures are analyzed by means of scanning electron microscopy and transmission electron microscopy. Several samples are fabricated to verify the method and investigate the accuracy of the in-plane alignment. Currently, layers can be aligned with an accuracy of about 10 nm. As an example, a ten-layer stack with a parabolic thickness profile is built that serves as phase plate for electrons, with the effect of focussing a plane electron wave (Fig. 2). In principle, phase plates with arbitrary shapes could be made by this approach.

The presented method surpass the limits of previous techniques for the assembly of van-der-Waals heterostructures. Having the individual layers as free-standing membranes, the 2D materials can be patterned with highest resolution prior to the stacking. Accurate alignment during the assembly is ensured by observation in an electron microscope. Together, the method enables the fabrication of 3D structures with highest spatial resolution.

[1] Haas, Jonas, et al. "Aligned Stacking of Nanopatterned 2D Materials for High-Resolution 3D Device Fabrication." *ACS Nano* 16.2 (2022): 1836-1846.

Fig. 1: (a) Schematic of the stacking process. (1) The free-standing 2D material is patterned, (2-3) brought into contact with a target support, and (4-5) detached from the initial support grid. The process is repeated for subsequent layers (6-10) under SEM observation, thereby enabling a precise lateral alignment. (b) Illustration of the setup used for the process. (c-h) SEM image sequence of placing a single layer. Scale bars are (c) 500 µm, (d,e) 10 µm and (f-h) 5 µm. Adapted from [1].

Fig. 2: (a) Ten-layer stack of 2D materials with increasing hole diameter that can be tailored to form a parabolic electron lens as shown in (b). (c-d) Intensity profile of a plane electron wave focused by a structure as shown in (a). Adapted from [1].

Fig. 1

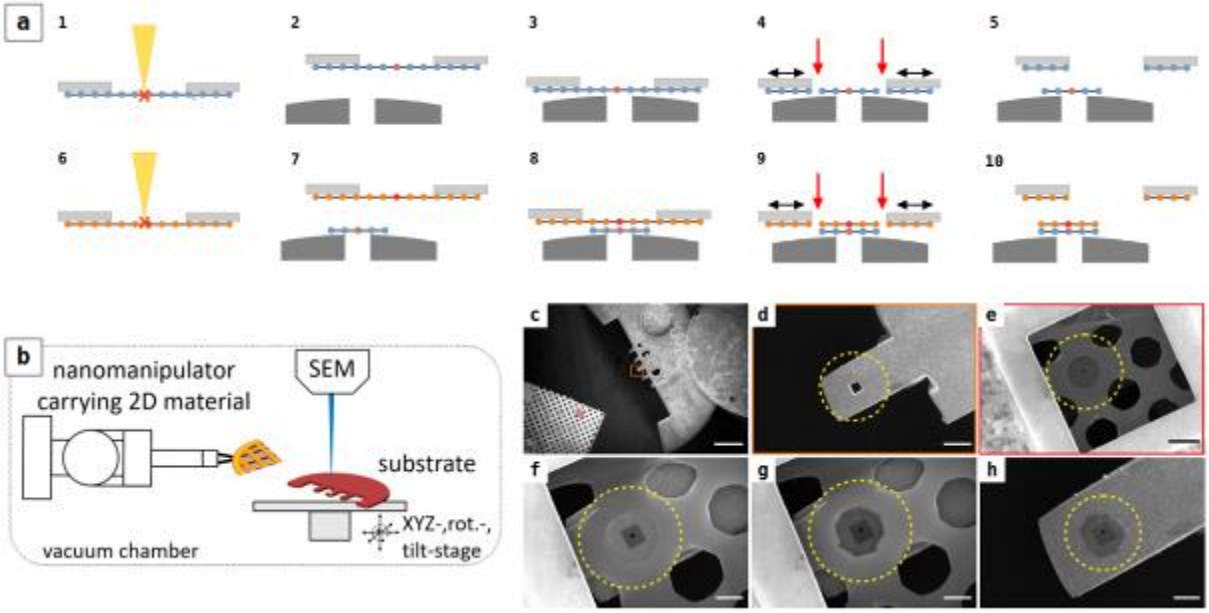
a
1
2
3
4
5
6
7
8
9
10
b
nanomanipulator
carrying 2D material
SEM
substrate
vacuum chamber
XYZ-,rot.-,
tilt-stage
c
d
e
f
g
h

Fig. 2

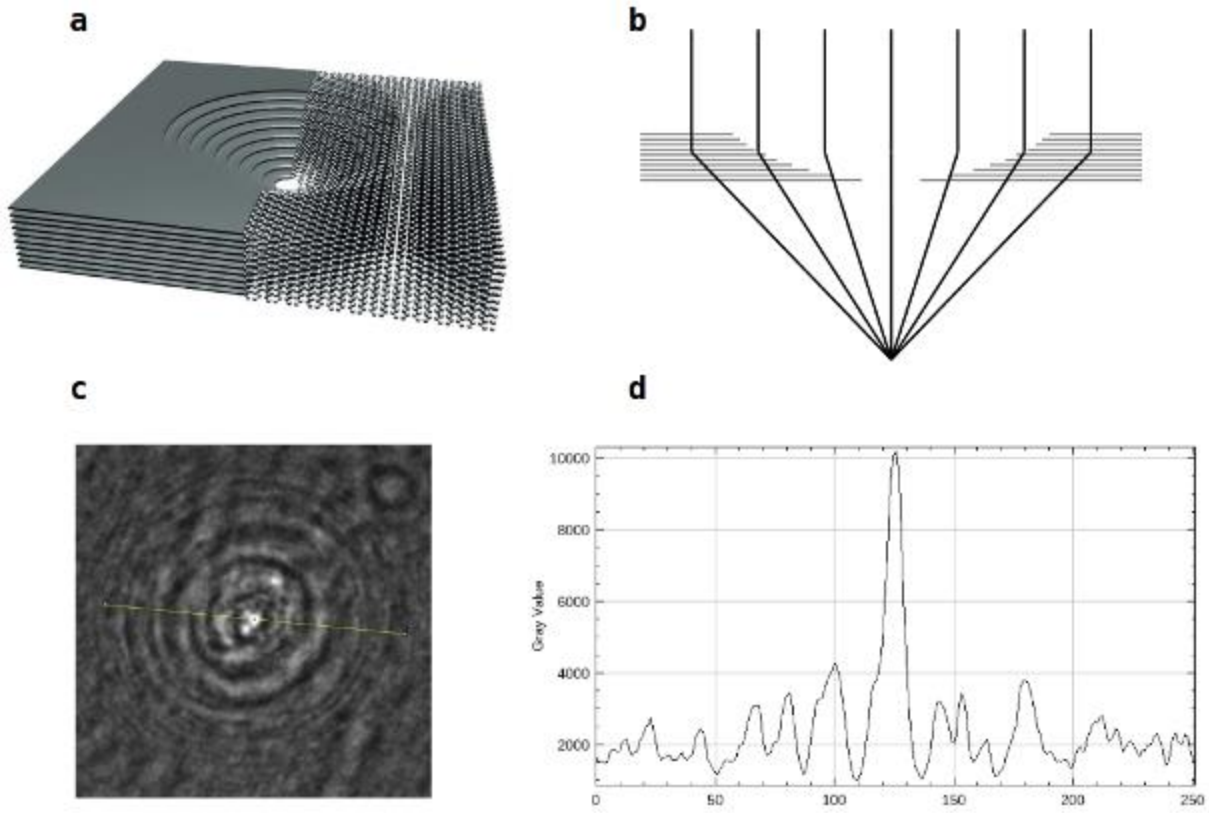
a
b
c
d
Grey Value
10000
8000
6000
4000
2000
0
50
100
150
200
250

MS3.P015

Correlative raman imaging characterizes crystal properties of 2D materials

U. Schmidt[1], J. Englert[1], T. Dieing[1], O. Hollricher[1]

[1]WITec GmbH, Applications, Ulm, Germany

Due to their unique optical and electronic properties, two-dimensional (2D) materials have great potential for application in optoelectronic devices. Diverse crystal properties such as the number of layers and growth defects influence the optical and electronic properties of the 2D materials. Research, development and quality control thus require powerful and non-destructive imaging techniques for monitoring these crystal properties and to evaluate synthesis processes. To comprehensively characterize the 2D material, it is advantageous to combine several imaging techniques. Here, we present correlative Raman imaging as a versatile tool for investigating prominent examples of 2D materials, namely graphene and the transition metal dichalcogenides (TMDs) molybdenum disulfide (MoS_2) and tungsten disulfide (WS_2). In combination with imaging techniques such as second harmonic generation (SHG), photoluminescence (PL), atomic force microscopy (AFM) or scanning electron microscopy (SEM), Raman imaging is able to provide a thorough characterization of the 2D materials. Crystal properties and features such as grain boundaries, surface structure, layer number, defect density, doping and strain fields can thus be identified and visualized.

Fig. 1:

Correlative imaging of a MoS_2 crystal using white light imaging (A), SHG intensity revealing grain boundaries (B), polarization dependent SHG characteristic for crystal orientation and strain (C), Raman spectrum of a monolayer of MoS_2 (D) intensity of the E_{2g} (E) and PL image revealing strain fields.

Fig. 1

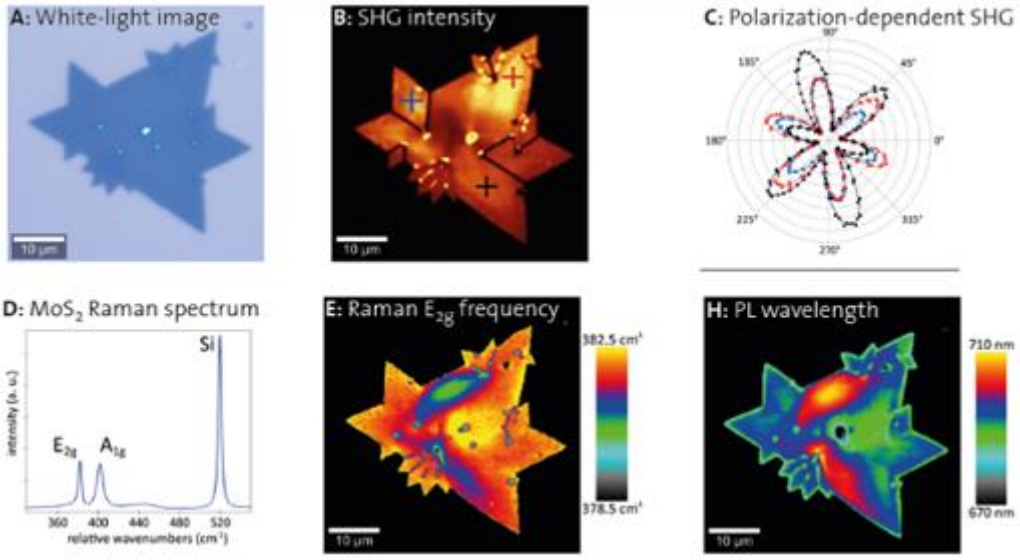

MS3.P016

Control and characterization of a piezo TEM stage for automated atomic-resolution and atomic-precision image mapping

K. Strobel[1,2], J. C. Meyer[1,2]

[1]University of Tübingen, Institute of Applied Physics, Tübingen, Germany
[2]NMI Natural and Medical Sciences Institute at the University of Tübingen, Reutlingen, Germany

The information gained from a native specimen is limited by the introduced dosage. One way to reduce dose, is to distribute it across an area, which is typically larger than the field of view of the detector, when acquiring atomically resolved TEM images. Therefore, in low dose experiments, a region of interest in the specimen can be mapped, by iterative displacements of the specimen, thus always exposing a fresh region of the sample. The stability and resolution of the TEM stage limits the quality of the final image map. This motivated the use of a piezo TEM stage for image mapping. The characterization of the lateral stepsize, the stage and imaging system control, as well as the automated low dose image acquisition was the objective of this work. The mapping system was implemented on an image corrected JEOL JEM-ARM200F microscope, equipped with a Gatan OneView. These systems were controlled via the backend of the Gatan and JEOL user interfaces (DigitalMicrograph, Temcenter), using custom python servers on each control computer. These servers were controlled simultaneously on a third computer, serving as a host. The stage was characterized by using a freestanding 2D material, and visible features served as a reference in the observed area, as illustrated in Figure 1. The reference was periodically displaced for 10,5 nm within the image and the stage start and end positions were recorded from the temcenter UI. The standard deviation from the start and end positions were smaller than 0,5 Å as well as the calculated step size at the lowest speed setting in the temcenter UI. The standard deviation of the start and end positions indicate that the stage is atomically precise, when conducting a unidirectional displacement. The step size was used in the mapping, to displace the specimen to a set of coordinates and to acquire a stack of images at each position, as illustrated in Figure 2. The electron beam was blanked during each displacement, reducing the dosage during mapping. In conclusion, the accuracy and precision of the piezo stage allows a mapping with non overlapping (or minimally overlapping) field of view in each exposure, which are closer packed together than for standard non piezo driven TEM stages. This enables the collection of low dose images from a smaller sample area, which might be especially helpful for 2D specimen with smaller patches of non-contaminated area or specimen with small regions of interest. Also, it enables the acquisition of an atomic resolution image from a large area (up to 380x380 nm) by stitching together a large number of exposures with a smaller field of view.

Figure 1: Characterization for the X direction of a piezo super fine stage of an JEOL ARM200F. The intended periodic forth and back displacement is indicated with arrows and the step size is illustrated as dimensioning arrows. The Precision is indicated along the edge of the reference structure (highlighted in red) with two barred lines.

Figure 2: Illustration of an atlas acquisition using the piezo stage of a JEOL JEM-ARM200F TEM. The field of view was 21,5x21,5 nm and the spacing along the stage x and y-axis were 18 nm. Videos for each spot were acquired with a Gatan OneView with 14fps.

Fig. 1

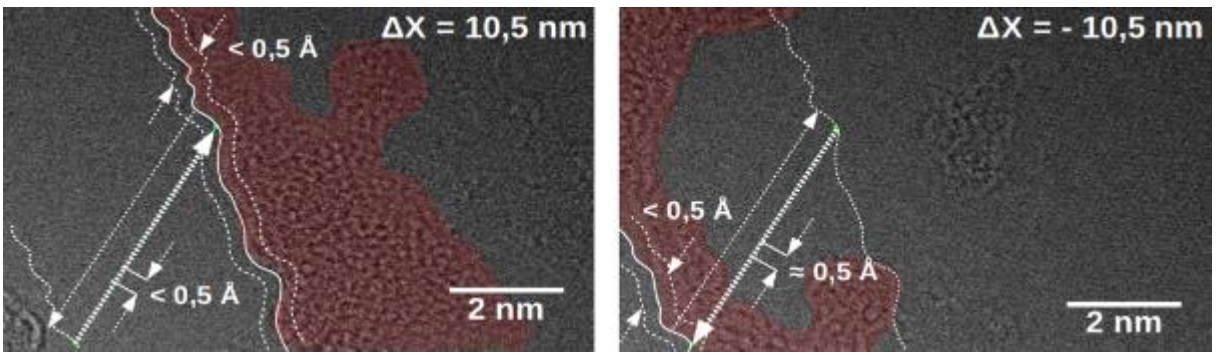

Fig. 2

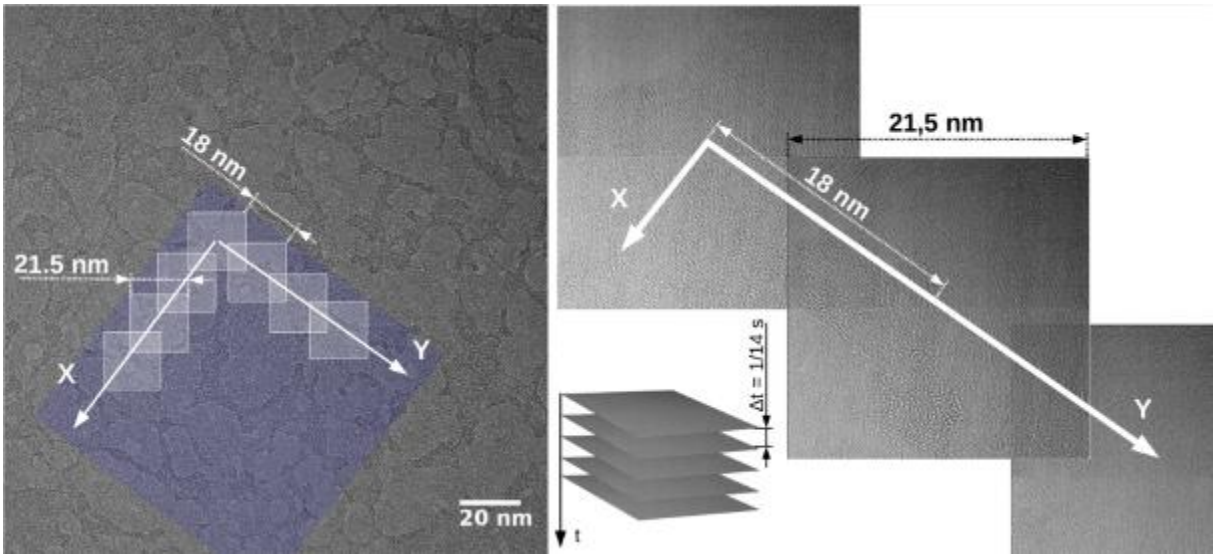

MS3.P017

Revealing the stacking configuration of ideal Moiré structures in CVD grown $MoSe_2$-WSe_2 heterobilayers

B. März[1], I. Bilgin[2], L. Richter[1], B. Diederichs[3], A. Högele[2], K. Müller-Caspary[1]

[1]Ludwig-Maximilians-University Munich, Department of Chemistry, Munich, Germany
[2]Ludwig-Maximilians-University Munich, Department of Physik, Munich, Germany
[3]Helmholtz Zentrum München, Munich, Germany

A $MoSe_2$-WSe_2 heterobilayer (HBL) consists of stacked monolayers (MLs) of each respective material. Because of slightly different lattice parameters a Moiré superstructure is formed by periodic self-reconstruction, with regions showing ideal Moiré patterns and according transitional regions in between [1]. When using chemical vapour deposition (CVD) to fabricate a HBL the actual stacking is hardly under control. In theory several R- and H-type ideal stacking configurations are possible. Depending on the Moiré interference pattern varying electrical and optical properties arise, as has been indicated by spectroscopic analysis [2]. In order to reliably link these properties to the respective stacking, knowledge is required about which Moiré structures are present. Due to the periodicity of the Moiré superstructure with small Moiré cells, and the limited spatial resolution of the applied spectroscopic methods, it could not yet be fully determined how the different properties relate to each stacking.

A probe-corrected STEM operated at 120kV was used for high-angle annular dark field (HAADF) imaging and recording of four-dimensional (4D) scanning transmission electron microscopy (STEM) data with a Merlin Medipix3 camera. The $MoSe_2$-WSe_2 HBL was prepared by CVD and transferred on a Cu Quantifoil TEM grid. Multislice simulations of 4D-STEM data of ideal Moiré patterns were conducted.

In this study the local Moiré stacking in $MoSe_2$-WSe_2 HBLs was identified using HAADF and 4D-STEM, supported by multislice simulations. We use both signals to determine the stacking order, vacancies and additional atoms. By evaluating the gradients of the pixel wise 4D-STEM and HAADF signals with respect to stacking, atom positions and vacancies we evaluate the validity of the results from the respective signals.

The atom structure in the experimental HAADF-STEM image shown in Fig.1(a) represent three groups of differently stacked atom columns because of their different Z-contrast. Simulated ADF-STEM signals of ideal Moiré patterns are shown in Fig.1(b-e). Ideal Moirés that, in contrast to the experiment, do not show an additional centred atom in the hexagonal ring were excluded. By comparing the relative intensities in the experimental HAADF image with the relative intensities expected from the respective atom columns and which constituting atom species are known, a R_X^M stacking depicted in Fig.1(e) was in best agreement with the experiment. The bright columns represent 1Mo+2Se, the darker ones W or 2Se atoms. The line profiles in Fig.1(f) highlight the differences in the ADF signal of each ideal Moiré. The according atomic structures are shown in Fig.2.

[1] S. Zhao *et al.* Excitons in mesoscopically reconstructed Moiré heterostructures, *pre-print*, (2022)
[2] M. Förg *et al.* Moiré excitons in $MoSe_2$-WSe_2 heterobilayers and heterotrilayers. *Nat Commun* **12,** 1656 (2021)
[3] We acknowledge financial support from the DFG under grant number EXC 2089/1-390776260 (e-conversion) and the EQAP project Munich.

Fig.1 Comparison of (a) an experimental HAADF-STEM image (noise filtered) with (b,c,d,e) simulated images of the ideal Moiré structures H_M^M, H_X^X, R_M^X and R_X^M of a $MoSe_2$-WSe_2 HBL. Profiles along red arrows are shown in (f); field of view in b,c,d,e is 1.5nm

Fig.2 Atomic structures of ideal Moiré configurations of the HBL; super- and subscript indices in the notation represent the top and bottom layer atoms stacked on top of another; R and H indicate the stacking type

Fig. 1

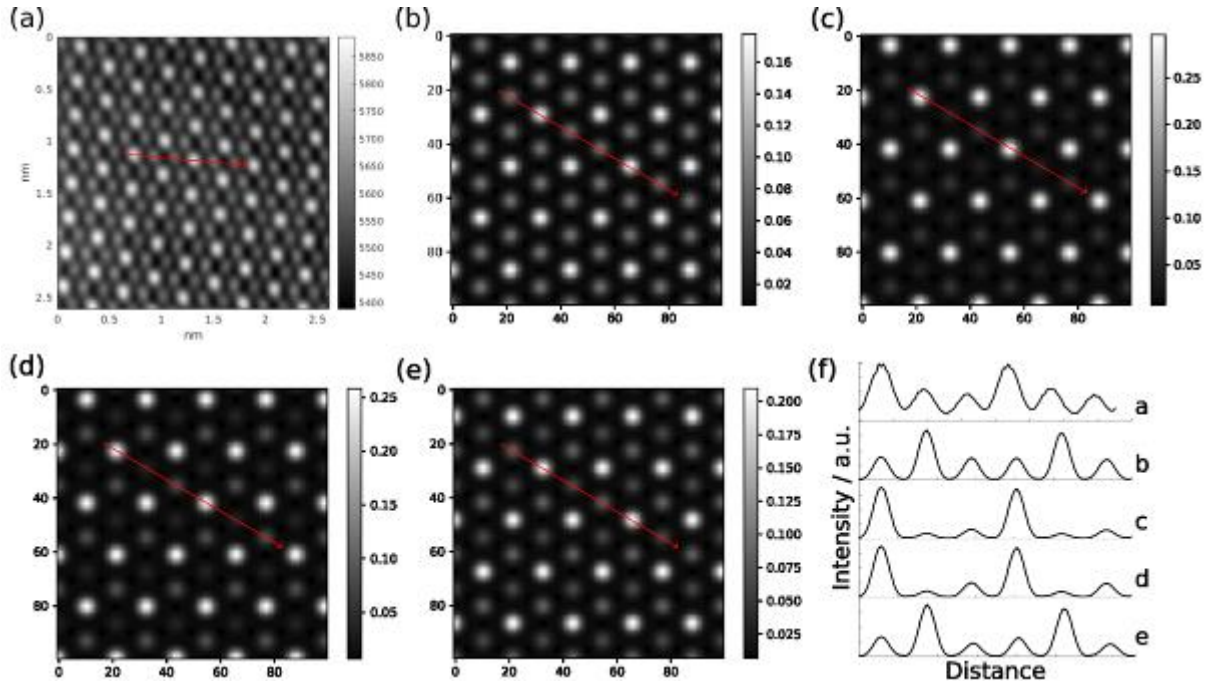
(a)
(b)
(c)
(d)
(e)
(f)
nm
Intensity / a.u.
Distance
a
b
c
d
e

Fig. 2

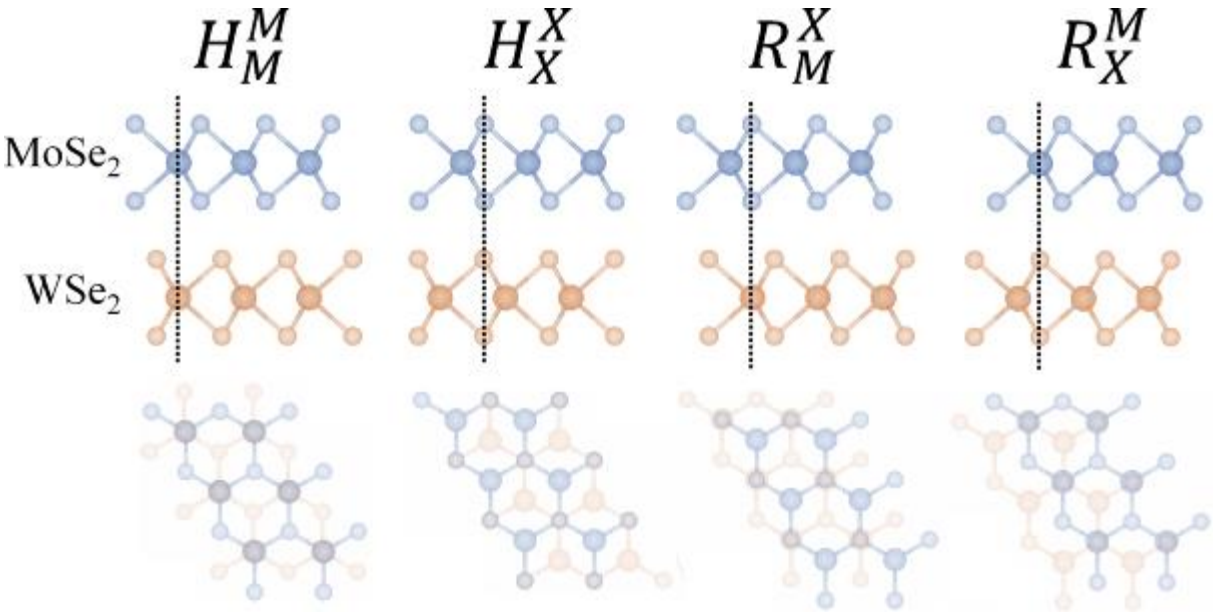
H_M^M
H_X^X
R_M^X
R_X^M
$MoSe_2$
WSe_2

MS3.P019

Structural transformations in transition metal phosphorus trichalcogenides studied by analytical transmission electron microscopy

A. Storm[1], J. Köster[1], M. Asl-Gohrbani[2], S. Kretschmer[2], T. Gorelik[1], A. Krasheninnikov[2,3], U. Kaiser[1]

[1]Ulm University, Ulm, Germany
[2]Helmholt-Zentrum Dresden-Rossendorf, Institute of Ion Beam Physics and Materials Research, Dresden, Germany
[3]Aalto University, Department of Applied Physics, Aalto, Finland

Few-layer transition metal phosphorous trichalcogenides (TMPTs) is a promising class of materials due to their inherent interesting properties [1], making these materials ideal candidates to study 2D magnetism [2], as well as promising candidates for future energy storage related applications [3].

In this work, we study structural modifications of few-layer TMPTs caused by electron-irradiation, as well as thermal annealing in transmission electron microscopy (TEM), and experiments are rationalized using ab-initio calculations.

Thin TMPT flakes were prepared with the help of a newly developed polymer-based preparation method [4], which significantly enhances the sample quality. The Cc/Cs-corrected Sub-Ångström Low Voltage Electron Microscope (SALVE) at 80kV was used to study structural modifications caused by the probing electrons. Furthermore, *in-situ* annealing experiments were conducted with a dedicated FEI NanoEx-i/v TEM specimen heating holder. Electronic, and magnetic properties of newly emerging phases were predicted using spin-polarized density functional theory (DFT) as implemented in VASP [5].

Continuous irradiation of 4-layer $NiPS_3$ showed a degradation of individual layers, thus single- and double-layer regions within the layer system emerge. Fig. 1 (a) presents a sulphur vacancy in double-layer $NiPS_3$. By using the McKinley-Feshbach formalism [6] estimated atom displacement cross-sections were calculated predicting the preferential removal of sulphur (see Fig. 1 (b)).

Further, the emergence of different MnS phases (e.g. Fig. 2 (a)) in $MnPS_3$, and MnSe phases in $MnPSe_3$ were observed due to structural modifications caused by the impinging electrons, and the growth of these ultrathin phases could be controlled by the illuminated area, and applied total electron dose. *In-situ* thermal annealing induced structural modifications showed the possibility of engineering various phases depending on the observed TMPT (e.g. $MnPSe_3$, and $NiPS_3$, transforms to MnSe (see Fig. 2 (b)), and NiP, respectively). Further, the phase transition temperatures of freestanding TMPTs in vacuum were determined. Eventually, ab-initio calculations predict distinct properties of the new phases, which strongly depend on the orientation and the thickness of the transformed facets.

In conclusion, displacement cross-sections predict that more S should be removed than P due to elastic interaction in the acceleration voltage range of 50-300kV. Further, our experiments show that structural modifiifations can attributed to the growth of specific phases in $MnPS_3$ and $MnPSe_3$, caused by electron-irradiation or thermal annealing.

Fig. 1. (a) 80kV Cc/Cs-corrected HRTEM image of a double-layer $NiPS_3$. A line-scan shows the position of a missing S atom. (b) Displacement cross-sections of sulphur and phosphorous in XPS_3 (X=Fe, Mn, Ni).

Fig. 2. (a) 80kV Cc/Cs-corrected HRTEM image of a -MnS crystal. A magnified area of the patch with overlaid structure model is shown beside. The structure emerged after irradiation of a $MnPS_3$ flake in TEM. (b) HRTEM image of an -MnSe crystal, which formed after annealing a $MnPSe_3$ in-situ to 600°C.

[1] Xu et al., Microstructures, 2, 2022011, (2022).

[2] Long et al., ACS Nano, 11, 11330-11336, (2017).

[3] Glass et al., J. Electrochem. Soc., 167, 110512, (2020).

[4] Köster et al., Nanotechnology, 32, 075704, (2021).

[5] Kresse et al., Phys. Rev. B, 54, 11169-11186, (1996).

[6] Meyer, et al., Phys. Rev. Lett., 108 (19), 196102, (2012).

Fig. 1

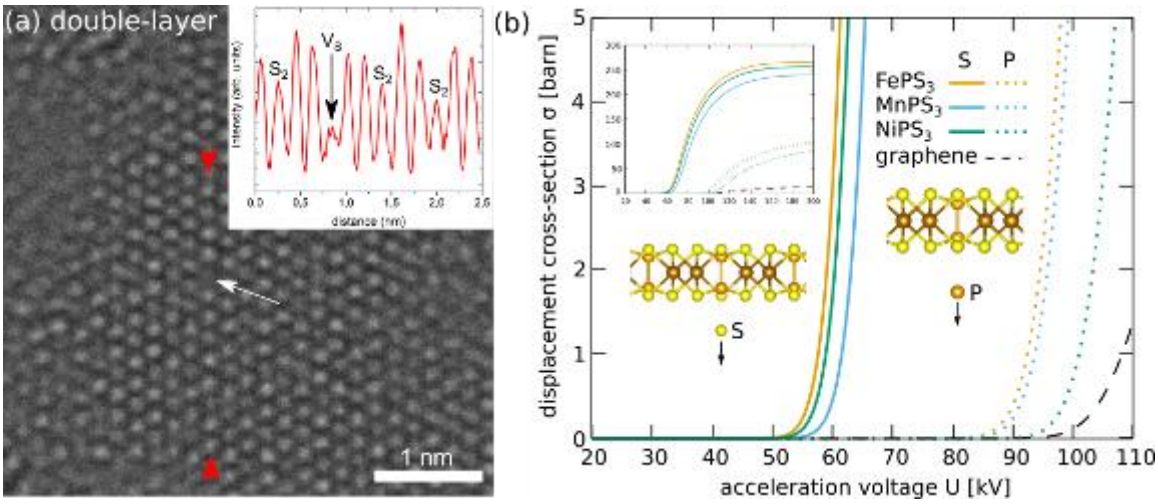
(a) double-layer
V_S
S_2
S_2
S_2
distance (nm)
1 nm
(b)
displacement cross-section σ [barn]
acceleration voltage U [kV]
S P
$FePS_3$
$MnPS_3$
$NiPS_3$
graphene
S
P

Fig. 2

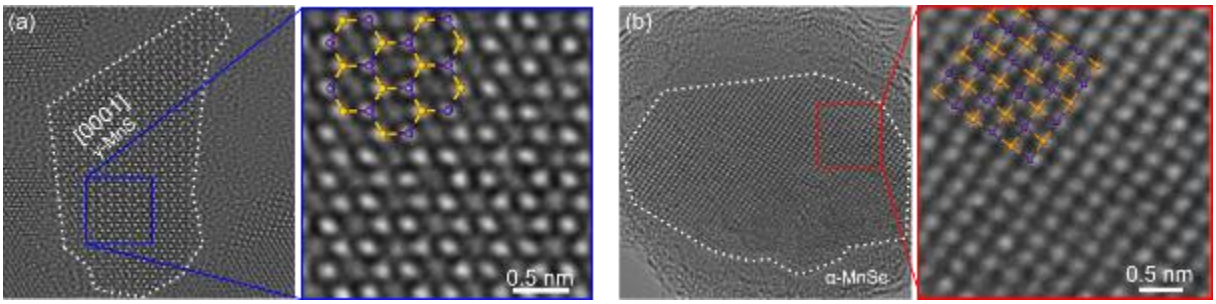
(a)
[001]
γ-MnS
0.5 nm
(b)
α-MnSe
0.5 nm

MS3.P020

Characterization of two-dimensional WSe_2 using differential phase contrast STEM

M. Groll[1], J. Bürger[1], I. Caltzidis[1], M. Sartison[1], K. D. Jöns[1], J. K. Lindner[1]

[1]University of Paderborn, Physics, Paderborn, Germany

Two-dimensional (2D) transition metal dichalcogenides (TMDs), such as MoS_2, $MoSe_2$, WS_2 and WSe_2, exhibit exciting electrical and optical properties due to their low dimensionality and are therefore promising candidates for next generation optoelectronic devices [1]. Comparable to graphene, TMDs consist of molecular layers which are bound to each other only by weak van der Waals interlayer interactions and are covalently bound within each layer. TMDs show varying physical properties depending on the number of stacked layers, such as a direct band gap for a monolayer of WSe_2 compared to an indirect band gap of its bulk form [2,3]. Many of these layer thickness-dependent properties are determined by the electric field and charge density distributions around individual atoms and defects within the crystal structure. However, only a few measurement methods allow characterization of electric fields with such a high spatial resolution. One of these is differential phase contrast (DPC) imaging in STEM, which, in combination with state-of-the-art Cs correction, allows the investigation of electric fields with subatomic resolution even at the sufficiently low acceleration voltage of 80 kV.

It is, thus, the objective of this study to image and quantify atomic electric fields and the field distribution of defects in mono- and multilayer WSe_2 using STEM-DPC imaging.

In order to investigate 2D WSe_2 by STEM-DPC, mechanically exfoliated WSe_2 flakes with different thicknesses are transferred to TEM grids. STEM-DPC imaging is performed using an eight-fold segmented STEM detector at an acceleration voltage of 80 kV. The measurement of electric fields by DPC in general relies on the measurement of the center of mass (CoM) of the bright-field intensity distribution. Due to Coulomb interaction of the incident electron beam with the electrostatic potential inside the specimen, a shift of the CoM in the detection plane can be measured in presence of electric fields. These electric fields can be quantified by the difference of intensity on opposing detector segments and an adequate calibration. Measurements are compared with corresponding multislice image simulations.

We show the atomic structure as well as the corresponding electric field and charge density distribution of 2D WSe_2, which are in good qualitative agreement with multislice image simulations. As 2D materials are prone to various defects which can influence physical properties, we also show the electric field distribution of defects and disclose characteristic changes in the electric field distribution in the vicinity of defects.

In conclusion, DPC measurements on atomically thin WSe_2 offer a great possibility to reveal the electronic structure achieve a deeper understanding of the optoelectronic properties of this material system.

[1] J. An, et al., Perspectives of 2D Materials for Optoelectronic Integration, Adv. Funct. Mater. 32 (2022) 2110119. https://doi.org/10.1002/adfm.202110119

[2] J. Gusakova, et al., Electronic Properties of Bulk and Monolayer TMDs: Theoretical Study Within DFT Framework (GVJ-2e Method), Phys. Status Solidi A. 214 (2017) 1700218. https://doi.org/10.1002/pssa.201700218.

[3] T. Yan, et al., Photoluminescence properties and exciton dynamics in monolayer WSe_2, Appl. Phys. Lett. 105 (2014) 101901. https://doi.org/10.1063/1.4895471.

MS3.P021

Characterization of two-dimensional transition metal dichalcogenides and their heterostructures by (S)TEM techniques

M. Mohn[1], A. Storm[1], J. Köster[1], T. Gorelik[1,2,3], J. Schulz[1], U. Kaiser[1]

[1]Ulm University, Central Facility Materials Science Electron Microscopy, Ulm, Germany
[2]Helmholtz Centre for Infection Research, Braunschweig, Germany
[3]Helmholtz Institute for Pharmaceutical Research Saarland (HIPS), Saarbrücken, Germany

In recent years, two-dimensional transition metal dichalcogenides (2D TMDs) have been intensively studied to explore their electronic and optical properties. While basic research on these materials can be conducted with exfoliated monolayers and manually assembled heterostructures, the focus is more and more placed on the application of materials prepared with scalable bottom-up techniques such as chemical vapor deposition (CVD). However, CVD-grown materials can have very different quality in terms of defect densities, grain sizes, and the number of layers.

In this study, we discuss how transmission electron microscopy techniques help to elucidate the relation between the growth parameters, atomic structure, number of layers, and electronic and optical properties of TMDs and their heterostructures. We investigate mono- and few-layer MoS_2 and $MoTe_2$, as well as lateral $MoSe_2$-WSe_2 heterostructures. The TEM techniques we apply include high-resolution TEM and STEM imaging at low voltages (20–80 kV), electron diffraction, energy-dispersive X-ray spectroscopy (EDX), and electron energy-loss spectroscopy (EELS). The results from all techniques are compared with simulations.

We first address the question of the exact number of layers in few-layer TMDs. We demonstrate that 3D electron diffraction and momentum-resolved EELS allow for unambiguous identification of 1–4 layers of MoS_2 or $MoTe_2$ [1]. Secondly, we show that the density of intrinsic defects in TMD monolayers can be obtained from atomically resolved Cc/Cs-corrected TEM images. The evaluation of the defect density can be performed very efficiently using convolutional neural networks, which can be trained using simulated TEM images and are able to identify atomic positions and chalcogen vacancies [2]. Thirdly and lastly, we evaluate that lateral heterostructures of monolayer TMDs can be best investigated with STEM, using the high-angle annular dark-field signal as well as EDX elemental mapping. These signals can be used to analyse the widths of interfaces between TMDs with different transition metals like Mo and W.

In summary, a variety of TEM techniques have been used to study 2D TMDs and their heterostructures. Specific applications have been found for each technique, be it the determination of the number of layers, the analysis of intrinsic defects, or the width of interfaces in lateral heterostructures.

We acknowledge funding from the European Union's Horizon 2020 research and innovation programme under Grant Agreement No. 881603 (GrapheneCore3).

[1] J. Köster, A. Storm, et al., Micron 160, 103303 (2022).
[2] J. Schulz, M.Sc. thesis, Ulm University (2022).

MS3.P022

Locally excited plasmon resonances of size-selected silver nanoparticles

K. Oldenburg[1,2], I. Barke[2,3], K. H. Meiwes-Broer[1,2,3]

[1]University of Rostock, ELMI-MV, Rostock, Germany
[2]University of Rostock, Department "Life, Light and Matter", Rostock, Germany
[3]University of Rostock, Institute of Physics, Rostock, Germany

Based on their plasmonic properties, noble metal nanoparticles find many technical applications including solar cells, catalysis, cancer treatment, sensors amongst others. Since the characterization of small individual free clusters remains extremely challenging due to the low interaction cross-section with light, most analysis is done by averaging over many clusters. Alternatively, plasmon resonances have been studied for deposited nanoparticles where the dielectric environment influences the plasmon resonance leading to diverse observations in literature [1,2]. In this contribution, we want to reassess the intrinsic plasmonic properties of size selected gas-phase deposited silver nanoparticles in the size range of 10 nm and well below. By means of STEM-EELS we investigate the locally excited plasmonic response of individual nanoparticles. Figure 1 exemplarily shows a HAADF STEM image of a 4 nm silver nanoparticle at the edge of a carbon substrate. Clearly visible is its plasmon resonance in the electron energy loss spectrum. The results are discussed with respect to the inhomogeneous dielectric surrounding, i.e. the substrate and possible surface adsorbates.

[1] A. Campos et al., Nature Physics 15 (2019), 275

[2] J. A. Scholl et al., Nature 483 (2012), 421

Figure 1: HAADF STEM image of a 4 nm silver nanoparticle at the edge of a carbon substrate together with the unprocessed electron energy loss spectrum taken at the marked position.

Fig. 1

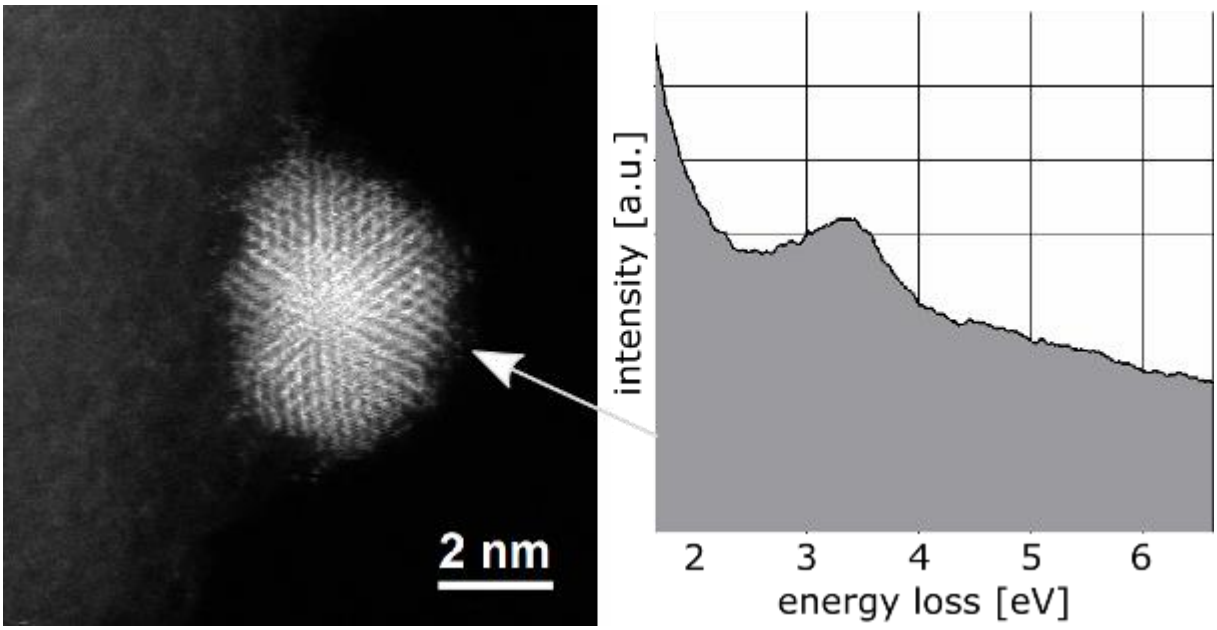

MS3.P023

Solving complex nanostructures with ptychographic atomic electron tomography

P. Pelz[1,2,3], S. Griffin[3], S. Stonemeyer[4,5], D. Popple[4,5,6,7], A. Zettl[4,5,6,7], P. Ercius[3], H. Devyldere[2], M. Scott[2,3], C. Ophus[3]

[1]Friedrich-Alexander-Universität Erlangen-Nürnberg, Materials Science, Nuremberg, Germany
[2]University of California, Berkeley, Materials Science & Engineering, Berkeley, CA, United States
[3]The Molecular Foundry, Lawrence Berkeley National Laboratory, Berkeley, CA, United States
[4]University of California, Berkeley, Physics, Berkeley, CA, United States
[5]University of California, Berkeley, Chemistry, Berkeley, CA, United States
[6]Kavli Energy NanoSciences Institute at the University of California at Berkeley, Physics, Berkeley, CA, United States
[7]Materials Sciences Division, Lawrence Berkeley National Laboratory, Berkeley, CA, United States

Knowledge of the three-dimensional atomic structure of natural and manufactured materials allows us to calculate their physical properties and deduce their function from first principles. Phase-contrast electron microscopy methods like ptychography are ideally suited to solve the 3D atomic structure of nanomaterials containing light and heavy elements. We perform mixed-state electron ptychography from 34.5 million diffraction patterns to reconstruct a high-resolution tilt series of a double wall-carbon nanotube (DW-CNT), encapsulating a complex ZrTe sandwich structure. Class averaging of the resulting reconstructions and subpixel localization of the atomic peaks in the reconstructed volume reveals the complex three-dimensional atomic structure of the core-shell heterostructure with 17 picometer precision.

MS3.P024

Atomic-scale study of the number of graphene layer-dependent growth of cesium iodide cluster deposited by electrospray ion-beam deposition

N. Vats[1], U. Kaiser[1]

[1]University of Ulm, Electron Microscopy Group of Materials Science, Ulm, Germany

The structure and morphology of an adsorbed atomic or molecular species depend critically on the interaction with the substrate that provides the energy landscape that governs the reaction dynamics and, in turn, influences the final product.[1-4] Surprisingly we found in an earlier scanning transmission electron microscopy study that the morphology and size of the forming cesium iodide (CsI) clusters drastically changes when adsorbed on single layer graphene (SLG) or bi-layer graphene (BLG) surfaces.[4] The formation of 2D-CsI crystals is observed explicitly on BLG and 3D-molecular clusters consisting of 4, 6, 7, and 8 atoms are only formed on SLG. As a possible hypothesis, the observed discrepancy in the adsorption behavior of the CsI clusters on SLG and BLG was discussed in the light of the presence of additional conjugated pi-electrons in the BLG, stimulating the growth of 2D crystals.4 However a thorough experimental study comparing the adsorption characteristic of CsI clusters in dependence on the numbers of graphene layers as well as on the TEM imaging parameters has not been performed so far.

Here, we investigate the structure, chemistry, and stability of 2D-CsI crystals for varying number of graphene layers (1-5) using the sub-angstrom low-voltage electron microscope (SALVE) operated at electron accelerating voltages from 40 to 80 kV. We used commercially available CVD-grown single and bi-layer graphene on a copper foil (Graphenea S.A.). In the first step, copper foil is etched in an 8% ammonium persulfate solution. Then the SLG and BLG are transferred to the platinum coated (thickness ~ 10 nm) perforated silicon nitride TEM grid. Subsequently, by directly stacking another SLG or BLG onto the already transferred SLG/BLG onto a TEM grid, a combination of two, three, four, and five stacked layers of graphene sheets are prepared. In order to minimize the hydrocarbon contamination, the TEM grid was annealed at 300^{o} C in the air for 30 minutes, where the platinum layer, deposited on the TEM grid, catalyzes the oxidation of the hydrocarbon contaminations. Finally, CsI cluster ions $(MX)_nM^+$ (where M and X represent the cation and anion, respectively) are deposited using the electrospray ion-beam deposition (ES-IBD) technique[5] on free-standing graphene TEM grids under high vacuum conditions. In addition, we employ ab-initio calculations to gain comprehensive insight regarding the stability of 2D-CsI crystals to the underlying graphene sheets.

In this work, we combine two unique techniques: low-voltage spherical and chromatic aberration-corrected transmission electron microscopy and highly pure, chemically selective deposition of mass-filtered molecular ion beams to further unravel the mystery of number of layer-dependent growth of 2D-CsI crystals. Furthermore, we anticipate that our atomically resolved number of graphene-layer-dependent and electron accelerating voltage-dependent analysis not only sheds light into the adsorption and growth behavior of CsI clusters but also helps to understand crystal growth of other alkali-iodide species on graphene.

References:
1. Hardcastle, T. P., et al. Physical Review B 87.19 (2013): 195430.
2. Al Balushi, Z. Y., et al. Nature materials 15.11 (2016): 1166-1171.
3. Shi, G., et al. Nature Chemistry 10.7 (2018): 776-779.
4. Vats, N., et al. ACS nano 14.4 (2020): 4626-4635.
5. Rauschenbach, S., et al. small 2.4 (2006): 540-547.

MS3.P025

Spatially-resolved properties of twisted 2D TMDs

R. Leiter[1], A. Storm[1], B. Haas[2], A. Eljarrat[2], C. T. Koch[2], U. Kaiser[1]

[1]Ulm University, Ulm, Germany
[2]Humboldt-Universität zu Berlin, Institut für Physik & IRIS Adlershof, Berlin, Germany

Since the discovery of superconductivity in twisted bilayer graphene at a so-called magic angle [1], there has been an increasing interest in twisted bilayers of two-dimensional materials. Various interesting electronic and optical phenomena have been shown or predicted for these materials [2], and the pronounced moiré patterns occurring at certain twist angles [3,4] have led to the materials also being referred to as "moiré materials". Furthermore, it has been shown that for low twist angles (typically <2°), the moiré structure may deviate from the static lattice by forming large domains of differently stacked layers [5].

Here, we elucidate the difference in the low-loss EELS data between single-, bilayer, and twisted bilayer tungsten diselenide at both high and low twist angles. For the latter, we analyze the local variations in the low-loss EELS data in conjunction with high-resolution (S)TEM imaging in order to correlate effects of local strains originating from domain formation.

We use mechanically exfoliated WSe_2 samples deposited on SiO_2 wafers, with a second layer stacked on top using a PMMA film. These are subsequently transferred to TEM grids using the KOH assisted method.

For high-resolution TEM imaging, we use the Cc/Cs-corrected SALVE TEM operated at 80 kV in order to minimize beam damage. For high-resolution STEM-EELS spectral imaging, we use the aberration-corrected and monochromated NION HERMES STEM instrument operated at an acceleration voltage of 60 kV.

Exciton peaks are fitted with Lorentzian functions on a linear background, which was adapted from the paradigm presented in [6].

We have developed a framework for analyzing exciton peak shifts of twisted bilayer TMD samples in low -loss EELS with high lateral resolution in order to match these shifts to features observed in the high-resolution TEM and STEM images. Care needs to be taken to avoid strong contamination, as we found that the exciton peaks vanish in the center of a trapped contamination bubble.

In the case of a boundary between a single layer and a twisted bilayer of WSe_2 at a twist angle of 8.7° (figure 1), investigation in high-resolution (S)TEM shows an atomically sharp, but jagged interface. When analyzing the scanning EELS data, we observe a reduction in the energy of the exciton peaks when crossing the boundary between the single layer and the bilayer region. Furthermore, comparing the maps of peak positions of the A and D excitons, respectively, we observe a broader transition area between the single- and bilayer for the former. We attribute this behavior to stronger delocalization at lower energies.

In the next step, we correlate high-resolution (S)TEM images with mapped peak shifts originating from strain due to lattice reconstruction at low twist angles.

Figure 1: 60 kV HAADF STEM image (a) and map of peak positions of A and D excitons (b and c, respectively), showing a broader transition area in the case of the A exciton.

[1] Cao *et al. Nature* **556** (2018)**,** 43–50

[2] Tran et al. Nature **567** (2019), 71–75

[3] Shallcross et al. Phys. Rev. B **81** (2010), 165105

[4] Campos-Delgado et al. Small **9** (2013), 3247-3251

[5] Weston et al. Nat. Nanotechnol. **15** (2020), 592–597

[6] Hong et al. Phys. Rev. Lett. **124** (2020), 087401

Fig. 1

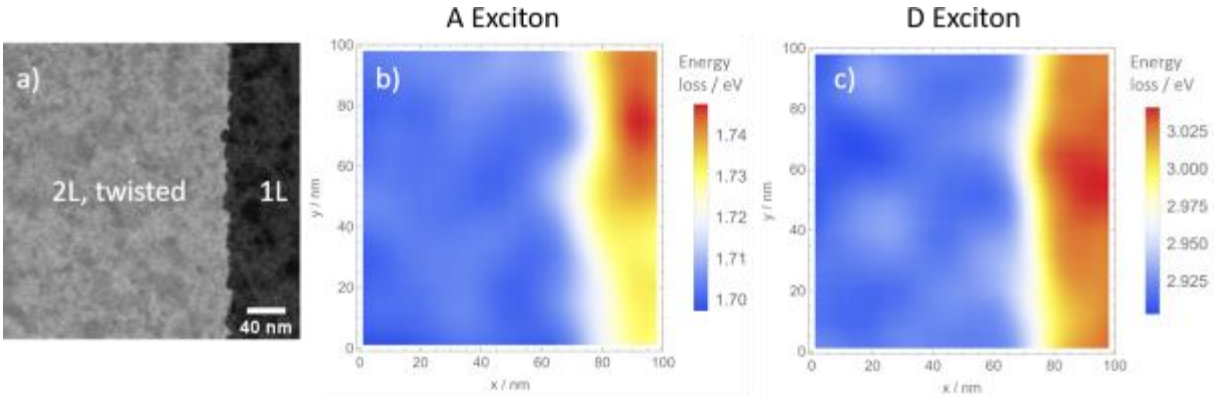
A Exciton
D Exciton
a)
2L, twisted
1L
40 nm
b)
c)
Energy loss / eV
1.74
1.73
1.72
1.71
1.70
3.025
3.000
2.975
2.950
2.925
y / nm
x / nm
0
20
40
60
80
100

MS4.001-invited

Planar defects in non-stoichiometric $SrFeO_{3-\delta}$ perovskite type thin films studied by analytical scanning transmission electron microscopy

R. Erni[1], M. D. Rossell[1]

[1]Empa, Swiss Federal Laboratories for Materials Science and Technology, Electron Microscopy Center, Dübendorf, Switzerland

Strontium-ferrite (SFO), $Sr_nFe_nO3_{n-1}$, provides a fascinating system in which stoichiometric changes can be explored in order to study their impact on the material's crystallographic structure, its properties, and, in particular, on defect formation. For n = 2, SFO adopts a brownmillerite-type structure of alternating layers of FeO_6 octahedra and FeO_4 tetrahedra with iron exclusively in +3 oxidation state. Increasing the oxygen content, with n = 4 and n = 8, SFO reveals tetragonal and orthorhombic structures with iron in +3 and +4 oxidation states (see, e.g., [2]). For the limiting case that $n \rightarrow \infty$, SFO is found in the stoichiometric, cubic perovskite structure as $SrFeO_3$, where Fe is uniquely in +4 oxidation state, forming the well-known FeO_6 octahedra as building blocks of the perovskite structure. From a properties point-of-view, SFO is known to be a mixed ionic-electronic conductor and consequently, tuning the structure and defects provides a mean to control its conductivity.

We present an experimental study of non-stoichiometric $SrFeO_{3-\delta}$, where the loss of oxygen ($\delta > 0$) must lead to oxygen vacancies, possibly structural defects, and thus resulting in changes in the oxidation state of Fe as well. We used HAADF- and ABF-STEM to develop a structural model of planar defects, which run "packman"-style along {001} planes in the SFO film grown on $SrTiO_3$, and which are formed due to the oxygen deficiency [2] (see Fig. 1). Atomic-resolution EDX spectroscopy reveals that the defective bands are formed by Fe_2O_2 double layers. The defects strongly resemble the $Sr_4Fe_6O_{12+\delta}$ structure viewed along the pseudocubic [107] direction, which consists of bands of corner-sharing FeO_6 octahedra separated by bands formed of periodically arranged FeO_5 polyhedra identified as trigonal bipyramids and tetragonal pyramids, respectively.

To assess the impact of these chemistry-driven structural defects on the physical properties, EELS was used to measure the Fe $L_{3,2}$ and the O K excitation edges. Subtle but significant differences in the fine structure of the O K edge at the defect planes compared to bulk spectra were identified and interpreted by complementing the experimental data with simulations using FEFF9. This analysis suggests an increased electron doping of the Fe 3d e_g bands in the Fe_2O_2 defect layers compared to the bulk $SrFeO_3$, which as a consequence must affect SFO's electron-hole conductivity. Moreover, analysis of the Fe $L_{3,2}$ excitation edge uncovers the expected change of the Fe oxidation state in the defective planes from +4 towards +3.

In summary, STEM imaging combined with EDX and EELS measurements revealed the nature of planar defects present in $SrFeO_{3-\delta}$ thin films grown on $SrTiO_3$ and their effect on the electron-hole conductivity. Controlling the amount of oxygen vacancies in these perovskite-based SFO thin films thus allows the electronic conductivity of these films to be adjusted.

Figure 1 HAADF STEM: overview (a) and detail (b) of the atomic structure of the planar defects formed in oxygen deficient, perovskite-type $SrFeO_3$.

References

[1] M. D. Rossell, A. M. Abakumov, Q. M. Ramasse, R. Erni, ACS Nano **7** (2013) 3078-3085.

[2] M. D. Rossell, P. Agrawal, M. Campanini, D. Passerone, R. Erni, Phys. Rev. Mater. **4** (2020) 075001.

[3] P. Agrawal and D. Passerone are kindly acknowledged for providing support for interpretation of the FEFF9 data, and we would like to thank M. Campanini providing the script for peak-pair analysis.

Fig. 1

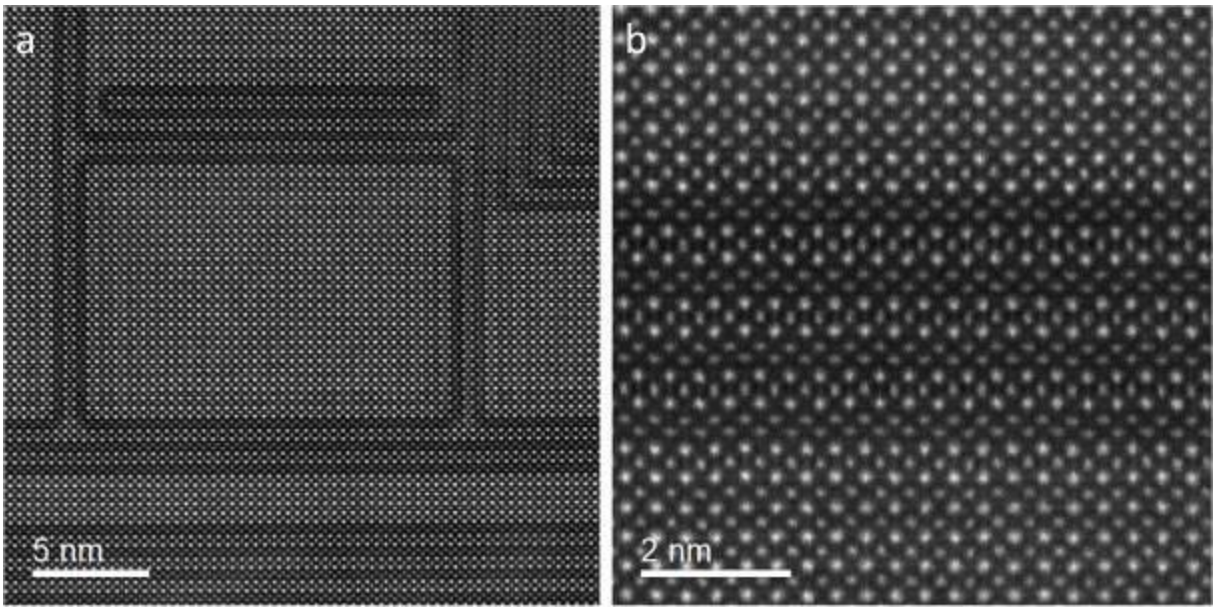

MS4.002

Tuning interface sharpness and interface superconductivity at La_2CuO_4 heterostructures

Y. E. Suyolcu[1], Y. M. Wu[1], G. Kim[1], G. Christiani[1], B. Keimer[1], G. Logvenov[1], P. A. van Aken[1]

[1]Max Planck Institute for Solid State Research, Stuttgart, Germany

Heterostructures of transition-metal oxides enable emerging unique physical properties at their interfaces [1]. The structural adaptability of La_2CuO_4 allows for designing different heterostructures, and superconductivity takes place at the interface between overdoped (metallic) and undoped (insulating) La_2CuO_4 layers grown by oxide molecular beam epitaxy (MBE)[2]. In addition to homo-epitaxial systems[3], heterogeneous multilayers of La_2CuO_4 with, for example, perovskite 113-type and 214-type lanthanum nickelate layers revealed the impact of the interface sharpness on thermoelectric and superconducting properties, respectively [4,5].

In this work, we fabricate $(La,Sr)_2CuO_4$–$SrMnO_3$–$LaMnO_3$–$La2CuO_4$ superlattices [6] using oxide MBE and focus on the interface sharpness and the related superconducting mechanism compared to *cuprate–cuprate* interfaces. We use scanning transmission electron microscopy (STEM) techniques, including high-angle annular dark-field (HAADF) and annular bright-field (ABF) imaging, electron energy-loss spectroscopy (EELS), and energy-dispersive X-ray spectroscopy (EDXS) to examine the interfaces. A JEOL JEM-ARM200F STEM equipped with a cold field-emission electron source, a probe Cs-corrector (DCOR, CEOS GmbH), a Gatan GIF Quantum ERS spectrometer and a large solid-angle JEOL Centurio SDD-type EDXS detector was used for atomic-resolution analyses.

Our findings demonstrate that hetero-epitaxial *cuprate–manganite* layers can achieve sharper Sr-doped La_2CuO_4 interfaces. The dopant distribution in La_2CuO_4 is affected by the elemental intermixing in the first atomic $LaMnO_3$ monolayer. We further underline that structurally sharp interfaces can be chemically rough (Fig. 1), and the chemical intermixing dominates the physical properties. Importantly, different superconducting behaviour (e.g., interface vs filamentary) can be customized with interfacial design [7].

References

[1] Y. E. Suyolcu, G. Christiani, P. A. van Aken, G. Logvenov, *J. Supercond. Nov. Magn.* **2020**, *33*, 107.

[2] A. Gozar, G. Logvenov, L. F. Kourkoutis, A. T. Bollinger, L. A. Giannuzzi, D. A. Muller, I. Bozovic, *Nature* **2008**, *455*, 782.

[3] Y. E. Suyolcu, Y. Wang, F. Baiutti, A. Al-Temimy, G. Gregori, G. Cristiani, W. Sigle, J. Maier, P. A. van Aken, G. Logvenov, *Sci. Rep.* **2017**, *7*, 453.

[4] F. Baiutti, G. Gregori, Y. E. Suyolcu, Y. Wang, G. Cristiani, W. Sigle, P. A. van Aken, G. Logvenov, J. Maier, *Nanoscale* **2018**, *10*, 8712.

[5] P. Kaya, G. Gregori, F. Baiutti, P. Yordanov, Y. E. Suyolcu, G. Cristiani, F. Wrobel, E. Benckiser, B. Keimer, P. A. van Aken, H.-U. Habermeier, G. Logvenov, J. Maier, *ACS Appl. Mater. Interfaces* **2018**.

[6] G. Kim, Y. Khaydukov, M. Bluschke, Y. E. Suyolcu, G. Christiani, K. Son, C. Dietl, T. Keller, E. Weschke, P. A. van Aken, G. Logvenov, B. Keimer, *Phys. Rev. Mater.* **2019**, *3*, 084420.

[7] This work has received funding the European Union's Horizon 2020 research and innovation programme under grant agreement No. 823717 – ESTEEM3.

Figure 1. (a) STEM-HAADF image of a La_2CuO_4–$SrMnO_3$–$LaMnO_3$–La_2CuO_4 superlattice demonstrating coherent "A" and "B" interfaces. (b) EDX line-scan profiles reveal Cu (red) and Mn (green) intermixing at the interfaces. Sr (orange) and La (blue) profiles are given as guides indicating the individual layers. The blue arrow depicts the region of the acquired EDX line scan profiles.

Fig. 1

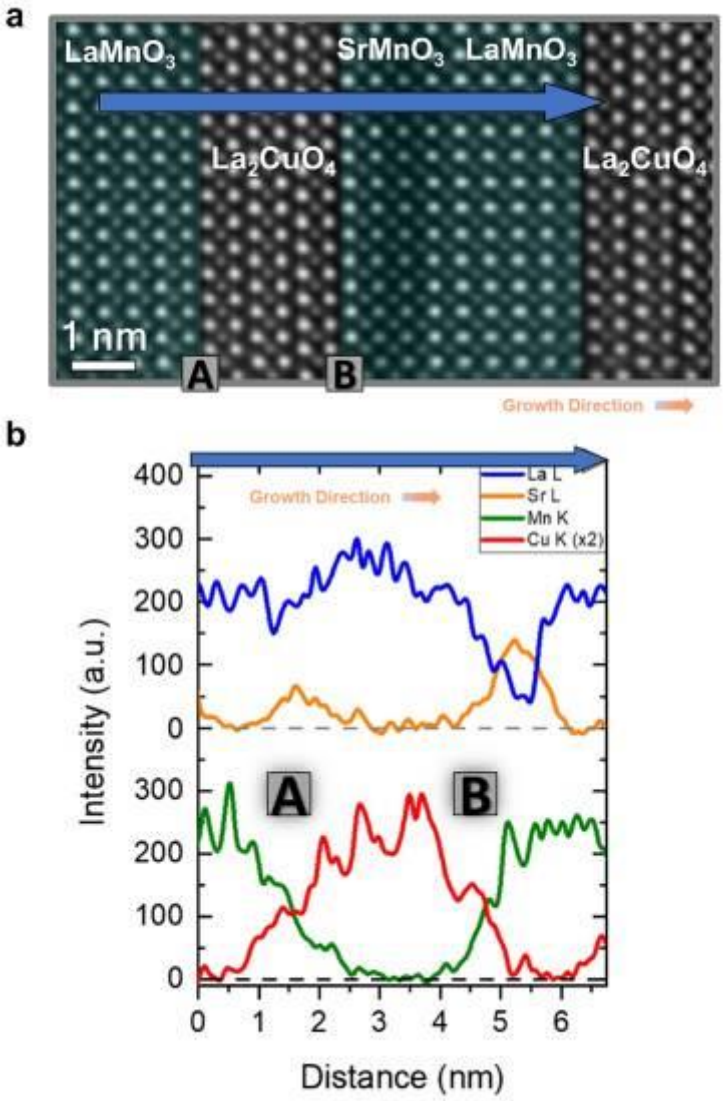
a
LaMnO3
SrMnO3
LaMnO3
La2CuO4
La2CuO4
1 nm
A
B
Growth Direction
b
Growth Direction
La L
Sr L
Mn K
Cu K (x2)
Intensity (a.u.)
A
B
Distance (nm)

MS4.003

Spatially localized electronic states at the $LaAlO_3/TiO_2$ interface: mapping of a 2D electron gas

M. Ederer[1], M. Oberaigner[2], G. Kothleitner[2,3], S. Löffler[1]

[1]TU Wien, USTEM, Vienna, Austria
[2]Graz University of Technology, Institute of Electron Microscopy and Nanoanalysis, Graz, Austria
[3]Graz Centre for Electron Microscopy, Graz, Austria

Perovskite heterostructures play an increasingly important role in optoelectronics applications, such as solar cells, LEDs and photo detectors [1]. The combination of two different semiconducting materials often leads to drastic changes of the electrical, magnetic or optical properties in the vicinity of the interface. Thus, full characterization of the localized electronic states is of utmost importance. We approach this goal with a combined *ab-initio* and experimental study of the electronic states localized at the $LaAlO_3/TiO_2$ interface.

The material of interest is a heterostructure consisting of the cubic perovskite $LaAlO_3$ and TiO_2 in anatase phase. Bulk anatase is typically a semiconductor with a few eV wide direct band gap. In combination with $LaAlO_3$, however, unoccupied states appear directly above the Fermi energy for 2-3 TiO_2 layers closest to the interface. When a small energy window is chosen for imaging, similar to elemental mapping albeit with a window of 0.5 eV or even smaller, the localized electronic states can be mapped in real space [2]. We compare the experimental results to inelastic channeling simulations of a Ti-La terminated interface based on [3].

The simulated spectrum image for an energy loss of 456.4 eV can be seen in **Figure 1(c).** Ti atoms at least 1 unit cell from the interface show negligible intensity or no intensity at all and can therefore be considered "bulk-like" in this context. Ti atoms close to the Ti-La terminated interface, however, show significant intensity at this energy loss, which is especially apparent in the second atomic column from the interface. The orbital there resembles the shape of a d_{xy}-orbital with x the horizontal axis and y the vertical axis in the figure. The experimental map of the Ti L_3-edge onset pre-peaks lies in close agreement with the simulations (see **Figure 1(b))**. Due to the difficult mapping conditions presented by the low signal-to-noise ratio and due to elastic channeling, the original shape of the orbitals is not exactly reproduced. More importantly, however, the spatial confinement of the relevant electronic orbitals and the resulting local increase in intensity is clearly visible.

Electrons occupying these states can, thus, be identified as a two-dimensional electron gas. The direct mapping of such an electron gas opens up new ways of investigating heterostructures in electronics with future application of understanding and designing new and improved optoelectronic materials. [4]

Figure 1. (a) HAADF image of a 12 nm thick heterostructure oriented in the [100] crystallographic directions of both anatase TiO_2 and $LaTiO_3$ recorded at a high tension of 300 kV. **(b)** STEM-EELS spectrum image for a collection semi-angle of 24 mrad and an energy window at the Ti L_3-edge onset. **(c)** Simulated spectrum image for an energy loss of 456.4 eV and a 1 unit cell thick sample with the same parameters as in **(a)** and **(b)**.

[1] Cheng et al., Adv. Optical Mater. **10**, 2102224 (2022)

[2] Löffler et al., Ultramicroscopy **177**, 26 (2017)

[3] Wang et al., Journal of Applied Physics **108**, 113701 (2010)

[4] The authors gratefully acknowledge funding from FWF under grant nr. I4309-N36.

Fig. 1

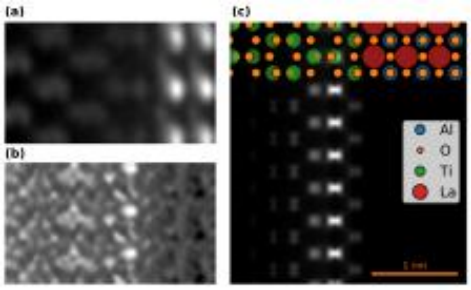

MS4.004-invited

Probing the interplay of atomic structure and properties in perovskite oxide thin films

D. T. L. Alexander[1], C. Domínguez[2], H. Meley[2], L. Varbaro[2], S. Gariglio[2], J. M. Triscone[2], B. Mundet[1,2]

[1]École Polytechnique Fédérale de Lausanne (EPFL), Electron Spectrometry and Microscopy Laboratory (LSME), Institute of Physics (IPHYS), Lausanne, Switzerland
[2]University of Geneva (UNIGE), Department of Quantum Matter Physics (DQMP), Geneva, Switzerland

Perovskite-structured oxide thin films provide a fascinating playground for the study of condensed matter physics, owing to the strong coupling of lattice composition and structural distortions to functional properties. Here, we illustrate how recent developments in electron microscopy are vital for study of their structure–property relationships.

Measurements are made in scanning transmission electron microscopy (STEM) mode using a double aberration-corrected FEI Titan Themis 60-300 at 200/300 kV. For measuring atomic structure, high angle annular dark field (HAADF) and annular dark field (ABF) 90° rotation image series are recorded, and then corrected for linear and non-linear scan distortions. Electron energy-loss spectroscopy (EELS) is carried out using a Gatan GIF Quantum ERS. Samples are prepared via mechanical polishing and broad ion beam milling, or by focused ion beam and lift out, and cleaned with an IBSS MCA.

First, we look at $NdNiO_3/SmNiO_3$ superlattices, where macroscopic measurements of a metal-to-insulator transition (MIT) show an unexpected transition from two electronic phases to a single one as layer thickness decreases below a critical value. Using monochromated EELS to measure subtle changes in the Ni L_3 and O K ionization edges, we not only confirm this behavior, but also map the electronic phases with a sub-nm spatial resolution [1]. STEM structure measurements show, however, that each layer retains the composition and lattice distortions of its parent lattice; a result that helps motivate a new Landau theory of electronic phase boundary energy [2]. To further study this behavior, we test decoupling the layers by incorporating $LaAlO_3$ interlayers into the superlattices. Here, atomic resolution STEM is essential for diagnosing deposition problems and for measuring the coupling of structural distortions across interfaces; see Fig. 1.

Lattice distortion connections next come to the fore in the study of $LaVO_3$ films. STEM helps show how epitaxial strain plays a key role in determining the film's orientation, giving an out-of-plane orthorhombic long axis under the tensile strain set by a (110) $DyScO_3$ substrate [3]. Since the $DyScO_3$ instead has an orthorhombic long axis that is in-plane, such a film inherently forces an interface that couples the incommensurate oxygen octahedra rotations of the two orthorhombic orientations. Remarkably, STEM reveals this rotation-coupled interface forms within film, rather than at the substrate/film interface, creating a sharp 90° domain boundary within a single compound. Justified by second principles energetic simulations, this finding promises new avenues for creating novel functional properties [4].

In summary, we illustrate myriad ways that aberration-corrected STEM is critical for uncovering the interplay between atomic structure and physical properties in functional thin films. Looking towards the future, in order to achieve further insights, our aim is to couple these precision measurements with variable sample conditions.

[1] B. Mundet *et al*., *Nano Lett.* **21**, 2437 (2021).

[2] C. Domínguez *et al*., *Nat. Mater.* **19**, 1182 (2020).

[3] H. Meley *et al*., *APL Mater.* **6**, 046102 (2018).

[4] D.T.L. Alexander *et al*., *under review.*

Fig. 1. (a) HAADF STEM image of a $NdNiO_3/SmNiO_3$ superlattice with $LaAlO_3$ interlayers. (b) depth profile of average Δy displacements of A-site cations from their "ideal" cubic positions (right) shows how each layer recovers the distortions of its parent compound.

Fig. 1

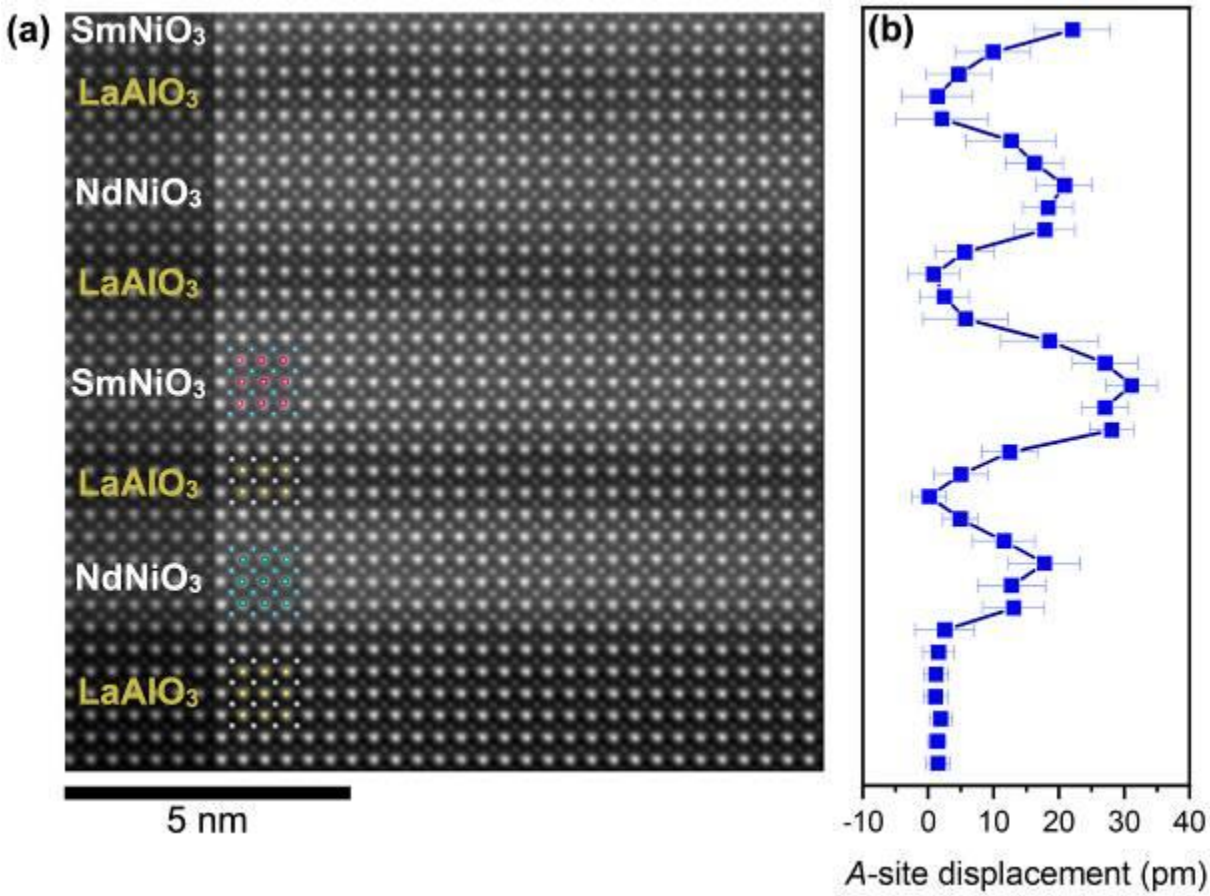
(a)
SmNiO3
LaAlO3
NdNiO3
LaAlO3
SmNiO3
LaAlO3
NdNiO3
LaAlO3
5 nm
(b)
-10
0
10
20
30
40
A-site displacement (pm)

MS4.005

Microstructure-functionality relationships of pulsed laser deposited CuI thin films

S. Selle[1], P. Storm[2,3], R. Busch[1], M. Lorenz[2], M. Grundmann[2]

[1]Fraunhofer IMWS, Microstructure of Optical Materials, Halle (Saale), Germany
[2]Felix Bloch Institute for Solid State Physics, Universität Leipzig, Leipzig, Germany
[3]Robert Bosch Semiconductor Manufacturing Dresden GmbH, Dresden, Germany

In the field of transparent p-type semiconductors, copper iodide (CuI) holds an outstanding position. It combines high transparency in the visible spectral range with excellent hole transport properties [1]. To make CuI thin films suitable for complementary electronics, i. e. to develop CuI into an equivalent partner for well investigated transparent n-type semiconductors, control of electrical and morphological properties is required.

Pulsed laser deposition (PLD) showed recently successful outcomes regarding film quality and systematic functionality tuning [2]. The use of powder-based targets allows a high flexibility regarding composition and can provide lateral and vertical composition gradients as well as controlled doping. With the possibility to change source targets in-situ, template layers can be grown to improve lattice match and surface smoothness due to the decrease of grain boundaries.

This works focuses on the microstructural investigation of (doped) CuI films employing EBSD, SEM, FIB, TEM and STEM-EDX. The obtained results are used to explore microstructure-functionality relationships by linking XRD findings and electrical properties with the results gained by the aforementioned electron microscopy techniques.

The first part of this work examines the impact of intentional p-doping with selenium (Se) on the film morphology. CuI with a lateral Se gradient was PLD grown on a two-inch diameter sapphire wafer. Site-specific TEM samples were prepared by focused ion beam (FIB) machining corresponding to a certain Se content. Whereas for each Se value, growth starts with the ´default´ zinc-blende γ-phase, high resolution TEM showed that a relatively high Se content seems to favor the CuI beta phase (trigonal crystal system) within the ongoing growth process. For a lower Se content, a new CuI phase, presumably with an up to now unpublished wurtzite 4H structure, was discovered with high-resolution TEM and related diffraction analysis (Fig. 1). This crystalline phase change also matches with results regarding XRD and electrical properties, where considerable changes occur for a selenium content above x(Se) = 1 at% [3].

The second part investigates the possibility to suppress rotational domains by employing PLD grown template layers such as sodium bromide (NaBr). By growing NaBr on cubic SrF_2 (111) substrates before depositing the CuI thin film, a heterostructure was constructed where the moisture sensitivity of NaBr could be employed to obtain free standing CuI thin films. XRD phi-scans showed single-crystallinity and no occurrence of rotational domains up to 1-2 µm film thickness. Nevertheless, films need to be sufficiently thicker to be utilized as, for example, front-back device processing. Samples out of reasonable thick films could be prepared for EBSD to visualize domain orientation, SEM to depict surface roughness and TEM to analyze grain boundaries to examine the cross-section as well as the front- and backside of the CuI film. It was shown that for thicknesses above 1-2 µm, the single crystallinity gets lost, probably due to accumulation of defects during the PLD growth [4].

[1] M. Grundmann et al., phys. stat. sol. (a) 210, 1671-1703 (2013).

[2] P. Storm et al., APL Mater. 8, 091115 (2020).

[3] P. Storm et al., Phys. Status Solidi RRL 15(8), 202100214:1-6 (2021).

[4] P. Storm et al., J. Mater. Chem. C 10, 4124-4127 (2022).

Fig. 1: CuI:Se film with lateral Se composition gradient on 2-inch diameter c-sapphire wafer with marked position for FIB sample extraction (left). High-resolution TEM images 1,2, and 3 close to the interface substrate-film (right).

Fig. 1

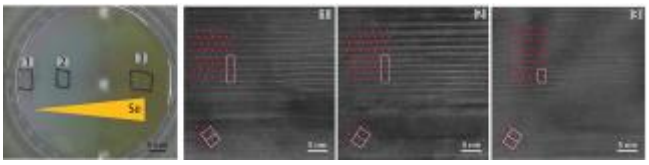

MS4.006

Seeing structural evolution of organic molecular nano-crystallites using 4D-scanning confocal electron diffraction (4D-SCED)

M. Wu[1], C. Harreiß[1], C. Ophus[2], M. Johnson[3], R. Fink[3], E. Spiecker[1]

[1]Friedrich-Alexander-Universität Erlagnen-Nürnberg, Materials Science, Erlangen, Germany
[2]Lawrence Berkeley National Laboratory, National Center for Electron Microscopy, Berkeley, CA, United States
[3]Friedrich-Alexander-Universität Erlagnen-Nürnber, Department of Chemistry und Pharmacy, Erlangen, Germany

Direct observation of organic molecular nanocrystals using electron microscopy is highly challenging, due to their radiation sensitivity and complex structure. 4D-STEM nano-beam diffraction (NBD) using small convergence α has been demonstrated to reveal the rich structural information in soft materials [1]. In this context, homogeneous beam-specimen interaction is desired to maximize dose/information efficiency before total structural damage, and spot diffraction signals are preferred for sensitivity and accuracy of Bragg peaks detection in dense reciprocal lattices typical in organic crystals. In NBD, the beam illuminates the sample with an Airy disk profile, and diffraction disks size is coupled to α, not optimized for dose efficiency and Bragg peaks detection due to spread signals and possible disks overlapping. Here, we introduce 4D-scanning confocal electron diffraction (4D-SCED) which combines high dose efficiency and high angular resolution. 4D-SCED applies defocused pencil beam illumination (Fig. 1b) on the sample and combines a confocal electron optic setup with a camera to record spot diffraction patterns (Fig. 1c). The defocused illumination reduces the dose with a homogenous beam sample interaction, and the confocal optics transfer spot-like diffraction signals, optimized for Bragg peaks detection. The spatial and angular resolution can be estimated using geometric considerations (Fig. 1d), which is largely decoupled from α.

We first compare SCED and NBD with a single crystal thin film of 2D molecular α,ω-DH6T bilayer (fig. 1e-h). An order-of-magnitude higher diffraction signal is seen in SCED compared to NBD, enabling accurate Bragg peak detection for structural studies, e.g. layer rotation relation. We apply 4D-SCED to study an active layer in organic solar cells, DRCN5T:PC71BM BHJ thin films after solvent vapor annealing (Fig. 2a-c). With careful balancing spatial and angular resolution for the given dose budget, structural details of DRCN5T nano-crystallites oriented both in- and out-of-plane are imaged at ~5 nm resolution and dose budget of ~5 e-/Å2. Finally, we use 4D-SCED to study the structural evolution during thermal annealing by in situ heating the thin film in the TEM (Fig. 2d). The evolution of crystallite size (coarsening) and texture, as well as the progressive enrichment of PC71BM at interfaces are directly revealed [2].

The unique combination of high dose efficiency and high angular resolution makes 4D-SCED an ideal technique for studying beam-sensitive soft materials. The new possibilities of the technique are currently employed to explore further soft materials.

Refs:
[1] Bustillo, K., et. al., Acc. Chem. Res. 11 (2021) 2543
[2] Wu, M., et. al. Nat. Commun. 13 (2022) 2911

The authors acknowledge financial support from DFG via projects GRK1896 and SFB953. Work at the Molecular Foundry has been supported by U.S. DoE under contract No. DE-AC02-05CH11231.

Fig 1. (a) STEM setup. (b) Defocusing the probe mitigates dose for beam-sensitive samples. (c) Scheme of SCED. (d) A geometric scheme for considering spatial and angular resolution. (e-h) Comparison of NBD and SCED applied to an α,ω-DH6T bilayer.
Fig 2. Visualizing (a) edge-on (with color wheel) domain orientation and (b) face-on (grayscale) domain location of the donor crystals in DRCN5T:PCBM blends. (c) Mapping the whole area with 4D-SCED dataset. (d) The structural evolution of donor nano-crystallites during an in situ annealing experiment in the TEM.

Fig. 1

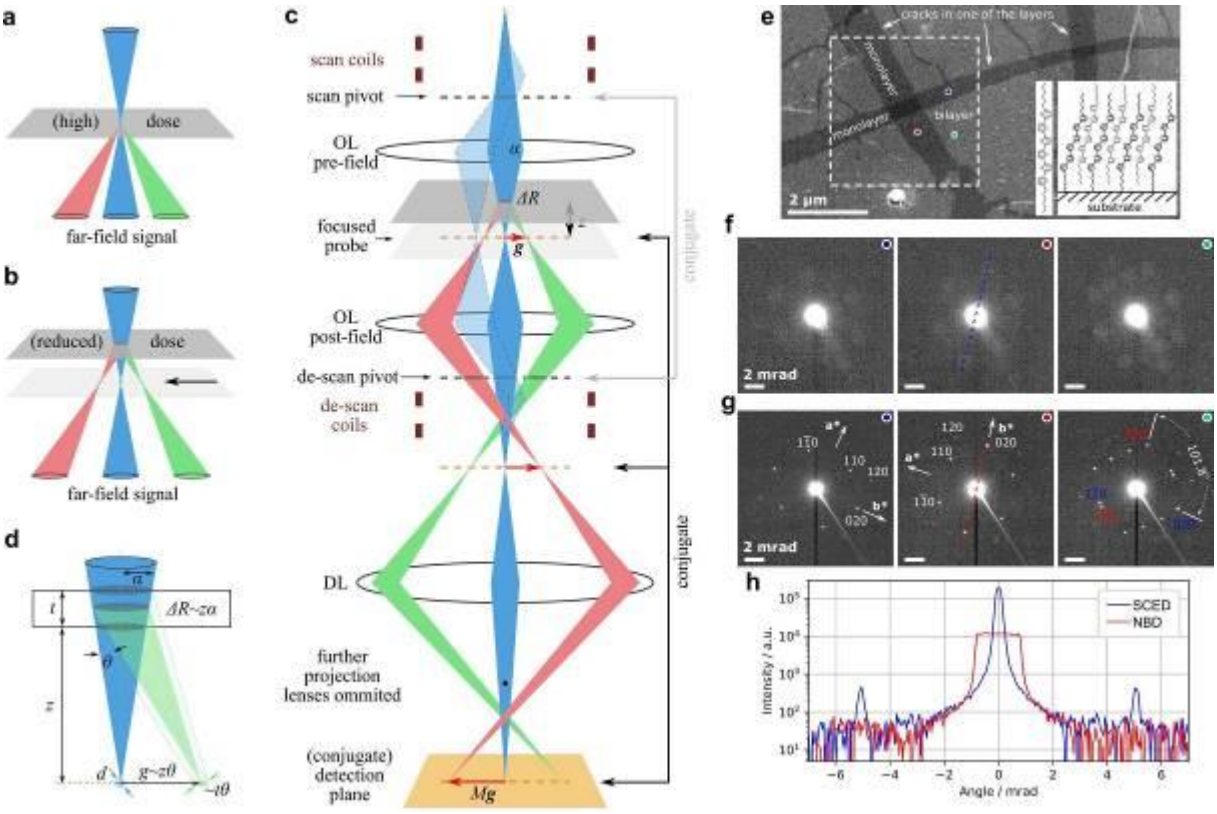
a
(high) dose
far-field signal
b
(reduced) dose
far-field signal
d
ΔR~zα
g~zθ
c
scan coils
scan pivot
OL pre-field
focused probe
OL post-field
de-scan pivot
de-scan coils
DL
further projection lenses ommited
(conjugate) detection plane
conjugate
conjugate
e
cracks in one of the layers
monolayer
monolayer
bilayer
2 μm
substrate
f
2 mrad
g
2 mrad
h
SCED
NBD
Intensity / a.u.
Angle / mrad

Fig. 2

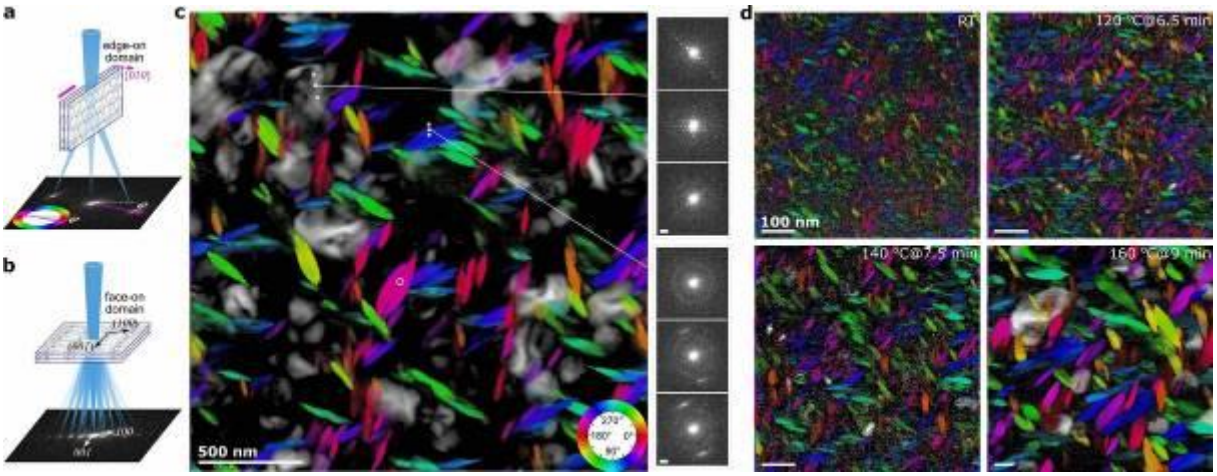
a
edge-on domain
b
face-on domain
c
500 nm
d
RT
120 °C@6.5 min
100 nm
140 °C@7.5 min
160 °C@9 min

MS4.P001

The impact of rapid thermal annealing on ferroelectric HfO2 analyzed by conventional TEM in plan-view and in cross-section

O. Gronenberg[1], R. Marquardt[2], U. Schürmann[1], H. Kohlstedt[2], L. Kienle[1]

[1]CAU, Institute for Material Science, Kiel, Germany
[2]CAU, Institute for Electrical Engineering and Information Engineering, Kiel, Germany

Introduction

HfO_2 and related compounds attracted considerable interest for different non-volatile storage elements. The functionality and device performance of memory related applications is strongly affected by oxygen vacancies, which can stabilize the metastable ferroelectric phase of HfO_2[1]. The wake-up effect of ferroelectric HfO2 was attributed to defect related changes[2], phase transitions[3] and structural transformations[4].

Objectives

Ferroelectric capacitors consisting of TiN electrodes and sputtered HfO_2 on an 1 cm^2 Si substrate showed different ferroelectric properties due to a temperature gradient during rapid thermal annealing (RTA). Devices from the hot corner had low remnant polarization of 10 µC/cm^2 without changing during field cycling, while devices from the cold corner showed a strong wake-up effect with 0 µC/cm^2 in pristine devices and up to 26 µC/cm^2 after 10^6 cycles. TEM analysis of devices from both positions was applied to correlate the electrical characteristics with microstructural differences.

Materials & methods

These devices were prepared by reactive sputtered TiN electrodes and RF sputtered HfO_2. TiN top electrodes were deposited after RTA and patterned with UV lithography. In the RTA set-up, approximately 600 °C were applied for 10 s in N_2 atmosphere. IR thermal imaging after RTA revealed a thermal gradient due to a disaligned filament inside the projector lamp used for heating.

Plan-view TEM samples from the hot and the cold corner were prepared by PIPS after the devices in the center were trained for 10^5 cycles with +/- 3 V (see Fig. 1). Additionally, cross-sectional TEM samples were prepared by FIB. TEM analysis in plan-view and in cross-section via electron diffraction (ED), HRTEM and EELS was correlated with the electrical characteristics.

Fig. 1: The Si substrate with TiN/HfO_2/TiN capacitors is shown on the left with trained devices marked with blue circles. On the right the PIPS sample is shown with two trained devices close to the hole.

Results

The combination of ED in plan-view and cross-sectional TEM analysis, revealed different microstructures and interfaces to the TiN top electrodes. At the interface to the TiN top electrode a TiO_xN_y interlayer was confirmed with EELS, which was thicker in the cold corner. Regarding the microstructure, the cold corner shows a stronger [110] texture while in the hot corner the <111> oriented grains became dominating due to Ostwald ripening. The in-plane polarization of the [110] textured HfO_2 and the observed structural transformation of the *ex situ* trained devices hints towards a ferroelastic switching during wake-up.

Conclusion

In-depth structural characterization in close correlation with the electrical response of ferroelectric TiN/HfO_2/TiN capacitors revealed a strong structural influence on the wake-up effect induced by a temperature gradient during RTA. The hot corner showed wake-up free remnent polarization due to increased <111> texture, while the cold corner has a strong wake-up effect due to [110] oriented grains with a pristine in-plane polarization. Gradual ferroelastic switching to [011] and [101] orientations increases the remnent polarization with field cycling.

References

1 T. Mittmann et al., Adv. Mater. Interfaces 1900042 (2019).

2 S. Starschich et al., Appl. Phys. Lett. **108**, 032903 (2016).

3 E.D. Grimley et al., Adv. Electron. Mater. **2**, 1600173 (2016).

4 T. Shimizu et al., Appl. Phys. Lett. **113**, 212901 (2018).

Fig. 1

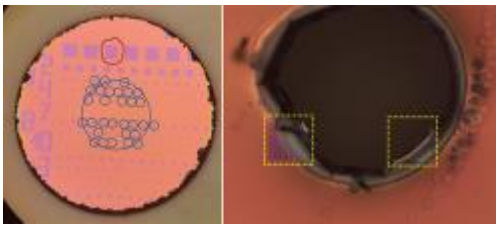

MS4.P002

Epitaxial growth mechanism of magnetic Fe_4N thin films - Intrinsic formation of metastable interface layers

M. Kamp[1], D. Seidler[1], J. McCord[1], L. Kienle[1], R. M. Islam[1]

[1]Materials Science, Kiel, Germany

Introduction

Due to its ferromagnetic properties, γ´´-Fe_4N can be applied in spintronic applications, while the microstructure and crystal orientation influence the switching behavior [1]. The focus of this contribution is set on the deposition of epitaxial thin films on single-crystal substrates like MgO by reactive magnetron sputtering. In contrast to other physical or chemical vapor deposition methods (molecular beam epitaxy, electron beam physical vapor deposition, atomic layer deposition) [2], phase-pure epitaxial vapor deposition by magnetron sputtering is more challenging, however, this method is much more widely used and allows easier scaling of the production process.

Objectives

The analysis of the γ´´-Fe_4N thin films allows to elucidate the growth conditions of epitaxial thin films. In particular, conclusions may be drawn about the nucleation phase of thin film growth by reactive DC magnetron sputter deposition. An interface layer, between the substrate and the film, might originate from a tetragonal distortion of the cubic γ´´-Fe_4N crystal structure or a phase transformation with local variations in chemical composition.

Materials & methods

The microstructure, chemical composition, and the magnetic properties of γ´´-Fe_4N thin films are investigated by XRD, vibrating sample magnetometry, magneto-optical microscopy, and spectrum imaging including high resolution scanning transmission electron microscopy, energy dispersive X-ray, and electron energy-loss spectroscopy. To verify the chemical composition of the thin (5 nm) interface layer, EDX and EELS spectroscopy has to be to be applied.

Results

The epitaxially grown γ´´-Fe_4N thin films indicate the formation of an interface layer between the substrate and the thin film with a tetragonal distortion of the cubic crystal structure and a lower nitrogen concentration. This observation indicates the formation of a metastable tetragonal phase such as α´´-Fe_8N [3]. Next to the inhomogeneous interface layer, the epitaxial γ´´-Fe_4N thin film is rotated against the substrate by 2.4° along the growth direction, which agrees with the observed tilting of cubic magnetocrystalline anisotropy.

Conclusion

The analysis of the chemical composition of the interfacial layer of γ´´-Fe_4N thin films provide insight into the growth conditions of epitaxial thin films. In particular, the nucleation phase of thin film growth by reactive DC magnetron sputter deposition is investigated. The intrinsic interface layer shows a tetragonal distortion of the cubic γ´´-Fe_4N crystal structure and a phase transformation with local variations in chemical composition.

1 Seema, P. Gupta, D. Kumar, V. R. Reddy and M. Gupta, *Applied Surface Science Advances*, 2021, **5**, 100088.

2 N. I. M. Nadzri, D. M. S. Ibrahim and S. Sompon, *IOP Conf. Ser.: Mater. Sci. Eng.*, 2019, **701**, 012047.

3 I. Dirba, P. Komissinskiy, O. Gutfleisch and L. Alff, *Journal of Applied Physics*, 2015, **117**, 173911.

MS4.P003

Extended grain boundary structures in quasi-epitaxial TiN_{1-x} electrode thin films grown on *c*-Al_2O_3

A. Zintler[1], R. Winkler[2], S. Petzold[2], S. U. Sharath[2], E. Bruder[2], N. Kaiser[2], L. Alff[2], L. Molina-Luna[2]

[1]Karlsruher Institut für Technologie (KIT), Laboratorium für Elektronenmikroskopie, Karlsruhe, Germany
[2]Technische Universität Darmstadt, Materialwissenschaften, Darmstadt, Germany

Titanium nitride (TiN) thin films are intensively studied in their application at room temperature (RT) as electrode materials in oxide electronics[1] and at low temperatures (LT) for microwave resonators and superconducting (SC) Josephson junctions.[2, 3] In these applications, low surface roughness, high electrical conductivity and high critical temperatures (TC) for SC applications are essential.[4]

Here, TiN_{1-x} films of 25 nm thickness have been deposited by reactive molecular beam epitaxy (RMBE) on *c*-cut sapphire substrates. For the sample series, increasing nitrogen deficiency was introduced by lowering the substrate temperature and increasing the Ti deposition rate. In their application as bottom electrodes in oxide electronic valence change memories (VCM) the nitrogen deficiency is discussed to enable electrical device performance.[5]

Besides characterization of the RT and LT electrical conductivity, a scale bridging set of characterization methods has been employed to create a global (mm scale) down to atomistic (Å scale) understanding of the microstructure and resulting grain boundaries. Starting from X-ray diffraction (XRD) over backscatter electron (BSE) imaging and ion channeling contrast imaging (iCCI) and atomic resolution high-angle annular dark-field (HAADF) STEM imaging, a comprehensive analysis has been carried out.

All samples showed highly textured out-of-plane growth (TiN (111)||Al_2O_3(001)) and two options for in-plane orientations, separated by 60°, for the TiN grains. iCC imaging revealed near identical grain sizes for all samples. For the low film thickness of 25 nm, the lateral grain size of over 100 nm indicated quasi-epitaxial growth introduced by domain matching epitaxy. The grain boundaries present are mainly twin boundaries of the <112> type. For the most deficient $TiN_{0.7}$ sample, these twin boundaries emit <112> {111} stacking faults, resulting in a low transparency for electrical transport of the extended grain boundary. Critical temperatures of up to 4.9 K are reported for the first time for TiN films of low thickness on *c*-cut sapphire.

Figure 1: (a,b) BSE images of the surfaces of the TiN (A) and TiN0.7 (B) thin film showing GBs in BSE contrast only for TiN0.7. **(c,d)** iCC images for the same samples, indication the two in-plane oriented grain types (60° in-plane rotation) and near identical grain sizes for both samples. **(e,f)** HAADF-STEM images of twin boundaries of the same samples, the TiN0.7 GB shows an extended GB structure resulting from the emission of stacking faults into the neighboring grain. **(g)** Temperature dependent resistivity measurements showing the anomalous increase in resistivity for the TiN0.7 sample and SC transition temperatures of the 25 nm TiN1-x films.

[1] Sharath SU, Vogel S, et al., Adv. Funct. Mater. 31 (2017) 10.1002/adfm.201700432
[2] Gao R, Yu W, et al., Phys. Rev. Materials 3 (2022) 10.1103/PhysRevMaterials.6.036202
[3] Krockenberger Y, Karimoto S, et al., Journal of Applied Physics 8 (2012) 10.1063/1.4759019
[4] Zintler A, Eilhardt R, et al.,(2022) 10.1021/acsomega.1c05505
[5] Niu G, Calka P, et al., 3 (2019) 10.1080/21663831.2018.1561535

Fig. 1

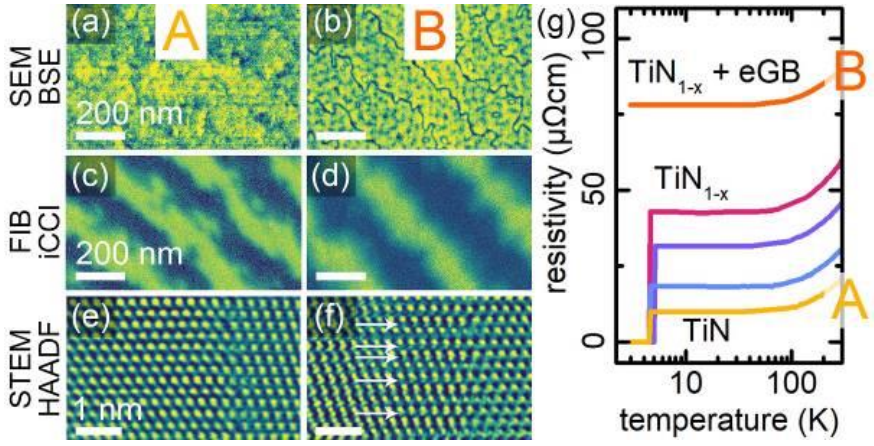

MS4.P004

Microstructure of GeTe-Sb_2Te_3 heterostructures grown by pulsed laser deposition

S. Cremer[1], L. Voss[2], N. Braun[1], L. Kienle[2], A. Lotnyk[1,3]

[1]Leibniz Institute of Surface Engineering e.V. (IOM), Leipzig, Germany
[2]University of Kiel, Faculty of Engineering, Kiel, Germany
[3]Ningbo University, Laboratory of Infrared Materials and Devices, Ningbo, China

Introduction: Ge-Sb-Te based phase change memory (PCM) is a highly promising technology for e.g., in memory or neuromorphic computing application. Relying on reversible amorphous-crystalline phase change, PCM is non-volatile, scalable, and fast. Heterostructured PCM show optimized performance, especially regarding power consumption and multi-level operation [1,2]. However, further investigations are necessary to understand in-detail the relationship of structure and properties.

Objectives: The influence of systematically varying deposition parameters on the microstructure of GeTe-Sb_2Te_3 heterostructured thin films was investigated to comprehend their outstanding properties.

Materials & methods: Non-periodic (npHS) and periodic (pHS) GeTe-Sb_2Te_3 heterostructures were deposited at room temperature by pulsed laser deposition (PLD). Detailed microstructure analysis was performed by combination of advanced transmission electron microscopy and X-Ray measurement techniques.

Results: For the npHS a decreased laser fluence and number of pulses resulted in a decreased layer thickness which goes along with an increased intermixing and a composition approaching $GeSb_2Te_4$ (Fig. 1a-d). Unlike amorphous GeTe layers, the Sb_2Te_3 layers are nanocrystalline after PLD growth. Similar to fully crystalline Sb_2Te_3 [3], the nanocrystals consist of different defects like grain boundaries and bi-layer defects (Fig. 2a, b). Moreover, the grain size and crystalline phases vary (Fig. 2a, c). Apart from the known t- and c-phases, a vacancy-ordered (vo) phase was observed [4]. Similar to vo-$Ge_2Sb_2Te_5$ [5], this structure transforms into the c-phase by electron beam exposure (Fig. 2d). Confirmed by XRD, overall, the Sb_2Te_3 layer mainly consists of {*00l*}-textured t-Sb_2Te_3 phase. Despite the small layer thickness, the layers of the pHS are still separated with alternating Sb- and Ge-rich layers, respectively (Fig. 1e-h).

Conclusion: Whereas the layers intermixing depends on the deposition parameters and despite the room temperature deposition as well as the use of an amorphous substrate, as-grown Sb_2Te_3 layers are nanocrystalline while GeTe layers are amorphous in the HS. Since for Sb_2Te_3-$GeSb_2Te_4$-HS already an enhanced operation energy efficiency was reported [6], the results of the present work provide a starting point to establish structure-property relationships for PLD grown GeTe-Sb_2Te_3-HS in addition.

References

[1] T. C. Chong et al., Appl. Phys. Lett. 88, 122114 (2006).

[2] L. Zhou et al., Adv. Electron. Mater. 6, 1900781 (2020).

[3] J.-J. Wang et al., Phys. Status Solidi RRL 13, 1900320 (2019).

[4] Y. Zheng et al., Nano Res. 9, 3453 (2016).

[5] A. Lotnyk et al., Acta Mater. 105, 1 (2016).

[6] J. Feng et al., ACS Appl. Mater. Interfaces 12, 33397 (2020).

Acknowledgements

We thank Mrs. A. Mill for assistance in the FIB preparation. This work was supported by the German Research Foundation (DFG 445693080).

Figure 1: Overview TEM images and EDX maps of npHS deposit with the highest (a,b) and lowest (c,d) laser fluence, respectively, and two pHS (e-h).

Figure 2: Local structure of npHS. TEM images showing Sb_2Te_3 nanocrystallites characterized by multiple grain sizes (a), crystal defects (a, b), and phases (c, d).

Fig. 1

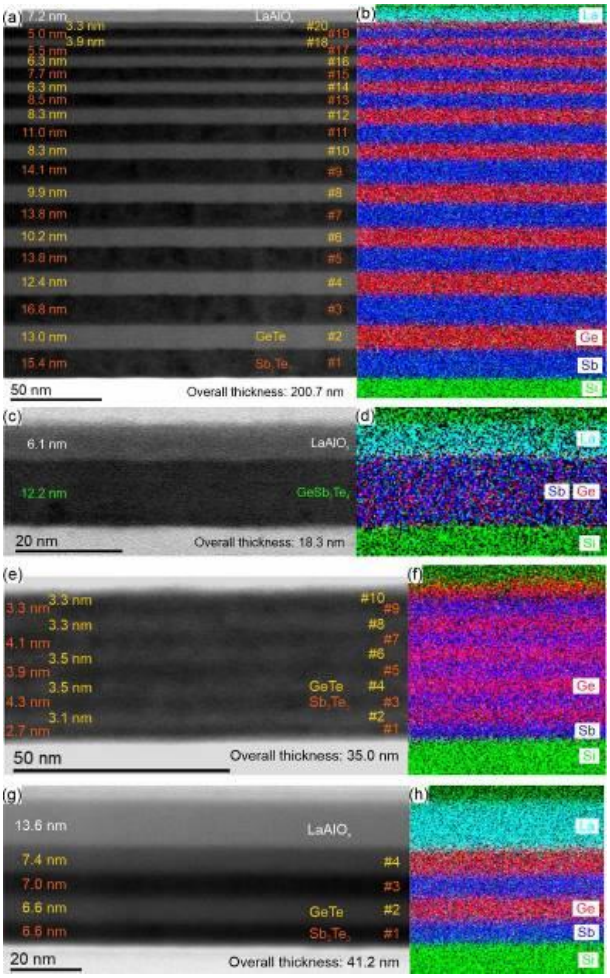

Fig. 2

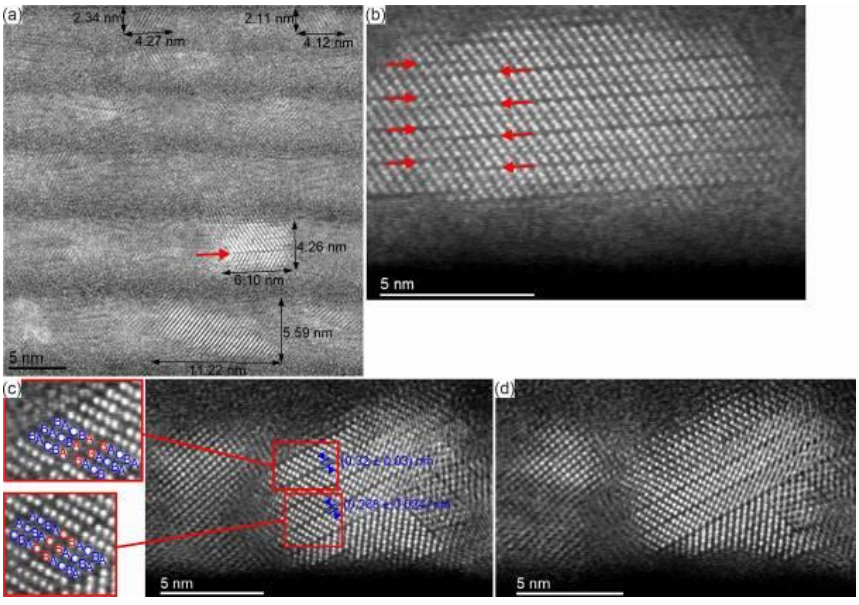

MS4.P005

Phase transitions in Cu-Sb_2Te_3 thin film systems induced by focused ion beam milling

N. Braun[1], V. Roddatis[2], A. Mill[1], S. Cremer[1], H. Bryja[1], L. Voss[3], S. Sun[4], L. Kienle[3], W. Zhang[4], A. Lotnyk[1,5,6]

[1]Leibniz Institute of Surface Engineering e.V. (IOM), Material Characterization and Analytical Service, Leipzig, Germany
[2]GFZ German Research Centre for Geosciences, Potsdam, Germany
[3]University of Kiel, Institute for Materials Science, Faculty of Engineering, Kiel, Germany
[4]Xi'an Jiaotong University, Center for Advancing Materials Performance from the Nanoscale, State Key Laboratory for Mechanical Behavior of Materials, Xi'an, China
[5]Ningbo University, Laboratory of Infrared Materials and Devices, The Research Institute of Advanced Technologies, Ningbo, China
[6]Harbin Engineering University, College of Physics and Optoelectronic Engineering, Harbin, China

Specimen preparation for transmission electron microscopy (TEM) using focused ion beam (FIB) is a commonly used method [1]. While it offers many advantages over other methods, like site specific specimen preparation, it also suffers from many disadvantages. Artifacts induced by FIB range from ion implantation to thermal effects [2,3]. In this work, we study the impact of FIB milling on the microstructure of Cu (electrode)-Sb_2Te_3 (thin films) systems used for memory applications [4]. The influence of different factors such as ion beam current, layer stacking sequence, Sb_2Te_3 structure and layer thickness are evaluated.

Sb_2Te_3 thin layers are epitaxially grown on p-type Si (111) substrates, while polycrystalline Sb_2Te_3 thin films are grown on SiO_2 using pulsed laser deposition (PLD) [4]. Cu, Pt/Cu and Cr layers are deposited by magnetron sputtering on top of the Sb_2Te_3 layers. TEM specimens are prepared at varied beam currents using a standard cross-section FIB preparation method [1]. FIB specimens are investigated using advanced methods of aberration-corrected scanning TEM such as atomic-scale HAADF imaging and atomic-scale chemical analysis (EDX and EELS). In situ x-ray diffraction heating of the Cu-Sb_2Te_3 thin film is performed to confirm structural changes.

Dependent on beam current used during FIB lamella preparation and Sb_2Te_3 layer thickness, hole formation in the Cu layer, thickness change and chemical changes of the Sb_2Te_3 layers are observed (Fig. 1). Samples with a 17 nm Sb_2Te_3 layer show uniform intercalation of Cu while a sample with 100 nm thick Sb_2Te_3 layer exhibits differential intercalation behavior. In specimen prepared from the in situ heated samples Sb_2Te_3 and Cu-Te grains are observed. The introduction of a Pt layer between the Cu electrode and Sb_2Te_3 layers hinders structural changes caused by FIB (Fig. 2). Moreover, Cr-Sb_2Te_3 and a Cu-GeTe layer systems show no modifications of Sb_2Te_3 and GeTe thin films during FIB preparation. In polycrystalline Sb_2Te_3 specimen the intercalation of Cu and formation of new phases is also observed.

This work demonstrates that structural changes in Sb_2Te_3 thin film systems can be induced during FIB specimen preparation of Cu (electrode)-Sb_2Te_3 (thin films) systems. The changes are thermally induced transitions caused by FIB process due to local heating, while redeposition of Cu plays a minor role.

The authors thank P. Hertel for magnetron sputtering. We acknowledge the financial support by the German Research Foundation (DFG 448667535).

[1] T. Ishitani, et al., Microscopy 43.5 (1994): 322-326.

[2] J. Mayer, et al., MRS bulletin 32.5 (2007): 400-407.

[3] R. Schmied, et al., Physical Chemistry Chemical Physics (2014), 6153.

[4] H. Bryja, et al., 2D Materials (2021), 045027.

Fig. 1: (a) EDX Map of a lamella prepared with FIB, (b-c) Overview HAADF-STEM images of specimen prepared with normal and reduced FIB beam currents. (d) Atomic-resolution HAADF-STEM image showing new Cu-Te phases.

Fig. 2: Cu/Pt/Sb_2Te_3 layer stack. (a) Overview HAADF-STEM image. (b) Overview EDX elemental map. (c) Atomic-resolution HAADF-STEM image, showing initial Sb_2Te_3 structure.

Fig. 1

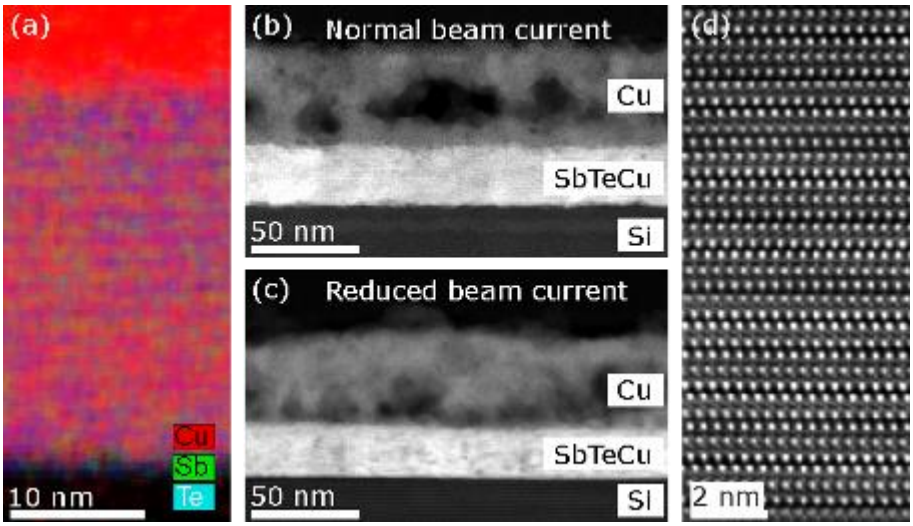
(a)
Cu
Sb
Te
10 nm
(b) Normal beam current
Cu
SbTeCu
50 nm
Si
(c) Reduced beam current
Cu
SbTeCu
50 nm
Si
(d)
2 nm

Fig. 2

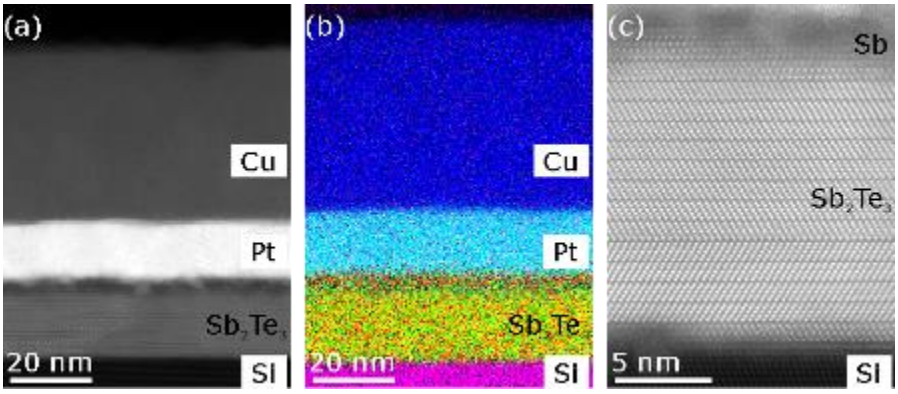
(a)
Cu
Pt
Sb2Te3
20 nm
Si
(b)
Cu
Pt
Sb2Te3
20 nm
Si
(c)
Sb
Sb2Te3
5 nm
Si

MS4.P006

Diffusion processes in HfO_2-based memristors investigated by *in situ* STEM and atom probe tomography

R. Winkler[1], T. Luo[2], A. Zintler[3], E. Matheret[1], T. Jiang[1], O. Recalde-Benitez[1], D. Nasiou[1], S. Petzold[4], N. Kaiser[4], E. Piros[4], T. Vogel[4], K. McKenna[5], L. Alff[4], B. Gault[2,6], L. Molina-Luna[1]

[1]TU Darmstadt, Advanced Electron Microscopy, Institute of Materials Science, Department of Materials and Earth Sciences, Darmstadt, Germany
[2]Max-Planck-Institut für Eisenforschung, Atom Probe Tomography, Department Microstructure Physics and Alloy Design, Düsseldorf, Germany
[3]Karlsruher Institut für Technologie (KIT), Laboratorium für Elektronenmikroskopie, Karlsruhe, Germany
[4]TU Darmstadt, Advanced Thin Film Technology, Institute of Materials Science, Department of Materials and Earth Sciences, Darmstadt, Germany
[5]University of York, Department of Physics, York, United Kingdom
[6]Imperial College, Department of Materials, Royal School of Mines, London, United Kingdom

Ionic movement is an essential part of Resistive Random Access Memory[1]. During resistive switching (RS) operations, the memory type determines the diffusing species: in the case of electrochemical metallization memory (ECM), the electrode material migrates and for the valence change memory (VCM) type, the oxygen anions and vacancies[2]. Moreover, the interfacial interactions in the metal-insulator-metal (MIM) RRAM cell can further impact RS[3].

To give insight into the diffusion processes for both ECM and VCM type HfO_2-based memristors we have employed in situ scanning transmission electron microscopy (STEM) in combination with atom probe tomography (APT). The goal is to reveal the role of the microstructure of the insulator and the impact of the metal electrode on the ionic migration process.

The investigated memristive devices consist of highly textured TiN (M) and HfO2 (I) thin films subsequently grown on *c*-cut sapphire by using reactive molecular beam epitaxy (RMBE), complemented by sputter deposition of Cu and Pt (M). These result in an ECM and VCM devices, respectively. From the VCM device, focused ion beam (FIB) lamellae for STEM and APT tips were prepared for a pristine device and a device that has been operated for 100 bipolar resistive switching (BRS) cycles. From the ECM device, FIB lamellae were transferred onto Micro Electrical Mechanical System (MEMS) based heating chips (DENSsolutions) for in situ STEM.

For the BRS cycled VCM device, Figure 1 shows the Hf+O density variation retrieved from one APT data set overlaid on a medium-angle annular dark-field (MAADF) STEM plan view image of TiN. The highest variation occurs along a distinct line which, based on the feature size, is related to a TiN grain boundary (GBs). This indicates that the RS operation could be confined to the TiN GBs. For the ECM device, a low-loss electron energy loss spectroscopy (EELS) spectrum image (SI) map is overlaid on a cross-sectional high-angle annular dark field (HAADF) STEM image after in situ heating, shown in Figure 2. Cu diffusion started at ~350°C and the Cu feature in the EELS map at ~19.6 eV becomes present at a HfO_2 GB. This demonstrates that Cu diffusion could primarily occur along GBs.

We have shown that GBs influence and locally confine diffusion processes. For filament-type RS like in metal-oxide based memristor, this could lead to an improvement in variability and reliability by providing pre-defined diffusion pathways and thus, avoiding random diffusion.

References:

[1] R. Waser *et al.*, Advanced Materials **21**, 2632 (2009).

[2] I. Valov, Semicond. Sci. Technol. **32**, 093006 (2017).

[3] S. R. Bradley *et al.*, Microelectronic Engineering **109**, 346 (2013).

Figure 1: The $Hf+O_2$ density variation retrieved from one APT data set for a VCM HfO_2-based memristor cycled for 100 BRS operations shows the highest variation along a distinct line. As overlaid here with a plan-view MAADF STEM image from TiN it becomes clear, that the feature shown in the Hf+O density variation must be related to a TiN grain boundary based on the feature size.

Figure 2: The EELS SI map overlaid on the cross-sectional AADFSTEM image of an ECM type HfO_2-based memristor after in situ heating reveals, that the Cu feature located at ~19.6 eV becomes present at the grain boundary (GB). This showcases, that Cu should primarily diffuse along GBs.

The authors acknowledge funding from the ERC "Horizon 2020" under Grant No. 805359-FOXON and Grant No. 957521-STARE.

Fig. 1

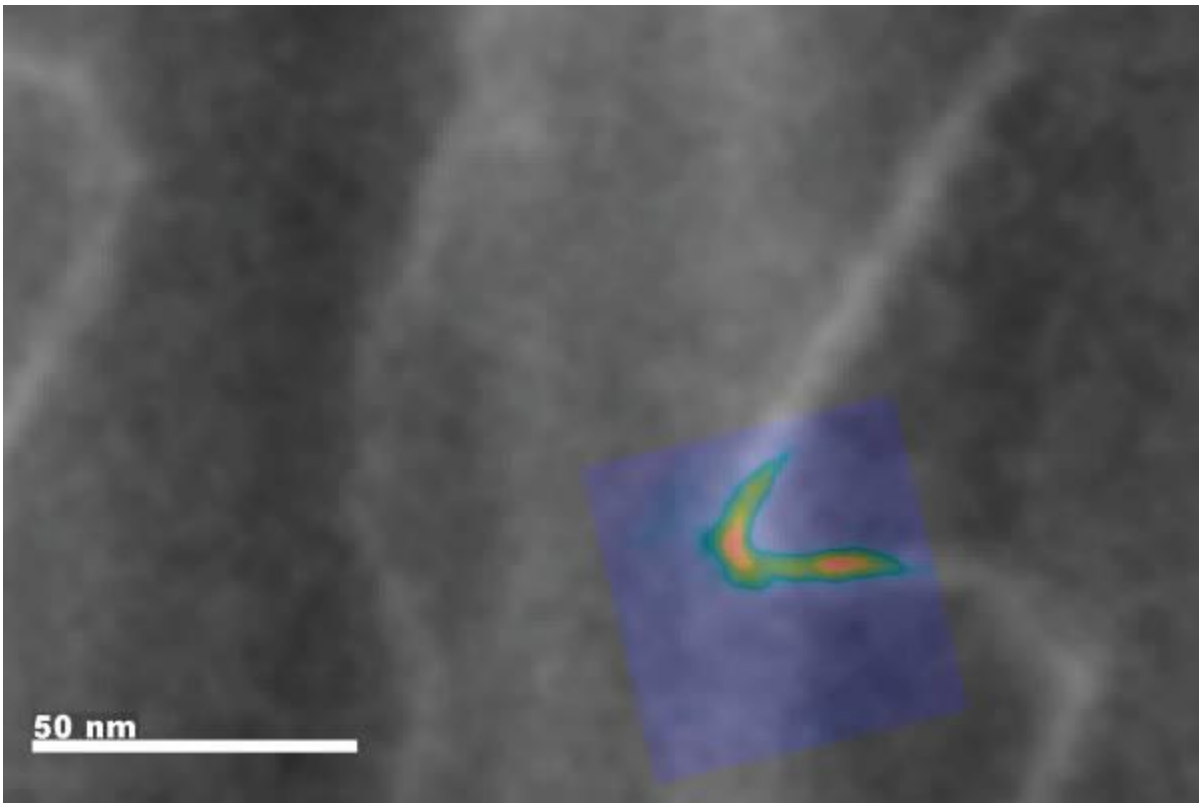

Fig. 2

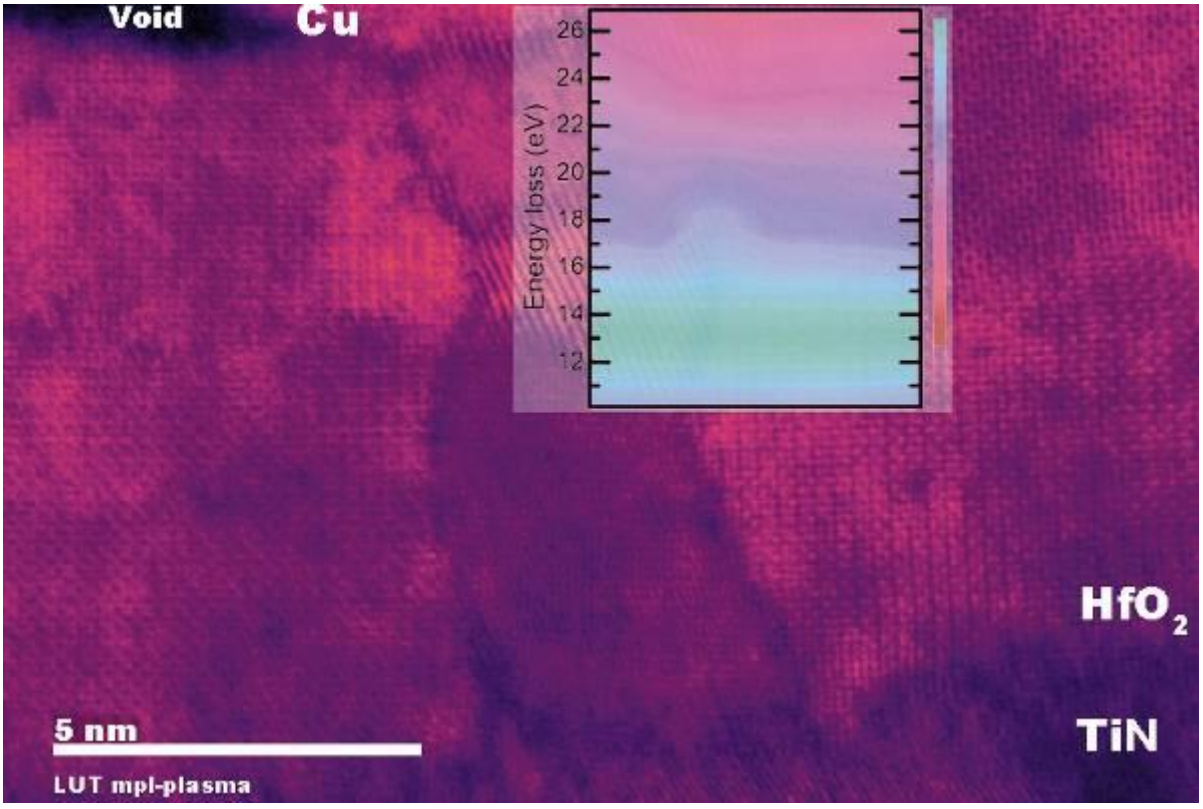

MS4.P007

Depicting atomic-resolution orbital occupation in hole doped high-t_c superconducting superlattices

N. Bonmassar[1], G. Christiani[1], G. Logvenov[1], Y. E. Suyolcu[1], P. A. van Aken[1]

[1]Max Planck Institute for Solid State Research, Stuttgart Center for Electron Microscopy, Stuttgart, Germany

La_2CuO_4 changes from an antiferromagnetic Mott-insulator into a superconductor upon hole doping. This phase transition can be observed via spectral features in the pre-edge region of the O-K edge by means of electron energy-loss spectroscopy (EELS). The O-K energy-loss near-edge structures (ELNES) allow the direct probing of this hole doping with atomic resolution.

We designed superlattices for the observation of evolving mobile carrier peaks (MCPs), the presence of the upper Hubbard band (UHB), and different Sr and Oxygen concentrations in direct proximity to each other. We link such electronic configurations and chemical distributions to the subsequent physical properties. Direct probing at the atomic-scale in order to differentiate between superconducting, metallic, and insulating parts in one single sample is unique, which to the best of our knowledge has not been shown before. This prospect, however, is of paramount interest for exploring future oxide-based quantum technologies, such as Josephson junctions.

The two heterostructures presented here consist of five repetitions of a bilayer with four and three unit cells La_2CuO_4 (LCO) and one unit cell Sr_2CuO_3 (SCO) with an additional capping layer of three and four unit cells La_2CuO_4, respectively. All superlattices have been grown via molecular-beam epitaxy (MBE) monitored by *in-situ* reflection high-energy electron diffraction (RHEED) under an ozone atmosphere on a $LaSrAlO_4$ (LSAO) (001)-oriented substrate. The samples have been characterized by resistance (R) versus temperature measurements, and scanning transmission electron microscopy (STEM); including EELS and high-angle annular dark-field (HAADF) imaging.

Transport properties of both heterostructures (Fig. 1) yield critical temperatures (T_c) of 32K for the 5x[4LCO + SCO] and 40K for the 5x[3LCO + SCO] superlattices, respectively. Due to the chemical potential between LCO and SCO, different amounts of intermixing between La and Sr can be observed at the top and bottom interfaces. This leads to a partial formation of insulating areas without charge carriers, superconducting areas with mobile carriers, and metallic areas with mobile carriers and oxygen vacancies. These phase-separated sample regions are further discussed with respect to their orbital occupation via a combination of atomically resolved EELS mappings and O-K ELNES analyses (Fig. 2). Further investigations of the blue-shaded area in Figure 2 highlight differences in the out-of-plane and in-plane orbital occupation by the introduced electron holes.

Here, we show for the first time that one can distinguish insulating, superconducting, and metallic areas within one single sample via O-K ELNES analyses and atomically resolved EELS. We want to highlight, that EELS experiments gave direct insights into the differences in orbital occupation of out-of-plane and in-plane orbitals, which open new possibilities for analyses of high-T_c superconductors answering open questions with respect to superconductivity.

Figure1: Resistance vs temperature of the two superlattices 5x[3LCO + SCO] (blue), and 5x[4LCO + SCO] (red).

Figure2: (a) 2D elemental EELS mapping (Sr: blue, Cu: green, La: red) of three different regions highlighting areas without Sr intermixing (red) and heavy Sr intermixing (blue). (b), (c) and (d) Gaussian fits with energy constraints for the MCP (blue) at 528 eV, the UHB (red) at 530.5 eV, and for the leading O-K edge-onset, a peak at 534 eV (turquoise).

Fig. 1

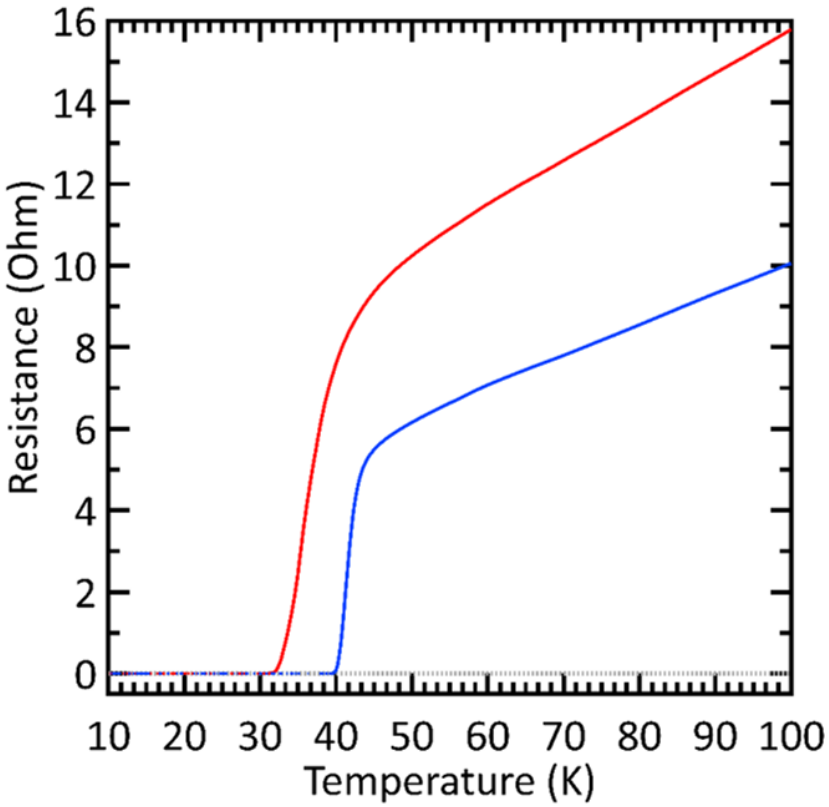
Resistance (Ohm)
Temperature (K)
0
2
4
6
8
10
12
14
16
10 20 30 40 50 60 70 80 90 100

Fig. 2

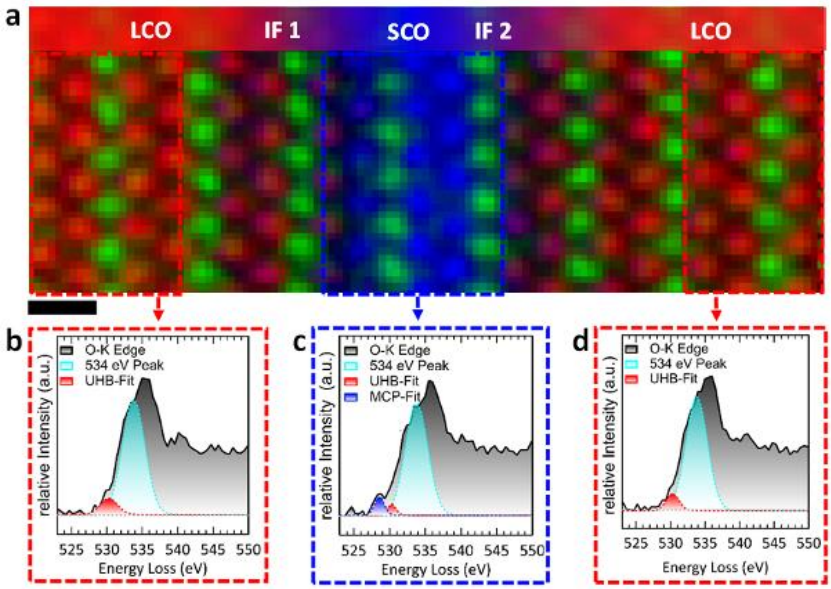
a
LCO
IF 1
SCO
IF 2
LCO
b
c
d
O-K Edge
534 eV Peak
UHB-Fit
MCP-Fit
relative Intensity (a.u.)
525 530 535 540 545 550
Energy Loss (eV)

MS4.P008

Revealing the nanostructure of filamentary HfO2-based memristors by scanning precession electron diffraction (SPED)

D. Nasiou[1], A. Zintler[2], R. Winkler[1], T. Vogel[3], T. Kim[3], O. Recalde-Benitez[1], T. Jiang[1], L. Alff[3], L. Molina-Luna[1]

[1]Technische Universität Darmstadt, Advanced Electron Microscopy, Darmstadt, Germany
[2]Karlsruher Institut für Technologie (KIT), Laboratorium für Elektronenmikroskopie, Karlsruhe, Germany
[3]Technische Universität Darmstadt, Advanced Thin Film Technology, Darmstadt, Germany

Introduction: Resistive random-access memory (RRAM) devices are under intense research as they have low-power consumption, excellent scalability, enhanced storage density and, high speed operation [1]. The resistive switching phenomenon is thought to be governed by the formation and dissolution of a conductive nanofilament when a voltage is applied [2,3]. As previously investigated, the electrical behaviour of hafnia-based RRAM devices is correlated to the local crystallographic texture and microstructure [4].

Objectives: SPED was used to investigate two different Cu/HfO2/Pt RRAM devices. The layer structure is shown in fig1(a). The goal was to map the microstructure and establish a structure-property correlation.

Materials & methods: By using reactive molecular beam epitaxy (RMBE) 20 nm thick HfO2 thin films were grown on top of sputtered Pt bottom electrodes. The top Cu electrode was deposited with different ways by an (i) ion beam etching (IBE) procedure and by (ii) simple lift out (SLO). Electron transparent cross sectional TEM lamellas were fabricated using a JEOL JIB 4600F Focused Ion Beam. For SPED acquisition, a scanning nanoprobe (in 2D real space) was controlled with a NanoMEGAS P1000 scanning unit integrated into a JEOL-ARM200F and a dynamic Medipix3 detector was used for synchronized electron diffraction patterns (EDP) acquisition (in 2D reciprocal space).

Results: Experimental EDP was cross correlated and statistically matched with suitable simulated EDP with the software ASTAR to generate the orientation fig2(a,c) and phase fig2(b,d) maps. For both devices the orientation and grain size (5 -20 nm) of the dielectric is similar as they were grown under the same conditions. From the phase maps, the monoclinic phase of the HfO2 is revealed and matches to the XRD data. The results show that the Cu is homogeneously grown on the SLO devices and that it is not well distributed in the IBE devices. In the last ones, unexpected Pt traces were found which might have an influence on the electrical performance of the device. In fig1(b) the leakage currents of both devices are shown, in SLO the magnitude is lower than in IBE which could be due to the inhomogeneous Cu and the Pt traces on top of HfO2.

Conclusion: The generated maps confirm the monoclinic phase of the HfO2 dielectric layer and reveal a similar grain distribution in both SLO and IBE devices. Also, from the phase maps, the SLO devices show well distributed layers which might explain their electrical performance.

[1] Zahoor et al. Nanoscale Res Lett 15 (90) (2020)

[2] R Waser et al., Adv. Mater. 21 (25–26) (2009) 2632-2663

[3] M. Lanza et al., Appl. Phys. Lett. 100 (12) (2012) 123508.

[4] S. Petzold, A. Zintler et al., Adv. Electron. Mater. 5 (10) (2019) 1900484

The authors acknowledge funding from the ERC "Horizon 2020" Program under Grant No. 805359-FOXON and Grant No. 957521-STARE, from the DFG grant No. 384682067, from the BMBF under contract 16ESE0298 and 16MEE0154, from the DAAD, from the EPSCR and support by the framework of the the WAKeMeUP and StorAIge projects.

Fig1: (a) The thin film stacks of the two different studied devices: IBE and SLO. (b) Their corresponding leakage current measurements.

Fig2: SLO *devices:* (a) orientation map of Cu/HfO2/Pt device. Each colour reveals an orientation and (b) phase map of the three layers: Cu in red, *m*-HfO2 in blue and Pt in green. IBE *devices:* (c) orientation map and (d) phase map. Scale bar: 50 nm.

Fig. 1

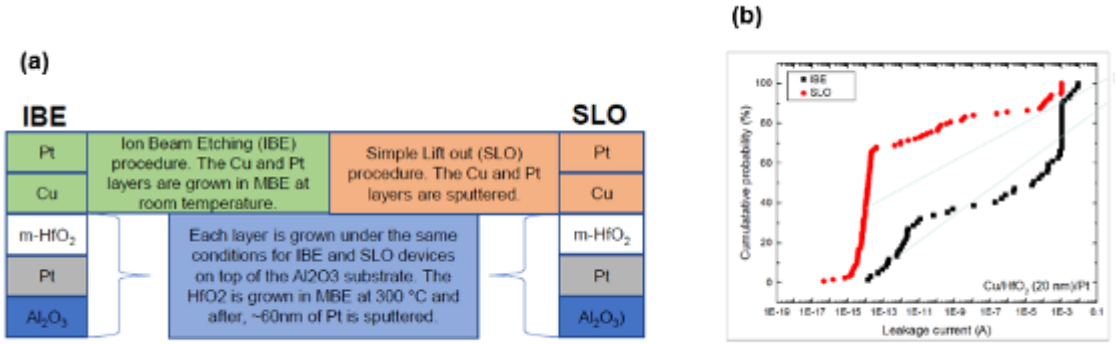
(a)
IBE
SLO
Pt
Cu
m-HfO2
Pt
Al2O3
Ion Beam Etching (IBE) procedure. The Cu and Pt layers are grown in MBE at room temperature.
Simple Lift out (SLO) procedure. The Cu and Pt layers are sputtered.
Each layer is grown under the same conditions for IBE and SLO devices on top of the Al2O3 substrate. The HfO2 is grown in MBE at 300 °C and after, ~60nm of Pt is sputtered.
(b)
IBE
SLO
Cumulative probability (%)
Leakage current (A)

Fig. 2

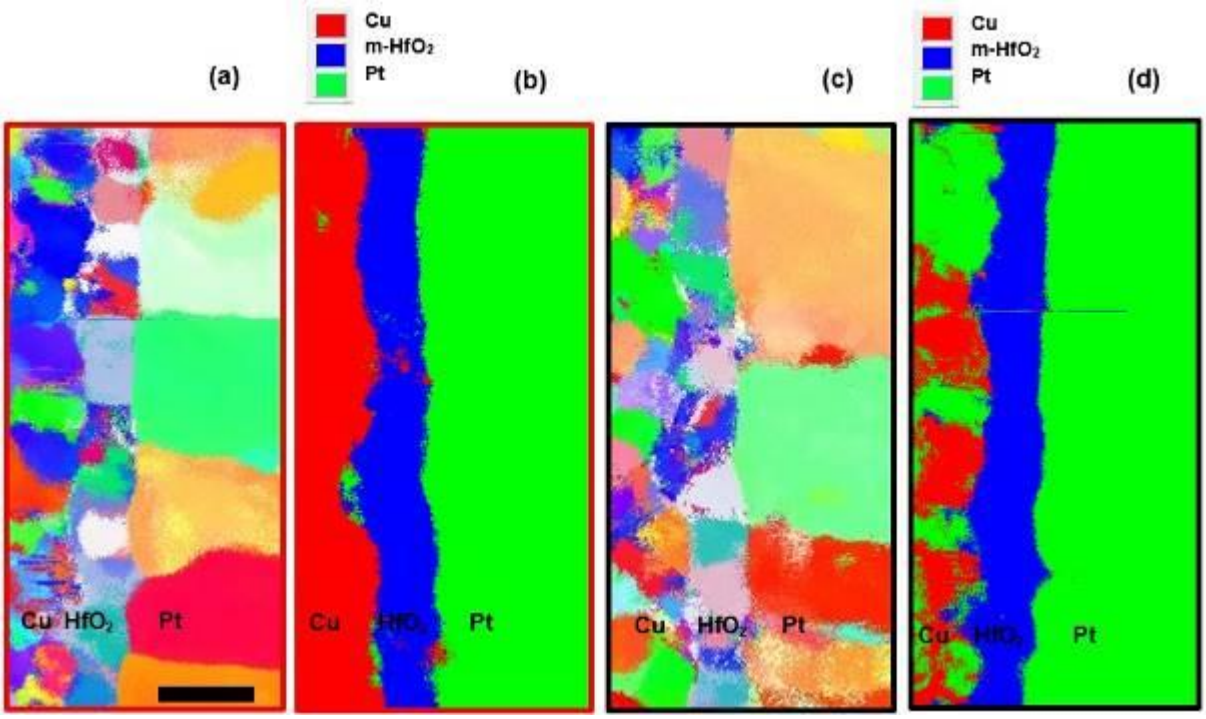
(a)
(b)
(c)
(d)
Cu
m-HfO2
Pt
Cu
HfO2
Pt

MS4.P009

Study of local indium concentration in $Ga_{(1-x)}In_xN$ quantum wells using quantitative scanning transmission electron microscopy

D. Park[1,2], J. Guckel[1,2], P. Horenburg[3], H. Bremers[3,2], U. Rossow[3], A. Hangleiter[3,2], H. Bosse[1,2]

[1]Physikalische Technische Bundesanstalt, Braunschweig, Germany
[2]Laboratory of Emerging Nanometrology (LENA), Braunschweig, Germany
[3]Technische Universität Braunschweig, Institute of Applied Physics, Braunschweig, Germany

Multiple quantum wells (MQW) and single quantum wells (SQW) of $Ga_{(1-x)}In_xN$ on GaN are promising candidates for nanooptical light emitters due to high quantum efficiency. The band gap of $Ga_{(1-x)}In_xN$ can be controlled over a wide wavelength range by tailoring the variation of the indium concentration [1]. In addition, the epitaxially grown quantum well structures can be easily modified using chemical etching for the formation of a pyramid containing quasi quantum dot structure. As the dimension of the quantum structure shrinks, the variation of the local indium concentration becomes detrimental to the optical properties. Therefore, a robust characterization technique is required to understand and optimize such complex structures on the atomic scale.

In this study, a single quantum well of $Ga_{(1-x)}In_xN$ between GaN layers on an Al_2O_3 substrate was grown using metal organic vapor phase epitaxy. The cross-sectional specimen was prepared using focused ion beam (FIB), including the final low kV milling step. The prepared specimen was characterized using a double-aberration corrected JEOL NeoARM 200F equipped with a cold field emission gun. We directly measured local lattice parameters based on the analysis of individual atomic column positions obtained from the high-angle annular dark-field (HAADF) image in real space. For a precise local lattice parameter analysis, drift-corrected HAADF imaging was utilized based on a sequential imaging technique with reasonably short acquisition time (1 sec/frame) accompanied by post rigid registration technique for drift correction between acquired images (Fig. 1). Then, the local indium concentration was derived using a modified Vegard's law including biaxial elastic strain effects. Fig. 2(a) shows the HAADF image of the epitaxially grown GaN/$Ga_{(1-x)}In_xN$/GaN structure and the individual indium contents derived using the modified Vegard's law is shown at the unit cell level in Fig. 2(b). The mean indium concentration inside the single quantum well from this analysis was 15.7 at. %, showing a very good agreement with the X-ray diffraction (XRD) analysis result. This result was compared with the local composition information obtained from a quantitative intensity analysis of the HAADF image. Absolute quantification of scanning transmission electron microscopy (STEM) - HAADF intensity (normalized intensity by the incident electron beam) was applied based on frozen phonon multislice calculation results [2]. The local thickness information obtained using position averaged convergent beam electron diffraction (PACBED) supported the quantitative intensity analysis [3]. In addition, the local composition information obtained from the intensity analysis was compared with the results from the quantitative STEM – electron energy-loss (EEL) spectroscopy analysis on the unit cell level.

The combination of STEM imaging, PACBED and spatially resolved EEL spectroscopy techniques shows the validation of Vegard"s law for the $Ga_{(1-x)}In_xN$ quantum well, providing more detailed information at the interfaces. The relationship between atomic structure and composition could be thoroughly studied. This robust combined STEM techniques will be ultimately applied to understand the effect of the changes in indium concentration on complex quantum dot structures.

[1] U. Rossow et. al., Phys. Status Solidi B, 258, (2021)

[2] J. LeBeau et. al., Physical review Letters, 100, (2008)

[3] J. LeBeau et. al., Ultramicroscopy, 110(2), (2010)

Fig. 1

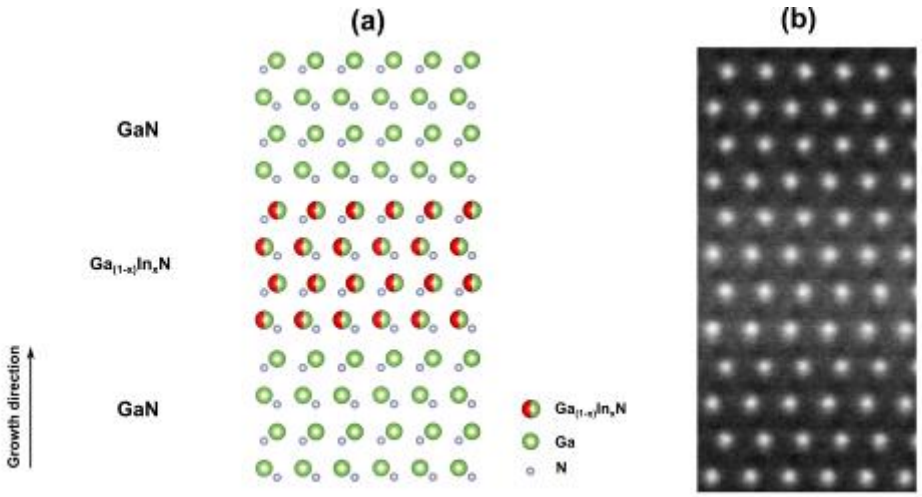

Figure 1: (a) the atomic model of the $Ga_{(1-x)}In_xN$ between the GaN layers and (b) the corresponding drift-corrected STEM HAADF image.

Fig. 2

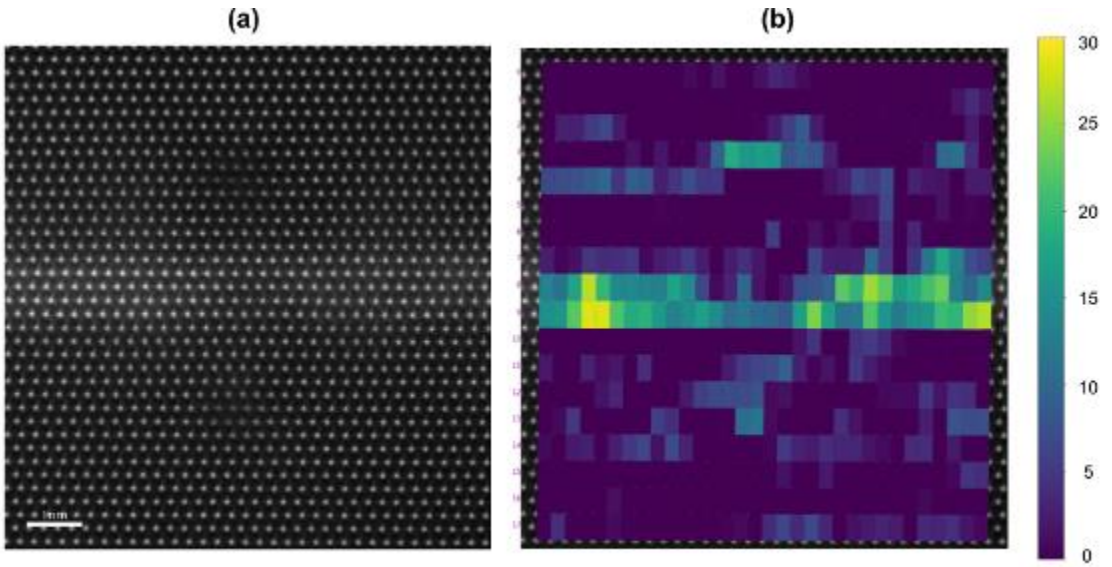

Figure 2: (a) the HAADF image of the $Ga_{(1-x)}In_xN$ between the GaN layers and (b) local indium concentration (at.%) calculated using modified Vegards's law based on the directly measured lattice parameters on the unit cell level.

MS4.P010

Identification of a new structural polymorph of quenched high-pressure $CrTe_3$ (*P*2/*m*)

L. Voss[1], M. Etter[2], N. Gaida[3], A. L. Hansen[4], N. Wolff[1], V. Duppel[5], A. Lotnyk[6,7], W. Bensch[8], L. Kienle[1]

[1]Christian-Albrechts-University Kiel, Technical Faculty, Kiel, Germany
[2]Deutsches Elektronen-Synchrotron DESY, Hamburg, Germany
[3]Nagoya University, Department of Materials Physics, Nagoya, Japan
[4]Karlsruher Institut of Technologie (KIT), Karlsruhe, Germany
[5]Max Planck Institute for Solid State Research, Stuttgart, Germany
[6]Leibniz Institute of Surface Engineering e.V. (IOM), Leipzig, Germany
[7]Laboratory of Infrared Materials and Devices, The Research Institute of Advanced Technologies, Zhejiang, China
[8]Christian-Albrechts-University Kiel, Inorganic Chemistry, Kiel, Germany

CrTe ($P2_1/c$) is of potential interest for spintronic devices because of its layered structural motif and antiferromagnetic and semiconducting properties (Eg = 0.3 eV)[1]. Modifying these properties towards a ferromagnetic state and metallic-like conduction upon structure deformation is suggested by theoretical studies which describe a high strain sensitivity of the material when the dimensions are reduced to a monolayer of $CrTe_3$ [2]. Such studies are motivation to investigate the CrTe3 system further.

In the past, structural polymorphs of binary TE have been identified and described using high-p and high-T experiments as a vital approach to explore structural modifications with unprecedented properties [3,4]. In this work, the layered phase of CrTe3 was used as a starting material and subjected to pressures as high as 6GPa at an applied temperature of 250°C to investigate new structural polymorphs of $CrTe_3$ and their magnetic properties.

The structural polymorph of the quenched $CrTe_3$ high-p phase was investigated by the combined methods of synchrotron radiation scattering experiments (PDF and XRD) and PED as well as atomic resolution STEM. Model-based simulations of STEM and ED data were conducted and compared with structural refinements by Rietveld analysis for structure determination.

With our experiments, we were able to identify a phase transition from the monoclinic $CrTe_3$ phase ($P2_1/c$) into a structural polymorph with space group *P*2/*m.* At first, the superposition of two potential structure candidates of $CrTe_2$ (*Pnn*2) and $CrTe_4$ ($P2_1/m$) were refined. These initial models were tested to PED data which excluded the $CrTe_2$ model and suggested the introduction of a 1/3 occupied Cr position at the corners of the unit cell into the supposed $CrTe_4$ structure to explain the kinematic intensity patterns. Further, large area EDX analysis confirmed the chemical homogeneity within large grains of the $CrTe_3$ polymorph with stoichiometry of Cr:Te 1:3. The here proposed structure of the new polymorph after refinement to the synchrotron diffraction data is depicted in Figure 1. Atomic scale imaging by aberration corrected STEM supported the proposed model by imaging the Te sub-structure.

In conclusion, a new structural polymorph of the $CrTe_3$ system was identified after high-pressure synthesis and subsequent quenching by the combined approach of TEM and synchrotron diffraction. In ongoing research, first SQUID measurements indicate interesting changes of the magnetic properties which could provide similarities to the theoretical calculations made by Z.-W. Lu et al[2].

[1] M. A. McGuire *et al.*, *Phys. Rev. B*, vol. 95, no. 14, p. 144421, Apr. 2017, doi: 10.1103/PhysRevB.95.144421.

[2] Z.-W. Lu, S.-B. Qiu, W.-Q. Xie, X.-B. Yang, and Y.-J. Zhao, *J. Appl. Phys.*, vol. 127, no. 3, p. 033903, Jan. 2020, doi: 10.1063/1.5126246.

[3] A. Pawbake *et al.*, *Phys. Rev. Lett.*, vol. 122, no. 14, p. 145701, Apr. 2019, doi: 10.1103/PhysRevLett.122.145701.

[4] W. C. Yu and P. J. Gielisse, *Mater. Res. Bull.*, vol. 6, no. 7, pp. 621–638, Jul. 1971, doi: 10.1016/0025-5408(71)90011-0.

Figure 1: Crystal structure of the quenched high-pressure phase of $CrTe_3$ with space group *P*2/*m* shown for a unit cell of 2x2x2 size. The corner-sharing motif can be best seen by a view along the crystallographic *b*-axis(a). Golden atoms are Te, blue are Cr. The edge-sharing motif and columnar ordering of the $CrTe_6$ octahedra can be best seen by a view along the crystallographic *c*-axis (b).

Fig. 1

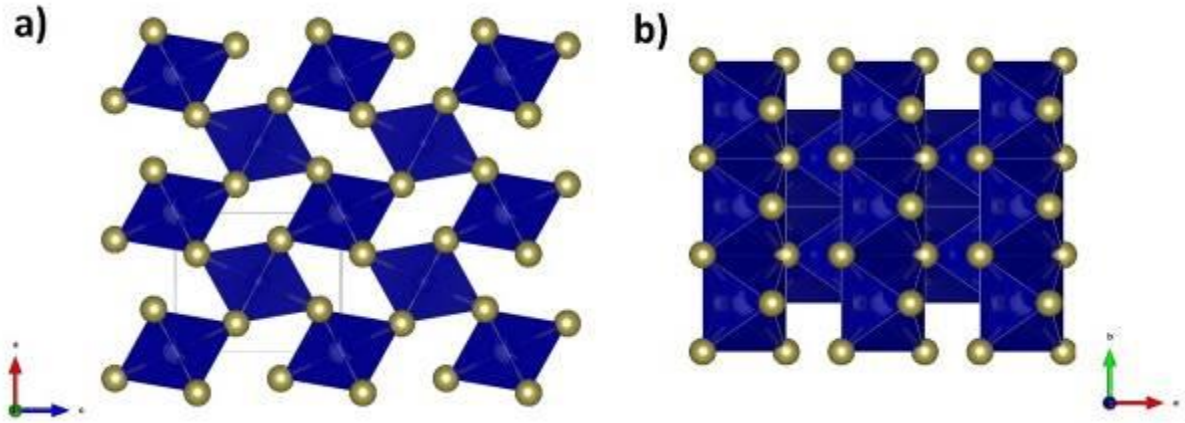

MS4.P011

Insight into the atomic structure and misfit relaxation mechanisms in micrometer-thick $SrMoO_3$ oxide electrodes grown on scandate substrates

T. Jiang[1], O. Recalde-Benitez[1], Y. Ruan[1], T. Zhang[1], F. Liang[1], L. Alff[1], P. Komissinsky[1], L. Molina-Luna[1]

[1]TU Darmstadt, Darmstadt, Germany

Introduction: Understanding the microstructure and related defect structures and their relationship with the physical properties is fundamental for the realization and optimization of oxide electronics-based devices. For instance, in the case of varactors or so-called metal-insulator-metal (MIM) tunable ferroelectric microwave capacitors, the tunable permittivity of the insulator layer and/or the thickness of the bottom oxide electrode exceeding the skin depth is crucial for its performance. To investigate the relationship between the thickness and other structural properties of these oxide thin films, i.e., alteration of stoichiometry and lattice constants, we performed Scanning Transmission Electron Microscopy along with X-ray diffraction (XRD) and Photoemission spectroscopy (PES).

Objectives: We characterized a set of heterostructure multilayer devices (scandates/SrTiO3/SrMoO3) by STEM. For the analysis of the HAADF-STEM images we implemented an automated-quantitative STEM method that allows to analyze a set of real-space images to (i) extract atomic position information and (ii) to identify local structural defects. The goal was to provide insight into the underlying strain accommodation mechanism in micrometer-thick SrMoO3 (SMO) oxide electrodes grown on various scandate substrates.

Materials and methods: The preparation procedure of the oxide-based multilayer devices can be found in P. Salg *et al.* [1]. The TEM lamellae were obtained using a JEOL JIB 4600F. For STEM, images with 5x5 frames along [001] and [100] directions of the epitaxial SMO layer were obtained using a JEOL ARM200F. Local in-plane/out-of-plane lattice constants were extracted along [001] growth direction by implementing customized codes, based on the python packages *Atomap* and *Hyperspy*. Picometer level precision was achieved. First principal calculations for SMO using density function theory (DFT) with the *CASTEP* package.

Results:

Both, XRD and STEM imaging (Fig.1a) confirmed the epitaxial growth (in-plane locked) of the SMO layer on top of all scandate substrates used. By performing automated-quantitative STEM analysis, atomic position information was obtained, as well as statistical out-of-plane/in-plane lattice constants (Fig.1b). The variation of this statistical lattice constants implies another strain accommodation mechanism, *i.e.,* off stoichiometry, in heterostructure material in addition to interfacial defects. The DFT calculations for SMO layer confirmed the relationship between the variation of lattice constants and the off stoichiometry.

Conclusions: A set of heterostructure multilayer devices were characterized by the combination of PES, XRD and STEM. The use of the automated-quantitative image analysis showed a reliable way to measure the local lattice constants with picometer-scale accuracy. Together with the help of DFT calculations, the relationship between the interfacial defects, the lattice constant, the off stoichiometry, and the accumulative strain was studied.

References:

[1] P. Salg, D. Walk and L. Zeinar *et al.*, APL Mater., **vol. 7** (2019), p. 051107. doi: 10.1063/1.5094855.

The authors acknowledge funding from the ERC "Horizon 2020" Program under Grant No. 805359-FOXON and Grant No. 957521-STARE.

Fig 1(a). HAADF-STEM image of heterostructure interface scandate/SrTiO3/SrMoO3. (b) Atom position information were extracted using customized codes based on the *Atomap* python package.

Fig. 1

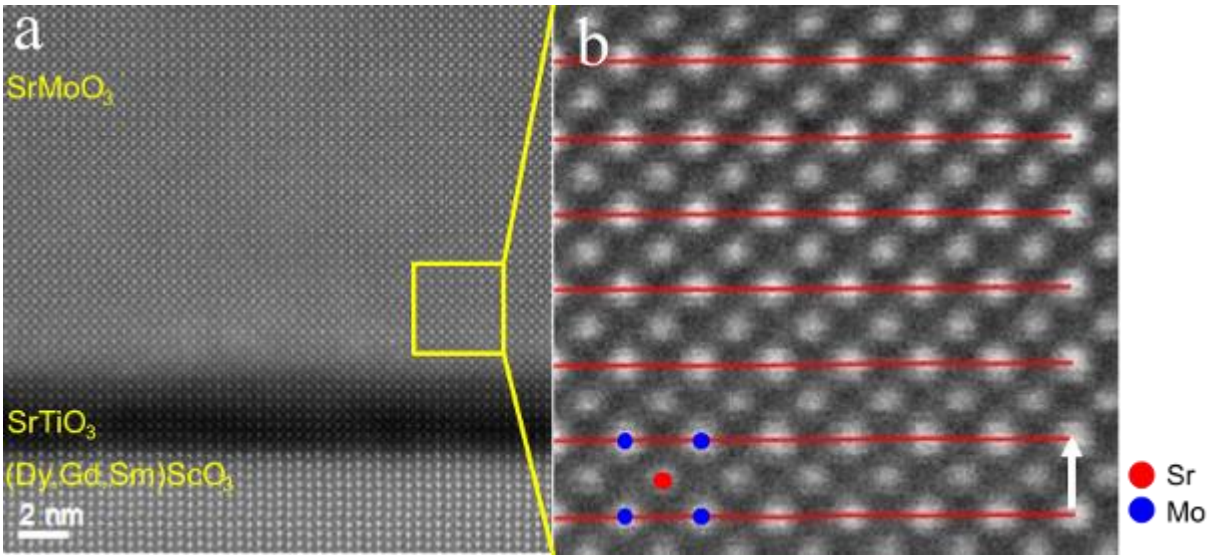

MS4.P012

Ordering of scandium into monolayers of aluminium nitride and its implication for AlScN based nitride semiconductor devices

U. Bläß[1], M. Wu[2], B. Epelbaum[1], E. Meißner[1,3]

[1]Fraunhofer Institute for Integrated Systems and Device Technology (IISB), Erlangen, Germany
[2]Institute of Micro- and Nanostructure Research (IMN) & Center for Nanoanalysis and Electron Microscopy (CENEM), Friedrich-Alexander-Universität Erlangen-Nürnberg, Erlangen, Germany
[3]Department of Electrical-Electronic-Communication Engineering, Chair of Electron Devices, Friedrich-Alexander-Universität Erlangen-Nürnberg, Erlangen, Germany

Recently the incorporation of scandium (Sc) into aluminium nitride (AlN) attracted severe attention for III-V nitride semiconductors. The sufficiently larger ionic size of Sc increases significantly the spontaneous polarisation of AlN (1), which is e.g. responsible for the formation of a two dimensional electron gas at the heterojunction to another, compositional slightly different nitride compound (2). This allows to fabricate high-electron mobility transistors (HEMT) with very high switching frequencies and high efficiencies.

However, the growths of well-crystalline AlScN material is impeded by a huge immiscibility gap between AlN and ScN. The material films deposited by magnetron sputtering or recently epitaxy are considered to exist only metastable (3). Intense annealing at temperatures beyond 1400°C for three hours, lead in this study to the formation of a layered structure of the compound, observed for the first time. The structural properties were intensely studies by atomic resolution STEM-HAADF images, EDS and EELS spectroscopy and will be reported in this contribution.

The results from STEM-HAADF images show clearly that bright atomic monolayers are developed every 5-8 layers, after annealing at 1700°C. They run straight through the whole crystal and extend several µm (Fig. 1a) along the basal plane. Following EDS data, the bright appearance is due to an ordering of Sc into these layers (Fig. 1 b,c) coupled to a strong increase in oxygen content. The Sc coordination changes from four-fold in the wurtzite structure to six-fold as preferred by Sc. Whereas the sequence of cation positions in atomic STEM-HAADF images is strongly determined, the sequence of bright layers varies randomly between 5 and 8, leading to a partial disorder along *c*-direction.

Further structural observations after annealing of samples at 1400°C allow some insight into their formation. Rarely platy seed of two octahedral Sc-bearing layers with only one intermittent AlN layers were observed. They are assumed to be thermodynamically favourable, similar to GdN platelets formed in Gd-doped GaN (4), but in contrast, significantly lower strain allows their two dimensional growths in the Sc-bearing system. Hence, this model of metastable formation resembles thermodynamical exsolution lamellae of mono-atomic widths.

The presented observations are not only intriguing from a structural point of view, the obtained insight into the material behaviour has also implications on the growths of future ScAlN material for semiconductor devices as well as their long-time stability during device operation.

References:

- (1) Akiyama et al., Adv. Mater. 21, 593–596 (2009).
- (2) Leone et al., Phys. Status Solidi RRL. 14, 1900535 (2020).
- (3) A. Moram and S. Zhang, J. Mater. Chem. A. 2, 6042–6050 (2014).
- (4) Wu et al., Acta Materialia. 76, 87–93 (2014).

Fig. 1: Left: atomic resolution STEM-HAADF image showing bright Sc-bearing layers at variable distance. Right: EDS elemental distribution maps and integrated counts perpendicular the layers.

Fig. 1

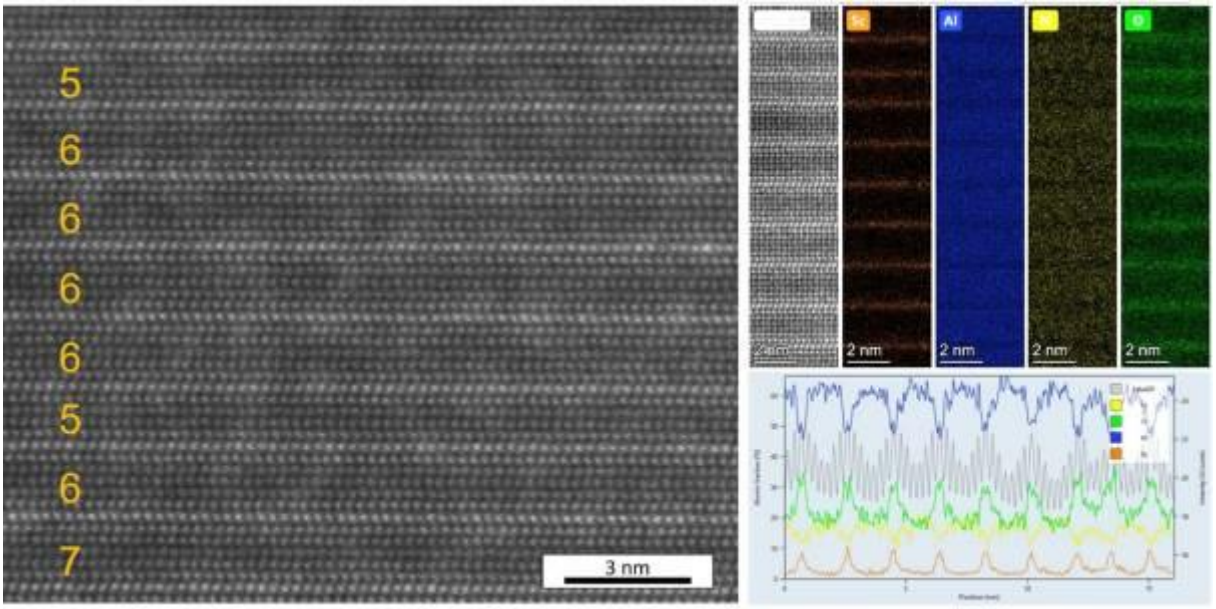

MS4.P013

The effect of metal concentration and annealing temperature on the growth of ultrasmall metallic nanoparticles inside a silica matrix

H. Jatav[1], D. Kabiraj[1], A. Mishra[1]

[1]Inter University Accelerator Centre, Materials science department, New Delhi, India

The nanocomposites (NCs) comprising ultra-small metallic Nanoparticles (NPs) embedded in silica matrix are more stable over time than chemically grown NPs and have shown improved practical efficiency, leading to a wide range of applications in plasmonics, nano-photonics, bio-medical and catalysis due to Localized Surface Plasmon Resonance (LSPR) [1-2]. The stability of these ultra-small NPs (diameter < 10 nm) is essential for high-temperature applications [3].The LSPR frequencies associated with NPs are strongly dependent on particle morphology and metal concentration, thus knowledge about the effect of metal concentration and the growth mechanisms of NPs at different annealing temperatures (ATs) are crucial to controlling the morphology of NPs for application purposes.

We have prepared Ag-SiO2 NC thin films using the atom beam co-sputtering technique at two different metal concentrations [4]. The evolution of silver NPs inside the silica matrix was discussed in Ref [4] utilising UV-Visible spectroscopy and High-Resolution Transmission Electron Microscopy (HRTEM) up to the annealing temperature of 400 °C. This work is now extended to the high annealing temperature of 900 °C. At each AT, HRTEM pictures, diffraction patterns, and STEM images are acquired to closely monitor the growth process of Ag NPs. A similar temperature-dependent growth investigation is also performed on Au and Au-Ag alloy NPs embedded in silica surrounds.

For Ag-SiO_2 NC, UV-Visible absorption spectra show a red shifting in the LSPR peak position, indicating the increase in the size of NPs with ATs. A quantum model simulation is combined with absorption results to estimate the size of the NPs at different ATs, suggesting the size of NPs is increasing. The morphological changes in NPs with ATs are monitored by HRTEM. We observed that the majority of the NPs are spherical in shape and remain in quantum size or ultra-small size regime (diameter < 10 nm). The diameter of the NPs varies from ~5 nm to 6.5 nm when the temperature rises from RT to 800 °C. However, exponential growth is observed at 900 °C. We observed that these ultra-small NPs have shown excellent stability up to the temperature of 800 °C, hence suitable for high-temperature applications. Similar primary results are observed for Au and Au-Ag alloy NCs, however, their detailed analysis is still ongoing. Based on the results, a three-stage mechanism is proposed to understand the process of nucleation and growth of the silica-embedded Ag NPs.

References:

[1] Campos, A., Troc, N., Cottancin, E., Pellarin, M., Weissker, H. C., Lermé, J.,& Hillenkamp, M. *Nature Physics* **2019**, *15*, 275-280.

[2] Amendola, V., Pilot, R., Frasconi, M., Marago, OM. Iati, MA. Jour. of Phy.: Cond. Mat. **2017**, 29, 203002.

[3] Goodman, E.D., Carlson, E.Z., Dietze, E.M., Tahsini, N., Johnson, A., Aitbekova, A., Taylor, T.N., Plessow, P.N. and Cargnello, M., *Nanoscale* ***13*****(2)**, 930-938 (2021)

[4] Jatav, Hemant, Ambuj Mishra, and D. Kabiraj. *Materials Today: Proceedings* 57 (2022): 234-238.

MS4.P014

Dimensionality-controlled interface properties in infinite-layer nickelate superlattices

C. Yang[1], Y. Wang[1,2], W. Sigle[1], R. A. Ortiz[1], H. Wang[1], E. Benckiser[1], B. Keimer[1], P. A. van Aken[1]

[1]Max Planck Institute for solid state research, Stuttgart, Germany
[2]Nanjing University of Aeronautics and Astronautics, Center for Microscopy and Analysis, Nanjing, China

The interface polarity plays a vital role in physical properties of oxide heterointerfaces since it can enforce the reconstruction of the electronic and atomic structure. A strong polar interface possibly exists in recently discovered nickelate superconductors and the superconductivity is absent in its bulk material, attracting increasing attentions on interface effects [1-4]. This motivated our investigation of the electronic and atomic structure at atomic scale at the interfaces of infinite-layer nickelates. Recently, we reported that advancedfour-dimensional scanning transmission electron microscopy (4D-STEM) technique can provide clear phase-contrast imaging of the oxygen sublattice [5].

Here, by employing 4D-STEM and atomic-resolution electron energy-loss spectroscopy (EELS), we systematically studied the oxygen distribution and atomic structure at the interface of infinite-layer $NdNiO_2$ (NNO) and $SrTiO_3$ (STO). Figure 1a shows an HAADF image of a 4NNO/2STO superlattice, where the STO and NNO layers can be easily identified due to their distinctly different mean inner potentials. It has been well accepted that the infinite layer of NNO can be synthesized by the topotactic reduction method. In order to understand the deintercalation process of oxygen ions and the variation of oxygen concentration in NNO layers, we acquired all oxygen positions by Gaussian fitting and then extracted the oxygen intensity map as displayed in Figure 1d. The corresponding intensity line profile of apical oxygen is presented in Figure 1e, identifying the reduction procedure about the local symmetry variations from octahedral to square planar.

By calculating the white-line ratio, we obtained the valence variations of Ni and Ti ions across the interfaces as shown in Figure 2. The valence of Ti intermixed on Ni sites for the 4NNO/2STO superlattice tends to be 3+ while it almost maintains 4+ for the 8NNO/4STO superlattice (Figure 2c and 2f). The Ni valence varies between 1+ and 2+ since it depends on the extent of deintercalation of the apical oxygen in the NNO inner layer. An apparent gradient variation of Ni valence is visible in the NNO layer for the 8NNO/4STO superlattice. Furthermore, we will discuss the effects of elemental intermixing, cation distortion, and oxygen distribution as well as occupancy on the observed valence variations near the interfaces.

References

[1] D. F. Li, et al. Nature 2019, 572 (7771), 624-627.

[2] B. H. Goodge, et al. arXiv:2201.03613, 2022.

[3] B. Geisler et al. Phys. Rev. B 2020, 102 (2), 020502.

[4] R. He et al. arXiv:2006.00656, 2020.

[5] C. Yang et al. Nano Lett. 2021, 21 (21), 9138-9145.

[6] This project has received funding from the European Union"s Horizon 2020 research and innovation programme under Grant Agreement 823717 – ESTEEM3.

Figure 1 Atomic structure of a 4NNO/2STO superlattice. (a) An overview HAADF image of a 4NNO/2STO superlattice. (b) An enlarged HAADF image and (c) the iCoM image obtained in the region marked by a yellow dashed box in (a). (d) The oxygen intensity map calculated from the oxygen columns in (c). (e) The extracted intensity line profile of apical oxygen columns from the white dashed line marked in (d).

Figure 2 Valence variations of Ni and Ti ions in 4NNO/2STO and 8NNO/4STO superlattices. HAADF images of (a) the 4NNO/2STO superlattice and (d) the 8NNO/4STO superlattice. (b) Ni L3/L2 intensity ratio and (c) Ti L3/L2 intensity ratio of the 4NNO/2STO superlattice. (e) Ni L3/L2 intensity ratio and (f) Ti L3/L2 intensity ratio of the 8NNO/4STO superlattice. The references of Ni3+ and Ni1+ valences are from our $NdNiO_3$ and $NdNiO_2$ samples, respectively. The Ni2+ reference is from a NiO film in the Gatan EELS database. The Ti4+ reference is from our $SrTiO_3$ sample.

Fig. 1

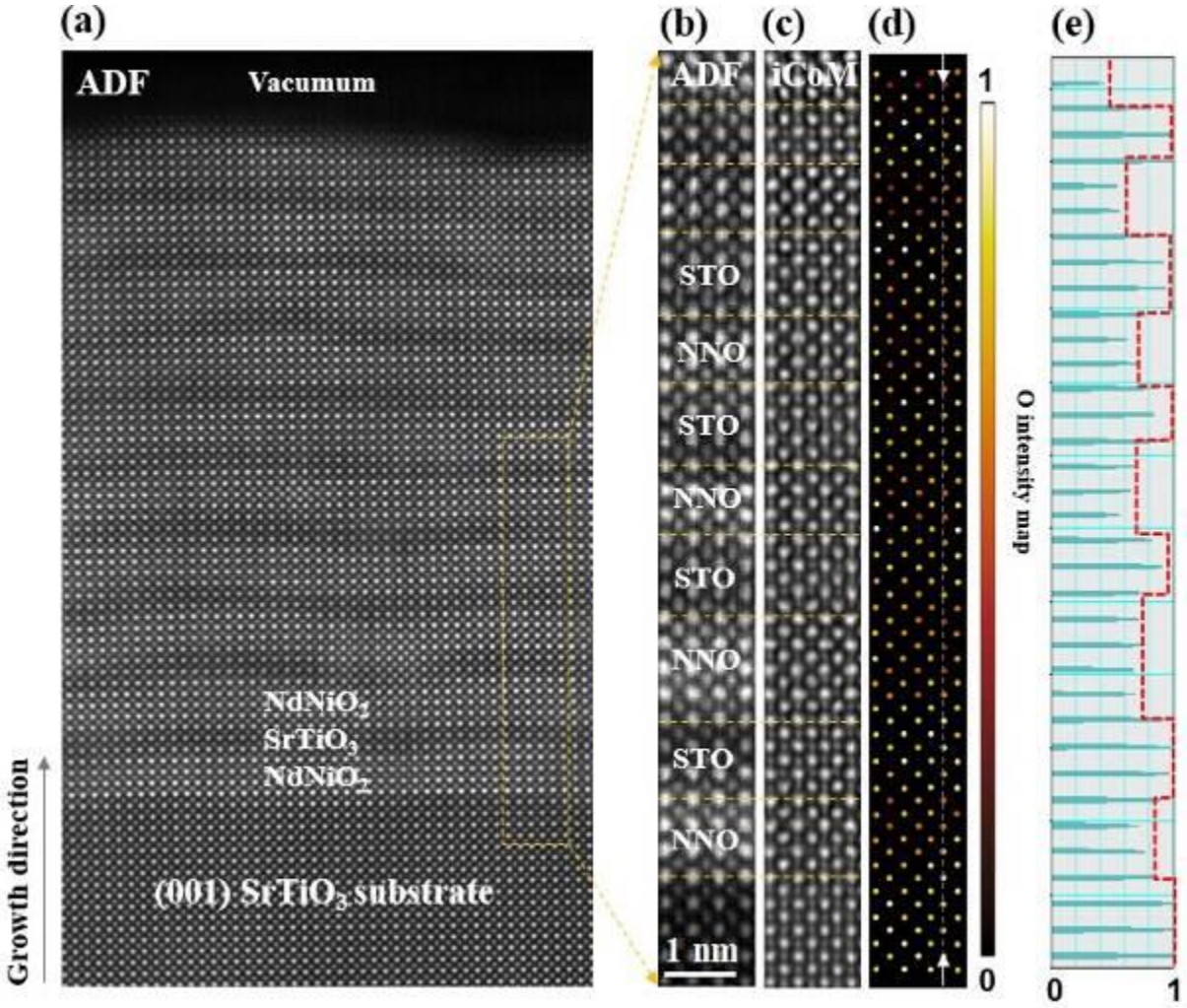
(a)
ADF
Vacumum
NdNiO2
SrTiO3
NdNiO2
(001) SrTiO3 substrate
Growth direction
(b)
(c)
(d)
(e)
ADF
iCoM
STO
NNO
STO
NNO
STO
NNO
STO
NNO
1 nm
1
0
O intensity map
0
1

Fig. 2

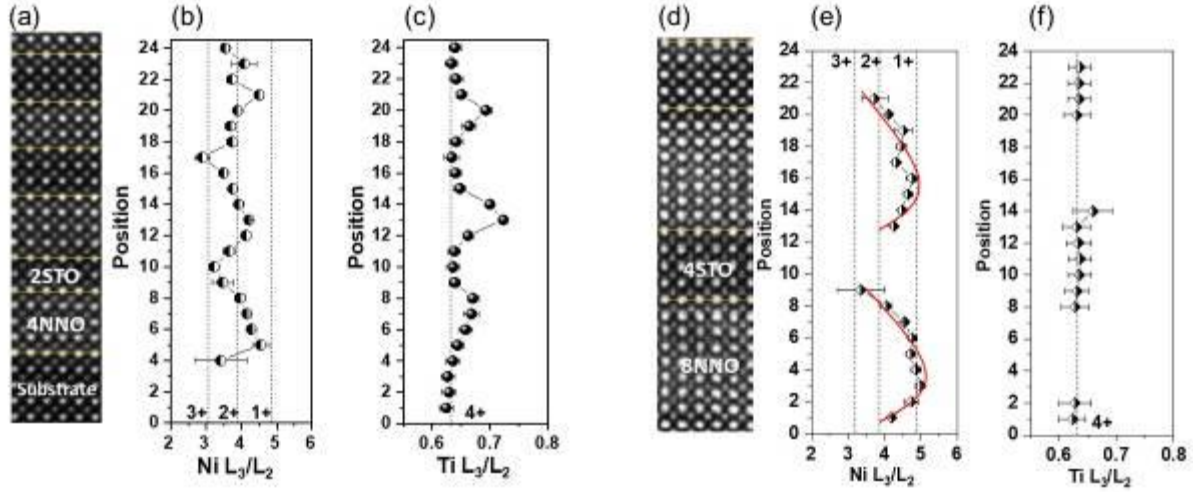
(a)
(b)
(c)
(d)
(e)
(f)
2STO
4NNO
Substrate
4STO
8NNO
Position
Ni L3/L2
Ti L3/L2
3+
2+
1+
4+

MS4.P015

Atomic-scale investigation of nickelate-based perovskite superlattices

F. Misják[1], R. A. Ortiz[2], D. Geiger[1], M. K. Kinyanjui[1], E. Benckiser[2], U. Kaiser[1]

[1]Ulm University, Central Facility of Electron Microscopy, Ulm, Germany
[2]Max Plank Institute for Solid State Research, Stuttgart, Germany

Nickelate-perovskite heterostructures offer outstanding oppportunities to design technologically relevant structures with functionalities such as unconventional magnetic, electric, catalytic features and even the possibility of superconductivity [1]. The wide variety of fuctional properties stems from the strong hybridisation between the Ni d and oxygen p orbitals. Targetted manipulation of the oxygen environment of the Ni can be realised by structural distortions, which are associated with the deformation or rotations of oxygen octahedra of the perovkites [2].

Superlattices consisting of dissimilar perovskite-oxides offer several tuning parameters for direct control over the octahedral network. Besides the epitaxial strain, spatial confinement, octahedral connectivity and symmetry mismatch at the heterointerfaces can alter the crystal structure and induce sizable changes in the electronic properties. However, targetted design of properties through the orbital-lattice interaction is impeded by poor understanding of the heterostructuring parameters on the structure and their resultant effect on the orbital response. In order to disentagle the effects of heterostructuring parameters and understand the underlaying mechanisms, atomic scale investigation of the oxygen octahedral network is necessary.

In this work, we investigated structural and transport properties of $LaNiO_3$/$LaGaO_3$ (LNO/LGO) superlattices (SLs). SLs with stacking sequences of LNO/LGO: 8/4, 4/4, and 4/8 pseudocubic unit cell were grown on (001) $SrTiO_3$ substrate by pulsed-laser deposition. Cross-sectional HRTEM specimens were prepared by focused ion beam. Negative-spherical-aberration imaging was used to resolve the oxygen atomic columns using C_S-corrected HRTEM (FEI TITAN) operated at an electron accelerating voltage of 300 kV. Electrical transport measurements were performed in van-der-Pauw geometry.

The results revealed, that the three stacking sequences of LNO/LGO stabilised different non-equilibrium states of the LNO. Within the LNO layers, we found significant variation in octahedral rotations and distortions in the vicinity of the LGO-LNO interface and away from the interface. We explained these results based on the varying contribution degree of epitaxial strain and spatial confinement by LGO on the structure evolution. The relative thickness ratio of the components also has an influence on the "strength" of the interfacial octahedral connectivity determining different structural distortions under the same epitaxial-strain condition. Thus the contribution of octahedral connectivity to epitaxial strain became tunable. Associated tunability of the electronic properties was comfirmed by transport measurements. The results show, that superlattices are effective platforms to optimize perovskite nickelate functionalities and manipulate the material properties in a controllable way.

Acknowledgements

We are grateful for financial support from DFG 323667265. We gratefully acknowledge Manuel Mundszinger for TEM sample preparation.

[1] S. Catalano, M. Gibert, J. Fowlie, J. Íñiguez, J.-M. Tricone, and J. Kreisel, Rep. Prog. Phys., 2018

[2] J.M. Rondinelli, S.J. May, and J.W. Freeland, MRS Bulletin, 2012

MS4.P017

Reproducibility and control of solid-state nanopore production by fast helium ion beam milling

M. Kögel[1], B. Schröppel[1], M. Mierzejewski[1], P. D. Jones[1], J. C. Meyer[1,2]

[1]NMI Natural and Medical Sciences Institute at the University of Tübingen, Reutlingen, Germany
[2]Eberhard Karls University of Tübingen, Institute for Applied Physics, Tübingen, Germany

Solid-state nanopores are of great interest for usage as an instrument for scalable and robust single-molecule measurements in life sciences. The nanopores are mechanically stable, and can withstand a wide range of environments, due to the materials used [1]. In order to further enhance the potential and usability of these nanopores, one of the main goals of our research is the fast and reliable fabrication.

Measurements of analytes with nanopores are typically done using simple flow cells, which incorporate a membrane chip. The membrane includes a single nanopore, therefore it forms the only possible ion conduction path between two bath chambers with electrodes, allowing the measurement of single molecules passing through the pore. The usage and further research of the solid-state nanopores as an instrument, requires fast fabrication methods. So far, nanopores were produced with a Transmission Electron Microscope (TEM), which requires manual control over the electron beam. Additionally a very frequent vacuum transfer of the single sample chip after each milling step is necessary.

Here we will present solid-state nanopores fabricated by a Helium Ion Microscope in silicon-nitride membranes. The HIM allows the etching of features smaller than 10 nm [2]. Furthermore, the depth of field is in the range of micrometres, which gives a better control over the aspect ratios of the pores. For high throughput production, this property is also useful, because the focus of the Helium Ion Beam does not need to be adjusted over a large field, which increases efficiency. We expect milling times 10-100x faster than TEM. Moreover, fast HIM scanning speeds allow low dwell times of the milling procedure (Fig. 3). Total dose each pore and dwell time - the time the Helium Ion Beam parks at one position - make up the precisely controllable parameters. The choice of these gives good control and reproducibility over the shapes of the pores, which was previously difficult to achieve by the fabrication using TEM.

Precise measurements of the sizes of the pores were done using a TEM (Fig. 1, 2). Electron energy loss spectroscopy (EELS) allows the measurement of the thicknesses, therefore aspect ratios are precisely determinable. We will present results on the reproducibility of different aspect ratios and sizes of silicon nitride nanopores.

Acknowledgements

We thank Christoph Blattert (Hahn-Schickard, Villingen-Schwenningen, Germany) for provided silicon nitride membranes. This work is supported by the project TechPat nano (Translational platform for nanosensor-based medical diagnostics, funding code 35 4223.10/10). We acknowledge financial support from the State Ministry of Baden Wuerttemberg for Economic Affairs , Labour and Tourism.

References

1. Xue, L. et al., doi: 10.1038/s41578-020-0229-6
2. Shixuan He et al., doi: 10.1088/2631-7990/abc673

Figure 1. TEM (80kV) phase-contrast image of a nanopore array fabricated by HIM. Different total doses were applied from right to left (10 nC/µm² .. 100 nC/µm²) and the dwell time was varied from top to bottom (1µs .. 10µs).

Figure 2. TEM (80kV) phase-contrast images of single nanopores, field of view 30 nm. With a dwell time of 1 µs, the total dose was varied from left to right: 40 nC/µm², 50 nC/µm², 100 nC/µm².

Figure 3. Milling procedure done by HIM. Diameter d sets the geometry. Repeats of the spiral milling pattern from inside to outside are dependent on the total dose and dwell time.

Fig. 1

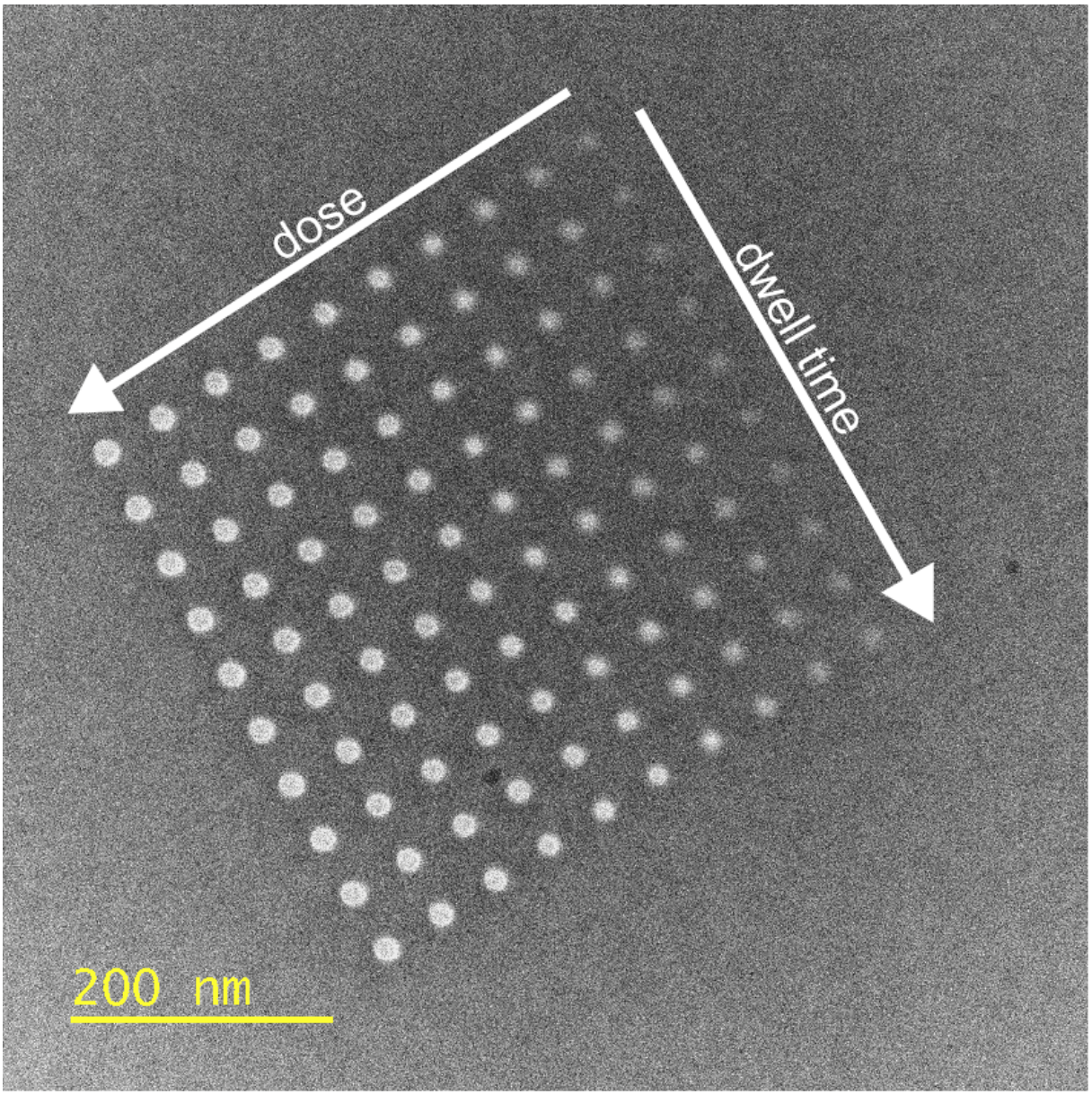

Fig. 2

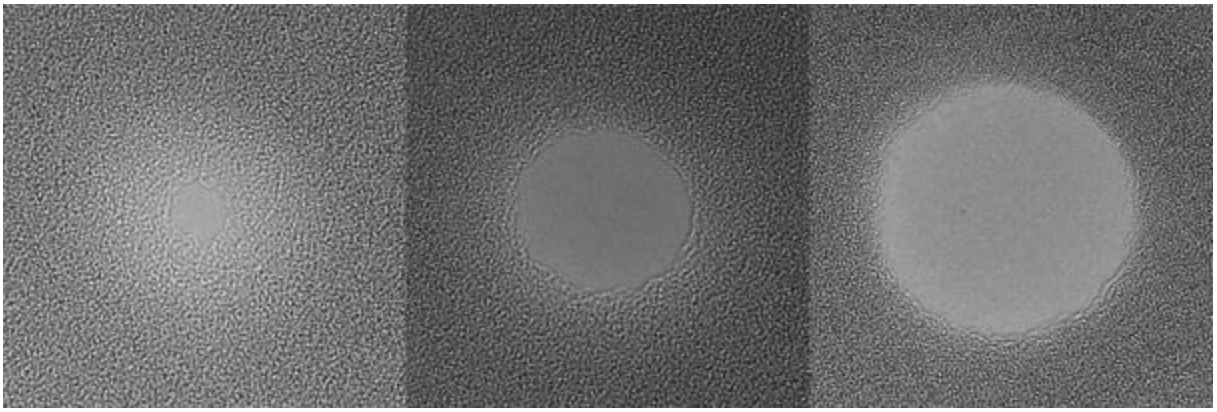

Fig. 3

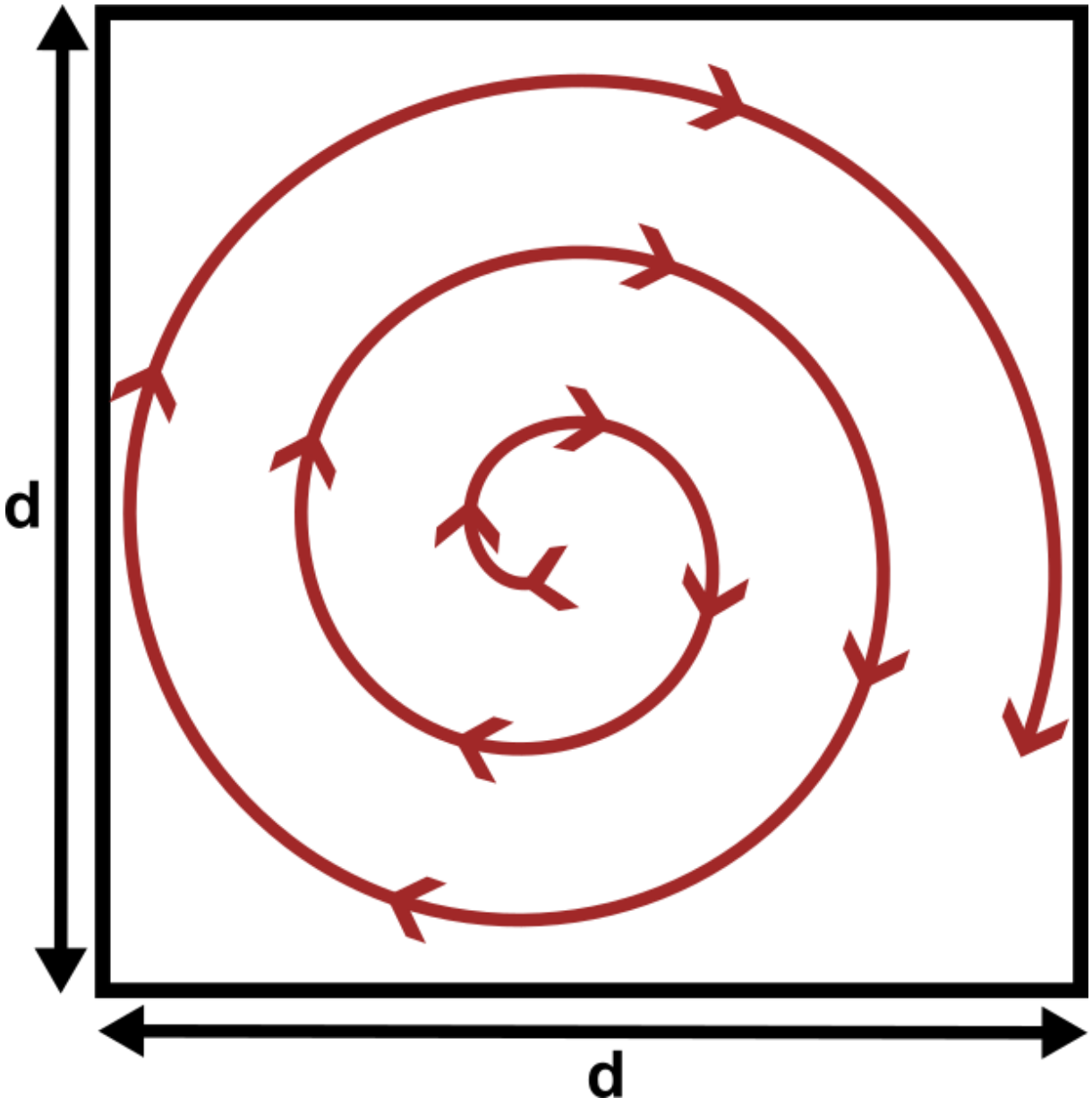

MS5.001-invited

Characterization of organic materials using four dimensional-scanning transmission electron microscopy (4D-STEM)

C. Ophus[1]

[1]Lawrence Berkeley National Laboratory, NCEM, Molecular Foundry, Berkeley, CA, United States

Organic materials remain challenging to characterize in electron microscopy due to their weak scattering from and high dose sensitivity to the electron beam. This talk will show how advances in detector technology and computational imaging have enabled four dimensional- scanning transmission electron microscopy (4D-STEM) characterization of functional organic thin films [1]. By carefully tuning the size of the converged electron probe, the distance between adjacent measurements, and the total exposure of the electron beam, we can maximize the amount of measurable information. This talk will show experimental examples characterizing the morphology of crystalline and semi-crystalline polymers and other organic thin films. It will also show several methods which can improve 4D-STEM characterization including cryogenic cooling, custom probe-forming apertures, 4D-scanning confocal electron diffraction (4D-SCED), and using machine learning methods to invert noisy and nonlinear diffraction measurements.

The primary goal of this research is to measure structural and morphological material properties from weakly-scattering and beam sensitive organic molecules. These properties include the degree of crystallinity, crystalline phase and orientation, and degree of short and medium range order present. We aim to map these properties over the functional length scale of the materials in question, where the field of view may range from nanometers to hundreds of micrometers.

Our experiments are performed using several FEI/ThemoFisher Titan and Themis platform STEM instruments. We typically use 300 kV accelerating voltage, and probe convergence semiangles from 0.1 to 4 mrads. We also make use of custom amplitude apertures in the probe-forming plane [2]. Our electron detectors range from scintillator-based cameras such as the Gatan Ultrascan, and direct electron detectors such as the Gatan K2 and K3. We also show results from the Berkeley Lab 4D Camera operating at 87 000 images/second [3]. The 4D-STEM experimental geometry and an example 4D-STEM sdataset is shown in Figure 1.

We also demonstrate alternative experimental geometries such as 4D-SCED which can minimize the electron beam damage induced by adjacent probe positions measurements [4]. Thick samples may also produce significant amounts of multiple scattering of the electron beam. In order to perform accurate measurements of these complex nonlinear diffraction signals at low electron dose, we have implemented machine learning methods [5]. Finally, all of our methods and datasets are freely available in the py4DSTEM open source analysis toolkit [6].

Figure 1 - 4D-STEM experimental geometry showing diffraction patterns measured at various probe positions for a small organic molecule sample. In each diffraction pattern, the pi-pi stacking direction(s) can be identified from the primary Bragg peak positions. The reconstructed sample morphology is shown above as an orientation map. Adapted from [7].

[C1] C Ophus, Microscopy and Microanalysis 25, 563 (2019).

[C2] S Zeltmann et al., Ultramicroscopy 209, 112890 (2020).

[C3] P Pelz et al., IEEE Signal Processing Magazine 39. 25 (2021).

[C4] M Wu et al., Nature Communications 13, 1 (2022).

[C5] J Munshi et al., arXiv:2202.00204 (2022).

[C6] B Savitzky et al., Microscopy and Microanalysis 27, 712 (2021).

[C7] K Bustillo et al., Accounts of Chemical Research 54, 2543 (2021)

Fig. 1

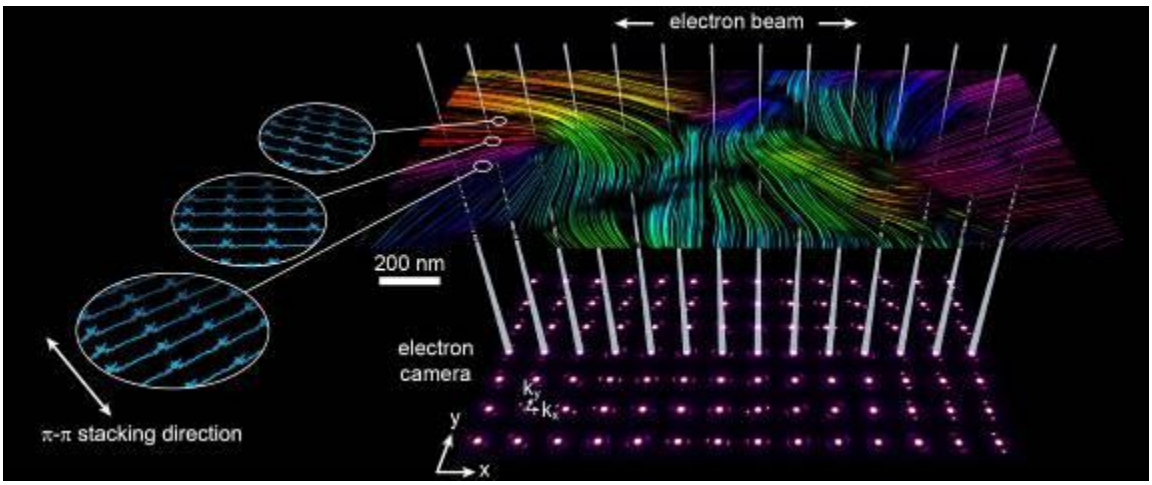
electron beam
200 nm
electron
camera
k_y
k_x
y
x
π-π stacking direction

MS5.002

Microscopy escorting the process from polymer synthesis to membranes fabrication

M. Held[1], E. Sperling[1], P. Georgopanos[1], K. Nieswandt[1], V. Abetz[1]

[1]Helmholtz-Zentrum Hereon, Institute of Membrane Research, Geesthacht, Germany

Tuning the morphology of block copolymer structures is an essential task in the development of polymer membranes.[1] This is even more important when thermoresponsive block such as the poly((dimethyl acrylamide)-*co*-(isopropyl acrylamide)) as a copolymer with polystyrene (P(DMA-*co*-NIPAM)-*b*-PS) is involved. Such membranes are formed via a non-equilibrium self-assembly process in solution. In order to observe all the steps of the process in detail, from the synthesis to the membrane fabrication, a bundle of microscopic methods are necessary to be employed.

From the formation of micelles during emulsion polymerization, via the morphology in the polymer bulk to the membrane"s pore structure, microscopy is required to complement and confirm integral analysis methods. Starting from the polymer fabrication,cryoTEM was employed to observe micelles in the emulsion reversible addition fragmentation chain transfer (RAFT) synthesis of the block copolymer, a precursor for structure formation during the solidification of the membrane.[2] Following that, TEM and AFM shed light onto the P(DMA-*co*-NIPAM)-*b*-PS bulk morphology as a first indicator for the final membrane structure. SEM investigations enable us to judge the quality of the final membrane. The images confirm the dynamic light scattering results regarding size and thermoresponsiveness, while also identifying the fabrication parameters for the final membrane. The structure of these thermoresponsive membranes would not have been identified without electron microscopic and atomic force microscopic imaging throughout their development.

[1]Müller and Abetz. Chemical Reviews 121 (22), 2021, p. 14189. DOI: 10.1021/acs.chemrev.1c00029

[2]Nieswandt et al. Polymers 14 (1), 2022, p. 62. DOI: 10.3390/polym14010062

Fig. 1

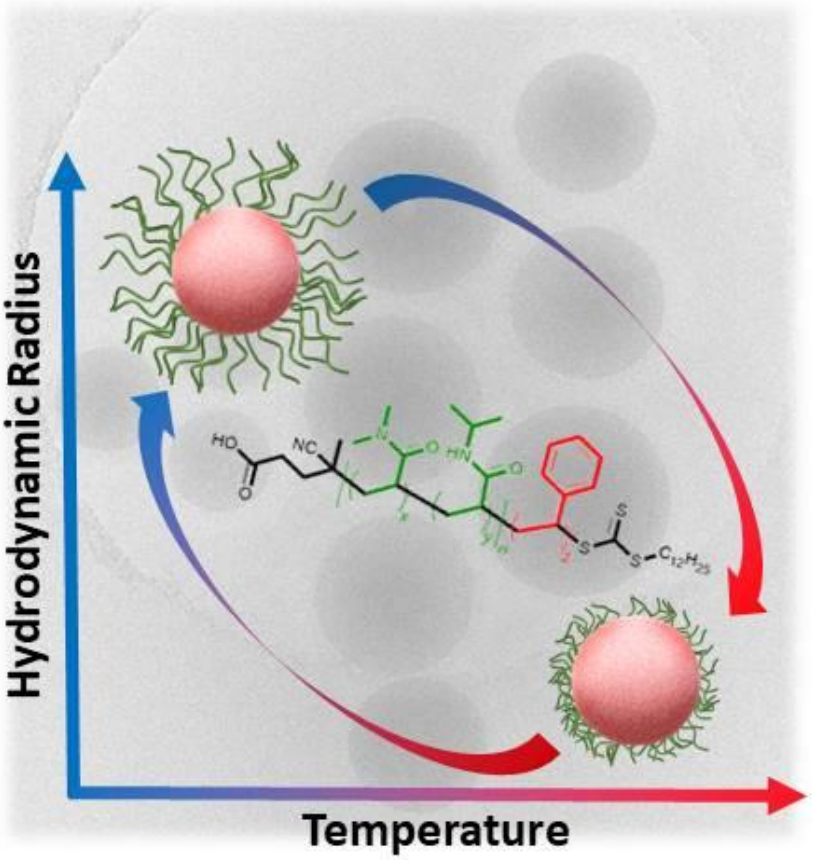

MS5.003

Enhancing the photocatalytic performance of carbon nitrides through controlled local structure modification

D. Piankova[1], H. Zschiesche[1], A. Tyutyunnik[2], E. Svensson[3], C. W. Tai[3], M. Antonietti[1], I. Teixeira[1,4], N. V. Tarakina[1]

[1]Max Planck Institute of Colloids and Interfaces, Potsdam, Germany
[2]Institute of Solid State Chemistry, Ural Branch of the Russian Academy of Sciences, Ekaterinburg, Russian Federation
[3]Stockholm University, Department of materials and environmental chemistry, Stockholm, Sweden
[4]Federal University of São Carlos, Department of Chemistry, São Carlos, Brazil

Carbon nitrides are the most studied sustainable metal-free photocatalysts: they can be synthesized by simple routes from abundant organic precursors, they are visible-light-active as well as thermally and chemically stable in photocatalytic reactions. However, most of them are poorly crystalline, which leads to a high recombination rate and difficulties in precise control and adjustment of their band structure.

Polyheptizine imides (M-PHIs) salts are one of the most crystalline carbon nitrides. They have high charge-separation efficiency, enabling storage of photogenerated electrons and the realization of so-called dark photocatalysis. In this work we show how the controlled modification of the local structure, obtained by varying the sizes and charges of metals as well as introducing a rotation between 2D heptazine layers, influences the energy band structure and allows to enhance the photocatalytic activity of M-PHIs. To realize this goal, we combined X-ray powder diffraction (XRD), low-dose HRTEM imaging, energy filtered electron radial distribution function (EF-eRDF) analysis obtained from rotational electron diffraction data and VEELS data with photocatalytic performance on M-PHI (M = Na, K, Mg, H) during the hydrogen evolution reaction (HER).

From low-dose HRTEM and XRD data and general assumptions about the structure from earlier works starting models for crystal structure refinement were proposed. PHI salts were found to crystalize in a trigonal unit cell; their idealized structure consists of heptazine units that are placed on top of each other in AAA stacking, forming continuous channels along the *c* direction. Based on XRD only we could not locate metal atoms uniquely in Mg-PHI and Na-PHI, thus we proposed 2 possible structural models. In order to find an unambiguous solution, we compared short-range order and the degree of crystallinity in different M-PHIs by performing an EF-eRDF analysis using rotational SAED data. The latter allowed to compensate for the preferential orientation of domains found in the M-PHI flakes. Fitting of EF-ePDF of Mg and Na salts showed that only one model with metal cations equally distributed between interlayer positions and bridging nitrogen atom positions in the channels is correct. The coherence lengths increase in the series H-, Na-, Mg-, K-PHI (reaching ~30 Å), indicatingan increase in crystallinity (Fig.1). The ePDF curves of Na- and Mg-PHI display broadening of the peaks beyond 8 Å pointing to a less pronounced fine structure compared to K-PHI, which is related with twists of layers found in these compounds.The rotation of layers by a random (usually only 2-8°) angle leads to the formation of "flower-like structures", while at specific rotation angles Moiré pattern lattices are formed. DFT calculations showed that both defects modify the band structure of these materials and should influence the HER.

Indeed, in tests as photocatalysts for the HER, Na- and Mg-PHI showed the best performance with the latter reaching an unprecedented quantum efficiency of 7.14%. This was attributed to the higher charge of Mg^{2+} compared to all other cations (Na^+, K^+, H^+), which leads to a more efficient polarization of the heptazine backbone and the promotion of the cleavage of the H-O bond during the water splitting as well as a considerably faster interlayer charge transfer in the presence of rotational defects.

We gratefully acknowledge financial support by the Max Planck Society.

Fig. 1

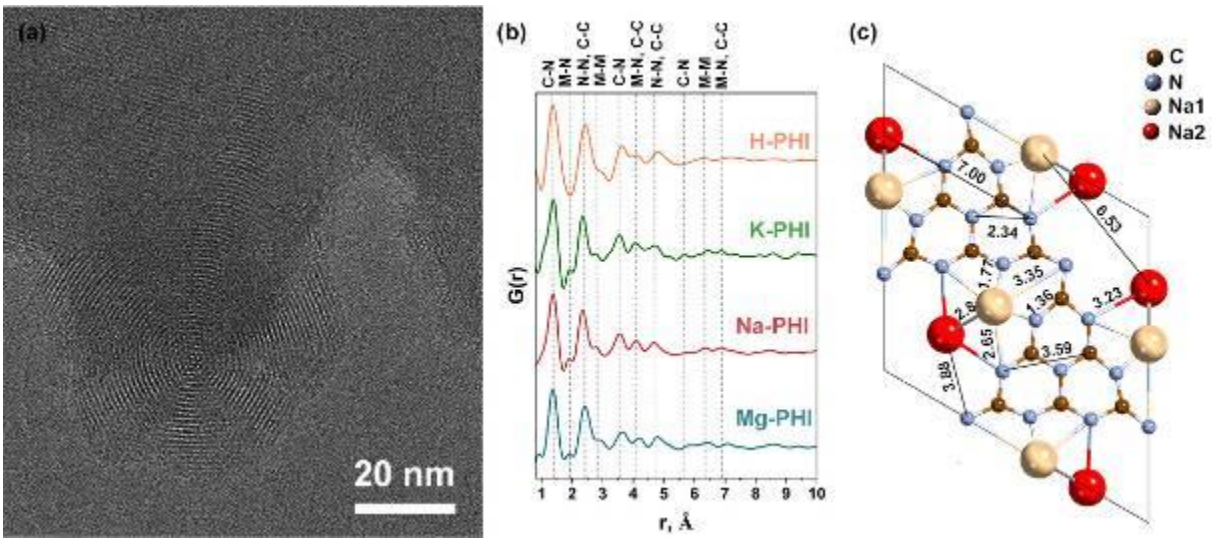
(a)
20 nm
(b)
C-N
M-N
N-N, C-C
M-M
C-N
M-N, C-C
N-N, C-C
C-N
M-M
M-N, C-C
H-PHI
K-PHI
Na-PHI
Mg-PHI
G(r)
1 2 3 4 5 6 7 8 9 10
r, Å
(c)
C
N
Na1
Na2
7.00
6.53
2.34
3.35
1.77
1.36
3.23
2.65
3.59
3.88

MS5.004

Revealing interfacial widths and line-edge roughnesses in cylinder-forming block copolymers using low keV analytical transmission electron microscopy

J. Bürger[1], H. Venugopal[1], D. Kool[1], T. de los Arcos[2], A. Gonzalez-Orive[3], G. Grundmeier[2], K. Brassat[2], J. K. Lindner[1]

[1]Paderborn University, Department of Physics, Paderborn, Germany
[2]Paderborn University, Department of Chemistry, Paderborn, Germany
[3]University of La Laguna, Institute of Materials and Nanotechnology, Santa Cruz de Tenerife, Spain

Lithography based on the self-assembly (SA) of block copolymers (BCP) is a competitive alternative to extreme UV lithography applied in semiconductor industries, since it allows to create regular arrays of motives with sub-ten nanometre feature size economically and on large areas [1]. During BCP-SA two blocks of immiscible polymer species, A and B, which are covalently bond to each other in a molecular chain, undergo a microphase separation. Depending on the BCP chain length ratio, this can result in various motives, e.g. hexagonally arranged cylinders of block A in a matrix of block B. For further lithography processes one of the blocks is selectively removed. Since the features after processing are a direct replica of their lithographic mask, the abruptness of the microphase interfaces (interfacial width) in the phase separated BCP film [2] and the line edge roughness (LER) of the resulting mask are crucial but difficult to measure. Previous studies have employed analytical techniques that either only allow to analyse the surface of the BCP mask or average the properties over a large area or provide comparatively low spatial resolution. However, future progress in BCP lithography requires high-resolution information on the internal interfaces of microphases at or below the single-nanometre scale.

Here, we investigate the quality of the BCP masks by employing advanced analytical (scanning) transmission electron microscopy ((S)TEM) at 60 kV in combination with XPS and PM-IRRAS to derive information about the size of the polymer domains, the interfacial width and LER, as well as the chemical changes occurring upon mask development using different polymer removal techniques.

BCP lithography masks are made from cylinder forming BCP consisting of the two polymer species polystyrene (PS) and polymethyl methacrylate (PMMA). Membranes of as-phase-separated as well as developed BCP films are studied, the latter after either wet chemical UV/acetic acid or Ar/O2 plasma treatment. Films are fabricated on a sacrificial SiO_2 substrate which for TEM preparation is removed by HF etching, followed by skimming of the BCP membrane with a Quantifoil TEM grid. Domain sizes, interfacial widths and LERs are calculated from high-resolution ADF STEM images using a self-written *MATLAB* application which is based on the analysis of angularly resolved radial intensity profiles of individual pores. This allows to monitor the LER of cylindrical mask openings at unprecedented, sub-nm resolution in different stages of the process chain and to detect the presence of pockets of the opposite polymer species protruding through the PS-PMMA interfaces. In addition, energy-filtered TEM element and thickness maps are acquired to analyse changes in chemistry and thickness of the BCP masks and it is shown that Ar/O_2 plasma treatment, while leading to smoother interfaces, also results in oxidised polymer surfaces [3].

[1] K. Brassat, J.K.N. Lindner, *Advanced Materials Interfaces* 7.5 (2020): 1901565.

[2] J. Bürger et al., *Nanomaterials* 10.1 (2020): 141.

[3] J. Bürger et al., *Advanced Materials Interfaces* (2022), accepted.

MS5.005

Understanding novel carbon-based sensor architectures by advanced STEM-EELS and 4D-STEM

C. O. Ogolla[1], M. Hepp[1], H. Wang[2], J. Ciston[3], C. Ophus[3], G. Panchal[4], S. Delacroix[5], D. Cruz[6,7], D. Kodja[4], A. Knop-Gericke[6,7], K. Habicht[4,8], B. Butz[1], V. Strauss[2]

[1]University of Siegen, Micro- and Nanoanalytics Group, Siegen, Germany
[2]Max-Planck-Institut für Kolloid- und Grenzflächenforschung, Potsdam, Germany
[3]Lawrence Berkeley National Laboratory, National Center for Electron Microscopy Facility, Molecular Foundry, Berkeley, CA, United States
[4]Helmholtz-Zentrum Berlin für Materialien und Energie GmbH, Dynamics and Transport in Quantum Materials, Berlin, Germany
[5]Ecole polytechnique, Institut Polytechnique de Paris, Paris, France
[6]Fritz-Haber-Institut der Max-Planck-Gesellschaft, Department of Inorganic Chemistry, Berlin, Germany
[7]Max Planck Institute for Chemical Energy Conversion, Department of Heterogeneous Reactions, Mülheim an der Ruhr, Germany
[8]University of Potsdam, Institute of Physics and Astronomy, Potsdam, Germany

Nitrogen-doped carbon materials (NCM) have emerged as cost-effective, environmentally friendly, and readily available starting materials for gas sensing device fabrication. They allow for the systematic tuning of properties for superior selectivity and sensitivity to specific analytes (volatile organic compounds and specific gases) by carefully choosing the precursor materials. CO_2 sensing is one of the major applications where such materials have been implemented. So far, miniaturized CO_2 sensors are based on sophisticated nanomaterials like selected, doped carbon nanotubes [1].

In this study, a one-step laser patterning procedure is applied to an optimized ink coating to directly generate complete and highly porous sensor architectures (~50 micrometer overall thickness) even on flexible PET substrates. The versatile ink is based on abundant organic precursors like adenine (nitrogen source for sensing functionality) and glucose as a pore-forming agent. Thermal laser treatment of the precursor material in an oxygen-containing environment allows us to fabricate complete sensor heterostructures with defined nitrogen and oxygen functionalities. The attenuation of the laser irradiation is depth dependent and results in the formation of a defined graphitic surface layer and a nitrogen-rich lower region (sensing layer) separated by a transition region.

To understand the structure formation by laser treatment as well as device functionality, a thorough scale-bridging investigation was conducted. Microtomic cross sectioning is employed to prepare high quality TEM cross-sections (0.25 - 0.5 t/λ) [2].

Elemental distribution maps from STEM-EELS data depicted a clear separation between the upper and lower layers. STEM-EELS chemical and bond analysis across the whole device allowed the clear differentiation between distinct amorphous and crystalline phases, and thus between different functional layers of the heterostructure. Therefore, principal component analyses were applied due to the complexity of the laser-generated material.

The distribution of the crystalline graphitic phase, the degree of ordering graphitization and the alignment of the basal planes were investigated in detail by 4D-STEM (see Fig 1.)as those parameters impact on the electrical conductivity of the sensor. In addition, the data analysis method employed, sparse correlation matching, as implemented in py4DSTEM [3] facilitates the detailed analysis of the structural peculiarities of the amorphous phases.

***Keywords**: laser-patterned CO2 sensor, graphitic, nitrogen-doped carbon*

Acknowledgements: We acknowledge funding support from the Fonds der Chemischen Industrie and the Max Planck Society, use of the DFG-funded Micro-and Nanoanalytics Facility (MNaF) at the University of Siegen (INST 221/131-1) and the National Center for Electron Microscopy (NCEM) in the Molecular Foundry (MF) at the Lawrence Berkeley National Laboratory (LBNL) supported by the Office of Science, Office of Basic Energy Sciences, of the U.S. Department of Energy under Contract No. DE-AC02-05CH11231

[1] Inagaki, Michio, et al. Carbon 2018, 132, 104-140.

[2] Hepp, Marco, et al. npj Flexible Electronics 2022, 6.1, 1-9.

[3] Ophus, Colin, et al. Microscopy and Microanalysis 2022, 28.2, 390-403.

Fig. 1

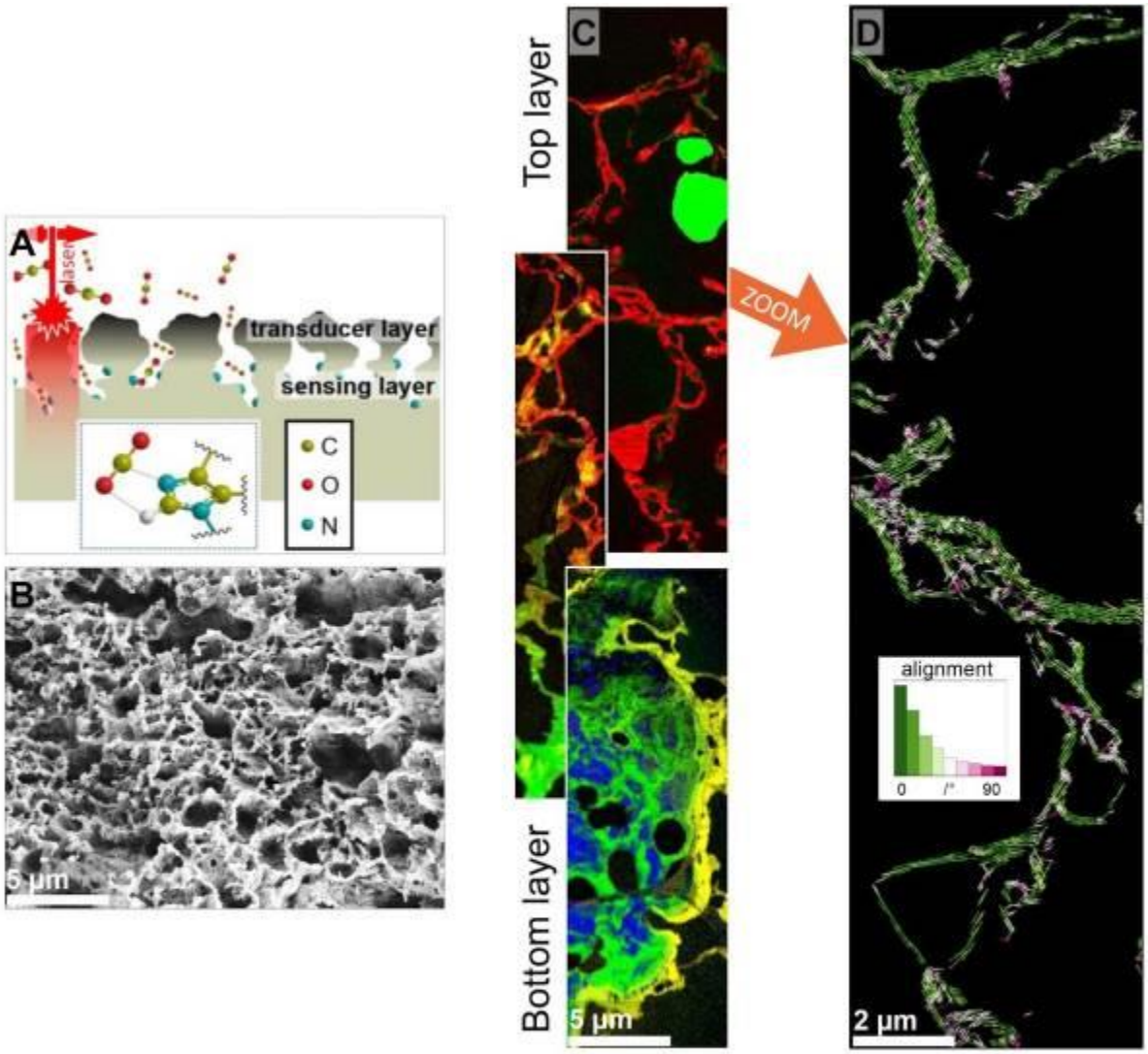

Figure 1. *A) Depth-dependent thermal laser irradiation; B) SEM top view of sensor film; C) Advanced STEM-EELS PCA bond state analysis; D) 4D-STEM analysis of upper part showing the local misalignment angle between the basal plane normal and pore surface normal.*

MS5.006

Advanced characterization of NP@MOF core-shell complexes using real-time electron tomography

T. Craig[1], A. A. Kadu[1], J. Batenburg[2], S. Bals[1]

[1]University of Antwerp, EMAT, Antwerp, Belgium
[2]Centrum Wiskunde & Informatica, Amsterdam, Netherlands

Metal-organic Frameworks (MOFs) are a diverse class of materials consisting of metal clusters and organic linkers arranged into a porous crystalline lattice. Due to their porosity, MOFs possess some of the largest surface areas of any known material. This is exploited for gas adsorption, catalysis and drug delivery. For drug delivery, a drug is incorporated within the MOF and release is initiated by stimuli induced MOF decomposition. Recent efforts have focused on incorporating stimuli responsive nanoparticles (NP) into the MOF, to induce thermal decomposition as a delivery mechanism. The morphology of these NP@MOF complexes is critical to their overall efficacy for drug delivery. [1]

Electron tomography (ET) is invaluable for characterizing their 3D morphology. However, ET requires long exposure times and high electron dosages which cause artefacts during imaging of NP@MOFs. Limiting beam exposure can be achieved by limiting the number of images acquired. Unfortunately, reducing the image number also induces undersampling artefacts. Hence, an optimum image number must be obtained. Optimization could be performed by comparing multiple 3D reconstructions acquired with variable image numbers, a time-consuming process. Furthermore, since each acquisition must be performed on a new sample due to beam exposure from the previous acquisition, reconstructions are not directly comparable and a microscopist must perform a qualitative judgement with uncertain reliability. [2]

Herein a protocol was propsed to estimate the optimum number of images from a single acquisition by combining a non-termination acquisition protocol, golden ratio scanning (grs) with real-time reconstruction. The protocol was tested using simulations and an experimentally acquired Au/Pd NP. Finally, the value of this procedure was highlighted by application to NP@MOF samples of ZIF-8 and NU-1000 containing Au nanoparticles. [3]

Fig. 1. In ET , images are collected (a) incrementally from the lowest angle to the highest angle. E.g. image 1 is collected at -70°, image 2 collected at -65° etc. Early termination results in a missing wedge. By collecting images using (b) grs, the ‚issing wedge is filled mostly in the first images and subsequent images improve sampling resolution. Real time reconstruction is used to monitor reconstruction quality and terminate acquisition. For Au/Pd@ZIF-8 viewed along the xy, xz and yz planes, undersampled (10 images) and oversampled (27) reconstructions have artefacts (red) not apparent in the determined optimum (13 images).

References

[1] Wang, L., Zheng, M., and Xie, Z. (2018) Nanoscale metal–organic frameworks for drug delivery: a conventional platform with new promise. *Journal of Materials Chemistry B*, **6** (5), 707–717

[2] Vanrompay, H., Béché, A., Verbeeck, J., and Bals, S. (2019) Experimental Evaluation of Undersampling Schemes for Electron Tomography of Nanoparticles. *Particle and Particle Systems Characterization*, **36** (7), 1–8.

[3] This project receives funding from the European Union"s Horizon 2020 research and innovation programme grant agreement No 860942 (HEATNMOF).

Fig. 1

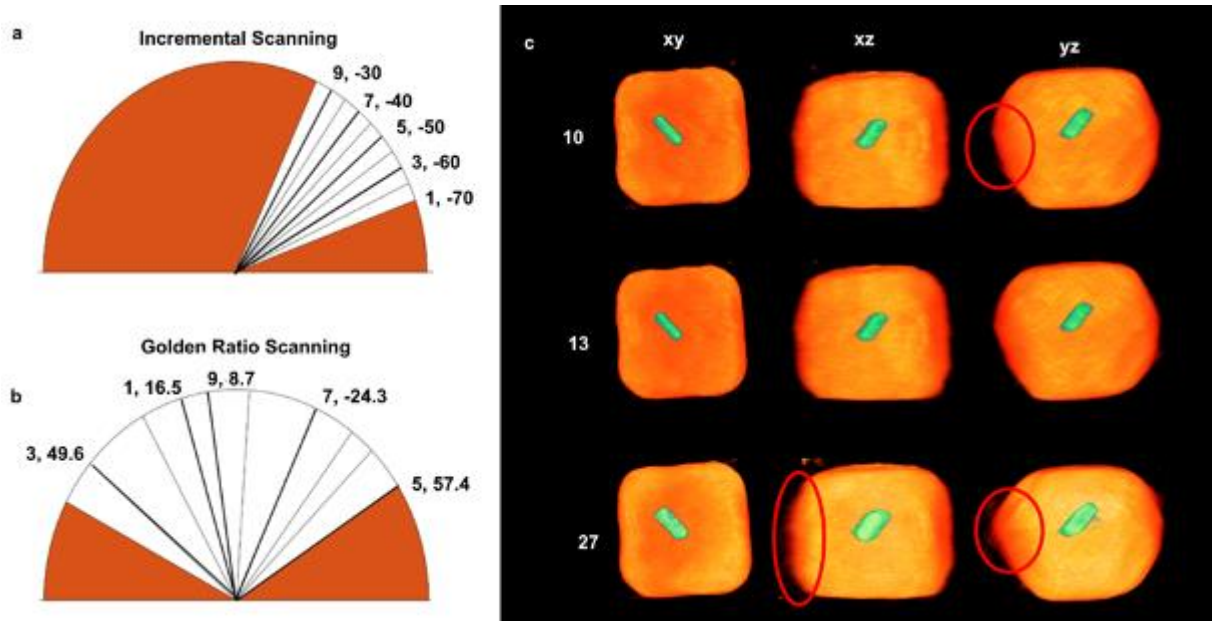
a
Incremental Scanning
9, -30
7, -40
5, -50
3, -60
1, -70
Golden Ratio Scanning
b
1, 16.5
9, 8.7
7, -24.3
3, 49.6
5, 57.4
c
xy
xz
yz
10
13
27

MS5.P001

Understanding the mechanism of molecular precursor condensation by *in-situ* TEM: towards the rational design of porous carbon materials for CO_2 absorption

D. Piankova[1], H. Zschiesche[1], N. V. Tarakina[1]

[1]Max Planck Institute of Colloids and Interfaces, Colloid Chemistry, Potsdam, Germany

Carbon-based materials are sustainable, metal-free functional materials used for various applications; for instance—owning to their porosity—they are often exploited for CO_2 capture. Their CO_2 uptake is usually enhanced by introducing heteroatoms (e.g., nitrogen) and adjusting the porous structure. While nitrogen doping can be achieved through one-step condensation of cheap nitrogen-containing molecular precursors, the porous structure—if no porogen or template is applied—can be adjusted only by synthesis conditions. The choice of the latter remains rather empirical due to the lack of a fundamental understanding of the condensation mechanism.

Our study aims to broaden the fundamental understanding of the condensation process and propose guidelines for designing new porous carbon materials for CO_2 absorption. To realize this goal, we performed *in-situ* heating experiments inside a TEM and followed the condensation *ex-situ* by analyzing the reaction products formed at different temperatures and pressures and evaluating their adsorption properties. As a model molecular precursor, we use uric acid, which forms carbonaceous materials with high nitrogen content. To distinguish the porosity in bulk and the surface of the studied particles, we combined bright-field STEM (internal structural information) with secondary electron imaging in STEM (morphological information).

The *in-situ* condensation in TEM starts at lower temperatures (250 °C) compared to synthesis in nitrogen atmosphere (425 °C from thermogravimetrical analysis). Figure 1 shows the secondary electron (SE) and bright-field (BF) signals from the same particle during heating. The surface of the particle is smooth at 25 ºC (Figure 1 a, SE) and becomes porous at 250 ºC (Figure 1b, SE, mesopores of ~21 nm), indicating the first temperature-induced changes – the beginning of the condensation process. Upon further isothermal heating at 250 ºC, the subsequent mass loss occurs from within the bulk of the particle through the porous surface resulting in the loss of mass first from the pre-surface area (Figure 1 c, BF) and after that from the bulk of the particle (Figure 1 d, BF).

Figure 1. Secondary electron (SE) and bright-field (BF) STEM images of the particle a) at 25 °C before the *in-situ* heating, b) immediately after reaching 250 °C, c) after 4 minutes at 250 °C, d) after 64 minutes at 250 °C.

We found that only samples in vacuum ($1.5 \cdot 10^{-4}$ bar) have pores of about 14 nm in diameter at the surface, while in nitrogen (1 bar), the surface of the samples appears smooth. The pressure in the reaction chamber influences the mass transfer from the surface of particles leading to more porous surfaces when synthesizing materials at low pressures, as observed in *ex-situ* samples in vacuum and during *in-situ* TEM heating ($3 \cdot 10^{-10}$ bar). As a result, vacuum samples demonstrate 2 times higher CO_2 uptake at 500 °C than nitrogen samples.

Thus, we reported the condensation of a molecular precursor *in-situ* for the first time. We showed that varying pressures and reaction rates result in particles with different porosity; the porosity of the surface of the particles during the early stages of condensation governs the subsequent release of volatiles and the development of a hierarchical pore structure.

We gratefully acknowledge financial support by the Max Planck Society and Dr. Janina Kossmann and Dr. Nieves Lopes for the synthesis and CO_2 sorption characterization

Fig. 1

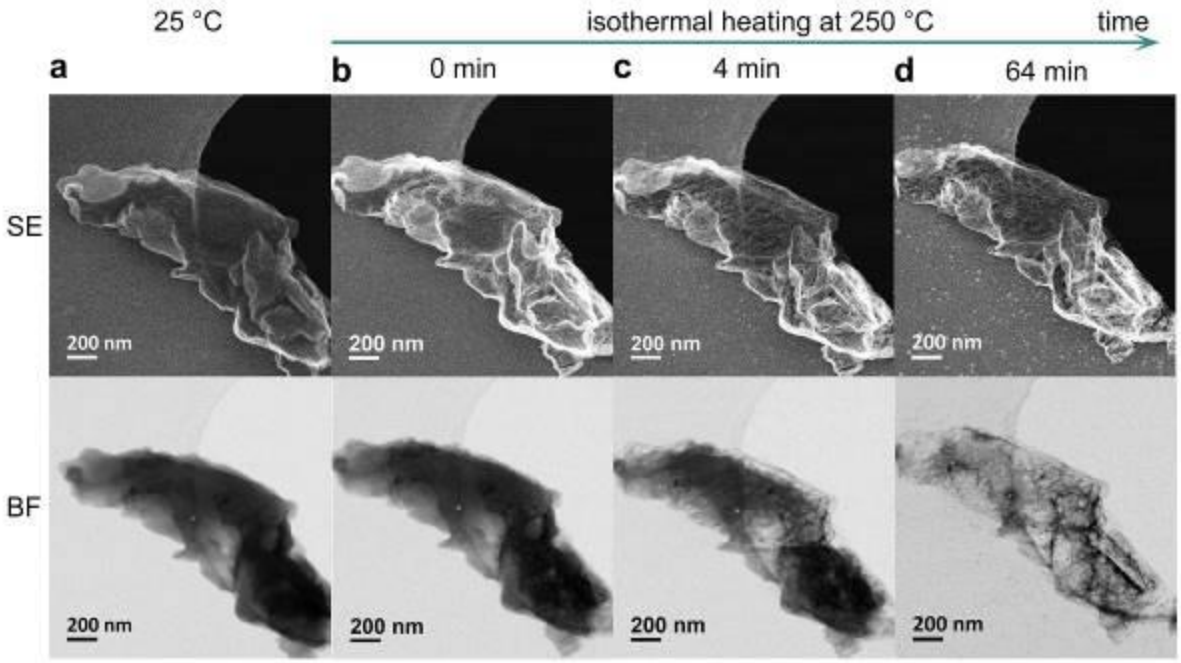
25 °C
isothermal heating at 250 °C
time
a
b
0 min
c
4 min
d
64 min
SE
BF
200 nm
200 nm
200 nm
200 nm
200 nm
200 nm
200 nm
200 nm

MS5.P002

Electron pair distribution function (ePDF) analysis of micro- and nanoplastic particles

C. Rohner[1], R. Schlögl[1,2], T. Lunkenbein[1]

[1]Fritz Haber Institute of the Max Planck Society, Department of Inorganic Chemistry, Berlin, Germany
[2]Max Planck Institute for Chemical Energy Conversion, Mülheim an der Ruhr, Germany

Micro- and nanoplastics (MNPs) are considered a possible threat to microorganisms in the aquatic environment. Here, we show that total scattering intensity analysis of electron diffraction (ED) data measured by transmission electron microscopy (TEM), which yields the electron pair distribution function (ePDF),[1] is a feasible method for the characterization and identification of MNPs down to 100 nm.

Polyethylene (PE), polypropylene (PP), polyethylene terephthalate (PET), and polyamide microparticles, and polystyrene (PS) nanoparticles were examined by TEM and serial ED under low dose, non-cryogenic conditions. Reduced pair density functions (RDF) were calculated from the processed and background subtracted ED data and compared to simulated RDF. Nanobeam diffraction was used for the measurements of the PS and SiO_2 nanoparticles.

High quality serial ED suitable for PDF analysis were measured on polymer microparticles (Figure 1) and nanoparticles. The ePDF method yields a qualitative agreement of experimentally determined and simulated RDFs (Figure 2). For the nanoparticulate PS, a distinction from SiO_2 particles can be made (Figure 3), where the SiO_2 particles are representative of the natural inorganic matrix. By analyzing a time series of ED, we are able to show the dose dependent structural changes in the materials in the series of RDFs. Those changes are qualitatively different for the two different dose rates that were applied, which is evident in particular in the peak intensities that can be attributed to C-H-bonds and C-C-bonds.

We show that detailed structural information can be gained on highly beam sensitive polymer materials by following a low dose, ePDF approach without applying cryogenic or staining techniques. The systematic appearance of C-H pair distance peaks in our measurements exemplifies an advantage of the ePDF method over X-ray based PDF, which usually cannot gain information about hydrogen.

Figure *1* ED *(top row)* and *T*EM *(bottom row)* of cryo ball milled PE*, PP, PET, and PA* microparticles.

Figure 2 Reduced pair density functions derived from serial ED measured on cryo ball milled PE, PP, PET, and PA microplastic particles, respectively. **A)** Results of measurements taken with a dose rate of ≈ 45 e/(nm2s). **B)** 3D model structures employed in the RDF simulation. **C)** Results of measurements taken with a dose rate of a dose rate of ≈ 160 e/(nm^2 s). Each graph in **A** and **C** shows the experimental time series of RDFs, G(r) (color lines), the calculated RDF of a model structure, G(r) model (grey lines), and the elemental pair distribution function of the model (stacked bar charts). The color scale bar indicates the total exposure time at the end of acquisition of an ED frame.

Figure 3 Comparison of ePDF of 100 nm sized PS with 100 nm sized a-SiO_2 spheres. **A**) TEM of PS particles after ED measurements. **B**) First frame of serial ED measured on a PS sphere, **C**) Shadow image of the beam (diameter ~75 nm, indicated by the red dashed line) on the PS sphere (indicated by the white dashed line). **D**) TEM of a-SiO2 particles after ED measurements. **E**) First frame of serial ED measured on an a-SiO_2 sphere **F**) Shadow image of the beam (diameter ~75 nm) on the a-SiO_2 sphere. **G**) Plots of corresponding RDFs of PS (top) and SiO2 (bottom). **H**) Structural model of PS **I**) Structural model of SiO_2.

(1) Gorelik TE et al. Acta Cryst. 2019;75:532–49.

Fig. 1

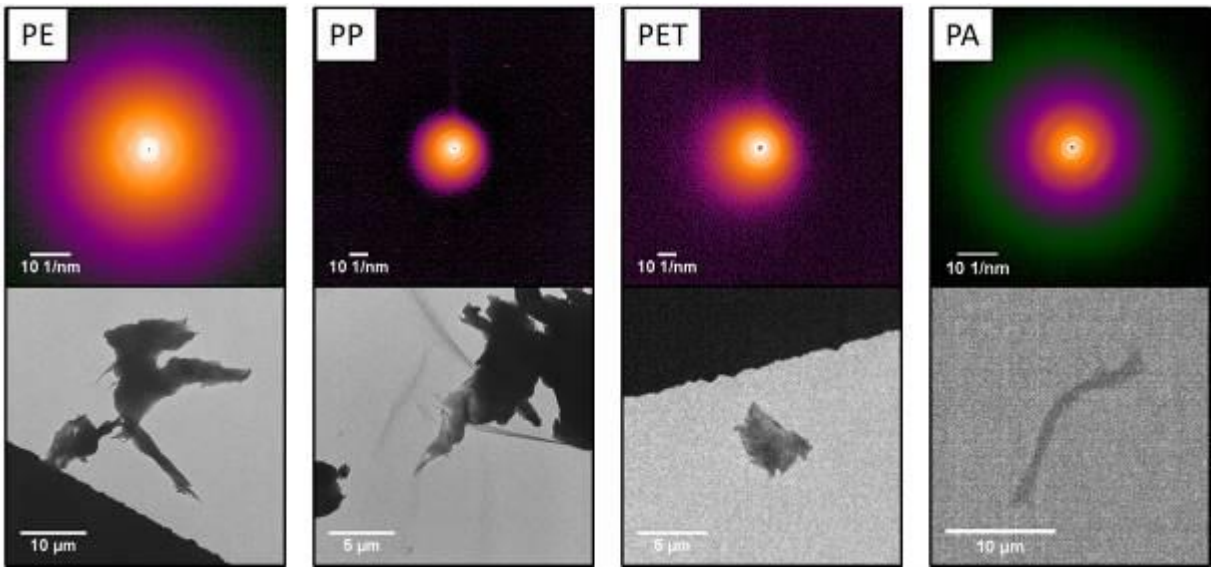
PE
PP
PET
PA
10 1/nm
10 µm
5 µm

Fig. 2

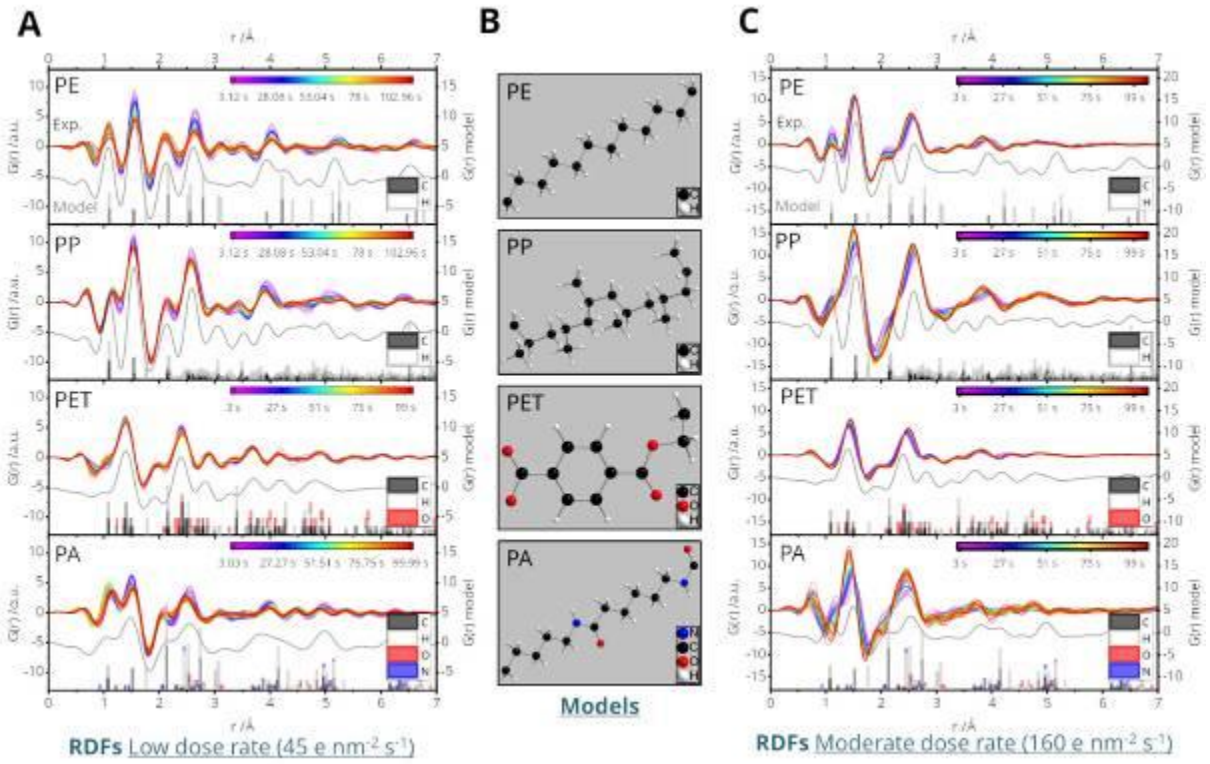
A
B
C
PE
PP
PET
PA
Exp.
Model
Models
RDFs Low dose rate (45 e nm⁻² s⁻¹)
RDFs Moderate dose rate (160 e nm⁻² s⁻¹)

Fig. 3

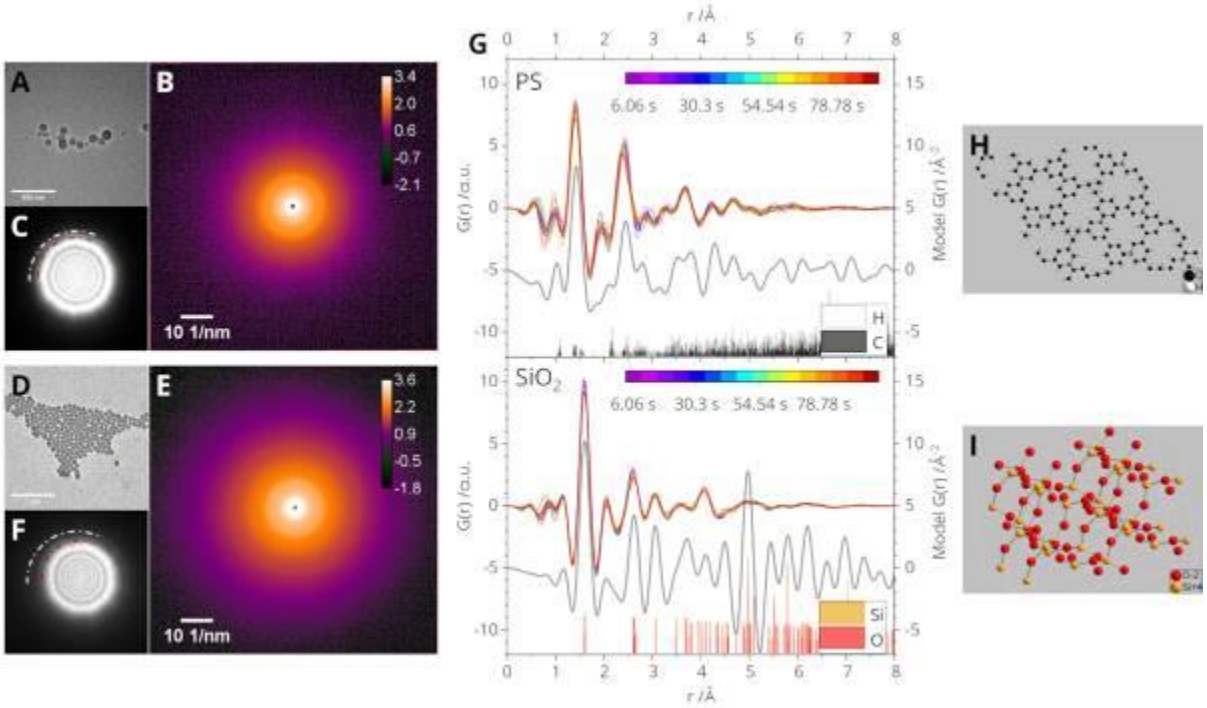
A
B
C
D
E
F
G
H
I
3.4
2.0
0.6
-0.7
-2.1
10 1/nm
3.6
2.2
0.9
-0.5
-1.8
10 1/nm
PS
6.06 s
30.3 s
54.54 s
78.78 s
H
C
SiO2
6.06 s
30.3 s
54.54 s
78.78 s
Si
O
G(r) /a.u.
Model G(r) /Å-2
r /Å

MS5.P003

Liquid phase (S)TEM of DNA origami: gold nanoparticle hybrids

A. Ong[1], D. Pohl[1], T. Jeong[2,3], A. Heerwig[3], M. Mertig[2,3], B. Rellinghaus[1]

[1]TU Dresden, Dresden Center for Nanoanalysis (DCN), Dresden, Germany
[2]TU Dresden, Physical Chemistry, Dresden, Germany
[3]Kurt-Schwabe-Institut für Mess- und Sensortechnik Meinsberg e.V, Waldheim, Germany

1. Introduction

DNA origami is a versatile and flexibly adaptable molecular template to control self-assembly of nanoparticles (NPs) and other nanoscopic building blocks [1]. Particle-particle and particle-substrate interactions can be controlled effectively by choosing appropriate functionalization of the NPs. As DNA-based processes require liquid environments, high-resolution microscopy applicable to liquids is needed to characterize, understand, and optimize the underlying physico-chemical mechanisms. Here, we use in-situ (scanning) transmission electron microscopy ((S)TEM) to study Au NPs, which are site-specificly bound to DNA origami structures directly in solution.

2. Objectives

The study focuses on imaging individual Au NPs adhered to DNA origami, determining the precision, to which particle sizes and positions can be measured in solution, and the characterization of beam-induced artefacts, which may impede the microscopic view and alter the solution chemistry and assembly.

3. Materials & methods

Au NPs (52±1 nm in diameter) were synthesized by seed-mediated growth and covered with DNA oligomers using a freeze-thaw approach [2]. 2 x 40 x 150 nm3 large quasi 2D DNA origami pads were designed and synthesized by scaffolded self-assembly [1,3]: Long ssDNA (*M13mp18*) is folded by oligonucleotides, some of which were extended by ssDNA, whose sequence is complementary to that on the Au NP surface. Two different sequences were used for positioning of Au NP dimers with defined spacing on the pad.

Ex-situ (S)TEM and in-situ liquid phase (S)TEM (LP-(S)TEM) were conducted on a *JEOL F-200* microscope equipped with a *Gatan OneView* camera and a HAADF detector at 200 kV. For LP-(S)TEM investigations, a *Protochips Poseidon Select* holder was used to keep the samples in a liquid environment that was sealed with SiN membranes against the high vacuum of the line tube.

4. Results

While ex-situ (S)TEM allows to clearly image Au NPs dried from solution and the individual DNA origami attached to them (despite large differences in contrast, see insert of Fig. 1), resolution and contrast of the LP-STEM images are reduced by beam-induced crystallization (predominantly of salts from solution). Nonetheless, upon optimizing the scanning parameters, a precision measurement of particle positions and distances is also possible in solution and first measurements indicate a preferred inter-particle distance as intended by the specifically "programmed" DNA pads (cf. Fig. 2). Indications are that complementary bright and dark field imaging may allow for a better resolution in STEM than in TEM.

5. Conclusion

LPEM bears a great potential for the quantitative characterization of NPs in solution. However, resolution-limiting artefacts and side effects render the continuous conduction of ex-situ control experiments indispensable.

Financial support by DFG through RTG 2767 and EU"s Horizon 2020 Programme (grant #964248) is gratefully acknowledged. We thank Gunnar Klös for nanoparticle synthesis and functionalization.

[1] J. Zessin et al., Nano Lett. 17 (2017) 5163.

[2] G. Klös et al., Zenodo (2022), https://doi.org/10.5281/zenodo.6516945.

[3] P.W.K. Rothemund, Nature 440 (2006) 297.

Fig. 1

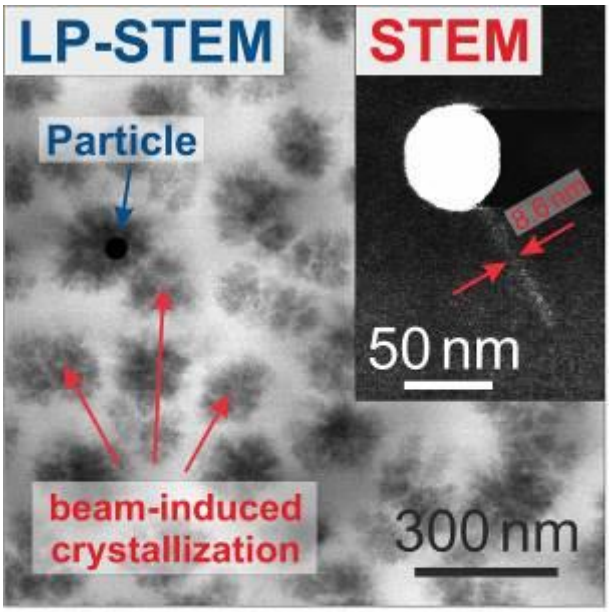

Fig. 1: Characterization of 50 nm Au nanoparticles with single rod-like 6HDNA origamis attached to them. Liquid phase STEM image (LP-STEM) of the particles in solution. Note the strong beam-induced crystallization artefacts. *Insert*: Single Au particle after drying from solution: Unlike with LP-STEM, the DNA origami is clearly visible with a measured width of 8.6 nm.

Fig. 2

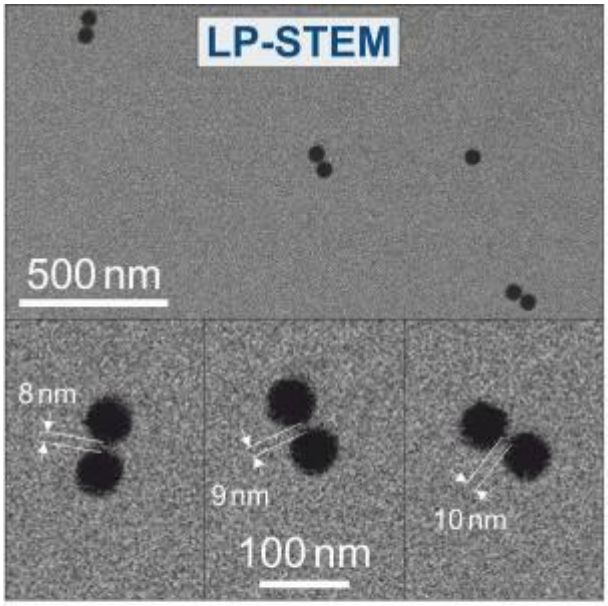

Fig. 2: Liquid phase STEM image (LP-STEM) of 50 nm Au nanoparticle dimers deposited on quasi 2D DNA pads composed of 16 neigboring double helice. Predefined patterns of chemical adhesion sites on the pads define a most probable inter-particle distance for particle dimers attached to them. This distance is measured to be 9 ±1 nm (limited by pixel size).

MS5.P005

Structures of Vitamin D derivatives by electron diffraction

K. K. Jha[1], M. Chodkiewicz[2], M. Wanat[2], B. Gruza[2], A. Kutner[3], T. Góral[1], P. Dominiak[2], K. Woźniak[1,2]

[1]University of Warsaw, CeNT, Warsaw, Poland
[2]University of Warsaw, Department of Chemistry, Warsaw, Poland
[3]Medical University of Warsaw, Department of Pharmacy, Warsaw, Poland

Introduction. Vitamins D are a group of fat-soluble secosteroids. Ergocalciferol (vitamin D2) and cholecalciferol (vitamin D3) are major forms of vitamins D which occur in fungi and animal organisms.[1] 1α,25-Dixydroxyvitamin D2 (ercalcitriol, 1,25(OH)2D2) and 1α,25-dihydroxyvitamin D3 (calcitriol, 1,25(OH)2D3) are the most active forms of vitamin D2 and D3, respectively. The biological activity of vitamins D (Fig. 1) is expressed mostly through the interactions with the nuclear vitamin D receptor (VDR). VDR, after binding natural agonists, calcitriol or ercalcitriol, forms the heterodimer with nuclear retinoid X receptor (RXR). This complex binds with DNA and regulate the vitamin D-dependent gene expression. Autoimmune diseases such as type 1 diabetes, multiple sclerosis, rheumatoid arthritis, and others such as influenza or tuberculosis occur more often in countries with limited access to sunlight and thus the lowered vitamin D endogenous production.

Objectives and results. We will present details of series of structures of the studied derivatives of the vitamin D resulting from kinematic refinement of the electron diffraction data collected in our Lab., comparison of the ED structures with known X-ray structures of the corresponding vitamin D derivatives, results of HAR and TAAM refinements [2] based on aspherical atomic electrostatic potentials and utilizing results of kinematic refinement, and, hopefully, also results of dynamical refinement [3] for the best ED data sets.

Materials. Only a small number of the vitamin D analogues crystalize well enough for structural X-ray studies [4-6]. We have previously solved the X-ray structure of the synthetic precursor of 1,25(OH)2D2, i.e. 1a-hydroxyvitamin D2 (1a-OH-D2) and showed that the molecule adopts exclusively an A-ring chair b-conformation [7]. Most vitamin D compounds form nanocrystals which can be structurally characterized only by more advanced techniques, including electron diffraction (ED). In this communication, we will also present ED structures of 1,25(OH)2D3 analogs, the side-chain, and A-ring modified VDR agonists coded PRI-2204 and PRI-1901, respectively.

References

1 A. Norman, Vitamin D; Elsevier, 2012; ISBN 978-0-323-14143-7; S. Kato, *J. Biochem. (Tokyo)* 127 (2000) 717

2 B. Gruza, M. L. Chodkiewicz, J. Krzeszczakowska, P. M. Dominiak, Acta Cryst.. A76 (2020) 92.

3 L. Palatinus, V. Petricek, C. A. Correa, Acta Cryst., A71 (2015) 235

4 M. Wanat, M. Malinska, A. Kutner, K. Woźniak, *Molecules,* 27(6) (2022) 1757

5 M. Wanat, M. Malińska, A. Kutner, K. Woźniak, *Molecules,* 25(8) (2020) 802

6 M. Wanat, M. Malińska, A. Kutner, K. Wozniak, *Cryst. Growth Des*. 18(6) (2018) 3385

7 WKołodziejski, K. Woźniak, P., J. Herold, M. Dominiak, A. Kutner*, J. Mol. Structure,*734, (2005) 149

Acknowledgments: This research was funded by the University of Warsaw IDUB grants BOB-IDUB-622-20/2021, IUDUB PSP: 501-D112-20-0006100 and by Polish NCN grant 2020/39/I/ST4/02904.

Figure 1. Structures and the numbering system of vitamins D: (a) 1,25(OH)2D2 (ercalcitiol) and (b) 1,25(OH)2D3 (calcitriol) and structures of the vitamin D analogs studied: (c) PRI-2204, (d) PRI-1901 (Solverol), (e) 1a-hydroxyvitamin D2 and (f) PRI-2191 (Tacalcitol). H-atoms omitted for clarity.

Fig. 1

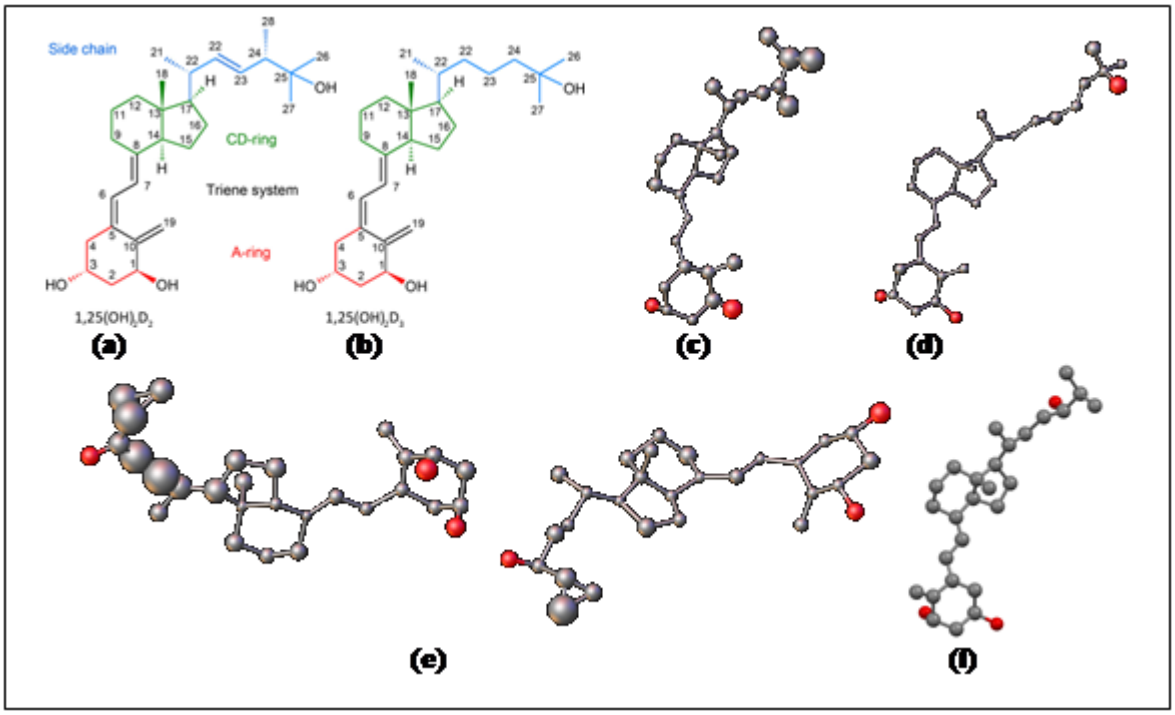
Side chain
CD-ring
Triene system
A-ring
1,25(OH)2D2
1,25(OH)2D3
(a)
(b)
(c)
(d)
(e)
(f)

MS5.P006

Polymer to carbon transition: *In Situ* pyrolysis of 3D printed microstructures

Q. Sun[1], C. Dolle[1], C. Kurpiers[2], P. Gumbsch[2,3], R. Schwaiger[4], Y. M. Eggeler[1]

[1]Karlsruher Institut of Technologie (KIT), Laboratory for Electron Microscopy (LEM), Karlsruhe, Germany
[2]Karlsruher Institut of Technologie (KIT), Institute for Applied Materials (IAM), Karlsruhe, Germany
[3]Fraunhofer Institute for Mechanics of Materials IWM, Freiburg, Germany
[4]Forschungszentrum Jülich GmbH, Institute of Energy and Climate Research (IEK), Jülich, Germany

Carbon has been well known as a compelling material to compete with silicon in the field of microchips. One promising method to fabricate micro- or nanoscale carbon architectures is to pyrolyze a pre-patterned polymer precursor [1]. Pyrolysis is, therefore, a crucial processing parameter. However, a mechanistic understanding of the pyrolysis process for sub-micrometer polymer geometries is still missing. In particular, for the temperature regime, where the highest mass loss and, in turn, the highest shrinkage is observed, a detailed analysis of the pyrolysis-induced shrinkage kinetics, geometry dependence shape deformation, the roles of atmosphere and surface area is still lacking [2].

In this work, we aim to fill this knowledge gap and provide a comprehensive understanding of morphological deformation upon pyrolysis. Here, we report a systematic study of *in situ* pyrolysis process by varying environment pressure, heating temperature, and sample geometry (surface-to-volume ratio) in an environmental SEM (ESEM). We use direct laser writing of IP-Dip photoresist to print microstructures directly on MEMS heating chips [3]. We focus on the early stage of carbonization from 450 to 550 °C, where polymer precursor experiences the greatest mass loss and structural shrinkage. The structural changes are directly tracked by secondary electron imaging.

We reveal the pyrolysis kinetics illustrating the temporal and temperature dependency of the deformation (Fig. 1). When evaluating the data pool by generating model-free master curves, we fully describe the dynamic process and extract the effective activation energy (Ea). After changing the environmental conditions, the shrinkage behavior turns out to be fundamentally different, largely kinetically hindered. A prevalence of the aspect ratio on kinetics and the final size becomes apparent, causing a dramatically lower Ea.

To complete the picture of the structural changes during pyrolysis-induced transformation, our ongoing experiments tackle focused ion beam (FIB) micromachined cross sections of the microstruts after isothermal exposure using scanning transmission electron microscopy (STEM). Not only morphological changes can be characterized but also local structural and chemical information by electron energy loss spectroscopy in 4D-spectrum images (EELS-SI), as shown in Fig. 2.

In conclusion, our *in situ* and scale-bridging study paves the way to a thorough understanding of morphological mechanisms upon pyrolysis and correlated property strengthening. The precise tuning of functional metamaterials by pyrolysis will facilitate the development of industrially relevant carbon device fabrication.

References:

[1] Schueller et al., Chem. Mater. 1997, 9, 6, 1399–1406.

[2] Sharma et al., Sci Rep 8, 16282 (2018).

[3] Sun et al., Microscopy and Microanalysis 27(S2) (2021) 83-84.

[4] The authors acknowledge financial funding by the German Research Foundation (DFG) under Germany"s Excellence Strategy (EXC-2082/1─390761711).

Fig. 1

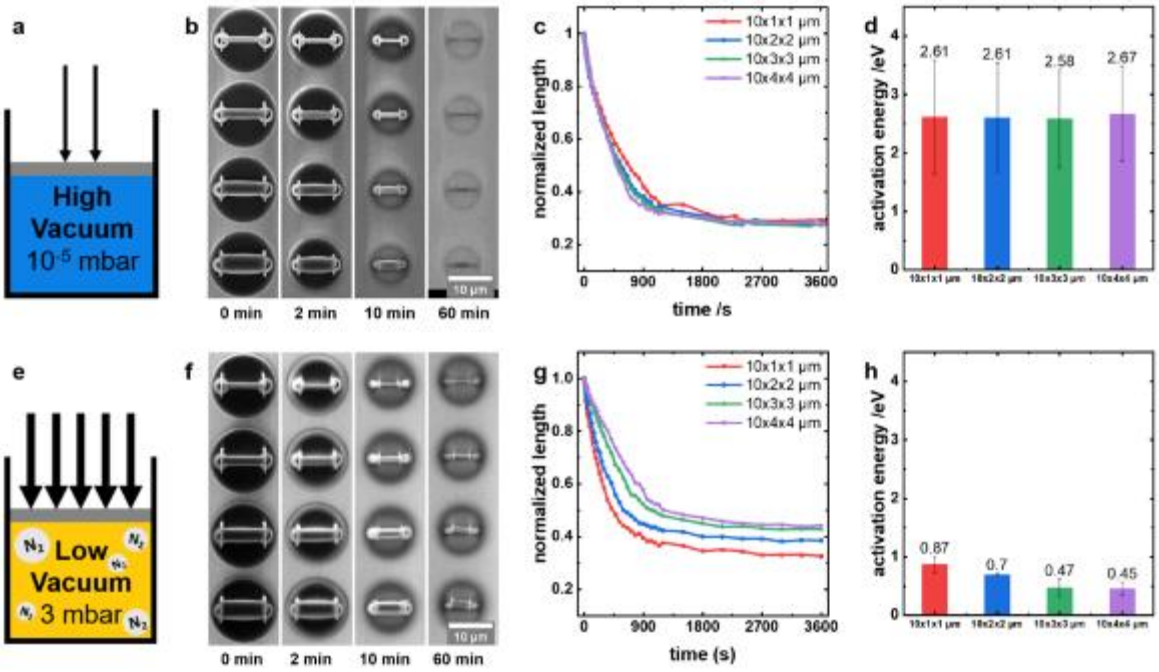

Figure 1 *In situ* pyrolysis in an ESEM. **a & e** Schematic representing the two investigated vacuum states. **b & f** SEM topview image montage of microstruts during isothermal heating at 500 °C as a function of time under high (**b**) and low (**f**) vacuum conditions. **c & g** Evolution of the microstrut length as a function of time extracted at 500 °C, under high (**c**) and low (**g**) vacuum conditions. **d & h** Effective activation energies calculated from pyrolysis kinetics showing great differences between high (**d**) and low (**h**) vacuum cases.

Fig. 2

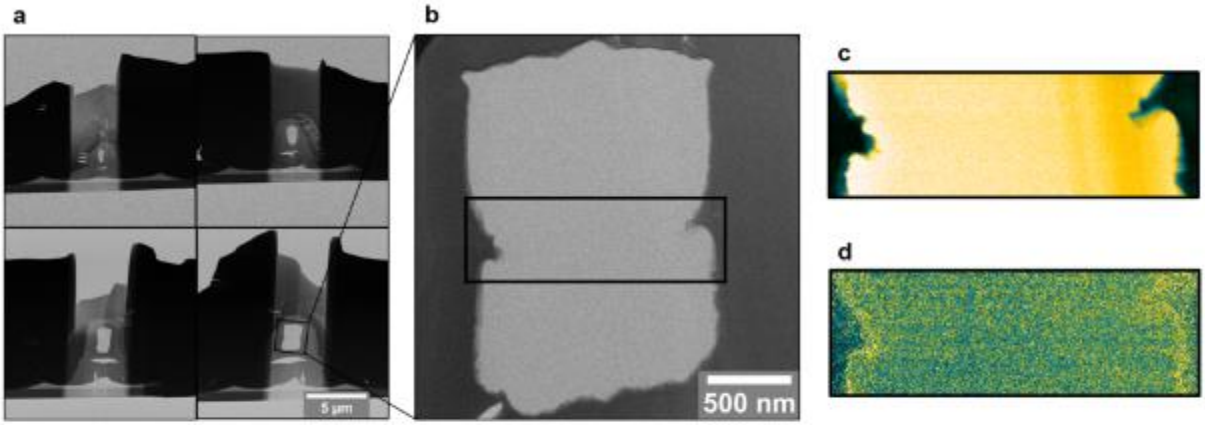

Figure 2 Cross-sectional study of pyrolyzed microstruts by STEM and EELS. **a** Overview bright field images of microstrut crossections heated at 450 °C in a low vacuum. **b** Zoomed-in micrograph of the thickest microstrut indicating the area of core-loss spectrum image from carbon K edge (**c**) to oxygen K edge (**d**), showing a cumulation of oxygen at the surface of microstruts.

MS5.P007

High-contrast electron microscopy imaging of polymer materials for Li-batteries

B. Förster[1], J. Allgaier[2], M. Ohl[2], S. Förster[2]

[1]Forschungszentrum Jülich GmbH, ER-C-1, Jülich, Germany
[2]Forschungszentrum Jülich GmbH, JCNS-1, Jülich, Germany

- Introduction

Ion-conducting polymers have attracted significant interest as electrolyte membrane materials for solid-state lithium batteries because of their excellent safety, mechanical stability and flexibility. The most commonly used ion-conducting polymer is polyethylene oxide (PEO) because the excellent solubility of lithium salts leads to high ionic conductivity. Block copolymers containing PEO covalently linked to hydrophobic polymer blocks such as polystyrene, polyisoprene or polybutadiene allow designing ordered nanoscale membranes with high ionic conductivity and mechanical stability via self-assembly. Self-assembly can be controlled via block lengths to tailor nanodomain phase morphology and macroscopic orientation. Electron microscopy allows visualizing the order and orientation of the conductive block copolymer domains to optimize the conductivity of the block copolymer membranes.

- Objectives

To correlate measured ionic conductivities of block copolymer membranes to block copolymer morphologies requires an in-depth structural characterization over length scales from nanometers to hundreds of micrometers, which can be provided by electron microscopy combining SEM and TEM images. Using cryo-ultramicrotomy we aim to show that LiTFSi-filled PEO-block copolymer membranes can be dry sectioned under humidity exclusion.

- Materials & methods

As block copolymers we investigated poly(butadiene-b-ethylene oxide) (PB-PEO) with/without added LiTFSi salt. Samples were solvent-cast into films. These were subsequently dry sectioned by cryo-ultramicrotomy and investigated by a JEOL F200 cryo TEM and Thermo Fisher Apreo Volumescope.

- Results

We obtained thin sections of LiTFSi-loaded PB-PEO using cryo-ultramicrotomy with thickness of about 80 nm. The thin sections can be imaged at high voltages of 200 kV with STEM without staining and at 30kV with STEM in SEM. Thin sections where prepared under cryo conditions and transferred to the TEM using a cryo holder. After investigation of the sections in TEM, they were transferred to the SEM without humidity control. We find that there is no structural change during air contact.

Images of loaded and unloaded samples can be compared to identify salt induced changes of the morphology.

The block copolymer domains in the ribbons can be imaged by TEM by high- and by SEM by low-voltage STEM without staining. Electron microscopy provides crucial information about the domain morphology, ordering and orientation within the membrane.

- Conclusion

We demonstrate that ultramicrotomed thin sections of block copolymers can be imaged with high contrast by STEM at voltages of 200 kV in TEM and 30 kV in SEM without staining. This allows to visualize the LiTFSi-conduction paths across the block copolymer membranes, which is of high importance to improve the conductivity of solid polymer electrolytes in Li-battery applications.

Bright field (figure 1) and dark field (figure 2) image of LiTFSi loaded PB-PEO block-co-polymer

Fig. 1

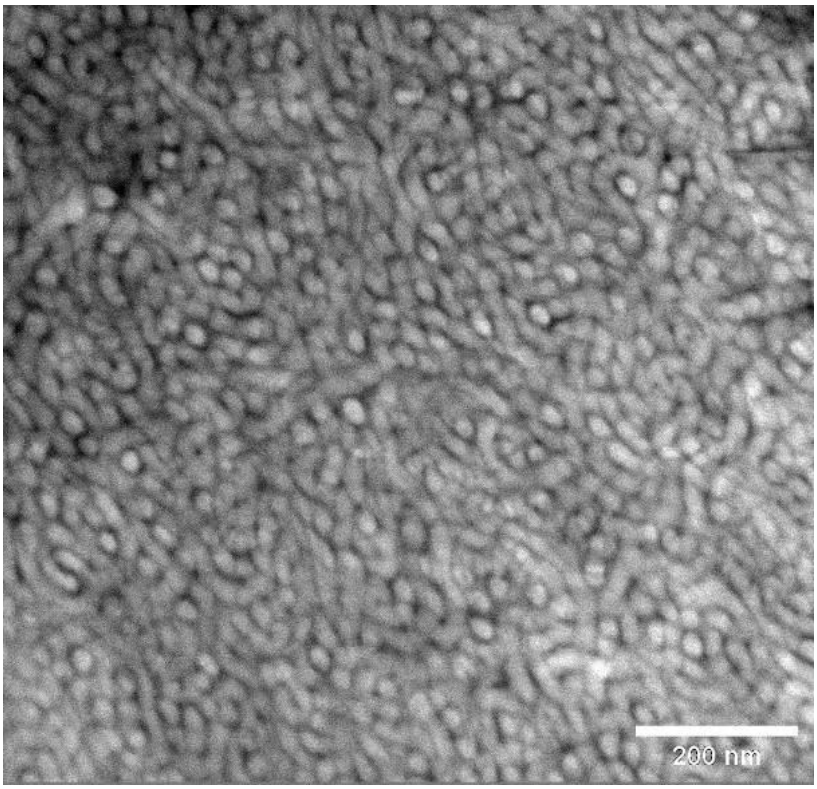

Fig. 2

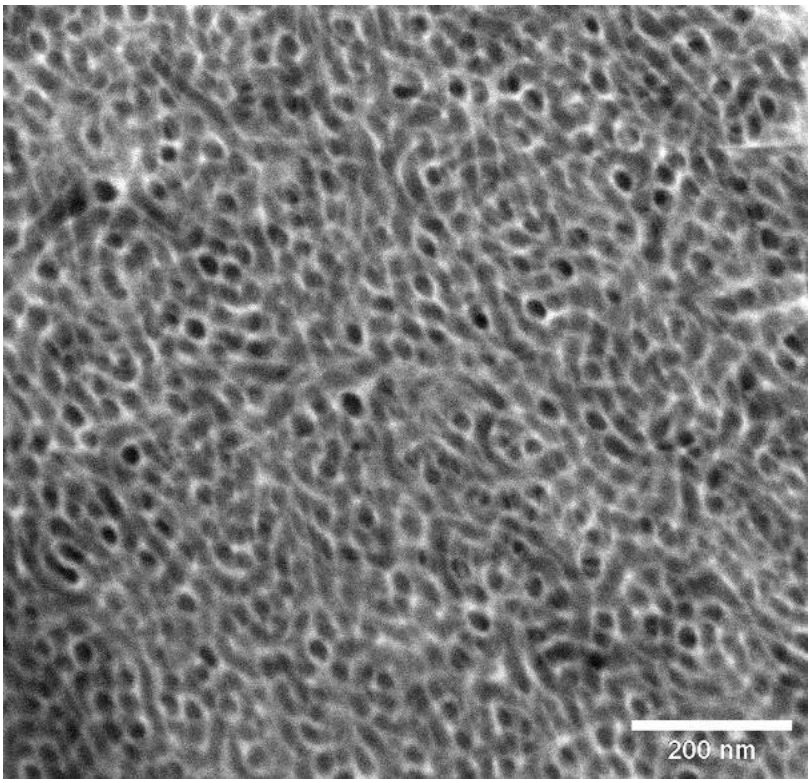

MS5.P008

Morphology of polylactide stereocomplexes in blends of poly[(L-lactide)-*co*-(ε-caprolactone) and -poly(D-lactic acid) with varying molar masses

Y. Pieper[1], P. Hommes-Schattmann[1], A. T. Neffe[1]

[1]Helmholtz-Zentrum Hereon, Institute of Active Polymers, Teltow, Germany

Introduction

Poly[(L-lactide)-*co* -(ε-caprolactone)] (PLC) and poly(D-lactic acid) (PDLA) are biodegradable polyesters that can be produced from renewable resources and are now widely used in standard, biomedical and pharmaceutical applications. Improving the mechanical properties and heat resistance of materials based on poly(ε-caprolactone) (PCL) and poly(lactic acid) (PLA)) is a major concern when they are used in biomedical and consumer products [1][2]. One of the most effective methods to improve the mechanical properties and thermal stability of PLA-based materials is the formation of stereocomplexes between poly(L-lactide) (PLLA) and poly(D-lactide). This stereocomplex (SC) formation is defined as stereocomplex crystallization between PLLA and PDLA and contributes significantly to the control of polymer properties [3].

Objectives

The aim of this study is to identify and visualize the different morphologies, especially crystallinity and stereocomplexation, in the blends of PLC and PDLA of different compositions prepared by solution casting, in order to understand the SC formation and the associated new properties of the polymer.

Materials and methods

The obtained polymer blends were morphologically studied by scanning electron microscopy (SEM) and transmission electron microscopy (TEM). Supporting analytical methods such as wide angle X-ray scattering (WAXS) and differential scanning calorimetry (DSC), were used to detect crystallization, while polymer characterization by GPC and NMR was employed to relate the morphology to polymer. Tensile tests were performed to determine the mechanical properties.

Results

Visualization of the morphology allowed identification of the amorphous and (stereo-) crystallizing regions. Together with the additional characterizations, maximal overall crystallization and, specifically, stereocrystallization was quantifiably shown. In polymer blends with too short lactide segment lengths, no SC could be detected. From a number average oligolactide sequence length $l_{LA} \geq 4.2$, the formation of SC was observed, which further increased with increasing lactide sequence and lattice content. However, the crystallites show a decrease in SC size, which can be attributed to phase dilution. Mixtures with a high PDLA mol mass yielded smaller SC crystallites than mixtures with lower mol mass. Limited SC formation exists due to steric hindrance of long molecular chains and partial crystallization of the homopolymer.

Conclusion

The totality of the applied analytical methods indicates that the adjustment of the morphology of the polymer blends at the nanoscale is necessary to achieve the desired macroscopic properties of the blends.

References

[1] A. T. Neffe et al., Nanomaterials 2021, 11, 1472.

[2] V. Izraylit et al., Eur. Polym. J. 2020, 137, 109916

[3] X. Su et al., Polymers 2020, 12, 2515.

MS5.P009

Flexible laser-patterned carbon coatings for sensing and energy applications

M. Hepp[1], H. Wang[2], C. O. Ogolla[1], K. Derr[1], V. Strauss[2], B. Butz[1]

[1]University of Siegen, Micro- and Nanoanalytics Group, Siegen, Germany
[2]Max Planck Institute of Colloids and Interfaces, Potsdam, Germany

Fabricating electronic devices from natural, renewable resources has been a common goal in engineering and materials science for many years. In this regard, carbon-based coatings are of significance due to high availability of the raw materials and their environmental degradability. Carbonized materials and composites thereof have been proven as promising candidates for a wide range of future applications in flexible electronics, optoelectronics, energy storage or catalytic systems. On the industrial scale, however, their application is inhibited by tedious and expensive preparation processes and a lack of control over the processing and material parameters.

A promising tool to tackle that challenge is carbon laser-pattering (CLaP) allowing for the defined and site-selective synthesis of functional carbon-based materials for flexible on-chip applications. Versatile inks, based on naturally occurring (molecular) starting materials are used to produce films, which are carbonized with a CO2-laser to obtain functional patterns of conductive porous carbon networks [1]. By chemical and physical fine-tuning of the laser-patterned carbons (LP-C), we developed high-performance flexible resistive chemical and mechanical sensors. Their properties make them applicable in many fields e.g., robotics, bionics and even health monitoring (Fig. 1).

In this contribution, we present both, the material"s synthesis and tailored properties as well as in-depth microscopic and spectroscopic cross-sectional analyses of such coatings (Fig. 2), which provide unprecedented insights into the microstructure and local chemistry/bonding of laser-patterned carbon [2,3]. In that regard, we as well discuss the challenges and solutions for cross-sectional preparation of such porous and sensitive structures by advanced ultramicrotomy. The gained insights in structure formation and local functionality pave the way for the utilization of alternative fast, large-scale carbonization methods such as rapid thermal annealing.

Part of this work was performed at the Micro-and Nanoanalytics Facility (MNaF) of the University of Siegen.

Fig. 1

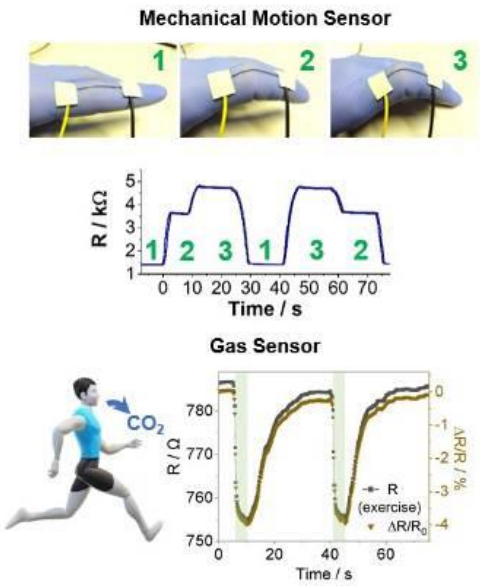

Fig. 1: Applications of LP-C sensor strips.

[1] Delacroix et al, Adv. Electron. Mater. 6 (2020) 2000463
[2] Hepp et al, NPJ Flex. Electron. 6 (2022) 3
[3] Wang et al, chemrxiv.org (2022) 6dlsg

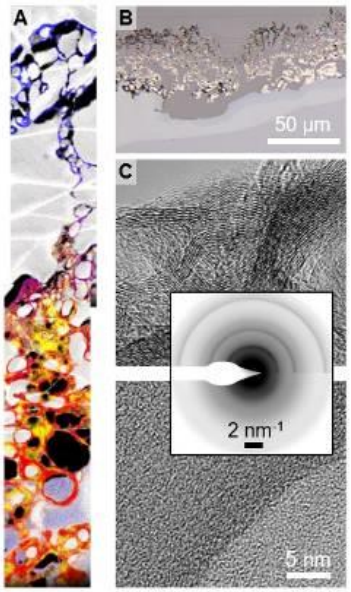

Fig. 2: Cross-sectional analysis of LP-C sensor strip. **A** EELS bond map. **B** Optical micrograph of resin infiltrated LP-C film. **C** HRTEM images from upper and lower film regions with related SAED pattern

MS6.001-invited

Stress-induced amorphization and grain boundary sliding in olivine

P. Cordier[1,2], I. ul Haq[3], A. Orekhov[3], D. Schryvers[3], H. Idrissi[3,4]

[1]University of Lille, UMET, Villeneuve d'Ascq, France
[2]Institut Universitaire de France, Paris, France
[3]University of Antwerp, EMAT, Antwerp, Belgium
[4]Université Catholique de Louvain, Louvain-la-Neuve, Belgium

$(Mg, Fe)_2SiO_4$ olivine is the most volumetric abundant mineral phase in the upper mantle down to 410 km depth and also the one which deforms the most and controls the rheology of the upper mantle. Deformation mechanisms in olivine have attracted considerable attention since several decades. One of the problems with this orthorhombic mineral is that there are not enough slip systems to produce a general deformation. The observation of a non-linear deformation regime depending on the grain size has led to the suggestion of the possibility of slip at the grain boundary [1], which has only recently been demonstrated microstructurally [2]. In this paper we show that under high stresses, this grain boundary sliding can be due to the amorphization of the grain boundary and to the flow of this amorphous intergranular phase. We show how nanomechanical testing in situ in the TEM allows to characterize this individual mechanism as well as the rheology of this amorphous olivine. We finally propose that this mechanism of stress-induced amorphization is an important deformation mechanism in its own right under conditions of high stress [3].

[1] Hirth, G., & Kohlstedt, D. (1995) Experimental constraints on the dynamics of the partially molten upper mantle: 2. Deformation in the dislocation creep regime, Journal of Geophysical Research, 100, 15,441–15,449,

[2] Bollinger, C., Marquardt, K. & Ferreira, F. (2019) Intragranular plasticity vs. grain boundary sliding (GBS) in forsterite: microstructural evidence at high pressures (3.5–5.0 GPa). American Mineralogist 104, 220–231.

[3] Idrissi, H., Carrez, P., & Cordier, P. (2022) On amorphization as a deformation mechanism under high stresses. Current Opinion in Solid State & Materials Science. 26(1), 100976

Fig. 1

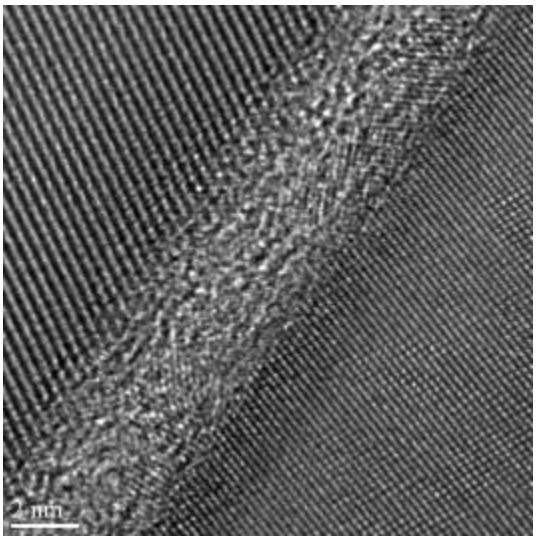

MS6.002-invited

Nucleation mechanism of Magnesium-Silicate-Hydrate (M-S-H) cement

R. A. Cristina[1]

[1]University Konstanz, Germany

Concrete is the most used artificial material of humankind. But despite the importance of concrete to our infrastructure, the production of its binder cement is contributing to a significant amount of the global CO2 emissions. [1] Actions to reduce cement"s massive carbon footprint involve strategies that include the utilization of abundant clays and minerals but also the development of low carbon binders. [2] Magnesium-Silicate-Hydrate (M-S-H) has caught the attention of material scientists as an alternative binder that could be produced from low carbon resources like seawater brines and the extraction of educts from abundant minerals like olivine. [2-3] Until now, most alternative binders are only scarcely researched and suffer from deficient material properties compared to traditional Portland cement.

Innovative binders must meet certain requirements, such as being environmentally friendly, sustainable, having suitable material properties while also being economically reasonable. Fundamental knowledge about the nucleation and growth mechanisms will be pivotal to control the formation and nanostructure of the cementitious material from the bottom up, via the use of designed polymeric or mineral additives formulations. Herein, we investigate first the early stages of M-S-H formation in an additive-free enviroment with physicochemical methods like analytical ultracentrifugation (AUC) coupled with ESI-MS and time-resolved potentiometric titration. This enable us to decipher the moieties present in the pre-nucleation phase and how they affect the postnucleation phase of theM-S-H. Characterization of the final product involves multiple state-of-the-art techniques used in the analysis of morphology and composition (TEM, SEM, IR, XRD).

[1] J. Lehne, F. Preston, Chatham House Report, Energy Enivronment and Resources Department: London, UK 2018, 1-66.

[2] E. Gartner, T. Sui, cement and concrete research 2018, 114, 27-39.

[3] S. Allan Nye, S. Vineet, O. Christopher, S. Barnaby, C. Chris, Frontiers in Built Environment 2021, 7.

MS6.003

Phase separation of olivine in basalt aggregate induced by fatigue damage of ultra-high performance concrete

G. Schaan[1,2], S. Rybczynski[2], F. Schmidt-Döhl[2], M. Ritter[1]

[1]Hamburg University of Technology, Electron Microscopy Unit, Hamburg, Germany
[2]Hamburg University of Technology, Institute of Materials, Physics and Chemistry of Buildings, Hamburg, Germany

Introduction

Ultra-high performance concrete (UHPC), a specialized form of concrete characterized by its high compressive strength of up to 200 N/mm^2, has garnered considerable interest since the first reports in the early 1990s.[1] Today, it is used mostly in structures with high strength requirements such as bridges, high-rise buildings and wind turbine towers.

Objectives

Due to the high cement content of fine-grained UHPC, its production entails the emission of large amounts of CO_2. In an attempt to mitigate this effect, we try to introduce conventional coarse aggregate from suitable high-strength rocks such as basalt or granite into the formula. However, the average and maximum lifetime of specimens during cyclic loading tests significantly decreases compared to UHPC not containing any coarse aggregate. One of our aims is to investigate the origins of this phenomenon using electron microscopy methods.

Materials and methods

UHPC was fabricated with ordinary Portland cement (CEM I), a water-to-cement ratio (w/c) of 0.24, quartz sand (maximum grain size ca. 500 µm) and quartz powder (20 µm) as aggregate, nanoscale silica fume and a PCE superplasticizer. Additionally, up to 30 vol.-% of basalt gravel (grain size 2 to 8 mm) were used as coarse aggregate. After hardening for at least 56 days, cylindrical samples were subjected to cyclic uniaxial compressive loading between lower and upper limits of 5 and 80%, respectively, of the short-term compressive strength. We performed testing until failure or until a desired point on the lifetime curve was reached. From whole specimens or suitable fragments, samples were extracted via mechanical as well as focused ion beam (FIB) methods and investigated using SEM, TEM and EDS spectral imaging.

Results

The basalt we used is a volcanic rock comprised of phenograins with a size of ca. 100 to 200 µm of mostly pyroxene (augite and jadeite), olivine and titanomagnetite embedded in a feldspar groundmass.

Figure 1: Large-area EDS map of basalt.

Additionally, we observe small phenograins of chloroapatite. Among olivine grains, most are affected by weathering in the shape of numerous cracks often permeating the entire grain. While this phenomenon has been known for decades,[2] we observe the conversion becoming more pronounced with progressing fatigue damage from cyclic loading. Cracks grow in width from 2 to 4 µm in the pristine state to up to 40 µm in post-failure specimens. Using EDS elemental mapping, we find a phase separation of olivine (magnesium iron silicate) into two or more separate compounds. Most cracks exhibit a distinct structure with an iron-rich outer region bordering the unaffected olivine mineral and a zigzag-shaped inner region rich in magnesium and silicon. In the very center of each crack, we observe enrichments of trace elements elements not commonly found in olivine such as aluminum and occasionally calcium, nickel or sulfur.

Figure 2: BSE-SEM image and EDS maps of phase separation in olivine.

Conclusion

We conclude that trace elements in olivine accumulate at interfaces. In the event of mechanical fatigue, inner friction occurs at these interfaces, resulting in a local rise in temperature that enables and promotes a phase separation of the mineral.

References

[1] D. H. Wang *et al.*, *Const. Build. Mater.* **2015**, *96*, 368-377.

[2] W. A. Deer, R. A. Howie, J. Zussman, *An Introduction to the Rock-Forming Minerals*, 3rd edition, Longmans, London, **2013**.

Fig. 1

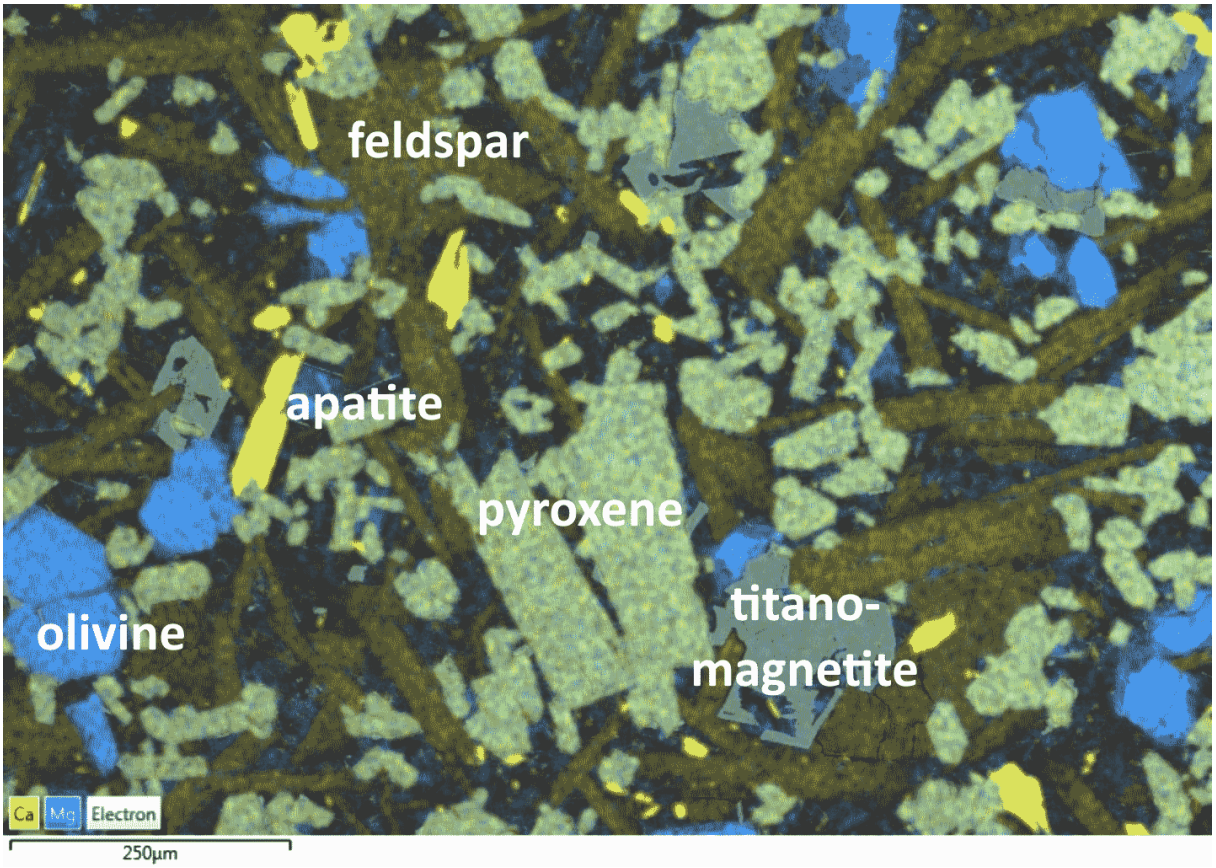

Fig. 2

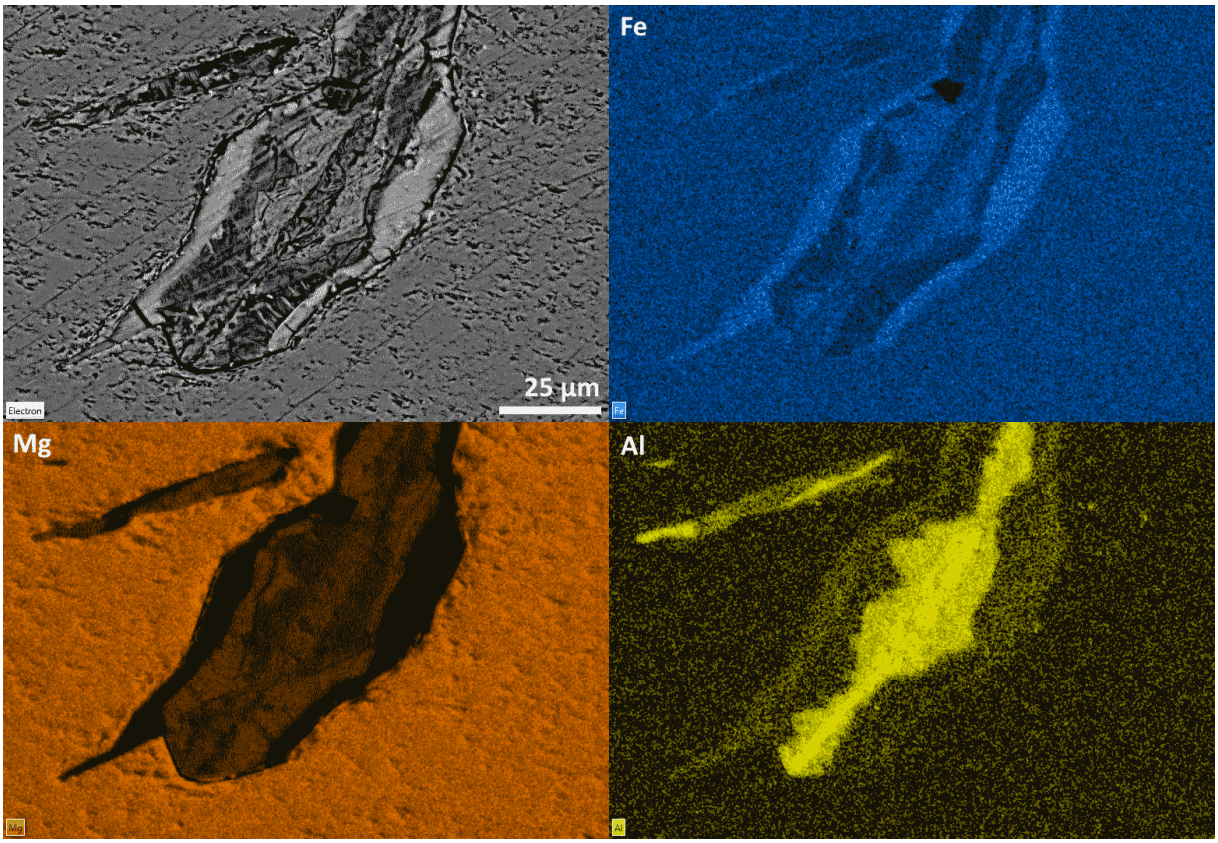

MS6.004

Alteration of Illite by Bad Nauheimer and Gerolsteiner Brine: implications on fluid permeability in geothermal projects

E. Götz[1], H. J. Kleebe[1], U. Kolb[2]

[1]Technical University Darmstadt, Darmstadt, Germany
[2]Johannes Gutenberg University Mainz, Mainz, Germany

Illite is one of the most abundant clay minerals on earth, yet its structure remains not fully resolved. Illites of the Remlinger sandstone display a fibrous growth around the detrital grains and form a meshwork within the pores of the sandstone. The meshwork and particles trapped therein during fluid flow lead to a dramatic decrease in permeability, which should be prevented in geothermal systems using for example such sandstones.

In autoclave experiments, the interaction of the Remlinger sandstone with two different natural brines, Bad Nauheimer and Gerolsteiner, were compared to an unaltered sandstone as reference, in order to determine possible changes in structure, stacking or shape of the illite fibers.

The surface of fluid-altered sandstone plugs was characterized using environmental scanning microscopy (ESEM). Grinded material of rim and core was examined by X-ray powder diffraction (XRPD). In addition, particles filtered from the fluid after the autoclave experiment were investigated employing transmission electron microscopy (TEM). Moreover, 3D electron diffraction experiments were performed using Automated Diffraction Tomography (ADT) (Kolb U., 2012; Rozhdestvenskaya et al., 2011).

Based on a 50 nm illite fiber, the structure of illite could be solved during TEM analysis using a single ADT data set. The reconstructed reciprocal space also revealed one-dimensional diffuse scattering, indicating a disorder in the stacking of the illite layers. The degree of disorder is dependent on the potassium content of the fluid, since the K+-ions of the interlayer can be released via the (010) habit plane. This reduces the stability of the structure, resulting in a high fragmentation and detachment of individual illite layers. Such mobile layer fragments can then be transported by mobile fluids to interact and entangle in the sandstone.

These new insights into the structure of illite fibers show a distinct dependence of the arrangement and local agglomeration of the fibers in the pores on the potassium content of the fluid (brine) used. The increased migration and interweaving of the fibers associated with a low potassium content can lead to severe clogging of the pores and thus to a reduction in fluid permeability. Altered sandstones with illitic pore filling are therefore less suitable for long-term geothermal projects.

Kolb U. 2012: Automated Diffraction Tomography. Uniting Electron Crystallography and Powder Diffraction. Springer, 314-326.

Rozhdestvenskaya E., Mugnaioli E., Czank M., Depmeier W., Kolb U., Merlino S. 2011: Essential Features of the Polytypic Charoite-96 Structure Compared to Charoite-90. Mineral. Magazine, 75, No. 6, 2833-2846.

MS6.005

Modification of common fluorescent dyes for the facilitated detection of micro- and nanoplastics with (scanning) transmission electron microscopy

A. C. Swertz[1], N. Pfänder[2], E. Schmidt[1]

[1]University of Wuppertal, Institute for Particle Technology, Wuppertal, Germany
[2]Max-Planck-Institut für Chemische Energiekonversion, Mülheim an der Ruhr, Germany

Introduction

In the environment, plastic litter has become a severe problem that gained much attention in recent times.[1] In this context, the term "microplastics" is commonly used to describe plastic particles with a diameter < 5 mm.[2] These particles are ubiquitously distributed in the environment – not only in marine ecosystems, but also in inland water bodies, the atmosphere, and soils. Plastic particles can degrade due to environmental impacts, including UV radiation, causing smaller particle sizes in the nanometer range.[3] These "nanoplastics" are difficult to detect because of their small particle size and low contrast in electron microscopy respectively.

Objectives

To facilitate the light microscopical analysis of small plastic particles, staining with fluorescent dyes is a widespread sample preparation technique. One commonly used dye suitable for the analysis of microplastics is Nile red. However, for smaller plastic particles, an electron microscopical analysis is required. As the contrast of polymeric nanoparticles decreases with smaller particle size for (S)TEM, heavy metal staining as applied for biological samples can help overcome this issue [4]. The aim of this study was to develop heavy metal stains by modifying the commonly used fluorescent dyes to allow a combined staining technique for light- and electron microscopy.

Materials & Methods

In this study, polymeric nanospheres and commercial polymer powders (e.g. PS, PE, PVC) were used to test the developed dyes. The dyes were based on Nile red, with the addition of previously produced heavy metal nanoparticles (e.g. Au and Pt). STEM images and EDX mappings were acquired using a C_S-corrected Hitachi HD-2700 dedicated STEM. SEM images were obtained using an FEI Quanta 450 FEG Environmental Scanning Electron Microscope.

Results

The addition of heavy metal nanoparticles on the surface of polymer nanoparticles can be observed by an increased contrast, especially in HAADF images, as shown in figure 1. Here polystyrene nanospheres were treated with an ethanolic solution of Pt-modified Nile red. The light microscopical analysis of this sample shows a successful reddish staining with fluorescence under UV light. The EDX analysis of the sample indicates an increased amount of nitrogen compared to the unstained sample, which could be associated with the Nile red staining.

Conclusion

The heavy metal modification of fluorescent dyes does not affect their ability to stain micro- and nanoplastics for light microscopical analysis. While the pure dyes as Nile red do not enhance the contrast in the electron microscope, the heavy metal modification facilitates tremendously the STEM analysis. So far, metallic nanoparticles have been attached to the fluorescent dyes for negative staining purpose. In future works, the fluorescent dyes are supposed to act as anchors for metal-ions or clusters, which allow a combined staining for light- and electron microscopy.

References

[1] Derraik, J. G., *Mar. Pollut. Bull.*, **44**(9), 842–852 (2002).

[2] Arthur, C., Baker, J. and Bamford, H., *National Oceanic and Atmospheric Administration Technical Memorandum NOS-OR&R-30*, p. 49 (2008).

[3] Mattsson, K., Hansson, L.-A. and Cedervall, T., *Environ. Sci.: Processes Impacts*, **17**, 1712-1721 (2015).

[4] Watson, M. L., J. *Biophysic. And Biochem. Cytol.*, **4**(4), 475 ff. (1958).

Figure 1: Example of stained polystyrene nanospheres: SE (left) and HAADF-STEM (right) images.

Fig. 1

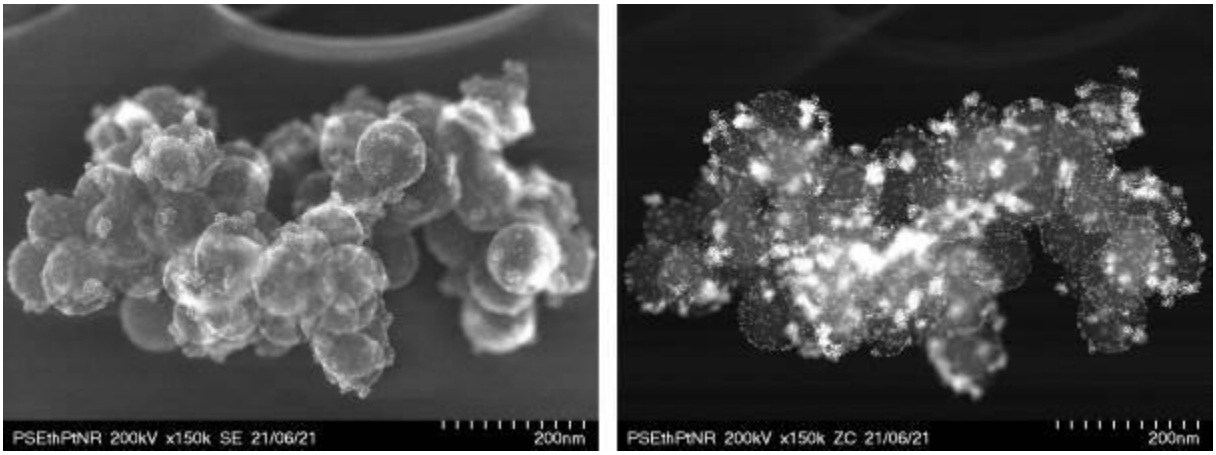

MS6.006

Strain hardening in garnet during deep crustal earthquakes

R. Dubosq[1], A. Camacho[2], D. A. Schneider[3], B. Gault[1,4]

[1]Max-Planck-Institüt für Eisenforschung GMBH, Microstructure physics and alloy design, Düsseldorf, Germany
[2]University of Manitoba, Department of Earth Sciences, Winnipeg, Canada
[3]University of Ottawa, Department of Earth and Environmental Sciences, Ottawa, Canada
[4]Imperial College London, Department of Materials, Royal School of Mines, London, United Kingdom

Mechanical models of the lithosphere assume a brittle upper layer and a ductile middle to lower layer separated by a steady-state transition occurring at a depth of ~15 km. Consequently, earthquakes typically occur in the upper continental crust[1]. Seismicity indicators such as pseudotachylytes in deeply exhumed rocks, however, evince earthquakes also occur in the lower crust (>50 km)[2]. Under these high-temperature conditions, rocks are expected to behave ductily therefore post-seismic ductile creep commonly obscures microstructures associated with seismic events in most crust-forming minerals[3]. Thus, the mechanics of seismic failure in the deeper crust remain largely unknown. Garnet, however, is a high-strength mineral and preserves structures that can be used to understand the rheological behaviour of the lower crust[4]. Herein, we study garnet porphyroclasts from an eclogite facies mylonite in the Musgrave province (central Australia) to investigate the mechanisms by which garnet is deformed under dry, lower crustal conditions. Our correlated microscopy approach combines 2D and 3D structural and geochemical analytical techniques including electron backscatter diffraction (EBSD), high-contrast backscatter electron (BSE) imaging, and atom probe tomography (APT). EBSD mapping and BSE imaging reveal bands of small, strain-free grains with scattered orientations, outlined by polygonal to lobate high-angle grain boundaries crosscutting the porphyroclasts in the vicinity of fractures. APT analysis of a high-angle grain boundary shows Fe enrichment in the form of planar and nearly equally spaced arrays of Fe-rich nanoclusters. The combined results demonstrate Fe segregation along grain boundaries of recrystallized garnet, resulting in the nucleation of Fe-rich clusters that can act as barriers for migrating dislocations and lead to strain-hardening and facilitate brittle fracture. Our findings potentially contribute to the mechanisms of mechanical failure in the lower continental crust that lead to deep seismicity.

[1]Green, H., Houston, H., 1995, The mechanics of deep earthquakes: Annual Review of Earth and Planetary Sciences, v. 23, p. 169–213.

[2]Austrheim, H., and Boundy, T., 1994, Pseudotachylytes generated during seismic faulting and eclogitization of the deep crust: Science, v. 265, p. 82–83.

[3]Kirkpatrick, J., and Rowe, C., 2013, Disappearing ink: How pseudotachylytes are lost from the rock record: Journal of Structural Geology, v. 52, p. 183–198.

[4]Mancktelow, N., Camacho, A., and Pennacchioni, G., 2022, Time-lapse record of an earthquake in the dry felsic lower continental crust preserved in a pseudotachylyte-bearing fault: Journal of Geophysical Research: Solid Earth, v. 127, p. 1–32.

MS6.P002

4D electron tomography of dislocation in MgO: an electron irradiation study

A. Mussi[1], P. Carrez[1], K. Gouriet[1], B. Hue[1], P. Cordier[1]

[1]Lille University, UMET - Unité Matériaux et Transformations - CNRS UMR 8207, Villeneuve d'Ascq, France

Introduction

The study of the fundamental plastic deformation mechanisms of crystalline materials requires detailed characterizations of defects. In case of dislocations, both determination of Burgers vectors and habit planes are required. Several techniques are well-established and available for characterizing Burgers vectors (extinction contrast criterion; equal thickness fringes method [1] and large angle convergent beam electron diffraction [2]), but geometrical characteristics like habit planes are more complex to obtain. Tilting experiments are routinely performed in the transmission electron microscope to extract 3-dimensional information, however strong limitations exist. The stereographic projection method can overcome this obstacle but it is time-consuming and burdensome.

Development

We have developed electron tomography of dislocations in Lille [3] with the aim of facilitating habit plane indexations. The main difficulty of this technique consists in keeping the contrast of dislocations constant during all the acquisition procedure. To go further with this technique, in particular with applications to beam-sensitive materials, we have developed dislocation electron tomography with few projected images [4]. This development allows us to catch evolution of microstructures with time, i.e. 4D dislocation electron tomography [5].

Results and conclusion

All these developments have contributed to characterize mechanisms which are difficult or even impossible to decipher with conventional methods such as colinear interactions [6], cross-slip, double cross-slip [7], the determination of specific glide plane, preferential slip systems, preferential mixed climb planes, among others…

[1] Y. Ishida, H. Ishida, K. Kohra, and H. Ichinose, *Determination of the Burgers vector of a dislocation by weak-beam imaging in a HVEM*, Philos. Mag. A 42 (1980), pp. 453–462.

[2] D. Cherns and A.R. Preston, *CBED Studies of Crystal Defects*, Proceedings of the 11th International Congress on Electron Microscopy Vol. 1, Kyoto, 1986, T. Imura, S. Marusa, and T. Suzuki, eds., Japan Society of Electron Microscopy, 1986, pp. 721–722.

[3] A. Mussi, P. Cordier, S. Demouchy, and C. Vanmansart, *Characterization of the glide planes of the [0 0 1] screw dislocations in olivine using electron tomography*, Phys. Chem. Miner. 41 (2014), pp. 537–545.

[4] A. Mussi, J. Gallet, O. Castelnau, P. Cordier, *Application of electron tomography of dislocations in beam-sensitive quartz to the determination of strain components*, Tectonophysics 803 (2021) 228754.

[5] A. Mussi, P. Carrez, K. Gouriet, B. Hue, and P. Cordier, *4D electron tomography of dislocations undergoing electron irradiation*, C. R. Phys. 22;S3 (2021), pp. 67–81.

[6] A. Mussi, P. Cordier, and S. Demouchy, *Characterization of dislocation interactions in olivine using electron tomography*, Philos. Mag. 95 (2015), pp. 335–345.

[7] A. Mussi, P. Cordier, S. Demouchy, and B. Hue, *Hardening mechanisms in olivine single crystal deformed at 1090 ◦C: an electron tomography study*. Philos. Mag. 97 (2017), pp. 3172–3185.

Fig. 1

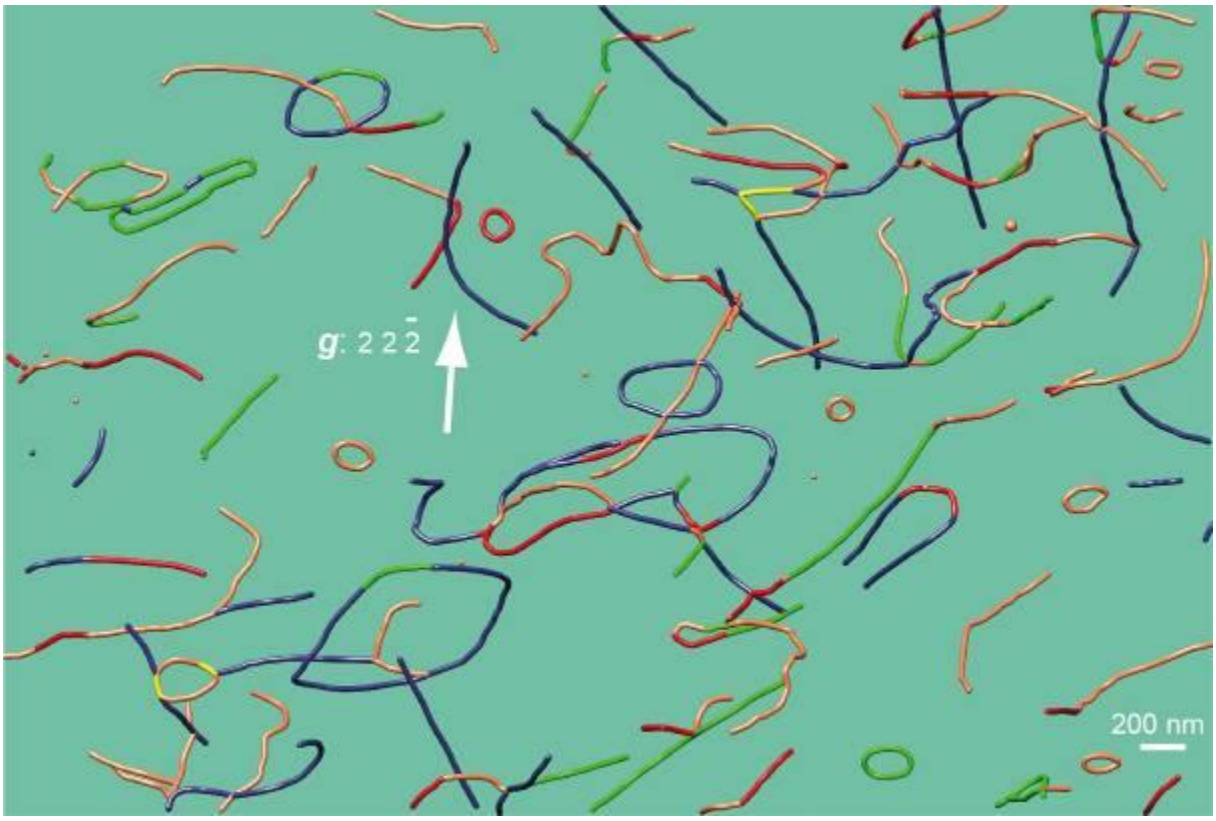

MS6.P003

Combining electron tomography of dislocations and continuum mechanics to investigate the rheology of minerals

T. Weidner[1], A. Mussi[1], K. Gouriet[1], P. Cordier[1]

[1]Université de Lille, Villeneuve d'Ascq, France

Transmission electron microscopy is the most precise technique to characterize dislocation microstructures. Several techniques are available to determine Burgers vectors be it via extinction contrast, by thickness fringes, or with LACBED. As a linear defect, a dislocation is also determined by its geometry, which gives important information on the deformation mechanisms like glide, climb, or cross-slip. In comparison to Burgers vectors, characterization of line orientations are less common and rely often on the use of the stereographic projection following tilting experiments.

Although applications of tomography in the transmission electron microscope (TEM) date back to the 70s, it is only in 2006 that it has been applied to dislocations [1]. The difficulty lies in the need to cover a large range of tilt while keeping the diffraction contrast rigorously constant. Using electron tomography of dislocations in the TEM provides a quantitative volumetric characterization of the dislocation microstructure. In this presentation, we show how this possibility can be exploited to build an interface with continuum mechanics. This allows in particular to identify the non-zero components of the strain tensor [2] or to determine the Nye tensor of dislocations. A further step is to implement the dislocation microstructure in a Dislocation Dynamics code (DD), NuMoDis [3] to investigate the temporal evolution of the microstructure under stress.

We present applications in quartz and olivine which are important mineral phases of the crust and the mantle respectively. Quartz presents the additional challenge of being very sensitive to electron irradiation which requires an adapted tilted series acquisition strategy.

[1] Barnard, J. S., Sharp, J., Tong, J. R., & Midgley, P. A. (2006). High-resolution three-dimensional imaging of dislocations. *Science*, *313*(5785), 319-319.

[2] Mussi, A., Gallet, J., Castelnau, O., & Cordier, P. (2021). Application of electron tomography of dislocations in beam-sensitive quartz to the determination of strain components. *Tectonophysics*, *803*, 228754.

[3] Drouet, J., Dupuy, L., Onimus, F., Mompiou, F., Perusin, S., Ambard, A. (2014): Dislocation dynamics simulations of interactions between gliding dislocations and radiation induced prismatic loops in zirconium. J. Nucl. Mater., 449, 252-262.

MS6.P004

Application of microscopic methods in the field of structural diagnostics: the drift seal of the Morsleben repository

H. J. Engelhardt[1], L. von Borstel[1]

[1]BGE TECHNOLOGY GmbH, Repository Safety, Peine, Germany

According to the multi-barrier concept, radioactive waste is isolated in geological repositories by the host rock and engineered barriers (seals). One group of sealing materials are concretes. During the emplacement and hardening of the concrete, processes can occur that could impair the effectiveness of the seals. As long as the mixture is fluid, the components can separate and air bubbles can escape. The heat of the chemical reactions results in a temperature rise and fall that could lead to volume changes, stresses, and cracking. Moreover, stresses and volume changes can be the result of mineral transformations and the build-up of a grain structure.

During the closure of the Morsleben repository drift seals will be erected. When using salt concrete, the contact zones to the host rock will be grouted. A pilot seal was built to investigate the spatial distribution of the sealing materials, their structure as well as the occurrence of cracks and their spatial distribution. The investigations included microscopic analyzes of the core seal, the contact zone to the host rock and the adjacent rock salt. Thick and thin sections were prepared from drill cores from all areas. For better visualization of cracks, the specimens were vacuum impregnated with blue colored resin and the surfaces of the specimens were polished. All specimens were examined with digital light microscopes. The non-transparent grout and concrete were viewed in reflected light. Moreover, thin section analysis and computed tomographic analysis were carried out. Rock salt could be viewed in reflected and transmitted light.

The work can be divided into an image analysis and a crack analysis. The aim of the image analysis was, for example, to describe the distribution of aggregates in the salt concrete (concrete edge zone), the shape of the contact area with the host rock and the spatial distribution of the grout. The blue-colored resin made it possible to draw conclusions about the depth of damage to the rock salt. In order to draw conclusions about the permeability of the damaged area, information on the extent, thickness, spatial position and cross-linking of the cracks is required. This task included the crack analysis. The basis of the analysis were sets of photos. The technique of image stacking was used to improve the depth of field (cf. Engelhardt 2016).

Measurement values of crack orientations were analyzed by the the numeric computing platform MATLAB. Photo stitching was used to get an overview of larger sample areas. Anaglyphs were made to get a three-dimensional impression of the structure of the rock salt. The ImageJ/Fiji software package was used for image and crack analysis.

The application is an example of the combined and successful use of microscopic methods in the field of structural diagnosis.

Engelhardt, H.-J. (2016) Der Einsatz von Focus-Stacking bei der Untersuchung von Flüssigkeitseinschlüssen im Steinsalz. Mikroskopie, 3 (07): 166-172.

Von Borstel, L.E.; Engelhardt, H.-J. & Köhler, M. (2012) Präparationstechnik zur Visualisierung des Porenraumes von kompaktiertem Salzgrus mittels Dünnschliffen. Schriftenreihe der Deutschen Gesellschaft für Geowissenschaften (SDGG), Heft 80, GeoHannover 2012, 1.–3.10.2012, p. 552.

MS6.P005

Discovering Baltic networks using TEM: Comparative material analysis on medieval age brass ornaments

M. K. Saleem[1], U. Schürmann[1], R. Shiroukhov[1], C. von-Carnap Bornheim[1], L. Kienle[1]

[1]Institute of Materials Science and Engineering, Kiel, Germany

Introduction:

Modern nano analysis can affectively help understand the material culture in the past societies by analyzing the excavated artefacts. In the recent past, increasingly sophisticated analytical methods have been used to study ancient artefacts to test various hypotheses related to the material aspects of these artefacts. In this research work advanced material analysis methods have been utilized to investigate the medieval age artefacts from East Baltic regions and Eastern Europe using nano analytical technique such as transmission electron microscopy (TEM).

Objectives

The objective of this research work is to test the hypotheses of possible immigration of population from East Baltic regions to Ostriv (present day Ukraine). Strong similarities between the physical attributes of the excavated artefacts from the two regions led to believe of a possible connection between the two regions. To explore this possible connection between the regions, laboratory analysis of the artefacts was planned to compare the production mechanism of the artefacts found in East Baltic regions and Ostriv.

Materials and Methods:

Two sets of samples belonging to the 11-12th century copper alloys were used such as fibulas, penannular brooches and flat ladder brooches. The first set of items was found in a cemetery by a group of Ukrainian scientists in Ostriv (Ukraine) within the skeletal graves. The other set of samples was received from Berlin Museum for Pre- and Early History that belonged to the East Baltic regions. The ornaments were studied by means of Energy Dispersive X-Ray (EDX) Spectroscopy in a Jeol JEM-2100 equipped with an EDX detector (Si/Li, EDAX). The analysis was performed on lamellae prepared from the surface of the ornaments into a depth of ca. 10 µm via Focused Ion Beam (FIB). EDX point measurements and elemental maps were performed in STEM mode.

Results:

The EDX analysis showed the presence of brass in the artefacts from Ostriv, however, the artefacts from East Baltic regions consisted of pure copper, brass and bronze. Additional surface limited signals from carbon, iron, lead, chlorides, sulphates, oxides and phosphates were also observed. TEM-EDX on the FIB lamellae showed Cu and Zn as the major constituents with traces of organic compounds and oxidation possibly as a result of secondary alteration. Astonishingly, the same physical features in the artefacts from East Baltic and Ostriv regions do not translate into same production mechanisms. The zinc content in the artefacts is also varying in the brass ornaments found in Ostriv cemetery.

Conclusion:

The advanced methodology for analyzing the archaeological artefacts is shown in this study. The study demonstrated the comparison of chemical compositions between the medieval age brass ornaments from East Baltic and Ostriv regions. The authors further demonstrate the modification of surface and subsurface of the archaeological artefacts, that are buried under the soil for thousands of years. The similar physical features but different elemental composition could suggest the transfer of technology through the population that migrated from East Baltic regions to Ostriv. Material composition of archaeological artefacts served as an important identifier to unearth technology exchange and network between medieval Baltic population.

MS6.P006

A full-field quantitative analysis of grain boundary sliding using digital image correlation (DIC) inside a transmission electron microscope

I. ul Haq[1], D. Schryvers[2], H. Idrissi[3], P. Cordier[4]

[1]University of Antwerp, Physics, Antwerp, Belgium
[2]University of Antwerp, Antwerp, Belgium
[3]Université Catholique de Louvain, Louvain-la-Neuve, Belgium
[4]Université de Lille, Lille, France

Abstract

In experimental mechanics, the digital image correlation (DIC) technique using scanning transmission electron microscope (SEM) images has been extensively used for quantitative deformation analysis [1]. In order to increase the sensitivity of DIC toward nanoscale strain detection, efforts are made to couple the DIC with transmission electron microscopy (TEM) images. At present, there are only a few experimental DIC studies available based on TEM [2, 3], hence exploiting this direction on various materials is desirable. In the present work, the grain boundary sliding deformation mechanism in olivine is investigated through the DIC technique coupled with TEM to get enhanced spatial resolution for mapping the small localized strain onset of the grain boundary sliding. For this purpose, forsterite nano-tensile specimens containing a single grain boundary or a triple point are prepared from synthetic forsterite (Mg-rich end member of olivine) by focused ion beam (FIB) after grain orientation mapping using ASTAR (see Fig. 01). Further, the surface of the tensile samples is decorated with nano-Pt particles during FIB. The in-situ nanomechanical test performed inside TEM uses high-angle annular dark field (HAADF) imaging to minimize the dynamical contrast. We demonstrate that during the deformation, strain localized at the grain boundaries triggers the sliding activity. These full-field quantitative nanoscale deformation investigations provide insight into the mechanisms that influence the macroscopic response.

[1] A. Weidner and H. Biermann, "Review on Strain Localization Phenomena Studied by High-Resolution Digital Image Correlation," *Adv. Eng. Mater.*, vol. 23, no. 4, 2021, doi: 10.1002/adem.202001409.

[2] X. Wang, Z. Pan, F. Fan, J. Wang, Y. Liu, Scott X. Mao, T. Zhu, and S. Xia, "Nanoscale deformation analysis with high-resolution transmission electron microscopy and digital image correlation," *J. Appl. Mech. Trans. ASME*, vol. 82, no. 12, pp. 1–9, 2015, doi: 10.1115/1.4031332.

[3] Y. Zhang, L. Feng, S. Dillon, and J. Lambros, "Full-field deformation measurements in the transmission electron microscope using digital image correlation and particle tracking," *Mater. Charact.*, vol. 183, no. July 2021, p. 111598, 2022, doi: 10.1016/j.matchar.2021.111598.

Fig. 01 Sample preparation and in-situ TEM nanomechanical experiment (a) FIB lamella showing the different grain boundaries and inset showing the ACOM-TEM from the selected area for cutting the tensile specimen (b) Push-To-Pull (PTP) device for in-situ TEM. A diamond flat punches the semicircular end on the top and opens the middle gap to strain the specimen. Inset shows the forsterite tensile specimen having a triple junction grain boundary before the fracture.

Fig. 1

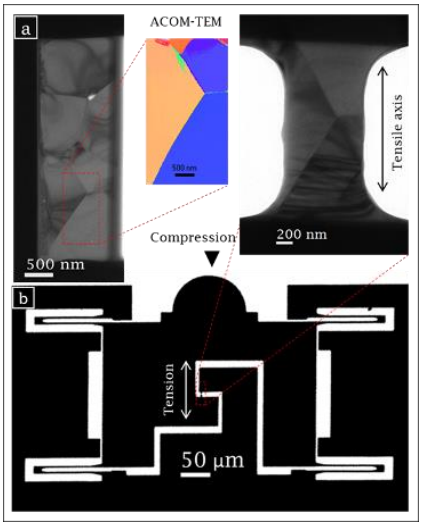

MS6.P007

The structure, character, and relative energies of grain boundaries in Mg_2SiO_4

A. Austin[1], M. Sedlak[1], F. Li[1], L. Rosset[2], S. Koizumi[3], K. Marquardt[1]

[1]Imperial College London, Materials, London, United Kingdom
[2]University of Oxford, Oxford, Germany
[3]University of Tokyo, Earthquake Research Institute, Tokyo, Japan

Mg_2SiO_4 is a ceramic with geological and engineering relevance. It is the most abundant mineral in the Earth's upper mantle, meaning its properties dominate mantle behaviour. Additionally, it is a refractory material with applications in microwave dielectric devices and promising bio-compatible properties.

It has been shown that the grain boundary energy is inversely correlated to the total area of that interface in a system(Li et al., 2009). The Grain Boundary Character Distribution (GBCD) shows the proportion of different types of interfaces in a system and is key to understanding melt extraction, texture formation, creep regimes, and electrical and optical properties of materials. It has also been shown that the relative grain boundary energy varies with grain size(Bojarski et al., 2013). In this study we aim to investigate these relationships in the Mg_2SiO_4 system, with studies of specific interfaces to determine their complexions.

Synthetic Mg_2SiO_4 samples with grain sizes of 0.4, 3.4, 7.8 and 5.4 µm were synthesised by vacuum sintering(Koizumi et al., 2010) and subsequently characterized with Electron Backscatter Diffraction (EBSD) and Atomic Force Microscopy (AFM). Over 230,000 grain boundary segments were extracted from EBSD maps encompassing over 70,000 grains to extract the Grain Boundary Character Distribution (GBCD) of each sample. Thermal etching was used to reveal grain boundary grooves which were mapped using AFM to extract their depth profile. From this data the relative grain boundary energy for different grain sizes was determined using a simplified Young's Equation. Finally, thin sections were prepared using mechanical and ion polishing for HRTEM imaging of individual interfaces.

Analysis of thermal grooves shows a decrease in average relative grain boundary energy with increasing grain size from 0.48 arbitrary units for 0.4 µm grain size to 0.41 for an average grain size of 7.8 µm. Furthermore we observe a difference in the relative grain boundary energy between normal and abnormally grown grains. We will discuss these results in relation to the GBCD and structure.

Bojarski, S. A., Knighting, J., Ma, S. L., Lenthe, W., Harmer, M. P., & Rohrer, G. S. (2013). The relationship between grain boundary energy, grain boundary complexion transitions, and grain size in Ca-doped Yttria. *Materials Science Forum*, *753*, 87–92. https://doi.org/10.4028/www.scientific.net/MSF.753.87

Koizumi, S., Hiraga, T., Tachibana, C., Tasaka, M., Miyazaki, T., Kobayashi, T., Takamasa, A., Ohashi, N., & Sano, S. (2010). Synthesis of highly dense and fine-grained aggregates of mantle composites by vacuum sintering of nano-sized mineral powders. *Physics and Chemistry of Minerals*, *37*(8), 505–518. https://doi.org/10.1007/s00269-009-0350-y

Li, J., Dillon, S. J., & Rohrer, G. S. (2009). Relative grain boundary area and energy distributions in nickel. *Acta Materialia*, *57*(14), 4304–4311. https://doi.org/10.1016/j.actamat.2009.06.004

MS6.P008

Networks of partially open grain and phase boundaries in magmatic and metamorphic rocks

J. H. Kruhl[1], E. Griesshaber[1], E. Raghami[1], W. W. Schmahl[1], C. Schrank[2], R. Wirth[3]

[1]Ludwig-Maximilians-University Munich, Department of Earth and Environmental Sciences, Munich, Germany
[2]Queensland University of Technology, School of Earth, Environmental and Biological Sciences, Brisbane, Australia
[3]GFZ German Research Centre For Geosciences, Section 3.5, Potsdam, Germany

TEM/FIB-based investigations have shown that grain and phase boundaries of various minerals in different metamorphic and magmatic rocks are lastingly open on the nanometer scale and partly to totally filled with secondary minerals [1, 2]. The most likely reason for opening is the exhumation of rocks and the associated temperature and pressure decrease, which leads to volume reduction and internal stresses on the grain scale and causes fracturing and opening of the boundaries. This is confirmed by 3D numerical modelling, combining contact mechanics and finite-element method [3]. It is assumed that opening starts below the temperature threshold for dislocation creep in the different minerals.

TEM investigations are restricted to small material volumes. Therefore, scanning electron microscopy (SEM) is applied to cm-large thin-section areas. The drastically enlarged data set provides statistically reliable information about conditions of opening and filling of boundaries in grain aggregates with different size and crystallographic orientation of grains. Investigated rocks and minerals include contact-metamorphic quartzite, deformed vein quartz, metagabbro, lherzolite, garnet-sillimanite rock, felsic granulite, calcsilicate rock, jadeite quartzite, syntectonic granitoid, and marble.

Over entire thin-section areas, roughly 90% of the boundaries are continuously open or partly filled with secondary minerals, independently of mineral type, and grain size, shape and crystallographic orientation. This confirms previous TEM investigations on a much broader data basis. The two crystal faces of an open boundary are mostly strictly parallel to each other. The width of opening remains generally constant between triple junctions, i.e., typically over tenth of micrometers. However, boundary kinks show that movement directions are often not perpendicular but oblique to the boundary. Open space is also developed between filling and crystal faces. This points to more than one stage of opening. Particularly in quartz, micrometer-large, often conical voids frequently occur along open boundaries indicating dissolution-precipitation processes. For quartz, a weak correlation exists between grain size and boundary opening width, however, is absent for the crystallographic orientation of boundaries and opening width. This confirms that cracking and opening of boundaries are controlled in a complex way by the development of stress on the grain scale and movements in the grain aggregate.

In general, these findings demonstrate that grain and phase boundaries are completely or partly open in all types of magmatic and metamorphic rocks and form pathways for fluid migration on thin-section scale but most likely also on larger scales. This represents a ubiquitous structural phenomenon of crystalline materials under at least upper-crust to surface conditions. It controls not only various physical properties of crystalline material but also governs its behavior during different natural and technical conditions as well as in experiment.

[1] Kruhl, J.H., Wirth, R., Morales, L.F.G., 2013. JGR Solid Earth. https://doi.org/10.1002/jgrb.50099

[2] Wirth, R., Kruhl, J.H., Morales, L.F.G., Schreiber, A., 2020. J. Metam. Geol. https://doi.org/10.1111/jmg.12610

[3] Raghami, E., Schrank, C., Kruhl, J.H., 2020. Tectonophysics. https://doi.org/10.1016/j.tecto.2019.228242

MS7.001-invited

Studying the crystallization of inorganic materials using correlated transmission electron microscopy

R. Drummond-Brydson[1], M. Ilett[1], M. Afzali[1], Z. Aslam[1]

[1]University of Leeds, School of Chemical and Process Engineering, Leeds, United Kingdom

Complex, electron-beam sensitive systems include organic crystals, polymers, hybrid organic-inorganic materials, some inorganic materials such as hydrates, as well as multiphase solid/liquid and solid/gas systems. Arguably they constitute the majority of systems of current interest across a wide range of scientific and engineering disciplines. We review the use of analytical transmission electron microscopy (TEM) for the characterisation of such beam-sensitive materials and complex, multiphase systems *in-situ* or close to their native state. Such materials are prone to damage by radiolysis which cannot be eliminated or switched off, requiring TEM analysis to be done within a dose budget so as to achieve an optimum dose-limited resolution and reliable, artefact-free results [1]. We highlight the importance of determining the damage sensitivity of a particular system in terms of characteristic changes that occur on irradiation under both an electron fluence and flux. We discuss the choice of electron beam accelerating voltage and detectors for optimizing resolution and outline the different strategies employed for low-dose microscopy in relation to the damage processes in operation. In particular, we discuss the use of scanning TEM (STEM) techniques for maximizing information content from high-resolution imaging and spectroscopy of materials and the use of cryogenic sample preservation methods.

As an example, we describe studies of crystallization processes in the calcium sulfate system using a correlated approach: a combination of liquid cell TEM (LCTEM), in-situ Raman spectroscopy and cryogenic TEM (cryo-TEM). Recent studies have suggested that the calcium sulfate polymorph gypsum (CaSO4.2H2O) can form in aqueous solution via a bassanite (CaSO4.0.5H2O) intermediate. Hence, initially we studied the transformation of bassanite nanorods to gypsum in an undersaturated aqueous solution of calcium sulfate. When coupled with Raman spectroscopy, the real-time data generated by LCTEM, and structural data obtained from time resolved cryo-TEM (i.e. crystallising solution samples vitrified at various time points) showed that bassanite can transform to gypsum via multiple pathways, the predominant one being dissolution/reprecipitation as opposed to the oriented attachment of nanorods and subsequent solid state transformation. Comparisons between LCTEM and cryo-TEM also showed significantly reduced kinetics within the confined liquid cell as compared with bulk solution, however the electron beam induced radiolysis of water (so lowering the local pH) can accelerate the transformation process [2]. Further studies focused on the direct formation of gypsum from aqueous solution using a range of different sample preparation methods: drop casting of solutions and drying, vacuum filtration, chemical quenching and drop casting, time-resolved cryogenic freezing, as well as LCTEM. Here we suggest that the observed crystallization pathway can be highly dependent on the degree of supersaturation experienced during the sample preparation method, which may lead to highly erroneous observations.

References:

[1] M. Ilett et al., Phil. Trans. R. Soc. A 378: 20190601 (2020). doi:10.1098/rsta.2019.0601.

[2] M. Ilett et al., J. Microscopy 2022, 288 : 155-168. doi: 10.1111/jmi.13102

MS7.002-invited

Interest of TEM for the development of new out-of-equilibrium materials by crystallisation from glass

M. Allix[1]

[1]CEMHTI - CNRS, ORLEANS, France

Crystallization from glass or high temperature melt is an original synthesis route allowing the elaboration of new non-equilibrium crystalline phases. The (partial) control of the nucleation and growth phenomena, by means of thermal treatments and adapted compositions, thus allows the synthesis of original materials not accessible by classical solid reaction. These innovative materials frequently show (micro)structural order and disorder phenomena. The use of transmission electron microscopy, coupled to other characterization techniques such as diffraction or NMR spectroscopy allows a fine and multi-scale description, opening the way to the understanding and control of some observed properties

Fig. 1

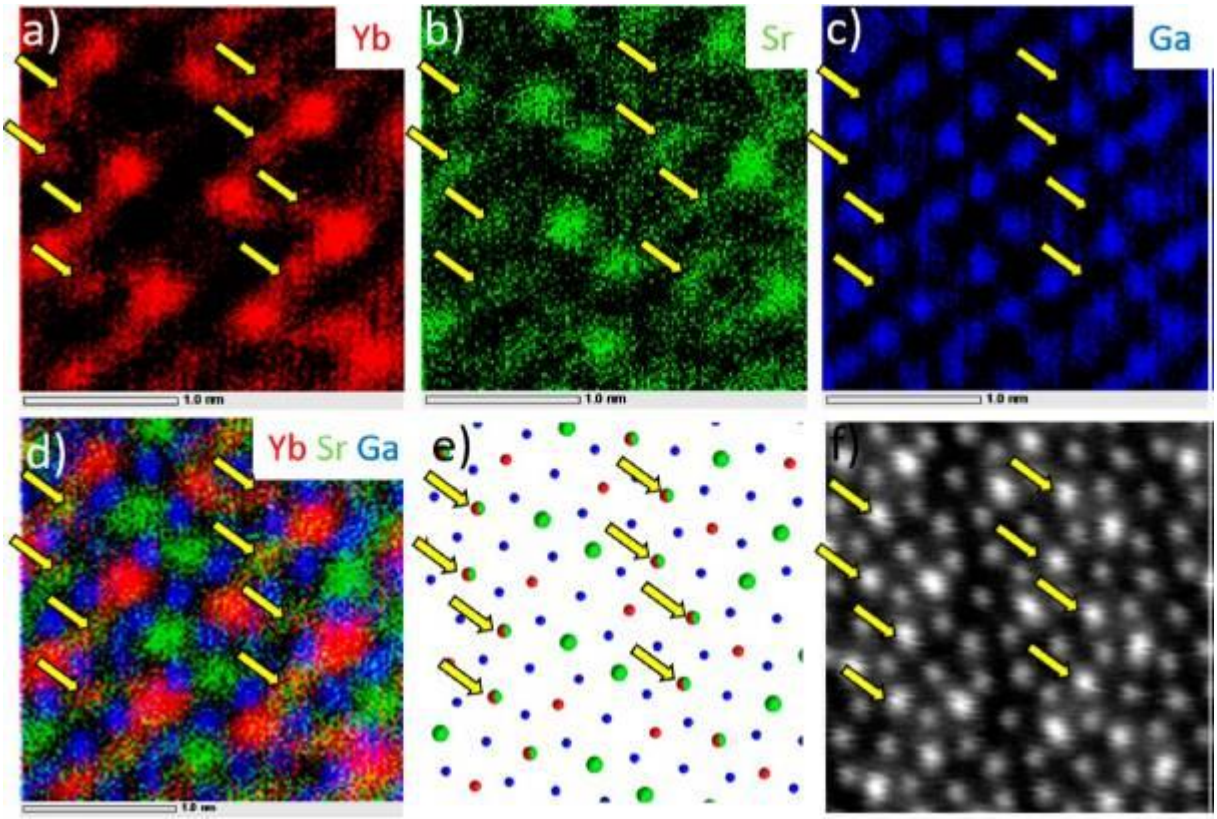

MS7.003

Structural adaptations in bronze-type niobium tungsten oxides enforced by varying stoichiometry

F. Krumeich[1]

[1]ETH Zurich, D-CHAB, Zurich, Switzerland

At present, niobium tungsten oxides are intensively studied as potential battery materials as their structural flexibility permits a reversible high-rate Li-ion exchange [1]. However, synthesis and characterization of phases in the pseudo-binary system Nb_2O_5-WO_3 was a major topic in structural research already in the 1960s [2]. Remarkably, the versatile structural chemistry was explored by HRTEM investigations right from the onset of this method in the early 1970s [3].

Several phases with odd but well defined stoichiometry appear in the system Nb_2O_5-WO_3. Their structures are based on frameworks of corner-sharing octahedra MO_6 (M = Nb,W) [4]. The structure of $Nb_8W_9O_{47}$ is closely related to that of the tetragonal tungsten bronzes (TTB) [5]: a part of the pentagonal tunnels (PTs) is filled by metal-oxygen strings in such a way that a threefold superstructure arises (Figure 1). This structure appears to be thermodynamically favored for the ratio oxygen:metal = 47:17, and any deviation from this ideal composition must somehow be compensated structurally. On the oxygen rich side of $Nb_8W_9O_{47}$, two simultaneously occurring effects accommodate an increased O/M ratio (Figure 1) [6]: (i) formation of little ordered variants with less PTs occupied (e. g. $Nb_6W_8O_{39}$); (ii) incorporation of single units of the neighboring phase $Nb_4W_7O_{31}$, an intergrowth of the TTB and the ReO_3 type as firstly determined by HRTEM [3]. The metal-rich side of $Nb_8W_9O_{47}$ towards the block phases is scarcely investigated yet. The HAADF-STEM characterization of samples with composition $Nb_{18}W_{16}O_{93}$ pointed to a denser occupation of the PTs: nano domains of units a yet unknow phase with composition $Nb_{12}W_{11}O_{63}$ and of $Nb_8W_9O_{47}$ appear [7]. The close relation of all these structures to the TTB-type substructure enables their intimate intergrowth as schematically shown in Figure 1 and demonstrated by the HRTEM image of a little ordered area shown in Figure 2.

The results discussed here confirm that the details of such a complex real structure as realized by niobium tungsten oxides can only be figured out by a direct visualization by high-resolution TEM or STEM [8].

Figure 1: Schemes and HAADF-STEM images of Nb-W oxides that are either superstructures of the tetragonal tungsten bronze (TTB) type (blue squares) or a coherent intergrowth of TTB and ReO3 type (orange square).

Figure 2: HRTEM image demonstrating the coherent intergrowth of Nb8W9O47 and Nb4W7O31 domains. The Fourier transform (inset) shows circular diffuse scattering besides the Bragg reflections of both phases.

References: [1] Griffith et al., *Nature* **559** (2018) 556. [2] Roth, Waring, *J. Res. Natl Bur. Stand.* **70A** (1966) 281. [3] Iijima, Allpress, *Acta Crystallogr. A* **30** (1974) 22. [4] Krumeich, *Chem. Mater.* ***34*** *(***2022**) 911. [5] Sleight, *Acta Chem. Scand.* **20** (1966) 1102. [6] Krumeich, *Acta Crystallogr. B* **54** *(1998)* 240. [7] Krumeich, *Crystals* **11** (*2021*) 1514. [8] Electron microscopy was done at ScopeM (ETH Zurich).

Fig. 1

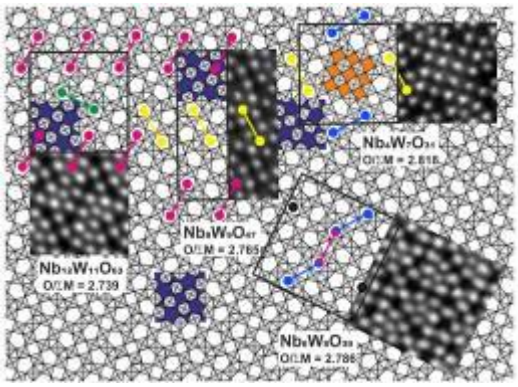

Fig. 2

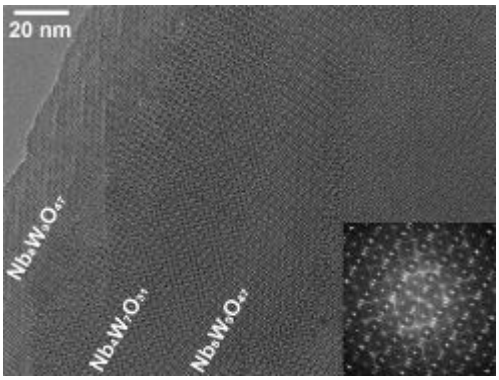

MS7.004

Crystallization of gel-derived SiO_2-TiO_2 amorphous nanobeads: an in situ high-temperature study

A. Zandonà[1], C. Genevois[1], A. Canizarès[1], E. Véron[1], J. Deubener[2], M. Allix[1]

[1]CNRS-CEMHTI, Orléans, France
[2]TU Clausthal, Institute of Non-Metallic Materials, Clausthal-Zellerfeld, Germany

SiO_2-TiO_2 glasses and gels have attracted a long-standing scientific and technological interest due to their very low thermal expansion [1] and to their use as precursors for the synthesis of photocatalytic glass-ceramic materials [2]. Despite their simple binary composition, the crystallization of SiO_2-TiO_2 glasses and gels can be rather complex and encompass several metastable stages marked by phase transformation between different TiO_2 polymorphs, such as TiO_2(B), anatase and rutile [2]. In this work, the structural ordering and compositional reorganization of spray-dried amorphous nanobeads of composition 50 SiO_2 – 50 TiO_2 and 83 SiO_2 – 17 TiO_2 is studied in situ at high temperature in a JEOL ARM200F cold FEG TEM, operating at 80 kV and equipped with a Protochips heating holder.

The nucleation and growth of TiO_2 crystals in a single amorphous nanobead (diameter ~50 nm) were first observed in the range 30-600 ºC, continuously acquiring TEM micrographs while heating. Subsequently, the role and evolution of compositional heterogeneities were evaluated in STEM-ADF mode, performing EELS mappings at various stages of heat treatment. Combined to in situ Raman spectroscopy and XRD, the results provide an unprecedentedly complete view of the crystallization mechanism in these materials: as-prepared nanobeads already contain TiO_2-enriched nanodomains, which evolve in size and composition with increasing temperature, eventually undergoing long-range ordering and yielding TiO_2 crystals. More generally, our study highlights potential, challenges and limitations of high-temperature (S)TEM experiments for the elucidation of crystallization processes in oxide materials.

Figure 1. Emergence and growth of anatase crystals in a nanobead of composition 50 SiO_2 – 50 TiO_2, observed in situ during heating in the TEM.

References

[1] Schultz, P. C. Binary Titania-Silica Glasses Containing 10 to 20 Wt% TiO_2. *Journal of the American Ceramic Society* **59**, 214–219 (1976)

[2] Zandona, A. *et al.* Spray-Dried TiO_2(B)-Containing Photocatalytic Glass-Ceramic Nanobeads. *Advanced Functional Materials* **31**, 2007760 (2021).

Fig. 1

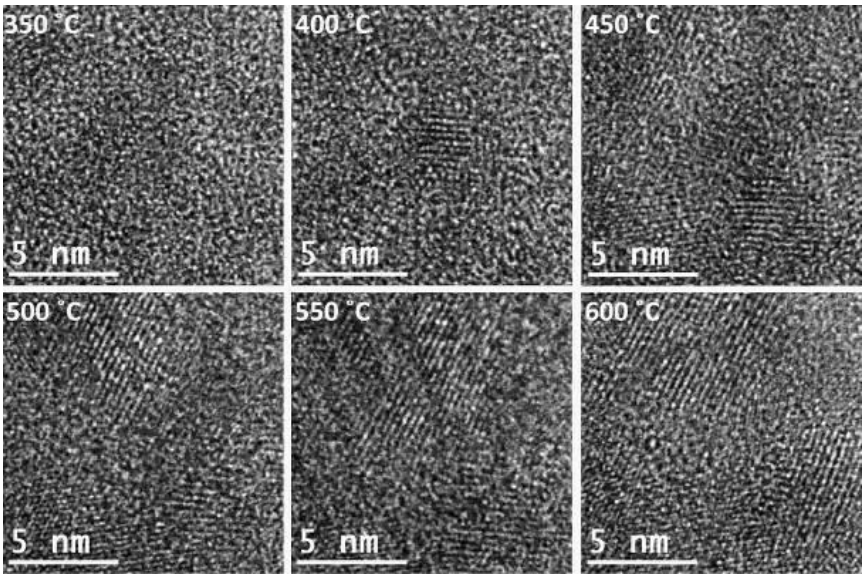

MS7.005

Investigation of the morphology of TiO2-CeO2 mixed-oxide nanoparticles for photocatalytic applications

M. Elis[1], M. Kamp[1], M. Hicke[1], J. Drewes[1], C. Aktas[1], F. Faupel[1], S. Veziroglu[1], L. Kienle[1]

[1]Institute for Materials Science, University of Kiel, Kiel, Germany

Introduction

Titanium(IV)oxide (TiO_2) nanoparticles are of high interest for a broad variety of applications, e.g. (photo)catalysis, self-cleaning and sensing. The photocatalytic performance of TiO_2 can be improved by controlling its crystal structure [1] as well as by the addition of noble metals [2] or oxides [3]. Combination of TiO_2 and other oxide especially with CeO_2 is one of the promising ways for effective electron-hole separation due to easy fluctuation of oxidation states of Ce [3].

Objectives

The presented research aims to find connections between the real structure of TiO_2-CeO_2 particles (i.e. crystal structure, morphology and composition) and their photocatalytic properties. Understanding these connections, allows to purposefully adapt the particles to the respective application and optimize their performance.

Materials & Methods

A custom-made gas aggregation cluster source (GAS) was used to synthesize mixed-oxide nanoparticles. Ti and Ce were sputtered from a custom build Ti-Ce target, agglomerated under admixture of O_2 as reactive gas and were deposited on Si wafer pieces. After deposition, the particles were heat treated at 700 °C under ambient conditions.

For TEM preparation the particles were scratched off the substrate and transferred to a Cu lacey TEM grid (Plano GmbH).

The particles were analyzed in a Jeol NeoArm JEM-ARM200F STEM equipped with two windowless EDX detectors. STEM-HAADF imaging in combination with EDX spectroscopy provides information on the particle morphology and the distribution of Ti and Ce. HRTEM as well as HRSTEM-HAADF images can reveal the nature of the interfaces between TiO_2 and CeO_2 crystals.

Results

First measurements on TiO_2-CeO_2 nanoparticles with a high concentration of Ce have shown demixing of a Ti-rich and a Ce-rich phases. Separate Ti-rich and Ce-rich particles have been observed as well as a core-shell type particle with a Ti-rich core covered by a Ce-rich shell. Ce-rich as well as Ti-rich phases where found to be crystalline. The crystal phase of CeO_2 was determined to be Fm-3m by electron diffraction. Due to the low Ti concentration, the crystal phase of TiO_2 was not determined by electron diffraction. Instead, the phase of TiO_2 was observed to be brookite phase in FFTs of HRTEM images. The investigation of further samples with different Ti/Ce-ratios synthesized at different process parameters are expected to show a broader variation in particle morphology and give an insight into the dependence of the particle morphology on Ti/Ce-ratio as well as GAS process parameters.

Conclusion

At high Ce concentration, demixing into different morphologies with a Ce-rich and a Ti-rich phase can be observed in the mixed-oxide nanoparticles. Both phases are crystalline. To achieve anatase phase, which is desirable for high photocatalytic activity, the GAS process parameters need to be adjusted. Earlier studies with pure TiO_2 particles have shown that the crystal phase can be varied by changing the magnetron voltage.

For further investigations, the magnetron voltage window for the synthesis of anatase phase TiO_2 in the mixed-oxide system will be investigated. In addition, the Ti/Ce ratio will be varied to study the influence of the particle composition on the morphology.

References

[1] A. Sclafani, J. M. Herrmann, *J. Phys. Chem.*, 1996, 100, 13655–13661

[2] S. Veziroglu *et al.*, *ACS Appl. Mater. Interfaces*, 2020, 12, 14983–14992

[3] S. Veziroglu *et al.*, *Nanoscale*, 2019, 11, 9840-9844

MS7.006

Precipitate-domain wall topologies in hardened Li-doped $NaNbO_3$

S. Gao[1], C. Zhao[1], M. Bohnen[2], R. Müller[2], J. Rödel[1], H. J. Kleebe[1]

[1]TU Darmstadt, Department of Materials and Earth Sciences, Darmstadt, Germany
[2]TU Darmstadt, Department of Civil and Environmental Engineering, Darmstadt, Germany

Ferroelectric hardening is an absolute requirement for potential applications of piezoceramics in high-power devices [1,2]. The state-of-the-art researches [3,4] demonstrate that ferroelectric hardening by pinning domain walls with precipitates introduced during processing is feasible, akin to precipitation hardening in metals [5]. With the precipitation of plate-like $LiNbO_3$ in Li-doped $NaNbO_3$ piezoceramics, ferroelectric hardening was achieved, exhibiting an enhanced mechanical quality factor (Q_m). The specific morphology and corresponding orientation of the $LiNbO_3$ platelets, exhibiting $\{110\}_{PC}$ habit planes, were characterized by transmission electron microscopy (TEM). The experimentally revealed crystallographic structures and strain incompatibility were found to correlate well with the thermodynamic simulation of the minimum-energy aspect ratio. In particular, the topology of the precipitate-domain wall assembly was clarified, revealing a full pinning on the domain walls by the incorporated plate-like precipitates. The revealed topology provides a fundamental basis for future optimization strategies for platelet hardening in new lead-free piezoceramics for high-power applications.

References:

[1] K.H. Hardtl, Electrical and mechanical losses in ferroelectric ceramics, Ceram. Int. 8 (1982) 121-127.

[2] K. Uchino, J.H. Zheng, Y.H. Chen, X.H. Du, J. Ryu, Y. Gao, S. Ural, S. Priya, S. Hirose, Loss mechanisms and high power piezoelectrics, J. Mater. Sci. 41 (2006) 217-228.

[3] C.H. Zhao, S. Gao, T.N. Yang, M. Scherer, J. Schultheiß, D. Meier, X.L. Tan, H.J. Kleebe, L.Q. Chen, J. Koruza, J. Rödel, Precipitation hardening in ferroelectric ceramics, Adv Mater. 33 (2021) 2102421.

[4] C.H. Zhao, S. Gao, H.J. Kleebe, X.L. Tan, J. Koruza, J. Rödel, Coherent precipitates with strong domain wall pinning in alkaline niobate ferroelectrics, Adv. Mater. Accepted, (2022).

[5] A.J. Ardell, Precipitation hardening, Metall. Mater. Trans. A 16A (1985) 2131-2165.

MS7.P001

Correlative light and electron microscopy of poly(L-lactic acid) spherulites for automatic detection

Y. Konyuba[1], H. Marubayashi[2], T. Haruta[1], H. Jinnai[2]

[1]JEOL Ltd., EM Business Unit, Tokyo, Japan
[2]IMRAM, Tohoku University, Miyagi, Japan

Crystalline polymers, such as polyethylene, are used in various applications because of their lightweight, low cost and excellent processability. The physical properties of crystalline polymers largely depend on their hierarchical solid-state structures with sizes spanning the nanometer to micrometer range. Understanding the hierarchical structure is essential for the structural design of crystalline polymeric materials. For this reason, it is desirable to have a method to analyze each level of the hierarchical structure at various scales.

Polarized optical microscopy (POM) has often been used to observe spherulites because the molecular orientation in the spherulite can be observed from the change in polarization state when linearly polarized light is incident on the sample. However, the resolution of POM is limited to a feature size of ~250nm, making it difficult to detect small spherulites on a submicron scale. The limitation of POM can be complemented using electron microscopy, such as transmission electron microscopy (TEM). One of the technical problems associated with TEM observations is the ultra-thin sectioned samples, which are often deformed during microtoming.

We observed poly(L-lactic acid) spherulite using POM and TEM in the same field of view. We attempted to combine the advantages of each technique - namely, molecular orientation information by POM and detailed scale morphology information by TEM [1]. To match the field of view of the TEM and POM images, a large number of TEM images were stitched together to produce a high-resolution large-area TEM image. After that, the deformations of the TEM ultrathin sections were corrected by reference to the POM images at the exact position of the sample, and large-area TEM images without deformations were successfully produced (Fig. 1).

We demonstrated a method to detect spherulites from the acquired large-area TEM image using YOLO, a well-known object detection system using convolutional neural networks. We obtained spherulites' number density and space-filling factor (relative crystallinity) within the desired region (Fig. 2). Such local structural information is key to understanding the nucleation and growth mechanisms of polymer spherulites. This detection process is speedy and much more powerful than manual processing and therefore is expected to analyze large amounts of image data. Furthermore, the present method would be more effective than the conventional methods in studying the heterogeneously distributed spherulites in materials (e.g., preferential nucleation at the filler surface in polymer composites).

References:

[1] Konyuba, Yuji, et al. "Correlative light and electron microscopy of poly (L-lactic acid) spherulites for fast morphological measurements using a convolutional neural network." *Microscopy* 71(2) (2022): 104-110.

Fig. 1. Same field of view of PLLA by polarized microscope (POM) and transmission electron microscope (TEM). (a) POM image. (b) Large-area TEM image of the same field of view as the POM image (deformations caused during ultrathin section preparation have been corrected). (c) Merged image of the POM and TEM images.

Fig. 2. Results of spherulite detection by the convolutional neural network. (a) Image of a 250 µm × 250 µm area from the large-area TEM image. (b) TEM image after spherulite detection. Each red frame shows a detected spherulite and its width and height.

Fig. 1

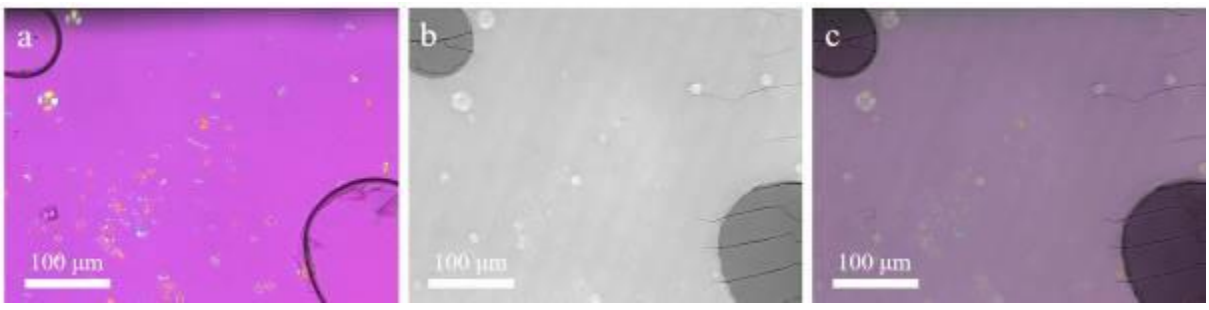

Fig. 2

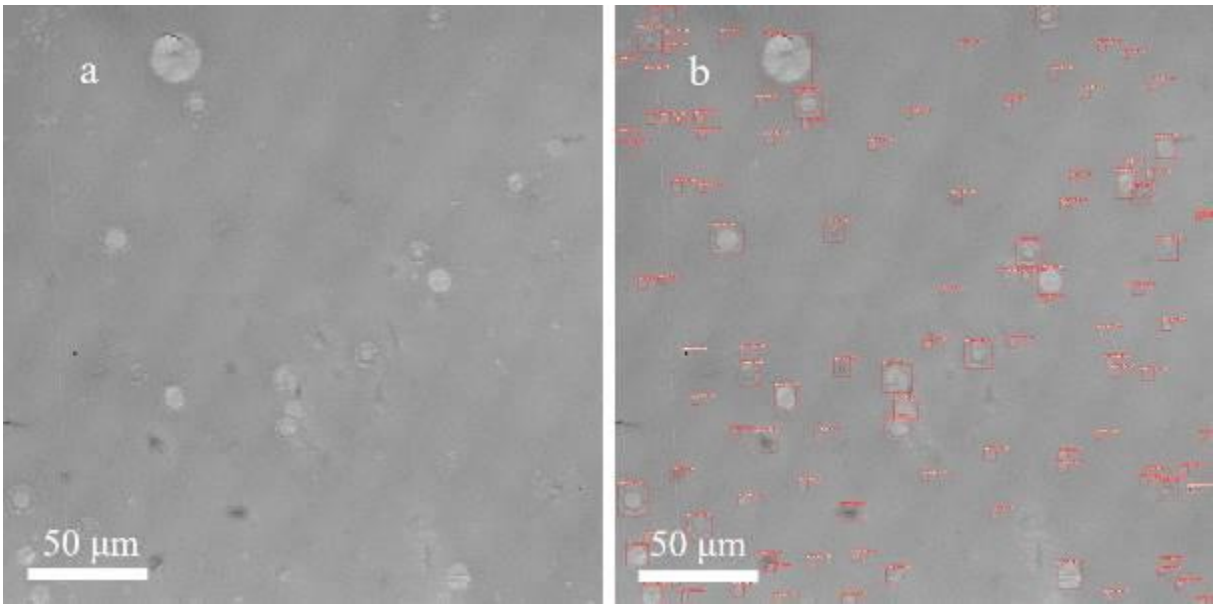

MS7.P002

Cryo-STEM analysis of electron beam sensitive anodic aluminum oxides

L. Daum[1], S. Ostendorp[1], M. Peterlechner[1], G. Wilde[1]

[1]Westfälische-Wilhelms-Universität Münster, Institute of Materials Physics, Münster, Germany

Aluminum alloys with predefined alloying elements are chosen regarding their performance in certain areas of industrial applications. Unfortunately, the natural forming protective alumina layer is suppressed in most alloys. Thus, the anodization of aluminum alloys is mandatory to achieve chemical resistance. The existence of segregations and stress fields inside the Al matrix hinders the formation of highly ordered anodic aluminum oxides (AAOs) as achievable using high-purity aluminum samples.

Depending on the thickness of the sample and anodization process, the electron beam damage of AAOs during transmission electron microscopy (TEM) investigations varies at a high level. This leads to severe artefacts and finally to the evaporation of the sample when performing experiments at room temperature. Previous scanning transmission electron microscopy (STEM) studies have shown that cryogenic temperatures can partially reduce the beam damage in electron beam sensitive materials as organics or AAOs [1,2]. In this study, the sample is characterized by nanobeam diffraction pattern (NBDP) analysis and electron dispersive x-ray spectroscopy (EDS) at cryogenic temperatures. The focus is set on the correlation of structural and chemical characterization of the participating segregations inside the AAOs and at the interface. For comparison the same measurements are done inside the Al 6xxx alloy close to the interface to the AAO.

Polished Al 6xxx samples are anodized with various anodization processes. An enhancement of the imaging quality of the high angle annular dark field (HAADF) detector is achieved by coating the pores with ZnO using atomic layer deposition (ALD). The sample preparation and milling are conducted with a focused ion beam using either Ga-ions or a mixture of Si/Au-ions. The samples were analyzed with a Gatan Double Tilt Liquid Nitrogen Cooling Holder 636 using a Titan Themis 60 – 300 at a temperature of ~96K. EDX spectra and energy-filtered NBDP are recorded with a quadrupole SuperXG2 detector and a CCD-GIF camera, respectively.

An exemplified measurement of the correlation between chemical and structural information is given in figure 1. In total, a dataset of 10.000 NBDP is acquired on a part of the subsequently conducted EDX map. The beam damage during acquisition was reduced in comparison to measurements at room temperature. The combination of both methods shows the amorphous AAO tubes which are coated with polycrystalline ZnO. However, the segregations inside the AAOs are remaining crystalline and are only partially anodized.

Based on the results, the segregations remain crystalline inside the amorphous AAOs. The decrease of chemical concentration assumes that one has to distinguish between segregation consisting of valve metals (e.g. Si, Al, Mg, etc.) and other elements (e.g. Mn).

[1] H. Ayoola, C.-H. Li, S. D. House, C. S. Bonifacio, K. Kisslinger, J. Jinschek, W. A. Saidi, and J. C. Yang.**Ultramicroscopy** 219 (2020), 113127

[2] A. M. Jasim, X. He, Y. Xing, T. A. White, and M. J. Young. **ACS Omega** 6.13 (2021), 8986–9000.

Fig. 1: STEM – EDX maps, HAADF and NBDP to analyze segregations inside the formed AAOs. As indicated in the HAADF signal, a smaller map for NBDP is recorded along the segregation. Areas which are enriched with Al are amorphous, whereas Zn enriched regions show polycrystalline NBDP. The diffraction pattern of the segregations indicate that the corresponding structure remains crystalline.

Fig. 1

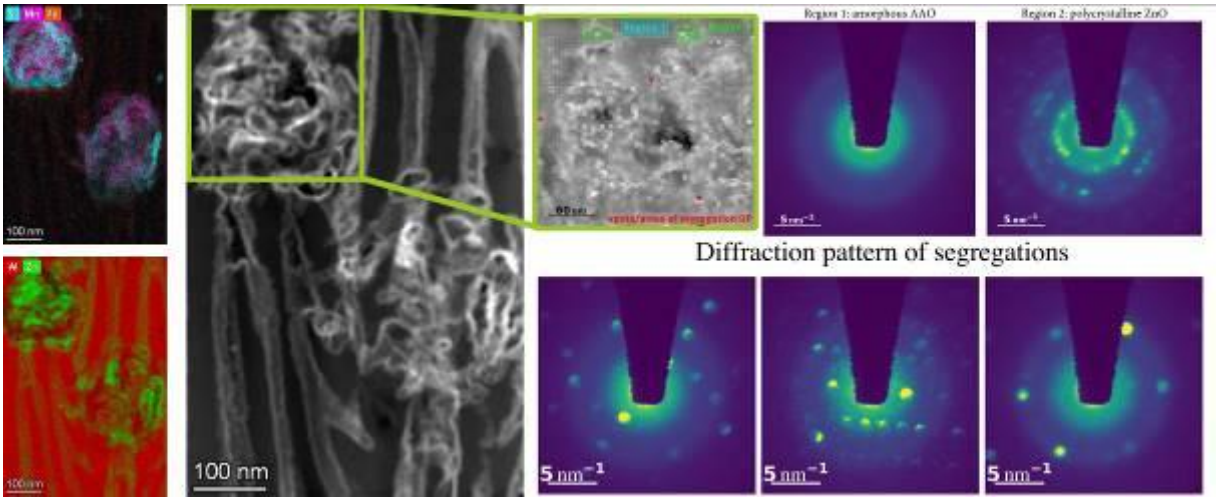
100 nm
Region 1: amorphous AAO
Region 2: polycrystalline ZnO
Diffraction pattern of segregations
5 nm⁻¹
5 nm⁻¹
5 nm⁻¹

MS7.P003

Electro-optical properties for BCZT and vanadium-doped BCZT nanoparticles using valence electron energy loss spectroscopy

G. Herrera-Perez[1]

[1]CONACYT-CIMAV, Physics of Materials, Chihuahua, Mexico

Valence electron energy loss spectroscopy, in transmission electron microscopy mode (VEELS-TEM) is an important tool to elucidate the complex dielectric function (CDF) and opto-electronic properties (O-EP) of insulators. The motivation of this work is to present a comparative study of CDF and the O-EP of lead-free $Ba_{0.8}Ca_{0.2}Ti_{0.9}Zr_{0.1}O_3$ (BCZT) and $Ba_{0.8}Ca_{0.2}Ti_{0.85}Zr_{0.1}V_{0.05}$ (BCZTV) electro-ceramics.

The samples were prepared by the modified Pechini method to obtain nanoparticles. A single tetragonal perovskite structure, considering the *P4mm* space group was stabilized at 700 °C for 1 h (1). This structure was confirmed by Rietveld refinement of the x-ray diffraction pattern for both compositions using Fullprof suite software. The microstructural parameters such as average crystallite size and shape in the nanometer range were simulated using the spherical harmonics method implemented in the GFourier program. The VEELS–TEM experiment scanned the energy interval from 0 to 50 eV was obtained with an electron energy loss spectrometer (EELS GAT–777 STEMPack) attached to a JEM2200FS (200 kV). All measurements were performed at room temperature. The system has an energy resolution of 1.00 eV, determined by the full-width-half-maximum of the zero-loss peak. The electron probe size was below 1 nm. The energy dispersion was set to 0.05 eV/channel, to maintain the energy resolution. The spectrum was collected with a parallel beam (convergence semi-angle $\alpha = 0$ mrad). The corresponding collection semi-angle was $\beta = 20.3$ mrad. For the EELS acquisition, 10 consecutive exposures were accumulated. The deconvolution and subtraction of the zero-loss peak (ZLP) from the VEELS region, the Fourier log method to remove plural scattering and Kramers-Kronig analysis performed in the single scattering distribution were carried out using the routines available in the Digital Micrograph™ Gatan Microscopy Suite (GMS 3) software. Absolute thickness of samples was determined via log ratio method with a value of 51.1 nm.

The spectroscopic analysis started with the chemical identification of the atoms that conforms the BCZT solid-solution. Bulk and surface plasmon were located at 27.2 eV and 12.9 eV for BCZT and 26.9 eV and 12.3 eV for BCZTV, respectively, in the normalized energy loss function. Dielectric constant was calculated from the real part of the complex dielectric function, while the inter-band transitions were identified in the joint density of states function. The refraction index n and the extinction coefficient k, as a function of energy, were obtained from the complex dielectric function. The band gap energy was determined using a polynomial fit in the optical absorption coefficient plot with an Eg = 3.2 eV (BCZT) and 3.18 eV (BCZTV) considering the relativistic correction using the difference method. The Cole-Cole plot corroborates the electronic contributions by the presence of two semicircles due to the inter-band transitions and plasmon region. As an important remark is that Vanadium plays an important role in the microstructural effects, in the covalent character and also in the opto-electronic properties of BCZT compounds.

G. Herrera-Perez would like to thank Mexico Catedra-CONACYT Grant No. 2563, SNI 1-CONACYT for complementary support and CONACyT–SEP Basic Research Project No. 253605.

References:

(1) G. Herrera-Pérez, et al. Micron 149 (2021) 103124.

MS7.P004

The nanoscale structure of relaxor ferroelectric $Na_{1/2}Bi_{1/2}TiO_3$-$BaTiO_3$ ceramics: A TEM investigation

A. K. Fetzer[1], A. Wohninsland[1], L. Kodumudi Venkataraman[1], H. J. Kleebe[1]

[1]Technical University Darmstadt, Department of Materials and Earth Sciences, Darmstadt, Germany

The EU directive for the Restriction of Hazardous Substances (RoHS) has driven researchers to look for alternatives in order to replace lead-containing components in electronic devices, due to growing concerns over health and environmental risks. The lead-free (1-*x*)$Na_{1/2}Bi_{1/2}TiO_3$-*x*$BaTiO_3$ (NBT-BT) system has gained considerable attention, especially for high-power and high-frequency applications, such as ultrasonic transducers.

The relaxor ferroelectric solid solution exhibits enhanced piezoelectric properties at its morphotropic phase boundary (MPB) near *x* = 0.06. Relaxors are characterized by the presence of nanometer-sized polar regions (PNRs/nanodomains), which allow for a high electromechanical response and high permittivity values. In the relaxor-ferroelectric transition of NBT-BT ceramics, the electromechanical properties are highly linked to a complex domain structure, which strongly varies with composition.

The local structure and phase assemblage of NBT-BT ceramics with 6, 9 and 12 mol % BaTiO3 (BT) was studied by using different imaging techniques and electron diffraction in transmission electron microscopy (TEM). Deploying dark-field (DF) imaging of superlattice reflections, the relaxor nanostructure is visualized, consisting of densely packed tetragonal *P*4*bm* nanodomains and a minor fraction of rhombohedral *R*3*c* nanodomains. The 5-30 nm sized *P*4*bm* regions display an elongated shape and are oriented along the $\{001\}_{pc}$ planes. Mapping the polar displacement in high-resolution high-angle annular dark field (HAADF) images reveals a heterogeneous local structure with short-range fluctuations of a few nanometres in size (PNRs). The nanoscale structure correlates to the frequency dispersion of the temperature-dependent permittivity, typical for relaxors. With increasing BT fraction, long-range ferroelectric lamellar domains of tetragonal *P*4*mm* symmetry emerge. Within these ferroelectric domains, the nanodomain contrast considerably declines, which is associated with the disappearance of octahedral tilting and a transition to the non-tilted *P*4*mm* structure, reflected in a more ferroelectric nature of BT-rich compositions. Nevertheless, a reduced population of both *P*4*bm* and *R*3*c* nanodomains remains embedded within the lamellar ferroelectric domains, indicating a complex hierarchical domain arrangement. The findings emphasize the important role of a direct microscopic analysis in order to elucidate on the nanostructure-property correlation in relaxor ferroelectric solid solutions.

MS7.P005

Probing the 3-dimensional structure of lead zirconate-based antiferroelectrics with a combined approach of TEM and NMR spectroscopy

H. Ding[1], S. Egert[2], B. X. Huang[3], A. Klein[3], G. Buntkowsky[3], H. J. Kleebe[3], L. Molina-Luna[3]

[1]MPIE, Düsseldorf, Germany
[2]University of St Andrews, St Andrews, United Kingdom
[3]TU Darmstadt, Darmstadt, Germany

The classical model of the prototype antiferroelectric material $PbZrO_3$ with antiparallel pairs of Pb displacements of equal magnitude has long been considered a principal guide for the understanding of antiferroelectricity. However, this simplistic picture has raised great concern as it is yet to be found in a real material, and a detailed examination of the 3-dimensional Pb positions is still lacking.

Here, not only the in-plane displacement but also the out-of-plane environment of Pb in $PbZrO_3$ and $(Pb,La)(Zr,Sn,Ti)O_3$ (PLZST) perovskite oxides is considered by jointly employing high-resolution scanning transmission electron microscopy (HRSTEM) and solid-state nuclear magnetic resonance (NMR) spectroscopy.

Displacement studies of PbZrO3 using the high-angle annular dark-field (HAADF) technique revealed an ordered four-fold modulation, which consists of two distinct segments that are nearly perpendicular to each other, contrasting the Kittel model. This ordered in-plane configuration is complemented by two discrete ^{207}Pb NMR signals reflecting alternating displacement magnitudes out-of-plane. On the other hand, PLZST is characterized by an inhomogeneous distribution of the Pb displacement modulation layers and Pb-O bond width calculated from annular bright-field (ABF) image, further manifested by a distribution of ^{207}Pb resonance frequencies revealing a significant increase in the displacement distribution width.

The combination of TEM and NMR techniques allows for a complementary exploration of the 3-dimensional crystal structure, correlating the microstructural displacements with the bulk displacement distribution both qualitatively and quantitatively. The findings rationalize our understanding of the complex polarization configuration in $PbZrO_3$-based antiferroelectrics that go beyond the Kittel model and highlight their highly disordered nature instead.

MS7.P006

TEM characterization of pseudomorphic polymer-derived ceramic papers: sample preparation and microstructure analysis

J. Peter[1], H. J. Kleebe[1]

[1]Institute of Applied Geosciences, Technical Unversity Darmstadt, Materials- and Geosciences, Darmstadt, Germany

Through the pyrolysis of polymeric precursor infiltrated cellulose-based paper templates, ceramic composites with paper-like morphology can be successfully manufactured. Such polymer-derived ceramic papers (PDCPs) are pseudomorphic after their template, closely resembling the original paper structure, with randomly interwoven carbonized fibers encased by a polymer-derived ceramic layer.

For this study, several PDCPs were prepared with varying synthesis parameters by pyrolysis of cellulose paper templates dip-coated with two different polysilazane-based single-source precursors, each modified with one of three different transition metals (Fe, Ni, Pd).

The resulting ceramic papers were studied by scanning electron microscopy (SEM), transmission electron microscopy (TEM), and energy-dispersive X-ray spectroscopy (EDS) analyses in combination with X-ray diffraction (XRD) as well as Raman and Fourier-transform infrared (FTIR) spectroscopy.

In order to reveal the in-situ generated microstructure, electron transparent thin-foils of the filigree and inherently brittle ceramic composites were prepared for TEM investigations. For this purpose, conventional polishing in combination with ion thinning as well as ultramicrotomy slice-cutting was comparatively employed to assess their suitability for these materials and to evaluate preparation artifacts introduced.

Overall, ultramicrotomy preparation led to a much better sample quality, allowing the core-shell structure of the composite ceramic fibers to be resolved in great detail (Figure 1). This points out that ultramicrotomy has high potential for TEM sample preparation of ceramic material systems, although it is seldomly used. Based on the results, the phase evolution and the role of the cellulose template during pyrolysis is discussed.

Figure 1: SEM BSE image (left) of a SiFeO(C,N)-based ceramic paper pyrolyzed in ammonia at 1000 °C and TEM BF image (middle) of an ultra-thin fiber cross-section prepared by ultramicrotomy preparation revealing the core-shell structure of the ceramic composite fibers. The electron diffraction patters (right) show that the ceramic layer is amorphous and contains numerous nanosized α-Fe particles, while the cellulose-derived fiber consists of semicrystalline turbostratic carbon.

Fig. 1

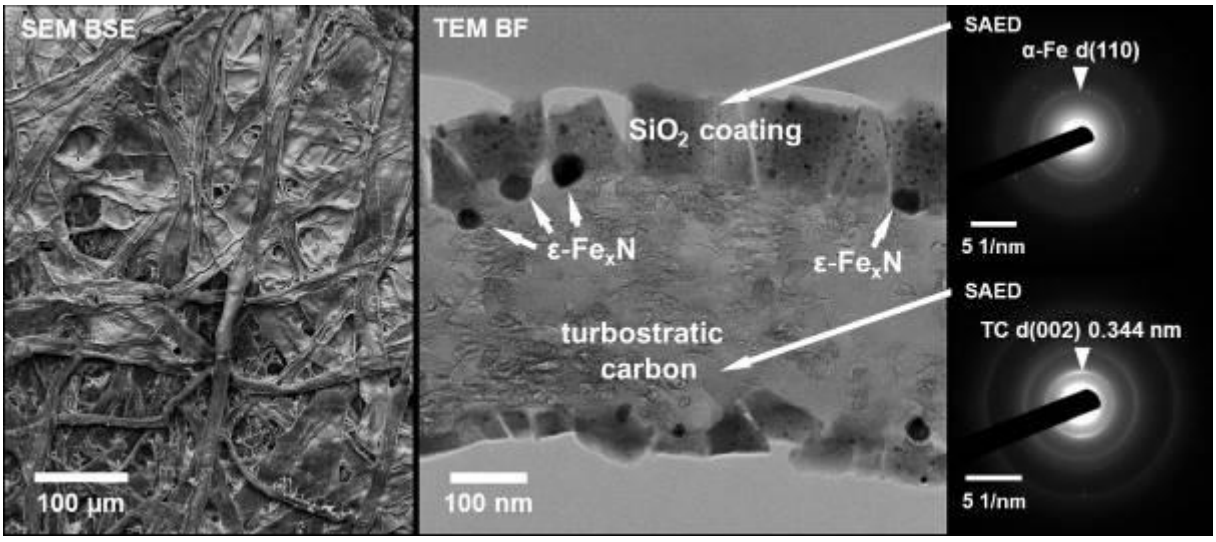

MS7.P007

Investigations on the amorphization of lithium-containing glass-ceramics during mechanochemical recycling

T. Necke[1,2], B. Balke[1], H. J. Kleebe[2], A. Weidenkaff[1]

[1]Fraunhofer IWKS, Energy Materials, Hanau, Germany
[2]TU Darmstadt, Geomaterial Science, Darmstadt, Germany

Due to its critical role in batteries, lithium has recently become a rather important element. Moreover, many efforts are being made to mine primary lithium sources, while lithium recycling and recovery are almost lacking. In addition to batteries, glasses and glass ceramics are an important and as yet unexploited source of lithium. Recently, we published an article on a novel mechanochemical recycling approach using end-of-life glass-ceramics from spend cooktops as feedstock for lithium extraction and simultaneous zeolite synthesis [1]. The experimental results indicate an effective particle size reduction and amorphization of the crystal structure of the high quartz lattice by intensive milling during the alkaline leaching process as the main driving forces for the reaction, significantly accelerating lithium extraction in parallel to zeolite synthesis.

The aim of this study is to investigate the physiochemical changes and amorphization of glass-ceramic material during ball milling without any chemical side reaction (mechanical activation).

In order to study the amorphization process, the glass-ceramic powder was mechanically activated in a planetary ball mill at 600 rpm in deionized water. After different times of 30, 60 and 120 min of ball milling, samples were taken and characterized by powder X-ray diffraction (PXRD), N2 adsorption/desorption analysis and transmission microscopy (TEM) including selected area electron diffraction (SAED).

Analysis of N2 adsorption/desorption by the Brunauer-Emmet-Teller (BET) method showed an increase in surface area with time, which can be attributed to a significant reduction in particle size due to intensive ball milling. With increasing time of mechanical activation, the PXRD measurements showed a decrease and broadening of the diffraction peaks. Moreover, the calculation on the crystallite size using Scherrer"s equation resulted in a clear trend to smaller crystallites with an increase of mechanical activation. Finally, TEM studies reveal the microstructural features of the samples, while the SAED patterns confirm the PXRD measurements and show the transformation of a well-ordered material into a (nano)crystalline or partially amorphous material.

The analytical results of BET, XRD and TEM/SAED measurements confirm a stepwise amorphization of the high-quartz structure and the transformation of a well-ordered source material into a (nano)polcrystalline material. Therefore, amorphization can be rationalized as the driving force for the mechanochemical reaction during lithium extraction and zeolite synthesis.

[1] Necke, T.; Wolf, D.M.; Bachmann, A.L.; Berberich, K.; Kleebe, H.-J.; Weidenkaff, A. Mechanochemical Lithium Extraction and Zeolite Synthesis from End-of-Life Glass−Ceramics, ACS Sustainable Chemistry & Engineering (advance online publication) 2022. https://pubs.acs.org/doi/10.1021/acssuschemeng.2c02342

MS7.P008

Microstructural evolution of novel Si(M)(BC)N polymer-derived ceramics upon different heat treatments

N. Thor[1], J. Bernauer[2], N. C. Petry[3], E. Ionescu[2,4], R. Riedel[2], A. Pundt[5], H. J. Kleebe[1]

[1]Institute of Applied Geoscience, Technische Universität Darmstadt, Darmstadt, Germany
[2]Institute of Materials Science, Technische Universität Darmstadt, Darmstadt, Germany
[3]Materials and Corrosion, Dechema Forschungsinstitut, Frankfurt am Main, Germany
[4]Materials Recycling and Resource Strategies, Fraunhofer Institution, Alzenau, Germany
[5]Institute of Applied Material, Karlsruher Institut für Technologie, Karlsruhe, Germany

Polymer-derived ceramics (PDCs) are promising candidates used as protective coatings on hard metal substrates for applications, requiring operating temperatures <1300°C. The polymer-to-ceramic synthesis route gives access to prepare ceramic coatings, such as environmental (EBC) or thermal barrier coatings (TBC) via several inexpensive liquid-phase deposition methods. Typically, PDCs consist of a highly refractory phase, such as early transition metal nitrides, carbides or borides, which are finely dispersed in a silica-former matrix phase (e.g., silicon carbide, silicon nitride, silicon(boro)carbonitride). As the microstructure and phase composition of a material strongly influence its high-temperature properties, a profound understanding of the microstructural development during its different processing steps is indispensable. During the synthesis of a PDC the starting preceramic polymers are firstly crosslinked at temperatures ranging from 200-1000°C and subsequently annealed at temperatures <1500°C, which induces phase separation and crystallization processes. To obtain dense monolithic materials, as-pyrolyzed powder samples are consolidated via spark plasma sintering. Dense monolithic ceramics are highly needed to gain information on mechanical properties and oxidation behaviour. In this context a series of novel PDCs were synthesized according to the polymer-to-ceramic route. As-pyrolyzed and subsequently annealed powder samples as well as spark plasma sintered (SPS) monolithic bulk materials in the Si(M)(BC)N system (M=Hf,Ta) were compared regarding their microstructural development upon different heat-treatments. Pyrolysis of Si(M)N powder samples was carried out at 1000°C under NH3 gas followed by an annealing at 1600°C in N2 atmosphere. As-pyrolyzed Si(M)(BC)N powders were sintered via SPS at 1950°C in vacuum employing different sintering parameters (different pressure & dwell times). The synthesized materials have been investigated via electron microscopy concerning their temperature-dependent microstructural evolution upon pyrolysis and subsequent heat treatments. Si(M)N powder samples as well as dense Si(M)(BC)N bulk materials were analysed via scanning (SEM) and transmission electron microscopy (TEM) with respect to their chemical composition, crystallization behaviour as well as their phase composition and distribution. The annealed Si(M)N powder samples revealed a microstructure consisting of two regions named bulk and surface regions, which differentiate in their intrinsic microstructure and phase composition. Bulk regions contain a silicon nitride-based matrix phase with finely dispersed nano-sized transition metal carbides (TMCs). In comparison, surface regions underwent phase separation, decomposition reactions and diffusion-controlled coarsening phenomena, showing a completely different microstructure, consisting of silicon carbide and grain coarsened TMCs. Similar microstructures were also found in the studied SPS dense monolithic materials. Former powder particles are consolidated via sintering, showing exactly the same above-mentioned two regions within the internal microstructure: surface and bulk. Furthermore, it is discussed, whether the microstructural evolution in powder samples compared to dense monolithic materials consolidated via SPS, show an almost identical microstructural development. A detailed microstructural evolution model for both, powder samples and dense monolithic materials is introduced.

Fig. 1

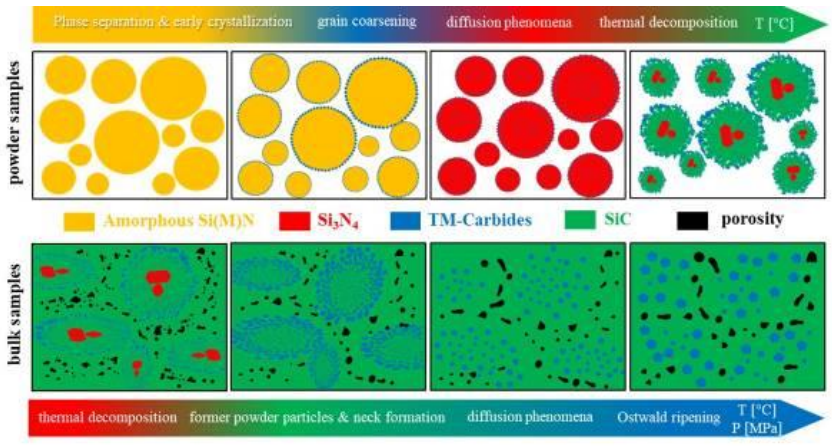

MS7.P009

Piezotronic ZnO bicrystals: A TEM study on interfacial segregation and properties of (0001) inversion boundaries

M. Trapp[1], H. J. Kleebe[1]

[1]Institute of Applied Geoscience, TU Darmstadt, Darmstadt, Germany

Zinc oxide is well-known for its non-linear current-voltage (I-V) characteristics and its respective application as varistor (*variable resistor*) ceramic.[1] The varistor effect itself is attributed to dopant-induced electrostatic potential barriers at ZnO grain boundaries.[1,2] In case of so-called piezotronic materials, semiconducting and piezoelectric properties are combined in order to tune such potential barriers. Therefore, ZnO – featuring piezoelectricity as well as intrinsic semiconduction – has received renewed scientific interest as piezotronic material and is considered to hold a large potential for the development of novel devices, such as strain-triggered transistors, diodes or sensors.[3,4] However, the dopant-related formation of varistor-type potential barriers in ZnO as well as the related semiconducting properties are still not completely elucidated, in particular, against the background of novel piezotronic applications, which imply conditions different from the established polycrystalline ZnO varistor ceramics. In the presented study, ZnO bicrystals with (0001) inversion boundaries were analyzed using atomic resolution (S)TEM methods, with a special focus on orientation and dopant segregation.[5,6] In doing so, different synthesis methods were applied and their effect on the interface properties was investigated. Based on the TEM findings and corresponding I-V measurements, a distinct correlation between interface coherency, degree of segregation and degree of non-linearity was observed. Since this correlation is attributed to basic principles of segregation and interfacial properties, the presented results are not only seen as a valuable contribution to the field of piezotronics and varistor ceramics, but also as adaptable for other material systems.

1. D. R. Clarke, "Varistor Ceramics," *J Am Ceram Soc,* 82[3] 485-502 (1999).
2. Y. Sato, T. Yamamoto, and Y. Ikuhara, "Atomic Structures and Electrical Properties of ZnO Grain Boundaries," *J Am Ceram Soc,* 90[2] 337-57 (2007).
3. X. D. Wang, J. Zhou, J. H. Song, J. Liu, N. S. Xu, and Z. L. Wang, "Piezoelectric Field Effect Transistor and Nanoforce Sensor Based on a Single ZnO Nanowire," *Nano Lett,* 6[12] 2768-72 (2006).
4. Z. L. Wang and W. Z. Wu, "Piezotronics and Piezo-Phototronics: Fundamentals and Applications," *Natl Sci Rev,* 1[1] 62-90 (2014).
5. M. Trapp, P. Keil, T. Frömling, J. Rödel, and H.-J. Kleebe, "Segregation and Properties at Curved vs Straight (0001 over bar) Inversion Boundaries in Piezotronic ZnO Bicrystals," *J Am Ceram Soc* (2019).
6. P. Keil, M. Trapp, N. Novak, T. Frömling, H.-J. Kleebe, and J. Rödel, "Piezotronic Tuning of Potential Barriers in ZnO Bicrystals," *Adv Mater,* 30[10] (2018).

MS7.P010

The prevention of SiC-fiber decomposition via the incorporation of a thin buffer layer in ZrB_2-based ultra-high temperature ceramics

K. Stricker[1], L. Silvestroni[2], H. J. Kleebe[1]

[1]Technical University Darmstadt, Institute of Applied Geoscience, Geomaterial Science, Darmstadt, Germany
[2]CNR - ISTEC Institute of Science and Technology for Ceramics, Structural and Functional Ceramics, Faenza, Italy

A ZrB_2–based ultra-high temperature ceramic (UHTC), containing short Hi-Nicalon SiC fibers, was separated from the outermost oxidation resistant ZrB_2-$MoSi_2$ layer by sandwiching it with a Mo-impermeable buffer layer, in order to prevent fiber decomposition.

This additional layer consisted of ZrB_2 doped with either Si_3N_4 or with the polymer-derived ceramics (PDCs) SiCN and SiHfBCN. Scanning in addition to transmission electron microscopy imaging (SEM/TEM) and elemental mapping via energy-dispersive X-ray spectroscopy (EDS) showed that this tailored sample geometry provides an effective Mo-diffusion barrier, preventing the SiC fibers from deterioration due to their reaction with Mo or Mo-compounds. In contrast, the structure of the SiC fibers in a reference sample without such a buffer layer is strongly degraded by $MoSi_2$ diffusion into the fiber core. The comparison of the three buffer-layer systems showed a moderate alteration of the fiber structure in the case of Si_3N_4 addition, whereas in the PDC-doped samples hardly any structural change within the SiC fibers was observed.

A stepwise reaction mechanism is proposed, based on the continuous progression of a reaction zone that propagates towards the ZrB_2-$MoSi_2$ top layer. The progression of such a reaction zone, which is seen as a consequence of the different eutectic melts forming in the different layers, i.e., first in the SiC-fiber containing bulk, followed by the buffer layer itself, and finally in the top ZrB_2-$MoSi_2$ layer at high temperature, allows for an effective separation of the oxidation resistant top layer from the SiC fibers that are embedded in the bulk.

Subsequent oxidation of the UHTCs at 1500°C and 1650°C for 15 min did not affect the efficacy of all three buffer layers containing Si_3N_4, SiCN or SiHfBCN, since no structural changes within the corresponding buffer layer as well as of the fibers were observed, as compared to the non-oxidized samples.

LS1.001-invited

Optimizing cryo-EM data acquisition

W. Hagen[1]

[1]EMBL Heidelberg, Heidelberg, Germany

Cryo-electron microscopy (cryo-EM) allows for the visualization of biomolecules at near-atomic resolution and has become an increasingly important tool for structural biologists. The presentation will discuss several strategies for optimizing cryo-EM data acquisition in order to improve the efficiency and throughput of experiments. Innovative approaches that have been developed over the years will be covered, such as aberration-free image shift (AFIS), and fringe-free imaging (FFI), which have been shown to improve the throughput of cryo-EM data collection. Additionally, the use of "Virtual Maps" for screening samples with problematic particle distribution will be discussed, a strategy that helps to prioritize areas of the sample for imaging and reduce the overall time and resources required for the experiment. Lastly, screening cryo-EM samples using an energy filter"s plasmon regime will be presented. Through the use of these optimization strategies, researchers can obtain high-quality data from cryo-EM experiments, leading to informative structural models, in a shorter amount of data acquisition time.

LS1.002-invited

Understanding redox protein mechanism through structure

B. J. Murphy[1]

[1]Max Planck Institute of Biophysics, Redox and Metalloproteins Research Group, Frankfurt am Main, Germany

Redox proteins carry out sophisticated reactions that shape our bodies, our planets and our climate. Understanding the mechanism of redox proteins depends on an atomic-level understanding not only of the protein structure, but of structural changes associated with reduction and oxidation processes. Because structural studies by single-particle cryo-EM have only recently achieved the resolutions that allow for atomic-level insight into mechanism, the tools for preparation of samples under defined redox conditions are lacking. As our group has worked toward understanding the structure and function of redox proteins, we have brought together a set of tools for better assessing redox-dependent structural changes. Applying these tools to proteins involved in hydrogen production and methanogenesis have allowed us to gain new insight into these processes.

LS1.003

Structure of the HOPS tethering complex, a lysosomal membrane fusion machinery

D. Shvarev[1], J. Schoppe[1], C. König[1], A. Perz[1], N. Füllbrunn[1], S. Kiontke[2], L. Langemeyer[1], D. Januliene[1], K. Schnelle[1], D. Kümmel[3], F. Fröhlich[1], A. Möller[1], C. Ungermann[1]

[1]Osnabrueck University, Osnabrück, Germany
[2]University of Marburg, Marburg, Germany
[3]University of Münster, Münster, Germany

Lysosomes are essential for cellular recycling, nutrient signaling, autophagy and the invasion of pathogenic bacteria and viruses. Lysosomal fusion is fundamental to cell survival and requires HOPS, a conserved heterohexameric tethering complex. On the membranes to be fused, HOPS binds small membrane-associated GTPases and assembles SNAREs for fusion, but how the complex fulfils its function remained speculative. Here, we used cryo-electron microscopy to reveal the structure of HOPS. Unlike previously reported, HOPS is surprisingly rigid and extensive flexibility is confined to its extremities, where GTPase binding occurs. The SNARE-binding module is rigidly attached to the core, therefore, ideally positioned between the membranes to catalyze fusion. Our results explain HOPS dual functionality and unravel why tethering complexes are an essential part of the membrane fusion machinery.

Figure 1. Composition and architecture of the yeast HOPS complex. A, Composite cryo-EM map from local refinement maps. B, Atomic model of the HOPS complex. C, Schematic representation of the HOPS complex.

References:

[1] Shvarev, Schoppe, König et al. (2022) *bioRxiv*, doi.org/10.1101/2022.05.05.490745.

Fig. 1

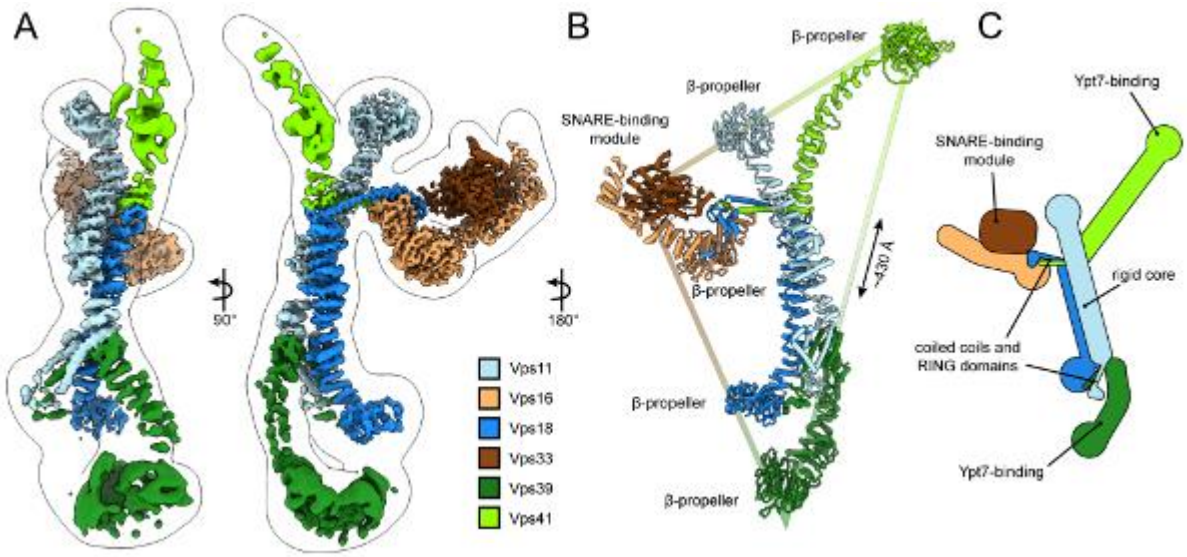

LS1.004

Cryo-EM structures of *C. glutamicum* pre- and posttranslocational 70S ribosome in complex with Kasugamycin

L. Jungbluth[1], S. Matamouros[2], D. Mann[1], J. Ortiz[1], M. Bott[2], C. Sachse[1]

[1]Forschungszentrum Juelich, Ernst-Ruska Centre: Structural Biology (ER-C-3), Jülich, Germany
[2]Forschungszentrum Juelich, Institute of Bio- and Geosciences: Biotechnology (IBG1), Jülich, Germany

The Actinobacteria *Corynebacterium glutamicum* is the workhorse in modern biotechnology, e.g. in industrial biosynthesis of amino acids and heterologous protein production. The detailed architecture of the *C. glutamicum* translation machinery, the 70S ribosome, is hitherto unknown, impeding its structure-function analysis, and limiting drug optimization. The majority of aminoglycoside antibiotic producers are Actinobacteria, still *C. glutamicum* is sensitive to the antibiotic Kasugamycin (KSG). Our study aims to understand the impact KSG has on the 70S ribosome of *C. glutamicum* (Cg70S) and how the simple mutations ΔbS22 and ΔKsgA contribute to resistance. Therefore, we present the three-dimensional structures of the wildtype, ΔbS22 and ΔKsgA ribosome solved to high resolution (<3 Å) with cryo-electron microscopy. By exploiting the potential of single particle analysis in the structural analysis of dynamic processes, particles were classified in 3D heterogeneous refinement according to their t-RNA position in the ribosome. We captured Cg70S ribosomes in the pre- and posttranslocational state in absence and presence of KSG. For both states, we were able to localize the KSG-binding pocket within the mRNA path and in close proximity to the P-tRNA binding site. In direct comparison of the molecular models derived from the WT, ΔbS22 and ΔKsgA EM density maps, it became clear that the deletions do not significantly alter the molecular structure of the KSG binding pocket. Interestingly however, depending on the absence or presence of KSG in wildtype- or ΔbS22-Cg70S the particle ratio between the two distinct states differs significantly, suggesting a role of bS22 in the stabilization of the pretranslocational state. ΔKsgA results in undermethylation of the 16s rRNA, but the structure of the KSG binding pocket is preserved. Here, the alteration of the protein content of the small ribosomal subunit, visible in the EM density maps, seems to be the key to resistance by influencing the presence of bS22 and other small ribosomal subunit proteins and thereby modifying ribosomal dynamics. The here presented cryo-EM structures of the *C. glutamicum* ribosome provide the structural framework for understanding antibiotic KSG resistance.

Fig. 1

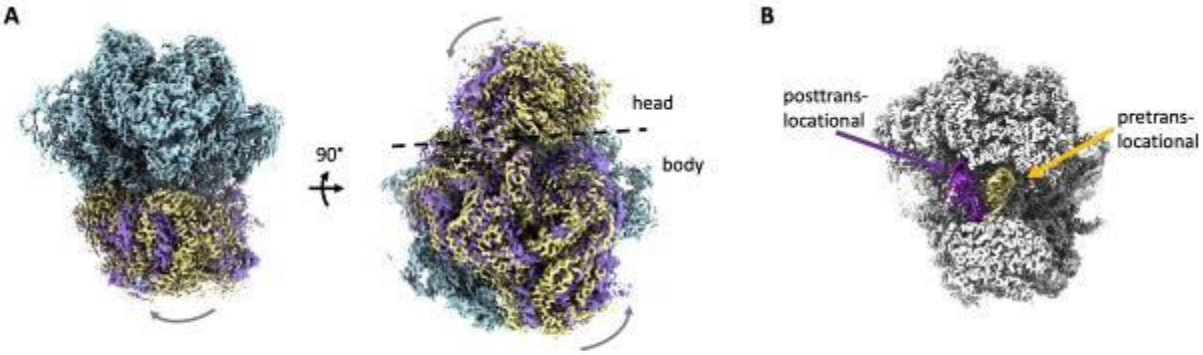

Figure 1: Alignment of cryo-EM density maps of pre- and posttranslocational state (WT)
A: Maps were aligned by superimposing the large ribosomal subunit (blue) of pre- (yellow) and posttranslocational (purple) state of WT Cg70S ribosomes to highlight the rotation of the small ribosomal subunit. **B:** Position of the t-RNA in pre- and posttranslocational state in the alignment of A.

LS1.005

Visualizing cellulose chains with cryo scanning transmission electron microscopy

D. Knez[1], P. Petschacher[2], H. Wiltsche[3], G. Kothleitner[1,4], T. Nypelö[5,6], S. Spirk[2]

[1]Graz University of Technology, Institute of Electron Microscopy and Nanoanalysis, Graz, Austria
[2]Graz University of Technology, Institute of Bioproducts and Paper Technology, Graz, Austria
[3]Graz University of Technology, Institute of Analytical Chemistry and Food Chemistry, Graz, Austria
[4]Graz Center for Electron Microscopy, Graz, Austria
[5]Chalmers University of Technology, Department of Chemistry and Chemical Engineering, Gothenburg, Sweden
[6]Chalmers University of Technology, Wallenberg Wood Science Center, Gothenburg, Sweden

Cellulose is the most abundant biopolymer on earth and is found in the cell walls of most plants and some algae, but also occurs in bacteria, fungi and even some sea animals. Plant cellulose, in particular, has a wide range of applications as a renewable, biodegradable and non-toxic material in papers, textiles, packaging and medical products, to name a few. Cellulose in plants is organized in supramolecular structures where the basic structural element the cellulose microfibril (CMF). The supramolecular cellulose comprises of ordered periodic crystalline regions that can be liberated by acid hydrolysis into nanoparticles, namely the cellulose nanocrystals (CNC), with dimensions of 100-200 nm in length and a few nanometers in width. Despite its abundance in nature and its technological relevance, the structural details of cellulose still remain elusive and various structural models have been proposed in recent years [1].

Transmission electron microscopy (TEM) under cryogenic conditions has proven to be a highly valuable technique for the structural analysis of such biomolecules. However, imaging cellulose at sufficiently high resolution has been challenging due to its very high susceptibility to electron beam damage, combined with the low contrast provided by its light constituents. These problems have been addressed in the past by applying contrast agents, staining with uranyl acetate or low voltage imaging [2]. While, by this, great progress has been made regarding the visualization of nanoscale cellulose features, atomic scale visualization still remains problematic [3].

Here, we report on the visualization of sulfated cellulose chains by low-dose cryo high-resolution scanning TEM (STEM). To this end we exploit the high contrast provided by indvidual heavy ions in annular dark field (ADF) imaging for visualization of cellulose chains.

For imaging a FEI Titan G2 STEM, operated at 300 kV, has been used. Samples were prepared by drop casting the CNCs, dispersed in water, on a TEM grid, which is covered by a 2-3 nm thick amorphous carbon film. During imaging the sample is kept at liquid nitrogen temperature.

In the obtained ADF images (Figure 1) the individual atoms providing contrast can clearly be discerned and exhibit a regular, linear arrangement along the long axis of the CNCs. By comparing the micrographs with multislice simulations based on atomistic structural models, we obtain information about possible arrangements of the sulfate groups, linked to the position of carbon 6 sites in the glucose unit within single CNC chains. Exemplary, a possible structural configuration on the amorphous carbon substrate is depicted in Figure 1c with the corresponding ADF multislice simulation shown in (f).

References

[1] Habibi, Youssef et al.; Chemical reviews 110 (6), pp. 3479–3500. DOI: 10.1021/cr900339w.

[2] Sugiyama, J. et al.; International Journal of Biological Macromolecules 9 (3), pp. 122–130. DOI: 10.1016/0141-8130(87)90039-0.

[2] Ogawa, Yu et al.; Cellulose 26 (1), pp. 5–15. DOI: 10.1007/s10570-018-2076-9.

Acknowledgements

The authors acknowledge financial support by the European Union"s Horizon 2020 research and innovation program under Grant 823717-ESTEEM3.

Fig. 1

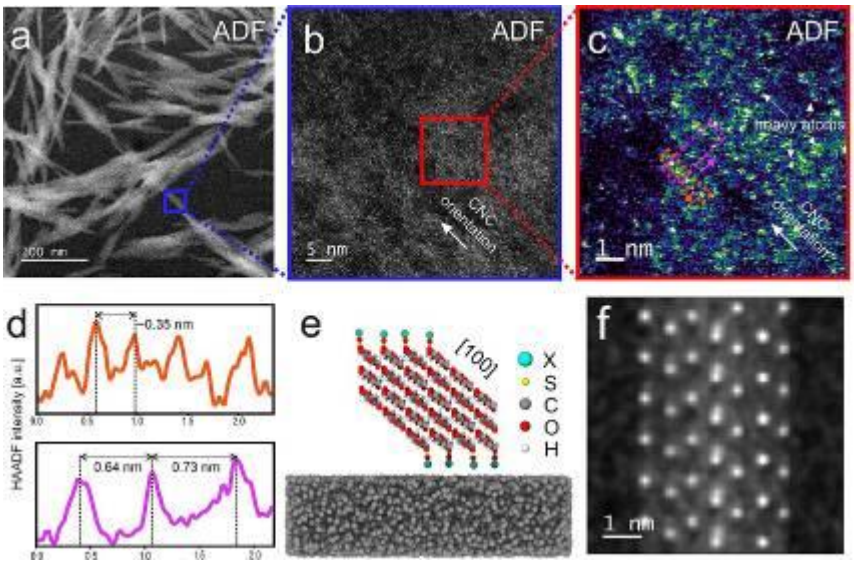
a
ADF
200 nm
b
ADF
5 nm
CNC orientation
c
ADF
heavy atoms
1 nm
d
0.35 nm
0.64 nm
0.73 nm
HAADF intensity (a.u.)
e
[100]
X
S
C
O
H
f
1 nm

LS1.006

Common structural features of ATTRwt and ATTRV30M amyloid fibrils from different patients

M. Schmidt[1], M. Steinebrei[1], J. Baur[1]

[1]Ulm University, Institute of Protein Biochemistry, Ulm, Germany

Introduction:

Wild type transthyretin-derived amyloid (ATTRwt) is the major component of non-hereditary transthyretin amyloidosis. Its accumulation in the heart of elderly patients is life threatening. A variety of genetic variants of transthyretin can lead to hereditary transthyretin amyloidosis, which shows different clinical symptoms, like age of onset and pattern of organ involvement. However, in the case of non-hereditary and in some cases of hereditary ATTR amyloidosis fibril deposits are located primarily in heart tissue.

Objectives:

The goal of this study was the analysis of ATTRwt amyloid fibrils structure from the heart of a patient with non-hereditary transthyretin amyloidosis and comparison with previous published structures.

Materials & methods:

Fibrils were extracted from the amyloidotic tissue of an explanted heart of a male ATTRwt patient. Cryo electron microscopy with subsequent structure modelling and mass spectrometry was used to study these fibrils.

Results:

A density map of ex vivo ATTRwt fibrils with a resolution of 2.78 Å was reconstructed. The structure is formed by stacked N- and C-terminal fragments of transthyretin forming an amyloid fibril which was confirmed with mass spectrometry. They form a spearhead like shape in their cross section. The N-terminal fragment has an extensive hydrophobic core. The C-terminal fragment on the other hand contains a big cavity surrounded by polar and charged amino acids and is probably filled with water.

Conclusion:

We compare the structure of ATTRwt fibrils with previously published V30M variants of ATTR fibrils extracted from heart and eye of different patients. All so far published structures show a remarkably similar cross-sectional shape of the N- and C-terminal fragments with only some minor differences. This demonstrates common features for ATTR fibrils despite differences in mutations and patients.

LS1.P002

Visualizing electrons by single particle cryo-EM

P. Wendler[1], C. Radon[1], G. MIttelstädt[2], S. Leimkühler[1], T. Mielke[3], J. Bürger[3]

[1]University of Potsdam, Potsdam, Germany
[2]Victoria University of Wellington, Ferrier Research Institute, Wellington, New Zealand
[3]Max-Planck Institute of Molecular Genetics, Berlin, Germany

Scattering of electrons by atoms in electron microscopy produces coulomb potential maps and hence EM maps reflect the charge of atoms in protein complexes. At resolution ranges between 5 Å and 10 Å, atomic scattering amplitudes are usually weaker the more negatively charged atoms are. Here, we compare the cryo EM structure of *Rhodobacter capsulatus* formate dehydrogenase (FDH) in the air oxidized, sodium azide inhibited state with an enzyme that is reduced by treatment with NADH. FDH catalyzes the reversible oxidation of formate to carbon dioxide. The electrons gained in this reaction at the active site molybdenum atom are transferred via an electron-transfer pathway formed by numerous FeS clusters and flavin mononucleotide (FMN) onto nicotinamide adenine dinucleotide (NAD+). At a resolution of about 3.25 Å, the difference map between the oxidized and NADH reduced states qualitatively visualizes negative charges on electron accepting atoms in the electron transfer chain of the reduced map.

LS1.P003

Aberration correctors for cryo electron microscopy

M. Linck[1], H. Müller[1], P. Hartel[1], S. Perl[1], S. Uhlemann[1], M. Haider[1]

[1]CEOS GmbH, Research and Development, Heidelberg, Germany

In cryo electron microscopy (cryo EM) the resolution of the TEM hasn"t been the limiting factor for a long time. Recently, however, cryo EM has reached the single Ångstrom level [1] where the aberrations of the TEM start to play a significant role in the process of image formation. There are multiple aspects where aberration correctors might be very useful for cryo EM techniques:

1. Coma-free alignment: The present spherical aberration requires extremely high accuracy and stability of beam tilt alignment to prevent beam tilt induced axial coma. This condition has to be stable for a very long time to allow for long-term automated data acquisition. In a Cs-corrected TEM a beam tilt of several mrad is acceptable without noticeably introducing axial coma.

2. Beam-image-shifts: To avoid mechanical specimen shifts and improve throughput, it is common practice to use combined beam-image-shifts during image recording rather than physical specimen shifts. These virtual object shifts are affected by the unavoidable off-axial coma of the objective lens (Fig.1). Precise simultaneous adjustment of beam tilt during beam-image-shift allows to compensate for this effect [2]. Alternatively, a Cs-corrector can actively compensate the shift-induced coma below the object during image shift and in that case the beam tilt above the specimen does not need to change hence remains flexible, e.g. for dispersion correction. Cs-correctors allow for aberration-free beam-image-shifts of up to 10µm, which is extremely useful for efficient work-flows for single particle reconstructions.

3. Large cameras with a high number of pixels are important to increase throughput: The large field of view which is captured at once, however, is affected by the off-axial coma in that the coma increases linearly from the center of the image towards the outer areas. While this effect is negligible for 2k cameras, it can have a distinct impact on 4k detectors with a similar pixel size. Fortunately, this limitation can be overcome by the off-axial coma corrector (BCOR) which enables aplanatic imaging, i.e. freedom from spherical aberration and off-axial coma [3].

4. Inelastically scattered electrons usually do not contribute to the high-resolution image contrast due to chromatic aberration. A Cc/Cs-corrector is expected to significantly improve contrast for larger sample thicknesses [4].

References:
[1] K.M. Yip et al., Nature 587, 157–161 (2020).
[2] Konings et al., Microsc. Microanal. 25 S2 (2019) 1012-1013.
[3] H. Müller et al., Nucl. Instrum. Methods Phys. Res. A 645 (2011) 20-27.
[4] J.L. Dickerson et al, Ultramicroscopy 237 (2022), 113510.
[€] CEOS GmbH has received funding from the European Union"s Horizon 2020 research and innovation program under grant agreement No. 823717 – ESTEEM3.

Fig. 1 – (a) Simultaneous use of beam and image deflectors for virtual object shifts is always affected by off-axial coma (b, red). Uncorrected TEMs require an additional simultaneous beam tilt to counterbalance off-axial coma effects (magenta). In Cs-corrected TEMs (blue), the corrector elements compensate the off-axial coma contribution and the beam tilt remains flexible. For large cameras the off-axial coma even changes the image quality within the camera's field of view. To remove this effect as well, a corrector for off-axial coma (e.g. BCOR) has to be used (cyan, dashed).

Fig. 1

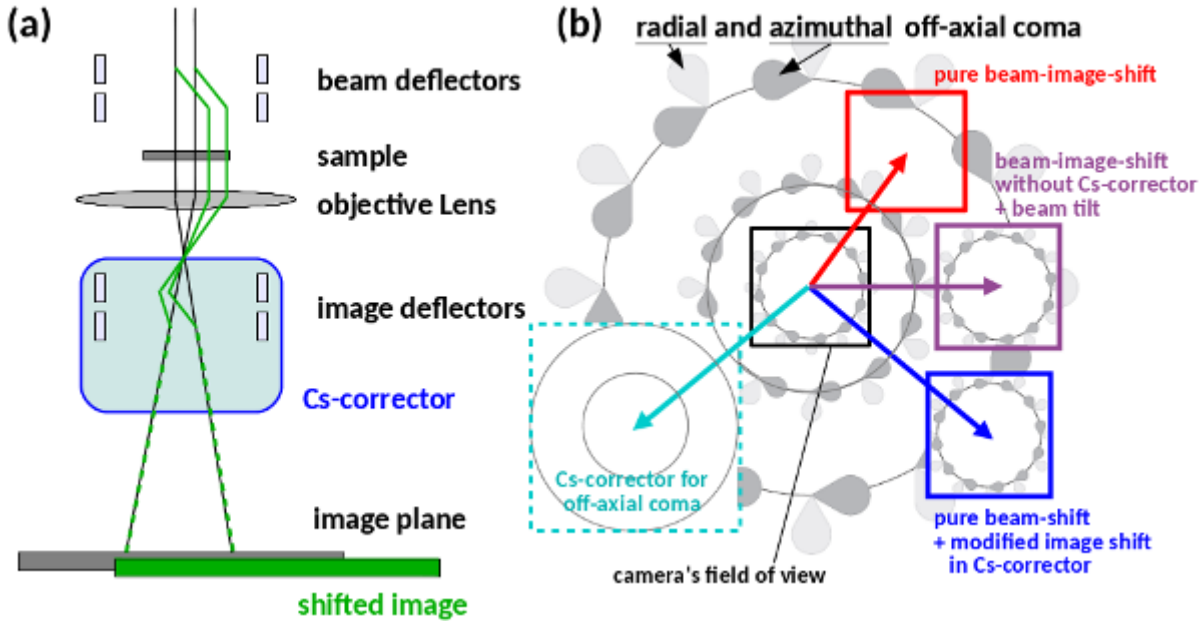
(a)
beam deflectors
sample
objective Lens
image deflectors
Cs-corrector
image plane
shifted image
(b)
radial and azimuthal off-axial coma
pure beam-image-shift
beam-image-shift
without Cs-corrector
+ beam tilt
Cs-corrector for
off-axial coma
pure beam-shift
+ modified image shift
in Cs-corrector
camera's field of view

LS1.P004

Effect of multiple scattering and the ice thickness on the information transfer in cryo transmission electron microscopy

M. L. Leidl[1,2], C. Sachse[1,3], K. Müller-Caspary[1,2]

[1]Forschungszentrum Jülich GmbH, Ernst Ruska-Centrum für Mikroskopie und Spektroskopie mit Elektronen (ER-C), Jülich, Germany
[2]Ludwig-Maximilians-University Munich, Chemistry, Munich, Germany
[3]Heinrich-Heine-Universität Düsseldorf, Biology, Düsseldorf, Germany

In the field of electron cryo-microscopy it remains a challenge to improve the resolution and to decrease the number of micrographs needed for challenging protein samples. To get a better understanding of the scattering inside a biological specimen and the surrounding glass-like ice, we performed multislice simulations of the tobacco mosaic virus (TMV) (PDBe: 6sag [1]) in ice. The molecular structure of ice was modelled by molecular dynamics (LAMMPS [2]) and the atomic model of TMV was added [3]. First, we varied the number of slices used for the multislice simulations. Secondly, we added additional ice above and below the TMV.

The contrast transfer, as seen in Fig.1 by the Fourier ring correlations (FRC) of the exit waves decreases when the number of slices is reduced. The effect is strongest at high spatial frequencies. However, even for a simulation of a single slice that accounts for the propagation to the same optical plane as the multislice simulation, the FRC values are larger than 0.75 up to a resolution of 2.3 Å. So, multiple scattering has only a small effect up to this resolution, which suggests the principal applicability of dose-efficient scanning TEM (STEM) techniques that are based on single scattering, such as integrated differential phase contrast (iDPC) [4] and the single side band (SSB) ptychographic reconstruction. Compared to CTEM simulations, iDPC and the phase of SSB in Fig. 1 are easier to interpret because both contrast transfer functions do not show contrast inversions.

To simulate the averaging of single particle reconstructions, we also calculated the average of 600 phase-corrected simulated CTEM images (defocus range: [-0.1,-1.0] µm, spherical aberration: 1.5 mm) for different ice thickness and compared the results to the ground truth, using the FRC curves (Fig. 2). The contrast transfer decreases with increasing ice thickness, which is reflected in a lower contrast in real space for TMVs and in lower FRC values. The decrease of the FRC values is stronger at higher spatial frequencies, with a plateau above a resolution of 3 Å (Fig. 2). The FRC decrease is most dominant when adding the first ice layers, whereas depositing further ice to form rather thick layer of up to 90nm affect the fidelity of the exit wave and the CTEM simulation as to the TMV less.

Our results will be discussed in the context of experimental applicability of momentum-resolved STEM techniques to biological specimen under low-dose cryo-conditions, and to which extent such new acquisition schemes might improve the structural characterisations of proteins.

Figure 1) (a): FRC curves of the exit waves for multislice simulations of TMV with different number of slices, the number is given in the legend. (b): iDPC reconstruction. (c): Angle of the SSB reconstruction.

Figure 2) (a) and (b): Phase of the exit wave of simulations with minimal and maximal ice thickness (thickness in the label). (c) and (d): CTEM simulations of the exit waves in (a) and (b) with a defocus of -500 nm and a spherical aberration of 1.5 mm. (e) and (f): FRC curves of the exit wave and the average of 600 phase corrected CTEM simulations (defocus: -0.1 µm to -1.0 µm, spherical aberration: 1.5 mm).

[1] Weis, et al. EMBO reports 20.11 (2019)

[2] Thompson, et al. Computer Physics Communications 271 (2022)

[3] Shang, et al. Journal of structural biology 180.1 (2012)

[4] Lazic, et al. (accepted for publication).

Fig. 1

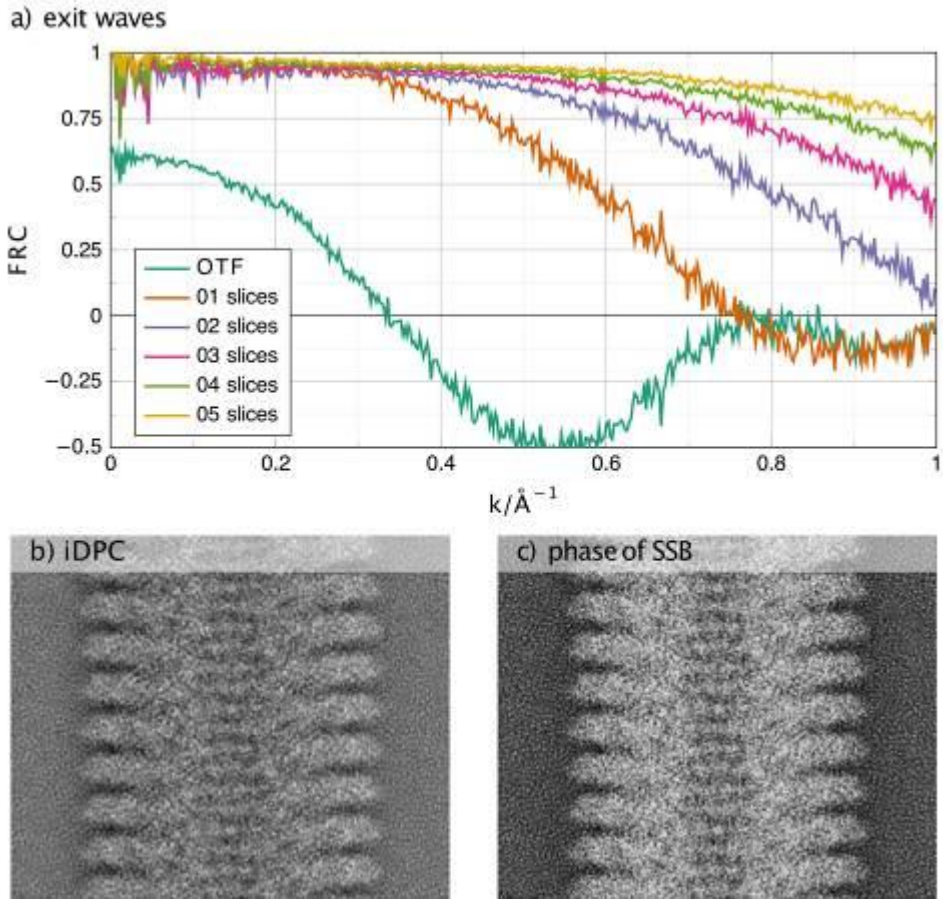
a) exit waves
FRC
k/Å^{-1}
OTF
01 slices
02 slices
03 slices
04 slices
05 slices
b) iDPC
c) phase of SSB

Fig. 2

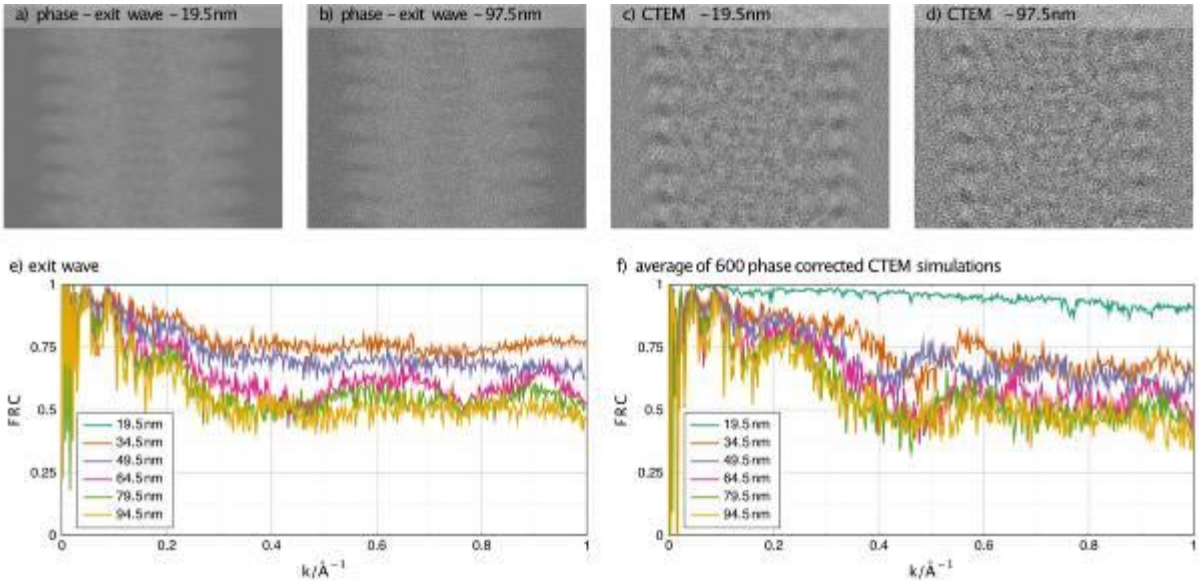
a) phase – exit wave – 19.5nm
b) phase – exit wave – 97.5nm
c) CTEM – 19.5nm
d) CTEM – 97.5nm
e) exit wave
f) average of 600 phase corrected CTEM simulations
FRC
k/Å^{-1}
19.5nm
34.5nm
49.5nm
64.5nm
79.5nm
94.5nm

LS1.P005

Design and deployment of a high-performance computing system for cryo-EM

K. Schnelle[1], A. Möller[1]

[1]University of Osnabrück, Structural Biology, Osnabrück, Germany

The constant development of faster electron detectors and microscope software and the analysis of flexible and dynamic macromolecular complexes demand powerful computing resources. While the microscope operation and image processing are getting increasingly automated and require less manual input, the design and deployment of an HPC system, suitable to fulfill such demands, is still very tedious and can quickly become overwhelming, especially for not professional system administrators.

Here we describe the design choices for our recent cryo-EM HPC system and explain how we automated its installation and deployment with a combination of Metal-As-A-Service (MAAS) and Ansible. The cluster incorporates multi-GPU nodes, highspeed Interconnection (InfiniBand HDR) and a parallel file system (BeeGFS). Our approach can be easily adapted to different storage and hardware systems and enables inexperienced personnel to set up an HPC with little time.

LS1.P007

Structural basis of TIRAP assembly revealed by cryo-EM

J. H. Schäfer[1], A. Möller[1]

[1]Osnabrueck University, Osnabrück, Germany

Toll-like receptors (TLRs) activate the innate immune response during pathogen infection. Upon ligand-induced receptor dimerization, intracellular adapter proteins, like TIRAP (TIR-domain containing adaptor protein), initiate the assembly of large signaling complexes. In resting TLR-positive cells, TIRAP multimerizes into filaments at the plasma membrane and is subsequently converted into dimers during TLR signaling. However, the exact process of TIRAP filament formation and interaction with TLR dimers remains unknown.

Here, we utilize negative-stain and cryo-EM to investigate the mechanism of TIRAP multimerization. We demonstrate that the full-length human TIRAP forms filaments in a temperature-dependent and reversible manner in the absence of TLRs. Our 3.2 Å cryo-EM structure, together with the negative-stain analysis, indicates a sequential filament formation, starting from stable dimers that polymerize into thin filamentous intermediates and tubes with a diameter of about 30 nm. Together, our data support the presence of TIRAP filaments in resting TLR-positive cells. Furthermore, filamentous TIRAP may provide a pool of required adapter proteins to stimulate TLR-based signal transduction.

Fig. 1

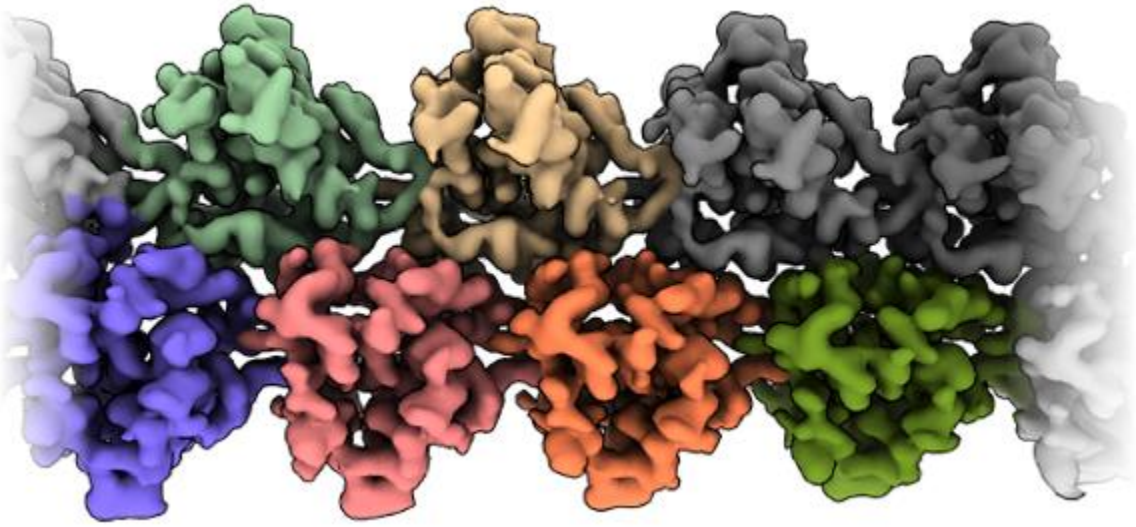

LS1.P008

Cryo-EM analyses of the conformational spectrum of an ABC transporter in various membrane mimics

L. Hoffmann[1], D. Januliene[1], J. Wong[1], A. Baier[1], D. Shvarev[1], A. Möller[1]

[1]University of Osnabrück, Structural biology, Osnabrück, Germany

Membrane proteins and especially ATP binding cassette (ABC) transporters play a major role in nature. ABC transporters are involved in numerous physiological processes and utilize ATP to translocate various compounds through the lipid bilayer. This process requires large-scale conformational changes and is highly dynamic. Therefore, structure determination is fundamental to understanding these transient proteins' function and mode of action.

Cryo-electron microscopy enables structure determination of proteins in solution to high-resolution and is, therefore, ideally suited to investigate such structural dynamics. However, particles must be extracted from the membrane and stabilized in artificial environments to facilitate cryo-EM sample preparation. To mimic the native environment, components such as detergents or lipid-based systems that form nanodisc can be used.

In this study, we investigated the impact of various hydrophobic environments on the archetypical ABC transporter MsbA which translocates the precursor of Lipopolysaccharide through the inner membrane of gram-negative bacteria.

In addition, to different activity intensities, measured by phosphate release during ATP hydrolysis, we notice a strong bias of the observed conformational spectrum to the respective membrane mimic which complicates the accurate determination of the protein''s behavior.

We hope our experiments can serve as a blueprint to calibrate reconstituted membrane protein systems and are now progressing to an alternative test specimen for validation.

LS1.P009

Towards structure of secretory immunoglobulin A with O-antigen substrate

B. M. Qureshi[1], Y. G. Turgay[2], B. Stadtmueller[3], E. Slack[2]

[1]ETH Zurich, Scientific Center for Optical and Electron Microscopy (ScopeM), Zurich, Switzerland
[2]ETH Zurich, Laboratory for Food Immunology, Institute of Food, Nutrition and Health, Department of Health Sciences and Technology, Zurich, Switzerland
[3]University of Illinois Urbana-Champaign, Urbana, Department of Biochemistry, Urbana, United States

Mucosal immune system is the largest component of immune system and mediates interactions with a diverse range of antigens from toxin molecules to pathogen organisms of dietary or environmental source. Moreover, it comprises physiologically diverse compartments such as ocular, oral, gastrointestinal, respiratory etc mucosae. *S*ecretory *I*mmuno*g*lobulin *A* (SIgA) is the major antibody of mammalian mucosa. It is a polymeric antibody and interacts with a large and diverse set of antigens. Mode of action for SIgA seems to be mostly non-inflammatory and involves coating, clumping, cross-linking (Kathrin Moor, et al. 2017). Structure of SIgA was recently solved (Kumar Bharathkar, Parker, et al. 2020) and comprises two copies of IgA with one *J*oining-*C*hain (JC). The full molecular assembly furthermore comprises Secretory *C*omponent (SC). However, the Fab fragments were not resolved likely due to high flexibility.

We characterized the SIgA using *cryo e*lectron *m*icroscopy (cryoEM) in presence of its substrate, the O-antigen. One SIgA and one O-antigen molecule comprise four Fabs and 50-60 repeating units, respectively. The molar ratio of SIgA/O-antigen is 2/1, which implies that two tetravalent SIgA molecules are bound to one molecule O-antigen comprising 50-60 antigen repeating units (corresponding to 1 Fab /6.25-7.5 antigen repeating units). Freshly glow discharged Quantifoil Cu R 2/2 grids were optimized for 0.5 mg/ml SIgA sample or its complex with O-antigen at a ratio of 2:1 using Vitrobot (3.5 µl, 22°C, 2-4 s blotting time). Data was collected using Titan Krios (Thermo Fisher Scientific) and GIF/K3 (Gatan) by applying 63 e/Å2 at 0.65 pix/Å. The collected 8060 movies were processed in cryoSPARC to solve the structure.

Few conclusions can be drawn from a comparison of the published SIgA structure with our SIgA structure or the SIgA-O-antigen complex. The obtained structure of the SIgA shows no change in the overall structure upon binding of the O-antigen. However, addition of the O-antigen markedly improves the resolution of the complex (currently ca. 3.2 Å) possibly resulting from a higher stability of complex. Furthermore, the obtained structure is similar to the published structure referred to earlier, but differences are observed especially for parts of the SC where the polypeptide chain is better resolved, and a different atomic model can be built. Besides, we are working currently to resolve the Fabs and Fab-antigen interaction using cryoEM and additional techniques such X-ray crystallization.

References:

Kumar Bharathkar, Parker, et al. eLife 2020;9:e56098. DOI: https://doi.org/10.7554/eLife.56098

Kathrin Moor, et al. Nature 2017; DOI:10.1038/nature22058

LS2.001-invited

On the way to objective tomogram analysis

B. Turoňová[1]

[1]Max Planck Institute of Biophysics, Molecular sociology, Frankfurt am Main, Germany

Cryo-electron tomography (Cryo-ET) has become an essential tool for in situ structural biology. Recent developments both in hardware and software lead to (relatively) high throughput in tilt-series acquisition as well as more automated tilt-series alignment and tomogram reconstruction. For subsequent tomogram analysis, most of the method development has been focused on automated particle picking and subtomogram averaging (STA). While these techniques are essential for high-resolution structure determination, they are often "blind" to the rich cellular environment from which the particles come and leave a large portion of the tomograms unexplored. In my talk I will discuss advantages and ways of incorporating contextual information into the particle picking and STA workflows and show how using meta data from STA can be used to analyze the remaining parts of cellular tomograms.

LS2.003

Structural basis of proteasome impairment by protein aggregates in ALS/FTD

Q. Guo[1,2], H. Riemenschneider[3], L. Qu[4,1], D. Edbauer[3,5,6], R. Fernandez-Busnadiego[4,1,7,8]

[1]Max Planck Institute of Biochemistry, Martinsried, Germany
[2]Peking University, Beijing, China
[3]German Center for Neurodegenerative Diseases, Munich, Germany
[4]University Medical Center Göttingen, Institute of Neuropathology, Göttingen, Germany
[5]Munich Cluster of Systems Neurology, Munich, Germany
[6]Ludwig-Maximilians-University Munich, Munich, Germany
[7]Cluster of Excellence "Multiscale Bioimaging: from Molecular Machines to Networks of Excitable Cells", Göttingen, Germany
[8]Aligning Science Across Parkinson's (ASAP) Collaborative Research Network, Chevy Chase, MD, United States

Protein aggregation is a hallmark of many neurodegenerative diseases, including amyotrophic lateral sclerosis (ALS) and frontotemporal dementia (FTD). However, the mechanisms linking aggregation to neurotoxicity remain poorly understood, partly because only limited information is available on the native structure of protein aggregates inside cells. We address this pressing issue utilizing the latest developments in cryo-electron tomography (cryo-ET). We use cryo-focused ion beam to prepare thin lamellas of vitrified cells containing protein aggregates, and subsequently image them in three dimensions by cryo-ET. This allows us to analyse aggregate structure within pristinely preserved cellular environments and at molecular resolution.

Using this approach, we analysed neuronal poly-GA and TDP-43 aggregates. The expansion of a GGGGCC repeat in the *C9orf72* gene is the most common cause of familial ALS/FTD. This mutation leads to the translation of poly-GA and other dipeptide repeat proteins, which aggregate in neurons. On the other hand, most ALS/FTD cases are sporadic and display aggregation of C-terminal fragments of TDP-43. Our *in situ* cryo-ET studies show that both poly-GA [ref #1; Fig.1] and TDP-43 [ref #2, Fig.2] aggregates recruit large amounts of proteasomes in neurons. Subtomogram averaging revealed that association with aggregates alters the conformational landscape of the proteasome. This leads to defects in proteasomal degradation and accumulation of proteasomal substrates in the cells. To understand these processes with mechanistic detail, we reconstituted the poly-GA/proteasome interaction *in vitro* [ref #3]. Combined single-particle, cryo-ET and biochemical analyses suggest a structural basis of proteasome impairment by poly-GA. Altogether, our studies highlight proteasome inhibition as an important factor of neurotoxicity in ALS/FTD, pointing to possible therapeutic avenues.

References

[1] Guo et al., *Cell* (2018) 172 (4), 696-705, DOI: 10.1016/j.cell.2017.12.030

[2] Riemenschneider et al., *EMBO Rep* (2022) 23 (6), e53890, DOI: 10.15252/embr.202153890

[3] Qu et al., *manuscript in preparation*

Legends

Fig 1. *C9orf72* poly-GA aggregates consist of polymorphic twisted ribbons (red) that recruit high numbers of proteasomes (light blue). Other large macromolecules, such as ribosomes (gold) or TRiC/CCT (purple) are mostly excluded from the aggregate and accumulate at its periphery. Further analysis of proteasome structure by subtomogram averaging suggests that poly-GA-associated proteasomes are functionally impaired. Guo et al., Cell (2018).

Fig 2. Aggregates formed by C-terminal fragments of TDP-43 ("TDP-25") appear amorphous (red) and recruit high numbers of proteasomes (light blue). Other large macromolecules, such as ribosomes (gold) or TRiC/CCT (green) are mostly excluded from the aggregate and accumulate at its periphery. Further analysis of proteasome structure by subtomogram averaging suggests that poly-GA-associated proteasomes are functionally impaired. Riemenschneider et al., EMBO Rep (2022).

Fig. 1

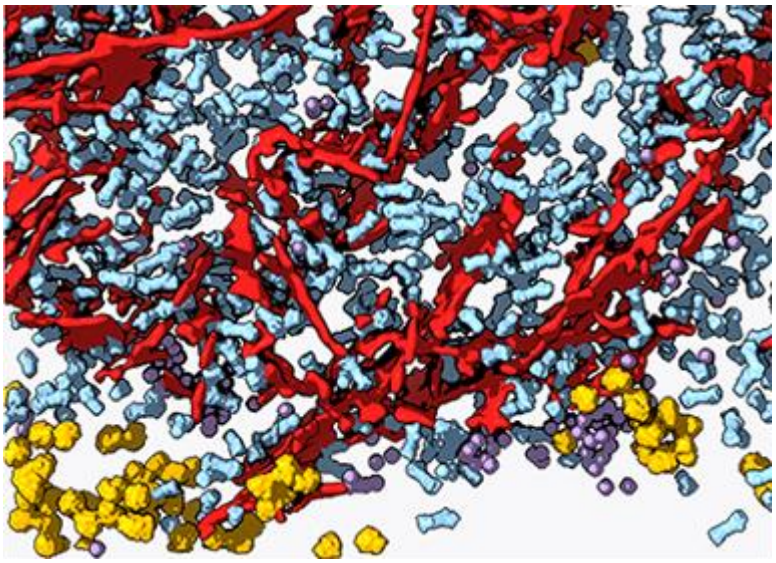

Fig. 2

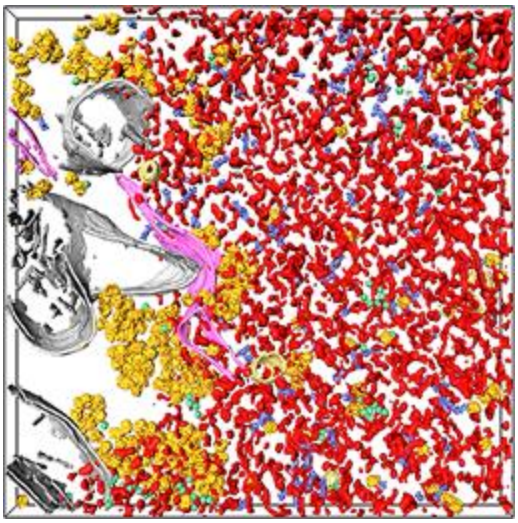

LS2.004

Cryo-electron tomography of SARS-CoV-2 replication and assembly sites reconstituted in cells

L. Zimmermann[1,2], X. Zhao[1,2], J. Makroczyova[1,2], M. Wachsmuth-Melm[1,2], V. Prasad[1,3], R. Bartenschlager[1,3,4,5], P. Chlanda[1,2]

[1]Heidelberg University Hospital, Heidelberg, Germany
[2]Virology, Infectious Diseases, Heidelberg, Germany
[3]Molecular Virology, Infectious Diseases, Heidelberg, Germany
[4]German Cancer Research Center (DKFZ), Division Virus-Associated Carcinogenesis, Heidelberg, Germany
[5]German Center for Infection Research (DZIF), Heidelberg, Germany

Severe Acute Respiratory Syndrome Coronavirus 2 (SARS-CoV-2) is an enveloped virus with a positive single-stranded RNA (ssRNA) genome. Upon infection, endoplasmic reticulum (ER)-derived double-membrane vesicles (DMVs) serve as replication organelles. Recently a structure spanning the DMVs was identified serving as a putative pore dedicated to the translocation of the newly synthesized viral genome and mRNAs from the DMV lumen into the cytoplasm. The viral membrane (M) and envelope (E) proteins drive virion budding and are responsible for the recruitment of the viral genome packaged by the nucleocapsid (N) protein at the ER-Golgi Intermediate Compartment (ERGIC). However, the exact roles of structural proteins in virus budding are poorly understood and the proteins involved in DMV biogenesis remain to be identified. Here we apply *in situ* cryo-electron tomography (cryo-ET) to reconstitute the formation of DMVs and virus assembly. To elucidate the DMV pore structure and the role of each structural protein in SARS-CoV-2 budding, we use a transfection-based system allowing us to express different combinations of viral proteins together with a fluorescent marker. Cryo-light microscopy is applied to target transfected cells for cryo-focused ion beam milling and produced lamellae are subjected to cryo-electron tomography. Our data provide information on VLP assembly and the composition and structure of the SARS-CoV-2 DMV pore. In summary, *in situ* cryo-ET of here established transfection-based system provides an invaluable tool to study SARS-CoV-2 replication and virus assembly at biosafety level 1 condition.

LS2.005

Characterization of vRNP clustering in influenza A virus-infected cells using in-situ cryo-electron tomography

M. Wachsmuth-Melm[1], S. Peterl[1], S. Vale-Costa[2], M. J. Amorim[2], P. Chlanda[1]

[1]Heidelberg University Hospital, Virology, Heidelberg, Germany
[2]Instituto Gulbenkian de Ciência, Oeiras, Portugal

Influenza A virus has an eight-segment single-stranded RNA genome. Each genome segment is packaged into a rod-shaped vRNP complex, eight of which form a bundle containing one copy of each genome segment. During viral assembly, newly produced vRNPs subvert the recycling endosome to travel from the ER exit sites, where they phase-separate in the presence of Rab11, to the plasma membrane where budding takes place. On this route, vRNP selection and bundle formation occur, yet neither the site of clustering nor the mechanism behind are fully understood on a molecular level.To shed light on this important step in the viral replication cycle, we employed *in-situ* cryo-electron tomography.

To analyze the spatial distribution of vRNPs inside cryoFIB-milled cells, we established a segmentation and cluster analysis workflow. Our data show that vRNPs localize to so far uncharacterized compartments that comprise double membranes zippered together by head-to-head interactions of viral hemagglutinin, which is the main mediator of viral entry. vRNPs cluster around these membranes, with numerous points of vRNP-vRNP and vRNP-membrane interactions. Taken together, our data show a previously unknown function of HA during viral assembly in intracellular membrane remodeling and vRNP clustering.

LS2.006

SavvyScan2: enhancements to a multichannel flexible scanning TEM system

S. Seifer[1], M. Elbaum[1]

[1]Weizmann Institute of Science, Chemical and Biological Physics, Rehovot, Israel

SavvyScan is a system that incorporates flexible pattern scanning and simultaneous acquisition from multiple diffraction detector segments in a Scanning Transmission Electron Microscope (STEM). The microscope operations are fully manageable by SerialEM while the extended hardware is based on multipurpose PC cards from Spectrum Instrumentation GmbH. Interface software is released as open source. In the first publication of the system we presented spiral scans of integrated differential phase contrast (iDPC) images and introduced the useful idea of splitting iDPC to separate depth contrast and phase contrast based on image shift corrections (1). Here we report on recent enhancements to the system. The range of image sizes has been extended based on first-in-first-out acquisition that is in principle limitless. The rate of digital averaging has been extended to maximum to improve signal to noise ratio and the channels are processed and recorded simultaneously to shorten acquisition time. The system now supports automated tilt series acquisition at multiple sites based on the navigation features in SerialEM. SavvyScan software recognizes the Record scans and save them in a multi-slice mrc format per detector channel. The newly supported remote Python scripting in SerialEM is utilized for special tasks such as automated alignment of the diffraction disk at high precision. Additional scan patterns have been introduced, including Lissajous curve and continuous 4X4 raster scans that may potentially reduce instability artifacts in single particle analysis. We learn to exploit the multiple signals from concentric annular segments on the Opal diode (El-Mul Technologies) and HAADF (Fischione) detectors for discrimination of materials on the basis of atomic stoichiometry.

(1) Seifer, S.; Houben, L.; Elbaum, M. Flexible STEM with Simultaneous Phase and Depth Contrast. Microscopy and Microanalysis 2021, 1–12. https://doi.org/10.1017/S1431927621012861.

LS2.P001

Visualisation of native Atg9 complexes using *in situ* cryo-EM

C. Ortmann de Percin Northumberland[1], M. Licheva[2], C. Kraft[2], C. Sachse[1]

[1]Forschungszentrum Juelich, Ernst-Ruska-Centre 3 Structural Biology, Jülich, Germany
[2]University of Freiburg, Institute of Biochemistry and Molecular Biology, Freiburg, Germany

Autophagy is a conserved process that allows for recycling of cellular components by sequestration into a double-membrane-bounded compartment which fuses with the lysosome for degradation. Among the core machinery that monitors the steps towards autophagy is Atg9, the only multi-spanning membrane protein. Atg9 forms a complex with Atg2 and Atg18 and is essential for extending the isolation membrane. So-called Atg9 vesicles, stored in the cytoplasm, provide a lipid reservoir for the growing isolation membrane. Recently a scramblase activity has been identified in both the human and yeast Atg9 [1,2]. In order to elucidate the exact mechanism of the Atg9-Atg2-Atg18 complex, I observed native Atg9 complexes and surrounding membrane environment in *S. cerevisiae* using cryo-confocal microscopy followed by focussed ion beam (FIB) milling and *in situ* tomography. Thus far, I established the reproducible preparation of FIB lamellae in yeast. I have screened a range of knock-out mutants, tested different fluorophores and growth conditions. These optimizations enriched Atg9-containing punctae around lysosomal membranes and will improve the success of localisation for down-stream FIB-milling and any associated image analysis such as subtomogram averaging. With functional mutants of the complex components *in situ* we will be able to address mechanistic questions of isolation membrane elongation.

References:

[1] Maeda, S. *et al.* Nat Struct Mol Biol **27**, 1194-1201 (2020).

[2] Matoba, K., *et al.* Nat Struct Mol Biol **27**, 1185-1193 (2020).

LS3.001-invited

Neuropathology on tape – applications of ATUM-based volume EM

M. Schifferer[1], G. Kislinger[2], C. Niemann[2], P. Androvic[3], I. Khalin[3], M. K. Fard[3], M. Kerschensteiner[3], C. Haass[3], N. Plesnila[3], M. Simons[2], O. Gokce[3], T. Misgeld[2]

[1]DZNE/SyNergy, Munich, Germany
[2]TUM, Munich, Germany
[3]LMU, Munich, Germany

Volume Electron Microscopy (vEM) reveals biological structures at nanometer resolution in three dimensions and resolves ambiguities of two-dimensional representations. However, as the structures of interest – like disease hallmarks emerging from neuropathology – are often rare but the field of view is small, this can easily turn a vEM project into a needle in a haystack problem. One solution for this is correlated light and electron microscopy (CLEM), which requires precise coordinate transfer between the two imaging modalities. With array tomography methods, serial ultrathin sections are collected into a storable tissue library, thus restoring precious samples like human biopsies and enabling repetitive imaging at different resolution levels for an SEM-based search strategy. For this, automated tape collecting ultramicrotomy (ATUM) has been developed to reliably collect serial ultrathin sections via a conveyor belt onto a plastic tape that is later mounted onto silicon wafers for serial scanning EM (SEM) (Kasthuri, Hayworth et al., 2015). The ATUM-SEM procedure is highly modular and enables targeting and high resolution imaging of specific structures. The variation of section thickness determines axial resolution and screening speed. We have developed ATUM hybrid methods that enable both, fast screening and targeted imaging at isotropic voxels (Kislinger, Gnägi et al., 2020). We exemplify targeted ATUM-SEM in mouse models for the reconstruction of Alzheimer"s disease plaques and for the visualization of Blood Brain Barrier leakage (Khalin, Adarsh et al., 2022). In order to correlate transcript levels with ultrastructure, we designed an indirect correlative method called SPcEM which combines ATUM-SEM with Spatial Transcriptomics (Androvic, Schifferer et al., 2022). In a mouse demyelination model adjacent cryosections are inspected by either of the two methods for sophisticated microglia classification.

Androvic P, Schifferer M, Anderson KP, Cantuti-Castelvetri L, Ji H, Liu L, Besson-Girard S, Knoferle J, Simons M, Gokce O (2022) Spatial Transcriptomics-correlated Electron Microscopy. *bioRxiv*: 2022.05.18.492475

Khalin I, Adarsh N, Schifferer M, Wehn A, Groschup B, Misgeld T, Klymchenko A, Plesnila N (2022) Size-Selective Transfer of Lipid Nanoparticle-Based Drug Carriers Across the Blood Brain Barrier Via Vascular Occlusions Following Traumatic Brain Injury. *Small (Weinheim an der Bergstrasse, Germany)* n/a: 2200302

Kislinger G, Gnägi H, Kerschensteiner M, Simons M, Misgeld T, Schifferer M (2020a) ATUM-FIB microscopy for targeting and multiscale imaging of rare events in mouse cortex. *STAR Protocols* 1: 100232Kislinger G, Gnägi H, Kerschensteiner M, Simons M, Misgeld T, Schifferer M (2020b) Multiscale ATUM-FIB Microscopy Enables Targeted Ultrastructural Analysis at Isotropic Resolution. *iScience* 23: 101290

Fig. 1 ATUM-SEM and ATUM-FIB of AD plaques

Fig. 2 BBB-CLEM with fluorescent and gold nanoparticles

Fig. 3 SPcEM in demyelinating disease

Fig. 1

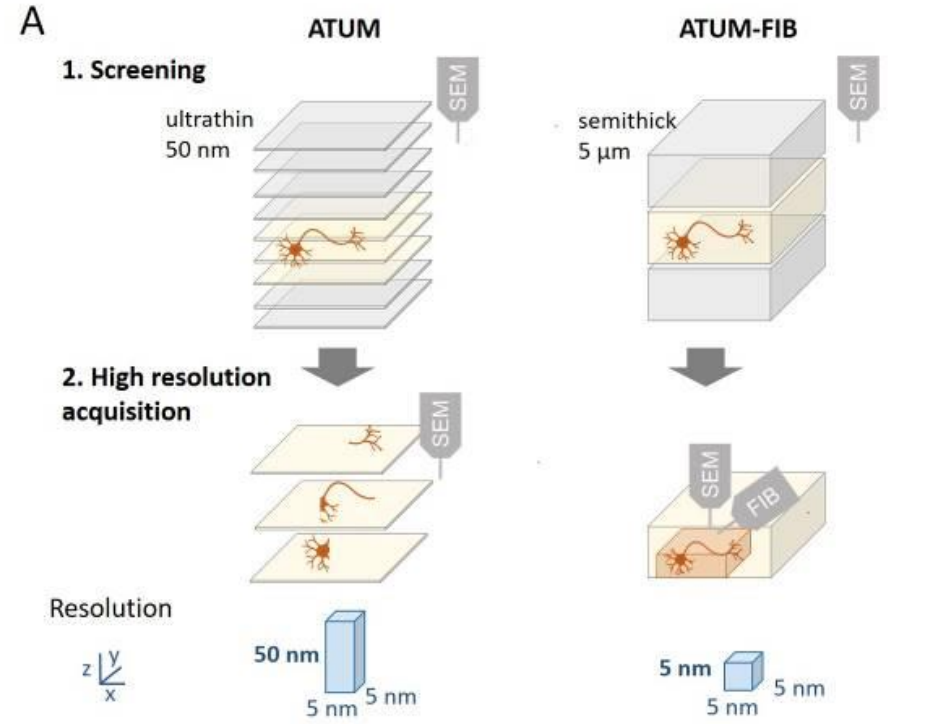
A
ATUM
ATUM-FIB
1. Screening
ultrathin
50 nm
SEM
semithick
5 µm
SEM
2. High resolution
acquisition
SEM
SEM
FIB
Resolution
z
y
x
50 nm
5 nm
5 nm
5 nm
5 nm
5 nm
B

Fig. 2

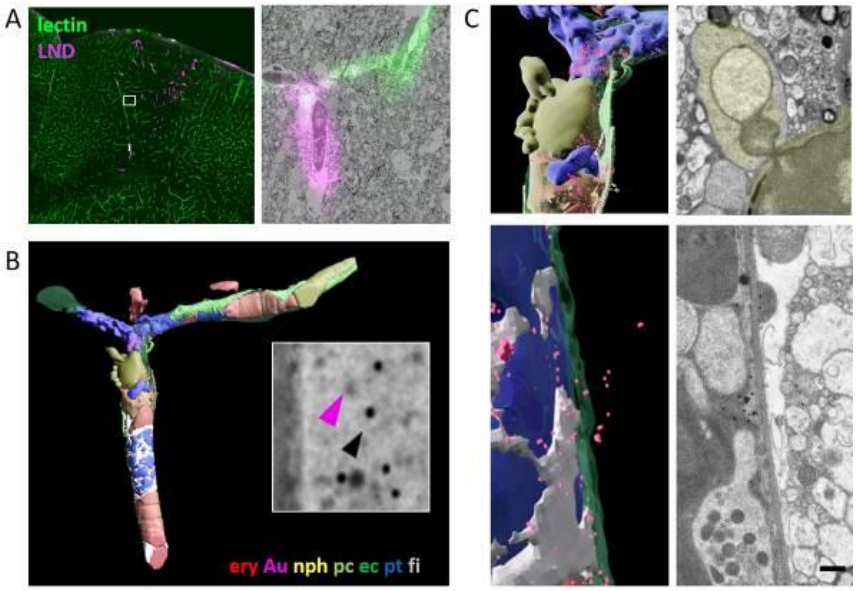
A
lectin
LND
B
ery Au nph pc ec pt fi
C

Fig. 3

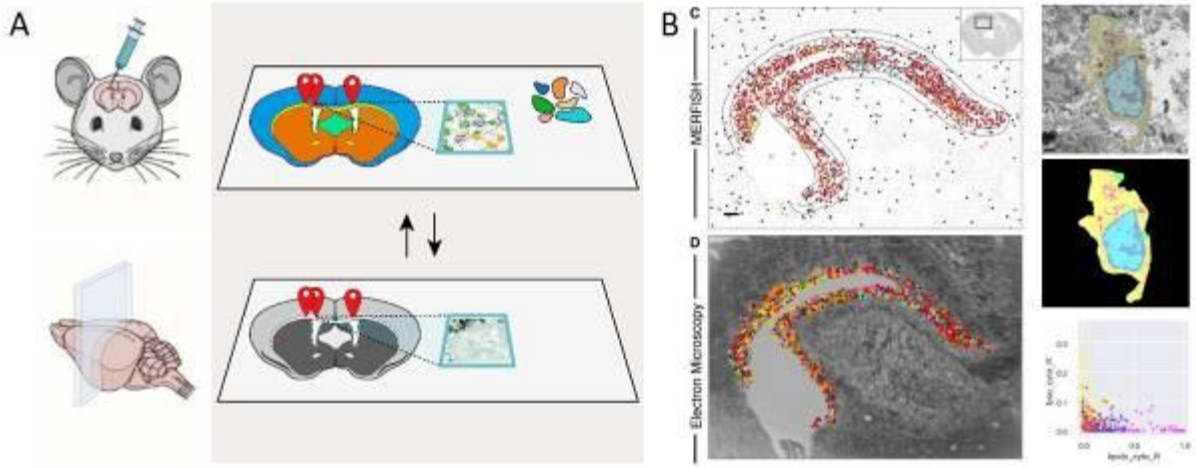

LS3.002-invited

Focus on the 3D architecture of mitotic spindles in human cells

G. Fabig[1], W. Conway[2,1,3,4], G. Ha[5], M. Basaran[4], R. Kiewisz[6], D. Needleman[3,4,7], T. Müller-Reichert[1]

[1]TU Dresden, Medizinische Fakultät, Dresden, Germany
[2]New York Structural Biology Center, Simons Electron Microscopy Center, New York, NY, United States
[3]Flatiron Institute, Center for Computational Biology, New York, NY, United States
[4]Department of Physics, Harvard University, Cambridge, United States
[5]Department of Systems Biology, Harvard University, Cambridge, United States
[6]New York Structural Biology Center, Simons Machine Learning Center, New York, NY, United States
[7]School of Engineering and Applied Sciences, Harvard University, Cambridge, United States

Mitosis in eukaryotes follows organism- as well as cell-specific patterns. One common feature of mitosis is the assembly of a bipolar spindle apparatus that is involved in the segregation of the genetic material to the newly forming daughter cells. The spindle is a complex microtubule-based cellular machinery. Within the spindle, microtubules are interacting with molecular motors and passive crosslinkers to align chromosomes in metaphase and move chromosome halves in anaphase. It is crucial to study the 3D complexity of mitotic spindles in order to better understand chromosome missegregation. Almost any chromosome missegregation results in aneuploidy, which is a hallmark of most types of cancer. Studying the 3D ultrastructure of the mitotic spindle apparatus at the level of microtubule organization requires electron microscopy. For 3D analysis, we apply high-pressure freezing, freeze substitution and resin embedding. Subsequently, we pre-screen embedded cells using confocal light microscopy to identify cells in desired stages of mitotic cell division. Once a cell has been chosen, we apply serial sectioning followed by electron tomography to reconstruct spindles *in silico* with single-microtubule resolution. For 3D reconstruction and quantitative analysis of spindle organization, we are applying a routine pipeline, which involves various software tools such as IMOD and Amira. With this approach, we recently analyzed bipolar spindles in HeLa cells (Kiewisz et al., Elife, 2022). During the meeting we will also report on our newest results on the ultrastructure of kinetochore microtubules (KMTs) in monopolar spindles in retinal pigment epithelial 1 (RPE1) cells. In both bipolar and monopolar mammalian spindles, KMTs are organized in so-called kinetochore (k)-fibers. Comparing spindle organization in various cell types, it is our goal to refine our recently developed biophysical model of k-fiber self-organization in mammalian cells (Conway et al., Elife, 2022).

Fig. 1

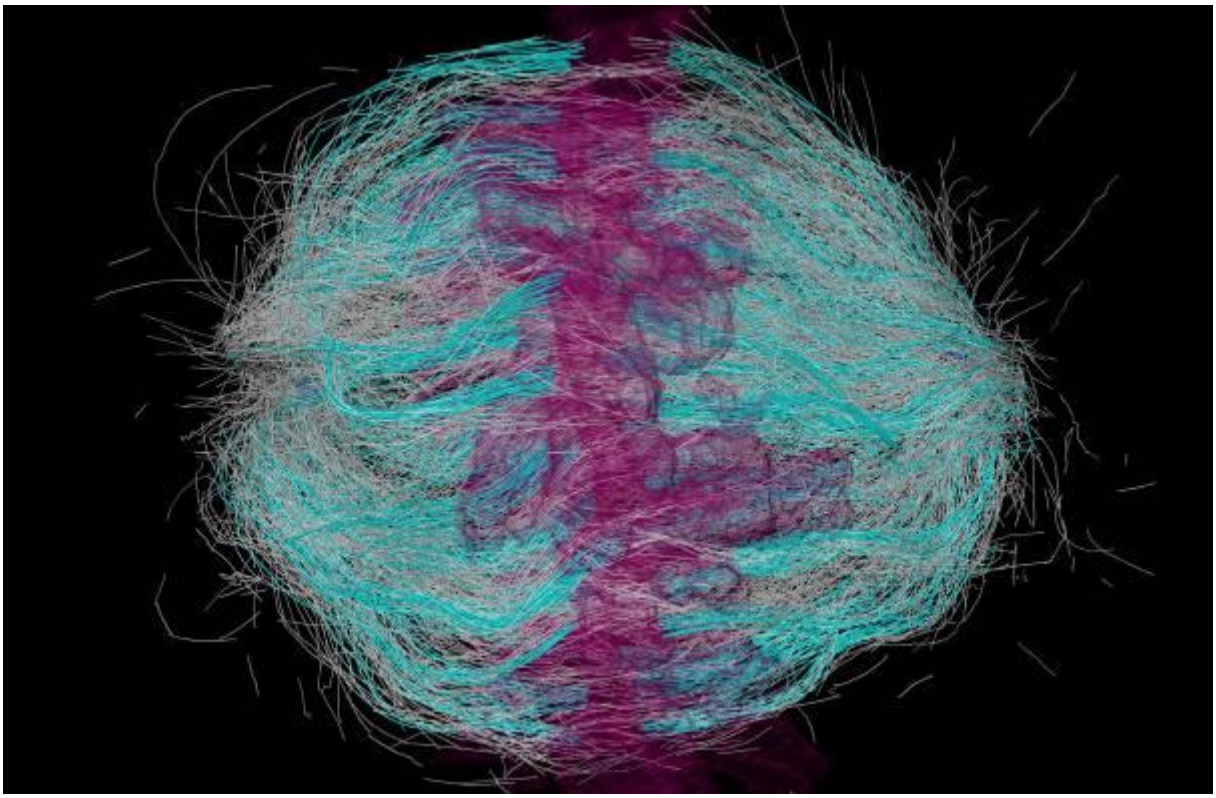

Fig. 2

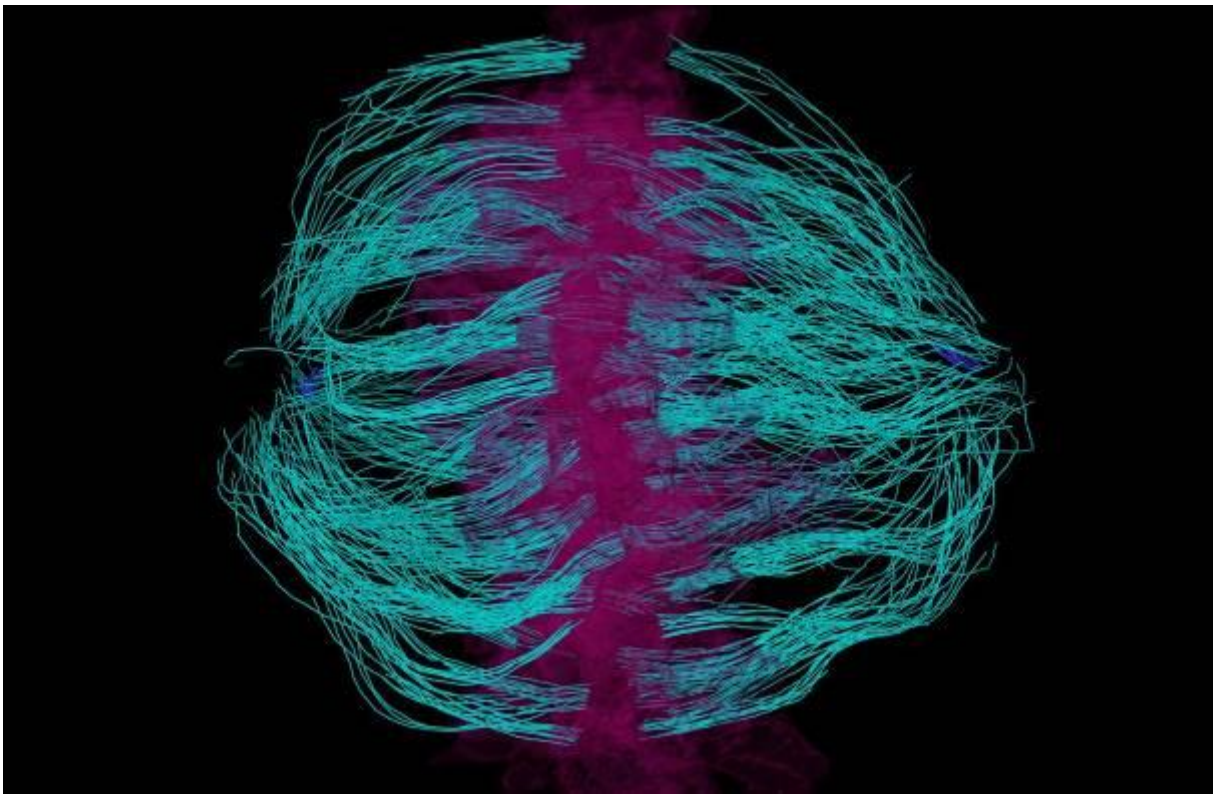

Fig. 3

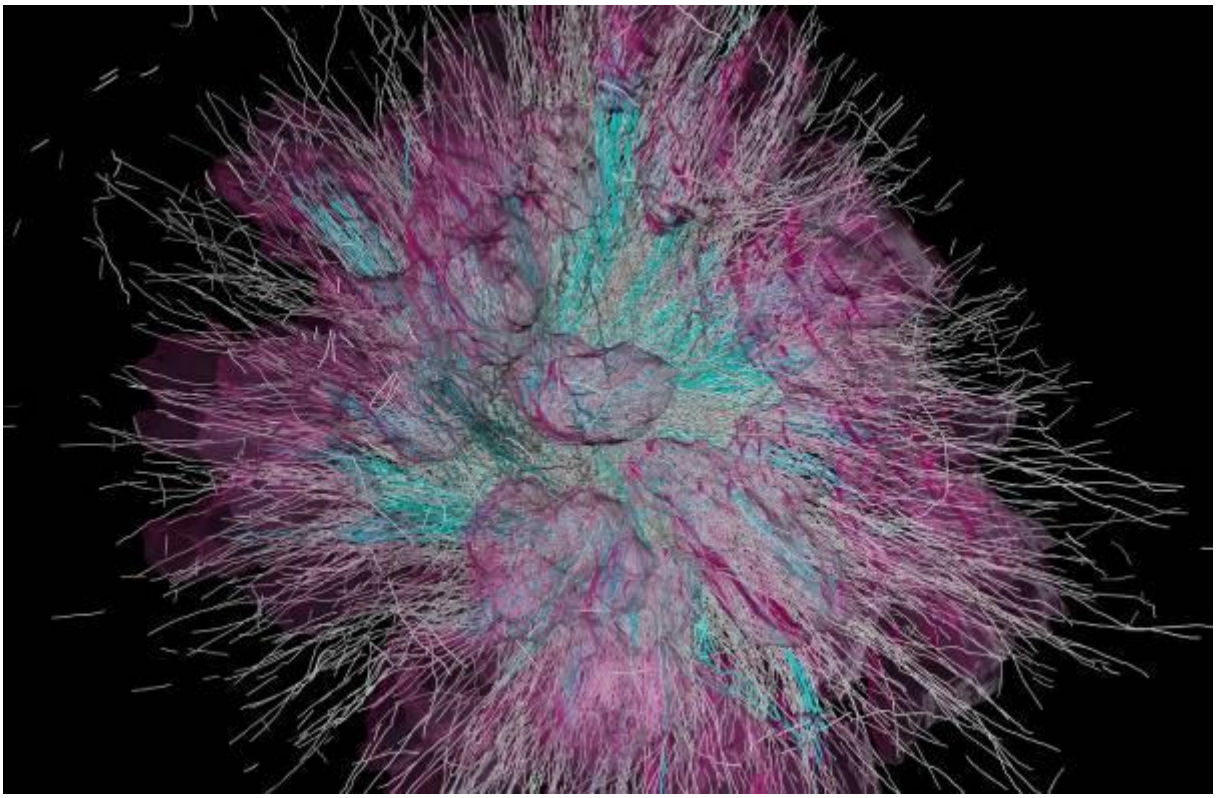

Fig. 4

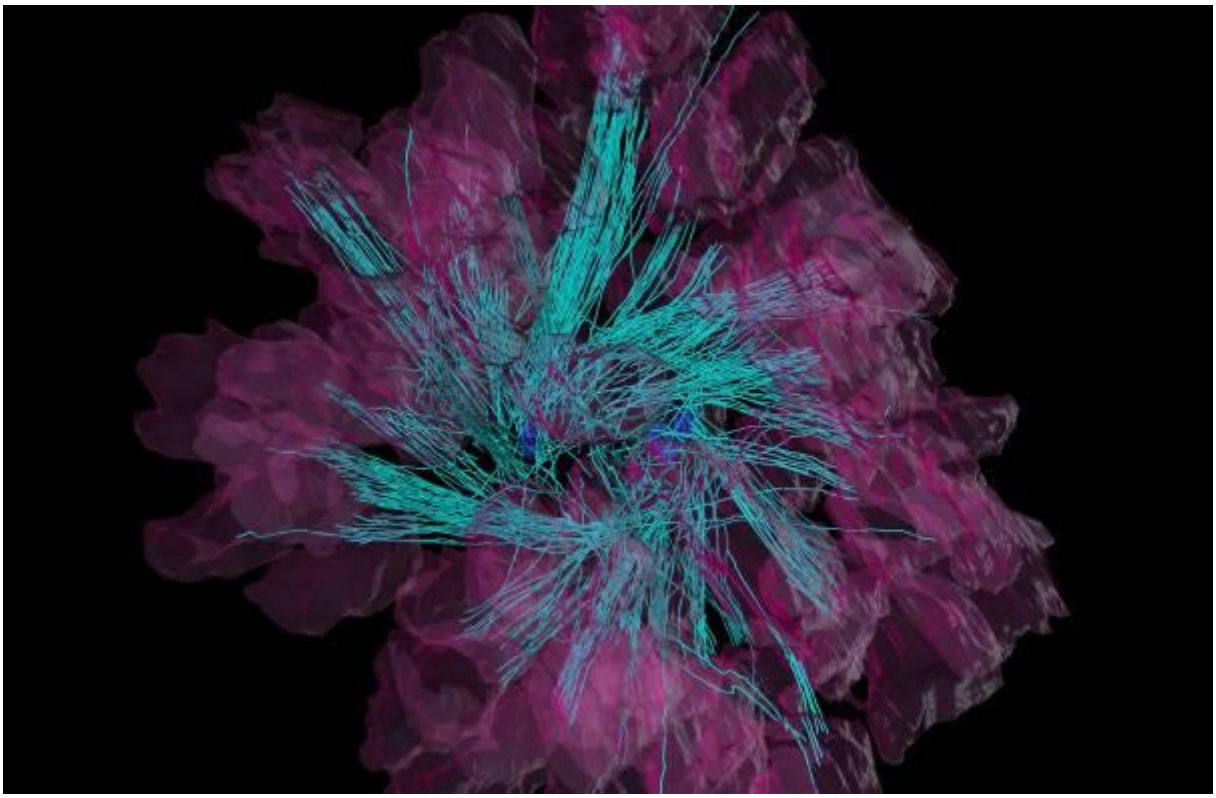

LS3.003

Structural analyses of the brown algae Ectocarpus

I. Koch[1], B. Sailer[1], P. Ronchi[2], A. Henschen[3], S. M. Coelho[3], K. Hipp[1]

[1]Max Planck Institute for Biology Tübingen, EM Facility, Tübingen, Germany
[2]EMBL Heidelberg, Electron Microscopy Core Facility, Heidelberg, Germany
[3]Max Planck Institute for Biology Tübingen, Department of Algal Development and Evolution, Tübingen, Germany

Brown algae belong to the stramenopiles and as such are phylogenetically distant from plants, animals and fungi. They have been evolving independently from plants and animals more than one billion years ago. Brown algae are one of only five eukaryotic lineages that have evolved independently to develop into complex multicellular organisms.

To contribute to the understanding of developmental processes that lead to the observed complex multicellularity in brown algae we have analysed *Ectocarpus siliculosus* on the ultrastructural level both by scanning and transmission electron microscopy. Several sample preparation techniques were tested to find optimal conditions for structure preservation for this organism. In order to characterise the morphology and ultrastructure of Ectocarpus we have compared the wild-type and a mutant that shows defects in the first cell divisions of the developing organism. Potential differences in Golgi morphology were analysed in datasets obtained by focused-ion beam scanning electron microscopy of plastic embedded samples of both the wild-type and the mutant.

LS3.004

Correlative light and serial block face electron microscopy for targeting and investigating oligodendrocyte-vasculature interactions

A. Battefeld[1], J. Palhol[1], E. Gontier[1]

[1]University of Bordeaux, CNRS, INSERM, Bordeaux Imaging Center, BIC UAR3420, Bordeaux, France

Cell-cell specific interactions occur between all major cell types in the brain. Although the investigation of cellular interactions with light microscopy is a standard approach, targeting specific cell-cell interactions with electron microscopy is highly challenging. In this project we investigated cellular interactions of oligodendrocyte cell bodies with the brain vasculature. This interaction has been has been previously identified, but organization and function of oligodendrocytes associated with the brain vasculature remains unknown. In preceding light microscopy experiments we estimated that in the neocortical grey matter about 17% of oligodendrocytes contact in majority capillaries. As the vasculature is highly organized and is formed by different cell types including endothelial cells, pericytes and astrocytes we wanted to further investigate vascular associated oligodendrocytes on the ultrastructural level to resolve the anatomical organization.

To specifically target and analyze oligodendrocyte vascular ensembles and obtain 3D reconstructions with electron microscopy we applied a correlative light and serial sectioning electron microscopy approach. We obtained fluorescent oligodendrocytes by using a transgenic mouse line that expressed membrane targeted EGFP under an oligodendrocytic specific promoter. After transcardial fixation of mice with 4% paraformaldehyde and 2.5% glutaraldehyde, the vasculature was labelled with fluorescent tomato lectin, a specific marker for the vasculature. After fixation, EGFP fluorescence remained and we identified oligodendrocyte-vasculature ensembles in 50 µm thick vibratome sections of the motor cortex using confocal imaging. After identification of ensembles we applied 2-photon branding (910 nm) of ensemble locations and included orientation marks of larger size for improved sample recovery. Subsequently the brain slices were prepared for serial block face electron microscopy (SBF-SEM), embedded in epon and mounted with silver containing conductive resin on sample pins. Using confocal microscopy z-stacks that we acquired during sample preparation, we re-identified the marked positions and proceeded with SBF-EM (Zeiss) to acquire backscattered images of the target regions at nanoscale resolution (pixel size of 10 x 10 x 30 nm). Data analysis included image post-processing, reconstruction of the structures of interest with Microscopy image browser and 3D rendering with Imaris (Fig 1).

By optimizing parameters of the sample preparation process we could detect the laser marked regions and identified oligodendrocyte-vasculature ensembles in electron microscopy. Analysis of the EM images revealed that the oligodendrocyte cell body and the vascular basement membrane are in direct contact (n = 3 cells, n = 2 mice,). Moreover, we detected Golgi apparatus, microtubules, endoplasmic reticulum, mitochondria and lipid inclusions in oligodendrocytes cell bodies (Fig 2). Astrocyte endfeet surrounded the oligodendrocyte cell body at non-contact sites suggesting a close interaction with astrocytes at the neuro-vascular-junction.

Our presented approach shows that a combination of fluorescence labelling, light microscopy and SBF-EM allows the investigation of the nanoscale structure of an oligodendroglial vascular niche. Our data suggest that oligodendrocytes are a component of the neuro-glia-vascular unit raising the possibility of direct signaling pathways and metabolite exchange with vascular cells.

Fig. 1

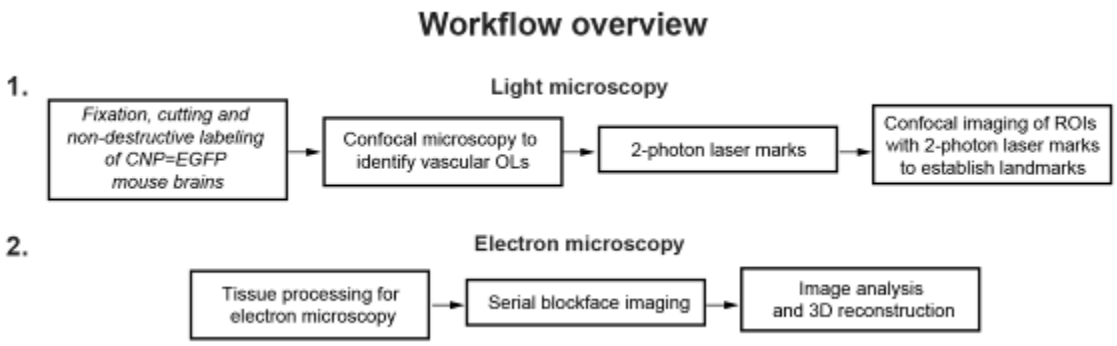

Fig. 2

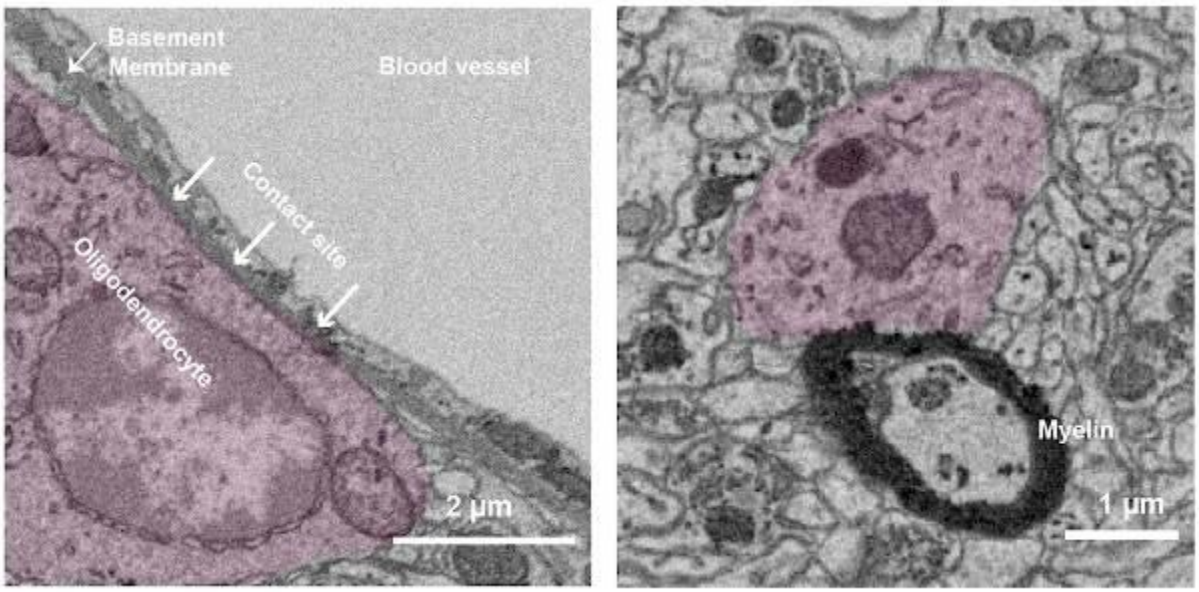
Basement
Membrane
Blood vessel
Contact site
Oligodendrocyte
2 µm
Myelin
1 µm

LS3.005

It is not easy being green: the technical path for the ultrastructural study of the locomotory apparatus of the moss *Physcomitrium patens*

A. L. Sousa[1], S. Gomes Pereira[2], A. J. Holmes[3], M. Schorb[4], J. D. Becker[5], M. Bettencourt-Dias[6], E. M. Tranfield[1]

[1]Instituto Gulbenkian de Ciencia, Electron Microscopy Facility, Oeiras, Portugal
[2]University of Geneva (UNIGE), Geneva, Switzerland
[3]University of Cambridge, Cambridge, United Kingdom
[4]European Molecular Biology Laboratory, Electron Microscopy Core Facility, Heidelberg, Germany
[5]Instituto de Tecnologia Quimica e Biologica Antonio Xavier - Universidade Nova de Lisboa, Oeiras, Portugal
[6]Instituto Gulbenkian de Ciencia, Cell Cycle Regulation, Oeiras, Portugal

Electron microscopy (EM) as a whole technique enables the ultrastructural studies of many samples from individual cells to full organisms. For the visualization of a single image under the electron beam, extensive time investment is made in technical preparation and several EM techniques often need to be applied until an image or model can be presented. The path is not always easy, and optimizations are commonly needed to avoid unintentional artifacts that can impact the final ultrastructural observation. This problem is even more pronounced when it comes to processing plant samples, such as the moss *Physcomitrium patens*, where there is a need to consider the existence of the cell wall, that provides rigidity and strength to cells, but also functions as a barrier for the chemicals needed to observe the ultrastructure using room temperature EM.

In this study, the challenge presented to our facility was the characterization of the locomotory apparatus of the moss *P.patens*, namely the *de novo* centriole assembly that is involved in the motility of the sperm cells during spermatogenesis. These sperm cells develop inside an antheridium located at the tip of the gametophore, a complex structure that contains leaves, rhizoids and both sexual organs (the antheridia and the archegonia). We addressed this question by combining the observations from Chemical Fixation, High-Pressure Freezing–Freeze Substitution, Correlative Light-Electron Microscopy and Electron Tomography.

Each of the different EM techniques helped to address different parts of the biological question. Chemical Fixation allowed to carefully identify the main stages of development and to do the initial ultrastructural characterization. High-Pressure Freezing – Freeze Substitution was used to confirm that the identified structures were not artifacts induced by chemical fixation and allowed a more accurate and detailed ultrastructural characterization of each structure. Electron Tomography gave three-dimensional models of the structures. Correlative Light-Electron Microscopy (CLEM) helped to elucidate the protein composition of the sperm cells" locomotory apparatus and associate the light microscopy results with the structures observed by electron microscopy.

Overall, this work shows how complex the technical path in an EM study of a larger specimen can be and how crucial it is to keep optimizing and developing EM techniques that supports the answering of biological questions even when using bigger and more intricate specimens.

Figure 1: 3D models of different stages in centriole assembly and maturation in *Physcomitrium patens*. **a)** Bicentriole stage; **b)** Sister centrioles associated with the multilayered structure (MLS); **c)** Asymmetrical sister centrioles docked to the cell membrane, serving as basal bodies for ciliogenesis. Cyan – astral microtubules; Light green – centriolar microtubules; Red – Centriolar cartwheel; Dark green – microtubular spline of the MLS; Yellow – lamellar strip of the MLS; Magenta – ciliary transition zone. Scale-bars = 200nm. Adapted from: The 3D architecture and molecular foundations of de novo centriole assembly via bicentrioles (2021).

Fig. 1

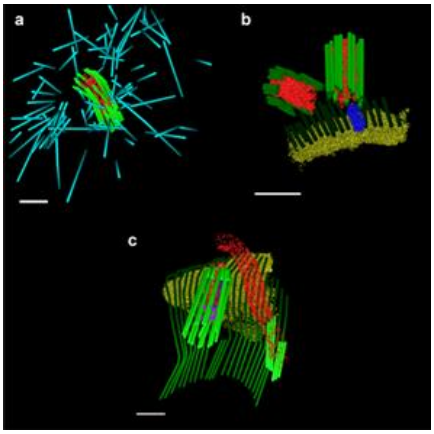

LS3.006

Structure of the endoplasmic reticulum during cell differentiation and stress

E. Jokitalo[1], L. Koistinen[1], Y. Asghar[1], I. Belevich[1], H. Vihinen[1]

[1]University of Helsinki, HiLIFE- Institute of Biotechnology, Electron Microscopy Unit, Helsinki, Finland

The endoplasmic reticulum (ER) consists of an elaborate network of flat cisternae (aka sheets) and tubules that extends throughout the cell and occupies a large fraction of the cytoplasmic volume. The ER contributes to the production and folding of approximately one third of cellular proteins, has a key role in coordinating lipid biosynthesis, and constitutes a reservoir of Ca2+ ions that act as signalling molecules to regulate essential cellular processes. The ER has a central role in organelle communication as it forms membrane contacts with most other organelles. Specific ER stress signaling pathways, collectively known as the unfolded protein response (UPR), are required for maintaining ER homeostasis. The UPR is triggered when ER protein folding capacity is overwhelmed by cellular demand. The UPR initially aims to restore ER homeostasis and normal cellular functions. However, prolonged UPR induces apoptosis to eliminate the defected cell. The continuity of the ER network, the extensive contacts with other organelles and its highly dynamic nature provides a mechanism to propagate various signals throughout the cell. The ER functions as a sensor of cell's well-being by integrating inter- and intracellular signals and inducing appropriate responses under various conditions during growth, division and differentiation.

The dynamic and complex organization of ER poses a major challenge on understanding how its functioning – maintenance of the structure, distribution of its functions and communication with other organelles – is orchestrated. We are utilizing CLEM and various volumeEM techniques in imaging of organelles, cells and tissue to carry out a detailed quantitative morphological characterization of the ER under physiological or pathological conditions such as ER stress, and during differentiation processes where cells adopt specialized functions. This will increase our understanding of fundamental aspects on the regulation of ER functioning and organization of the organelle communication.

Figure 1: hiPSC prior (left) and after (middle and right from stage 7) differentiation to pancreatic secretory cells. ER is depicted in yellow.

Fig. 1

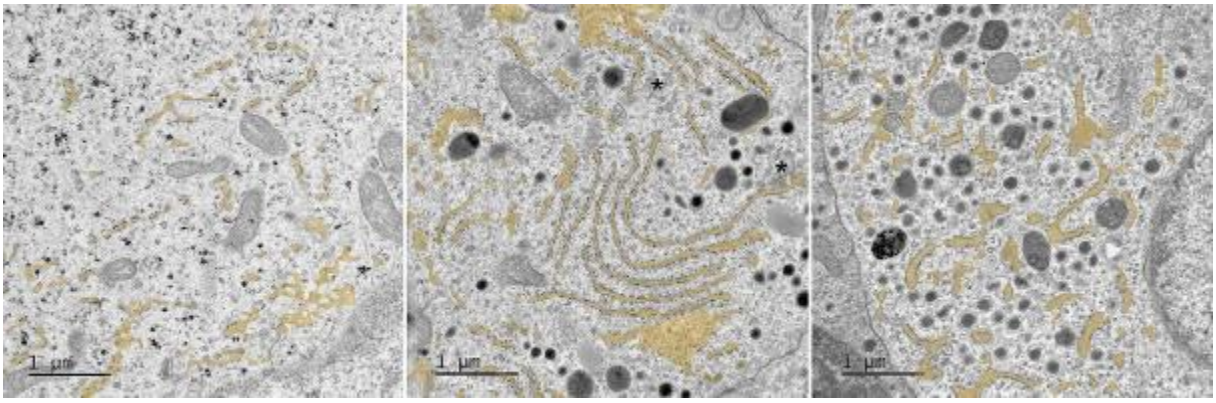

LS3.P001

Structural and metabolic dynamics of plant cells in context of heat acclimation

C. Seydel[1], M. Heß[1], A. Klingl[1], T. Nägele[1]

[1]Ludwig-Maximilians-University Munich, Munich, Germany

In order to survive sub-lethal heat stress, plants possess the ability to acclimate to moderately elevated temperatures. They are altering their physiology in many different ways to maintain cellular homeostasis despite the change in environmental conditions. The carbohydrate metabolism is important for energy storage and biomass production and is also involved in regulation of heat acclimation response. To accurately resolve subcellular metabolic fluxes and compartment-specific metabolite concentrations in the model organism *Arabidopsis thaliana*, it is necessary to combine metabolic and ultrastructural data. To achieve this, we combined a non-aqueous fractionation procedure to generate subcellular metabolite concentrations with 3D imaging of leaf tissue by serial block-face scanning electron microscopy, which resulted in two datasets of control and heat treated leaf tissue, spanning approximately 150 µm in x and y and 50 µm in z-direction. We were able to calculate effective metabolite concentrations in three compartments of the cell, namely chloroplast, cytosol and vacuole. Applying a kinetic model of carbohydrate metabolism, subcellular fluxes were estimated which revealed metabolic heat acclimation strategies of plant metabolism and provide evidence for a tightly regulated metabolic network.

Denk, W., & Horstmann, H. (2004). Serial block-face scanning electron microscopy to reconstruct three-dimensional tissue nanostructure. *PLoS Biol*, *2*(11), e329. https://doi.org/10.1371/journal.pbio.0020329

Fürtauer, L., Weckwerth, W., & Nägele, T. (2016). A benchtop fractionation procedure for subcellular analysis of the plant metabolome. *Front Plant Sci*, 7, 1912. https://doi.org/10.3389/fpls.2016.01912

Seydel, C., Kitashova, A., Fürtauer, L., & Nägele, T. (2022). Temperature-induced dynamics of plant carbohydrate metabolism. *Physiol. Plant, 174*(1). e13602. https://doi.org/10.1111/ppl.13602

LS3.P002

3D tomographic analysis to reveal intermediate stages of primary cilia formation

R. Rachel[1], K. Schmidt[2], K. Buerger[2], O. Maier[2], A. Zuegner[2], R. Witzgall[2]

[1]University of Regensburg, Center for Electron Microscopy, Regensburg, Germany
[2]University of Regensburg, Institute for Molecular and Cellular Anatomy, Regensburg, Germany

1. Introduction

The intracellular ciliogenesis pathway includes binding of vesicles to the distal appendage and their fusion to generate one ciliary vesicle. In the following, it elongates into the ciliary membrane and the axoneme grows out.

2. Objectives

We aim to describe these consecutive stages of the ciliogenesis pathway using electron tomographic investigations in three dimensions (3D) and also by CLEM (correlative light and electron microscopy).

3. Materials & methods

We use a protocol for correlative light and electron microscopy (CLEM) to analyse the timing of Rab8 recruitment to the basal body and to visualize membrane remodelling processes which take place in early stages of cilia formation. From human retinal pigment epithelial 1 (hRPE1) cells, stably expressing CENTRIN1 and RAB8A with fluorescent tags, fluorescence light microscopy images (focal stacks) are recorded after formaldehyde fixation, specifically the hRPE1 centriolar region. For electron microscopy, cells were fixed using glutardialdehyde, en-bloc contrasted (OsO4, UAc), dehydrated, resin-embedded, and sectioned (600 – 900 nm). On cells containing fluorescent signals at the centrosom, STEM tomograms were recorded, reconstructed (IMOD), and segmented. Correlation of positions of fluorescent proteins with ultrastructural features was done using the software eC-CLEM.

4. Results

By using fluorescence microscopy, we identified a dot-like pattern (mCherry-Rab8a) to one of the two Centrin1-GFP-positive centrioles in. In STEM tomograms of the centrosomal regions and in 3D models (by manual segmentation), novel intermediate stages of cilia formation were revealed; we named them the donut-shaped stage, and the biconcave, erythrocyte-shaped stage. Our data let us conclude that distal appendage vesicles fuse side-by-side to first build a C-shaped structure, which later employs the shape of a donut. Centripetal fusion events result in a biconcave membrane structure, later forming a cap-shaped ciliary membrane. Overlays (CLEM) showed that the earliest stage of ciliogenesis in which mCherry-Rab8a localized to the basal body in our set-up was the C-shaped ciliary membrane structure. To get insight into the cellular compartments that serve as a source for the early ciliary membrane compartment, we incubated cells with the lectin wheat germ agglutinin (WGA) conjugated to horseradish peroxidase (HRP), a tag helping to visualise the fusion protein by EM within its cellular context. Interestingly, we detected electron dense membrane material generated by HRP at the developing ciliary membrane during early cilia formation. This observation suggests that endocytosed membrane material contributes to the formation of the early ciliary membrane compartment.

5. Conclusion

We extend the stages of primary cilia formation during the intracellular cilia assembly pathway by identifying the donut-shaped and the biconcave stage, and we present evidence that endocytic trafficking routes contribute to the early ciliary membrane compartment.

Lit.: Rachel et al 2020 J Struct Biol 211: 107551

Buerger et al 2021 Meth Cell Biol 162: 171-203

Fig. 1: images show (left, middle) two *xy* planes (thickness 2.7 nm; 54 nm apart from each other) of a STEM tomogram (IMOD). The slice was cropped to the region of the basal body. Bar, 200 nm; (right) 3D model of the

reconstructed volume after manual segmentation of the STEM tomogram; top view, to best visualize the donut shape of the centriolar vesicle

Fig. 1

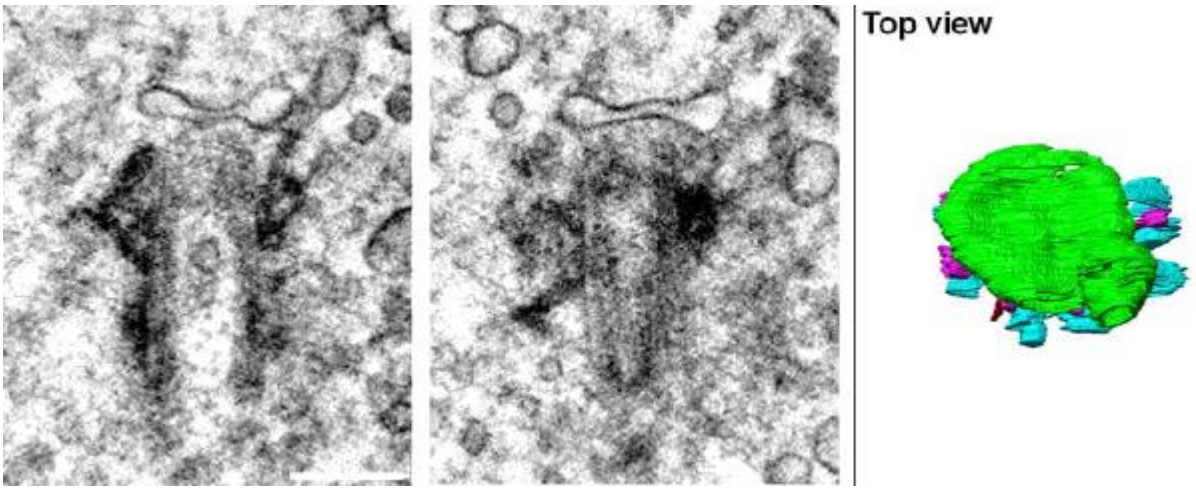

LS3.P003

SEM array tomography with TEM like resolution in X and Y

P. Walther[1], N. Wenske[2], A. Caroll[1], D. D'Souza[1], J. von Einem[3], C. Read (Villinger)[1]

[1]Ulm University, Central Facility for Electron Microscopy, Ulm, Germany
[2]Universitaet Ulm, Central Facility for Electron Microscopy, Ulm, Germany
[3]Ulm University, Virology, Ulm, Germany

Several approaches for volume scanning electron microscopy have been established during the last years. This article deals with array tomography by collecting SEM images of serial sections of high pressure frozen, freeze substituted and plastic embedded cultivated cells.

The objective of the study is to obtain TEM like resolution with an SEM on serial thin sections mounted on silicon chips.

Human cytomegalovirus (HCMV) infected human foreskin fibroblasts were grown on sapphire disks, high pressure frozen, freeze substituted with 0.2 % osmium tetroxide, 0.1 % uranyl acetate and 5 % of water in acetone and embedded in Epon. Serial thin sections (100 nm) were collected on silicon chips, partially post stained with lead citrate trihydrate (3% liquid) and imaged in a Hitachi S-5200 SEM at an accelerating voltage of 2 kV for recording the so-called composite signal, which consists of secondary electrons type 3 (that are produced by backscattered electrons) for intermediate magnifications (Fig. A), or with 5 kV accelerating voltage and recording the regular secondary electron signal for high magnifications (Figs. B and C).

When the sections were not poststained with lead, the secondary electron as well as the backscattered electron signal were very noisy. We first tried plasma cleaning to remove some of the Epon and to make the heavy metal better amenable, but in our hands, this did not significantly improve image quality. The breakthrough was post staining of the sections on the silicon chips with lead citrate. It was then possible to record 62 consecutive sections of cells infected with HCMV and make a three-dimensional reconstruction. Figure A shows a portion of one section at an intermediate magnification. Chromosomes, microtubules and the centriols are visible on this section.

Figures B and C show higher magnification images of an area of the cytoplasm with a viral particle in a vesicle. The images were recorded at 2 and at 5 kV. Best resolution was obtained at an accelerating voltage of 5 kV. The leaflets of the membrane bilayer are well visible and better resolved at 5 kV. These results fit well with our earlier studies of freeze substituted samples in FIB-SEM (Villinger et al., 2012, Histochem Cell Biol 138, 549-556)

With the presented approach it was possible to obtain very good resolution in X and Y of serial sections. All details visible in TEM on similar samples can also be seen in our SEM images. Best results were obtained after lead post staining at 5 kV accelerating voltage and using the secondary electron signal. The best accelerating voltage is a tradeoff of the smaller beam diameter and the higher penetration depth at 5 kV compared to 2 kV. The resolution in Z is obviously defined by the thickness of the sections and is 100 nm in the presented dataset.

Fig. 1

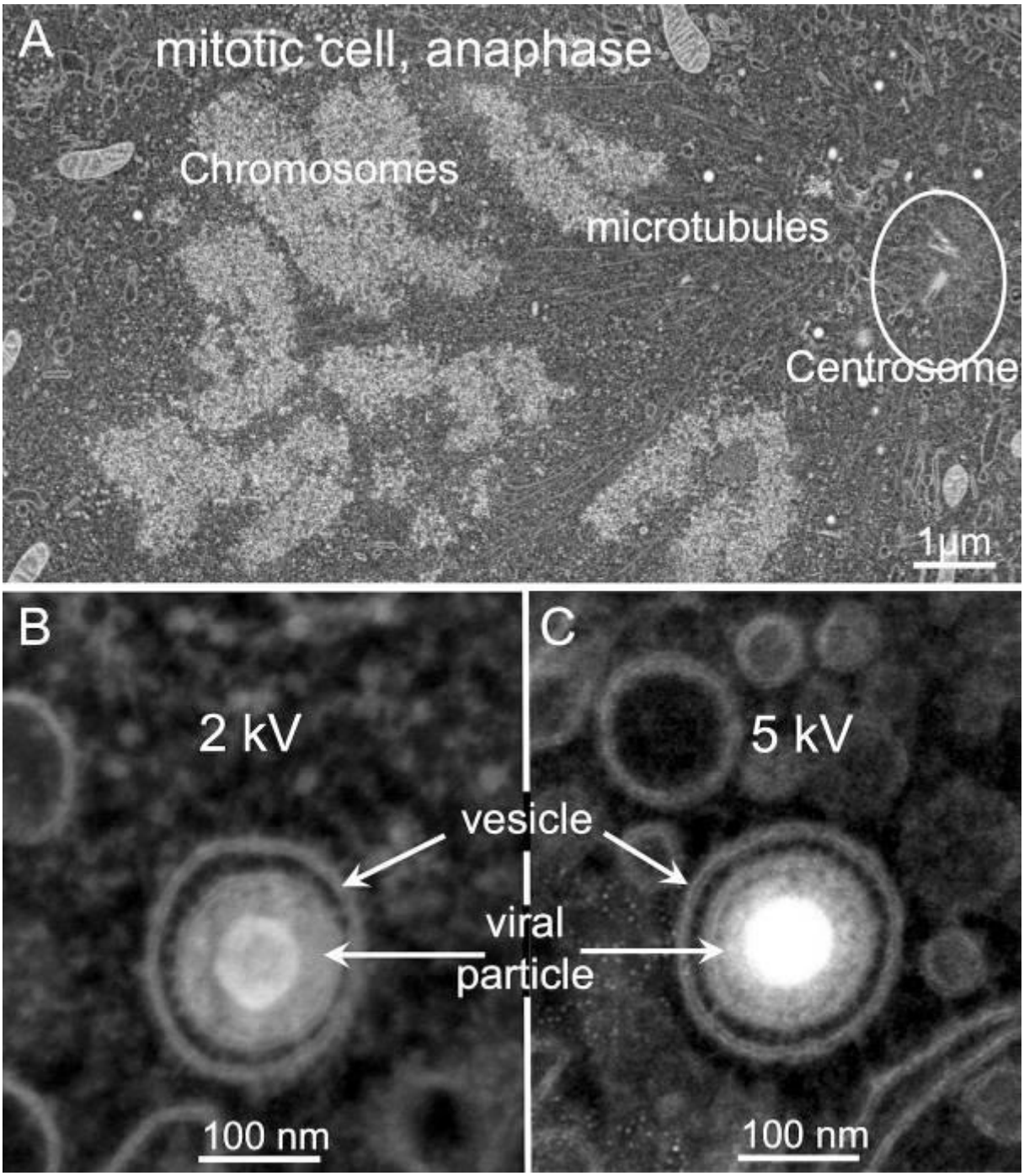
A
mitotic cell, anaphase
Chromosomes
microtubules
Centrosome
1µm
B
2 kV
C
5 kV
vesicle
viral
particle
100 nm
100 nm

LS3.P004

Why software is key for designing your volume EM experiment.

M. Schorb[1]

[1]EMBL Heidelberg, EM Core Facility, Heidelberg, Germany

The biological questions that drive a volume EM study set the key parameters of an acquisition such as the desired resolution, the volume extent and the number of replicates. These determine the imaging method and corresponding limitations in throughput and dimensions. Software can play a crucial role in overcoming limitations during acquisition by means of automation. Turning the acquired raw data into the final volume representation requires dedicated software for aligning serial images or reconstructing tomographic tilt series. Transforming voxel intensities into quantitative measures can be a final important procedure towards biological interpretation of the data that also heavily relies on software. Often these post-acquisition procedures are a bottleneck and thus need to be considered thoroughly when planning a volume EM study. Various projects from EMBL's EM Core Facility illustrate how software development enable scaling up different volume EM pipelines enabling new scientific applications.

LS3.P005

Comparative morphology of mitochondria in optic nerve and cell body of retinal ganglion cells in a mouse model of spastic paraplegia type 2

L. C. Schadt[1], T. Ruhwedel[1], D. Riedel[1], A. M. Steyer[2], K. A. Nave[3], W. Möbius[1]

[1]Max Planck Institute for Multidiscipinary Sciences, EM Facility Faßberg Campus, Göttingen, Germany
[2]EMBL Heidelberg, Imaging Center, Heidelberg, Germany
[3]Max Planck Institute for Multidisciplinary Sciences, Neurogenetics, Göttingen, Germany

Oligodendrocytes facilitate rapid action potential propagation by ensheathing central nervous system axons, thereby existing in a close metabolic relationship with the myelinated axon. This "axo-glial" unit critically depends on proper energy supply by axonal mitochondria to meet their high energy demands for saltatory action potential propagation. In neurodegenerative diseases such as *PLP1*-related disorders, axonal swellings together with alterations in morphology and function of axonal mitochondria serve as hallmarks for dys- and demyelinating disease states. So far it remained elusive how lack of proteolipid protein (PLP) in oligodendrocytes and myelin impairs axonal function, but a deficit in axonal energy supply due to mitochondrial dysfunction is one plausible explanation. Here we used retinal ganglion cells (RGCs) with their myelinated axons in the optic nerve as model tissue for studying axonal mitochondria in a *Plp*-deficient mouse model of spastic paraplegia type 2.

To investigate the influence of myelin on the local mitochondrial heterogeneity in RGC neurons we compared mitochondrial morphology in myelinated and non-myelinated parts of the axon. For this purpose, we developed a method to reliably target RGC mitochondria in distinct regions: the optic nerve, the optic nerve head (ONH), and the retinal ganglion cell body for electron microscopy and 3D reconstruction.

A hybrid method was established in combining chemical fixation with high-pressure freezing (HPF) and freeze substitution to obtain a well-preserved mitochondrial ultrastructure. HPF is a well-established method to study the ultrastructure of cells and tissue in a close-to-native state, but complex tissue requires dissection before freezing. To minimize handling artefacts and disturbance of tissue organization, prefixed tissue was sliced with a vibratome producing sections of required thickness, from which the most suitable sections were selected for HPF. Careful vibratome sectioning of the eye was indispensable for targeting the optic nerve head. For the structural investigation, we applied transmission electron microscopy (TEM) and electron tomography for 3D analysis of individual mitochondria.

Mitochondria in the RG cell body and optic nerve head region revealed very little morphologic difference between wild-type mice and $Plp^{-/y}$ mice. However, we observed inclusions in RGC mitochondria of $Plp^{-/y}$ mice, a finding that requires further investigation. At the ONH, mitochondrial clusters containing mitochondria with a round shape and mostly tubular cristae were prominent in both genotypes. The optic nerve revealed clear genotype-dependent changes in mitochondrial morphology. This is consistent with a recent study by Steyer *et al.* 2020, *J Struc Biol* 210(2):107492), in which 3D reconstruction of data sets obtained by focused ion beam scanning electron microscopy (FIB-SEM) showed that axons in $Plp^{-/y}$ mice contain twice as many mitochondria per 10 µm axon, with the mitochondria additionally appearing shorter and rounder.

Overall, we were able to develop a method to reliably target the optic nerve head with attached retina and optic nerve to study mitochondrial heterogeneity in RGC axons in a mouse model of spastic paraplegia type 2. This will help us to better understand the consequences for axonal mitochondria architecture and function in *Plp*-deficiency.

LS3.P006

Ultrastructural characterization and reconstruction of cultured xenapses

N. Glyvuk[1], Y. Tsytsyura[1], J. Duan[1], J. Klingauf[1]

[1]Institute of Medical Physics and Biophysics, Cellular Biophysics, Münster, Germany

In our lab, we have developed a new model to study the neurotransmission process in neurons. Using click-chemistry microstructured glass coverslips were functionalized to grow xenapses - TIRF-amenable presynaptic boutons on the glass surface. The new model system required not only functional but also ultrastructural characterization, and comparison to synapses in conventional neuronal cultures and slices. Given the size of structures of interest, and the resolution required, we chose to perform 3D reconstructions from serial sections of plastic-embedded xenapses. Mouse neurons, grown on functionalized, carbon-coated coverslips, were fixed by immersion in a mix of 1% glutaraldehyde with 1% osmium tetroxide in 0.1 M sodium cacodylate buffer on ice, additionally post-fixed at room temperature with 1% osmium tetroxide in the same buffer, and *en bloc* stained with either uranyl or samarium acetate. Samples were dehydrated in an ethanol series and embedded in Epon. The cured Epon blocks had a medium hardness. The region of interest was identified by visual inspection in a light microscope after removal of the glass and then additionally embedded in Epon for stabilization and protection of the sample during sectioning. After trimming the block with a diamond knife to obtain highly polished edges, the serial sections were cut at 40-50 nm and ribbons of 40-50 sections were collected on Formvar-coated slot TEM grids. Imaging was performed with a TEM Philips CM-10 equipped with a bottom-mounted TemCam F-416 camera. Image series were aligned and rendered in Reconstruct. Morphological analysis (size and distribution of synaptic vesicles (SV) within the acquired volume) was performed with MetaMorph software.
Data obtained from EM are in good accordance with our live cell imaging, electrophysiology, and immunofluorescence data and confirmed that xenapses showed all the hallmarks of presynaptic boutons in culture or in brain slices. Xenapses are filled with numerous SVs, analogous in size to SVs in standard cultures; they also harbor other structures typical to presynaptic boutons – like mitochondria, endosomes/cisternae, cytoskeleton elements, multi-vesicular bodies, large dense core and clathrin-coated vesicles. SVs distributed within xenapse's volume may represent the resting and recycling pools of vesicles, whereas the ones at the footprint are analogous to the readily releasable pool of SVs in normal synapses as revealed in experiments with TIRF microscopy. Taken together our data indicate that the new model shows all structural features of standard presynapses and enables live-cell imaging of single vesicle exo- and endocytosis in space and time.

LS4.001-invited

DeepHEMNMA approach for analyzing continuous conformational heterogeneity in single-particle cryo-EM images

S. Jonic[1]

[1]IMPMC - UMR 7590 CNRS, Sorbonne Université, MNHN, Paris, France, Paris, France

Introduction: Single-particle cryo electron microscopy (cryo-EM) allows 3D reconstruction of multiple conformations of purified biomolecular complexes from their 2D images. The elucidation of different conformations is the key to understand the molecular mechanisms behind the biological functions of the complexes and the key to novel drug discovery. The standard cryo-EM data analysis procedures involve many rounds of 2D and 3D classifications to disentangle and interpret the combined conformational, orientational, and translational heterogeneity. Gradual conformational transitions give raise to many intermediate conformational states. Continuous conformational heterogeneity in cryo-EM data (a mixture of many intermediate conformational states), due to such gradual conformational transitions, is both an obstacle for high-resolution 3D reconstruction of different states and an opportunity to obtain the information about multiple coexisting states at once.

Objective: We aim at developing new methods for analyzing continuous conformational heterogeneity in cryo-EM data, which will be fast, user-friendly, and allow obtaining the full conformational landscape.

Methods: HEMNMA method [1], that we specifically developed for analyzing continuous conformational heterogeneity in cryo-EM data, determines the conformation, orientation, and position of the complex in each single particle image by analyzing images using normal modes (motion directions simulated for a given atomic structure or EM map), which in turn allows determining the full conformational space of the complex but at the price of high computational cost. To speed up HEMNMA, we recently combined it with a deep learning approach. This deep learning extension of HEMNMA is referred to as DeepHEMNMA [2].

Results: With a synthetic dataset, we have shown that DeepHEMNMA is more than 40 times faster than HEMNMA [2]. With an experimental dataset, we have shown that DeepHEMNMA reveals the conformational heterogeneity that is out of reach of standard methods [2].

Conclusion: DeepHEMNMA is a fast and user-friendly software that allows obtaining the full conformational landscape of biomolecules. It is available in ContinuousFlex, open-source software package that we are developing. ContinuousFlex provides user-friendly graphical interface to several methods for analyzing continuous conformational heterogeneity in vitro [1-3] and in situ [4-5], and it is available as a plugin for Scipion [6-7]. In this talk, I will present DeepHEMNMA and its performance using synthetic and experimental cryo-EM images. Also, I will briefly introduce ContinuousFlex.

[1] https://doi.org/10.1016/j.str.2014.01.004

[2] https://doi.org/10.3389/fmolb.2022.965645

[3] https://doi.org/10.1016/j.jmb.2022.167483

[4] https://doi.org/10.3389/fmolb.2021.663121

[5] https://doi.org/10.1016/j.jmb.2021.167381

[6] https://doi.org/10.1016/j.jsb.2022.107906

[7] https://pypi.org/project/scipion-em-continuousflex

LS4.002-invited

Microscopy image restoration and downstream analysis – recent improvements and hopes for the future

F. Jug[1]

[1]Human Technopole, Jug Group, Computational Biology Research Centre, Milan, Italy

The necessity to analyze scientific images is as old as the ability to acquire such data. While this analysis did initially happen by observation only, modern microscopy techniques now enable us to image at unprecedented spatial and temporal resolutions, through the 'eyes' of many and very diverse imaging modalities.
The unfathomable amounts of data acquired in the context of biomedical research cannot any longer be analyzed by manual observation alone. Instead, algorithmic solutions are helping researchers to study and quantify large image data.

In the past years, our abilities to use artificial neural networks (ANNs) for the automated analysis of scientific image data gained significant traction, and many important analysis problems have now much improved solutions based on ANNs. At the same time, we start being aware of limitations that come with this new set of machine learning approaches.

In my talk I would like to update you on some of the latest algorithmic developments from our and other labs. More specifically, I will talk about improved but easy to use image restoration and segmentation methods and the efforts of our community to store, share, and run ANN based methods via the BioImage Model Zoo -- a Horizon Europe funded infrastructure we are currently establishing.

Finally, I will carefully attempt to look into the future and share my predictions about how artificial intelligence will help us make valuable scientific discoveries at elevated pace.

LS4.P002

Influence of segmentation protocols on simulations based on 3D X-ray microscopy images

M. Izidoro Santos[1], D. Damberga[2], R. Wehrspohn[1], A. Greiner[2], J. Martins de Souza e Silva[3]

[1]Martin-Luther University of Halle-Wittenberg, Institute of Physics - Chair of Microstructure-Based Material Design, Halle (Saale), Germany
[2]University of Bayreuth, Faculty of Biology, Chemistry and Earth Sciences - Chair of Macromolecular Chemistry II, Bayreuth, Germany
[3]Fraunhofer Institute for Microstructure of Materials and Systems IMWS, Halle (Saale), Germany

The study of filtration properties, such as solvent permeability and diffusion through a material, is an essential step in developing efficient filter elements. Aiming at flexible and efficient filter production processes, fluid flow simulations can complement the empirical determination of these parameters with help from 3D X-ray images of real filters. Phase-contrast X-ray microscopy imaging is a technique suitable for imaging materials with low electron density. However, the segmentation of phase-contrast images is not trivial, frequently leading to unreliable results. Here, we analyzed a fibrous matrix of a filter material using different phase-contrast X-ray imaging conditions and evaluated the effects of a semi-automatic segmentation protocol in the simulation of solvent permeability and diffusion properties. We observed that the segmentation strongly influences the results output, causing significant variations in the values of diffusion coefficients (k) and apparent molecular diffusivity. Therefore, before running the simulations, there is a need to apply segmentation protocols that can be validated by other imaging techniques to guarantee relevant results.

LS4.P003

High-throughput transmission electron microscopy for screening yeast deletion mutants

M. Mayer[1], C. Schug[1], S. Geimer[1], B. Westermann[1], T. Klecker[1]

[1]Institute of Cell Biology, University Bayreuth, Bayreuth, Germany

The yeast *Saccharomyces cerevisiae* is a well-established model organism for cell biological research. The availability of large mutant collections, the fast growth and easy handling make it ideally suited for systematic large-scale analyses. However, sample preparation of yeast cells for transmission electron microscopy (TEM) of thin sections is a time-consuming process, limiting the feasibility of large-scale screening for yeast mutants with altered ultrastructure by TEM. Here, we present two approaches to reduce the time necessary for conducting a systematic TEM-based screen of yeast deletion mutants. First, we apply pooling of ten different strains to increase the amount of mutants that can be simultaneously screened for a specific ultrastructural phenotype. In a proof of concept experiment, we were able to reliably identify samples containing mutants with altered mitochondrial ultrastructure. Second, we employ a microwave-assisted protocol to accelerate sample preparation. This reduces the time requirement for chemical fixation and Epon embedding to less than 24 hours, making it ideally suited when dealing with a high number of samples. Taken together, both approaches facilitate large-scale screening of yeast deletion mutants.

LS4.P004

Step-by-step pre-processing of 3D SEM images of neurons

S. Radulović[1], L. Chalet[2], B. Gottschalk[1], S. Wernitznig[1], A. Zankel[3], G. Leitinger[1]

[1]Medical University of Graz, Graz, Austria
[2]University of Franche Comté, Besançon, France
[3]Graz University of Technology, Graz, Austria

Introduction

Traditionally, neuron reconstructions from serial EM micrographs and synapses localizations are done manually, which is extremely time consuming. Currently used, semi-automatic selection tools for segmenting are faster compared to manual selection. In order for those tools to work properly, prior to segmentation, noise reduction is necessary, while keeping membrane integrity and structural features of synapses preserved at the same time.

Objectives

Here we introduce a solution, which includes pre-processing of electron micrographs. Pre-processed images are suitable for the use of more advanced, fast selecting tools, which significantly shorten the amount of time needed for segmentation.

Materials and methods

Stacks of serial electron micrographs of identified neurons of the locust, Locusta migratoria were produced by serial block face scanning electron microscopy. This was followed by multiple image processing steps on these stacks by Image J software.

First preprocessing step: A histogram matching algorithm was used to homogenize the initial brightness levels within the stack, followed by a low pass Fourier transform band-filter to isolate small structures like cell-membranes. Further a rolling ball algorithm was used to give the cell membranes a higher contrast and thereby the stack was set up for an automated Otsu threshold. The thresholded stacks were analyzed with the particle analyzer implemented in ImageJ to filter out small irregular components present in the original stack not belonging to the cell membranes. In parallel, the particle analyzer was used once more with settings that enabled keeping the large particles such as mitochondria. The result was subtracted from the result of the first round with the particle analyzer.

Second preprocessing step: mitochondria, representing an obstacle during and after segmentation, where the target. For this purpose the histogram - matched stacks were filtered with a median filter after a contrasting step. Finally a Huang´s auto threshold was used to get a binary image (that contained the mitochondria) which was subtracted from the first preprocessing step.

Results

The first step successfully removed many structures inside the cells, but mitochondria attached to the membranes were still visible, compromising the results of the following segmenting steps. This can slow down fast selection tools subsequently used for segmentation (such as "Blow" in Amira). (Fig. 1B)

During the second preprocessing step most of the structures inside the cells were deleted. However, at certain locations the membranes appeared discontinuous. Nevertheless combining both steps with fast selection tools significantly enhanced segmentation efficiency compared to a traditional manual approach. (Fig. 1C)

Conclusion

Pre-processing can improve the accuracy and efficiency of segmenting algorithms.

LS4.P005

Membrane analysis toolkit: a quantitative way to analyse protein lipid mixtures from cryo-EM images

P. Schönnenbeck[1], B. Junglas[1], C. Sachse[1]

[1]Forschungszentrum Jülich, Ernst Ruska-Centrum 3, Jülich, Germany

Cryo-EM is a powerful tool to study protein membrane interactions as it delivers high-resolution images of vitrified macromolecules including biological membranes. The quantitative analysis of protein-induced effects on the membrane structure is a challenging and time-consuming task as they are not amenable to established single-particle image reconstruction techniques. However, due to the high contrast of phospholipid bilayers, the images are suitable for detailed analysis and can yield characteristic lipid features and membrane shapes. Currently, localisation of such membrane structures and the extraction of their features is often performed interactively and is, therefore, subjective and a time-consuming task.

Here we present the "membrane analysis toolkit", a toolkit currently in development which aims to automate the membrane analysis and facilitate quantitative comparison of large functional datasets, e.g capturing the variations such as protein mutations and lipid compositions. The membrane structures are localized using convolutional neural networks and sequentially analysed by a variety of image processing techniques. Typical determined features are membrane thickness, curvature and distance structures along the membranes in addition to shape information about the continuous membrane structures like total area and shape classification.

The membrane analysis toolkit can be used for any sample containing lipid bilayers and can lead to a more quantitative understanding of membrane-active proteins or other environmental influences.

LS5.001-invited

Intravital correlative microscopy of metastatic cancer cells at the blood-brain-barrier

M. A. Karreman[1]

[1]University Hospital Heidelberg and German Cancer Research Center (DKFZ) Heidelberg, Neurology/Clinical Cooperation Unit Neurooncology, Heidelberg, Germany

Introduction

Patients suffering from malignant melanoma, breast cancer and lung cancer are at high risk of developing brain metastases (BM), which are at this time incurable and have devasting consequences for quality of life, already at the time of the diagnosis. The underlying mechanisms of brain colonisation of the metastatic cancer cells, immune cell infiltration and interaction with the unique brain microenvironment are yet to be uncovered and are challenging to study in preclinical models.

Objectives

The focus of our work is to better understand how metastatic cancer cells derived from extracranial tumors surpass the blood-brain-barrier, seed the brain and how the cross-talk with immune-cells and brain-resident cells influences BM growth and development. Here, we set out to target relevant cellular processes with brain-penetrant therapeutic agents at an early stage of brain colonisation in order to prevent the formation of large, uncurable brain metastases.

Materials & methods

Our preclinical models of breast cancer and melanoma brain metastases enable to monitor long-term the dynamic development of BM in mice using intravital microscopy (IVM) through chronic cranial window. In order to achieve high-resolution insight into these processes, we perform intravital correlative microscopy, combining IVM, x-ray micro-CT and 3D electron microscopy.

Results

Here, I will disuss different projects aiming to reduce BM growth in vivo by by targeting early and critical events during brain colonisation. Intravital correlative microscopy was used to reveal how metastatic cancer cells cross the blood-brain-barrier. We found that this process is MMP9 dependent, and that the main source of the MMP9 is the cancer cell itself (Karreman et al, in revision). Moreover, we demonstrate that low-dose PI3K/mTOR inhibition in a preventative setting hinders melanoma brain metastatic growth in vivo (Tehranian et al, Neuro-oncology, 2021). Finally, using newly developed mouse models, we identified a new route for T cells to enter the brain and target melanoma brain metastases (Messmer et al, submitted for publication).

Conclusion

There is a pressing need to develop new therapeutic approaches against BM development. Targeting the earliest steps of this disease enables to circumvent more aggressive and often ineffective treatments. Intravital (correlative) microscopy on various models of brain metastases enabled us to uncover important mechanisms of brain colonisation and thus inform new treatment strategies.

LS5.002-invited

Uncovering new roles of actin cytoskeleton using correlative light and electron microscopy

A. Melero Carrillo[1], S. G. Martin[1]

[1]University of Lausanne, Fundamental Microbiology Department, Lausanne, Switzerland

Sterols are key lipids for biological membranes, thereby their abundance and distribution must be tightly regulated. At subcellular level, organelles such as endosomes are central hubs for sterol distribution, mediating sterol transfer between the diverse subcellular destinations. Sterols reach and leave endosomes via small vesicular carriers or via sterol transfer proteins at short-range membrane contact sites. How endosomal sterol transfer is orchestrated is poorly understood. Using a genetically encoded sterol biosensor (D4H) in the fission yeast Schizosaccharomyces pombe, we have found that sterol steady-state distribution can be re-routed from the plasma membrane to endosomal structures upon pharmacological inhibition of branched actin assembly. In yeast, branched actin plays major roles in plasma membrane reshaping, whereas in complex eukaryotes branched actin also facilitates membrane trafficking in endosomes, however the role of actin at endosomes remains unclear. We show that upon inhibition of Arp2/3 complex, essential for actin branching, endosomes undergo ultrastructural remodeling from elongated to round organelles and become sterol rich. Upon reactivation of Arp2/3 complex, sterols rapidly redistribute to the plasma membrane and endosomes regain their elongated ultrastructure. Using correlative light and electron tomography (CLEM) we have found that under Arp2/3 inhibition, endosomes are smooth ellipsoidal organelles with no evidence of active membrane remodeling. Processing cells for CLEM immediately after Arp2/3 complex re-activation revealed that endosomes undergo intense ultrastructural remodeling into morphologically complex organelles with tubulations, fenestrations and budding events. Altogether our findings suggest a novel role for branched actin facilitating membrane remodeling at early endosomes. We investigate the mode of activation of Arp2/3 at endosomes and the role of endosomal ultrastructure on sterol trafficking. We propose that branched actin is necessary for endosome tubulation, facilitating membrane remodeling by trafficking complexes and thus enabling sterol trafficking through the endosomal system.

LS5.003

Correlative microscopy and imaging secondary ion mass spectrometry for high resolution nano-analytics on biological tissue

A. Biesemeier[1], T. Taubitz[1], O. De Castro[1], H. Quang Hung[1], J. N. Audinot[1], W. Tom[1]

[1]Luxembourg Institute of Science and Technology (LIST), MRT - Materials Research and Technology Department, Belvaux, Luxembourg

Introduction

Applications featuring sub-20 nm-imaging and chemical analysis at the same time typically rely on electron microscopy, which can be directly coupled to energy dispersive x-ray microanalysis (EDX) or used in combination with other tools like imaging mass spectrometry. Our group develops integrated focused ion beam (FIB)-based instruments featuring electron and/or ion primary beams, coupled to a double focusing magnetic sector secondary ion mass spectrometry (SIMS) system. This allows for correlative investigation of ultrastructure and chemical mapping within the same instrument at a lateral resolution of below 15 nm1.

Objectives

Presentation of a selection of application fields of FIB-SIMS in biology, nanotoxicology and beyond.

Material and Methods

Correlative electron (SE, BSE) and SIMS imaging of biological samples was performed using integrated FIB-SIMS instruments developed at LIST (e.g. Zeiss Orion Nanofab-SIMS, FEI Scios-SIMS). They yielded highly resolved chemical maps of elemental ions, their isotopes and respective small or large cluster molecules. Localisation and identification of pristine nanoparticles, but also metals embedded in complex matrices like tissue sections are performed. Additional detectors for e.g. transmitted helium beam detection on a Gas Field Ion Source (GFIS) equipped prototype instrument, called npSCOPE2, allow also correlative TEM-like imaging and analysis capabilities with helium beam at 20 - 30 keV and at temperatures down to -145°C thanks to the incorporation of cryo-setup capabilities.

Results

Uptake of foodborne nanoparticles by epithelial cells or bacteria, and nanoparticular redistribution of tattoo ink in skin phantoms and internal ion distributions of physiological elements are demonstrated.

Conclusion

High-resolution SIMS (< 15 nm resolution) enables detection of nanosized metal particles in biological tissue samples. In comparison to SEM-EDX at 10 keV, SIMS with 20-30 keV primary ion beams features both higher lateral resolution and sensitivity and provides isotopic information over a wide mass range. A cryo-workflow for the npSCOPE is currently under development (see abstract by Taubitz et al.) and will facilitate close to native chemical analysis of diagnostic, environmental and nanotoxicology samples.

Funding information: This project has received funding from the European Union"s Horizon 2020 Research and Innovation Programme under grant agreement No. 720964 and by the Luxembourg National Research Fund via the project INTER/DFG/19/13992454. Ink samples investigated as part of the COST COMULIS round robin study for novel correlative multimodal analyses (CA17121).

References:

1 Audinot et al. Highest resolution chemical imaging based on secondary ion mass spectrometry performed on the helium ion microscope. Rep Prog Phys 2021;84(10). doi: 10.1088/1361-6633/ac1e32.

2 De Castro, O. et al. npSCOPE: A New Multimodal Instrument for In Situ Correlative Analysis of Nanoparticles. Anal.

LS5.004

Identification and characterization of uncultivated archaeal virocells using correlative fluorescence and scanning electron microscopy

I. Banas[1], V. Turzynski[1], M. Hasenberg[2], A. Klingl[3], A. Probst[1,4]

[1]University Duisburg-Essen, Chemistry, Essen, Germany
[2]University Duisburg-Essen, Imaging Center Essen, EMU, Essen, Germany
[3]LMU München, Pflanzliche Entwicklungsbiologie & Elektronenmikroskopie, Planegg-Martinsried, Germany
[4]University Duisburg-Essen, Centre of Water and Environmental Research (ZWU), Essen, Germany

Microbes and their interactions with viruses play important roles in biogeochemical cycles and shape Earth"s biomes. However, information on viral interactions has largely been extrapolated from a very small fraction of cultivated exemplars – the large majority of microbes remains uncultivated. Viral infections of key environmental microbes with their respective viruses forming so-called virocells, are hard to visualize and characterize in environmental samples[1]. Emerging methods in fluorescence microscopy enlighten smaller and less frequent structures within microbial cells. For example, it is now possible to design fluorescent probes to target viruses infecting uncultivated hosts and identify different infection stages in environmental samples using virusFISH[2]. Here we introduce the correlation of virusFISH with scanning electron microscopy for locating virocells and studying their morphology in environmental samples.

VirusFISH for identifying viral infections of *Candidatus* Altiarchaeum hamiconexum within environmental biofilms was performed as described previously[2], but modified specifically to carry out the correlation. After localizing virocells using fluorescence microscopy on a gridded coverslip, samples were processed for scanning electron microscopy using osmium tetroxide and an acetone dehydration series, followed by critical point drying and coating using Pt/Pd. The gridded coverslip facilitated the correlation of the micrographs using GIMP, showing that the biofilms stayed attached to the grid throughout sample preparation. Similar to cultivation-based studies, it was possible to identify morphological changes of virocells. However unlike other archaea, where a significant increase of cell size over several orders of magnitude was observed[3], *Candidatus* Altiarchaeum hamiconexum only shows a slight, but significant increase of cell size by 10-20%. Within virocells a spatial separation of host DNA and viral reproduction was observed allowing conclusions regarding spatial and functional organization within virocells. Besides the study of virocells itself, this study also supports previous hypotheses that cell lysis due to viral infection fuels the growth of heterotrophic organisms in the deep subsurface.

We conclude that the correlation of virusFISH with electron microscopy enables the characterization of virus-host interactions in environmental samples. In the future, this approach will support hypothesizes based on *in silico* studies to shed like on a board range of interactions of uncultivated microorganisms.

1. DeLong, J. P. *et al.* Towards an integrative view of virus phenotypes. *Nat Rev Microbiol* **20**, 83–94 (2022).
2. Turzynski, V., Monsees, I., Moraru, C. & Probst, A. J. Imaging Techniques for Detecting Prokaryotic Viruses in Environmental Samples. *Viruses* **13**, 2126 (2021).
3. Liu, J. *et al.* Virus-induced cell gigantism and asymmetric cell division in archaea. *Proceedings of the National Academy of Sciences* **118**, e2022578118 (2021).

LS5.005

Correlative and volumetric EM imaging of inflammatory dynamics in skin vessels

L. Breitsprecher[1], K. Mildner[2], S. M. Currie[3], R. I. Stegmeyer[3], M. Stasch[4], S. Volkery[4], O. E. Psathaki[1], D. Vestweber[3], D. Zeuschner[2]

[1]University of Osnabrück, Microbiology / Integrated Bioimaging Facility Osnabrück, Osnabrück, Germany
[2]Max Planck Institute for Molecular Biomedicine, Electron Microscopy Unit, Münster, Germany
[3]Max Planck Institute for Molecular Biomedicine, Department of Vascular Cell Biology, Münster, Germany
[4]Max Planck Institute for Molecular Biomedicine, BioOptic Service Unit, Münster, Germany

Introduction: Serial block-face scanning electron microscopy (SBF-SEM) increases reliability, availability and throughput of 3D-EM. The ability to resolve nanoscales with a large field of view and great depths, can provide insight to many biological fields. However, analysis of cellular dynamics remains exclusive to fluorescent markers, visualized in light microscopy. Pairing both processes in a complicated, correlative (CLEM) approach is therefore necessary and new reliable workflows have to be established, taking into consideration mismatch of resolution and targeting on nano-scale level. For instance, tissue homeostasis and its balance upon inflammatory events often lead to severe changes regarding permeability of blood vessels and transmigration of neutrophils and platelets. Neutrophils may leave the vessel in a controlled process[1], whereas platelets seal the endothelial barrier, preventing vascular leakage[2]. Interaction dynamics of both have been observed at sites of inflammation[3] but to this day lacked ultrastructural investigation.

Objectives: Observe the interaction of platelets and leukocytes following an inflammation stimulus via intravital microscopy (IVM) before fixation. Relocate that specific vessel and region of interest led by artificial and natural landmarks to allow subsequent ultrastructural investigation. Adapt the fixation and staining protocol for complex, multi-layered skin samples and enable consistent SBF-SEM imaging.

M&M: A dorsal skinfold chamber frame was attached to anesthetized and depilated LysMeGFP mice, injected with immunolabelled PECAM-1 (vascular endothelium) and GPIbβ (platelets) and subjected to immune-complex mediated vasculitis. Neutrophil recruitment and inflammatory bleeding events within a designated stamp-labelled area were imaged for 90-120 min. Subsequent sample fixation and introduction of additional landmarks included perforation of the skin, allowing penetration of fluids, biopsy-punching the area of interest and glueing it on carbon-gridded coverslips. To enhance contrast it was crucial to increase the temperature to 40 °C during all incubation steps of the adapted protocol for SBF-SEM imaging. Beneath extensive Osmium staining, infiltration was performed with a mixture of Ketjenblack to account for charge accumulation during SBF-SEM imaging.

Results: The use of natural and artificial landmarks enabled precise relocation of distinct vessels and targeted trimming. IVM in response to inflammation stimuli reveals that neutrophils leave vessels through partial openings of endothelial junctions. Additionally, rare occasions of co-interaction in which an increased number of platelets follow the transmigration of neutrophils can be observed. Adaptations to the staining protocol enables volumetric serial block-face imaging to detect complete platelets transferring the basement membrane barrier.

Conclusion: Many CLEM projects remain challenging throughout all steps, reaching from sample preparation towards relocation and final imaging. The workflow presented had to be optimized step-by-step. Finally, SBF-SEM offers the ability to visualize complex, volumetric cell interactions. Combination of state-of-the-art LM tools can help guide and address relevant biological questions.

Fig.1: Representative IVM MIP and SBF-SEM volume merge of neutrophil recruitment.

[1]Vestweber D (2015) How leukocytes cross the vascular endothelium

[2]Braun LJ et al. (2020) Platelets docking to VWF prevent leaks during leukocyte extravasation by stimulating Tie-2

[3]Lisman T (2018) Platelet-neutrophil interactions as drivers of inflammatory and thrombotic disease

Fig. 1

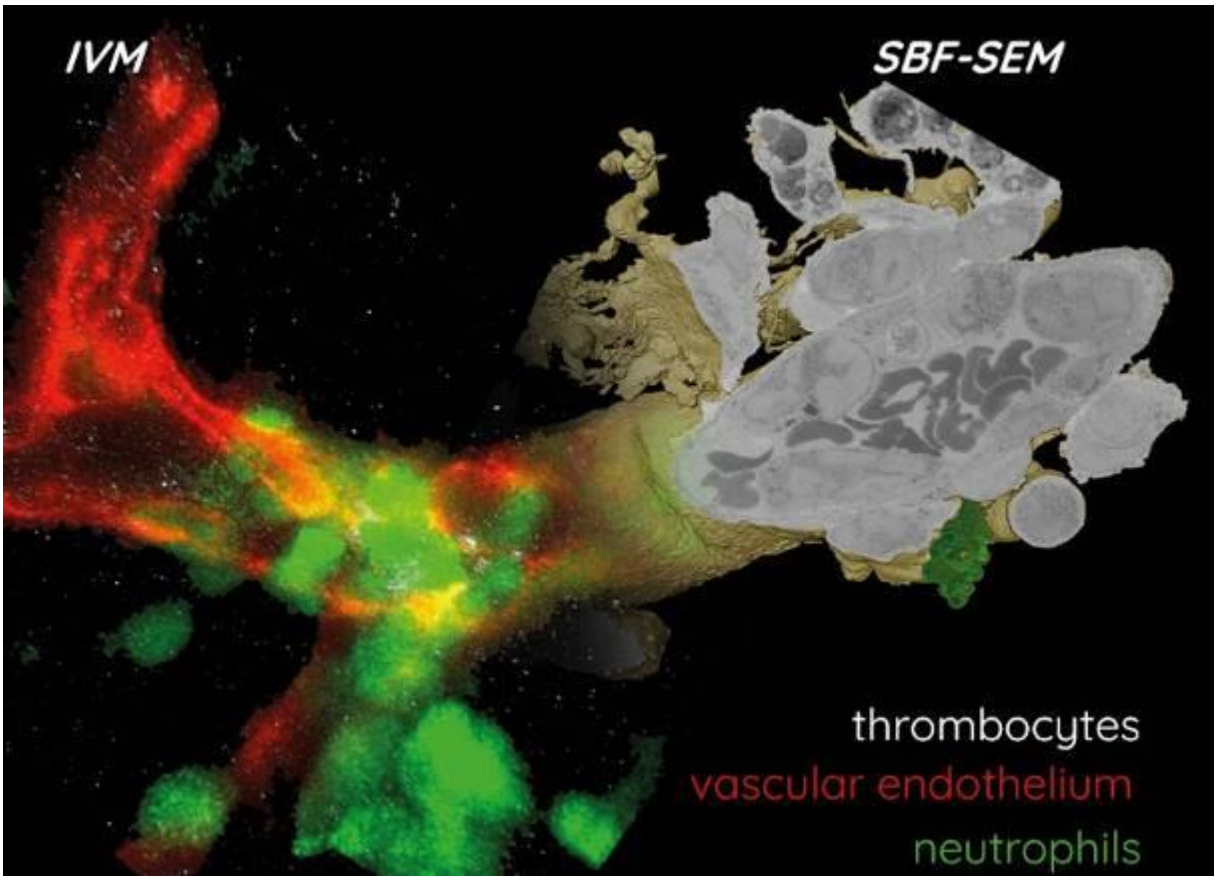
IVM
SBF-SEM
thrombocytes
vascular endothelium
neutrophils

LS5.P001

STEM-in-SEM of biological specimens in correlation with TEM

E. Müller[1], H. Störmer[1], S. Fritsch-Decker[2], C. Weiss[2], D. Gerthsen[1]

[1]Karlsruher Institut of Technologie (KIT), Laboratory for Electron Microscopy (LEM), Karlsruhe, Germany
[2]Karlsruher Institut of Technologie (KIT), Institute of Biological and Chemical Systems, Karlsruhe, Germany

1. Introduction

Scanning transmission electron microscopy in scanning electron microscopes (STEM-in-SEM) at low primary electron energies (≤ 30 keV) yields a pronounced image contrast for weakly scattering biological materials [1] and provides a complementary technique to transmission electron microscopy (TEM) at high electron energies. SEMs are widely available and can be equipped with a STEM detector. Further advantages compared to TEM are reduced maintenance costs and less demanding alignment procedures. STEM-imaging can be combined with secondary electron imaging, rendering STEM-in-SEM a multimodal technique for imaging both surface and subsurface features [2].

2. Objectives

In this work, the competitiveness of STEM-in-SEM as an alternative to TEM is explored. The two techniques are compared with respect to their resolution and signal-to-noise ratio.

3. Materials and Methods

Thin microtome slices of A549 lung carcinoma cells exposed to silica nanoparticles (NPs) are used for 200 keV TEM imaging in a Philips CM200. Bright-field (BF) STEM-in-SEM images are taken from the same region of interest in a FEI Helios G4 FX at 30 keV. The two techniques are compared by evaluating the spatial resolution and the contrast-to-noise-ratio $CNR = (S-B)/\sigma_B$ (S: signal, B: background intensity, σ_B: standard deviation of B) of the images. As the contrast in TEM depends also on defocus and aperture settings, the beam convergence and detection angles for the images in Figure 2 are chosen such that similar image signals can be expected due to the reciprocity theorem for STEM and TEM [3].

4. Results

Figure 1 shows images of the same region of a cell section with NPs. To improve the contrast, the TEM image (Figure 1a) was taken with a defocus 1.5 µm. A line scan over a small feature reveals a feature size of 2 nm, estimated by the full-width-at-half-maximum (FWHM). The same feature in the BF-STEM image (Fig. 1b) also shows a resolution of 2 nm.

The evaluation of the CNR is shown in Figure 2. A line scan through one of the dark particles reveals a more pronounced noise in the TEM image (Figure 2a) with CNR=3. The 30 keV BF-STEM image in Figure 1b shows a reduced noise with CNR=20.

4. Conclusions

STEM-in-SEM is a powerful technique for analyzing biological specimens, combining good CNR with a high spatial resolution. The resolution is sufficient for many applications making STEM-in-SEM well competitive to TEM.

Figure 1. Spatial resolution of 2 nm estimated by the FWHM of a linescan over a small feature. a) TEM image with a defocus of 1.5 µm. b) BF-STEM image of the same region.

Figure 2. Line scan over a NP. a) CNR=3 for the TEM image. b) CNR=20 for the BF-STEM image

[1] U Kaiser et al., Ultramicroscopy **111** (2011), p. 1239. doi: 10.1016/j.ultramic.2011.03.012

[2] C Sun et al., J Mater Sci 55 (2020), p. 13824. doi: 10.1007/s10853-020-04970-3

[3] CB Carter and DB Williams, "Transmission Electron Microscopy", Plenum Press, New York, 1996

Fig. 1

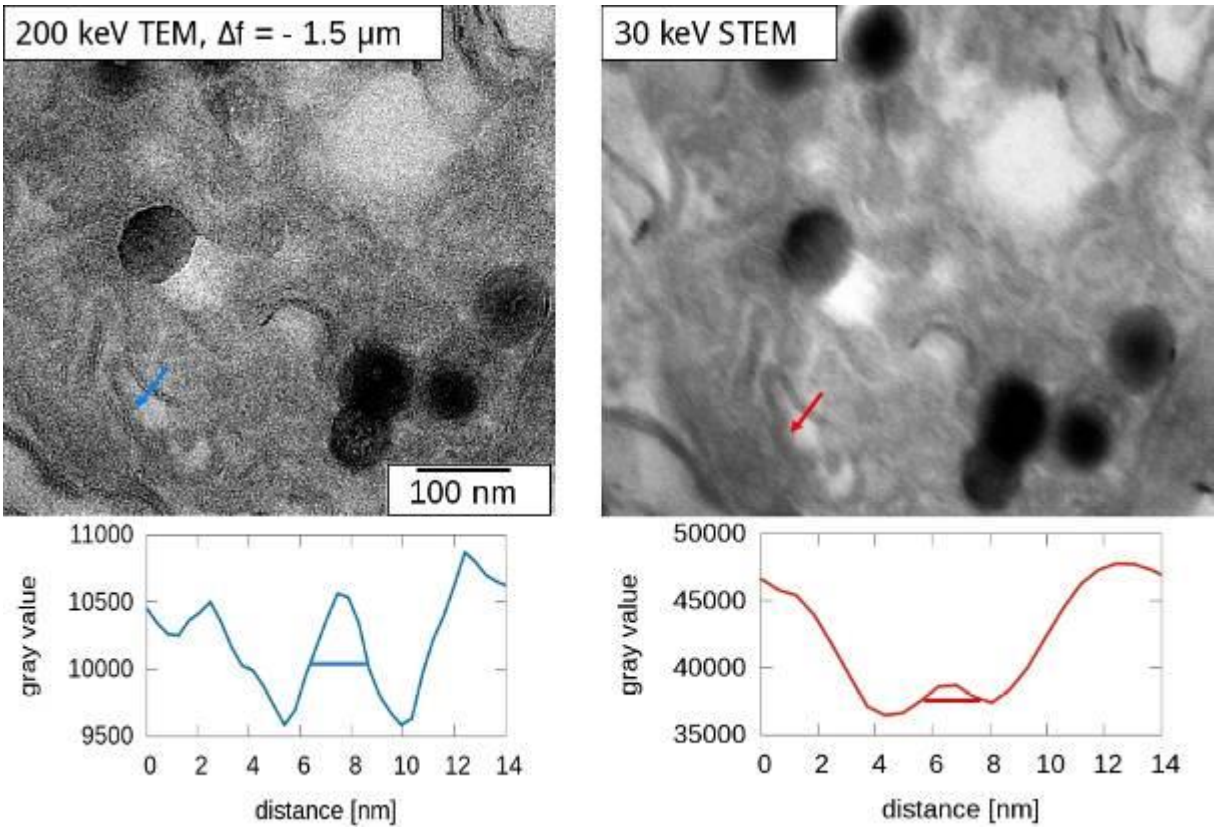

Fig. 2

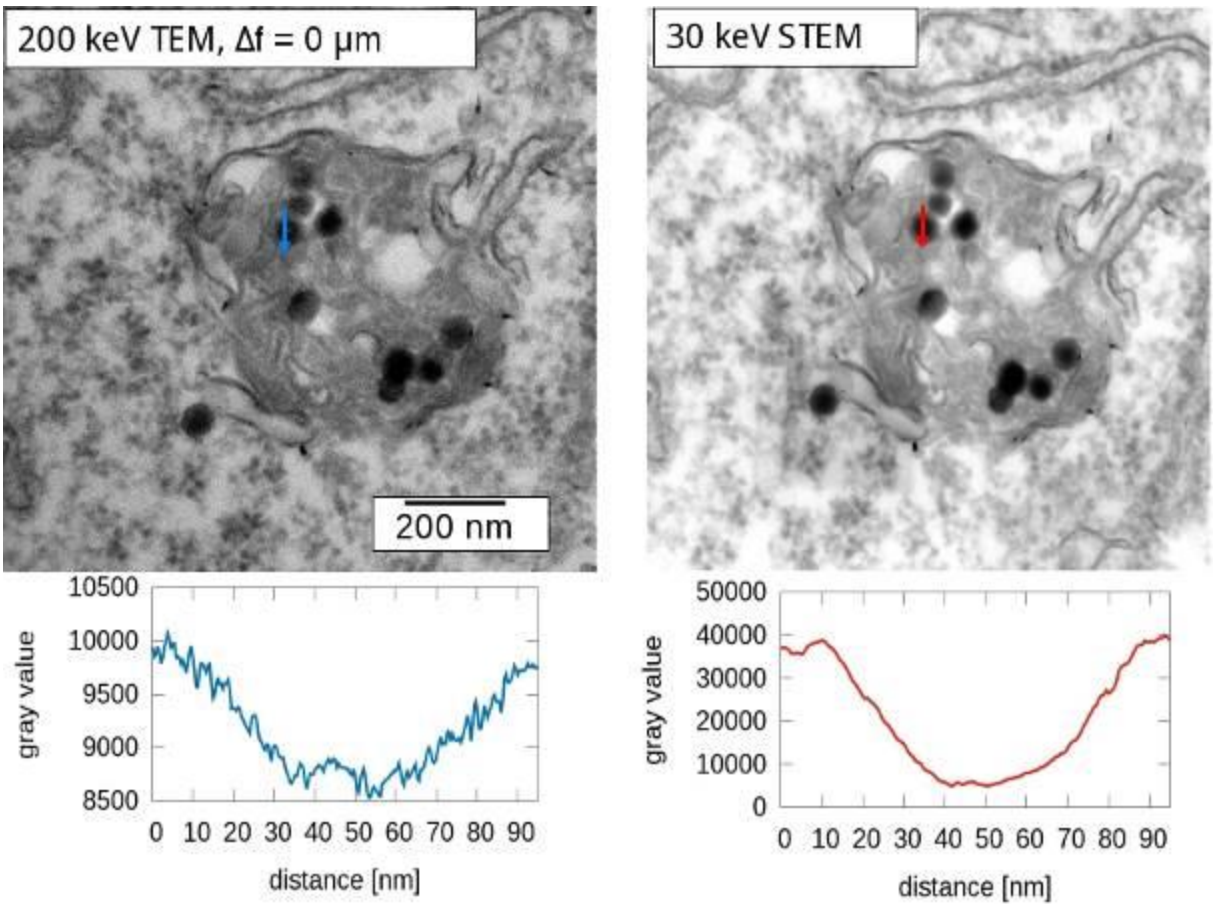

LS5.P002

Multiscale imaging pipeline integrating x-ray tomography, classical histology, and SEM to target sub-volumes in conventional paraffin samples

E. R. Curticean[1], J. Reiser[2], I. Wacker[1,2], W. Wagner[2], R. R. Schröder[1,2]

[1]Universität Heidelberg, Heidelberg, Germany
[2]University Hospital, Heidelberg, Germany

Introduction: Paraffin samples still remain the primary source of pathological diagnosis and for understanding disease development and progression. Due to the vast amount of paraffin samples available to scientific laboratories and universities around the world [1], we need to rethink modalities for imaging targeted structures that go beyond the limits of standard light microscopy (LM) and that achieve higher resolution. Objectives: Our goal is to develop a correlated workflow for targeting volumes of interest within a standard paraffin block. Starting with X-ray based imaging to create a reference volume, we then combine LM and SEM imaging to address specific subvolumes. Materials & Methods: Samples - Tissue from human lungs affected by COVID-19 was fixed in formalin and embedded in paraffin (FFPE) according to standard protocols. X-ray microscopy - Entire paraffin blocks were µCT-imaged (Phase Contrast CT) using a synchrotron radiation-based system (SRCT, Synchrotron Elettra, Trieste), initially with an isometric voxel size of 4µm. Based on the 3D scan of the entire block, targeted punch biopsies (cylinders with a diameter of 4 mm) were taken and scanned again with a voxel size of 2µm. Histology - Serial sections (5µm thick) were cut from a selected volume, stained (AB-PAS) and imaged using digital LM (slide scanner). Electron microscopy - Sections were stained with 3% uranyl acetate and lead citrate or/and sputtered with 3nm of Pt/Pd (80/20%). SEM (Zeiss Ultra 55) analysis was performed on regions pre-defined in the LM scan. Integration – To adjust possible deformations of the sections due to LM/SEM preparation, the data was registered with ,,Fuxlastix" [2] Results: Comparison of a virtual slice from an X-ray volume (fig 1A) with a physical section cut from the corresponding paraffin block and stained for glycoproteins (fig 1B) shows perivascular fibrotic tissue formation in both modalities. SEM imaging (fig 1C, D) of regions defined in the LM scan illustrates the amount of detail obtainable at high resolution. By integrating the LM and SEM data into the X-ray volume, it is possible to identify and segment extended extracellular matrix elements such as the elastin cables (yellow in fig 2B & C) within the volume. Combining a cross-section of an alveolar tip (insets fig 2A) highlighted in purple in the X-ray volume (fig 2 B top) with the segmented elastin cables (fig 2B bottom) indicates where the elastin cables "penetrate" the alveolar tip. Conclusion: The use of X-ray tomography for non-destructive targeting is a goal-oriented method. We have developed a consistent correlative workflow for imaging paraffin samples in order to go beyond the restricted spatial resolution offered by traditional LM analysis. Furthermore, by using SRCT-based segmentations, we are able to make interpretations of their 3D context and represent them ultrastructurally by imaging the slice in the SEM. [1] L Cheng, DG Bostwick, (Eds.) - Essentials of Anatomic Pathology, Humana Press, 2002 [2] J Albers et al. - Elastic transformation of histological slices allows precise co-registration with microCT data sets for a refined virtual histology approach, Scientific Reports, 2021

Fig. 1

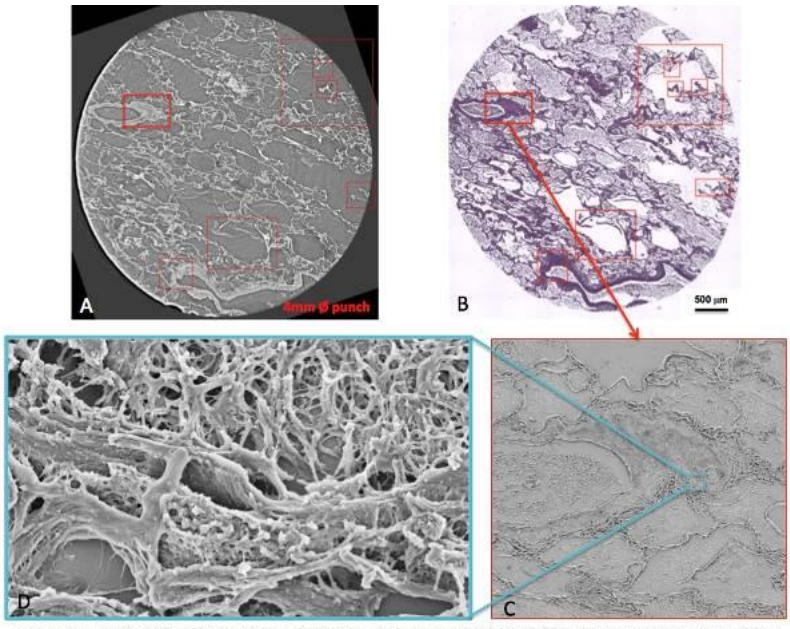

Figure 1 : Perivascular fibrotic tissue formation in human Covid lung: Correlative imaging using phase contrast µCT (A), AB-PAS histology (B) and SEM (C, D)

Fig. 2

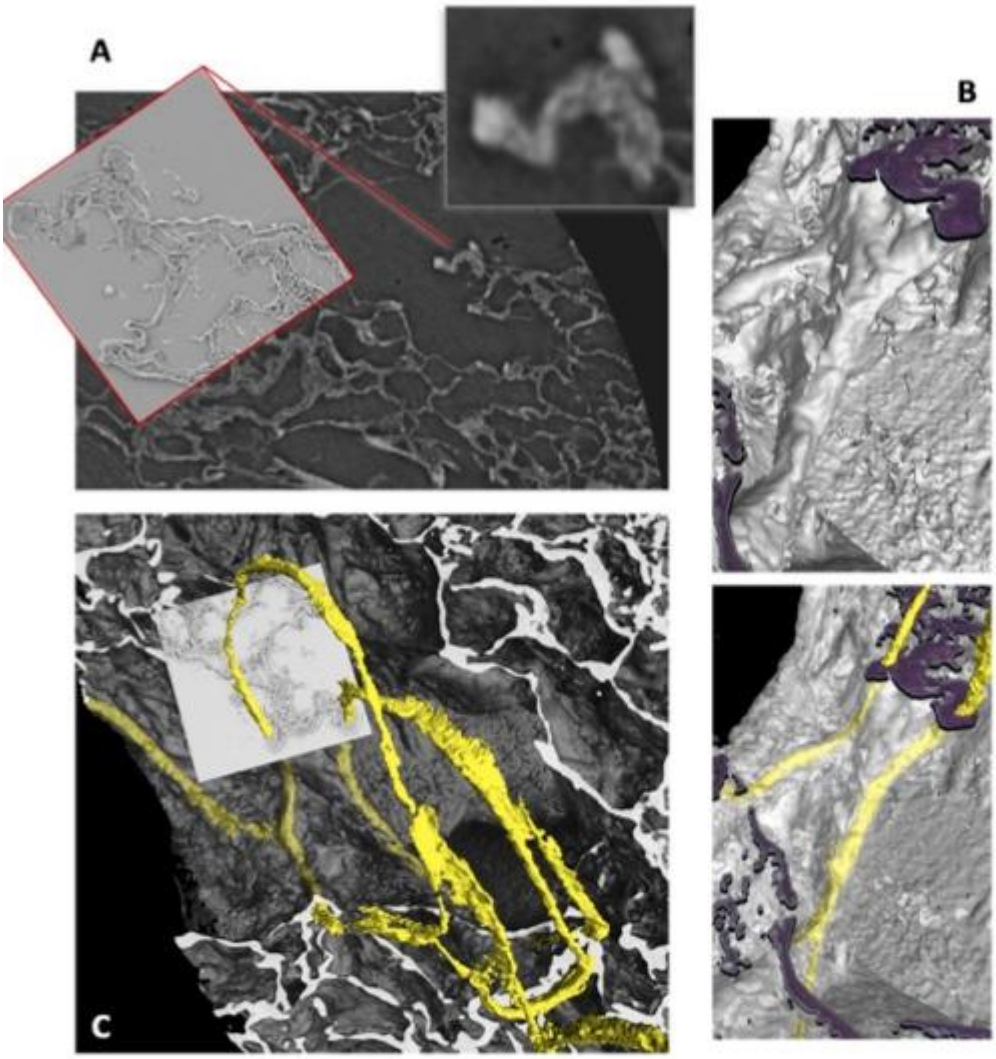

Figure 2: SEM-guided segmentation of the X-ray tomographic volume: Integration of SEM data into X-ray volume (A) and comparison of the appearance of an alveolar septal tip in SEM (insert left) and XRM (insert right). Segmentation of alveolar septal tips in purple (B) and axial connective tissue system (elastin cables) in yellow (B bottom, C). Fitting of SEM data into the larger context of the axial connective tissue system (C).

LS5.P003

Magnetic resonance microscopy for the 3D-non-destructive analysis of the tendon micro-structure under strong mechanical load supported by polarization sensitive optical microscopy and SEM data

A. Berg[1,2], M. Stoiber[1]

[1]Medical University of Vienna, Center for Medical Physics and Biomedical Engineering, Vienna, Austria
[2]Medical University of Vienna, High-field MR Center, Vienna, Austria

1 Introduction

Magnetic Resonance Microscopy (MRM) is limited in spatial resolution (a≈10µm) and sensitivity compared to optical microscopy (OM) or SEM but offers the advantages of being non-destructive, 3-Dimensional imaging of intact 3D biological tissue and a multifold variety of different contrast weightings (eg. T2/T1, magn. susceptibility, diffusivity, chemical information). These features qualify MRM for investigating biological samples and delineation of microstructural changes as a consequence of biological or mechanical impact.

The elementary functional element of the tendon is represented by collagen filaments. These are arranged to larger fiber bundles, surrounded by the MR-bright endotenon, in a hierarchical, self-similar way from primary to tertiary fiber bundles[1]. Strong mechanical load without rupture, e.g. by abrupt trauma in sport or repetitive dynamic fatigue overload might change the microstructural arrangement of fiber bundles permanently and therefore might result in increased risk for permanent fatigue aches and even rupture within routine sport activities.

2 Objectives

1 Can high resolution MRM delineate permanent changes in the microstructure of tendons as a consequence of strong mechanical load?

2 What are these microstructural changes and can they be related to the results of ex-vivo investigations on human tendons using OP or SEM? What bio-physical model could be used for the interpretation of the observed changes in T2* contrast MRM?

3 Materials/Methods

3.1 MR-microscopy

The spatial encoding in 2DFT-MR-imaging is obtained via slice selective excitation, phase- and frequency encoding of the sample emitted radiofrequency (rf) signal. The extraordinary high microscopic spatial resolution on an Ultra-High-Field (B=7T) human MR-scanner was achieved using a prototype strong magn. field gradient insert with sensitive rf-detectors[2]. 2D and 3D- T2*-weighted images (VS: 64x64x60µm^3) were obtained with short encoding time TE for visualization of tendon tissue with short relaxation time T2*.

3.2 Tendon-tissue samples

Several samples (l≈5cm) from cattle Achilles tendon were halved into two parts; one segment was exposed to a mechanical load (F≈600N). The samples were scanned with orientation of the main tendon axis and mechanical load parallel to the outer static magnetic field **B** of the MR-scanner.

4 Results

An MR-microscopic axial slice out of a Multi-slice MR data set (fig.1) and a sagittal view reconstructed from a high-resolution isotropic 3D data set are shown exemplarily below (fig.2).

The MRM images were compared to polarization sensitive OM and SEM of the rat tendon under mechanical load[3]. The main direction of tendon fiber filaments changes for a length of about 60µm (crimp structure of tendon) until being oriented back again. The number and angle of this crimp misalignment reduces with load (flattening triangle model)

and was also observed in MRM (disappearing of the hyperintense filaments) as a consequence of the Magic angle effect[4] in MR.

5 Conclusion

Advanced MR-technology based on prototype insert hardware on UHF scanners is capable of the non-destructive visualization of permanent changes in the microstructure of tendons with load below rupture level. The MR appearance can be interpreted within a flattening alignment model of the tendon crimp structure. Thus, MR-microimaging offers perspectives for the early diagnosis of pre-damage to tendons and interpretation of undefined tendon aches.

Fig. 1

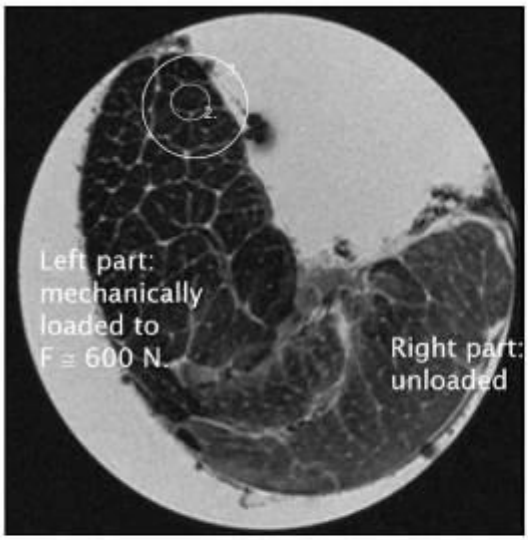

*Fig. 1 T2*w- MR-microscopic image (transverse) of the bovine tendon (Vs: 70x70x300 µm³, TE = 2.44 ms). The left hypointense part experienced a mechanical load of F ≈ 600 N. The right part appears brighter by an undefined noisy-type background. Both parts show the tertiary (3.) and secondary (2.) sub-structure of the self-similar architecture of the tendon.*

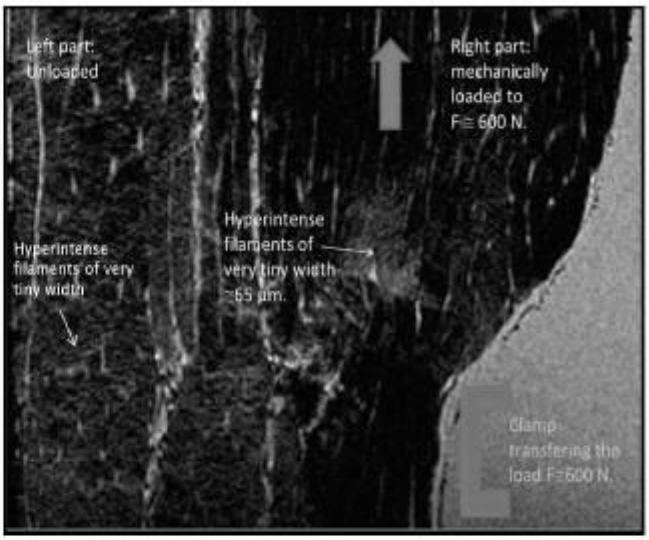

*Fig. 2 Sagittal view, taken from a high-resolution (Vs: 64x60x60 µm³) 3D data set of MRM-images. At this high resolution the reason for the noisy background in the T2*w axial images with less spatial resolution becomes visible: hyperintense filaments, indicating fiber subsegments, which are not oriented parallel to the outer magnetic field (tendon crimp structure). The blue arrow indicates the direction of the outer magnetic field B0, here parallel to the mechanical load.*

Fig. 2

6 References

[1] Kannus P; *Structure of the tendon connective tissue*. Scandinavian Journal of Medicine & Science in Sports, 10: 312-320 (2000),

[2] Berg A, Potthast A, Starewicz P; *MR-Microscopy on a human 7T-Scanner*. Proc. ISMRM/ESMRMB 2010,1048, Stockholm, Sweden (2010).

[3] Franchi M, Fini M, Quaranta M, De Pasquale V, Raspanti M, Giavaresi G, Ottani V, Ruggeri A; *Crimp morphology in relaxed and stretched rat Achilles tendon*. J Anat ; 210: 1–7 (2007).

[4] Hager, B, Schreiner, MM, Walzer, SM, Hirtler, L, Mlynarik, V, Berg, A, Deligianni, X, Bieri, O, Windhager, R, Trattnig, S and Juras, V; *Transverse Relaxation Anisotropy of the Achilles and Patellar Tendon Studied by MR Microscopy*. J Magn Reson Imaging (2022).

LS5.P004

Morphological evaluation of the stomach of the African giant-pouched rat (*Cricetomys gambianus)* using gross anatomy, histology and scanning electron microscopy

C. Igbokwe[1], F. Ejikeme Mbajiorgu[2,3]

[1]university of nigeria nsukka, veterinary anatomy, Nsukka, Nigeria
[2]SCHOOL OF ANATOMICAL SCIENCES, HISTOLOGY, Johannesburg, South Africa
[3]FACULTY OF HEALTHSCIENCES, HISTOLOGY DIVISION, UNIVERSITY OF WITSWATERSRAND, JOHANNESBURG, SOUTH AFRICA, SCHOOL OF ANATOMICAL SCIENCES, FACULTY OF HEALTH SCIENCES, HISTOLOGY, Johannesburg, South Africa

The African giant pouched-rat (AGR) is semi-fossorial, nocturnal and omnivorous wild rodent that is widely distributed in sub-Saharan Africa.. AGR is used to detect land mines and for tuberculosis investigation and other biomedical uses. The stomach plays important roles in the physical and digestive process. There are reports on gross anatomy, morphometric and histology of the digestive tract of AGR (Knight and Knight-Eloff; 1987). Detailed investigations on the internal morphology of the stomach of AGR are scant, and studies that used scanning electron microscopic technique (SEM) for investigation rare. This study therefore seeks to examine the relationship between stomach structure and food habits by gross dissection, stereomicroscopy, and histology and scanning electron microscopic techniques. Six adult rats of either sex captured from the wild at night with metal-cage traps were used. Grossly, the stomach externally showed a U-shaped compartmentalized parts with copious sacculations. Well developed oesophageal groove, numerous papillae (corpus of non-glandular zone) and pyloric pouch were identified. An internal limiting ridge demarcated glandular from non-glandular part (FIGS.1A-1D). The four regions of the glandular stomach are cardiac, fundus, pylorus and antrum, while non-glandular zone consists of coma-shaped fundus and out-pocketing saccus cecum. Internally non-glandular zones are comprised of protruded papillae-like structures and thick wall, the glandular part showed smooth fundic mucosa, pyloric sphincter and gastric diverticular folds. The mean weight and length and width of the stomach were 27.7g, 19.5 cm and 3.9 cm respectively. Histologically (Fig. 2A), the arrangement of stomach tissues was as seen in typical mammalian pattern with variations in the glandular and non-glandular compartments. The wall of the stomach in the glandular and non-glandular regions showed four layers; mucosa supported by lamina propria, submucosa (loose connective tissue, vessels and nerves), muscularis (inner oblique, inner circular and out longitudinal muscle layers) and serosa. Non-glandular corpus and fornix ventriculi was covered in the lumen by numerous papilla lined by stratified keratinized epithelium. The glandular part is folded into rugae and the complex epithelial/ glandular lining contains depressions (gastric pits) which provided entrance into gastric glands lined by five types of typical epithelial cells There were variations of these components in the parts of the glandular antrum, cardiac, fundic and pyloric glands. The presence of neutral and acidic mucins in the gastric pits was demonstrated by PAS and AB reactions. Under SEM, the mucosal surface of the non-glandular compartment showed projections of robust papillae with longitudinal invaginations and desquamated keratinous structures of the papillae(Figs.2B-D). In fundic glandular part, gastric plicae with numeous openings of gastric glands were apparent and several longitudinal rigdes were seen amongst the plicae in the pyloric antrum. The study demonstrated that the stomach of AGR is complex as in other Cricetids (Perrin and Kokkin, 1986). The presence of sacculations, well-developed, numerous papillae, and pyloric pouch makes it remarkably different from other wild rats and supports its omnivorous dietary habit and symbiotic bacteria role in the stomach.

Knight & Knight-Eloff (1986). J. Zool., 213:7-22

Perrin & Kokkin (1986). South Afr. J. Zool., 21(3):202-210

Fig. 1

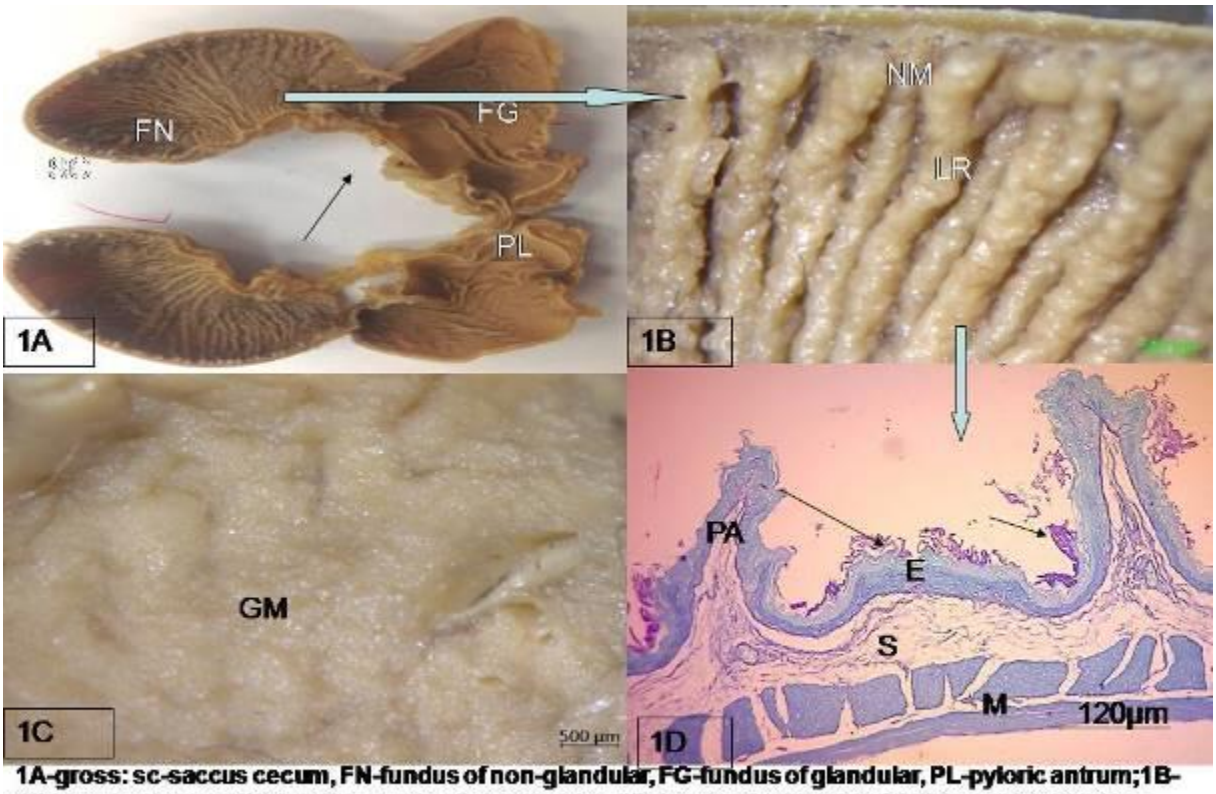

1A-gross: sc-saccus cecum, FN-fundus of non-glandular, FG-fundus of glandular, PL-pyloric antrum;1B-stereomicroscopy:NM-fundic non glandular mucosa, LR-longitudinal ridges; 1C-Stereomiscroscopy: fundic glandular mucosa;1D-Histology (PAS): fundic non glandular compartment with PA-papillae, E-keratinized epithelium, S-submucosa, M-muscularis (smooth muscle layers), arrow-keratin layers that stain PAS positive for mucins

Fig. 2

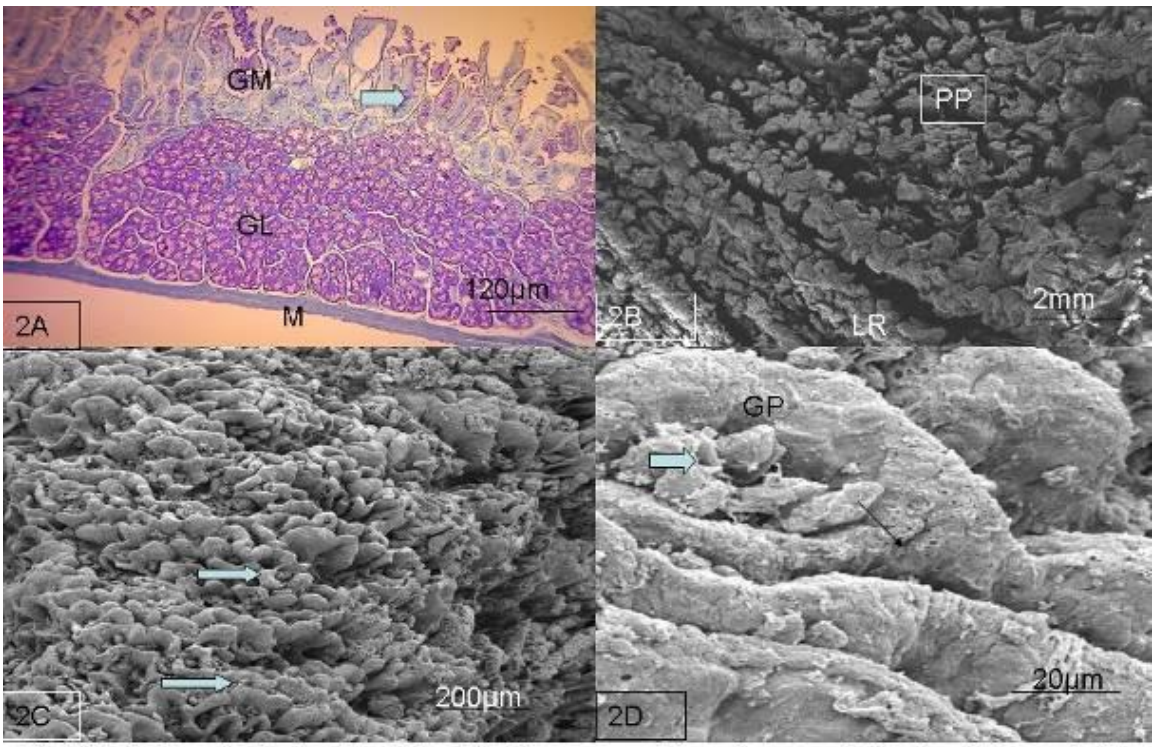

2A; Histology: pyloric glands: GM-epithelia mucosa, GL- submucosal glands, M-muscularis layers;2B: SEM photos-Non-glandular with papillae (pp) on longitudinal ridges (LR);2C-SEM photos of glandular mucosa low power with gastric plica (arrows)-2D-SEM higher power: gastric plica (GP) with pits for mucin and enzymatic secretions (arrows)

LS5.P005

Micro- and nanoplastics contamination detection in plant samples by correlative microscopy

J. Wissler[1], P. Häfner[2], A. Aberle[2], N. Loerler[2], D. Mamdouh[3,4], D. Szwajgier[5], H. A. Reimann[2]

[1]TESCAN, Dortmund, Germany
[2]University of Applied Sciences Ansbach, Fakultät Technik, Ansbach, Germany
[3]University of Applied Sciences Weihenstephan-Triesdorf, Department of Plant Food Processing, Agricultural Faculty, Weidenbach, Germany
[4]Al-Azhar University, Botany & Microbiology Department, Faculty of Science, Cairo, Egypt
[5]University of Life Science in Lublin, Dept. of Biotechnology, Microbiology and Human Nutrition, Lublin, Poland

Correlative light electron microscopy (CLEM) has been used for the detection of plastics pollution with plants. Entries of the ubiquitous world-wide plastics pollution into nature thus enter the human food chain as degradation products, influencing environmental habitat and health. Micro- and nanoplastics as foreign bodies contaminating beverages and foods are likely to have a long-term impact on nutrition growth, public and personal health.

Nanoparticles and their spatial location are generally difficult to detect in biological specimens, especially plastic particles due to their analogous hydrocarbon-based matrix. Reliable analysis methods for the discovery of micro- and nanoplastic particles in entities are not fully established yet.

We determined that light microscopy (LM) is usable for a coarse estimation of the contamination grade of plant samples. Light microscopy, due to its optical diffraction limit, rather detects nanoparticle patches than single particles, shown using fluorescent polymer nanoparticles. Scanning electron microscopy (SEM) instead provides higher resolution, especially for single particle detection. But it requires extended EM sample staining preparation to depict hydrocarbon-based specimens.

Using both microscopy types in a CLEM approach with TESCAN CORAL, the necessary insights to the contaminated plant areas are provided with single nanoparticle resolution. It reveals that nanoparticles seem to be tightly attached to the plant material (cf. Fig. 1). It indicates further that basic food cleaning procedures might be insufficient for full particle removal. The presented approach circumvents correlative topography issues of the 3D-plant samples. CLEM provided a fast and reliable analysis method for the semiquantitative analysis & detection of micro- and nanoparticles plant contamination.

(**Fig.1:** Nanoplastics particles attached to the leaf surface)

Fig. 1

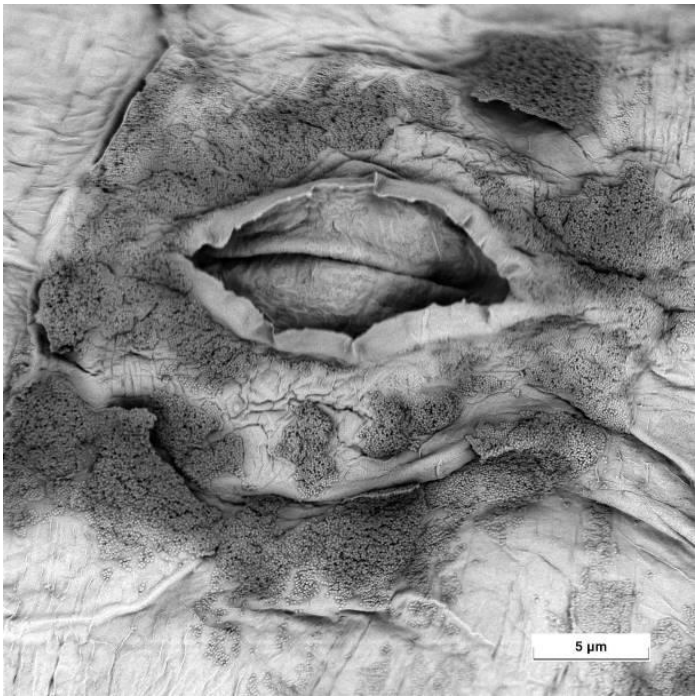

LS5.P007

Comparative morphological features of the stomach (Proventriculus and Gizzard) in two species of Columbidae (Red-eyed turtle dove: *Stretopelia semitoquarta*; Domestic pigeon: *Columba livia domestica*) in the wild and domestic environment

C. Igbokwe[1], F. Ejikeme Mbajiorgu[2,3]

[1]university of nigeria nsukka, veterinary anatomy, Nsukka, Nigeria
[2]SCHOOL OF ANATOMICAL SCIENCES, HISTOLOGY, Johannesburg, South Africa
[3]university of witswatersrand, Johannesburg, south africa, SCHOOL OF ANATOMICAL SCIENCES, FACULTY OF HEALTH SCIENCES, HISTOLOGY, Johannesburg, South Africa

INTRODUCTION: Among the different bird species, the shape, size and structure of the stomach varies with diet (Duke, 1997). The avian stomach is composed of two definite compartments separated by a constriction: the cranial glandular proventriculus (PV) and a larger caudal non-glandular gizzard (GZ). The stomach of flesh-eating species of birds is primarily a storage organ appropriate for chemical digestion of soft diet. But, the stomach of herbivorous and omnivorous birds is adapted for mechanical degradation of tougher food materials through strong muscular development of the stomach (King and McLelland, 1975). The red-eyed dove (RD) and domestic pigeon (DP) belong to the Columbidae which feed primarily on seeds, fruits, and plants. But the domestic and wild feeding habitats of the species could influence their granivorous and omnivorous habits and subsequently impact on the structure of the stomach. Large-sized grains were specifically recovered from stomach of RD unlike the small-sized grains from the DP. Studies have been carried out on the histology of the proventriculus and gizzard in many species especially poultry (fowl, guinea fowl and turkeys, quail) and few feral species (common starlings, hooded crow and Australian passerines). Few reports have described the stomach linings of the *Columbidae* especially wild doves by ultrastructural evaluation. The present investigation seeks to evaluate the structural features of the proventriculus and gizzard in the wild RD and DP and related the features with dietary habits. METHODOLOGY: The work used gross dissection, stereomicroscopy, histology and scanning electron microscopy following routine protocols. Six adult RD (body weight: 148.69g) and 6 DP (body weight: 293.56g) birds of either sex were used. Humane handling and cervical dislocation for euthanasia were used. RESULTS: Gross results showed that the relationship of the stomach to the left lobe of liver, duodenum, spleen and abdominal air sacs was similar in both species. Grossly typical features of cone-shaped PV and lens-shaped GZ were present (**Figs 1a-e**). It was located within intestinal peritoneal sac. The total GIT weight and stomach weight for were 12.06g, 27.61g and 5.12g, 8.51g respectively for RD and DP. The stomach represented 41.4% and 30.1% of the GIT in RD and DP respectively. It showed 3.4% and 2.8% of body weight in RD and DP respectively. Under SEM (**Figs 2a-f**), PV formed spiral folds (plicae) around a central glandular opening and the number and anastomotic arrangement varied in the species. The glandular openings were surrounded by longitudinal and transverse mucosal folds of the epithelium. Evidence of secretory activity of mucin-like substances was apparent. Surface structures resembling variably shaped projections of membrane were in the gizzard of the birds by SEM. Histologically **(Figs. 2g-i),** four typical tunics were represented in the two species. Large proventricular glands were tubuloalveolar lobules with secretory ducts and arranged were in a definite row and shape in the *muscularis mucosa*. The koilin membrane and *tunica muscularis* of GZ was thicker in the RD. Simple tubular glands were with the thick muscular layers. CONCLUSION:The morphological features of the stomach did not differ significantly in the two birds indicating convergence of dietary components.

King and Mclelland (1975). Outlines of Avian Anatomy, Bailliere Tindall, London

Duke (1997). Proc. Nurt. Soc., 56, 1049-1056.

Fig. 1

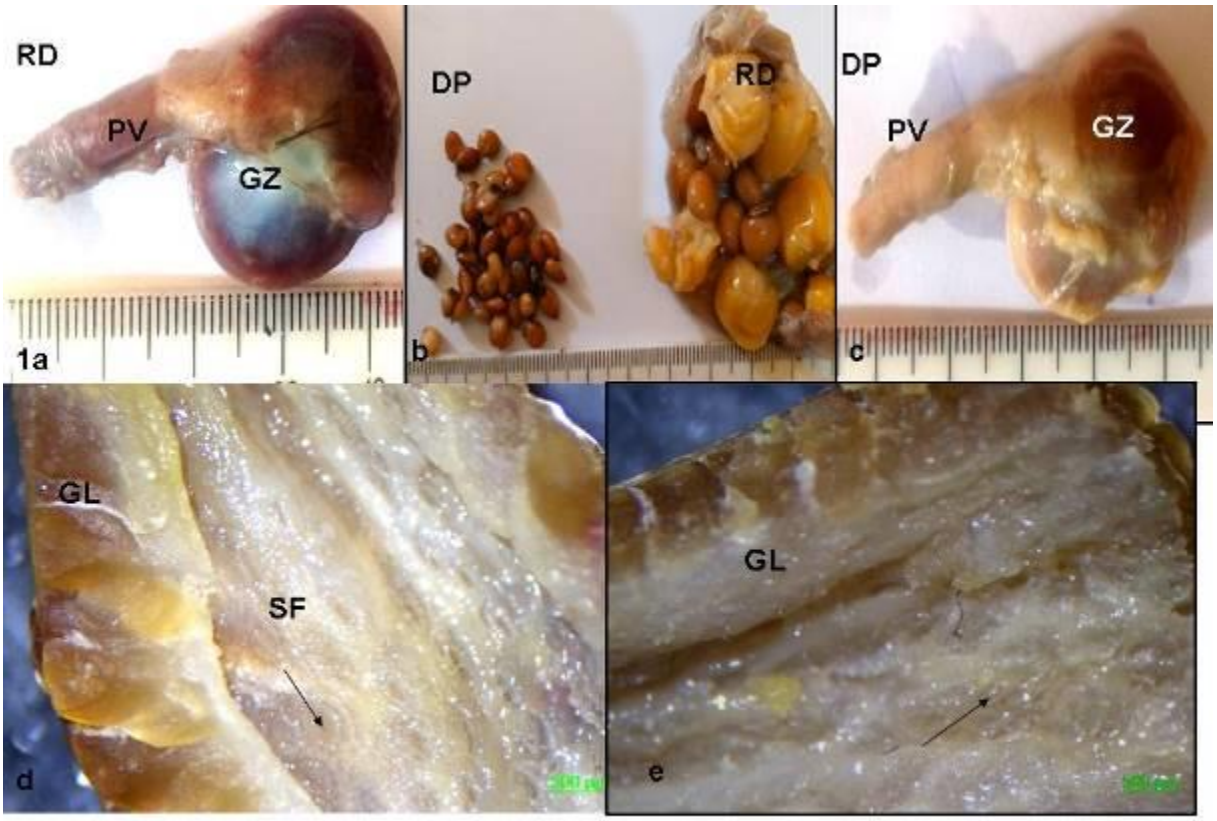

1a-c:gross photos of proventruclus (PV) and gizzard (**GZ**) of dove (**RD**) and pigeon (**DP**) with size of grains consumed **(1b); 1d-e:** shows **stereomicrograph of surface of PV in dove (1d) &** pigeon **(1e)** with papillae (arrows).

Fig. 2

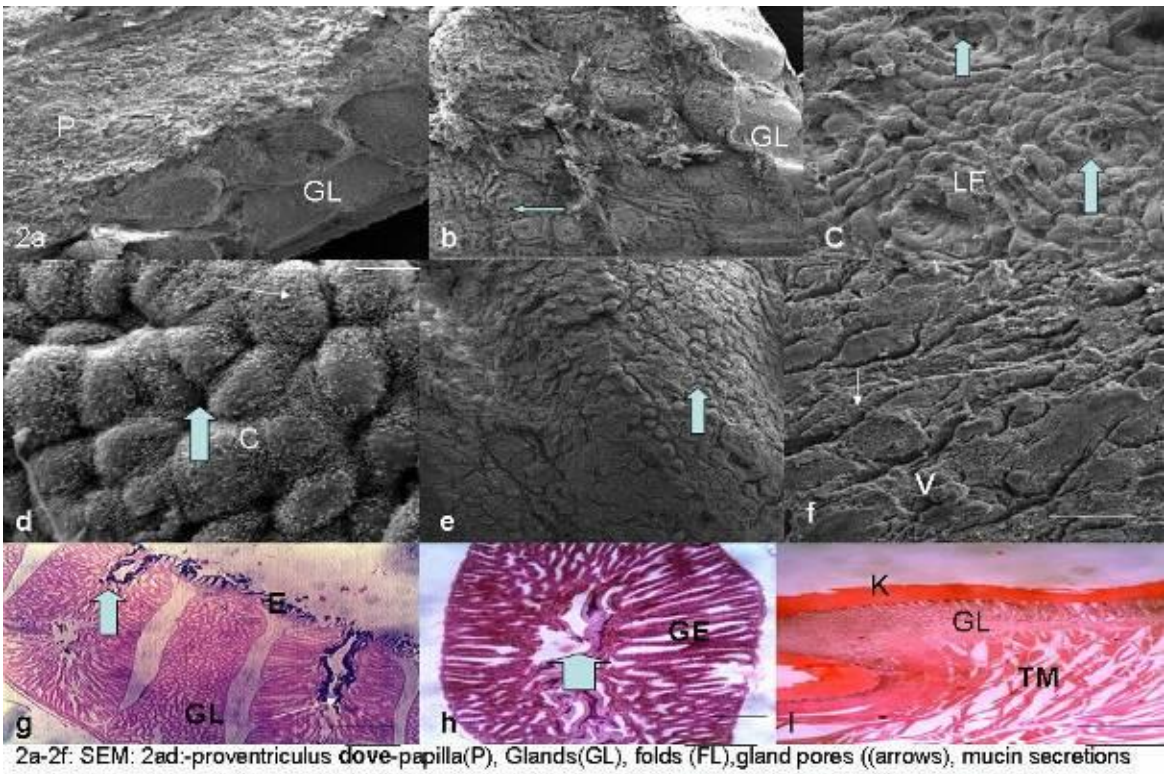

2a-2f: SEM: 2ad:-proventriculus **dove**-papilla(P), Glands(GL), folds (FL),gland pores ((arrows), mucin secretions on surface (small arrows); **2e-f: gizzard dove-**:Koilin surface like vertical rods (arrow)-2f: **pigeon; 2g-h:** histomicrographs showing proventrular gland of **dove** (GL) with mucins (AB-PAS), E (epithelium),acinus and cells (GE). **I-** gizzard of pigeon: koilin (K) & muscular layer (TM) and glands (GL):Bar scale2a-f): 500, 500,200,5,500,200µm; 2g-1: 120, 40,120µm

Fig. 3

Table 1: showing average values of parameters related to the proventriculus (PROV) and gizzard (GIZ) of red-eyed dove (RD) and domestic pigeon (DP)

	RD		DP	
PARAMETER (cm)	PROV	GIZ	PROV	GIZ
Length (long axis)	1.5	2.9	1.9	3.1
Diameter (short axis)	0.5	2.1	0.9	2.4
Thickness (tissue wall)	0.2	1.6	0.3	1.9

LS5.P008

Fluorescent dyes for in-resin CLEM with conventional EPON embedding

R. Franzkoch[1,2,3], V. Liss[1,2,3], O. E. Psathaki[1,2], M. Hensel[2,3]

[1]Universitaet Osnabrueck, Integrated Bioimaging Facility Osnabrueck, Osnabrück, Germany
[2]Universitaet Osnabrueck, Center of Cellular Nanoanalytics, Osnabrück, Germany
[3]Universitaet Osnabrueck, Microbiology, Osnabrück, Germany

1. Introduction

In-resin correlative light and electron microscopy (CLEM) facilitates a high-precision registration of the fluorescence signal upon the EM image. Current approaches most often employ acrylic resins, such as Lowicryl HM20, for preserving fluorescence while compromising the ultrastructural preservation (Buerger *et al.*, 2021). Epoxy resins, such as EPON 812, on the other hand are the optimal choice for preserving ultrastructure. However, embedding samples in epoxy resins leads to a reduction in antigenicity and fluorescence. Nevertheless, it was shown that on-section CLEM following a conventional sample preparation including chemical fixation, post-fixation with osmium tetroxide, dehydration at room temperature and embedding in epoxy resins is possible with partly specifically adapted fluorescent proteins or protein tags labelled with certain dyes (Müller *et al.*, 2017; Peng *et al.*, 2022).

2. Objectives

We set out to further test the broad applicability of different fluorescent dyes in a conventional in-resin CLEM workflow with embedding in EPON. We plan to demonstrate the robustness of this by application to different cellular organelles, which allows us to achieve a high-precision registration with minimal effort in terms of sample preparation.

3. Materials & methods

Cell lines and cell culture

HeLa cells expressing the HaloTag fused to various markers were labelled with different fluorescent ligands, imaged by confocal laser scanning microscopy (cLSM), if needed, and further processed for EM.

Sample preparation for on-section CLEM

Cells were fixed with 2.5 % glutaraldehyde and post-fixed for 30 min using 1 % OsO4 and 1.5 % K4[Fe(CN6)] on ice. Samples were dehydrated and embedded in EPON. After polymerization, 250 nm thin sections were cut, collected on mesh grids and imaged at a cLSM.

4. Results

The fluorescence of mitochondria, Golgi apparatus and *Salmonella* effector proteins labelled with TMR or JFX554 is preserved after conventional sample preparation and embedding in EPON.

5. Conclusion

The in-resin CLEM workflow devised in this study offers a very promising tool for cases in which Lowicryl embedding cannot or does not need to be used, but a registration of the LM to the EM image with high accuracy is desirable. Live-cell imaging and direct fixation on the LM stage can be easily integrated.

References

Buerger, K., Schmidt, K.N., Fokkema, J., Gerritsen, H.C., Maier, O., de Vries, U., Zaytseva, Y., Rachel, R., and Witzgall, R. (2021). Chapter 8 - On-section correlative light and electron microscopy of large cellular volumes using STEM tomography. In Methods Cell Biol, T. Müller-Reichert, and P. Verkade, eds. (Academic Press), pp. 171-203.

Müller, A., Neukam, M., Ivanova, A., Sönmez, A., Münster, C., Kretschmar, S., Kalaidzidis, Y., Kurth, T., Verbavatz, J.-M., and Solimena, M. (2017). A Global Approach for Quantitative Super Resolution and Electron Microscopy on Cryo and Epoxy Sections Using Self-labeling Protein Tags. Scientific Reports *7*, 23.

Peng, D., Li, N., He, W., Drasbek, K.R., Xu, T., Zhang, M., and Xu, P. (2022). Improved Fluorescent Proteins for Dual-Colour Post-Embedding CLEM. Cells *11*, 1077.

Figure Legends

Fig. 1: Conventional in-resin CLEM with EPON embedding of mitochondria labelled with fluorescent dyes. Fluorescence of Tom20-HaloTag stained with JaneliaFluorX 554 (A-C) or TMR (D-F) is preserved after conventional embedding in EPON. Scale bars: 2 µm.

Fig. 1

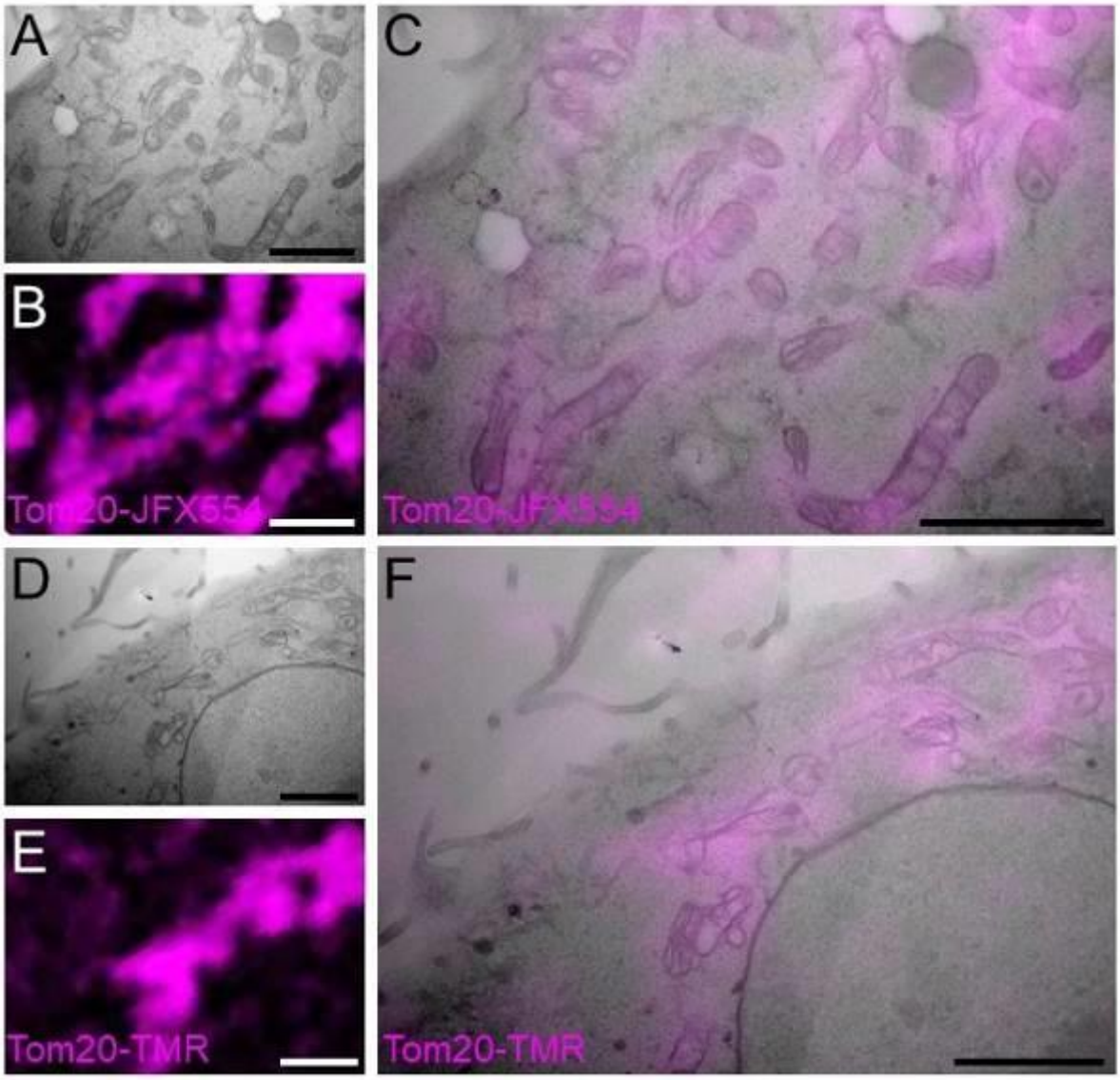

LS6.001-invited

Zooming into the spread and entry of influenza A viruses by correlative light and electron microscopy

C. Lahr[1], S. Klein[1], C. Schneider[1], C. Funaya[2], P. Chlanda[1]

[1]University Hospital Heidelberg, Schaller Research Groups, Department of Infectious Diseases, Virology, Heidelberg, Germany
[2]Heidelberg University, 2) Electron microscopy core facility, Heidelberg, Germany

Influenza A viruses (IAV) cause annual epidemics and occasional pandemics typically resulting from zoonotic transfers. While it has been well established that the IAV are highly pleomorphic forming filamentous virions typically found in human isolates and spherical particles after lab adaptation, the benefits of filamentous virions in spread and entry inside lungs are not fully understood. Here, we used reverse genetics to create spherical and filamentous reporter viruses with the same genetic background. We apply cryo-correlative light and electron tomography to elucidate IAV entry in endosomes and established a correlative light and scanning electron microscopy to study IAV spread in a quantitative manner using plaque assays. Our data show differences in the spread of spherical and filamentous virions in different cell lines.

LS6.002-invited

Dissecting the lifecycle of uropathogens by directly analyzing patient samples with cryo-ET

G. Weiss[1]

[1]ETH Zurich, Institute of Molecular Biology & Biophysics, Zurich, Switzerland

Urinary tract infections (UTIs) are among the most common bacterial infections in humans. Besides being generally considered to be extracellular infections and easily treated with antibiotics, they are often incompletely resolved. About 25% of patients experience a recurrent UTI and the resulting repetitive administration of antibiotics contributed to higher antibiotic resistance rates in uropathogens. Up to 90% of UTIs are caused by uropathogenic E. coli (UPEC), which can proliferate in the bladder lumen but are also capable of invading uroepithelial cells where they form intracellular bacterial communities, protecting the pathogen from host defenses and antibiotics.

By using an integrative approach of mass spectrometry, (cryo-correlative) light microscopy, cryo-focused ion beam (FIB) milling and cryo-electron tomography (cryo-ET), we aim to dissect the different infection stages of UPEC in vitro and directly in patient samples. In a first step, we resolved the architecture of the most abundant protein in our urine, uromodulin, and could show how it serves as a multivalent antagonist against UPEC adhesion. However, many bacteria can overcome the uromodulin barrier and infect bladder epithelial cells to form intracellular communities. We optimized an infection protocol and transferred it to cells seeded on electron microscopy (EM) grids. By using cryo-fluorescent light microscopy, we correlate our subsequent cryo-FIB milling step to different maturation stages of intracellular bacterial communities to reveal their native in situ architecture and composition. To transfer our insights to actual patients, we are working on analyzing infected cells found in patient urine and in bladder biopsies with cryo-ET.

LS6.003

The role of vaccinia virus protein A6 for correct assembly

S. Tonnemacher[1], R. Eberle[1], R. Kunz[2], P. Walther[2], J. Krijnse Locker[1]

[1]Paul-Ehrlich-Institut, Loewe DRUID, Langen, Germany
[2]Universität Ulm, Zentrale Einrichtung Elektronenmikroskopie, Ulm, Germany

Introduction: Enveloped viruses acquire their membrane from the host, but for the large DNA-virus vaccinia virus (VACV), member of the poxviridae, the origin and biogenesis of its membrane remains controversial until this date. By electron microscopy (EM) newly synthesized VACV membranes appear as short, half-moon shaped units (the crescents) that grow into membrane spheres, the immature virus (IV). Upon DNA-uptake, the IV matures in to the infectious brick-shaped mature virus (MV) [1]. The gene product of A6, a 43 kDa protein, is one of five VACV proteins that seem to be required for viral membrane biogenesis and the formation of infectious virus, collectively called virus membrane associated proteins (VMAPs) [2].

Objectives: It is known, that the VMAPs play an essential role in the assembly of the VACV. In this study, the role of A6 in VACV-assembly was further investigated.

Materials & methods: Hela cells were infected with a recombinant VACV where the synthesis of A6 can be conditionally induced. Cells infected with or without A6 synthesis were fixed at different time points and prepared for EM-imaging. Complementary EM-imaging methods were applied: conventional thin section EM, EM-immuno-labeling and scanning transmission electron tomography.

Results: When the expression of A6 is blocked, IV- and MV-formation is absent [3]. Instead aberrant virally induced structures accumulate in a time dependent manner; fragmented core accumulations, and large spherical membranes, resembling IVs, but devoid of viral core proteins.

Conclusion: It seems that A6 plays a role in the interaction of core protein and crescents.

Reference:

[1] DOI: 10.1016/j.virol.2015.02.003
[2] DOI: 10.1128/JVI.02405-16
[3] DOI: 10.1128/JVI.00877-09

LS6.004

Influence of iron overload on the structure of amyloid beta fibrils in the human brain

S. Sunkara[1], R. Megjidi[1], S. Patz[1], W. Sattler[1], G. Leitinger[1]

[1]Medical University of Graz, Graz, Austria

Introduction:

Organotypic cultures (OTC) represent a promising method to study neurodegenerative diseases with the advantage of preservation of original architecture and connections. We established Alzheimer"s disease (AD) condition *ex-vivo* in the hippocampus region of the porcine brain and the human brain. We designed a simple protocol to generate the fibrils from the amyloid beta (Aβ) peptide prior to our treatments. We used this as our model to study the influence of iron accumulation in AD pathology. Iron is an essential and most abundant trace element in the human body. Iron deposition in AD is correlated with free radical damage, oxidative stress, amyloid beta plaques, etc1,2. Several studies report the increase in toxicity of AD due to iron overload3. Hence, we hypothesize that the unexplained toxicity due to the accumulation of iron in the brain could be due to its effect on the structure of the Aβ fibrils. To understand the same, we plan to mimic the iron accumulation in the brain using ferric citrate as the iron (Fe+3) donor in our *ex-vivo* 3D model - organotypic culture induced with Aβ.

Objectives:

1. To establish an authentic *ex-vivo* Alzheimer"s model in the human brain to enable the closer study of AD pathology.
2. To establish iron overload in the brain using ferric citrate as the iron donor.
3. To study the effect of iron overload on the structure of Aβ fibrils.

Materials and methods:

Human brain specimen was obtained either from the glioma surgery or from the post-autopsy routine of patients. The specimen was sectioned into 160µm thickness using vibratome. The slices were immediately shifted onto a porous membrane over neurobasal media and maintained for several days. To induce artificial AD and iron overload conditions in the culture *ex-vivo*, the exogenous Aβ1-42 peptides and ferric citrate were added respectively to the serum-free neurobasal media. Harvested sections were processed accordingly for immunofluorescent staining and electron microscopy imaging. The embedded tissue was sectioned into 70nm thickness and used for routine electron microscopy and negative contrasting. We plan to use ATUMtome to produce serial sections for electron tomography to study the effect of iron on the fibrils" structure in detail.

Results:

We compared the morphology of the samples obtained from post-mortem porcine samples with OTC samples and found that the cell integrity and the neuronal connections are viable and the cells are in an active state. The slices exposed to Aβ peptides polymerized and formed aggregates and displayed a mesh-like appearance in the extracellular matrix when observed in the electron microscope. Having established this model, we now plan to induce iron accumulation in the brain to characterize the structure of Aβ fibrils in former condition using 2D electron micrographs and perform electron tomography to understand the structural changes in the fibrils in 3D.

Conclusion:

Organotypic culture systems have been a long-standing tool in neuroscience. However, in neuropathological conditions like AD, most of the studies opt for transgenic mice models to study the disease. We hope that this *ex-vivo* model system of AD from the human brain with slight modifications serves as an excellent alternative to studying the AD pathological conditions and the factors contributing to it. (The project is funded by FWF – Austrian Science fund - P 29370).

LS6.005

SARS-CoV2 induced membrane remodelling and assembly revisited in high-pressure frozen and freeze substituted cells

T. Bergner[1], F. Zech[2], M. Hirschenberger[2], K. M. J. Sparrer[2], P. Walther[1], C. Read (Villinger)[1,3]

[1]Ulm University, Central Facility for Electron Microscopy, Ulm, Germany
[2]Ulm University, Institute of Molecular Virology, Ulm, Germany
[3]Ulm University, Institute of Virology, Ulm, Germany

The severe acute respiratory syndrome coronavirus 2 (SARS-CoV-2), the causative of the still ongoing COVID-19 pandemic, is a highly pathogenic β-coronavirus. During the replication of this virus, viral RNA (vRNA) synthesis takes place in double-membrane vesicles (DMVs). The newly synthesized vRNA exit the DMVs, presumably through a molecular pore (1). Virion assembly is initiated by clustering of the nucleocapsid protein complexed with genomic vRNA at the cytoplasmic face of single membrane vesicle (SMV) membranes. This induces membrane curvature and budding of virions into the SMV lumen. Important structural insights into the SARS-CoV2 replication cycle have so far been obtained by EM. Mainly chemically fixed, conventionally dehydrated samples were used for room temperature TEM or frozen hydrated samples were analyzed by cryoTEM.

We analyzed remodeling of cellular structures upon SARS-CoV-2 infection in high-pressure frozen (HPF), freeze substituted (FS) and Epon embedded cells, aiming for high-quality structural preservation and membrane visibility. That is a pre-requisite for scanning transmission electron microscopy (STEM) tomography to visualize the different stages of SARS-CoV2 virion assembly in 3D.

Cells were cultivated on carbon-coated sapphire discs, infected with SARS-CoV-2 for 24h, and inactivated with 4 % PFA for 1 hour at 4°C. Immediately, samples were prepared by HPF, FS (5% H2O, 0.2% OsO4 and 0.1% UA in acetone for 17h) and Epon embedding, as published in (2). For TEM, 70 nm thick sections were collected on glow-discharged grids coated with a carbon reinforced formvar film and imaged with a JEOL JEM-1400 TEM at 120 kV acceleration voltage. For STEM tomography, 700-800 nm thick sections were cut, collected on freshly glow-discharged grids with parallel bars, shortly immersed into a colloidal gold-suspension, and coated with a 5 nm carbon layer. A series of 97 STEM bright-field-images (-72° to +72° with 1.5° increment) was recorded with a JEOL JEM-2100F at 200 kV acceleration voltage. Tomograms were reconstructed using the IMOD software package (3,4).

Through HPF-FS and Epon embedding, membrane profiles were well preserved. The clear membrane visibility allowed characterization of the cytopathological alterations in SARS-CoV-2 infected cells, such as the compartmentation of the cytoplasm. Further, DMVs and SMVs could be well resolved, showing the power of the HPF-FS technique. Both membranes of the DMVs appeared often tightly apposed and showed minimal deformation. Although imaging of numerous DMVs, the postulated nuclear pore connecting the DMV interior with the cytoplasm discovered by cryoTEM (1) was not detected by TEM. In one case, we identified a structure in a STEM tomogram that resembled the molecular pore. However, compared to multiple pores per DMV detected by (1), only a single pore spanned the membranes of the DMV in our study. Furthermore, a detailed view into the virus budding process at SMVs (Fig1) allowed temporal resolution of the assembly process.

We show that HPF-FS allows visualization of structures related to SARS-CoV2 infection comparable to advanced cryoEM techniques, opening the door for further studies. STEM tomography provided a detailed insight into SARS-CoV-2 virion assembly.

Fig1: Virtual STEM section of SARS-CoV2 virion assembly

(1) Wolff et al. (2020) Science

(2) Read et al. (2019) J Virol.

(3) Wieland et al (2021) Histochem Cell Biol.

(4) Kremer et al. (1996) J Struct Biol.

Fig. 1

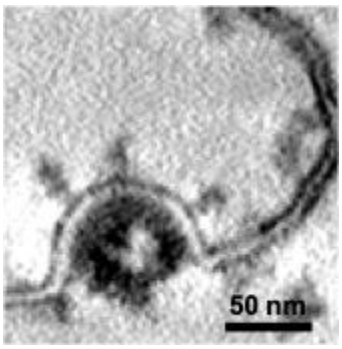

LS6.006

The emerging key features of latency in tobamoviruses

K. Richert-Pöggeler[1], R. Ilyas[1], H. Ziebell[1]

[1]Julius Kühn-Institut, Institute for Epidemiology and Pathogen Diagnostics, Braunschweig, Germany

Introduction

Tobacco mosaic virus (TMV), the first plant virus imaged in electron microscopy, is the type member of the genus *Tobamovirus*, family *Virgaviridae*.

Typically, tobamoviruses cause systemic infections with severe symptoms on the host leading to major yield loss. For new emerging and highly virulent members such as the tomato brown rugose fruit virus infecting tomato quarantine measures, apply.

The diseased phenotype can consist of mosaic patterns, leaf mottling and/or deformations in early infection stages that develop to reduced growth and necrosis in new emerging leaves. All diseased tissues are associated with major disruptions and reorganizations in their ultrastructure.

The tropical plant *Hoya* ssp. is susceptible to both virulent as well as latent tobamoviruses. Hoya tobamovirus 2 (HoTV-2) has been isolated from asymptomatic hoya plants (Gaafar et al., 2020) and serves as model system to investigate the ultrastructure of latent, asymptomatic tobamovirus infections.

Objectives

1. Analysis of serological relationship of HoTV-2 with other tobamoviruses
2. Identification of cellular features during latent (HoTV-2) compared to virulent (TMV) tobamovirus infections.
3. Characterization of viral interferences in mixed infections comprising HoTV-2 and TMV
4. Analyses of cellular ultrastructure in compatible and resistant tobacco species
5. Identification of HoTV-2 virions and viral RNA respectively in associated compartments of infected cells using IEM

Material and Methods

HoTV-2 was isolated from infected hoya plants using a bioassay. Therefore, healthy *Nicotiana* ssp. were mechanically inoculated with HoTV-2 infected hoya leaves. Negative stain and ISEM were used for virus detection in plant sap homogenates (Richert-Pöggeler et al., 2018; Gaafar et al., 2020). Embedding and generation of ultrathin sections were performed as described in (Erokhina et al., 2017).

Results

1. HoTV-2 is serological cross-reacting with Youcai mosaic virus (YoMV) antiserum (DSMZ, Germany) but not with other tested tobamoviruses.
2. Whereas phenotypically no differences of systemic HoTV-2 infections are visible when the virus is transmitted among asterid hosts from its primary host (*Apocynyceae*, *Gentianales*) to susceptible *Nicotiana* ssp. (*Solanaceae*, *Solanales*), the cellular ultrastructure indicates differences in viral replication. Only in *Solanales* virus particles were detected.
3. The number of virions was significantly reduced in latent (HoTV-2) compared to virulent (TMV) tobamovirus infections.
4. YoMV antiserum can be used in IEM, but lacks specificty for efficient immunogold labeling.

Conclusions

Ultrastructural analysis provided evidence that the asymptomatic phenotype is associated with reduced viral replication.

References

Erokhina, T. N., Lazareva, E. A., Richert-Pöggeler, K. R., Sheval, E. V., Solovyev, A. G., and Morozov, S. Y. (2017). Subcellular Localization and Detection of Tobacco mosaic virus ORF6 Protein by Immunoelectron Microscopy. *Biochemistry (Mosc)* 82, 60–66. doi: 10.1134/S0006297917010060

Gaafar, Y., Richert-Pöggeler, K. R., Hartrick, J., Lüddecke, P., Maaß, C., Schuhmann, S., et al. (2020). A new tobamovirus infecting *Hoya* spp. *New Dis. Rep.* 42, 10. doi: 10.5197/j.2044-0588.2020.042.010

Richert-Pöggeler, K. R., Franzke, K., Hipp, K., and Kleespies, R. G. (2018). Electron Microscopy Methods for Virus Diagnosis and High Resolution Analysis of Viruses. *Front Microbiol* 9, 3255. doi: 10.3389/fmicb.2018.03255

LS6.P001

Virus diagnosis can be easily optimized by the combination of electron microscopy and molecular biology

S. Richter[1], S. Revilla-Fernández[1]

[1]Austrian Agency for Health and Food Safety, Inst. for Veterinary Disease Control Moedling, Moedling, Austria

Introduction: In past, EM was involved with the detection and identification of a broad range of viruses some of which have impact on human, veterinary and wildlife health. However, since pathogen identification was performed mainly by molecular biology the use of diagnostic EM declined radically. With whole genome sequencing and metagenomic approaches the perspectives for molecular pathogen diagnostics changed from a primer-based testing system to a kit-independent diagnostic tool [Metzker, M.L. (2010): Genetic 11:31-45]. But molecular biology can still detect only genetic components of a pathogen whereas EM gives you a morphological picture of the virus. In the present study the method of EM virus screening followed by PCR described by Johnson at al. 2006 [J. Virol. Methods. 134:92-98] was further developed.

Material & methods: Viruses of different genera were investigated by negative staining in a TEM (Zeiss EM 906) at 80kv. Negative staining with 0,5% UA, 0,5% PTA or 4% NdAC was performed with pure or inactivated samples. Samples were provided from feces, cell supensions and biopsy material. Some samples were inactivated with 4% PFA; final PFA-concentration was 2%. For some samples the enrichment method by ultracentrifugation at 84000g (Beckmann airfuge) was used. The stained grids were exposed to the EM beam for 30-180min. Some grids were also stored 1 week before further processing. After EM analysis, virus RNA or DNA was obtained from the virus particles adhering to the 400 mesh copper grid(s) by placing the grid(s) into a vial and adding 180µl lysis buffer. The grid(s) were incubated in lysis buffer for 10min. Then 200µl of PBS was added and the solution with the grid(s) was vortexed for 1 min. The grid(s) was/were then removed before the sample was processed for nucleic acid amplification. The further steps of (RT-)PCR were routinely performed.

Results: Virus detection with EM combined with PCR was successful – in nearly all samples viruses could be detected by both methods. Since it is not possible to quantify the correct amount of viruses on a grid we will only present here a qualitative result (yes/no decision). Exposure to the electron beam does not significantly affect the diagnosis. Storage of grids for a short time (1 week) before processing to the lysis buffer also had no influence except for a slight decrease in viral copies. Enrichment by airfuge or eludation of more than one grid in 180µl lysis buffer naturally resulted in an increase of viral copies. Virus nucleic acids could be detected by PCR in pure or PFA inactivated samples. Viruses were also detected by PCR after using different stains. All used staining solutionsdid not inhibit essentially the amplification process. This is important in so far as NdAC (Neodymium (III)acetate), not toxic and easy to use, is an excellent stain for negative staining [Kuipers J. & Giepmans B, 2020. Histochemistry and Cell Biology 153:271-277]. It replaces the toxic and radioactive uranyl acetate.

Conclusion: Molecular biologists and electron microscopists should be aware that their methods bear a lot of uncertainties in their technical procedure. The results show that a combined EM/Molecular Biology method based on the same sample material eluted from a grid can be performed in an easy and fast procedure. Thus - with the simultanous use of both methods - diagnosis can be confirmed and false negative or positive diagnostic results can be prevented.

LS6.P002

Ultrastructural + mechanical properties of spidersilk or why do Schwann cells like spider silk?

L. Ploszczanski[1], K. Peter[1], G. Sinn[1], A. Naghilou[2], S. Stadlmayr[2], C. Radtke[2], H. Lichtenegger[1]

[1]University of Natural Resources and Life Sciences, Institute of Physics and Materials Science, Vienna, Austria
[2]Med Uni Vienna/Vienna General Hospital, Plastic and Reconstructive Surgery, Vienna, Austria

Spider silk (SPSI) has been established as one of nature"s most fascinating materials due to its unique properties. A remarkable application of the SPSI is its use in reconstructive medicine as nerve guidance structure/filament for nerve regeneration [1]. The Schwann cells (SCs), which are a crucial part of the nerve regeneration process adhere to SPSI and migrate along it to support axonal elongation [2]. SPSI degrades without inflammatory response or physiological pH changes. However, the interaction between the SCs and the silk and by that the SPSI properties, that promote SC adhesion are still unclear. The aim of this project is to elucidate material properties of SPSI, that are crucial for its unique performance in nerve regeneration. Not all spider silks show the same medical success, and we believe that properties such as composition, ultrastructure, and mechanical behaviour have a pronounced influence on the acceptance of SPSI by SCs. Therefore, by combining experiments consisting of in vitro studies and the material characterization of various SPSIs, the properties, which are responsible for the advanced success of SPSI in nerve regeneration, will be clarified.

Figure 1. Force-displacement curves and SEM micrographs of the native and autoclaved *N. edulis* MAG SPSI

- [1] Radtke, C., et al., *Spider Silk Constructs Enhance Axonal Regeneration and Remyelination in Long Nerve Defects in Sheep*. *PLOS ONE*, **2011**. 6(2): p. e16990.
- [2] Kornfeld T, et al. *Spider silk nerve graft promotes axonal regeneration on long distance nerve defect in a sheep model, Biomaterials,* **2021** Feb 2;271:120692. doi: 10.1016/j.biomaterials.2021.120692.
- [3] Riekel, C., et al., *Nanoscale X-Ray Diffraction of Silk Fibers,* Frontiers in Materials, **2019**. 6(315).

Fig. 1

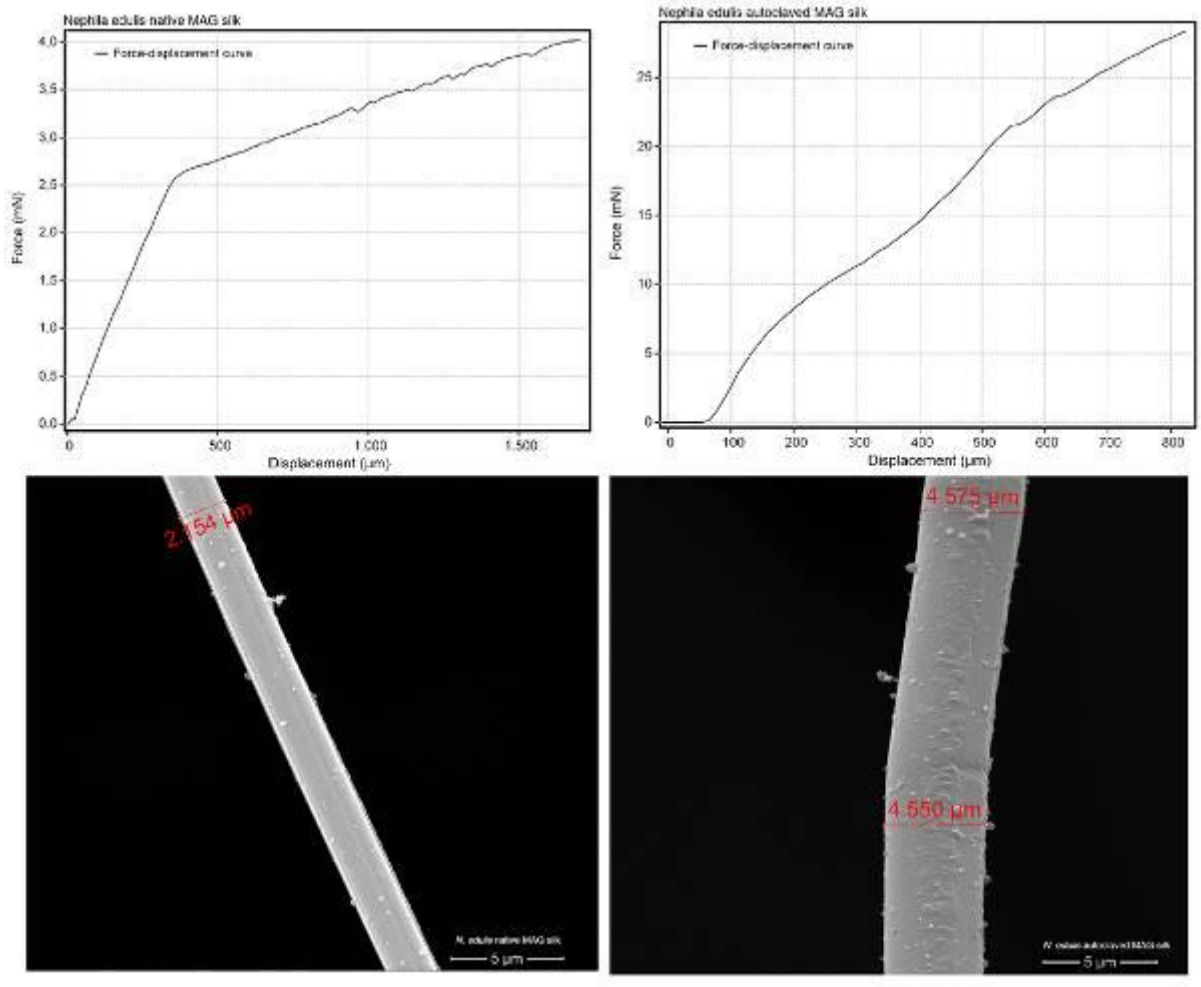

LS6.P003

Initiation of human cytomegalovirus secondary envelopment requires the gM/gN glycoprotein complex and its palmitoylation

C. Read (Villinger)[1,2], L. Cortez Rayas[2], R. Rogg[2], A. Omokinwa[1], D. Lieber[2], J. von Einem[2]

[1]Ulm University, Central Facility for Electron Microscopy, Ulm, Germany
[2]Ulm University, Institute of Virology, Ulm, Germany

The human cytomegalovirus (HCMV) belongs to the family of herpesviruses. As all herpesviruses, its complex maturation pathway includes two distinct envelopment processes in the host cell: primary envelopment on the way from the nucleus into the cytoplasm, and secondary envelopment in the cytoplasmic viral assembly complex (cVAC), the process that provides the virions with their final envelope. HCMV glycoprotein M (gM) forms a protein complex with glycoprotein N (gN), whose precise function in viral morphogenesis is poorly understood. Both proteins are highly conserved among herpesviruses and presumably exert similar functions in assembly and egress, with the gM/gN complex being essential in HCMV.

Ultrastructural analyses using TEM imaging and STEM tomography of high-pressure frozen and freeze substitution were applied in combination with viral mutant and siRNA knockdown experiments to clarify at which step of secondary envelopment the gM/gN complex is involved.

In wild-type virus infected cells, most capsids at the cVAC are enveloped and only a few partially tegumented but naked capsids can be found. Furthermore, naked and enveloped capsids are homogeneously distributed throughout the entire cVAC area/volume. In contrast, TEM of a palmitoylation-deficient gN mutant virus (TB-gNmutC123S) showed few enveloped virions at the cVAC, however, many partially tegumented and not enveloped nucleocapsids accumulated in the outer region of the cVAC. The centre of the cVAC was devoid of capsids. Detailed analysis of the various stages of secondary envelopment revealed that most nucleocapsids in TB-gNmutC123S-infected cells either did not contact cellular membranes at all or, if they did, showed no sign of membrane curvature that marks the initiation of secondary envelopment. In addition, large protein aggregates were found in and adjacent to the cVAC, surrounded by numerous naked, partially tegumented capsids. This ultrastructural phenotype was accompanied with a pronounced release defect. A very similar phenotype concerning capsid distribution, defect in secondary envelopment, protein aggregates and release defect was found in wild-type virus infected cells transfected with siRNA against gM. Furthermore, wild-type virus infection after inhibition of palmitoylation by 2-BP resulted in an altered nucleocapsid distribution in the outer region of the cVAC, as observed in the TB-gNmutC123S mutant.

Taken together, our results show that the gM/gN complex and its palmitoylation are essential for the initiation of secondary envelopment of partially tegumented capsids at the cVAC.

LS6.P004

Comparative ultrastructural studies of conidia and blastospores of the entomopathogenic fungus *Metarhizium brunneum*

R. G. Kleespies[1]

[1]Julius Kühn-Institut, Institut für Biologischen Pflanzenschutz, Dossenheim, Germany

Introduction

For biological control of economically important herbivorous insects, entomopathogenic fungi are efficiently used. They are established as an eco-friendly control tool in organic farming. Products of *Metarhizium brunneum* are successfully used against several pest insects, such as Western Corn Rootworm (*Diabrotica virgifera*), Japanese Beetle (*Popillia japonica*), Black Wine Weevil (*Otiorhynchus sulcatus*), and thrips (*Frankliniella occidentalis*) (https://ec.europa.eu/food/plant/pesticides/eu-pesticides-database/active-substances/?event=search.as). This fungus can be produced on selective solid and liquid artificial media, resulting in different spore types. On solid media, areal conidia are formed, while in liquid media often so-called blastospores are produced.

Objectives

Conidia and blastospores differ in their physiology, e. g. germination of blastospores is much faster compared to conidia. Ultrastructure of both spore types was investigated in transmission electron microscopy to elucidate differences in their metabolism and will be presented in several micrographs.

Materials & methods

For best results of observing ultrastructure of conidia and blastospores, the two spore types had to be fixed and embedded in different ways. Conidia were fixed in 3.5% glutaraldehyde, 2% osmium tetroxide and embedded in Methacrylate, while blastospores were fixed in 4% glutaraldehyde, 2% osmium tetroxide and embedded in Epon. Materials and methods protocol with detailed information will be provided.

Results

Studies on the ultrastructure of the two spore types illustrated that blastospores are in a physiologically active state and therefore capable of immediate germination, while conidia are in a kind of dormant condition. In contrast to conidia, blastospores have numerous mitochondria, many ribosomes and endoplasmic reticulum as well as densely enriched storage substances (Fig. 1).

Fig. 1. Micrograph of an ultrathin section of a *Metarhizium brunneum* blastopore. Active metabolism is obvious by numerous ribosomes (r), mitochondria (m), droplets of storage substances (o = oil, l = lipid) and by endoplasmic reticulum (er), n = nucleus.

Perspective

Production of blastospores of *M. brunneum* in liquid media is fast, and enables a high number of spore yield. One advantage of blastospores is their ability to germinate within a few hours. Therefore, penetration through insect cuticle and killing of its host can proceed in shorter time compared to conidia. Entomopathogenic fungi are susceptible to UV-light, high temperatures and dryness. The application of *M. brunneum* blastospores could therefore be of great advantage for biocontrol of pest insects.

Fig. 1

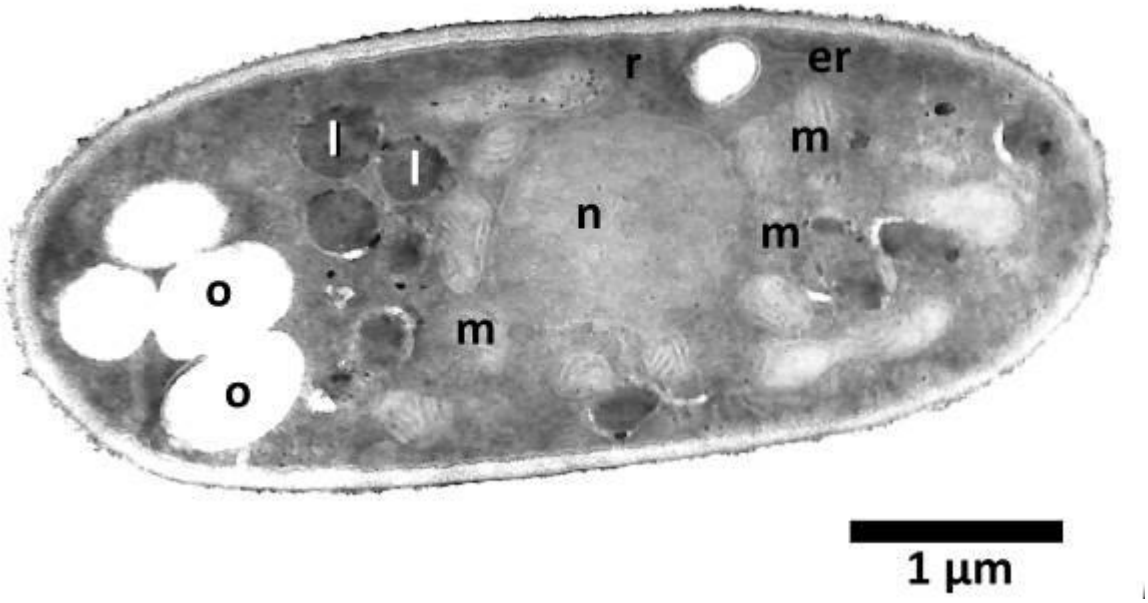

LS6.P005

Ultrastructural investigation of samples from monkeypox virus and coronavirus infected patients using thin section electron microscop

M. Laue[1]

[1]Robert Koch Institute, Advanced Light and Electron Microscopy (ZBS 4), Berlin, Germany

The recent outbreak of monkeypox and the ongoing COVID-19 pandemic emphasize the importance of studying infectious diseases as one of the major threats of human health. While molecular diagnostics is sensitive, specific and efficient in the diagnosis of viruses, immunohistochemistry and in-situ hybridization techniques allow the localization of virus protein or nucleic acids in patient samples by using special probes at the light microscopy level and its correlation with classical histopathology. However, all of these methods only detect either molecules of viruses or effects of virus infection and not the intact virus itself which is the infectious unit. Electron microscopy (EM) is the only technique which is capable to directly identify virus particles and their precursor structures in patient samples by using their typical morphological features (size, shape, special surface pattern) [1]. The reliable identification of viruses in patient samples is important to discriminate between direct and indirect effects caused by the infection and, thus, for the understanding of the pathogenesis of the disease, which, at the end, is the basis for a better treatment of patients.

Thin section EM of patient samples (e.g. from biopsies or autopsies) offer the possibility to localize virus particles in the cellular context of the affected tissue and to correlate it with (histo-) pathological findings. However, investigation of the complex ultrastructure of human tissue and identification of virus particles need experience which seems to vanish as the many mis-interpretations of putative coronavirus particles published during the last years demonstrate [2, 3]. Here, I present the strategies (e.g. sampling, sample preparation for EM, microscopy) which we have applied to study the ultrastructural pathology of coronavirus and monkeypox virus infection in patient material (see Figure) and what we have learned from the results [e.g. 4, 5].

Figure Caption:

(A) Mature monkeypox virus particles in the cytoplasm of a fibroblast in the lamina propria mucosae of the colon. Different section profiles of the complex mature virus particles are seen, e.g. a side view (arrowhead) showing the dumbbell-shaped core and a view in top-down direction (arrow) which reveals the brick-shaped form of the virus particle. (B) Part of an isolated naso-pharyngeal ciliated mucosa cell which is regularly found in extracted swab material used for PCR-testing. Coronavirus particles are seen in the extracellular space (arrows) among the base of the cilia and within membrane-bound compartments (arrowheads) of the cytoplasm. Scale bars = 200 nm.

References:

[1] Miller (1986) Journal of Electron Microscopy Technique (doi.org/1002/jemt.1060040305)

[2] Dittmayer et al. (2020) The Lancet 20 (doi.org/10.1016/ S01406736(20)320791)

[3] Krasemann et al. (2022) eBioMedicine (doi.org/10.1016/j. ebiom.2022.104193)

[4] Meinhardt et al. (2021) Nature Neuroscience (doi.org/10.1038/s41593-020-00758-5)

[5] Cortese et al. (2022) Virchows Archive (doi.org/10.1007/s00428-022-03308-5)

Fig. 1

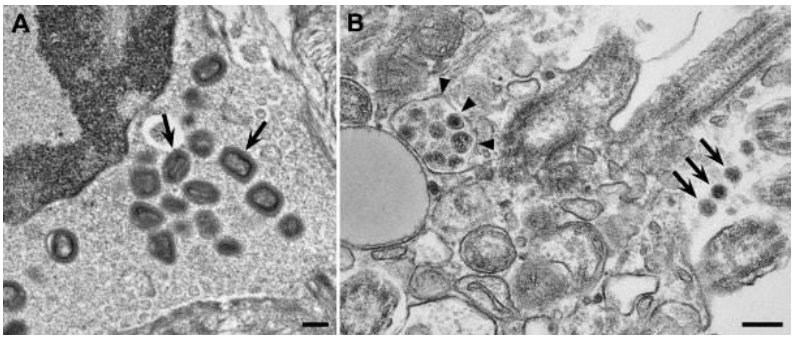

LS6.P006

Histochemical examination of vascular tissues of PCR-negative patients after SARS-CoV2 infection

S. Gonca[1], O. Şen[2], S. Eltutan[2], Ü. Uslu[3], G. Erkanli Şentürk[4], S. Kurnaz Özbek[1]

[1]Kocaeli University Faculty of Medicine, Histology and Embryology, Kocaeli, Turkey
[2]Istanbul Mehmet Akif Ersoy Thoracic and Cardiovascular Surgery Training and Research Hospital, Department of Cardiovascular Surgery, Istanbul, Turkey
[3]İstanbul Medeniyet University Faculty of Medicine, Histology and Embryology, Istanbul, Turkey
[4]Istanbul Üniversitesi-Cerrahpaşa, Cerrahpaşa Faculty of Medicine, Histology and Embryology, Istanbul, Turkey

1. Introduction

The Coronavirus (Covid-19) disease emerged in 2019 December in Wuhan District of China, was accepted as a pandemic by WHO due to its rapid spread and a mortality rate of 3.4% as determined in 2020 March (1).

Although the main effect of the Covid-19 is on the respiratory system, as the majority of patients showed signs of cardiac damage, cardiovascular features of the disease began to be taken into consideration. Especially the mortality and morbidity rates of the disease are thought to be connected to circulatory system (CVS) involvement (2).

More than a direct viral effect on endothelial cells or perivascular inflammation, the profound decrease in pericytes and observed apoptosis strongly suggest that the alteration of pericytes by a direct effect of SARS-CoV-2 could be the initial trigger of the micro-vasculopathy (3,4).

2. Objectives

The study of the effect of the SARS-CoV2 infection on the vascular structure and determining the morphological defects in endothelial cells and vascular wall will contribute crucially to the enlightenment of the pathogenesis and the treatment by providing valuable information.

3. Materials & methods

Saphenous vein and mammarial artery samples were obtained from postcovid and SARS-CoV2 negative patients that undergo bypass graft operation. And then, we investigated alpha smooth muscle actin (α-SMA) immunoexpression.

4. Results

Alpha smooth muscle actin activity in the saphaneous vein increased dramatically in post Covid-19 patients compared to the control group. Whereas, a significant increase in same marker activity was observed in the mammarial artery of the control group.

5. Conclusion

α-SMA activity observed in the patient group veins is an evidence for smooth muscle cell proliferation. Whereas decrease of the same marker in the arteries supports fibrosis.

Although the precise mechanism for the development of myocardial or vascular injury associated with COVID-19 is not fully understood, a combination of direct and indirect pathogenic factors, such as ACE2-mediated SARS-CoV-2 infection of cardiomyocytes, hypoxia and cytokine storm, may contribute to the development of myocardial and vascular injury and other adverse events which aggravate conditions and increase mortality.

References

1. Sohrabi, C., Alsafi, Z., ... & Agha, R. (2020). World Health Organization declares global emergency: A review of the 2019 novel coronavirus (COVID-19). International journal of surgery, 76, 71-76.
2. Guo, T., Fan, Y., ... & Lu, Z. (2020). Cardiovascular implications of fatal outcomes of patients with coronavirus disease 2019 (COVID-19). JAMA cardiology, 5(7), 811-818.

3. Cardot-Leccia, N., Hubiche, T., … & Passeron, T. (2020). Pericyte alteration sheds light on micro-vasculopathy in COVID-19 infection. *Intensive care medicine*, *46*(9), 1777-1778.
4. Geng, Y. J., Wei, Z. Y., … & Castriotta, R. J. (2020). Pathophysiological characteristics and therapeutic approaches for pulmonary injury and cardiovascular complications of coronavirus disease 2019. *Cardiovascular Pathology*, *47*, 107228.

Fig. 1A. SARS-CoV-2 negative mammarial artery. Especially in the media layer prominent α-SMA distribution is seenx20. **B.** SARS-CoV-2 positive mammarial arter. Especially in the media layer, immunoexpression of the α-SMA is decreased x20.

Fig. 2A. SARS-CoV-2 negative saphenous ven. Whole vascular wall showed immunostaining of the α-SMAx20. **B.** SARS-CoV-2 positive saphenous ven. Vascular wall showed immunostaining of the α-SMAx20.

Fig. 1

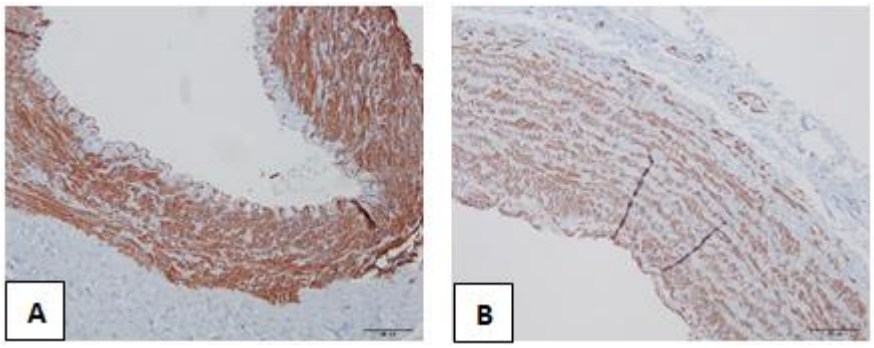

Fig. 2

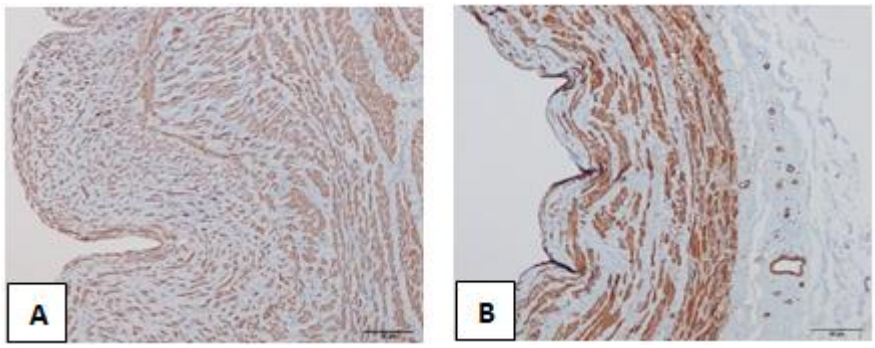

LS7.001-invited

Combining cryo-microscopy and expansion microscopy to reveal the molecular architecture of the cell

P. Guichard[1]

[1]University of Geneva, Dept of Molecular and Cellular Biology, Geneva, Switzerland

The centriole (also called basal body) is an evolutionary conserved organelle that coordinates fundamental biological processes including cell division, cellular signaling, and cell motility. This organelle, 500 nm long and 250 nm in diameter, is composed of about 100 different proteins, some of which have been associated with human diseases. How these proteins are organized at the level of the centriole architecture and how associated mutations could be involved in pathologies is still poorly understood. I will present the latest work from my laboratory, which tackle these fundamental structural cell biology questions using cryo-tomography, cell biology, and ultrastructure expansion microscopy (U-ExM) methods.

Fig. 1

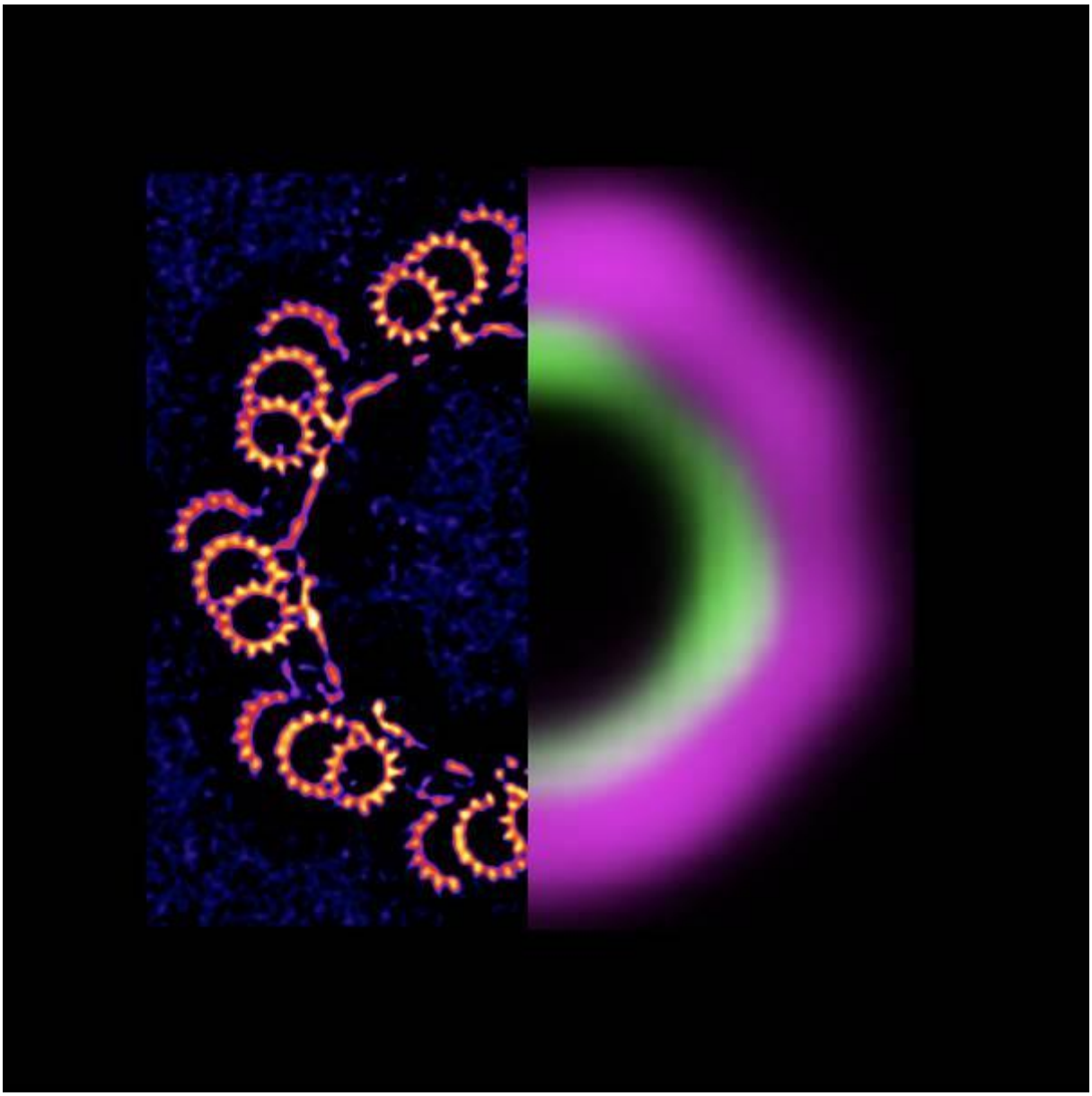

LS7.002-invited

New ways to tackle challenges in sample preparation in single particle cryoEM for improved sample quality and time-resolved studies

S. Muench[1,2], R. Thompson[1,2]

[1]University of Leeds, Biomedical Sciences, Leeds, United Kingdom
[2]University of Leeds, Leeds, United Kingdom

Recent developments in the electron microscopy (EM) field have led to a step change in our ability to solve the "high resolution" structure of previously intractable systems. This is exemplified by the sudden expansion in membrane protein structures solved revealing new insights into structure, mechanism and regulation. Advances in the size of data sets that can be collected and processed by electron microscopy (EM) and the broad range of samples that can be studied makes it ideally suited to time-resolved studies. This talk will describe the ongoing developments of a cryo-electron microscopy grid preparation device that permits rapid mixing and vitrification of samples within ~10 ms allowing us to pull out non-equilibrium states on a range of systems from membrane proteins to viruses. Moreover, rapid grid preparation has also provided new insights into factors that can be detrimental to sample preparation and the talk will discuss ways to improve grid making for single particle cryoEM. A significant focus of the talk will be in our new findings in factors that are detrimental to sample preparation, especially those caused by interactions with the air-water-interface. The talk will conclude with our current overview of the challenges in sample preparation for both conventional cryoEM and time-resolved studies and look towards future developments in the field.

LS7.003

Scanning electron microscopy (SEM) preparation and imaging techniques to visualize cell-material interaction on hydrogels and thermoplastic printed scaffold

M. Koch[1], P. Gudeti[2], M. Gladysz[3], M. Wlodarczyk-Biegun[2,3]

[1]INM - Leibniz Institute for New Materials, Physical Analytics, Saarbrücken, Germany
[2]Silesian University of Technology, Biotechnology Centre, Gliwice, Poland
[3]Zernike Institute for Advanced Materials, Polymer Science, Groningen, Netherlands

1. Introduction

Among several imaging methods to study cell-material interaction, Scanning Electron Microscopy (SEM) is capable of resolving both materials and cellular structures down to the nanometer scale. However, Scanning Electron Microscope typically works under high vacuum conditions, which requires special sample preparation. Cells and water containing substrates need to be dehydrated and dried before investigation at room temperature. Dehydration using a row of water/ethanol mixtures with increasing ethanol concentration and drying using hexamethyldisilazane (HMDS) is an established preparation route to visualize cells on vacuum stable substrates by SEM. For water-containing substrates like hydrogels, cryo-SEM or ESEM can be used to study cells material interactions without morphological changes of the substrate due to drying (1).

2. Objectives

Here we show different preparation and imaging protocols to visualize with minimalized artifacts resulting from sample preparation, cells" performance (i.e. distribution and morphology) on two types of bio-fabricated substrates commonly used for tissue engineering – hydrogels and thermoplastic (polycaprolactone, PCL) printed scaffolds.

3. Materials & methods

3-dimensional cell culture scaffolds were obtained using 3D printing: hydrogels samples were obtained via extrusion process of alginate-based ink, PCL constructs were prepared using melt electrowriting approach. Mouse fibroblast (NIH3T3) cells were cultured on the scaffolds and visualized using SEM. Cell-seeded PCL scaffolds were investigated by SEM after dehydration and drying using a row of water/ethanol mixtures and HMDS. Hydrogel samples were imaged using cryo-SEM and ESEM following optimized protocols.

4. Results

SEM of PCL scaffolds allowed detailed observation of cell-material interactions. Focal adhesion points after 3 days of growth were frequently observed with high resolution. Cells grown inside the PCL scaffold can be imaged by embedding the dehydrated and dried sample in frozen ethanol and cutting thin slices by a blade under a stereomicroscope.

Cryo-SEM of hydrogel samples, following the proposed preparation procedure, allowed to study cell attachments without morphological change of substrate and cells. For the investigation of cells and substrates in fully wet/swollen conditions, ESEM was performed at 3°C and 750 Pa water vapor pressure. Due to the limited field of view (diameter of the pressure limiting aperture is 500 µm) stitching of individual images is necessary to visualize the complete scaffold. Using ESEM starting at 3°C and 750 Pa water vapor pressure an in-situ freeze-drying experiment shows the morphological change of gelatin from a dense hydrogel to a porous polymer structure during temperature and pressure decrease according to the pressure-temperature phase diagram of gelatin (see Fig. 1).

5. Conclusion

SEM is a powerful tool to study cell-material interactions. For water-containing substrates like hydrogels cryo-SEM or ESEM can be used to prevent morphological changes of the substrate due to drying inside vacuum/under atmospheric conditions at room temperature. SEM of freeze-dried samples should be avoided when characterizing hydrogel-based materials in detail.

1. *Koch, M. and Wlodarczyk-Biegun, M. K., Bioprinting 20, e00098 (2020)*

Fig. 1: Morphological change of aqueous 1.8 wt.% gelatin during in-situ freeze-drying using ESEM.

Fig. 1

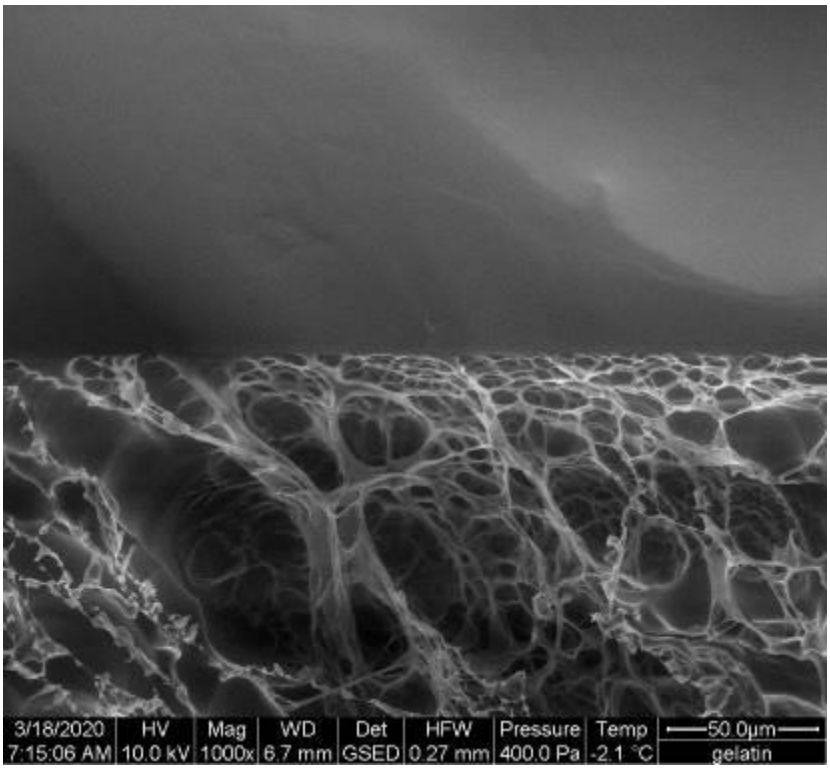

LS7.004

Breaking the ice with new Samples: cryo sample preparation during field studies

A. M. Steyer[1], K. Mocaer[1], C. le Kieffre[2], J. Decelle[2], Y. Schwab[1]

[1]European Molecular Biology Laboratory, Heidelberg, Germany
[2]Laboratoire Physiologie Cellulaire & Végétale, Grenoble, France

The set of tools combined in correlative light and electron microscopy have seen new developments in the last couple of years allowing to address new research questions or revisiting old questions in a different way. The ability to combine dynamic and targeted imaging in the light microscope to their ultrastructural composition in electron microscopy provides insights into functional traits, subcellular dynamics and ultrastructure on a single organelle level. At the same time new developments for software and hardware for high-end scanning and transmission electron microscopes have allowed the resolution of protein structures inside cells to be pushed to atomic level. Combining advanced sample preparation strategies and being able to target precisely subcellular regions with high-end transmission electron microscopy has allowed unprecedented insights into biological processes. Sample preparation in a standardized, well-controlled laboratory environment with humidity-controlled rooms and access to ideal set-ups has been becoming rather standard. As a new emerging field of research, planetary biology spanning multiple ecosystems has the aim to understand how microbes, plants and animals respond to each other and to their environment. To be able to achieve this goal, field studies with controlled laboratory research are combined to understand the influence of environmental parameters on the molecular mechanisms underlying biological processes.

To be able to use newest imaging technologies on field samples, we have been working on bringing different high-end sample preparation tools such as plunge freezer and high-pressure freezer to the field to prepare samples in the best possible way. Following pilot studies collecting Plankton from different ecological habitats in warmer and colder climates, during the TREC (Traversing European Coastline) project and beyond, EMBL mobile laboratories will bring this cutting-edge technology and methodology to the field.

Here I would like to discuss cryo workflows, different sample preparation strategies and challenges of sample preparation during field expeditions. I will show sample preparation for volume electron microscopy using the focused ion beam scanning electron microscope workflow under cryogenic conditions, using cryo light microscopy to select structures of interest in different species of Plankton, followed by focused ion beam scanning electron microscopy at cryogenic temperatures to acquire 3D data.

Figure 1. Overlay of a cryo confocal image and scanning electron microscopic image of Acantharia (marine skeleton-bearing planktonic protists) (left, scale bar 50 µm). Green: autofluorescence of host, red: chlorophyll of symbionts (microalgae). Overlay of cryo-volume imaging FIB-SEM and cryo-confocal imaging (right, scale bar 5 µm).

Fig. 1

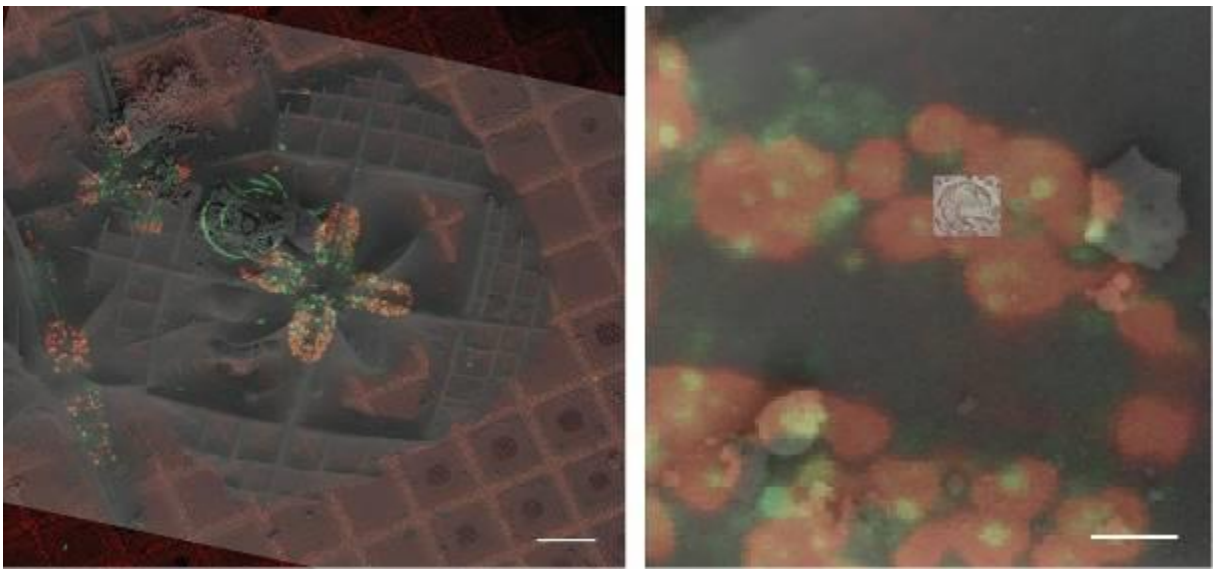

LS7.005

Tokuyasu sample preparation for TEM, STEM and SEM

V. Oorschot[1]

[1]EMBL Heidelberg, EMCF, Heidelberg, Germany

Cell biologist are frequently looking for tools to localize proteins of interest in biological samples. **Specific antibodies** are used to solve the questions on a fluorescent light microscopy level. But one would prefer to resolve the intracellular structure together with the immunolabeling pattern at higher resolution (e.g. electron microscopy). For IEM, samples are chemically fixed and embedded in a support layer. Ultrathin sections of 70 nm are cut and immunolabelled with the antibody of choice followed by a binding step with an electron dense Gold particle (visible in EM).

The most efficient immunolabelling procedure is the **Tokuyasu** cryosectioning technique. Hereby a biological sample is fixed with mild chemicals like glutaraldehyde and paraformaldehyde (either directly or by High Pressure Freezing and Automatic Freeze Substitution). After fixation the sample is embedded in a gelatin support, infused in sucrose and frozen in LN2. Thin sections are cut in a ultracryotome at -120˚C using a diamond knife. Sections are retrieved, thawed, placed on EM-grids and immunolabelled followed by EM analysis. Unfortunately, high antigenicity only goes together with mild fixation and therefor good morphology is sacrificed.

The protocols are challenging and skill demanding. The Tokuyasu method can be applied to a large range of samples including small organisms, tissue samples, and cells. Sections can be used for immunofluorescent- and high-resolution Gold labeling. In this presentation the focus will be on the pitfalls and difficulties of Tokuyasu protocols.

LS7.006

High temporal resolution electron microscopy (flash-and-freeze) reveals vesicle compound fusion at ribbon synapses of zebrafish retina

S. Markert[1], T. Mulligan[2], L. Zhang[2], J. Thierer[2], J. Mumm[2], S. Watanabe[2]

[1]University of Würzburg, Imaging Core Facility, Würzburg, Germany
[2]Johns Hopkins University, Baltimore, MD, United States

Our eyes offer us a window into the world. This is made possible first and foremost by the photoreceptor neurons in our retinas. These neurons perceive light and translate it into electrical nerve signals that our brain can understand and process. This translation from light to nerve signals is achieved at so-called ribbon synapses. There, neurotransmitter is released from vesicles that are lined up at ribbon structures. The amount of transmitter release over time is inversely correlated with light intensity: more light, less transmitter. In the dark, the rate of release is at maximum. In particular, right at light-dark transition, a huge amount of transmitter is released within milliseconds. It is unknown how such bursts of release can be achieved in such a short amount of time. The field has been arguing about possible models for decades. The process is too fast, and vesicles are too small to visualize by live-cell fluorescence microscopy. However, with a new technique called flash-and-freeze, this question can finally be answered.

The flash-and-freeze technique is uniquely able to visualize cellular processes with extremely high spatial *and* temporal resolution. Retinas of adult zebrafish were subjected to light-dark transitions to elicit the transmitter bursts. During the bursts, the retinas were frozen under high pressure within milliseconds. This halts the cellular processes that produce the bursts, thus enabling us to examine these extremely fast events. We then use electron microscopy to visualize the ribbon synapses with nanometer-resolution.

Our data show unusually large vesicles at synaptic ribbons several milliseconds after light-off. Fusion events where sometimes captured in action. At later time points, these large vesicles are not observed anymore. In light-on controls, all vesicles remain their usual size.

Our data strongly suggest that vesicles undergo so-called compound fusion: They are lined up at the ribbon to fuse with each other to form super-vesicles. These giant vesicles then release a huge amount of transmitter at once, thus explaining the bursts. We are now investigating the molecular mechanisms of compound fusion.

The flash-and-freeze technique can be adapted to investigate other fast cellular processes at extremely high spatial and temporal resolutions.

Fig. 1

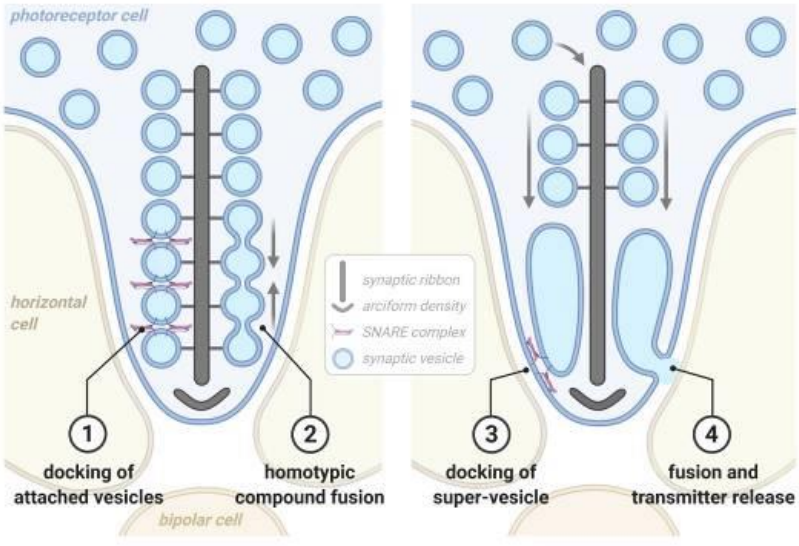

Fig. 2

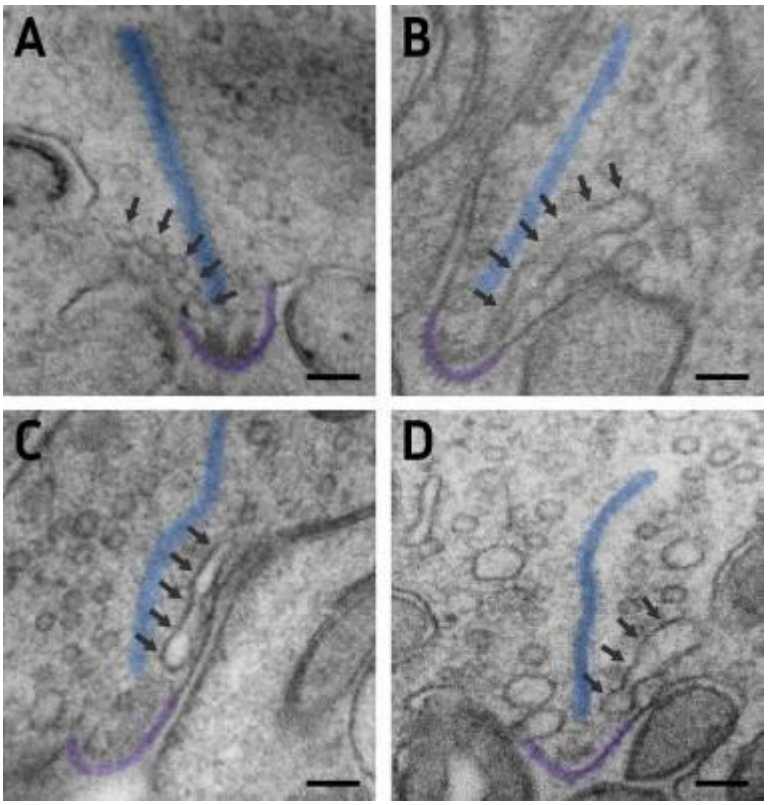

LS7.P001

naRNA is a canonical neutrophil extracellular trap component

B. Sailer[1], I. Koch[1], F. Bork[2], A. N. R. Weber[2], K. Hipp[1]

[1]Max Planck Institute for Biology Tübingen, EM Facility, Tübingen, Germany
[2]University of Tübingen, Interfaculty Institute for Cell Biology, Department of Immunology, Tübingen, Germany

Neutrophil extracellular traps (NETs) have been established as a key feature of cellular innate immunity that is mediated by polymorphonuclear neutrophils (PMNs), the primary leukocyte population in humans. NETs form web-like structures that are composed of DNA, histones, and antimicrobial proteins. They trap and kill microbial invaders thereby enhancing host defense. Whilst DNA has been in focus as a primary structural component of NETs, we here characterize naRNA (NET-associated RNA), as a new canonical, abundant, and largely unexplored NET component.

In order to contribute to the understanding of the localization of these RNAs and the composition of the NET structures we have analysed PMNs on the ultrastructural level both by scanning and transmission electron microscopy. Immunolabeling using anti-rRNA antibodies confirmed the presence of RNA in NET structures on ultrathin sections of plastic embedded samples corroborating fluorescence microscopy date. To show the localization of RNA to the NET structures also in SEM we established an immunolabeling protocol for this kind of samples.

LS7.P002

Electron microscopic analysis of wrapping glial differentiation in adult Drosophila

S. Rey[1], H. Ohm[1], C. Klämbt[1]

[1]WWU Münster, Neurobiology, Münster, Germany

Axonal wrapping starts in the developing Drosophila larva and is similar to the non-myelinating Schwann cell in the vertebrate PNS. Myelin is a more sophisticated form of axonal wrapping in vertebrates but has not been reported for Drosophila so far. Nevertheless, myelin-like structures have been described in several invertebrate species, e.g., in earthworms, shrimps, prawns, and cockroaches. Here we demonstrate that myelin-like structures also exist in the Drosophila nervous system. Abutting the myelinated axon segments, we found a prominent lacunar system formed by glial cell processes. The glial lacunar system comprises an exceptionally wide, liquid-filled extracellular space that possibly constitutes an ion reservoir meeting the high demand for ions needed for sustained firing of action potentials. We therefore analysed the localization of the only voltage-gated sodium channel encoded by the Drosophila genome termed Para. Antibody labelling indicates that Para predominantly localizes in motor axons at a position that coincides with the localization of the glial lacunae. To further test this we labelled the endogenous Para protein by inserting an Apex2 encoding exon, which allows to detect Para protein localization in the electron microscope. Our findings will be discussed in the light of the evolution of fast and precise signal transduction in the peripheral nervous system.

LS7.P003

Constructing artificial membrane structures on graphene to resolve membrane protein conformational dynamics

L. Jorde[1], J. Wong[1], D. Januliene[1], J. Piehler[2,3], C. You[2,3], A. Möller[1]

[1]University of Osnabrück, Structural Biology, Osnabrück, Germany
[2]University of Osnabrück, Biology/Chemistry, Osnabrück, Germany
[3]University of Osnabrück, Center of Cellular Nanoanalytics (CellNanOs), Osnabrück, Germany

Mechanistic understanding of membrane-based processes requires detailed insights of the membrane environment and its impact on protein structure and function. Membrane properties such as fluidity, curvature, and lipid phase segregation have tremendous influence to membrane protein structure. To explore the conformational spectra of membrane protein on variable membrane structures, we tether liposomes as membrane curvature models and fuse them into planar lipid bilayer on graphene-coated substrate. For this purpose, ultra small unilamellar vesicles (USUVs) are prepared with a mean hydrodynamic diameter of 40±15nm. Using biotin-streptavidin interaction, stable immobilization of the USUVs on graphene-supported lipid monolayer (GSLM) is confirmed by negative staining electron microscopy (EM). The USUVs can thus be used to integrate individual ABC transporter MsbA per liposome on graphene-coated EM grid to determine the correlation of protein structure with membrane curvature. By fusing the USUVs on GSLM on glass substrate, fluorescence recovery after photobleaching reveals a fluidic membrane structure. Based on these artificial membrane structures on graphene, we aim to combine single molecule fluorescence microscopy and cryo-EM to correlatively investigate the time-resolved conformational dynamics of membrane protein in controlled membrane environment.

LS7.P005

A fast and uranium-free method for platinum replica preparation of membrane cortices

Y. Tsytsyura[1], N. Glyvuk[1], J. Duan[1], J. Klingauf[1]

[1]Institute of Medical Physics and Biophysics, Cellular Biophysics, Münster, Germany

Conventional room-temperature preparation of biological samples for electron microscopy (EM) is often time-consuming and involves treatment of the sample with different fixation agents to stabilize the structure and enable its later observation in a vacuum under a high-energy electron beam. The fixation agents in general are extremely hazardous chemicals, some of which are subject to strict regulations, with uranium salts being the most complicated due to radioactivity. Some alternatives to uranium were proposed, but their use is mostly limited to post-staining of sections or negative staining. Here we propose to expand the range of their use by substituting uranyl acetate (UA) in the production of the platinum replicas from cell cortices. Our sample preparation procedure is based on previously published methods (1, 2). Cells, cultured on the glass coverslips, washed off culture medium with Ca^{2+}-free Ringer solution, additionally "glued" using PLL 0.1 mg/ml, swollen in hypotonic buffer (1/3 of normal PHEM concentration), and subsequently unroofed by sonication in PHEM buffer of normal concentration. Cell cortices were immediately fixed in a mixture of glutaraldehyde and tannic acid in PHEM. After extensive wash with deionized water the samples were post-fixed with different metal salts in water, then dehydrated in ethanol series followed by hexamethyldisilazane, and air dried instead of critical-point drying to spare time. Platinum replicas were made by coating samples with 2 nm Pt/C; no baking out with carbon was used. Replicas were released with the help of HF acid and after extensive wash transferred to Formvar-coated 75 mesh TEM grids. Images were then acquired with a high-resolution SEM Hitachi S5000 or TEM Philips CM10 with bottom-mounted camera TemCam F-416 (in the latter case the images were digitally inverted to resemble SEM). The quality of all samples was compared to UA-treated sample taken as standard. Experiments revealed that UA could be substituted by gadolinium, hafnium, or iron chloride, as well as acetate salts of gadolinium, neodymium, samarium, or ammonium molybdate or osmium tetroxide without losing sample quality. Negligible sample thickness after unroofing allowed to shorten the time down to two hours from starting the preparation to image acquisition. With little modifications, it could be adapted for CLEM or gold-immuno EM by altering the primary fixation and introducing immunolabelling prior EM preparation procedure, and thus is a good alternative to existing routines.

1. Heuser, J. Traffic, 2000, 1, 545-52
2. Sochacki, K. A. & Taraska, J. W. 2017, 1663, 219-230

IM1.001-invited

Micron-sized magnetic multipole devices for charge particle optics

A. Lubk[1,2], R. Huber[1], F. Kern[1], D. Karnaushenko[3], A. Thampi[1], B. Büchner[1,2], D. Karnaushenko[3], O. Schmidt[3]

[1]Leibniz Institute for Solid State and Materials Research Dresden, Institute for Solid State Research, Dresden, Germany
[2]TU Dresden, Institute of Solid State and Materials Physics, Dresden, Germany
[3]TU Chemnitz, enter for Materials, Architectures and Integration of Nanomembranes, Chemnitz, Germany

Introduction: Tunable electromagnets and corresponding devices, such as magnetic lenses or stigmators, are the backbone of numerous charged particle optical (CPO) instruments, such as electron microscopes. However, the built-in electromagnets are typically macroscopic conducting coils, which cannot generate swiftly changing magnetic fields due to their large resistivity and inductivity, require active cooling, and are structurally bulky. These restriction make them unsuitable for fast beam manipulation and miniaturized applications. To overcome these limitations, miniaturization of tuneable magnetic devices is required.

Objectives: We seek on-chip microsized magnetic charged particle optics, which can be fabricated by microprocessing technologies, such as lithography. These devices should generate alternating magnetic fields of several 100 mT at frequencies up to GHz, supplying sufficiently large optical power for CPO applications. That particular includes fast spatio-temporal electron beam modulation such as electron beam deflection, focusing, and wave front shaping.

Methods: Recently developed microcoil technology [1] allows overcoming the obstacles haunting miniaturization of magnetic CPO devices[PR3]. These microcoils (diameter: several 10 µms) are fabricated via lithography-patterned microelectronic structures, which assemble into 3D tubular architectures due to strain engineering within the multilayered polymer structure (Fig. 1a). The current-carrying copper layer of more than 100 nm thickness sustains more than 100 mA current in vacuum that generates a field of several mT depending on the number of windings. That field is further increases by introducing a soft-ferromagnetic wire (radius 5µm, saturation magnetization 0.2T, relative permeability 1000) into the zero-pitch microcoils (Fig. 1a).

Results: Adapting the previously described microcoil technology, the whole platform was fabricated directly around an aperture plate in a multipolar arrangement (i.e., as monopole, dipole and quadrupole, Fig. 1b). The micron-sized devices were then mounted in dedicated high-frequency aperture holders, facilitating fast switching of the devices within a TEM. With that, alternating magnetic fields of about ±100 mT up to a hundred MHz, supplying sufficiently large optical power for numerous CPO applications is feasible (Fig. 2), including fast beam blanking and focusing for stroboscopic imaging. Notably, the quadrupole devices allow switchable line foci of a focal length of ca. 5 cm at 300 kV acceleration voltage, which is comparable to macroscopic bulk devices [2].

[1] D. Karnaushenko, T. Kang, V. K. Bandari, F. Zhu, and O. G. Schmidt. Adv. Mat. 32.15 (2020), 1902994.

[2] R. Huber, F.L. Kern, D. Karnaushenko, E. Eisner, P. Lepucki, A. Thampi, A. Mirhajivarzaneh, C. Becker, T. Kang, S. Baunack, B. Büchner, D. Karnaushenko, O. Schmidt, A. Lubk, Nat. Comm. 13 (2022), 3220

[3] We acknowledge funding from the European Research Council (ERC) under the Horizon 2020 research and innovation program of the European Union (grant agreement no. 715620).

Fig.1: Fabrication of microcoil charge particle optic devices: (a) strain-engineered multilayer architecture and rolling process. (b) Schematics of quadrupole devices and SEM image of central part of QP device.

Fig.2: Performance characteristics of quadrupole device. Switchable line foci at 70 mA coil current and high-frequency deflection measurement demonstrating ca. 100 MHz cut-off frequency.

Fig. 1

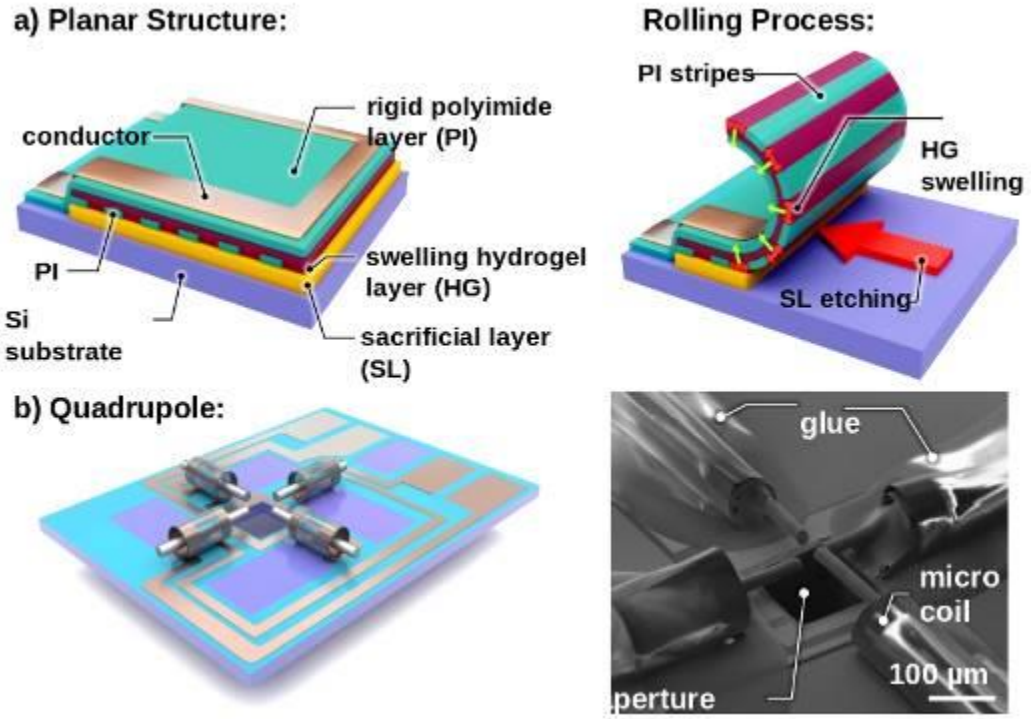
a) Planar Structure:
conductor
rigid polyimide layer (PI)
PI
swelling hydrogel layer (HG)
Si substrate
sacrificial layer (SL)
Rolling Process:
PI stripes
HG swelling
SL etching
b) Quadrupole:
glue
micro coil
100 µm
perture

Fig. 2

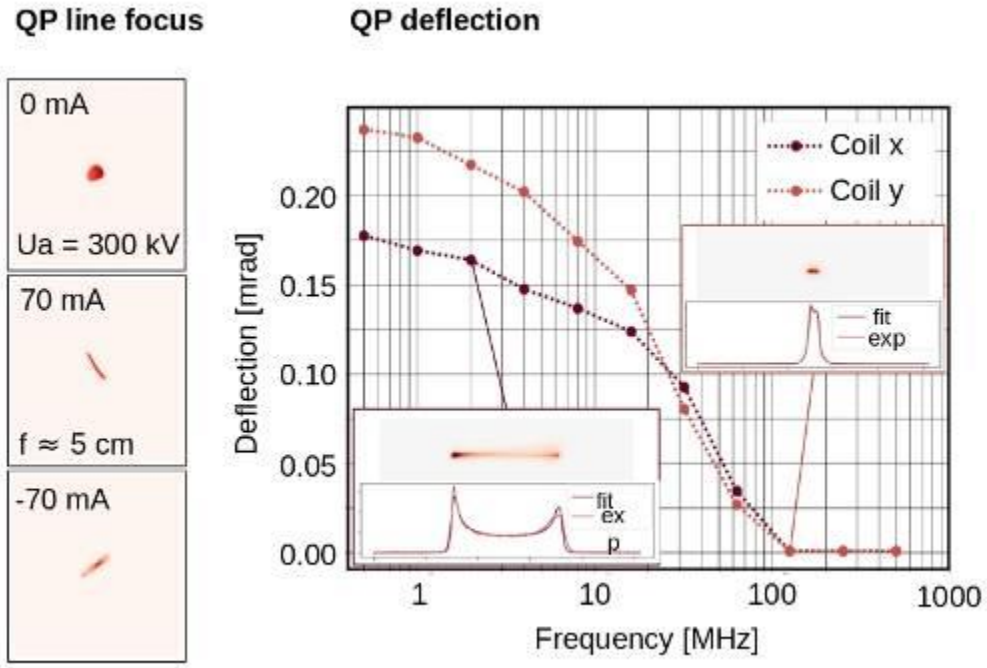
QP line focus
0 mA
Ua = 300 kV
70 mA
f ≈ 5 cm
-70 mA
QP deflection
Coil x
Coil y
fit
exp
Deflection [mrad]
0.20
0.15
0.10
0.05
0.00
1
10
100
1000
Frequency [MHz]

IM1.002-invited

Coupling electron microscopes with lasers: ultrafast charge dynamics and the laser-assisted nanoscale Kirkendall effect

R. M. van der Veen[1]

[1]Helmholtz Zentrum Berlin, Abteilung Atomare Dynamik in Licht-Energie Umwandlung, Berlin, Germany

While transmission electron microscopy (TEM) has evolved into a powerful tool for atomic-scale structure determination, temporal resolution in TEM has received far less attention, with detector and beam-current limits being on the order of microseconds. In this talk, I will describe how time resolution limits can be pushed by coupling ultrafast pulsed lasers to otherwise conventional TEMs. After briefly describing the experimental setup, I will present some of our recent work on transient lensing from photoemitted electron clouds on the picosecond time scale. I will also show how lasers coupled to TEMs can be used to induce nanoscale structural changes in nanomaterials on much slower time scales.

IM1.003-invited

ER-C 2.0: An update on plans for new electron microscopes at the Ernst Ruska-Centre in Forschungszentrum Jülich

R. E. Dunin-Borkowski[1], J. Mayer[1], C. Sachse[1]

[1]Forschungszentrum Jülich GmbH, Ernst Ruska-Centre for Microscopy and Spectroscopy with Electrons, Jülich, Germany

The Ernst Ruska-Centre for Microscopy and Spectroscopy with Electrons (ER-C) in Forschungszentrum Jülich has operated a user facility in advanced transmission electron microscopy (TEM) jointly with RWTH Aachen University since 2004. Following a competitive selection process, the ER-C succeeded in being placed on the National Roadmap for Research Infrastructure of the German Federal Ministry of Education and Research in 2019 based on its "ER-C 2.0" application for a "National research infrastructure for high-resolution electron microscopy".

The ER-C 2.0 project is based on five next-generation electron microscopes, which are not currently available commercially and will be delivered in 2024 and 2025. The microscopes will be operated jointly by Forschungszentrum Jülich, RWTH Aachen University and Heinrich Heine University in Düsseldorf. Their development and operation will also be supported by associated partners in Humboldt University Berlin, the University of Göttingen, Maastricht University and the Max-Planck-Institut für Eisenforschung in Düsseldorf.

The basic specifications of the five instruments, which are presently being designed by different column manufacturers in consultation with companies specializing in aberration corrector, detector and sample transfer technologies, as well as in ultra-high vacuum (UHV) equipment and correlative techniques, are as follows:

1. TOMO: An aberration corrected UHV TEM combined in a single instrument with a co-located laser-equipped atom probe tomography capability and a cartridge-based liquid-helium-cooled specimen holder.

2. OPERANDO: An aberration corrected fully bakeable UHV TEM equipped with *in situ* deposition of a wide range of materials using the technique of thermal laser epitaxy, with connectivity to a cryo UHV focused ion beam scanning electron microscope equipped with a secondary ion mass spectrometer and to a scanning probe microscope.

3. FEMTO: Two time-resolved laser-driven aberration corrected field emission TEMs for ultrafast and dynamic studies of reversible and irreversible processes in materials over the widest range of temporal resolutions, featuring unique electron gun designs, magnetic-field-free imaging with atomic spatial resolution, an ultra-wide pole-piece gap and cryo workflows.

4. SPECTRO: An ultra-high-energy-resolution aberration corrected scanning TEM equipped with light injection and collection, helium cooling of the specimen, magnetic-field-free imaging with atomic spatial resolution, gas injection and connectivity to a high pressure scanning electron microscope equipped with co-located cathodolouminescence and Raman spectroscopy.

5. BIO: A chromatic and spherical aberration corrected next generation cryo TEM equipped with liquid helium cooling of the specimen and additional electron optical elements for novel phase plate designs.

Access to the microscopes will be provided based on scientific proposals, which will be assessed by an external review panel. Successful applicants will be supervised by experienced scientists, who will offer hands-on support with experiments, analysis and data science. In this talk, I will present an update about the current status of the project.

IM1.004

Interference gating: a novel way for the dynamic investigation of switching semiconductor nanostructures by time-resolved electron holography

T. Wagner[1], D. Berger[2], I. Häusler[3], H. Çelik[1], M. Lehmann[1]

[1]Technische Universität Berlin, Institut für Optik und Atomare Physik, Berlin, Germany
[2]Technische Universität Berlin, Zentraleinrichtung Elektronenmikroskopie, Berlin, Germany
[3]Humboldt-Universität, Institut für Physik, Berlin, Germany

Off-axis electron holography deepens TEM"s insight even further by providing access to amplitudes and phases of reconstructed electron waves. The latter contain spatially resolved information about projected electromagnetic potentials, making electron holography (EH) an excellent tool for the investigation of electric potential distributions in semiconductor nanodevices, especially when they are operated during investigations using special in situ specimen holders. Since existing methods for the realization of time-resolved measurements in a TEM by stroboscopic illumination have proven to be disadvantageous for EH [1,2], such investigations have so far been limited to static measurements.

Recently, a simple, yet promising approach to realize time-resolved measurements of periodic processes with nanosecond time resolution in an electron holographic setup by means of interference gating (iGate) was presented [3]. As shown in fig. 1a, the basic idea of interference gating is a synchronized destruction of the interference pattern, realized by introducing random phase shifts $\varphi_g(t)$ to the electron wave, for a defined period of time during an interferometric measurement such as electron holography (EH). The holographic reconstruction process acts as a temporal filter that only retains the information of the undisturbed interferogram outside this period (fig. 1b). By shifting the undisturbed time interval ? (gate) along an synchronized externally controlled periodic process (e.g. due to an applied voltage signal), the whole period can be sampled in a pump-probe (or lock-in) manner.

In a first materials scientific application, interference gating was used to investigate dynamic electric potential distribution in an externally driven nanostructured general purpose silicon diode during switching in reverse-biased condition shown in fig. 2. An added value of this type of investigations is the simultaneous combination of high spatial and temporal resolutions. In the analysis of single frames of the investigated process (every 11.1 ns), different potential dynamics are revealed depending on the location. Thus, switching times in vacuum between free-standing electrodes (grey circles) correlate very well with the applied signal as measured in parallel by an oscilloscope (blue line), whereas switching delays (transients) appear as expected within the space charge region (red circles). Interference gating, thus, paves the way for the investigation of dynamic electrical effects in semiconductor nanostructures directly at the site of the event.

[1] A. Feist et al., Ultramicroscopy, vol. 176, pp. 63–73, 2017.
[2] F. Houdellier et al., Ultramicroscopy, vol. 186, pp. 128–138, 2018.
[3] T. Wagner et al., Ultramicroscopy, vol. 206, p. 112 824, 2019.

Figure 1: a) Dynamic phase shift $\varphi_g(t)$ producing time-dependent electron hologram $I_{hol}(r, t)$ (red and blue lines represent exemplary wave fronts for different times t). b) Dynamic phase sequence for generating time-resolved electron holograms with gating length ? and respective Fourier transformations of $I_{hol}(r, t)$ (disturbed case: only centerband, undisturbed: also sidebands).

Figure 2: Plot of the control signal $U_{in}(t)$ (blue line) applied to the prepared diode measured by the oscilloscope and plots of the phase slopes $d/dx\ \varphi_{el}(x, tgi)$ (vacuum: grey circles, depletion region of the diode: red circles) calculated for 30 gate positions t_{gi} in two different areas with the standard deviation as error bars.

Fig. 1

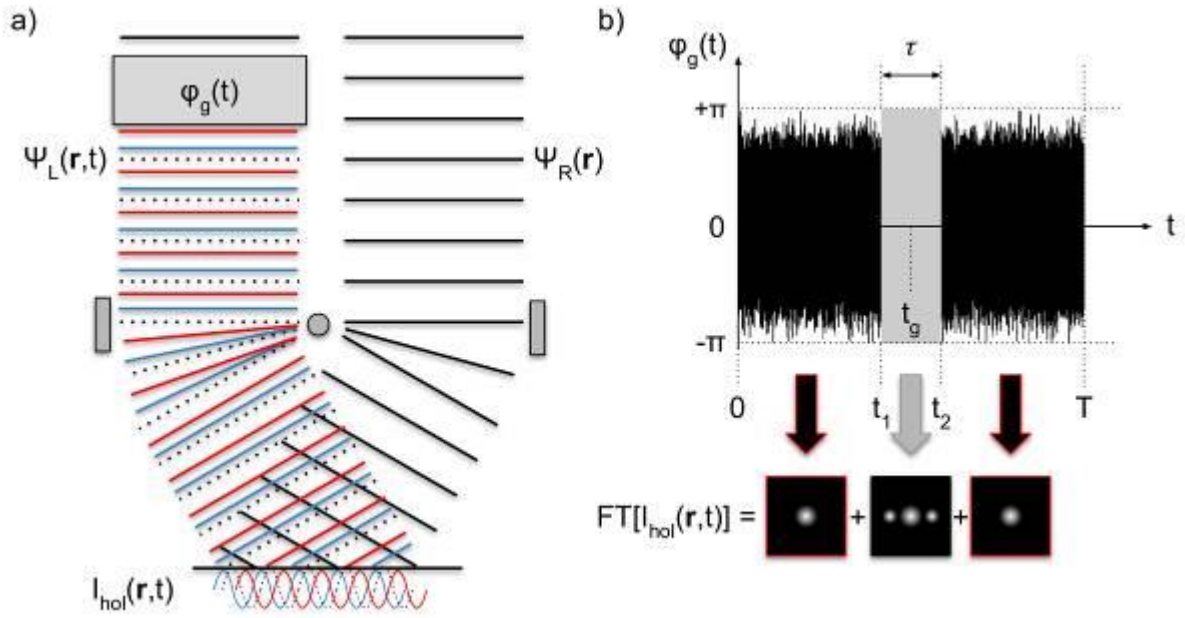
a)
$\varphi_g(t)$
$\Psi_L(\mathbf{r},t)$
$\Psi_R(\mathbf{r})$
$I_{hol}(\mathbf{r},t)$
b)
$\varphi_g(t)$
τ
+π
0
-π
t
t_g
0
t_1
t_2
T
$FT[I_{hol}(\mathbf{r},t)]$ =

Fig. 2

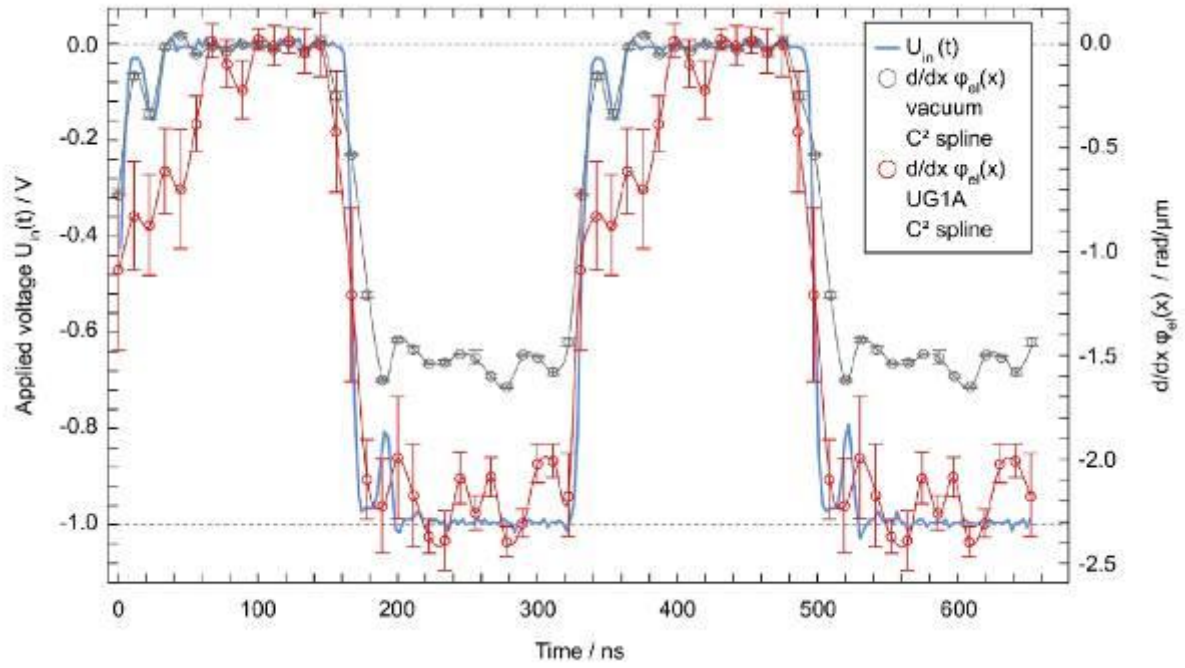
U_{in} (t)
d/dx φ_{el}(x) vacuum C² spline
d/dx φ_{el}(x) UG1A C² spline
Applied voltage U_{in}(t) / V
d/dx φ_{el}(x) / rad/µm
Time / ns
0.0
-0.2
-0.4
-0.6
-0.8
-1.0
-0.5
-1.5
-2.0
-2.5
0
100
200
300
400
500
600

IM1.005

Evaluation a 48 pixel programmable phase plate for electron wavefront shaping

J. Verbeeck[1], F. Vega Ibañez[1], A. Béché[1]

[1]University of Antwerp, Physics, EMAT, Antwerp, Belgium

We report on advances in the development of a versatile programmable phase plate for use in electron microscopy. The current design provides up to 48 individually addressable electrostatic phase shifting elements that can be laid out in multiple design patterns depending on the target application. The phase plate state can be synchronously updated at up to 100 kHz rate providing an attractive route for high speed adaptive algorithms shaping the electron probe while optimizing a goal function. We discuss different phase plate implementations and their usefulness towards applications. We show the realization of dipolar, quadrupolar and vortex phase symmetries in sub nm electron probes when placing the phase plate in the condenser plane of a modern STEM microscope. We demonstrate adaptive algorithms maximizing for contrast in HAADF STEM images as well as discussing their prospects for focusing inside thick samples, increasing depth of field and use in ptychography.

Figure 1. Example of two prototype phase plate realisations showing a 36 pixels cartesian design (left) and a polar segmented 48 pixel design.

[1] J. Verbeeck et al. "Demonstration of a 2×2 programmable phase plate for electrons." Ultramicroscopy 190 (2018): 58-65.

[2] Patents EP3474308, US11062872 B2.

[3] The authors acknowledge the financial support of the Research Foundation Flanders (FWO, Belgium) project G042820N. The ADAPTEM project is funded by the European Research Council as an ERC POC project under grant nr: DLV-789598.

Fig. 1

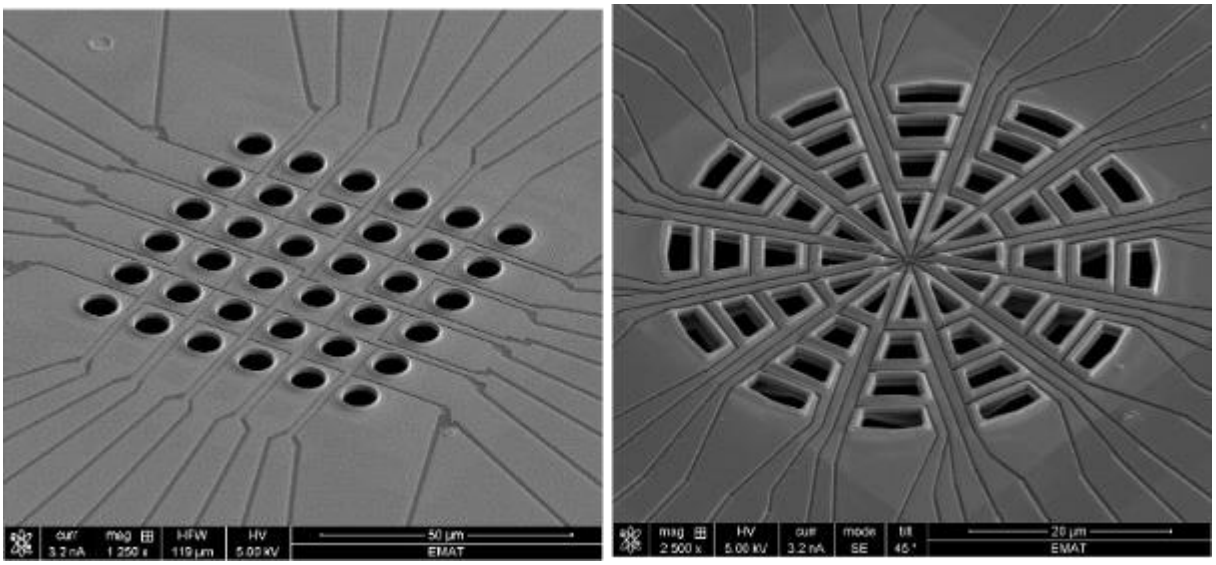

IM1.006

Hexapole correctors for STEM: CESCOR, DCOR, ASCOR and beyond ...

P. Hartel[1], S. Uhlemann[1], T. Riedel[1], S. Perl[1], M. Linck[1], H. Müller[1], V. Gerheim[1], M. Haider[1]

[1]CEOS GmbH, Heidelberg, Germany

The success of hardware aberration correction in transmission electron microscopy started 25 years ago with the first resolution improvements achieved with a two-hexapole design in TEM [1] and a quadrupole-octupole design in STEM [2]. The two-hexapole design was used in STEM later as well [3]. A careful redesign lead to the advanced two-hexapole corrector (DCOR/ASCOR) with full fourth-order correction and effectively vanishing fifth-order aberrations [4]. This design is still state-of-the-art – independent from using additional A5 stigmators or not [5,6].

After these achievements it has been argued, that the usable aperture semi-angle for two-hexapole and even three-hexapole correctors is finally limited by the three-lobe aberration of sixth order D6 [7]. For an objective lens with a medium gap size around 5mm, e.g. for analytical applications, the π/4-phase shift limit due to this intrinsic aberration is just below 40mrad (Fig. 1). As investigated theoretically [4,5] and verified experimentally [6,8,9], these advanced correctors are sufficient for modern CFEG-equipped microscopes to touch the high-resolution limit set by the chromatic aberration. D6 hardly limits the obtainable resolution, if additional D6 phase shifts up to several π/4 are reasonably-well counterbalanced by lower-order three-fold aberrations [6,10]. However, if the intrinsic D6 can be eliminated a-priori in the optics, the counterbalancing techniques wouldn"t be necessary in most situations. This is especially valuable in case of monochromated illumination, which allows for even larger apertures, enabling not only better xy- but also improved z-resolution [11].

Recently, we found first evidence that a novel three-hexapole design can eliminate the three-lobe aberration of sixth order D6 together with higher-order spherical aberrations. Consequently, the theoretical π/4-limit due to intrinsic residual aberrations is shifted further out to 70mrad. Again, compensation techniques can extend the usable aperture even beyond this value. Fig. 2 shows very promising results of experimentally obtained ronchigrams with a radius of ≥80mrad recorded at 200kV. [12, 13]

[1] M. Haider et al., Nature **392**, 768 (1998).
[2] P.E. Batson, N. Dellby, O.L. Krivanek, Nature **418**, 617-620 (2002).
[3] H. Sawada et al, Microscopy **54** (2), 119-121 (2005).
[4] H. Müller et al., Microscopy and Microanalysis **12** (6), 442–445 (2006).
[5] P. Hartel et. al., Ultramicroscopy **206**, 112821 (2019).
[6] R. Sagawa et al., Ultramicroscopy **233**, 113440 (2022).
[7] S. Morishita et al., Microscopy 67 (2018) 156-163.
[8] M. Watanabe et al., Microsc. Microanal. 22 (2016) 310-311.
[9] M. Bischoff et al., Microsc. Microanal. 24 (2018) 1134-1135.
[10] S. Morishita et al., Phys.Rev.Let. 117 (2016) 153004.
[11] R. Ishikawa et al., Ultramicroscopy 151 (2015) 122-129.
[12] We acknowledge and highly appreciate the collaboration and support by JEOL company.
[13] CEOS GmbH has received funding from the European Union"s Horizon 2020 research and innovation program under grant agreement No. 823717 – ESTEEM3.

Figure 1: Hexapole corrector generations. The typical size of the intrinsic aberrations and the resulting π/4-limits for 30..300kV are indicated, assuming a medium-size objective lens gap.

Figure 2: A comparison of experimental in-focus ronchigrams at 200kV: a) advanved hexapole corrector with D6 ≈ 2mm b) calibration with gold c) new corrector with D6 ≈ 0.

Fig. 1

OL gap ≈ 5mm	no corrector	conventional ($C_S \approx 0$)	advanced ($A_5 \approx 0$)	new corrector ($D_6 \approx 0$)
π/4-limit	5...7mrad	27...30mrad	35...40mrad	≥70mrad
first residual	$C_S \approx 1$mm	$A_5 = 6...3$mm	$D_6 = 9...2$mm	$G_7 \approx 0.5$mm, $D_8 \approx 8$mm

Fig. 2

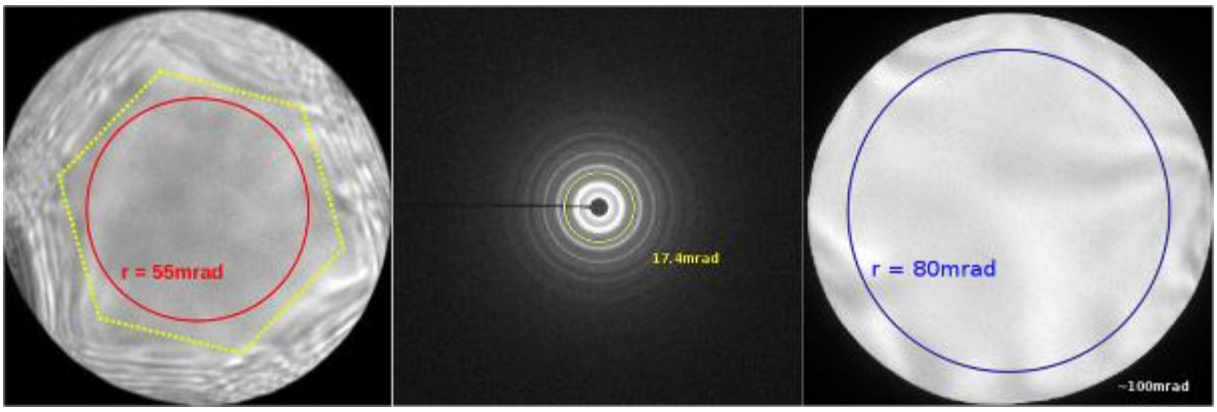

IM1.007

Energy-filtered ultrafast electron microscopy with chirped photoelectrons

O. H. Kwon[1]

[1]Ulsan National Institute of Science and Technology, Chemistry, Ulsan, South Korea

1. Introduction

Ultrafast electron microscopy (UEM) enables time-resolved imaging with a spatial resolution approaching (sub)nanometer precision. The temporal resolution has been governed by the duration of the imaging electron pulse at the specimen. The energy spread of the electron pulses develops a chirp, an energy–time correlation, resulting in the temporal broadening of the pulses because the leading electrons with higher energies accelerate and those with lower energies are retarded during propagation.

2. Objectives

We demonstrate energy-filtered UEM (EFUEM), which exhibits a femtosecond resolution with a conventional energy filter for use in a TEM without pulse compression. The temporal resolution is controlled by selecting chirped photoelectrons of distinct kinetic energies using the post-specimen energy filter. We demonstrate ultrafast real-space imaging using EFUEM, observing the phase-transition dynamics of VO2 to study its heterogeneous nature with different strains exerted on individual nanoparticles (NPs) in an ensemble.

3. Materials & methods

A proof-of-concept experiment was performed with a polycrystalline VO2 film, which exhibits insulator-to-metal transition (IMT) from a low-temperature semiconducting phase with a low-symmetry monoclinic structure, *M*1, to a high-temperature metallic phase with a high-symmetry rutile structure, *R*. Excitation using femtosecond optical pulses provides a route to the ultrafast transition from the *M*1 to the *R* phase. To demonstrate the temporal resolution approaching the time window of IMT, time-resolved micrographs were obtained by energy filtering the photoelectrons with various slit widths. By gating the detection range of electron energy, the frame time of images is controllable.

4. Results

The temporal resolution is determined by the slit width of the energy filter, reaching the resolution of ~700 fs, which is mainly limited to the duration of optical excitation pulses (550 fs). The concept enables resolution of ultrafast structural responses in matter beneath temporally broad photoelectron bunch without delicate instrumental modification or compromising the large number of electrons. In our approach, the temporal resolution of ultrafast imaging was additionally limited by the degree and dispersion of the chirps of probing electron pulses, the spectral jitter of the energy filter, and the duration of the optical excitation pulses to initiate structural change. If these factors are improved, the temporal resolution of ultrafast imaging may reach <100 fs, which surpasses the timescale of serial atomic displacement. Using the energy-filtered photoelectrons, the ultrafast IMTs of VO2 NPs were visualized, revealing their unique behaviors associated with nanoscale strain. A NP under a negligible strain, such as the bulk single-crystalline VO2, transforms from the initial *M*1 phase directly to the *R* phase upon photoexcitation. When a NP in the *M*1 phase is partially strained, its metallic *M*2 phase emerges for the first few picoseconds, retaining the parent lattice structure, which then subsequently undergoes the structural transition to the *R* phase.

5. Conclusion

Our approach enables electron microscopy to access the timescale of elementary nuclear motion to visualize the onset of the structural dynamics of matter at the nanoscale

IM1.P001

Adaptive probe correction with electrostatic phase plate

C. P. Yu[1], F. Vega Ibañez[1], A. Béché[1], S. van Aert[1], J. Verbeeck[1]

[1]University of Antwerp, Antwerp, Belgium

Introduction

Scherzer theorem [1] states that to correct spherical aberration of an electron optical system, one needs either electromagnetic lenses that break rotational symmetry, time variant fields, or the existence of space charge. While the effectiveness of the first solution has been widely proven, we implemented the last one as an alternative. In this project, an electrostatic phase plate that creates local electric potential is installed in the microscope, altering the phase of the electron wave. In this manner, the phase plate compensates aberrations to some degree and increases the resolving power of the probe. With this principle, an adaptive aberration correction method is proposed.

Objectives

To correct the electron probe using phase plate without measuring the aberrations, but through maximizing a chosen quality indicator computed from annular dark field (ADF) images instead.

Methods

Multiple algorithms are used to search for the best phase configuration, all of them aim to minimize specific loss functions that are coupled with different scanning modes. For line scans, the standard deviation of the intensity is used, while for raster scans, other loss functions can be added, such as BRISQUE image quality assessment [2] and symmetry analysis of the probe.

The optimization goes in two steps. In the first step, the resulting image with different phase configurations is acquired by changing the voltage of the phase elements either grouped in rings or as lobes (Fig. 1). To avoid local minima, simulated annealing is used to search rather widely in the space of possible phase configurations. In the second step, gradient descend is applied with complete freedom of possible phase configuration allowed by the phase plate in order to further improve the result from the first step, and thus less symmetric aberrations and local variations in the phase response of the phase plate can be corrected.

Results

The simulated results (Fig. 1) of the probe and ADF images formed with a circular aperture, phase plate, and corrected phase plate at different stages of the process. The contrast and resolving power increase at each stage, accompanied by sharpening of the probe intensity profile.

Conclusion

An automatic probe correction scheme with phase plate is presented and experimentally realized on the microscope. Comparing the ADF image generated with the phase plate before and after the process clearer atomic features are observed, even with the unavoidable tail spread-out imposed by the finite fill factor of the phase plate [3]. The project shows a promising method for the probe correction of a less critical optical system and also a significant progress in fully automating electron microscopy experiments.

Reference

[1] O, Scherzer. "Über einige fehler von elektronenlinsen." *Zeitschrift für Physik* 101.9 (1936): 593-603.

[2] A. Mittal, et al. "Blind/referenceless image spatial quality evaluator." *2011 conference record of the forty fifth asilomar conference on signals, systems and computers*. IEEE, 2011.

[3] F. Vega Ibáñez, et al. "Can a Programmable Phase Plate serve as an Aberration Corrector in the Transmission Electron Microscope (TEM)?." *arXiv e-prints* (2022): arXiv-2205.

Fig. 1 The probe shape at different stage of probe correction and their corresponding ADF image. The probe gradually converges to a sharp point with increasing resolving power. The sample shown is gold [1 1 1] on amorphous carbon.

Fig. 1

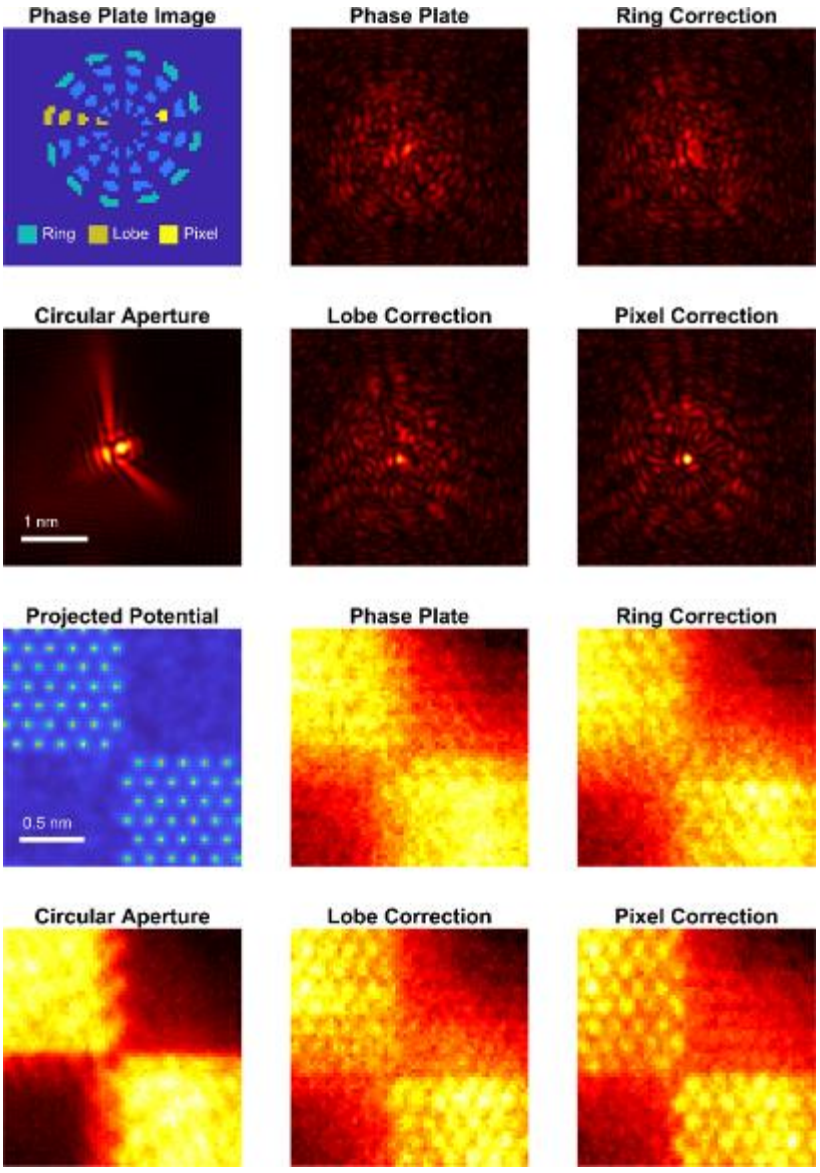

IM1.P002

Secondary electron imaging in scanning transmission electron microscopy for material science

E. Vlasov[1], D. Wang[1], J. Verstraelen[1], W. Heyvaert[1], A. Béché[1], J. Verbeeck[1], S. Bals[1]

[1]University of Antwerp, Electron Microscopy for Materials Science (EMAT), Antwerp, Belgium

(Scanning) transmission electron microscopy ((S)TEM) is a rapidly developing field with a large variety of techniques widely used in modern material science. Signals generated within TEM during electron-matter interaction provide information about the composition, crystallography, mass-thickness, and local electromagnetic fields [1]. Secondary electrons (SEs) are electrons ejected from a sample after electron beam irradiation. SEs originate from the near-surface region of the sample, so these electrons are often exploited in scanning electron microscopy to form images that are sensitive to the surface topology. Topographic information from SEs would greatly aid the interpretation of conventional 2-dimensional STEM images [2], but unfortunately, SE imaging is not available on most conventional STEM instruments. In this work, we demonstrate the capabilities and benefits of SE imaging in STEM as an alternative 3D characterization method.

SE images were obtained using an aberration-corrected "cubed" Thermo Fisher Themis Z instrument operated at an acceleration voltage of 200 kV and a beam current of 250 pA. We used a recently proposed methodology to detect SEs using electron beam-induced current (SEEBIC) [3]. A homemade transimpedance amplifier (TIA), electrically connected to the sample via a DENS Solutions Wildfire holder, was used to convert the SEEBIC signal into a voltage signal digitized by the Gatan Digiscan II unit along with the HAADF-STEM detector signal.

SE images contain topography information, so they enable revealing the information hidden in conventional HAADF-STEM. We demonstrate this effect on self-assemblies of rounded $Fe_xO/CoFe_2O_4$ nanocubes in spherical confinement [4]. Figure 1 shows the five-fold symmetry of an icosahedron, and demonstrates the presence of stacking faults. It should be noted that retrieving the information about such complex morphologies from a single or a few images is very important when the acquisition of tilt series for electron tomography is not possible due to various factors. These approaches are inspired by techniques used in scanning electron microscopy for surface metrology. We demonstrate our first attempts to retrieve 3D information using the shape-from-shading and structure-from-motion algorithms. Another important direction is the investigation of surface facets. The surface nature of the SE signal can greatly aid the understanding of the microscopy data.

Figure 1. (a) HAADF-STEM and (b) SEEBIC images of self-assemblies of $Fe_xO/CoFe_2O_4$ nanocubes.

In conclusion, we have demonstrated the versatility of SE imaging in modern material science for various purposes. The surface origin of the SE contrast enables to extract morphological information that can be hidden in conventional STEM images. The use of novel techniques for 3D reconstructions was discussed as an alternative to conventional electron tomography.

The project has received funding from European Research Council (ERC Consolidator Grant 815128, REALNANO).

1. D. B. Williams, C. B. Carter, *Transmission Electron Microscopy: A Textbook for Materials Science* (2009).
2. C. Mignot, et al., *Micros. Today,* 26 – 3 (2018).
3. M. Mecklenburg, et al., *Ultramicroscopy*, 207 – 112852 (2019).
4. D. Wang, et al., *Nat. Commun.*, 9 – 2228 (2018).

Fig. 1

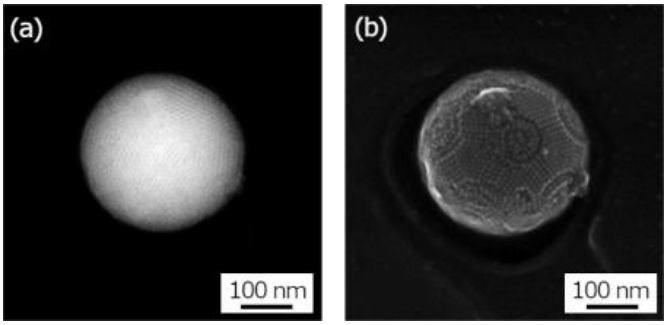

IM1.P003

Low voltage transmission electron diffraction in SEM as a powerful tool for wide field of view characterization of crystalline materials

A. Orekhov[1,2], N. Denisov[1,2], D. Jannis[1,2], N. Gauquelin[1,2], J. Verbeeck[1,2]

[1]University of Antwerp, Electron Microscopy for Materials Science (EMAT), Antwerp, Belgium
[2]University of Antwerp, NANOlab Center of Excellence, Antwerp, Belgium

The study of the structure of nanocrystalline materials is often difficult as standard X-ray diffraction techniques break down for sub micrometer particles, especially when occurring in a mixture. Here, we present a tool for structural analysis of a wide range of layered materials and nanosized powder samples based on a conventional scanning electron microscope. An hybrid pixel electron detector below the sample makes it possible to record two dimensional diffraction patterns for every probe position on the sample surface, in transmission mode, thus performing a 4d-STEM (scanning transmission electron microscopy) analysis. This offers a field of view up to 2 mm2, while providing spatial resolution in the nm range, enabling the collection of statistical data on grain size, relative orientation angle, bilayer stacking, strain, *etc.* which can be mined through a custom-made open-source Python based code. Diffraction pattern acquisition is performed using an Advacam®MiniPix detector with a 300 ?m Si active layer and a 13bit depth dynamic range. We use a standard JEOL JSM-5510 SEM with a W electron source, enabling wide adoption of our proposed setup. Samples are mounted on a Thorlabs 30 mm optical cage system, giving an adjustable sample to detector distance (camera length) ranging from 5 to 50 mm (Fig. 1) [1]. The direct geometrical projection of the diffraction pattern onto the hybrid pixel detector provides a robust calibration of the scattering angles not influenced by lens drift and optical distortions.

Fig. 1. **(a)** Schematic drawing of the experiment, consisting of a layered material and a hybrid pixel detector at the bottom, inside an SEM sample chamber. **(b)** Picture of the setup. The Thorlabs optical cage system allows camera length adjustment.

The authors acknowledge the financial support from EU FLAG-ERA JTC 2017 GRAPH-EYE, FWO SBO AutomatED S000121N from the Research Foundation Flanders.

Fig. 1

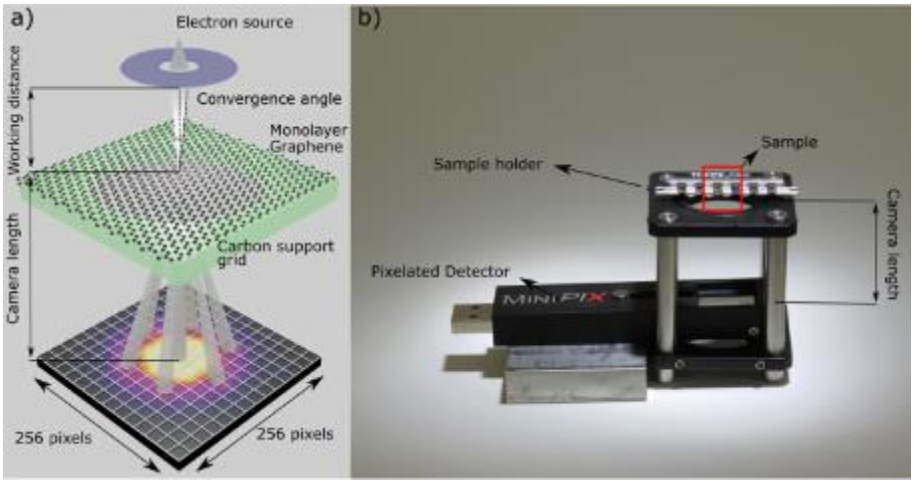

IM1.P004

Improving the time-resolution of event-based electron cameras using neural networks trained by femtosecond electron pulse detection

A. Schröder[1], C. Rathje[1], L. van Velzen[2], M. Kelder[2], S. Schäfer[1]

[1]University of Oldenburg, Oldenburg, Germany
[2]Amsterdam Scientific Instruments (ASI), Amsterdam, Netherlands

Introduction

In the recent two decades, ultrafast transmission electron microscopy (UTEM) has successfully enabled investigation of ultrafast dynamics on the nanoscale by combining femtosecond electron probe pulses with a synchronized optical sample excitation [1]. With increasing availability of sufficiently fast event-based electron detectors, dynamics down to the nanosecond timescale can also be imaged by continuous-beam TEM. For example, with the TimePix3 chip architecture [2] electron events are registered with a bin width of about 1.6 ns. However, the achievable spatial and temporal resolution in experiments is often limited due to the stochastic electron trajectories in the sensor chip [3]. Neural network approaches have already enabled increased spatial resolution [4].

Objectives

Here, we report on the development of a neural network architecture trained by experimental electron pulse data to improve the temporal resolution of the TimePix3 detector.

Materials & methods

As a high-precision electron arrival time standard, we utilized 200-fs electron pulses (400-kHz repetition rate, 200-keV electron energy, 1.3 electrons/pulse) using the Oldenburg UTEM (Fig. 1a). With a TimePix3 detector (Cheetah T3, Amsterdam Scientific Instruments), we experimentally collected a dataset of electron detection events for 4×10^6 electron pulses. For accurate synchronization, the TimePix3 detector additionally assigns timestamps to each photoemission laser pulse. For every event, relative detector position, time of arrival (ToA) and time over threshold (ToT) are stored and clustered according to their arrival time and position (on average 6 events per cluster). To predict the arrival time of the primary electron, a fully connected deep neural network model is trained using event data from 1.6×10^5 time-scrambled event cluster.

Results

The unprocessed ToA data, using individual unclustered event data, shows a temporal spread of about 10 ns FWHM (Fig. 1b (gray)). Already by identifying event clusters and considering the average ToA in each cluster, the temporal spread in the histogram can be reduced to 7 ns (red). With the neural network, the predicted ToA distribution (for a part of the data not involved in the training) is narrowed to 4.7 ns (FWHM, 2 ns rms, blue). Remarkably, the tailed ToA distribution in the previous cases is transformed to an almost Gaussian distribution by the neural network. An example of imaging data for the unprocessed and neural-network-filtered case is shown in Fig. 1c and d, respectively.

Conclusion

In conclusion, we demonstrate the application of neural networks trained by femtosecond electron pulse data to predict the accurate ToA, substantially increasing the temporal resolution of the TimePix3 detector. We expect that future versions of the TimePix chip with shorter time bins will likely benefit even more from sophisticated event data analysis.

[1] A. Feist et al., Ultramicroscopy 176, 63 (2017).

[2] T. Poikela et al., JINST 9, C05013 (2014).

[3] F. Pitters et al., JINST 14, P05022 (2019).

[4] J. P. van Schayck et al., Ultramicroscopy 218, 113091 (2020).

Figure 1: (a) Schematic setup of Oldenburg UTEM with TimePix3 detector. (b) Histogram of the time of arrival for uncorrected (gray), cluster mean corrected ToA (red), and the neural network predicted ToA (blue). (c,d) Image for uncorrected (c) and neural network predicted ToA (d). Color scale: ToA of electron event.

Fig. 1

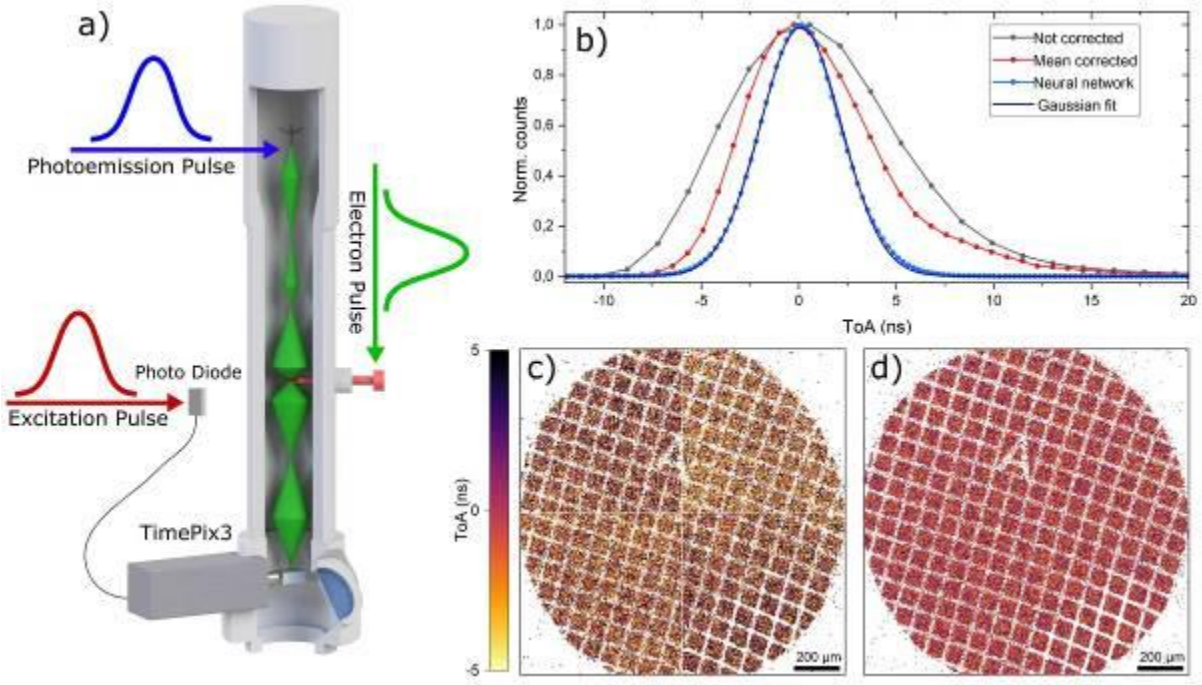

IM1.P005

A diffusion model for electron beam damage in STEM

D. Jannis[1,2], A. Velazco[1,2,3], A. Béché[1,2], J. Verbeeck[1,2]

[1]University of Antwerp, Physics, Antwerp, Belgium
[2]NANOlab Center of Excellence, Sciences, Antwerp, Belgium
[3]The Rosalind Franklin Institute, Science, Oxford, United Kingdom

Even though the advent of the aberration-corrected microscopes has enabled the possibility to perform STEM up to and below 50 pm resolution it is still not trivial to achieve atomic resolved images for each material. This is not because of the optics of the electron microscope but due to the electron beam damage which occurs when the highly energetic incoming electron interacts with the specimen. The common method to reduce the induced damage is by reducing the total dose, by making short exposure times, or reducing the electron beam current. Both result in lower signal-to-noise ratio images limiting the accuracy and precision of the quantified parameters extracted from such data. Experimental evidence has pointed out that not only the dose and dose rate influence the damage which occurs in a specimen during a STEM acquisition but that even the scan sequence and dwell time can modify the induced damage on a specimen [1,2]. One clear experimental evidence is found in the work of *Velazco et al.* [1] where a substantial decrease in damage is observed on a Linde Type A zeolite when decreasing the dwell time or changing the scan pattern while keeping the total dose and dose rate equal.

In the present work, the aim is to qualitatively model the damage observed using a minimal amount of physical parameters (diffusion constant and threshold). A diffusion-based model is chosen since the damage was experimentally found to depend on the scan sequence indicating a non-local component where the induced damage depends on the time at which the neighboring pixels are visited. By only taking the diffusion of a quantity to describe the damage there is no difference in the total induced damage when changing the scan sequence. Therefore, a threshold is introduced below which no damage is induced. Note that no assumption is made on which physical parameter is diffusing and why. Furthermore, the experimental observations observed in *Velazco et al. [1]* are used to estimate the two parameters of the model and verify the applicability of the model to describe the experiments. By developing such model, it is possible to predict how the scan sequence and dwell time can influence the total induced damage. In the future these predictions could be taken as guidelines to optimize experiments for different samples.

References:

[1] Velazco A. *et al.*, (2022), Ultramicroscopy, 232, 113398.

[2] Jones L. *et al.* (2018), Microscopy, Issue 67, Pages i98-i113

[3] Jannis, D. *et al*. (2022), Ultramicroscopy, 240, 113568

[4] Acknowledgment: AB, AV, DJ and JV acknowledge financial support from the Flemish region through FWO grants G093417N and G042920N innovation program under grant agreement No 101017720, FET-Proactive EBEAM

IM1.P006

A hamiltonian mechanics framework for straight and curved charge particle optics systems

A. Lubk[1,2]

[1]Leibniz Institute for Solid State and Materials Research Dresden, Institute for Solid State Research, Dresden, Germany
[2]TU Dresden, Institute of Solid State and Materials Physics, Dresden, Germany

Introduction

The theoretical formulation of charge particle optics typically concerns the systematic analysis of charge particle trajectories close to some design trajectory / optical axis in a device producing deliberately configured electrostatic and magnetostatic fields. Cornerstone results consider the expansion of path deviations into a hierarchical system of differential equations, which may be solved in an iterative manner to yield paraxial and subsequent aberration optical properties of the system under consideration [1]. Note, however, that considerable technical difficulties arise when analyzing high-order aberrations, e.g., those of curved system, relativistic systems of combined electrical and magnetic fields, which are related to complex expressions, exploitation of symmetries (e.g., symplectic), or numerical implementation.

Objectives

Here, we seek to develop a particularly compact solution to the charge particle optics program employing Hamiltonian formulation of mechanics. That includes phase space coordinates adapted to (curved) optical axis, systematic expansion into a hierarchy of first order differential equations, simplification of equation system by employing adapted physical gauges, and symplectic symmetries. Finally, we seek to provide compact analysis of archetypal elements such as multipoles or magnetic lenses to high aberration orders.

Methods

The charge particle optics problem is considered as the propagation of deviation vectors, between design particles moving along the optical axis of a given device and particles in close vicinity to that design particles, along the optical axis [2]. In the Hamiltonian formulation of classical mechanics, these vectors are defined in phase space, i.e., contain both spatial and momentum difference to the design particle. We employ a canonical transformation to transform this conventional phase space into an adapted extended phase space containing time and energy as additional dimensions, which also implies a reparameterization of the trajectory parameter from time to optical axis coordinate. The latter is particularly well suited for description of particle coordinates in planes perpendicular to the optical axis. We finally employ a modified physical gauge (i.e., related to hyperaxial gauge), which is particularly well adapted to the tube-like geometry of the particle pencils around (curved) optical axis. The gauge simplifies expressions considerably and leads to explicit expressions of the potentials in terms of integrals of the physical electrostatic and magnetostatic fields. Last but not least, we also discuss the numerical implementation of this method within the boundary element formalism.

Results

Employing the above formalism, we set up a compact system of first order differential equations in 6 dimensional extended phase space describing paraxial and aberrational properties of general (curved) optical systems in a hierarchical manner. The equations obey symplectic symmetries at each expansion level, leading, e.g., to interdependencies among error paths or aberration coefficients. We solve these equations for a number of typical optical devices, such as quadrupole and magnetic lens.

[1] P.W. Hawkes, E. Kasper, Principles of Electron Optics Vol. 1: Basic geometrical optics, Principles of Electron Optics.

[2] F. Kern, J. Krehl, A. Thampi, A. Lubk, Optik 242, 167242.

[3] We acknowledge funding from the Deutsche Forschungsgemeinschaft (DFG) (No. 461150024.)

IM1.P007

Dealing with carbon contamination as a consequence of wet TEM sample preparation

J. Menten[1], D. Ramermann[1], N. Pfänder[1], R. Schlögl[1,2], W. Hetaba[1]

[1]Max Planck Institute for Chemical Energy Conversion, Mülheim an der Ruhr, Germany
[2]Fritz Haber Institute of the Max Planck Society, Berlin, Germany

Introduction

In order to achieve the desired data quality in transmission electron microscopy (TEM) measurements, careful sample preparation forms a crucial step for these experiments. For many samples, dispersing the specimens in solvent and applying the sample as a solution on the grid is a well-suited method. One big obstacle is the formation of carbon contamination on the specimens which can result from organic residues, e.g. solvents.

Objectives

We investigate the impact of different solvents on TEM measurements and apply cleaning and preparation strategies in order to minimize the carbon contamination during TEM investigations. The amount of accumulated contamination resulting from different solvents was evaluated by high-angle annular dark field (HAADF) measurements and electron energy loss spectroscopy (EELS). The sample preparation in our sample cleaning setup was customized based on the specimens" properties and utilized solvent in order to prevent contamination.

Material & Methods

Thickness measurements by evaluating HAADF image contrast and EELS analysis were performed with a Thermo Scientific Talos F200X transmission electron microscope. For specific sample pretreatments, a self-made heatable vacuum setup was utilized in order to perform specialized sample preparation methods. All samples were prepared by applying 1 µL of solvent to a holey carbon copper grid and dried for 10 minutes before sample insertion into the TEM.

Results

HAADF and EELS measurements can be utilized for determining the thickness of deposited carbon contamination. The grids were exposed to the electron beam for different durations immediately after sample insertion and again 30 minutes later. For both toluene and THF as solvents, the determined amount of accumulated carbon showed a linear increase with longer exposure times. When the samples were exposed after 30 min in the TEM vacuum again, the observed carbon layer was significantly less (Fig. 1).

In order to prevent solvent outgassing in the microscope environment, a dedicated sample cleaning setup with a cold trap was utilized to prepare the TEM samples by removing solvent residues before sample insertion. Evaluation of decrease in pressure while pumping with a freshly prepared sample grid inserted, gives insight in the necessary drying times in order to reduce contamination during TEM investigations (Fig. 2).

Conclusion

Our experiments emphasize the crucial impact of the sample preparation in order to achieve best data quality and to keep a clean microscope environment. Based on our experiments, we can prepare our samples in a way resulting in less contamination on the specimen surface and introducing less volatile organic molecules to the microscopes.

Fig. 1: Carbon contamination depending on the beam exposure times of toluene (black) and THF (red) immediately after sample insertion (filled in dots) and after 30 min (circles) in the TEM. For each measurement, an area of 173 nm x 173 nm was exposed to the electron beam. Less volatile solvents like toluene lead to far more contamination, though the solvent can outgas in the TEM vacuum.

Fig. 2: Pressure measurements of pumping a toluene sample compared to a reference measurement (empty TEM grids). The pressure values are measured above and below a baffle cooler. The pressure difference between the sample and the reference above of the cooler indicates the presence of outgassing molecules.

Fig. 1

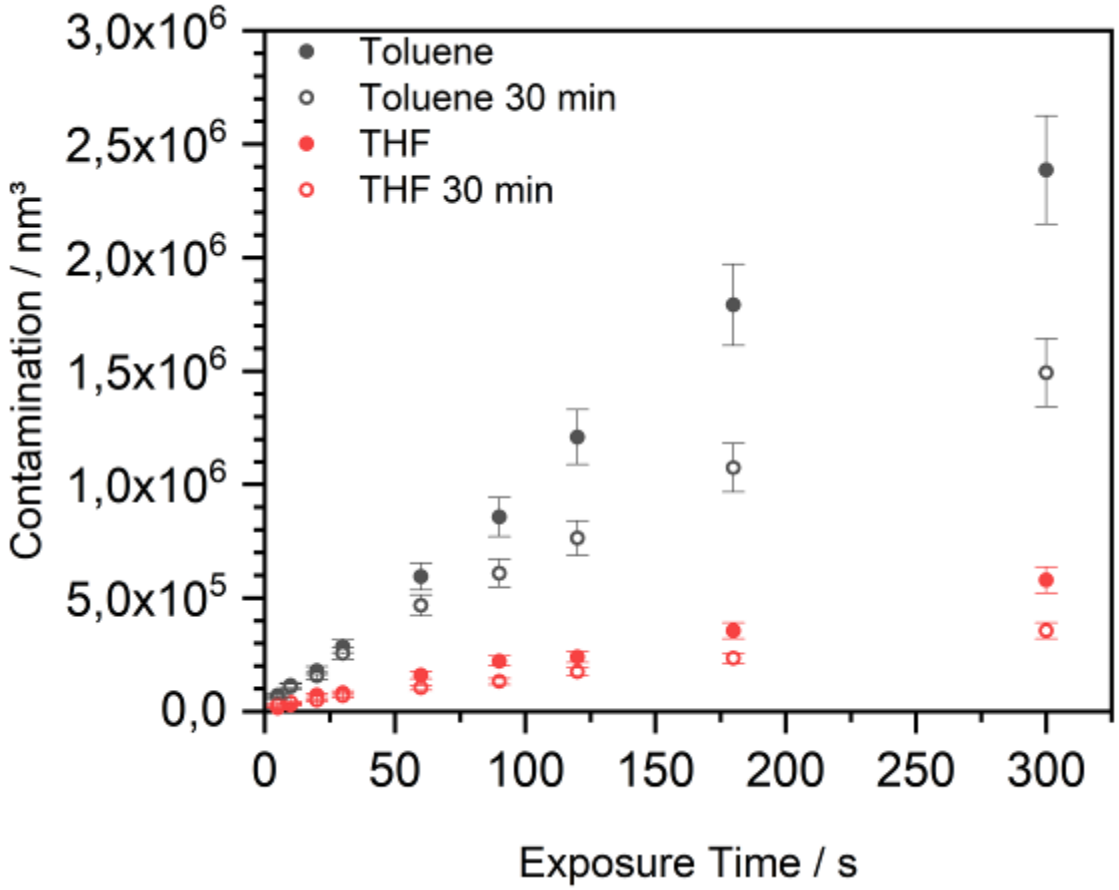
Contamination / nm³
3,0x10⁶
2,5x10⁶
2,0x10⁶
1,5x10⁶
1,0x10⁶
5,0x10⁵
0,0
Toluene
Toluene 30 min
THF
THF 30 min
0
50
100
150
200
250
300
Exposure Time / s

Fig. 2

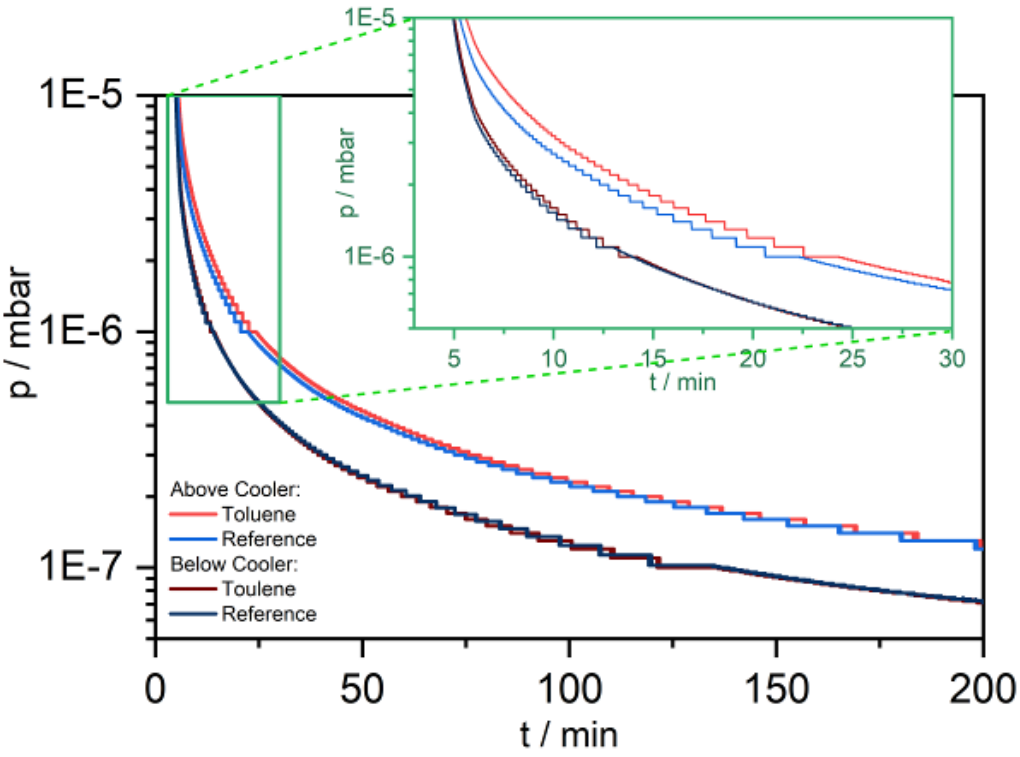
p / mbar
1E-5
1E-6
1E-7
0
50
100
150
200
t / min
Above Cooler:
Toluene
Reference
Below Cooler:
Toulene
Reference
1E-5
1E-6
p / mbar
5
10
15
20
25
30
t / min

IM1.P008

Study of beam sensitive and nanostructured materials by low-kV and low-dose optimized EBSD

T. Przybilla[1], M. Dierner[1], R. de Kloe[2], H. A. Afify[3,4,5], J. Will[1], W. Heiss[3,5], E. Spiecker[1]

[1]Institute of Micro- and Nanostructure Research (IMN) and Center for Nanoanalysis and Electron Microscopy (CENEM), Department of Material Science, FAU Erlangen-Nuremberg, Erlangen, Germany
[2]EDAX/Ametek BV, Tilburg, Netherlands
[3]Materials for Electronics and Energy Technology (i-MEET), Department of Material Science, FAU Erlangen-Nuremberg, Erlangen, Germany
[4]National Institute of Laser Enhanced Sciences (NILES), Department of Laser Sciences and Interactions, Cairo University, Giza, Egypt
[5]Materials for Electronics and Energy Technology (i-MEET), Department of Material Science, Energy Campus Nuremberg, Nuremberg, Germany

EBSD analysis on beam sensitive and nanostructured materials demands in many cases low-kV, low-dose or low-vacuum operation with careful beam budget design and sensitive detectors in order to avoid sample degradation, minimize image drift, satisfy spatial resolution requirements and gain sufficient signal-to-noise level for indexable Kikuchi patterns [1-3]. The stated requirements play a major role for the structural characterization of metal-halide-perovskite (MHP) thin films/crystallites, which revolutionized the field of thin-film semiconductor technology, due to their favorable optoelectronic properties and facile solution processing e.g. by inkjet-printing [4]. Best device efficiencies require structural coherence on the atomic scale, which can be achieved by epitaxial growth on lattice matching substrates [4]. In this work, we demonstrate the capability of recent sensitive EBSD cameras for the structural characterization of beam sensitive MHP crystallites ($CsPbBr_3$, $FACsPbBr_3$, $MAPbBr_3$) grown on various substrates (PbS, mica). In particular new direct detection based cameras allow to obtain indexable Kikuchi patterns from MHPs at strongly decreased electron dose at low-kV compared to their indirect detection based counterparts (Figure 1a), which is crucial for a reliable and statistically relevant EBSD characterization. Based on this, we present EBSD results underlining the homogeneous hetero-epitaxial growth over large scale of $CsPbBr_3$ and $FACsPbBr_3$ crystallites on single crystalline PbS substrates fabricated via inkjet-printing and further substantiate the theory of lattice-anchoring and stabilization of the cubic crystal structure of MHPs as indicated in former studies [4, 5] (Figure 1b). Further, we present results on the orientation-dependent growth characteristic of $FACsPbBr_3$ crystallites on flexible and single crystalline mica substrates. Here, various different cubic crystal orientations with characteristic morphologies are observed. Most crystals feature a [101] out-of-plane orientation which is parallel to the [001] axis of the substrate and grow along (110) planes, with a few of them obtaining an in-plane orientation of [101] parallel to the [010] direction of the substrate. Further advantages of low-kV and low-dose sensitive EBSD detectors lie in the achievable spatial resolution, making them perfectly suitable for the analysis of nanomaterials. This benefit evolves particularly in conjunction with low-vacuum operation, since any need for conductive coating of the sample surface, which damps the EBSD signal, but is often required to minimize sample drift, is reduced. Referring to this, we present in Figure 2 EBSD results on the texture analysis on nano-grained and low Z-number thin films (AlN) based on Pt/Ti/SiO2/Si substrates, revealing an average grain size of ~30 nm and a crystal fiber texture with an out of-plane <0001> alignment. Further analyses focus on the local clustering of neighboring grains with similar orientation. Overall, we show that the application of low-kV and low-dose EBSD paves the way for a reliable and efficient structural characterization of beam sensitive and nanomaterials and enables new insights into epitaxial growth and the orientation-dependent growth of MHPs on large scale.

[1] Adhyaksa et al., 10.1002/adma.201804792

[2] Leonhard, et al., 10.1002/ente.201800989

[3] Luo et al., 10.1021/acs.jpcc.0c06733

[4] Sytnyk et al., 10.1002/adfm.202004612

[5] Afify et al., 10.1002/adom.202200237

Fig. 1

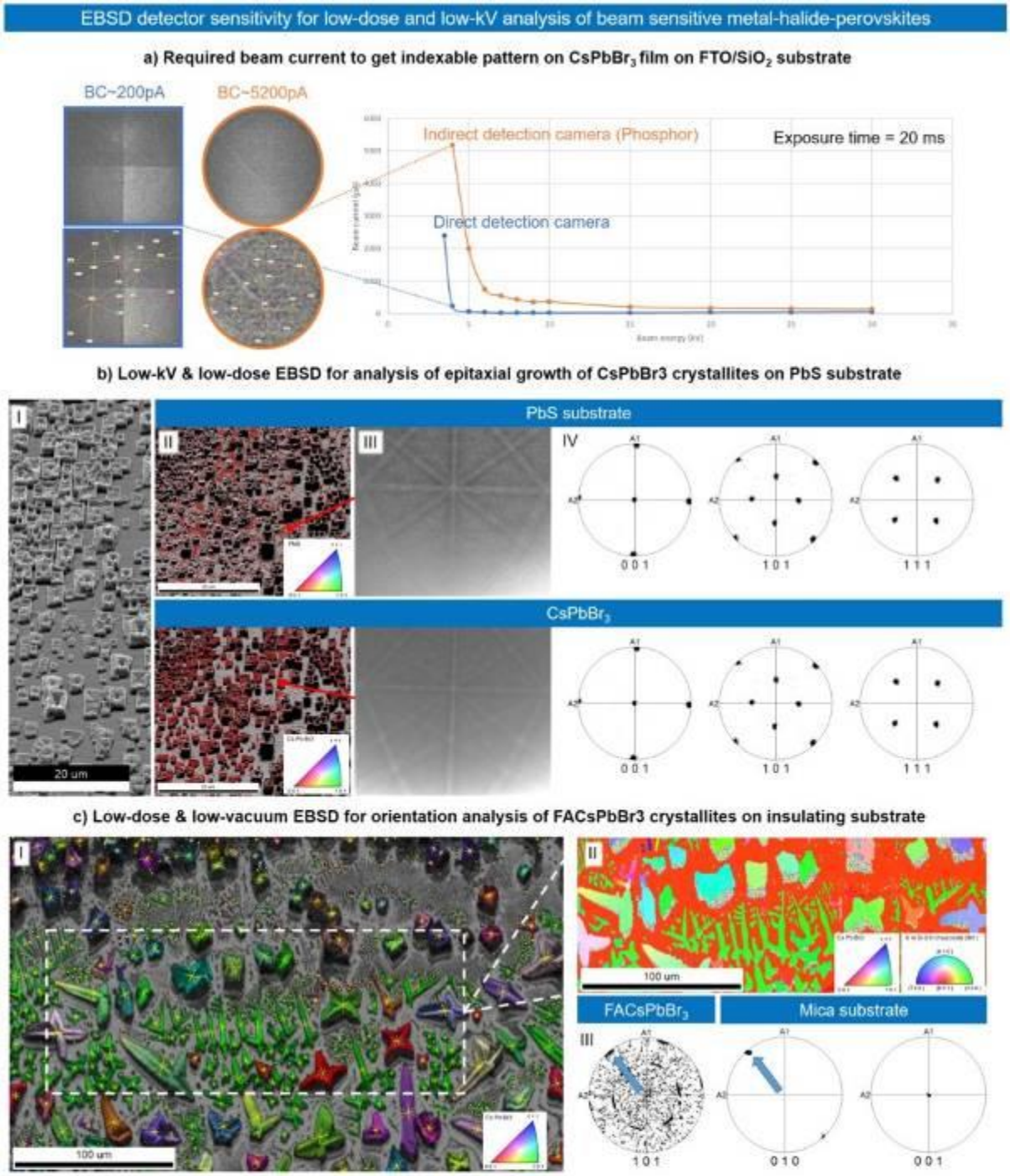

Figure 1: a) Comparison of low-kV and low-dose detector sensitivity between direct detection camera ("Clarity Super", Ametek) and Phosphor-based camera system ("Velocity", Ametek). The minimum required beam current (BC) to get indexable patterns on $CsPbBr_3$ at 4 kV beam energy is around 26x lower in case of the direct detection based camera (~200 pA vs. 5200 pA). b) Low-kV (8 kV) and low-dose (100pA) EBSD analysis to study the epitaxial growth of $CsPbBr_3$ crystallites on PbS substrate. b-I) SEM overview image. b)-II IPF maps (out-of-plane) overlaid on BSE images. b-III) Corresponding Kikuchi patterns of PbS and $CsPbBr_3$ phases. b-IV) Matching pole figures of both phases indicate epitaxial relationship. c) Low-dose (900 pA) & low-vacuum (20 Pa) EBSD analysis for orientation analysis of $FACsPbBr_3$ crystallites on insulating mica substrate, featuring a high indexing success rate of 86%, which is hardly possible without a low-vacuum mode due to charging/sample drift and the need for conductive layers. c-I) Pattern quality map with overlaid IPF orientation mapping reveals the out-of-plane orientation from the perovskite crystallites and the matching/alignment between crystal <110> planes (indicated as yellow lines) and crystal shapes. c-II) IPF orientation mapping revealing the [001] out-of-plane orientation of the substrate. c-III) Corresponding PFs of perovskite crystals and substrate reveal a textured crystal growth with a few crystals being aligned in-plane with [101] parallel to the [010] axis of the substrate.

Fig. 2

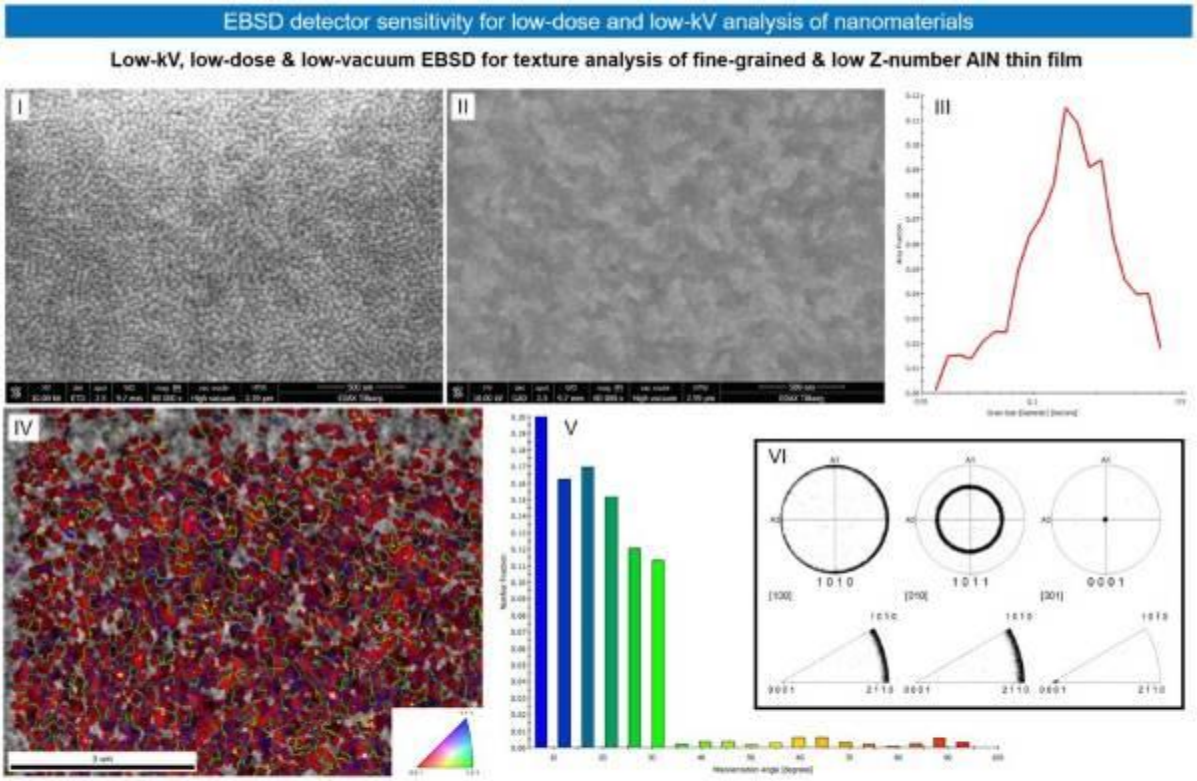

Figure 2: Low-kV (8 kV), low-dose (80 pA) & low-vacuum (10 Pa) EBSD texture analysis of fine-grained & low Z-number AlN thin film. SE imaging (I) reveals the individual fine grain structure, while BSE imaging (II) indicates larger grain domains with similar crystal orientation. The subsequent EBSD analyses (III, IV, V, VI) reveal a grain size distribution (III) with minimum grain sizes ~30 nm, a crystal fiber texture with an out of-plane <0001> alignment (visible in the PFs and IPFs in VI) and the out-of-plain orientation of each individual grain with the misorientation angle distribution (V), overlaid on the pattern quality map (IV).

IM1.P009

New Performance for SEM with an Annular Switchable Gain BSE Detector Diode

S. Mazloomzadeh[1], M. Schmid[1], S. Aschauer[1], H. Soltau[1]

[1]PNDetector GmbH, Munich, Germany

Using the whole energy spectrum of the SEM has been always an issue by installation of just one Back Scattered Electron Detector (BSD) to get high quality images in each scanning speed and energy range for every application. Despite of the state-of-the-art BSDs with all premium features as a GCE up to 85%, a DCE up to 55% at 1 keV (see Fig. 1), and a high signal to noise (S/N) ratio, there is still lack of a feature which closes the gap between low and high keV range when high scan speed and high throughput are needed. This applies specially for life science and bio science applications where the sensitive samples need to be scanned at low keV conditions but at the same time with high image acquisition.

In order to be able to maintain the scan speed relatively high at very low energies, one needs to increase the gain of the BSD collecting as much signal as possible to optimize the signal to noise (S/N) ratio. A typical BSD is not capable of changing the gain once the higher value is needed since the gain is already fixed in the preamplifier. There is no more need to exchange the BSD while working under this situation. Instead with PNDetector"s new Switchable Gain Advanced BSD (SWG-BSD) one can overcome this issue and switch the gain manually to a higher value in a fraction of a second while scanning the sample so that the scan speed is not sacrificed and significantly reduced to get high resolution images. Here we show how the new detector enables this technique.

The SWG-BSD is equipped with two preamplification gains in the preamplifier integrated into a compact vacuum compatible housing shown in Fig. 2. The gain values are adjusted to and V/A. The lower value is called "high speed" mode and the higher value is called "high gain" mode. With switching between these two modes one is capable of adjusting the gain while changing the energy in order to maintain the desired scan speed and optimize the S/N. When the SWG-BSD is used in high speed mode the typical rise time achieved by the detector is down to 30ns (the real TV speed) and very high resolution single frame images without smearing can be taken under 0.1 sec with 0.8 MP once the sample is scanned at high energies such as 30keV. The typical example of such application is in semiconductor industry to surf the samples very fast and search for hot spots. Once the spot is found and focused it is now the time to switch to high gain mode and zoom the spot for detail inspection to get an optimized image while reducing the scan speed not that low as it is normally used with traditional BSDs. The SWG-BSD enables the possibility of maintaining the scan speed relatively high under 1000ns rise times and the result will be a superior SEM image of the spot in e.g. 31 sec at 1 keV (see Fig. 3). Other common application for SWG-BSD is observation of sensitive samples like tissues for which very low energies under 1keV are needed to ensure minimal interaction between the electron and the sample and reduce damage and charging.

The two gain settings adjusted for SWG-BSD is used in combination with the main amplifier with a Python based GUI software enabling the switch action by a single button designed in the software. The SWG-BSD comes also with the complete motorized retractable system shown in Fig. 2 with all vacuum compatible parts to be installed directly in the SEM.

Figure 1.

Figure 2.

Figure 3. Two SEM images taken by SWG-BSD in (left) high speed and (right) high gain modes.

Fig. 1

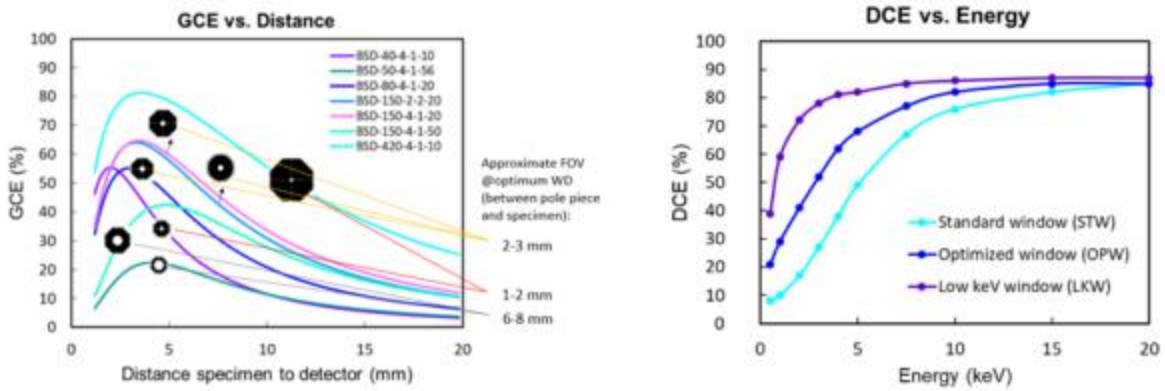

Fig. 2

Fig. 3

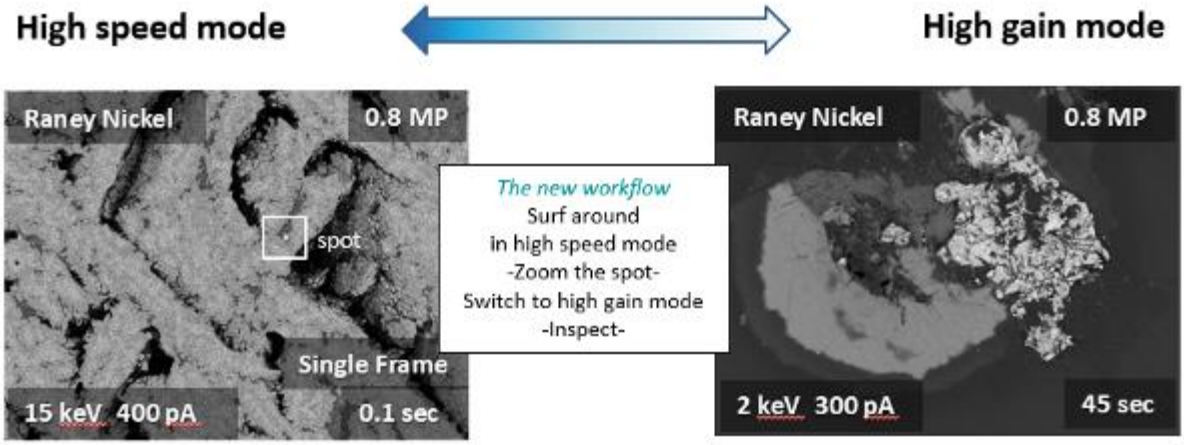

IM1.P010

A ground-potential monochromator design

F. Börrnert[1], S. Uhlemann[1], V. Gerheim[1], M. Haider[1]

[1]CEOS GmbH, Heidelberg, Germany

Electron energy loss spectroscopy with high energy resolution is interesting for a wide range of applications ranging from analytics of organic matter at very small dimensions to determining the optical properties in two-dimensional materials. In (scanning) transmission electron microscopy ((S)TEM), the energy resolving power of the instrument was determined by the type of the electron source and limited to about 300 meV before the advent of electron monochromators for (S)TEM instruments about two decades ago. In the meantime, several different designs of monochromators have been implemented and can be bought as an option to most high-end microscopes [1-4].

There are two meaningful positions for monochromators along the optical path: Before or after the accelerator, that is, at high potential or at ground potential, respectively. While most monochromator implementations today are at high potential, ground-potential monochromators have some notable advantages, such as less sensitivity to selection-slit interactions and magnetic stray fields, independence of acceleration voltage instabilities, no performance deterioration from Boersch or Loeffler effect, and the possibility to retrofit it to existing instruments.

One of the major general drawbacks in the use of a monochromator for imaging or spectroscopy is the loss of current in the electron beam, and thus, loss of interpretable signal. Therefore, the most interesting parameter besides the actual energy resolution is the available current at this very energy resolution at a certain primary electron energy.

Here, we present a design for a ground-potential monochromator that can be retrofit to existing microscope columns. Performance estimates are given for primary electron energies of 300 keV and 30 keV with instruments equipped with a cold field emission electron source.

References:

[1] H. Rose, Ultramicroscopy **78**, 13-25 (1999).

[2] P. C. Tiemeijer, Inst. Phys. Conf. Ser. **161**, 191-194 (1999).

[3] O. L. Krivanek *et al.*, Philos. Trans. R. Soc. London. Sec. A **367**, 3683-3697 (2009)

[4] M. Mukai *et al.*, Ultramicroscopy **140**, 37-43 (2014).

IM1.P011

Optimization and new tools for 3DED data collection

M. Santucci[1], U. Kolb[1]

[1]JGU Mainz, Institut für Physikalische Chemie, JGU Mainz, Mainz, Germany

Introduction 3D Electron Diffraction (3DED), become the "low dose" technique for crystal structure determination of nanocrystals and a wide range of materials. The criteria for a successful crystal structure solution is data completeness while a sufficient refinement is data quality dependent.[1] Several methods for 3DED data acquisition using different hardware have been established, but in order to spread the usage of 3DED a standardization is needed to overcome two major challenges intrinsic in the hardware used.[2]

Objectives 3DED needs to become user friendly thanks to automatized data acquisition and diffractometer alignment. Secondly, the uncertainties intrinsically present in our microscopes need to be dumped which make it difficult to measure crystals with domains less than 100nm requiring smaller beam sizes. With these improvements, 3DED will be accessible to a wider community and will show its true potential compared to XRD analysis.

Methods The methods currently available use two major approaches, Nano-Beam Electron Diffraction (NBED) and Selected Area Electron Diffraction (SAED). SAED has several advantages, such as beam size down up to 200nm, small crystal shift during the tilt series. Combined with Instamatic, these features enable rapid dissemination of SAED, especially to JEOL users.[3] However, NBED can achieve beam sizes down to a few nm, reduce image dose rates up to 40-fold in STEM images, and use HAADF to generate Z-image contrast. It often shows higher quality datasets compared to SAED and allows multiple datasets acquisition from the same crystal, due to localized beam damage.[4] The concepts of the NBED technique are implemented in Fast-Automated Diffraction Tomography (Fast-ADT), a user-friendly DigitalMicrograph© (DM) script for 3DED acquisition and tracking.[5]

Results Here we report our improvement to the 3DED technique. Fast-ADT has been translated and implemented from DM© in Python. The script is based on the Temscript package, allowing use for the majority of the FEI microscopes and future expansion to JEOL microscopes using PyJEM.[6] Fast-ADT allows TEM/STEM SAED and NBED in Precession ED Tomography (PEDT) and Continuous Rotation ED (CRED). This way, FEI machines could use one universal tool for conventional 3DED experiment, with the potential to be deployed and customized to design its personal 3DED experiments. To enhance the 3DED automation, an automatic eucentric height tool is implemented in Fast-ADT, which performs the Z control of the target crystal in a more precise and reproducible way. This is essential for NBED, which plays a role to counterbalance the target drift during data collection and is the major responsible of a 3DED data collection failure.

Conclusion With these improvements, one of the last challenges that could be solved by software is the design of a more robust 3DED crystal tracking routine. This implementation is important for NBED because it is easier to lose the target during the tilt series than in SAED, where the beam size is higher. In conclusion, Fast-ADT has the potential to be used more efficiently and be spread easier to all the 3DED labs as a complete package for 3DED data acquisition.

[1]https://doi.org/10.1107/S2052520619006711

[2]https://doi.org/10.1021/acscentsci.9b00394

[3]https://doi.org/10.1107/S2052252519007681

[4]https://doi.org/10.1557/PROC-1184-GG01-05

[5]https://doi.org/10.1016/j.ultramic.2020.112951

[6]https://github.com/niermann/temscript

IM2.002-invited

Modelling spatially-resolved electron energy-loss spectra in the low-loss region

A. Konečná[1]

[1]CEITEC, Brno University of Technology, Brno, Czech Republic

Mapping low-energy excitations such as plasmons, excitons, or phonons with high spatial and spectral detail is key for understanding and engineering nanostructured materials' optical, electrical, or thermal properties. One of the experimental techniques allowing for analyzing the low-energy excitations and their interaction down to the atomic scale is electron energy-loss spectroscopy (EELS) in a scanning transmission electron microscope (STEM), which enables the acquisition of spectra with a few-meV/Å spectral/spatial resolution [1,2].

Most of the recent state-of-the-art STEM-EELS experiments have been complemented or even guided by theoretical modelling and predictions. This talk will review two main approaches for simulating low-loss EEL spectra, using either classical electrodynamics or ab-initio methods. I will show that the macroscopic electrodynamics calculations are suitable for describing polaritonic excitations, such as plasmon or phonon polaritons that typically emerge in metals or ionic crystals, respectively. I will discuss examples of spatially-resolved EELS of electron-beam excitation of phonon polaritons in hexagonal boron nitride [3] and a system sustaining plasmon and phonon polaritons, which are engineered to strongly couple [4].

On the other hand, STEM-EELS of molecular systems or momentum-resolved EELS requires modelling at a truly microscopic level, which I will demonstrate with an example of a hBN-like molecule. The theoretically predicted results obtained with ab-initio calculations demonstrate that a single isotope impurity in this molecule would significantly affect the EELS probability [5]. Finally, we will discuss possible future directions in STEM-EELS, considering both theoretical and experimental efforts.

[1] FS Hage et al., Science **367** (2020), p. 1124-1127. doi:10.1126/science.aba1136

[2] X Yan et al., Nature **589** (2021), p. 65-69. doi:10.1038/s41586-020-03049-y

[3] A Konečná et al., Small **17** (2021), p. 2170201. doi:10.1002/smll.202170201

[4] P Gallina et al., arXiv:2112.12832 (2021), https://arxiv.org/pdf/2112.12832.pdf

[5] A Konečná, F Iyikanat and FJ García de Abajo, ACS Nano **15** (2021), p. 9890-9899. doi: 10.1021/acsnano.1c01071

IM2.003

Spectroscopic coincidence experiments at nanoseconds time resolution in TEM

D. Jannis[1,2], A. Béché[1,2], K. Müller-Caspary[3], J. Verbeeck[1,2]

[1]University of Antwerp, Physics, Antwerp, Belgium
[2]NANOlab Center of Excellence, Sciences, Antwerp, Belgium
[3]Ludwig-Maximilians-University Munich, Department of Chemistry and NanoScience, Munich, Germany

Electron energy loss spectroscopy (EELS) and energy dispersive spectroscopy (EDX) are two frequently used analytical techniques in transmission electron microscopy. Both techniques rely on the inelastic scattering of the incoming electron with the core level states of an atom to determine the chemical composition of the material. The two techniques differ with respect to which particle is detected. For EELS the energy of the inelastically scattered electron is measured and in EDX the energy of an emitted X-ray, which is created during the decay of the excited atom, is detected. Hence, for every X-ray emitted there was at least one electron that gave part of its energy to excite the atom which could give the impression that they convey very similar information. However, the energy resolution for EDX is typically 100 times worse compared to EELS due to the detection mechanism of X-rays (100 eV). On the other hand, EELS has a low signal-to-background ratio, (SNR) making it hard to detect low concentration elements. Since these two techniques arise from the same physical process, it should be possible to find a correlation in time between such an inelastic electron and x-ray. By only selecting an electron when an X-ray is detected nearby in time *Kruit el al.* [1] were able to detect this time correlation between the electrons and X-rays.

Since individual electron and X-ray events need to be detected at nanosecond time resolution, a dedicated setup needed to be developed. In the present work, the current setup will be described where we were able to get a temporal resolution of ~250 ns without filtering events on the hardware level. Hence the conventional EELS and EDX signals are retained. Furthermore, we will show how by applying such a time correlation constraint it is possible to remove the background signal in EELS (see Fig.1) and obtain EDX spectra without having any prior knowledge on the shape of this background [2]. This is especially valuable for EELS where conventionally an empirical power-law function is used to fit the background where a pre-edge is needed to extrapolate a fitted background signal. Additionally, it will be shown how one can determine the collection efficiency [JV1] of both EELS and EDX without having the need for a reference sample and knowledge on beam current. Finally, it is discussed how using the time correlation between EELS and EDX can improve the signal-to-noise ratio for trace elements where the signal-to-background is too low for EELS and the energy resolution for EDX is insufficient to discriminate between overlapping x-ray peaks.

[1] P. Kruit et al. Detection of X-rays and electron energy loss events in time coincidence. *Ultramicroscopy*, 13(3):205-213,1984.

[2] D. Jannis, K. Müller-Caspary et al., Spectroscopic coincidence experiments in transmission electron microscope, *Appl. Phys. Lett.* **114**, 143101 (2019)

[3] D. Jannis et al., Coincidence Detection of EELS and EDX Spectral Events in the Electron Microscope, *Appl. Sci.* 2021, 11, 9058

[4] D.J., A.B. and J.V. acknowledge funding from the Flemish Research Fund FWO under project no. G093417N and G042920N, J.V. acknowledges funding from No 823717 ESTEEM3[JV1] , K.M.-C. acknowledges funding from the FWO under contract G042920N

Fig. 1

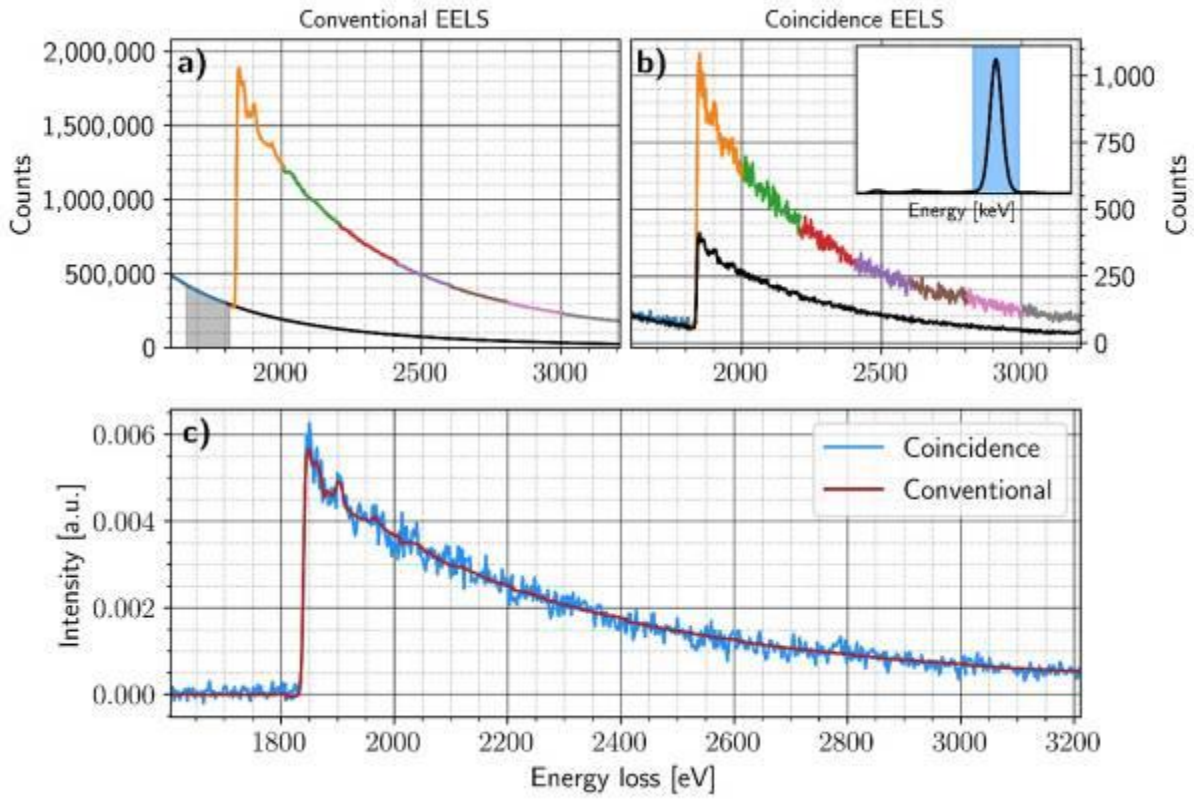
Conventional EELS
Coincidence EELS
a)
b)
c)
Counts
Counts
Energy [keV]
Intensity [a.u.]
Energy loss [eV]
Coincidence
Conventional
2,000,000
1,500,000
1,000,000
500,000
0
1,000
750
500
250
0.006
0.004
0.002
0.000
2000
2500
3000
1800
2200
2400
2600
2800
3200

IM2.004

Mapping local phonon modes in silicon grain boundaries at atomic resolution

B. Haas[1], T. Boland[2], C. Elsässer[3], A. Singh[4], K. March[5], J. Barthel[6], C. T. Koch[1], P. Rez[4]

[1]Humboldt-Universität zu Berlin, Department of Physics and IRIS Adlershof, Berlin, Germany
[2]Arizona State University, School for Engineering of Matter Transport and Energy, Tempe, AZ, United States
[3]Fraunhofer Institute for Mechanics of Materials IWM, Freiburg, Germany
[4]Arizona State University, Department of Physics, Tempe, AZ, United States
[5]Sorbonne Université, Institut de Minéralogie, de Physique des Matériaux et de Cosmochimie, Paris, France
[6]Forschungszentrum Jülich, Ernst Ruska-Centre (ER-C 2), Jülich, Germany

INTRODUCTION

In the last few years, mapping of phonon modes by scanning transmission electron microscopy electron energy loss spectroscopy (STEM-EELS) has become possible [1-2]. Phonons, the quantized collective vibrations of atoms, play a fundamental role in many physical properties of materials, especially thermal and electrical conductivity. Changes in the atomic structure at grain boundaries (GBs) affect the local density of states (LDOS) of phonons and thus these physical properties.

OBJECTIVES

Here, we measure the LDOS across different GBs in silicon at atomic resolution and compare them to results of theoretical calculations. Such measurements have the potential to contribute to our understanding of thermal conductivity across internal interfaces, to the optimization of polycrystalline Si solar cells, and to the design of phononic devices.

MATERIALS & METHODS

The Si sample in [110] zone axis exhibiting different GBs was prepared from an ingot by FIB and further thinned and cleaned using Ar ions.

The experiments were performed in a Nion HERMES whose IRIS spectrometer was fitted with a Dectris ELA direct electron detector. For the atomic-resolution spectral maps (exposure time: 1 ms, dispersion: 1 meV per channel), a probe convergence semi-angle of 30 mrad and a spectrometer collection angle of 45 mrad were used. The energy resolution (FWHM of the zero-loss peak in vacuum) was 8.9 meV. To correct for slow sample drift, series of spectrum images were acquired and non-rigidly registered and integrated [3]. In addition, high-angle annular dark-field (HAADF) images were acquired using 36 mrad convergence angle with greater magnification in the monochromator to increase spatial coherence.

Theoretical phonon DOS and LDOS were calculated from velocity-velocity correlation functions of molecular dynamics trajectories using the empirical Tersoff potential [4].

RESULTS

Fig. 1 (a) shows an overview image of the sample exhibiting different GBs. In (b) the triple point of two meeting symmetric Σ3 and one symmetric Σ9 can be seen. A raw bulk spectrum, background fit and resulting phonon DOS are depicted in (c), marking the optic phonon peak around 62 meV that is analyzed in the following.

In Fig. 2 for three different boundaries (symmetric Σ3, symmetric Σ9 and asymmetric Σ9), the atomic structure (via high-resolution HAADF), a HAADF image acquired simultaneously with the EELS signal, a map of the EELS intensity around 62meV, a line profile across it, and calculated LDOS are given. This observation allows us to correlate the changes in atomic structure with changes in the phonon LDOS from virtually no effect at all for the symmetric Σ3 to drastic modification (compared to bulk) for asymmetric Σ9.

CONCLUSION

We demonstrated mapping of localized phonon modes at GBs in Si at atomic resolution. The more structurally distorted the boundary configuration is, the stronger the suppression of the phonon LDOS - in agreement with theory.

We expect that this research contributes to controlling phonon propagation and to minimizing decoherence in Si-based quantum computing using phonon entanglement.

[1] F.S. Hage et al., *Science* **367**, 1124 (2020).

[2] X. Yan et al., *Nature* **589**, 65 (2021).

[3] L. Jones et al., *Microscopy* **67**, 98 (2018).

[4] P. Rez et al., *Microsc. Microanal.* ***28***, 672 (2022).

Fig. 1: (a) Overview of Si sample, (b) high-resolution of GBs, (c) EELS in bulk with fit.

Fig. 2: Structure, EELS and simulation for different GBs.

Fig. 1

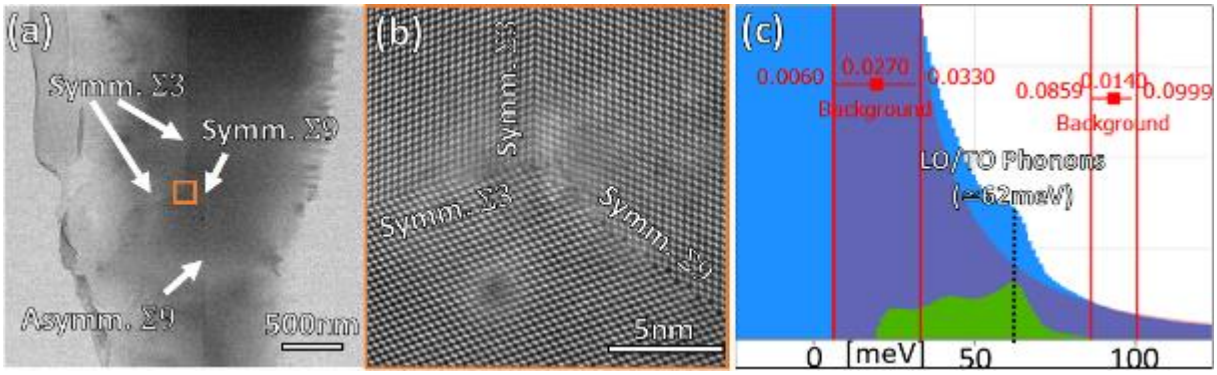

Fig. 2

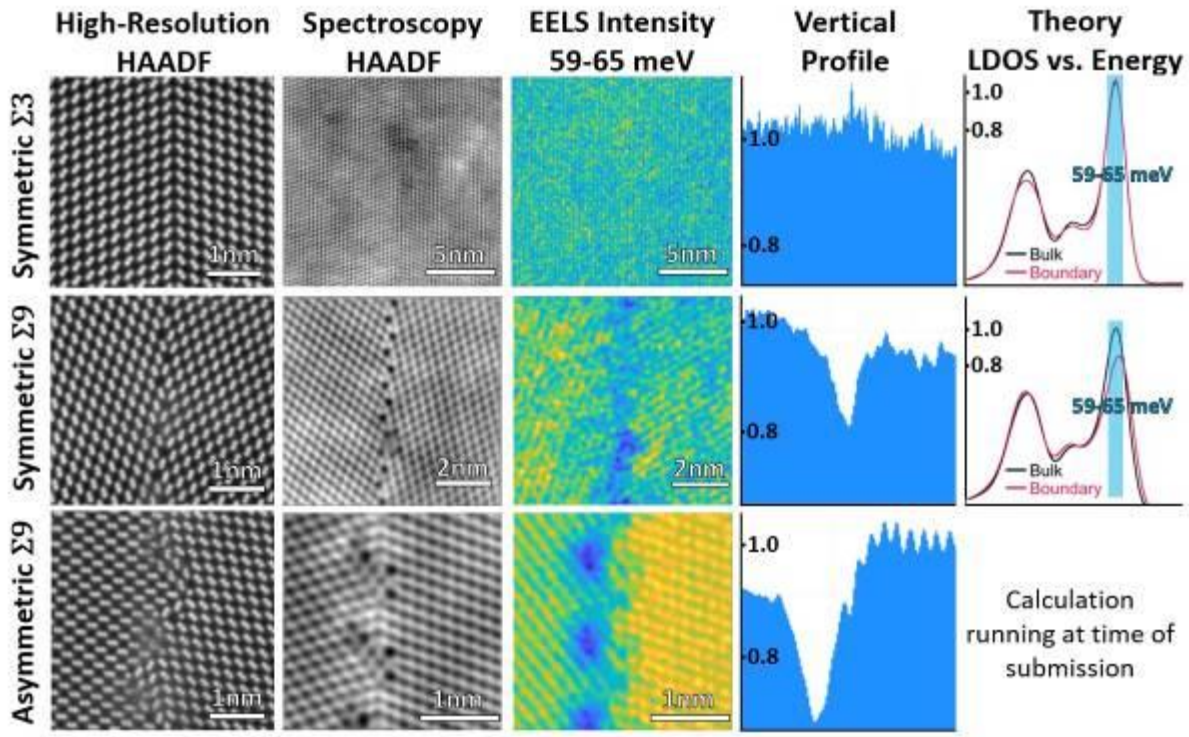

IM2.005

Beyond conventional chemical mapping: prospects and challenges of orbital mapping

S. Löffler[1], M. Ederer[1], M. Oberaigner[2], M. Mohn[3], J. Biskupek[3], U. Kaiser[3], G. Kothleitner[2,4], Q. Ramasse[5,6], D. Kepaptsoglou[5,7], M. Bugnet[5,6,8]

[1]TU Wien, USTEM, Vienna, Austria
[2]Graz University of Technology, Institute of Electron Microscopy and Nanoanalysis, Graz, Austria
[3]Universität Ulm, Materialwissenschaftliche Elektronenmikroskopie, Ulm, Germany
[4]Graz Centre for Electron Microscopy, Graz, Austria
[5]SuperSTEM Laboratory, Daresbury, United Kingdom
[6]University of Leeds, Leeds, United Kingdom
[7]University of York, York, United Kingdom
[8]University of Lyon, Lyon, France

It is well-known that core-loss EELS data contains not only information about the chemical elements present in the sample, but also about the scattering atoms" chemical environment, which manifests itself in the near-edge fine structure (ELNES). This enables some more advanced characterization techniques such as the fingerprinting of chemical compounds and the mapping of oxidation states. In this work, we explore the possibilities of fine structure mapping at "sub-atomic" spatial resolution, i.e., the real-space mapping of transitions to individual orbitals such as p_z or d_{xy} inside the sample.

Arguably, an electron is more likely to trigger a transition from, say, a 1s core-electron to an unoccupied p_x state if it passes close to the region where the 1s-p_x-overlap is large than it is when passing "far away". Therefore, it is conceivable that by mapping the inelastic scattering probability (i.e., an EEL spectrum) with very high spatial resolution allows to map the orientation and shape of the p_x orbital. Indeed, this is corroborated by detailed theoretical calculations [1] as well as proof-of-principle experiments [2,3]. Fig. 1 shows an example from the mapping of Ti-e_g-like states in Rutile oriented along the [0 0 1] zone axis at 80 kV. Despite the noise, the 90° rotation between adjacent Ti atoms is clearly visible.

In this work, we discuss the fundamental requirements for successfully performing orbital mapping, include conditions on the sample (such as geometry, symmetry and stability), the experimental setup (such as spatial resolution, energy resolution and high-tension), and the detection process (such as the signal to noise levels). In particular, it is shown that a low symmetry in the chosen orientation is required to clearly separate the ELNES peaks of different orbitals, that narrow energy ranges are generally necessary, and that high incident doses are required, even with direct electron detectors.

Despite the technical challenges, the prospect of mapping the electronic transitions between individual orbitals is exciting not only from a fundamental quantum mechanical point of view, but also for its possibilities for the design and characterization of novel materials in many fields, including electronics, energy storage, and catalysis. [4]

[1] Löffler et al., Ultramicroscopy 131 (2013) 39
[2] Löffler et al., Ultramicroscopy 177 (2017) 26
[3] Bugnet et al., PRL 128 (2022) 116401
[4] The authors acknowledge financial support by the Austrian Science Fund (FWF) under grant nr. I4309-N36.

Fig. 1: Example of mapping transitions to Ti-e_g-like orbitals in Rutile. a) EELS spectrum with selected energy range (yellow). b) charge density calculated with WIEN2k. c) Experimental imaging after averaging over several unit cells. d) Same as c after Gaussian filtering. e) Simulated image at infinite dose. f) Simulated image at realistic dose. g) Same as f after Gaussian filtering. All scalebars indicate 5 Å. Adapted from [2].

Fig. 1

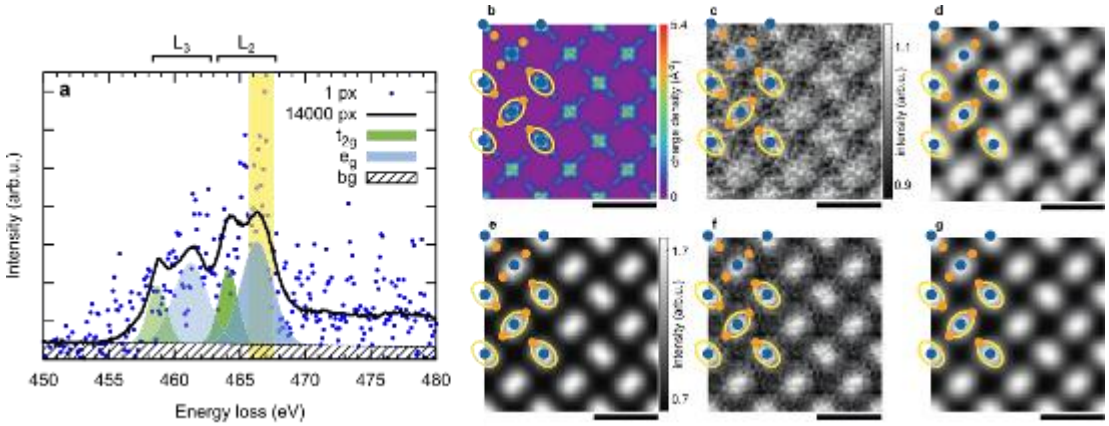
a
L3
L2
1 px
14000 px
t2g
eg
bg
Intensity (arb. u.)
450
455
460
465
470
475
480
Energy loss (eV)
b
c
d
e
f
g

IM2.006

Simulations of electron energy loss spectra at ultra-low energy losses

J. Rusz[1], P. Zeiger[1]

[1]Uppsala University, Department of Physics and Astronomy, Uppsala, Sweden

Recent hardware developments in monochromation of the electron beam [1] in scanning transmission electron microscopy (STEM) have opened new domains of physics to the spectroscopic studies at down to atomic resolution. Most notably, excitation of phonons, happening in the tens to few hundreds of meV range, has been observed at unprecedented spatial resolutions [2,3,4]. Compared to other spectroscopic methods, high spatial resolution is the primary advantage of STEM. It gives access to local changes in the electron energy loss spectra (EELS) near interfaces or defects, also within this ultra-low energy-loss range [3,4]. The primary objects of interest for STEM-EELS are thus local changes of the low energy excitations.

To predict and properly interpret the experimental data, reliable simulation methods are necessary. Such methods also need to have a favorable scaling with respect to system sizes (number of atoms, Nat). For instance, a structure model with an interface or a localized defect needs to be sufficiently large to avoid self-interaction of the defect with its periodic images. As an example, an fcc silicon structure model of 1000 atoms would be a cube of dimensions 2.73 nm3. Realistic sample thicknesses are often an order of manitude larger and lateral dimensions may often need to be larger to contain the spreading electron beam wavefunction in multislice calculations. Thus system sizes of tens of thousands of atoms are often needed.

Transition potential multislice-based approaches for calculation of inelastic scattering [5,6] provide a transparent and accurate way of simulating STEM-EELS of phonons, and similarly with Bloch-waves based approaches [7] they allow to both include electron challeling effects as well as spectroscopic information. Nevertheless, these approaches require explicit knowledge of phonon modes, which requires diagonalization of dynamical matrix scaling with the third power of Nat. In the domain of tens of thousands of atoms such approaches quickly become computationally too expensive.

We have recently presented a method named frequency resolved frozen phonon multislice method (FRFPMS; [8]), which has computing costs scaling linearly with Nat. We will discuss its capabilities and recent developments. This method is also a starting point for a description of another type of excitations in solid state, in particular, the excitations of a magnetic subsystem called magnons. Magnons occupy approximately the same energy range as phonons, however compared to phonons their interaction with electron beam is significantly weaker. Diffuse scattering due to magnons [9] and a semi-classical theory of scattering of electron beams on magnons [10] have been presented recently. We will discuss our recent developments in the theory of magnon scattering in STEM-EELS and routes to potential detection of this type of quasiparticle excitations by monochromated STEM.

References:

[1] O. Krivanek et al., Nature 514, 209 (2014).
[2] F. Hage et al., Phys. Rev. Lett. 122, 016103 (2019).
[3] F. Hage et al., Science 367, 1124 (2020).
[4] X. Yan et al., Nature 589, 65 (2021).
[5] B. D. Forbes and L. Allen, Phys. Rev. B 94, 014110 (2016).
[6] C. Dwyer, Phys. Rev. B 96, 224102 (2017).
[7] P. Rez and A. Singh, Ultramic. 220, 113162 (2021).
[8] P. M. Zeiger and J. Rusz, Phys. Rev. Lett. 124, 025501 (2020).
[9] K. Lyon et al., Phys. Rev. B 104, 214418 (2021).
[10] B. Mendis, Ultramic. 230, 113390 (2021).

IM2.P002

Probing charge distribution at complex oxide interfaces via EELS

H. Wang[1], V. Srot[1], H. Boschker[1], J. Mannhart[1], P. A. van Aken[1]

[1]Max Planck Institute for Solid State Research, Stuttgart, Germany

Heterointerfaces in complex oxide materials promote emergent physical properties like colossal magnetoresistance, magneto-electric coupling, fractional quantum Hall Effect, and high-Tc superconductivity, which are not found in their bulk constituents. These properties can be attributed to the reconstruction of charge, spin, and orbital ordering at interfaces. Of particular concern is the charge distribution at interfaces, which is a crucial factor in controlling the interface transport behavior. However, the study of the charge distribution is very challenging due to its small length scale and the intricate structure and chemistry at interfaces. Furthermore, the underlying origin of the interfacial charge distribution has been rarely studied in-depth and is still poorly understood.

In this study [1], we performed atomic-scale investigations of the microstructure and electronic structure at $SrTiO_3$ (STO)-$SrMnO_3$ (SMO) heterointerfaces by high-angle annular dark-field, annular bright-field imaging and electron energy-loss spectroscopy (EELS) using an aberration-corrected scanning transmission electron microscope (STEM). EELS analysis confirms that the charge density attains the maximum of 0.13 ± 0.07 e^-/unit cell (uc) at the first SMO monolayer (Fig. 1). Based on quantitative atomic-scale STEM analysis and first-principle calculations, we explore the origin of the interfacial charge accumulation in terms of epitaxial strain-favored oxygen vacancies, cationic interdiffusion, interfacial charge transfer, and space-charge effects.

Based on EELS studies and theoretical calculations, this work provides a comprehensive description of the charge distribution and related mechanisms at SMO/STO heterointerfaces, which is beneficial for the manipulation of the functionality via charge engineering at interfaces.

Fig. 1 Electronic charge density as a function of atomic position near the interface

References:

[1] H. Wang, V. Srot, X. Jiang, M. Yi, Y. Wang, H. Boschker, R. Merkle, R. W. Stark, J. Mannhart, and P. A. van Aken. ACS Nano 14, 12697-12707 (2020).

Fig. 1

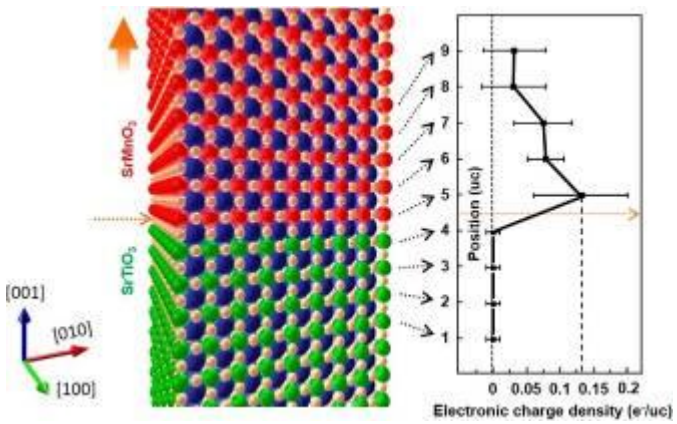

IM2.P003

Different image contrasts between atomic resolution HAADF and EELS mapping in rutile TiO_2

C. Iwashimizu[1], M. Haruta[1], H. Kurata[1]

[1]Institute for Chemical Research, Kyoto University, Uji-city, Japan

<Introduction and objectives>

Recently, we reported on the anisotropic electron orbital mapping of oxygen 2*p*-state in $SrTiO_3$ using STEM-ELNES mapping [1]. It is important to understand the origin of shape in ELNES mapping for further development of this field because even conventional elemental maps with the intensity of a wide energy region of ELNES, can generate artifacts, for instance due to volcano effect [2], delocalization of inelastic scattering [3] and so on. Here, we report different image contrasts between atomic resolution HAADF and EELS mapping in rutile TiO_2 due to the unique electron channeling and the difference of scattering potentials.

<Materials and method>

HAADF images and EELS spectra (Ti $L_{2,3}$- and O *K*-ELNES) were simultaneously obtained along [001] axis of rutile TiO_2 by spectrum imaging (SI) mode using a JEOL ARM200F operated at 60 kV. The well averaged dark reference was subtracted from the SI data to randomize the dark noise [4]. Next, the distorted SI data were corrected using a non-rigid registration technique [5]. Finally, more than six thousand templates of SI data were accumulated to improve S/N ratio. μSTEM software was used to calculate HAADF image, elemental maps (Ti $L_{2,3}$- and O *K*-edges) and probe propagation in the TiO_2 crystal [6].

<Results>

The elemental maps of Ti and O visualize each elemental site with atomic resolution and the O map exhibits projected octahedral structures rotating 90 degrees for their neighbors (Fig. 1 (e, f)). The Ti $L_{2,3}$ map shows an anisotropic ellipsoidal distribution extending along the axial bonds of the projected octahedral structure, while Ti atomic columns in the HAADF image do not show such anisotropy (Fig. 1 (d)). The simulated images agree well with the experimental images (Fig. 1 (g-i)). Probe propagation inside of the TiO_2 crystal was also simulated and revealed that the causes of the anisotropic intensity distribution of Ti $L_{2,3}$-signal are the unique channeling effects of the rutile structure and the differences of scattering potential between HAADF and EELS.

<Conclusion>

It has elucidated that the channeling effects could influence on the shape of atomic contrast in elemental mapping by STEM-EELS. Therefore, it is important to well understand the origin of the shape of image contrasts in elemental and orbital mapping for correct interpretation.

<Reference>

[1] C. Iwashimizu, M. Haruta and H. Kurata, *Appl. Phys. Lett.* **119**, (2021) 232902

[2] A. J. D"Alfonso, S. D. Findlay, M. P. Oxley and L. J. Allen, *Ultramicroscopy,* **108** (2008) 677

[3] P. Wang, A. J. D"Alfonso, S. D. Findlay, L. J. Allen and A. L. Bleloch, *Phys. Rev. Lett.* **101** (2008) 236102

[4] M. Haruta, Y. Fujiyoshi, T. Nemoto, A. Ishizuka, K. Ishizuka and H. Kurata, *Ultramicroscopy,* **207** (2019) 112827

[5] L. Jones, H. Yang, T.J. Pennycook, M.S.J. Marshall, S. Van Aert, N.D. Browning, M. R. Castell and P. D. Nellist, *Advanced Structural and Chemical Imaging*, **1** (2015) 8

[6] L.J.Allen, A.J.D′Alfonso and S.D.Findlay, *Ultramicroscopy*, **151** (2015) 11

<Acknowledge>

This work was supported by Kakenhi Grants-in-Aid No. 22H01956 from the Japan Society for the Promotion of Science (JSPS)

<Figure legend>

Figure 1 (a) Crystal structure of rutile TiO_2. (b) Crystal structure projected along [001] axis. (c) EELS spectrum. (d) Experimental HAADF image, (e) Ti-$L_{2,3}$ map and (f) O-K map, respectively. (g-j) Simulated images corresponding to (d-f).

Fig. 1

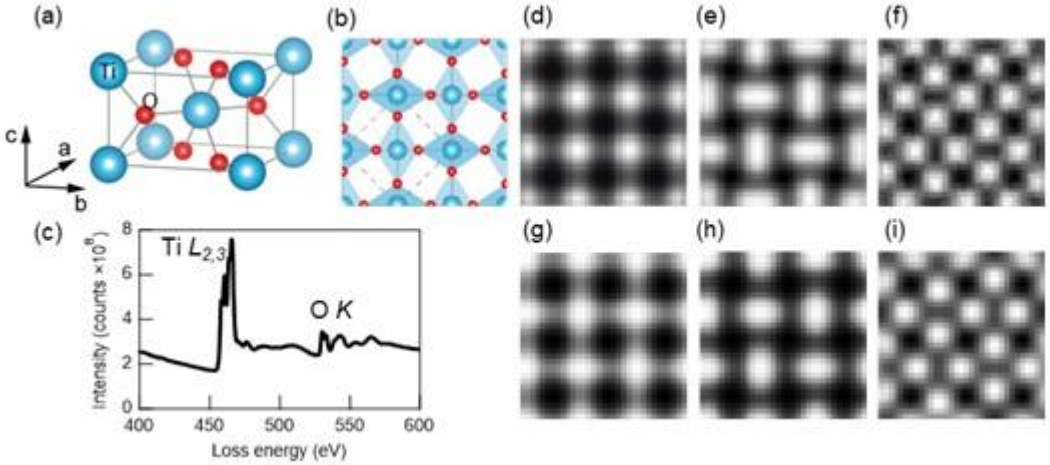

IM2.P004

Quantitative understanding of the thermal vibration effect on Ti $L_{2,3}$-edge spectrum

I. C. Lin[1], M. Haruta[1], T. Nemoto[1], H. Kurata[1]

[1]Kyoto University, Institute for Chemical Research, Uji-city, Japan

The effect of anisotropic atomic vibrations on Ti $L_{2,3}$-edge spectrum of $SrTiO_3$ was reported in previous research[1]. Our group revealed that the Ti $L_{2,3}$-edge experimental spectra could be reproduced by crystal field multiplet calculation considering the anisotropic atomic vibrations model. The thermal vibration factors are very sensitive to the reproduction of spectral shape, but not all elemental thermal vibration factors have the same effect. Therefore, in the present work, we report the relation between individual atomic vibration and $L_{2,3}$-edge spectrum quantitatively by monochromated STEM-EELS and crystal field multiplet calculation.

Firstly, we investigated the importance of individual thermal vibration factors to the Ti $L_{2,3}$-edge spectrum in the perovskite cubic structure. In $SrTiO_3$, Ti and Sr show isotropic vibration, and oxygen atoms show anisotropic ellipsoid thermal vibration, as shown in **Figure 1**. Our result indicated that the effect of atomic vibrations on the $L_{2,3}$-edge is related to specific elements in the crystal and their vibration directions. It reveals that thermal vibrations of Ti and O have effects on the Ti $L_{2,3}$-edge spectral shape, whereas Sr has almost no effect on it. In particular, the vibration effect on the spectrum is mainly dominated by the oxygen thermal factor along the Ti-O direction ($U_{O(Ti)}$); thermal vibration of Ti (U_{Ti}) and oxygen along SrO plane ($U_{O(Sr)}$) show small and similar effects. Hence, as the inverse problem, we tried to extract the temperature dependence of Debye-Waller factors of oxygen from the experimental Ti $L_{2,3}$-edge spectrum by fitting with the multiplet calculation spectrum. High-temperature Debye-Waller factors are difficult to be refined in diffraction experiments because of the low intensity and experiment instability. In this case, using STEM-EELS, the spectra can be obtained with small sample thermal drift and high S/N ratio in local region. As a result, temperature-depended anisotropic Debye-Waller factor of oxygen can be obtained and shows good agreement with those determined by theoretical calculation[2], gamma-ray[3], synchrotron[4], and x-ray[5] experiment, as shown in **Figure 2**.

This work presents a method that can potentially extract thermal factors in local regions such as interface and surface, which cannot be obtained in other ways. In the presentation, we will discuss the thermal factor extraction method and atomic vibration effects on the Ti $L_{2,3}$-edge spectrum in detail.

This work was supported by Kakenhi Grants-in-Aid No. 22H01956 from the Japan Society for the Promotion of Science (JSPS).

Reference:
[1] M. Haruta et al., Appl. Phys. Lett., 119, 232901 (2021).
[2] A. Uldry et al., Phys. Rev. B 85, 125133 (2012).
[3] W. Jauch and M. Reehuis, Acta Cryst. A61, 411-417 (2005)
[4] E. N. Maslen et al., Acta Cryst. B51.939-942 (1995)
[5] Y. A. Abramov et al., Acta Cryst. B51, 942 (1995).

Figure1: Graphic representation of the anisotropic thermal ellipsoids for $SrTiO_3$.

Figure 2: Anisotropic thermal factors of oxygen extracted from experimental Ti L-edge in $SrTiO_3$ (blue) comparing with theoretical values[2] (gray), gamma-ray[3] (green), and x-ray[5] (red). The circle marker represents $U_{O(Ti)}$, and the square marker represents $U_{O(Sr)}$. The data points are averaged of 3 fitting results, and the error bar corresponds to the stander deviation of each fitting result.

Fig. 1

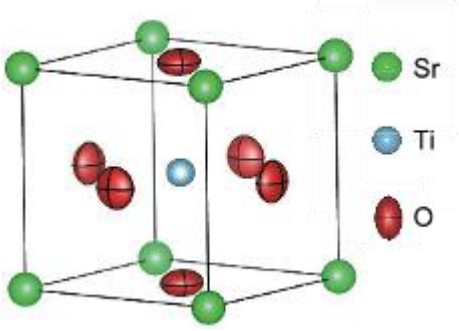

Fig. 2

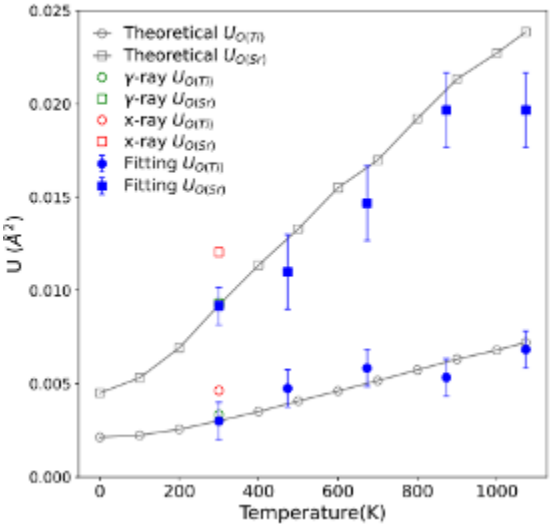
Theoretical $U_{O(Ti)}$
Theoretical $U_{O(Sn)}$
γ-ray $U_{O(Ti)}$
γ-ray $U_{O(Sn)}$
x-ray $U_{O(Ti)}$
x-ray $U_{O(Sn)}$
Fitting $U_{O(Ti)}$
Fitting $U_{O(Sn)}$
U ($Å^2$)
0.025
0.020
0.015
0.010
0.005
0.000
0
200
400
600
800
1000
Temperature(K)

IM2.P005

Structural resolution of $Ca_3GaZn_{0.5}Ge_{4.5}O_{14}$, a three isoelectronic cation langasite structure, using quantitative 2D-EDS mapping

C. Genevois[1], H. Bazzaoui[1], D. Massiot[1], V. Sarou-Kanian[1], E. Véron[1], S. Chenu[2], P. Beran[3], M. J. Pitcher[1], M. Allix[1], A. Zandonà[1]

[1]CNRS-CEMHTI, Orléans, France
[2]Rennes Institute of Chemical Sciences, Rennes, France
[3]Nuclear Physics Institute of the CAS, Rez, Czech Republic

Crystallisation of zinc gallogermanate glasses is of interest for the synthesis of new transparent ceramics. In this context, we were interested in the solid solution $Ca_3Ga_{2-2x}Zn_xGe_{4+x}O_{14}$ ($0 \leq x \leq 1$) and its detailed structural characterization. Powder diffraction was used to determine that this new compound adopt the trigonal langasite structure type, offering three possible crystallographic sites for the coordination of isoelectronic Zn^{2+}, Ga^{3+} and Ge^{4+}. The distribution determination through the different sites of the three isoelectronic cations for the complex intermediate member $Ca_3GaZn_{0.5}Ge_{4.5}O_{14}$ is not possible using only Rietveld refinement from neutron diffraction. For this compound, we have developed an original approach using quantitative 2D analysis of atomic-resolution STEM-EDS maps.[1]

In order to visualise the 2D structural projection of $Ca_3GaZn_{0.5}Ge_{4.5}O_{14}$ and to distinguish the three type of crystallographic site, the sample was oriented along the [001]* direction and imaged in STEM-HAADF mode at the atomic scale (Fig a-b). However, as Ge, Ga and Zn are of similar atomic number, it is not possible to determine the distribution of these 3 cations using only the intensities of the STEM-HAADF images. Consequently, EDS mapping at the atomic scale was carried out and show that one site is clearly visible and composed only of Ca as expected, whilst another one contains only Ge, and the last two are mixed occupied (Ga^{3+}/Ge^{4+}/Zn^{2+}) (Fig c-d). In order to gain more information and determine the Ga, Ge and Zn cation ratio on the different sites, a 1D profile analysis was first performed by extracting an intensity profile through the sites from the EDS maps, using a Gaussian decomposition and assuming that the area under the curve is proportional to the element content. In a second time, to reduce certain limitations of this approach such as the application of a Wiener filter on the elementary maps, which can induce a bias, as well as the inability to integrate the signal through the entire sites due to the small distance between the neighbouring, a two-dimensional fitting approach has been tested (Fig e-f).[2-3] The results were then compared with those obtained by Rietveld refinement of NPD data whose model was built following the STEM-EDS mapping analyses. The quantitative 2D refinement of atomic-resolution STEM-EDS maps could be applicable to materials where multiple cations with poor scattering contrast are distributed over different crystallographic sites in a crystal structure.

[1] H. Bazzaoui et al., Inorg. Chem. 2022, 61, 9339-9351

[2] P. Lu et al., Microsc. Microanal.2014, 20, 1782-1790

[3] P. Lu et al., Sci. Rep. 2014, 4, 3945

Figure a) Scheme of the $Ca_3GaZn_{0.5}Ge_{4.5}O_{14}$ structure projection along [001]. b) Corresponding STEM-HAADF image. c) and d) Overlaid EDS maps of "Ca (blue), Ge (red), Ga (green)" and "Ca (blue), Ge (red), Zn (green)". e) and f) 3-D representation of the Ge signal extracted from the STEM-EDS 2D-maps and the corresponding fit.

Fig. 1

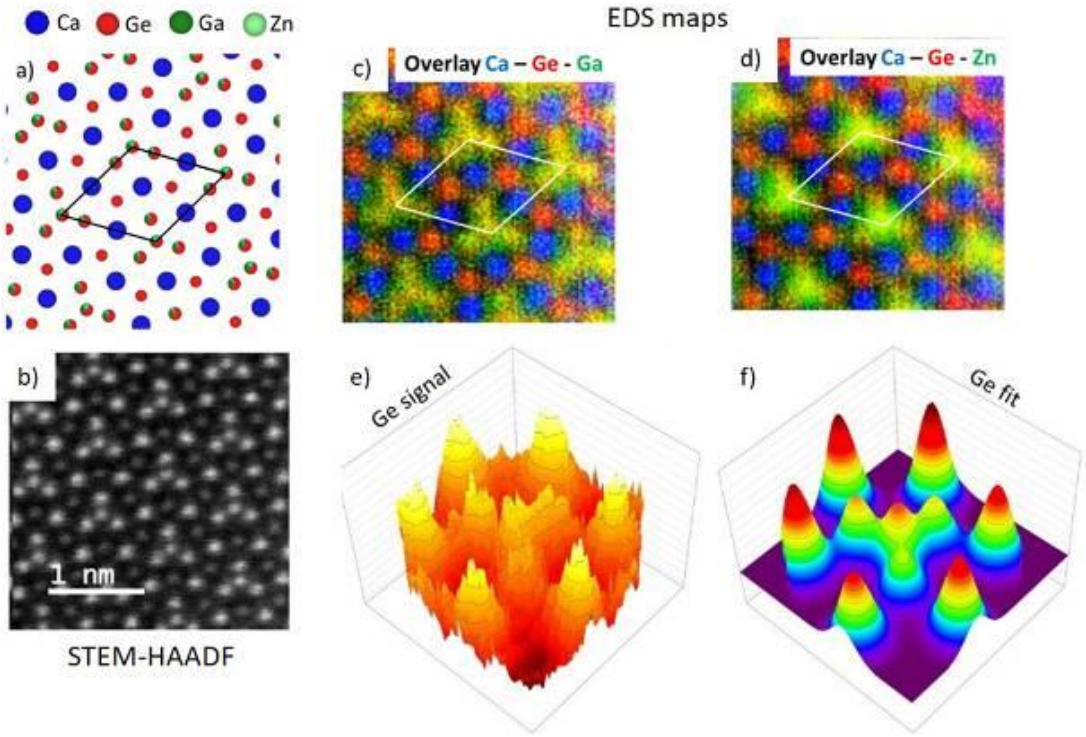
Ca
Ge
Ga
Zn
a)
b)
1 nm
STEM-HAADF
EDS maps
c)
Overlay Ca – Ge - Ga
d)
Overlay Ca – Ge - Zn
e)
Ge signal
f)
Ge fit

IM2.P006

Evolution of low-energy plasmons in patterned aluminum nanostructures on graphene

K. Elibol[1], P. A. van Aken[1]

[1]Max Planck Institute for Solid State Research, Stuttgart Center for Electron Microscopy, Stuttgart, Germany

A charge transfer plasmon (CTP) emerges via a direct charge transfer between linked nanoparticles or via quantum tunneling between nearly touching nanoparticles. [1,2] CTPs find applications in single-molecule sensing and functional devices including ultrafast nanoswitches and terahertz frequency photonic devices. [3] Unlike conventional plasmonic materials such as gold and silver, aluminum (Al) supports plasmon excitations in visible and ultraviolet regions of the spectrum. A natural oxide covering the surface of metallic Al protects not only its further oxidation, but also induces an energy red shift of the plasmon modes. [4] In addition, a support film underlying the plasmonics can induce a mode mixing and a red shift in plasmon modes. [5] Although electron-beam lithography (EBL) enables fabricating robust Al plasmonic devices, producing patterned Al nanostructures with a sub 5 nm gap by EBL is challenging due to a 3-5 nm-thick oxide layer surrounding metallic Al.

Here we monitor the evolution of low-energy plasmon modes in linked Al nanostructures produced by EBL on graphene via a gradual manipulation of their junctions. Moreover, we expect to reduce substrate-induced mode mixing and redshift by locating plasmonics on an ultra-thin substrate such as suspended monolayer graphene.

To overcome the difficulties in fabricating patterned Al nanostructures with a sub 5 nm gap, we manipulate the conductive junctions of linked Al nanoprims via a focused electron beam. The gradual manipulation of junctions enables monitoring the evolution of low-energy plasmon modes by low-loss EELS measurements in a monochromated scanning transmission electron microscope (STEM). The plasmon modes measured by EELS are further analyzed and confirmed by an LC circuit model and full electromagnetic simulations performed with boundary-element and frequency-domain methods.

The EELS measurements indicate that the CTP resonances of linked nanoprisms depend strongly on the kinetic inductance of the conductive junction. With the increase of junction width, the CTP resonances of linked nanoprisms blueshift, whereas their lifetimes decay monotonically on the femtosecond time-scale. In contrast to CTPs, their 3λ/2 and λ resonances display a redshift. After shrinking the junction width via electron-beam irradiation, the CTP, 3λ/2 and λ modes explicitly redshift. When the nanoprisms are separated completely by a focused electron–beam, the CTP vanishes and a new bonding-type gap mode appears. In addition, the 3λ/2 and λ resonances evolve into bonding dipolar and antibonding dipolar localized surface plasmon resonances (LSPRs).

References

[1] F. Wen *et al.*, *ACS Nano* **2015,** *9* (6), 6428-6435.

[2] O. Pérez-González *et al.*, *Nano Letters* **2010,** *10* (8), 3090-3095.

[3] J. Gu, *et al.*, Nature Communications 2012, 3 (1), 1151.

[4] M. W. Knight *et al.*, ACS Nano 2014, 8 (1), 834-840.

[5] C. Cherqui *et al.*, *The Journal of Physical Chemistry Letters* **2018,** *9* (3), 504-512.

IM2.P007

A post-column imaging energy filter compatible with multiple detectors

H. Müller[1], G. Guzzinati[1], M. Linck[1], P. Kükelhan[1], D. Lörks[1], A. Leibscher[1], I. Maßmann[1], V. Gerheim[1]

[1]CEOS GmbH, Heidelberg, Germany

Recent developments of detector technologies and acquisition schemes cause a demand for modular post-column energy filters with good performance for EFTEM and EELS experiments. Owing to decades of research in academia and at Gatan company for post-column filters and at Zeiss and JEOL companies for in-column filters these techniques are well established [1,2]. At CEOS we re-investigated the optical design and technology and identified some incremental improvements by using design methods, manufacturing technologies and alignment strategies originally developed for aberration correctors. Complementary to established plug-and-play solutions which primarily allow for a predefined combination of microscope / spectrometer / detector, we provide an open platform with utmost freedom in the selection of components, regarding both hardware and software.

The optics design of the CEOS Energy-Filtering and Imaging Device (CEFID) is based on a highly optimized sector magnet combined with two 12-pole elements. For all other focusing elements we use pure quadrupoles supplemented by some deflectors and separate two- and three-fold stigmators. This approach already allows for a 12mm entrance aperture with a peak-to-peak non-isochromaticity below 1eV at 200kV (Fig. 1) and a root-mean-square geometric distortion below 0.35% in imaging mode. In spectroscopy mode dispersions from 1meV/channel up to 1eV/channel are possible even at 80kV. The use of well-designed quadrupole elements made from high-quality soft iron helps to largely avoid remanence effects and improves the reproducibility of alignments. The filter design introduces a clear separation between pre- and post-slit alignments. All second- and higher-order spectrum aberrations can be measured and tuned at the slit plane by using identical methods for EFTEM and EELS modes [3]. This simplifies operation and enables to switch between imaging and spectroscopy modes with different dispersions or even different detectors with no or only little re-tuning. With an entrance aperture of 5 mm an energy resolution in the sub-20meV range should be possible and a drift of less than 1eV over 12 hours at 300 kV has been achieved.

Multiple pixelated detectors can be added at different distance from the final cross-over, e.g. large-field of view scintillator-coupled or direct-detection CMOS cameras or frame- or event-based hybrid-pixel detectors with a large pixel size (Fig. 2). Our Python-based software targets for open interfaces and flexibility for user-scripting also for unusual experimental setups. EFTEM and EELS including STEM spectrum imaging are readily possible [4].

References:
[1] Reimer, L. (1995) Energy-filtering transmission electron microscopy. Springer, Berlin.
[2] Egerton, R. F. (2011) Electron energy-loss spectroscopy in the electron microscope. Springer, Berlin.
[3] F. Kahl et al. (2019) AIEP 212 including Proceedings CPO-10.
[4] A. Ruiz-Caridad et al. (2022) Micron 160, Volume 160.

Figure1. Non-isochromaticity measured at 200kV for the full Ø12mm entrance aperture and the inner Ø8mm area with increased post-filter magnification.

Figure 2. CAD Model with a selection of currently possible pre-filter and post-filter detectors. Typically only two post-filter detectors are installed on the same system.

Fig. 1

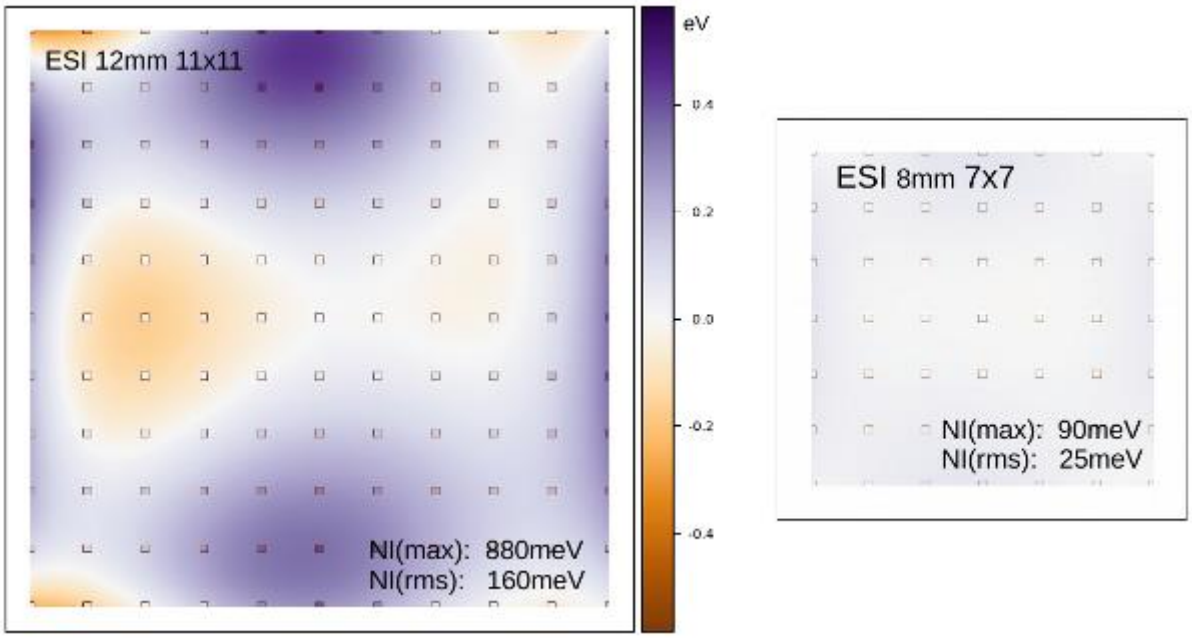
ESI 12mm 11x11
eV
0.4
0.2
0.0
-0.2
-0.4
NI(max): 880meV
NI(rms): 160meV
ESI 8mm 7x7
NI(max): 90meV
NI(rms): 25meV

Fig. 2

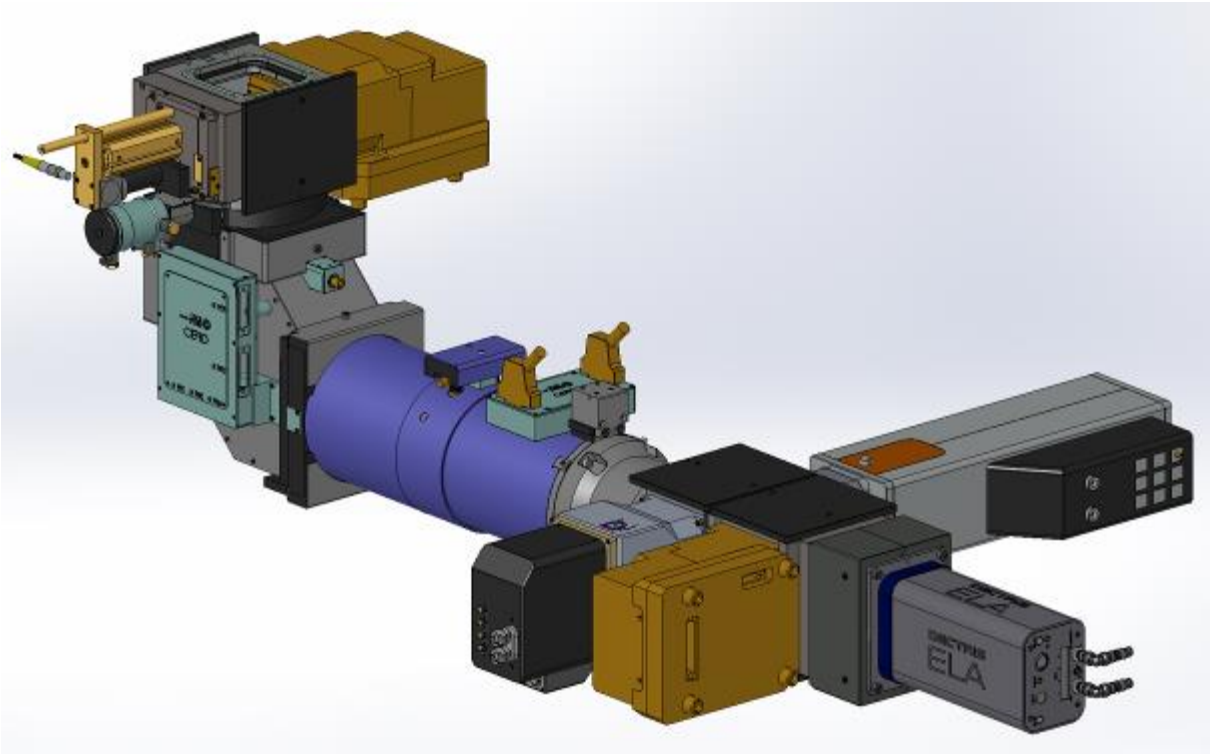

IM2.P008

Panta Rhei: a software platform for acquisition and processing of image and spectral data

D. Lörks[1], A. Leibscher[1], M. Krieger[1], G. Guzzinati[1], H. Müller[1], M. Linck[1], P. Kükelhan[1], I. Maßmann[1]

[1]CEOS GmbH, Heidelberg, Germany

Recent developments of add-on equipment in transmission electron microscopy cause a demand for modular and flexible data acquisition software. Fully integrated commercial solutions exist, but these are typically tailored towards a certain combination of proprietary hardware components from one manufacturer. For off-line data analysis and very specific high-throughput workflows open source software packages became available during the last years. Nevertheless, a lack of highly interactive software directly usable during the operation of the instrument with its different components is obvious. To close this gap, CEOS Panta Rhei is designed as an interactive platform for data acquisition, processing and visualization in electron microscopy written in Python using the Qt, ZMQ and numpy libraries.

The primary purpose of Panta Rhei is to enable simple steering and supervision of workflows combining the control of the microscope and its accessories with data acquisition, online data analysis, and direct visual feedback. The capabilities for online data evaluation are progressing. We currently concentrate on functionality for quick and meaningful assessment of data quality and online session planning like image filters, data statistics, diffractograms, live 4D-STEM evaluation, and elemental mapping and quantification for EELS as well as EFTEM. Data can be interchanged with other software using common file formats like npz, hspy, and tiff. The acquisition (via cameras or scan detectors) typically generates high volume data which has to be transferred and processed efficiently. Therefore, a central component of Panta Rhei is a separate server process called Repository providing access to a managed shared memory. As soon as an acquisition device stores data in the Repository other clients are notified and can directly access the data with minimal CPU load and memory consumption. Clients themselves may also use the Repository to store processed data.

The Panta Rhei GUI is an application to acquire, display and process data and control hardware components which connects as client to the Repository. It displays Views of data from the Repository via a multiple document interface (MDI). Views are used to live display certain aspects of the data and the numerous available DataTools continuously calculate dependent data from updated input. The name Panta Rhei (πάντα ῥεῖ -- everything flows) is motivated by these chains of transformations that may even run in separate processes. For custom extensions, a scripting interface provides control of data processing and display tools as well as hardware devices. For easy external access to hardware control, an RPC-interface is available.

Currently, device interfaces for the TEMs of three manufacturers, five families of detectors, two different scan generators, and the CEOS Imaging Energy Filter (CEFID [1]) exist. We expect that the number of compatible devices will continuously grow over time.

References:

[1] F. Kahl et al. (2019) AIEP 212 including Proceedings CPO-10.

Figure 1: Software architecture of the CEOS Panta Rhei platform.

Figure 2: Screenshot of CEOS Panta Rhei with Views for different imaging and spectroscopy workflows.

Fig. 1

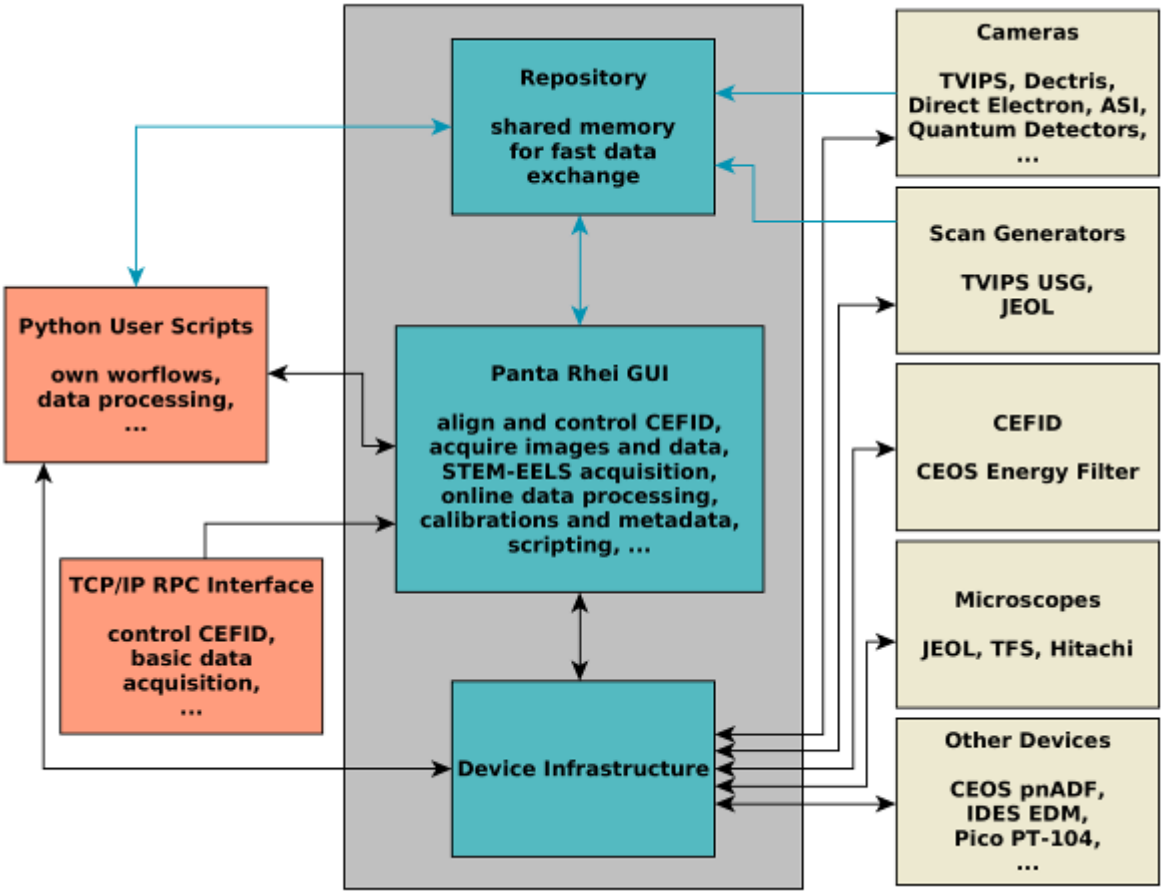
Repository
shared memory for fast data exchange
Cameras
TVIPS, Dectris, Direct Electron, ASI, Quantum Detectors, ...
Scan Generators
TVIPS USG, JEOL
Python User Scripts
own worflows, data processing, ...
Panta Rhei GUI
align and control CEFID, acquire images and data, STEM-EELS acquisition, online data processing, calibrations and metadata, scripting, ...
CEFID
CEOS Energy Filter
TCP/IP RPC Interface
control CEFID, basic data acquisition, ...
Microscopes
JEOL, TFS, Hitachi
Device Infrastructure
Other Devices
CEOS pnADF, IDES EDM, Pico PT-104, ...

Fig. 2

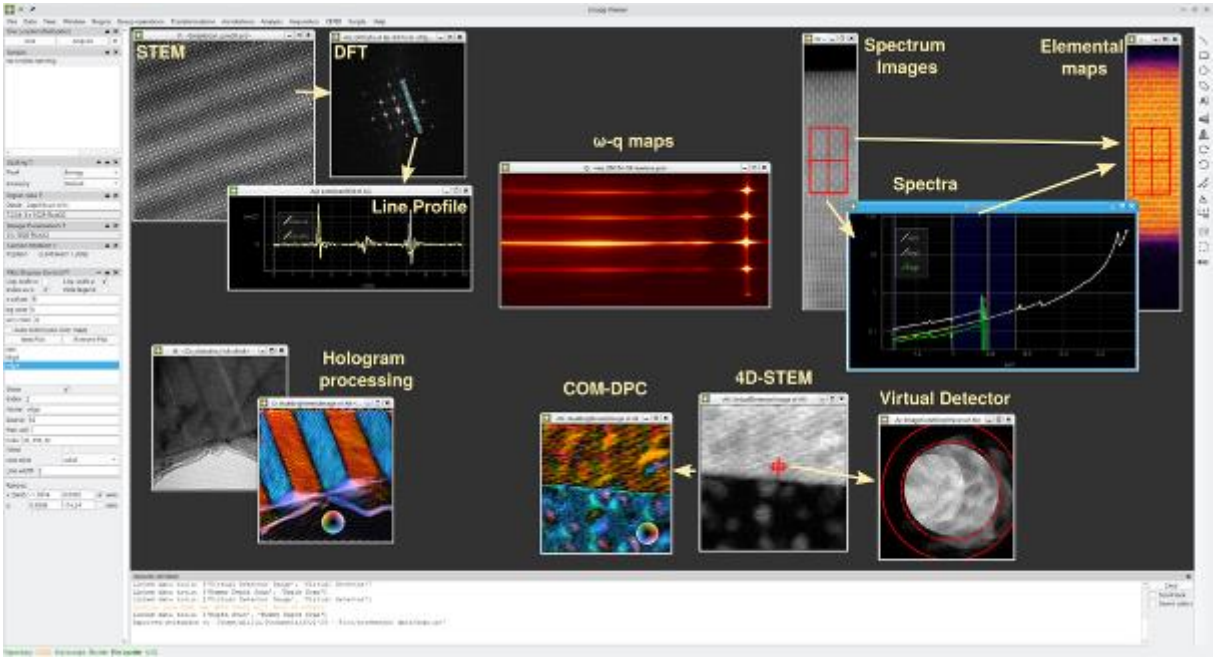
STEM
DFT
Line Profile
ω-q maps
Spectrum Images
Elemental maps
Spectra
Hologram processing
COM-DPC
4D-STEM
Virtual Detector

IM2.P009

Detection limits of direct-counting CMOS and CCD cameras in EELS experiments

M. Haruta[1], J. Kikkawa[2], K. Kimoto[2], H. Kurata[1]

[1]Kyoto University, Institute for Chemical Research, Uji-city, Japan
[2]National Institute for Materials Science, Tsukuba, Japan

Introduction

Spatially resolved STEM-EELS is widely used to investigate local elemental and electronic structures at an atomic scale. However, acquiring spectra with both a high signal-to-noise ratio (SNR) and a high spatial resolution is difficult even if we use advanced direct counting CMOS camera because of the limitations imposed by practical experimental conditions (e.g., instrument instability, electron damage to the sample, limited dynamic range and low probe current). Hence, a multiple acquisition technique is sometimes useful and can improve the SNR, avoiding both sample damage and image drift.

Objectives

Previously, we reported the detection of extremely low count in EELS multiple spectrum imaging (SI) experiments by randomizing the CCD dark reference noise [1]. Although a direct-detection CMOS camera is useful, it does not always provide superior performance compared with a CCD camera. Thus, understanding the advantages and disadvantages of direct-detection and CCD cameras is important for obtaining optimal experimental data. Here, we compare the performance and detection limits for a CMOS K2 camera operated in counting mode and a conventional CCD camera in EELS experiments. We investigate the detection limit by focusing on the electron dose entering the camera [2].

Materials & methods

STEM–EELS experiments were carried out on a Themis Z (300 kV) equipped with a GIF Quantum970 spectrometer. The spectra were recorded using a direct-detection K2-IS camera and an UltraScan CCD camera (Gatan). The test spectra of Ti $L_{2,3}$-edge were measured from $SrTiO_3$.

Results

In the case of a single spectrum acquired at the shortest dwell times (2.5 ms for K2 and 1 μs for CCD), the detection limit, defined as three times the standard deviation of the spectral noise (3σ), was very low (1 e^-/channel) in the K2 camera compared with that acquired with the CCD camera (5 e^-/channel). By contrast, the spectral noise of the K2 camera changed depending on the dwell time because of the multiple read-outs related to its fixed frame rate (400 fps). The spectral noise of the K2 camera was larger than that of the CCD camera when the dwell time was longer than ~30 ms. Thus, the CCD camera was found to be still useful when detecting a very small number of electrons with a long acquisition time. However, in the case of an accumulated spectrum obtained by acquiring 10,000 spectra after subtracting the average dark reference signal, the detection limits per read-out were ~0.016 and ~0.025 e^-/channel/read-out for the K2 and CCD cameras, respectively.

Conclusion

Because both cameras have advantages and disadvantages with respect to their detection limit, speed, and dynamic range, their proper use is important.

Reference

[1] M. Haruta, Y. Fujiyoshi, T. Nemoto, A. Ishizuka, K. Ishizuka and H. Kurata, *Ultramicroscopy*, **207** (2019) 112827.

[1] M. Haruta, K. Kikkawa, K. Kimoto and H. Kurata, *Ultramicroscopy*, **240** (2019) 113577.

This work was supported by Kakenhi Grants-in-Aid No. 22H01956 from the Japan Society for the Promotion of Science (JSPS).

IM2.P010

Computation of generalised oscillator strengths for the simulation and quantification of energy loss spectra

G. Guzzinati[1], L. Segger[2], H. Müller[1], H. Kohl[2]

[1]CEOS GmbH, Heidelberg, Germany
[2]Institute of Physics, University of Münster, Münster, Germany

The extraction of quantitative compositional data from anelectron energy loss spectrum relies on the theoretical modeling and simulation of the core-loss (ionisation) edges. This allows to fit a simulated spectrum to theexperimental one, using the concentrations of each element as a free parameter. Cross sections can be obtained from the "generalised oscillator strengths" (GOS) which in turn depend on the wave functions of the target atoms which cannot be analytically described except in the hydrogen atom [1]. While the hydrogenic model is adequate to describe the K edges which is useful for some light elements, many elements require more complex computations in order to be quantified. While these calculations can be quite fast on a modern computer, tabulating the results is the most efficient approach for a wide deployment. Progress in methods for quantitative EELS has beenlimited by the existing GOS tables, which have been computed 40 years ago [2] and are not freely available.

To remedy this, we have computed a high-resolution GOS dataset covering all known EELS edges, which is now freely available [3]. We calculated the atomic wave functions self-consistently within the local density approximation, using the exchange correlation potential after Perdew [4]. For this a modified version of a program by Hamann is used [5]. Using this atomic potential, the wave function of the ejected free electron is calculated. To normalize the free wave functions they are matched to spherical Bessel and Neumann functions at large distances from the core. The remaining integral constitutes a spherical Bessel transform. Using the convolution theorem this integral is solved with a fast Fourier transformation. More details can be found in [6].

We assess the quality of the resulting data by comparing it to existing sets [2]. The agreement is good, but the new data offers better sampling, covers a larger number of edges (many minor ones), and is available over a wider range of energy and momentum. The comparison between the simulated edges, including ones simulated based on the hydrogenic model, offers good agreement across the board.

Finally, we have devised a HDF5-based file format for the distribution of GOS data which can be used in the future to ensure that new GOS data is immediately compatible with existing software.

The data, the code, and format specifications are freely available [3]. The new data can be used in CEOS Panta Rhei and in hyperspy.

[1] R. Egerton, (2011) Electron Energy-Loss Spectroscopy in the Electron Microscope, Springer

[2] R. D. Leapman, P. Rez and F. Mayers, J. Chem. Phys 72 (1980), p. 1232

[3] L. Segger, G. Guzzinati and H. Kohl, DOI: 10.5281/zenodo.6599071

[4] J. P. Perdew and A. Zunger, Phys. Rev. B 23 (1981), p. 5048

[5] D. R. Hamann, Phys. Rev. B 40 (1989), p. 2980

[6] L. Segger and H. Kohl, EMC 2020 Proceedings, 181

Fig.1. Comparison between generalised oscillator strengthsfor the Ti L3 edge. Our new data is compared to an existing reference [2], across energy and momentum (top row) and for specific energies (bottom row). The datasets show good agreement, but the new data has a finer sampling and covers a wider parameter space.

Fig. 2. Simulated edges for the different GOS datasets, and the hydrogenic approximation. The two tabulated datasets are in good agreement, while the hydrogenic data diverges significantly already for the L edges, and is not computed for higher edges.

Fig. 1

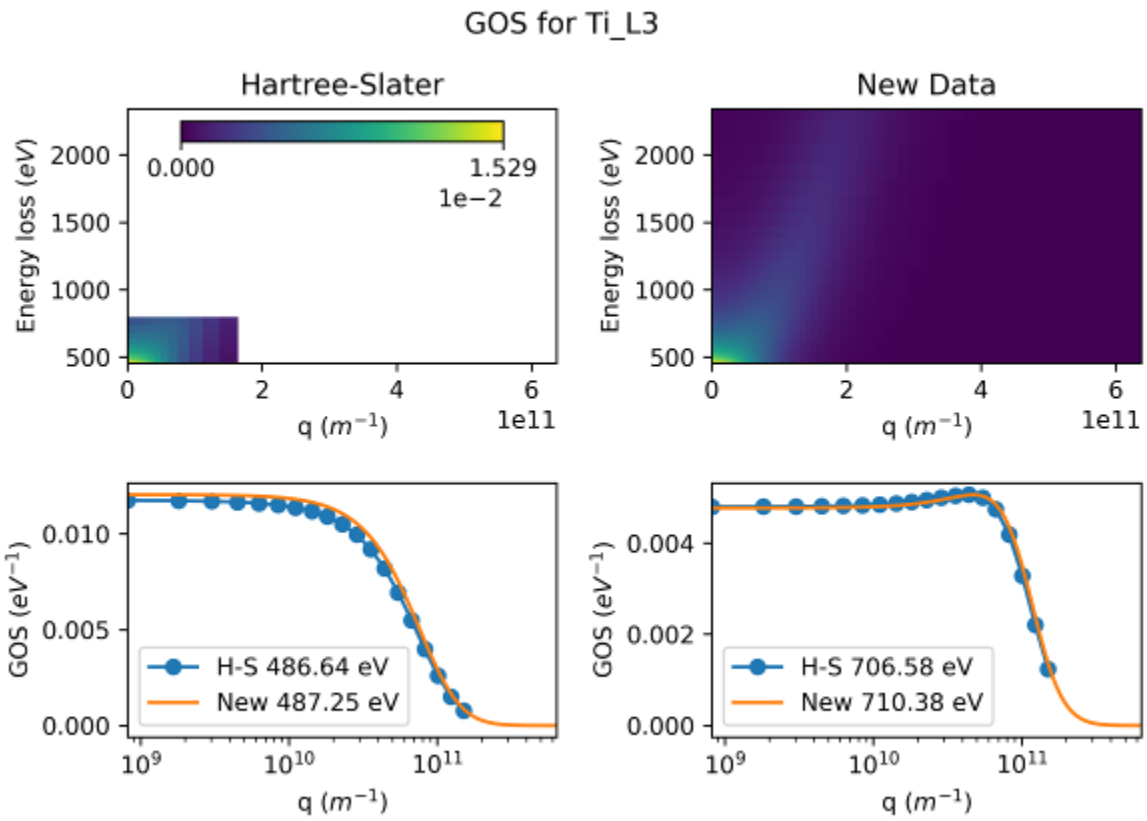
GOS for Ti_L3
Hartree-Slater
New Data
Energy loss (eV)
0.000
1.529
1e−2
q (m^{-1})
1e11
GOS (eV^{-1})
H-S 486.64 eV
New 487.25 eV
H-S 706.58 eV
New 710.38 eV

Fig. 2

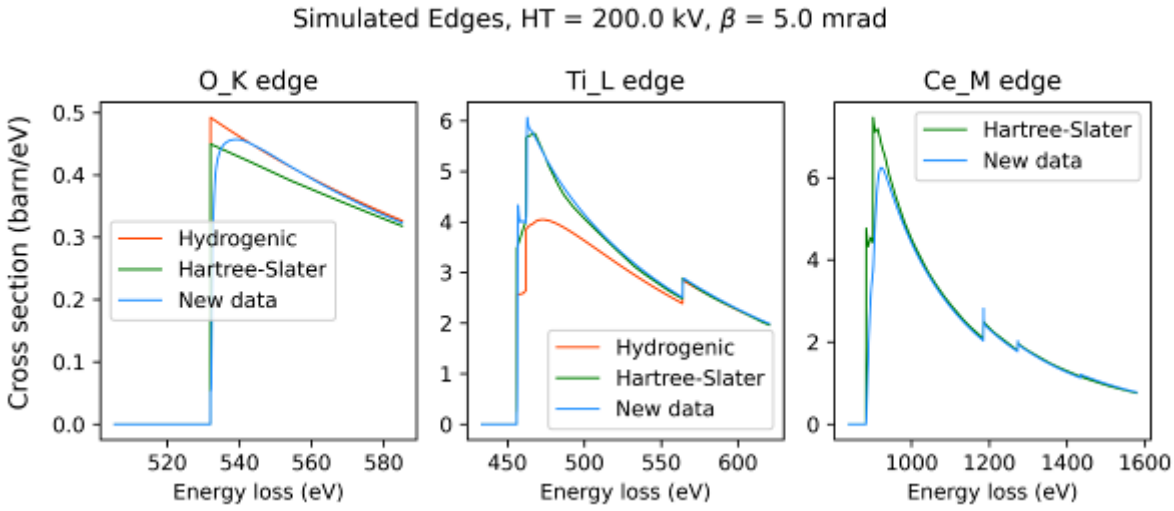
Simulated Edges, HT = 200.0 kV, β = 5.0 mrad
O_K edge
Ti_L edge
Ce_M edge
Cross section (barn/eV)
Hydrogenic
Hartree-Slater
New data
Energy loss (eV)

IM2.P011

Fast predictions of ADF-EDX scattering cross-sections for elemental quantification of nanostructures

Z. Zhang[1,2], A. De Backer[1], I. Lobato[1], S. van Aert[1], P. Nellist[2]

[1]University of Antwerp, NANOlab Center of Excellence, Antwerp, Belgium
[2]University of Oxford, Department of Materials, Oxford, United Kingdom

To understand the structure-property relationship in nanostructured materials, we need to probe their crystal structures and compositions at the atomic scale. Advanced materials usually consist of multiple elements in a complicated structure. Significant difficulties remain to disentangle the contributions of composition and thickness in STEM due to dynamic scattering, which needs to be taken into account by detailed simulations. However, the combination of the computational cost of the multislice calculation and the enormous ordering possibilities for a given composition makes the quantification of mixed columns almost impossible. To address these challenges, we here report the development of an incoherent non-linear method for the fast prediction of ADF-EDX scattering cross-sections of mixed columns under channelling conditions.

Due to electron channelling, ADF and EDX have a non-linear relationship against thickness and composition, particularly at the atomic scale in zone axis orientation. However, preliminary experiments indicate a linear dependence between EDX and ADF scattering cross-sections, which are defined as the integration of signal intensities for each atomic column. We performed frozen phonon multislice calculations for a pure Au crystal and investigated the linear dependence of the ADF-EDX scattering cross-sections using the coefficient of determinantion R2 for different ADF inner and outer collection angles. Since EDX can be considered as a perfect incoherent reference, an R2 value equal to 1 suggests perfect longitudinal incoherence of the ADF, which is the case for high angles.

Because of the incoherent signal mode, we can treat dynamical scattering as a superposition of individual atoms focussing the incident electrons. Here we expanded the so-called atomic lensing model [1] (developed previously for ADF) to spectroscopy to enable fast generation of EDX scattering cross-sections with the ordering of elements taken into account under the channelling condition. As shown in Fig. 1 for a core-shell Au-Pt nanorod, scattering cross-sections extracted from the multislice calculations agree reasonably well with the atomic lensing model predictions but are very different from those of the linear model where the signal is assumed to scale linearly with the number of atoms for each type. To deploy the atomic lensing model to experimental results, we can incorporate the experimentally measured EDX partial cross-section [2], that bypasses the difficult characterisation of the EDX detector. We can also make use of the linear dependence between the signal modes as a constraint for simultaneous ADF-EDX atom counting. This method allows us to explore the enormous ordering possibilities of heterogeneous materials with multiple elements.

[1] K.H.W. van den Bos, A. De Backer, G.T. Martinez, N. Winckelmans, S. Bals, P.D. Nellist, S. Van Aert, *Physical Review Letters* 116 (2016) p. 246101.

[2] A. Varambhia, L. Jones, A. London, D. Ozkaya, P.D. Nellist, & S. Lozano-Perez, *Micron* 113 (2018) p. 69-82.

[3] The authors acknowledge financial support from the Research Foundation Flanders (FWO) through Project No. G.0502.18N and a post-doctoral grant to ADB. This project has received funding from the European Research Council (ERC) under the European Union"s Horizon 2020 research and innovation programme No. 770887 PICOMETRICS and No. 823717 ESTEEM3

Fig.1 Comparing the simulated and predicted scattering cross-sections (SCS) of ADF and EDX for an Au-Pt core-shell nanorod.

Fig. 1

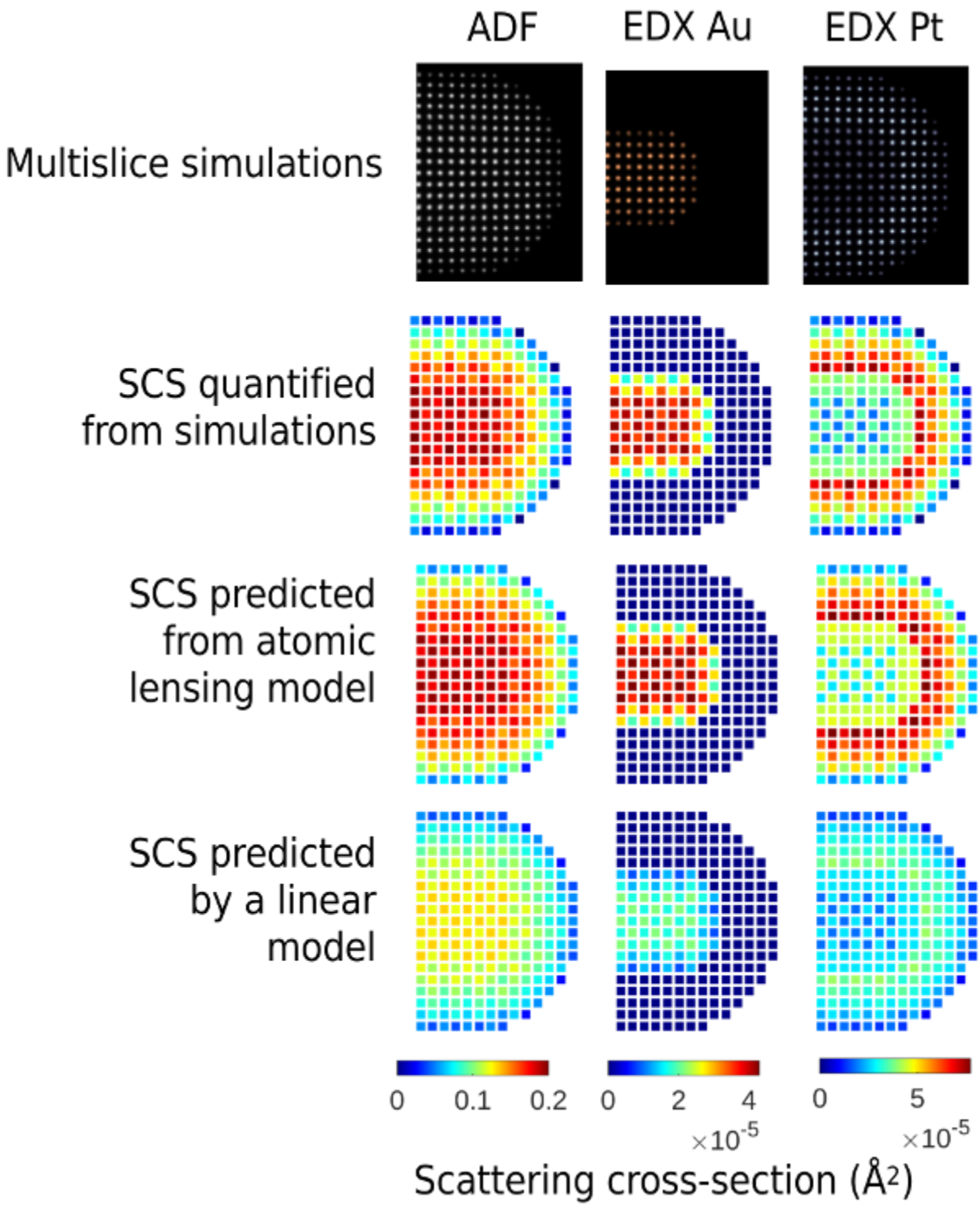
ADF
EDX Au
EDX Pt
Multislice simulations
SCS quantified from simulations
SCS predicted from atomic lensing model
SCS predicted by a linear model
0
0.1
0.2
0
2
4
×10-5
0
5
×10-5
Scattering cross-section (Å2)

IM2.P012

Experimental progress to achieve atomic resolution EMCD measurements

H. Ali[1], J. Rusz[1], B. Hjörvarsson[1], K. Leifer[1]

[1]Uppsala University, Uppsala, Sweden

Electron magnetic circular dichroism (EMCD) [1] is an electron energy loss spectroscopy (EELS) based technique in the TEM which can measure element specific magnetic moments of the materials. When used in STEM mode, the spatial resolution of EMCD analysis is defined by the size of the electron probe which in the modern instruments can easily reach atomic resolution. Although atomic resolution EMCD should be feasible, it is quite demanding due to various challenges.

Classical EMCD experiments are performed with the crystal tilted into two (or three) beam condition and acquisition of two (or four) conjugate EELS spectra at specific off-axis angular positions in the reciprocal space. A disadvantage of using such diffraction geometry is that the atomic planes are parallel to the electron probe, losing the atomic column resolution. Atomic-plane resolved EMCD measurements[2] have been demonstrated using such diffraction geometry. To achieve the atomic (column) resolution, the crystal must be tilted to a zone axis. The EMCD experiments in a zone axis are non-trivial due to complex distribution of the magnetic signal and high dynamical diffraction effects.

In this work, we have used different custom-made hardware apertures to address various challenges in the EMCD experiments. We have used double hole and quadruple apertures to simultaneously acquire the multiple EELS spectra required for the EMCD experiment, removing the need of multiple electron beam scans [3], [4]. We have also demonstrated the simultaneous acquisition of the EMCD signals and the crystal orientation which allowed us to study the effects of small crystal mistilts on the EMCD signals. Finally, we have used complex shaped apertures to acquire the EMDC signals in the zone axis geometry. We demonstrated the detection of EMCD signals under atomic resolution conditions using such apertures[5]. We also propose strategies based on the use of virtual apertures to achieve atomic resolution EMCD measurements.

[1] P. Schattschneider *et al.*, "Detection of magnetic circular dichroism using a transmission electron microscope," *Nature*, vol. 441, no. 7092, pp. 486–488, May 2006, doi: 10.1038/nature04778.

[2] Z. Wang *et al.*, "Atomic scale imaging of magnetic circular dichroism by achromatic electron microscopy," *Nature Materials 2018 17:3*, vol. 17, no. 3, pp. 221–225, Feb. 2018, doi: 10.1038/S41563-017-0010-4.

[3] H. Ali, T. Warnatz, L. Xie, B. Hjörvarsson, and K. Leifer, "Quantitative EMCD by use of a double aperture for simultaneous acquisition of EELS," *Ultramicroscopy*, vol. 196, pp. 192–196, Jan. 2019, doi: 10.1016/j.ultramic.2018.10.012.

[4] H. Ali, J. Rusz, T. Warnatz, B. Hjörvarsson, and K. Leifer, "Simultaneous mapping of EMCD signals and crystal orientations in a transmission electron microscope," *Scientific Reports*, vol. 11, no. 1, p. 2180, Dec. 2021, doi: 10.1038/s41598-021-81071-4.

[5] H. Ali, D. Negi, T. Warnatz, B. Hjörvarsson, J. Rusz, and K. Leifer, "Atomic resolution energy-loss magnetic chiral dichroism measurements enabled by patterned apertures," *Physical Review Research*, vol. 2, no. 2, p. 023330, Jun. 2020, doi: 10.1103/physrevresearch.2.023330.

Fig. 1

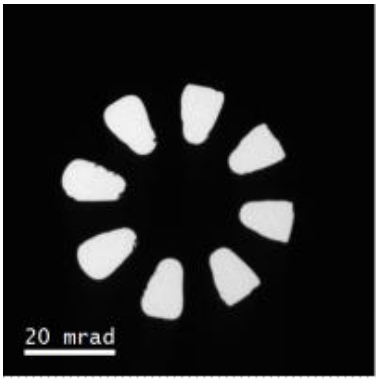

A custom-built ventilator aperture

Fig. 2

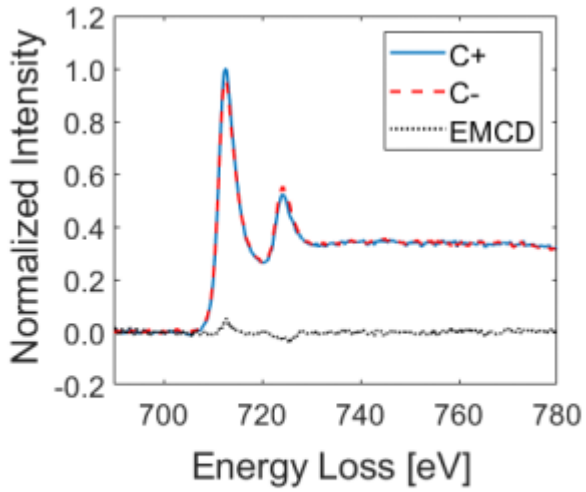

Chiral + and chiral - EELS spectra acquired under zone axis using a beam convergence angle of 10 mrad. A clear EMCD signal is detected.

IM2.P013

How to compress STEM spectrum-images into a linear combination of meaningful endmembers

P. Potapov[1], A. Lubk[1]

[1]IFW-Dresden, Dresden, Germany

1. Introduction

Modern STEM instruments now deliver routinely EELS and EDX spectrum-images of huge size. This opens the possibility to apply the methods of Multivariate Statistical Analysis (MSA) for improving the quality and interpretability of results. In particular, Principal Component Analysis (PCA) was routinely applied for denoising data [1]. However, PCA delivers results in the abstract, uninterpretable form. This issue can be addressed by another family of the MSA methods – unmixing algorithms. Unlike PCA, an unmixing approach decomposes the data on a linear combination of endmembers – the spectra with clear physical meaning, corresponding for instance to the real compounds constituting the object.

2. Objectives

In this work, we develop an unmixing algorithm based on the Vortex Component Analysis (VCA) [2]. The original VCA strategy is not well suited for STEM spectrum-imaging and must be significantly modified. First, the treatment should consider noise always present in STEM data. Second, the VCA results often appear non-unique while the reproducibility is a key requirement for a robust algorithm. We elaborate this issue by the combination of the VCA approach with Bayesian inference and clustering.

3. Materials & methods

The present unmixing algorithm was tested in a number of synthetic and experimental datasets. The experiments involved atomically resolved layered ceramic nanolayers and nanostructured semiconductor devices investigated by Electron Energy-Loss Spectroscopy (EELS) and Energy Dispersive X-ray Spectroscopy (EDX).

4. Results

The processing starts with the PCA reduction of data dimensionality down to typically 5-10 dimensions. This pre-treatment facilitates strongly the retrieval of reasonable endmembers while also implying a drastic denoising and compression of data. Analyzing data distribution in such a reduced factor space allows to retrieve the endmembers as shown in exemplary EELS dataset in Fig. 1. Namely, the VCA procedure is repeatably applied providing a set of potential endmembers as suggested by Spiegelberg [3]. Finally, the output is subjected to the statistical treatment, which includes Bayesian inference and clustering. The different modifications of the method, e.g. Bayesian priors and various clustering strategies are discussed.

Fig. 1: Data distribution in the factor space formed by (a) 1st and 2nd or, alternatively (b) 2nd and 3rd PCA components. The positions of the retrieved endmembers are denoted by the colored spots. (c) EEL spectra and abundancies of the extracted endmembers, which allow to identify them with the actual compounds constituting the device: TiN, HfO2, SiO2, Si and TaN.

5. Conclusion

The suggested method represents STEM spectrum-images as a compact linear mixture of few physically interpretable components, which greatly facilitates collection, storage, interpretation and quantification of huge volumes of spectrum-imaging data.

[1] see for example: M.Watanabe et al, Micr. Anal. (2009) p.6.

[2] J.M.P. Nascimento, J.M.B. Dias, IEEE trans. Geoscience Remote Sensing 43 (2005) p.898.

[3] J. Spiegelberg et al., Ultramicroscopy 182 (2017) 205-211.

The authors appreciate support from ERC (grant 715620 under the Horizon 2020 program) and DFG project 431448015.

Fig. 1

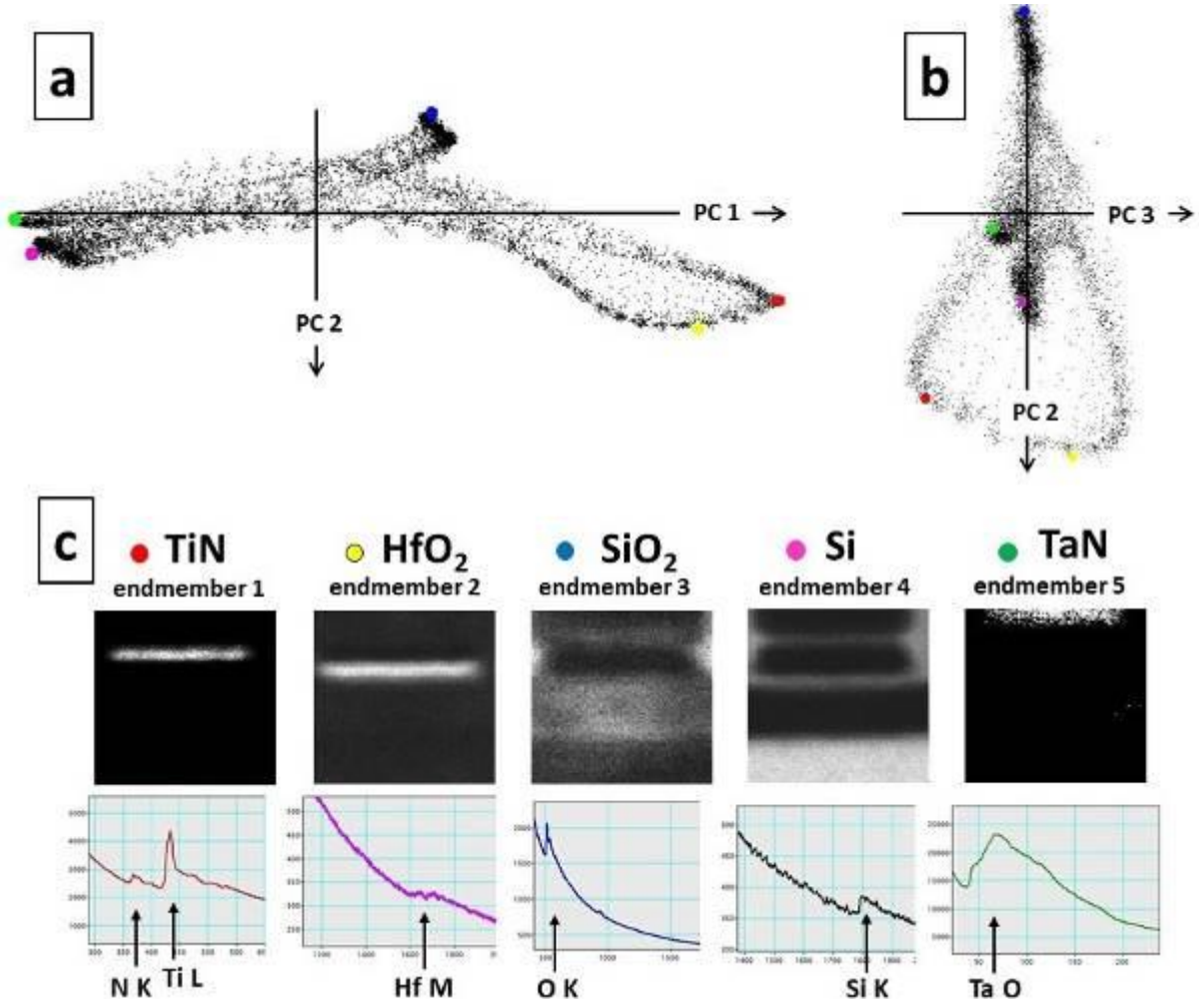

IM2.P014

Anderson localization of surface plasmons in two-dimensional Au-nanostructures

J. Schultz[1], K. Hiekel[2], P. Potapov[1], P. Khavlyuk[2], A. Eychmüller[2], A. Lubk[1]

[1]Leibniz-Institut für Festkörper- und Werkstoffforschung Dresden e. V., IFF, Dresden, Germany
[2]TU Dresden, Physical Chemistry, Dresden, Germany

Surface Plasmons (SPs) are collective charge oscillations in solids which arise at interfaces of media with opposite sign of the dielectric functions. By confining SP to plasmonic nanoparticles, nanoantennas, etc., the electromagnetic fields of the plasmon oscillations are localized both spatially and spectrally including a strong field amplification, which is exploited in various applications, such as Surface Enhanced Raman Spectroscopy or energy harvesting.

To further enhance localization and field amplification, disorder-induced localization (induced by Anderson localization mechanism) have been proposed and controversially discussed previously [1,2]. To further elucidate this localization mechanism, we study recently discovered ultrathin randomly disordered gold webs [3] (see lower right image in Fig. 1 b) by using Electron Energy Loss Spectroscopy (EELS) in combination with Scanning Transmission Electron Microscopy (STEM). This technique allows probing both, the spatial and spectral localization of the SPs at highest resolution (Δx~1nm and ΔE~60meV). The experimental data is compared to simulations employing Babinet"s principle equating holes of the web with thin oblate nanodiscs, which are mutually interacting through their dipole moments. This trick (i.e. simulation of inverse structure as coupled discrete dipoles) allows to handle large webs of several microns diameter, which are not accessible by conventional boundary element or FTDT methods. Within the discrete dipole model localization of resonant modes is quantified, among others, by so-called inverse participation number, which corresponds to the average number of active hotspots within resonant modes that are experimentally obtained by analyzing the number of hotspots within a narrow energy band.

Both, the experimental and simulated participation numbers decrease with increasing excitation energy until ~1.7eV. At this frequency, maximal spatial and spectral localization of dipole coupled modes is observable, leading to very high quality factors (strong field enhancement) close to the theoretical maximum. Beyond 1.7eV dipole coupled localized SPs modes are completely suppressed. Our simulations show that the threshold may be deliberately tuned by material and geometry parameters of the nets, which opens interesting prospects for strong light absorption and energy conversion by those ultrathin networks.

[1] V. A. Markel, J. Phys. Condens. Matter **18**, (2006).

[2] S. Grésillon et al., Phys. Rev. Lett. **82**, (1999).

[3] K. Hiekel et al., Angew. Chem. Int. Ed. **59**, (2020).

[4] This project was funded by the European Research Council (ERC) under the Horizon 2020 research and innovation program of the European Union (grant agreement no. 715620) and the Deutsche Forschungsgemeinschaft (DFG, German Research Foundation) under Germany's Excellence Strategy through Würzburg-Dresden Cluster of Excellence on Complexity and Topology in Quantum Matter - ct.qmat (EXC 2147, project-id 390858490).

Fig. 1: *a) EEL spectra collected at different spatial subsets, revealing numerous LSP modes. b) STEM image of the investigated map collected with the High-angle annular dark-field detector (lower right) and spatially resolved loss probability maps at different loss energies. The loss probability maps show increasing localization of the field hot spots with increasing energy.*

Fig. 2: *Experimental and simulated participation number, which reflects the increasing localization observable in Fig. 1.*

Fig. 1

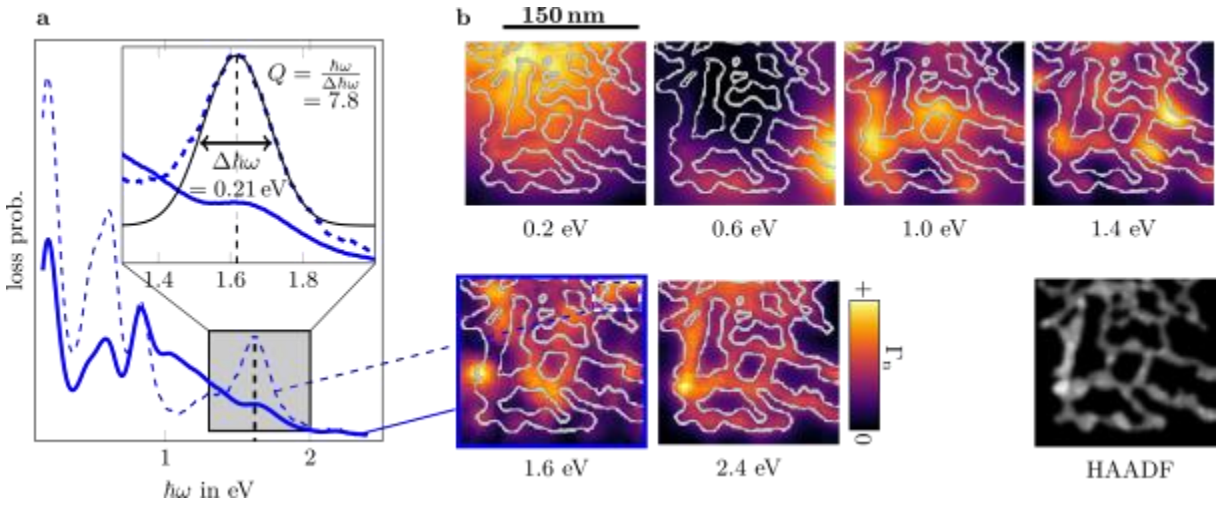
a
b
150 nm
loss prob.
$Q = \frac{\hbar\omega}{\Delta\hbar\omega} = 7.8$
$\Delta\hbar\omega = 0.21$ eV
1.4
1.6
1.8
1
2
$\hbar\omega$ in eV
0.2 eV
0.6 eV
1.0 eV
1.4 eV
1.6 eV
2.4 eV
+
0
Γ_n
HAADF

Fig. 2

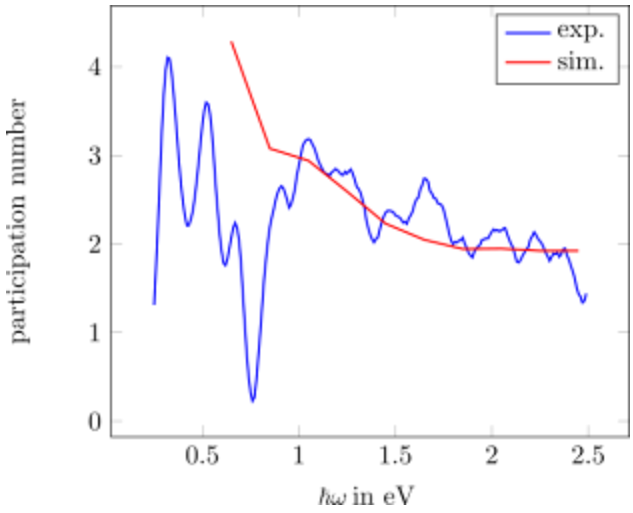
exp.
sim.
participation number
0
1
2
3
4
0.5
1
1.5
2
2.5
$\hbar\omega$ in eV

IM2.P015

Momentum-resolved spectrum imaging for electromagnetic field mapping in plamonic nanostructures

J. Schultz[1], J. Krehl[1], G. Guzzinati[2], P. Potapov[1], J. Verbeeck[2], A. Lubk[1]

[1]Leibniz-Institut für Festkörper- und Werkstoffforschung Dresden e. V., IFF, Dresden, Germany
[2]University of Antwerp, EMAT, Antwerp, Belgium

Surface plasmons (SPs) are resonances occurring at interfaces of media with opposite sign of the dielectric functions. They are characterized by strongly enhanced and localized electric fields, which can be exploited in several applications, e.g., Surface Enhanced Raman Spectroscopy or plasmonic waveguides.

To investigate SPs on nanostructures at highest spatial and spectral resolution, electron energy-loss spectroscopy is frequently employed in combination with scanning transmission electron microscopy (so-called plasmon mapping) [1], which provides spatial resolved loss probability maps that reveal the character (dipolar, quadrupolar, etc.) of different SP modes. While the loss probability is proportional to the longitudinal (i.e., parallel to e-beam) field component, transverse field components (e.g., containing magnetic contributions) cannot be probed. To overcome this limitation, momentum transfer by transverse field components to the beam electrons must be measured with spectral and spatial resolution.

Here, one option is to record energy-filtered diffraction patterns in the far field at different probe positions (see lower row in Fig. 1 a) [2]. From the overall intensity in the discs, a spatial resolved loss probability map can be extracted (see Fig. 1 a). The shift of the center of mass of the intensity, on the other hand, corresponds to the transverse momentum transfer to the beam electrons, i.e., to the transverse electromagnetic field (see Fig. 1 b). In this mode, the filtered spectral region is determined by a slit aperture in the energy dispersive plane and is hence limited to ~1eV.

An alternative approach is to acquire ω-q maps with one spectral and one momentum dimension recorded at different probe positions. Here, the sampled direction in q-space is determined by a slit aperture in a diffraction plane. By rotating the sample with respect to the aperture, different directions of momentum transfer can be probed serially (see upper rows in Fig. 2 for two different q-space directions). Integrating the intensity along the q-dimension at each scanning position, leads again to spatially resolved loss probability maps (see lower row in Fig. 2).

Our proof-of-concept experiments show that both setups are suitable to measure transverse electromagnetic field components of SPs. Here, the highest spectral resolution can be obtained by acquiring ω-q maps. Recording energy-filtered diffraction patterns, on the other hand, provides parallel acquisition of the momentum transfer in all q-space directions.

[1] J. Nelayah, et al., Nat. Phys. **3**, (2007).

[2] J. Krehl et al., Nat. Comm. **9**, (2018).

[3] This project was funded by the European Research Council (ERC) under the Horizon 2020 research and innovation program of the European Union (grant agreement no. 715620).

Fig. 1: *Transverse momentum transfer/ electric field components reconstructed from energy-filtered diffraction discs of an Al nanorod. a) Loss probability map (upper image) and diffraction discs (lower row) recorded at probe position 1-4. b) Transverse electric field components derived from the center of mass of the intensity (orange diamonds) in the diffraction discs shown in a).*

Fig. 2: *Transverse momentum transfer and loss probability maps reconstructed from ω-q mapping of an Al split ring resonator. a) Lateral momentum transfer along two different directions in q-space (indicated by the arrows). b) Corresponding loss probability maps.*

Fig. 1

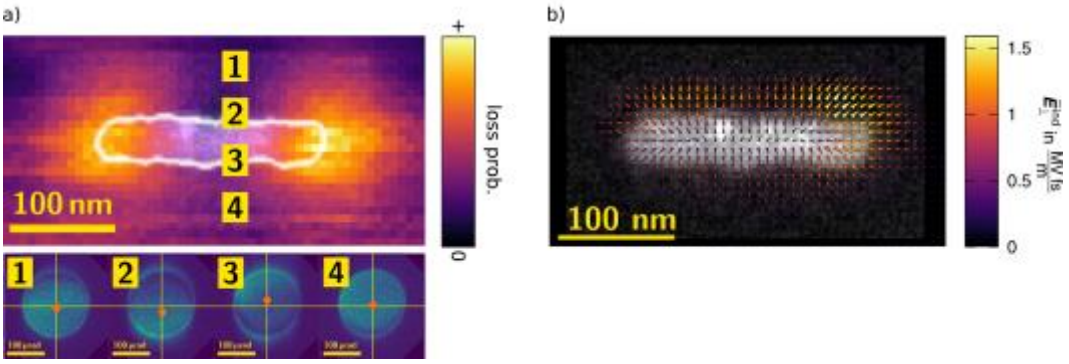
a)
1
2
3
4
100 nm
+
loss prob.
0
b)
100 nm
1.5
1
0.5
0

Fig. 2

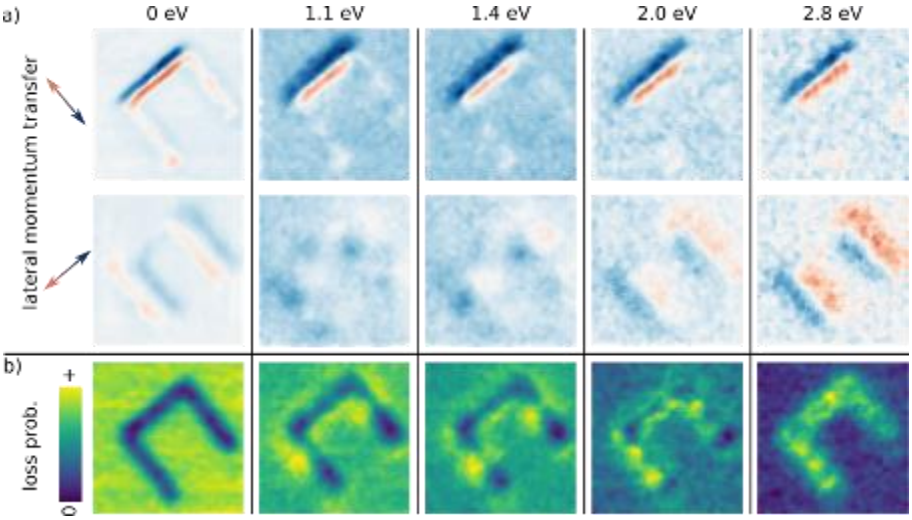
a)
0 eV
1.1 eV
1.4 eV
2.0 eV
2.8 eV
lateral momentum transfer
b)
loss prob.
+
0

IM2.P016

Combining HAADF STEM and EDX for element specific atom-counting

A. De Backer[1], Z. Zhang[1,2], K. H. W. van den Bos[1], E. Bladt[1], A. Sànchez-Iglesias[3], L. M. Liz-Marzán[3,4], P. Nellist[2], S. Bals[1], S. van Aert[1]

[1]EMAT and NANOlab Center of Excellence, University of Antwerp, Antwerp, Belgium
[2]Department of Materials, University of Oxford, Oxford, United Kingdom
[3]CIC biomaGUNE, Basque Research and Technology Alliance (BRTA), San Sebastian, Spain
[4]Ikerbasque, Basque Foundation for Science, Bilbao, Spain

Multimetallic nanocrystals are of great scientific and technological interest because of their unique electronic, optical, or catalytic properties. These properties are largely determined by the atomic structure and composition of the nanocrystal. Therefore, quantitative structure determination is essential for the development of new nanocrystals. For homogeneous nanoparticles, the number of atoms can be counted from high resolution annular dark field scanning transmission electron microscopy (HAADF STEM) images [1] where intensities scale with the number of atoms and the atomic number Z. For heterogeneous structures, however, the presence of this so-called Z-contrast complicates this atom-counting procedure since the different elements and their exact 3D arrangement in each atomic column will contribute differently to the image intensity [2]. Therefore, we developed a new methodology, which combines HAADF STEM imaging and elemental mapping by energy dispersive X-ray (EDX) spectroscopy.

The so-called scattering cross-section (SCS), corresponding to the total intensity of electrons scattered by a single atomic column, has been shown to be a successful performance measure for atom-counting and composition determination in HAADF STEM [1,4-6]. Similarly, EDX STEM SCSs can be defined from elemental maps. Since both HAADF STEM and EDX imaging are incoherent techniques, a linear relationship between the EDX and HAADF STEM SCSs exists. By exploiting this linear relationship, the experimental SCSs are matched to the simulated SCSs by estimating normalization constants for the EDX SCSs, using an iterative weighted least squares minimization.

As a proof of concept, the combination of EDX and HAADF STEM images is used to count the number of atoms for a Au@Ag nanorod. Figure 1(a) shows a times series for both the STEM images and the Ag and Au EDX maps. The resulting number of Ag and Au atoms for each atomic column are shown in Figure 1(b). With this methodology we also explored the possibility of the characterization of a simulated Au@Pt nanorod, with adjacent atomic numbers (Figure 2). Those analyses quantitatively demonstrate the new opportunities to count the number of atoms corresponding to each specific element, even when the difference in atomic number is only one [7].

References

[1] S. Van Aert et al., Physical Review B 87 (2013), p. 064107.

[2] K.H.W. van den Bos et al., Physical Review Letters 116 (2016), p. 246101.

[3] A.J. D"Alfonso et al., Physical Review B 81 (2010), p. 100101.

[4] S. Van Aert et al., Ultramicroscopy 109 (2009), p. 1236.

[5] H. E et al., Ultramicroscopy 133 (2013), p. 109.

[6] G.T. Martinez et al., Ultramicroscopy 187 (2018), p. 84.

[7] This work was supported by the European Research Council (Grant 770887 PICOMETRICS to SVA and Grant 815128 REALNANO to SB, Grant 823717 ESTEEM3). The authors acknowledge financial support from the Research Foundation Flanders (FWO, Belgium) through project fundings and postdoctoral grants to ADB and EB.

Figure 1 (a) Experimental HAADF STEM images and EDX elemental maps for Ag and Au. (b) The total number of atoms and the number of Au and Ag atoms.

Figure 2 (a) Example of a simulated time-series of HAADF STEM images and Pt and Au elemental maps with 5% collection efficiency and an incident dose of $5\times10^4 e^-/Å^2$ per frame for the HAADF STEM images and $5\times10^6 e^-/Å^2$ per frame for the EDX elemental maps. (b) Root mean squared error per atomic column for Pt, Au, and the total number of atoms.

Fig. 1

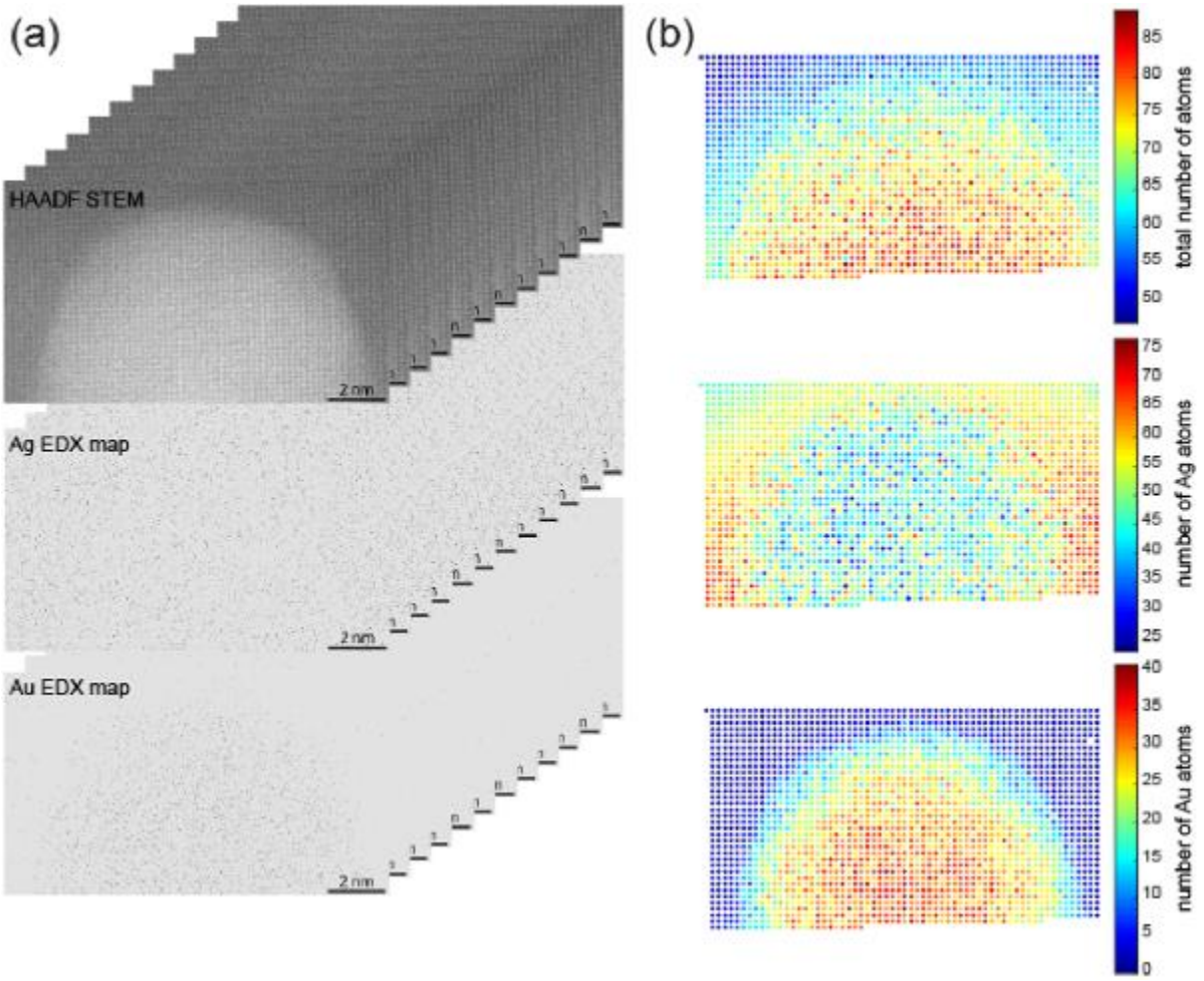
(a)
HAADF STEM
2 nm
Ag EDX map
2 nm
Au EDX map
2 nm
(b)
total number of atoms
number of Ag atoms
number of Au atoms

Fig. 2

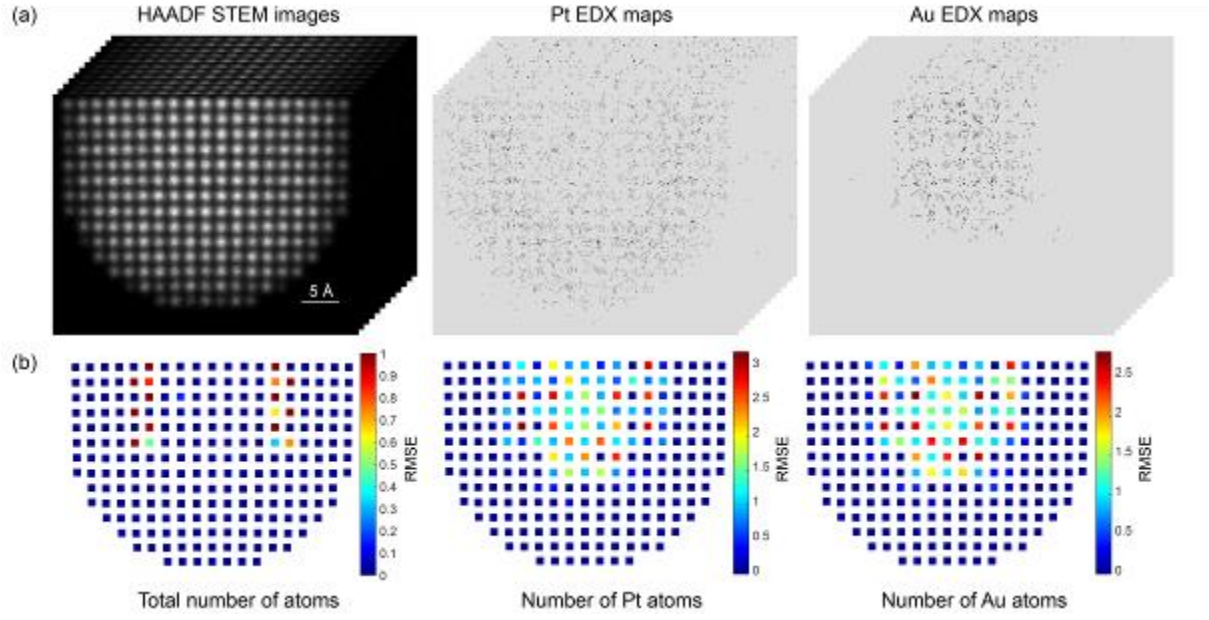
(a)
HAADF STEM images
Pt EDX maps
Au EDX maps
5 Å
(b)
RMSE
Total number of atoms
Number of Pt atoms
Number of Au atoms

IM2.P017

Simulations of magnon diffuse scattering in STEM at different temperatures

J. Á. Castellanos-Reyes[1], A. Bergman[1], P. Zeiger[1], J. Rusz[1]

[1]Uppsala University, Department of Physics and Astronomy, Uppsala, Sweden

Introduction

The latest monochromator and spectrometer improvements in scanning transmission electron microscopy (STEM) currently allow energy resolutions below 10 meV [1-4]. This has extended the capabilities of STEM electron energy loss spectroscopy (EELS) to perform, for example, vibrational spectroscopy with high spatial resolution in STEM [3, 4].

The energy losses due to magnons are in the same range as the typical energies of vibrational modes (tens or few hundreds of meV) [5]. Hence, it might be possible to probe magnons with STEM-EELS at both high-spatial and high-energy resolutions. This would bring new possibilities for studying magnetic ordering phenomena, benefiting fields such as spintronics and spin caloritronics.

Probing magnons with STEM-EELS is technically challenging, especially since the vibrational (phonon) signal, due to thermal diffuse scattering (TDS) of electrons, can be four orders of magnitude greater than the magnon diffuse scattering (MDS) signal [5]. However, there are circumstances in which the relative strengths of the magnetic signals can reach a few percent [6–8]. Therefore, it is important to find conditions in which MDS and TDS signals can be separated. For this, temperature could play a key role: it is likely that temperature dependence of magnon and phonon signals qualitatively differ.

Objectives

In this work, we will present STEM MDS simulations for BCC iron at different temperatures. We will compare our results with TDS calculations, focusing on the distinguishability of the signals.

Materials & methods

We will follow the methodology of Ref. [5], in which the MDS signal is computed from the magnon analog of the frozen phonon multislice (FPMS) method [9, 10], combining the magnetic-fields-aware multislice method [6] and atomistic spin dynamics (ASD) simulations [11].

Results

We will present results using classic and quantum thermostats in ASD simulations. In particular, we will show that the MDS signal increases up to T_c and then decreases. We will discuss the implications of our results for experimental measurements of MDS signals.

Conclusions:

We will show that temperature could be a key factor in successful MDS measurements in STEM. In particular, as for the case of BCC iron, temperatures close to T_c might enhance MDS signals, potentially allowing for the separation of MDS and TDS signals.

References

[1] O. L. Krivanek et al., Nature 514, 209 (2014).

[2] O. L. Krivanek et al., Ultramic. 203, 60 (2019).

[3] M. J. Lagos et al., Microscopy 71, i174 (2022).

[4] N. Dellby et al., Microsc. Microanal. 28(S1), 2640 (2022).

[5] K. Lyon et al., Phys. Rev. B 104, 214418 (2021).

[6] A. Edström et al., Phys. Rev. Lett. 116, 127203 (2016).

[7] A. Edström et al., Phys. Rev. B 94, 174414 (2016).

[8] A. Edström et al., Phys. Rev. B 99, 174428 (2019).

[9] R. F. Loane et al., Acta Cryst. A47, 267 (1991).

[10] P. M. Zeiger and J. Rusz, Phys. Rev. Lett. 124, 025501 (2020).

[11] O. Eriksson et al., *Atomistic Spin Dynamics: Foundations and Applications* (Oxford University Press, Oxford, 2017).

IM2.P018

Backscattered electron energy loss spectroscopy: on the way to fluorophore imaging in the SEM

D. Ryklin[1], F. Schmidt-Kaler[1], D. Wrege[1], R. R. Schröder[1]

[1]Universität Heidelberg, Bioquant Institut, Heidelberg, Germany

Introduction

With the use of organic materials in electronic devices, as well as in biological and bioinspired functional nano-materials, the need for novel characterization methods becomes paramount. Such materials are in general highly beam sensitive and common electron microscopic techniques cannot be applied in general. In particular metal sputtering, heavy metal staining and beam induced degradation of the sample are obstacles hampering the direct observation of organic materials.

Objectives

In our study we want to overcome obstacles listed above using ultra-low voltage Scanning Electron Microscopy (SEM) for direct imaging of organic materials with high spatial resolution, surface sensitivity, and significantly reduced beam-damage. For electron energies below 1 keV the SEM image contrast and imaging quality in particular for low-dose imaging of organic materials is significantly improved.

In addition, we introduce Electron Energy Loss Spectroscopy (EELS) to SEM. Applying electron spectroscopic imaging of backscattered electrons (BSE) we can for the first time in a SEM identify excited states (e.g. plasmon and fluorescence excitations) and use them for low-dose material characterization.

Materials and Methods

We use a prototype of an electron-spectroscopic SEM, i.e. Zeiss Delta-SEM [1] for recording backscattered EEL spectra (bsEELS). As prerequisite for spectroscopic data collection we can achieve sub-nanometer imaging resolution in a wide energy range from a few keV (as in conventional SEM) down to ultra-low landing energies around 20 eV.

Results

As initial model system we studied QDots, which – as inorganic material – showed a strong bsEELS shoulder at the corresponding excitation energy (data not shown). As first organic system we obtain spectral data from graphene on silicon wafer (SiO_2), materials where TEM-EELS measurements can be used as reference [2,3]. Fig. 1 shows measured bsEEL spectra together with a correlating naïve model fit derived from TEM-EELS data. Although the energy resolution of our prototype is limited (worse than about 5eV), we find a good agreement of the SEM spectral data to e.g. the known characteristic surface plasmon signal of graphene. We show here for the first time that backscattered electrons carry specific material information from their elastic and inelastic interaction with the sample.

Next we study organic samples such as DNA and DNA labelled with fluorophores (Fig. 2). The results show that beam damage is minimized and contrast heavily increased for organic materials at ultra-low electrons energies. In Fig. 2 we show the first results of bsEEL spectra of DNA origamis and fluorophores. Although the spatial and energy resolution still needs to be improved, the bsEEL spectra show a pronounced signal of the UV DNA absorption as well as the excitation signal of the bound fluorophores.

Conclusion

bsEELS provides a new, powerful characterization tool for the direct visualization and spectroscopy of organic materials.

Acknowledgements: The authors thank Enrico Lemma (KIT Karlsruhe, Germany), Yannick Dreher and Kerstin Göpfrich (MPI Heidelberg, Germany) for samples. Research funded by DFG (German Research Foundation) via the Excellence Cluster "3D Matter Made to Order" (EXC-2082/1-390761711).

[1] RR Schröder et al., Microsc. Microanal. 24 (Suppl 1), 2018

[2] Wachsmuth et al, Physical Review B 90, 235434, 2014

[3] Park et al, Ultramicroscopy 109, 9, 2009

Fig. 1

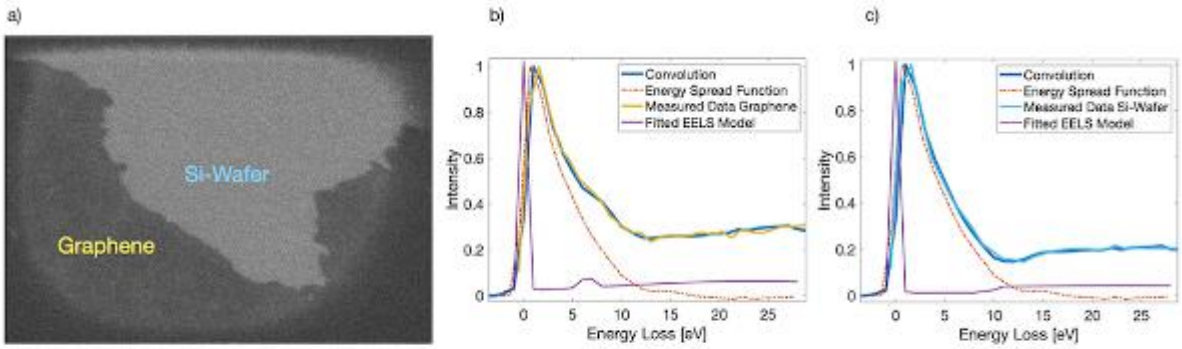

Figure 1: a) BSE Image of a graphene flake on Si-Wafer. The field of view is framed by clearly visible beam-induced contamination, whereas the central window is cleared of contaminants by the beam. b) for graphene and c) for SiO_2 show a naïve model fit (blue) of the expected EELS data simulated from TEM measurements (purple, [2] and [3] respectively). The TEM spectra are convoluted with the measured energy spread function of the detection electron path (red, dotted) and agree then very well to the measured data of graphene (yellow) and silicon oxide (light blue) respectively.

Fig. 2

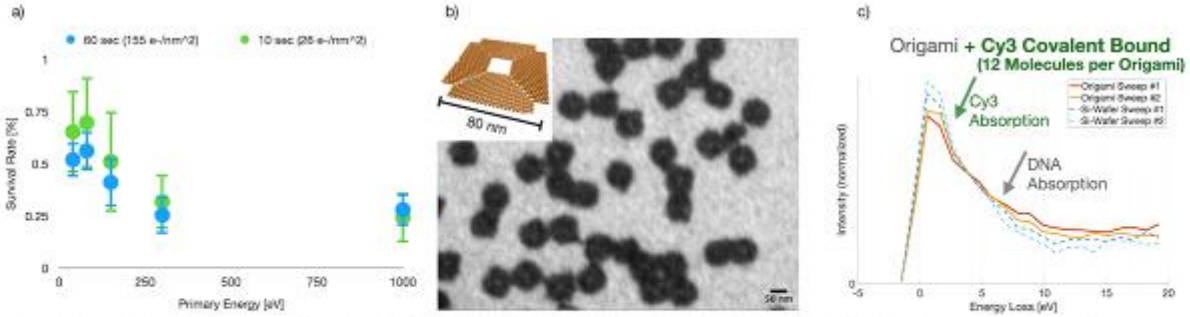

Figure 2: a) Survival rate of fluorescence signal from DNA labeled with Cy5 and Cy3 fluorophores after electrons irradiation depending on the electron primary energy. The survival rate increases with decreasing electron energy. b) BSE image of DNA-Origami (flat platelets, 2nm thickness, 40-50 atoms per nm^2 pixel size) on Si-Wafer. Inset shows the Origami design. c) First bsEEL spectra of DNA Origami with fluorescent label: Red curve shows the signal of a contaminated sample, yellow curve shows the same sample spectrum after beam-induced cleaning. An additional energy loss signal at around 2 eV can be observed for the cleaned Origami. This shoulder can be attributed to the excitation of the fluorescent label and is not observed on unlabeled DNA (data not shown). Dotted blue and light blue curves show the corresponding reference signal from the silicon-wafer for the contaminated and cleaned sample, respectively. The additional EELS signal of the Origami spectra above 5eV energy loss compared to the Si-Wafer reference can be attributed to the absorption energy of DNA.

IM2.P019

Large solid angle racetrack-shaped SDDs for efficient EDX analysis in SEMs and TEMs down to Lithium

A. Niculae[1], S. Aschauer[1], M. Bornschlegl[1], K. Hermenau[1], H. Soltau[1], L. Strüder[2]

[1]PNDetector GmbH, Munich, Germany
[2]PNSensor GmbH, Munich, Germany

The progress made over the last decade in high resolution electron microscopy (EM) has pushed the instrument abilities towards new frontiers. Higher beam currents, smaller spot sizes, more accurate and fast detectors – all these features enable sample imaging and elemental mapping at atomic scale resolution in real time. Often equipped with one or more Energy Dispersive X-Ray (EDX) detectors, the analytical capabilities of the electron microscopes have gained more and more significance over the last years.

For high resolution EMs like TEMs or HR-SEMs, the working distance between the upper pole-piece and sample is very small; thus, when using an EDX detector of a certain size, the maximum achievable solid angle for collecting the x-ray signal is mainly determined by the minimum distance at which the detector can be positioned relative to the sample point. For these cases, using a racetrack-shaped detector with its reduced vertical dimension enables a closer positioning of the detector with respect to the sample point (see Fig. 1a) and therefore a substantial increase in solid angle (Fig. 1b).

With more than 20 years of experience in developing and manufacturing of high-quality Silicon Drift Detectors (SDD), we at PNDetector have been continuously working on tailoring the detector performance to keep pace with the new application trends in EDX microanalysis. With respect to the maximum achievable solid angle, the well-established Racetrack detector series comprising sensors with active areas from 60 mm^2 to 200 mm^2 (see Fig.2) has been already introduced for some time [1]. From the various detector sizes, especially the 100 mm^2 SDD Racetrack is being successfully used for many years as a large solid angle EDX detector in many TEMs or in HR-SEMs. Depending on the pole-shoe configuration, solid angle values of up to 1 sr can be achieved. The solid angle can be doubled by using a dual-detector configuration.

In the research field of renewable energies, Lithium is a key element for the development of efficient batteries. Detection of Lithium in various compounds by EDX is not a trivial task and necessitates a state-of-the-art EDX detector with minimum noise level and high detection efficiency. Extending the energy detection limits of the SDDs for ultra-light elements down to Lithium (54 eV) has become one of our major development objectives over the past years [2].

Combining the large solid angle of x-ray collection with the very low-noise SDD^{plus} technology makes the racetrack-shaped detectors ideal for Lithium detection and mapping in an electron microscope. Figure 3 shows a Lithium spectrum measured on a SEM with a 100 mm^2 SDD^{plus} Racetrack detector in windowless configuration. In this contribution we will presents newest developments and spectroscopic results obtained with various racetrack-shaped detector configurations.

[1] A. Niculae et al., Microscopy and Microanalysis 22 (Supl3), 2016.

[2] A. Niculae et al., Microscopy and Microanalysis 25 (Supl2), 2019.

Fig. 1 (a) Schematic view of a TEM pole-piece with a round EDX detector on the left and a racetrack-shaped detector of similar area on the right-hand side; (b) Detector solid angle distribution as a function of the distance from detector to the sample and detector area.

Fig. 2: Three racetrack-shaped SDD geometries with total active areas of 200 mm^2, 100 mm^2 and 60 mm^2.

Fig. 3. Spectrum from a pure Li sample measured in SEM with a 100 mm^2 Racetrack SDD^{plus} detector

Fig. 1

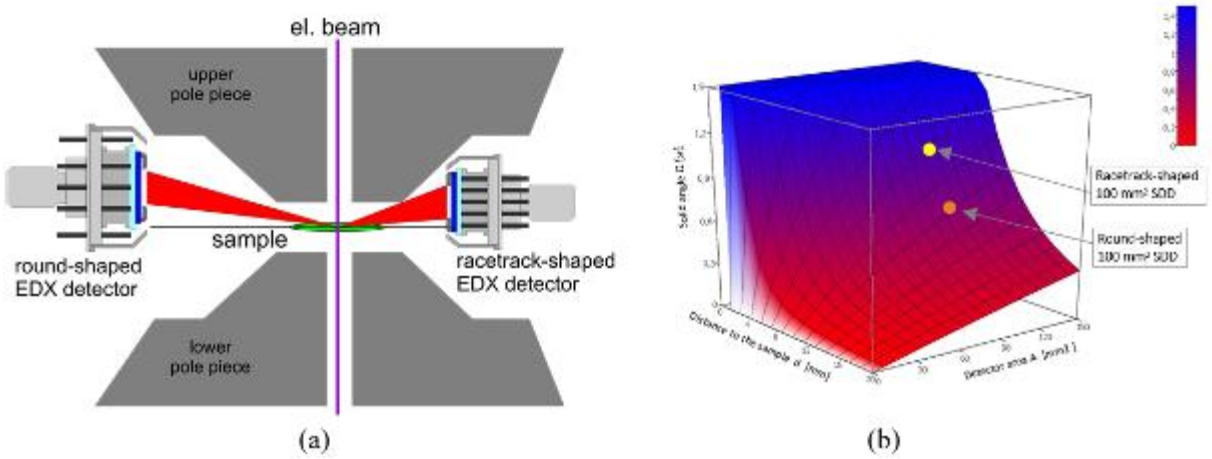

Fig. 2

Fig. 3

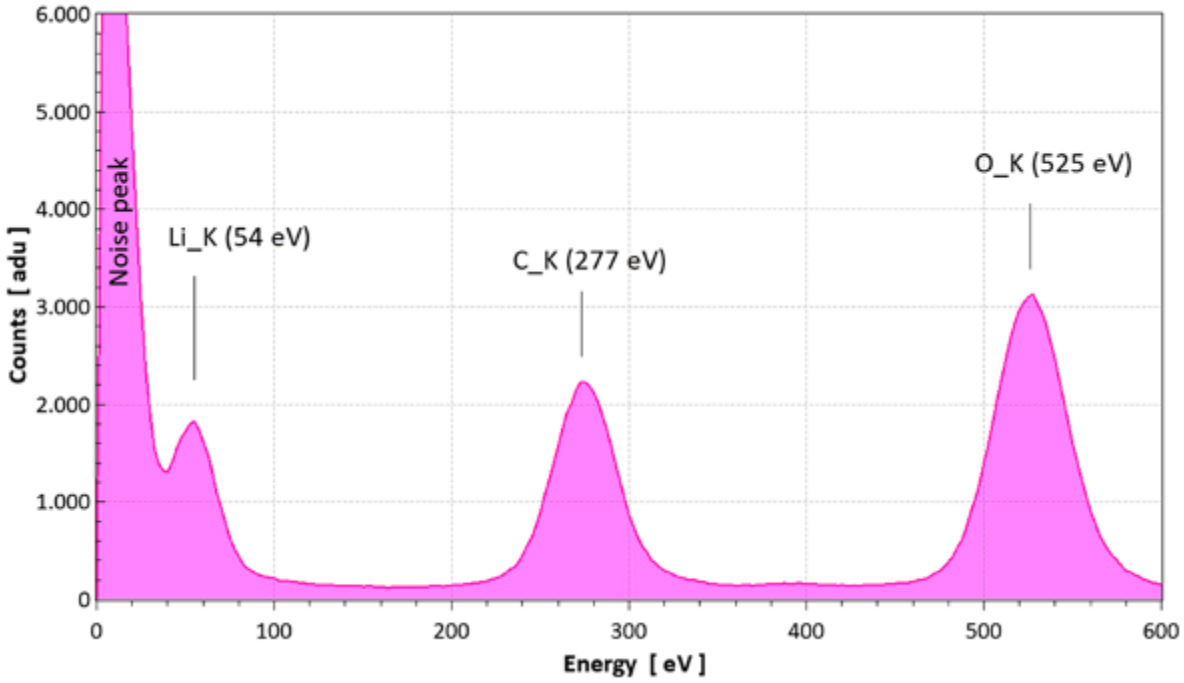

IM2.P020

EELS accessible for non-expert TEM users: adding a ChemiTEM workflow for EELS-related techniques to the portfolio

D. Ramermann[1], J. Menten[1], E. H. Wolf[1], W. Hetaba[1]

[1]Max-Planck-Institut für Chemische Energiekonversion, Mülheim an der Ruhr, Germany

Introduction

Analytical Transmission Electron Microscopy is used for a wide range of applications. Usually TEM-experts perform most of the analytical techniques. However, easy access for non-expert users to different TEM methods is provided by ChemiTEM workflows [1]. These workflows are implemented in an app guiding the users step by step through the measurements. This enables non-expert users to perform standardised measurements including TEM imaging, STEM/HRSTEM and EDS. In addition in this work we present a workflow for measuring EELS-related techniques which includes measurement of sample thickness, mapping selected elements and investigation of the oxidation state of a material.

Objectives

As addition to the ChemiTEM app a workflow for EELS, aiming at the three most common measurement scenarios, is developed: Thickness measurement, elemental mapping and oxidation state determination. It guides the user step by step through the measurement procedures. This allows non-expert TEM users to perform these techniques, which increases the throughput for a research institute while maintaining a high standard in data quality and comparability.

Methods & Results

To assess which EELS techniques are mostly used, the EELS measurement tasks of 9 months at the Max Planck Institute for Chemical Energy Conversion have been evaluated and rated with respect to the demand on the TEM operator. Out of 54 samples 29 needed EELS elemental mapping as well as oxidation state determination, while 25 required thickness evaluation. In the EELS workflow a first set of questions about the sample helps the user to judge whether a measurement can be successfully performed by a non-expert user. A decision-tree based based workflow (Fig. 1) guides the user through sample preparation, choosing a suitable measurement region, alignment of the spectrometer including safety precautions for the camera and acquisition settings to achieve a good signal to noise ratio of the desired signal. The workflow distinguishes between the three scenarios mentioned before: For thickness measurements the focus lies on acquisition of the zero loss peak and low loss region as well as camera protection. For elemental mappings the workflow helps to determine which parts of the spectrum to acquire with respect to dispersion and drift tube voltage in a window between 200 and 1200 eV. Finally, for the oxidation state investigations the acquisition of the oxygen K edge and the zero loss peak in case of dual EELS measurements are covered in the workflow. In each case data analysis using appropriate software packages is also included.

The presented EELS workflow is tailored for a FEI Talos F200X microscope equipped with a Gatan Continuum S spectrometer, however, it can be adapted to other setups with minor effort.

To assess the designed EELS workflows, users which were trained using the ChemiTEM workflows and an experience of less than 10 sessions, more than 20 sessions and an expert TEM user evaluated the same sample and the results have been compared.

Conclusion

The large amount of training an expert TEM user needs cannot be replaced, but parts of the tasks that can be performed in a standardised way can be carried out by non-expert TEM users using our EELS workflow, making this sophisticated TEM technique available to a larger community.

[1] Hetaba et al., Chemistry-Methods 2021, 1, 401-407

Fig.1: Schematic decision-tree of the ChemiTEM EELS workflow.

Fig. 1

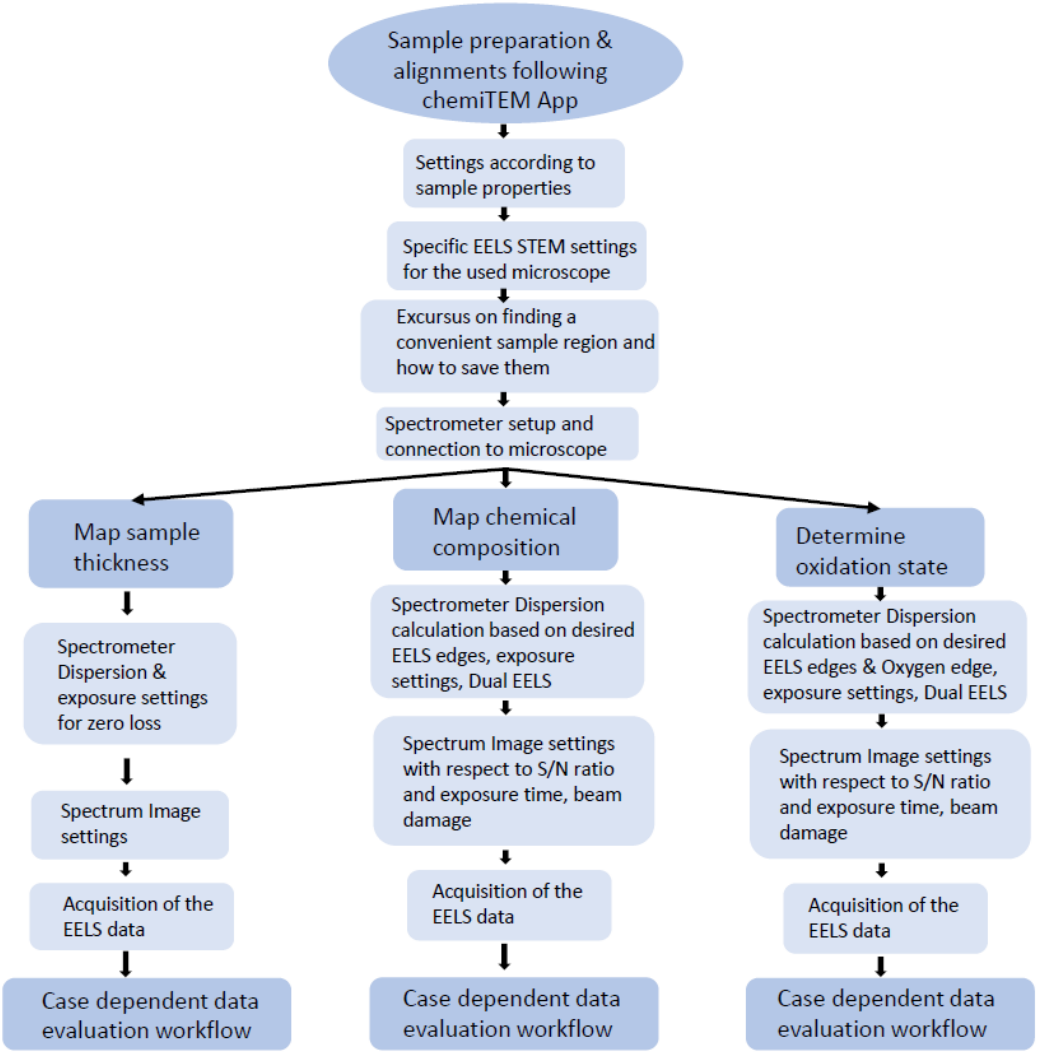
Sample preparation & alignments following chemiTEM App
Settings according to sample properties
Specific EELS STEM settings for the used microscope
Excursus on finding a convenient sample region and how to save them
Spectrometer setup and connection to microscope
Map sample thickness
Spectrometer Dispersion & exposure settings for zero loss
Spectrum Image settings
Acquisition of the EELS data
Case dependent data evaluation workflow
Map chemical composition
Spectrometer Dispersion calculation based on desired EELS edges, exposure settings, Dual EELS
Spectrum Image settings with respect to S/N ratio and exposure time, beam damage
Acquisition of the EELS data
Case dependent data evaluation workflow
Determine oxidation state
Spectrometer Dispersion calculation based on desired EELS edges & Oxygen edge, exposure settings, Dual EELS
Spectrum Image settings with respect to S/N ratio and exposure time, beam damage
Acquisition of the EELS data
Case dependent data evaluation workflow

IM2.P021

General oscillation strength of core-shell electron excitation by fast electrons based on Dirac solutions

Z. Zhang[1,2], I. Lobato[3,1], S. van Aert[3,1], P. Nellist[2]

[1]University of Antwerp, NANOlab Center of Excellence, Antwerp, Belgium
[2]University of Oxford, Department of Materials, Oxford, United Kingdom
[3]University of Antwerp, EMAT, Department of Physics, Antwerp, Belgium

STEM-EELS is widely used for probing the local structure, composition and electronic states of materials at the atomic scale. The rich information of EELS comes from the complex inelastic scattering process where fast electrons transfer their energy and momentum to the atoms by exciting the associated atomic electrons to higher unoccupied states, which is elemental specific and local density of states sensitive. To quantify EELS, a common practice is to fit the observed spectrum [1] with the scattering cross-sections calculated from the experimental parameters and general oscillation strength (GOS) database. The current GOS is based on the Hartree-Fock solution of atomic orbitals [2], which does not include the full relativistic effects but can apply the first order correction through (1) the relativistic mass correction for the kinetic energy (2) spin-orbital coupling and (3) the Darwin term -- the inherent error can be significant for heavy elements where the electron relativistic effect is significant. Also, the relativistic electrodynamics during the scattering is not considered in the transition matrix equation, which has been shown to be critical for the correct prediction of magic angle and orientation anisotropy [3] of EELS and energy-filtered CBED [4]. In addition, due to the limited computing resources at that time, the GOS database has limited energy-momentum ranges with coarse sampling.

For better quantification of EELS, here we developed an inelastic scattering physics code for the database generation of GOS based on Dirac solutions with relativistic electrodynamics. In this treatment, the spin-orbital splitting is naturally included, for instance for Ti L23 shown in Fig.1. The sampling is finely chosen for a much wider energy-momentum space than before. We hope the newly developed GOS database can benefit the EELS community for both academic use and industry integration. For future development, we will follow the same inelastic scattering physics for simulating EELS and EDX in the multislice algorithm under channeling conditions.

Reference:

[1]Verbeeck, J., and S. Van Aert. "Model based quantification of EELS spectra." Ultramicroscopy 101.2-4 (2004): 207-224.

[2]Leapman, R. D., P. Rez, and D. F. Mayers. "K, L, and M shell generalized oscillator strengths and ionization cross sections for fast electron collisions." The Journal of Chemical Physics 72.2 (1980): 1232-1243.

[3]Schattschneider, P., Hébert, C., Franco, H., & Jouffrey. "Anisotropic relativistic cross sections for inelastic electron scattering, and the magic angle." Physical Review B 72.4 (2005): 045142.

[4]Dwyer, C. "Relativistic effects in atomic inner-shell ionization by a focused electron probe." Physical Review B 72.14 (2005): 144102.

Fig.1 Plots of GOS as a function of momentum and energy losses for Ti L23 edges. The difference due to spin-orbital splitting is also included.

Fig. 1

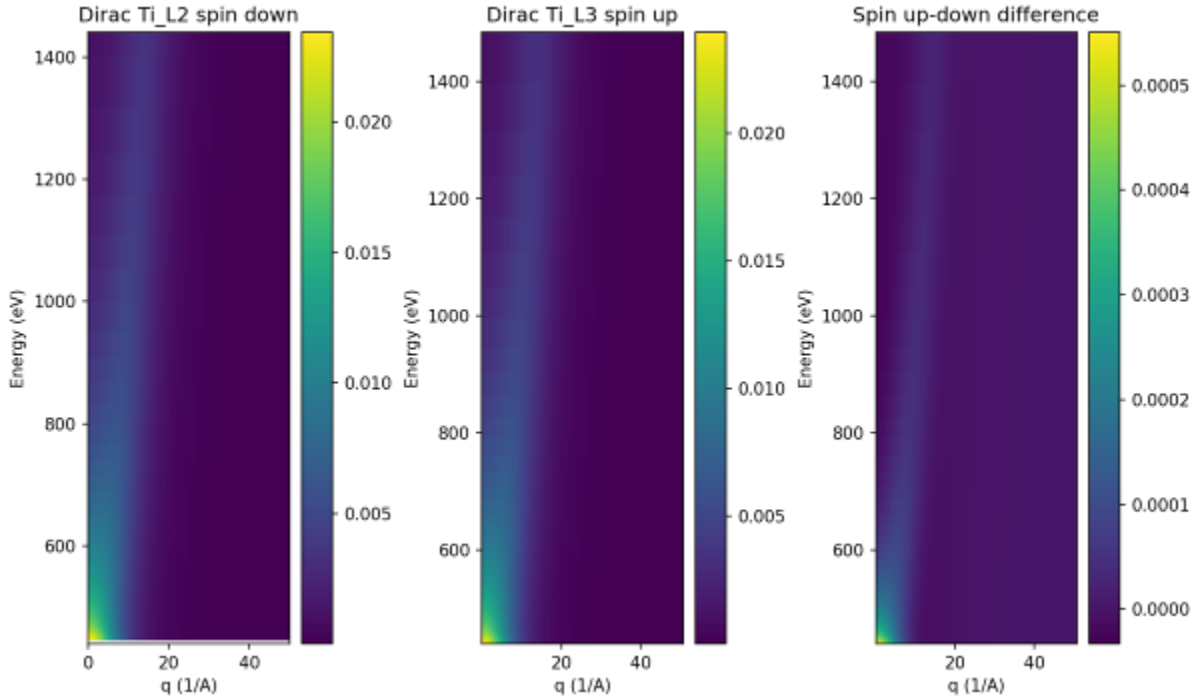
Dirac Ti_L2 spin down
Dirac Ti_L3 spin up
Spin up-down difference
Energy (eV)
q (1/A)
1400
1200
1000
800
600
0
20
40
0.020
0.015
0.010
0.005
0.0005
0.0004
0.0003
0.0002
0.0001
0.0000

IM2.P022

A new sampling paradigm for FRFPMS simulations of high energy resolution (STEM)-EELS experiments

P. Zeiger[1], J. Á. Castellanos-Reyes[1], J. Rusz[1]

[1]Uppsala University, Physics and Astronomy, Uppsala, Sweden

The development of high energy resolution EELS [1] has enabled the study of phonon properties of materials at the atomic scale, see for example Refs. [2,3]. One thereby exploits so-called impact scattering of electrons on the atomic nuclei itself, which is similar to the scattering of neutrons on phonons, albeit with a different atomic scattering factor [4,5]. With these tools it is now possible to locally probe the behaviour of phonons and thereby the flow of heat near interfaces [6-9], which is of large practical interest in the design of nano-scale devices and a unique capability of monochromated ultra high energy resolution STEM.

From a theoretical point of view, impact scattering on thicker specimen is difficult to model in a single inelastic scattering picture considering every possible transition due to the large amount of final states of the phonon system as well as the strong elastic interaction of the electron beam and the sample, the so-called dynamical diffraction. If one wants to consider a system containing an interface in such simulations, computational requirements may become prohibitive due to the large unit cells of suitable structure models. However topics such as electron channeling effects and delocalization of the vibrational (impact scattering) signal have not been fully addressed in literature yet, but are of high relevance for the correct interpretation of experiments.

We have introduced a qualitatively motivated extension of the Frozen Phonon Multislice (FPMS) method, the Frequency-Resolved FPMS (FRFPMS) method, which relies on molecular dynamics simulations using a frequency-selective thermostat rather than an explicit knowledge of phonon modes. The methodside-steps in this waysome of the computational complexity of simulations of inelastic phonon scattering in the STEM[10,11], but includes the effects of dynamical diffraction and is able to consider different scattering geometries. In this contribution, we first review the FRFPMS method and showcase some of the results obtained so far. We then consider a new sampling paradigm for the FRFPMS method, which relies on Fourier filtering of MD trajectories rather than a frequency-selective thermostat, and discuss it critically in comparison with the old scheme. This new sampling scheme promises a technicalsimplification of the calculation as well as a reduction of computational requirements.

IM2.P023

Machine learning for unmixing overlapping phases with low SNR STEM-EDXS data

H. Chen[1], D. T. L. Alexander[1], C. Hébert[1]

[1]École Polytechnique Fédérale de Lausanne (EPFL), Lausanne, Switzerland

The combination of Energy-Dispersive X-ray Spectroscopy (EDXS) and Scanning Transmission Electron Microscopy (STEM) is a rapid and robust technique for the chemical analysis of materials from microscale to nanoscale. However, suppose the sample is made of several phases that overlap in the thickness of the specimen. In that case, the technique cannot deliver an individual quantification of each phase but only an averaged composition. Many machine learning algorithms have therefore been explored to un-mix overlapping phases, among which the most promising is Non-negative Matrix Factorization (NMF) [1]. It considers that the mixture model between all individual components is linear, which applies well to EDXS in thin TEM specimens. Further, it constrains both the individual components and their weightings to be non-negative during computation, which is consistent with the physics of EDXS. Nevertheless, the effectiveness of NMF in un-mixing phases depends on the characters of the phases themselves and the signal-to-noise ratio (SNR) of the collected dataset. Under the circumstances that the concerned phases share some elements and the specimen is beam-sensitive, NMF would fail to achieve correct phase segmentation. In this paper, we seek to address this challenging case by appropriately adapting a clustering method [2] into the framework of NMF decomposition.

The sample examined is a deep Earth mantle mineral assemblage synthesized at 88 GPa and around 3000 K in a laser-heated diamond anvil cell. Figure 1(a) is the high-angle annular dark-field (HAADF) image, and Figure 1(b)-(d) are elemental maps of the assemblage. It consists of three mineral phases, Ferropericlase (i.e., a magnesium-enriched oxide), Calcium perovskite (i.e., a calcium-enriched silicate), and Bridgmanite (i.e., a magnesium-enriched silicate). Herein we name them Fp, CaPv, and Brg. The two precipitates are embedded in the matrix phase, Brg, and they overlap with each other. First, the standard NMF of scikit-learn [3] was applied, and its results are displayed in Figure 2(a)-(f). A minor phase, CaPv failed to be retrieved. The second component correctly captures the chemical features of Fp, while the first component contains much less Mg compared with the ground truth spectrum of Brg. The result is understandable since Mg is a common element shared by Brg and Fp, and the SNR of the dataset is at a low level. In contrast, the results of adapted NMF are shown in Figure 2(g)-(l). All the relevant three phases are correctly identified and segmented. Despite a few imperfections observed, the decomposed three components correctly represent phases' chemical features and their distributions.

Fig. 1. (a) The HAADF image of the mineral assemblage; (c) overlaid Mg Kα and Ca Kα elemental maps to reveal the distribution of Fp and CaPv; (b) and (d) elemental maps of Si Kα and O Kα.

Fig. 2. (a)-(c) The abundance maps, and (d)-(f) the spectra of the components of the standard NMF decomposition; (g)-(i) the abundance maps, and (j)-(l) the spectra of the components of the adapted NMF decomposition.

References:

[1] D. D. Lee, H. S. Seung, Nature 401 (6755) (1999)

[2] HW Zhang et al. International Conference on Image Processing, ICIP, 10 (2020)

[3] F Pedregosa et al. Journal of Machine Learning Research 12 (2011) 2825–2830.

Fig. 1

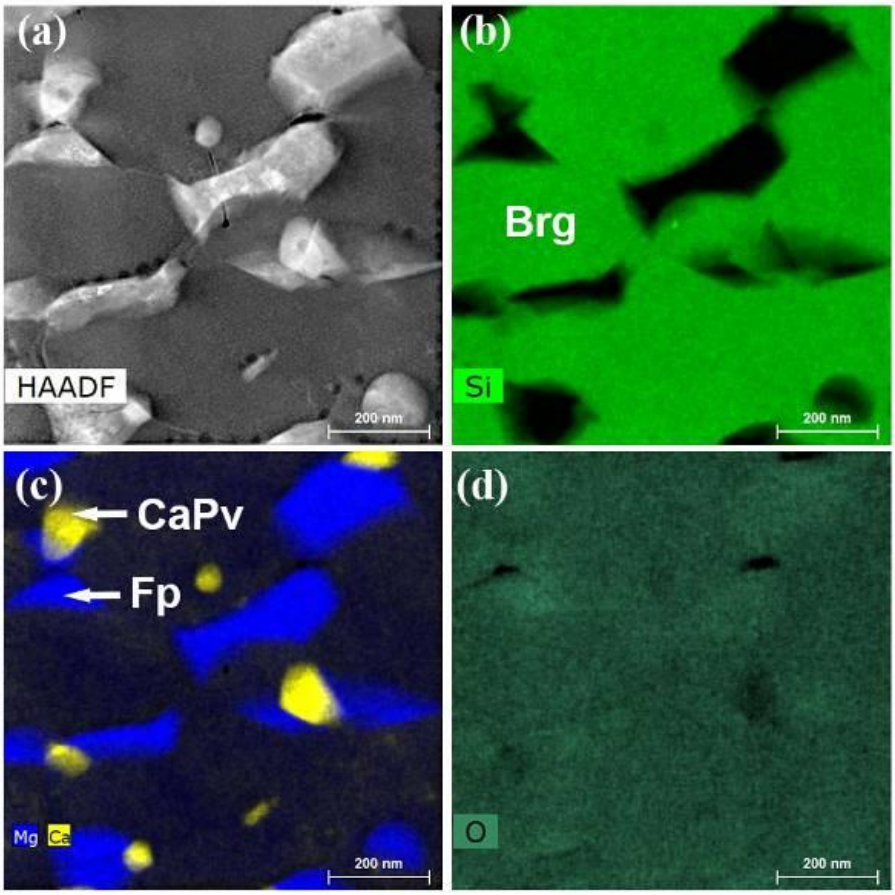
(a)
HAADF
200 nm
(b)
Brg
Si
200 nm
(c)
CaPv
Fp
Mg
Ca
200 nm
(d)
O
200 nm

Fig. 2

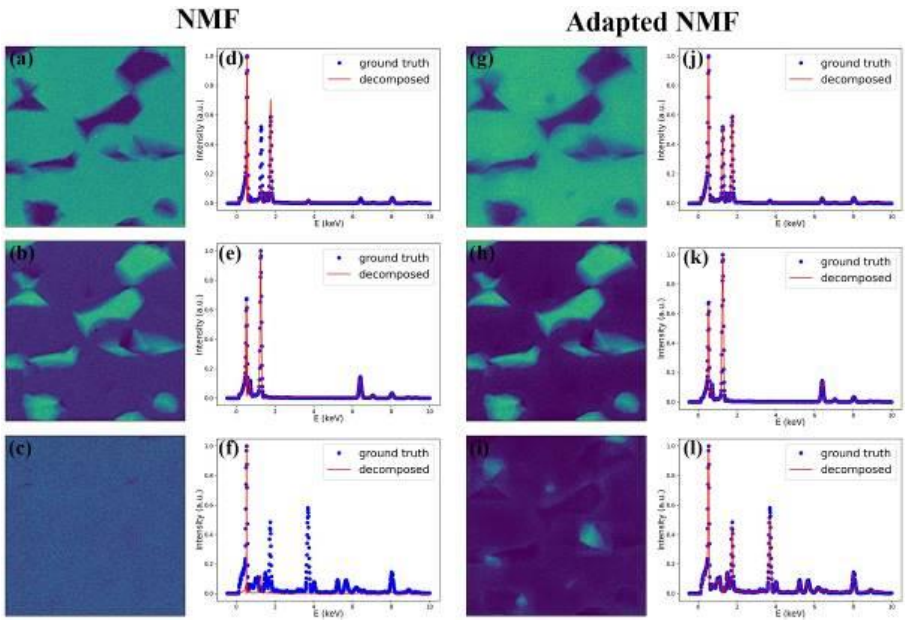
NMF
Adapted NMF
(a)
(b)
(c)
(d)
(e)
(f)
(g)
(h)
(i)
(j)
(k)
(l)
ground truth
decomposed
Intensity (a.u.)
E (keV)

IM3.001-invited

Hyperspectral visualization of picometric motion

K. MacDonald[1], T. Liu[1], J. Y. Ou[1], N. Zheludev[1,2]

[1]University of Southampton, Southampton, United Kingdom
[2]Nanyang Technological Uiversity, Singapore, Singapore

The motion of nanostructures can be measured with picometric resolution using scattering of free electrons at sharp edges of the structures.

Motion at the nano- to atomic scale is of growing technological importance and fundamental interest, in nano-electro-mechanical systems (NEMS), advanced materials (e.g. nanowires, 2D materials), mechanically reconfigurable photonic metamaterials; and in the study of systems governed by Van der Waals and Casimir forces, and quantum phenomena. However, there are no routinely available technologies for quantifying and spatially mapping fast, complex movements of picometric amplitude in nanostructures. We show how the spectrally resolved detection of scattering from a tightly-focused free-electron beam incident on the sharp edges of a nano-object can provide for quantitative 3D visualization of motion at the picoscale.

For a range of nano/microstructures, from simple cantilevers to photonic metamaterials and MEMS comb-drive actuators, we demonstrate measurements of thermal (cf. Brownian) motion amplitudes down to a noise-equivalent displacement level of 1 pm/Hz1/2, and the mapping of driven-motion oscillatory "mode shapes" with spatial (SEM imaging) resolution far beyond the diffraction limit applicable to optical vibrometry techniques.

We also report on the first observation of short-timescale "ballistic" thermal motion in the flexural mode of a nanomembrane cantilever, driven by thermal fluctuation of flexural phonon numbers in the membrane: over intervals <10 µs, the membrane is found to move ballistically, at an average constant velocity of ~300 µm/s, while Brownian-like dynamics emerge for longer observation times. Access to the ballistic regime provides verification of the equipartition theorem and Maxwell-Boltzmann statistics for flexural modes and presents opportunities in fast thermometry and mass sensing.

IM3.002

Simultaneous acquisition of real and reciprocal space information in transmission SEM

P. Denninger[1], P. Schweizer[2], E. Spiecker[1]

[1]Friedrich-Alexander-Universität Erlangen-Nürnberg, Institute of Micro- and Nanostructure Research (IMN), Erlangen, Germany
[2]EMPA, Thun, Switzerland

In the recent years, a variety of transmission diffraction setups entered the field of scanning electron microscopy (SEM) to prove the worthwhile implementation of diffraction analysis in combination with lower energetic electrons and the analytical capabilities of a SEM [1-3]. The broad accessibility and simpler setup facilitate such developments compared to the more complex transmission electron microscopy (TEM). Moreover, the large microscope chamber offers a straightforward implementation and enough space for unique in situ systems [4-5]. Even state-of-the-art direct electron detection cameras combined with the popular 4D-STEM technique are available for SEM´s with the benefits of reduced knock-on damage and increased contrast [2]. However, in relation to in situ experiments, where a continuous observation of the occurring phenomena is indispensable, these cameras are not suitable for such an experiment, even with the fastest acquisition rate.

Based on the limitations regarding parallel acquisition of real and reciprocal space information in situ, we introduce a unique setup in SEM, which solves the current restrictions. Figure 1a shows schematically the concept of our developed system, which is similar to our existing diffraction setup (LEND) [3]. The basis is a fluorescent screen positioned below the sample and an in-chamber mounted CMOS [WJ1] camera responsible for recording of the generated diffraction patterns on the screen. To enable the additional acquisition of the real space signal, a flexible STEM detector is installed below the fluorescent screen, which contains a concentric hole allowing the electrons to pass through and contribute to image formation. Figure 1b depicts the setup installed in our SEM. The combination of a simple integrating detector (STEM) with the parallel acquisition of the averaged diffraction patterns offers high frame rates linked to the corresponding reciprocal space information. In addition, all occurring signals in SEM can be collected.

Here, we investigate a thin MoS2 flake covered with gold nanoparticles as model system for acquiring the four simultaneously available signals in one run (Figure 2). The sample topography is depicted by secondary electrons (SE), where all small particles and surface contamination are visible. Back-scattered electrons (BSE) offer elemental contrast, which facilitates to distinguish between the gold particles and MoS2. The inner sample structure can be investigated by bright-field (BF) STEM and the acquired diffraction pattern reveal the present crystal structure of MoS2. Besides BF STEM imaging, the fluorescent screen, together with the STEM detector, can be moved to switch to dark-field (DF) imaging by selecting a suitable diffraction spot.

In the future, we are planning to perform dedicated heating experiments while acquiring real and reciprocal space information in situ. An upgrade of the current setup to an in situ chip-based heating stage will expand strongly the analytical potential of this concept. The real time monitoring of an ongoing process by STEM and diffraction signal will help to reveal appearing phenomena and mechanism in several material aspects [6].

[1] 10.1016/j.ultramic.2018.09.006

[2] 10.1016/j.ultramic.2020.113137

[3] 10.1016/j.ultramic.2020.112956

[4] 10.1017/S143192762100951X

[5] 10.1017/S1431927621003974

[6] The authors acknowledge funding by the German Research Foundation (DFG) via the Research Training Group GRK 1896

Fig. 1

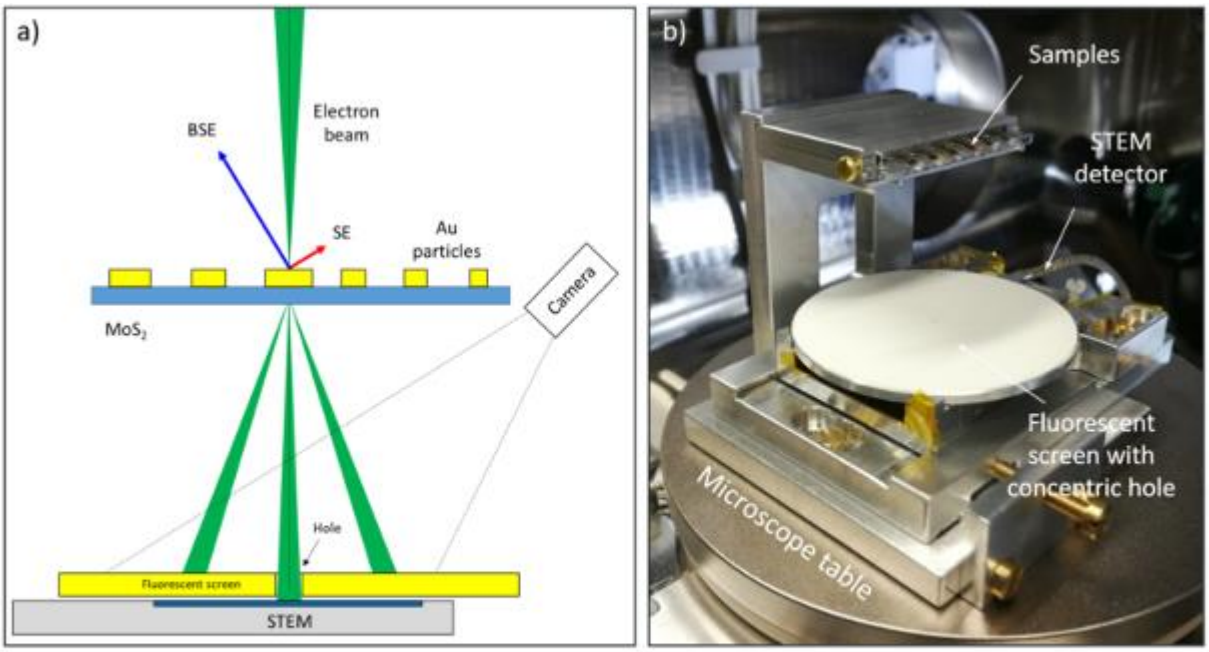

Figure 1: Parallel acquisition of STEM imaging and diffraction analysis. a) Schematic illustration of our developed setup. It combines a fluorescent screen and an independent STEM detector, which is installed underneath. The in-chamber mounted CMOS camera records all occurring (averaged) diffraction patterns. b) Installed setup in the SEM.

Fig. 2

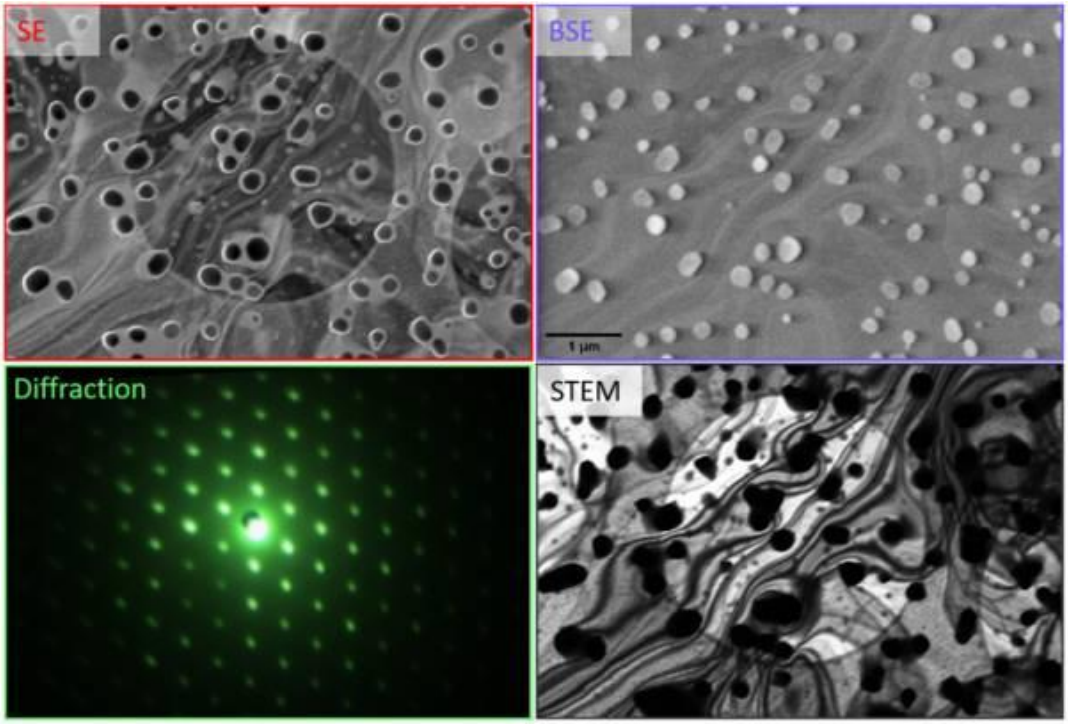

Figure 2: MoS_2 flake covered with gold nanoparticles. All presented images are acquired simultaneously. Topographic information is provided by SE (red), BSE (blue) offers elemental contrast, the averaged diffraction pattern (green) reveals the crystallographic structure and STEM (BF) exhibits the inner structure (dominated by mass-thickness and Bragg contrast).

IM3.003

Cryo focussed ion beam secondary ion mass spectrometry analysis of Galinstan

L. Berner[1], R. R. Schröder[1], I. Wacker[1]

[1]Bioquant, Heidelberg, Germany

Introduction

The combination of a focused ion beam and scanning electron microscope (FIB/SEM) with a time of flight secondary ion mass spectrometer (ToF-SIMS) [1] offers new possibilities for materials samples investigation. The combination of different information, such as highly sensitive 3D chemical mapping, in-situ sample preparation and high resolution imaging yield valuable insights into the samples. When adding cryo sample temperatures by using a cryo stage a number of experiments are possible for e.g. liquid metals, such as Galinstan, a Ga, In, Sn alloy.

Galinstan can be printed into 3D shapes at room temperature [2]. As it solidifies only at about -19°C [2], it is the general expectation that printed structures are stabilized by a thin galliumoxide layer, which forms around the alloy by passivation. As Galinstan is liquid at room temperature, it is generally difficult to investigate the oxide layer with conventional spectroscopic methods.

Objectives

In our study we want to detect the stabilizing oxide layer with ToF-SIMS facilitated by the Gallium ion beam in a FIB/SEM. To prevent material mixing within the liquid metal we solidified the printed Galinstan by cooling it down on a cryo stage. This allows also the study of the alloy demixing of Galinstan when cooled down, which can have an influence of Galinstan"s electrical properties at low temperatures.

Materials & Methods

Printed Galinstan lines are cooled down below the solidification temperature in-situ. Afterwards ToF-SIMS analyses of the sample surface can be conducted (Figure 1a). For the cross section analyses, the Galinstan is cut with the FIB and then tilted to an angle of 54° (Figure 1d). Either negative ions (GaO) or positive ions (Ga, In, Sn) can be detected by ToF-SIMS.

Results

We can visualize the enclosing galliumoxide layer in two different detection geometries: First, on the surface of the lines (Figure 1b,c) and second, along the line surface adjacent to a cross section (Figure 1e,f). As additional finding we see that the alloy separates into a Ga and In-Sn phase at temperatures lower than -25°C (Figure 2). However, we found a number of experimental sample and instrument parameters influencing the secondary ion signal, such as sample geometry, the presence of oxygen (matrix effect [3]) and the charging of the sample. Moreover, water freezing out on the sample surface during the cooling process can strongly influence the ion signal.

Conclusion

In our study we showed a first application of our cryo FIBSIMS instrumental combination yielding valuable results for the investigation of Galinstan. It was possible to visualize the galliumoxide layer and phase separation of the cooled down alloy. The secondary ion detection shows strong influence of the detection geometry and the investigated sample. In future, we want to expand this novel analysis tool to investigate fully printed, flexible electronics. This might yield valuable information for both the design of new devices and their quality control.

Acknowledgements: The author thanks Navid Hussain, Jasmin Aghassi-Hagmann, and Michael Hirtz (Karlsruher Institut für Technologie) for the samples. Research funded by DFG via the Excellence Cluster "3D Matter Made to Order" (EXC-2082/1-390761711)

[1] Pillatsch et al., Progr. Cryst. Growth Charact. Mater., 65(1):1–19, 2019

[2] Hussain et al., Adv. Mater. Technol., 29:2100650, 2021

[3] Priebe et al., J. Anal. Atom. Spectrom., 35(6):1156–1166, 2020

Fig. 1

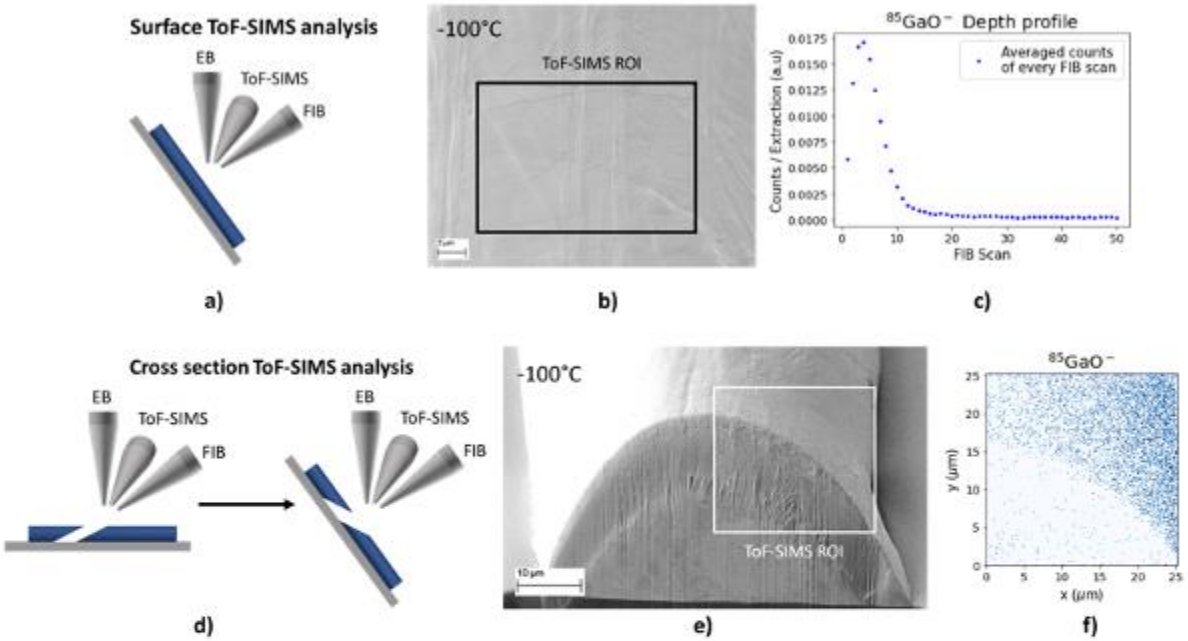

Figure 1: Visualization of the galliumoxide layer. a) Scheme of the sample orientation in the microscope. (EB: Electron beam). b) SEM image of the analysed region of interest. c) ToF-SIMS depth profile of $^{85}GaO^-$. At around 10 FIB Scans the $^{85}GaO^-$ signal has decreased vastly showing the boundary between the oxide layer and alloy. d) Developed two-step sample preparation for ToF-SIMS analyses of the cross section. e) SEM image of the analysed region (Adopted from [2]). f) As expected, the $^{85}GaO^-$ is detected on the surface of the line, but not on the cross section, showing the presence of the galliumoxide layer.

Fig. 2

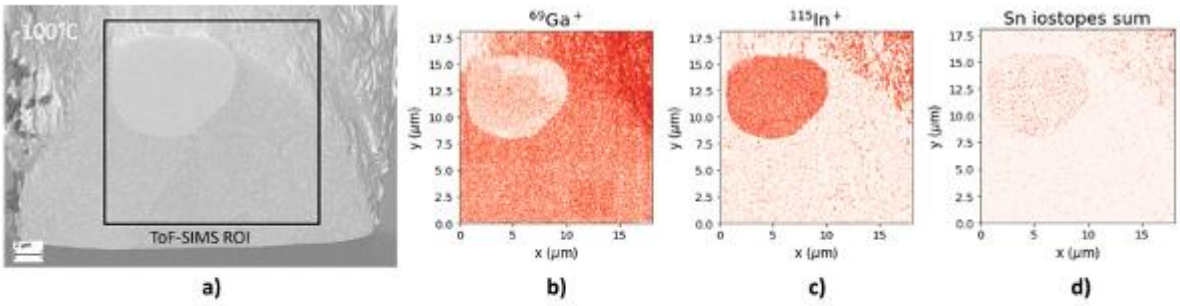

Figure 2: a) The SEM image of a cross section shows a separation of Galinstan in two material phases at low temperatures. b) – d) Performing a ToF-SIMS analysis reveals that the phases consist of Ga and In-Sn.

IM3.005

3D-reconstruction of hierarchical nanoporous structures using multi-modal deep learning models trained on synthetic multi-voltage FIB tomography data

T. Sardhara[1], R. C. Aydin[2], A. Shkurmanov[3], M. Ritter[3], C. J. Cyron[1,2]

[1]Hamburg University of Technology, Institute for Continuum and Material Mechanics, Hamburg, Germany
[2]Helmholtz-Zentrum Hereon, Institute of Material Systems Modeling, Geesthacht, Germany
[3]Hamburg University of Technology, Electron Microscopy Unit, Hamburg, Germany

3D reconstruction of hierarchical nanoporous structures requires high-resolution imaging data in the range of a few nanometers. Focused ion beam (FIB) tomography can be combined with a scanning electron microscope (SEM) to collect high-resolution images of nanostructures in the range of 1 nm in the SEM plane and 10 nm in the out-of-plane direction [1]. FIB tomography collects data layer-wise, where a FIB milling process follows each imaging process by an SEM. However, these consecutive series of cross-sectional images have artefacts, such as the "shine-through effect" [2]. Due to this effect, some structures become visible from posterior regions of the currently milled plane, and it is not straightforward to map pixel intensities with the material phase uniquely. Therefore, such images cannot be segmented accurately using conventional methods like thresholding or the k-means algorithm. Earlier, [3] presented a machine learning-based approach to reconstruct hierarchical nanoporous materials accurately. [3] also demonstrated a method to generate synthetic FIB-SEM images of any complex nanoporous structures to overcome the lack of training data. In this study, we present two ways to improve 3D reconstruction results. The first approach is to use a multi-modal machine learning method to take advantage of more information from the same region. In this case, we train a machine learning model using synthetic multi-voltage FIB tomography data generated by changing the accelerating voltage and simulating images of the same regions (Figure 1). Figure 2 shows pixel intensity profiles of images simulated using different accelerating voltages and the actual structure. The second approach is to make synthetic FIB-SEM data more similar to the real electron microscopy images using machine learning-based domain adaptation techniques. We show that using these approaches, our segmentation methods can suppress the "shine-through effect" and improve upon the methods presented in [3].

[1] Knott et al., Journal of Neuroscience, 28(12):2959–2964 (2008)

[2] Prill et al., J Microsc., 250(2):77-87 (2013)

[3] Sardhara et al., Frontiers in Materials, 9 2296-8016 (2022)

Fig. 1

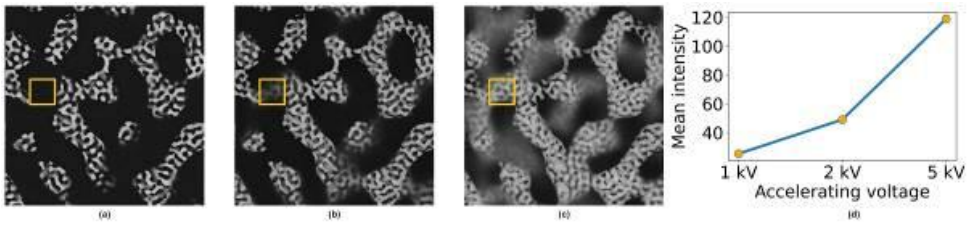

Figure 1: Simulated FIB tomography images of hierarchical nanoporous gold using voltage values (a) 1 kV, (b) 2 kV and (c) 5 kV, and (d) mean intensity values of the highlighted area

Fig. 2

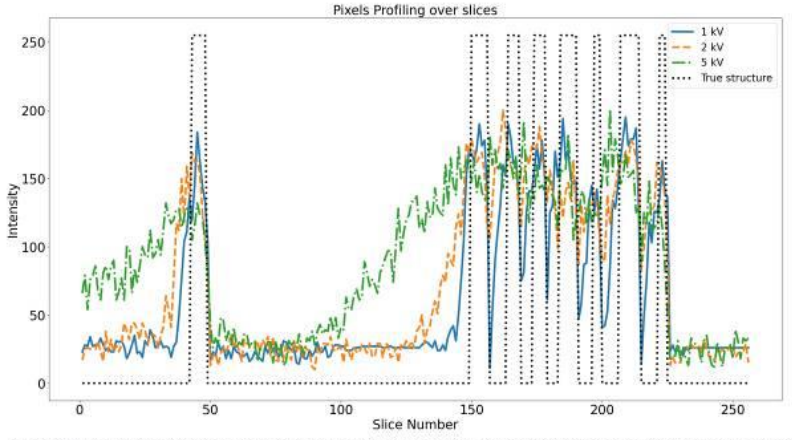

Figure 2: Intensities of a pixel located at a random location in the xy-plane of hnpg images simulated using accelerating voltages: 1 kV (blue), 2 kV (orange), 5 kV (green) and true structure (black)

IM3.006

FIB-notch: a novel method towards ultra-high throughput TEM sample preparation

R. Busch[1], G. Moldovan[2], G. Schusser[1], M. Krause[1], T. Höche[1]

[1]Fraunhofer Institute for Microstructure of Materials and Systems IMWS, Optical Materials and Technologies, Halle (Saale), Germany
[2]point electronic GmbH, Halle (Saale), Germany

Transmission electron microscopy (TEM) has become a routinely used technique in a wide range of industries. With an ever-increasing number of analyses performed, lowest time-to-sample is now a central demand on sample preparation. Here, conventional focused ion beam (FIB) preparation routines are facing a fundamental physical limitation: milling is either performed rapidly at high currents or accurately at very low currents [1]. The final thinning and polishing steps thus become a bottleneck for the whole process.

FIB-Notch is a novel, FIB-based preparation approach designed to overcome the dichotomy between accurate and fast milling. It employs a special sample geometry, where a notch is cut into a thick lamella [2]. Upon glancing-angle milling of the sample, enhanced erosion occurs at the elevated notch faces, leading to the formation of a receded, electron-transparent terrace region (Fig. 1). The key advantage of this patented technique is that spatial localization is governed by the notch geometry rather than the ion beam profile, making the erosion process essentially self-aligned. This allows for rapid thinning to be performed at high beam currents in a quasi-broad ion beam setting, speeding up the preparation process significantly (Fig. 2).

In order to control the final thickness of the lamella in the terrace region, the notch geometry needs to be matched to the initial thickness of the lamella. Accurate determination of this parameter is thus required, preferably performed in-situ. A quantitative thickness measurement technique based on electron beam absorbed current (EBAC) [3] was developed to for this purpose.

First experiments performed on a VION plasma FIB and a customized Zeiss Auriga 40 instrument will be presented, where electron-transparent samples could directly be created with nA-range ion beam currents. The physical principles governing the erosion of a notched lamella will be discussed, which were studied analytically and numerically using a two-dimensional, kinetic model of sputter erosion. Finally, an outlook on further potential applications of the technique to tasks such as sample sectioning will be given. Future work will focus on validation of the thickness determination method and automation of the preparation process.

Figure 1. Erosion of a notched lamella (schematic depiction).

Figure 2. SEM micrograph of a TEM lamella prepared with the FIB-Notch technique, using a Xe plasma FIB at 180 nA.

Financial support by the European Union via the Europäischer Fonds für Regionale Entwicklung (EFRE) and the Investitionsbank Sachsen-Anhalt (Germany) through the project FIBNotch under the grant number 2004/00071 is gratefully acknowledged.

[1] Bassim N, Scott K. and Giannuzzi LA, *MRS Bulletin* 39, 317-325 (2014)

[2] Busch R, Krause M, Coyle S, and Höche T, *Micron* 107, 35-42 (2018)

[3] Moldovan, G. *Microscopy and Microanalysis*, 25(S2), 532-533. (2019)

Fig. 1

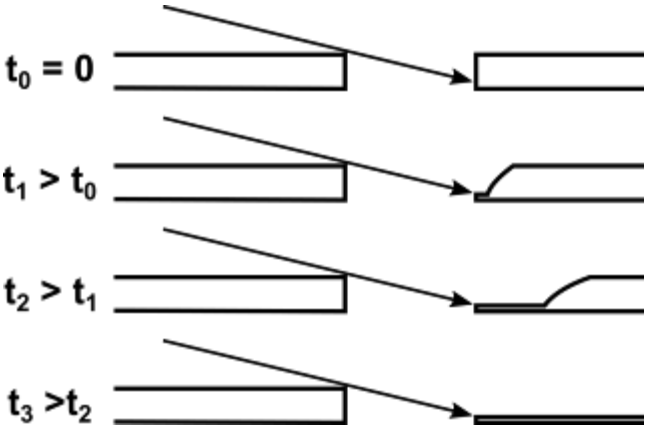

Fig. 2

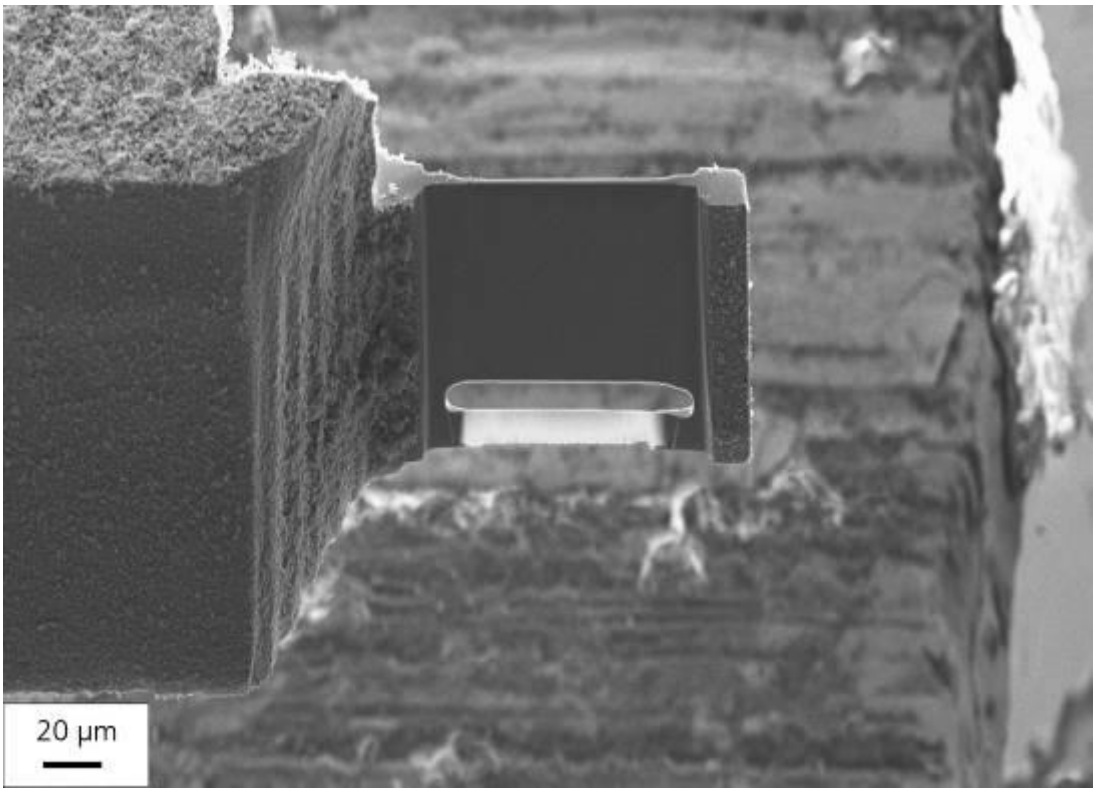

IM3.P001

Characterisation of a timepix detector for use in SEM acceleration voltage range

N. Denisov[1], D. Jannis[1], A. Orekhov[1], K. Müller-Caspary[2], J. Verbeeck[1]

[1]University of Antwerp, Physics, EMAT, Antwerp, Belgium
[2]Ludwig-Maximilians-University Munich, Chemistry and Pharmacy, Physical Chemistry, Munich, Germany

Introduction

Hybrid pixel direct electron detectors are getting more popular in electron microscopy due to their excellent properties. These cameras can be affordable which makes them ideal tools for experimentation especially in combination with an SEM setup. To support this, a full detector characterisation of an Advacam Minipix detector system in the 15-30keV range was made. At low beam currents, detector layer behaviour should be dominant, which could make the findings equally applicable to Medipix and TImepix3 sensors provided the same detector layer is used.

Objectives

Determine modulation transfer function (MTF) and detective quantum efficiency (DQE) of the Advacam Minipix detector for acceleration voltages of 15 – 30 keV and different detector thresholds.

Materials & methods

Advacam Minipix (TimePix) with 300 µm thick Si sensor 256x256 pixels of 55 µm size; Tescan Mira FEG SEM; 16 µm FIB aperture.

The MTF is obtained via Fourier transform of the Point Spread Function (PSF) acquired with single spot illumination [1], mechanically scanning over individual pixels with a 16 µm FIB fabricated mask mounted on a piezo stage.

The DQE is calculated from separate homogeneous illumination measurements of DQE(0) corrected with cluster size estimation [2], Noise Power Spectrum and MTF with same conditions [3].

Results

Fig.1 and Fig.2 represent MTF and DQE obtained for beam energies of 15 – 30 keV and detector threshold settings 5 – 25 keV. It is seen that the MTF is quite close to ideal. MTF gets further from ideal with an increase of HT at constant threshold. Higher thresholds improves MTF but at the cost of reducing the number of detected electrons and thus a worse DQE.

Figure 1. MTF of TimePix detector depending on Acceleration voltage (HT) and camera threshold.

Figure 2. DQE of TimePix detector depending on Acceleration voltage (HT) and camera threshold.

Conclusion

We provide a full MTF and DQE characterisation of an Advacam Minipix detector for beam energies in the SEM range. We observe a near ideal MTF with only minor effects from clustering. In this sense the detector is very close to its theoretical limit. The DQE on the other hand remains always under 65% which we speculate to be due to a combination of backscattering and absorption in the front metal contact that is deposited on the detector layer.

References

[1] Tore Niermann et al. "A new linear transfer theory and characterization method for image detectors. Part II: Experiment", https://doi.org/10.1016/j.ultramic.2012.01.011

[2] D. Jannis et al. "Event driven 4D STEM acquisition with a Timepix3 detector: Microsecond dwell time and faster scans for high precision and low dose applications" https://doi.org/10.1016/j.ultramic.2021.113423

[3] G.McMullan et al. "Detective quantum efficiency of electron area detectors in electron microscopy", https://doi.org/10.1016/j.ultramic.2009.04.002

[4] The authors acknowledge the financial support of the Research Foundation Flanders (FWO, Belgium) project SBO S000121N.

[5] The authors are grateful to Dr. Ivan Lobato for productive discussion of methods

Fig. 1

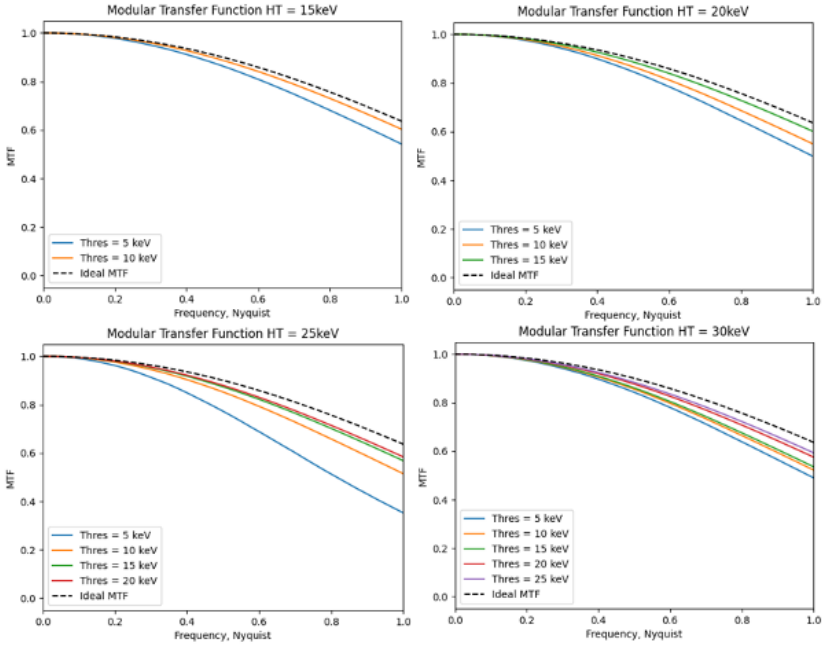

Fig. 2

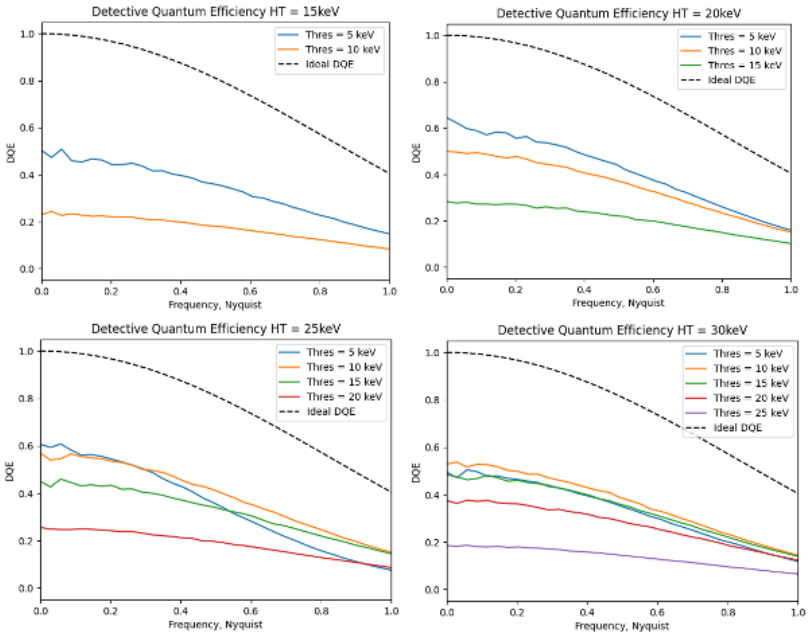

IM3.P002

A novel ion source for Lithium-ion microscopy and 3D tomography

T. Richter[1], J. Stodolka[1], L. Bruchhaus[1], A. Nadzeyka[1]

[1]Raith GmbH, Dortmund, Germany

Liquid Metal Alloy Ion Source (LMAIS) is an emerging Focused Ion Beam (FIB) source technology. It has been established for nanofabrication over the last years [1]. Most recently, ion imaging with Lithium ions from GaBiLi eutectic alloy has become feasible [2]. Multiple ion species such as Lithium and Bismuth are emitted simultaneously from a single source and are separated in a subsequent Wien filter. Different ion species, light or heavy and fast or slow, can be selected quickly without any mechanical sample or column adjustment [3].

Lithium is the lightest ion available from LMAIS. It features the smallest virtual source diameter and lowest energy spread [4]. Hence Lithium offers the smallest probe size of all ions emitted from eutectic alloys, resulting in sub 2nm image resolution

Besides Lithium, also Gallium and Bismuth ions as well as Bi clusters are available from the same source. Bismuth ions and in particular Bi clusters have an excellent depth resolution for sample delayering. The combination of Bi and provides outstanding ion beam imaging capabilities.

Switching between Li and Bi can be accomplished within a few seconds and enables access to different ion beams within the same FIB column. This setup allows stable imaging of 3D structures and sample reconstruction. With the FIB system presented (here), Ion beams are always perpendicular to the sample and no stage movement or sample tilt is needed resulting in a stable and reliable process for tomography and 3D sample reconstruction.

In this contribution we describe the working principle and capabilities of LMAIS with a focus on GaBiLi. Results of 2D Lithium-ion microscopy and workflows for stable 3D tomography by Bismuth milling and Li imaging will be presented.

Figure 1: Li ion image of Sn/C

Figure 2: Li ion image of graphite

Figure 3: Region of interest (RIO) for tomography. Box created by 80 Bi+ milling steps and in between Li+ ion imaging

Figure 4: 3D reconstruction of semiconductor chip Stack of Li images from RIO (Figures 3)

[1] J. Gierak et al, Journal of Vacuum Science & Technology B 36, 06J101 (2018)

[2] N. Klinger et al, Beilstein J. Nanotechnology, 11, 1742–1749 (2020)

[3] W. Pilz et al, Journal of Vacuum Science & Technology B 37, 021802 (2019)

[4] L. Bischoff et al, Appl. Phys. Rev. 3, 021101 (2016)

Fig. 1

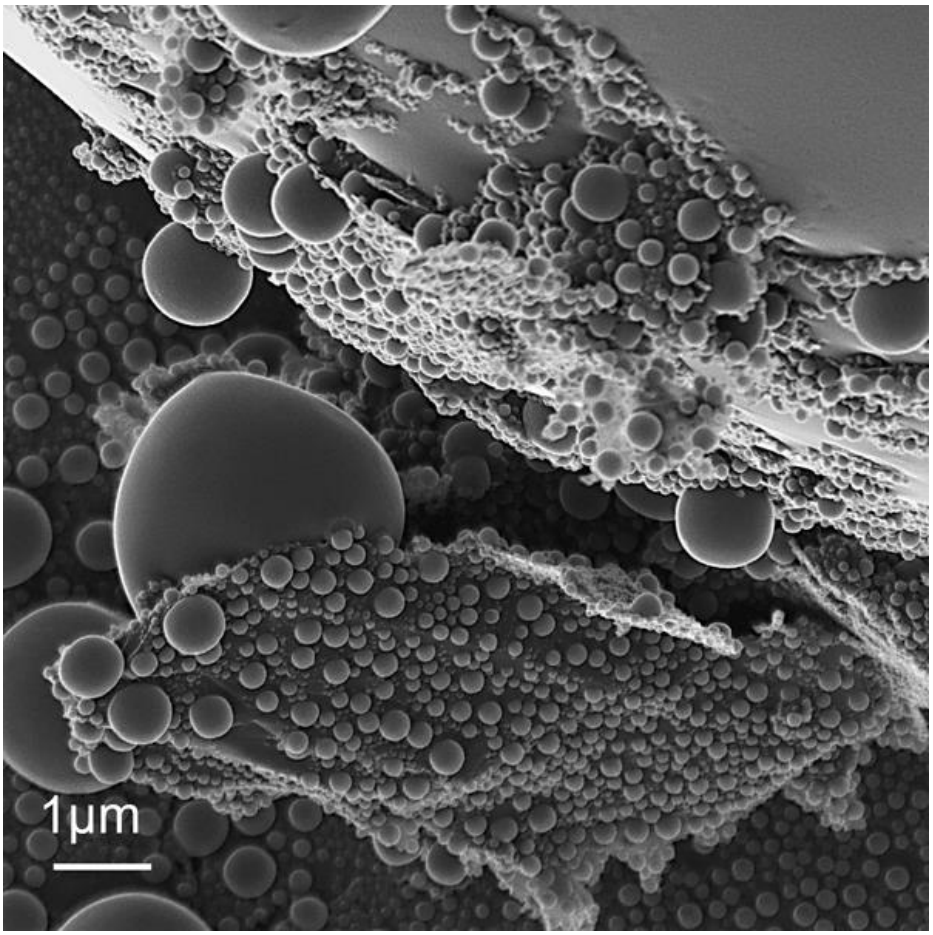

Fig. 2

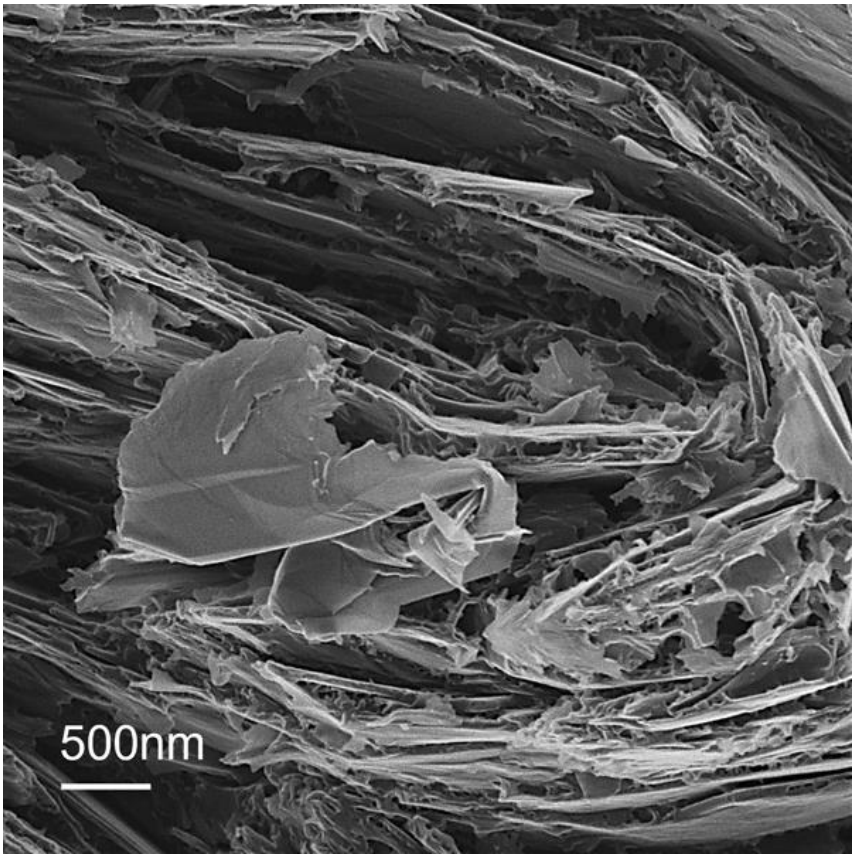

Fig. 3

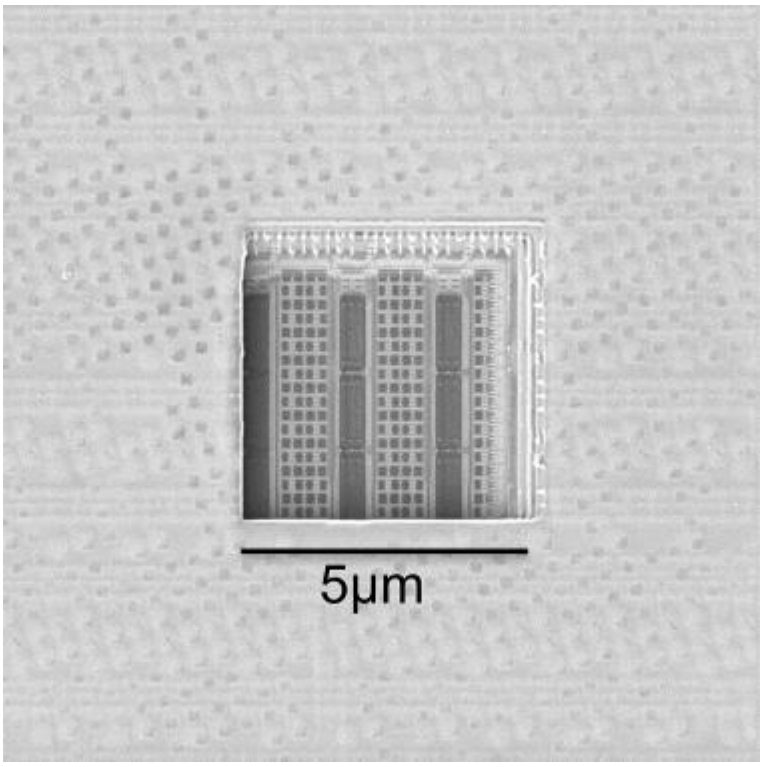

Fig. 4

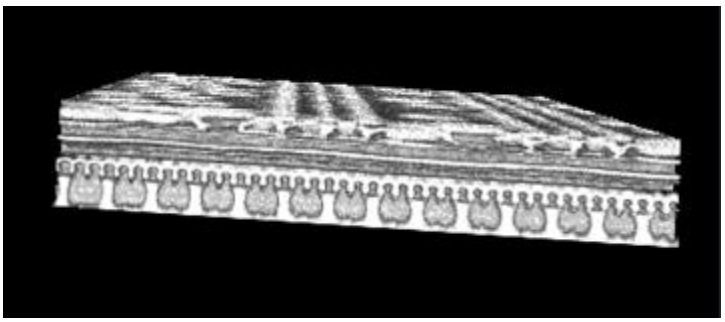

IM3.P003

Multi-voltage FIB-tomography of the hierarchical nanoporous gold

A. Shkurmanov[1], T. Sardhara[2], M. Ritter[1]

[1]TUHH, Electron Microscopy Unit (BEEM), Hamburg, Germany
[2]TUHH, Institute for continuum and Material Mechanics, Hamburg, Germany

Hierarchical nanoporous metals have attracted scientific interest due to their enhanced mechanical properties, e.g., strength and stiffness, in comparison to the continuous metals [1]. Hierarchical nanoporous gold (HNPG) represents a uniform network of nanoscale pores and solid metal ligaments with a size in a range of 15-110 nm.

FIB-tomography where a slice-by-slice FIB milling of the HNPG sample is followed by a subsequent imaging of the obtained block faces by using high-resolution SEM, allows to reconstruct the investigated HNPG volume with a high precission [2]. However, in order to do so, the impact of the so-called shine-through-effect should be considered during the reconstruction process [3]. This effect though, might not only seen as an artifact but contribute additional information of the ligaments" shapes and positions when simultaneously imaged different accelerating voltages. Thus, the images obtained at the higher voltage will contain more information from the depth of the sample while the low-voltage images would give the information about the shallow level as presented in Fig.1.

However, it is challenging to interpret this information accurately as there is no unique mapping between material and intensities. In such situations, more complex reconstruction methods such as machine learning-based segmentation methods over classical thresholding methods should be preferred [4]. Additionally, our multi-voltage images, together with a different machine learning method, can further improve segmentation performance and reconstruct the nanostructures more accurately.

Figure 1. SEM images of the HNPG structure obtained at 1kV (A), 2kV (B) and 4 kV(C) and the mean intensity of the specified area (red dashed square) as a function of the accelerating voltage (D).

[1] Shi et al., Science 371 1026 (2021)
[2] Winter et al., J Micros 233(3):372–383 (2009)
[3] Moroni, Thiele, Ultramicroscopy 219 113090 (2020)
[4] Sardhara et al., Frontiers in Materials 9 2296-8016 (2022)

Fig. 1

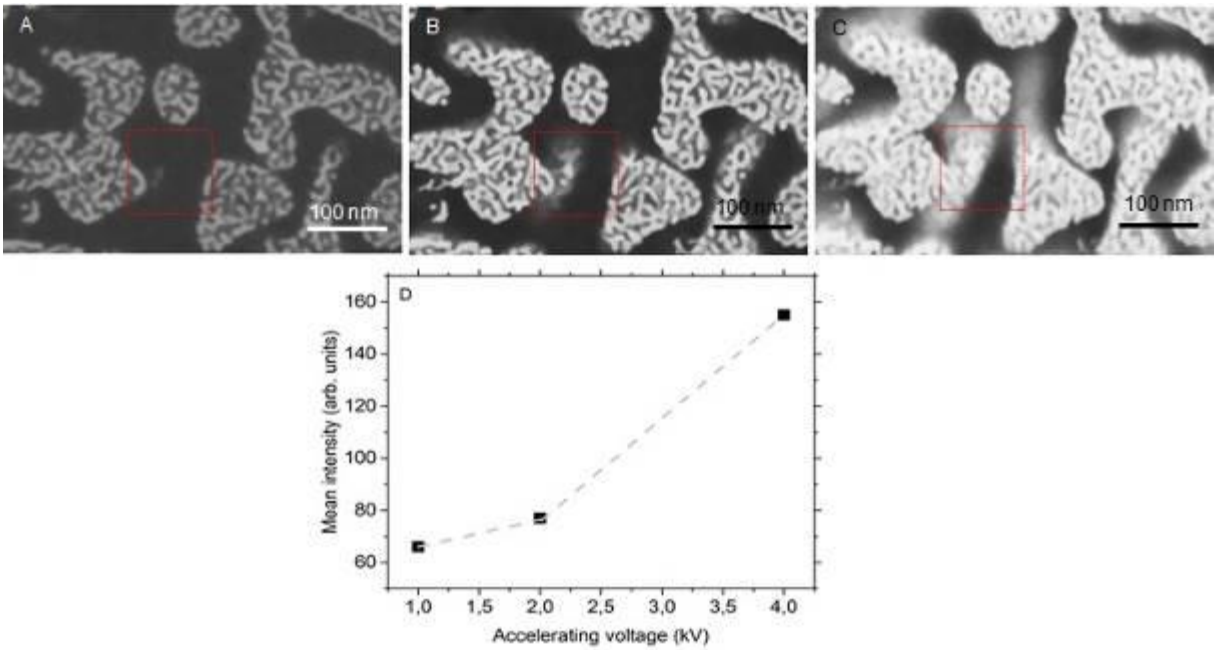

IM3.P004

Implementation of elastic and inelastic scattering processes for electrons with energies below 30 keV in Geant4 for the simulation of SEM

M. Hermann[1], D. Hüser[1], A. Meyer-Plath[2], T. Klein[1]

[1]Physikalisch-Technische Bundesanstalt, 5.24 Electron Microscopy, Braunschweig, Germany
[2]Bundesanstalt für Arbeitsschutz und Arbeitsmedizin, Unit 4.5 Particulate Hazardous Substances, Advanced Materials, Berlin, Germany

A Monte Carlo tool called Geant4SEM is presented for the simulation of secondary electron (SE) emission, back scattered electron (BSE) trajectories and transmission signal in a scanning electron microscope (SEM). The tool is based on the powerful open source platform Geant4 [1]. Although initially it was developed for high energy physics simulations, the toolkit is well suited for analyzing interactions of particles with matter in many areas and has been used for similar purposes before [2]. Within Geant4, physics models can easily be implemented and tested individually.

Thus far, four physics models have been implemented into the framework of Geant4. Mott cross-sections based on ELSEPA [3] have been used for the elastic scattering model. A dielectric function theory approach for cross sections of inelastic scattering and generation of SEs coming with JMONSEL [4] according to Shinotsuka et al. [5] has been adopted. Additionally, an inelastic scattering model for electron-phonon interaction based on Ganachaud and Mokrani [6] has been implemented as well as a model for boundary crossing of electrons. The detection of electrons can be set to occur right after exiting the sample or at a distance and can be filtered by electron properties such as kinetic energy and emission angle.

Aforementioned models have been validated against experimental results. Figure 1 shows a comparison of simulated SE yields of gold at multiple primary electron energies with other simulations and experimental results of Walker et. al. [7].
Fig 2 displays signal profiles of an SEM image of a nominally 100 nm high and a 250 nm wide silicon step on a silicon wafer at a beam energy of 1.3 keV and an equivalent simulation. To achieve a quantitative comparison between the two, the exponential decay of the SEM signal has been fit to the simulated data and to the over multiple lines averaged measured data from the left edge towards the center of the silicon step sample. The exponential factor of our simulation lies within the margin of error of the experimental data's fit.

It is demonstrated that Geant4SEM is capable of quantitative predictions of experimental SEM images. It deepens our understanding of the SEM imaging process and enables accurate measurements of nanosize structures such as semiconductor structures, fibers and particles of varying sizes, shapes and materials.

[1] S. Agostinelli et al., Nucl. Instrum. Methods Phys. Res. Sect. A 506, 250-303 (2003)

[2] E. Kieft, E. Bosch, J. Phys. D: Appl. Phys. 41, 215310 (2008)

[3] F. Salvat et al., omput. Phys. Commun. 165, 157-190 (2005)

[4] J. Villarubia et al., Ultramicroscopy 154, 15-28 (2015)

[5] Shinotsuka, Tanuma, Powell, Surf. Interface Anal. 51, 427-457 (2019)

[6] J.P. Ganachaud, A. Mokrani, Surface Science 334, 329-341 (1995)

[7] Walker et al. Scanning. 30. 365-80. (2008)

Fig. 1

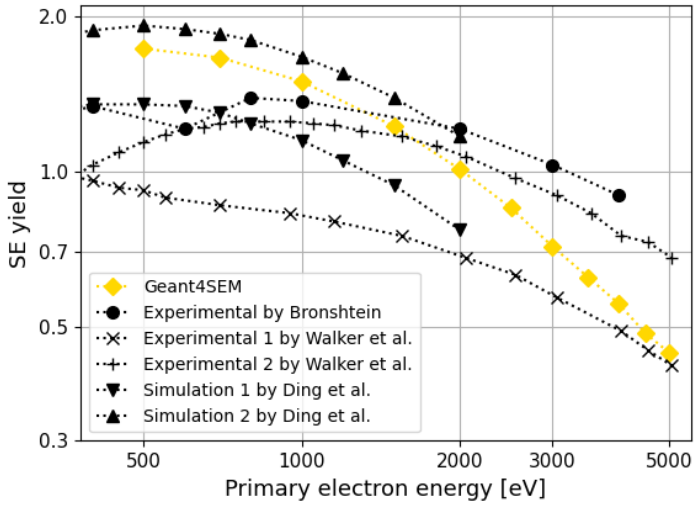

Fig 1. SE yields of gold at different primary electron energies. Experimental results 1 by Walker et al. used an as-inserted sample while the second one used a cleaned sample. Ding et al. simulation results 1 uses the method where the SEs are assumed to come from a distribution of electron energies in the valence band, while simulation 2 assumes SEs originate from the Fermi level.

Fig. 2

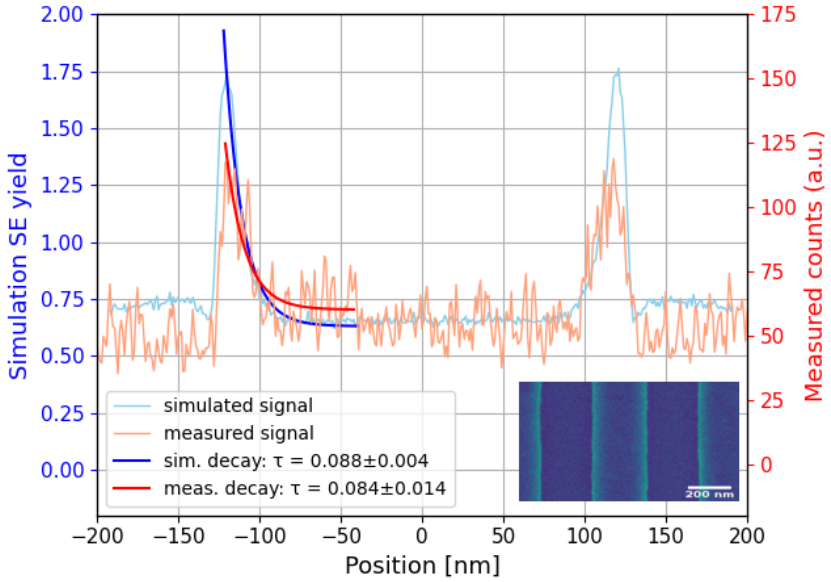

Fig 2. Averaged SEM signal of a nominally 250 nm wide and 100 nm high silicon step at low electron dose to avoid sample damage (red, right y-axes) and signal of an equivalent simulation (blue, left y-axis). The exponential decay of the signals from the left edge towards the center of the silicon step has been fit for quantitative comparison.

IM3.P005

Video frame interpolation neural network for FIB-SEM tomography

L. Gambini[1], C. Gabbett[1], L. Doolan[1], L. Jones[1], J. Coleman[1], S. Sanvito[1]

[1]Trinity College Dublin, Dublin, Ireland

Introduction

Focused-Ion-Beam Scanning-Electron-Microscope (FIB-SEM) tomography is a destructive imaging technique useful to investigate the 3D internal structure, and therefore the properties, of various materials composites. This technology is often employed for the study of nanomaterials, such as graphene nanosheet networks, whose mechanical and electrical properties are highly dependent on the material morphology. Through serial milling and imaging hundreds of network cross-sections, a high-fidelity 3D reconstruction of a nanostructured network can be produced and analysed [1].

The typical slice thickness is about 10-20 nm, while the resolution in the cross section is about 5 nm. It would be advisable to have the same resolution along the milling direction, this will result in a 3D reconstruction made of cubic voxels, which facilitate the studies of certain morphological properties. However, most imaging systems do not allow to produce thinner slices of the material and the process would be more expensive. In addition thinner slices have the disadvantage that the damage produced during one cut can propagate down to the next one.

Objectives

The solution proposed in this work [2] is to use a neural network developed for video frame interpolation, namely RIFE [3], to generate the missing slices between the collected images, and therefore obtain cubic voxels.

Materials and methods

The first application of the model was performed on a dataset made of graphene nanosheet networks, with pixel size of 5 nm and slice thickness of 17 nm.

Along with computer vision metrics, such as mean squared error (MSE) and structural similarity index (SSIM), the evaluation of the network porosity in each frame was used to quantitatively compare the results to the ground truth and a simple linear interpolation method.

Results

The results show that the proposed model successfully generates the missing frames and outperforms the linear interpolation method on the graphene dataset. The application was extended to datasets of materials of a different scale generated using various imaging techniques, such as micro CT scans and serial block face SEM.

Conclusion

This work demonstrates that the resolution along the cut direction of FIB-SEM data, or other imaging techniques, can be improved by employing a neural network developed for video frame interpolation. Thanks to this model, it is possible to obtain cubic voxels in the 3D reconstruction despite the acquisition of thick slices, which facilitates the imaging process.

[1] Gabbett, C. Electrical, Mechanical & Morphological Characterisation of Nanosheet Networks. Diss. Trinity College Dublin, 2021.

[2] Gambini, L., Gabbett, C., Coleman, J. N., Jones, L., Sanvito S. Video frame interpolation Neural Network for FIB-SEM tomography. In preparation.

[3] Huang Z., Zhang T., Heng W., Shi B., Zhou S. Real-time intermediate flow estimation for video frame interpolation. In: Proceedings of the European Conference on Computer Vision (ECCV), 2022.

IM3.P006

Traceable size measurement of polysterene particles with sizes up to 500 nm using STEM-in-SEM together with simulation-based image analysis

T. Klein[1], D. Hüser[1], D. Bergmann[1], A. Nowak[2], E. Buhr[1]

[1]Physikalisch-Technische Bundesanstalt (PTB), 5.24 Electron Microscopy, Braunschweig, Germany
[2]Physikalisch-Technische Bundesanstalt (PTB), 3.43 Aerosol and Particle Measurements, Braunschweig, Germany

Nano and micro particles possess size-dependent, desirable properties, but also pose risks to health and the environment. For this reason, exhaust emission standards such as Euro6 stipulate limits for the number of emitted particles, which are checked in exhaust emission tests (AU). Such official measurements must be traceable to SI units. Hence, a traceable sizing method for polysterene particles with sizes between 200 nm and 500 nm has been developed. For this purpose, an already existing procedure for smaller particles [1] has been adapted to the new task.

The experimental procedure has already been described in Ref. [1]. In short, the polysterene particles are deposited on a TEM grid and imaged by STEM-in-SEM (or TSEM), using the bright field detector, see Fig. 1. The traceability to the SI unit meter is ensured by means of a two-dimensional grating standard.

For size determination, the image pixels belonging to the particle must be separated from the background pixels. To achieve highly accurate measurements, the signal profiles are linearly interpolated and an individual threshold dependent on the particle size is used [1]. For relatively large polysterene particles, the threshold is located in the outer, non-linear section of the signal profile. Thus, a two-step approach has been chosen as depicted in Fig. 2: First, a preliminary value for the size is determined at a fixed threshold of 60%, which lies in the linear region of the signal profile. To obtain the final size, a tabulated value is added that has been determined by Monte Carlo simulations in advance.

The simulation of the image formation process is performed using Geant4SEM. For this purpose, we have added our own physics classes [2] for single scattering processes of electrons to the powerful open source Monte Carlo framework Geant4 [3]. The elastic scattering cross sections have been calculated using ELSEPA [4] with muffin-tin radii. For the inelastic scattering cross sections**,** we have implemented a phenomenological model approximating the dielectric function.

We measured polysterene particles with three different nominal sizes: 200 nm (PSL200), 300 nm (PSL300), and 500 nm (PSL500). Table 1 lists our results in comparison to the reference values of two international intercomparisons [5, 6] and the manufacturer's data sheet for PSL500, respectively. In all three cases, a very good agreement is shown. In addition, preliminary studies reveal that the uncertainty of our measurements is generally smaller than the pixel size.

References

[1] T. Klein et al., Meas. Sci. Technol. **22**, 094002 (2011)
[2] See also the MC2023 contribution of Martin Hermann et al.
[3] J. Allison et al., Nucl. Instrum. Methods Phys. Res. **835**, 186 (2016)
[4] F. Salvat et al., Comput. Phys. Commun. **261**, 107704 (2021)
[5] F. Meli et al., Meas. Sci. Technol. **23**, 125005 (2012)
[6] H.-L. Lin et al., Metrologia **56**, 04004 (2019)

Fig. 1

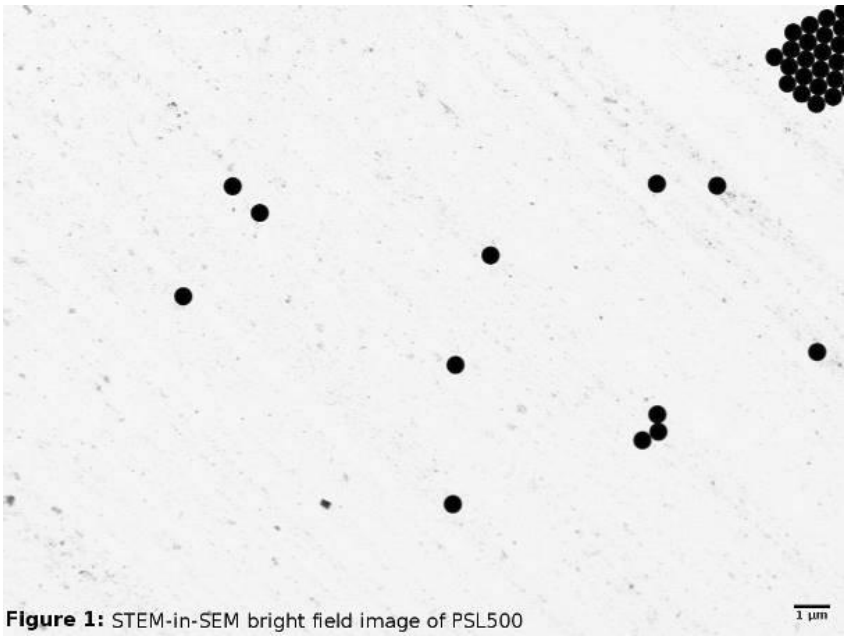

Figure 1: STEM-in-SEM bright field image of PSL500

Fig. 2

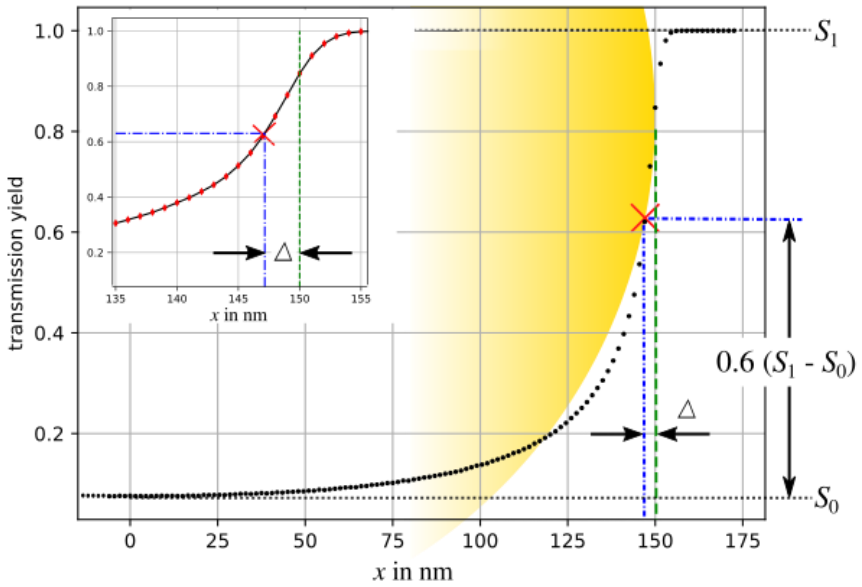

Figure 2: The preliminary particle size at 60% signal level is adjusted by 2Δ to obtain the final size.

Fig. 3

	d in nm	d_ref in nm	U_ref in nm
PSL200	197.0	197.68	4.54
PSL300	306.9	305.73	1.18
PSL500	511.7	510	7

Table 1: Measured particle size d together with reference value d_ref and its expanded uncertainty U_ref.

IM3.P007

JEOL`s JSM-IT800 series: high performance SEM for all users

T. Harzer[1]

[1]JEOL (Germany) GmbH, Freising, Germany

Looking for a modern, high-resolution SEM allrounder that fits to your individual needs? JEOL"s popular FE-SEM JSM-IT800 will serve you for fast and crisp high-resolution image acquisition, high throughput while maintaining maximum ease of use. The microscope now comes in 3 "flavors" in form of 3 objective lenses "HL" "SHL" and the new "i" – a model line-up, exactly designed for your individual purposes.

Understand how tailored lens-technologies will enhance your results and how easy and automated it is to operate JEOL"s flagship SEM featuring the fully integrated JEOL EDS system.

IM3.P008

Advanced focused ion beam milling techniques for TEM specimen preparation of solid bulk samples

L. Kibkalo[1], M. Kruth[1], L. Risters[1]

[1]Ernst Ruska-Centre for Microscopy and spectroscopy with Electrons, Forschungszentrum Jülich GmbH, Germany, Jülich, Germany

Introduction:

In contrast to time-consuming conventional TEM-specimen preparation methods, the focused ion beam (FIB) sputtering in a dual beam SEM system allows to produce high-quality specimens for various TEM studies automatically and quickly. Different TEM based techniques require specific considerations during the specimen preparation.

Objectives:

In this work, we discuss three special FIB preparation methods: cutting of the electron beam shaping device from a bulk sample, preparation of the Ga ion beam sensitive nanotube cross-section and transport of the SiN-Membrane with magnetic structure on the surface.

Materials and methods:

For the preparation of specimens, we used focused Ga ion beams in FEI Helios dual-beam scanning electron microscopes.

Results:

Figure 1 shows the beam-shaping device for off-axis measurement of the phase shift around the vertical current. The U-shape cross-section TEM lamella of a Ga ion beam sensitive nanotube can be seen in the figure 2. Figure 3 illustrates the cross-section TEM lamella of the magnetic structure on the surface of a SiN membrane.

Focused Ga ion beam sputtering is used to prepare high quality electron transparent specimens for different TEM experiments as well as to prepare some non-conventional specimens considering desired geometry, topology and material beam sensitivity.

Fig. 1

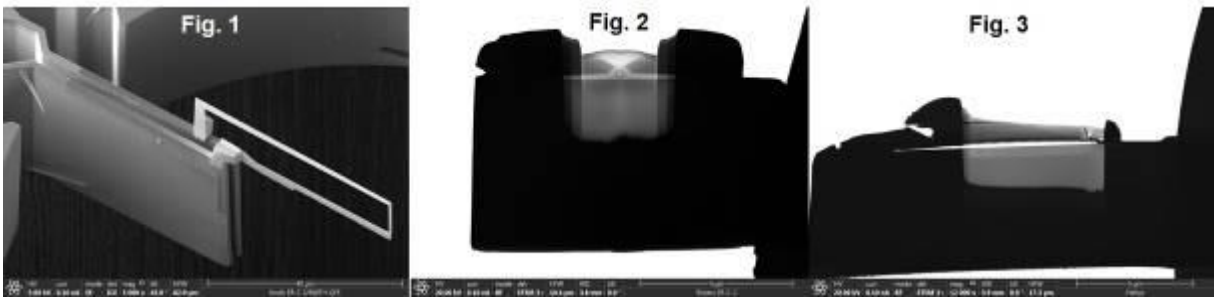

IM3.P009

TEM sample preparation with high-energy Xenon ions and focused low-energy Argon by plasma FIB

D. Phifer[1]

[1]Thermo Fisher Scientific, Eindhoven, Netherlands

Optimizing ion species for specific (S)TEM sample preparation tasks is not only becoming common with multi-ion species plasma FIB, but rather, essential as our understanding from experience and simulation data grows. Xenon ions provide a high sputter yield and are excellent for large 3D-volume-data-acquisition and correlated microscopy applications. Reactive oxygen ion beam processing has proven to dramatically improve milling quality for carbon-carbon bonding materials by smoothing the cut-face very effectively during sputtering. In this presentation, recent progress of low-energy-focused-argon ion beam cleaning is explored from trials with a Helios 5 Hydra Plasma FIB for TEM specimen preparation. Argon ion beam can be used down to 500 eV for specimen preparation, which is producing lower damage in finished samples.

Ions species selection is critical for near "damage-free" TEM specimen preparation. Xenon plasma FIB first opened an opportunity for "gallium-free" TEM specimen preparation and had a benefit of lower amorphous layer thickness than gallium. However, Xenon ions induce higher vacancy-density in target materials. With conventional gallium FIB, there is a challenge to reduce or eliminate gallium in TEM specimen. Unfortunately, gallium implantation commonly leads to reactions and migration with many materials (e.g., steel, aluminum alloy, GaN/AlGN etc).

Experimentation with the Helios Hydra for making (S)TEM samples has confirmed that the focused argon ion beam is suitable for near damage-free TEM specimen preparation guided by the investigation of ion-solid interaction SRIM data [1]. With Plasma FIB argon ion energy at 500 eV, it is becoming routine to produce near "damage-free" TEM specimens of these reactive materials which opens new opportunities for better material structure-property-function investigation.

[1] C. Jiao, J. Graham, Xu Xu, T. Burnett, and B. van Leer. Low Energy 500 eV Focused Argon Ion Beam Provided by Multi-Ions Species Plasma FIB for Material Science Sample Preparations. Microsc.Microanal. 27 (Spupl 1). 2021

IM3.P010

Using machine learning and topographic SEM imaging for software assisted fractography

M. Hemmleb[1], D. Bettge[2], L. Schmies[2], U. Sonntag[3], B. Botsch[3]

[1]point electronic GmbH, Halle (Saale), Germany
[2]BAM, Berlin, Germany
[3]GFaI, Berlin, Germany

The aim of a fractographic investigation is the evaluation of macroscopic and microscopic fracture surface characteristics and, as a result, the determination of the fracture mechanism of a component from a failure case. The basis for such evaluations of fracture characteristics comes from actual comparative mechanical testing and from the literature. A fractographic analysis can be very complex and, in any case, requires considerable experience.

In the IGF project "iFrakto", software is being developed that quantitatively determines fracture characteristics and fracture mechanisms utilizing digitized expert knowledge, machine learning, and standard 2D and topographical data from SEM imaging. Topographical data are obtained from 4QBSE detector using shape-from-shading technology (Fig. 1). The developed software tool provides knowledge-based suggestions for the evaluation of fracture surfaces (Fig. 2). As a basis for this, round robins were carried out among fractographers to create a knowledge base, to query the practice-relevant requirements for such tools and to carry out first practical tests.

The approach described can be used with all scanning electron microscopes. The results presented here were generated with a Tescan Vega3 and the BSE detector based topography measurement system DISS6 from point electronic GmbH. The investigations were mainly carried out on various metallic fracture surfaces.

The results show that the use of machine learning software together with SEM image and topography data makes an important contribution to the quantification of fracture surfaces and effectively supports the operator in the interpretation of fracture surfaces.

Fig. 1

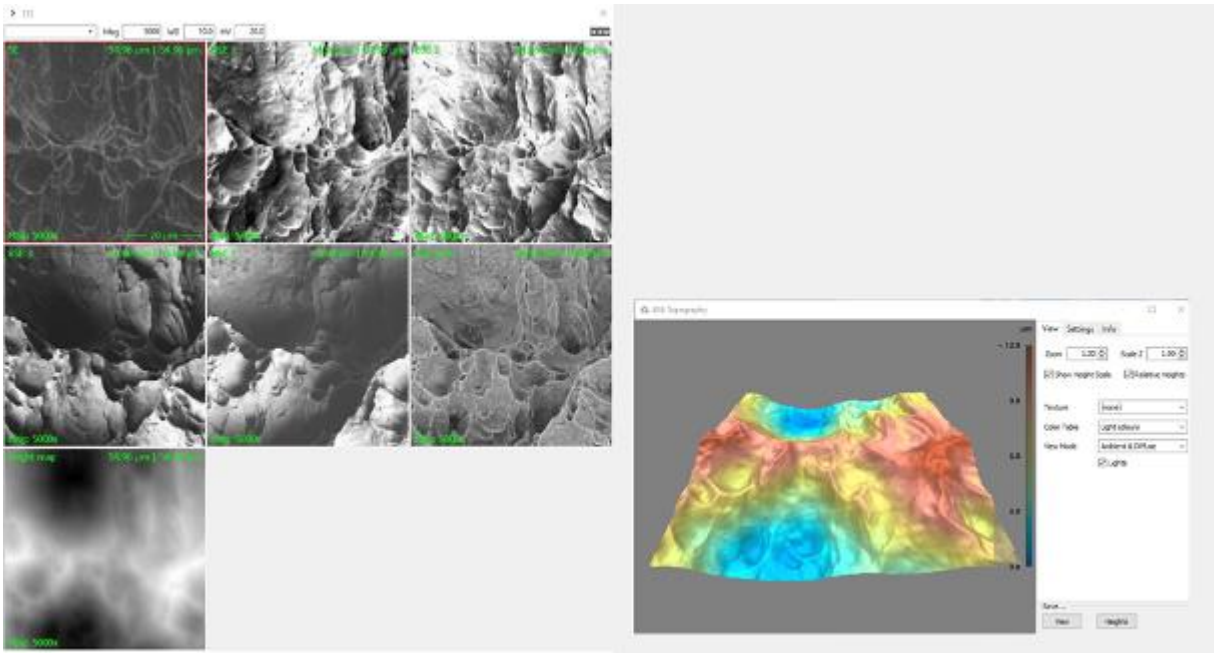

Fig. 2

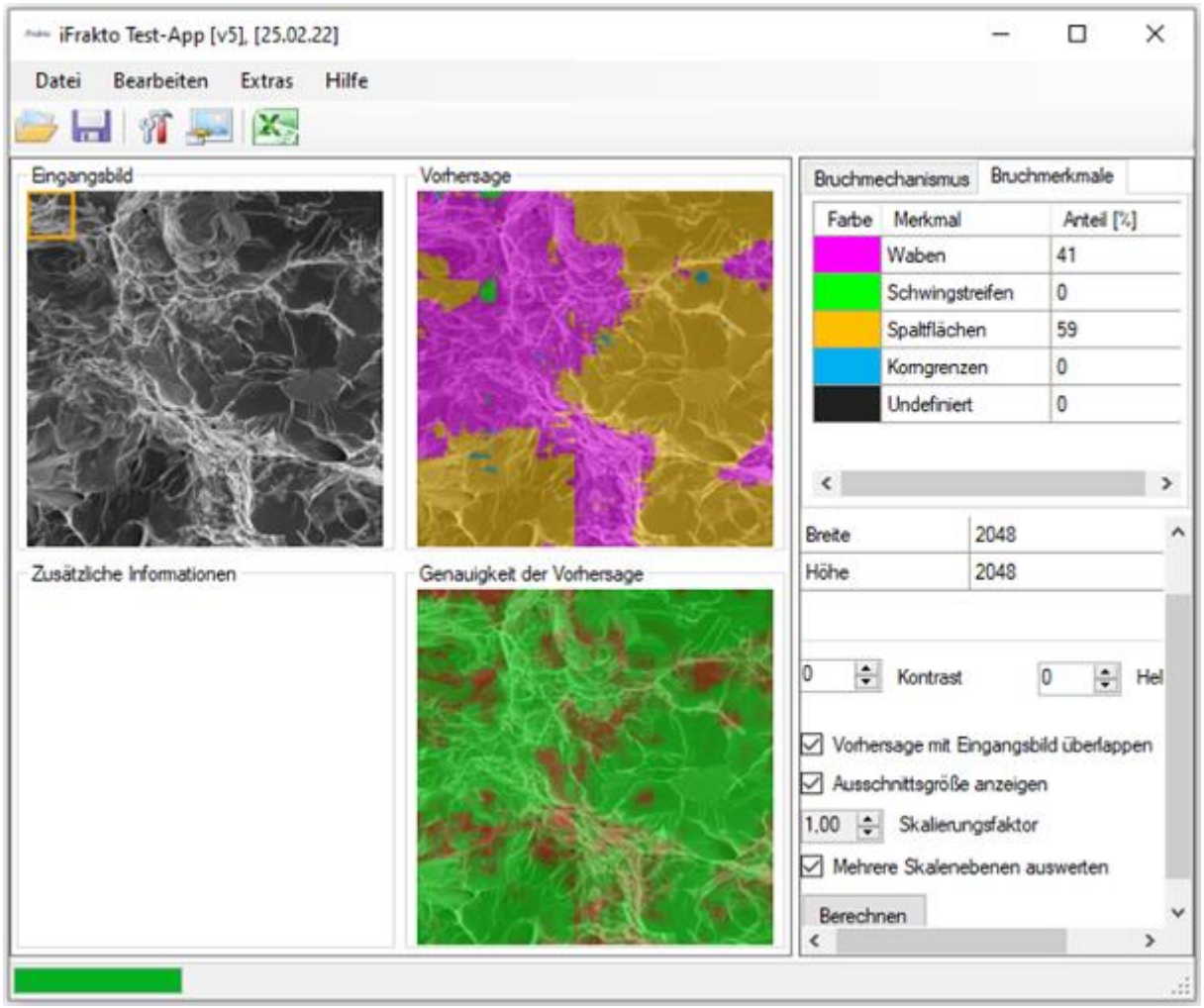
iFrakto Test-App [v5], [25.02.22]
Datei
Bearbeiten
Extras
Hilfe
Eingangsbild
Vorhersage
Zusätzliche Informationen
Genauigkeit der Vorhersage
Bruchmechanismus
Bruchmerkmale
Farbe
Merkmal
Anteil [%]
Waben
41
Schwingstreifen
0
Spaltflächen
59
Korngrenzen
0
Undefiniert
0
Breite
2048
Höhe
2048
Kontrast
Vorhersage mit Eingangsbild überlappen
Ausschnittsgröße anzeigen
1.00
Skalierungsfaktor
Mehrere Skalenebenen auswerten
Berechnen

IM4.001-invited

Cryo-STEM tomography – a powerful technique

M. Elbaum[1]

[1]Weizmann Institute of Science, Dept of Chemical and Biological Physics, Rehovot, Israel

For many years, life science cryo-EM has been practically synonymous with wide-field imaging in transmission. This modality has been famously successful in determination of macromolecular structure at near-atomic resolution, based on the combination of phase contrast generated by defocus with image averaging. The same wide-field TEM approach was further employed for pioneering works in 3D imaging of cells by tomography. An alternative modality is STEM, scanning transmission EM. STEM uses a focused probe and a variety of detectors to collect one or more signals pixel by pixel. Its popularity in the materials sciences has not yet been matched in cryo-EM for biological materials, due mainly to the impression that STEM is incompatible with beam-sensitive specimens. To the contrary, STEM may be more dose-efficient than TEM. A case in point is tomography of thick samples, where the energy filter required for conventional TEM can be avoided. 4D STEM and multi-segment detectors can collect every electron, but the means to combine the information they contribute are still under development. These include angle-resolved STEM, ptychography, and differential phase contrast in various configurations. The power of the scanning probe methods lies in their flexibility, and the fact that multiple image contrast modes may be generated in a single scan. The talk will describe progress and prospects for cryo-STEM in life science applications with an emphasis on cellular cryo-tomography.

IM4.002-invited

Microsecond time-resolved cryo-electron microscopy

U. Lorenz[1]

[1]EPFL, Lausanne, Switzerland

While cryo-electron microscopy (cryo-EM) is rapidly becoming the dominant method in structural biology, its time resolution is currently insufficient to directly observe proteins in action, leaving our understanding of these nanoscale machines fundamentally incomplete. Here, we demonstrate a novel approach to time-resolved cryo-EM that affords microsecond time resolution. Our method is illustrated in Fig. 1. It involves melting a cryo sample with a laser beam (a), which allows dynamics of the embedded particles to occur in liquid once a suitable stimulus is provided, for example by releasing a caged compound (b). While the dynamics occur, the heating laser is switched off at a well-defined point in time (c), causing the sample to rapidly recool, so that it vitrifies, and the particles are trapped in their transient configurations (d), in which they can subsequently be imaged (e). We demonstrate that our approach affords a time resolution of 5 µs or better. Moreover, near-atomic resolution reconstructions can be obtained from revitrified samples, showing that the revitrification process does not damage the protein structure. Finally, we present a microsecond time-resolved pH jump experiment, in which we observe the dynamics of the capsid of CCMV, an icosahedral plant virus. These results highlight the potential of our method to fundamentally advance our understanding of protein function through direct observation.

Figure 1. Experimental concept for microsecond time-resolved cryo-EM.

Fig. 1

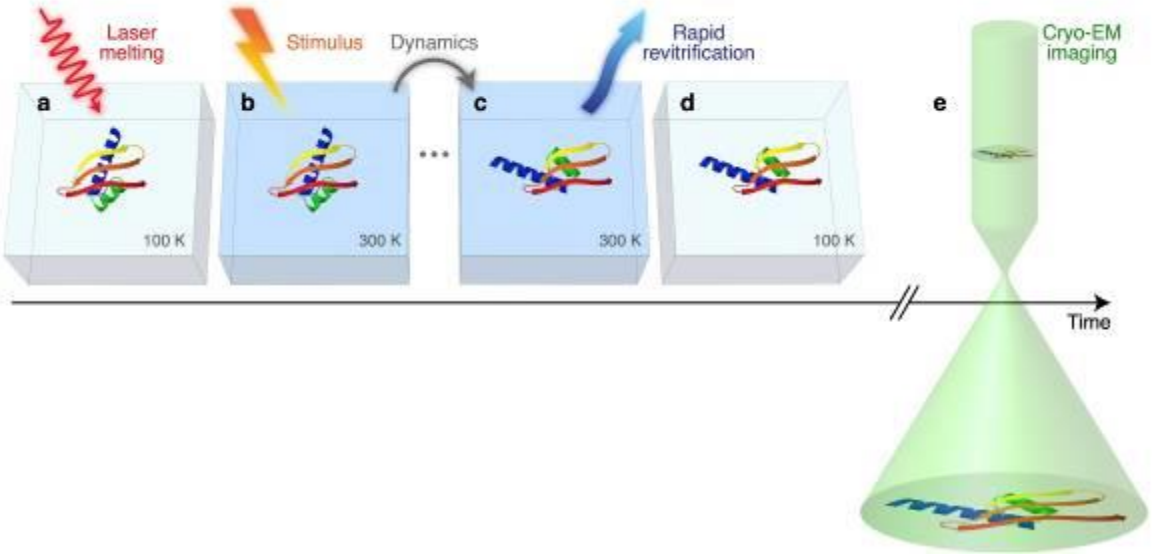

IM4.003

Towards multimodal *in situ* cryo-FIB-SIMS imaging in biological systems

T. Taubitz[1], A. Biesemeier[1], O. De Castro[1], J. N. Audinot[1], T. Wirtz[1]

[1]Luxembourg Institute of Science and Technology (LIST), Materials Research and Technology department, Belvaux, Luxembourg

Introduction: One of the struggles of correlative multimodal imaging in biological systems is the necessity for utilizing several analytical instruments to permit high-resolution and high-sensitivity morphological and chemical analyses. This induces time-consuming sample transfers and subsequent data processing and correlation. For cryo-investigations, not only is there a limited availability of cryo-compatible instruments, but there is the additional concern of contaminating or even damaging the frozen-hydrated sample during sample-transfer due to ambient temperature and humidity.

Our group specializes in incorporating several complimentary techniques into one individual instrument to streamline such correlative analytical workflows, all the while focusing on the vital key characteristics, i.e. high spatial resolution, chemical sensitivity, dynamic range (for the detection and mapping of atoms and small clusters with concentrations varying over several orders of magnitude) and isotopic selectivity.

Objectives: We present a novel instrument devised for multimodal *in situ* imaging and chemical analysis of biological samples in a close to native cryogenic state.

Materials & Methods: Previously, we described the in-house developed npSCOPE instrument [1], based on a Gas Field Ion Source using finely focused Helium and Neon ion beams and capable of performing: a) Secondary Electron (SE) imaging (providing morphological and topographical information; lateral resolution: < 1 nm); b) Scanning Transmission Ion Microscopy (STIM, providing bright and dark field imaging; lateral resolution: < 6 nm); and c) Secondary Ion Mass Spectrometry (SIMS, employing a compact high-performance double-focussing magnetic sector mass spectrometer equipped with a continuous focal plane detector, allowing a full mass spectrum to be recorded for each single pixel; lateral resolution: < 15 nm).

Here, we describe new developments that allow the investigation of frozen-hydrated biological samples at temperatures < -140° C close to their native state on the npSCOPE under high vacuum conditions. To achieve this, we equipped the instrument with a custom-built cryogenic sample stage, and we developed a customized cryo-sample transfer system structured around a prototype cryogenic-glovebox, ensuring optimal environmental conditions during sample handling.

Results: We present proof-of-principle results comparing data obtained on various chemically fixed room temperature (RT)-compatible samples which were investigated both at RT and at < -140° C that show that all three imaging modes function artefact-free at cryogenic temperatures, as well as early results obtained from frozen-hydrated samples.

Conclusion: The here presented cryo-workflow on the npSCOPE will allow the chemical analysis of biological samples from various fields of research under close to native conditions.

Funding: This project has received funding from the European Union's Horizon 2020 Research and Innovation Programme under grant agreement No. 720964 and by the Luxembourg National Research Fund via the project INTER/DFG/19/13992454.

References:

[1] O. De Castro *et al.*, "npSCOPE: A New Multimodal Instrument for In Situ Correlative Analysis of Nanoparticles," *Anal. Chem.*, vol. 93, no. 43, pp. 14417–14424, Nov. 2021, doi: 10.1021/acs.analchem.1c02337.

IM4.004

Mechanisms for radiation damage in biological specimens revealed by vibrational EELS

B. Haas[1], K. March[2], O. Krivanek[1,3,4], C. T. Koch[1], Z. Kochovski[5], P. Rez[3]

[1]Humboldt-Universität zu Berlin, Department of Physics and IRIS Adlershof, Berlin, Germany
[2]Sorbonne Université, Institut de Minéralogie, de Physique des Matériaux et de Cosmochimie, Paris, France
[3]Arizona State University, Department of Physics, Tempe, AZ, United States
[4]Nion Company, R&D, Kirkland, WA, United States
[5]Helmholtz-Zentrum Berlin für Materialien und Energie, Department for Electrochemical Energy Storage, Berlin, Germany

INTRODUCTION

Radiation damage fundamentally limits the attainable spatial resolution in the electron microscopy of biological specimens. To determine protein structures with the resolution needed to understand biological function it is necessary to average over multiple copies of a molecule of interest. The need for averaging limits studies of how macromolecules interact e.g. in an organelle. Traditionally, the effects of radiation damage have been assessed by measuring spot fading in crystals [1], or by monitoring mass loss from EELS spectra [2].

OBJECTIVES

It is highly desirable to understand the mechanisms of radiation damage, which bonds are breaking, and when they can reform. Recent developments make it possible to record vibrational spectra in the electron microscope - equivalent to IR but at the nanometer scale. We acquired data on guanine and vitreous ice to quantitatively measure the structural changes through the vibrational signal from different chemical bonds as a function of electron exposure.

MATERIALS & METHODS

We used a Nion HERMES microscope at 60kV with Dectris ELA direct detector attached to the IRIS spectrometer. We used guanine fish scales [3] and vitreous ice from plunge freezing. Spectrum images were recorded by repeatedly scanning a defocused probe over an area (typically 100x100 nm²). The spectra from each map were aligned and summed, yielding average spectra vs. fluence at below 8 meV energy resolution. The intensities of peaks corresponding to different bonds were extracted by fitting power laws over multiple windows.

RESULTS

Spectra of guanine and vitreous ice are given in Fig. 1 and show vibrational modes linked to different bonds. Fig. 2 shows different peak heights (normalized to zero loss) versus fluence. In the early stages, the C=O intensity from guanine at room temperature does not change while the XH intensity is drastically, cf. Fig. 2 (a). This indicates that the CH and NH bonds break first and is consistent with the observation of hydrogen bubbles [4]. At higher electron exposure up to 1000 e-/ Å2 the C=O bonds are broken as seen in Fig. 2 (b). Eventually, a steady state of broken bonds is reached but mass loss from sputtering continues (increased zero-loss intensity, not shown). Fig. 2 (c) shows that cooling to liquid N2 temperatures reaches the steady state earlier but does not change the general behavior. For vitreous ice, it appears from Fig. 2 (d) that single OH bonds break first releasing free H, as seen from the decrease in the OH stretch peak.

CONCLUSION

At a low electron fluence of up to 100 e-/ Å2 CH, NH and OH bonds are the first to break. They presumably release hydrogen that can accumulate as bubbles. As the electron exposure increases other bonds such as the C=O in guanine are broken. However, many of these bonds are also being reformed as damage proceeds. We are now studying hydrogen exchanges via deuteration.

[1] H. Stark et al, Ultramicr. **63**, 75 (1996).

[2] P. Li and R.F. Egerton, Ultamicr. **101**, 161 (2004).

[3] P. Rez et al, Nat. Commun. **7**, 10945 (2016).

[4] R.D. Leapman and S. Sun, Ultramicr. **59**, 71 (1995).

Fig. 1 (a) Background subtracted spectrum of guanine and (b) spectrum of vitreous ice. Variation of peak intensities (normalized to zero-loss) versus fluence for (c) guanine at room temperature and low fluence, (d) increased fluence, (e) cooled and (f) for vitreous ice.

Fig. 1

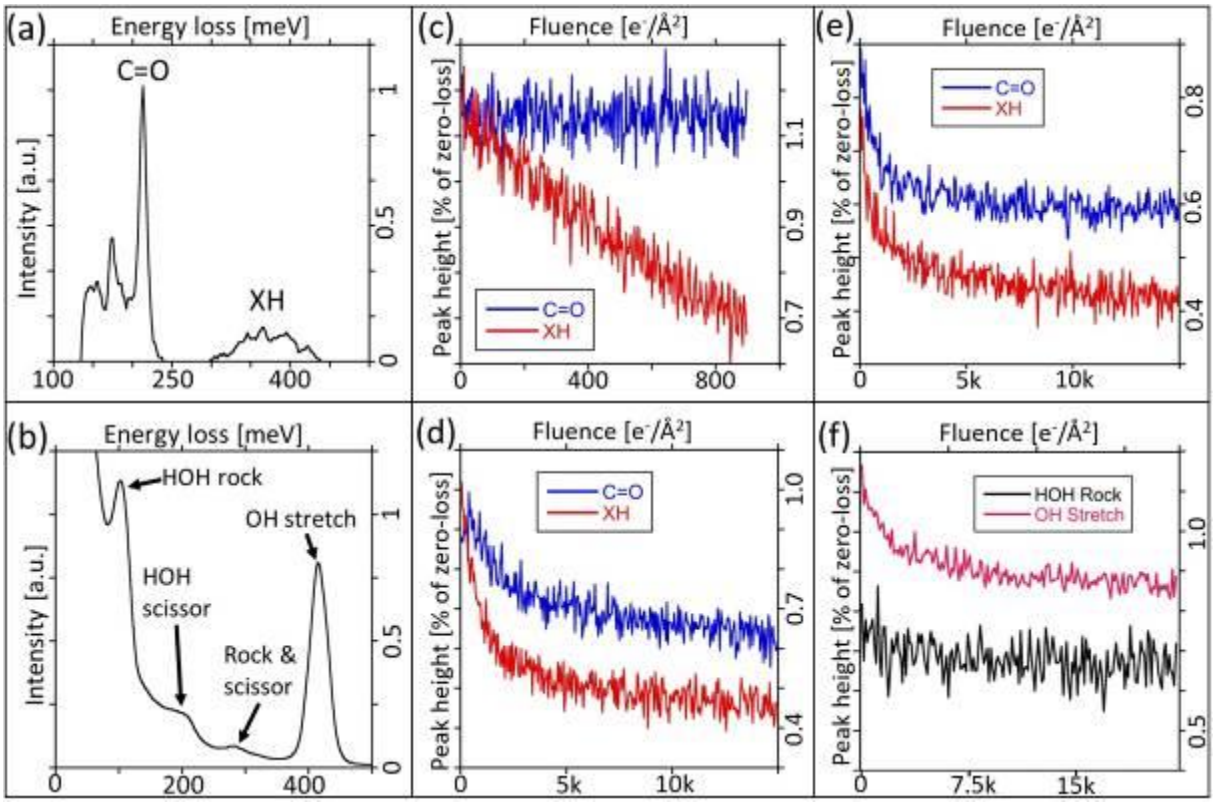

IM4.005

Cryo-STEM imaging for single particle structure determination

C. Sachse[1,2], I. Lazić[3], M. Wirix[3], M. L. Leidl[1,4], D. Mann[1], M. Beckers[1,5], E. V. Pechnikova[3], K. Müller-Caspary[4], F. de Haas[3]

[1]Forschungszentrum Jülich, Ernst-Ruska Centre 3 / Structural Biology, Jülich, Germany
[2]Heinrich Heine University, Department biology, Düsseldorf, Germany
[3]Thermo Fisher Scientific, Materials and Structural Analysis Division, Eindhoven, Netherlands
[4]Ludwig-Maximilians-University Munich, Department of Chemistry and Centre for NanoScience, Munich, Germany
[5]European Molecular Biology Laboratory (EMBL), Structural and Computational Biology Unit, Heidelberg, Germany

In electron cryo-microscopy (cryo-EM), molecular images of vitrified biological samples are obtained by conventional transmission electron microcopy (CTEM) using large underfocuses and subsequently computationally combined into a high-resolution 3D structure. Although scanning transmission electron microscopy (STEM) has been successfully applied to organic and inorganic materials and achieved exceptionally high resolution, its capability to resolve biological structures with high resolution is still to be determined. Here, we apply STEM using the integrated differential phase contrast mode also known as iDPC-STEM (*1*) to two cryo-EM test specimens, keyhole limpet hemocyanin (KLH) (*2*) and tobacco mosaic virus (TMV) (*3*). The micrographs show complete contrast transfer to high resolution and enable the cryo-EM structure determination for KLH at 6.5 Å resolution, as well as for TMV at 3.5 Å resolution using single-particle reconstruction methods, which share identical features with maps obtained by CTEM of a previously acquired same-sized TMV data set. The estimated B-factor from iDPC-STEM of 93 Å2 indicates that the accomplished micrograph quality exceeds CTEM recordings from 2015 using 2nd generation direct electron detection devices. These data show that STEM imaging in general, and in particular the iDPC-STEM approach, can be applied to vitrified single-particle specimens to determine near-atomic resolution cryo-EM structures of biological macromolecules. Our proof-of-principle study introduces high-resolution STEM to biological cryo-EM (*4*).

1. I. Lazić, E. G. T. Bosch, S. Lazar, Phase contrast STEM for thin samples: Integrated differential phase contrast. *Ultramicroscopy*. **160**, 265–280 (2016).
2. C. Gatsogiannis, J. Markl, Keyhole Limpet Hemocyanin: 9-Å CryoEM Structure and Molecular Model of the KLH1 Didecamer Reveal the Interfaces and Intricate Topology of the 160 Functional Units. *J. Mol. Biol.* **385**, 963–983 (2009).
3. S. A. Fromm, T. A. M. Bharat, A. J. Jakobi, W. J. H. Hagen, C. Sachse, Seeing tobacco mosaic virus through direct electron detectors. *J. Struct. Biol.* **189**, 87–97 (2015).
4. I. Lazić, M. Wirix, M. L. Leidl, F. de Haas, M. Beckers, E. V. Pechnikova, K. Müller-Caspary, R. Egoavil, E. G. T. Bosch, C. Sachse, "Single-particle cryo-EM structures from iDPC-STEM at near-atomic resolution" (preprint, Biophysics, 2021), , doi:10.1101/2021.10.12.464113. *Accepted at Nature Methods*

Fig.1 Cryo-iDPC-STEM resolves biological test specimens up to near-atomic resolution.

(a) Optical path of STEM, including the convergence semi-angle (α), the average electron path (red line) and the center of mass (COM) of the intensity at the detector. (b) Raster geometry and beam dimensions over the field of view. (c) iDPC-STEM micrograph of keyhole limpet hemocyanin (left) and corresponding 6.5-Å resolution map with superimposed atomic model (right). Scale bar is 100 nm. (d) iDPC-STEM micrograph of tobacco mosaic virus (left) and corresponding 3.5-Å resolution density (based on the 0.143 Fourier shell correlation (FSC) cutoff criterion) with superimposed atomic model. Scale bar is 100 nm. ADF, annular dark field; BF, bright field; E, electric field; f, focal length of the lens; rp, position of the probe in real space; V, electrostatic potential field.

Fig. 1

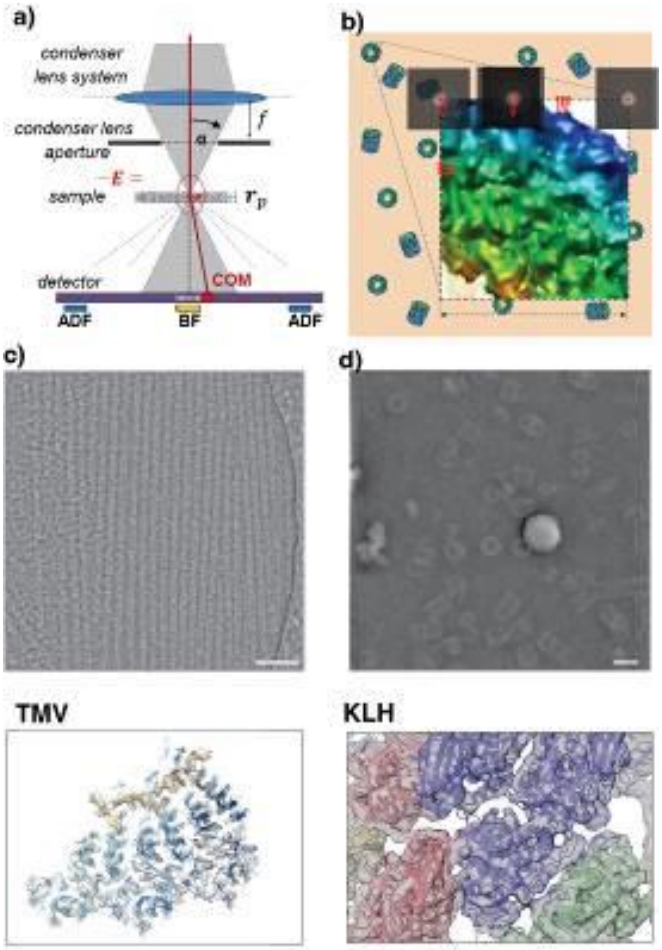
a)
condenser lens system
condenser lens aperture
sample
detector
COM
ADF
BF
ADF
b)
c)
d)
TMV
KLH

IM4.006

New principle and robot for vitrification of cryo-EM samples with controllable sample thickness and real-time optical inspection

R. I. Koning[1], H. Vader[2], M. van Nugteren[2], P. A. Grocutt[2], W. Yang[3], L. L. R. Renault[3], A. J. Koster[1], A. C. F. Kamp[2], M. Schwertner[2]

[1]Leiden University Medical Center, Electron Microscopy, Cell and Chemical Biology, Leiden, Netherlands
[2]Linkam Scientific Instruments Ltd., R&D, Salfords, United Kingdom
[3]NeCen, Leiden University, Institute of Biology, Leiden, Netherlands

Keywords: Vitrification of biological samples, blotting-free ethane plunging, sample preparation robot, cryo-Electron Microscopy (cryo-EM), Single Particle Tomography (SPT), cryo-Electron Tomography (cryo-ET)

Introduction

Cryo-EM, cryo-tomography, Single Particle Tomography (SPT) and cryo-CLEM (Correlative Light and Electron Microscopy) have become standard tools for the investigation of protein 3D structures, cellular structures and more in the last decade. Despite the progress with cryo-EM instruments and automated sample loading and imaging the routine preparation of cryo-samples can be challenging. Ice layer thickness and uniformity are key parameters for obtaining high quality data.
Cryo-plunging techniques most widely used for vitrification are based on paper-blotting to adjust the thickness of the vitrified layer. We have identified this as a key drawback in the process because the blotting paper soaks up moisture while inside the high-humidity chamber leading to characteristics that are challenging and not always repeatable [2][3].

Objectives

In this work we aim to address the difficulties of cryo-sample preparation for cryo-EM and cryo-ET by means of automation and by introducing the principle of suction to adjust the film thickness on the grid before plunging.

Materials & methods: comparison with conventional blotting, robot design

Fig 1 compares the traditional cryo sample preparation technique (top row, sample pipetted onto EM grid with support film followed by blotting in humidity chamber) with the method proposed here: sample application via dipping followed by film thickness adjustment via suction (bottom row) [1].

Filter paper used in the traditional technique soaks up moisture from the environment of the humidity chamber, changing properties.
The suction used by our method can be adjusted (flow rate and duration) to control film thickness. It also gives access for direct optical real-time imaging that is used to assess sample conditions and to determine the best moment to trigger plunging [1]. The desktop plunging system is shown in fig. 2, the internal elements in fig. 3.

Results

We built a robotic cryo-plunger and demonstrated the use for protein suspensions, lipid vesicles, bacteria and human cells.
See [1] for additional details.

Conclusion

We have identified the blotting process in the traditional plunging setups as a key drawback in the process and propose a novel method where fluid is removed for the sample thickness adjustment by means of a calibrated and programmed suction process. Key benefits are repeatability, straightforward automation and direct optical access to the sample for real-time monitoring and control of sample film thickness. The thin-film interference and the liquid surface characteristics observed in the optical microscope give control over the optimisation of film thickness (see [1]). Importantly, the optical image acquired immediately before plunging allows good prediction of sample ice quality – saving valuable EM beam time. The new setup improves repeatability, removes potential risks from manual sample handling and increases speed and throughput via automation.

References

[1] Nature Communications, (2022) 13:2985, https://doi.org/10.1038/s41467-022-30562-7

[2] Nature Methods, VOL 18, May 2021, 463–471, P. J. Peters, et al. https://doi.org/10.1038/s41592-021-01130-6

[3] J. of Microsc., Vol. 276, Issue 1 2019, pp. 39–45 doi: 10.1111/jmi.12834

Fig. 1

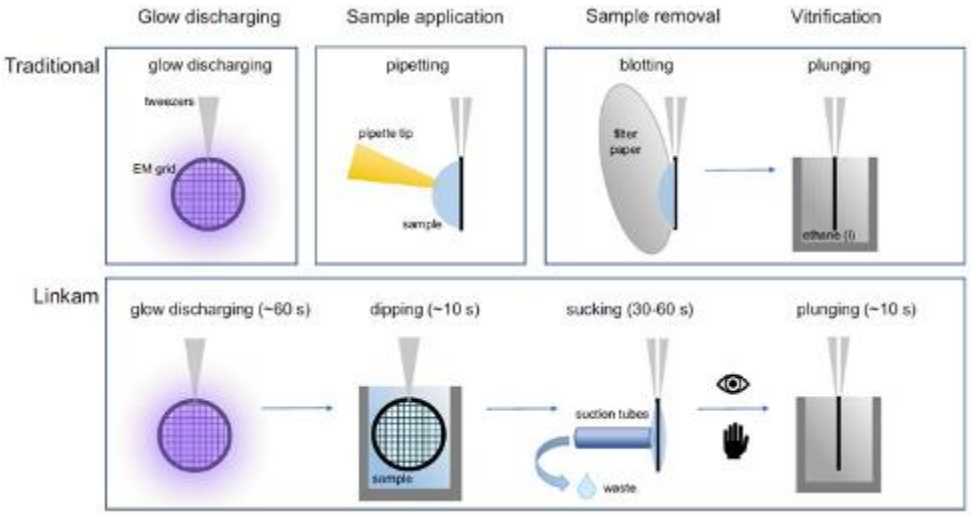

Fig. 2

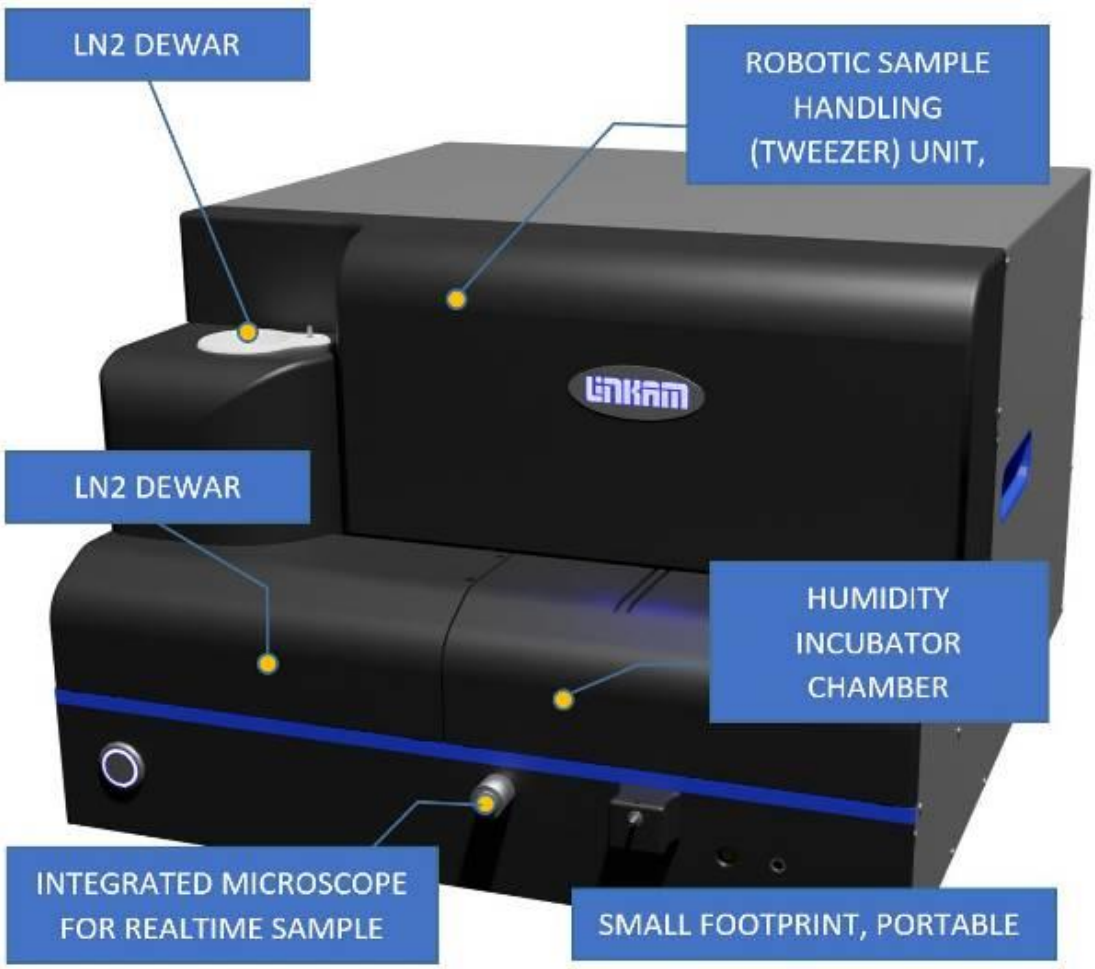

Fig. 3


FROZEN GRID STORE
SAMPLE DIPPING
ETHANE BATH, LIQUIFICATION
MICROSCOPE
TWEEZERS
GRID OBSERVATION
GLOW DISCHARGE UNIT
GRID PICKUP
LN2 BATH (NO COVER)
SUCTION UNIT FOR THICKNESS ADJUSTMENT
HUMIDITY CHAMBER WITH DEW-POINT CONTROL

IM4.P001

Improved performance with CRYO ARM II series

E. Katzmann[1]

[1]JEOL (Germany) GmbH, Freising, Germany

1. Introduction

According to EMDB and PDB data bases the number of data entries (solved structures) in the last 10 years (2011 – 2021) has been grown almost in an exponential manner by 23-fold. This is an enormous increase which is a result of several advances in cryo electron microscopy technology. Camera models with higher sensitivity and speed, more robust and user-friendly cryo transmission electron microscopes (cryo TEM), refined sample preparation tools and constantly improving analysis software paved the way to this development.

2. Objectives

Recent developments and achievements with the CRYO ARMTM series from JEOL will be presented along selected application examples.

3. Materials & methods

JEOL is one of the largest manufacturers of electron microscopes worldwide and from early on contributed to the current success in the field of cryo electron microscopy. Since the early 1980th JEOL has released the 8th generation of cryo TEM"s the CRYO ARMTM series. Basically, two version are available comprising unique features like a cold field emission source which was pioneered by the CRYO ARM series for the cryo electron microscopy community as well as in-column energy filters and outstanding resolution performance without sophisticated and expensive add-ons like correctors and monochromators.

4. Results

Higher throughput in terms of moves per hour were achieved by more efficient data collections routines and microscope alignments. Multi images per hole routines together with "Koehler mode" set up resulted in > 500 images per hour depending on the detector used. New direct detector camera generations were evaluated and gave rise to high resolution data sets for tomography, single particle (SPA) and MicroED applications.

5. Conclusion

All together these data demonstrate the high flexibility and robustness of the latest generation CRYO ARMTM II series for the needs of current and future applications in the field of structural biology.

Fig. 1

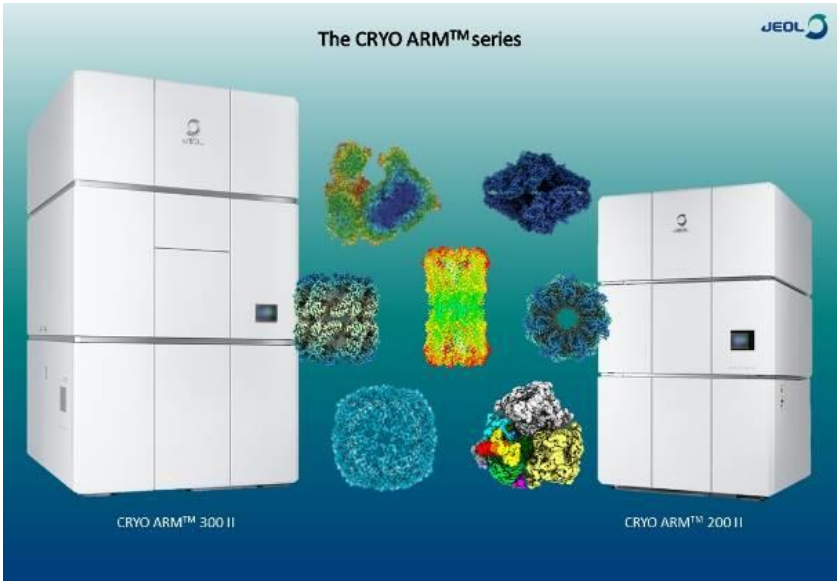

IM5.001-invited

Advances in ptychography with a focus on low-dose and 3D applications

M. Schloz[1], T. C. Pekin[1], J. Müller[1], A. Gladyshev[1], B. Haas[1], C. T. Koch[1]

[1]Humboldt Universität zu Berlin, Physik, Berlin, Germany

The use of fast pixelated detectors optimized for four-dimensional scanning transmission electron microscopy (4D-STEM) experiments has revolutionized the type and amount of data that can nowadays be acquired at an electron microscope. In combination with the development of new computational hardware and reconstruction algorithms, microscopy techniques, such as ptychography, are about to replace conventional STEM imaging methods due to their superior image resolution of electron radiation-sensitive materials [1,2]. Ptychography in particular has already become a mature electron microscopy technique and has experienced immense advances in the last years [3-5]. The current research to further improve this technique is driven by the desire to investigate thick samples as well as to measure with a low electron dose.

Here, we will discuss the advances in ptychography during the last couple of years. We will take a look at how researches have tried to relax the strict scanning constraint, which is required for obtaining information redundancy through consecutively overlapping probes. For example, we will look at one approach that involves a defocused probe rastered across the specimen, with a less dense scan pattern and discuss its drawbacks and suggest alternatives. Further, we will examine the measures that have been taken to generate high resolution 3D images of thicker samples. We will discuss possible improvements of the conditioning of the 3D reconstruction problem in order to extent the depth resolution and we will compare the results to those of other STEM techniques. Finally, we will outline future research directions and unresolved problems for ptychography [6].

References:

[1] Jiang, Yi, et al. "Electron ptychography of 2D materials to deep sub-ångström resolution." Nature 559.7714 (2018): 343-349.
[2] Chen, Zhen, et al. "Electron ptychography achieves atomic-resolution limits set by lattice vibrations." Science 372.6544 (2021): 826-831.
[3] Wakonig, Klaus, et al. "PtychoShelves, a versatile high-level framework for high-performance analysis of ptychographic data." Journal of applied crystallography 53.2 (2020): 574-586.
[4] Schloz, Marcel, et al. "Overcoming information reduced data and experimentally uncertain parameters in ptychography with regularized optimization." Optics Express 28.19 (2020): 28306-28323.
[5] Pelz, Philipp M., et al. "Solving Complex Nanostructures With Ptychographic Atomic Electron Tomography." arXiv preprint arXiv:2206.08958 (2022).
[6] M.S., T.C.P. and C.T.K. acknowledge financial support from the Deutsche Forschungsgemeinschaft (DFG, German Research Foundation) - Project-ID 414984028 - SFB 1404. J.M. acknowledges support by the DFG Grant No. KO 2911/12-1, KO 2911/13-1, BR 5095/2-1 and Project-ID 182087777 - SFB951. M.S. and J.M. acknowledge financial support by the Volkswagen Foundation (Initiative: "Experiment!", Project: "Beyond mechanical stiffness").

IM5.002-invited

Organic crystal structure refinement from 3D electron diffraction data with application of dynamical theory and more accurate scattering factors

P. Dominiak[1], B. Olech[1], P. Brazda[2], L. Palatinus[2], M. Malinska[1], K. K. Jha[3], T. Góral[3], K. Woźniak[1,3]

[1]University of Warsaw, Biological and Chemical Research Centre, Department of Chemistry, Warsaw, Poland
[2]Institute of Physics of the Czech Academy of Sciences, Prague, Czech Republic
[3]University of Warsaw, CeNT, Warsaw, Poland

In recent years, one can observe spectacular developments in the 3D electron diffraction (3D ED) methods. Practitioners of this method are learning how to improve data collection, among others how to diminish radiation damage and how to deal with dynamical scattering, data processing, and refinement. Currently, available structures from 3D ED reach R-factors even below 10% and resolution around *dmin* = 0.5 Å. Refinement with a dynamical approach [1] against such data allows for observation of residual density in bonding paths or lone electron pair regions. Therefore, it is possible and profitable to use more sophisticated aspherical models of atomic electrostatic potential instead of the standard independent atom model (IAM).

We have already proposed transferable aspherical atom model (TAAM) refinements against 3D ED data in kinematic approximation [2]. The TAAM was parametrized with the Multipolar Atom Types from Theory and Statistical clustering (MATTS) databank (successor of UBDB2018 [3]). Now TAAM is coupled with dynamical refinement and available in Jana2020 [4]. Here, we present refinements of exemplary organic crystal structures, urea, and α-glycine, with the application of the kinematic approach. Next, we show the refinement of 1-methyluracil crystal structure against *dmin* = 0.56 Å data with TAAM in the dynamical approach. There is a visible clearing of the residual density maps, also lowering of the maximum and minimum residual values, and a further lowering of R-factors. The combination of various variants of TAAM with the dynamical approach allows us to conclude that quantitative information about electron density distribution due to chemical bonding, the presence of lone electron pairs, partial charges on atoms, and charge density polarization due to intermolecular interactions can be extracted from the 3D ED data (Fig.1). In the future, we will go beyond TAAM and refine the parameters of the multipole model of electron density.

Fig. 1. Residual electrostatic potential maps for dynamical refinements of 1-methyluracil crystal structure with application of IAM (left), TAAM (middle), and periodic TAAM (right) scattering models. Contour level 0.13 eÅ-1, yellow: positive, cyan: negative. Thermal ellipsoids with 50% probability.

References

[1] L. Palatinus, V. Petricek, and C. A. Correa, *Acta Crystallogr. A*, **71** (2015), 235–244.
[2] B. Gruza, M. L. Chodkiewicz, J. Krzeszczakowska, and P. M. Dominiak, *Acta Crystallogr. A*, **76** (2020), 92–109.
[3] P. Kumar, B. Gruza, S. A. Bojarowski, P. M. Dominiak, *Acta Crystallogr. A*, **75** (2019), 398-408.
[4] V. Petrícek, M. Dusek, and L. Palatinus, *Zeitschrift für Krist. - Cryst. Mater.,* **229** (2014), 345–352.

Acknowledgments: This research was funded by National Science Centre, Poland 2020/39/I/ST4/02904 and University of Warsaw IDUB grant BOB-IDUB-622-20/2021 (,,Infrastructure for Cryomicroscopy and Electron Diffraction Core Facility").

Fig. 1

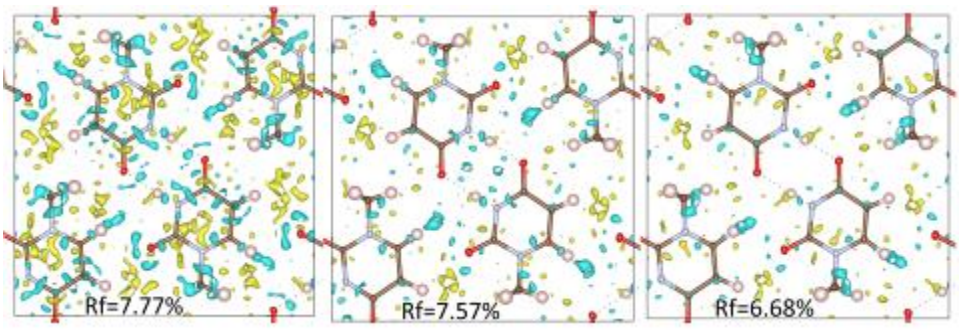

IM5.003

Probing 3D reciprocal space of textured nanocrystalline thin films using electron diffraction tomography

I. Kraus[1], M. Wu[1], S. Rechberger[1], C. Harreiß[1], J. Will[1], W. Gruber[2], S. Maiti[2], T. Unruh[2], E. Spiecker[1]

[1]Institute of Micro- and Nanostructure Research & Center for Nanoanalysis and Electron Microscpy (CENEM), Friedrich-Alexander-Universität Erlangen-Nürnberg, Materials Science, Erlangen, Germany
[2]Institute for Crystallography and Structural Physics, Friedrich-Alexander-Universität Erlangen-Nürnberg, Erlangen, Germany

Texture in crystalline materials dictates their anisotropy properties, e.g. opto-electronic properties in light harvesting polycrystalline semiconductors. Texture is conventionally evaluated by probing the reciprocal space using X-ray and/or electron diffraction (ED) methods. In organic bulk heterojunctions of organic solar cells (OSCs) grazing incidence wide angle X-ray scattering (GIWAXS) is a well-established method. However, real space information is missing to correlate domain structure with crystal texture. TEM can deliver both real and reciprocal space as well as analytical signals. However, ED in OSCs is not well explored largely due to radiation damage challenges. In this work we establish a method to probe the 3D reciprocal space of textured nanocrystalline thin films by means of electron diffraction tomography (EDT), complemented by 4D-STEM analysis.

As sample systems a radiation robust AlN thin film (Fig. 1) and a radiation sensitive active layer of OSC blend (Fig. 2) are chosen. A tilt series of ED patterns over ±70° is acquired with a single-axis tilt holder. A 3D reciprocal space representation of the data is reconstructed using Process Electron Tilt Series (PETS) software and the corresponding 2D slices are extracted (cf. Fig. 1b and Fig. 2e) for comparison with GIWAXS. The texture is further studied using 4D-STEM and 4D-SCED [1].

The AlN thin film shows a pronounced fiber texture (columnar grains of ~50 nm diameter and ~500 nm length grown along direction, Fig. 1a) and its beam robustness qualifies it as reference for the described method. Figure 1b shows an overview of the EDT workflow. The 3D reciprocal lattice pattern confirms random in-plane rotation of grains and small out-of-plane tilt. The local grain orientation, mapped with ACOM [2] based on nano-beam ED 4D-STEM data (Fig. 1c), shows that the tilted grains are clustered in groups.

For the OSC samples, composed of small molecule donor DRCN5T and acceptor PC71BM, dominating texture of π-stacking face-on and edge-on were identified based on GIWAXS studies (Fig. 2c and ref. [3]). In TEM energy-filtering of SAED (EF-SAED) is necessary to suppress inelastic background scattering. Due to the limited dose budget, each ED pattern in the tilt series was acquired at fresh sample areas. The reconstructed 3D reciprocal lattice is compared with the GIWAXS data showing good agreement. A fully quantitative comparison is underway and will be presented together with pros and cons of the two methods.

[1] M. Wu, et. al., Nat. Commun. (2022) 13, 2911

[2] C. Ophus, et. al., Microsc. Microanal. (2022) 28, 390

[3] M. Berlinghof, et. al., Z. Kristallogr. (2020) 235, 15

The authors gratefully acknowledge financial support by the DFG via the Collaborative Research Centre SFB 953 "Synthetic Carbon Allotropes".

Figure 1: Characterization of highly textured columnar AlN thin film. (a) BF TEM images. (b) ED patterns from a tilt series, principle of 3D reciprocal space reconstruction and 3D view of the reciprocal space. (c) visualized texture maps based on 4D-STEM data.

Figure 2: Characterization of active layer DRCN5T:PC71BM after solvent vapour annealing. (a) molecule structure of donor DRCN5T (sulphur-rich) and acceptor PC71BM (carbon-rich) and scheme of donor crystal structure. (b) EF-SAED, (c) GIWAXS, (d) nano-morphology based on STEM-EELS data. (e) 3D reciprocal space from EF-SAED EDT. (f) face-on (grayscale) and edge-on (coloured) donor domains revealed in 4D-SCED data.

Fig. 1

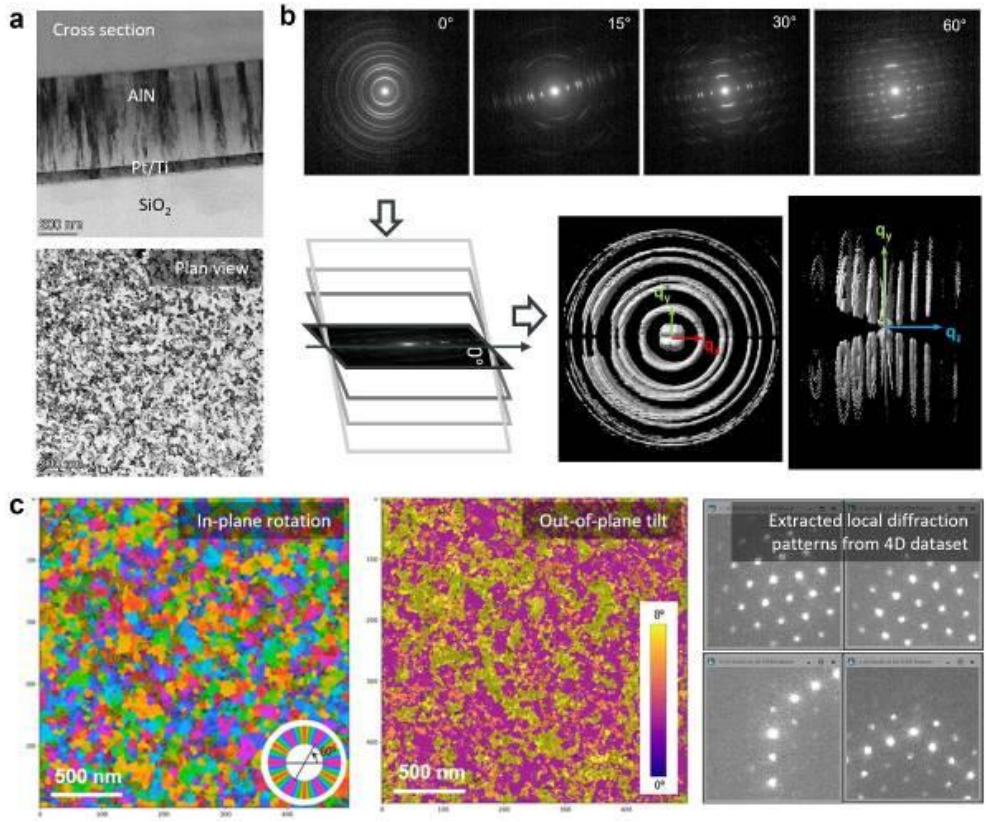
a
Cross section
AlN
Pt/Ti
SiO_2
Plan view
b
0°
15°
30°
60°
q_y
q_z
c
In-plane rotation
Out-of-plane tilt
Extracted local diffraction patterns from 4D dataset
500 nm
500 nm

Fig. 2

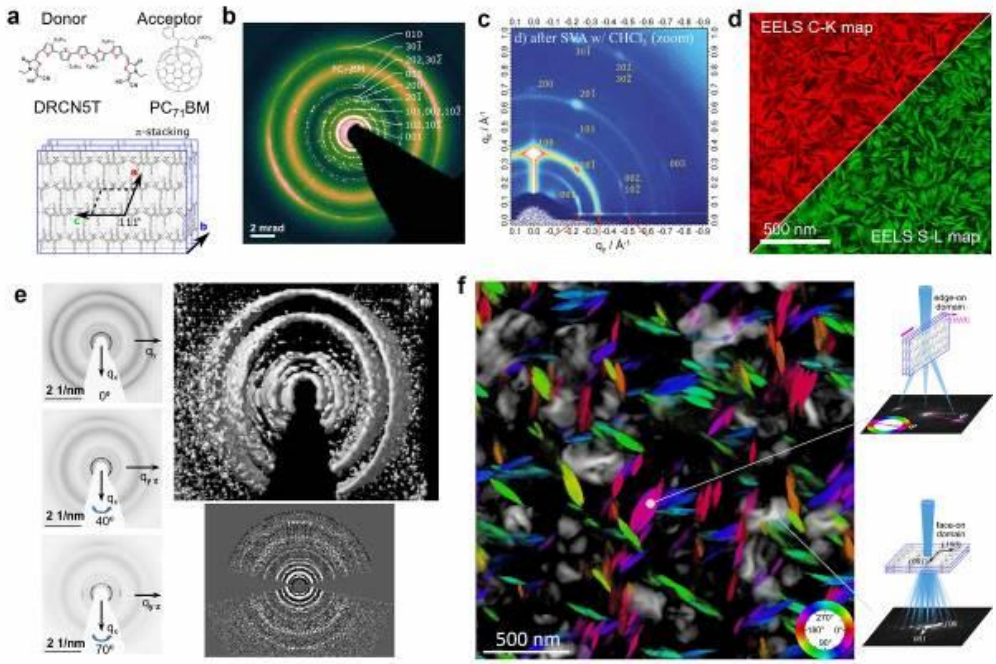
a
Donor
Acceptor
DRCN5T
$PC_{71}BM$
π-stacking
b
2 mrad
c
d) after SVA w/ $CHCl_3$ (zoom)
d
EELS C-K map
500 nm
EELS S-L map
e
2 1/nm
2 1/nm
2 1/nm
f
500 nm

IM5.004

Parametrized diffraction inversion by gradient-based optimization employing a fully differentiable multislice

B. Diederichs[1,2], L. Richter[2], F. Filbir[1], K. Müller-Caspary[2]

[1]Helmholtz Zentrum München, Institute of Biological and Medical Imaging, Neuherberg, Germany
[2]Ludwig-Maximilians-University Munich, Department of Chemistry and Center for NanoScience, Munich, Germany

With the availability of momentum-resolved STEM data, a multitude of phase retrieval methods were established. Most can be grouped into two categories; direct inversions employing a single object transmission function (OTF) and iterative techniques capable of reconstructing both single- and multiple slice OTFs as well as the STEM probe. Importantly, these optimization schemes act on the pixel-wise distribution of amplitude and phase of OTF and probe.

In fact, the diffraction patterns (DP) correspond to a relatively sparse set [P] of parameters, e.g., aberration coefficients, positions and types of atoms, specimen tilt, coherence parameters and probe positions. The goal of an inversion procedure is the retrieval of [P] iteratively from a starting guess using the gradients with respect to [P]. We introduce a fully differentiable multislice scheme TorchSlice implemented in Pytorch, utilizing GPUs. Gradients are obtained by backpropagation, a method widely used in machine learning. Using backpropagation for inverse multislice was introduced in [1, 2].

Here, we demonstrate the capability of this approach in two steps. First, we employ the availability of gradients to study optimum experimental designs. In particular, a 4D STEM simulation of 2D and bulk MoS2 including vacancies is performed, resembling an experimental data set. A parametrized perfect crystal is then assumed to calculate the gradients with respect to the presence or absence of atoms at their native sites, for different STEM signals, doses, probe foci and aberrations. Fig 1 depicts the success rate for the detection of a vacancy in dependence of dose and focus for the 4D STEM and the STEM bright field signals. It is concluded that 4D STEM is a lot more dose-efficient and robust than BF imaging with respect to vacancy detection.

Secondly, we address the retrieval of bonding effects from 4D STEM data of hBN and GaAs. DFT simulations are used to generate DP including electron redistributions due to chemical bonding. Then, a model based on isolated atoms is set up as initialization for a gradient-based optimization. That allows to evaluate a priori what dose levels and experimental setups are most promising to detect bonding effects. The hBN monolayer required a significantly higher dose level, electrons per DP, while the bonding effect of a 12nm GaAs crystal appeared already at electrons per DP. It is conceivable that an elevated thickness helps to detect bonding effects. Fig 2 depicts the successful reconstruction of bonding effects for GaAs.

Finally, we address further prospects and show first reconstructions of experimental data of 2D heterostructures and ferroelectrics, where we determined the cation displacements from slightly misoriented PZT crystals.

Figure 1: detection probability of a vacancy depending on the dose and the defocus, respectively and from bright field or 4d-stem data, respectively. Probabilities were calculated over 70 runs

Figure 2: Phase grating (PG) in the isolated atom approximation for GaAs on the left; Difference between PG with bonding and PG at the end of reconstruction on the right. The PG was recovered at the area covered by the probes

[1] W. Van den Broek and C. T. Koch, *Physical review letters*, 2012, 10.1103/PhysRevLett.109.245502

[2] W. Van den Broek and C. T. Koch, *Physical Review B,* 2013, 10.1103/PhysRevB.87.184108

[3] Support from Helmholtz under contracts VH-NG 1317, ZT-I-0025 and ZT-I-PF-5-028 is gratefully acknowledged.

Fig. 1

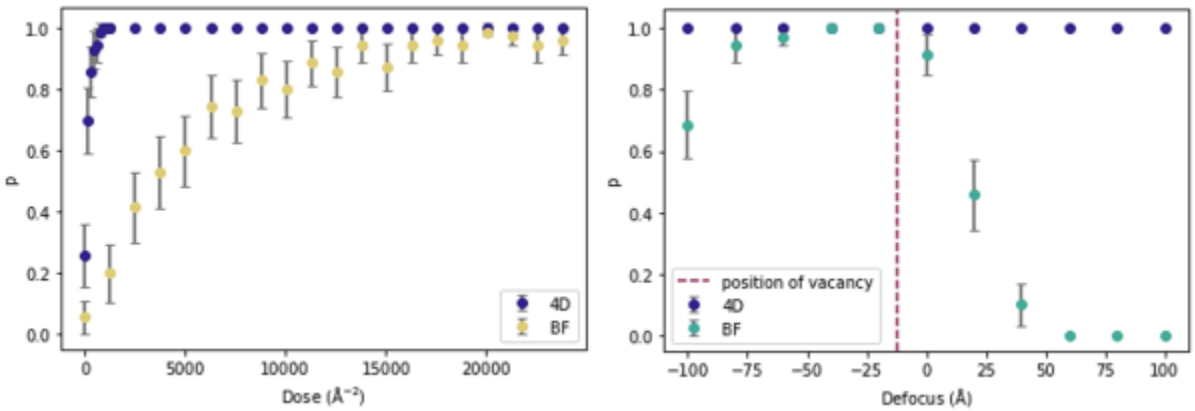
p
Dose (Å^{-2})
4D
BF
position of vacancy
Defocus (Å)

Fig. 2

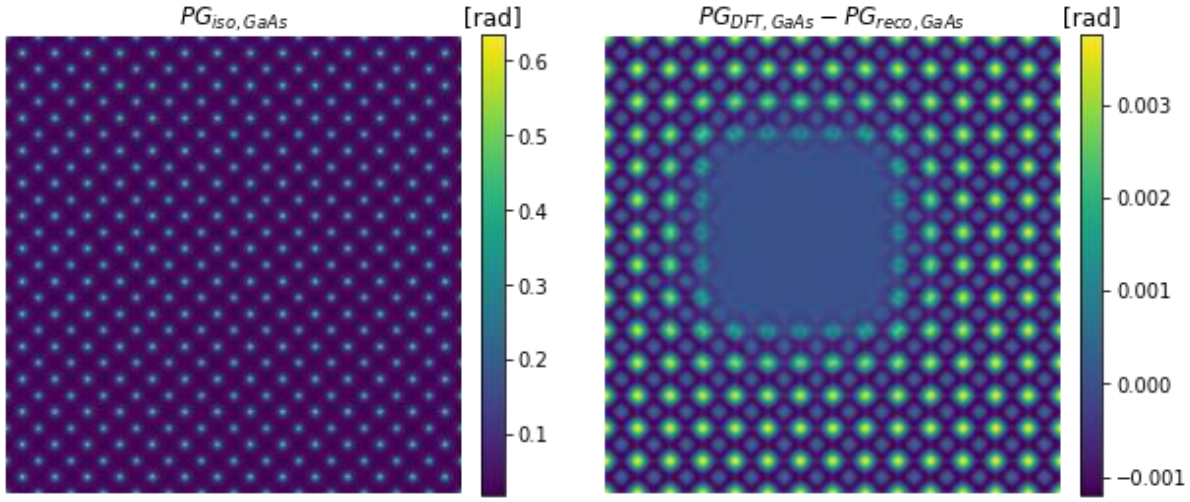
$PG_{iso,GaAs}$
[rad]
$PG_{DFT,GaAs} - PG_{reco,GaAs}$
[rad]

IM5.005

Optimized segmentation for quantitative 3D analysis of electron tomography reconstructions

S. Kavak[1], A. Sànchez-Iglesias[2], A. A. Kadu[1], N. Claes[1], L. M. Liz-Marzán[2], S. Bals[1]

[1]EMAT and NANOlab Center of Excellence, Physics, Antwerp, Belgium
[2]Bionanoplasmonics Laboratory, CIC biomaGUNE, San Sebastian, Spain

Nanoparticle assemblies are of great interest due to their tunable structure and properties, and their application in various fields.1,2 For example, the coexistence of Au nanoparticle and quantum dots (QDs) enables dual imaging, fluorescence and light scattering, and/or photothermal treatment of cancer cells.3 By changing the number of particles, and/or the interparticle distances, it becomes possible to reach specifically desired structures and properties for targeted usage.4 Hereby, it is very important to investigate the structure-property relationship of the nanoparticle assemblies. In order to extract quantitative information of the 3D structure, an accurate characterization at the nanometer level is required. Transmission electron microscopy (TEM) is a useful technique to study nanomaterials. However, since conventional TEM is limited to 2D projections, it is important to perform electron tomography experiments to obtain reliable information for 3D structures. An important step to extract quantitative 3D information is the segmentation of the 3D data set. Manual segmentation is hereby the most conventional but also most time consuming technique. To overcome this limitations, advanced reconstruction algorithms, such as the discrete algebraic reconstruction technique (DART),5 and the sparse sphere reconstruction algorithm (SSR) 6 have been developed in which segmentation is part of the 3D reconstruction. However, they are computationally expensive and might not be ideal for assemblies where the nanoparticles are agglomerated or not uniform in size. In this work, we therefore focused on the optimization of the segmentation process and we have compared three different segmentation methods to extract quantitative parameters from the 3D reconstructions. In additional to the manual segmentation (**Figure 1**), we made use of a watershed function7, which separates the agglomerated particles from their catchment points for each local minima, and a spherical Hough function, which detects each particle separately by defining their radius and center point.8 Results showed that the spherical Hough function, is the most promising technique to extract quantitative information from the 3D reconstructions of the nanoassemblies. In this contribution, I will present the results and comparison of these segmentation methods, including their advantages and limitations.

1. Hanske, C. et al. M. Advanced Materials 30, 1707003 (2018).

2. Colloidal Synthesis of Plasmonic Nanometals. (2020).

3. Jin, Y. & Gao, X. Nature Nanotechnology 4, 571–576 (2009).

4. Hollingsworth, J. A. et al. MRS Bulletin 40, 768–776 (2015).

5. Batenburg, K. J. et al. Ultramicroscopy 109, 730–740 (2009).

6. Zanaga, D. et al. Nanoscale 8, 292–299 (2016).

7. Beucher, S. & Meyer, F. in Mathematical Morphology in Image Processing (CRC Press, 1993).

8. Hough, P. V. C. Method and Means for Recognizing Complex Patterns. (1962).

Figure 1: *The samples: CdSe/CdS quantum dots encapsulated by polymeric micelles (**a,e**), Au nanosphere and CDSe/CdS quantum dots encapsulated by polymeric micelles (**b,f**), Au nanorod and CdSe/CdS quantum dots assembled on silica shell (**c,g**), and Au nanorod and PbS quantum dots assembled on silica shell (**d,h**). The first row (**a-d**); 3D visualizations of the reconstructions of nanoassemblies, and the second row (**e-h**); manual segmentation of the same structures. (Scale bars represent 30 nm).*

Fig. 1

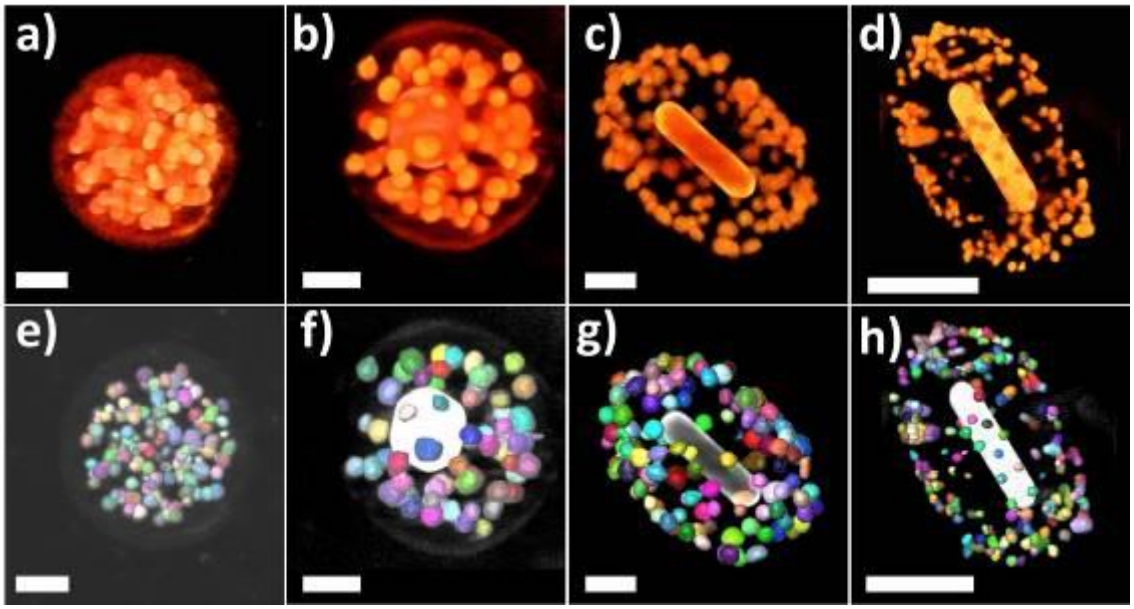

IM5.006

Theory challenges of the two-beam electron tomography of real crystals

F. Chukhovskii[1]

[1]A.V. Shubnikov Institute of Crystallography of Federal Scientific Research Centre “Crystallography and Photonics” RAS, X-ray Analysis Methods and CY, Moscow, Russian Federation

In regard to the digital electron microscopy tomography (DEMT), an issue of decoding reference data in the electron tomography is discussed, in particular: the general solution of the 3D *inverse* Radon"s transform issue (*i.e.,* to recover a 3D picture using the 2D image patterns) and denoising of the corresponding 2D image patterns (IPs) recorded in a process of rotating the crystal sample.

Based on the Takagi-Taupin (TT) and Howie-Wheelan (HW) equations (see [1]), the boundary Cauchy problem of the two-beam electron scattering in distorted crystals has been formulated in the form of the matrix integral TT- and HW-equations, respectively.

The self-consistent transport model approximations of the integral TT- and HW- equations have been derived and accordingly, analytical *abschließsicher* solutions have been built up. As example how the *abschließsicher* solutions work, the bright- and dark-field contrast of the edge dislocation in the middle of the crystal slab eight extinction lengths thick have been evaluated and compared with the corresponding ones numerically calculated [1].

In general, analytical model solutions of the two-beam electron diffraction open a door to solving the *inverse* 3D Radon"s transform issue that will allow to facilitate and justify investigations of crystal-lattice defects by *ab initio* DEMT technique.

In general, analytical model solutions of the two-beam electron diffraction open a door to solving the *inverse* 3D Radon"s transform issue.

In report, on the example of the Coulomb-types point defect described in terms of the HW equations by the 3D displacement field function $f_{pdCt}(\mathbf{r}\text{-}\mathbf{r}_0)$, the 3D Radon"s transform issue is considered to retrieve function **.** Such the procedure assumes numerically to recover the function $f_{pdCt}(\mathbf{r}\text{-}\mathbf{r}_0)$ by using a number of the 2D IPs by means of optimizing the DEDT target function.

For this, one applies the joint iterative algorithm based on a quasi-Newton Levenberg-Marquardt (qNLM) gradient descent [2] and Simulated Annealing (SA) [3] algorithms. The results of recovering the cross-section of $f_{pdCt}(\mathbf{r}\text{-}\mathbf{r}_0)$ have been obtained by using the SA algorithm code [3].

Separately, in the report, denoising the reference DEMT data, the 2D IPs, by using the different filtering methods such as the Wiener-Kolmogorov Filter (WKF), Guided Image Filter (GIF) and Statistical Acquisition Filter (SAF) is discussed. The examples of applying the SAF to the Gaussian noisy 2D IPs are given [4].

References

1. P. B. Hirsh, A. Howie, R.B. Nicholson, D.W. Pashley & M. J. Whelan. *Electron Microscopy of Thin Crystals*. LONDON BUTTERWORTHS, PP. 549 (1965).
2. J. J. Moré. *The Levenberg-Marquardt algorithm: Implementation and theory*. In G.A. Watson (eds) Numerical Analysis. Lecture Notes in Mathematics, vol. **630** Springer, PP. 105-116. Springer-Verlag, Berlin and New York. 1978. DOI: 10.1007/BFb0067700 .
3. S. Kirkpatrick, C. D. Gelatt, M. P. Vecci*. Science* **220** (4598), 671-80 (1983). DOI: 10.1126/science.220.4598.671.
4. V.I. Bondarenko*,* P.V. Konarev & F.N. Chukhovskii. *Crystallography Reports* **65**, 821-826 (2020). DOI: 10.31857/S0023476120060090.

IM5.P001

Including inelastic plasmon scattering in multislice simulations for STEM: a real space integration scheme

F. F. Krause[1], T. Grieb[1], M. Schowalter[1], A. Beyer[2], S. Firoozabadi[2], P. Kükelhan[2], H. L. Robert[3], K. Müller-Caspary[3,4], K. Volz[2], A. Rosenauer[1]

[1]Universität Bremen, Institut für Festkörperphysik, Bremen, Germany
[2]Universität Marburg, Marburg, Germany
[3]Forschungszentrum Jülich, Ernst Ruska Center, Jülich, Germany
[4]Ludwig-Maximilians-University Munich, Departement Chemie, Munich, Germany

The use of multislice simulations of the electron beam propagating through the specimen as reference data to evaluate experimental STEM images is a well-established technique for quantitative evaluation. Using the frozen phonon method to include inelastic phonon scattering, the simulations include thermal diffuse scattering (TDS) and Bragg diffraction, the two major scattering mechanisms. Especially for micrographs acquired from HAADF scattering such simulations have been proven to allow accurate precise evaluation of thickness or composition at atomic resolution.

The transfer of these successes into the medium- and low-angle regime however, has proven difficult: The measured intensity at low scattering angles is found to be higher than expected from frozen phonon simulations. This can be largely attributed to plasmon scattering, as energy filtered, angle resolved experiments confirm that plasmon loss diffraction patterns show an elevated intensity between semi-convergence angle and ~40 mrad [1].

The inclusion of plasmon scattering into multislice simulations is hence of high interest to restore the possibility for accurate evaluations in the low-angle regime. This work presents the implementation of the inelastic plasmon scattering events by inclusion of transition-potentials into the multislice routine. Because the energy loss due to a plasmon excitation is more than four magnitudes smaller than the probe electron energy, the characteristic scattering angle that mainly determines the shape of the transition potentials is only of few µrad. Simultaneously it is necessary to have a reciprocal space extent of several hundred mrad to accurately model TDS. As computational limitations limit the numerical grid size to few thousands of pixels in each direction, the plasmon transition potential is usually undersampled. This can cause a severe overestimation of lowest-angle scattering resulting in an underestimation of the influence of plasmons in the simulation. An integration scheme is proposed to mend this for the simulation of diffraction intensities.

Beyond the characteristic angle, the Lorentzian-shaped transition potential drops quickly to very small values, which has led other authors to the proposal of introducing a critical cuttoff angle, which has been shown to work accurately for conventional energy filtered TEM simulations [2]. In the present work it is shown, that plasmon scattering from the central beam to angles up to ~45 mrad even though improbable is the main contribution to the difference between simulations with and without the inclusion of plasmons. This is due to the very large intensity disparity between central beam and the outer diffraction pattern. It is thus of utmost importance to fully model the transition potentials without a cutoff to high angles, where they are dominated by a term derived from the plasmon dispersion relation.

When the simulation results including plasmon effects are compared to energy filtered experimental diffraction patterns of silicon, they are generally able to reproduce the amount and angle distribution of the plasmon scattering. Remaining discrepancies can be attributed to other effects as is discussed [3].

[1] A. Beyer *et al.*, Scientific Reports **10** (2020), p. 1

[2] J. Verbeeck et al., Ultramicroscopy **102** (2005), p. 239

[3] F. Krause *et al.*, Ultramicroscopy **161** (2016), p. 146

Fig. 1

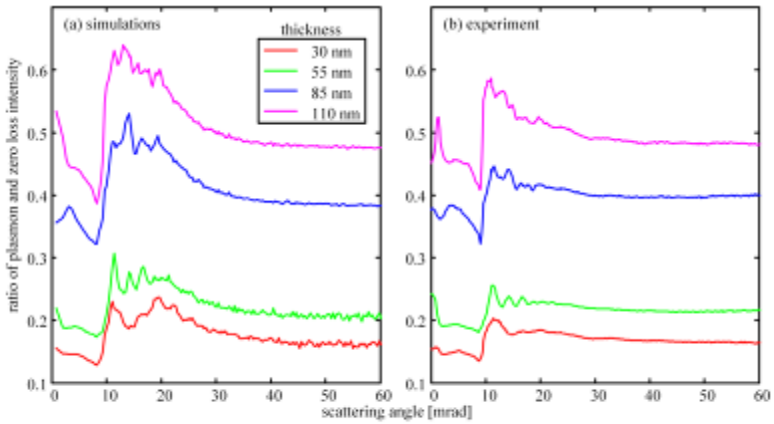

Figure 1: Ratios of the intensities of plasmon loss and zero loss filtered diffraction patterns of silicon in [100] direction for different thicknesses as a function of scattering angle. The acceleration voltage was 300 kV at a semiconvergence angle of 9 mrad. (a) shows the simulation results according to the described method, (b) shows experimental results using a GIF imaging filter. Despite some discrepancies, the amount and angle distribution of the plasmon scattering is in fair agreement with the experiment and decidedly better than for simulations without plasmon scattering.

IM5.P002

Dose-efficient acquisition of EDX-maps: a proposal for an adaptive scanning scheme

F. F. Krause[1], A. Rosenauer[1]

[1]Universität Bremen, Institut für Festkörperphysik, Bremen, Germany

Energy-dispersive X-ray spectroscopy (EDX) maps are usually acquired by scanning with a regular raster of scan positions, where at every scan point the characteristic X-ray emission caused by the electron beam in the sample is detected. In this way, a three-dimensional dataset with two spatial dimensions (scan raster) and one energy dimension (one spectrum for each scan point) is created. After the acquisition, the spectrums can be evaluated and composition information about the specimen can be extracted by, e.g., the Cliff-Lorimer-method. This methodology of evaluation is well-established and largely automated. With modern EDX-detectors that cover an extremely large solid angle and have a high detective efficiency, atomic resolution of the composition maps can be achieved.

However, one of the most critical limiting factors for such EDX map acquisitions is beam damage. Because the X-ray gain per electron dose is relatively small, an electron dose that is magnitudes larger than required for, e.g., a HAADF-STEM image is needed. This can be a problem for beam-sensitive samples, which either deteriorate under the electron beam or have to be prepared in such a way, that a strong contamination occurs. Here, the critical dose, where the resulting images do not longer represent the original sample, is often reached before a sufficient X-ray signal has been acquired. As a result, the spectra are not evaluable at an atomic resolution.

While this dose problem generally is of fundamental nature and cannot completely be avoided, this work proposes a scheme to alleviate the issue. It is based on the observation that the respective excitation cross sections are relatively small and centered around the atoms: For a scan conducted with a sample oriented in a crystallographic direction, the EDX signal from beam positions on atomic columns is significantly stronger than from interstitial positions, if all scan positions receive the same dose – as is the case during a regular scan. The signal retrieved per dose is therefore advantageous directly on the atomic columns.

Given these deliberations, a scanning scheme, where the beam is quickly shifted from column to column, thereby spending little time in the interstitial area, promises an elevated EDX signal for the same specimen dose compared to a regular scan of the same time. Consequently, it should be possible to acquire better spectra per atomic column before the specimen deteriorates.

Quantitative inelastic multislice simulations are used to study the achievable EDX signal improvement for different electron probes and materials. Because any experimental realisation will not be able to target the center of each column flawlessly, the impact the positioning and atom column detection precision is investigated. Finally, possible experimental and instrumental realisations of the proposed technique are discussed.

IM5.P003

Analysing gold nanorod STEM-in-SEM signals at 20 and 30 keV beam energies using a simulation combining explicite diffraction calculations with Monte Carlo strategies

D. Hüser[1], W. Häßler-Grohne[2], S. Strnat[3], C. Bick[2], T. Klein[2]

[1]Physikalisch-Technische Bundesanstalt, 5 Precision Engineering, Braunschweig, Germany
[2]Physikalisch-Technische Bundesanstalt, 5.24 Electron Microscopy, Braunschweig, Germany
[3]Physikalisch-Technische Bundesanstalt, Fundamental Physics for Metrology, Braunschweig, Germany

Environmental and health care issues demand for a quantification of the size of nanoparticles (NP) necessitating the characterization of the geometrical dimensions and shapes. NP of simple geometries such as rods and spheres reveal varying STEM-in-SEM signals for identical thickness, even identical particles, depending on a varying history of exposure [1], see Fig. 1.

Models of the geometry and as well physical models of the beam-sample interaction are required to interpret the transmission signals to defer size information.

We have measured gold nanorods (Au-NRs) using a SEM in transmission mode with beam energies of 20 and 30 keV, a beam current of 50 pA and various dwell times. The Au-NRs have been prepared on a carbon support film of a thickness of 12.5 ± 2.5 nm. Simulations have been carried out using ELSEPA [2] to calculate the scattering amplitudes, thus cross sections, of elastic scattering with a muffin tin radius for gold of 0.147 nm and using cross sections for inelastic scattering coming with JMONSEL [3] according to Shinotsuka et al. [4]. Both types of cross-sections have been implemented as concrete physics C++ classes into the framework of Geant4 [5]. The complex waves with their elastic scattering amplitudes of "independent" gold atoms, their potentials being limited within a sphere (muffin tin) and the atoms being positioned at the gold lattice have been superimposed to calculate the Laue diffraction.

The propagation of beam electrons as trajectories with paths and vertices, with the vertices being the positions where scattering events occur, has been simulated by a Monte Carlo (MC) model. The path lengths s are diced according to the mean free path L by $s = -L \log(R)$ with R being a uniformly distributed random number, such that vertices are randomly positioned without any crystal lattice relationship. The signal of the bright field detector simulated by such MC simulations complies with the second scan taken 12 seconds after the first, see in Fig. 1 the blue, purple dash-dotted and yellow curves. A sequence of scans show changing signals of the identical particle. Some NR even have stripes of varying intensity that lie parallel to the scanning direction. It is assumed that the higher transmission yield is obtained due to channeling effects dependent on crystallization. The polar diagrams of the diffraction images in Fig. 2 depict the resultant distribution of the scattering; left: that of a single atom representing the differential cross section as generally used for MCs; right: the diffraction pattern of a Laue diffraction calculation on a lattice with 704 atoms. Comparing the two intensity distributions reveals that in case of crystal diffraction, the electron's wave amplitudes are channeled into the center of the bright field detector. The probability of interacting inelastically, thus incoherently and mostly scattered outside the bright field detector, is 45.2%. If channeling occurs, expect for the small fraction of intensity of the secondary maxima, most of the remaining 54.8% hit the bright field detector. We have observed 53.8% intensity on the bright field detector, see Fig. 1 red curves.

For a quantitative determination of NP sizes, appropriate physical modeling is required. Therefore, a combination of a Monte Carlo approach accounting for the randomness of size and orientation of crystal domains and of inelastic scattering processes with crystal diffraction is under development.

Fig. 1

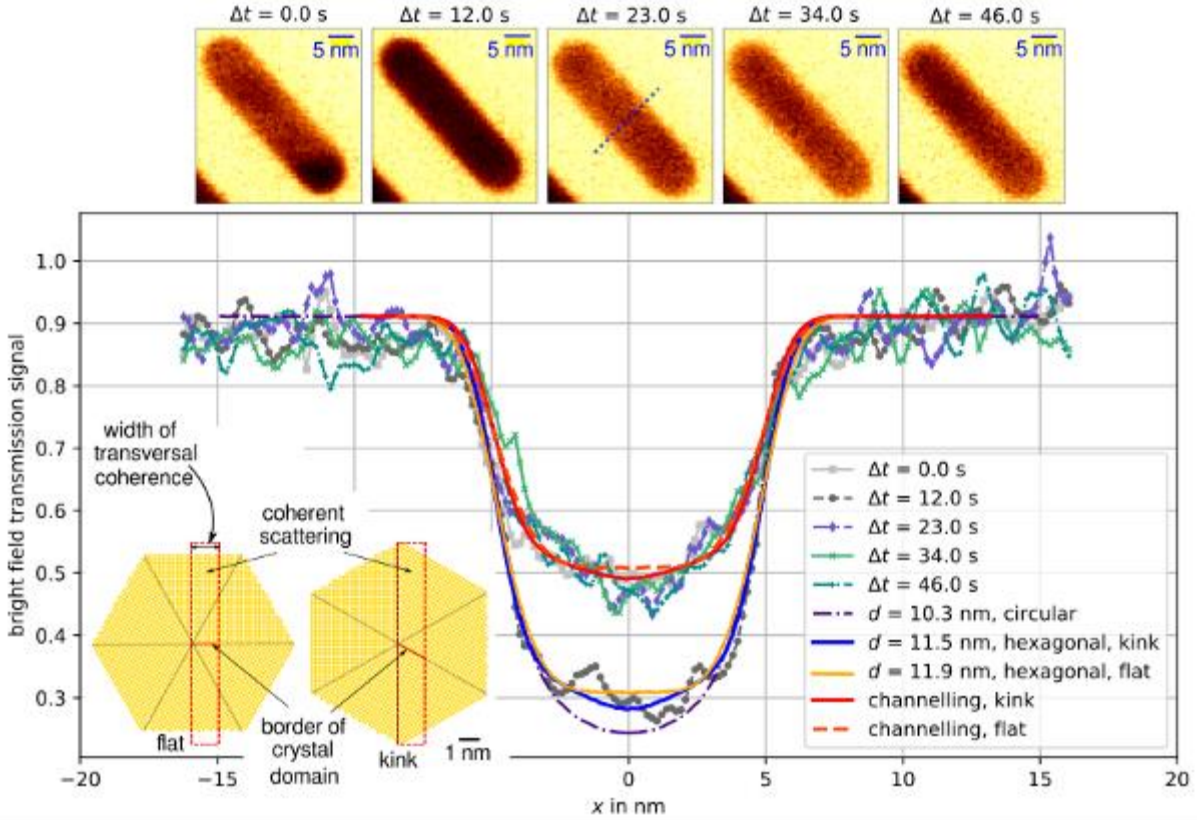

Figure 1: Micrographs taken subsequently with 1600 ns dwell time, 50 pA beam current, 30 keV beam energy and pixel sizes of 0.49 nm each; diagram of the profiles along the axis perpendicular to the rod axis at the mid of the rod; inset: drawings indicating the rods as being of hexagonal structure in cross sectional view [6].

Fig. 2

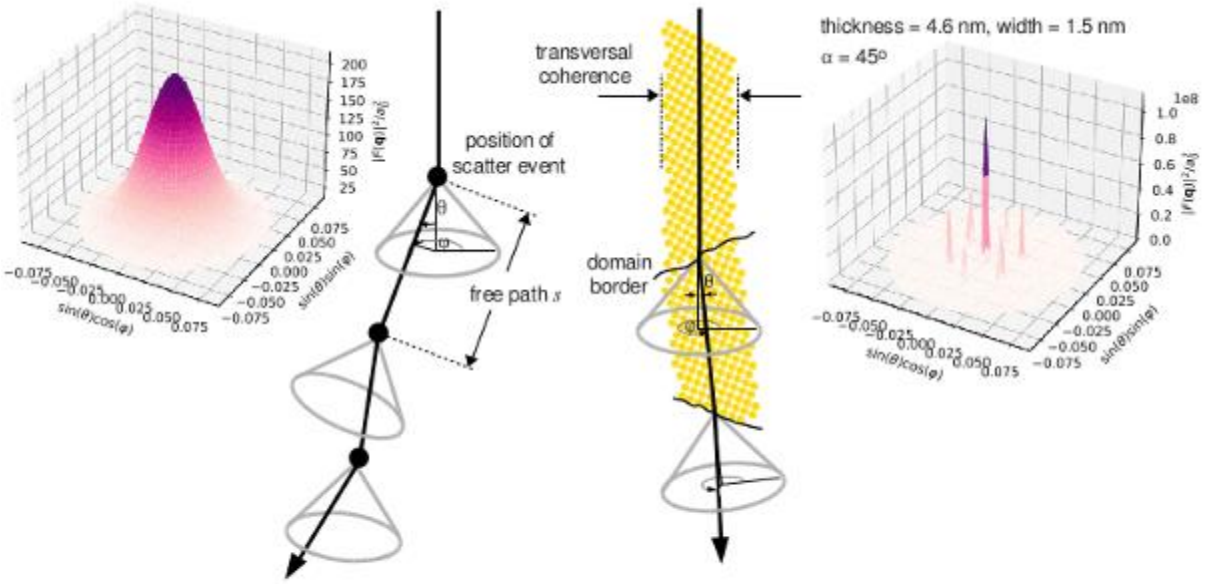

Figure 2: Principles of STEM-in-SEM Monte Carlo approaches without and with crystal domains (center); scattering resp. diffraction intensity distributions (left and right), the diffraction distribution on the right is obtained from a lattice of an area of 1.59 nm x 1.59 nm complying with the transversal coherence length and a height of 4.6 nm with 704 atoms.

Fig. 3

[1] Kisielowski, *Observing Atoms at Work by Controlling Beam-Sample Interactions, Adv. Mater.* **27** (2015), 5838-5844, doi:10.1002/adma.201500082

[2] Salvat , Jablonski, Powell, ELSEPA - *Dirac partial-wave calculation of elastic scattering of electrons and positrons by atoms, positive ions and molecules_*, Computer Physics Communications **165** (2005) 157-190, doi:10.1016/j.cpc.2004.09.006

[3] Villarrubia, Vladár, Ming, Kline, Sunday, Chawla, List, *Scanning electron microscope measurement of width and shape of 10 nm patterned lines using a JMONSEL-modeled library*, Ultramicroscopy **154** (2015) 15-28, doi:10.1016/j.ultramic.2015.01.004

[4] Shinotsuka, Tanuma, Powell, Penn *Calculations of electron inelastic mean free paths. XII. Data for 42 inorganic compounds over the 50 eV to 200 keV range with the full Penn algorithm*, Surf. Interface Anal. **51** (2019), 427-457, doi:10.1002/sia.6598

[5] GEANT4-Collaboration: S. Agostinelli and others, *Geant4 - a simulation toolkit*, Nuclear Instruments and Methods in Physics Research Section A: Accelerators, Spectrometers, Detectors and Associated Equipment **506** (2003), 250-303, doi:10.1016/S0168-9002(03)01368-8

[6] Carbo-Argibay et al, *The Crystalline Structure of Gold Nanorods Revisited: Evidence for Higher-Index Lateral Facets*, Angew. Chem. Int. Ed. **49** (2010), 9397-9400, doi:10.1002/anic.201004910

IM5.P004

Measurement of electron dose in TEM mode at a JEOL TEM/STEM JEM 2200FS

H. Kirmse[1], F. Bär[1], C. T. Koch[1]

[1]Humboldt University of Berlin, Physics, SEM group, Berlin, Germany

1. Introduction

Electron radiation sensitive materials are subject of vivid fundamental research using transmission electron microscopy. But, organic materials [1] and hybrid inorganic/organic systems [2] suffer from high electron dose. There are several means to avoid radiation damage by e.g., low-dose, specimen cooling, and scanning TEM [3]. In order to tailor TEM measurements to the needs of both, specimen and TEM technique the electron dose has to be quantified and a good compromise has to be identified.

2. Objectives

This work aims at the quantification of the electron dose in a JEOL TEM/STEM JEM 2200FS running in TEM mode. Experimental parameters shall be given for preserving the TEM specimen from radiation damage and for optimum signal-to-noise ratio of the particular investigation technique.

3. Materials & methods

Measurement of beam current is performed with an in-built viewing screen connected to ground instead of using a Faraday cup. A large hole in the specimen enables electrons passing vacuum exclusively. Parallel beam is ensured by sharp diffraction spots of a GaAs single crystal.

The electron dose mainly depends on two parameters: spot size and alpha selector setting. Spot size is controlled by condenser lens (CL) 1. It defines the number of electrons passing the CL aperture (Fig. 1). Alpha is controlled by CL2 and defines the area illuminated by the identical number of electrons passing the CL aperture (Fig. 2).

Subsequently, the measured beam current I is correlated with the illuminated area A. Finally, the electron dose D is calculated with q being the elementary charge:

$$D = I / (A \times q)$$

Beam current measurement and dose calculation are performed for all combinations of spot size and alpha.

4. Results

In Fig. 3 the beam current is exemplarily given for the combination of spot size 3 and alpha 3 as a function of magnification and CL aperture size. Filled dots mark measurements where the electron beam covers an area smaller than the viewing screen. Hence, the measured current does not follow the inverse quadratic dependence on the magnification anymore and can be directly related to the illuminated area. The error bars of the measurement range within the size of the markers.

Fig. 4 gives the full data set of experimentally derived electron dose on logarithmic scale. Lowest dose is found for spot size 5 and alpha 3 with about 0.3 e-/Å2×s. Highest dose is found for spot size 1 and alpha 1 with about 42 e-/Å2×s. There is no overlap of electron dose values between the different alpha settings. The dose goes down with gradually changing from spot size 1 to spot size 5 for fixed alpha. To enter lower dose level, one has to switch to the next alpha value (e.g. from 1 to 2) and start with spot size 1 again.

5. Conclusion

This work delivers quantitative values of the electron dose. Spot size and alpha setting for minimum and maximum dose are found. A good compromise for suppression of radiation damage but still good performance of TEM technique seems to be the combination of spot size 5 and alpha 1 giving a dose of about 16 e-/Å2×s.

Ref:

[1] Z.J.W.A. Leijten et al., J. Phys. Chem. C 121 (2017) 10552.

[2] S. Chen et al., Science Bulletin 65 (2020) 1643.

[3] R.F. Egerton, Ultramicroscopy 127 (2013) 100.

[4] Fig. adapted from the instruction manual of the JEOL JEM 2200FS.

Fig. legends:

Fig. 1: Spot size control with CL1.

Fig. 2: Alpha control by CL2 [4].

Fig. 3: Beam current density (spot 3, alpha 3).

Fig. 4: Electron dose.

Fig. 1

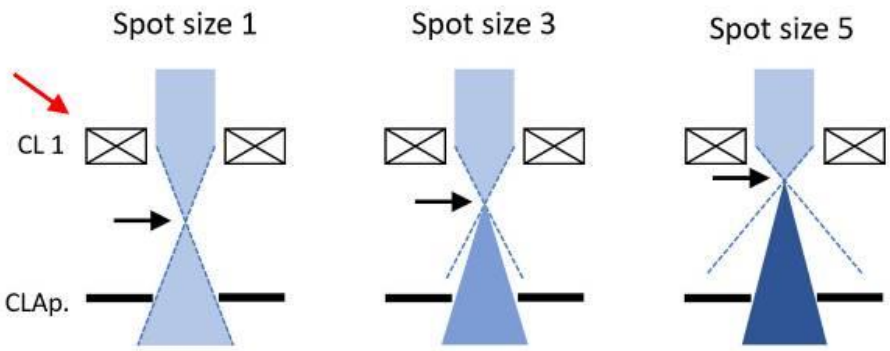

Fig. 2

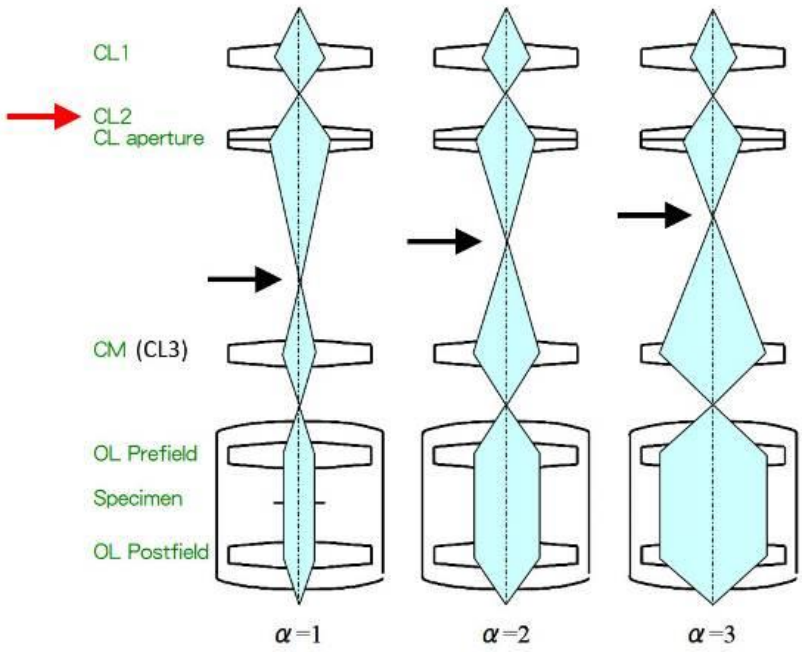

Fig. 3

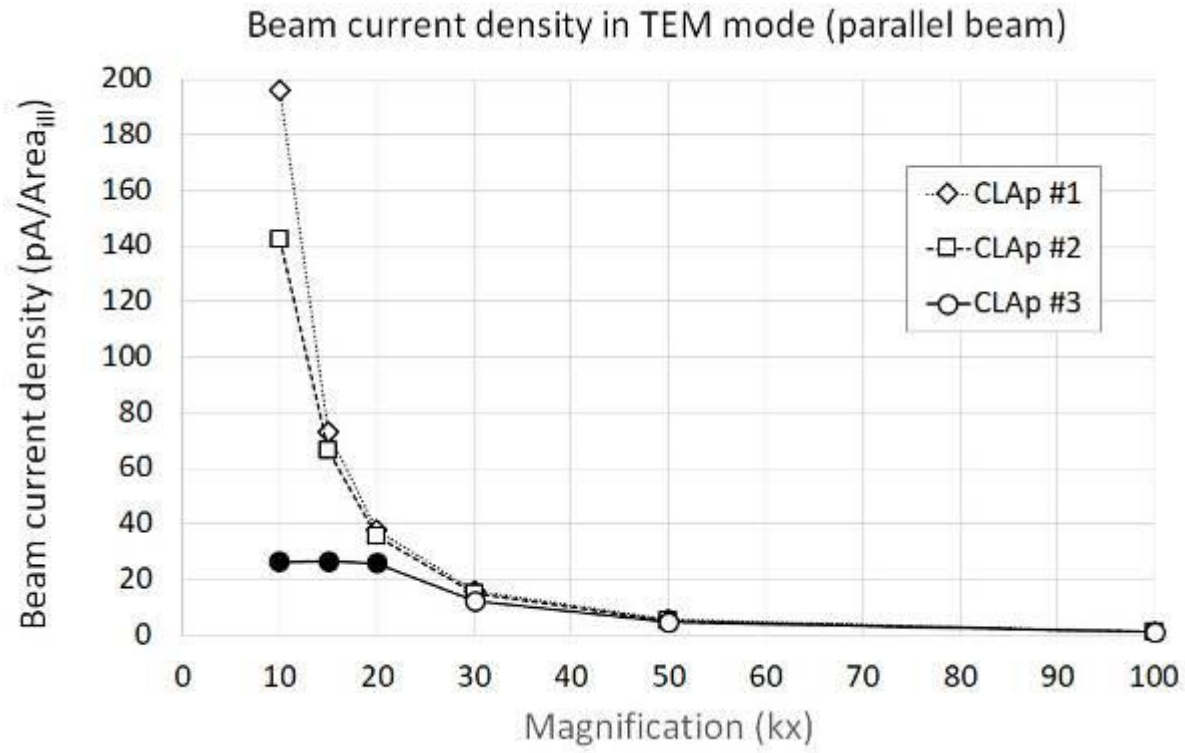
Beam current density in TEM mode (parallel beam)
Beam current density (pA/Area$_{ill}$)
200
180
160
140
120
100
80
60
40
20
0
0
10
20
30
40
50
60
70
80
90
100
Magnification (kx)
CLAp #1
CLAp #2
CLAp #3

Fig. 4

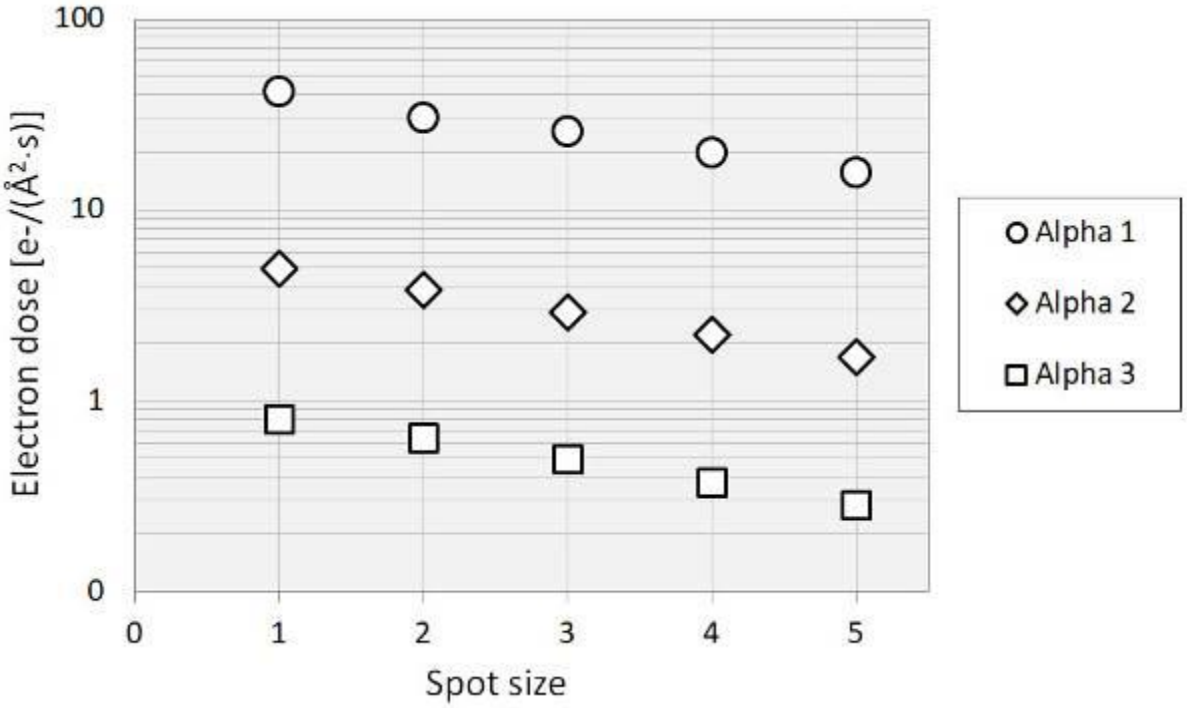
100
10
1
0
Electron dose [e-/(Å^2·s)]
0
1
2
3
4
5
Spot size
Alpha 1
Alpha 2
Alpha 3

IM5.P005

TEM characterization of amorphous molecular clusters for directional white-light generation

J. Belz[1], J. Haust[1], A. Beyer[1], K. Volz[1]

[1]Philipps-University Marburg, Department of Physics & Structure & Technology Research Laboratory, Marburg, Germany

Motivated by the discovery of a highly non-linear optical response, occurring as directional white-light emission (WLE) in tin-sulfide-clusters [1], we investigate structurally similar organic functionalized diamondoids as well as inorganic cluster molecules.

The goal of our TEM (transmission electron microscopy) study is to identify the structure as well as chemical bonding by analyzing the pair distribution functions (PDF) and the electron energy loss spectra (EELS) of these materials in the low and high loss regime. These shall be correlated to the optoelectronic properties of the materials to discover structural prerequisites for the WLE mechanism.

In order to achieve high quality samples for TEM that have a suitable thickness, we embed the specimens in epoxy and cut them into 50 nm thick slices using a LEICA ULTRACUT UCT ultramicrotome (UMT).

The electron scattering measurements to derive the pair distribution function (PDF) are carried out with a JEOL JEM-3010 TEM equipped with a TVIPS-XF416 ES camera. The EELS measurements are done with a double-aberration corrected JEOL JEM-2200FS (S)TEM that is additionally equipped with a PNDetector pnCCD direct electron camera with full frame rate of 2000 fps. An additional precession electron diffraction (PED) unit (Nanomegas) is used on both microscopes.

By using conventional and precession diffraction we derive pair distribution functions (PDFs) of the typically amorphous materials providing the inter- and intramolecular arrangements of these molecules (Fig. 1). These properties are considered to play a fundamental role in the process of white light emission since the inclusion of nanometer scale crystallites can suppress the WLE [2]. By using diffraction experiments the PDFs can be used to investigated molecules in a dose efficient manner which is shown to be critical for some of the organic clusters [3].

In conjunction with a scanning unit we acquire spatially resolved diffraction patterns in 4-dimensional datasets. We investigate the limits of scanned PDF measurements with and without precession in terms of accuracy and dose requirements aiming for a spatial resolution down to a few nanometers.

Finally, we consolidate our findings with X-ray scattering experiments, scattering simulations and density functional theory calculations.

References:

[1] N. W. Rosemann et al., Science 352, 1301 (2016).

[2] J. Haust et al., ChemPhotoChem 6 (2022).

[3] J. Belz et al., The Journal of Physical Chemistry C 126, 9843 (2022).

Fig 1: Electron diffraction and the derived PDF of an amorphous WLE showing a characteristic ring pattern which relates to molecular and atomic arrangements.

Fig. 1

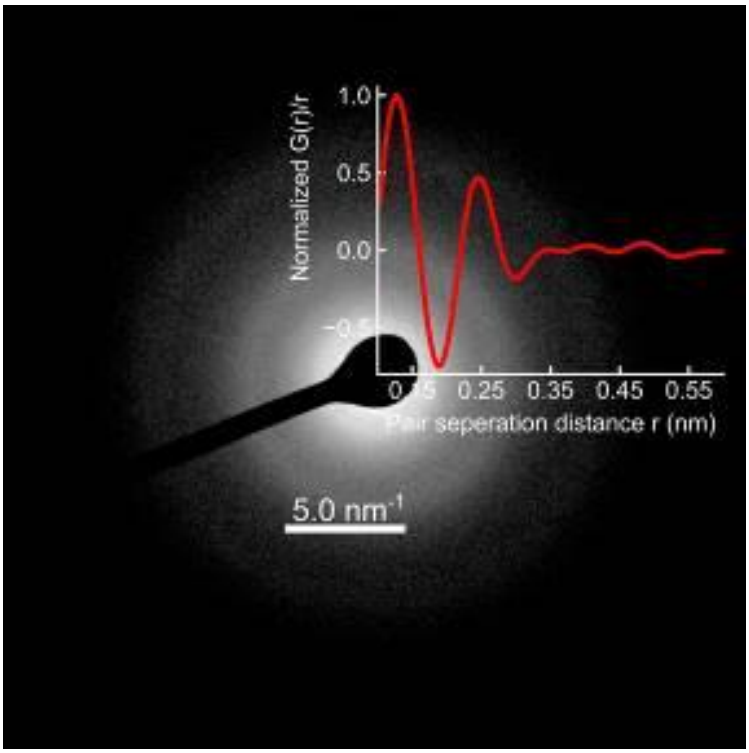
Normalized G(r)/r
1.0
0.5
0.0
0.25
0.35
0.45
0.55
Pair seperation distance r (nm)
5.0 nm-1

IM5.P006

The effect of muffin-tin radii on potentials used for multislice simulations

C. Bick[1], D. Hüser[1]

[1]Physikalisch-Technische Bundesanstalt, 5.24 Electron Microscopy, Braunschweig, Germany

Advancements in the semiconductor industry allow for ever smaller miniaturization. The simulation of scanning transmission electron microscopy (STEM) images can assist in understanding measurements necessary for the characterization of those nanoscale structures.

In multislice simulations of STEM images the total potential of the specimen commonly gets constructed by a linear superposition of atomic potentials, while the atomic potentials themselves are related to scattering amplitudes in the first Born approximation. This approach is called independent atom model, since bonding effects are neglected [1]. On the other hand, the muffin-tin approximation is a common method to account for the differences in the electron distribution in solids [2], in which the atomic potentials are assumed to be radially symmetric inside a sphere around the nucleus and constant outside of it.

In this work we compare the results of differently derived potentials to gain a better understanding of the impact of those potentials on multislice simulations. We compare independent atom model potentials using a common parametrization [1] with atomic potentials derived from charge densities limited by muffin-tin radii, which are based on the ELSEPA software package [2]. We further compare those results with the full density functional theory (DFT) calculations of Susi et al. [3].

The potentials show a significant deviation between free atoms and those limited by the muffin-tin spheres as well as the DFT results. Comparison with experimental data will reveal the appropriateness of models.

[1] E. J. Kirkland, "Advanced computing in electron microscopy" (Springer, 2020).
[2] F. Salvat et al., Computer Physics Communications 165, 157-190 (2005).
[3] T. Susi et al., Ultramicroscopy 197, 16-22 (2019).

IM5.P007

Contribution of strain and relaxation to dynamical diffraction in 4D-STEM signals

F. Otto[1], L. Niermann[1], T. Niermann[1], M. Lehmann[1]

[1]Technische Universität Berlin, Instutitut für Optik und Atomare Physik, Berlin, Germany

Novel semiconductor devices have continuously been decreasing in size over the last few decades. With decreasing dimensions, a devices" electronical properties are mostly governed by effects from material interfaces, opening up a wide range of parameters used for modern semiconductor engineering. Strain engineering, for example, can lead to much desired quantities like high carrier mobilities in silicon transistors [1]. For the further advancement of semiconductor engineering and device growth, knowledge of strain fields is crucial feedback for the growth process.

Anyhow, gaining knowledge of growth-induced strain and strain relaxation effects on a nanometer scale can be challenging. One commonly used method for mapping strain is Nanobeam Electron Diffraction (NBED) [2] where one calculates the displacement from the variation of the recorded diffraction spots. In NBED measurements, however, the intensity in a diffraction spot can vary due to dynamical diffraction effects, posing a common problem for spot position detection [3]. To minimize these effects, one typically tries to use a collimated electron beam and focus solely on the relative distance of the diffraction spots. Nevertheless, by doing this, spatial resolution is limited by the beam diameter which typically is in the order of a few nanometers.

In this work, we have chosen an alternative way by investigating the patterns in diffraction discs. We acquired 4D-STEM signals of (Al,Ga)N quantum wells (QWs) in a GaN matrix using a convergent electron beam. This results in a much smaller beam diameter at the specimen surface. At every scan position, this yields a disc shaped diffraction spot mimicking the shape of the used condenser aperture where each disk contains features of dynamical diffraction. We evaluate these features for diffraction spots for a systematic row perpendicular to the QW layers. Figure 1 shows one measurement obtained this way, using a representation of the dataset reduced from four into two dimensions: This is achieved by spatially averaging the data along the y-axis and in reciprocal space along the axis perpendicular to the systematic row. The recorded pattern changes visibly in the region of the QW layer. However, these changes also extend further into the unstrained GaN. We compare the obtained results to beam-calculations solving Darwin-Howie-Whelan equation. The strain field was simulated using finite element calculations (Figure 2). As a result, we attribute long range changes in the recorded patterns to relaxation effects of specimen surfaces. For varying QW sizes and specimen thicknesses, we employ this method to investigate relaxation effects.

[1] Friedrich Schäffler 1997 Semicond. Sci. Technol. 12 1515
[2] V. B. Ozdol et al Appl. Phys. Lett. 106, 253107 (2015)
[3] T.C. Pekin et al., Ultramicroscopy 176 (2017) 170–176

Figure 1: 2D representation of 4D STEM data scanning across an AlGaN/GaN QW structure. In the highlighted region shifts of the diffraction disc and changes in patterns from dynamical diffraction become visible.

Figure 2: Calculated displacement relative to a GaN reference lattice showing the effects of relaxation. The simulated beam direction runs from bottom to top, meaning a positive displacement effectively points downwards.

Fig. 1

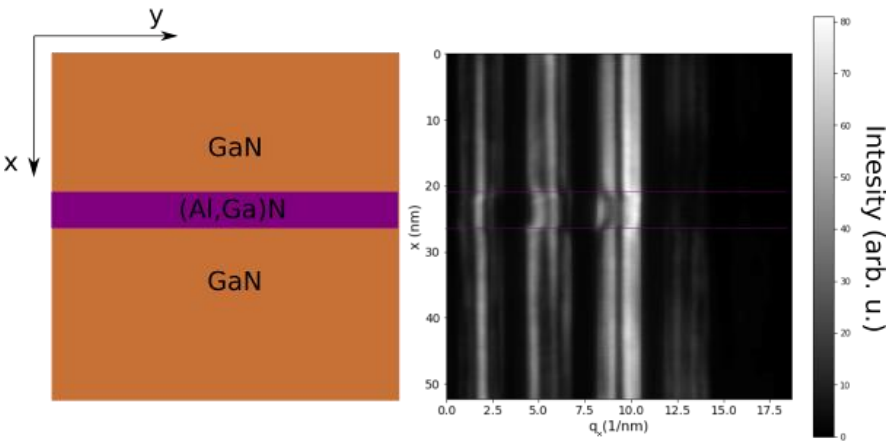
y
x
GaN
(Al,Ga)N
GaN
x (nm)
0
10
20
30
40
50
0.0
2.5
5.0
7.5
10.0
12.5
15.0
17.5
q_x(1/nm)
Intesity (arb. u.)
0
10
20
30
40
50
60
70
80

Fig. 2

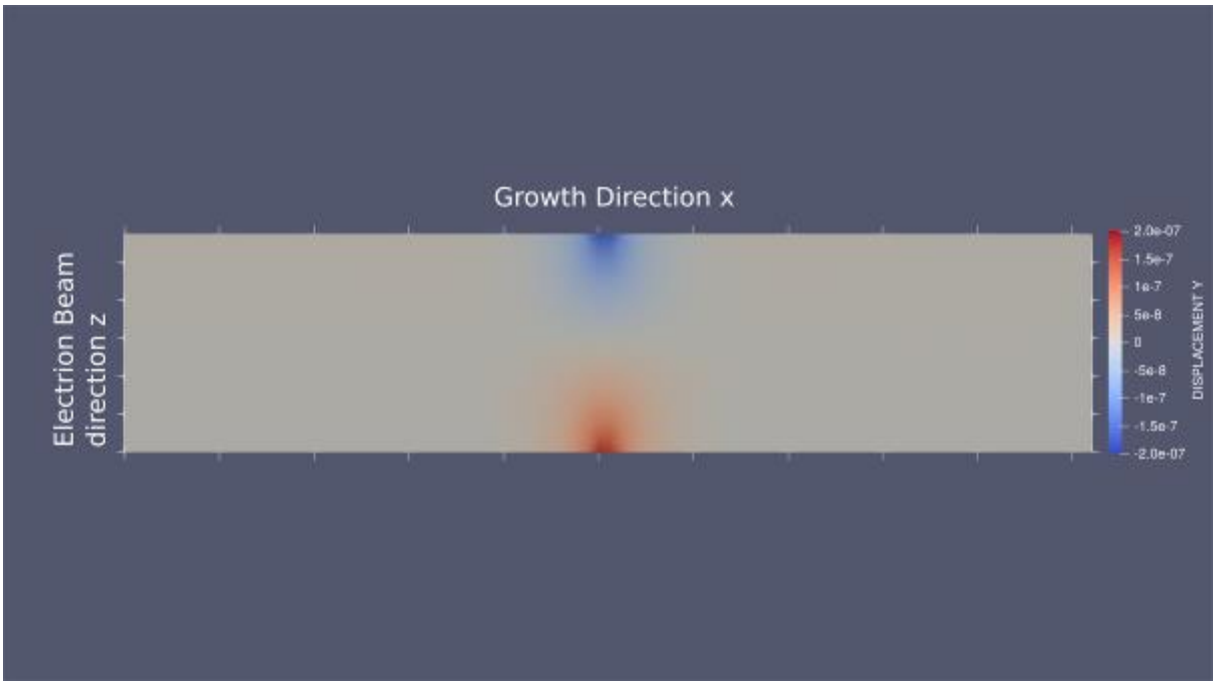
Growth Direction x
Electrion Beam
direction z
2.0e-07
1.5e-7
1e-7
5e-8
0
-5e-8
-1e-7
-1.5e-7
-2.0e-07
DISPLACEMENT Y

IM5.P008

Enhancing relative aberration measurements in the TEM by PCTF-corrected cross-correlation

M. Linck[1]

[1]CEOS GmbH, Research and Development, Heidelberg, Germany

In transmission electron microscopy, the evaluation of Thon ring patterns in diffractograms of defocused amorphous objects is the most often applied method to determine the present aberrations of the TEM: an individual diffractogram provides access to defocus C1 and two-fold astigmatism A1 and a tilt tableau of diffractograms enables the measurement of the existing higher order aberration coefficients by analysing tilt-induced C1A1 contributions [1].

Complementary, the cross-correlation (XC) analysis is a valuable tool to determine image displacements in between two or more subsequent images. This is often used for drift analysis but can also be used in a systematic tilt tableau to assess the existing aberration function by analysis of tilt-induced image displacements [2].

In the case of weak phase objects (WPO), it turns out that the phase contrast transfer function (PCTF) can have a considerable effect on the quality of the XC analysis. This is mainly due to the fact that the PCTF can cause contrast reversals between the two images which leads to mixed partial correlation and anti-correlation of the two respective images. As an example, Fig. 1 shows the XC of an over-/ underfocus image pair. Fortunately, this partial anti-correlation effect, which corresponds to a frequency-dependend phase jump by pi in the XC's Fourier phase, can quite simply be corrected for. As a consequence, the resulting PCTF-corrected XC becomes much more robust and more easy to interpret in terms of image shift.

In the WPO approximation antisymmetric aberrations such as coma can be considered as frequency-depenend image shifts (point-spread function = coma tail). Therefore, it becomes possible to recover relative changes of 2nd order aberrations, i.e. three-fold astigmatism A2 and axial coma B2 in between two images, if PCTF artifacts are properly corrected. Fig. 2 shows the PCTF-corrected XC of two images comprising a hexapole change in between. Subsequently, the relative A2B2 changes can be recovered from the Fourier phase of the XC image.

The PCTF-corrected XC can help a lot to improve the precision of image shift determination, and moreover reduces the required number of images for calibrations on second-order aberration changes. Alternatively, the analysis of the existing tilt tableau method can benefit from additional information on relative A2B2-changes during tilted illumination. [€]

References:
[1] F. Zemlin et al., Ultramicroscopy 3 (1978), 49-60.
[2] A.J. Koster et al., Ultramicroscopy 38 (1991), 235-240.
[€] CEOS GmbH has received funding from the European Union"s Horizon 2020 research and innovation program under grant agreement No. 823717 – ESTEEM3.

Fig.1: (a) The XC of two images in under-/overfocus is not a peak any more because of partial contrast reversals between the images. These show up as pi phase jumps in the XC's Fourier phase. (b) Since C1A1 of both images can be determined at the same time, the sign of the contrast contributions can be properly corrected to obtain a sharp XC peak with a uniform wedge-shaped Fourier phase.

Fig.2: (a) The pure XC of two images taken with different hexapole excitations is difficult to analyse. (b) Using the PCTF-corrected XC, however, further analysis in terms of three-fold astigmatism is straight forward. (inlay: robust phase contours by Hanning-window)

Fig. 1

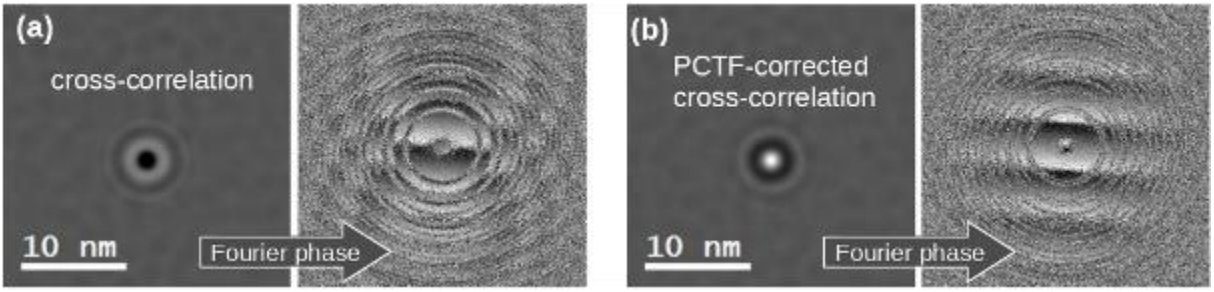
(a)
cross-correlation
10 nm
Fourier phase
(b)
PCTF-corrected
cross-correlation
10 nm
Fourier phase

Fig. 2

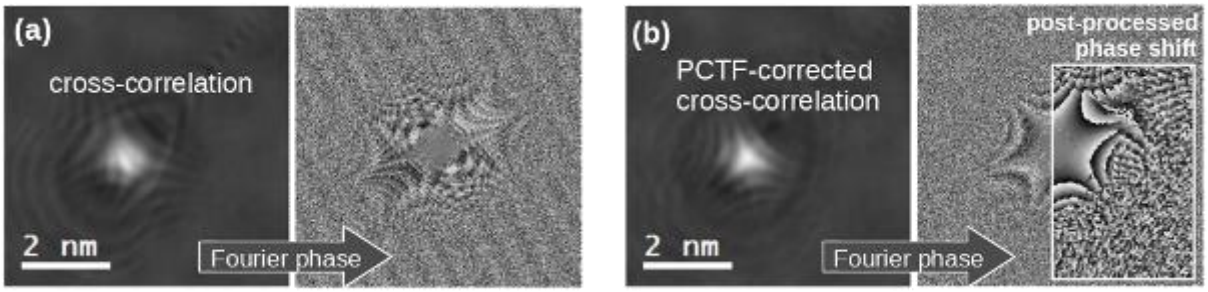
(a)
cross-correlation
2 nm
Fourier phase
(b)
PCTF-corrected
cross-correlation
2 nm
Fourier phase
post-processed
phase shift

IM5.P009

Deep learning pipeline for statistical quantification of amorphous two-dimensional materials and dynamic tracking

C. Leist[1], H. Qi[1], U. Kaiser[1]

[1]University Ulm, Central Facility Electron Microscopy Materials Science Electron Microscopy, Ulm, Germany

Recent years have witnessed the rise of amorphous 2D (*a*-2D) materials. The combination of atomic thinness and lack of long-range order has endowed *a*-2D materials with unique characteristics, such as ultra-high uniformity, excellent mechanical and chemical stability, and abundance in catalytic-active sites. Owing to the atomic thinness of *a*-2D materials, direct observation of atomic arrangements can be well achieved using aberration-corrected high-resolution transmission electron microscopy (HRTEM) (*1*). However, extracting structural information from HRTEM images of *a*-2D materials is a nontrivial work because every individual atom in the HRTEM image (Fig. 1a) needs to be pinpointed. Moreover, research on reaction dynamics, such as amorphous-crystalline phase transition within an *a*-2D material, requires analysis of every frame from the time-resolved image series, leading to an exponential increase in the workload.

In this work, we developed a U-net-based neural network (NN) for comprehensive image analysis in *a*-2D materials. HRTEM has been conducted on the *C*c/*C*s-corrected microscope operated at 80 kV, resolving single atoms with strong contrast (*2*). The NN is capable of atom coordinate identification and segmentation of evaluation-suitable regions with high precision. This has been achieved by training the NN exclusively on simulated images. A semi-random atomic model with porous and bilayer areas led to the successful recognition of complex attributes in experimental images, including disorder, micropore, and surface contaminations. The NN"s robustness against intensity inhomogeneity was further enhanced by introducing intensity gradients in the training datasets. Implementation on the experimental images of monolayer *a*-carbon and *a*-polymer provided multifold statistical datasets and direct visualization of the short-range-ordered structures. Although designed for *a*-materials, our deep learning pipeline is readily generalizable to crystalline samples, enabling the identification of local defects and grain boundaries. We envisage that automated quantification of short-range order will bring new insights into the structural understanding of *a*-2D systems, laying the foundation for the establishment of structure-property correlation in this rising class of materials. The deep learning approach may also pave the way for probing dynamic processes with efficiency and precision, e.g., amorphous-crystalline transition, amorphization, nucleation and crystal growth.

Acknowledgement

This research is funded by the Deutsche Forschungsgemeinschaft (DFG, German Research Foundation) – 424798828; 492191310 and the European Union's Horizon2020 research and innovation program (No. 881603, GrapheneCore3). We thank Dr. Xue Liu for providing the *a*-2D carbon monolayer samples.

Reference

1. P. Huang et al. *Science,* **342**, 224, 2013
2. M. Linck et al. *Phys. Rev. Lett.* **117**, 76101, 2016

Fig. 1. Challenges of automated image analysis. a, HRTEM image of monolayer *a*-carbon. b-d, Cropped out images from the boxed regions in (a), showing areas of disorder (b), micropore (c), and surface contamination (d).

Fig. 2. Automated image evaluation via NN. a, 80 kV HRTEM image of monolayer *a*-carbon. b, Segmentation applied to (a) for removal of non-monolayer regions (black) and micropores (purple). c, Enlarged image from the boxed region in (a). d, NN mapping of polygons. e-g, Statistical histogram of bond angles, lengths, and polygon frequency. Scale bar: 2 nm (a); 1 nm (c)

Fig. 1

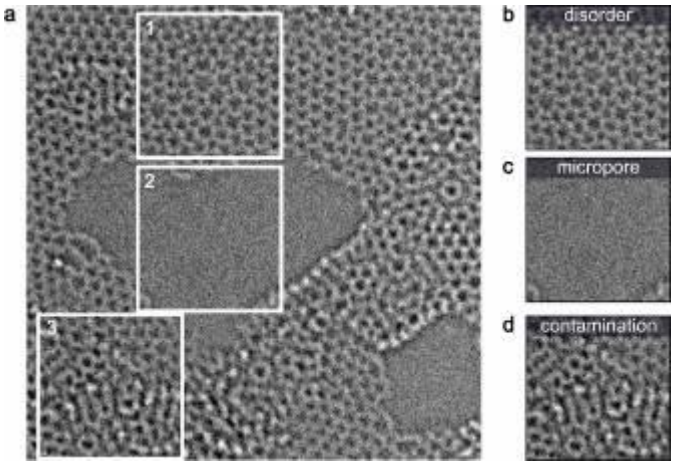
a
1
2
3
b
disorder
c
micropore
d
contamination

Fig. 2

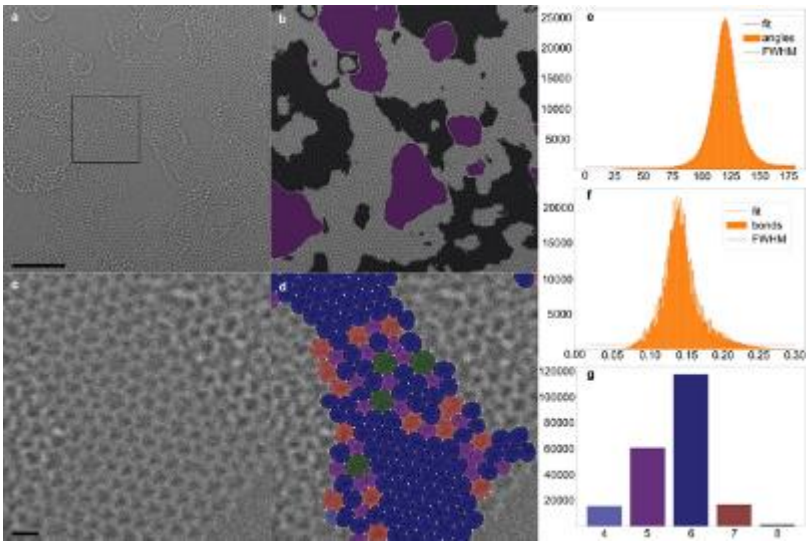
a
b
c
d
e
fit
angles
FWHM
f
fit
bonds
FWHM
g
4
5
6
7
8

IM5.P0010

Investigation of the impact of multiple plasmon-loss on low-angle electron diffraction by energy-filtered 4D-STEM

H. L. Robert[1,2], K. Müller-Caspary[1,3]

[1]Forschungszentrum Jülich, Ernst Ruska-Centre, Jülich, Germany
[2]RWTH Aachen University, Aachen, Germany
[3]Ludwig-Maximilians-University Munich, Department of Chemistry, Munich, Germany

The introduction of momentum-resolution in STEM, thanks to fast cameras [1], brought new motivations for the quantitative understanding of low-angle electron diffraction, which, due for instance to its richness in inelastic contributions [2], is challenging to simulate. Previous work, employing energy-filtering, led to the observation of intensity redistribution in diffraction space following the excitation of a volume plasmon mode [3]. This process could be included in calculations by use of a transition potential, following a dipolar approximation. A qualitative agreement between simulation and experiment was thus obtained, though rigorous quantitative approaches require the introduction of further contributions [4].

In this context, the influence of multiple plasmon-losses was left out. Nevertheless, whether the redistribution process is the same from each successive transition, in terms of the recorded intensity, remains an open question. In particular, by removing the propagation of the mutually incoherent wave-functions created by each distinct energy-loss, it becomes possible to express the inelastic intensity as the convolution of the elastic intensity by a Lorentzian kernel.

An energy-filtered 4D-STEM experiment was thus performed on a 74 nm-thick Al specimen, using an aberration-corrected Hitachi HF5000 instrument equipped with a CEFID energy filter leading to a Medipix3 camera. 10 eV-wide windows were positioned on the first five plasmon peaks of the EEL spectrum (PL_n) as well as on the zero-loss peak ($ZL=PL_0$) [5]. The resulting angle-dependent measurements are plotted in fig. 1.a and show a similar spreading of diffracted intensity as previously reported [3]. This is further verified by the ratios plotted in fig. 1.b, displaying a peak at the angle where the intensity tends to be redistributed to.

For each transition, e.g. PL_0 to PL_1, PL_1 to PL_2, etc…, the convolution approximation was tested by optimizing a Lorentzian L_n, to minimize the sum of $|(L_n \otimes PL_{n-1})-PL_n|^2$ in diffraction space. The resulting intensity curves are depicted in fig. 2.a-e and show a high quality of fit, thus demonstrating the accuracy of the approximation. The extracted kernels, depicted in fig. 2.f, are found to differ slightly from one another, though the characteristic spatial frequency $q_{\delta E}$ remains in an interval of 0.15 to 0.23 nm^{-1}. Similar results were obtained in regions of higher thickness.

Those findings constitute experimental evidence for the validity of an empirical convolutional approach to account for multiple plasmon scattering. Aspects of simulation efficiency, reliability of Lorentzian parameters, and propagation, are also to be discussed.

Fig.1: a) Angle-dependent profiles obtained from each recording, expressed as proportions of incident intensity by Sr. b) Ratio of successive profiles. c) PACBED patterns. d) BF images.

Fig.2: a-e) Plots of successive transitions, with depiction of pre-transition and post-transition intensities normalized to incident beam, and result of convolution. f) Extracted Lorentzian kernels.

Fundings from the Initiative and Network Fund of the Helmholtz Association under contracts VH-NG-1317 and ZT-I-0025 are gratefully acknowledged.

[1] H. Ryll ; J. instr. 11, P04006 (2016)

[2] K. Müller-Caspary et al.; Sci. rep. 6, 37146 (2016)

[3] A. Beyer et. al. ; Sci. rep. 10, 17890 (2020)

[4] T. Grieb et. al. ; Ultram. 221, 113175 (2021)

[5] H. L. Robert et. al. ; App. Phys. Lett. (submitted)

Fig. 1

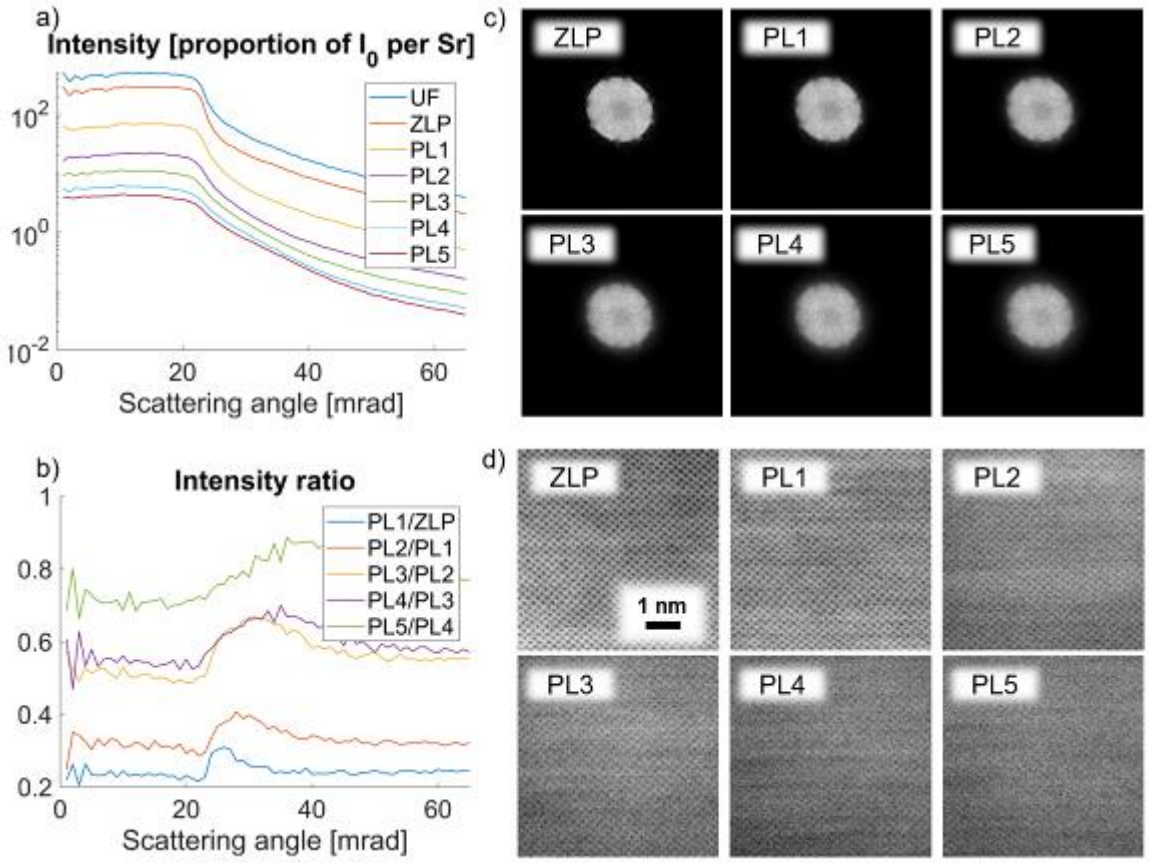
a)
Intensity [proportion of I_0 per Sr]
UF
ZLP
PL1
PL2
PL3
PL4
PL5
Scattering angle [mrad]
b)
Intensity ratio
PL1/ZLP
PL2/PL1
PL3/PL2
PL4/PL3
PL5/PL4
Scattering angle [mrad]
c)
ZLP
PL1
PL2
PL3
PL4
PL5
d)
ZLP
PL1
PL2
1 nm
PL3
PL4
PL5

Fig. 2

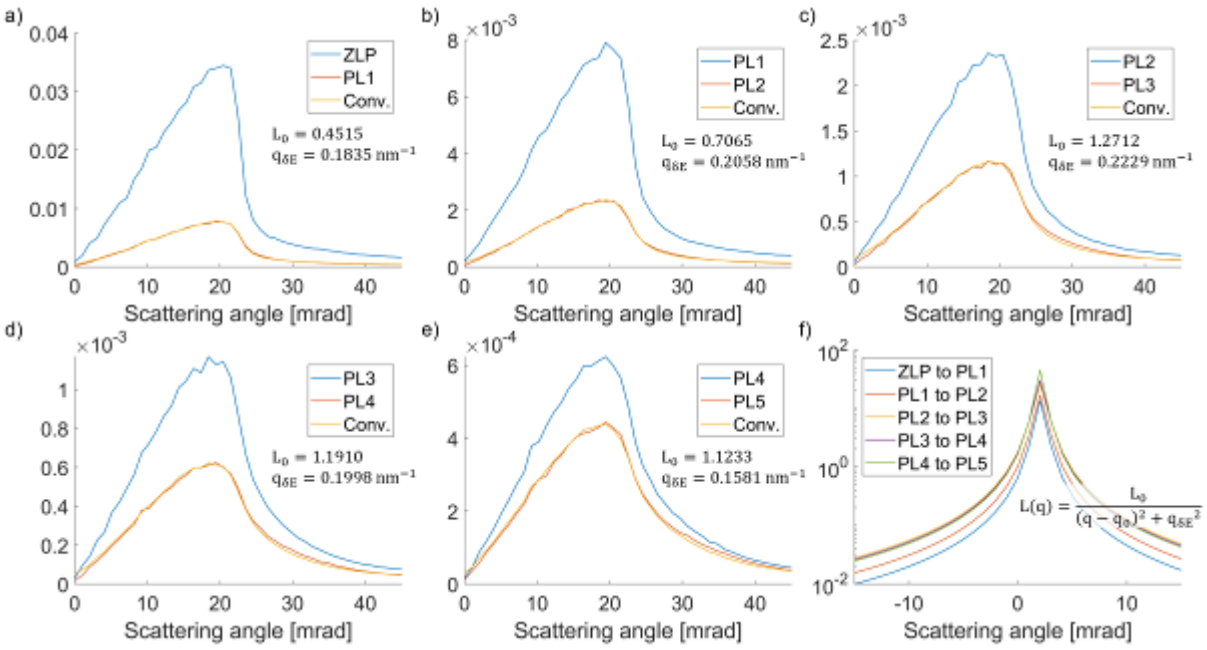
a)
ZLP
PL1
Conv.
$L_0 = 0.4515$
$q_{\delta E} = 0.1835\ nm^{-1}$
Scattering angle [mrad]
b)
PL1
PL2
Conv.
$L_0 = 0.7065$
$q_{\delta E} = 0.2058\ nm^{-1}$
Scattering angle [mrad]
c)
PL2
PL3
Conv.
$L_0 = 1.2712$
$q_{\delta E} = 0.2229\ nm^{-1}$
Scattering angle [mrad]
d)
PL3
PL4
Conv.
$L_0 = 1.1910$
$q_{\delta E} = 0.1998\ nm^{-1}$
Scattering angle [mrad]
e)
PL4
PL5
Conv.
$L_0 = 1.1233$
$q_{\delta E} = 0.1581\ nm^{-1}$
Scattering angle [mrad]
f)
ZLP to PL1
PL1 to PL2
PL2 to PL3
PL3 to PL4
PL4 to PL5
$L(q) = \frac{L_0}{(q-q_0)^2 + q_{\delta E}^2}$
Scattering angle [mrad]

IM5.P0011

A semiconductor-type segmented STEM annular dark-field detector

P. Kükelhan[1], H. Müller[1], G. Guzzinati[1], M. Linck[1], M. Schmid[2], H. Soltau[2]

[1]CEOS GmbH, Heidelberg, Germany
[2]PNDetector GmbH, Munich, Germany

Spectrum imaging has developed into a very useful analytical technique. Behind the energy filter or spectrometer the EEL spectrum is recorded by a fast pixelated detector. For sample navigation and drift correction it is beneficial to simultaneously record an ADF STEM signal.

In order to capture enough signal to form a high-quality EEL spectrum a small camera length of the STEM projective has to be used. As a consequence, for many existing microscopes the inner detector angle for the available ADF detector becomes rather large leading to a small signal-to-noise ratio in the ADF images. In this situation, an additional, dedicated ADF detector inserted directly above the filter entrance aperture and adapted to its geometry can significantly improve the signal quality.

Here, we use a commercially available segmented electron detector (product of PNDetector GmbH [1]) originally developed for back-scattered electron imaging in SEM combined with a modified pre-amplifier configuration. The pneumatic insertion mechanism has been developed to be compatible with the CEOS pre-filter camera housing. The simultaneous acquisition of STEM EELS and ADF signals is fully integrated into the spectrum imaging workflows of our software CEOS Panta Rhei.

The semiconductor-type detector based on fully depleted ultra-pure silicon has a very high sensitivity up to 300 kV, a very low dark current level resulting in an excellent signal-to-noise ratio and allows for fast readout. The detector can be provided in a light insensitive version. The detector with an inner and outer diameter of Ø 5.6mm and Ø 12mm, respectively, is placed in front of the Ø 5mm entrance aperture for the CEOS Energy-Filtering and Imaging Device (CEFID [2]). While the integrated pre-amplifier provides a fixed gain, the main amplifier allows for adjustment of brightness and contrast levels. The signal from the four segments can be combined freely with a 4:1 readout using one main amplifier, while a 4:2 readout resulting in two simultaneous differential signals for orthogonal directions is possible with a second main amplifier. Additionally, the high sensitivity and discrete electron signals allow for quantitative STEM [3].

In this contribution, we exemplify different use cases and features of the detector, especially for high-resolution STEM at very small camera length.

References:
[1] Schmid et al. (2018), New Possibilities for State-of-the-Art Electron Microscopy with Fast Backscattered Electron Detectors, Microscopy and Microanalysis 24

[2] Kahl et al. (2019), Test and characterization of a new post-column imaging energy filter, Advances in Imaging and Electron Physics, Volume 212

[3] Ishikawa et al. (2014), Quantitative Annular Dark Field Electron Microscopy Using Single Electron Signals, Microscopy and Microanalysis 20

[4] CEOS GmbH has received funding from the European Union"s Horizon 2020 research and innovation program under grant agreement No. 823717 – ESTEEM3.

Figure 1: Detector mechanism with ADF STEM detector head and flange suitable for mounting to CEOS camera housing.

Figure 2: STEM image of Au particles on carbon film and corresponding histogram. The discrete electron events in the histogram allow for easily calibrate for quantitative STEM [3].

Fig. 1

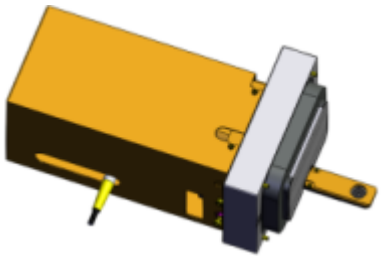

Fig. 2

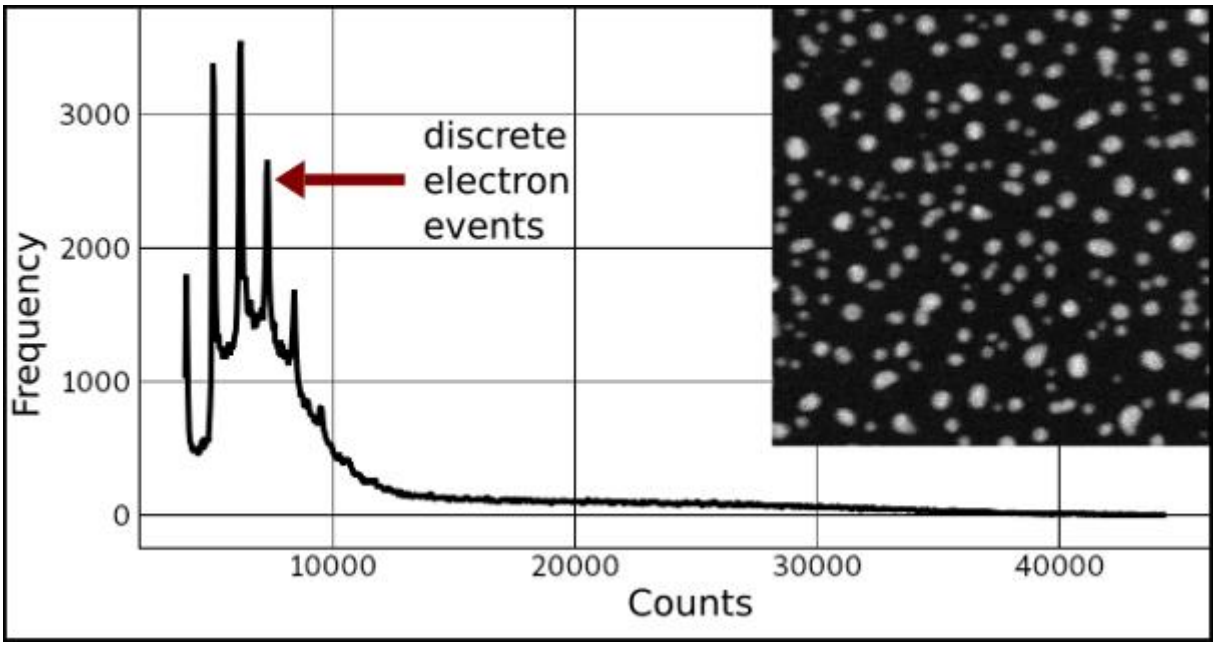
3000
2000
1000
0
Frequency
discrete
electron
events
10000
20000
30000
40000
Counts

IM5.P0012

Change of basis: a compression method for ptychography

1. Gladyshev[1,2], M. Schloz[1,2], T. C. Pekin[1,2], B. Haas[1,2], B. Plotkin-Swing[3], A. Mittelberger[3], C. T. Koch[1,2]

[1]Humboldt-Universität zu Berlin, Institut für Physik, Berlin, Germany
[2]IRIS Adlershof, Berlin, Germany
[3]Nion Company, Kirkland, WA, United States

Introduction

Electron ptychography is a computational imaging technique used to recover the phase of a specimen from a four-dimensional scanning transmission electron microscopy (4D-STEM) dataset consisting of two-dimensional diffraction patterns recorded from overlapping illuminated areas [1].

Objectives

Ptychography is a rapidly growing field, but several practical challenges limit its scope. The amount of data acquired is a major issue. One way to resolve this limitation is to find a lossy compression method for the diffraction patterns. Here we compare various methods that are based on a change of a basis spanning the detector plane.

Materials and Methods

A 4D-STEM dataset was simulated using qstem [2], including thermal diffuse scattering, an effective source of size 0.5 Å and a finite electron dose. To perform electron ptychography we reconfigured a gradient-based optimization framework ADORYM [3]. The object was reconstructed by minimizing the L2 norm of the difference between magnitudes of the experimentally measured diffraction patterns and the ones generated by the model. The loss calculation included transformations that allowed us to use basis sets with fewer elements than the number of pixels and therefore describe the patterns more efficiently.

Results

In the bright field area we compared three basis options: binning, Zernike polynomials and basis vectors generated by the Gram-Schmidt algorithm applied to diffraction patterns recorded before the main acquisition. The dark field region of the patterns was described by a single value accounting for the constant offset. The results are presented in Figure 1.

Figure 1. a) Si crystal ground truth potential used in qstem. **B)-d)** Reconstructed phases of the complex transmission functions obtained using three orthonormal basis sets. The lowest possible number of basis vectors and electron doses (shown in the lower right corners of **b)-d)**) were used. The basis in **b)** consisted of 15 randomly selected diffraction patterns, in **c)** of the first 36 Zernike Polynomials and in **d)** of 45 binning masks. **E)** Fourier shell correlations between compressed reconstructions and ground truth. **F)** A typical log-scaled diffraction pattern. Enlarged bright field basis vectors are shown in **g)-h). g)** shows a basis vector used in **b)**, generated from a recorded pattern. **H)** shows a Zernike polynomial. Binning basis vectors denoted with individual colors are presented in **i)**.

Conclusion

Compressed datasets were 5,000-15,000 times smaller than the original. We show that it is possible to achieve atomic resolution in ptychographic reconstructions even with partial spatial coherence of the electron source and a finite electron dose. The proposed compression approach takes the specific geometry of diffraction patterns into account and retains a sufficient amount of the “intact” information after the transformation. No specific constraints, e.g. a regularization, were used, but as previously shown [4], this could improve the quality of the reconstructions.

[1] W Hoppe, Acta Crystallogr. (1969). Pp. 495-514.
[2] C Koch, PhD thesis, Arizona State University (2002)
[3] M Du et al. Optical Express 29 (2021), pp. 10000-10035. Doi: 10.1364/OE.418296
[4] M Schloz et al., Optical Express 28 (2020), pp. 28306-28323. Doi: 10.1364/ OE.396925
[5] The authors acknowledge financial support through the DFG (SFB 951 and SFB 1404).

Fig. 1

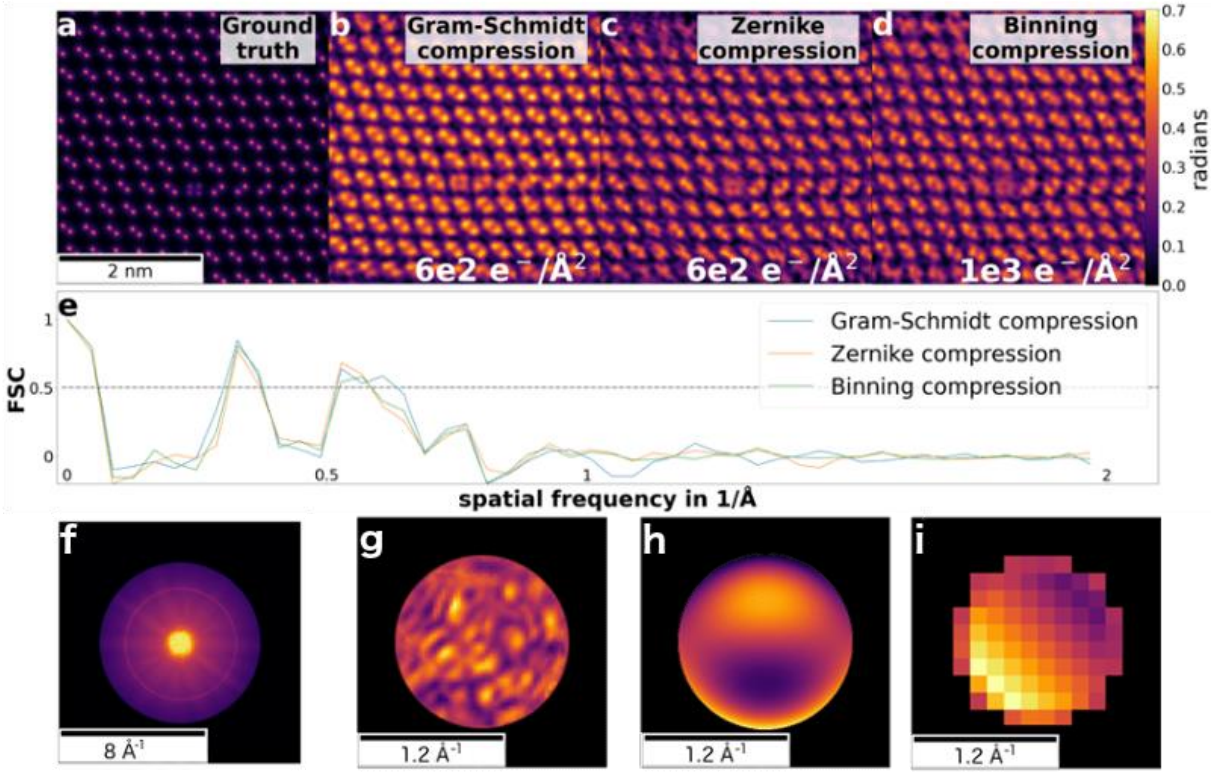
a
Ground truth
b
Gram-Schmidt compression
c
Zernike compression
d
Binning compression
2 nm
6e2 e⁻/Å²
6e2 e⁻/Å²
1e3 e⁻/Å²
0.7
0.6
0.5
0.4
0.3
0.2
0.1
0.0
radians
e
FSC
1
0.5
0
0
0.5
1
2
spatial frequency in 1/Å
Gram-Schmidt compression
Zernike compression
Binning compression
f
8 Å⁻¹
g
1.2 Å⁻¹
h
1.2 Å⁻¹
i
1.2 Å⁻¹

IM5.P0013

Second moment STEM tomography

S. Sturm[1], L. Richter[1], B. Diederichs[2], H. L. Robert[3,4], K. Müller-Caspary[1]

[1]Ludwig-Maximilians-University Munich, Department of Chemistry, Munich, Germany
[2]Helmholtz Zentrum München, Deutsches Forschungszentrum für Gesundheit und Umwelt (GmbH), Munich, Germany
[3]RWTH Aachen University, 2nd Institute of Physics, Aachen, Germany
[4]Forschungszentrum Jülich, Ernst Ruska-Centre for Microscopy and Spectroscopy with Electrons (ER-C), Jülich, Germany

Electron Tomography is able to reconstruct nanoscopic three dimensional structures via acquisition of a tilt series of projections [1].

While different types of signal have been exploited in the past (e.g. holographically obtained phase [2]), the tomographic reconstruction still relies to a great extent on the fulfillment of the projection requirement, requesting the signal to reassemble a linear integral of a 3D distribution along the projection direction.

For STEM Tomography in particular, the HAADF signal, among others, can be exploited to gain quantitative results when approximated as Lambert−Beer-exponentially attenuated with the coefficient

μα [3]. However, the often observed so-called cupping artifacts indicate that there is still considerable deviation from an ideal projection. Especially when dynamical scattering gets significant, as in case of close to zone axis orientations, the assumption of linearity gets problematic.

Recently, with the advent of new fast direct electron detectors, momentum-resolved STEM [4, 5] becomes increasingly more accessible, enabling users to shape the entity of the detected signal in dedicated new ways.

In this study, for a 10nm sized truncated gold nanocube (relaxation using Tersoff potentials, implemented in LAMMPS software), a whole tilt series has been simulated (+- 180° in 5° steps, 8mrad semi-convergence angle, 600x600 scan points, 15x15x15nm³ (with 15 slices), 4096x4096px² diffraction pattern, 8mrad ring detectors, 5 frozen phonon configurations) , using a highly efficient STEM multislice simulation code, running on several V100 GPUs. Gold was chosen, due to its high atomic number, leading to violation of linearity already at very low specimen thickness. Several STEM signals have been compared as to their linearity using the a priori known projected depth as reference. The second moment in momentum space (in this case from 8mrad to 64mrad) has been found to be almost linear (Fig. 1).

Fig. 2 shows the final second moment tomogram, reconstructed using a WSIRT algorithm with 5 iterations [2]. Even though it was not the aim of this study, at least under the ideal conditions of this simulation (high amount of projections along crystal axes, 180° tilt range), atomic resolution was easily achieved. Notably, there are virtually no cupping artifacts. Of course, experimental conditions like coherence, misalignment or noise would affect reconstruction quality. Nevertheless, second moment tomography should be highly beneficial e.g. at medium resolution.

Figure 1: Simulated tilt series of a truncated Au-Nanocube.

(a) - (d) Second moment projections at 0°, 15°, 30° and 45°, respectively.

(e) - (h) Profiles of (a) - (d) summed up in tilt direction (green). For each tilt the likewise obtained profiles of projected thickness (black), HAADF detector (orange) and from HAADF retrieved Lambert-Beer attenuation μα (blue) are given as reference.

Figure 2: Second Moment STEM Tomogram

(a) Volume rendering with indication of a (1,0,0) plane.

(b) Slice through the indicated (1,0,0) plane in (a).

References:
[1] M WEYLAND et al. Materials Today, 2004, 10.1016/S1369-7021(04)00569-3
[2] D WOLF et al. et al. Ultramicroscopy, 2010, 10.1016/j.ultramic.2009.12.015
[3] D WOLF et al. Nano Letters 2018, 10.1021/acs.nanolett.8b01270
[4] K MÜLLER, et al. Nature communications, 2014, 10.1038/ncomms6653

[5] H ROBERT, et al. Ultramicroscopy, 2022, 10.1016/j.ultramic.2021.113425
[6] K. M.-C. acknowledges funding from the DFG, contract EXC 2089/1 – 390776260 (e-conversion).

Fig. 1

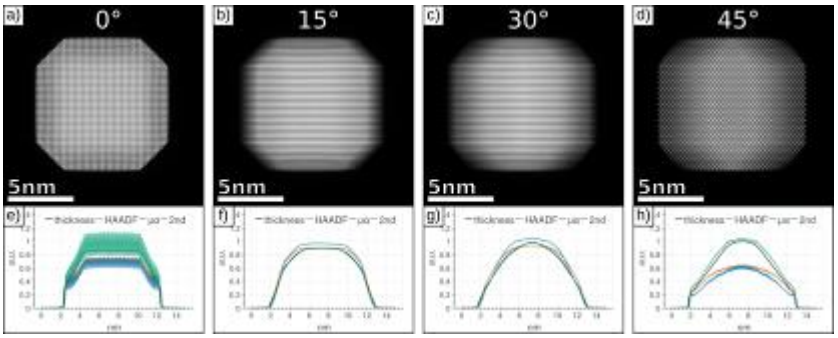

Fig. 2

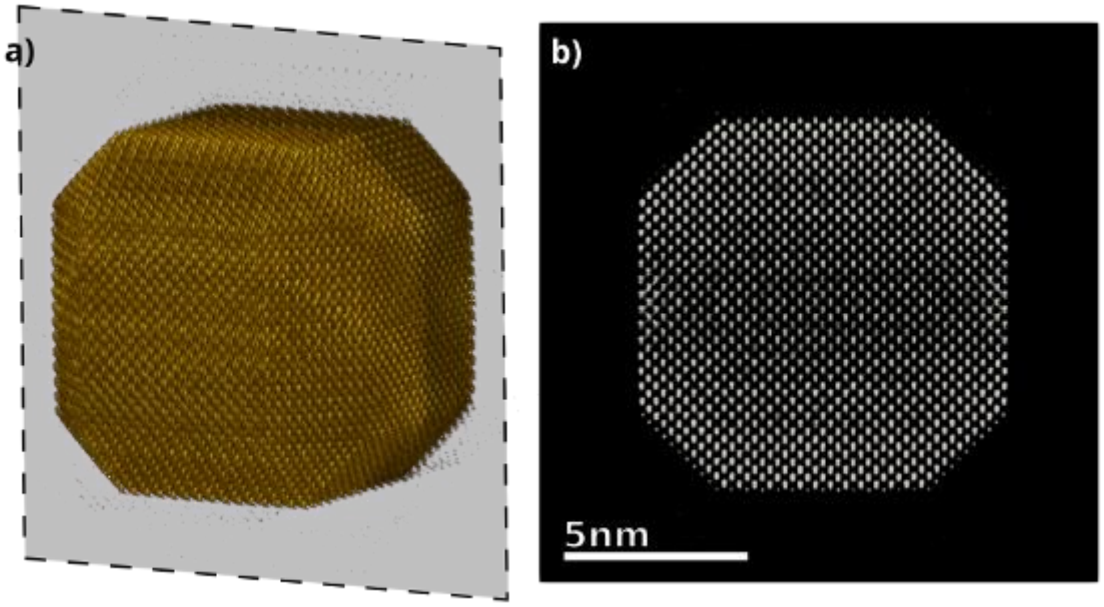

IM5.P0014

Procedure for 3D atomic resolution reconstructions using atom-counting and a Bayesian genetic algorithm

A. De Backer[1], S. van Aert[1], C. Faes[2], E. Arslan Irmak[1], P. Nellist[3], L. Jones[4]

[1]EMAT and NANOlab Center of Excellence, University of Antwerp, Antwerp, Belgium
[2]I-BioStat, Data Science Institute, Hasselt University, Hasselt, Belgium
[3]Department of Materials, University of Oxford, Oxford, United Kingdom
[4]CRANN & School of Physics, Trinity College Dublin, Dublin, Ireland

To understand the catalytic properties of metallic nanoparticles (NPs), a 3D characterization at high resolution is often required. Although electron tomography is a valuable tool to get insight in the 3D shape of NPs, this approach is often not feasible when investigating small beam-sensitive catalysts or dynamical processes. Therefore, alternative methods have been developed where 3D atomic models are reconstructed from a single ADF STEM projection [1-4]. For this purpose, atom counts are used to create an initial atomic model which serves as an input for an energy minimization to obtain a relaxed 3D reconstruction.

The existing methods often show some limitations. Either the finite atom-counting precision is ignored, or the final reconstruction ends up in a global energy minimum while the NP"s structure deviates from a ground state configuration. To overcome these limitations, we developed a Bayesian genetic algorithm. Bayesian methods are powerful tools to rationally combine a priori information with observed data and genetic algorithms are typically used for solving large optimization problems [4,5]. Our novel method enables to minimize the NP"s energy while utilizing a priori information about the finite precision of the atom-counting results and neighbour-mass relations.

In an extensive simulation study, the quality of the obtained reconstructions is quantitatively evaluated in terms of the surface atoms, which are of general interest for catalysis. Fig. 1 shows the fraction of correctly reconstructed surface atoms of a simulated Pt NP. As a reference, the results for the reconstructions without prior knowledge are also included. We also applied the method to study an experimental time-series of a catalyst Pt NP. To reliably count the number of atoms from the time series, we used a hidden Markov model which explicitly describes the possibility of structural changes over time [6]. The reconstructed models are schematically represented in Fig. 2.

In summary, a significant improvement is observed when including more relevant prior knowledge, especially at lower doses. Therefore, the method is very promising for obtaining reliable reconstructions of beam-sensitive NPs during dynamical processes from images acquired with lower incident electron doses [7].

References

[1] S. Bals et al., Nat. Comm. 3 (2012) 897

[2] L. Jones et al., Nano Lett. 14 (2014) 6336

[3] A. De Backer et al., Nanoscale 9 (2017) 8791

[4] M. Yu et al., ACS Nano 10 (2016) 4031

[5] Aarons et al., Nano Lett. 17 (2017) 4003

[6] De wael et al., Phys. Rev. Lett. 124 (2020) 106105

[7] This work was supported by the European Research Council (Grant 770887 PICOMETRICS to SVA and Grant 823717 ESTEEM3). The authors acknowledge financial support from the Research Foundation Flanders (FWO Belgium) through project fundings and a postdoctoral grant to ADB. LJ acknowledges Science Foundation Ireland (SFI), the Royal Society, and the AMBER Centre.

Figure 1 Fraction of the correctly reconstructed surface atoms l as a function of the incident electron dose. The inset shows the ground truth reconstruction of the Pt NP where the colouring of the Pt atoms indicates the nearest-neighbour coordination.

Figure 2 a) ADF STEM time series. b) corresponding reconstructed 3D atomic models for the time sequence viewed along the beam direction. c) Rotated models to show the dominant surface facets. The colouring of the atoms corresponds to the nearest-neighbour coordination.

Fig. 1

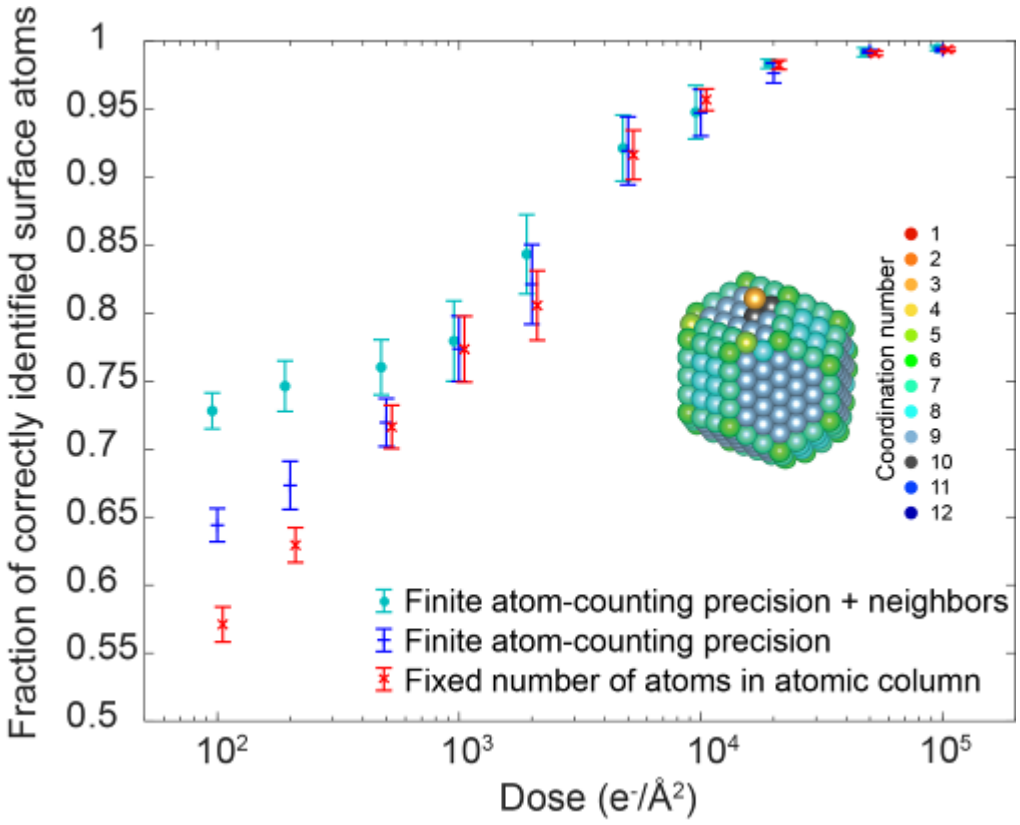

Fig. 2

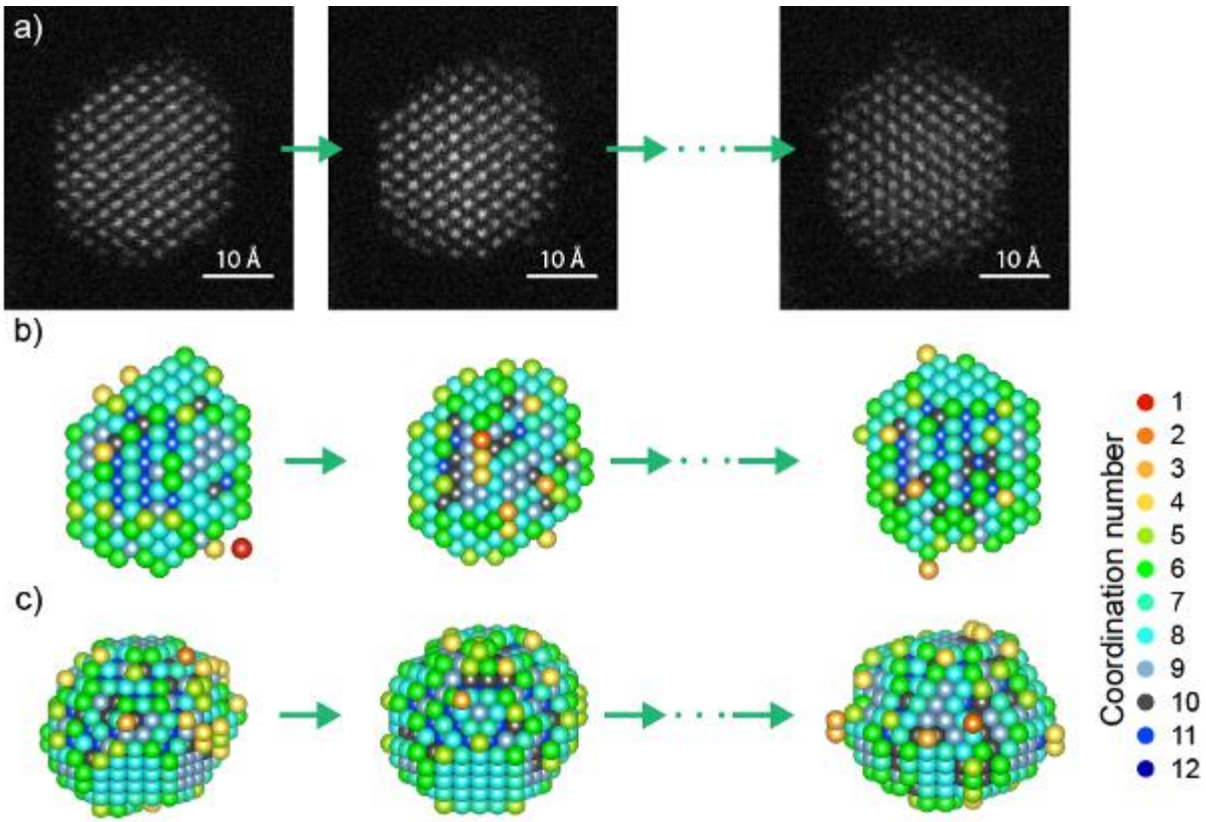

IM5.P0015

Increasing the spatial resolution of pixelated semiconductor tracking detectors using convolutional neural networks

B. Eckert[1]

[1]PNDetector GmbH, Munich, Germany

Energetic electrons do not deposit their energy locally at their Point of Entry (PoE) into the detector volume but statistically produce three-dimensional trajectories by multiple scattering. The energy deposition happens along these trajectories, typically extending over several pixels. The output of the pixelated semiconductor-based detector system is a binned two-dimensional projection of the energy deposition. However, to get images with a high spatial resolution, not the energy deposition into the detector volume is of interest but the precise PoE of the primary electrons into the detector volume.

We developed a convolutional neural network (CNN) whose output is a frame-wise probability map. The probability map describes the probability that each physical pixel contains a PoE map with values between zero and one. The CNN has no fully-connected layers and, therefore, applies to different physical detector sizes without retraining. The modular design of the CNN also enables the fast adaptation to different primary energies and physical pixel sizes via transfer learning.

For a primary energy of 300 keV, a modulation transfer function (MTF) of 0.77 at a Nyquist frequency of 0.5 is obtained from a slanted edge [1, 2]. For comparison, the MTF obtained using conventional state-of-the-art PoE reconstruction methods is below 0.4 at a Nyquist frequency of 0.5 [2]. The MTF is constant up to a rate of 0.04 e -/pix/frame and decreases slowly for higher rates. Therefore, the CNN can provide a precise reconstruction even with higher electron rates.

Moreover, the CNN can be expanded by a super-resolution module to enable probability maps with subpixel resolution of a factor of four by four. The super-resolution shows its full power for primary energies below 120 keV. For these energies, the energy depositions in the pixel structure are dominated by systematic effects like diffusion and repulsion and not by stochastic effects like multiple scattering. Therefore, a more precise reconstruction of the PoE is possible.

Using the presented CNN to reconstruct the PoE of individual primary electrons frame-wise enables a high spatial resolution, which can be extended to subpixel resolution for lower primary energies. Application examples will be provided.

[1] B. Eckert et al., Electron Imaging Reconstruction for Pixelated Semiconductor Tracking Detectors Using the Approach of Convolutional Neural Networks, submitted to IEEE, Transaction on Nuclear Science (2021)

[2] International Organization for Standardization, Photography - Electronic Still Picture Imaging-Resolution and Spatial Frequency Responses, ISO 12233:2017, ISO (2017)

IM5.P0016

TEM data compression and denoising by autoencoders and convolutional neural networks

S. Pylypenko[1], A. Lubk[1], Y. Fasano[2]

[1]Leibniz Institute for Solid State and Materials Research Dresden, Institute for Solid State Research, Dresden, Germany
[2]Instituto Balseiro and Centro Atomico Bariloche, Bariloche, Argentina

Introduction

Machine learning methods such as Principal Component Analysis are widely employed for data denoising and compression in Electron Microscopy and Spectroscopy [1]. Recently, neural network based methods have been successfully introduced to the field, potentially increasing robustness toward noise , while increasing the application range.

Objectives

Here, we apply suitable autoencoder neural networks [2,3,4] to denoise and compress electron microscopy data comprising magnetic imaging and spectrum imaging. Our focus is removal of ubiquitous Poissonian noise, scattering artifacts and identification of optimal compression thresholds.

Materials and Methods

Electron Microscopy datasets comprise different types of magnetic images. It can be vortex matter or electron energy loss / energy dispersive x-ray spectrum images. In particularly the latter is notoriously affected by Poissonian noise as the spectra comprise regions of very low and large intensity.

The autoencoder neural network consist of a 2-3 layers of convolutionary and pooling type on the encoder side and their analogues on the decoder side. As training data we employed several images with lowest noise level. In this work were used just 4 images. For extending of training dataset was applied scaling with different scale factors. All neural networks were implemented utilizing the Tensorflow and Keras frameworks.

Results

Autoencoder network as applied to denoising of magnetic images in Fig. 1a.

Fig. 1a Magnetic image before denoising Fig. 1b Image after denoising

In this example the image data contains a regular hexagonal structure. Due to not perfect sample composition, not optimal exposure, image drift and other experimental challenges, the image contains a lot of sharp artifacts, contrast variations and of course the experimental noise.

The application of the autoencoder (Fig. 1b) removes a large part of the noise, rendering the dataset amenable to, e.g., vortex positions and anomalies analysis. Closer analysis reveals that the data compression is similar to a truncation of the Fourier basis in this particular example, where the periodic repetition of the contrast is the dominating feature.

Conclusion

Autoencoder neural networks represent a viable alternative to conventional denoising algorithms for treatment of electron microscopy imaging and spectrum imaging data. We demonstrate successful denoising utilizing relatively simple network designs and when applied to different types of images.

References

1. Jolliffe, I.T.: Principal component analysis, 2nd edn. Springer Verlag, Berlin (2002)

2. Lovedeep Gondara, "Medical Image Denoising Using Convolutional Denoising Autoencoders", 2016 IEEE 16th International Conference on Data Mining Workshops (ICDMW).

3.Yasenko, Y. Klyatchenko and O. Tarasenko-Klyatchenko, "Image noise reduction by denoising autoencoder", 2020 IEEE 11th International Conference on Dependable Systems Services and Technologies (DESSERT), pp. 351-355, 2020.

4.https://keras.io/examples/vision/autoencoder

Fig. 1

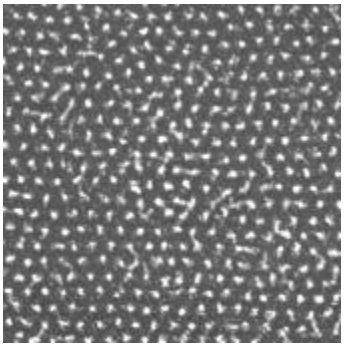

Fig. 2

IM5.P0017

Investigating the influence of reconstruction and segmentation algorithms on the volume reconstruction in electron tomography

T. Krekeler[1], D. Rings[1], M. Brinker[2], P. Huber[2], M. Ritter[1]

[1]Hamburg University of Technology, Electron Microscopy Unit, Hamburg, Germany
[2]Hamburg University of Technology, Institute for Materials and X-Ray Physics, Hamburg, Germany

Electron tomography is a valuable tool to obtain the 3D structure of specimen in the nm or even sub-nm range. The general workflow is to acquire a series of projections from the specimen from different angles or orientations, computationally reconstruct the volume and segment the volume data into different components or phases. Over the last decades a variety of reconstruction, segmentation and filtering algorithms have emerged, providing the scientist with a large toolset for his tasks. However, by favoring one algorithm over the other, the resulting tomographic reconstruction may deviate from the true 3D structure.

In this work we present the influence of reconstruction and segmentation algorithms on the final 3D structure of a nanoporous silicon sample with known porosity.

The sample material consist of electrochemically anodized silicon with cylindrical pores of a diameter <10 nm and a solid-fraction of 50% determined by nitrogen sorption isotherm. A tomography needle of 150 nm diameter was prepared by standard FIB liftout technique. A tilt series of 161 projections (-80° - +80° with 1° spacing) was acquired using a Talos F200X TEM in HAADF-STEM mode.

After image registration of the unfiltered projections, the volume was reconstructed using WBP, SIRT, SART and EM algorithms. A representative volume of the reconstructed volume was chosen for histogram based thresholding segmentation using Otsu, Max Entropy, K-means and Percentile (50%).

The solid-void ratio, homogeneity of density and noise of the segmented volume were analyzed and compared using ImageJ.

While SIRT and EM result in high contrast and low-noise volume reconstructions, the intensity distribution show significant density inhomogeneity inside the reconstructed volume (see Fig. 1). WBP and SART result in more homogenous density inside the specimen but the noisy data makes histogram based segmentation of the unfiltered data difficult.

Besides the obvious percentile (50%) result, segmentation using Otsu and K-means gave solid-fractions closest to the theoretical value of 50% regardless of reconstruction method (see Fig. 2).

These results show that prior knowledge about sample properties (like porosity) is useful during the segmentation step as some segmentation algorithms strongly deviate from the true structure. One should be aware that the human factor is a significant influence of on the quality and validity of tomographic reconstructions in electron tomography.

Fig. 1: YZ-orthoslices of reconstructed volumes.

Fig. 2: Table of calculated solid-fractions of reconstructed volumes.

Fig. 1

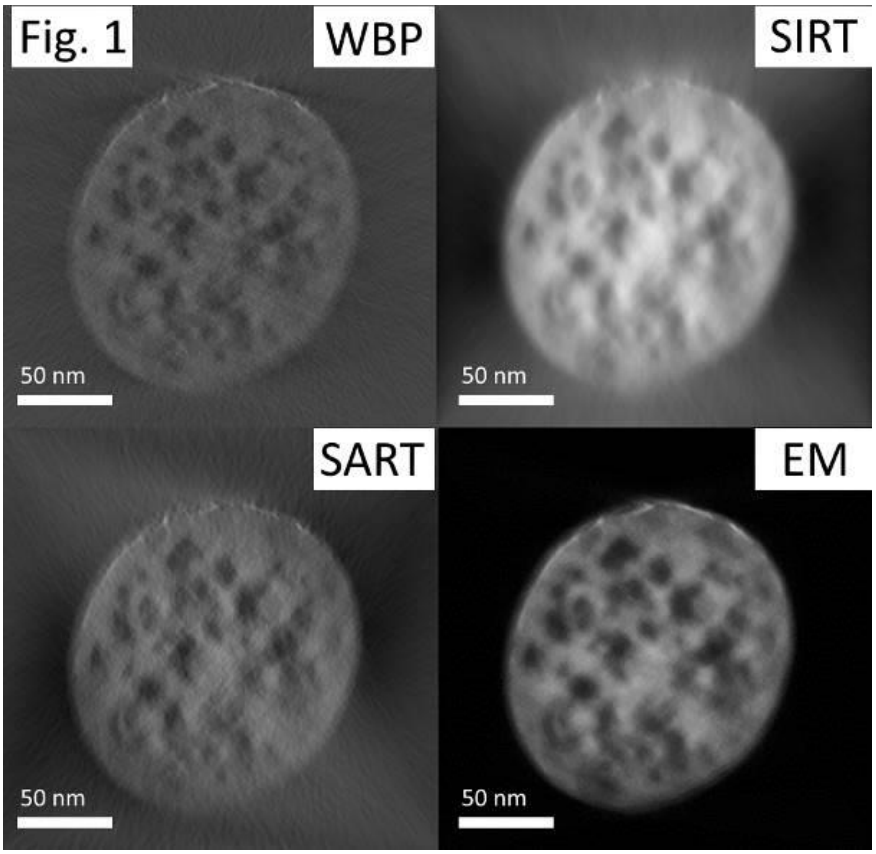

Fig. 2

	WBP	SIRT	SART	EM
Otsu	51.7	51.4	54.0	48.2
Max Entropy	72.7	56.6	66.4	39.6
K-means (n=2)	47.5	51.3	53.9	47.8
Percentile (50%)	50.1	50.4	50.0	50.1

IM5.P0018

Quantitative field mapping around electrically biased needles by STEM & holography

J. F. Dushimineza[1,2], J. Jo[1], R. E. Dunin-Borkowski[1], K. Müller-Caspary[1,2]

[1]Forschungszentrum Jülich GmbH, Physics of Nanoscale Systems (ER-C-1), Jülich, Germany
[2]Ludwig-Maximilians-University Munich, Department of Chemistry and Center for NanoScience, Munich, Germany

Quantitative electric field mapping from mesoscopic scales down to sub-atomic distances is of fundamental interest with respect to materials science and device design. However, the direct probing of, e.g., polarisation-induced electric fields in a specimen via TEM is currently hampered by dynamical scattering. Consequently, quantifying intrinsic electric fields occurring in thicker specimens remains a challenge, for which a prerequisite is the quantification of electric fields in the absence of dynamical scattering, and obtaining consistency among different TEM methodologies. In this work, the stray electric fields produced by two biased gold needles (Fig. 1a) employing momentum-resolved STEM and electron holography (EH) have been studied in comprehensive simulations and were compared to experiments. Via finite element (FE) simulations, the 3D electric potential V was calculated (Fig. 1b). By projection along the *z*-direction, the projected potential Vpz is obtained (Fig. 1c). Subsequently, the projected electric field Ep is given by the gradient of Vpz (Fig. 1d) in *x*- or *y*-direction. This was done for different geometries, e.g., relative needle shifts and tip curvatures. For example, the line profiles in Fig 1e taken along the half axis show that a relative needle shift reduces and shifts the maximum significantly. The impact of further parameters such as needle shape and gap distance are also elucidated, as well as the impact of propagation through the large-scale electric potential for different acceleration voltages. The reliability of the simulation was examined by comparison with a STEM experiment in which Ep was measured using the centre of mass (COM) method where a respective line profile was extracted (Fig. 1f). Considering slightly deviating geometry parameters, i.e., the inaccurately known 3D tip shape, simulation and experiment are in good agreement. By experimentally probing Ep under alike conditions via EH, a discrepancy of about 50% between COM and EH became apparent. The EH geometry in Fig. 2a, however, suggests that the reconstructed phase is significantly affected by the perturbed reference wave effect (PRE), opposite to STEM where the field-free reference was recorded subsequently with unbiased needles. To numerically quantify the PRE in EH, Vpz gained from FE simulations (Fig. 2a) has been divided into two regions O and R of width w. In EH, the electron beam transmits both regions which are brought to interference via a biprism. Effectively, the measured projected electric potential in EH within the interference region is then given by the difference of Vpz in O and R. Ep is calculated from the gradient of the reconstructed phase, which would ideally equal Fig. 2b and yield the circled profile in Fig. 2c. However, the PRE causes the reconstructed Ep to be reduced by 50V as shown by the crosses in Fig. 2c which agree well with the EH experiment. Finally, Fig. 2d demonstrates that the experimentally measured differences between COM and EH are well reproduced by the FE simulation if the PRE is included. Consequently, COM measurements in this case provide a more direct access to absolute electric fields due to the subsequent unbiased reference measurement, whereas EH is quantitatively understood by accompanying FE simulations, at least for the EH geometry used here.

[K. M.-C. acknowlegdes support under contract from the Helmholtz-Association and from moreSTEM VH-NG 1317]

Fig. 1

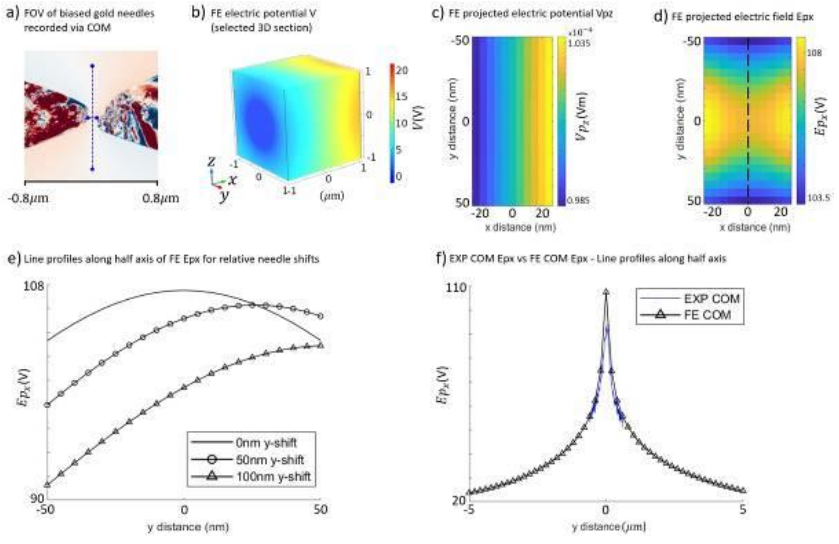

Fig. 2

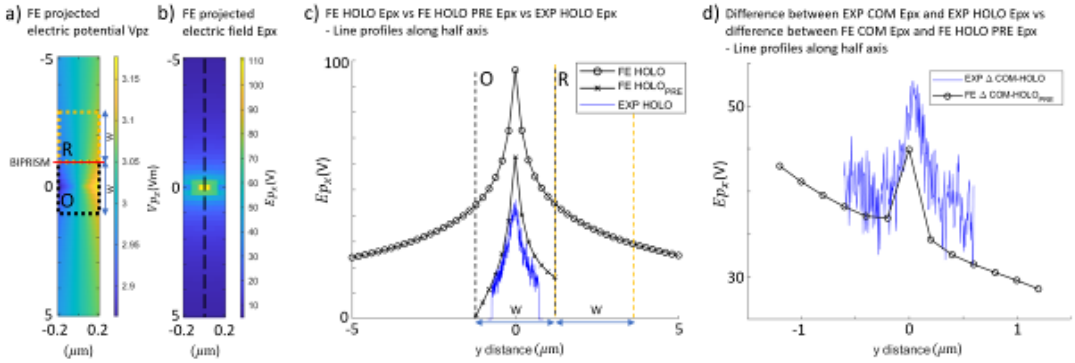
a) FE projected electric potential Vpz
b) FE projected electric field Epx
c) FE HOLO Epx vs FE HOLO PRE Epx vs EXP HOLO Epx - Line profiles along half axis
d) Difference between EXP COM Epx and EXP HOLO Epx vs difference between FE COM Epx and FE HOLO PRE Epx - Line profiles along half axis
BIPRISM
R
O
w
y distance (μm)
FE HOLO
EXP HOLO
EXP Δ COM-HOLO

IM5.P0019

Quantitative imaging of single cesium atoms in the channels of a Beryl crystal

D. Knez[1], C. Gspan[2], N. Šimić[2], S. Mitsche[1], H. Fitzek[2], G. Kothleitner[1], W. Grogger[1], F. Hofer[1]

[1]Graz University of Technology, Institute of Electron Microscopy and Nanoanalysis, Graz, Austria
[2]Graz Centre for Electron Microscopy, Graz, Austria

Aberration-corrected scanning transmission electron microscopy (STEM) allows the imaging of single atoms in bulk crystals, usually with high angle annular dark field (HAADF) images [1], but in special cases also with STEM spectroscopy methods [2]. However, the detection of single atoms in a bulk crystal is challenging and depends on various experimental parameters such as specimen thickness, crystal orientation, composition of the matrix and the type of dopants. For substitutional dopants, the channeling of the electron waves in the crystal must be considered, whereas for single atoms on interstitial sites such as in porous materials, other difficulties such as the electron probe confinement arise [3].

In this work, we show how single atoms in the channels of a beryl crystal can be detected and quantified. Beryl ($Be_3Al_2Si_6O_{18}$) has a hexagonal ring structure with crystal channels of about 0.5 nm diameter aligned parallel to the c-axis. Foreign atoms such as alkali ions or H_2O molecules can be embedded in these channels. Recently, atoms were detected in the channels using STEM-HAADF and it was assumed that these were Fe^{2+} ions [4].

Here we study a beryl that had Fe and Cs concentrations of 0.3% and 0.03%, respectively. The ion-milled crystal was investigated with a probe-corrected Titan^3 (Thermo Fisher) operated with an X-FEG at a convergence angle of 15 mrad. The angular ranges of the detectors are from 62 to 214 mrad (FEI) and from 20 to 73 mrad (Gatan). The experimental results were validated by density functional theory (DFT) calculations and the images were simulated with the program QSTEM (C. Koch, Berlin).

The experimental HAADF images in Fig. 1 show the crystal structure parallel to the c-axis. The specimen thickness is 10 nm. The central channel is occupied by at least one atom, it shows the highest brightness of all occupied channels in this crystal, whereas the other channels in this image are unoccupied. The occupied channels are unevenly distributed over the crystal. Since several ions can be incorporated into these channels, we have simulated images of Na, K and Cs but also with Fe in the top crystal layer. The intensity ratio of the Si and Al columns with the central channel clearly shows that we have a single Cs ion present very close to the uppermost crystal plane. This is also in agreement with crystal chemical considerations. Thus, the qualitative assumption of Arivazhagan [4] that the contrast in the channels is due to Fe ions can be clearly refuted.

Fig. 2 shows the intensity distributions of the channels and the Al and Si columns. While the Si columns show a narrow distribution, the intensities of the Al columns vary strongly, which can be attributed to Fe atoms that preferentially sit on the octahedral Al sites. This is confirmed by DFT calculations and by STEM-EDX measurements.

References:

[1] J. Hwang et al., Phys. Rev. Lett. 111 (2013) 266101.

[2] M. Varela et al., Phys. Rev. Lett. 92 (2004) 095502.

[3] K. Kimoto et al., Appl. Phys. Lett. 94 (2009) 041908.

[4] V. Arivazhagan et al., J. Microsc. 265 (2017) 245.

Fig. 1 Experimental STEM images of the brightest channel occupant compared with multi slice simulations viewed along the [001] direction; with various dopants in the channel position Z=0 for a specimen thickness of 10 nm.

Fig. 2 Intensity distributions of the columns in the FEI HAADF image (left), intensity integration map (middle) and histogram showing the channels, Si-O and of Al-Fe columns (right).

Fig. 1

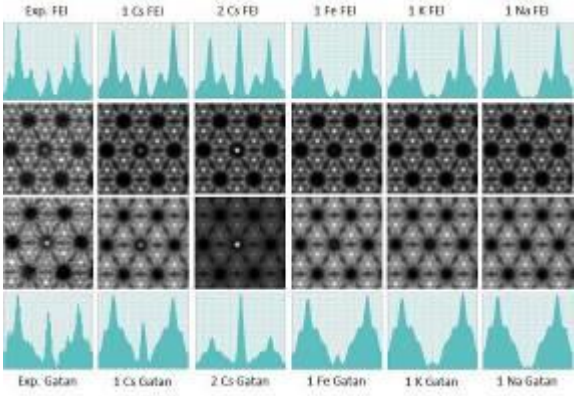
Exp. FEI
1 Cs FEI
2 Cs FEI
1 Fe FEI
1 K FEI
1 Na FEI
Exp. Gatan
1 Cs Gatan
2 Cs Gatan
1 Fe Gatan
1 K Gatan
1 Na Gatan

Fig. 2

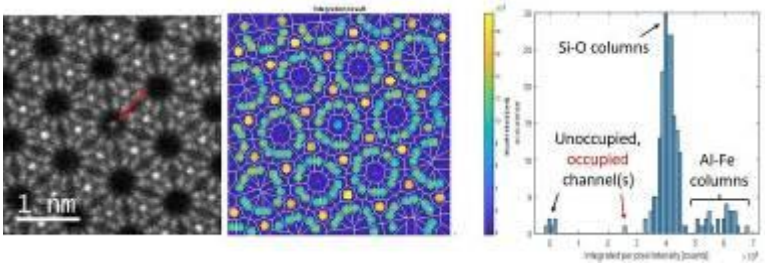
1 nm
Si-O columns
Unoccupied,
occupied
channel(s)
Al-Fe
columns

IM5.P0020

Atom-counting from multiple ADF STEM images

D. G. Sentürk[1,2], C. P. Yu[1,2], A. De Backer[1,2], S. van Aert[1,2]

[1]EMAT and NANOlab Center of Excellence, University of Antwerp, Antwerp, Belgium
[2]NANOlab Center of Excellence, University of Antwerp, Antwerp, Belgium

To understand the structure-property relationship of nanostructures, reliably quantifying parameters, such as the number of atoms, is important. Advanced statistical methodologies have made it possible to count the number of atoms for monotype crystalline nanoparticles from a single ADF STEM image [1,2]. However, recent developments enable one to simultaneously acquire multiple ADF STEM images. Therefore, we extended the statistics-based atom-counting method in order to enhance the accuracy and precision of the atom counts.

So-called scattering cross-sections have been introduced corresponding to the total fraction of scattered intensity attributed to each atomic column to count atoms [3]. Within the univariate approach, the distribution of scattering cross sections (SCSs) is modelled by a one-dimensional Gaussian mixture model (GMM) (Fig 1b) [4]. The number of components often corresponds to a local minimum in the evaluation of an order selection criterion (ICL – Fig 1d). When having two independent sets of SCSs, the distribution can be represented in a scatter plot (Fig 1c). A multivariate approach is then required to estimate the locations and number of components for this 2D GMM. By comparing the ICL criteria from the 1D and 2D GMM analysis, it is clear that the second set of SCSs improves the selection of the correct number of components in the GMM.

In a more extensive simulation study, we evaluated quantitatively the performance of the 1D vs 2D GMM analysis. For this purpose, a more realistic distribution of SCSs is simulated corresponding to a nanoparticle having a thickness up to 20 atoms. The results of this study are presented in Table 1 for different amounts of overlap of the Gaussian components (σ/δ). Typically, this overlap increases when lowering the electron dose. The low performance of the 1D GMM analysis for the low detector angles is the result of an underestimation of the number of components by the ICL criterion leading to missing components in the thickness range where SCSs of columns with different number of atoms have a similar magnitude. From this table, it is clear that the percentage of correctly determined number of components significantly increases when evaluating the 2D dataset.

In conclusion, we present a statistics-based method for atom-counting from independent multiple STEM images which improves the accuracy and allows one to retrieve precise information, especially from low-dose images [5].

Figure 1: Illustration of the concept. (a) Input structure. (b) Histogram of the SCSs obtained from a single image (115-157 mrad) together with the 1D GMM. (c) Distribution of the SCSs extracted from two images (35-45 mrad and 115-157 mrad). (d) ICL criterion evaluated as a function of the number of components of the GMM.

Table1: Percentage of correctly determined number of components from simulated data by using 1D and 2D GMM analysis for different amounts of overlap of the Gaussian components (σ/δ as indicated in Figure 1b).

REFERENCES

[1] A. De Backer et al., Nanoscale 9 (2017) 8791-8798

[2] T. Altantzis et al., Nanoletters 19 (2019) 477-481

[3] A. De Backer et al., Ultramicroscopy 134 (2013) 23-33

[4] G. McLachlan, D. Peel, Finite Mixture Models, Wiley Series in Probability and Statistics, John Wiley and Sons, Inc, 2000

[5] This work was supported by the European Research Council (Grant 770887 PICOMETRICS to SVA and Grant 823717 ESTEEM3). The authors acknowledge financial support from the Research Foundation Flanders (FWO Belgium) through project fundings and a postdoctoral grant to ADB.

Fig. 1

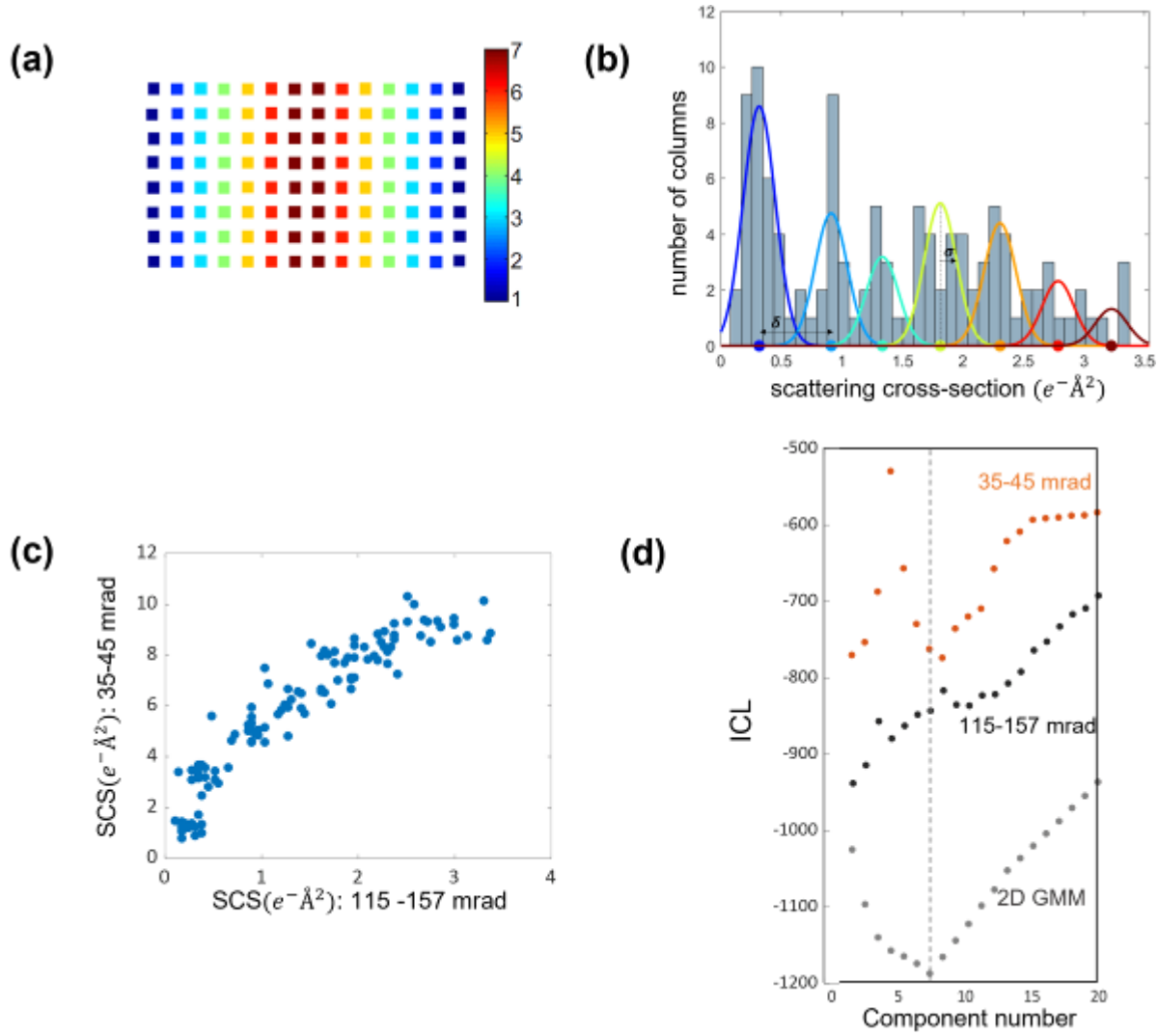

Fig. 2

Detector	σ/δ=0.25		σ/δ=0.30	
	1D GMM	2D GMM	1D GMM	2D GMM
D1: 35-45 mrad	2	97	1	63
D2: 115-157 mrad	78		50	

IM5.P0021

Dynamic range compression in iDPC imaging enables visualisation of light atoms closely surrounded by heavy elements

P. Lu[1], L. Jin[1], E. G. T. Bosch[2], I. Lazić[2], R. E. Dunin-Borkowski[1]

[1]Forschungszentrum Juelich, Ernst Ruska-Centre for Microscopy and Spectroscopy with Electrons and Peter Grünberg Institute, Jülich, Germany
[2]Thermo Fisher Scientific, Materials and Structural Analysis, Eindhoven, Netherlands

Integrated differential phase contrast (iDPC) imaging in scanning transmission electron microscopy (STEM) was theoretically proposed 45 years ago [1] and has only been experimentally implemented until recent years [2]. This is based on the fact that the shift of the centre of mass (CoM) of a far-field convergent beam electron diffraction (CBED) pattern is linearly related to the projected electric (and magnetic, if exists) field in the specimen. The value of CoM along two orthogonal directions can be approximated by the difference of signals in two opposite quadrant detectors, which leads to the name of DPC. By integrating such signals one can produce the so-called iDPC (or iCoM) image that is linearly proportional to the phase shift of the specimen. This has been used to visualise weak phase objects such as biological tissues [3] as well as light atoms at atomic resolution [4].

Particularly for the latter case, it will become more difficult if there are much heavier (or effectively heavier because of different number of atoms along the column in a unit cell) elements to be detected at the same time (finite dynamic range) and extremely challenging if those heavier elements are more closely adjacent to the light atoms. We simulated iDPC images for a model system with different artificial light filler atoms 140 pm away from neighbouring Sb (Z=51) atoms (Sb : filler = 2 : 1 in a unit cell) in a CoSb3 skutterudite thermoelectric material (Fig 1a). Interestingly, by reducing the outer collection angle below the objective aperture, the peaks of light filler atoms start to become resolvable and higher, while that of Sb atoms is shortened (Fig 1b). This recalls the dynamic range compression in audio signal processing, which reduces the volume of loud sounds and/or amplifies quiet sounds, thus allowing the magnetic tape with limited dynamic range for recording. In fact, this is precisely the reason. We simulated CBED images at the points that are 40 pm upward from the Sb and B atom centre (Fig 2a, c, d), and then calculated the accumulative CoM_y from the difference between North and South quadrants as a function of different collection angles. The results demonstrated that, by reducing the outer collection angle to around 70% of the objective aperture, the CoM_y at the point close to B atoms is boosted while that close to Sb atoms is diminished (Fig 2b, e, f).

Such an electron optical (rather than digital) image dynamic range compression eventually expands the detectable dynamic range and helps resolve light atoms in the extreme cases. This is also experimentally proved and will be shown in the presentation.

References

[1] H. Rose, Ultramicroscopy 2, 251 (1977).

[2] I. Lazić *et al*., Ultramicroscopy 160, 265 (2016).

[3] X. Li *et al*., Journal of Structural Biology 214, 107837 (2022).

[4] S. de Graaf *et al*., Science Advances 6, eaay4312 (2020).

Fig 1. (a) Simulated sample model. CoSb3 skutterudite with different artificial light filler atoms (from H to Cl), 140 pm away from neighbouring Sb atoms (Sb : filler = 2 : 1 in a unit cell). (b) iDPC images as a function of collection angles with line profile along the red arrow.

Fig 2. (a, c, d) Simulated CBED images at the points that are 40 pm upward from the Sb and B atom centre. (b, e, f) Accumulative CoM_y (difference between North and South quadrants) as a function of collection angles.

Fig. 1

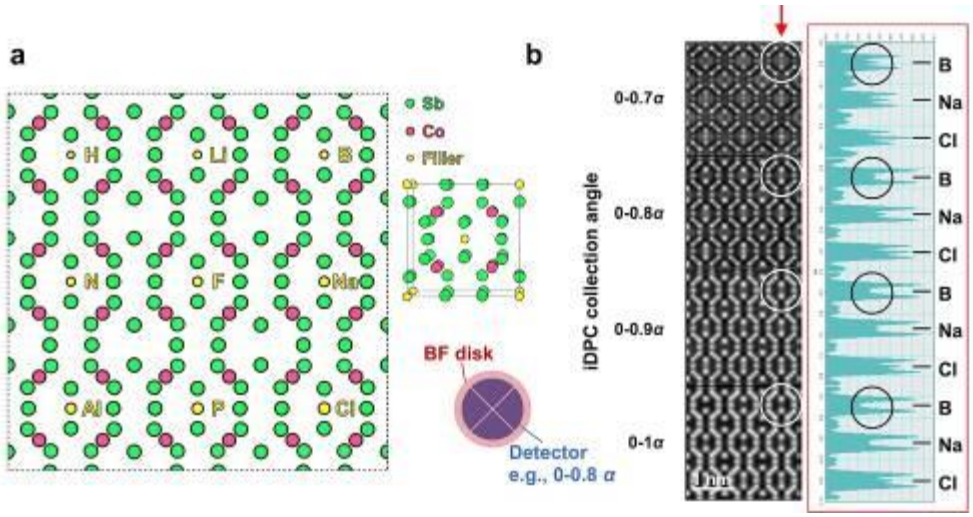
a
b
H
Li
B
N
F
Na
Al
P
Cl
Sb
Co
Filler
BF disk
Detector
e.g., 0-0.8 α
iDPC collection angle
0-0.7α
0-0.8α
0-0.9α
0-1α
1 nm
B
Na
Cl
B
Na
Cl
B
Na
Cl
B
Na
Cl

Fig. 2

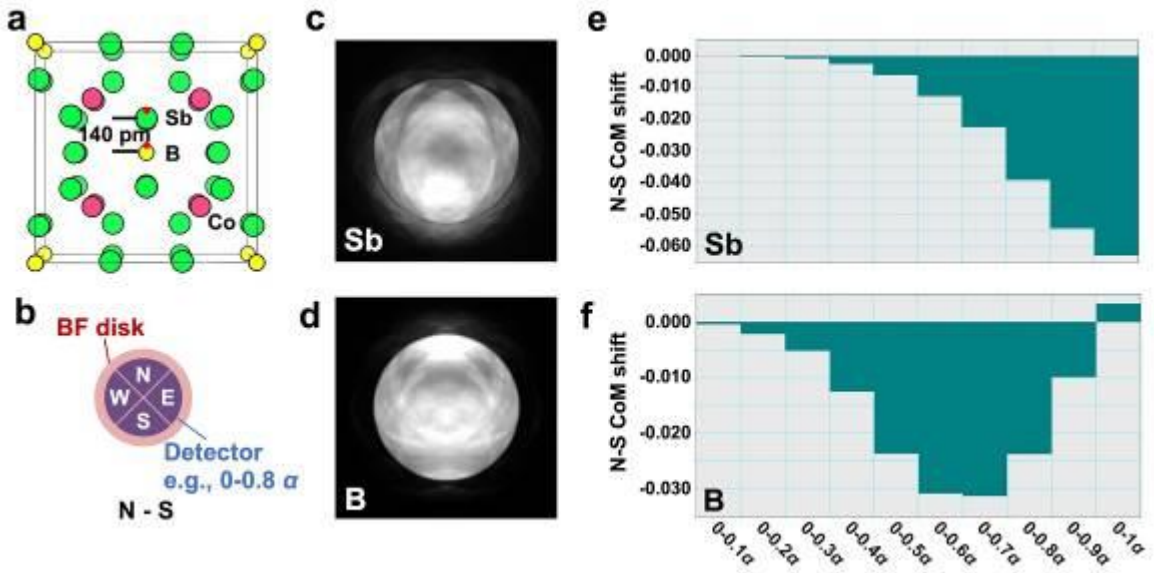
a
Sb
140 pm
B
Co
b
BF disk
N
W
E
S
Detector
e.g., 0-0.8 α
N - S
c
Sb
d
B
e
N-S CoM shift
0.000
-0.010
-0.020
-0.030
-0.040
-0.050
-0.060
Sb
f
N-S CoM shift
0.000
-0.010
-0.020
-0.030
B
0-0.1α
0-0.2α
0-0.3α
0-0.4α
0-0.5α
0-0.6α
0-0.7α
0-0.8α
0-0.9α
0-1α

IM5.P0022

Do we really need to see the atoms?

M. Petrik[1,2]

[1]Philipps-University Marburg, Marburg, Germany
[2]Formerly Philipps-Universität, Marburgg, Marburg, Germany

Introduction

Atomic resolution in electron microscopy is almost taken for granted today. In some cases it is regarded as a necessity. – Is imagination and inductive reasoning threatened by blind belief in only what one can see with one"s eyes?

Objectives

Employing an example from the recent literature we shall demonstrate that it does not necessarily take state-of-the-art atomically resolved TEM (transmission electron microscopy) to elucidate, say, the structure of a multiple twin of an intermetallic compound on the atomic scale. Less advanced TEM images from as long as forty years ago will do.

Materials and Methods

Wolfgang Hornfeck and colleagues in Dieter Herlach"s group recently proposed an intriguing atomistic model for the nucleation of tenfold cyclic twins of orthorhombic (CrB type) NiZr from the melt [1]. They postulated a quasicrystalline nucleus which, when viewed as a 2D projection on a (001) plane, grows in spirals leading to a chiral structure (s. Figure, left). In order to gain further insight, they used HAADF-STEM (high-angle annular dark field scanning TEM) in collaboration with the group of Denis Gratias who also carried out further work on the NiZr twins [2]. In spite of these efforts they were actually unable to produce a TEM image of the tenfold twin"s nucleus and, therefore, had to be contented with the mere plausibility of their model which was at least consistent with the atomically resolved structure of the twin boundary.

We asked ourselves in what other ways a tenfold twin might possibly arise given the orthorhombic NiZr structure. By means of pencil and paper and using elongated hexagons of half the volume of the orthorhombic NiZr unit cell as building blocks, we found two other plausible structures, the simpler one of which is depicted here (s. Figure, centre). The representation of these types of structure by elongated hexagons goes back to the group of K. H. Kuo at the Beijing Laboratory of Electron Microscopy in the early nineties [3].

Now, the question is how one or the other of these theoretical twin structures might be experimentally verified.

Results

As pointed out above, the most advanced atomically resolved TEM technique did not yield information on the structure of the tenfold twin"s nucleus. We, however, were intrigued by a paper from the group of K. H. Kuo published way back in 1985 [4]. They had succeeded in producing a HR-TEM (high-resolution TEM) micrograph of a partially formed NiZr tenfold twin nucleus (s. Figure, right).

Without atomic resolution, using conventional phase contrast HR-TEM under varying defocus conditions, they were able to get an image of the arrangement of the loci of highest electron density which are the centres of the elongated hexagons depicted here (s. Figure).

Conclusion

Comparing the three schematic drawings shown (s. Figure, lower parts – solid lines pass along segments" centres), it is seen that the twin structure in the HR-TEM micrograph of 1985 [4] must have been the one proposed here. Only recently did we learn that K. H. Kuo and colleagues had in fact proposed (merely as an aside) the same tenfold twin structure for NiZr already thirty years ago [5].

Lessons learned:

* Imagination is more important than mere imaging.

* Old literature is still vital.

[1] *Nature Comm.* **2018**, *9*, 4054.

[2] *Acta Cryst.* **2018**, *A74*, 647.

[3] *Philos. Mag. B* **1992**, *65*, 525.

[4] *Philos. Mag. A* **1985**, *52*, L53.

[5] *Philos. Mag. B* **1992**, *66*, 117, p. 122.

Fig. 1

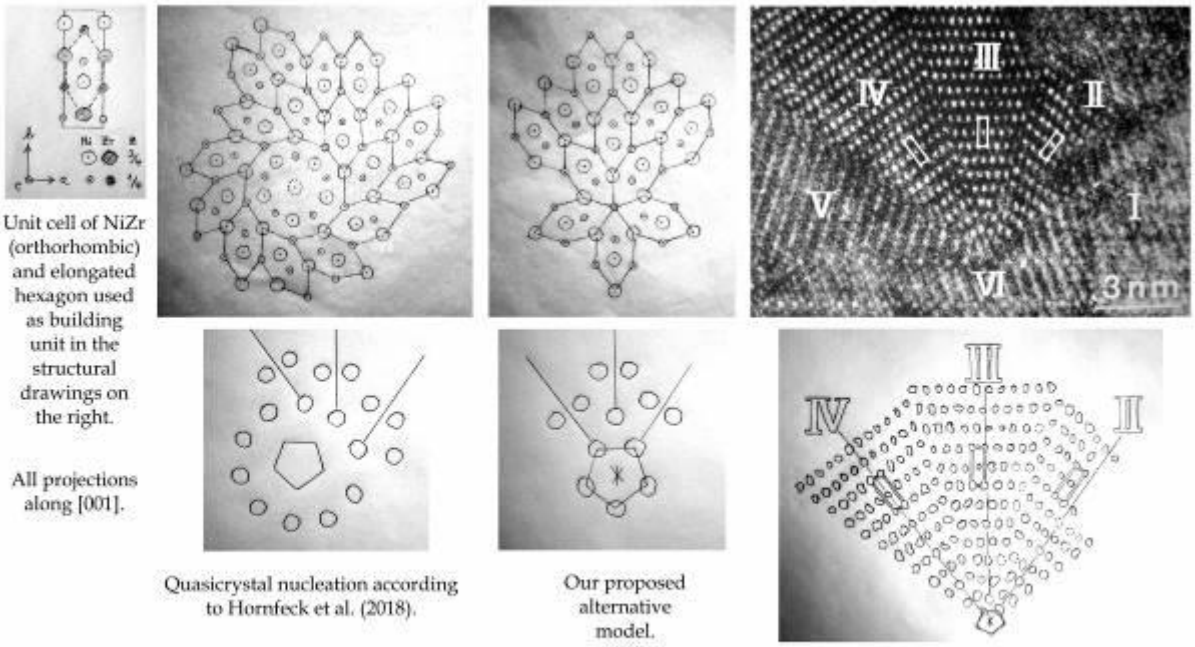

IM6.001-invited

Nanoscale 3D imaging of magnetic spin textures with holographic vector-field electron tomography

D. Wolf[1], A. Lubk[1,2]

[1]IFW Dresden, Dresden, Germany
[2]TU Dresden, Institute of Solid State and Material Physics, Dresden, Germany

Lorentz transmission electron microscopy (LTEM) and off-axis electron holography (EH) are the methods of choice to image magnetism at the nanometer scale. Both techniques exploit the electro-magnetic Aharonov-Bohm effect imprinting a phase shift on the wave function of highly-energetic electrons after transmitting a thin sample. However, for investigation of three-dimensional (3D) nanomagnetism [1], which involves complex 3D magnetic configurations such as exotic domain walls (e.g. of Bloch point type) or magnetic textures (e.g. (braided) Skyrmion tubes, chiral bobbers, Hopfions), these 2D techniques are insufficient for a unique mapping of the underlying magnetic structure. To overcome this problem EH is combined with electron tomography to holographic vector-field electron tomography (VFET). After recording and reconstructing holographic tilt series, the resulting phase image tilt series are input in tomographic reconstruction algorithms to obtain both the mean inner potential (MIP) and the magnetic induction $\boldsymbol{B}$ in 3D. Here, at least three tilt series are required to reconstruct two linearly-independent $\boldsymbol{B}$-field components, and the MIP contribution to the phase. The latter is sensitive to the 3D morphology and chemical composition of the sample. The third $\boldsymbol{B}$-field component can be computed by solving div.$\boldsymbol{B}$=0.

We discuss state-of-the-art VFET including comparison to x-ray-based magnetic vector-field reconstruction and methodological challenges, e.g., imperfect and incomplete projection data, alignment errors, as well as regularization schemes in the tomographic reconstruction algorithms. Moreover, we present examples how VFET has been applied to obtain 3D magnetic vector fields with a few nanometer resolution: (I) We reconstructed in 3D two remanent magnetic states including their peculiar domain walls in CoNi nanowires with large transversal magnetocrystalline anisotropy [2]. (II) We revealed with holographic VFET Bloch-type Skyrmion tubes (SkTs) in an FeGe needle-shaped specimen [3]. This experiment is challenging because it has to be performed under cryogenic conditions (provided by an LN-cooled sample holder) in the presence of an out-of-plane applied $\boldsymbol{B}$-field (provided by a ring magnet of Sm_2Co_{17} underneath the specimen), stabilizing the Skyrmion lattice in the FeGe needle. Fig. 1 shows a 3D reconstruction obtained from three holographic tilt series recorded over a tilt range of ±66° in 3° steps. The 3D MIP distribution was determined from a tilt series recorded at room temperature, at which FeGe is paramagnetic. The resulting tomogram was then subtracted from tomograms reconstructed from two tilt series recorded at 95 K to determine the 3D $\boldsymbol{B}$-field of the FeGe sample in its Skyrmion phase. These results give direct insights into 3D Skyrmion spin texture. An analysis of, e.g., planar energy density maps across the SkTs reflecting the interplay between symmetric exchange and antisymmetric Dzyaloshinskii–Moriya interaction, as well as a comparison with micromagnetic simulations is presented.

Figure 1. 3D magnetic induction of the skyrmions in an FeGe sample. Left: Color-coded components B_x and B_y with arrow plots show the direction and magnitude of the magnetic field. Right: Extracted single SkT with arrow plots at a top, middle and bottom plane.

[1] A. Fernandez-Pacheco *et al.*, Nat Commun **8**, 15756 (2017)

[2] I. M. Andersen *et al.*, Phys. Rev. Res. **3**, 033085 (2021)

[3] D. Wolf *et al*., Nat. Nanotechnol. **17,** 250 (2022)

Fig. 1

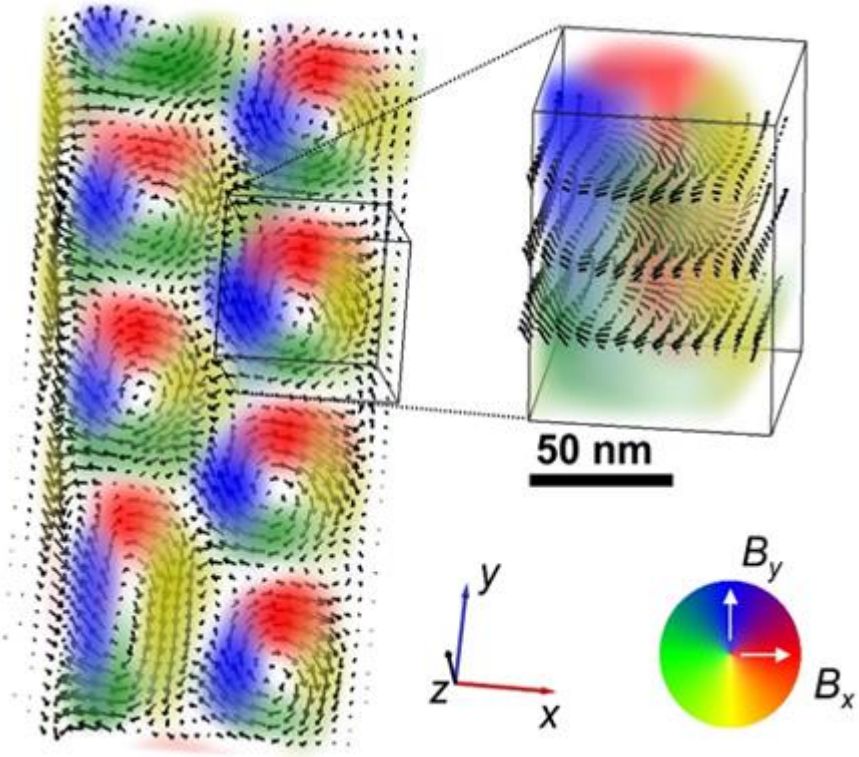

IM6.002-invited

4D STEM – characterisation of materials and contrast enhancement in light matter

K. Müller-Caspary[1], B. März[1], A. Strauch[2], B. Diederichs[1,3], T. Lorenzen[1], Z. Herdegen[1], M. L. Leidl[1,2], H. L. Robert[2], S. Sturm[1], J. F. Dushimineza[1,2]

[1]LMU Munich, Chemistry, Munich, Germany
[2]Forschungszentrum Jülich, Jülich, Germany
[3]HMGU Munich, Applied Mathematics, Munich, Germany

The simultaneous availability of densely sampled real- and diffraction space data in momentum-resolved (MR) STEM increases the versatility of established imaging modes and enables the development of a multitude of new techniques. Prominent ones are first moment (FM) STEM imaging and ptychography, which will be outlined as to basic concepts, limitations and paradigm applications. Then, first results in the field of imaging weakly scattering organic specimens will be shown.

The flexibility provided by MR STEM as to the generation of FM, bright field (BF), dark field (DF) and annular BF (ABF) signals implies it being termed a universal imaging mode. However, it is found that many signals obey their own focus dependence already at moderate specimen thicknesses [1], as demonstrated in a 4D STEM focal series experiment in Fig. 1a, yielding the contrast dependencies in Fig. 1b. A simultaneous recording of, e.g., Z-contrast and FM STEM data at their optimum foci is thus usually not possible. Moreover, we discuss the second moment of the diffracted intensity as to its capability to recover the locations of the specimen surfaces in beam direction. Another important factor to be considered for the quantitative understanding of low-angle scattering is the redistribution of diffracted intensity due to (multiple) plasmon scattering [2], which we demonstrate by energy-filtered MR STEM as depicted in Fig. 1c. Here, the validity of a convolutional Lorentzian model is checked to account for multiple plasmon scattering.

By interpreting FM STEM using Ehrenfest"s theorem [3], electric field quantification in 2D materials is now possible at atomic scale as shown in Fig. 2. In addition, spontaneous, piezo- and ferroelectric specimens have thicknesses of several tens of nanometers, requiring a careful assessment of dynamical scattering. Whereas this leads to moderate systematic errors in unit cell averaged FM data in wurtzite GaN [4], field quantification in Pb- and Ba-based ferroelectrics is shown to be prone to substantial errors arising from dynamical scattering, mistilt and bonding, as demonstrated in a combined experimental and simulation study. In Fig. 3a, a PbZrTiO example is used to illustrate the presence of crystallographic tilt gradients across domain boundaries in 90° domains, leading to systematic errors easily misinterpreted as polarisation-induced electric fields. As a remedy, we present the gradient-based retrieval of the ferroelectric structure using mistilt-corrected, parametrised inverse multislice methods applied to the same 4D data set as depicted in Fig. 3b, from which ionic displacements can be measured accurately.

Whereas ptychographic phase retrieval is complicated in the presence of dynamical scattering, organic matter such as covalent organic frameworks (COFs) and proteins can be treated as (weak) phase objects. We present a study of the validity of this assumption by dose-dependent multislice simulations of viruses in amorphous ice, justifying the application of single-sideband and Wigner distribution deconvolution ptychography, and the quantitative interpretation of differential phase contrast (DPC) STEM [5], as exemplified for a COF in Fig. 4. These basic results will be used to envisage possible future directions to combine physical and life science microscopy.

[1] Ultramicroscopy 233, 113425 (2022)

[2] APL 121, 213502 (2022)

[3] Nat. Comm. 5, 5653 (2014)

[4] PRL 122, 106102 (2019)

[5] Nat. Methods 19, 01586 (2022)

Fig. 1

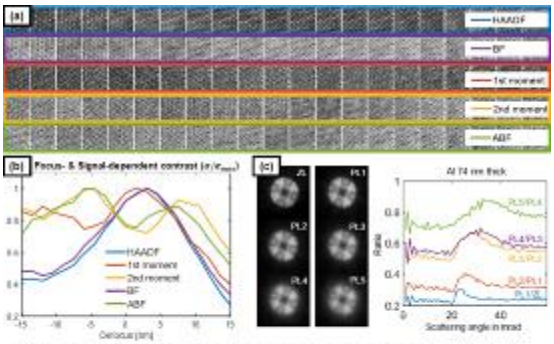

Figure 1 (a) Focal-series 4D STEM for a 13 nm thick In_2Se_3 specimen. The maximum contrast of selected signals is reached for different foci. (b) Standard deviation (normalised) of data in (a). (c) Energy-filtered 4D STEM of an Al specimen with position-averaged CBED patterns recorded at different plasmon peaks and the elastic peak, as well as the angular dependencies of the azimuthally integrated intensity. With increasing plasmon loss, an increased broadening is observed.

Fig. 2

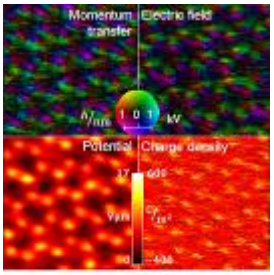

Figure 2 Imaging of WSe_2 by momentum-resolved STEM. The first moment is proportional to the momentum transfer (top left), from which the projected electric field, the charge density and the Coulomb potential can be derived.

Fig. 3

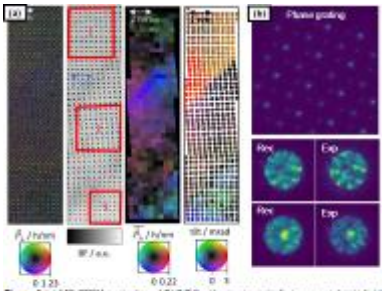

Figure 3 (a) MR STEM evaluation of Pb2/SiO with atomic-scale first moment, bright field data, unit-cell-averaged first moment and mistilt map. The region shows three domains aligned by 90 degrees, and an abrupt tilt gradient at the domain boundaries, leading to large systematic errors. (b) Result of a parametrised inverse multislice reconstruction of the central domain in (a), yielding accurate atom positions. Bottom: selected experimental and simulated diffraction patterns, the latter using the reconstructed structure as input.

Fig. 4

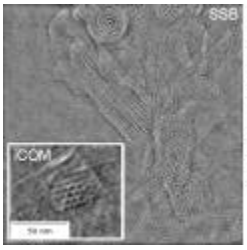

Figure 4 In-focus MR STEM imaging of the fibrils and pores of a covalent organic framework (COF). The large area shows the result of a single-sideband ptychography evaluation (SSB). The inset depicts the integrated first moment data obtained by a reciprocity approach employing the precession of the incident beam direction in plane-wave illumination TEM combined with an ultrafast Medipix Merlin 4EM camera.

IM6.003

Electrical fields in AlN/GaN-nanowires measured with aberration-corrected 4D-STEM

F. F. Krause[1], T. Grieb[1], C. Mahr[1], M. Schowalter[1], T. Mehrtens[1], R. Hötzel[1], S. Figge[1], M. Eickhoff[1], A. Rosenauer[1]

[1]Universität Bremen, Institut für Festkörperphysik, Bremen, Germany

The functionality and efficiency of electronic or optoelectronic devices can be critically influenced by electric fields in the structures. Such fields may arise from inhomogeneous doping, spontaneous or piezoelectric polarisation or occur during operation due to an externally applied voltage. A prominent example is the quantum-confined Stark effect, which can strongly diminish the output of light emitting structures even if crystalline quality and composition homogeneity are otherwise excellent. This is especially the case for crystals with an inherent polarisation as found in the wurtzite-structured AlN/GaN material system.

A position resolved measurement of the electric field strength inside of epitaxially grown structures – ideally with the ability to apply voltages to the specimens in-situ – is hence an important tool for the investigation and optimisation of their growth and subsequent operation. As aberration-corrected STEM allows for imaging with atomic resolution, it is an ideal method for such investigations. But while other specimen properties such as composition or geometry can be characterised from strongly integrated STEM signals acquired with large annular detectors, the signal footprint of electric fields in the sample is more delicate: They mostly manifest in a slight redistribution of intensity in the diffraction patterns. For quantitative field measurements, it is hence necessary to acquire and evaluate 4D-STEM datasets, where the diffraction pattern for each scan point is recorded. From these sets, field strengths can be derived under certain conditions and assumptions.

This work focusses on 4D-STEM field measurements in AlN/GaN nanowire heterostructures. These wires are grown by MBE and investigated with a probe-corrected TEM equipped with an ultrafast, pixelated, direct electron detection detector. The measurements are accompanied by multislice simulations to assess their accuracy and precision. Prerequisites for quantitative measurement of polarisation-induced fields are discussed and the management of possible artefacts due to changes in the mean inner potential are addressed. Based on these considerations, experimental results of high-resolution 4D-STEM field-measurements are presented. The conversion into maps of electrostatic potential or charge density is discussed.

Due to the high resolution inherent to STEM, the measured signal is at first dominated by the very large atomic fields that obscure the polarisation-induced fields. An appropriate averaging process is therefore warranted and is discussed in detail. One exemplary evaluation is shown in Fig. 1. The resulting mesoscalic fields are compared to the theoretical expectations.

In order to investigate the influence of external fields, wires are contacted by electron lithography on ultrathin silicon nitride membranes. Different voltages are applied in-situ employing a dedicated electrical biasing specimen holder. These results can be related to photoluminescence spectra of the same wires.

Fig. 1: Measurement of fields in an AlN/GaN layer structure in a nanowire. A 4D-STEM dataset was acquired in the marked area of the overview on the left. It was evaluated yielding a map of electric field strength in growth direction shown in the top right. The different spontaneous and piezoelectric fields in AlN and GaN can be measured.

Fig. 1

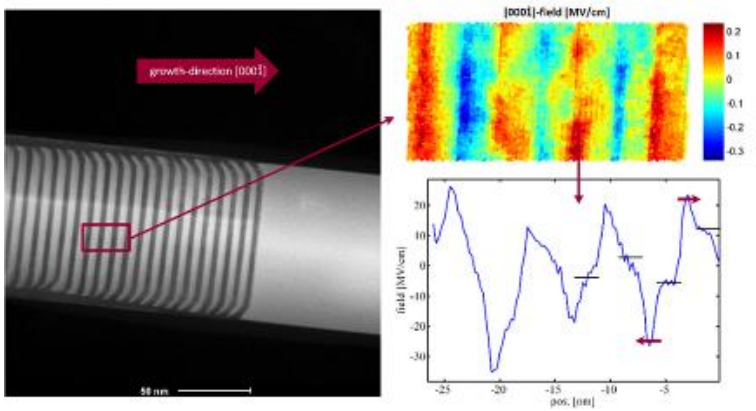

IM6.004

Quantitative electric field determination in semiconductor homo- and hetero-interfaces using electron diffraction and 4D-STEM

V. S. Chejarla[1], A. Beyer[1], D. Heimes[1], J. Scheunert[1], S. Ahmed[1], K. Volz[1]

[1]Philipps-University Marburg, Physics, Marburg, Germany

Introduction:

Nanometer scale characterization of electric fields at semiconductor interfaces is necessary for most electronic devices such as lasers, transistors, solar cells and batteries in order to understand the performance of those devices. Various experimental methods such as electron holography [1], differential phase contrast (DPC) imaging [2], the Fresnel method [3] and the Focault method [4] have been reported in the past for the imaging of built-in electric fields. Recently, we reported the quantitative evaluation on the electric field across a GaAs-based pn-junction using the center of mass (COM) shift of the central beam by 4D-STEM [5].

Objectives:

We aim for the quantification of long-range electric fields that build up at the homo- and hetero-interfaces by measuring the COM shift of the central beam disc by combining precession electron diffraction (PED) with 4D-STEM.

Materials and methods:

In the present study, we use a Nanomegas ASTAR PED system attached to a double aberration corrected JEOL JEM2200FS for quantifying the fields across both homo- and hetero-interfaces. Therefore, we use the parallel beam scanning mode where the convergence angles are in the range of 1-3mrad. Accordingly, dynamical diffraction effects, which destroy the signal at hetero-junctions are reduced as we precess the beam around the optical axis of the microscope. In this way, we manage to get rid of the signal from the atomic fields improving the resolution for the much weaker long-range fields.

Results:

GaAs-based pn-junctions with different doping concentrations are analyzed to show the potential of this method. We optimize the parameters for observing the COM shift of the central beam disc which is determined by the built-in electric field, the polarity and the doping concentrations of the pn-junction. Fig.1 shows the COM evaluations performed on the GaAs-based pn-junction. Further, we apply this method to hetero-interfaces such as AlAs/GaAs and GaP/Si. Apparently, the observed COM shift at the hetero-interfaces also relates to the change in the mean inner potential (MIP). Fig.2 shows the experimental results across the AlAs/GaAs hetero-interface.

Conclusions:

Our results clearly indicate that the presence of electric fields caused by doping or interatomic bonding at the interface can be detected. The presentation will explain the PED-4D STEM experiments, the optimum parameters for those as well as will give some experimental examples.

Fig 1: Experimental measurements of a GaAs-based pn-junction (a) Virtual Bright Field (BF) image with an inset showing the central beam disc with precession of 0.45° (b) COM shift across the depletion region perpendicular to the growth direction [001] (c) COM shift and electric field profiles at the depletion region and linear fits to the rise and fall of the peak in electric field.

Fig 2: Experimental measurements of a AlAs/GaAs heterointerface (a) Virtual BF image with an inset showing the central beam disc with precession 0.45° (b) COM shift at the interface perpendicular to the growth direction [001] (c) COM shift and electric field profiles across the interface.

References:

1. Sasaki et al. Microscopy 63, pp.235 (2014).
2. Shibata et al., Sci. Rep. 5, pp.10040 (2015).

3. Merli et al Phys. Status Solidi 1973, 16 (2), K89−K91.
4. Titchmarsh el al status solidi (b), 34(2), K83-K86.
5. Beyer. A. et al Nano Lett. (2021),21,5, 2018-2025.

Fig. 1

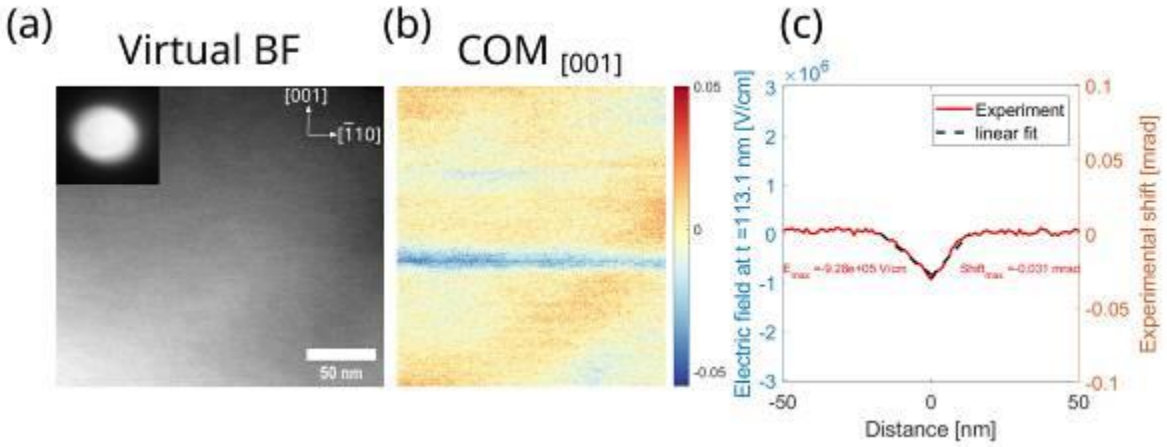

Fig. 2

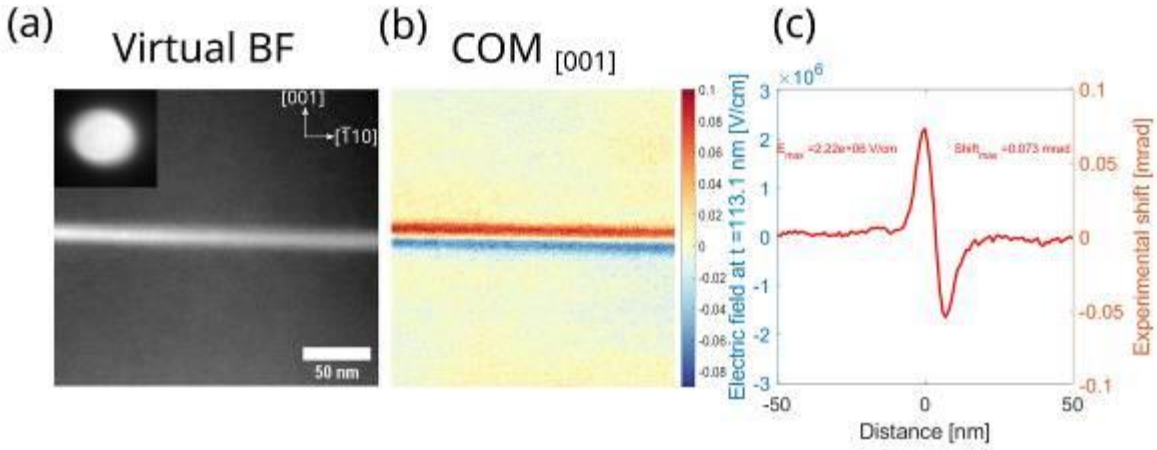

IM6.005

Can we enhance the depth of focus/depth resolution in STEM with an electrostatic phase plate?

F. Vega Ibañez[1,2], A. Béché[1,2], J. Verbeeck[1,2]

[1]University of Antwerp, EMAT, Antwerp, Belgium
[2]University of Antwerp, NANOlab Center of Excellence, Antwerp, Belgium

Introduction

In STEM, a trade-off appears between in-plane (xy) and out-of-plane z-resolution due to higher-order aberrations limiting the beam's convergence angle (α). The z-resolution can be demonstrated to scale with $1/\alpha^2$, whereas the xy resolution scales with $1/\alpha$, so we get that the z-resolution is a factor of α lower.

In other applications such as tomography, it is necessary to have all features throughout the thickness of a sample in focus to obtain an accurate geometric projection. In this case, the depth of field needs to be increased as much as possible.

In this report, we will investigate if the emerging capability of shaping the wavefront of an electron beam with programmable Phase Plates (PP) would offer more freedom.

Objectives

- (1) To enhance the z-resolution by correcting the higher-order aberrations with a PP
- (2) To enlarge the depth of field attainable in the STEM using an adaptive PP.

Methods

To achieve objective (1), we correct for higher-order aberrations with a PP, following the lessons learned in our previous study (Fig. 1) [1]. Once we have a design for the PP, we do multislice simulations to observe defects at different depths in a crystal.

Fig. 1 Round ap. at 25mrad (a) vs. PP at 40mrad (b), the propagated probe is shown next to each aperture.

For objective (2), we propose a novel imaging scheme (see Fig. 2) that takes advantage of the fast and reliable tuneability of the PP that we have demonstrated before [2]; by incoherently adding up different probe configurations, we can create a Bessel-like probe that remains in focus at larger propagation lengths.

Fig. 2 Proposed imaging scheme for enhanced depth of field.

Results

The results show that for objective (1), we can design an aperture capable of correcting higher-order aberrations, thus obtaining an enhanced z-resolution without compromising the xy resolution.

For objective (2), we can enlarge the propagation length of the probe by incoherently adding several probes during a dwell time *t* (up to 5x at α=5mrad).

Conclusion

We demonstrated how a PP could be used to enhance z-resolution and enlarge the depth of field. However, such implementations need further work to overcome design constraints and the non-ideal effects that arise in real experimental setups. Nonetheless, such PP can potentially adapt to the sample, thus enhancing the imaging capabilities of the instrument.

References

[1] Vega F, Béché A, and Verbeeck J, "Can a Programmable Phase Plate serve as an Aberration Corrector in the Transmission Electron Microscope (TEM)?" arXiv e-prints (2022): arXiv-2205

[2] Verbeeck J, Vega F, and Béché A, "Demonstration of a 48-pixel programmable phase plate for adaptive electron optics," in *Electron Beam Spectroscopy for Nano-Optics*, Jun. 2021

[3] Acknowledgments to the financial support of the Research Foundation Flanders (FWO, Belgium) project G042820N. The European Research Council funds ADAPTEM as an ERC POC project under grant nr: DLV-789598. This project has received funding from the European Union"s Horizon 2020 Research Infrastructure - Integrating Activities for Advanced Communities under grant agreement No 823717 – ESTEEM3

Fig. 1

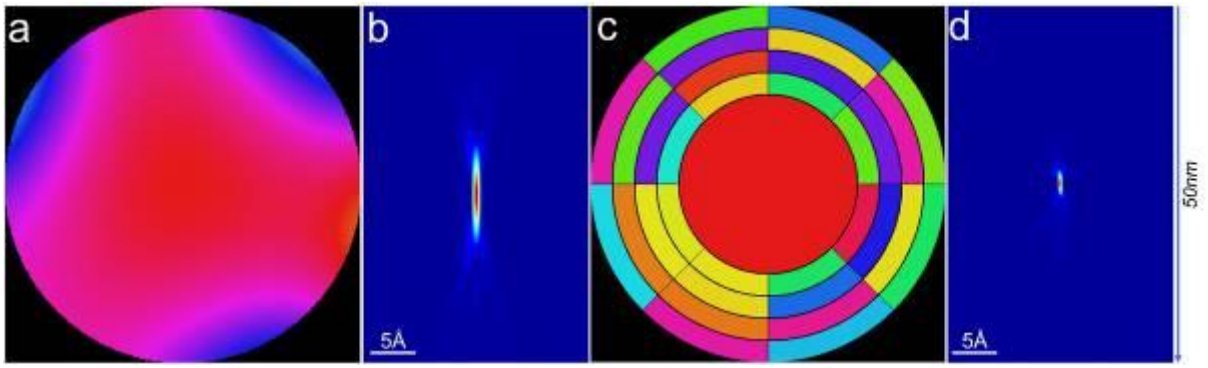

Fig. 2

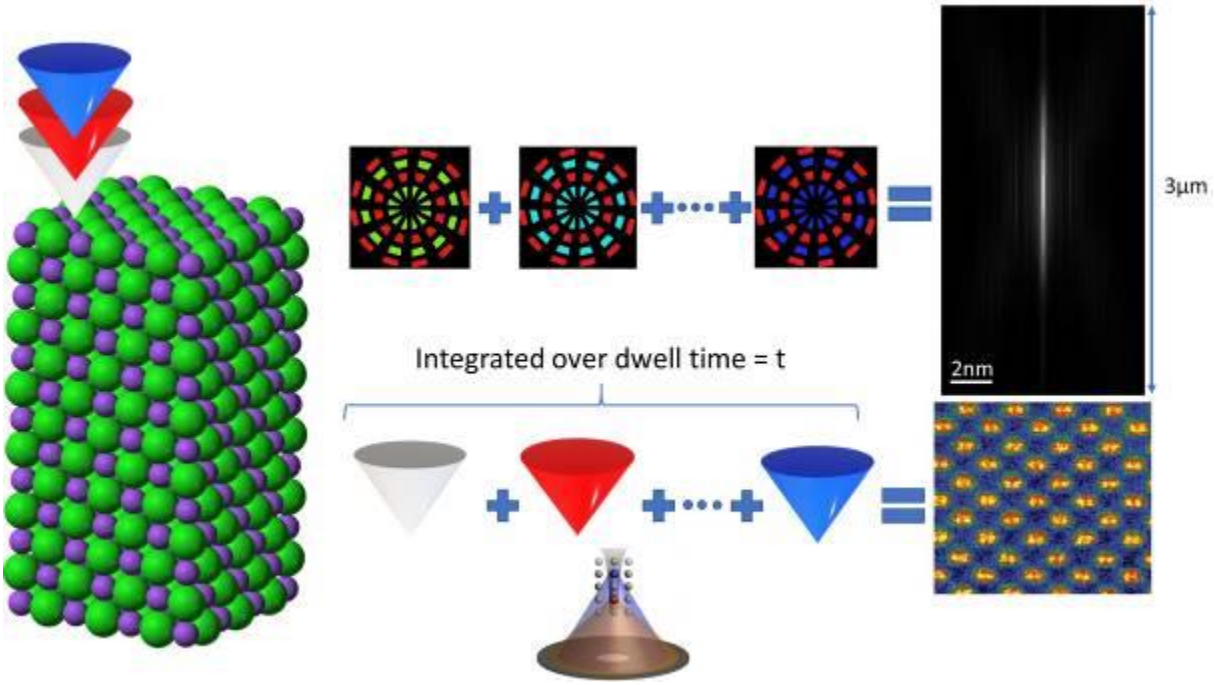

IM6.006

Structured illumination electron ptychography: probe design and experimental implementation

P. Lu[1], S. You[2], T. Schachinger[3,4], F. Allars[2], Y. Lu[1], R. E. Dunin-Borkowski[1], A. M. Maiden[2,5]

[1]Forschungszentrum Juelich, Ernst Ruska-Centre for Microscopy and Spectroscopy with Electrons and Peter Grünberg Institute, Jülich, Germany
[2]University of Sheffield, Department of Electronic and Electrical Engineering, Sheffield, United Kingdom
[3]TU Wien, Institute of Solid State Physics, Vienna, Austria
[4]TU Wien, University Service Centre for Transmission Electron Microscopy, Vienna, Austria
[5]Diamond Light Source Ltd., Didcot, United Kingdom

Ptychography measures a correlated matrix of diffraction patterns with sufficient real space overlapping between adjoining data, and reconstructs both amplitude and phase of the object as well as of the probe. In a ptychographic measurement, the multiply of real space sampling, i.e. scanning step size, ΔR (Fig. 1a) and reciprocal space sampling, $\Delta\theta$ (Fig. 1b), should be smaller than half of the wavelength [1]. A factor of ½ here is because only amplitude information is recorded in the diffraction patterns and phase information is lost (phase problem). We can then define a sampling figure of merit $S = \lambda / 2 / \Delta\theta / \Delta R$ (λ, wavelength), which must be larger than 1. In practice S is usually larger than 3 and typically takes a value of 10 to 20 (oversampling). With the additional information of the target reconstructed image pixel size (related to spatial resolution) p, detector pixel numbers N_d, one can determine the scanning step size $\Delta R = N_d * p / 2 / S$. Depending on the overlapping ratio, a proper probe size can then be calculated, especially for defocused probe ptychography.

Instead of applying defocus aberration, one could realise the desired enlarged probe in focus by adding certain population of vortices in the probe (Fig. 2c) [2, 3]. This can be realised with a patterned Si_3N_4 thin film phase mask putting in the condenser aperture plane. It would produce a structured enlarged probe with rather uniform intensity level over a wide lateral extent (Fig. 2d). If instead using an amplitude mask or a phase mask with wrong phase shift, the central spot will be much brighter than the surrounding structures and therefore diminish the advantages of the structured illumination. Following the calculation above, we can also determine the population of vortices, if the desired probe size and image pixel size is given, so the fabricated phase mask can match with the designed experimental set up.

Structured illumination is also of vital importance in near-field ptychography. In this case, the probe becomes a full-field illumination and the detector measures Fresnel (near-field) instead of Fraunhofer diffraction. Without a structured probe, each diffraction image carries the same information except it is laterally shifted, and thus the ptychography reconstruction reduces to a single phase retrieval loop. We have experimentally demonstrated near-field ptychography with electrons using a thin film phase diffuser [4] and now extended this with an amplitude mask (Fig. 2a, b) which proves to work well and avoids the inelastic scattering from the phase diffuser.

References

[1] D. J. Batey *et al*., Physical Review A 89, 043812 (2014).

[2] P. M. Pelz *et al*., Scientific Reports 7, 9883 (2017).

[3] W. Van den Broek *et al*., Microscopy and Microanalysis 25 (S2), 58 (2019).

[4] F. Allars *et al*., Ultramicroscopy 231, 113257 (2021).

Fig. 1. Illustration of real space sampling (a) and reciprocal space sampling (b) in ptychographic measurements.

Fig. 2. (a-b) Amplitude diffuser for near-field ptychography. (a) SEM image of a FIB-fabricated amplitude diffuser. (b) Experimentally reconstructed amplitude of the probe from a near-field electron ptychography measurement using the diffuser in (a). (c-d) Phase diffuser for far-field ptychography. (c) Design of a phase diffuser. (d) Experimentally measured in-focus probe structured by a FIB-fabricated Si3N4 thin film phase diffuser based on the design in (c).

Fig. 1

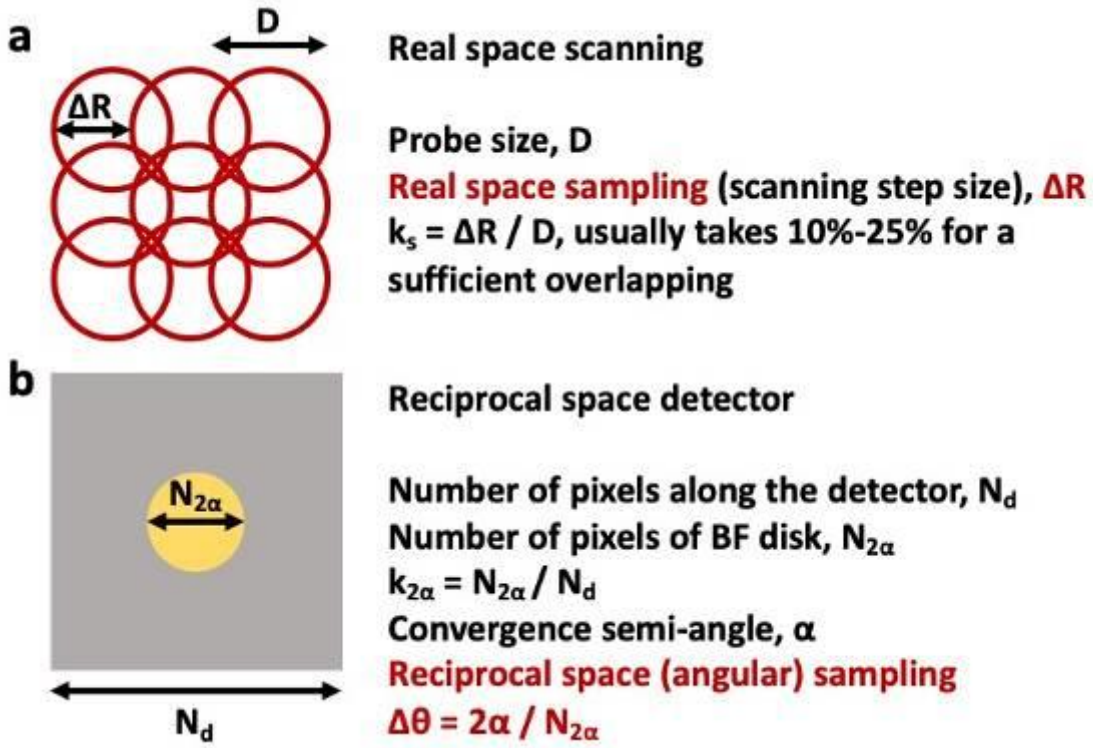
a
D
ΔR
b
$N_{2\alpha}$
N_d
Real space scanning
Probe size, D
Real space sampling (scanning step size), ΔR
$k_s = \Delta R / D$, usually takes 10%-25% for a sufficient overlapping
Reciprocal space detector
Number of pixels along the detector, N_d
Number of pixels of BF disk, $N_{2\alpha}$
$k_{2\alpha} = N_{2\alpha} / N_d$
Convergence semi-angle, α
Reciprocal space (angular) sampling
$\Delta\theta = 2\alpha / N_{2\alpha}$

Fig. 2

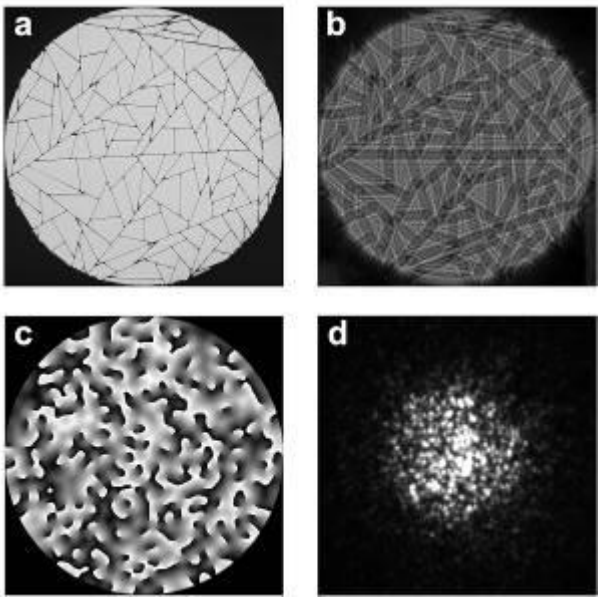
a
b
c
d

IM6.P001

Can a difference in mean inner potential be measured from a shift of the central disc in nano-beam electron diffraction?

C. Mahr[1], T. Grieb[1], F. F. Krause[1], M. Schowalter[1], A. Rosenauer[1]

[1]University of Bremen, Institute of Solid State Physics, Bremen, Germany

Measurement of electric fields in scanning transmission electron microscopy is a field of research that has seen a lot of development during the last years. The basic idea of the method is that an electric field leads to a tilt of the focused probe that can be detected as a shift in the back focal plane. Although this principle seems rather simple, a quantitative field measurement is not always possible and sometimes only approximations can be obtained. Shifts of the beam in the back focal plane were first analysed in differential phase contrast scanning transmission electron microscopy (DPC-STEM) using segmented STEM detectors[1]. Many impressive results were obtained with this technique and huge improvement has also been achieved regarding the quantitative interpretability[2,3]. The development of new hardware[4] paved the way for the fast acquisition of the full diffraction pattern while the focussed electron beam is scanned across the sample. Using a probe with a high convergence angle, atomic electric fields can be measured evaluating the centre of mass of the diffraction pattern for samples with a thickness below 5nm[5]. Using a broader probe results in diffraction patterns with non-overlapping diffraction discs. Long-range electric fields can be measured from a shift of the central disc applying disc detection techniques[6,7].Whereas in some materials electric fields are expected at interfaces between two materials[7], in the present contribution[8] we show that a shift of the diffraction pattern occurs also at interfaces in a non-polar silicon germanium sample, where no electric fields are expected (see Fig. 1). We investigate by evaluation of simulations and experiment, whether this shift can be interpreted as originating from an electric field caused by differences in the mean inner potential between regions with different chemical composition.

Fig.1: A shift of the central disc is measured in nano-beam electron diffraction at interfaces between regions with different composition.

The mean inner potential has an influence on the measured shift indeed. On the other hand, the measured shift depends on several parameters such as specimen thickness and sample orientation with respect to the electron beam, all of them leading to changes in dynamic diffraction. Even the measured field direction changes with thickness (see Fig. 2). An improvement can be achieved if electron beam precession is used. This minimizes the effects of dynamic diffraction, still preserving information stemming from the change in mean inner potential. *Fig. 2: Measured shift converted to electric field as a function of scan position and sample thickness. Direction and magnitude of the measured field strongly depend on the sample thickness.* In conclusion, we show that the simple interpretation of the measured shift of the diffraction pattern as originating from an electric field only caused by differences in mean inner potential is not correct and will be misleading in the majority of cases.

[1] H. Rose et al., Ultramicroscopy **2** (1976), p.251.

[2] J. Zweck et al., J. Magn. Magn. Mater. **104** (1992), p.315.

[3] N. Shibata et al., Nat. Physics **8** (2012), p.611.

[4] V. Özdol et al., Micros. Microanal. **20** (2014), p.1046.

[5] K. Müller et al., Nat. Commun. **5** (2014), p.5653.

[6] K. Müller et al., Micros. Microanal. **18** (2012), p. 995.

[7] T. Grieb et al., Ultramicroscopy **228** (2021) p.113321.

[8] C. Mahr et al., Ultramicroscopy **236** (2022), p.113503.

Fig. 1

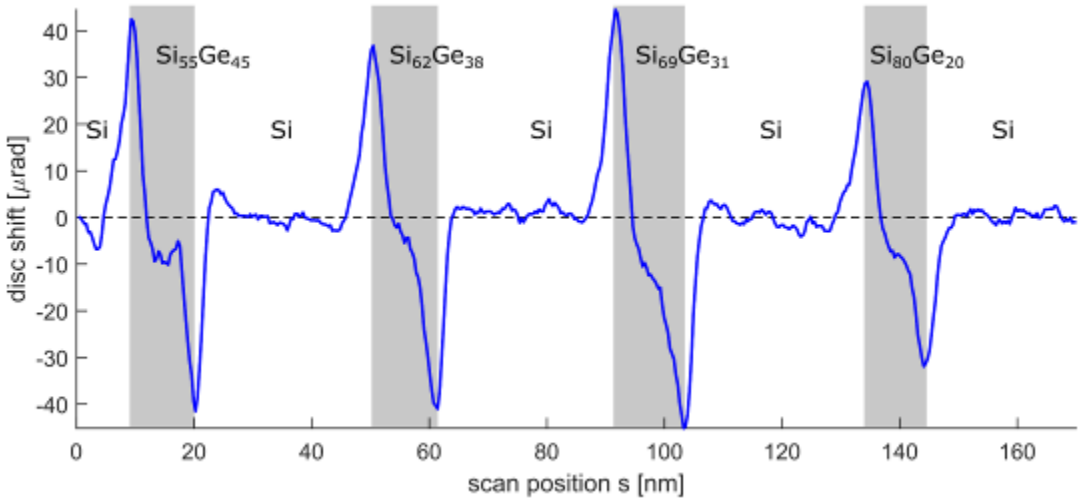
Si
Si55Ge45
Si
Si62Ge38
Si
Si69Ge31
Si
Si80Ge20
Si
disc shift [μrad]
scan position s [nm]

Fig. 2

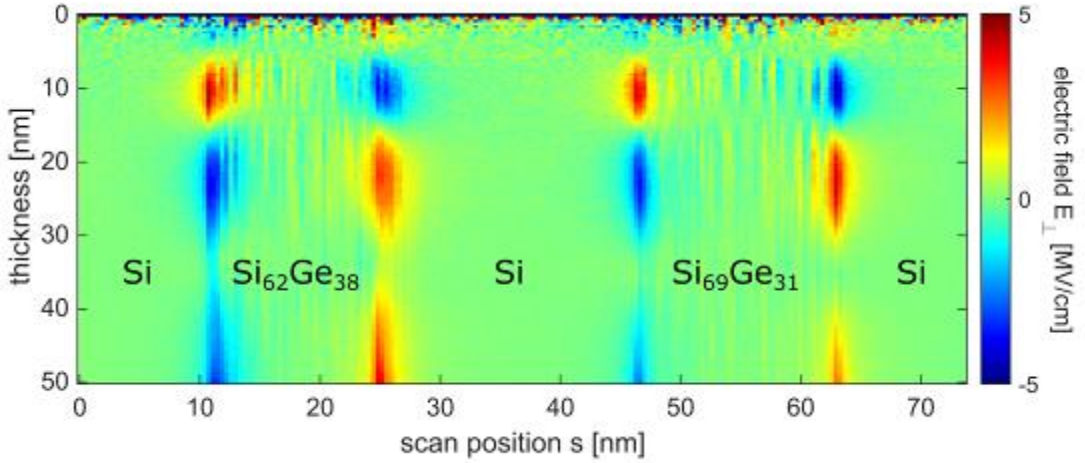
Si
Si62Ge38
Si
Si69Ge31
Si
thickness [nm]
scan position s [nm]
electric field E⊥ [MV/cm]

IM6.P002

GaN atomic electric fields from STEM: Panther vs. EMPAD

T. Grieb[1], F. F. Krause[1], T. Mehrtens[1], C. Mahr[1], M. Schowalter[1], A. Rosenauer[1]

[1]University of Bremen, Bremen, Germany

1 Introduction

High-resolution scanning transmission electron microscopy (STEM) in principle allows to measure the atomic electric fields in a specimen as the beam electrons are deflected due to electrostatic forces. To measure the electric fields, for each scan point, information of the angular distribution of the transmitted electrons need to be obtained (4D-STEM). Two different approaches for acquisition are compared: using a pixelated camera which benefits from high resolution in momentum space and a segmented electron detector which is much faster than the camera but limited by the number of segments.

2 Objectives

Using 4D-STEM, the center of mass (COM) of the intensity distribution of the transmitted electrons was measured for each scan point in an STEM image. From the COM the effective momentum transfer of the beam electrons caused by the interaction with the atomic potentials can be calculated [1,2]. The corresponding quantities such as electric field, charge density and coulomb potential are compared for the two detector types and additionally checked by quantitative simulations. The pros and cons of these techniques are discussed as well as for which conditions a quantitative measurement is possible.

3 Materials and methods

A thin GaN crystal was analysed in a Thermo Fisher (TF) Spectra 300 TEM. The electric field seen by the scanning electron beam was measured with two different detector designs: (i) Using 4D STEM with a pixelated EMPAD electron detector, for each scan point the diffraction pattern was recorded. (ii) Using a 16-segmented TF Panther detector from the which the COM is calculated by weighting the measured intensity on each detector segment.

4 Results

Fig. 1a shows the experimental dark-field intensity for pure GaN obtained by the outer segments of the Panther. Figs. 1 b-e show the projected electric field (in units of V) for experimental and simulated Panther and EMPAD detectors in a color-wheel representation. Qualitatively and quantitatively, there is a good agreement between experiment and simulation but also between the results obtained by Panther and EMPAD detector.

5 Conclusions

We show that GaN atomic electric fields can be measured with 4D-STEM using either a pixelated EMPAD camera or a segmented Panther detector in case of thin GaN layer. The experimental results are in good agreement with quantitative simulations.

FIG1. (a) Dark-field intensity obtained from outer Panther segments. (b-e) Projected electric field in GaN calculated from the centre of mass of the transmitted-electron intensity obtained by 4D-STEM in color-wheel representation: color shows direction, brightness shows the strength with a maximum (absolute) value given in the red box in each subfigure. Data (b,c) from the segmented Panther detector (b: experiment, c: simulation) and (d,e) from the pixelated EMPAD camera (d: experiment, e: simulation).

[1] K. Müller et al., Nature Communications 5 (2014), 5653

[2] N. Shibata et al., Nature Communications 8 (2017), 15631

Fig. 1

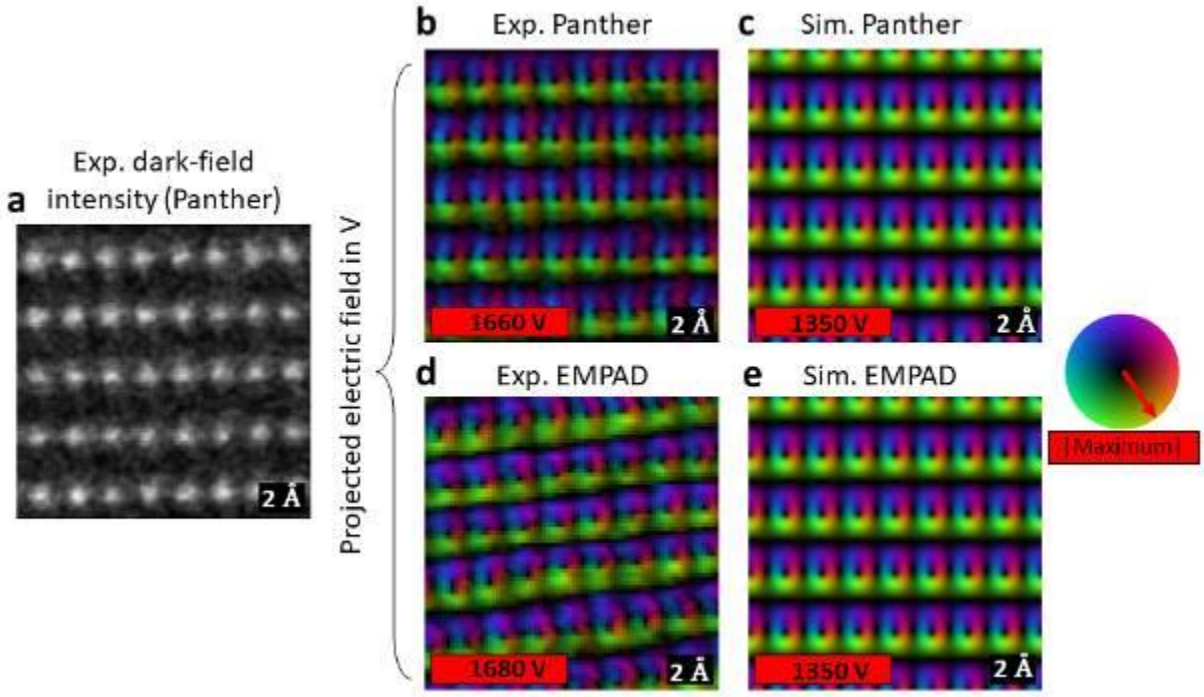
a
Exp. dark-field intensity (Panther)
2 Å
b
Exp. Panther
1660 V
2 Å
c
Sim. Panther
1350 V
2 Å
Projected electric field in V
d
Exp. EMPAD
1680 V
2 Å
e
Sim. EMPAD
1350 V
2 Å
[Maximum]

IM6.P003

Towards quantitative electric field measurements at hetero interfaces via precessing 4D-STEM

J. Scheunert[1], V. Lider[1], D. Heimes[1], A. Beyer[1], K. Volz[1]

[1]Philipps-University Marburg, Wissenschaftliches Zentrum für Materialwissenschaften, Marburg, Germany

Recently, four-dimensional scanning transmission electron microscopy (4D STEM) has been established to investigate internal electric fields on nanometer length scales [shibata, AB, …]. To achieve this, the shift of the electron-beam caused by the fields is measured. This becomes especially difficult at interfaces, where additional shifts, e.g., due to the different scattering potentials or tilt can occur.

In this work, we analyse whether precession electron diffraction (PED) is capable of removing dynamic effects that lead to a thickness-dependent oscillation of the detected beam-shift. Furthermore, we investigate if the shift momentum transfer of the field to the probe is determined more accurately by edge-detection or by the calculation of the centre-of-mass (COM) of the intensity. Finally, the ideal settings of a STEM for determining the displacing fields shall be found.

Using the STEMsalabim [JOE] multi-slice algorithm, we simulate electron scattering patterns assuming a precessing electron-beam. For that, we use p-n-homo- as well as hetero-interfaces, i.e., p-GaAs/n-GaAs, AlAs/GaAs and GaP/Si interfaces. From these we determine the COM of the direct beam and subsequently calculate E-fields and potentials across the junctions. In turn, we compare these with experimental results which were derived using a JEOL JEM 2200FS STEM equipped with a Nanomegas ASTAR PED system and a fast pnCCD pixelated detector.

Our investigations show that the precessing electron-beam does indeed reduce dynamic effects. However, we obtain clear deviations for the potential drop across the interfaces derived from the simulations and the experiments. In particular, thickness-dependent peculiarities are recognized, i.e. the difference of potentials at interfaces decreases with increasing sample-thickness in simulations.

In conclusion, we find that the method of precessing electron-beams still needs significant development to obtain the results that we expect.

This contribution will summarize our progress in the quantitative evaluation of internal electric fields at hetero-interfaces.

Fig. 1

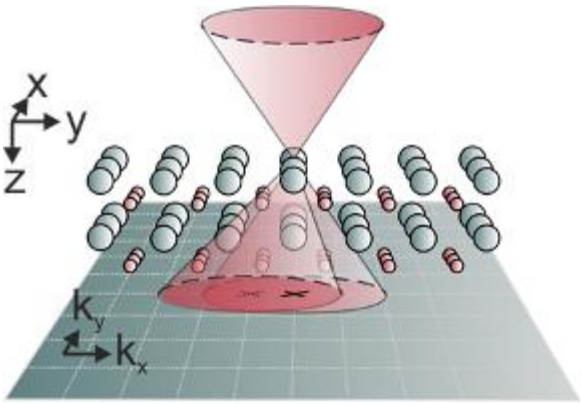

IM6.P004

Phase retrieval of WS_2 with rPIE

J. Haust[1], A. Jerath[1], O. Maßmeyer[1], J. Belz[1], A. Beyer[1], K. Volz[1]

[1]Philipps-University Marburg, Fachbereich Physik, STRL, Marburg, Germany

Introduction:

Phase retrieval in scanning transmission electron microscopy (STEM) by different ptychography algorithms gained more and more attention. It allows sub-angström resolution[1] in 2D materials, is suitable for light elements and dose efficient[2]. Furthermore, by combining ptychography with the multislice approach its application can also be extended to thicker samples[3].

Objectives:

The extended ptychographical iterative engine (ePIE) was already applied successfully for imaging 2D materials[1]. In this work we aim at utilizing an improved algorithm, the regularized PIE (rPIE)[4,5], for the phase retrieval of 2D structures as well as thicker samples e.g. given for battery materials.

Materials and Methods:

rPIE solves the phase problem by taking the recorded diffraction patterns one by one and by iteratively revising the probe and the object[4,5]. It has an improved update function, which allows more control over the update rate and gives an enhanced robustness and stability in comparison to ePIE[4,5].

In this work we benchmark the rPIE approach by simulated data in a first step and later on with experimental data. For STEM simulations our in-house developed multislice algorithm STEMsalabim[6] is used. The experimental images are acquired with an aberration-corrected JEOL JEM-2200FS STEM equipped with a fast pixelated direct electron detector (DED) by PNDetectors.

Results:

In a first benchmark test rPIE is already applied to a simulated dataset of tungsten disulfide (WS_2). The calculated phase as well as the amplitude image, as shown in figure 1, exhibit a clearly enhanced resolution in comparison to the annular dark field (ADF) image. With a subsequent simulation study, the optimal instrumental parameters like scan density, cutoff angle, and angular resolution will be determined, which will allow later on efficient acquisition of experimental data suitable for phase reconstruction. Also, the probability of extending rPIE with the multislice approach will be investigated.

Conclusion:

rPIE could be successfully applied on a simulated WS_2 dataset. This opens the path for the first experimental datasets and as well as the extension of the rPIE algorithm.

Figure 1. a) ADF image of a simulated WS_2 dataset with 80 kV acceleration voltage and 21 mrad semi-convergence angle. b) and c) Object amplitude and phase obtained with rPIE after 10 iterations.

References:

[1] Jiang, Y. et al. Nature **559**, 343–349 (2018).

[2] Song, W. et al. Joule **6**, 1049–1065 (2022).

[3] Chen, Z. et al. Science **372**, 826–831 (2021).

[4] Maiden, A. et al Optica **4**, 736 (2017).

[5] Springer Handbook of Microscopy, 819-904 (2019).

[6] Oelerich, J. O. et al. Ultramicroscopy **177**, 91–96 (2017).

Fig. 1

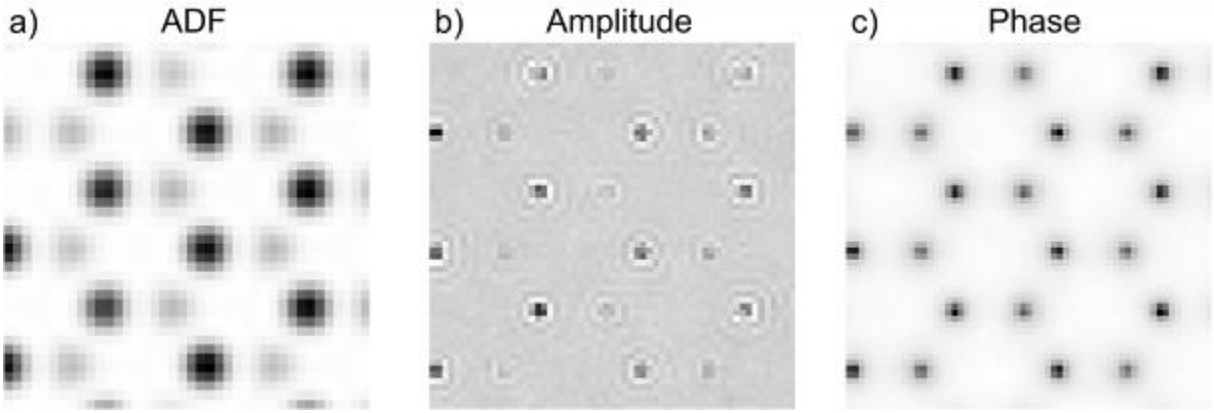

IM6.P005

Impact of dynamical scattering on first moment imaging of a ferroelectric $PbZr_{0.2}Ti_{0.8}O_3$

A. Strauch[1,2], B. März[3], M. Cattaneo[1,2], T. Denneulin[1], A. Rosenauer[4], K. Müller-Caspary[1,3]

[1]Forschungszentrum Jülich, Ernst Ruska-Centrum, Jülich, Germany
[2]RWTH Aachen University, Aachen, Germany
[3]Ludwig-Maximilians-University Munich, Department of Chemistry and Center for NanoScience, Munich, Germany
[4]Universität Bremen, IFP, Bremen, Germany

Ferroelectrics remain an important research field due to a wide range of possible nanoelectronic devices, e.g., high electron mobility transistors or ferroelectric tunnel junctions. Thus, (S)TEM methods that allow for the quantitative mapping of polarisation-induced electric fields down to the unit-cell scale are desirable to characterize and fundamentally understand such devices.

Nowadays, ultrafast cameras allow for high momentum and spatial resolution in aberration-corrected STEM. Especially, momentum-resolved STEM (MR-STEM) enabled first moment-based imaging of subatomic electric fields in thin specimens [1,2]. Recently, polarisation-induced fields in semiconductors were mapped by unit-cell averaged (uc.a.) MR-STEM data [3]. This method assumes that long-range components of the electric field are dominant over atomic ones in the uc.a. first moments. The validity of this assumption depends on crystal symmetry and experimental parameters such as specimen thickness or tilt, leading to a systematic error δ whose magnitude needs to be addressed in simulations to allow for a quantitative interpretation of mesoscopic electric field measurements.

Here, MR-STEM of non-ferroelectric $SrTiO_3$ (STO) and ferroelectric $PbZr_{0.2}Ti_{0.8}O_3$ (PZT) is considered in comprehensive experimental and simulation studies. A unit cell segmentation is performed to yield the uc.a momentum transfers P. Ideally, this corresponds to a potentially present local polarisation-induced electric field, however, a detailed assessment of δ reveals systematic errors of at least the same magnitude. First, we determine the mistilt from [100] zone axis and the in-plane rotation from Kikuchi bands. This exhibits strong domain contrast in PZT, too, which requires a careful interpretation of the apparent electric field contrast among domains determined from uc.a P, because also δ varies strongly in dependence of tilt. A striking example is STO, where the uc.a P takes partly large values although no internal electric fields are present.

The experimental uc.a P are compared to thickness- and tilt-dependent multislice simulations for each PZT domain with the experimental conditions as input. Using an isolated atom model with periodic boundary conditions in STEMsim [4], we find that all non-zero uc.a. first moments arise from dynamical scattering and symmetry breaking (mistilt and atom displacements in PZT). We finally address sources of ambiguities in measuring the momentum space origin arising from perturbed reference data, similar to perturbed reference waves in electron holography.

For non-ferroelectric STO, Fig. 1 shows that the uc.a. P varies with tilt and thickness of the sample. Here, only the systematic error δ can be the cause. For ferroelectric PZT, Fig. 2 shows that the uc.a. P gives domain contrast, that could erroneously be interpreted as different polarisation-induced electric fields. However, the contrast is mainly caused by crystallographic tilt and rotation.

To conclude, the contrast in unit-cell averaged first moments is mainly caused by structural effects and dynamical scattering and not by a polarisation-induced electric field.

Fig. 1: a) P, b) uc.a. P and c) tilt of an STO data set.

Fig. 2: a) P, b) uc.a. P and c) tilt of a PZT data set.

[1] Nat. Commun. 5 p. 5653 (2014)

[2] Ultramicroscopy 178 p. 62 (2017)

[3] Phys. Rev. Lett. 122 p. 106102 (2019)

[4] Mat. 120 p. 1316 (2007)

[5] Funding: Initiative and Network Fund (Helmholtz), contract VH-NG-1317

Fig. 1

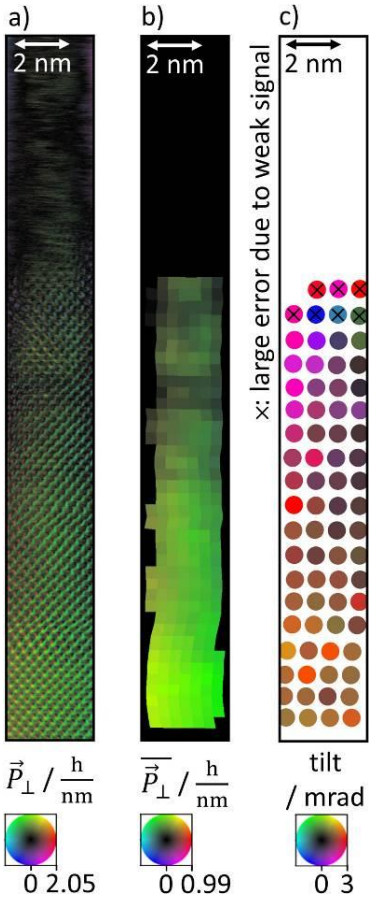

Fig. 2

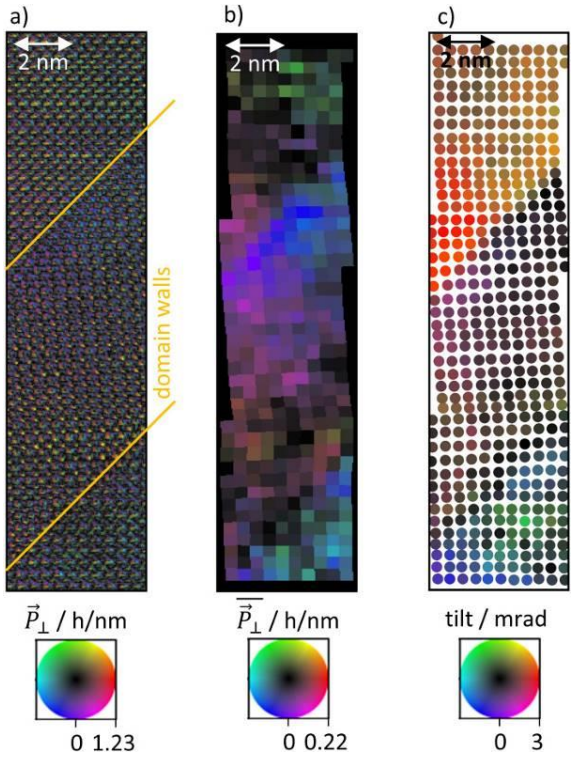

IM6.P006

Towards quantitative measurements of electric fields in TEM: a synergy of electrical biasing STEBIC and off-axis electron holography

F. Otto[1], T. Wagner[1], S. Koloffon[1], H. Çelik[1], D. Berger[2], C. Günther[2], M. Lehmann[1]

[1]Technische Universität Berlin, Instutitut für Optik und Atomare Physik, Berlin, Germany
[2]Technische Universität Berlin, Zentraleinrichtung Elektronenmikroskopie (ZELMI), Berlin, Germany

Most of today"s electronic devices, like solar cells or transistors, are based on electric fields at the junctions of doped semiconductors. As electronic devices keep shrinking, identifying electric fields on an increasingly smaller scale is an important part of the optimization of these devices. Two possible options to map electric fields with a high spatial resolution are electron beam induced current (EBIC) in a (S)TEM and off-axis electron holography (EH). In EBIC, the current induced by the electron beam scanning over the specimen is measured, while EH detects a shift to the electron phase by an electrostatic potential.

Although EH has been studied intensively over the past decades, it still faces several challenges, hindering quantitative determination of electrostatic potentials. Especially the changes of the properties of an effectively two-dimensional p-n junction when reducing a sample to TEM specimen still pose several problems [1]. Previous works have shown that electric stray fields outside the specimen have an influence on the measurement of the build-in potential in off-axis electron holography [2]. EBIC has, in the past, been used for the mapping of electric fields in SEM. Although, by performing EBIC in a (S)TEM (STEBIC), a higher spatial resolution is achieved [3], it is not yet a common practice and has only recently gained traction due to advancements in the development of biasing holders and STEM units. Now, STEBIC faces similar challenges that EH had to overcome, while others are still relevant for both methods.

In this work, knowledge gained through EH is used in order to deepen the understanding of collected charge carriers induced by the electron beam in such an effectively two-dimensional p-n junction. As a first step of unifying both methods, STEBIC and EH experiments are performed under the same conditions (i.e. in the same microscope). A symmetrically doped p-n junction in silicon is investigated by both EH and STEBIC (Figure 1). The negative EBIC current measured by STEBIC is proportional to the electric fields in a silicon p-n junction, while the phase shift (Φ) measured in EH is proportional to the electrostatic potential. Thus, its derivation $d/dy\ \Phi$ is comparable to the STEBIC signal. By setting both signals side to side, the STEBIC signal, contrary to EH, mimics the symmetry of the junction"s doping concentration (Figure 2). Under reverse bias (-2 V), the expected increase of the electric field at the junction can be observed. Based on the similar behavior that both methods exhibit under bias, we conduct further exploration of the methods with focus on the width of the recorded profiles. Through finding similarities and differences between the two methods, a pathway to quantitative investigations of electric fields in TEM seems feasible.

[1] Ankur Nipane et al., J. Appl. Phys. 122, 194501 (2017)
[2] T. Wagner, PhD-Thesis, TU Berlin (2022)
[3] Aidan P. Conlan et al., J. Appl. Phys. 129, 135701 (2021)

Fig. 1: Overview of the symmetric p-n junction in silicon. Exemplary EBIC, phase and d/dy phase images from the marked areas.

Fig. 2: Electric field in a pn-junction in terms of negative EBIC current from STEBIC and d/dy phase profiles from EH according to marked areas in Fig. 1.

Fig. 1

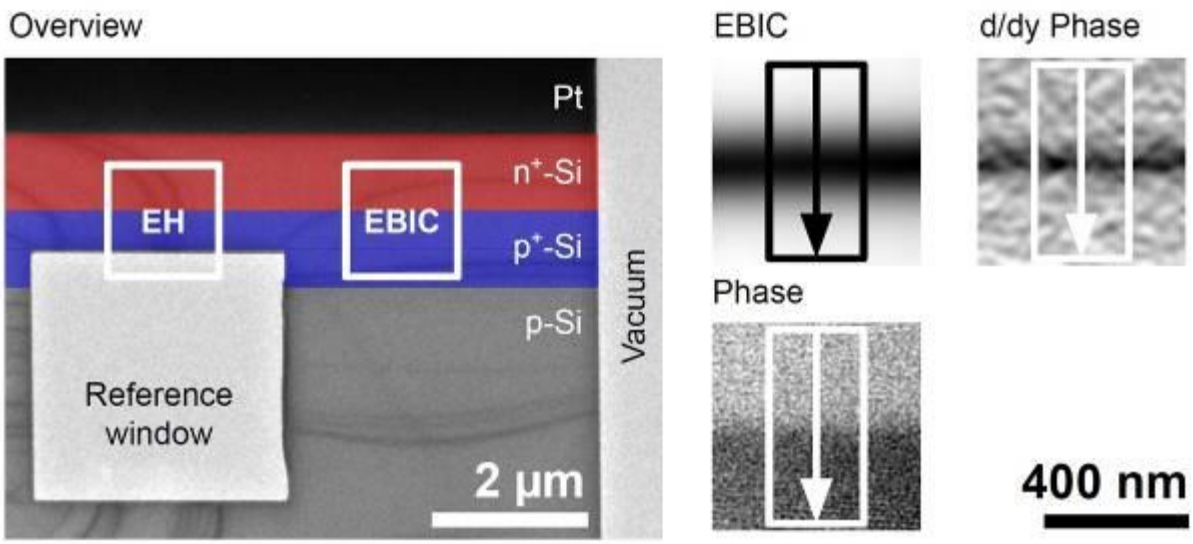
Overview
Pt
n+-Si
p+-Si
p-Si
EH
EBIC
Reference window
2 µm
Vacuum
EBIC
Phase
d/dy Phase
400 nm

Fig. 2

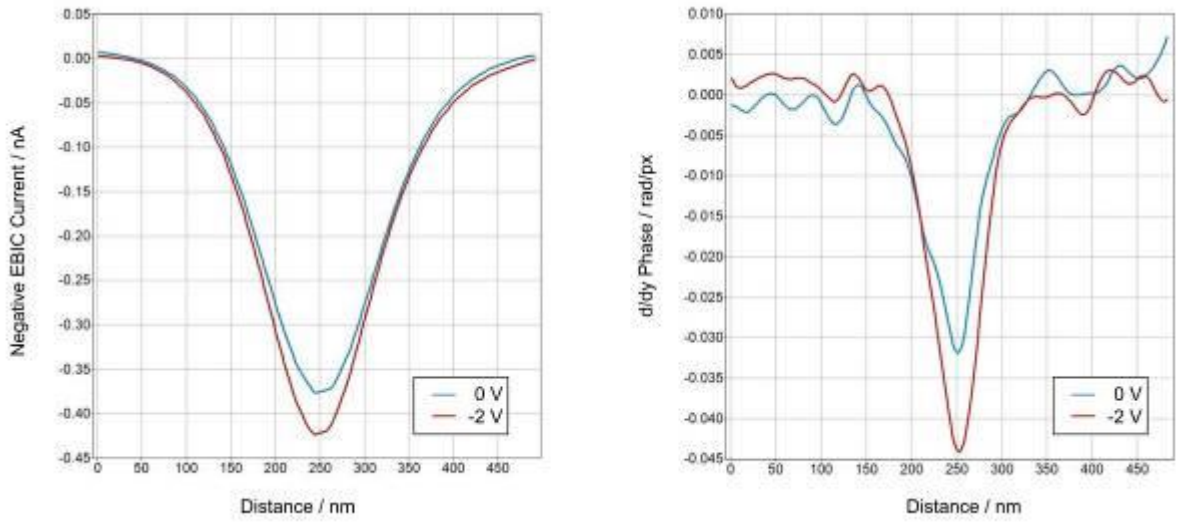
Negative EBIC Current / nA
Distance / nm
0 V
-2 V
d/dy Phase / rad/px
Distance / nm
0 V
-2 V

IM6.P007

Shape sensitivity in momentum resolved STEM

H. Dulisch[1,2], H. L. Robert[1,2], P. Lu[1,2], F. Kirner[3], E. Sturm[3], R. E. Dunin-Borkowski[1,2], K. Müller-Caspary[4]

[1]RWTH Aachen University, Aachen, Germany
[2]Forschungszentrum Jülich, Ernst Ruska-Centre, Jülich, Germany
[3]Ludwig-Maximilians-University Munich, Department of Earth and Environmental Sciences, Munich, Germany
[4]Ludwig-Maximilians-University Munich, Department of Chemistry, Munich, Germany

In 4D STEM, the Center of Mass (COM) signal is commonly used to measure electromagnetic fields. Its direct interpretation relies on the use of Ehrenfest's theorem and on the Phase Object Approximation (POA)[1]. One challenging aspect to quantify in such measurements is the signal arising at interfaces with different mean inner potentials (MIP). This component of the COM is therefore dependent on the shape of the investigated specimen. Nonetheless, in general, the direct interpretation of this contrast is not as straightforward as previously described. This is due to atomic electric fields, which makes it necessary to take the effects of propagation and multiple scattering into account [2].

In this work, we studied to which extent dedicated conditions can suppress the influence of high spatial frequency components, and where the specimen can be described with a continuous model (CM), with the inclusion of propagation and scattering effects at interfaces via multislice (MS) calculations. There, the specimen-beam interaction simplifies to a refraction-like behaviour.

This model is tested through MIP measurements of large (~100 nm) amorphous latex spheres. The projected potential is retrieved via integration in Fourier space of the electric fields, calculated from the COM data, and the polar average around the center of the sphere is fitted via linear least squares. Our extracted result of 5.92 V from the experimental curve in figure 1 shows deviations from previous measurements [3]. The curve also shows a mismatch in shape, which can be explained by including charging heuristically with the help of MS simulations within the CM approach.

We then employ this model on facetted gold nanoparticles (≤30 nm) [4] in an attempt to deduce their projected shape. Our findings show that this type of model is only applicable under certain conditions and can then only be used to understand qualitative features as those visible in figure 2. Quantitative agreement is hindered by thickness and orientation dependency of the effective MIP acting on the electron travelling through a crystalline specimen.

Funding from the Initative and Network Fund of the Helmholtz Association under contracts VH-NG-1317 and ZT-I-0025 are gratefully acknowledged

Figure 1: a) Measurement of an experimentally retrieved projected potential of a latex sphere next to a simulated one in figure 1 b). The simulated one is only half the size as in the experiment, but includes additional heuristic charging potentials to fit better to the experimental data. c) Normalized profile curves from from spheres in a) and b), with the addition of a simulated uncharged sphere. The filled blue region marks the curve of a perfect sphere. The curves from a) and b) deviate from the perfect sphere but show good qualitative agreement between each other.

Figure 2: Comparison between experimental (left) and simulated (right) COM. The COM is depicted in color wheel representation. The simulation shows good qualitative agreement with the experimental data within the marked region of interest (white doted square). The model used for the MS is visible in the bottom right corner.

References:

[1] Knut Mu ̈ller et al. In: Nat. Com. 5.1 (2014), p. 5653.

[2] Christoph Mahr et al. In: Ultram. 236 (2022), p. 113503.

[3] Frederick Allars et al. In: Ultram. 231 (2021), p. 113257.

[4] Felizitas Kirner et al. In: J. Mater. Chem. C 8 (31 2020), pp. 10844–10851.

Fig. 1

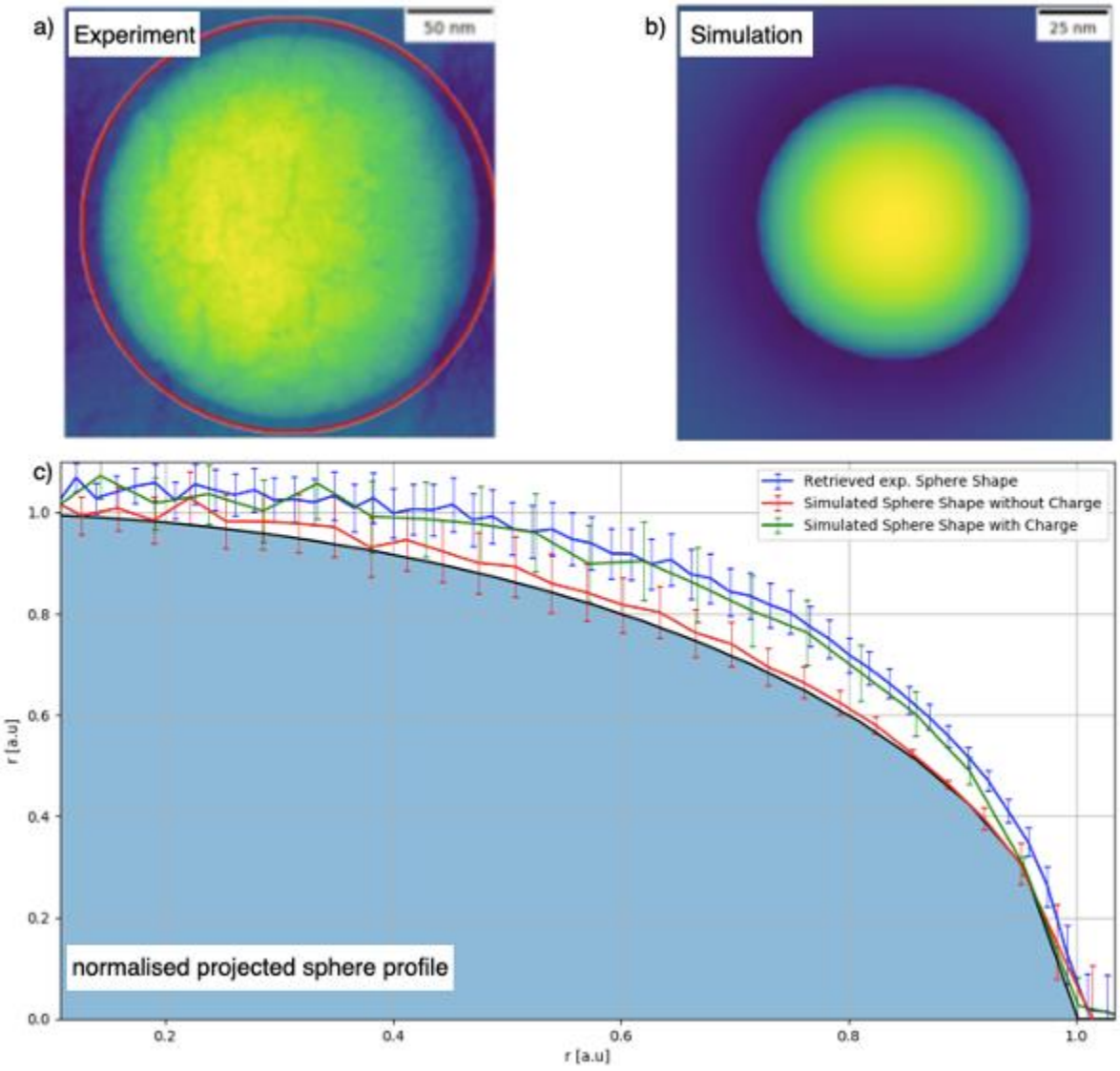
a)
Experiment
50 nm
b)
Simulation
25 nm
c)
Retrieved exp. Sphere Shape
Simulated Sphere Shape without Charge
Simulated Sphere Shape with Charge
normalised projected sphere profile
r [a.u]
r [a.u]
0.0
0.2
0.4
0.6
0.8
1.0

Fig. 2

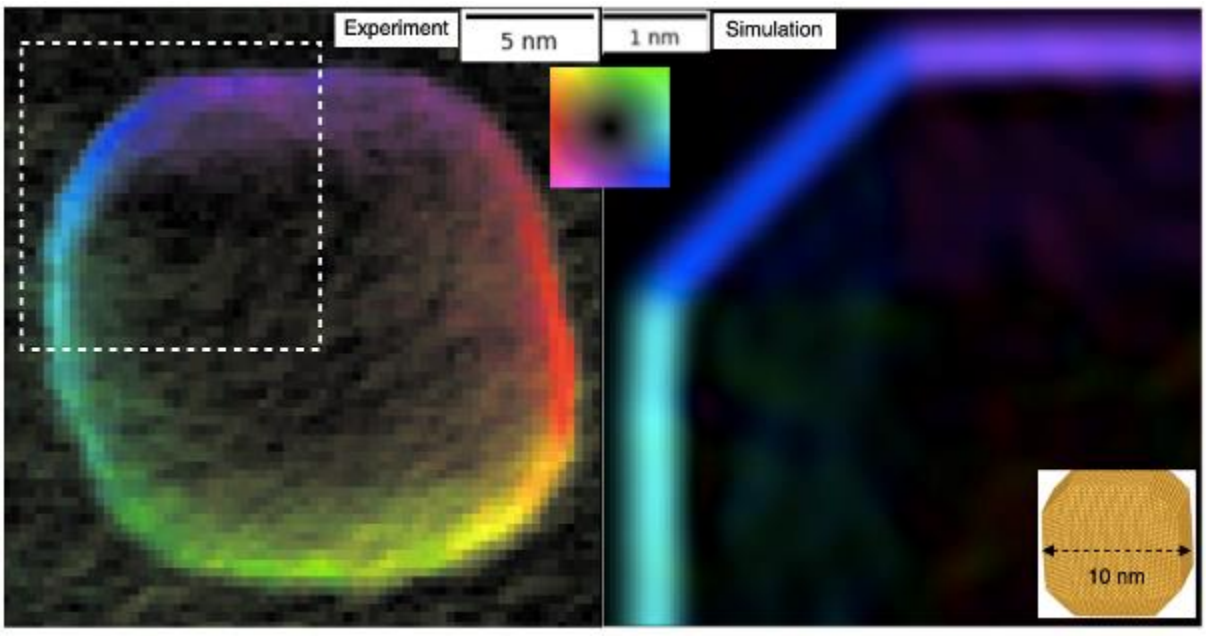
Experiment
5 nm
1 nm
Simulation
10 nm

IM6.P008

Electron ptychographic phase imaging of beam-sensitive all-inorganic halide perovskites using 4D-STEM

A. Scheid[1], Y. Wang[2], M. Jung[3], T. Heil[1], D. Moia[3], J. Maier[3], P. A. van Aken[1]

[1]Max Planck Institute for Solid State Research, Stuttgart Center for Electron Microscopy, Stuttgart, Germany
[2]Nanjing University of Aeronautics and Astronautics, Center for Microscopy and Analysis, Nanjing, China
[3]Max Planck Institute for Solid State Research, Physical Chemistry of Solids, Stuttgart, Germany

Halide perovskites have remarkable electronic properties that make them promising for applications in photovoltaics and optoelectronics. Despite the latest advances in performance optimization and low-cost manufacturing, halide perovskites still face significant challenges with chemical instability. In this context, a great interest has emerged in the chemistry and perovskite community to comprehend the chemical (in)stability and to develop engineering strategies for improving the robustness of perovskite devices [1].

To date, the sensitivity of halide perovskites to the electron beam limits a deeper understanding of the fine structure at the atomic level, which would provide valuable guidance for the optimization of the device performance. Under irradiation, the atomic structure of all-inorganic halide perovskites is disrupted by electron-beam-induced stimulated desorption of halide species. Due to this sensitivity, many of the conventional investigation techniques often utilized for optoelectronic materials, such as bright-field and dark-field scanning transmission electron microscopy (STEM) or spectroscopic methods, are not an option for atomic-scale characterization [2, 3].

In this study, we demonstrate that ptychographic phase reconstructions from 4D-STEM datasets offer great potential to fill this gap for atomic structure investigations with low electron-dose exposure. Recent progress in the development of direct electron cameras (DECs) allows for the acquisition of low-dose, sparse binary diffraction patterns at high frame rates. Specific sample information, such as high-angle scattering to generate synthetic dark-field images or the bright-field disc necessary for phase reconstructions, can be extracted in post-processing steps. With Single-Sideband (SSB) and Wigner-Distribution-Deconvolution (WDD) algorithms, it is possible to reconstruct the electrostatic potential of the sample and thereby obtain high signal-to-noise ratio (SNR) images with a strong phase contrast for all atomic species [4, 5]. The superior dose-efficiency of ptychography with improved SNR allows visualization of fine structural details, invisible in synthetic dark-field images, computed from the same dataset. Atomically resolved phase images of three all-inorganic halide perovskites, CsPbBr3, CsPbIBr2, and CsPbI3, are presented with a resolution down to the aperture-constrained diffraction limit. In addition, we show that even for slightly thicker samples, low-dose ptychographic reconstructions give a representation of the atomic structure [6].

References

[1] T. A. Berhe et al., Energy Environ. Sci., **9**, 2 (2016).

[2] X.-G. Zhou et al., J. Phys. Chem. C, **125**, 19 (2021).

[3] S. Chen et al., Journal of Applied Physics. **128**, 1 (2020).

[4] C. M. O'Leary et al., Appl. Phys. Lett. **116**, 12 (2020).

[5] J.M. Rodenburg et al.,Phil. Trans. R. Soc. Lond. A. **339**, 1655 (1992).

[6] This work is received funding the European Union's Horizon 2020 research and innovation programme under grant agreement No. 823717 – ESTEEM3.

Figure 1. Synthetic LAADF and phase-reconstructed atomic structure images from 4D-STEM datasets. (a)-(c) CsPbBr3, acquired under conventional STEM imaging conditions. (d)-(f) CsPbIBr2, acquired under low dose conditions with an average dose of ~4070 e-/Å2. The inset shows structural overlays of possible crystallographic directions, indistinguishable in the LAADF image. (g)-(i) CsPbI3, acquired with an average dose of ~3540 e-/Å2.

Fig. 1

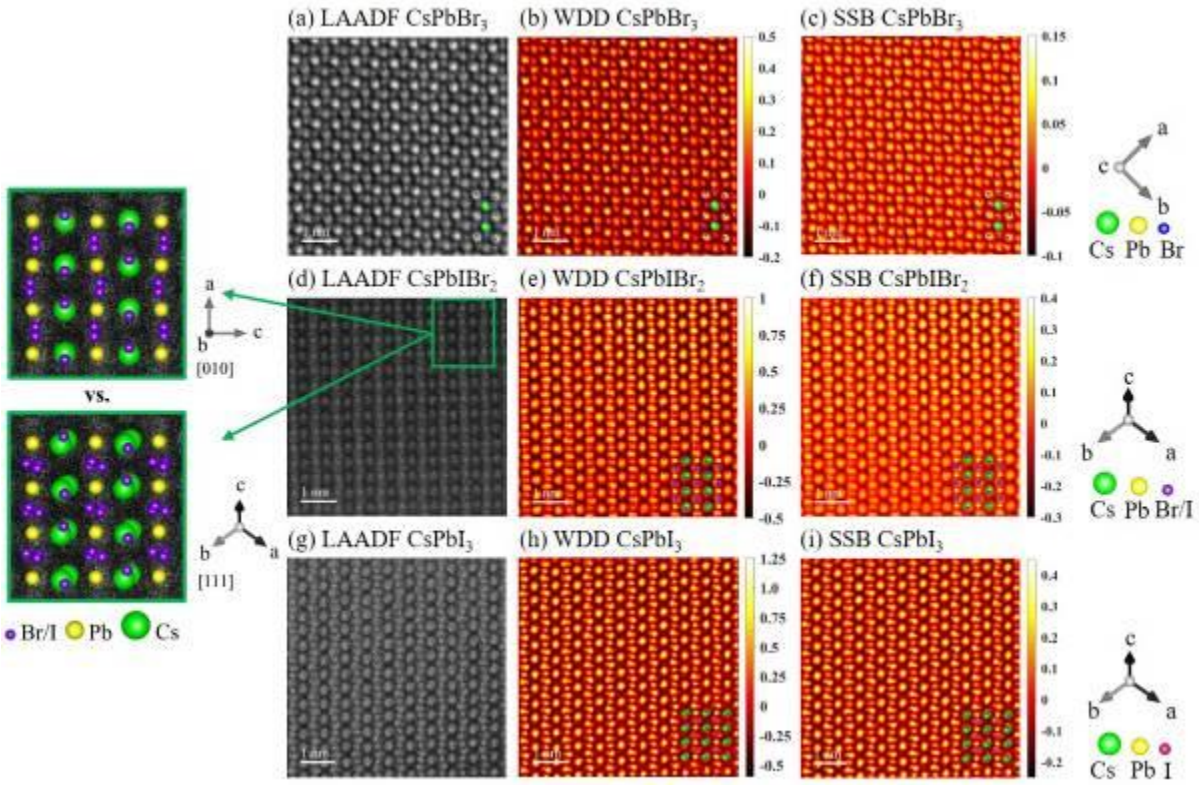
(a) LAADF $CsPbBr_3$
(b) WDD $CsPbBr_3$
(c) SSB $CsPbBr_3$
(d) LAADF $CsPbIBr_2$
(e) WDD $CsPbIBr_2$
(f) SSB $CsPbIBr_2$
(g) LAADF $CsPbI_3$
(h) WDD $CsPbI_3$
(i) SSB $CsPbI_3$
vs.
[010]
[111]
Br/I Pb Cs
Cs Pb Br
Cs Pb Br/I
Cs Pb I

IM6.P009

Simultaneous mapping of magnetic and atomic structure of ferromagnetic metallic glass using Ltz-4D-STEM

S. Kang[1,2], D. Wang[1,3], C. Minnert[4], K. Durst[4], C. Kübel[1,2,3], X. Mu[1]

[1]Karlsruher Institut of Technologie (KIT), Institute of Nanotechnology, Eggenstein-Leopoldshafen, Germany
[2]Technical University Darmstadt, Joint Research Laboratory Nanomaterials, Darmstadt, Germany
[3]Karlsruher Institut of Technologie (KIT), Karlsruhe Nano Micro Facility, Eggenstein-Leopoldshafen, Germany
[4]Technical University Darmstadt, Department of Materials Science, Darmstadt, Germany

Magnetic materials consist of a domain structure where the magnetic fields of dipoles are grouped together and aligned to minimize magnetostatic energy. The formation of the magnetic domains is associated with magnetic anisotropies which tun the local configuration of spins. According to magneto-elastic coupling, magnetic anisotropies are coupled to local atomic displacement [1]. Therefore, a strain field within a material can induce rearrangement of the domain structure giving rise to the complicated magnetic responses of magnets [2]. For soft ferromagnetic metallic glass (SFMG), which originally possess an isotropic atomic structure, the magnetic domain rearrangement of SFMGs is extremely sensitive to the local deviatoric distortion at the atomic scale [1, 3]. Highly sensitive measurement of strain, magnetic field, and atomic structure in SFMGs at the nanometer scale is desired for new material designs.

Here, we developed Lorentz 4-dimensional scanning transmission electron microscopy (Ltz-4D-STEM) for correlative mapping of the magnetic structure, strain field, and atomic density of a Fe-based SFMG. A quasi-parallel electron probe is focused to ~10 nm diameter on the soft magnetic TEM sample under field-free conditions as illustrated in Figure 1**A**. Electron diffraction patterns are acquired from the nano-volume at each scan position during stepwise scanning of the probe over the area of interest. Diffraction patterns are shown in the background. As illustrated in Figure 1**B,** measuring the center positions of each local diffraction pattern provides a magnetic domain map. Measuring the strength and orientation of elliptical deviation of each local diffraction pattern provides strain fields and a corresponding map of elastic energy. Quantifying the area encircled by the 1st ring of each diffraction pattern provides an atomic packing density map [4]. Thus, this method simultaneously provides a correlative visualization of multi-field and atomic structure information with a pixel-level correlation. Figure 1**C** shows typical results from the Lorentz 4D-STEM. The magnetic field , first principal strain , and relative atomic packing density are simultaneously measured from a deformed SFMG.

Figure 1. Schematic illustration of Lorentz 4D-STEM. (**A**) The electron probe is focused on the soft magnetic TEM sample under field-free conditions. Spatially-resolved diffraction patterns are collected during scanning over a shear band in a deformed metallic glass. (**B**) Data processing: the center of mass (CoM) of a direct beam measures the momentum transfer in the diffraction pattern by the magnetic field (Lorentz forces) inside of the sample under the probe positions. The principal strains (and) are calculated from the elliptic distortion of the diffraction ring from a perfect circle. The local atomic packing density is quantified by the area encircled by the 1st ring of each diffraction pattern. (**C**) Obtained data, magnetic field , strain field and relative atomic packing density from a deformed soft magnetic Fe85.2Si0.5B9.5P4Cu0.8 MG ribbon.

[1] Shen et al, *Nat. Commun.* 9, 4414, (2018)

[2] Lei, N. et al. *Nat. Commun*. 4, 1378 (2013)

[3] Pascarelli, S. et al.. *Phys. Rev. Lett*. 99, 237204 (2007)

[4] Kang et al, *Nat. Commun*, Under review. Currently available at *Nature portfolio* https://doi.org/10.21203/rs.3.rs-1545335/v1%20(2022) (2022)

Fig. 1

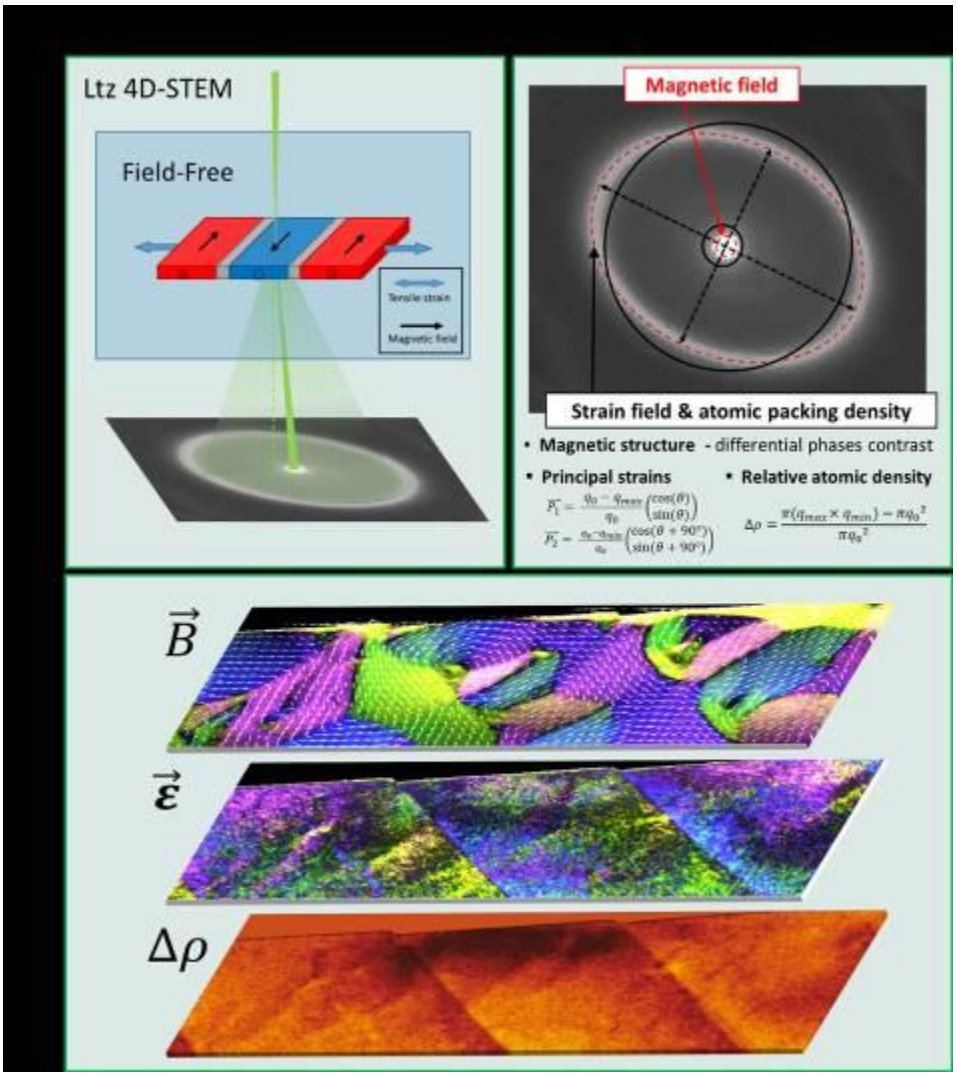
Ltz 4D-STEM
Field-Free
Tensile strain
Magnetic field
Magnetic field
Strain field & atomic packing density
• Magnetic structure - differential phases contrast
• Principal strains
• Relative atomic density
$\vec{B}$
$\vec{\varepsilon}$
$\Delta\rho$

IM6.P010

In-situ electric fields mapping of potential-induced processes by pixelated-DPC

P. Ranieri[1], R. Ignatans[1], V. Boureau[2], V. Tileli[1]

[1]École Polytechnique Fédérale de Lausanne (EPFL), Institute of Materials, Lausanne, Switzerland
[2]École Polytechnique Fédérale de Lausanne (EPFL), Interdisciplinary Center for Electron Microscopy (CIME), Lausanne, Switzerland

Mapping the local electric field of ferroelectric materials under biasing conditions can enlighten the mechanisms of switching domain evolution phenomena [1], with consequences in energy harvesting and computing applications. Quantification of the electric field in ferroelectric perovskite oxides, inside a transmission electron microscope (TEM), has been demonstrated using off-axis electron holography [2]. However, this technique is limited by the need for a vacuum region close to the area of interest which make these measurements under applied bias challenging. On the other hand, differential phase contrast (DPC) technique performed in 4D scanning TEM (STEM) configuration can provide an evaluation of the electric field without these restrictions [3].

Pixelated-DPC can provide an evaluation of electric fields but quantitative measurements are prone to artifacts. The result of the measurement is also influenced by the material characteristics since from these depends the mean inner potential. Our objective is to evaluate the accuracy of the technique in vacuum for the mapping of electrostatic fields in a model system. For this purpose, we used a coplanar micrometric capacitor fabricated on a MEMS chip for in-situ biasing.

A DensSolutions Lightning holder was used to apply a potential to the plates of the capacitor and 4D-STEM acquisition was performed in a Thermo Fisher Scientific Titan Themis microscope operated at 300 kV equipped with a MerlinEM detector. The electric field generated by the micro-device was simulated with finite element modeling (FEM) using COMSOL 5.5 software. This allows for a direct comparison of the electric field of the model system with the pixelated-DPC experiment.

The electron beam deflection induced by the capacitor is mapped and then quantitatively converted into electric field using the center of mass (COM) method that allows to quantify the shift of the transmitted beam [4]. The difference of COM maps (object and reference) is used to measure the beam deflection free from descan artifacts. This results in a measure of the integral of the in-plane component of the electric field over the electron path. This quantitative measurement is directly compared to the FEM model by computing the projection (or integral) of the field along the z direction, assumed as the direction of electron propagation. Overall, the pixelated-DPC measurement shows a quantitative agreement with the model. Although the sensitivity of the measurement is very good, the accuracy of the measurement suffers from artifacts.

In conclusion, we developed a workflow for quantitative evaluation of electric fields in vacuum using a model capacitor system, which results in reasonable agreement with the simulated projected field.

References:

[1] R. Ignatans et al., Physical Review Letters 127.16 (2021)
[2] T. Matsumoto et al., Applied Physics Letters 92 (2008)
[3] K. Moore et al., APL Materials 9.2 (2021)
[4] V. Boureau et al., Journal of Physics D: Applied Physics, 54 (8) (2021)

IM6.P011

Reciprocity based phase contrast in a conventional TEM setup

T. Lorenzen[1], B. März[1], I. Kaminska[1], A. Beyer[2], K. Volz[2], P. Tinnefeld[1], K. Müller-Caspary[1]

[1]Ludwig-Maximilians-University Munich, Department of Chemistry, Munich, Germany
[2]Philipps-University Marburg, Department of Physics, Marburg, Germany

The advent of fast pixelated detectors has greatly increased the capabilities for phase retrieval in scanning transmission electron microscopes (STEM) using center of mass (COM) imaging or various ptychographic techniques. In a conventional TEM (CTEM) setup phase contrast either requires modification of the instrument by using phase plates or applying a defocus, thereby limiting the interpretability and resolution.

Here a method is presented by which reciprocity is exploited to create STEM datasets in a CTEM setup from a series of beam tilts. The reciprocity theorem equates a single CTEM beam tilt with a STEM detector pixel, furthermore the radius of the objective aperture and the convergence semi angle of the STEM probe are related [1].

In a STEM setup the whole diffraction pattern is created for each scan point but only parts are sampled by the detector. However, in most cases the crucial information is carried by a small portion of the Ronchigram. Hence a method would be desirable to dedicatedly record the required reciprocal information, especially for low-dose applications. By exploiting the reciprocity relation only the wanted parts of the diffraction space are created. This can be used to reduce measurement times and increase dose efficiency, for example by not sampling the center of the primary beam which does not contain much information [2].

In this work, two specimen were investigated. The application of the method to semiconductor crystals allowed the visualization of the weak built-in electric fields of a pn junction, a feature formerly restricted to STEM setups employing pixelated, DPC detectors or electron holography (Figure 1).

Application to DNA Origamis showed greatly increased contrast when compared to normal CTEM images (Figure 2). Even the minimum of four different tilts around the edge of an aperture greatly increased contrast. The measurement time is reduced drastically compared to similar STEM acquisitions (1 s per 2k x 2k image, four images total).

The recording time can be reduced further by precessing the beam around the edge of the aperture while simultaneously recording images using a fast camera. In this approach the measurement time is not delayed by the speed of the beam tilt coils or delays resulting from the used software interface. Using a Merlin detector 100 images were recorded in 0.1 seconds which reduced the influence of specimen drift.

Of particular interest is the application to biological or other dose-sensitive specimen, due to the promise of increased contrast while keeping measurement times low. Additionally the method allows the introduction of phase contrast into labs which do not have scanning units or segmented detectors. The relation between the chosen beam tilts and the observed contrast transfer is shown and problems like specimen drift will be discussed.

[1] Cowley, J. M. (1969). *Applied Physics Letters*, *15*(2), 58-59.

[2] Lazić, I., Bosch, E. G., & Lazar, S. (2016). *Ultramicroscopy*, *160*, 265-280.

[3] K. M.-C., B. M. and T.L. acknowledge funding from the DFG, contract EXC 2089/1 – 390776260 (e-conversion).

Figure 1: CTEM image of the GaAs specimen (a), the pn-junction is contained between the AlAs marker layers. While invisble in the CTEM image, the pn-junction is visible in the x-component of the COM (b), the average COM-shift perpendicular to the pn-junction is shown.

Figure 2: CTEM image of L-shaped DNA Origamis (a) and calculated integrated COM of the same area (b).

Fig. 1

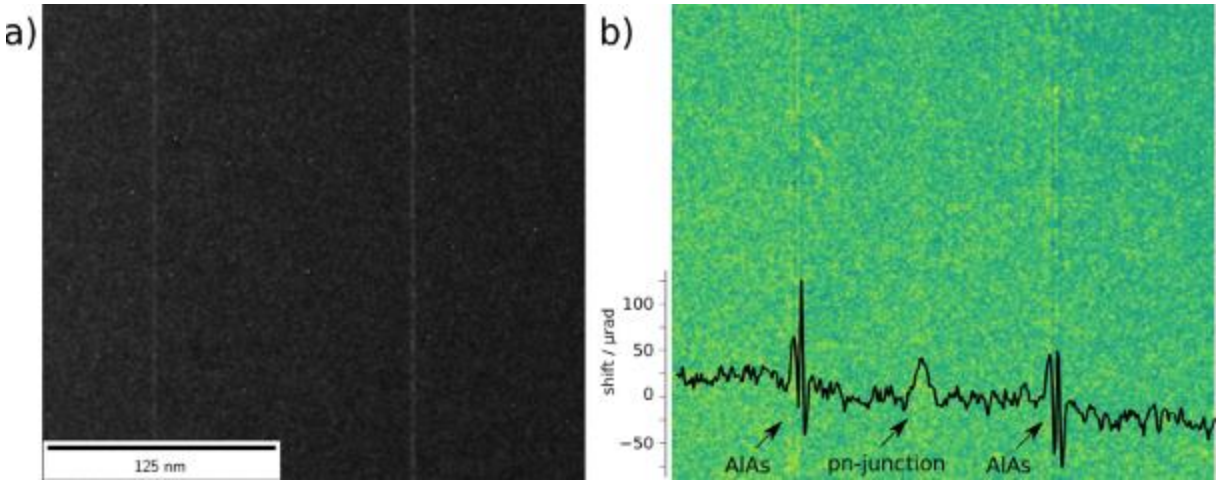

Fig. 2

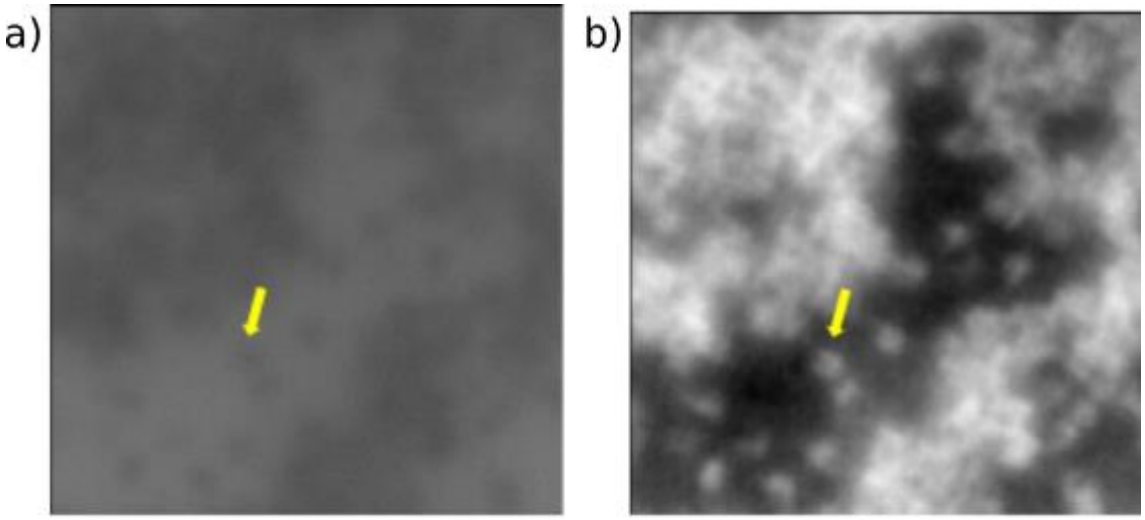

IM6.P012

Optimum BF (OBF) STEM using the SAAF detector

P. Wachsmuth[1]

[1]JEOL (Germany) GmbH, Freising, Germany

Introduction & Objectives

Imaging beam-sensitive materials at low-dose conditions remains a very challenging topic in transmission electron microscopy (TEM), especially if the goal is the direct observation of the atomic structure in these materials. In particular, electron beam induced damage during image tuning can make visualizing the sample at atomic resolution an extremely difficult task.

Methods & Results

In this presentation we will discuss a new ultra-high contrast Scanning transmission electron microscopy (STEM) technique that has recently become available on JEOL TEMs called optimum bright-field (OBF) STEM [1]. This method works with both segmented as well as pixelated STEM detectors and has been shown to be highly dose efficient while at the same time allowing for real-time imaging under low-dose conditions. The capability to image beam sensitive materials in real time under low-dose conditions promises to make TEM work on these materials significantly easier.

Outlook

Here we will give a brief overview of the OBF STEM Method and present several application examples on different materials highlighting the performance and capabilities of this new imaging technique.

References

[1] Kousuke Ooe et al., Ultram*icroscopy 220*, **2021**, 113133

IM6.P013

Integrated differential phase contrast (iDPC) STEM for ultimate low dose imaging at atomic resolution, including cryo nano particles

I. Lazić[1], C. Sachse[2,3,4], M. Wirix[1], M. L. Leidl[2,5,3,6], D. Mann[2,3], M. Beckers[2,7], E. V. Pechnikova[1], K. Müller-Caspary[5,6], A. Meingast[1], A. Carlsson[1], F. de Haas[1], E. G. T. Bosch[1]

[1]Thermo Fisher Scientific, Materials and Structural Analysis, Eindhoven, Netherlands
[2]Ernst Ruska-Centre for Microscopy and Spectroscopy with Electrons, Structural Biology (ER-C-3), Jülich, Germany
[3]Institute for Biological Information Processing, Cellular Structural Biology (IBI-6), Jülich, Germany
[4]Heinrich Heine University, Department of Biology, Düsseldorf, Germany
[5]Ludwig-Maximilians-University Munich, Department of Chemistry and Centre for NanoScience, Munich, Germany
[6]Ernst Ruska-Centre for Microscopy and Spectroscopy with Electrons, Physics of Nanoscale Systems (ER-C-1), Jülich, Germany
[7]European Molecular Biology Laboratory (EMBL), Structural and Computational Biology Unit, Heidelberg, Germany

Historically, beam sensitive materials have been imaged using conventional transmission electron microscopy (CTEM) applying parallel electron illumination. Through single particle analysis (SPA) and cryo CTEM has found its way towards life science (LS) and biological applications. In these directions, scanning TEM (STEM) applying focused electron illumination, has played considerably smaller role, especially in revealing nano particle structures at atomic and near atomic resolution.

With integrated differential phase contrast (iDPC) STEM [1] mode a strong capacity to image light next to heavy elements at atomic resolution [2, 3, 4, 5] has been revealed, also within structures that are highly sensitive to electron radiation [6, 7]. Experimentally, capability to image metal organic frameworks (MOF-s) [6] and zeolites including single molecules [7, 8] with unprecedented resolution has been proven. In Fig. 1a, an iDPC-STEM image of a MOF, MIL-101 structure is shown with resolution of 2 Å using total electron dose of 42 e-/Å^2, while in Fig. 1b, an image of MOF, UiO-66 structure is shown with resolution of 1.4 Å obtained using electron dose of 54 e-/Å^2. This strongly encourages STEM investigation in LS applications [9], including imaging of biological cryo nano particles at near-atomic resolution [10]. For example, iDPC-STEM imaging of Keyhole Limpet Hemocyanin (KLH) protein and Tobacco Mosaic Virus (TMV), well-known and in-depth studied specimens [11] are shown in Fig. 2. The iDPC-STEM micrographs show complete signal transfer to high resolution, enabling 3D structure SPA reconstruction at 3.5 Å.

iDPC-STEM is utilized as the integration of the DPC vector field to resolve the iDPC scalar field [1]. For a thin sample the DPC vector field represents the projected electric field, which, when integrated into iDPC, yields the projected electrostatic potential field of the sample [1, 2]. Consequently, iDPC-STEM is directly interpretable since the potential field has maxima at the atomic core positions.

Here, iDPC-STEM low dose specifics and imaging of various extremely beam sensitive organic and inorganic materials (as in Fig. 1) will be shown, as well as LS cryo-EM specimens (as in Fig. 2) at near atomic resolution.

Figure 1. 200kV iDPC-STEM with 10 mrad convergence semi-angle (CSA) beam (Sample courtesy: Prof. Y. Han, KAUST Catalysis Center) **a)** Image of MOF, MIL-101, el. dose 42 e-/A^2, resolution 2 Å **b)** Image of MOF, UiO-66, el. dose 54 e-/Å^2, resolution 1.41 Å

Figure 2. 300kV iDPC-STEM with 3.5 mrad CSA beam, el. dose 35 e-/Å^2, cryo SPA. **Top:** KLH **a)** 2D projections **b)** 3D reconstruction at 6.5 Å resolution **Bottom:** TMV **c)** iDPC-STEM micrograph **d)** 3D reconstruction and molecular model fit at 3.5 Å resolution

References:

[1] I. Lazić, *et al.*, Ultramicroscopy **160** (2016), 265.

[2] I. Lazić and E.G.T. Bosch, Advances in Imaging and Electron Physics **199** (2017), 75.

[3] E. Yücelen, *et al.*, Scientific Reports **8** (2018), 2676.

[4] D. Song *et al.*, Advanced Functional Materials **29** (2019), 1903843.

[5] S. de Graaf *et al.*, Science Advances **6** (2020), eaay4312.

[6] B. Shen *et al.*, Nature Communications **11** (2020), 2692.

[7] B. Shen *et al.*, Nature **592** (2021), 541.

[8] B. Shen *et al.*, Nature **607** (2022), 703.

[9] X. Li, *et al.*, Journal of Structural Biology **214** (2022), 107837.

[10] I. Lazić, *et. al.*, Nature Methods, accepted, (2022), preprint https://doi.org/10.1101/2021.10.12.464113

[11] S.A. Fromm *et.al.*, Journal of Structural Biology, **189** (2015) 87.

Fig. 1

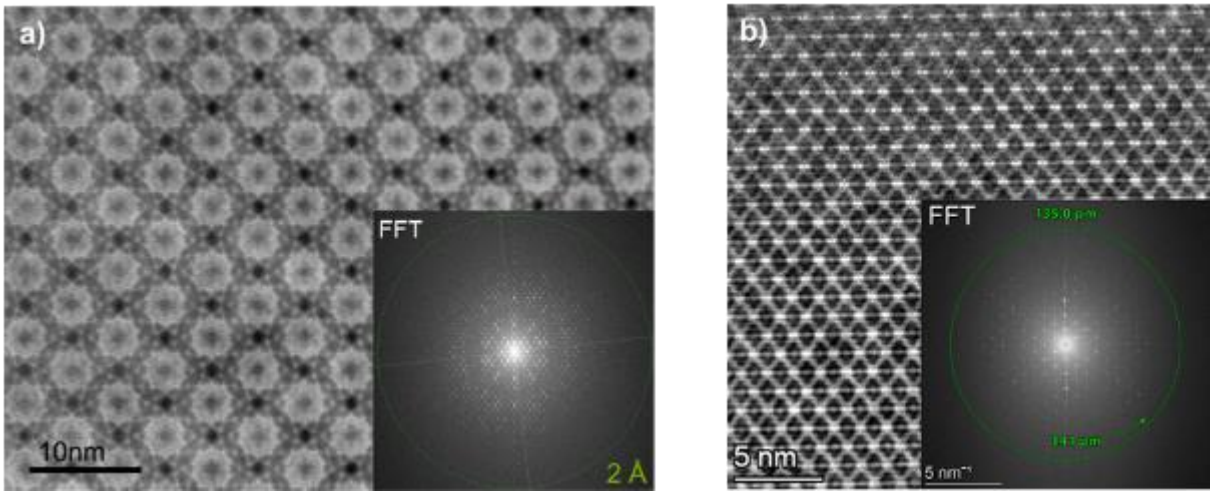

Fig. 2

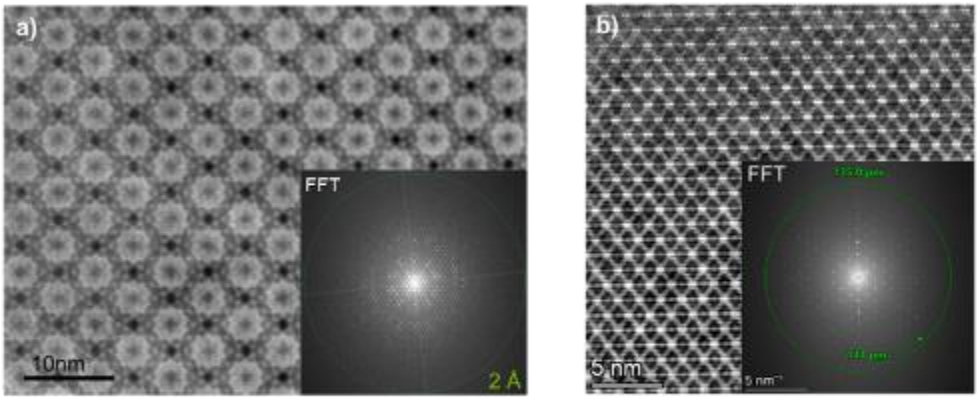

Figure 1. 200kV iDPC-STEM imaging, convergence semi-angle (CSA) 10 mrad (Sample courtesy: Prof. Y. Han, KAUST Catalysis Center; Images: Arno Meingast and Anna Carlsson) **a)** *Image of* metal organic framework MOF, MIL-101 acquired with total electron dose of 42 e^-/A^2, showing resolution of 2 Å **b)** Image of MOF, UiO-66 acquired with total electron dose of 54 $e^-/Å^2$, showing resolution of 1.41 Å

Fig. 3

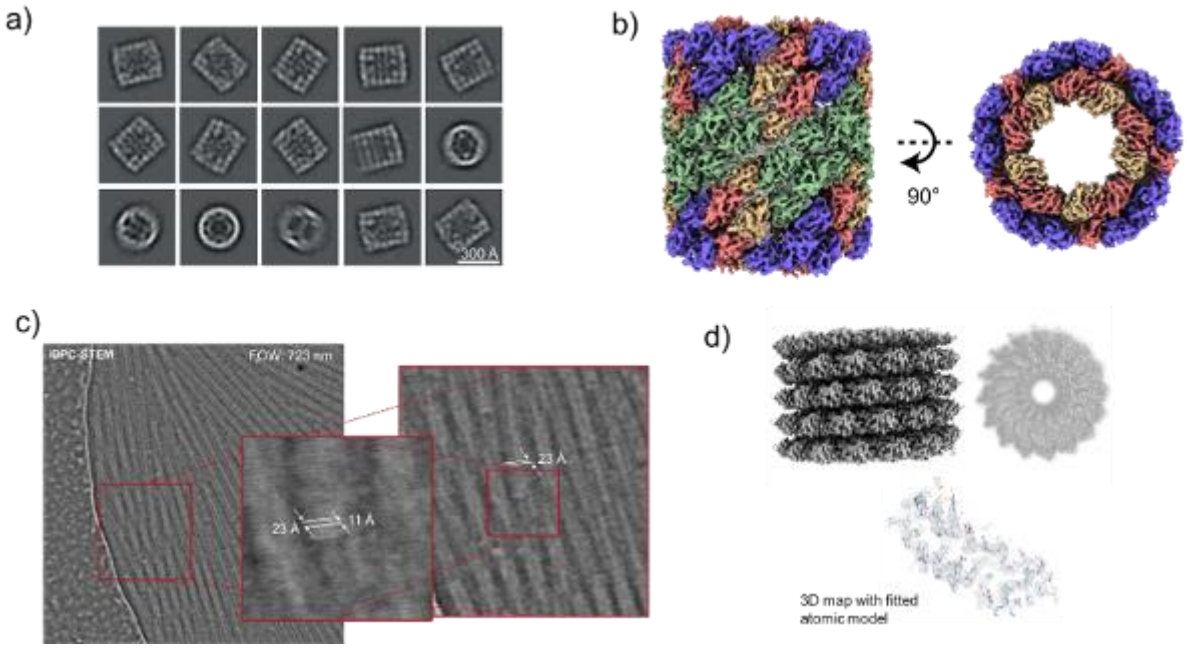

Fig. 4

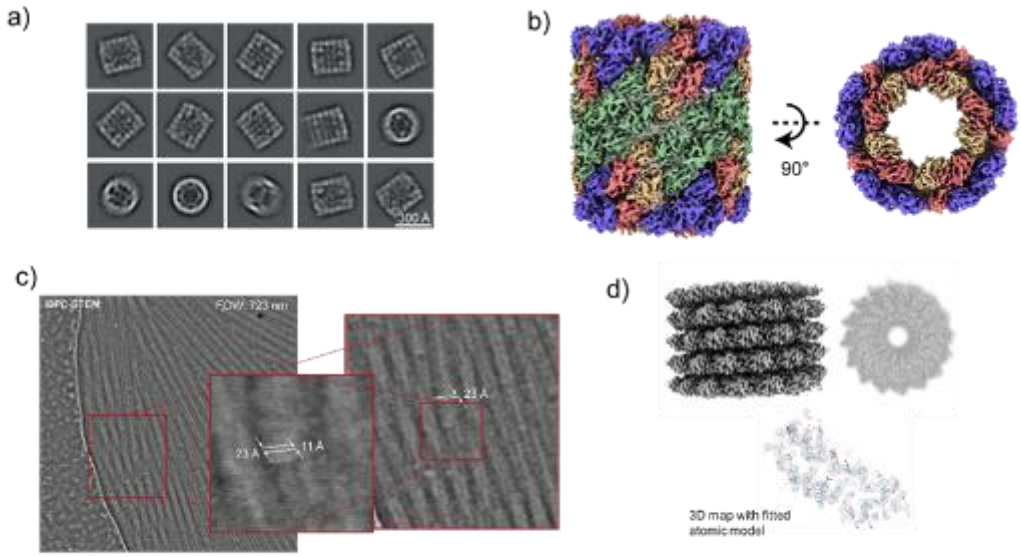

Figure 2. 300kV iDPC-STEM cryo SPA examples. **Top:** KLH at 3.5 mrad convergence semi-angle (CSA). **a)** 2D projections **b)** 3D volume reconstruction, side and top view, resolution determined at 3.5 Å. **Bottom:** TMV at 3.5 mrad CSA beam **c)** Example of iDPC-STEM micrograph **d)** Reconstructed 3D volume (side and top view) and molecular model fit, resolution determined at 3.5 Å

IM6.P014

Towards quantification of electric fields at interfaces in battery materials

S. Ahmed[1], V. S. Chejarla[1], D. Heimes[1], A. Beyer[1], J. Janek[2], K. Volz[1]

[1]Structure and Technology Research Laboratory, Department of Physics, Marburg, Germany
[2]Physikalisch-Chemisches Institut, Giessen, Germany

Introduction:

The characterization of long-range electric fields and space-charge layer effects at the few to tens of nanometer scale is of supreme importance at various interfaces in Lithium-ion battery materials. Relevant interfaces include grain boundaries in cathode materials as well as the interface between cathode materials and solid electrolytes,[1,2] etc. The momentum transfer of the electric field to a scanning electron probe can be used to derive the electric field as it can be quantitatively measured using fast electron detectors. This method has been shown to yield quantitative data for GaAs p-n-homojunctions.[3] Characterizing long-range electric fields across junctions of different materials or materials in different orientations, however, requires employing a low semi-convergence angle (<2 mrad) in scanning beam mode. Furthermore, applying precession on top of this helps to reduce dynamical effects.[4] Typically, the scanning transmission electron microscope (STEM) modes of most microscopes with aberration correctors are not optimized to form a low semi-convergence angle (<2 mrad). One possibility is to use the TEM mode of the microscope with the smallest available condenser lens aperture. However, two major difficulties are usually associated with the TEM mode. First, the TEM modes of most microscopes do not allow the scanning of the electron beam. In such cases, the electron beam can be scanned by external scanners. Secondly, the TEM modes of most microscopes do not allow the insertion of annular dark field and bright field detectors, which makes the simple tasks of searching the region quite tedious.

Objectives

Being able to form a low semi-convergence angle with precession in the STEM mode allows us to use the microscope's internal scanner with annular detectors.

Methods and Materials:

Here we discuss methods to achieve a low semi-convergence angle in STEM mode and compare its pros and cons with the TEM mode with the external scanner. We also apply precession using the NanoMegas P2000 unit. Since aligning precession requires switching between diffraction and imaging modes, the precession alignment procedures in STEM mode are also outlined. We also comment on the highest attainable precession frequency, which is of supreme importance when taking datasets with a fast pixelated direct electron detector.

Results:

Finally, we acquire 4D STEM datasets using a pnCCD by employing a low semi-convergence angle (1.73 mrad) and precession (0.1º) at the grain boundary (GB) region in a Ni-rich lithium-ion battery layered cathode material (NCM622). The initial results are shown in Figure 1.

Fig. 1: Scanning-precession images at a GB-region in NCM622, (a) High-angle annular dark field (HAADF), (b) Virtual Bright Field (VBF), (c) Center-of-Mass (COM) x-component & (d) COM y-component.

References:

[1] L. Wang, R. Xie, B. Chen, X. Yu, J. Ma, C. Li, Z. Hu, X. Sun, C. Xu, S. Dong, T.-S. Chan, J. Luo, G. Cui, L. Chen, *Nat. Commun.* **2020**, *11*, 5889.

[2] J. Haruyama, K. Sodeyama, L. Han, K. Takada, Y. Tateyama, *Chem. Mater.* **2014**, *26*, 4248.

[3] A. Beyer, M. S. Munde, S. Firoozabadi, D. Heimes, T. Grieb, A. Rosenauer, K. Müller-Caspary, K. Volz, *Nano Lett.* **2021**, *21*, 2018.

[4] T. Mawson, A. Nakamura, T. C. Petersen, N. Shibata, H. Sasaki, D. M. Paganin, M. J. Morgan, S. D. Findlay, *Ultramicroscopy* **2020**, *219*, 113097.

Fig. 1

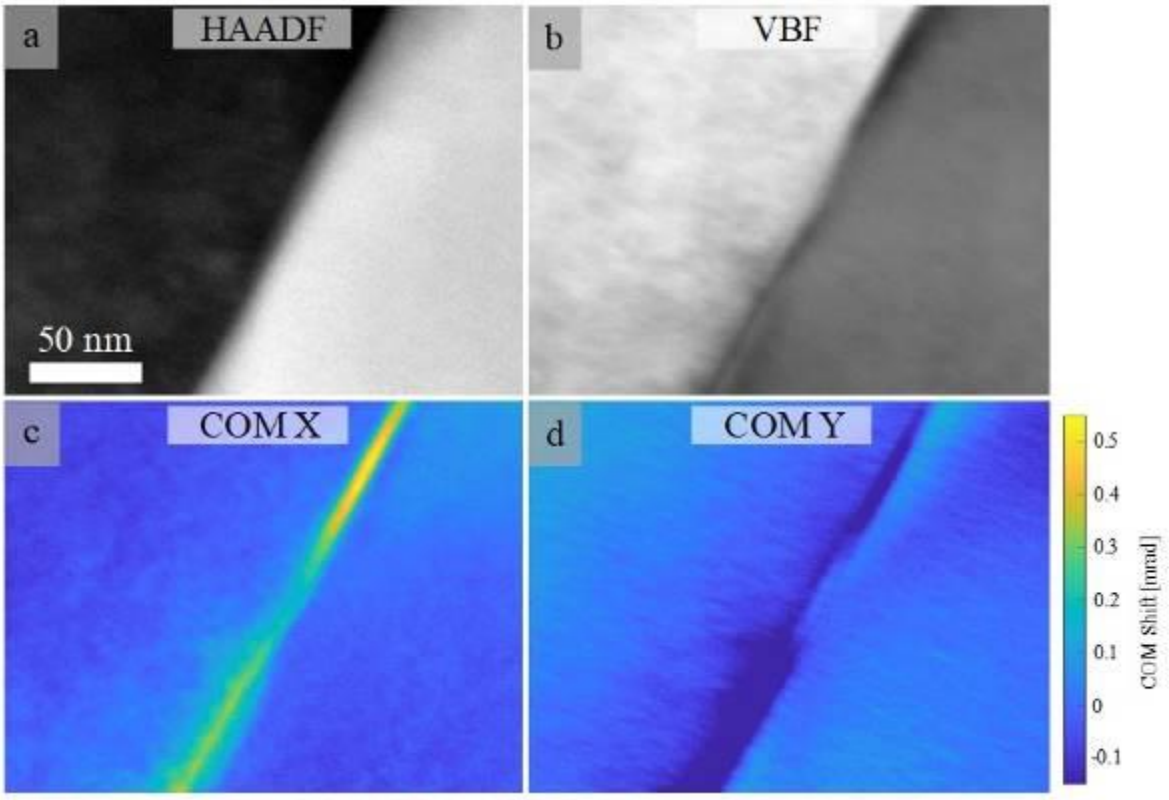

IM6.P015

Correlative microstructural, compositional and magnetic characterization of phase-separated high entropy alloys

A. Kovács[1], Q. Lan[1], R. E. Dunin-Borkowski[1]

[1]Forschungszentrum Jülich, Ernst Ruska Centre, Jülich, Germany

High entropy alloys (HEAs) or complex concentrated alloys (CCAs) are a novel class of material that offers remarkable structural and functional performance in a wide range of applications. Their properties can be tuned by using different combinations of elements and/or processing strategies. Although their mechanical properties have been widely studied, fewer investigations have been performed about their magnetic properties. Here, we perform correlative characterization of the microstructure, chemical composition and magnetic properties of Al0.3CoFeNi and AlCo(Cr)FeNi alloys using transmission electron microscopy (TEM) methods. Off-axis electron holography and the Fresnel mode of Lorentz TEM are used to determine the magnetic states of precipitates, the coercivity mechanism and the widths of magnetic domain walls in the alloy.

A plate-shaped arc-melted ingot of Al0.3CoFeNi was homogenized at 1200 ºC for 1 h and cold-rolled to 90%. It was then either solutionized at 1200 ºC for 5 min or solutionized and annealed at 600 ºC for 50 h . Electron-transparent TEM specimens were prepared using focused ion beam sputtering in a dual beam scanning electron microscope (FEI Helios 400). Microstructural, chemical and magnetic imaging was carried out using probe-corrected and image-corrected TEMs (FEI Titan 80-200 and FEI Titan 60-300 operated at 200 and 300 kV, respectively).

The Al0.3CoFeNi alloy consists of L12-ordered precipitates embedded in an FCC single crystal. Extended annealing at 600 ºC induced lamellar phase separation consisting of FCC+L12 and BCC+B2 regions. High-resolution *in situ* investigations showed that the magnetization reversal process changes from a nucleation-type mechanism in the FCC+L12 microstructure to a pinning-type mechanism in the lamellar microstructure, with a significant decrease in domain wall width from 171 to 35 nm. At the same time, the magnetic coercivity increased from 2.5 to 160 Oe, while the yield strength and hardness increased by a factor of 2.

The AlCo(Cr)FeNi alloy consists of highly complex hierarchically-decomposed B2 and BCC phases with different dimensions and arrangements [1]. Quantitative measurements of the magnetic phase shift using off-axis electron holography (Fig. 1(a)) and reconstruction of the in-plane magnetization using model-based iterative reconstruction (Fig. 1(b)) were used to reveal the distinct magnetic characteristics of the constituent states, which include magnetic vortices (Fig. 1(c)) and single domains with paramagnetic inclusions [1].

The authors are grateful to N. Balaji, R. Banerjee, J. Caron, V. Chaudhary, S. Dasari, H. Du, R. V. Ramanujan and D. Song for valuable contributions to these results. This work was supported by the European Union"s Horizon 2020 Research and Innovation Programme (Grant No. 856538, project ""3D MAGiC"") and the DFG through CRC/TRR 270 (Project ID 405553726).

Figure 1. (a) Magnetic phase image of the BCC phase in the B2 matrix of an AlCo(Cr)FeNi CCA [1]. Each dark or bright contrast feature is associated with a well-defined magnetic vortex state. (b) Projected in-plane magnetization map of the marked precipitate in (a) generated from the magnetic phase image. (c) Magnetic induction map showing vortices. The contour spacing is 2π/24 radians.

[1] Q. Lan et al., iScience 25 (2022) 104047.

[2] A. Kovács, R.E. Dunin-Borkowski, In Handbook of Magnetic Materials; Brück, E., Ed.; Elsevier: 2018; Vol. 27, 59.

Fig. 1

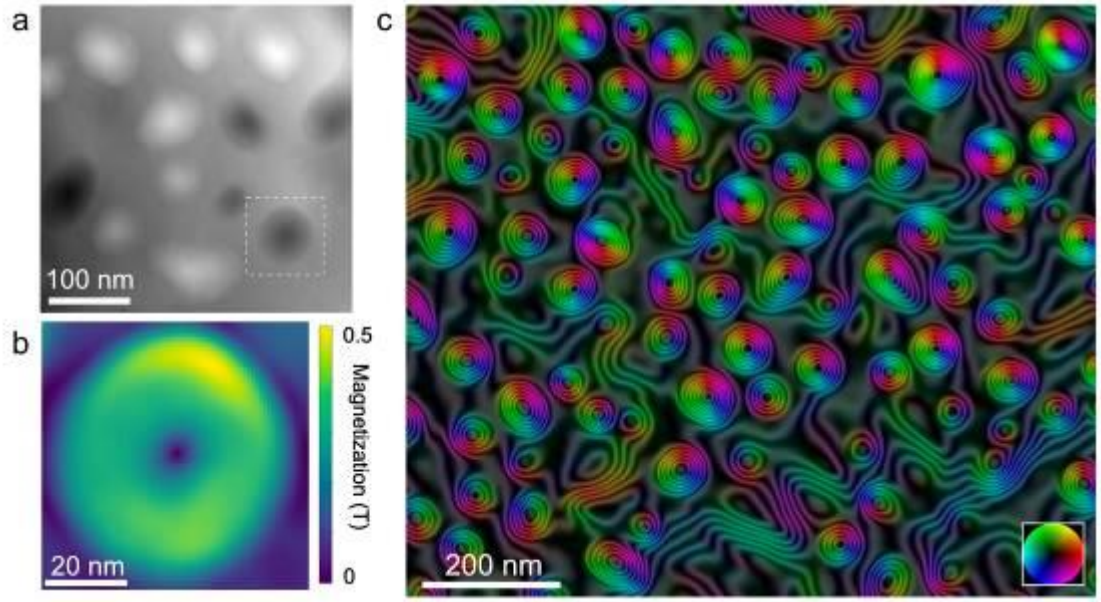

IM6.P016

Fast pixelated direct detector with center hole to enable simultaneous 4D-STEM and EELS

M. Huth[1]

[1]PNDetector GmbH, Munich, Germany

Recently the method of four-dimensional scanning transmission electron microscopy (4D STEM) imaging, where a focused beam of electrons scans the sample in a two-dimensional (2D) raster pattern, has gained significant interest and a continuous growing community. An ultrafast and direct electron detection system like the pnCCD (S)TEM camera [1] having single electron sensitivity is ideally suited for all kinds of 4D STEM applications. The pnCCD (S)TEM camera can be operated at 7500 frames per second, and is compatible with electron energies ranging from 20 keV to 300 keV.

With the possibility of coherent STEM imaging, enabling quantitative phase contrast imaging, the range of materials which can be analyzed with STEM has been extended down to light elements like carbon.

Attractive additional information about the sample like phonon or plasmon excitation or core loss phenomena can be obtained from electron energy loss spectroscopy (EELS). With the currently available detector systems, the decision needs to be made if either a 4D STEM or an EELS measurement is taken.

We present a new pnCCD chip design with a center hole in the middle of the detector (diameter 2.5 mm, see in Fig. 1), which lets the center part of the electron beam pass through into the EELS spectrometer, while the outer bright field disc as well as parts of the dark field signal can be observed on the pixelated 4D STEM detector simultaneously. Calculations have already shown that e.g. Ptychographic phase contrast reconstruction is very robust against loss of the center part of the bright field disc [2].

The contribution will show preliminary detector data and calculations using 4D STEM data.

Figure 1: Schematic showing the dimensions of the center hole in the pixelated 4 D STEM detector. The physical hole has a diameter of 2.5 mm, while the insensitive region in the detector plane has a diameter of 4 mm.

Figure 2: Picture of a pixelated 4D STEM detector with a center hole in the middle, which allows to combine 4D STEM and EELS measurements.

References:

[1] Ryll, H., et al, Journal of Instrumentation **11** (2016)

[2] Song B., et al, Physical Review Letters **121** (2018)

Fig. 1

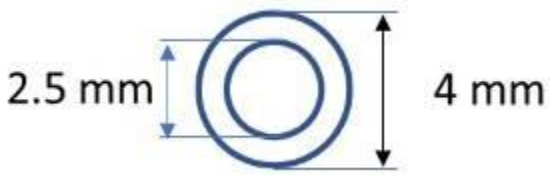

Fig. 2

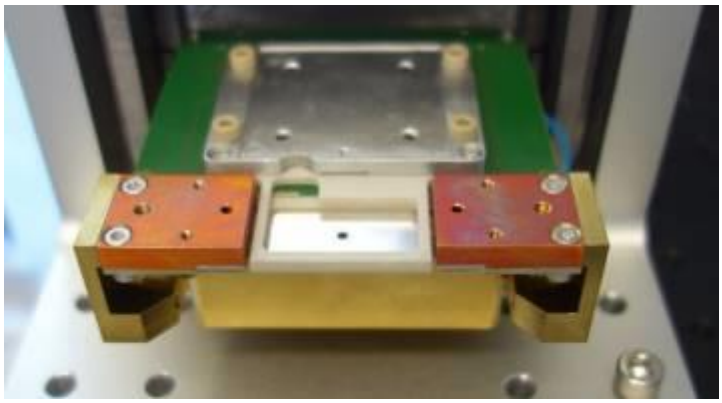

IM6.P017

Application of phase-shifting off-axis holography to the reconstruction of atomic-resolution exit waves

U. Ross[1], J. Lindner[2], T. Meyer[2], V. Boureau[3], M. Seibt[1], C. Jooss[2,4]

[1]Georg-August-University Göttingen, IV Physics, Göttingen, Germany
[2]Georg-August-University Göttingen, Institute of Materials Physics, Göttingen, Germany
[3]École Polytechnique Fédérale de Lausanne (EPFL), Lausanne, Switzerland
[4]International Center for Advanced Studies of Energy Conversion, Göttingen, Germany

Transmission electron off-axis holography is a phase retrieval technique which enables access to the full complex-valued exit-wave of thin samples. At atomic resolution, the reconstructed phase allows direct determination of the projected potential of the lattice arrangement. In the field of catalyst research electrostatic surface fields are of particular interest, since they can be assumed to play a major role in reaction mechanisms such as the oxygen evolution reaction[1].

Conventional off-axis holography reconstruction operates via the Fourier domain. As a consequence, the accessible range of spatial frequencies is band-limited by the carrier frequency of the hologram. Various studies have demonstrated high-resolution recording of lattice images by Fourier reconstruction[2]. However, a trade-off is always necessary in order to optimize fringe frequency, visibility and phase-contrast transfer strongly depending on the instrument stability[3].

In phase-shifting holography[4] a series of tilts of the incident wave shifts the hologram fringes over the sample. The resulting series of holograms after careful correction for sample and biprism drift is then used to carry out a linear fit of the local phase and amplitude of the fringe modulation due to the object potential. This obviates the use of a reconstruction aperture, and the upper bound of the spatial resolution is thus only limited by the performance characteristics of the instrument, while the low-frequency information is also retained.

We demonstrate the implementation of phase-shifting holography at sub-nm resolution on a single-biprism setup, which is combined with the in-situ capabilities of a third-order aberration-corrected environmental TEM in order to investigate catalytic platinum samples under low-pressure gaseous environments. The resulting high-resolution exit-waves are successfully matched to multislice image simulations. Lens aberrations up to second order are corrected via minimization of the amplitude contrast in propagated exit-waves. The method enables in-situ investigation of atomic structure and surface effects in polycrystalline platinum under the influence of up to 5e-2 mbar of O_2 and H_2O.

Figure 1: Principle of phase-shifting holography. The pixel projection of an aligned holographic tilt series yields the fit of local phase θ, centerband amplitude a and sideband amplitude modulation b. The reference phase shift φ_n is corrected from a vacuum reference region.

Figure 2: Reconstructed exit-wave of a Pt[110] surface, supercell-averaged amplitude and phase before and after 2nd-order correction, at n-6nm numerical defocus.

1 I.E.L. Stephens, A.S. Bondarenko, U. Grønbjerg, J. Rossmeisl, and I. Chorkendorff, Energy Environ. Sci. **5**, 6744 (2012).

2 F. Winkler, J. Barthel, A.H. Tavabi, S. Borghardt, B.E. Kardynal, and R.E. Dunin-Borkowski, Phys. Rev. Lett. **120**, 156101 (2018).

3 M. Linck, Ultramicroscopy **124**, 77 (2013).

4 Q. Ru, G. Lai, K. Aoyama, J. Endo, and A. Tonomura, Ultramicroscopy **55**, 209 (1994).

Fig. 1

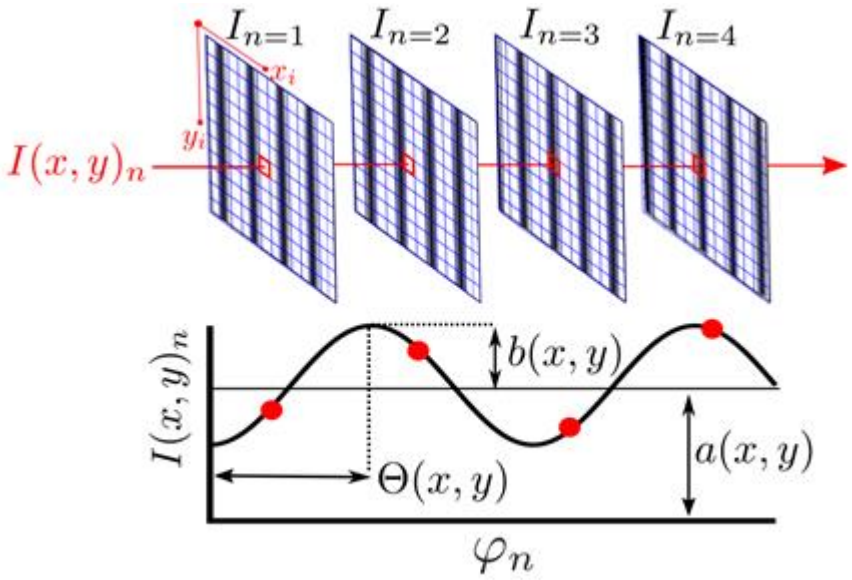
$I_{n=1}$
$I_{n=2}$
$I_{n=3}$
$I_{n=4}$
x_i
y_i
$I(x,y)_n$
$b(x,y)$
$a(x,y)$
$\Theta(x,y)$
$I(x,y)_n$
φ_n

Fig. 2

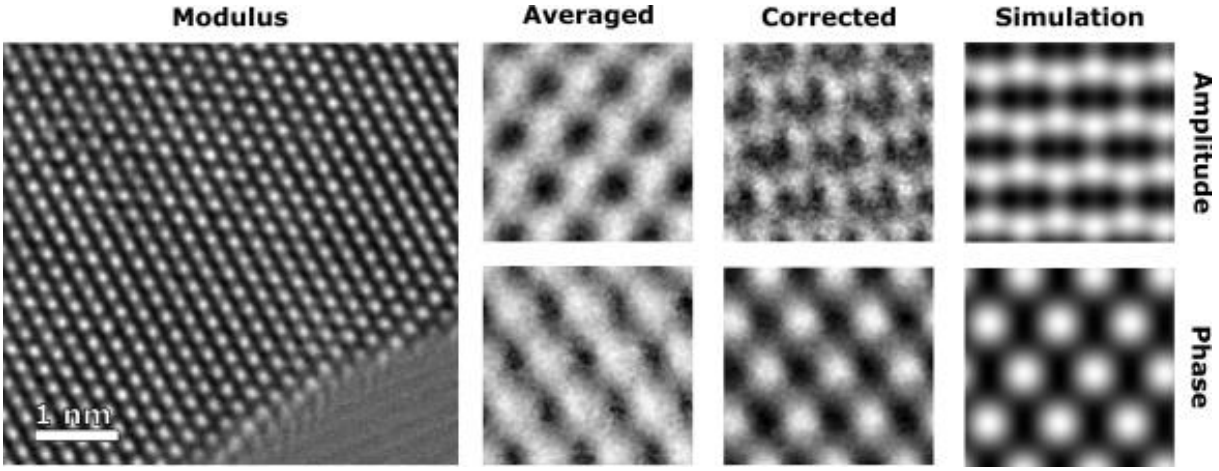
Modulus
Averaged
Corrected
Simulation
Amplitude
Phase
1 nm

IM6.P018

DPC-Toolbox, a software for post-processing and analysis of differential phase contrast STEM images

J. Bürger[1], M. Groll[1], J. K. Lindner[1]

[1]Paderborn University, Department of Physics, Paderborn, Germany

Differential phase contrast (DPC) in scanning transmission electron microscopy (STEM) allows the visualization and quantification of electric and magnetic fields. In combination with state-of-the-art C_s-correction, it is even possible to map the projected electric field distribution and the corresponding charge density with subatomic resolution [1]. The DPC method is based on the measurement of transferred momenta which are imposed on the incident electron beam by the Coulomb interaction with the electrostatic potentials of the specimen at each pixel of the scan. The transferred momentum is closely linked to phase differentials within the electron wave and measurable as a lateral change of the center of mass of the intensity distribution in the detector plane [1]. This change can be determined using a position sensitive detector, such as a segmented or pixelated detector. However, to obtain quantitative information, substantial and careful post-processing including precise calibration and removal of machine related image artefacts need to be conducted.

Here we report on the development of a software enabling microscopists to readily do a quantitative analysis of DPC measurements including removal of various image artefacts, reduction of image noises and precise determination of atomic column positions.

The software can be executed as a stand-alone version for post-processing and as an "in-line" tool during the specimen analysis, enabling the prompt correction of misalignments. All images (dark-field image, images of all detector segments, constructed (annular) bright-field images) are saved in a single project file, in which all calculated maps, the image information such as calibration and acceleration voltage, as well as a history of processing steps are stored. This allows for a simple handling of data and facilitates collaboration. To calculate quantitative maps, the toolbox uses dedicated calibration files which can be tailored for the microscope settings (camera length, accelerating voltage, etc.) used during the measurement. One of these optimizations performable with the DPC-Toolbox is the correction of rotation of the deflection direction. In addition, the calculation of the scattergram, which is a 2D histogram of the transferred momentum, and a subsequent correction of the beam centering is implemented. Especially the scattergram is an excellent tool to detect possible image artifacts arising from e.g. wrong centering of the beam, lens aberrations and dynamical diffraction effects ("in-line") during the analysis [2]. Furthermore, a background signal, which results from a scanning of the beam in the detector plane and is typically observed on microscopes without descanning coils, can be drastically reduced in post-processing. Further functions of the DPC-Toolbox include noise reductions using rigid and non-rigid image registration algorithms, determination of atomic column position by fitting Gaussian functions to the intensity of individual atomic columns in dark-field images, characterization of magnetic domain walls and determination of magnetic domain sizes. Moreover, the software includes a recipe function to correct and analyze a series of DPC images and thus facilitates a fast processing of DPC data. The software is made freely available by contacting the authors.

[1] K. Müller-Caspary et al., *Ultramicroscopy* 178 (2017): 62-80.

[2] J. Bürger et al., *Ultramicroscopy* 219 (2020): 113118.

IM6.P019

Influence of plasmon-excitation electrons on ptychography phase imaging

Z. Ding[1], A. I. Kirkland[1,2,3], P. Nellist[1]

[1]University of Oxford, Department of Materials, Oxford, United Kingdom
[2]Diamond Light Source Ltd., Electron Physical Sciences Imaging Centre, Didcot, United Kingdom
[3]The Rosalind Franklin Institute, Didcot, United Kingdom

Introduction

Electron ptychography is a phase retrieval method in transmission electron microscopes (TEM) in which the phase of exit wavefunction is reconstructed from electron diffraction patterns[1]. It is used for a wide range of specimens for atomic-scale imaging, including sensitive battery materials[2] and biological structures[3]. As a method of coherent imaging, contrast of electron ptychography is based on coherence of electron beam. However, inelastic scattering that happens in the interaction between beam and specimen introduces an energy distribution of the exit beam. With increased thickness of the sample, the proportion of inelastic scattered electrons (most of which are plasmon-excited electrons) increases.

Objective

In this work, we investigate the influence of inelastic electrons, especially plasmon-excited electrons on ptychographic reconstruction.

Materials & Methods

To explore the influence of inelastic scattered electrons, in an aberration-corrected TEM at 200kV, 4D-STEM datasets with and without energy filter were recorded at different defocus conditions on a sample of gold nanoparticles and carbon film. The convergence angle of the electron beam is 22 mrad. Then ptychography reconstructions were carried out on recorded 4D-STEM datasets using the ePIE algorithm[4].

Results

The reconstruction results shows that phase contrast images for atomic-scale resolution are stable whether or not the inelastic scattered electrons are filtered. This result is in line with the prediction based on characteristic scattering angle for inelastic scattering. For this experiment, the characteristic scatter angle of plasmon-exited electrons (energy loss: 20 eV) is 0.005 mrad. However, the pixel size of 4D-STEM detector used in the experiment is 0.25 mrad, which is far bigger than the characteristic scatter angle. This means that statistically, most electrons will still be detected by the same pixel whether or not they are inelastic scattered along with the image-forming elastic scattering. Therefore, the normalized intensity distribution of recorded diffraction patterns with or without energy filter are almost the same.

However, if a smaller pixel size is used, i.e. a larger camera length, for a beam with a smaller convergence angle, the situation is different. For example, if a convergence angle of 1~2 mrad is used for large field-of-view ptychographic imaging[3], the pixel size on detector may be comparable to characteristic scatter angle under a similar experimental condition. In this situation, the influence of inelastic scattered electrons on electron ptychography should not be ignored.

Conclusion

In summary, plasmon-excitation electrons, which are the majority amount of inelastically scattered electrons, have a negligible effect on atomic resolution ptychography.

Reference

[1] Nellist, P., McCallum, B. & Rodenburg, J. M. *Nature* **374**, 630-632 (1995).

[2] Lozano, J. G., Martinez, G. T., Jin, L., Nellist, P. D. & Bruce, P. G. *Nano letters* **18**, 6850-6855 (2018).

[3] Zhou, L. *et al. Nature communications* **11**, 1-9 (2020).

[4] Maiden, A. M. & Rodenburg, J. M. *Ultramicroscopy* **109**, 1256-1262 (2009).

figure legends:

Figure 1: Ptychographic phase reconstructions (a) without energy filter, i.e. elastic and inelastic scattered electrons are both recorded, and (b) with energy filter, i.e. only elastic scattered electrons are recorded. Defocus value is -14 nm.

Fig. 1

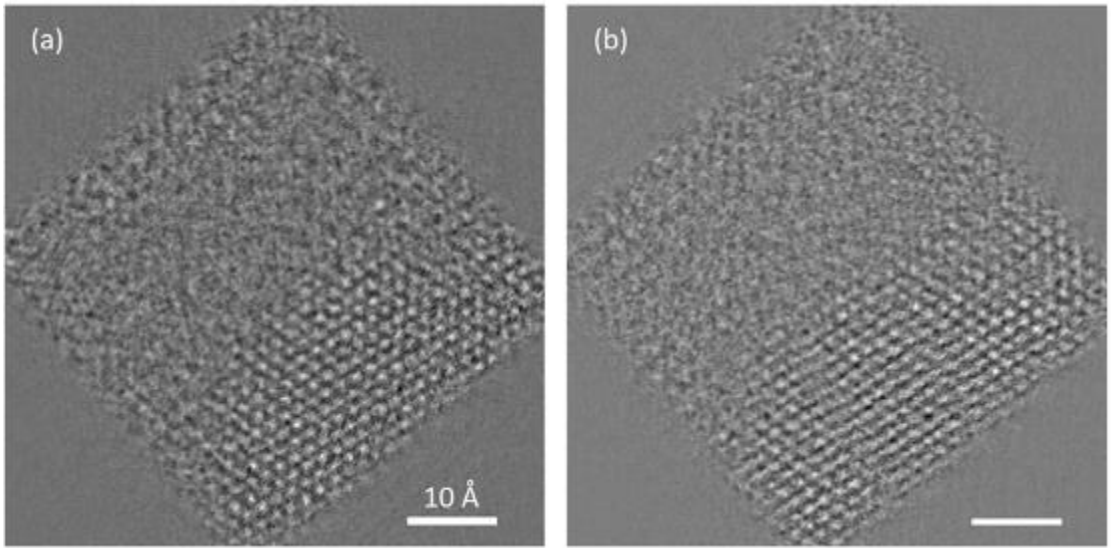

IM6.P020

Wirtinger Flow: the effect of different noise models for low-dose scanning electron transmission microscopy

M. L. Leidl[1,2], P. Römer[3,4], F. Filbir[3,4], C. Sachse[1,5], K. Müller-Caspary[1,2]

[1]Forschungszentrum Jülich GmbH, Ernst Ruska-Centrum für Mikroskopie und Spektroskopie mit Elektronen (ER-C), Jülich, Germany
[2]Ludwig-Maximilians-University Munich, Chemistry, Munich, Germany
[3]Technical University of Munich, Mathematics, Munich, Germany
[4]Helmholtz Zentrum München German Research Center for Environmental Health Strategy and Digitalization, Mathematical Imaging & Data Analysis, Munich, Germany
[5]Heinrich-Heine-Universität Düsseldorf, Biology, Düsseldorf, Germany

The Wirtinger Flow (WF) is a variational approach to the phase retrieval problem. It minimizes a loss function which is adapted to a specific noise model. It was studied in the mathematical literature in greater detail [1-3] for a least squared loss function

$$l_g(\bar{y},y) = |\bar{y} - y|^2$$

that is related to an additive Gaussian noise and to a loss function derived for Poisson noise

$$l_p(\bar{y},y) = y \cdot log(\bar{y}) - \bar{y},$$

where $\bar{y}$ is the guess and y the measurement. However, in the situation of low-dose measurements these results do not apply as the gradient has singularities.

The widely used reconstruction algorithms like the extended iterative engine (ePIE) and the Wigner deconvolution can be analysed for a Gaussian noise model. However, for the Poisson noise model the analysis is missing. In contrast, the WF method can be adapted even for lowest-dose measurements. This is of particular importance when dose sensitive samples like viruses have to be imaged. However, the low dose case is not well examined and WF is mostly tested on simulated [1,2] or x-ray data [3].

We compare unblinded (known illumination) WF reconstructions of low-dose scanning transmission electron microscopy (STEM) simulations with a convergence semi-angle of 5 mrad and a dose of 30 e/Å² of apoferritin (PDBe: 7a6a [4]) in vacuum. A Gaussian, Poissonian and an approximation of the Poissonian probability distribution [5] are assumed during the reconstruction. The reconstructions are compared with the object transmission function (ground truth) and an integrated centre of mass (iCOM) reconstruction in real space and by using the Fourier ring correlations (FRC).

Our results show that the differences between the different reconstructions are rather small (Fig. 1). However, all WF reconstructions show a higher dose efficiency for most of the resolution shells and less noise at low frequencies than the iCOM reconstruction. However, the loss function based on Poissonian noise, which is theoretical favourable at low dose, does not perform better than a Gaussian loss function at a dose of 30 e/Å². A reason is the singularity that is included in the logarithm of the Poissonian loss function. Therefore, it is difficult to control the gradient update for the Poissonian loss function. We will discuss the difficulties of the Poissonian loss function, the possibility to combine the Gaussian and Possonian loss function and demonstrate further dose-dependent WF reconstructions of experimental STEM data of 2D materials for comparison.

Figure 1: (a) iCOM reconstruct. (b) to (d) WF reconstructions with different loss functions that are given in the label. (e) FRC curves that compare the iCOM reconstruction and the phase of the WF reconstructions with the phase of the ground truth.

[1] Candes, et al. IEEE Transactions on Information Theory 61.4 (2015)

[2] Bian, et al. Scientific reports 6.1 (2016)

[3] Thibault, et al. New Journal of Physics 14.6 (2012)

[4] Yip, et al. Nature 587.7832 (2020)

[5] Thibault, et al. New Journal of Physics 14.6 (2012)

Fig. 1

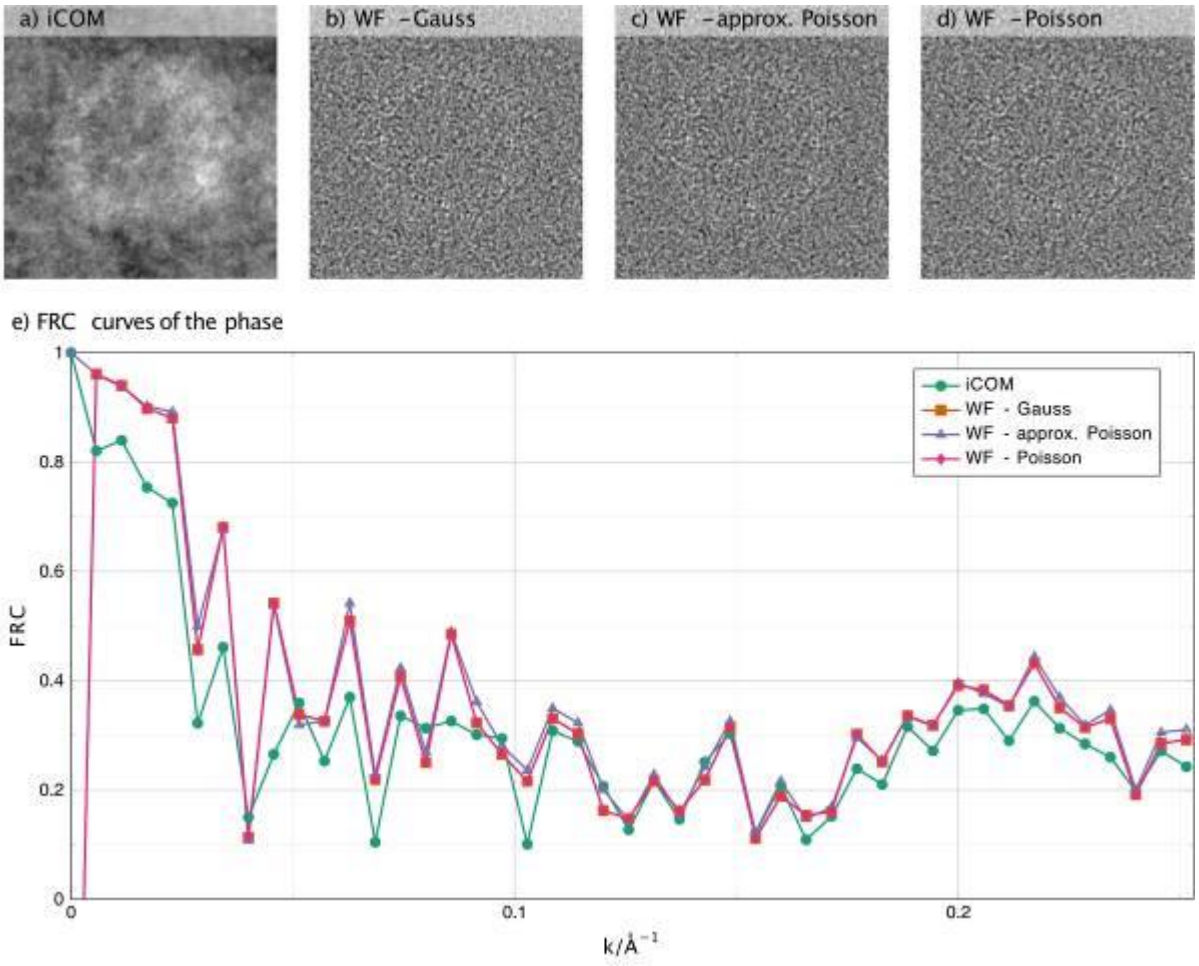

IM6.P021

Large-scale 3D phase-contrast imaging from scanning diffraction measurements

P. Pelz[1,2,3], M. Scott[2,3], M. G. Cho[2], C. Ophus[3]

[1]Friedrich-Alexander-Universität Erlangen-Nürnberg, Materials Science, Nuremberg, Germany
[2]University of California, Berkeley, Materials Science & Engineering, Berkeley, CA, United States
[3]The Molecular Foundry, Lawrence Berkeley National Laboratory, Berkeley, CA, United States

Scanning diffraction microscopy in the form of ptychography is a powerful method for materials characterization with X-rays and electrons at the nano- and the atomic scale. As radiation sources become brighter and detectors faster, scale-bridging studies and multi-scale phenomena become accessible by this method. However, the current reconstruction algorithms scale poorly to large field of view and thick samples. Here we present an unsupervised reconstruction algorithm inspired by a fast simulation method for scanning transmission electron microscopy (STEM), that offers more than 100x speedup compared to existing 3D phase-reconstruction methods for large fields of view with more than 10^6 diffraction measurements. We demonstrate the approach experimentally in STEM at atomic resolution by sectioning through a highly strained Co3O4 /Mn3O4 core-shell nanoparticle and revealing its 3D structure from a single view.

IM6.P022

Electrostatic shaping of magnetic transition regions in $La_{0.7}Sr_{0.3}MnO_3$

Q. Lan[1], C. Wang[2], L. Jin[1], M. Schnedler[1], L. Freter[1], X. Wei[1], T. Denneulin[1], A. Kovács[1], P. Ebert[1], X. Zhong[1], R. E. Dunin-Borkowski[1]

[1]Forschungszentrum Jülich, Ernst Ruska-Center, Jülich, Germany
[2]Southern University of Science and Technology, Department of Physics, Shenzhen, China

Magnetic domain walls are magnetic transition regions where the magnetization changes gradually between adjacent domains, typically by rotation. Bulaevskii and Ginsburg predicted the existence of a magnetic domain wall without rotation of magnetization near the Curie temperature, where the transition is achieved by a gradual change in the magnitude of the magnetization [1]. However, such a magnetic domain wall had not been observed experimentally, in part because a variation in the magnitude of the magnetization is rare in classical ferromagnets.

Here, we report a magnetic transition region in a La0.7Sr0.3MnO3 film, where the magnitude of the magnetization changes gradually without rotation below the Curie temperature. [2] The microstructure, composition, electronic structure and magnetization distribution in the transition region of the La0.7Sr0.3MnO3 film were investigated using correlative electron microscopy techniques, including spectroscopy and off-axis electron holography. The results reveal that the fundamental mechanism of the change in the magnitude of the magnetization is diffusion and drift-induced charge carrier redistribution, which changes the Mn valence state and thereby the magnitude of the magnetization, governed by the Mn3+ and Mn4+ double exchange interaction. The width of the magnetic transition region is approximately 50 nm, which is similar to the classical magnetic domain wall width in perovskite-type oxide materials. However, the underlying physical mechanism is different. The magnetic transition region that we observe is governed solely by electrostatics, while classical magnetic domain walls are governed by minimization of the total magnetic energy. Thus, our results demonstrate a case of the electrostatic shaping of magnetic transition regions.

References

[1] L. N. Bulaevskii and V. L. Ginzburg, Sov Phys Jetp-Ussr **18**, 530 (1964).

[2] Q. Lan *et al.*, Phys. Rev. Lett. **129**, 057201 (2022).

IM6.P023

Playground 4D-STEM in SEMs: a rich toolbox for a wide range of applications

J. Müller[1], M. Schloz[1], J. Schmehr[2], J. Cao[2], C. Mirek[1], B. Haas[1], S. Shabih[1], W. van den Broek[1], J. Becker[2], C. T. Koch[1]

[1]Humboldt-Universität zu Berlin, Department of Physics, Berlin, Germany
[2]X-Spectrum GmbH, Hamburg, Germany

1. Introduction

A wide range of diffraction-based techniques have recently been developed for 4D-STEM [1], many of these techniques can also be employed in conventional SEMs by inserting a fast camera below the electron-transparent sample. We developed two different camera-based sub-stages to realize 4D-STEM in SEMs, which can acquire transmission diffraction patterns with up to 2000 fps. Compared to dedicated transmission electron microscopes, using SEMs as a base platform allows for simpler, more easily customizable, and more economical systems. In addition, the lower acceleration voltage of 0.5kV to 30kV results in stronger scattering (beneficial, e.g. in 2D materials) as well as reduced knock-on damage. We will present our two SEM sub-stages and show a summary of our implemented methods and applications.

2. Objectives

Our goal is to add 4D-STEM to SEMs and FIB/SEMs to expand their vast range of applications, we ultimately aim for enabling ptychography [2] in SEM to increase their spatial resolution well beyond the instruments limit.

3. Material & methods

The two different camera-based transmission diffraction sub-stages are mountable to the SEM stage within our Zeiss GeminiSEM 500. The first setup consists of a Medipix 3 direct electron detector [3] and the second setup utilizes a compact 2.5x2.5x1.1cm³ CMOS camera with a fiber-coupled scintillator mounted inside a hexapod stage. We merged the hard- and software in-house, giving us full control over the whole system. This enables us to implement new methods, like live-feedback systems, and existing 4D-STEM-based methods.

4. Results

We applied our SEM diffraction setups to map material properties like layer thickness, crystal orientations, crystallite size, crystallinity and other crystallographic information. We also looked into improving the stability between sample and electron beam to apply more advanced methods like ptychography by investigating unwanted shifts resulting from floor vibrations, acoustic and electro-magnetic noise. For that purpose, we implemented a proof of concept feedback system using shadow images of a hole in a carbon TEM grid to minimize the relative movement between electron beam and sample.

5. Conclusion

4D-STEM in SEMs with direct and scintillator-based cameras is a feasible and well-working tool to investigate thin bulk and low-dimensional materials in SEMs, adding to their versatility. Having full control over the microscope setup also allows for implementing new methods like live-feedback systems. Minimizing unwanted movement between sample and electron beam, will allow for ptychography in standard SEMs increasing the spatial resolution well beyond the instrument limit and increasing their application range.

References:
[1] C. Ophus, Microscopy and Microanalysis, Vol. 25, Issue 3, June 2019, pp. 563-582 (2019)
[2] M. Schloz, et al, Optics Express, Vol. 28, Issue 19, pp. 28306-28323 (2020)
[3] https://x-spectrum.de
[4] LiberTEM, DOI: 10.5281/zenodo.6927963

We acknowledge financial support by the German Research Foundation (DFG grant nrs. KO 2911/12-1, KO 2911/13-1, BR 5095/2-1 and Projektnummer 182087777 - SFB951) and by the Volkswagen Foundation (Initiative: "Experiment!", Project "Beyond mechanical stiffness"). We thank Harald Niebel, Björn Gamm, Markus Boese from Carl Zeiss Microscopy GmbH for help with controlling the SEM.

Fig. 1

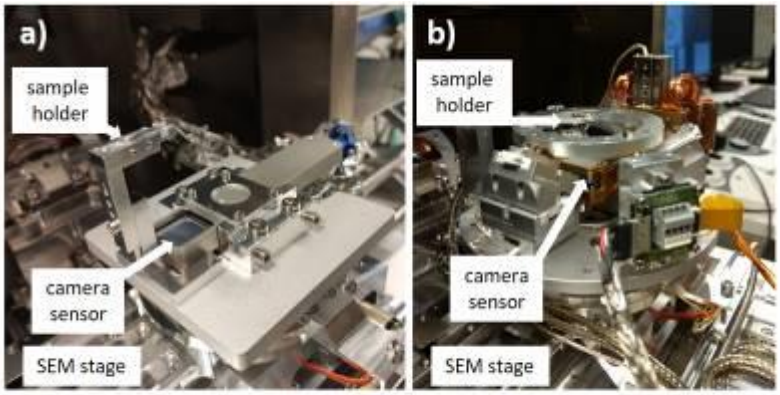

a) First setup with a Medipix 3 sensor from X-Spectrum GmbH. b) Second setup consisting of a compact 2.5x2.5x1.1cm³ CMOS camera with a fiber-coupled scintillator mounted inside a hexapod stage.

Fig. 2

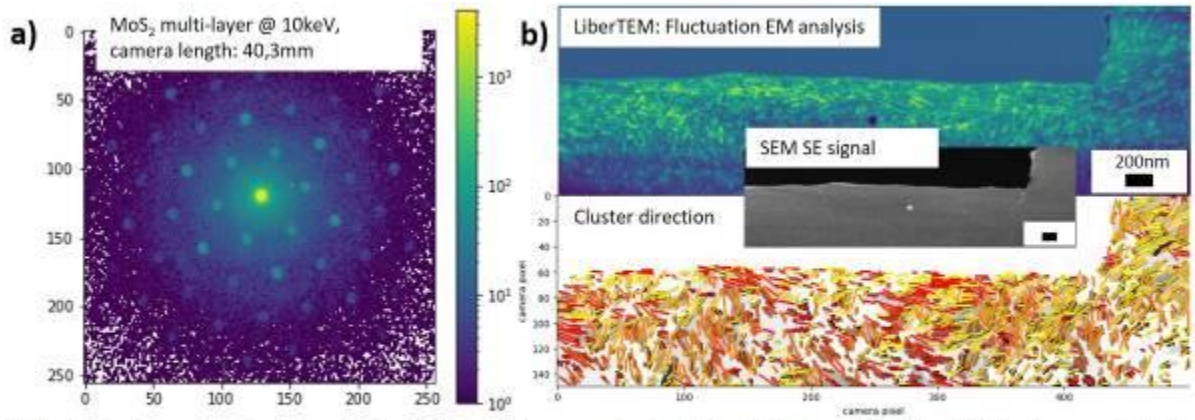

a) One diffraction pattern in log scale of a MoS_2 multi-layer acquired with the first setup using the Medipix 3 sensor (10keV electron energy, 10ms shutter). b) 4D-STEM dataset acquired with the second setup (20keV electron energy) of a human tooth prepared with a Jeol IB-09060CIS Cyro Ion Slicer, top: Fluctuation EM analysis with LiberTEM [4] showing crystallites, middle: simultaneously acquired SEM inlens signal, bottom: Cluster analysis with their long axis (color indicates direction).

IM6.P024

Breaking the resolution limit of electron microscopy of magnetic materials using 4D-STEM ptychography

M. Töllner[1], X. Mu[1]

[1]Karlsruher Institut of Technologie (KIT), INT, Karlsruhe, Germany

Nanometer and sub-nanometer resolution is crucial for the correlation of magnetic properties and devices to their intrinsic and nanoscale atomic structure for applications.The applications are in the range from nanostructured permanent magnets, high density magnetic memory storage, magnetic glasses and magnetic shape memory alloys. These can be used for crucial developments in the areas of energy efficient generators and motors, magnetic cooling systems and new IT infrastructure solutions. STEM is one of the few techniques, which is able to image the atomic structure of the material and the magnetic induction field at the nanoscale. The aim of this work is to break the current resolution limit and therefore enhance the developments in magnetic materials.

STEM nowadays can easily reach sub-nm resolution in the range of 30 to 60 pm. For magnetic imaging especially DPC imaging the resolution is between 5-10 nm. The reason for the decrease in resolution is, that the objective lenses of the microscope needs to be turned off as the magnetic field produced by the objective lenses is up to 2 T and these strong magnetic fields interfere with the magnetic structure of the samples. Therefore, the condenser lens which is far away from the sample is used for focusing the probe. Another issue is the influence of Bragg diffraction and dynamic scattering in crystalline materials. This leads to artifacts at grain boundaries and due to bend contours limiting the research in magnetic nanostructures.

In order to overcome the resolution limit and to create a robust interpretable contrast, the phase reconstruction method ptychography is used. The magnetic information is stored in the phase gradient of the sample. Electron ptychography leads to higher spatial resolution and quantifiable information than the optical limit of the instrument. For the phase reconstruction a two-stage process is used. In the first stage the Wigner Distribution Deconvolution (WDD) reconstruction algorithm is used. This algorithm uses the global approach which is more resistant against noise, but this algorithm does not lead to super resolution. In the second stage the newly developed Alternating Amplitude Flow algorithm is used. This algorithm is an iterative algorithm comparable to ePIE. In comparison to ePIE, it is more robust, always converges and is faster in tests with simulated data. Finally, the first derivative of the reconstructed phase is used to calculate the magnetic structure.

Additionally, a new pre-information analysis is used for getting a better approximation of the object. The object assumption is normally set to be pure vacuum in X-ray ptychography. Instead of this with the new approach a first approximation of the phase and amplitude of the object is generated by iDPC and brightfield data before the data is transferred into the algorithms. Furthermore, in the preprocessing stage the data is improved by the removal of noise and correction of the diffraction pattern positioning.

A preliminary result can be seen in Figures 1&2, there an iDPC image (left) of an FeRh thin film with precipitates and the reconstruction from the ptychography algorithm (right) can be seen. The reconstruction is optimized for running stable in this point of time. An enhancement to superresolution is the next step.

Fig. 1

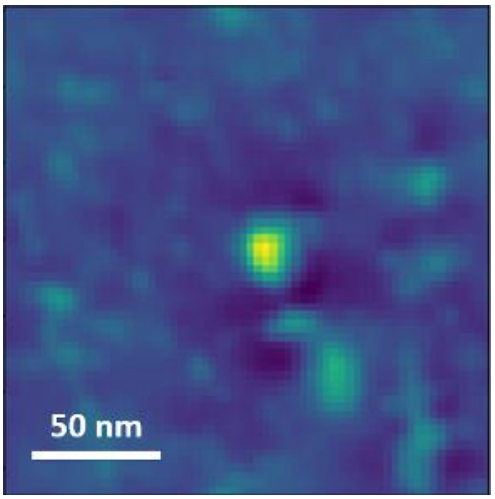

Fig. 2

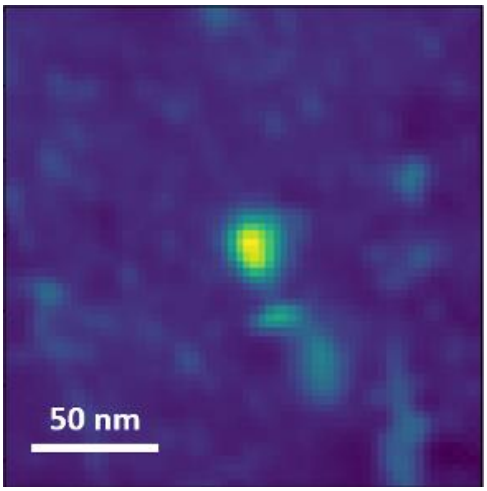

IM6.P025

Mapping nanoscale strain fields in metallic glass composites via precession nanobeam electron diffraction

L. Schretter[1], H. Sheng[1], S. Fellner[1], J. Eckert[1,2], B. Sarac[1], C. Gammer[1]

[1]Erich Schmid Institute of Materials Science of the Austrian Academy of Sciences, Leoben, Austria
[2]Chair of Materials Physics, Montanunversität Leoben, Leoben, Austria

Introduction: Accurate strain determination in both crystalline and amorphous materials is crucial for a fundamental understanding of a materials response to applied loads at the atomic level. Using the widely adopted nanobeam electron diffraction (NBED) technique, it is possible to accurately measure in-plane strains in crystalline TEM samples by peak detection using phase- or cross-correlation techniques as demonstrated by many authors before. For amorphous materials such as metallic glasses, the in-plane strains can be determined by fitting an elliptic shape function to the amorphous halo in the diffraction space. However, the desired experimental conditions for these two experiments have a key difference. Peak detection in crystalline samples works best for large diffraction disks up to the point where they almost start to overlap. For amorphous materials, such large convergence angles would result in a very diffuse, low intensity halo making fitting an ellipse impossible. Therefore, strain mapping experiments on non-crystalline materials must be conducted using an, ideally, parallel beam.

Objectives: The objective of this study is to show the possibility to measure strain in both crystalline and amorphous samples in a single experiment with high precision and accuracy by using a small convergence angle as recently shown by Sheng et al. [1].

Materials & methods: This study was carried out on a CuZrAl glass forming alloy. The sample was prepared via suction mold casting. Homogenously distributed Cu10Zr7 crystals precipitated while the matrix transformed into the glassy state, resulting in a metallic glass composite (MGC). An electron transparent lamella of this sample, prepared via FIB, was subsequently investigated via 4DSTEM. A fast CCD camera was used to capture the full diffraction patterns. For the reasons stated above, a semi-convergence angle of about 0.7 mrad and an illumination time of 200 ms were used to ensure strong signals. The analyzed region was chosen to be at the phase boundary between the amorphous matrix and a crystal in [001] zone axis.

Results: The results show that strain determination in the crystalline region via correlation methods works well even when using a small convergence angle. The strain fields show a very gradual transition between regions of different strain levels, indicating the low level of noise in the maps. Thus, it can be assumed that a disk size of 46 pixel in diameter is sufficient for accurate peak detection. In the amorphous region, the strain maps show greater deviations across the scan area. The standard deviations of 0.63, 0.08 and 0.66 % for exx, exy and eyy indicate significant inhomogeneities in the material. Nevertheless, the fitting resulted in an average RMS value of 2·10-9 for a mean ring intensity of 663 counts. Therefore, it can be stated that the fitting procedure was successful and the results in the amorphous region are accurate.

Conclusion: We have determined the atomic level elastic strains in a MGC by using cross-correlation techniques in the crystalline and ellipse fitting in the amorphous region in the same experiment. This opens the possibility for future in-situ deformation experiments on MGCs on the quest for better understanding of the deformation mechanism and the interplay between the two phases.

[1] H. Sheng, D. Sopu, S. fellner, J. Eckert and C. Gammer, Physical Review Letters 218, 245501 (2022)

We acknowledge support from the Austrian Science Fund (FWF):Y1236-N37

Fig. 1

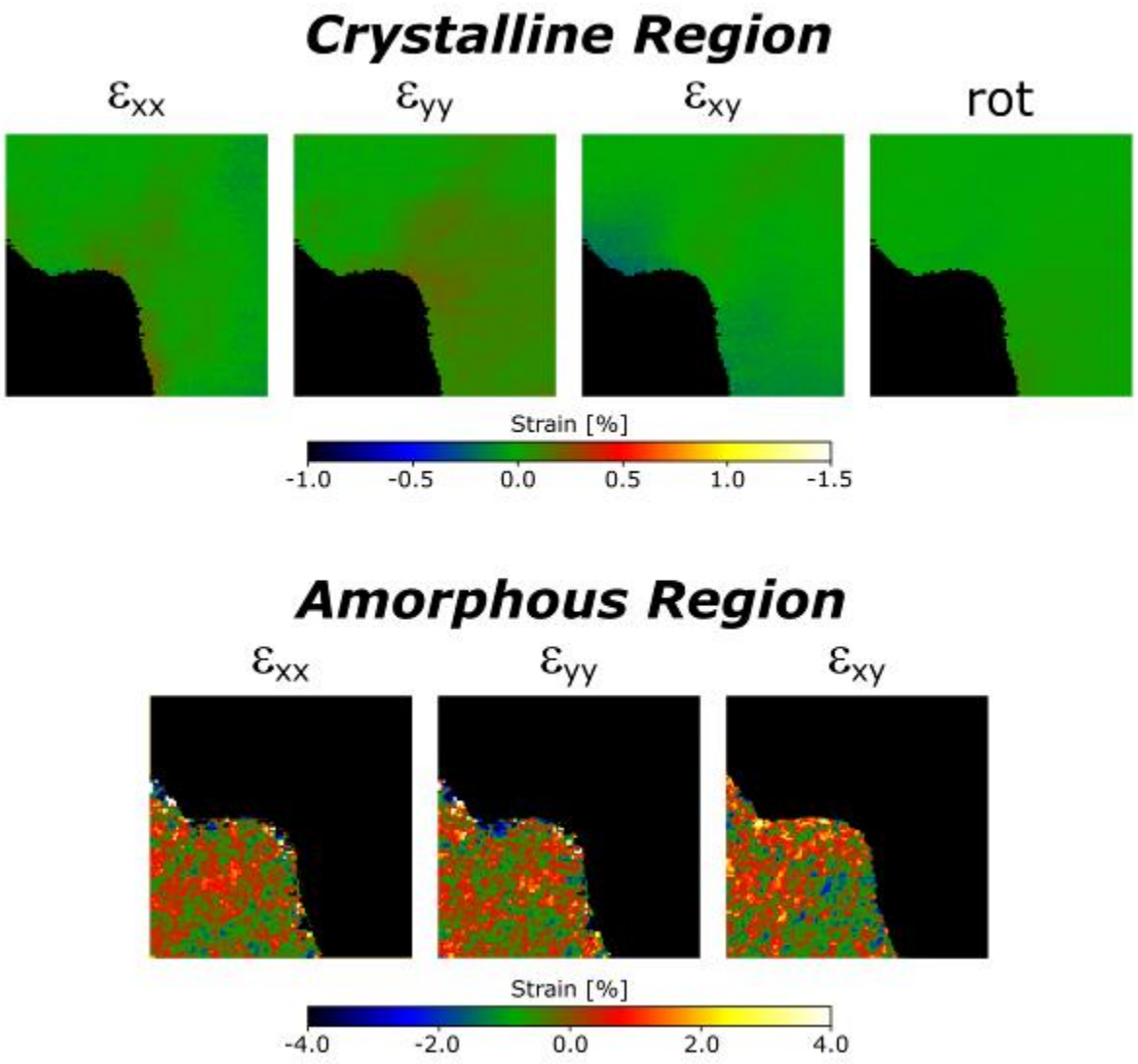
Crystalline Region
εxx
εyy
εxy
rot
Strain [%]
-1.0
-0.5
0.0
0.5
1.0
-1.5
Amorphous Region
εxx
εyy
εxy
Strain [%]
-4.0
-2.0
0.0
2.0
4.0

IM6.P026

Fast ptychographic reconstruction for low dose, binary 4D STEM

E. Hedley[1], B. Eckert[2], H. Soltau[2], P. Nellist[1]

[1]University of Oxford, Materials, Oxford, United Kingdom
[2]PNDetector GmbH, Munich, Germany

The popularity of 4D-STEM and ptychography has expanded significantly in recent years since the development of fast pixelated detectors such as the pnCCD[1], which enable new applications of 4D-STEM to beam sensitive materials which require low dose capabilities. A strong focus has developed on dose efficient method of imaging highly beam sensitive materials including, battery materials, [2]. However despite the data sets becoming very low dose and therefore the number electron recorded being small the size of the datasets remains a challenge for fast data processing.

It has previously been demonstrated by O"Leary et al. that high quality ptychographic reconstructions can be obtained from sparse binary CBED patterns such that within individual diffraction patterns electron events recorded by the detector do not overlap and cumulative doses as low as 1000eÅ-2 [3]. It was demonstrated that despite the very low bit-depth in the diffraction information that high quality reconstructions could be obtained by single side band reconstruction.

We simplify the analysis of these datasets by only storing coordinates at which electrons are recorded, which in the case of the low dose data is very few. We then aim to demonstrate the advantage of this significantly reduces dataset for further processing and perform the ptychography reconstruction on this significantly reduced dataset.

The JEOL 4D Canvas used here is a charge integrating detector with a high sensitivity, to reduce the data to a binary list of electron detection events with a pre-set threshold level for the integrated signal to be registered as an electron detection event. Instead of storing the entire pixel array we transform the dataset into an event-stream of 4D-coordinates where electrons are detected. Fig 1. Shows an example of a low dose image (a) and relevant 4D-STEM diffraction pattern (b) with a summary of the initial lines of the 4D-hitlist (c).

The slowest step in the ptychographic reconstruction process usually the Fourier Transform of the square modulus of 4D dataset which is recorded by the detector. This can be very fast in the case of sparse binary data, especially when the number of electrons detected is low; the speed of the Fourier Transform scales linearly with the number of events recorded.

In this presentation we will demonstrate the memory and time improvement potential in this workflow for low dose ptychographic reconstructions and demonstrate that there is no decreased performance in terms of the quality of reconstruction. We demonstrate the promising capabilities of this to enable a shift towards real-time ptychographic reconstructions.

[1] H. Ryll *et al.*, J. Instrum. **11** (2016)

[2] J.G. Lozano, G.T. Martinez, L. Jin, P.D. Nellist, P.G. Bruce, Nano Lett. **18** (2018) 6850–6855.

[3] C.M. O"Leary *et al* , Appl. Phys. Lett. **116** (2020)..

[4] The authors acknowledge use of characterization facilities within the David Cockayne Centre for Electron Microscopy, Department of Materials, University of Oxford and in particular the Faraday Institution (FIRG007, FIRG008), the EPSRC (EP/K040375/1 "South of England Analytical Electron Microscope") and additional instrument provision from the Henry Royce Institute (Grant reference EP/R010145/1).

Figure 1. a) Low dose ADF image of Au nanoparticle. b) Single diffraction pattern acquired on JEOL 4D Canvas equipped with a pnCCD® (S)TEM Camera® System. c) Edit of 4D-hitlist of electron interaction events.

Fig. 1

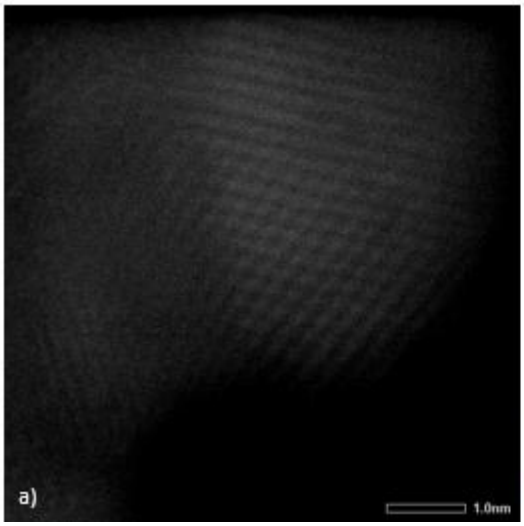

b)

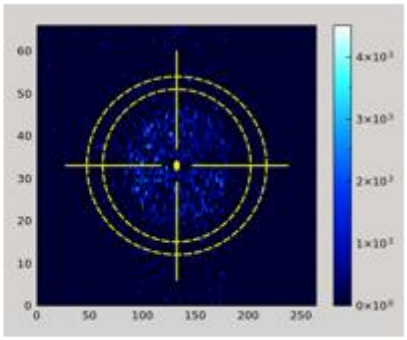

c)

Read hitlist

	event_id	frame_id	id_x	id_y	energy
0	2069022797950602579	0	0	90	588
1	2069022797950602579	0	0	91	1000
2	2069022797950602579	0	0	92	92

IM6.P027

Disentangling the contributions to the 4D-STEM signal at interfaces by muti-slice simulations

A. Beyer[1], V. S. Chejarla[1], J. Scheunert[1], V. Lider[1], K. Volz[1]

[1]Philipps-University Marburg, Materials Science Centre and Department of Physics, Marburg, Germany

The introduction pixelated detectors for scanning transmission electron microscopy (STEM) having frame rates of several thousand fps opened the exciting new field of 4DSTEM, since they allow to acquire a full diffraction pattern at each scan point. This facilitates to measure built-in electric fields using momentum-resolved STEM (MRSTEM) by evaluating the introduced shift of the diffraction pattern e.g. by tracking the direct beam or calculating the center-of-mass (COM) of the pattern"s intensity. In this way, fields with extensions in the atomic range or even longer-ranges up to micrometers, which are present in actual devices, like solar cells or batteries, can be addressed. As an example, recently, MRSTEM was used to determine the electric fields in GaAs-based pn-junctions quantitatively [1].

Real-life devices, however, generally do not consist of one material only but are composed of different ones. Accordingly, key properties, like the crystal structure, crystal orientation, the mean inner potential (MIP) or the strain state can change across the interfaces involved, complicating the determination of the electric fields.

In this contribution, we investigate the different contributions to the COM signal at interfaces with the help of systematic multi-slice simulations utilizing the STEMsalabim code [2]. These simulations are probably the only way to disentangle the different contributions of COM, since the input parameters like MIP and internal fields, e.g. due to built-in charges, can be varied independently. Moreover, optimum experimental parameters can be derived before the actual experiment. To this end, we utilize various well-defined model interfaces, i.e. GaP/Si, GaAs/GaInP, GaAs/AlAs, in which a notable difference in MIP is present and/or an intentional doping was applied to create an additional electric field . To verify our theoretical findings, complementary 4DSTEM datasets were acquired in an aberration corrected JEOL JEM 2200FS operating at 200 kV, equipped with a pnCCD detector and a NanoMEGAS Astar precession electron diffraction (PED) system.

It turns out that the choice of experimental parameters is indeed crucial to measure meaningful signals, e.g. low convergence angles of a few mrad proved to be beneficial. In addition, we find that dynamic diffraction leads to thickness-dependent oscillations in the COM signal, which do not reflect the internal fields anymore. However, PED can be applied to minimize the impact of dynamic diffraction at the cost of a reduction of spatial resolution. Under optimum conditions, MIP and fields can be detected via MRSTEM. This is shown in Fig. 1 with the example of a simulated GaAs/AlAs interface. The fields and potentials derived from the simulated COM data are in very good agreement to the input data.

In this contribution, we elucidate the different contributions to the COM signal at interfaces.

Fig1.: Simulation study of the GaAs/AlAs interface: The Input electric fields (dashed black lines) are shown alongside the fields derived from the simulated COM data (solid red lines), considering the difference in mean inner potential (MIP) only (a), an internal electric field only (b) and both MIP and field (c). The corresponding calculated potential profiles are shown in (d) – (f).

[1] A. Beyer et al., *Nano Lett.* **2021**, *21* (5), 2018–2025.

[2] J. O. Oelerich et al., Ultramicroscopy 2017, 177.

Fig. 1

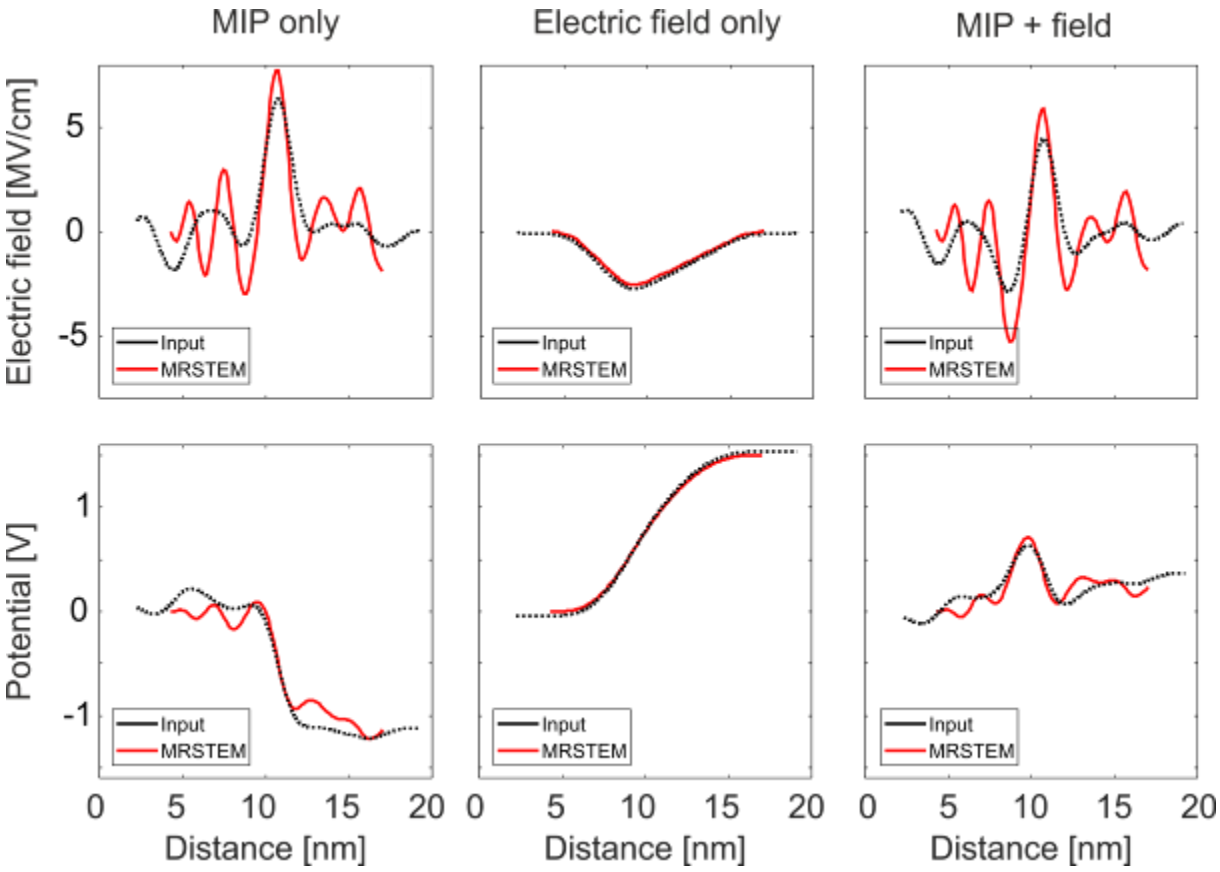
MIP only
Electric field only
MIP + field
Electric field [MV/cm]
5
0
-5
Input
MRSTEM
Potential [V]
1
0
-1
0
5
10
15
20
Distance [nm]

IM6.P028

Magnetic phase imaging using Lorentz near-field electron ptychography

S. You[1], P. Lu[2], T. Schachinger[3,4], F. Allars[1], A. Kovács[2], R. E. Dunin-Borkowski[2], A. M. Maiden[1,5]

[1]The University of Sheffield, Electronic and Electrical Engineering, Sheffield, United Kingdom
[2]Forschungszentrum Juelich, Ernst Ruska-Centre for Microscopy and Spectroscopy with Electrons and Peter Grünberg Institute, Jülich, Germany
[3]TU Wien, Institute of Solid State Physics, Vienna, Austria
[4]TU Wien, University Service Centre for Transmission Electron Microscopy, Vienna, Austria
[5]Diamond Light Source Ltd., Harwell Science and Innovation Campus, Oxford, United Kingdom

Ptychography is a phase-retrieval approach that has been widely used in electron microscopy society. It uses a localised "probe" beam of illumination to scan through the sample with overlapping between adjacent scan positions. The intensity from recorded diffraction pattern is iteratively calculated to recover the complex transfer function of both sample and illumination probe. The redundancy introduced by the overlapping probes makes ptychography robust and insensitive to noise.

Over the past few years, near-field ptychography has drawn more attention for its ability to recover a large field of view with fewer diffraction patterns [1, 2]. Near-field ptychography replace the localised probe with a full-field structured illumination and move the detector from far-field to near-field. Recent research showed that by using a diffuser, the field of view can be as large as 100 , while only using a few diffraction patterns [3].

In this talk, we experimentally demonstrate that near-field electron ptychography can be used to reconstruct magnetic sample under Lorentz mode with various illumination sizes. We move the diffuser from selected area aperture to condenser lens. This improves the does efficiency and allow us to use different illumination sizes, while keeping the merits such as large field of view with few diffraction patterns. The purposed-designed amplitude diffuser will eliminate inelastic scattering and make the illumination more coherent. A parallel beam of electrons will illuminate onto the specimen. A system diagram is shown in Figure 1, together with a picture of the amplitude diffuser and an example of diffraction pattern. The reconstructed sample results are shown in Figure 2.

We would like to acknowledge the funding from European Union"s Horizon 2020 research and innovation programme under grant agreement No. 823717 (ESTEEM 3) and No. 856538 ("3D MAGiC"), and Royal Society International Exchange Award No. IESR2192202.

Reference

[1]. M. Stockmar, et al, Sci. Rep. 3(1), (2013).

[2]. S. McDermott and A. Maiden, Opt. Express 26(19), 25471–25480 (2018).

[3]. F Allars and P Lu, Ultramicroscopy,231, (2021), p.113257.

Figure 1: System diagram of near-field electron ptychography. The amplitude diffuser, shown in (a), is inserted at condenser lens aperture. An example of diffraction pattern is shown in (b), this diffraction pattern is under conventional TEM mode with latex sphere as sample. Under Lorentz mode, both upper and lower objective lens will be turned off due to the use of magnetic sample.

Figure 2. Latex sphere and Mo-doped Permalloy sampled reconstructed results under Lorentz mode. (a) and (b) are the reconstructed amplitude and phase of latex sphere sample. (c) and (d) are the reconstructed amplitude and phase of Mo-doped Permalloy. As for the magnetic sample (sub-figure c and d), these are still preliminary results, we will keep improving these.

Fig. 1

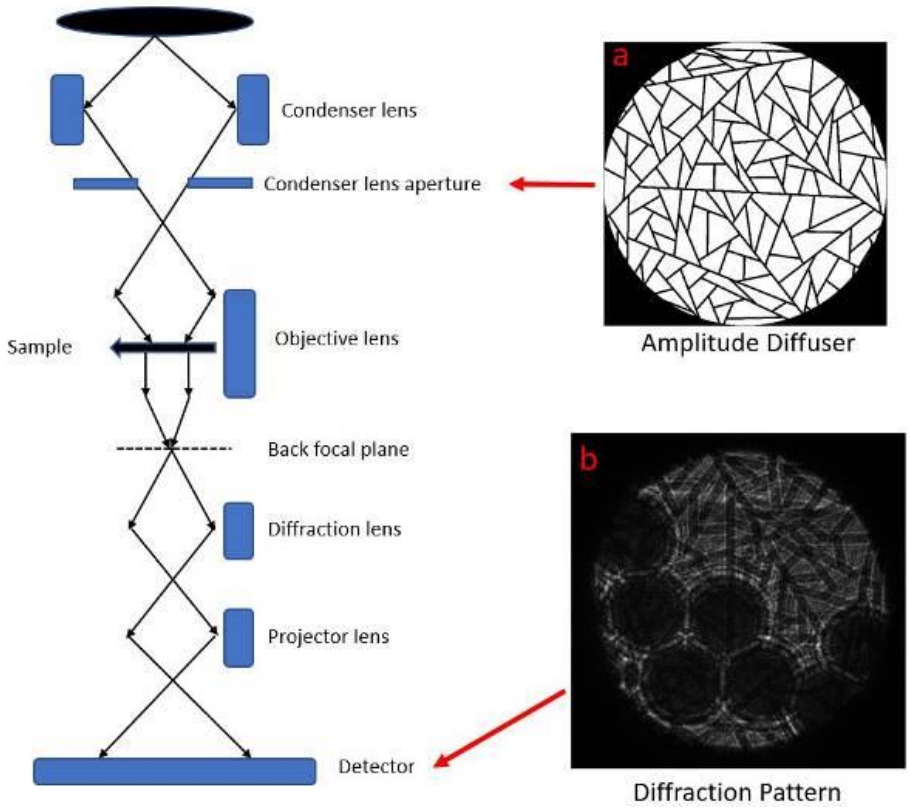
Condenser lens
Condenser lens aperture
Sample
Objective lens
Back focal plane
Diffraction lens
Projector lens
Detector
a
Amplitude Diffuser
b
Diffraction Pattern

Fig. 2

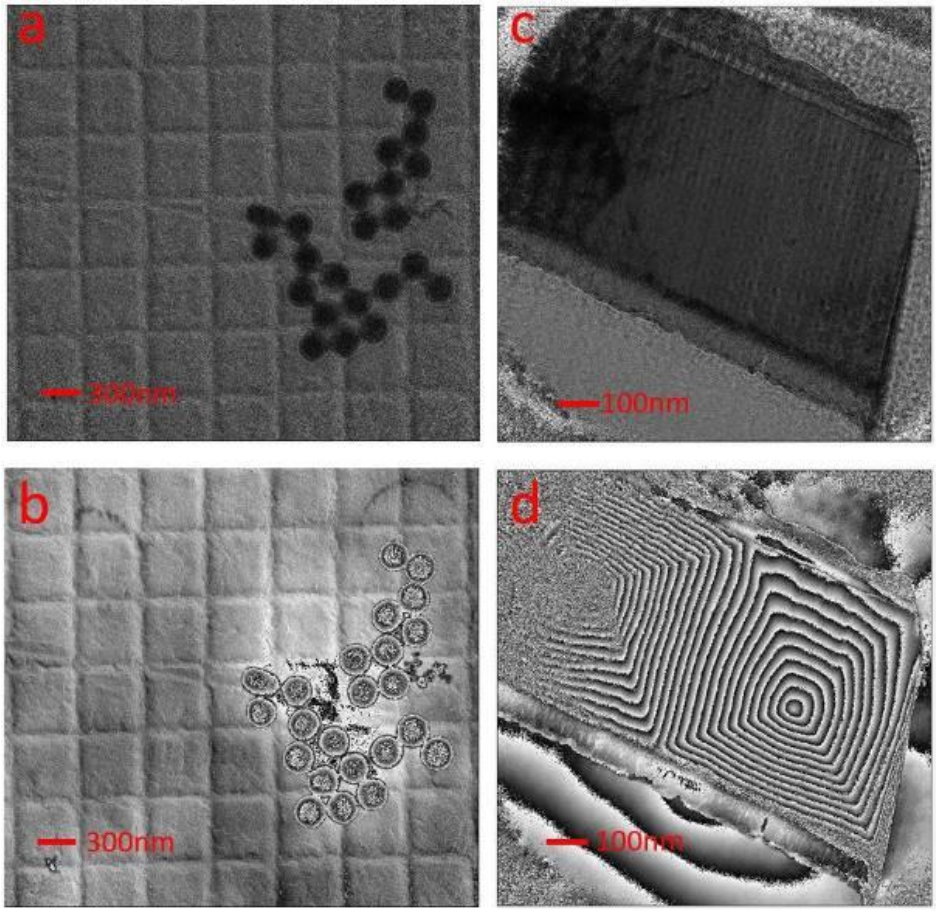
a
300nm
c
100nm
b
300nm
d
100nm

IM6.P029

Quantitative comparison of long-range electric field measurements using off-axis electron holography and 4D STEM

J. Jo[1], I. Lazić[2], E. G. T. Bosch[2], G. Pozzi[3], R. E. Dunin-Borkowski[1]

[1]Research Centre Juelich, Jülich, Germany
[2]Thermo Fisher Scientific, Eindhoven, Netherlands
[3]University of Bologna, Bologna, Italy

Quantitative measurements of nanoscale electromagnetic fields are of great interest for fundamental research, as well as for the development of next-generation electronic and spintronic devices. Off-axis electron holography (EH) is a well-established transmission electron microscopy (TEM) technique for measuring potentials and fields within and outside materials with nm spatial resolution.[1,2] 4-dimensional scanning TEM (4D STEM) is a rapidly developing technique for measuring potentials and fields, which is usually based on the recording of diffracted intensity on a pixelated detector.[3,4]

Here, we present a quantitative comparison of long-range electrostatic field and potential measurements recorded from the same sample using EH and 4D STEM based on scanning nanobeam electron diffraction. The sample comprised two Au needles, which were loaded into a Nanofactory STM-TEM specimen holder and separated by a distance of 200 nm. A bias of +50 V was applied to one of the needles, as shown in Fig. 1. Surprisingly, measurements recorded using the two techniques revealed that the projected potential and the magnitude of the *y* component of the projected in-plane electric field (*Ey*) were much smaller when measured using EH than 4D STEM, whereas the magnitude of the *x* component of the projected in-plane electric field (*Ex*) was almost the same. The difference between the two measurements is thought to originate from the effect of a perturbed reference wave (PRW) when using EH, as the long-range electric field from the needles affects the vacuum reference and hence primarily *Ey*, thereby reducing the potential and field measured using EH. In order to confirm this hypothesis, electrostatic potentials were calculated in various ways, as shown in Fig. 2. A measurement of the potential based on an analytical equation that does not consider the PRW (Fig. 2d) is similar to that measured using 4D STEM (Fig. 2b). The inclusion of the PRW effect into the analytical expression (Fig. 2e) closely reproduces the apparent potential measured using EH. This comparison is consistent with the explanation that the PRW can significantly affect measurements of long-range potentials and fields using EH.

[1] A. Tonomura, *Rev. Mod. Phys.*, **59,** 639 (1987)

[2] H. Lichte *et al.*, *Ann. Rev. Mat.*, **37,** 539 (2008)

[3] J.N. Chapman *et al.*, *Ultramicroscopy*, **3,** 203 (1978)

[4] N. Shibata *et al.*, *Sci. Rep.* **5,** 10040 (2015)

Fig. 1. Comparison between measurements recorded from two biased Au needles using (a-d) EH and (e-h) 4D STEM. The figures show (a, e) projected electrostatic potential; (b, f) magnitude of the projected in-plane electric field *E*; (c, g) *x* component of the projected in-plane electric field *Ex* (d, h) *y* component of the projected in-plane electric field (*Ey*) . The arrows in (b, f) represent the direction of the projected in-plane electric field. The same scales and scale bars are used for the same physical quantities. The units are V·nm and V for the projected electrostatic potential and projected electric field, respectively.

Fig. 2. Comparison between measurements of projected electrostatic potential around the biased Au needles recorded using (a) EH; (b) 4D STEM. (c) Application of model-based iterative algorithm to the phase image recorded using EH; (d) Application of analytical expression based on line charges; (e) Application of analytical expression based on line charges but including PRW effect. The black dashed lines in the figures represent the outlines of the Au needles. The units are V·nm for the projected electrostatic potential. The contours have a spacing of 10^4 V·nm.

Fig. 1

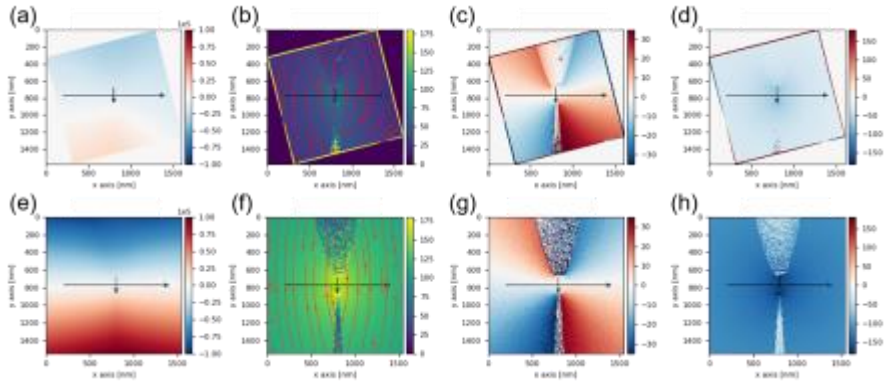

Fig. 2

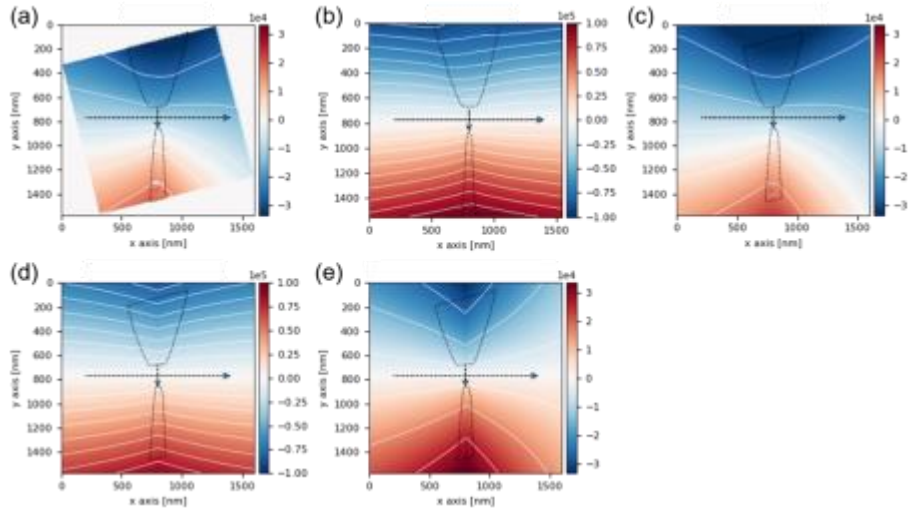

IM6.P030

Adaptation of the wsirt algorithm for vector field tomography

S. Sturm[1], K. Müller-Caspary[1], A. Lubk[2]

[1]Ludwig-Maximilians-University Munich, Department of Chemistry, Munich, Germany
[2]Leibniz-Institut für Festkörper- und Werkstoffforschung Dresden e. V., Institute for Solid State Research, Dresden, Germany

Electron Tomography allows retrieval of the 3D structure of nanoscopic objects inside a TEM, by acquisition of a tilt series of 2D projections [1]. Electron holographic tomography [2] in particular makes use of the phase, which apart from the electrostatic potential distribution (e.g. mean inner potential) also probes the magnetic field via the Aharonov–Bohm effect [3]. After separation of both using opposing projections, this allows vector-field tomography [3, 4]. Each 2D projection contains two independent projected vector components of the 3D field. However, only the component parallel to a single tilt axis is always referring to the same vector component of the 3D field, whereas the other is constantly changing in accordance to the reference frame of the tilted object. Even though the information of the latter is for dual axis tomography redundant to the third component as retrieved via Maxwell's laws [4], by directly incorporating it in the reconstruction scheme, a variety of new tilt geometries becomes possible to use for vector field tomography. Therefore, a back-projection in 3D vector space, throwing back the 2D vector projection from arbitrary projection directions, has been implemented in a WSIRT algorithm [2] adaptation in python, enabling reconstruction for any given tilt geometry. The according weighting in 3D Fourier space accounts for over representation of lower spacial frequencies and possibly for non-uniform representation of the 3D vector components. As a proof of principle, a double conical tilt geometry (incl. zero tilt) has been simulated. Fig. 1, shows all projection directions with their corresponding 2D vector projections. As a reference object (with 128x128x128 pixels), a homogeneously (in direction of the knot) magnetized torus knot (3, -4) was chosen, as it exhibits features in multiple different directions. Fig. 2 shows the reconstruction after one iteration in comparison to the original reference object. The simulation proves, that such tilt geometries can indeed be used for 3D vector field reconstruction and suggests a high fidelity of this reconstruction algorithm with only small variations of the magnetization directions within the object. Fig 1. Double Conical Setup: Tilt geometry used for the simulation in Fig. 2. Each 3D vector is color coded according to its direction (x green, y blue, z red), while each 2D vector projection is color coded according to its own reference frame (x green, y blue, no z axis). Please note, that experimentally, it would still be required to additionally record each opposing projection, in order to separate electric and magnetic field. Fig. 2 Reconstruction of a simulated reference object: Comparison reference object (top row, with 3 different views) with WSIRT reconstruction after 1 iteration (bottom row, with the corresponding 3 views). Each 3D vector is color coded according to its direction (x green, y blue, z red). For visualization, a threshold was used to limit the number of plotted arrows and only every 23rd vector has been plotted for both. References: [1] M WEYLAND, et al. Electron tomography. Materials Today, 2004 [2] D Wolf, et al. Towards automated electron holographic tomography [...], Ultramicroscopy, 2010 [3] G LAI, et al. Three-dimensional reconstruction of magnetic vector fields [..]. Journal of Applied Physics, 1994 [4] D WOLF, et al. Holographic vector field electron tomography [...]. Communications Physics, 2019 [5] K. M.-C. acknowledges funding from the DFG, contract EXC 2089/1 – 390776260 (e-conversion). A. L. received funding from the European Research Council (ERC) under the Horizon 2020 Research and Innovation Program of the European Union (grant agreement number 715620).

Fig. 1

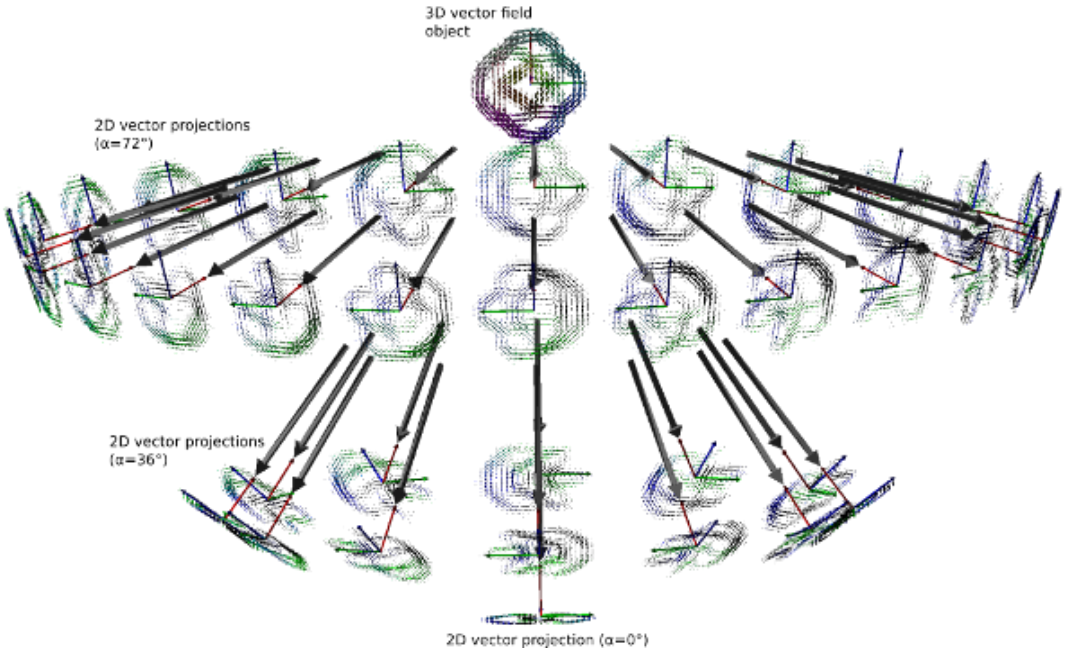
3D vector field object
2D vector projections (α=72°)
2D vector projections (α=36°)
2D vector projection (α=0°)

Fig. 2

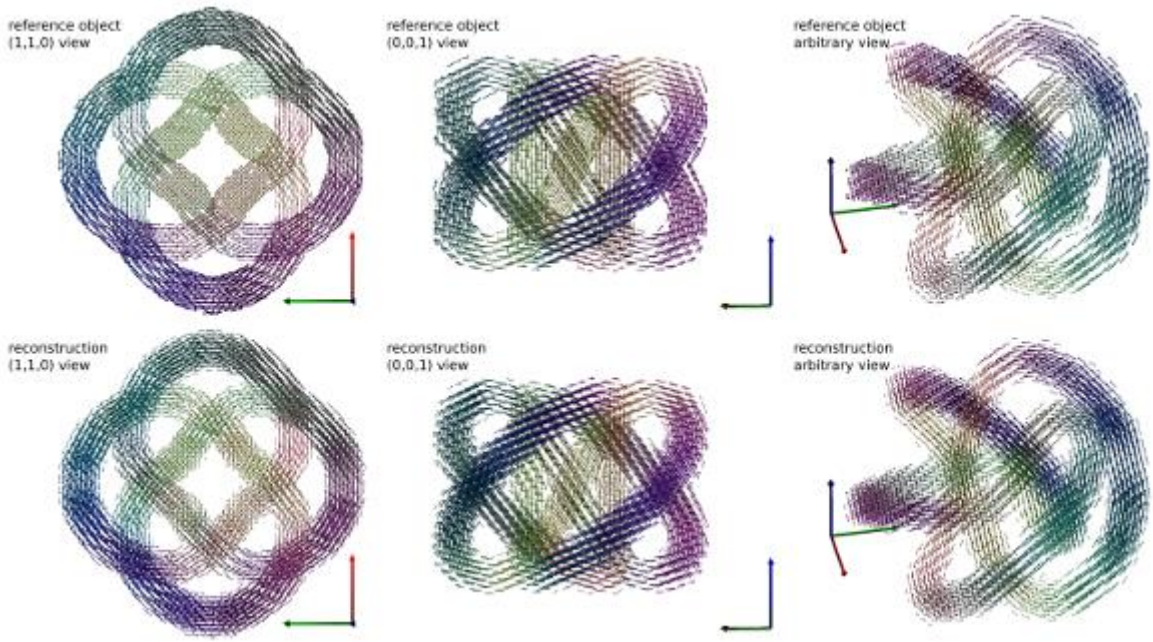
reference object (1,1,0) view
reference object (0,0,1) view
reference object arbitrary view
reconstruction (1,1,0) view
reconstruction (0,0,1) view
reconstruction arbitrary view

IM6.P031

First experimental results with the latest generation hybrid-pixel detector from DECTRIS for 4D STEM

E. Müller[1], E. Poghosyan[1], T. J. Pennycook[2], C. Hofer[2], D. Grando Stroppa[3], C. Hoermann[3], M. Meffert[3], L. Piazza[3]

[1]Paul Scherrer Institute, Electron Microscopy Facility, Villigen, Switzerland
[2]University of Antwerp, EMAT, Antwerp, Belgium
[3]DECTRIS Ltd., Baden-Daettwil, Switzerland

Unlike "conventional" STEM, 4D STEM allows the electron microscopist to not restrict data acquisition to one specific technique. The acquisition of a full-frame diffraction pattern per probe position allows one to reconstruct different images at a later time, including integrating over different scattering angles with virtural detectors, mapping electromagnetic fields via DPC or CoM based methods, or mapping crystallographic orientation and strain via diffraction pattern identification. Additionally, such a 4D dataset can be used for ptychography, which provides for instance extremely high dose efficiency and light atom detection.

The bottleneck for 4D STEM acquisition is the camera, which has previously been a severe limitation for the technique. The camera needs high sensitivity, a large dynamic range, low noise and a very high speed. Ideally, it should not require slower scans than conventional imaging modes in order to minimize problems with beam-damage, contamination and drift. High speed also facilitates high quality parallel acquisition of conventional signals such as ADF or secondary electron images.

We have tested the latest generation hybrid-pixel direct electron detector DECTRIS ARINA with our probe-corrected 200kV JEOL NeoARM. The ARINA fulfills the requirements of high sensitivity and a very low noise level. Its high counting speed, up to 10pA per detector pixel, allows simultaneous acquisition of both the intense BF disk and far less intense higher angle scattering – an important prerequisite for being able to construct all possible signals from the 4D data. Very importantly, the DECTRIS ARINA reaches very high frame rates: while at a full resolution of 192x192 pixels, a frame rate of 20kHz is possible, and even up to 120kHz is possible at a resolution of 96x96 pixels, corresponding to a dwell-time shorter than 10us.

We performed our first experiments with the ARINA with beam-tolerant Si, $SrTiO_3$ and SmB_6 for STEM imaging, permalloy and $NdMn_2Ge_2$ for DPC/CoM and metals for orientation mapping. Already these first experiments prove ARINA is suitable for STEM imaging, DPC/CoM and orientation mapping. Ptychography results from both the materials and life sciences will be presented under normal and low-dose conditions. Thanks to the high dynamic range, high sensitivity, low noise and very high frame-rate, the Dectris ARINA is very versatile and is perfectly suited for the above-mentioned very diverse applications, about which we will present an overview.

IM7.001-invited

Unveiling the dynamic behavior of electrocatalysts through operando microscopy and spectroscopy

B. Roldan Cuenya[1]

[1]Fritz-Haber Institute of the Max Planck Society, Department of Interface Science, Berlin, Germany

Climate change concerns have spurred a growing interest in developing environmentally friendly technologies for energy generation, including green H2 production from water splitting. Moreover, concerted attempts are also being made to re-utilize CO2 by electrocatalytically converting it into value-added chemicals and fuels, offering the possibility to store renewable energy into chemical bonds. Thus, efficient, selective and durable electrocatalysts that can operate under mild reaction conditions are urgently needed. However, the latter challenging goal can only be achieved when fundamental understanding of the electrocatalyst structure and surface composition under reaction conditions becomes available. It should also be kept in mind that even morphologically and chemically well-defined pre-catalysts are commonly susceptible to drastic modifications under operando conditions, especially when the reaction conditions themselves change dynamically. Here, a synergistic experimental approach taking advantage of a variety of cutting-edge microscopy (EC-AFM, EC-TEM, LEEM/XPEEM), spectroscopy (NAP-XPS, XAS, Raman Spect., GC/MS) and diffraction (XRD) will be employed to unveil the complexity of energy conversion electrocatalysts.

In particular, I will provide new insights into the electrocatalytic reduction of CO2 and Nitrate as well as the oxygen evolution reaction using operando characterization methods while targeting model pre-catalyst systems ranging from single crystals to metal nanoparticles. Some of the aspects that will be discussed include: (i) the design of size- and shape-controlled catalytically active nanoparticle pre-catalysts (Cu, Cu2O cubes, CoOx NPs, Fe/NiO octahedra), (ii) the understanding of the active state formation and (iii) the correlation between the dynamically evolving structure and composition of these electrocatalysts under operando reaction conditions and their activity, selectivity and durability.

Our results are expected to open up new routes for the reutilization of CO2 through its direct conversion into industrially valuable chemicals such as ethylene and ethanol, the electrochemical synthesis of ammonia and the generation of H2 through water splitting.

IM7.002-invited

Dynamic observations of compositionally complex alloys by *in situ* TEM

C. Liebscher[1], Z. Li[2], D. Raabe[1], G. Dehm[1], W. Lu[3]

[1]Max-Planck-Institut für Eisenforschung, Düsseldorf, Germany
[2]Central South University, School of Materials Science and Engineering, Changsha, China
[3]Southern University of Science and Technology, Department of Mechanical and Energy Engineering, Shenzhen, China

Introduction

The development of multicomponent high entropy alloys (HEAs) has opened the door to sculpt advanced microstructures in the near-infinite compositional space, resulting in materials with unprecedented mechanical and functional properties. Understanding the underlying phase transformation mechanisms during processing and application of these compositionally complex alloys is a key requirement to further advance alloy design strategies. *In situ*transmission electron microscopy (TEM) techniques nowadays make it possible to probe even compositionally complex alloys under varying temperatures or strains, while being able to dynamically observe microstructure evolution down to the atomic level.

Objectives

The present talk focuses on *in situ* probing strategies in the TEM to observe plastic deformation and temperature dependent phase transformations in HEAs. I will show a novel mechanism of transformation induced plasticity in an FeMnCoCr alloy revealed by *in situ* straining in the TEM. In a further example, *in situ* heating experiments in the TEM will be used to track temperature induced phase transformations and secondary phase formation in a carbon (C) doped FeMnCoCrNi alloy.

Materials & methods

The HEAs are fabricated by vacuum induction melting and investment casting using at least 99.5 wt.% pure metals. Thermo-mechanical treatment is used to homogenize the alloys and adjust the desired starting microstructure. *In situ* tensile straining experiments are performed using a custom-built straining inset in a model 654 Gatan straining holder. Samples are heated *in situ* in the TEM using a DENSsolutions Lightning heating/biasing holder, while using both TEM and scanning TEM to observe microstructural changes in Titan Themis (Thermo Fisher Scientific) microscopes.

Results

The dual-phase $Fe_{50}Mn_{30}Co_{10}Cr_{10}$ (at.%) alloy is primarily deforming via displacive phase transformation from the face-centered cubic (FCC) to the hexagonal close packed (HCP) structure. Our *in situ* tensile straining reveals that a bi-directional transformation is active, where FCC transforms to HCP and back to FCC upon straining. This strain induced phase transformation leads to dynamic microstructural refinement, which equips the alloy with outstanding work-hardening capabilities.

Such a nanostructure provides excellent room temperature properties, but rapidly coarsens at elevated temperatures leading to a loss in mechanical properties. Interstitial doping with C is a way to stabilize the microstructure and our *in situ* TEM observations reveal the underlying phase transformation mechanisms. At intermediate temperatures of ~300ºC we observe the formation of nano-twinned FCC originating from an initial HCP grain. Upon further heating to 700ºC, elongated nanoscale carbides are forming along the FCC twin boundaries, which can stabilize the nano-twinned regions up to 900ºC. Atomic scale observations at extreme temperatures at >900ºC reveal the dissolution of the carbide phases and associated de-twinning, providing insights into microstructural evolution in the compositionally complex alloys.

Conclusions

In the present talk, we showed that *in situ* straining and heating in the TEM provides unprecedented insights into the phase transformation mechanisms in compositionally complex alloy systems. *In situ* probing is pivotal in observing the underlying transformation dynamics and is able to reveal previously overlooked phase transformation mechanisms.

IM7.003-invited

STEM EBIC mapping of ferroelectric polarization in thin film hafnia

H. L. Chan[1], S. Fields[2], Y. Chen[1], T. O'Neill[1], W. Hubbard[3], J. Ihlefeld[2], B. C. Regan[1,3]

[1]UCLA, Physics and Astronomy, Los Angeles, CA, United States
[2]University of Virginia, Materials Science and Engineering, Charlottesville, VA, United States
[3]NanoElectronic Imaging, Inc., Los Angeles, CA, United States

In its primary imaging mode, a scanning transmission electron microscope (STEM) can locate individual atoms. With various spectroscopic attachments, a STEM can even determine the chemical identity of those atoms. However, while it excels at determining a sample"s physical and chemical structure, traditional STEM struggles to map electronic structure. Inter-atom electric fields are small compared intra-atom electric fields, so visualizing the former generally requires advanced techniques such as holography or differential phase contrast imaging. These techniques are analysis intensive and can produce complicated images that are difficult to interpret.

In electron beam induced current (EBIC) imaging, a transimpedance amplifier electrically connected to the sample collects the current induced by a scanning electron beam. Associating that current with the beam position produces an image. In samples with intrinsic electric fields, a raw EBIC image can sometimes be quickly and quantitatively interpreted to give the local electric field magnitude and direction.

To illustrate STEM EBIC imaging"s capabilities for high-resolution, *in situ* electric field mapping, we fabricate electron-transparent TaN/HZO/TaN capacitors (30/20/30 nm) on 20-nm thick silicon nitride membranes. The tantalum nitride is deposited via DC sputtering and the zirconium-doped hafnia ($Hf_{0.5}Zr_{0.5}O_2$, HZO) is deposited via plasma-enhanced atomic layer deposition [1]. Using traditional transport measurements, we determine the dielectric's polarization as a function of the applied electric field *in situ* over various ranges of the electric field. Interleaved with the P(E) measurements, we perform STEM EBIC imaging to map the remanent polarization as a function of position in the capacitor.

Collecting the EBIC separately from the two electrodes of the capacitor allows us to separate the standard EBIC, which depends on the electric fields internal to the sample, from the EBIC caused by the ejection of secondary electrons from the sample [2]. The former appears in the difference EBIC images (Fig. 1), while the latter appears in the sum (not shown). Subtracting a polarization "up" differential EBIC image from a polarization "down" EBIC image beautifully reveals the spatial variation of the switching fraction (Fig. 2). The switching fraction further varies with the switching history.

References

1.Fields, S. S. et al. Compositional and phase dependence of elastic modulus of crystalline and amorphous $Hf_{1-x}Zr_xO_2$ thin films. Appl. Phys. Lett. 118, 102901 (2021).

2.Hubbard, W. A., Mecklenburg, M., Chan, H. L. & Regan, B. C. STEM Imaging with Beam-Induced Hole and Secondary Electron Currents. Phys. Rev. Applied 10, 044066 (2018).

This work was supported by National Science Foundation (NSF) award DMR-2004897 and by NSF Science and Technology Center (STC) award DMR-1548924 (STROBE).

Figure 1. (left to right) Bright field, annular dark field, differential EBIC with polarization "up", and differential EBIC with polarization "down" images. The field of view is 11 μm on a side.

Figure 2. (left) The difference between the fourth and the third images from Fig. 1. Areas with a switchable remanent polarization appear black. (right) A higher magnification view (acquired separately, but analyzed in the same way) of the region indicated by the red box reveals ferroelectric domains. Here the field of view is 1.9 μm on a side.

Fig. 1

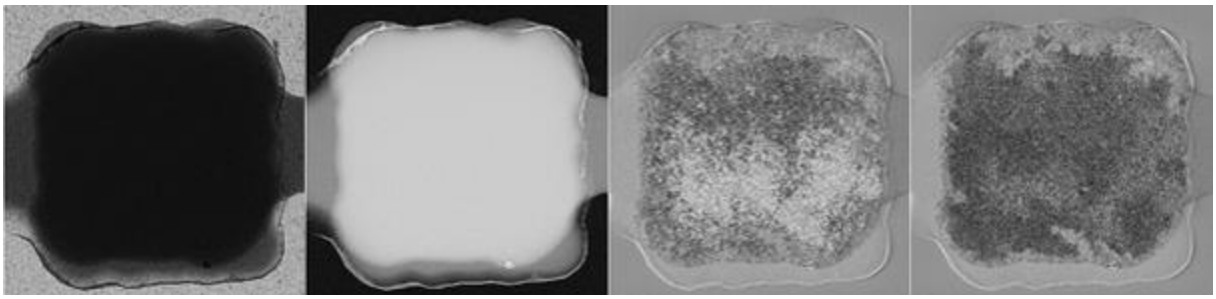

Fig. 2

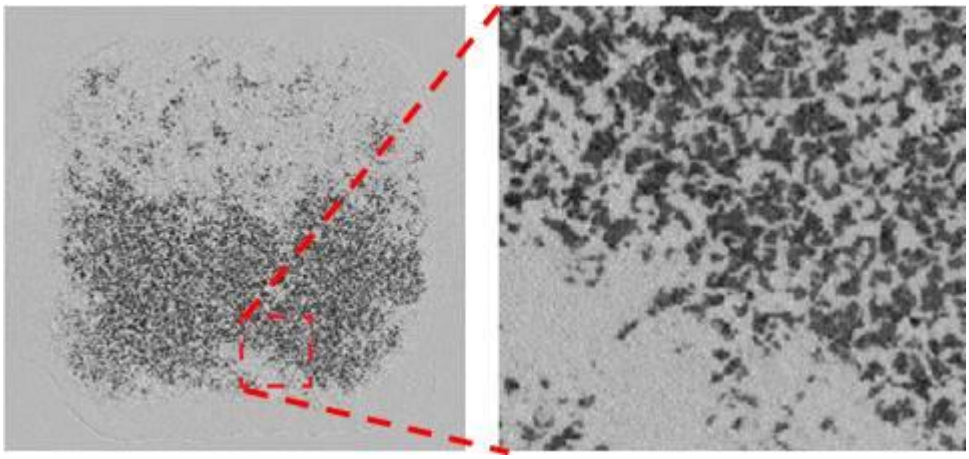

IM7.004

Growth mechanisms of nanomaterials studied by atomic-resolution liquid-phase scanning transmission electron microscopy

W. Dachraoui[1], D. Keller[1], A. Vogel[1,2], R. Erni[1]

[1]Swiss Federal Laboratories for Materials Science and Technology (EMPA), Dübendorf, Switzerland
[2]ETHZ—Swiss Federal Institute of Technology Zürich, Materials, Zurich, Switzerland

Understanding the chemical and the physical processes of nanomaterials (NMs) in liquid media is a crucial challenge and of fundamental interest to modern materials science, chemistry and biology.1 For example, observing the initial steps of nucleation and the growth of solids and following the exact pathway of the formation of bimetallic NMs are of highest importance for the development of novel materials. This requires techniques allowing the study of NMs in their liquid environments with the corresponding resolution necessary to observe processes at the atomic scale. The most attractive and unique capabilities of a scanning/transmission electron microscope (S/TEM) is its high spatial resolution, enabling the study of materials at the atomic scale. Nevertheless, a key limitation of this technique is the need of high vacuum conditions to analyse samples. In recent years, a new frontier in the field of TEM has emerged to observe specimens in liquid environments under high-vacuum conditions, by separating the liquid sample from the vacuum column using thin impermeable/electron transparent membranes.2 Recent advances in microfabrication technology have led to a number of commercially available liquid cell TEM holders, where the liquid cells are made of two micro-fabricated silicon nitride electron transparent thin films. This liquid cell consists of liquids normally exceeding 100 nm in thickness encapsulated by SiN windows that are several tens of nanometer in thickness as well, and thus are unsuitable for atomic scale observations. Graphene-based liquid cell electron microscopy (GLC) has demonstrated a better imaging resolution3 (Fig 1).

In this study, we optimized graphene-based liquid cells to realize in real time atomic scale observations of nucleation and growth of Platinum (Pt) nanoparticles (NPs) and the formation of Pt-Pd core-shell NPs in liquid mode. We investigate the exact growth mechanisms of platinum NPs from single atoms to final crystals by in-situ liquid phase STEM at atomic-scale. After nucleation, we show that the nanocrystals grow via two main stages: atomic attachment in the first stage, followed by the second stage of growth, which is based on particle attachment by different atomic pathways (Fig 2). In addition, we investigated the exact atomic mechanisms underlying the growth of Pt-Pd core-shell NPs, where growth mechanisms of the Pt shell on Pd nanocubes are studied in aqueous solution at the atomic level. We found that Pd-Pt core-shell NPs are formed via two distinct mechanisms: (i) at low concentration of Pt atoms, an ultra-thin skin of only a few atomic layers is formed *via* atom-by-atom deposition and (ii) at higher concentration of Pt atoms, inhomogeneous islands and thick shells are formed via attachment of Pt clusters (Fig 3).3, 4

Figure 1: Encapsulated Pt precursor with GLC: (a) schematic illustration, (b) formation of Pt atoms in liquid.

Figure 2: Nucleation and growth of nanoparticles: (a) ADF-STEM time lapse and (b) schematic illustration. (Reproduced from ref. 3)

Figure 3: Pd NCs core and Pt shell STEM analysis. Pd nanocube (a) with thin layer of Pt shell (b) with Pt shell islands. (Reproduced from ref.4)

REFERENCES

1Unocic, R. R. U*Microsc. Microanal* 2015, **21**, 1972-1973

2Alloyeau, D.; Dachraoui, W.; Javed, Y.; et al. *Nano Letters* 2015, **5**, 2574-2581

3Dachraoui, W.; Henninen, T. R..; Keller D.; Erni, R. *Scientific Reports* 2021, **11**, 23965

4Dachraoui, W.; Bodnarchuk, M. I.; Vogel, A.; Kovalenko, M. V.; Erni, R. *Applied Physics Reviews* 2021, **8**, 041407

Fig. 1

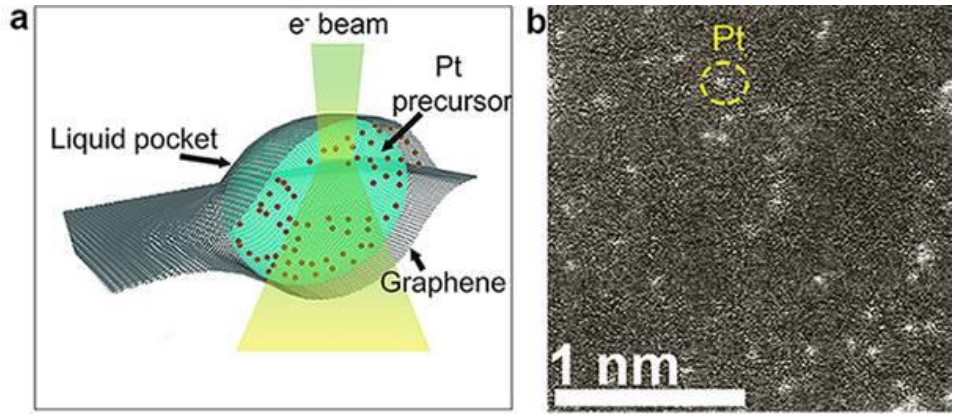

Fig. 2

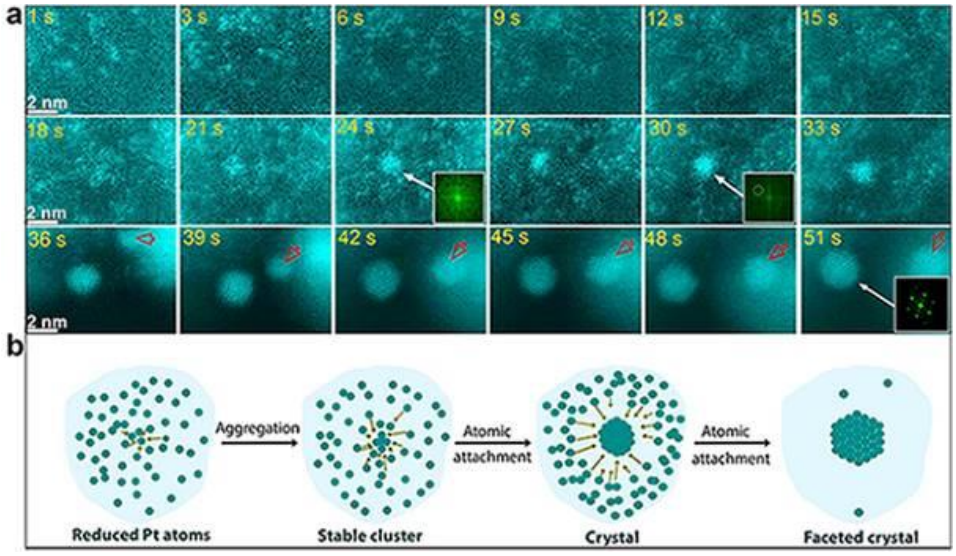

Fig. 3

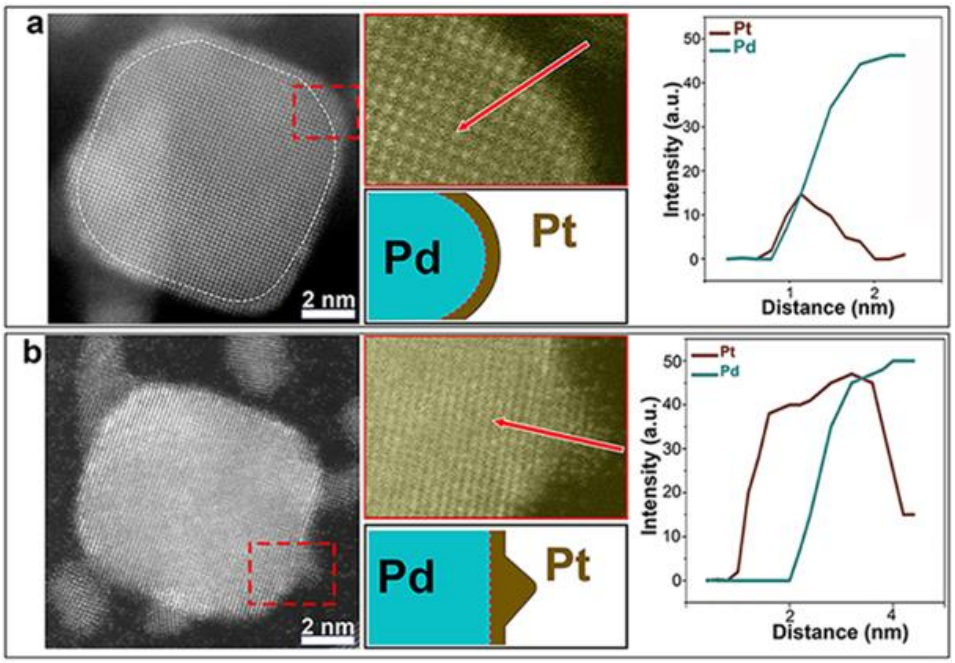

IM7.005

Investigation of the underlying mechanism of the Ag-induced layer exchange by *in situ* studies in SEM and TEM

P. Denninger[1], A. Greppmair[1], T. Schwope[1], D. Drobek[1], M. Buwen[1], B. Apeleo Zubiri[1], P. Schweizer[2], E. Spiecker[1]

[1]Friedrich-Alexander-Universität Erlangen-Nürnberg, Institute of Micro- and Nanostructure Research (IMN), Erlangen, Germany
[2]EMPA, Thun, Switzerland

Thin film semiconductors are indispensable in modern technology and a key element for future applications. In particular, highly crystalline thin film semiconductors are of great interest due to their outstanding performance by reducing the detrimental influence of grain boundaries [1]. Preparing such thin film crystalline semiconductors on foreign (amorphous) substrates can even improve their performance and enable future applications like flexible devices. However, the fabrication on amorphous and/or heat-sensitive substrates are quiet challenging and expensive. A smart approach is the crystallization of the semiconductor directly on the needed substrate. Here, the metal-induced layer exchange (MILE) process offers a direct crystallization route by contacting the amorphous semiconductor with a metal layer, which decreases dramatically the necessary crystallization temperature [2]. Applications of the MILE process are widespread due to the great variety of semiconductor – metal systems. Although this process has been known for a long time, the mechanism behind it is still under debate [3].

In our work, we investigated the layer exchange (LE) process within the silver-silicon system (AgILE). Especially, the early stages before the initial LE starts are studied by in situ microscopy. The sample composition comprises a poly-crystalline Ag layer on the substrate (SiN), an oxide layer and an amorphous Si top layer. During heating, both layers change their position and the Si crystalizes (illustrated in Figure 1a).

Pre-characterization and analysis of the process dynamics are performed by in situ light microscopy (see Figure 1b) and ex situ electron microscopy (see Figure 1d). In situ annealing experiments in SEM are performed by our custom-built chip-based heating stage (illustrated in Figure 1c) [4]. Especially, STEM High Angle Annular Dark-Field (HAADF) imaging facilitates the discrimination between Ag and Si due to the Z-dependency of the signal. To study the occurring reactions in more detail, additional heating experiments in the TEM are executed.

Both heating experiments (700 °C) revealed similar reactions before the initial LE occurs. Figure 2a-d displays the observed reactions in the SEM. After a short initial annealing time, Ag push-ups appear followed by a second reaction, where a new Si-rich phase grows within the appeared Ag push-ups. Afterwards, the LE starts exactly at one previously occurred push-up and grows subsequently through the whole sample. The final state consist of pure Si-crystals (black), reacted area (dark gray) and some unreacted regions (bright).

To gain insights into the inner sample structure, lift-out analysis and non-destructively electron tomography are performed. The results of the lift-out samples revealed a crystalline Si phase in the bottom layer, whereas the top layer consist of initial amorphous Si and pushed-up Ag grains (see Figure 2e). Figure 2g indicates the Ag is pushed up by the lateral growing c-Si. Interrupted in situ heating experiments in the TEM were performed to acquire a tilt series of the present sample state. The resulting 3D tomograms verify the distribution of Ag and Si in both layers (see Figure 2f).

Accordingly, we propose a refined model of the AgILE process due to our detailed microscopic study and observed reactions [5].

[1] 10.1063/1.91832

[2] 10.1088/1361-6463/ab91ec

[3] 10.1002/adem.200800340

[4] 10.1016/j.ultramic.2020.112956

[5] Financial support by DFG via GRK

Fig. 1

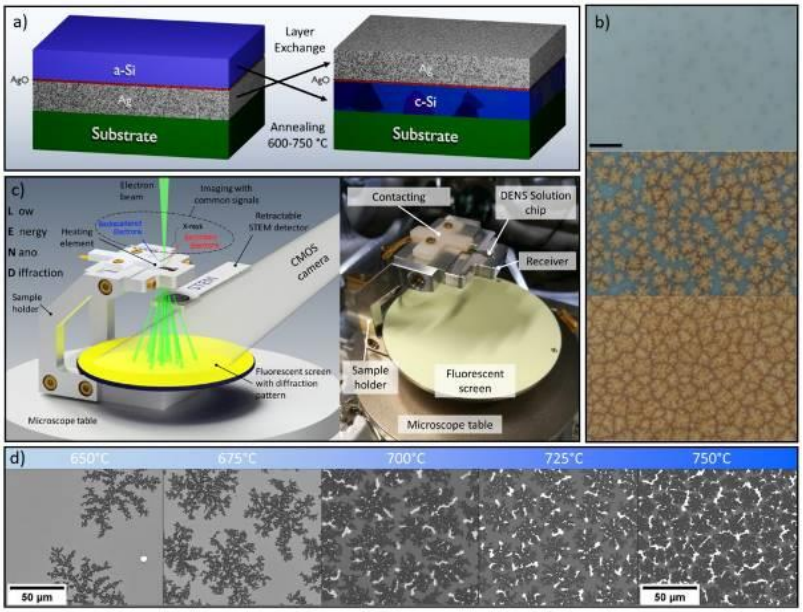

Figure 1: Overview of the AgILE process. a) Schematic illustration of the process. The initial sample consist of an Ag/a-Si layer stack. During annealing, both layer changes their position and the Si crystalizes (c-Si/Ag). b) Pre-characterization by *in situ* light microscopy to study the reaction dynamics. c) Custom-built chip-based heating stage in SEM. d) Ex situ characterization of the temperature dependency in the process.

Fig. 2

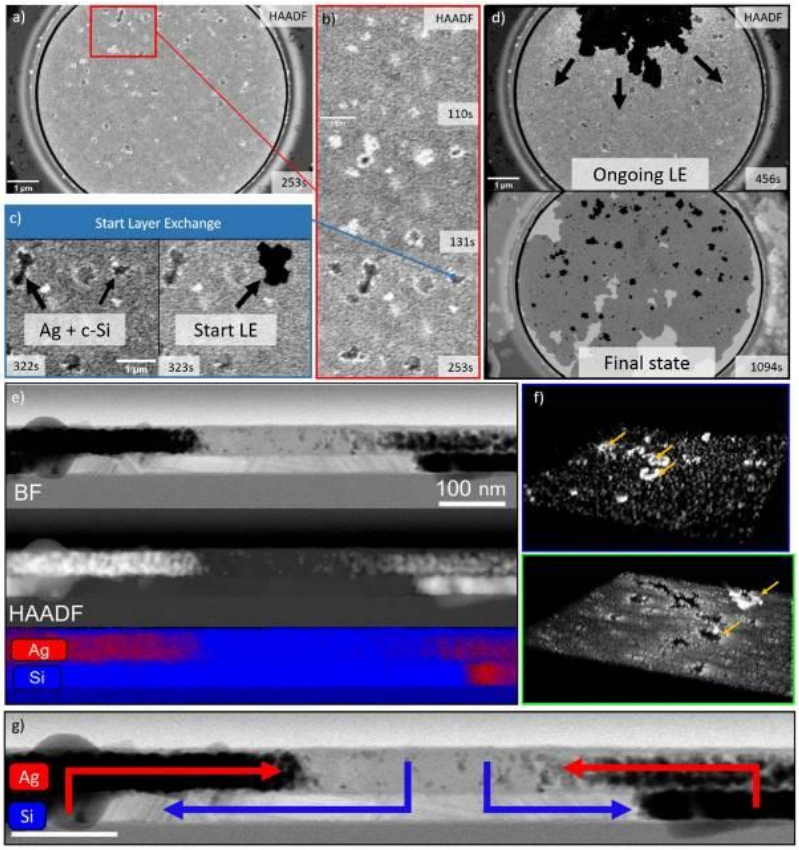

Figure 2: *In situ* heating experiments and post-characterization. a-b) Ag push-up (bright contrast) formation after a short annealing time (110 - 253 s) with a subsequent growth of a Si-rich phase within those push-ups (darker contrast). c) The LE starts at one observed push-up (see bottom left) and grows through the whole sample. d) Ongoing LE and final sample state, which comprises of pure Si crystals (black), reacted regions (completed LE, darker contrast) and unreacted, initial regions (brighter contrast). e) Analysis of the lift-out by STEM BF and HAADF imaging. The bottom layer consists of c-Si and residuals of the initial Ag layer. The top layer consists of a-Si and pushed-up Ag grains. The corresponding EDX map support the observations. f) 3D reconstruction of the interrupted and final sample enables to study the sample in all three dimensions. g) Illustration of the material flow within the AgILE process. c-Si grows laterally and pushes the initial Ag layer into the top layer, which consists of a-Si.

IM7.006

In-situ correlation of the anomalous Hall effect with the occurrence of topological and non-topological magnetic phases in $Mn_{1.4}PtSn$

D. Pohl[1], B. Rellinghaus[1], S. Schneider[1], D. Krieger[2,3], Y. Lee[2], P. Vir[4], C. Felser[4], M. Winter[1,4], A. Thomas[2,3]

[1]TU Dresden, Dresden Center for Nanoanalysis (DCN), Dresden, Germany
[2]Leibniz Institute for Solid State and Materials Research Dresden, Dresden, Germany
[3]TU Dresden, Institute of Solid State and Materials Physics, Dresden, Germany
[4]Max Planck Institute for Chemical Physics of Solids, Dresden, Germany

1. Introduction

(Anti-)skyrmions are potential future nanoscale information carriers, since they can be electrically manipulated and detected. So far, Hall effect measurements on skyrmionic samples are conducted on samples with different thicknesses and confinements as compared to those used for magnetic imaging in a transmission electron microscope (TEM) [1,2], which has proven extremely valuable for unveiling the details of skyrmionic spin textures even in 3D [3]. Since the stability of (anti-)skyrmions depends sensitively on the sample geometry, a correlation of magneto-transport and TEM data are problematic, if not conducted on identical samples.

2. Objectives

We have therefore devised an in-situ measurement platform that bridges this gap and allows for the conduction magneto-transport measurements in-situ in a TEM. The current investigation aims at correlating the anomalous Hall effect in the Heusler compound $Mn_{1.4}PtSn$ with the magnetic field dependent occurrence of non-topological (NT) and topologically protected magnetic phases such as the helical phase, NT bubbles and anti-skyrmions.

3. Materials & methods

In-situ Lorentz-TEM (L-TEM) investigations were conducted on a *JEOL F-200* microscope (200 kV, cold FEG) equipped with a *Gatan OneView* camera. A *Protochips Fusion Select* holder with gold-plated spring contacts connected to electrical feedthroughs is used to measure the anomalous Hall effect. A TEM lamella was cut from a $Mn_{1.4}PtSn$ single crystal [4] using a focused ion beam system (FIB), deposited on a measurement chip with a SixN window, and soldered to the pre-defined contact pads by Pt deposition in the FIB.

In Lorentz mode, the objective lens of the microscope was used to apply a magnetic field perpendicular to the sample plane. Acquisition of L-TEM images and concurrent measurements of the Hall voltage as function of the magnetic field were conducted automatically utilizing Python scripting.

4. Results

The L-TEM-images in Fig. 1 reveal that upon increasing the magnetic field **B** (i) the density of helices (as manifested by a stripe contrast) is reduced and (ii) the magnetization process is governed by growth of (preferred) helical domains – very alike that of conventional ferromagnets. At fields above roughly B = 300 mT, where the Hall voltage exceeds the otherwise linear increase with **B** (cf. Fig. 2), we observe (i) a transition from a continuous to a discontinuous helical phase and (ii) finally the formation of NT bubbles and/or anti-skyrmions, which then slow down the approach towards saturation. The formation of anti-skyrmion lattices was, however, only observed after subsequent variations of the magnitude and direction of **B**. The subtle effect of the latter on the Hall effect of the sample is subject of ongoing research and will be discussed.

5. Conclusion

Our new setup allows us for the first time to follow in detail the field dependence of the Hall voltage while simultaneously monitoring the magnetic phases in $Mn_{1.4}PtSn$, thereby providing valuable insights into the existence and nature of an intensely debated electrical signature of skyrmionics structures.

A.T. and B.R. gratefully acknowledge financial support by the DFG within SPP 2137. M.W. thanks the Max Planck Society for funding through IMPRS-CPQM.

[1] M. J. Stolt et al., Adv. Func. Mater. 2019 (2019) 1805418.

[2] R. Schlitz et al., Nano Lett. 19 (2019) 2366.

[3] D. Wolf et al., Nature Nanotechnology 17 (2021) 250.

[4] P. Vir et al., Chem. Mater. 31 (2019) 5876.

Fig. 1

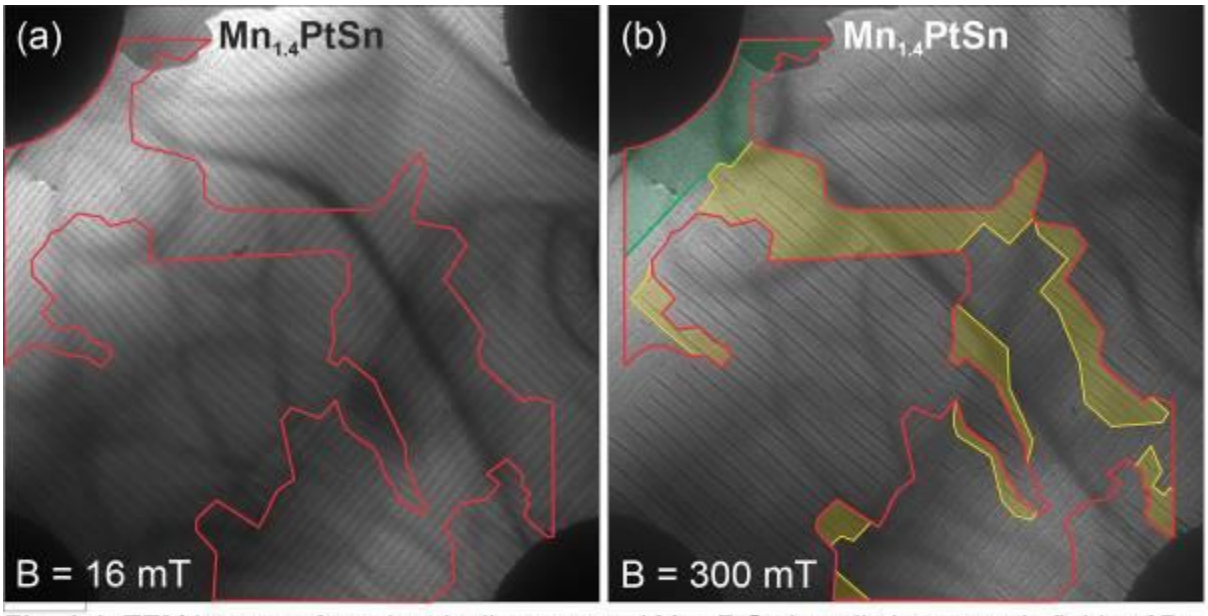

Fig. 1: L-TEM images of an electrically contacted $Mn_{1.4}PtSn$ lamella in magnetic fields of B = 16 mT (a) and B = 300 mT (b) as provided by the objective lens of the microscope. The red lines border the area of a uniformly oriented helical domain in (a). The yellow and green areas in (b) indicate regions, where this domain is shrunk at the expense of a perpendicularly oriented helical phase or areas of perpendicular saturation, respectively.

Fig. 2

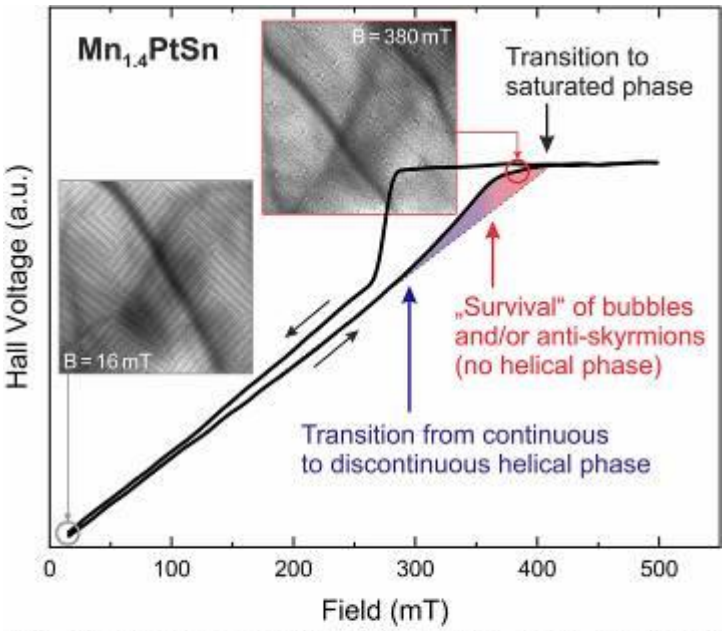

Fig. 2: Anomalous Hall effect of $Mn_{1.4}PtSn$ measured during the acquisition of the images shown in Fig. 1. The L-TEM images reveal that the stronger than linear approach towards saturation (cf. blue-red shaded area) coincides with the break-up of the continuous helical phase and the occurrence of non-topological bubbles and/or anti-skyrmions with increasing magnetic field.

IM7.007

Enabling In situ TEM biasing of Two-terminal Oxide-based Nanodevices using MEMS-based chips and gas cells

O. Recalde-Benitez[1], T. Jiang[1], R. Winkler[1], D. Nasiou[1], Y. Ruan[1], A. Zintler[2], E. Adabifiroozjaei[1], A. Arzumanov[1], Y. Pivak[3], H. H. Perez Garza[3], L. Alff[1], P. Komissinsky[1], L. Molina-Luna[1]

[1]TU Darmstadt, Materials Science, Darmstadt, Germany
[2]Karlsruher Institut für Technologie (KIT), Laboratorium für Elektronenmikroskopie, Karlsruhe, Germany
[3]DENSsolutions B.V. Netherlands, Delft, Netherlands

Introduction: Materials characterization of two-terminal oxide-based electronic devices at the nano and sub-nanometer scale in operative conditions is undoubtedly reliant on existing in situ transmission electron microscopy (TEM) methods. However, electrical biasing experiments using MEMS-based platforms have been highly challenging up-to-date due to the complex Focused Ion Beam (FIB)-based methodologies involved, in which stray leakage current paths formed during TEM lamellae preparation, might lead to over-estimated electric responses and therefore, ambiguous in situ observations. Moreover, the electrical properties of oxide-based stack devices in actual conditions are strongly influenced by, for instance, gas flow and/or temperature [1]. Hence, a systematic in situ TEM investigation of leakage current in operando conditions is crucial to understanding device behavior at the micro and nanoscale.

Objectives: To reproduce the electrical responses of micrometer-sized oxide-based stack devices in the corresponding TEM lamella devices using a short-circuit-free FIB-based preparation approach. To establish a structure (chemical)-property correlations in operando conditions (i.e., gas and/or temperature) with the use of in situ (S)TEM techniques.

Materials and Methods: Micrometer-sized epitaxially grown SrTiO3 (STO)-based memristors and BaSrTiO3 (BST)-based high-performance capacitors have been grown by Pulsed Laser Deposition (PLD). TEM lamellae of both types of heterostructures were prepared using a Focused Ion Beam (FIB). The TEM lamellas were mounted on DENSsolutions MEMS-based chips for biasing, heating, and gas experiments. High-angle annular dark-field (HAADF)-STEM, bright field (BF)-STEM, and electron energy loss spectroscopy (EELS) data were obtained while operating TEM lamella devices under gas and biasing stimuli.

Results: Our short-circuit-free FIB methodology yielded current measurements of TEM lamellae devices as low as 10-12 A, mimicking the expected micrometer-sized electrical response. Operative TEM lamellae-based memristor devices could be measured inside the microscope. Additionally, high-performance capacitors (varactors) with high leakage currents have been exposed to an O2-rich environment and heated by the effect of electron beam irradiation while simultaneously tracking the suppression of the device leakage current inside a TEM (Fig. 1).

Conclusions: Our methodology enables current measurements e.g., STO-based memristors of at least six orders of magnitude in leakage current in comparison with conventional-FIB approaches and reported literature values [2], allowing for realistic and reproducible biasing operations of various oxide-based TEM lamella devices inside a TEM under heating or gas stimuli.

References:[1]L. Zeinar et al., "Matching conflicting oxidation conditions and strain accommodation in perovskite epitaxial thin-film ferroelectric varactors," Journal of Applied Physics, vol. 128, no. 21, p. 214104, Dec. 2020, doi: 10.1063/5.0021097. [2] D. Cooper and M. Bryan, "Reproducible in-situ electrical biasing of resistive memory materials using piezo-controlled electrical contacts and chip-based systems.," Microsc Microanal, vol. 27, no. S1, pp. 164–166, Aug. 2021, doi: 10.1017/S1431927621001197.

Fig. 1. Suppression of the leakage current of a TEM-lamella extracted from a BST-varactor device exposed to an O2 environment inside a TEM. A systematic electron beam irradiation (heating) study was performed.

Fig. 1

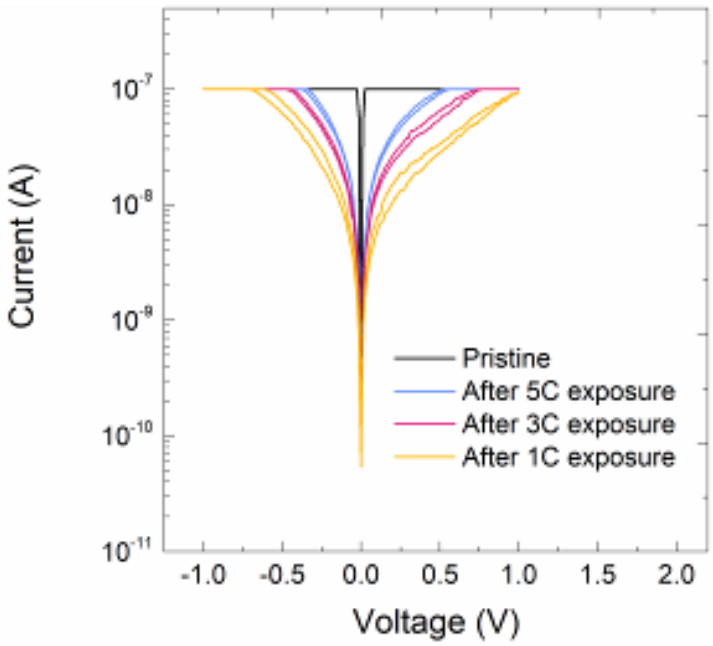
Current (A)
10^{-7}
10^{-8}
10^{-9}
10^{-10}
10^{-11}
-1.0
-0.5
0.0
0.5
1.0
1.5
2.0
Voltage (V)
Pristine
After 5C exposure
After 3C exposure
After 1C exposure

IM7.P001

In situ electrochemistry in TEM with controlled mass transport for electro-conversion

A. F. Beker[1], H. Sun[1], J. T. van Omme[1], V. Papadimitrious[1], H. H. Perez Garza[1], A. Rozene[1]

[1]DENSsolutions B.V. Netherlands, R&D, Delft, Netherlands

Introduction

In order to overcome the current energy challenges, the study of new materials for energy or feedstocks conversion becomes urgent. Liquid Phase Transmission Electron Microscopy (LPTEM) combined with electrodes for electrochemistry is a relevant technique for innovation in electro-conversion.

Objectives

We present an electrochemical flow Nano-Cell (LPTEM) allowing in situ observation of materials in relevant reaction conditions. It combines the advantages of ultra-microelectrodes - probing fast kinetics - and microfluidics**(1)** to switch from mass transport- to electron transfer rate-limited reaction kinetics, with the high resolution imaging capabilities of TEM and its chemical analysis toolbox, allowing the study of catalytic nanoparticles in operando or their synthesis.

The redox kinetics are controlled in this flow cell configuration by flow rate control and electrical potential control in liquid using microfabricated electrodes. We address how to limit radiolysis from a microfabrication point and which electrode materials can best link classic electrochemical methods to LPTEM conditions.

Materials & methods

In order to characterize the MEMS-based Nano-Cell mass transport characteristics, a one electron redox molecule with fast electron transfer rate is used experimentally and modelled using finite element analysis.

Results

We show the stability of both flow and electric potential in our LPTEM Nano-Cell (Figure 1) and show examples of in situ nanoparticle synthesis

Conclusion

This technique can lead to new insights in catalysts synthesis for electro-conversion by linking a material"s nanoscale morphology to its functionality.

Figure 1: Cyclic voltammetry of 1mM Ferrocenemethanol + 0.1M KCl, for different flowrates using the same Nano-Cell. For each flowrate value, 10 cycles were run at 10mV/s. The plots overlapping shows the stability of the electric potential measurement and flow speed at the electrode surface.

References

1 I. Dumitrescu, D. F. Yancey and R. M. Crooks, *Lab Chip*, 2012, **12**, 986.

Fig. 1

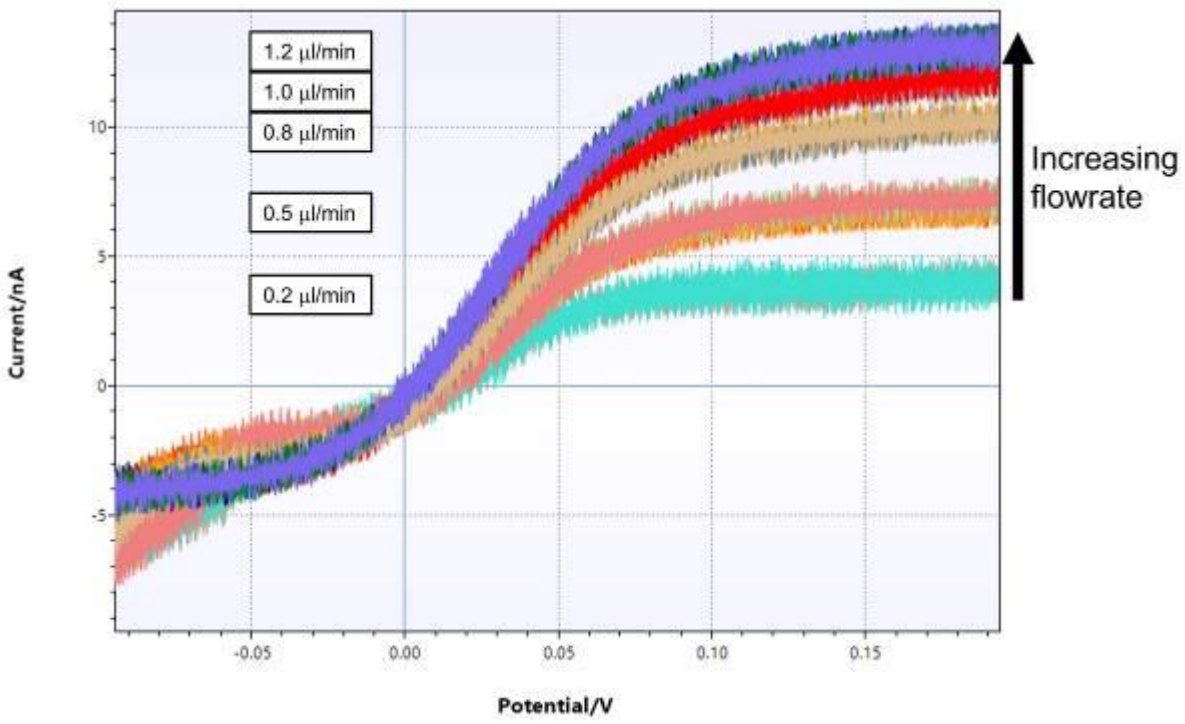
1.2 µl/min
1.0 µl/min
0.8 µl/min
0.5 µl/min
0.2 µl/min
Increasing flowrate
Current/nA
Potential/V
10
5
0
-5
-0.05
0.00
0.05
0.10
0.15

IM7.P003

In situ force measurements and temperature control: the FIB/SEM as a mechanical characterization tool

A. J. Smith[1], K. Schock[1], A. Rummel[1], S. Kleindiek[1]

[1]Kleindiek Nanotechnik, Reutlingen, Germany

Introduction

Mechanically characterizing materials inside FIB/SEMs is a common task with a myriad of use cases in various fields of research. In addition, when studying material properties, taking the sample temperature into account can be of great importance. Furthermore, some materials (e.g. certain polymers) do not lend themselves to observation in the SEM as the energy introduced by the electron beam may alter the sample (e.g. melting). Such effects can be suppressed by reducing the sample"s temperature using a cooling stage.

Objectives

In this work, the authors will present several examples of how in situ force measurements can be performed using different setups inside the FIB/SEM's chamber, thus utilizing the FIB/SEMs capability to modify, customize or otherwise prepare samples for testing as well as image samples from different angles for a more comprehensive set of images for later analysis.

Materials & methods

The described measurements are achieved using one of three setups: 1. Smallest forces - in the range of some nN - can be measured using self-sensing, piezo-resistive AFM cantilevers. 2. Another option is to utilize moveable sample holders with precisely calibrated spring constants. In this manner the deflection observed in the FIB/SEM can be used to calculate the applied force. By choosing from spring loaded sample holders with varying spring constants, a wider range of forces can be addressed. 3. Force transducers can be used to measure large forces up to several N. Each approach has its own distinct use cases, advantages, and disadvantages. These will be discussed, as well. Several the proposed force measurement applications can be combined with a compact heating and cooling stage for temperature control during the experiment.

Results

Examples include bending FIB cut beams and comparing EBSD results obtained pre and post bend (Fig. 1: FIB cut beam after bending failure (courtesy Archie, MPIE)), flat punch experiments for elucidating forging properties of novel superalloys (Fig. 2: Flat punch of a super alloy cube set in a FIB-cut base (courtesy Roesler, TU Braunschweig)), characterizing nanowires,CNTs, and other structures, etc.

Conclusion

With the appropriate set of tools, a wide range of mechanical characterization experiments can be performed inside a FIB/SEM"s chamber thereby harnessing the power of the high SEM"s resolution imaging, the FIB"s secondary viewing angle as well as the ability to modify/shape small samples for site-specific micro-analyses, in addition to the myriad of other detectors and add-ons such as EBSD, EDX, STEM, etc.

Fig. 1

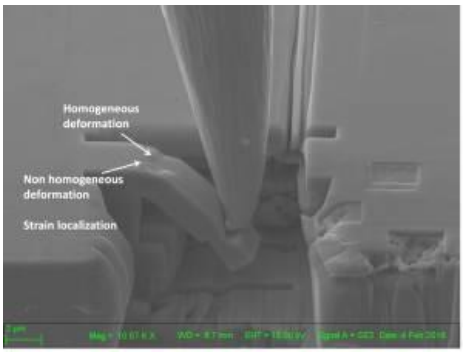
Homogeneous deformation
Non homogeneous deformation
Strain localization

Fig. 2

IM7.P004

High resolution and analytical transmission electron microscopy in a liquid flow cell via gas purging

H. Sun[1], J. Park[2], S. Basak[2], A. F. Beker[1], J. T. van Omme[1], Y. Pivak[1], H. H. P. Garza[1]

[1]DENSsolutions B.V. Netherlands, Delft, Netherlands
[2]Forschungszentrum Jülich GmbH, Institute of Energy and Climate Research, Fundamental Electrochemistry (IEK-9), Jülich, Germany

Liquid phase electron microscopy (LPEM) based on sandwiched MEMS sample carriers provides the means to

observe time-resolved dynamics in a liquid state. Until now, LPEM has been widely used in materials science, energy and life science, providing fundamental insights into nucleation and growth, the dynamical evolution of key materials in batteries and fuel cells, as well as the 3D imaging of biomolecules [1]. Compared to liquid cells without a flowing function (such as static graphene pocket cells), liquid flow cells have obvious advantages. This includes the control of the liquid environment, the modulation of the effect of electron beam irradiation [2] and the integration of functional electrodes for heating or/and biasing. Due to the pressure difference between the TEM column (~ 0 bar) and the enclosed liquid cell (~1 bar), the two membranes (silicon nitride with a typical thickness of ~50 nm) bulge outwards, resulting in a thick liquid layer, which can reach more than 1 micrometer in the cell center region. Therefore, performing high resolution and analytical electron microscopy studies in a liquid flow cell comes with a multitude of challenges.

Several strategies have been proposed to solve this issue, including (1) decreasing the membrane thickness or replacing it with ultrathin materials e.g. graphene, h-BN, MoS2, etc. [3], (2) developing novel cell configurations, namely hole array patterns [4] and nanochannel [5], to avoid or decrease the bulging, (3) generating a gas bubble via electron beam irradiation [6,7], (4) generating a gas bubble via electrochemical water splitting [8] and (5) mitigating the window´s bulging by changing the pressure difference between the cell and TEM column, either via an external pressure controller [9,10] or via the internal Laplace pressure [10]. Those methods have been proven useful in high resolution and analytical electron microscopy studies in LPEM, however, there are also intrinsic limitations in each method.

In this work, we propose a general and robust method to perform high resolution and analytical electron microscopy studies in a flow cell (the Stream Nano-Cell), which can be implemented during liquid heating or liquid biasing experiments. Thanks to the on-chip flow channel of the Stream Nano-Cell [11], the liquid in the field of view can be removed by flowing gas (including inert gases to avoid problems with air sensitivity), which is termed "purging". This purging method enables the acquisition of high-resolution TEM images, chemical composition and valence analysis through energy-dispersive X-ray spectroscopy (EDX) mapping and Electron Energy-Loss Spectroscopy (EELS), respectively. In addition, the purging approach is both reversible and reproducible, which therefore enables the alternation between a full cell and a thin liquid configuration to study liquid-thickness-dependent physical and chemical phenomena.

References

1. F. M. Ross. Science, 2015, 350, aaa9886.
2. N. M. Schneider, et al. J. Phys. Chem. C, 2014, 118, 22373.
3. G. Dunn, et al., ACS Nano, 2020, 14, 9637.
4. S. Nagashima, et al. Nano Lett., 2019, 19, 10, 7000.
5. M. N. Yesibolati, et al. Phys. Rev. Lett., 2020, 124, 065502.
6. G. Zhu, et al. Chem. Commun. 2013, 49, 10944.
7. U. Mirsaidov, et al. Soft Matter, 2012, 8, 7108.
8. R. Serra-Maia, et al. ACS Nano 2021, 15, 10228.
9. S. Keskin, et al. Nano Lett., 2019, 19, 4608.
10. H. Wu, et al. Small Methods, 2021, 5, 2001287.
11. A. F. Beker, et al. Nanoscale, 2020, 12, 22192.

IM7.P006

In situ extreme micromechanics: recent innovations and prospects

R. Widmer[1], N. Randall[1], R. Pero[1], J. M. Breguet[1]

[1]Alemnis AG, Thun, Switzerland

In situ micro- and nanomechanical testing is an indispensable technique for materials design as well as for fundamental mechanics. Many new protocols and testing geometries beyond traditional nanoindentation now enable the study of microstructure–property relationships, material intrinsic behaviour including orientation-dependence and plasticity, fracture dynamics, or the performance of novel µ3D-printed metamaterials, to name but a few.

Thanks to its versatility, micromechanics is contributing to numerous scientific domains, including thin films and coatings, metallurgy, glasses and ceramics, semiconductors, biomechanics, or architectured materials. Performing micromechanical tests *in situ* in a SEM offers two important advantages: (1) unmatched control, stability, and positioning accuracy, and (2) the possibility to perform unique correlative experiments based, for example, on the combination of mechanical data with direct imaging or EBSD measurements.

An increasingly important branch of micromechanical testing can be found in the simulation of real-world, extreme operation conditions, such as high temperatures in engines, cryogenic temperatures in hydrogen storage, dynamic loading under shock or impact, high frequency cyclic fatigue, or a combination thereof. Progress in the understanding of material behaviour at such conditions is clearly linked to the availability of laboratory equipment that can perform reliable tests under such conditions.

We present the most recent developments in instrumentation for *in situ* extreme mechanics testing at the micro- and nanoscale. In the focus is a testing platform capable of strain rate dependent testing over the range from 0.0001 s^{-1} up to 10000 s^{-1} (8 orders of magnitude) with simultaneous high-speed actuation and sensing capabilities with nanometer and micronewton resolution, respectively. Furthermore, the challenges and solutions to performing extreme micromechanics over the temperature range from -150 °C to 1000 °C, and the inherent advantages of using small volumes of sample material will be discussed. Finally, we present examples of such extreme micromechanical *in situ* tests and discuss future research directions in the field of extreme micromechanics.

Fig. 1

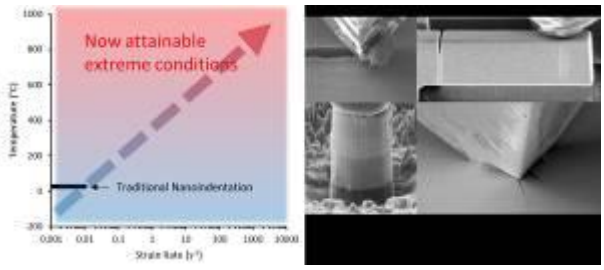

IM7.P007

Implementation of a microplasma cell for in situ TEM

U. Schürmann[1], N. Kohlmann[1], L. Hansen[2], H. Kersten[2], L. Kienle[1]

[1]Christian-Albrechts-University Kiel, Institute for Materials Science, Kiel, Germany
[2]Christian-Albrechts-University Kiel, Institute for Experimental and Applied Physics, Kiel, Germany

Introduction

We built an *in situ* microplasma cell for integration into a TEM holder. The goal is *in situ* investigation of plasma surface processes on the nanoscale. Here we present the current state as well as preliminary results.

Objectives

In situ transmission electron microscopy is an area of growing interest. Observation and analysis of fabrication and/or modification processes of nanostructured materials and surfaces are essential for basic plasma physics and materials science. Also, plasma processes are a suitable method to modify nanostructures but have been largely neglected so far and are not part of the standard repertoire of *in situ* TEM investigations. To date, plasma treatment and material analysis are mostly separated in two steps including a sample transfer from the plasma environment into the electron microscope. To overcome this separation a microplasma cell for *in situ* plasma treatment inside a TEM based on the idea of Tai *et al.* [1] was chosen and further developed.

Materials & Methods

We use a custom sample holder from Hummingbird Scientific with high voltage capabilitites. The cell design is optimized for vacuum-tightness and reproducibility, see Fig. 1. Due to the single-shot design cells can be tested for function and being vacuum sealed before introduction into the TEM. Principle TEM studies were carried out using a JEOL JEM-2100.

Results

The choice of the geometry and discharge parameters to create a stable plasma is critical and challenging. On the one hand, gas and its purity and pressure as well as the electrical parameters to ignite the plasma have, on the other hand, to be combined with the design of a vacuum-proof but electron beam transparent cell. A stable atmospheric pressure DC normal glow microplasma discharge was studied outside the TEM fulfilling the demands in stability and size for the *in situ* TEM integration. The operation in the normal glow regime could be proved by electrical and optical diagnostics [2].

Conclusion

The current design and potential impact of a microplasma cell for TEM integration is given. The authors further present an outlook for adaptation of plasma treatment experiments to the microcell environment.

Acknowledgements

The authors thank the Deutsche Forschungsgemeinschaft (DFG, german research foundation) for funding (KI 1263/17-1, KE 574/8-1).

Figure 1: Sketch of the Design of the *in situ* microplasma cell.

References

[1] K. Tai *et al*., Scientific Reports, Vol. 3, pp 1325, year 2013.

[2] L. Hansen *et al.*, 2022 Plasma Sources Sci. Technol. 31 035013

Fig. 1

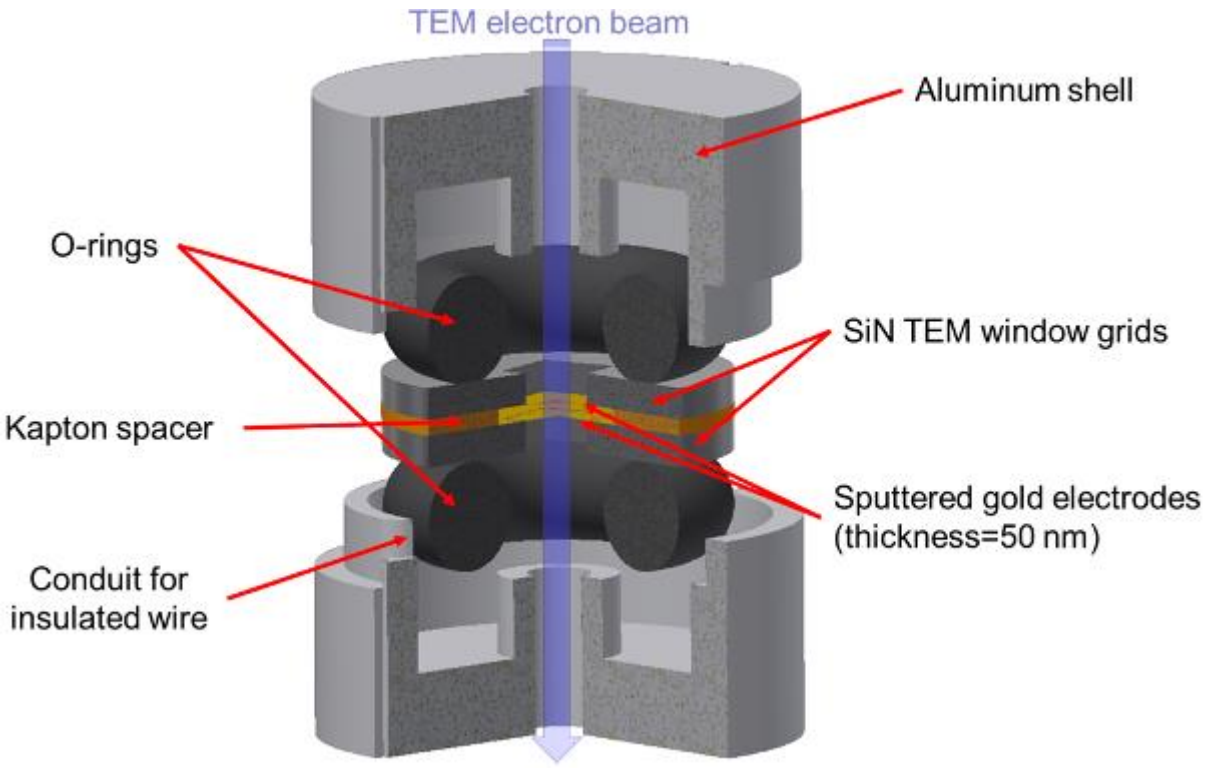
TEM electron beam
Aluminum shell
O-rings
SiN TEM window grids
Kapton spacer
Sputtered gold electrodes
(thickness=50 nm)
Conduit for
insulated wire

IM7.P008

Fast STEM tomography on sensitive materials using multiscale environmental electron microscopies

L. M. Lebas[1], A. Zulfiqar[2], A. Bekel[1], L. Roiban[1], K. Masenelli-Varlot[1]

[1]Univ Lyon, INSA Lyon, UCBL, CNRS, MATEIS, UMR5510, Villeurbanne, France
[2]Leibniz Institute for Solid State and Materials Research Dresden, Saarbrücken, Germany

Environmental electron microscopy has been developed to study specimens under water or gas partial pressure [1]. It allows the preservation of hydrated samples with minimum preparation. In ESEM, the spatial resolution can reach the nanometer, and in ETEM the Ångström. Using a specific tomographic sample holder, tilt series can be recorded and reconstructed in a 3D volume [2, 3].

This work aims to establish liquid-phase and three-dimensional scanning electron microscopy (LPSTEM) as a new technique for characterizing biological or materials science samples at the nanoscale, by addressing two of the remaining limitations. The electron dose should be reduced and quantified, especially for sensitive materials. The acquisition time should be commensurate with the events to be studied, i.e. no more than few minutes in most of *operando* experiments.

We show here automated acquisitions of ± 70° tilt series in LPSTEM in less than 5 minutes in ESEM and ETEM. SE, BF and HAADF images are simultaneously recorded. Moreover, the electron dose can be precisely controlled. We use a ThermoFisher (FEI) QuattroS ESEM operated at 30 kV and a ThermoFisher (FEI) Titan 80-300 ETEM at 300 kV.

Researches are conducted on SBA latex and on different types of gels: silica aerogels and different types of aluminium hydroxide wet gel suspensions. The specimen are deposited on a TEM grid coated with a holey carbon film, itself fixed on a home-made prototype of wet-STEM tomography sample holder (ESEM), or on a dedicated sample holder (ETEM) [4]. Images are recorded with our home-made software M-SIS based on Python, using Autoscript and Digital Micrograph libraries. It features automatic eucentric, drift correction and various helps for automatic acquisition. The tilt series are aligned with the TomoJ and data are segmented with 3D Slicer.

The 3D models exhibit a spatial resolution around 10 nm (ESEM) or around few nanometers (ETEM) whereas the electron dose can be finely controlled and can be kept below the viability threshold of a biological cell. Hence the morphology of the samples and their porosity are studied. The limits will also be exposed in term of sample thickness, liquid film thickness control, spatial resolution, electron dose and total imaging time.

These results open the way to perform fast multiscale studies in liquid-phase STEM tomography with easy sample preparation, both in ESEM and ETEM. This low-dose process could be applied for various types of hydrated or liquid samples and could be widely used in materials characterization.

[1] Schuh, T., de Jonge, N. (2014) "Liquid scanning transmission electron microscopy: Nanoscale imaging in micrometers-thick liquids" Comptes Rendus Physique, 15(2-3)

[2] Masenelli-Varlot, K. et al. (2014) "Wet-STEM Tomography: Principles, Potentialities and Limitations", Microscopy and Microanalysis, 20(2).

[3] de Jonge, N. (2018) "Theory of the spatial resolution of (scanning) transmission electron microscopy in liquid water or ice layers", Ultramicroscopy, 187.

[4] Jiao, X. et al. (2019) "Electron tomography on latex particles suspended in water using environmental scanning electron microscopy", Micron, 117.

Figure 1: From upper-left to bottom-right: YZ, XY and XZ ortho-slices of the reconstructed silica airgel volume from images
recorded at different tilt angles a) in BF mode, b) in HAADF mode. Scale bar is 500 nm.

Fig. 1

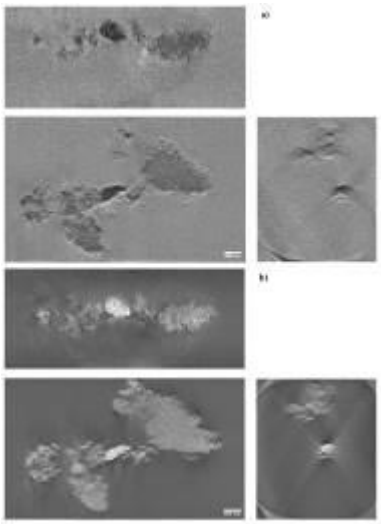

IM7.P009

Control of film thickness in liquid cell transmission electron microscopy depending on mechanical clamping conditions

R. Klemmt[1,2], A. Chiring[3], G. Wittstock[3], S. Schäfer[1], V. Solovyeva[1]

[1]University of Oldenburg, Institute of Physics, Oldenburg, Germany
[2]Aarhus University, INANO, Aarhus, Denmark
[3]University of Oldenburg, Institute of Chemistry, Oldenburg, Germany

Introduction

Liquid-cell transmission electron microscopy (LC-TEM) is a rapidly developing electron microscopy technique employed to study the structure and dynamics of samples in a liquid environment [1]. The achievable spatial resolution is typically limited by elastic and inelastic electron scattering in the liquid layer and the enclosing membranes and ultrathin layers are therefore desirable.

In early silicon-nitride(SiN)-based LC-TEM sample designs utilizing large membrane areas, the thinnest achievable liquid layer was typically determined by the bulging of the viewing membranes and partially by the height of membrane spacers defining the liquid flow channel. In contrast, for novel LC-TEM systems with largely reduced membrane areas other secondary effects start to determine the liquid thickness.

Objectives

To characterize the achievable film thickness in a commercial liquid cell TEM sample holder, we analyzed in detail the impact of mechanical clamping conditions of the cell stack and the effect of relative positioning and orientation of the membranes in the stack.

Materials & Methods

In the utilized LC TEM holder (Stream, DENSSolution; for JEOL TEM), the liquid is encapsulated by two 50-nm thick SiN-membranes (200 µm x 12 µm area) with patterned Pt electrodes. For determining the thickness of the enclosed water layer, we used a mass-thickness-contrast method [2] and electron-energy-loss spectroscopy. Different experimental conditions were adopted, including variations in the liquid inlet/outlet pressure, flow speed, relative chip orientation and various designs for the mechanical components clamping the two membranes. The resulting film thickness is compared to numerical models.

Results

For the geometry of the DENS Stream holder, numerical calculations including bulging effects and spacer height, result in an estimated liquid thickness of ∼600 nm for an internal absolute liquid pressure of 1600 mbar. However, experimentally, we find liquid thicknesses of about 1500 nm, largely independent from inlet/outlet pressure and flow speed (Fig. 1). Changing the mechanical clamping conditions by different top lid geometries and additional foil spacers drastically reduces the film thickness to ∼900 nm (Fig. 1). Optical microscopy images of the assembled stack demonstrate that for the optimized clamping conditions chip bending is minimized. Curiously, we also observed that the bending is depending on the relative orientation of the rectangular membranes (cross/parallel configuration), putatively due to the difference in the mechanical properties of the assembly, and a generally lower thickness is observed in the parallel case. With these modifications and utilizing the inhomogeneous bending across the membranes, a minimal liquid thickness of ∼420 nm was found in the parallel configuration (Fig. 2).

Conclusion

We demonstrated that mechanical clamping conditions of the liquid cell stack can be the limiting factor determining the film thickness for small area membrane cells. With optimized clamping close to ideal liquid thicknesses are experimentally achieved.

References

[1] S. Pu et al., Roy. Soc. Open Sci. 7, 191204 (2020).

[2] H. Wu et al., Small Methods 5, 2001287 (2021).

Fig. 1

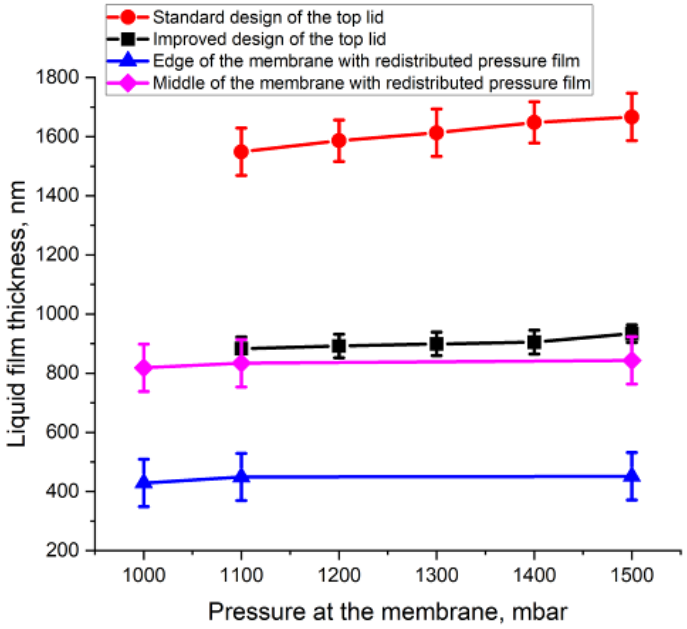

Fig. 2

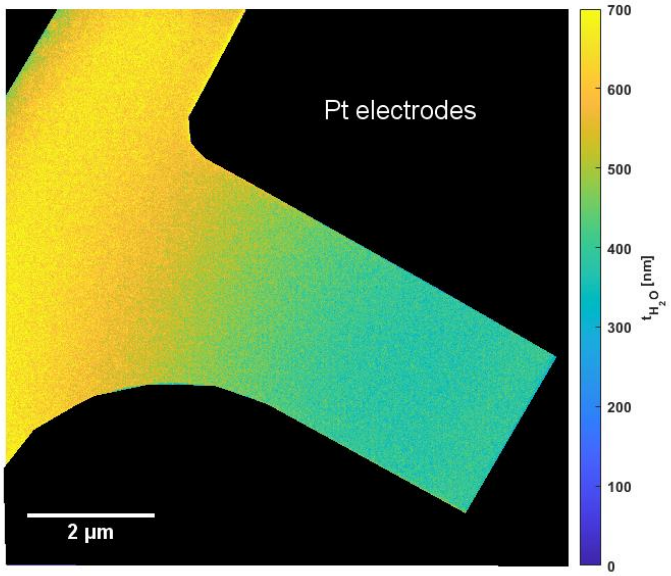

IM7.P010

Quasi in situ TEM investigation on the activation of commercial wüstite precursors

K. Dembélé[1,2], M. Swoboda[1], R. Schlögl[1,2], T. Lunkenbein[1]

[1]Fritz-Haber Institute of the Max-Planck Society, Inorganic Chemistry, Berlin, Germany
[2]Max-Planck Institue for Chemical Energy Conversion, Department of Heteregeneous Reactions, Mülheim an der Ruhr, Germany

Introduction: The development of *in situ* and *operando* transmission electron microscopy (TEM) has substantialy improved our understanding on the materials during their operation at realistic conditions which are generally different from the vacuum. However, the atmospheric pressure mainly used by *in situ* and *operando* TEM may be still too low and therefore unsuitable for investigating lots of catalytic reactions such as ammonia synthesis, methanol synthesis and Fischer-Topsch synthesis. Hence the *quasi in situ* TEM[1] approach, – which consists of studying the sample before and after the treatment at relevant conditions (high pressure and temperature) – appears as a powerfull tool to investigate the local changes that occur during the activation and operation of the catalysts. In this case, the sample is treated in a special TEM grid-reactor outside the TEM, then later transfered to the TEM without exposing to ambient air.

Objectives: In order to understand the morphology and microstructure of the iron catalyst used in the NH_3-synthesis, we have investigated by *quasi in situ* TEM the reduction of iron oxide precursors so called wüstite. This is crucial for optimizing the active catalyst before the NH3 synthesis process.[2,3]

Materials and Methods: We have developped a high-pressure TEM grid-reactor for the *quasi in situ* studies. This has allowed us to investigate the reduction of a commercial wüstite sample from Sigma-Aldrich under relevant activation condition (H2/N2=3:1,10 bar, 500 °C). In addition, we conducted identical location imaging (ILI) using a double Cs corrected Jeol ARM 200F electron microscope that was operated at 200 kV.

Results: The wüstite precursors presented inhomogenous grains size (from 0.2 to few micrometer) with defective and polycristalline FeO structure (Fig. 1a-c). After the activation/reduction treatment (H2/N2=3:1, 10 bar, 500 °C), ILI revealed morpholological changes corresponding to the formation of core-shell-like structures due to the fragmentation of pristine particle into smaller particles agglomerates (Fig. 1d-e). Electron diffraction analysis (Fig. 1f) indicates the full reduction of wüstite into metallic iron.

Conclusions: *Quasi in situ* TEM study using a high-pressure TEM grid-reactor is powerful for investigating local changes on the morphology and structure of the catalysts at relevant activation conditions. Furthermore, this approach will be extended to study the pressure dependencies during the reductive activation.

References

[1] L. Masliuk, M. Swoboda, G. Algara-Siller, R. Schlögl, T. Lunkenbein, *Ultramicroscopy* **2018**, *195*, 121–128.

[2] J. R. Jennings, Ed., *Catalytic Ammonia Synthesis: Fundamentals and Practice*, Springer US, **1991**.

[3] H. Liu, W. Han, *Catalysis Today* **2017**, *297*, 276–291.

Figure 1: (a) Identical location TEM investigation and electron diffraction of a commercial wüstite sample before (a, b and c) and after (d, e and f) exposure to a total flow of 4 mL/min of a H_2/N_2 =3:1 mixture at 10 bar and 500 °C.

Fig. 1

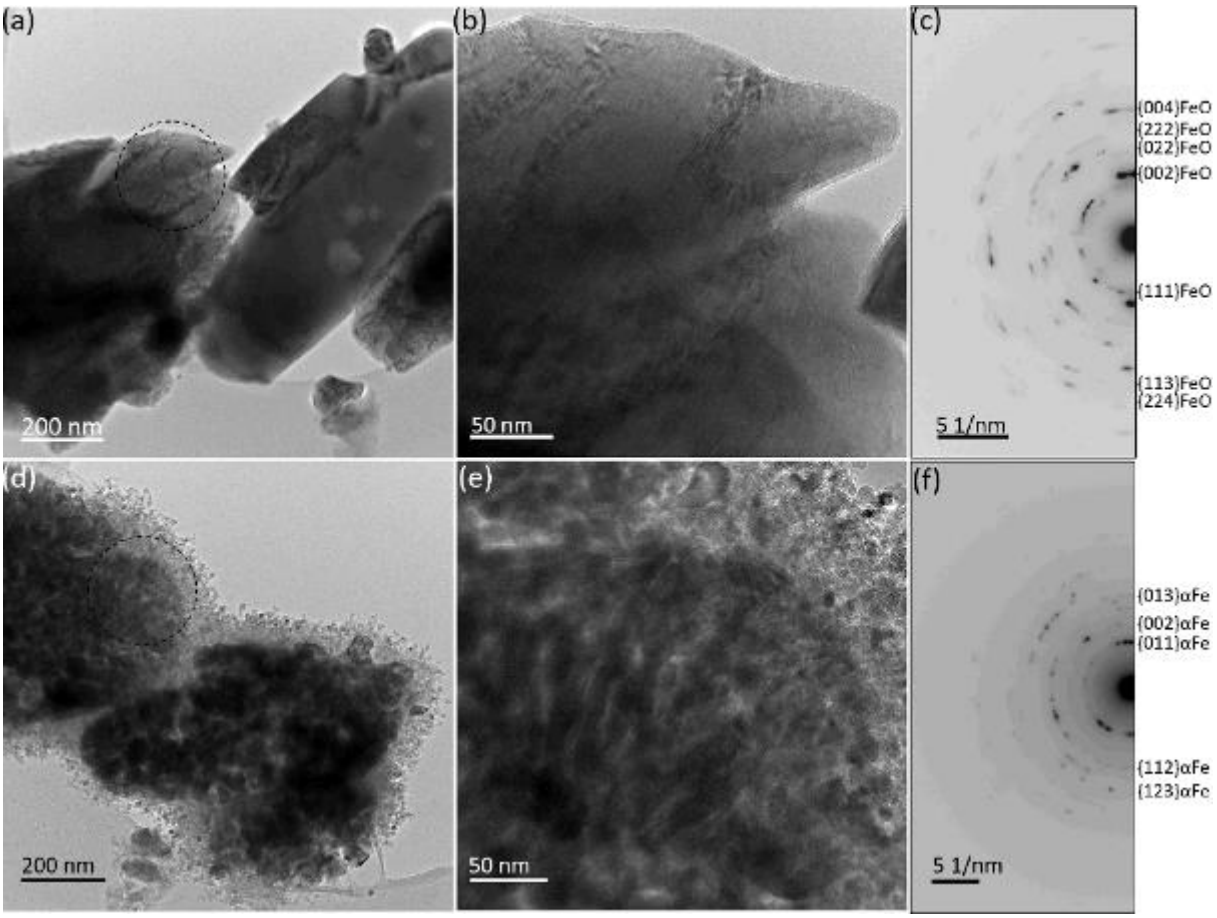
(a)
200 nm
(b)
50 nm
(c)
(004)FeO
(222)FeO
(022)FeO
(002)FeO
(111)FeO
(113)FeO
(224)FeO
5 1/nm
(d)
200 nm
(e)
50 nm
(f)
(013)αFe
(002)αFe
(011)αFe
(112)αFe
(123)αFe
5 1/nm

IM7.P011

In-situ liquid phase transmission electron microscopy as a disruptive tool for life science applications

H. Sun[1], A. Rozene[1], V. Papadimitrious[1], M. Pen[1], Y. Pivak[1], H. H. Perez Garza[1]

[1]DENSsolutions B.V. Netherlands, Delft, Netherlands

We introduce the "Stream System" to enable in-situ liquid phase transmission electron microscopy (LPTEM). The Stream system raises the impact in single-particle research as well as in pharmaceutical development, as it overcomes historical limitations and enables real-time studies of biological processes, in their native liquid state, as a function of different stimuli.

The "Stream System" is a plug-and-play system for TEMs. It relies on a customized side-entry holder with integrated tubing to supply liquid into a microfluidic Lab-on-a-Chip device acting as a smart specimen carrier, referred to as the Nano-Cell, which contains on-chip inlet and outlet to create a defined fluidic path, as well as an integrated set of biasing electrodes or a microheater. The liquid control is enabled via a Liquid Supply System (LSS), which can independently control the pressure at the inlet and the outlet. The fluid containing the sample (e.g. liposome, vesicles, viruses, proteins, etc) is flown from the LSS into the inlet of the sample carrier to initialize the in-situ experiment. The fluid coming out of the outlet is then re-collected in an empty Eppendorf tube on the LSS, to enable downstream biochemical analysis. These capabilities enable dynamic studies for life science and pharmaceutical research as a function of temperature/biasing/pressure/flow rate.

The system enables high level of control over the microfluidics and high throughput studies. In the case of Single Particle Analysis (e.g. SPA of proteins), the Brownian motion of the particle can be used to resolve its 3D structure while being in liquid. This technology has therefore enabled the possibility to resolve the 3D structure of apoferritin and an RNA polymerase while being in liquid. Furthermore, the user can avoid this liquid-air interface. Additionally, the system allows to control the mass transport, enabling the user to optimize the biochemistry on-the-fly. Liquid phase TEM can be used to visualize in-situ the synthesis of liposomes (e.g. for drug delivery purposes). The tip of the liquid holder is removable, creating a "Lab-on-a-Cartridge" (i.e. tip + Nano-Cell) that can be independently used to enable interoperability with other tools (e.g. SEM, Fluorescent Microscope, Synchrotron, etc.) and correlative studies.

Our development provides the unique possibility to visualize biological processes in real time with high resolution, while the sample is in its native environment (as a function of different stimuli). This opens up several possibilities such as SPA (proteins, viruses, exosomes, etc), biomedical/pharmaceutical applications (e.g. disease biomarkers, drug delivery vehicles or vaccines) and fundamental studies in biophysics and biochemistry. We believe that this technique will become a very powerful complementary technique to cryo electron microscopy.

References:

[1] G Battaglia et al, "4D imaging of soft matter in liquid water" (2021), DOI:10.1101/2021.01.21.427613

[2] J Cookman, "Visualising early-stage liquid phase organic crystal growth via liquid cell electron microscopy" Nanoscale, 7 (2020).

[3] A Ianiro, et al. "Liquid–liquid phase separation during amphiphilic self-assembly", Nature Chemistry, 11, 320–328 (2019), https://doi.org/10.1038/s41557-019-0210-4

[4] A Rizvi, "Observation of Liquid–Liquid-Phase Separation and Vesicle Spreading during Supported Bilayer Formation via Liquid-Phase Transmission Electron Microscopy", Nano Letters, 10325–10332 (2021)

IM7.P012

Correlative *in situ* light and electron microscopy studies on the deformation behavior of silver nanowires on polymer substrates

M. Moninger[1], L. Vogl[2], P. Schweizer[2], P. Denninger[1], P. Smolka[1], E. Spiecker[1]

[1]University of Erlangen–Nuremberg, Materials Science and Engineering Chair of Micro- and Nanostructure Research, Erlangen, Germany
[2]Swiss Federal Laboratories for Materials Science and Technology (EMPA), Thun, Germany

Ongoing developments in the field of flexible electronics led to a need for transparent flexible electrodes. In this area, percolation-based electrodes have shown promising characteristics. Especially, networks based on silver nanowires (AgNWs) inhabit a very appealing combination of properties for the application case. Since, flexibility is one of the most important characteristics of these electrodes it is necessary to understand the wire behavior under different loading scenarios revealing the influence of mechanical loading on the device performance.

Within the network, the mechanical response can be governed by complex interaction of the wires with one another. Therefore, for our testing purposes a scaled back approach was chosen, investigating isolated wires placed on varying polymer substrates (PDMS, PET, LDPE). As a first step, an alignment setup up utilizing doctor blading was developed, to investigate tensile and compressive behavior independently. In this context, the compressive loading is achieved via the constriction of the polymer substrates on AgNWs directed perpendicular to the initial straining direction (plastic Poisson"s effect). To cover all facets of the nanowire deformation mechanism, a correlative workflow combining complementary microscopy techniques was selected. Stopped *in situ* straining tests were performed under the light microscope (LM) since visible light has in contrast to electrons no deteriorative interaction with the AgNWs. For a more detailed post characterization, ex situ scanning electron microcopy (SEM) and transmission electron microcopy (TEM) were used (see Fig.1). Here, the AgNWs are transferred to the TEM by a workflow incorporating a sacrificial PEDOT:PSS layer.

We observed that the wires on PET compensate an applied compressive load with the formation of sharp angled kink structures. Subsequent TEM studies revealed the kinks to be locations for newly formed grain boundaries (GBs). The formation of GBs in combination with a folding mechanisms enables the wire to withstand high amount of compression without failing. Changing the substrate material from PET to the elastomer PDMS opened up the ability to perform fatigue tests on the AgNWs. In contrast to the wires on PET, the wires on PDMS show a sinusoidal elastic deformation behavior before at a critical strain amount they switch to an acute plastic kink. Furthermore, additional fatigue tests uncovered the elastic deformation to be completely reversible. Whereas, the introduced GBs in the wire act as a fracture location when repeatedly strained. Overall, we demonstrate that the combination of LM and EM gives fundamental insight into the underlying deformation mechanisms of AgNWs on different substrates as well as loading conditions. We believe, that those findings are highly relevant to further improve the mechanical properties of AgNW electrodes in application of flexible devices.

Fig. 1

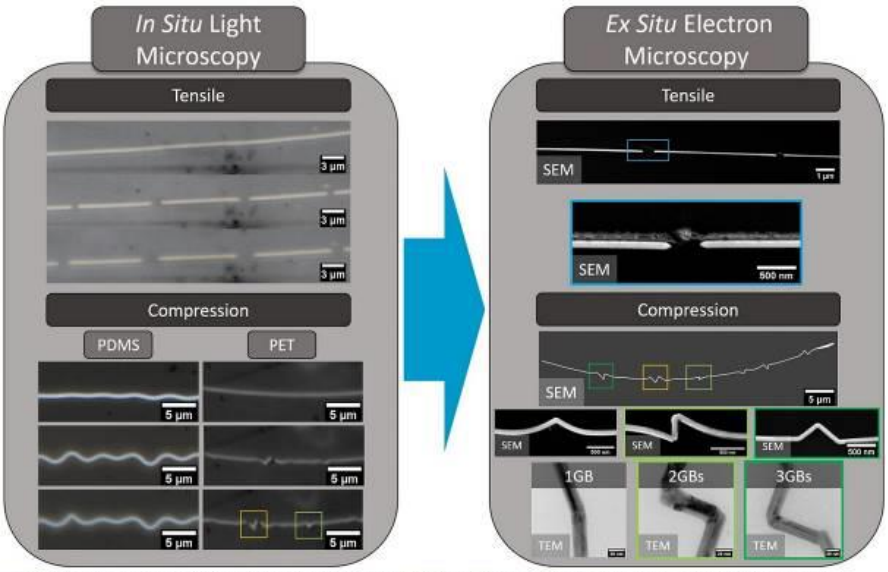

Figure 1: Schematic illustration of the correlative microscopy workflow. Interrupted in situ tensile and compression straining tests on polymer substrates were performed in the light microscope to monitor the mechanical behavior without misleading contamination caused by the electron beam. Post-characterization by complementary transmission and scanning electron microscopy techniques was utilized to gather more detailed information about the deformation mechanisms.

IM7.P013

Integrated liquid mixing supply module for *in-situ* liquid phase transmission electron microscopy

A. Rozene[1], H. Sun[1], J. T. van Omme[1], H. H. Perez Garza[1]

[1]DENSsolutions B.V. Netherlands, Delft, Netherlands

Advances in in-situ LPEM have made it possible to image a wide variety of dynamic processes in liquid samples. One dynamic parameter of interest is the chemical composition of the liquid surrounding the sample. Liquid composition can be controlled through flow or by mixing liquids prior to the imaging area. Current mixing strategies in LPEM rely on the use of syringe pumps and sample carriers with "bathtub" designs. They otherwise rely on pre-mixing on a sample vial or on combining two adjacent cells with small amounts of liquid under the electron beam. However, certain processes such as chemical precipitation induce changes shortly after combining the reagents and require constant refreshing of the liquid in the sample area. To overcome this limitation, we present the Liquid Supply System (LSS) with integrated liquid mixing. This technology allows to change the composition of the liquid environment on-the-fly and improves the controllability of liquid properties. Also, thanks to the design of the Nano-Cell sample carrier, it is guaranteed that the mixed phase passes through the imaging area. The LSS with liquid mixing consists of two individual liquid lines, each carrying one reagent. The liquid lines are combined in a mixing element prior to reaching the window area. Each liquid line is equipped with a precise pressure-based microfluidic flow control system that allows fine control of the concentration of the resulting mixture. We show the advantages of the liquid mixing module applied to nucleation and growth of calcium carbonate, a phenomenon of great interest across several academic and industrial fields. For this study, we use the Stream system, which consists of a smart MEMS-based liquid sample carrier, a Stream holder and the LSS with integrated liquid mixing. To study the early stages of calcium carbonate nucleation and growth we use two sample vials. One is filled with 50 mM of sodium bicarbonate (NaHCO3), dissolved in Milli-Q water, and the other with 50 mM of calcium chloride anhydrous (CaCl2), also dissolved in Milli-Q water. We use a Thermo Fisher Scientific Tecnai T20 G2, 160 kV TEM for image acquisition. We first flow a 1:1 mixture of both reagents at a rate of 10µl/min which induces the growth of calcite. We then replace the liquid with air, change the ratio of the mixture to 1:2 (double the amount of calcium chloride) and observe the formation of amorphous calcium carbonate as well as a lower number of calcite crystals. Our results show unprecedented control over the concentration of the mixed phase and allows to control kinetics-on-the-fly. The design of the Stream system guarantees that a predictable flow path is followed increasing the reproducibility of experiments. We expect that this technique will have applications not only in the field of biomineralization but in the fields of nanoparticle nucleation, growth, self-assembly and coarsening, in Liquid–Liquid Phase Separation of proteins, peptide self-assembly, vesicles studies and others.

Figure 1 legend: Calcite particles resulting from a 1:1 mixture of sodium bicarbonate and calcium chloride (top) with diffraction (bottom)

Figure 2 legend: Amorphous calcium carbonate (top) and calcite (bottom) particles obtained from flowing a 1:2 mixture of sodium bicarbonate and calcium chloride. Corresponding Diffraction in inset

Fig. 1

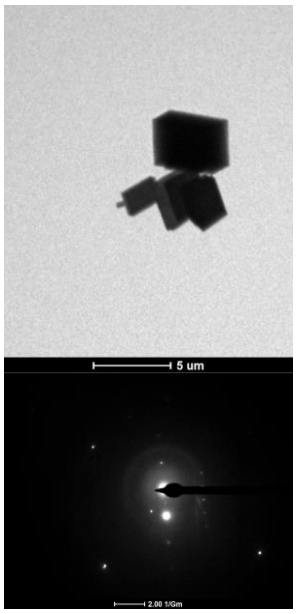

Fig. 2

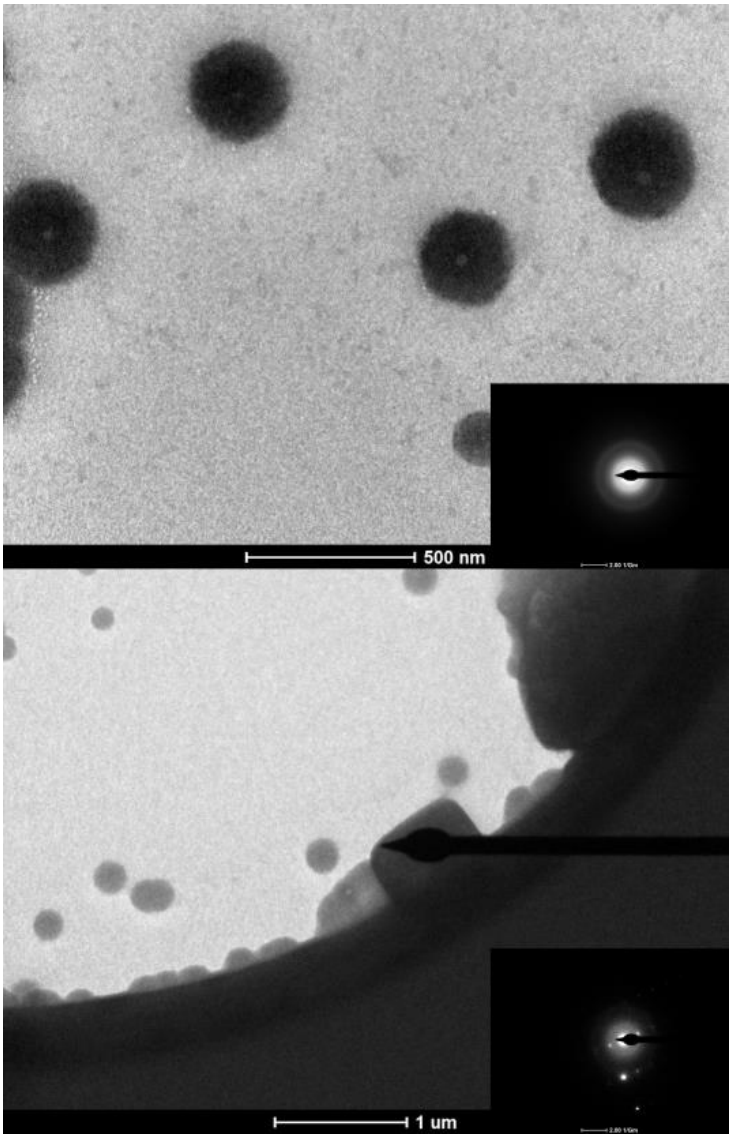

IM7.P015

Observation of chemical state changes during sample cooling using a soft X-ray emission spectrometer

T. Murano[1], S. Koshiya[1], Y. Yamamoto[2]

[1]JEOL Ltd., SA Business Unit, Akishima, Japan
[2]JEOL Ltd., EP Business Unit, Akishima, Japan

Introduction / Objective:

In recent years, the needs for chemical state analysis of materials in bulk samples using a scanning electron microscope (SEM) has increased in the fields such as batteries, steel and polymer materials, and more and more research results have been reported.

Terauchi et al. reported the development of a wavelength-dispersive soft X-ray emission spectrometer (WD-SXES) combined with a transmission electron microscope, and demonstrated high energy-resolution [1,2]. We have developed and commercialized a general-purpose soft X-ray emission spectrometer (SXES) that can be mounted on a kind of scanning electron microscope (SEM/EPMA*) based on the Terauchi"s spectrometer [3]. This contributes to the generalization of chemical state analysis in bulk samples.

In addition, the technique of observing a sample while it is cooled on a SEM system is becoming more common. It is known that cooling a sample changes its chemical state, but only a limited number have been reported. In this study, the correlation between sample temperature and chemical state was investigated using SXES.

In a pioneering work, Skinner experimentally and theoretically reported that the intensity distribution near the Fermi level (Fermi edge) in the soft X-ray emission spectrum becomes sharp as the sample cooled [4]. The observed edge width is 0.22 eV at 300 deg C and 0.14 eV at 110 deg C for metal Al.

In this study, similar experiments were carried out using a SEM equipped with a liquid nitrogen cooling stage and a high energy resolution SXES , and the comparison and interpretation of the obtained spectra are reported.

Materials & Methods:

A JSM-IT800HL SEM and an SS-94000SXES spectrometer from JEOL, a C1003 Liquid nitrogen cooling stage from GATAN, Inc. were used. Metal aluminum (Al) was used for the sample.

Results:

The Al $L_{2,3}$-M-emission SXES spectra obtained at different sample temperatures from room temperature to -185 deg C are shown in Figure 1. The intensity rise from around 73.0 eV to the lower energy side is the L_3-edge corresponding to the Fermi edge. As shown in the figure, the width of the intensity rise changes with sample cooling and shows a correlation with the sample temperature (from 0.110 eV to 0.088 eV).

This indicates that the Fermi level of the valence electron is broadened by the temperature factor. In other words, we have observed a phenomenon corresponding to the temperature dependence of the Fermi-Dirac distribution function.

Conclusions:

We have shown that by combining a general-purpose SXES commercialized by JEOL and a sample cooling mechanism, it becomes possible to acquire higher energy-resolution SXES spectra with reduced blurring due to the temperature factor. We think that this resolution improvement is of great benefit for more detailed chemical state analysis of materials.

[1] Terauchi, M., & Kawana, M. (2006). *Ultramicroscopy*, **106**, 1069-1075. doi: 10.1016/j.ultramic.2006.04.021

[2] Terauchi, M *et al.* (2012). *J. Electron Microsc*., **61**, 1-8. doi: 10.1093/jmicro/dfr076

[3] Takahashi, H *et al.* (2016). *IOP Conf. Ser.: Mater. Sci. Eng.*, **109**, 012017. doi: 10.1088/1757-899X/109/1/012017

[4] Skinner, H. W. B. (1940). *Philos. Trans. R. Soc. A*, **239**, 95-134. doi: 10.1098/rsta.1940.0009

* Electron Probe Microanalyzer

Fig. 1

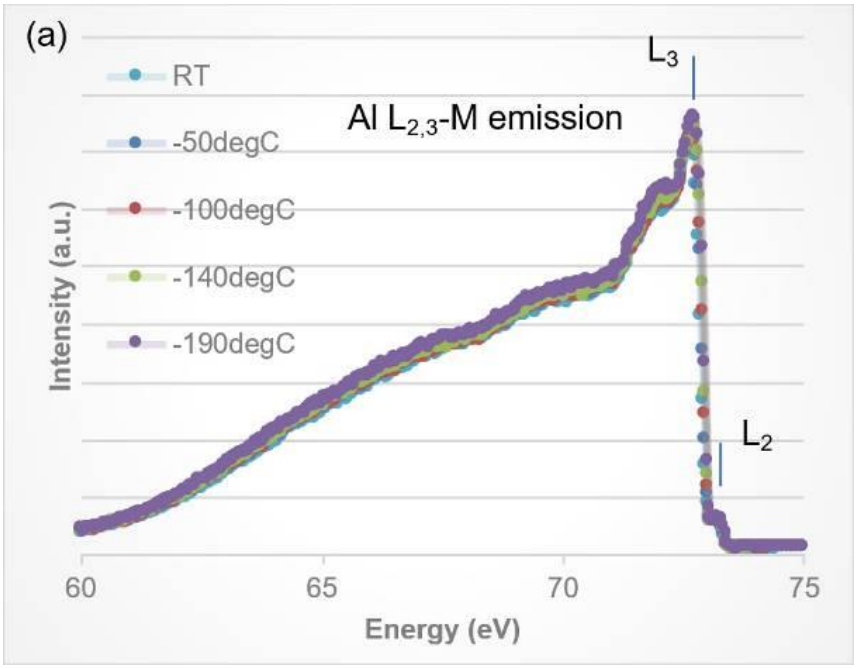

Fig. 2

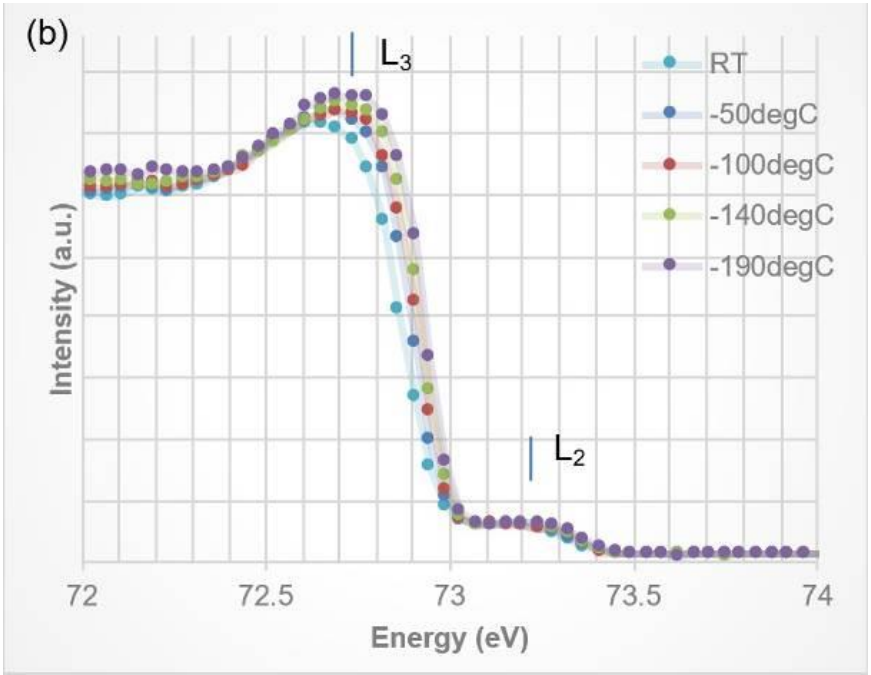

IM7.P016

In situ (S)TEM observation of PZT ferroelectric capacitor fatigue-related phenomena under bipolar electric field cycling

D. Chezganov[1], N. Gauquelin[1], M. T. D. Nguyen[2], G. Koster[2], E. Houwman[2], G. Rijnders[2], S. van Aert[1], J. Verbeeck[1]

[1]University of Antwerp, EMAT, Department of Physics, Faculty of Science, Antwerp, Belgium
[2]University of Twente, Enschede, Netherlands

Ferroelectric materials have been used in many applications such as non-volatile ferroelectric random access memories and micro-electromechanical systems. However, the suppression of the polarization in ferroelectric films under repeated electric field cycling (ferroelectric fatigue), leads to rapid degradation and reduced performance of these devices. Recently, a model has been proposed to clarify the causes and mechanisms, in which the $Pb(Zr,Ti)O_3$ (PZT) ferroelectric capacitor fatigue was discussed as an interface-related effect [1]. However, there is little experimental information about the relation between the interface features and the fatigue behaviour as well as the modification of the interface during fatigue treatments.

S(TEM) is a powerful technique to study ferroelectric material with the highest spatial resolution. In-situ biasing in S(TEM) has been exploited successfully to trace domain and crystal structure evolution, phase transition, etc. So far only limited STEM investigation has been performed on fatigue mechanisms in ferroelectric devices.

Here we report an in situ S(TEM) study of ferroelectric capacitor fatigue-related phenomena under bipolar electric field cycling.

The samples were $Pt/PbZr_{0.52}Ti_{0.48}O_3/SrRuO_3$ (Pt/PZT/SRO) capacitors grown by pulsed laser deposition. The epitaxial PZT film was 250 nm in thickness and samples were prepared by FIB milling and placed on a DENS-solution In Situ TEM biasing MEMS-chip. HAADF-STEM was used for atomic resolution imaging of the interface degradation. DF-TEM in two-beam condition was utilized to track the domain distribution with a Gatan K2 IS direct electron detector. EDX spectroscopy was applied for element distribution mapping. The measurements were performed on Thermo Fisher Titan instruments operated at 300 kV. A function generator was employed for the application of up to 10^9 fatigue cycles of bipolar triangular voltage pulses.

A time series of HAADF-STEM images of the Pt/PZT interface were acquired after a different number of cycles. The images were aligned and stacked to trace the changes (Fig. 1a). The data demonstrates the metal/ferroelectric interface structural and elemental modification during cycling, resulting in a non-ferroelectric degraded layer [1] (Fig. 1).

We have analyzed the domain structure evolution during "slow" switching before and after fatigue by tracking image similarity relative to voltage amplitude. The sample's fatigue resulted in the appearance of partially non-switchable areas and increased threshold fields.

Fig. 1 (a) The evolution of metal/ferroelectric interface upon electric field cycling, (b) EDX elemental profile across the interface.

Our results enable studies of dynamic processes in ferroelectric thin films under an applied bias voltage and provide a path to identify the causes and clarify the physical mechanisms of polarization fatigue.

References

[1]. M. T. Do, N. Gauquelin, M. D. Nguyen et al., APL Mater. 9, 021113 (2021).

[2] The authors acknowledge the financial support from a TOP/BOF project from the University of Antwerp. This project has received funding from the European Union"s Horizon 2020 Research Infrastructure - Integrating Activities for Advanced Communities under grant agreement No 823717 – ESTEEM3.

Fig. 1

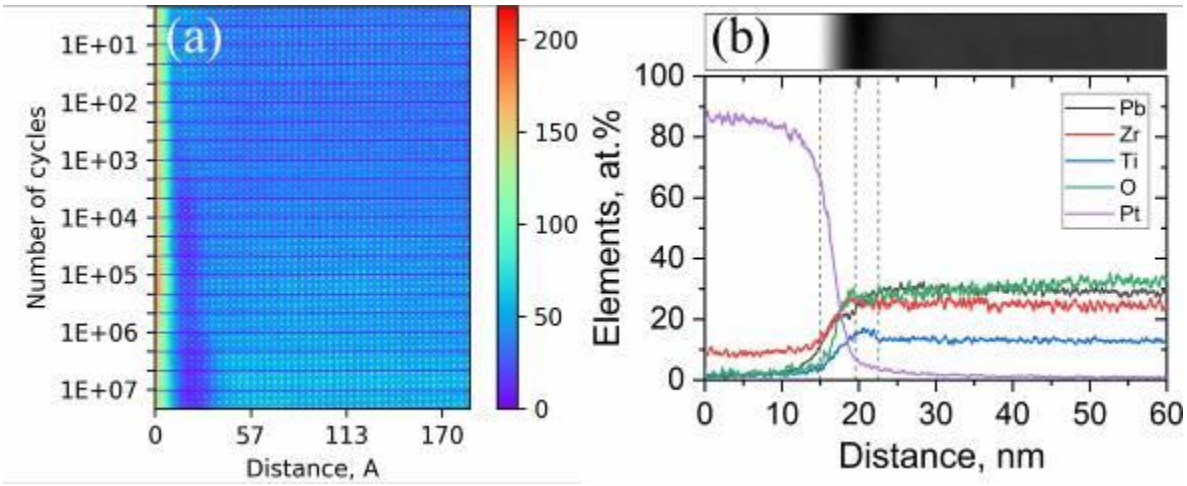
(a)
Number of cycles
1E+01
1E+02
1E+03
1E+04
1E+05
1E+06
1E+07
0
57
113
170
Distance, A
200
150
100
50
0
(b)
Elements, at.%
100
80
60
40
20
0
0
10
20
30
40
50
60
Distance, nm
Pb
Zr
Ti
O
Pt

IM7.P018

Reactivity and advanced electron microscopy of mass selected pt clusters deposited on CeO_2 supports for co oxidation catalysis

A. R. Lakshmi Nilayam[1], C. B. Maliakkal[1], R. Shadkam[1], M. V. Kante[1], D. Wang[1], H. Hahn[1], C. Kübel[1,2]

[1]Karlsruher Institut of Technologie (KIT), Institute of Nanotechnology, Eggenstein-Leopoldshafen, Germany
[2]Karlsruher Institut of Technologie (KIT), Karlsruhe Nano Micro Facility (KNMF), Eggenstein-Leopoldshafen, Germany

The study of model catalyst systems with mass selected Pt, Pd and Pt-Pd clusters on nanostructured metal oxide supports like CeO_2, Al_2O_3 in exhaust gas environments can be helpful to understand the fundamental processes in catalytic reactions of exhaust gases, to unravel the complex relationship between the structure and the catalytic properties. During a catalytic reaction, the active metal clusters/ particles dynamically change their structure due to the interaction with the gas environment at elevated temperatures. *In-situ* TEM can be of aid to track the the dynamic transient stages involved, structure/morphology changes of clusters under catalytic reaction conditions.

We aim to study the behavior of size selected Pt clusters (50-1000 atoms) deposited on CeO_2 support, under pure gas environments (H_2, Ar, O_2, CO, CO_2) and during CO oxidation (with CO and O_2 as input gases) using *in-situ* TEM with Micro Electro Mechanical Systems (MEMS) based nanoreactors. Size selected Pt clusters are deposited on top of Pulsed Laser Deposition (PLD) deposited CeO_2 thin films on MEMS chips using a magnetron sputtering cluster source integrated into an Ultra High Vacuum (UHV) Cluster Ion Beam Deposition (CIBD) system[1]. The atomic structural evolution and oreintation changes in the clusters, cluster-support interaction, cluster-gas interaction etc. can be studied realtime in exhaust gas environments using in-situ STEM imaging & spectroscopy. Quantitative analysis of the product gases from the MEMS based nanoreactors will be done using high sensitivity Residual Gas Analyzer (RGA).

An exemplary HAADF STEM image of CIBD deposited Pt clusters (200 atoms) on CeO_2 support is as shown in Fig. 1. The size distribution of Pt200 clusters (~1000 clusters) deposited on standard Lacey Carbon TEM grid is shown in Fig. 2. The size distribution showed a narrow peak at around 1.9 nm, matching perfectly to the expected diameter of 200-atom cluster. The second peak at around 2.5 nm could be attributed to the merging of two primary clusters. The size, three dimensional shape, orientation and atomic arrangement of size selected Pt clusters that are soft landed on the TEM grid can be determined using HAADF imaging with aberration corrected HRSTEM along with simple imaging simulations[2]. The acquired HRSTEM image of Pt_{1000} clusters is shown in Fig. 3. The single Pt atoms displaced out from the cluster (circled in red) are due to the electron beam induced knock on damage. Moreover, the clusters seem to be unstable under electron beam with changes in the inherent structure (distortion and/ or rotation, twinning etc) with longer beam exposure. A low voltage HRTEM imaging with high senstiticve detectors is preferable for the detailed analysis of the clusters in atomic resolution to understand the stable configurations possible for each cluster size thus complementing the observations of structural evolution of the supported clusters in the exhaust gas environments from the *in-situ* TEM experiments.

References

1. A. Fischer, R. Kruk, H. Hahn, *Rev Sci Instrum* **2015,** 86, (2), 023304.
2. Z. Y. Li, N. P. Young, M. Di Vece, S. Palomba, R. E. Palmer, A. L. Bleloch, B. C. Curley, R. L. Johnston, J. Jiang, J. Yuan, *Nature* **2008**, 451, 46-48.

Fig. 1

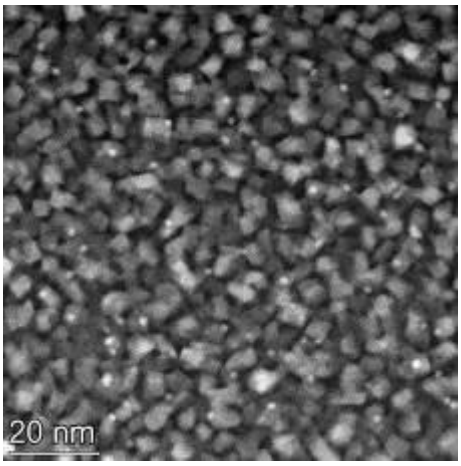

Fig. 2

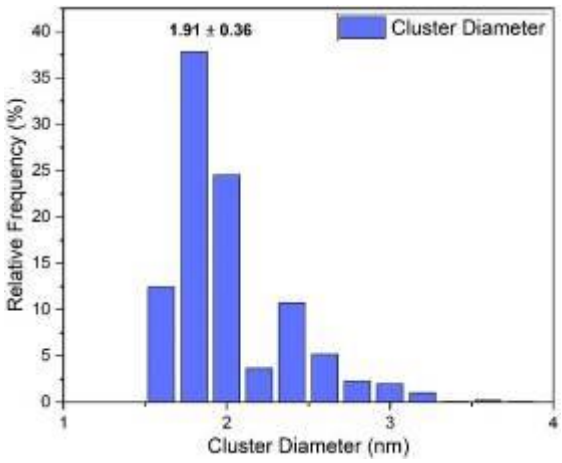

Fig. 3

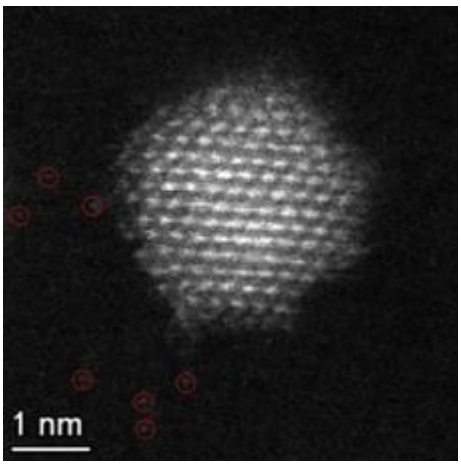

IM7.P021

Magnetoresistive effects on the electron beam induced coulomb explosion of gold microparticles

W. Feng[1,2], I. Gonzalez-Martinez[1], T. Gemming[1], B. Büchner[1,2]

[1]IFW, Dresden, Germany
[2]Technische Universität Dresden, Dresden, Germany

1. Introduction In situ transmission electron microscopy (TEM) offers a unique approach to observe dynamic physical and chemical processes in real time and with atomic-scale resolution. Due to several advances in electron microscopy including aberration corrected optics, specimen environment control, custom stages, fast and sensitive data acquisition, the electron microscope has become an increasingly popular tool to synthesize nanostructures of all three dimensions [1, 2]. Furthermore, the diverse radiation damage mechanisms that are a hurdle to high resolution electron microscopy [3] are put to the experimenter"s advantage when the microscope is repurposed for nanoengineering processes. We focus on the influence of an experimental aspect of beam-induced fragmentation which can offer direct insights into the physical nature of this process, namely, the influence of the magnetic field originating from the pole pieces in the TEM. Our findings show that the presence or absence of the magnetic field affects the fragmentation of the particles in ways that are consistent with an explanation based on beam-induced charging. 2. Materials and Methods We deposited Au microparticles onto the amorphous carbon (a-C) film of a commercial TEM grid by direct dry transfer. We then irradiated the particles under two irradiation conditions: first, in bright field (BF) mode, where the magnetic field around the microparticles is of around 2 T, and second, in Lorenz mode of TEM, where the field is turned off. The irradiation protocol is the same for both irradiation conditions and it is schematically represented in Figure 1 a) and b). Initially, the Au microparticle is stable as long as the irradiating current density is below a critical threshold value JT (Fig. 1 a) and c)). Above JT , the particle begins to shrink as its outermost layers are expelled and form Au nanoparticles deposited on the a-C substrate (Fig. 1 b) and d)). 3. Results The irradiation procedures with and without magnetic field allow us to investigate if and how magnetoresistive effects on the Au/a-C interface modulate JT at which fragmentation occurs. We found that the presence or absence of the field significantly affects the fragmentation of the particles: Au microparticles subjected to convergent irradiation in Lorentz mode (B = 0 T) fragment or "shrink" at average lower current densities than particles subjected to the same protocol in BF mode (B = 2 T). This can be observed in Figure 2 where JT at which the shrinking of the particles begins is plotted as a function of the particle"s mass. The results are consistent with the beam-induced charging paradigm. 4. Conclusion The role of the magnetoresistive mechanism as inferred from the field-dependent variation of the critical current density to initiate the fragmentation of the Au particles strongly4. Conclusion The role of the magnetoresistive mechanism as inferred from the field-dependent variation of the critical current density to initiate the fragmentation of the Au particles strongly indicates that the fragmentation phenomenon is electrostatically driven instead of thermally triggered. Furthermore, the magnetoresistive effect seems to be negative, which is consistent with current knowledge about the electrical properties of a-C films [4]. This leads us to conclude that beam-induced fragmentation is a phenomenon that should be conceptualized as an instance of Coulomb explosion.

Fig. 1

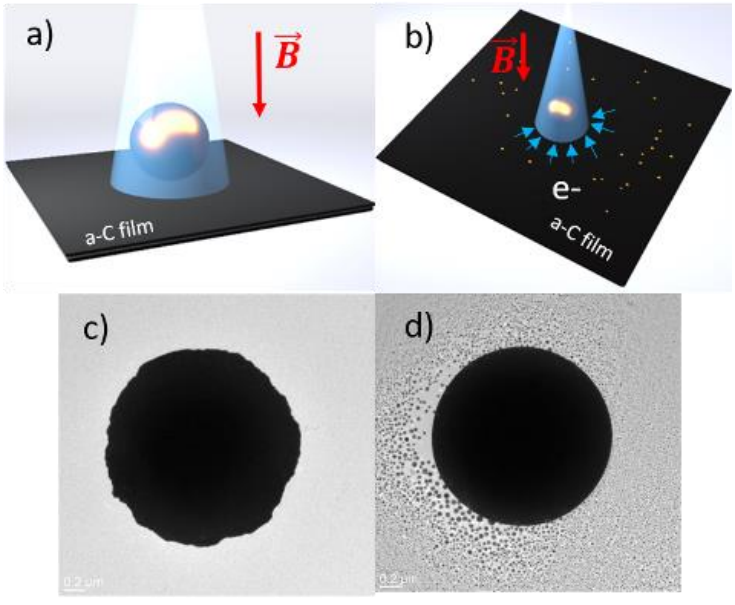

Fig. 2

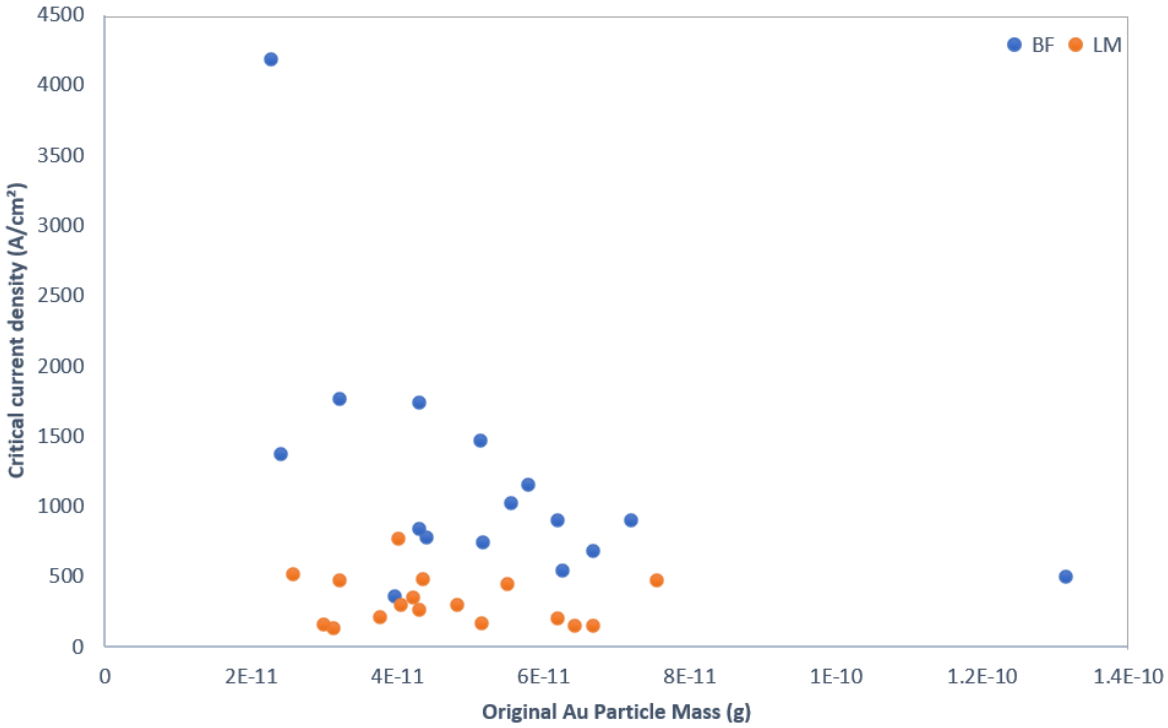
BF
LM
Critical current density (A/cm²)
4500
4000
3500
3000
2500
2000
1500
1000
500
0
0
2E-11
4E-11
6E-11
8E-11
1E-10
1.2E-10
1.4E-10
Original Au Particle Mass (g)

IM7.P023

Atmospheric gas and heating TEM with water vapor

D. Zhou[1], R. G. Spruit[1], H. H. Perez Garza[1], Z. Su[1,2,3], C. Lu[3], X. Liu[1,2], J. Carter[4], G. Hutchings[4], X. Zhang[5], F. Zhang[5], W. Liu[5]

[1]DENSsolutions B.V. Netherlands, Delft, Netherlands
[2]Shanghai Jiao Tong University, School of Chemistry and Chemical Engineering, In situ Center for Physical Sciences, Shanghai, China
[3]Xi'an Jiaotong University, Department of Nuclear Science and Technology, School of Energy and Power Engineering, Xi'an, China
[4]Cardiff University, Max Planck-Cardiff Centre on the Fundamentals of Heterogeneous Catalysis FUNCAT, Cardiff Catalysis Institute, School of Chemistry, Cardiff, United Kingdom
[5]Dalian Institute of Chemical Physics (DICP), Chinese Academy of Sciences, Dalian National Laboratory for Clean Energy, Dalian, China

Water"s negative effects on metal corrosion and catalyst deactivation are well known and under study for decades. On the positive side, water can act as reactants in hydrogen production reactions, like water-gas shift reaction (product in reverse water-gas shift reaction (RWGS)). With the introduction of aberration correctors, in-situ and operando gas and heating TEM can reveal structure and composition down to atomic resolution in their working status. However, the investigations on water"s influence inside a TEM are limited due to limited control over the water vapor flow and fear of potential leak to contaminate the TEM columns. In this work, we will present three application examples of our recently developed vaporizer for MEMS-based gas and heating TEM. One is the corrosion of FeCrAl alloy, one is the reversible growth and dispersion of the Au nanoparticles on support materials and another is the oscillatory reduction and oxidation of NiAu nanoparticles.

Material and Methods

DENSsolutions" Climate G+ system, including 3 feeds GSS, TEM sample holder, vaporizer componnets between GSS and TEM holder, gas and heating nano-reactor and Impulse software, DENSsolutions gas analyzer, and a FEI Titan (TEM) operated at 300 kV were used in this work. FeCrAl alloy was firstly cut and thinned by focused ion beam and then transferred to Climate nano-reactor. Au nanoparticles on support materials and NiAu nanoparticles were firstly dissoved in ethanol and then transferred to the Climate nano-reactor by drop-casting.

Results

Interrupted cooling water cycle could cause nuclear cladding material Zr to react much faster under water vapor condition than in vacuum or in dry oxygen. This can cause Zr break and release a lot of explosive hydrogen gas. As an alternative material to Zr, the FeCrAl alloy"s performance under water vapor heating and vacuum heating were investigated in this work.

Au dispersed on reducible support materials has important applications in low temperature water-gas shift reactions. Research on deactivation mechanism of such material under realistic gas environment can help to find more resistant ones. In our work, we visualized the agglomeration of Au nanoparticles from CeZrO4 support under wet gas environment and afterwards redispersion under dry oxygen environment. The results show complex dynamics and possible regeneration of Au nanoparticles under proper conditions and thus gives practical applications better scopes.

For NiAu nanoparticles, we firstly investigated three extreme situations, i.e. reduction condition without vapor (H2 & He), reduction condition with highest humidity vapor (H2, H2O & He) and only vapor at highest humidity level (H2O & He), as shown in Figure 1. The particle retained in a structure of Ni core and Au shell in H2 & He. Loose NiO structure formed outside the particle upon introduction of high humidity vapor (H2, H2O & He), and then condensed upon disappearance of H2 in the inlet gas (H2O & He).Then we varies humidity level from 0 to ~50% with H2 and without H2. We found an interesting oscillative transition between loose and condensed NiO layer formation, whose periodicity influenced by humidity level.

More experimental details and interpretations will be presented on-site.

Conclusion

Development and application of such vaporizer are expected to help design more sustainable metal materials and catalysts from fundamental failure mechanism studies.

Fig. 1

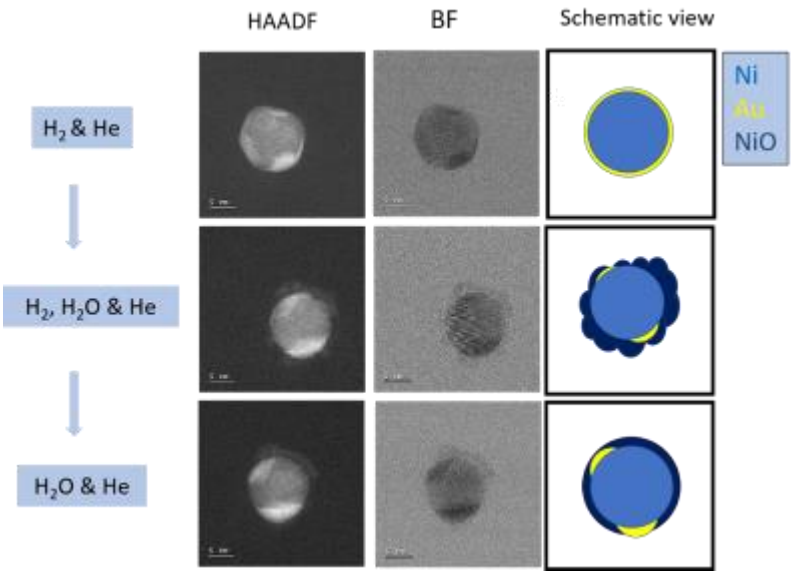

IM7.P024

Atomic-resolution 3D imaging of metallic nanoparticles under realistic conditions

E. Arslan Irmak[1], P. Liu[1], S. Bals[1], S. van Aert[1]

[1]EMAT and NANOlab Center of Excellence, University of Antwerp, Antwerp, Belgium

Determining the three-dimensional (3D) atomic structure of nanoparticles (NPs) is critical to understand their functional properties for many applications. It is hereby essential to perform such analyses under conditions relevant to the envisioned application. In this talk, a refined methodology will be presented for the 3D atomically resolved structural characterization of metallic NPs on an oxide support at elevated temperatures, relevant for catalytic applications.

In situ scanning transmission electron microscopy (STEM) experiments are valuable to analyze NPs under application-relevant conditions. Nonetheless, these investigations are usually inadequate because they only provide a projected image of a 3D structure. Electron tomography is a powerful method for the 3D reconstructions of NPs, but the long acquisition time required to collect a tilt series limits this technique when one wants to observe dynamic changes with atomic resolution. As an alternative, the 3D atomic structure of NPs can be extracted from annular dark-field (ADF) STEM images acquired along a single zone axis orientation during *in situ* experiments. Due to the thickness sensitivity of ADF STEM images, the number of atoms can be reliably estimated by the so-called atom counting method. The outcome serves as an input for energy minimization by Monte Carlo (MC) or molecular dynamics (MD) simulations. [1,2] However, this approach cannot be directly applied to supported metal NPs at elevated temperatures. The reason is that increased thermal displacements of atoms and particle-support interactions should also be taken into account as they influence the morphology of the particle. Moreover, it is expected that the structure of NPs at elevated temperatures may significantly deviate from their ground state configuration, which is difficult to determine using purely energy minimization approaches.

To overcome these limitations, we proposed an iterative local minima search algorithm based on atom-counting results by taking both the temperature effect and the particle-support interaction into account. The proposed method explores different local minima in the energy landscape while quantitatively validating the reconstructed structure with the observations from ADF STEM images (Fig 1). It has been demonstrated that our approach outperformed the previously applied methodologies (Fig 2) and enabled 3D atomic-scale investigations of both stable and metastable states of the NPs that may appear at high temperatures. [3]

References

[1] A. De Backer et al., *Nanoscale* 9 (2017), 8791.

[2] T. Altantzis, I. Lobato et al., *Nano Lett*. 19 (2019), 1, 477–481.

[3] E. Arslan Irmak et al., *Small Methods* 5 (2021), 2101150.

[4] This work was supported by the European Research Council (770887 PICOMETRICS to SVA and 815128 REALNANO to SB, 823717 ESTEEM3), and Research Foundation Flanders (G.0267.18N, G.0502.18N, and G.0346.21N).

Fig 1. 3D reconstruction from an experimental ADF STEM image of a supported NP (a) by combining atom-counting (b) and the iterative local minima search algorithm (c) resulting in final 3D model (d).

Fig 2. Comparison of different approaches. a) Original test structure. The final structures obtained from the combination of atom counting and b) MC, c) MD and d) the proposed approach. e) Comparison of the surface structure of the reconstructed NPs and the original NP based on the coordination number (CN) of the atoms.

Fig. 1

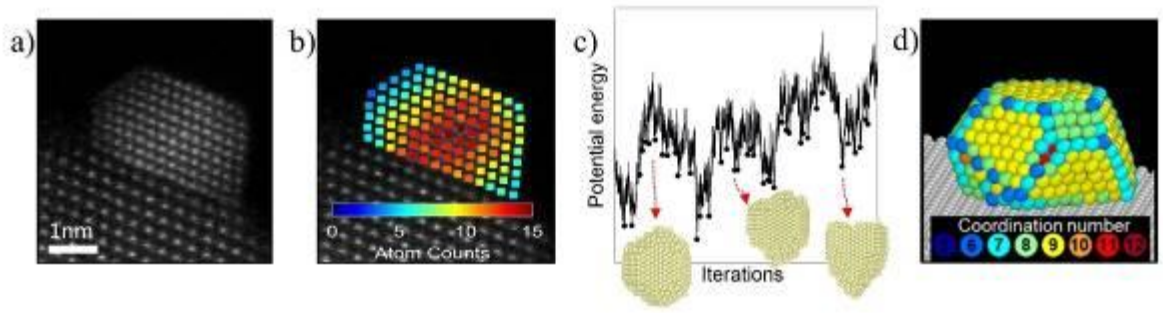
a)
1nm
b)
0
5
10
15
Atom Counts
c)
Potential energy
Iterations
d)
Coordination number
6
7
8
9
10
11
12

Fig. 2

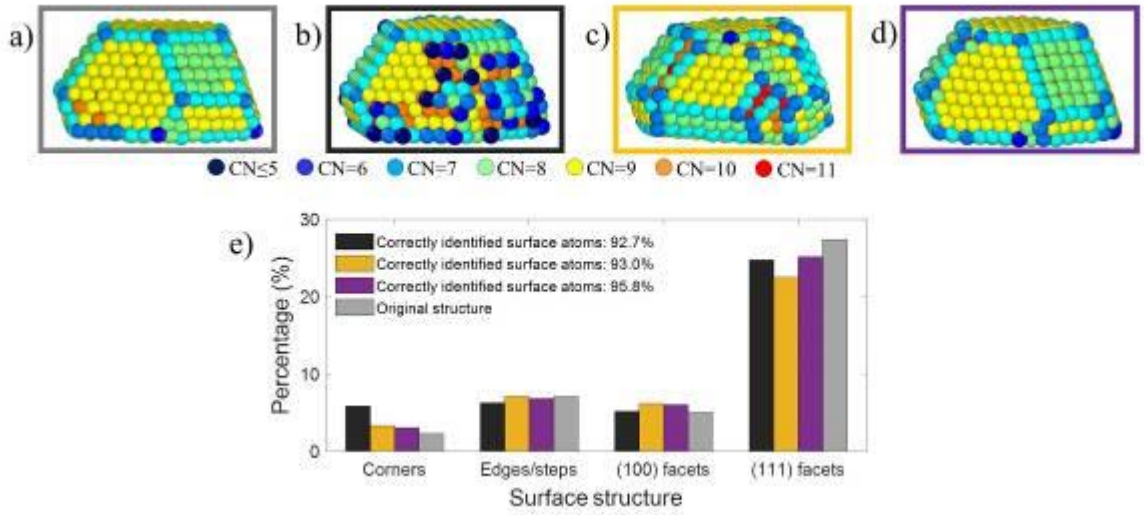
a)
b)
c)
d)
CN≤5
CN=6
CN=7
CN=8
CN=9
CN=10
CN=11
e)
Correctly identified surface atoms: 92.7%
Correctly identified surface atoms: 93.0%
Correctly identified surface atoms: 95.8%
Original structure
Percentage (%)
0
10
20
30
Corners
Edges/steps
(100) facets
(111) facets
Surface structure

IM7.P025

In-situ mapping of Bloch and Neel domain walls in magnetic thin films

A. Thampi[1,2], J. Schöpf[3], Y. Lee[1], D. Wolf[1], A. Thomas[1], I. Lindfors-Vrejoiu[3], A. Lubk[1,2]

[1]Leibniz Institute for Solid State and Materials Research Dresden, Institute for Solid State Research, Dresden, Germany
[2]TU Dresden, Physics, Dresden, Germany
[3]University of Cologne, Physics Institute, Cologne, Germany

Magnetic domain walls (DWs) in ferromagnetic thin films exhibit a rich variety of configurations and corresponding dynamic properties depending on parameters like film thickness, defect density, magnetocrystalline anisotropy, exchange stiffness, and Dzyaloshinskii–Moriya interaction (DMI). These may be tuned by corresponding synthesis strategies such as multilayer growth, strain engineering, etc., which holds great potential for next-generation magnetic memory or logical devices utilizing moving DWs.

Here, we study epitaxial ferromagnetic multilayer devices of $La_{0.7}Sr_{0.3}Mn_{1-x}Ru_xO_3$, consisting 8 nm thick manganite layers with varying Ru/Mn content, in order to engineer symmetric and antisymmetric exchange interaction and magnetic anisotropy across the multilayer stack. We particularly map the DW states as a function of temperature and external out-of-plane magnetic fields employing high-resolution magnetic imaging in the Transmission Electron Microscopy (TEM), in order to reveal the dominating magnetic interaction mechanisms and the impact of inversion symmetry breaking at the interfaces. Moreover, we develop and apply a high-frequency in-situ electric biasing holder facilitating the manipulation of magnetic textures and show first results on in-situ domain wall motion in soft magnetic thin films.

Lorentz TEM and transport of intensity phase reconstruction is used to characterize the magnetic domains and DWs formed as a function of temperature and perpendicular magnetic field strength. Mapping of magnetization dynamics at the nanometer scale, including DWs, is performed by application of very short current pulses in a specially designed high-frequency electric biasing holder and parallel imaging via Lorentz microscopy.

Fig. 1 shows a characteristic pattern of stripe domains. Varying the external out-of-plane magnetic field from 0 mT to -350 mT (and back) leads to hysteretic growth of one domain type with respect to the other allowing to identify the domains as out-of-plane type stabilized by magnetocrystalline anisotropy. Careful analysis of the DW contrast assisted by micromagnetic simulations furthermore allows to identify the DWs as chiral Néel type. This observation indicates the crucial impact of interfacial DMI in their formation, which is corroborated by micromagnetic simulations. We finally observe a split of the domains into bubbles of diameter smaller than 100 nms with magnetic texture characteristic of Néel skyrmions at certain field strengths.

To demonstrate the possibility of DW manipulation by (ultrashort) electric pulses and the induced spin-torque effect, we prepared thin Ni and Permalloy (Py) films on a Si_3N_4 membrane and observed the current induced DW variations by Lorentz TEM. Here, the DW shifts are quantitatively analyzed with respect to the current density and also with heat energy. We demonstrate that we can achieve current densities in the range of 10^{11}-10^{13} A/m^2 as required for spin torque DW motion in Py.

High-resolution magnetic field mapping of $La_{0.7}Sr_{0.3}Mn_{1-x}Ru_xO_3$ multilayer system demonstrates the possibility to engineer chiral Neel domain walls and skyrmions. First steps toward spin-torque driven in-situ manipulation of DWs thin film is demonstrated using a dedicated biasing holder and sample design.

Fig. 1

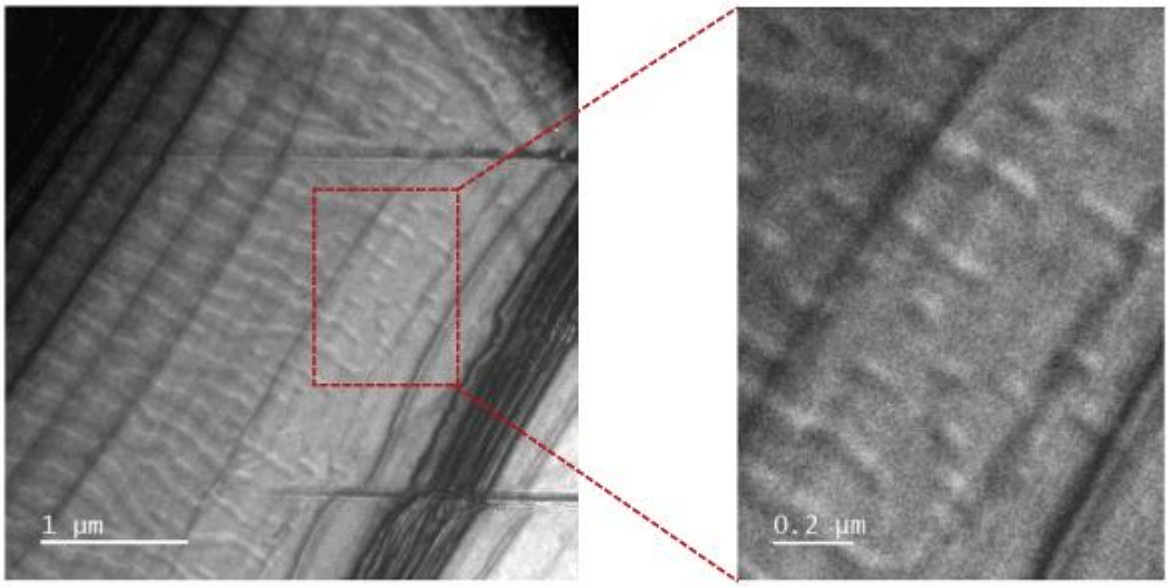

Fig.1 Lorentz TEM image of $La_{0.7}Sr_{0.3}Mn_{1-x}Ru_xO_3$ thin film at a temperature of 235 K and applied magnetic field of -157 mT. The inset shows the Neel bubbles.

Fig. 2

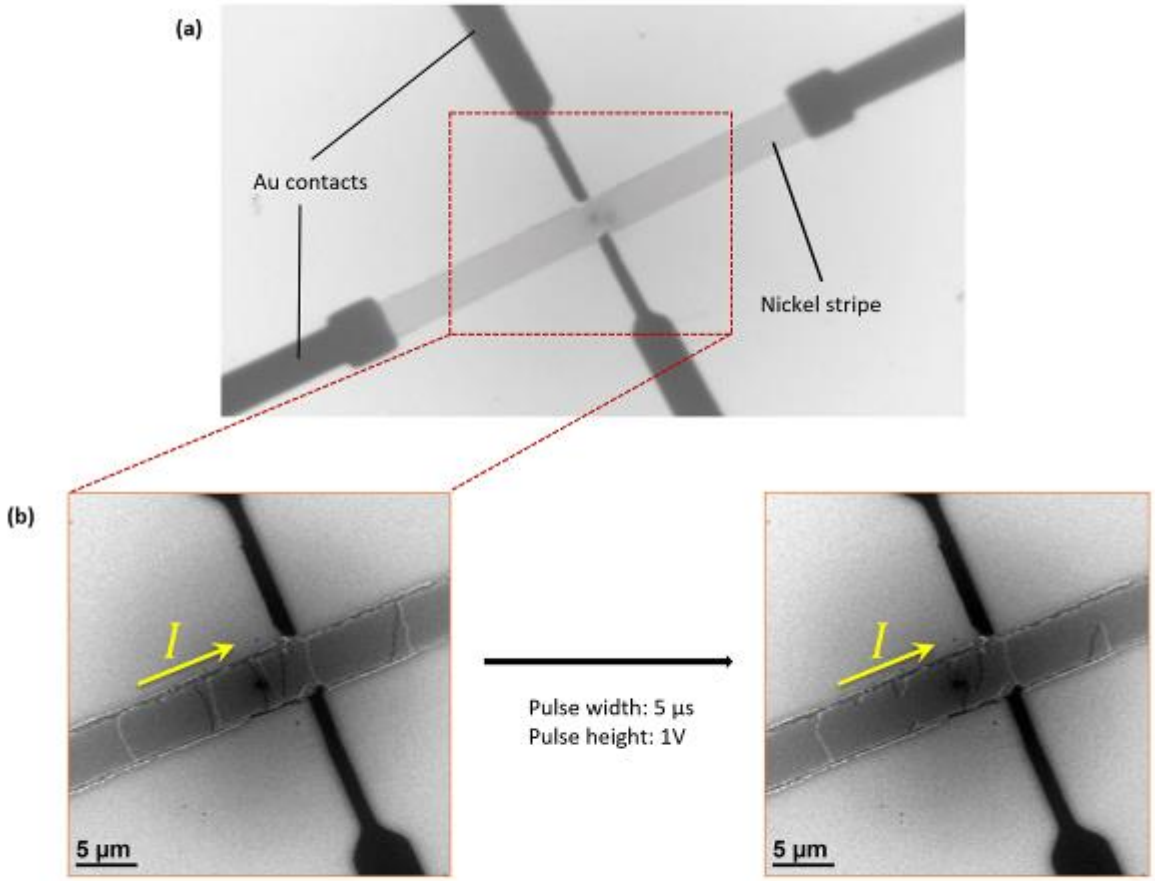

Fig.2 Lorentz TEM Image of current induced domain wall motion in thin Ni stripe. (a) Geometry of the system showing how the Ni stripe is connected to the gold contacts. (b) Domain wall motion in the system with respect to the induced electric pulses.

IM7.P026

In-situ correlative microscopy using AFM-in-SEM

V. Hegrová[1], R. Dao[1], J. Neuman[1]

[1]NenoVision s. r. o., Brno, Czech Republic

Correlative microscopy has become an essential tool helping us understand the complexity of the sample properties. It combines different imaging systems and benefits for understanding the principles of materials. Correlation of atomic force microscopy (AFM) and complementary technique, scanning electron microscopy (SEM), has several advantages, such as multimodal analyses under in-situ conditions, with precise localization to the area of interest.

With the ever-increasing number of battery-powered devices around us, the importance of optimizing our means of energy storage grows. Therefore, getting to know how the processes in batteries work in nanoscale is crucial. Cathode Active Materials, such as $LiNiO_2$, are the core ingredient of a battery. These micro-particle powders have their grains coated to prevent unwanted chemical reactions but conserve high conductivity. The result is a rechargeable battery with a longer lifetime.

To be able to measure such powders, we used AFM-in-SEM, LiteScope, to image the conductivity and the topography of such coated particles. Since the powdered cathode material prone to immediate oxidation upon air exposure, it is a very difficult sample for separate AFM and SEM systems and needs to be analyzed in-situ. The correlated data in 3D conductive AFM and CPEM view (Correlative Probe and Electron Microscopy) show surprisingly complex coating structure, see fig. 1.

Thus, the AFM-in-SEM solution allows us analyses under in-situ conditions of several AFM modes – such as 3D topography, electrical, magnetic, or mechanical properties – and SEM capabilities like fast imaging, chemical analysis, or surface modification. This way, the Correlative Microscopy is essential not only in battery research, but also in other fields of Material science, Nanotechnology, Life science, and other areas in both research and industry.

Fig. 1: Correlative analysis of LiNiO2 cathode powder: SEM provided fast navigation, elemental analysis (EDX) and material contrast. AFM provided 3D topography and conductivity mapping. The 3D CPEM view merged AFM topography and SEM signal.

Fig. 1

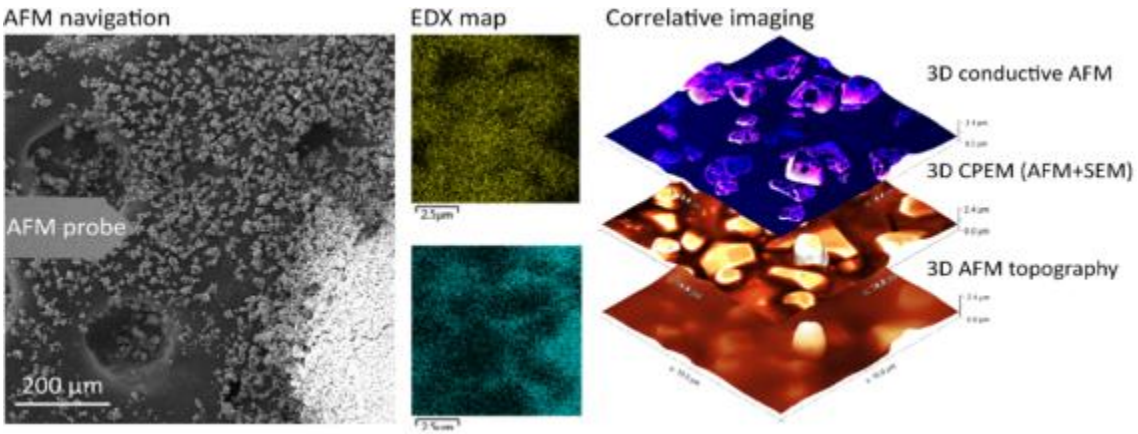

IM7.P027

Advanced denoising methods for Pt/C electrocatalyst studies with electrochemical liquid phase TEM

R. Girod[1], S. Toleukhanova[1], V. Tileli[1]

[1]EPFL, Institute of Materials, Lausanne, Switzerland

Electrochemical liquid phase transmission electron microscopy (TEM) provides *operando* insights at the nanoscale for electrocatalyst evolution during reactions. However, resolution in both temporal and spatial dimensions remains limited by the thickness of conventional MEMS-based liquid cells and by the low electron dose required to advert beam-induced radiolytic processes[1]. Denoising methods leveraging the capabilities of deep learning (DL) are promising for overcoming this resolution limit but they typically require training on extensive ground truth datasets[2]. In the context of liquid phase TEM, these are often difficult to access experimentally or to obtain from simulation for complex samples and, as such, implementation of unsupervised and easy-to-train denoising methods is necessary.

Herein, we tested unsupervised training schemes based on the Noise2Noise[3] and Noise2Void[4] frameworks on *in situ* and *operando* datasets of Pt nanocatalysts (2-3 nm diameter) dispersed on Ketjenblack microporous carbon supports. They represent a challenging test case due to the spatial resolution requirement, the temporal resolution needed to analyze degradation events, and the low dose limitation to prevent beam-induced carbon corrosion. Datasets were acquired in bright-field (BF)-TEM mode, using a liquid cell electrochemical holder and custom electrochemical chips featuring a glassy carbon working electrode. Implementation and training of the DL models was done in python using the CSBdeep toolbox[5]. Performance comparison with the block-matching and 3D filtering (BM3D) and non-local means (NLM) algorithms was performed based on Q-metric results, resolution estimation with Fourier ring correlation, and segmentation accuracy. We find that across the range of metrics, the DL-based methods outperform conventional denoising algorithms and enable studies of challenging systems such as potential-induced Pt/C electrocatalyst evolution in real time. This work demonstrates that careful selection of denoising strategies can improve the spatial and temporal resolution of *in situ* electrochemical TEM, which paves the way towards new insights in beam-sensitive systems.

[1] N. de Jonge, L. Houben, R. E. Dunin-Borkowski, F. M. Ross, *Nature Reviews Materials* **2019**, *4*, 61.

[2] C. Belthangady, L. A. Royer, *Nat Methods* **2019**, *16*, 1215.

[3] J. Lehtinen, J. Munkberg, J. Hasselgren, S. Laine, T. Karras, M. Aittala, T. Aila, *arxiv.org:1803.04189* **2018**.

[4] A. Krull, T.-O. Buchholz, F. Jug, *arXiv:1811.10980* **2019**.

[5] M. Weigert, U. Schmidt, T. Boothe, A. Müller, A. Dibrov, A. Jain, B. Wilhelm, D. Schmidt, C. Broaddus, S. Culley, M. Rocha-Martins, F. Segovia-Miranda, C. Norden, R. Henriques, M. Zerial, M. Solimena, J. Rink, P. Tomancak, L. Royer, F. Jug, E. W. Myers, *Nat Methods* **2018**, *15*, 1090.

IM7.P029

Studying the structural transformation behavior of tailored metallic glass composites by *in-situ* techniques in the TEM

S. Fellner[1], J. Eckert[1,2], C. Gammer[1]

[1]Erich Schmid Institute of Materials Science / Austrian Academy of Sciences, Leoben, Austria
[2]Montanuniversität Leoben, Department of Materials Science, Leoben, Austria

Introduction:

Properties of nanomaterials are not only dependent on chemistry but also on the manufacturing process. Every structural change induced by thermal or mechanical stresses alters the material properties. In metallic glasses, a material class exhibiting a disordered amorphous structure, the fundamental deformation mechanisms are still not yet fully understood [1]. Therefore, they are subject to intensive research. The introduction of secondary crystalline phases or highly rejuvenated regions renders transformation mechanisms in metallic glasses even more complex. Due to the emergence of novel dedicated specimen holders, in-situ TEM measurements are a powerful tool allowing to perform direct measurements on the deformation behavior of these tailored nanocomposites [2].

Objectives:

In this work, we study the effect of local heterogeneities on the structural transformation mechanisms in metallic glass composites by combined in-situ TEM techniques. A direct electron detector is used allowing to perform the experiments with high temporal resolution.

Materials and Methods:

The as-cast specimen material was prepared using a Suction Cast Arc Melter with 1.6 mm plate thickness. To provide tailored composites a combination of severe plastic deformation using high pressure torsion deformation and controlled heating is used. Quantitative in-situ nanomechanical deformation experiment were performed using a Hysitron PI 95 PicoIndenter from Bruker. Scanning transmission electron microscopy (STEM) images were taken on a JEOL 2200FS equipped with Omega energy filter A QuantumDetectors MerlinEM pixelated 512x512 direct electron detector was used to acquire 4D-STEM datasets during the in-situ experiments [3]. The analysis was performed using custom Python scripts and Digital Micrograph software.

Results & Conclusions:

The metallic glass composites produced in the present work show highly complex microstructures, including a heterogeneous disordered amorphous phase and multiple homogeneously distributed crystalline phase precipitates. It is shown that the nanocomposites exhibit a strain localization that correlates with the scaling of local heterogeneities. Advanced in-situ TEM experiments using a fast direct electron detector are able to unravel quantitative local deformation mechanisms on the nanoscale. Specifically, we use 4D-STEM to measure the strain at the nanoscale. This provides new insights into the evolution of local elastic and global plastic strains during the in situ experiments and thus helps to draw a more direct link between structure and properties of the metallic glass composites.

The authors gratefully acknowledge the financial support from the Austrian Science Fund (FWF): Y1236-N37.

Fig. 1: STEM HAADF image showing complex strain softened regions before deformation

References

[1] A.L. Greer, Metallic glasses on the threshold, Mater. Today 12 (1-2) (2009);

[2] H. Sheng, L. Zhang, H. Zhang, J. Wang, J. Eckert, C. Gammer In-situ TEM observation of phase transformation in bulk metallic glass composites, Materials Research Letters, 9 (2021) 190-195;

[3] H. Sheng, D. Şopu, S. Fellner, J. Eckert, C. Gammer PHYSICAL REVIEW LETTERS 128 (2022) 245501.

Fig. 1

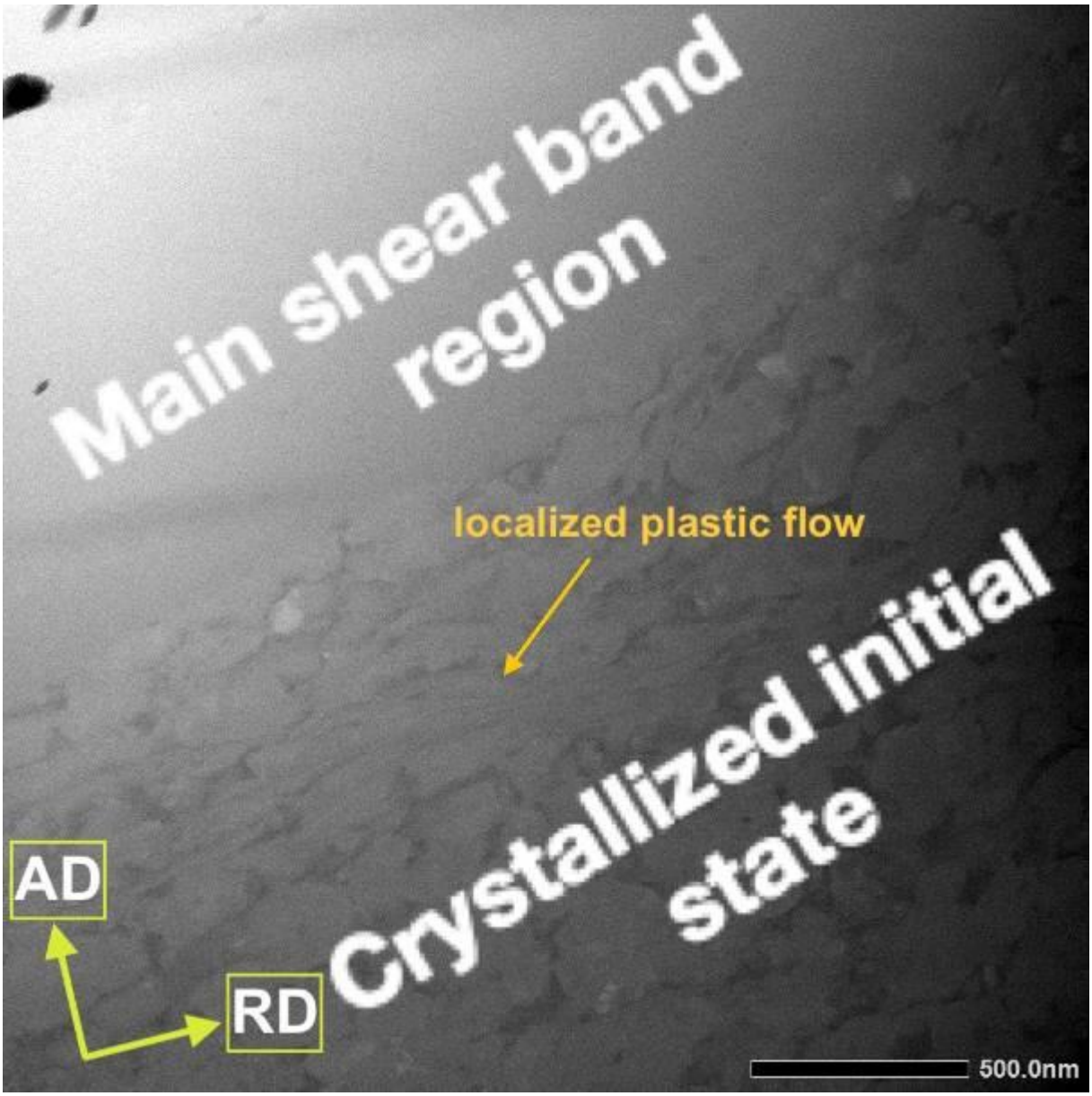
Main shear band region
localized plastic flow
Crystallized initial state
AD
RD
500.0nm

IM7.P030

Damage induced by electric field (DIEF) of gold microparticles on silicon oxide substrate in the scanning electron microscope (SEM)

K. Weinel[1], L. Agudo Jácome[1], I. Gonzalez-Martinez[2], B. Büchner[2,3]

[1]Bundesanstalt für Materialforschung und -Prüfung, Berlin, Germany
[2]Leibniz-Institute for solid state and materials research, Dresden, Germany
[3]Technische Universität Dresden, Dresden, Germany

Introduction

A normally unwanted process that can arise when converging an electron beam onto, e.g. microparticles, has been called "damage induced by electric field" (DIEF) [1]. By DIEF, the convergent electron beam (CEB) imparts a high amount of energy to the microparticle locally and strongly interacts with its atoms. At a specific current density ***J***, which can be controlled by the convergence angle *α*, the irradiated material begins to transform. The phenomenon of expelling nanomaterial from microparticles under the influence of a convergent electron beam (CB) in a transmission electron microscope (TEM) has been largely studied [2]. Several types of nanoparticles (NPs) have been observed for different metallic materials and metal oxides after specific CB protocols (P) in the TEM. Thus, DIEF can be used as a promising synthesis method controlled changes of micrometric material to create new nanometric material compositions and morphologies.

While these reactions have been observed in situ at the high acceleration voltages associated with TEM, it remains unclear whether the SEM can also be used to fabricate NPs via DIEF. In contrast to TEM there is no possibility to statically convert the electron beam to a range of *α* to reach the needed ***J*** as in TEM. Instead, the scanning parameters and the magnification can be manipulated so as to find an integrated ***J***. Considering that the scanning electron microscope (SEM) is easier to use, more accessible and cheaper than a TEM, here we explore the possibility to transfer the concepts of DIEF known to operate in the TEM for in situ NP generation SEM.

Objectives

The main goal is to determine whether DIEF can be translated to the SEM perform to controlled in situ fabrication of nanoparticles from microparticles, using gold microparticles on amorphous SiO substrate as precursors. We determine what experimental parameters must be taken into account to create SEM-based CBPs for NP creation in the SEM with these materials.

Materials & methods

Gold microparticles with diameter of around 1 to 3 µm were deposited on electron transparent amorphous SiO/SiO_2 substrate. Using a convergent electron beam protocol (CBP) in a scanning electron microscope (SEM) at an acceleration voltage of 30 kV, the gold microparticles were irradiated until a production of NPs takes place as shown in figure 1. The beam current varied between 16 and 23 nA.

Results

Depending on the CBP parameters, either only Au NPs or a mixture of Au and Si NPs are produced. The particle size ranges from a few nm up to 100 nm, and it depends on the distance of the NP to the initial position of the microparticle. Further beam parameters such as the dwell time, the effective irradiated volume and particle size determine whether NPs are produced or if the microparticles only are expelled from the substrate without reacting.

Conclusion

The SEM can be used as an instrument for synthesizing nanomaterials via DIEF. Different CBP protocols can be applied for obtaining either gold nanoparticles or silicon + gold nanoparticles

[2]I. Gonzalez-Martinez, A. Bachmatiuk, et al.; *Electron-beam induced synthesis of nanostructures: A review*; Nanoscale (**2016**),11340

[1]N. Jiang; *Damage mechanisms in electron microscopy of insulating materials*; J. Phys. D: Appl. Phys. (**2013**),305502

Fig1: Convergent beam protocol on a gold microparticle deposited on a silicon oxided substrate. a) initial state b) after CBP c) selected area electron diffraction analysis and simulation.

Fig. 1

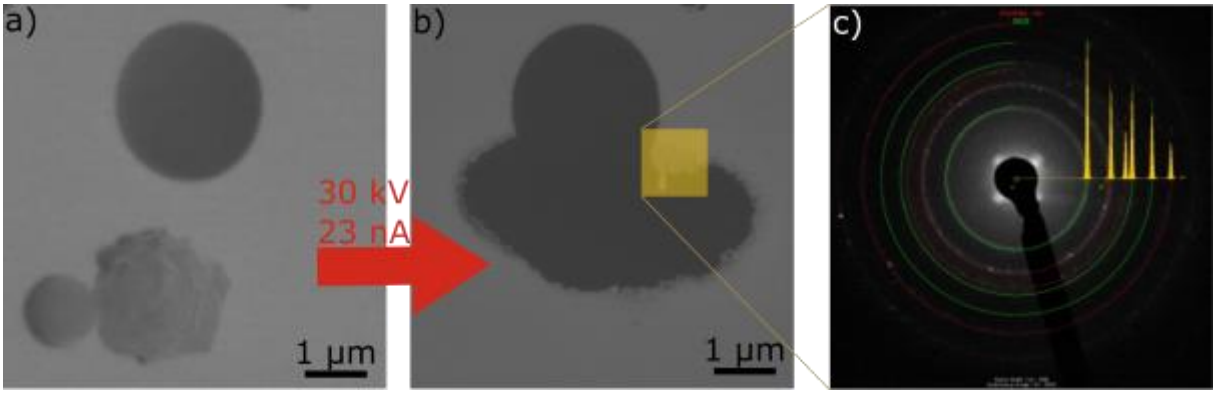

IM7.P031

In-situ SEM mechanical testing of bond coating at extreme temperatures

J. Lukes[1], S. Bhowmick[2], E. Hintsala[2], U. Hangen[1]

[1]Bruker Nano GmbH, Bruker Nano Surfaces and Metrology, Berlin, Germany
[2]Bruker Nano GmbH, Bruker Nano Surfaces and Metrology, Eden Prairie, MN, United States

Pt-aluminide (PtAl) bond coats are an integral part of thermal barrier coating (TBC) systems operating in aggressive environments such as gas turbine engines. We explored deformation mechanisms of diffusion bond coats and Ni-based superalloys at elevated and at cryogenic temperatures.

An advanced in situ SEM nanomechanical instrument, Hysitron PI 89 PicoIndenter (Bruker, Minneapolis, USA) with an integrated 1000°C high-temperature stage and active 1000°C tip heating was used to conduct uniaxial compression of micropillar samples. An integrated cryogenic stage was used to conduct pillar compression tests at -130°C.

Micropillars of dimensions 8 µm x 8 µm in cross-section and 25 µm in height were prepared from the outer layer of PtNiAl coating and Ni-base superalloy region by focused ion beam (FIB) machining. Using the displacement-controlled feedback mode of the system, the pillars were compressed to 5-12% strain at a strain rate of 10-3 s-1.

A switch in plasticity mechanism to grain boundary sliding at higher temperature was observed on the surface of the bond coating pillars (fig. 1). The elastic modulus of the bond coating remains nearly constant up to 900°C, whereas yield stress of the coating decreases to ~50% (fig. 2).

Fig.1 Morphology of bond coating pillar after compression at 700°C.

Fig. 2 Stress-strain curves of bond coating at different temperatures

Fig. 1

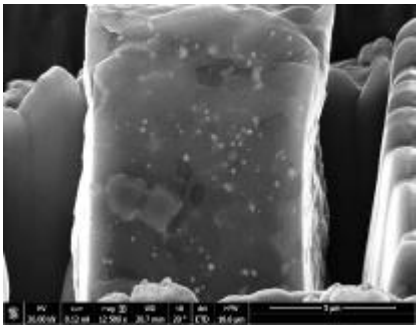

Fig. 2

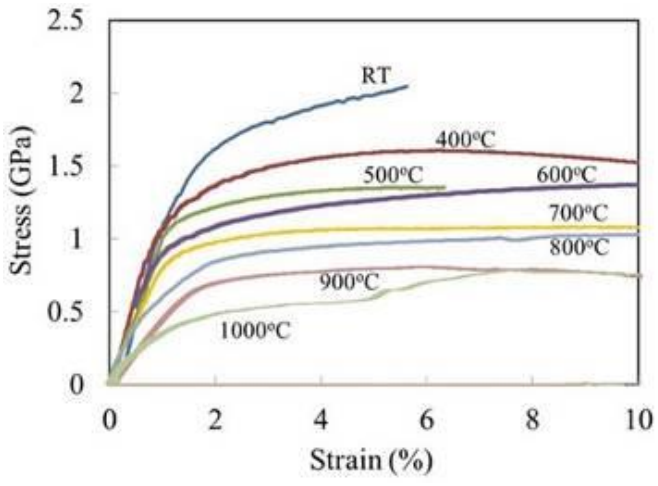

IM7.P032

Simultaneous conductivity and electric field mapping with multi-modal STEM EBIC

W. Hubbard[1], H. L. Chan[2], B. C. Regan[1,2]

[1]NanoElectronic Imaging, Inc., Riverside, CA, United States
[2]University of California, Los Angeles, Dept. of Physics and Astronomy, Los Angeles, CA, United States

The transmission electron microscope (TEM) excels at physical characterization, with modern systems capable of precisely determining the type, number, and arrangement of atoms in a sample. TEM detection of electronic and thermal signals is also possible but often requires cutting-edge hardware, substantial computation, and an ideal sample. These signals are more elusive because standard TEM-based techniques are insensitive to electronic and thermal structure compared to physical and chemical structure. Often, especially when studying devices, the former are much more important than the latter.

Electron beam-induced current (EBIC) measures the current generated in a sample by an electron beam. In the "standard" EBIC mode, current is generated when electron-hole pairs are separated by local electric fields. In a recently demonstrated mode of EBIC, secondary electron emission EBIC (SEEBIC), the current consists of holes produced by secondary electron emission (1). SEEBIC is ~1000× smaller than std. EBIC, accessible at high resolution (2), and generates straightforward contrast related to electronic signals, including conductivity (3,4), and temperature (5). Here we demonstrate obvious electronic contrast in TEM via measurement of two EBIC modes simultaneously, mapping resistance, via SEEBIC, and electric field, via std. EBIC, within a single image.

Figs. 1 (A) and (B) show annular dark-field (ADF) STEM and STEM EBIC images, respectively, of a GeSbTe (GST) strip patterned between two TiN electrodes on a SiN membrane. At each TiN/GST interface, the Schottky barrier between the materials creates an electric field that produces std. EBIC contrast. The EBIC in these regions indicates both the direction (current polarity) and magnitude of the field. SEEBIC dominates in the rest of the device, where there is no electric field, and indicates the resistance at each pixel to the left, grounded electrode (3). For example, signal is darkest (resistance lowest) near the grounded left electrode because it provides a lower resistance path to ground; less holes produced there reach the EBIC amplifier via the right electrode (Fig. 1C).

STEM EBIC imaging generates obvious electronic contrast that would otherwise be either difficult (electric field) or impossible (conductivity) to visualize in the TEM. Complementing TEM's physical contrast, STEM EBIC provides a unique opportunity to study *electronic* dynamics in *electronic* devices at high resolution.

References:

(1) W. A. Hubbard, *et al.,* Phys. Rev. Appl., **10** (2018), p. 044066.

(2) M. Mecklenburg, *et al*., Ultramicroscopy, **207** (2019), p. 112852.

(3) W. A. Hubbard, *et al*., Appl. Phys. Lett., **115** (2019), p. 133502.

(4) W. A. Hubbard, *et al*., Adv. Funct. Mater., **32** (2022), p. 2102313.

(5) W. A. Hubbard, *et al*., Microsc. Microanal., **26 S2** (2020), p. 3124.

Figure 1. STEM EBIC resistance and electric field mapping. The ADF STEM image (A) shows a TiN/GST/TiN device. The STEM EBIC image (B) has bright (dark) contrast at the left (right) GST/TiN interface due to std. EBIC at the Schottky barriers. Outside of these interfaces SEEBIC dominates. SEEBIC is largest in the TiN connected to the EBIC amplifier, decreases right-to-left along the GST, and is lowest on the left TiN electrode. The diagram (C) depicts SEEBIC current generation in the GST strip. Holes are more likely to reach ground via the left or right electrode depending on the relative resistance to each, generating resistance contrast in the image.

Fig. 1

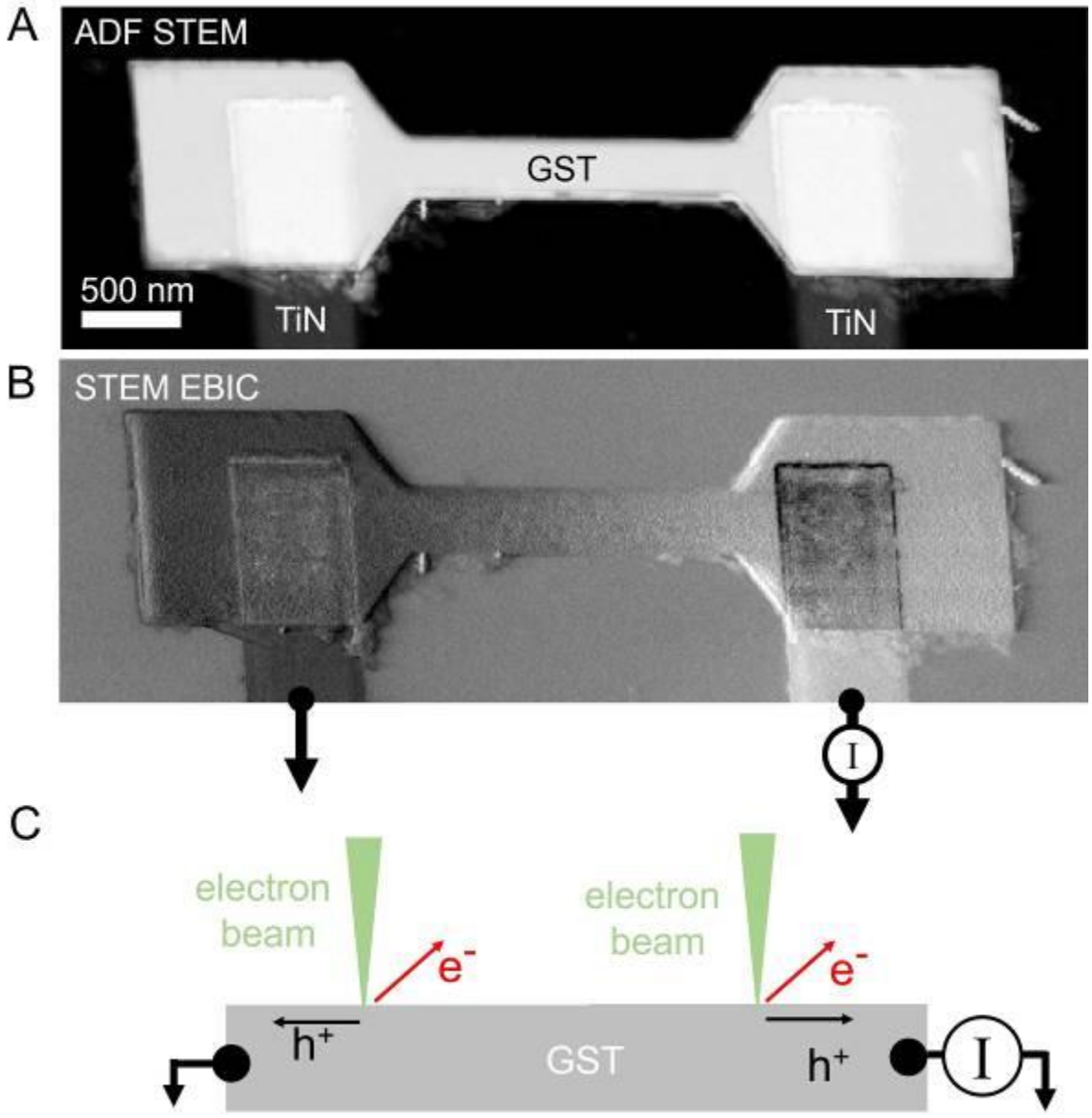
A
ADF STEM
GST
500 nm
TiN
TiN
B
STEM EBIC
I
C
electron
beam
e-
electron
beam
e-
h+
GST
h+
I

IM7.P033

An *in situ* heating STEM study of Cu related catalysts

F. Ruiz-Zepeda[1], M. Gatalo[1], M. Azeezulla Nazrulla[1], M. Bele[1], G. Dražić[1], M. Gaberšček[1], N. Hodnik[1]

[1]National Institute of Chemistry, Department of Materials Chemistry, Ljubljana, Slovenia

In this work we have studied the thermal annealing process of carbon supported Cu3Pt nanoparticles that can be employed as a cathode material for the oxygen reduction reaction (ORR) in fuel cells [1]. By following the growth mechanism at different temperatures we have been able to observe that there is a Cu enrichment during the heat treatment, since there is a relatively large surplus of CuO needle-like particles from the previously double passivation galvanic displacement step. This process seems to involve the migration of Cu single atoms *via* the carbon support. At temperatures up to 500 °C, other effects were observed such as particle reshaping as well as ordering of the crystal lattice which is due to the Cu enrichment of the initial Pt-Cu nanoparticles giving as a result the Cu3Pt structure. Heating up till 800 °C, the growth is mainly due to coalescence. Ostwald ripening was apperently not observed to play a significant role in the nanoparticle size. And due to the partial vapor pressure at this temperature Cu loss was experienced. These findings, aside from providing insights into the morphological and structural characteirstics in the alloys (and relating it to the performance as catlaysts), can serve as a framework to stablish equally designed expeimetns for similar Cu related systems.

References

[1] M. Gatalo, F. Ruiz-Zepeda, N. Hodnik, G. Dražić, M. Bele, M. Gaberšček. Insights into thermal annealing of highly-active PtCu3/C Oxygen Reduction Reaction electrocatalyst: An *in-situ* heating transmission Electron microscopy study. Nano Energy 63 (2019) 103892.

Aknowledgements

Authors would like to thank the European Research Council (ERC) Starting Grant 123STABLE (Grant agreement ID: 852208).

MSLB.P001

Probing atomic tilt coupling in oxide superlattices $Pr_{0.7}Ca_{0.3}MnO_3/SrRuO_3$ using quantitative electron microscopy

C. Liu[1,2], P. Lu[1], L. Jin[1], R. E. Dunin-Borkowski[1]

[1]Forschungszentrum Jülich, Ernst Ruska-Centre, Jülich, Germany
[2]Leibniz Institut für Kristallzüchtung / Forschungszentrum Jülich, Berlin, Germany

Perovskite oxides have a wide range of tuneable physical properties and are of interest for electronic and energy-related applications. In superlattices of $Pr_{0.7}Ca_{0.3}MnO_3/SrRuO_3$ (PCMO/SRO), the anomalous Hall effect depends sensitively on the crystal structures of the $SrRuO_3$ layers, while the field dependence of the Hall resistivity is related to the PCMO layer thickness. Here, we use integrated differential phase contrast (iDPC) scanning transmission electron microscopy (STEM) to study the influence of layer thickness on the structures of PCMO/SRO superlattices. As high angle annular dark field (HAADF) images have poor sensitivity to light elements such as oxygen, especially in close proximity to heavy elements, we use iDPC imaging for the simultaneous visualisation of oxygen and metal atoms in real space. We determine atomic positions with sub-pixel precision and measure atomic tilt angles quantitatively. We use simulation results to establish an approximately linear relationship between optimal defocus and sample thickness in SRO, which provides a guide for tuning the defocus experimentally during iDPC STEM experiments. Our results show that atomic tilt angles in the SRO layers depend on the thicknesses of the PCMO layers, with thicker PCMO layers resulting in smaller oxygen tilt angles and different magnetic properties.

MSLB.P004

Simultaneous raman and SEM imaging of mineral sections

D. Premužić[1], P. Johnson[2], D. Nutting[2], T. Batten[2]

[1]Renishaw GmbH, Pliezhausen, Germany
[2]Renishaw Plc., Wotton-under-Edge, Gloucestershire, United Kingdom

Raman spectroscopy is an excellent tool for analysing the chemical bonding and structure in mineral sections with high specificity. Raman mapping/imaging is typically combined with optical microscopy to provide correlated information on samples. Sometimes, optical imaging provides less contrast for mineralogical samples compared to scanning electron microscopy (SEM) images. However, combined SEM Raman instruments are relatively uncommon and often require the sample to be moved within the SEM chamber to a different analysis position. This movement makes it challenging to ensure the SEM and Raman measurements are accurately co-localised.

In this work, we demonstrate a combined SEM Raman system that is capable of simultaneous SEM and Raman imaging from the same sample area. Figure 1 illustrates a SEM image and a Raman image taken from a mineral section. Here, there is clear and accurate overlay between SEM and Raman features. Additionally, Raman imaging detected the presence of biotite which is not visible in the SEM image.

Figure 1: a) SEM image of mineral section b) Corresponding Raman image illustrating the distribution of rutile (green), oligoclase (red), biotite (blue) and amphibole (purple)

Fig. 1

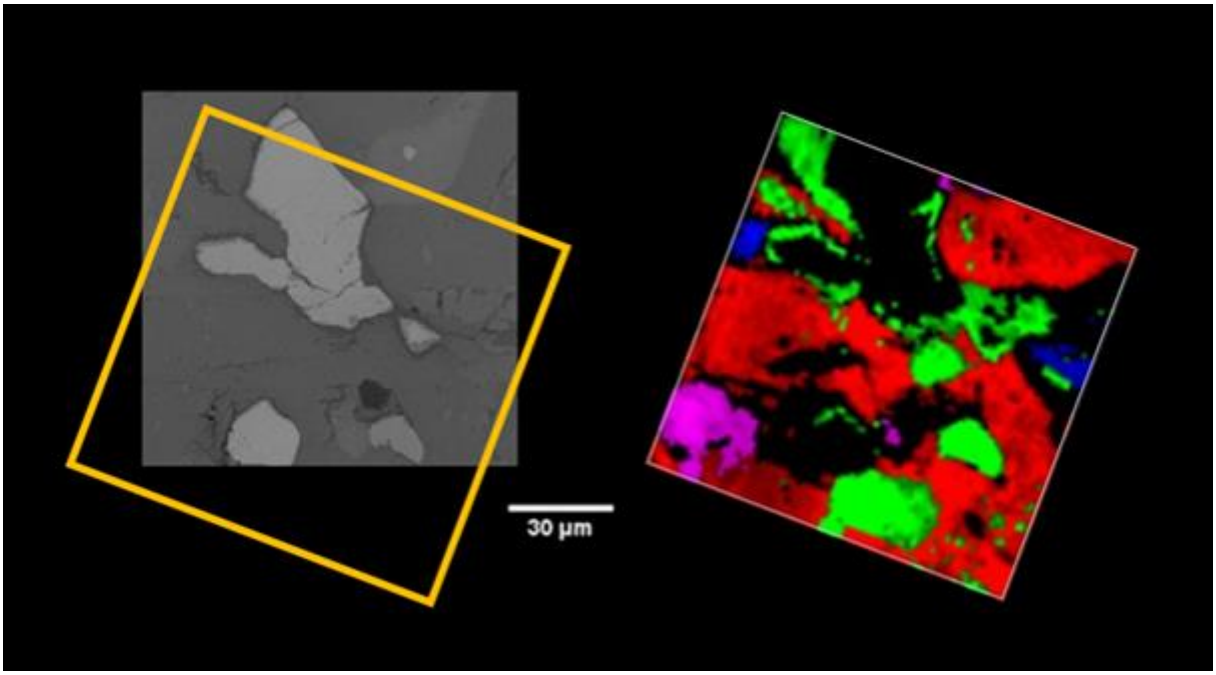

MSLB.P005

Characterization of high density (111) textured nanotwinned Ag thin film evaporated on an 8-inch Si wafer

T. H. Chuang[1]

[1]National Taiwan University, Department of Materials Science and Engineering, Taipei, Taiwan

It is known that the atomic diffusivity of (111)- orientation surface is 3 to 5 order of magnitude higher than (110) and (100) surfaces, leading to the decrease of Cu to Cu bonding temperature to 150℃. In the present study, an 8-inch Si wafer has been evaporated firstly with Ag nanotwinned thin film with a thickness about 4 μm using the assistance of ion beam bombardment. FIB cross-sectional image reveals many columnar grains with an average width about 0.5 μm containing numerous parallelly aligned Ag nanotwins. XRD spectrum showed a strong Ag (111) peak without any other crystal orientations both in the central and edge regions, indicated the (111)- preferred orientation of the Ag nanotwinned films. The results are consistent with the top-view EBSD inverse pole figure analysis showing that a very high density of (111) orientation of 85.2% on the surface of the Si wafer. Furthermore, TEM analyses indicated that the twin characteristics of the grain structure in the Ag thin film can be evidenced from the symmetry relationship between the ( )M/( )M and ( )T/( )T diffraction patterns through the inset selected area electron diffraction (SAED) analysis taken from the [011] zone axis. The twin spacing can also be measured from the HR-TEM micrograph, which are ranged from 2 to 15 nm with an average value about 6 nm. It can also be observed from the HR-TEM analyses that the Ag (111) twin boundaries revealed a very fine atomic spacing about 0.2 nm. Finally, the direct wafer bonding at quite low temperatures ranging from 250 to 100℃ has been performed.

Fig.1 XRD and FIB analyses of the Ag nanotwins on Si wafer.

Fig.2 EBSD and TEM analyses of the Ag nanotwins on Si wafer and low temperature direct bonding of the wafers.

Fig. 1

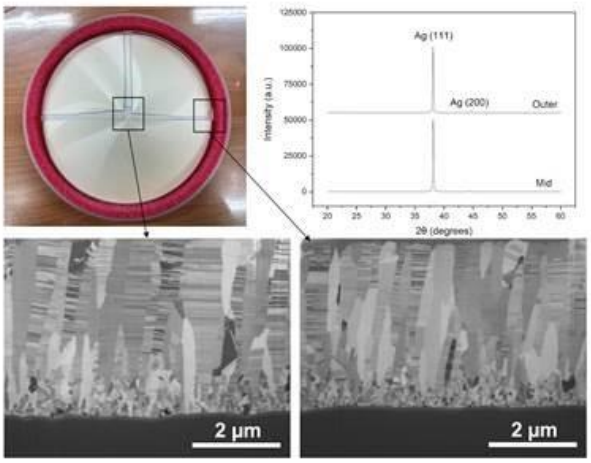

Fig. 2

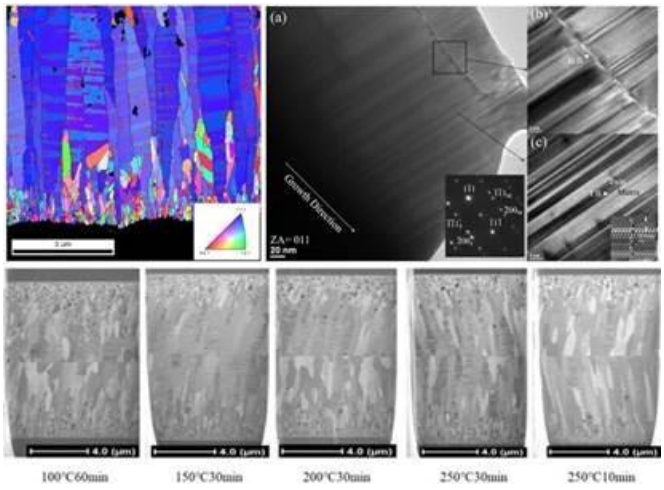

MSLB.P006

Atomic study of structural changes of LiNiO2 at high cutoff-voltage in lithium ion batteries

J. Chen[1], R. House[1], P. Adamson[1], P. Bruce[1]

[1]University of Oxford, Department of Materials, Oxford, United Kingdom

The demand of high-energy lithium-ion batteries boosts the interest in increasing Ni content in cathodes and/or raising charge cutoff voltage. The Co-free LiNiO2 (LNO) has the advantage of lower production cost, high discharge capacity and high energy density compared to traditional LiCoO2, whilst the underlying mechanisms of their capacity loss and degradation when highly charged are not fully understood. The issues along with high charged states include surface O2 evolution and structural degradation. Finding pathways to unlock extra capacity is contingent upon an exact understanding of their structural behaviours. Several decades of effort worldwide have been devoted to developing characterization techniques across multiscale to study the mechanisms involved LNO charge storage but the knowledge still lacks regarding the nanoscale evolution. Here, we use the atomic-resolution annular dark-field scanning transmission electron microscopy (ADF-STEM) combined with electron energy loss spectroscopy (EELS) to directly examine intrigue structural and chemical change mechanisms during the LNO electrochemical process. We have directly visualised the surface densification, void formation at the bulk, stacking fault evolution of LNO over charging to high cut-off voltage. We also provide detailed EELS spectroscopy analysis of Ni oxidation changes at different charged states, comparing the trends at different distances to the surface. This offers atomic-level insights of structural behaviours and degradation mechanisms of highly charge LNO in lithium-ion batteries.

MSLB.P007

Conductive filler networks in flexible conductive composites

D. Perius[1], A. Taranovskyy[1], L. González-García[2], T. Kister[1], T. Kraus[1,3]

[1]INM Leibniz institute for new materials, Structure Formation, Saarbrücken, Germany
[2]INM Leibniz institute for new materials, Electrofluids, Saarbrücken, Germany
[3]Saarland University, Colloid and Interface Chemistry, Saarbrücken, Germany

Flexible, electronic hybrid, and composite materials combine mechanical elasticity and electrical conductivity by forming a conductive particle network. The performance of such "network materials", i.e., particle-based composites, battery materials, etc., is dominated by the morphology of the conductive filler particle network and the contact resistances between particles.

Here, we study the structure of the particle network of conductive silver spheres in a silicone elastomer matrix. A conductive network with macroscopic conductive paths is formed at the concentration required to meet the vol% of the percolation threshold in the electrically insulating. We investigate selected morphological parameters as a function of filler volume fraction and correlate the trends with macroscopic electrical conductivities.

Spherical silver particles (average diameter 2.5µm) were dispersed in a polydimethylsiloxane (PDMS) elastomer matrix with different silver volume fractions from 25 - 45 vol%. Macroscopic four-point measurements were performed at different volume fractions to analyze the electrical conductivity of the composites. We use Focused Ion Beam – nanotomography (FIB-nt) of volumes with a statistical number of particles to reveal the 3D particle network structure for each silver volume fraction (Figure 1). Post-processing of the 3D reconstruction provided information such as geometric tortuosity distributions, particle coordination number distributions, percolation fractions, particle-particle contact area distributions, and the number of shortest paths.

The mean tortuosity decreased with increased filler volume fraction, indicating shorter conductive paths with fewer interfaces. The mean coordination number increased with the volume fraction, increasing the number of potentially conductive contacts. We observe an increase of the average contact area with volume fraction which indicates an increasingly jammed packing of the particles above the percolation threshold. The overall increase in conductivity could be explained by a more interconnected network with reduced particle contact resistances.

Fig. 1

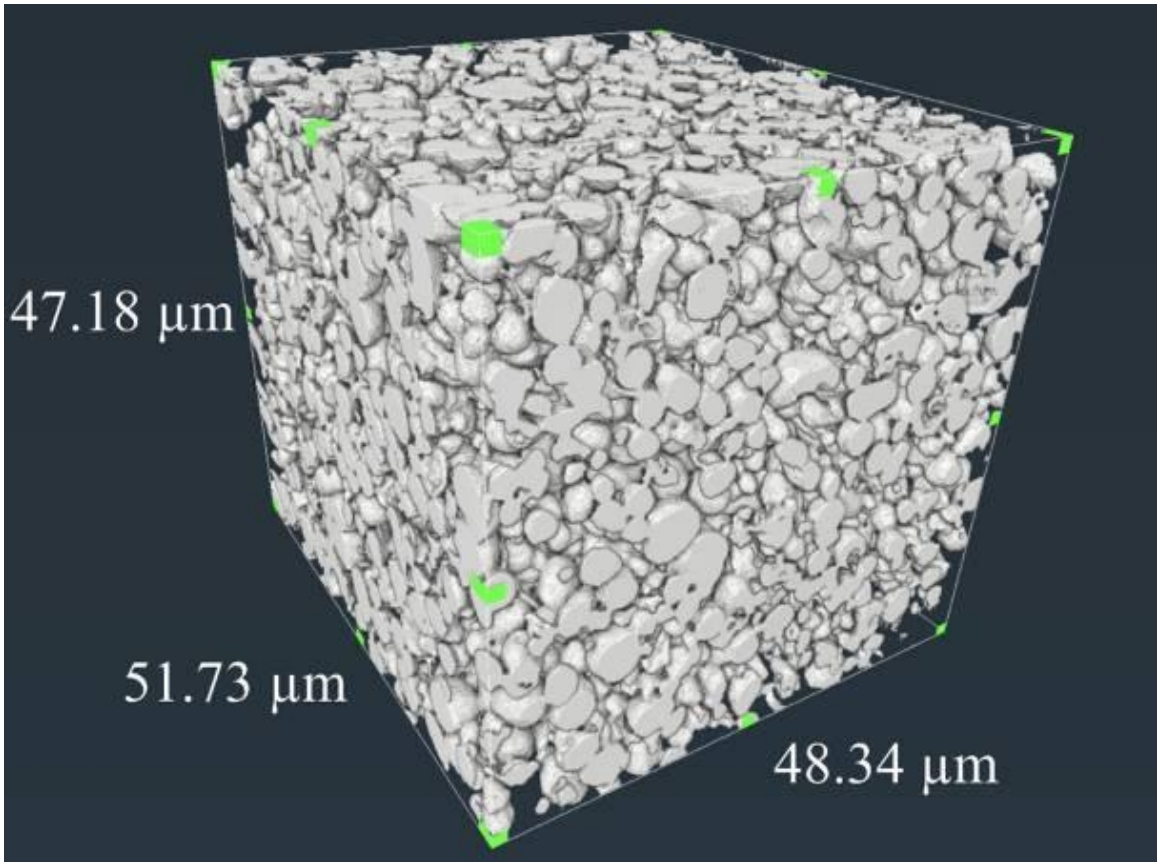

MSLB.P008

Synthesis and morphological and electrochemical characterization of graphene quantum dots

R. Ortiz[1,2], H. Osorio[1,2], C. Santacruz[1,2], K. Encalada[1,2]

[1]Escuela Politécnica Nacional, Física, Quito, Ecuador
[2]Escuela Politécnica Nacional, Quito, Ecuador

Graphene quantum dots (GQDots) have outstanding properties such as low toxicity, high biocompatibility, tunable fluorescent emission, high stability, and great versatility due to their abundant edges that allow their chemical functionalization. In this sense, it is necessary to have synthesis methods that allow their production in a controlled manner, being of low cost and low environmental impact. Therefore, in this study GQDots functionalized with amino groups were obtained by means of hydrothermal synthesis. The synthesis starts by obtaining graphene through the electrochemical exfoliation of graphite, its subsequent oxidation by the modified Hummers' method, and finally applying the hydrothermal treatment to this oxide. The materials obtained in this process were characterized by different microscopic and spectroscopic techniques. Atomic force microscopy confirmed that graphene nanosheets of 6.02 ± 2.73 nm wide and 1.04 ± 0.32 µm long were obtained. On the other hand, spectroscopic techniques (UV-Vis and FTIR) allowed for verifying the effectiveness of Hummers' method for the oxidation of graphene nanosheets. After applying the hydrothermal treatment to the graphene oxide, using different reaction times and temperatures, the formation of GQDots was verified by atomic force microscopy. The expected amino functionalization of the GQDots was verified by FTIR spectroscopy. The optical properties of these quantum dots were studied by UV-Vis and fluorescence spectroscopy, showing that absorption mechanisms in UV-Vis spectrum function as secondary mechanisms of fluorescent emission. Also, GQDots with higher reaction times have stronger fluorescent emission. Finally, the GQDots were used to modify the surface of a glassy carbon electrode, studying the change in the electrochemical sensitivity of this electrode using cyclic voltammetry. GQDots under certain synthesis parameters can increase the electrochemical signal detected. However, the phenomenon that shields the interaction of the modified electrode surface is still unknown.

Fig. 1

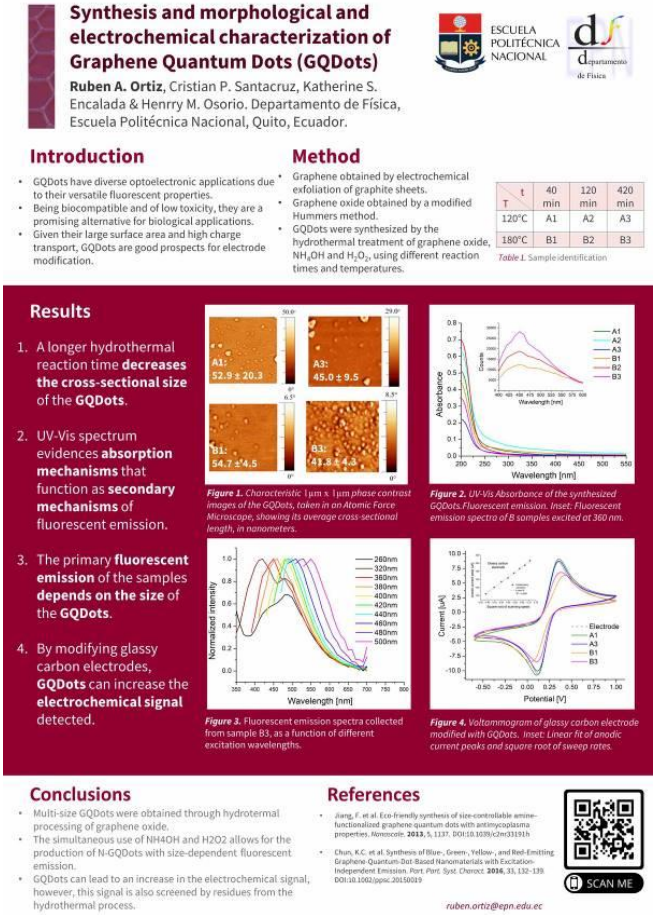

Fig. 2

Synthesis and morphological and electrochemical characterization of Graphene Quantum Dots (GQDots)

Ruben A. Ortiz, Cristian P. Santacruz, Katherine S. Encalada & Henrry M. Osorio. Departamento de Física, Escuela Politécnica Nacional, Quito, Ecuador.

ESCUELA POLITÉCNICA NACIONAL

departamento de Física

Supplementary information

Graphene morphology

- 143 nanosheets were studied.
- The obtained graphene exhibits suitable dimensions to be a precursor for the synthesis of GQDots.

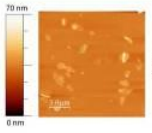

Figure 5. 10 x 10 µm characteristic image taken under an atomic force microscope. Graphene nanosheets are characterized.

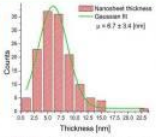

Figure 6. Thickness distribution for the studied graphene nanosheets.

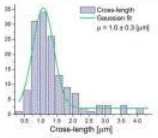

Figure 7. Cross-length distribution for the studied graphene nanosheets.

Graphene oxidation

- Infrared spectroscopy exhibits the resonance of oxygenated bonds through carbonyl, hydroxyl and alkoxy groups.

Figure 8. Schematic of graphene oxidation by the modified Hummers' method.

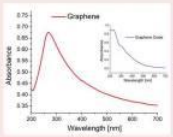

Figure 9. UV-Vis absorption spectra. Oxidation of graphene is verified by the emergence of the absorption band centered at 301 nm.

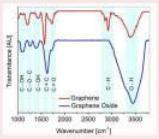

Figure 10. FTIR spectra of precursor materials. Oxidation of graphene confirmed by finding new peaks associated with oxygenated functional groups

Amine functionalization

FTIR spectroscopy shows the resonance of nitrogenated bonds, associated with amine groups. GQDots with higher reaction times have stronger fluorescent emission.

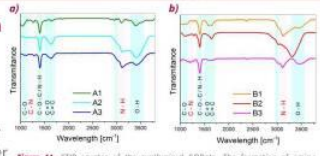

Figure 11. FTIR spectra of the synthesized GQDots. The formation of amine functional groups is confirmed by the appearance of peaks associated with the deformation of the N - H and N - C bonds. (a) A samples. (b) B samples.

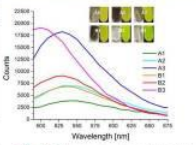

Figure 12. Fluorescence spectra collected under 460 nm excitation. Inset: fluorescent emission shown under 470 nm excitation.

Cyclic voltammetry assays

Peak anode current values adjust linearly to the square root of scan rates, showing that doping with graphene quantum dots does not change the charge transport mechanism.

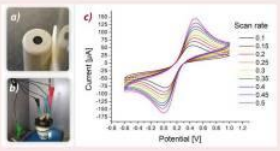

Figure 13. a) GQDot modified glassy carbon electrode. b) Three-electrode experimental arrangement. c) Cyclic voltammetry tests measured at different sweep rates.

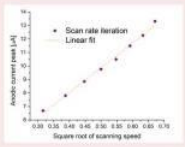

Figure 14. a) GQDot modified glassy carbon electrode. b) Three-electrode experimental arrangement. c) Cyclic voltammetry tests measured at different sweep rates.

ruben.ortiz@epn.edu.ec

MSLB.P009

Ti-6Al-4V ELI alloy subjected to mechanical surface modification and gas nitriding

L. Maj[1], J. Morgiel[1], D. Tobola[2], M. Pomorska[1], M. Wytrwal-Sarna[3]

[1]Institute of Metallurgy and Materials Science, Polish Academy of Sciences, Krakow, Poland
[2]Łukasiewicz Research Network – Krakow Institute of Technology, Krakow, Poland
[3]Academic Centre for Materials and Nanotechnology, AGH University of Science and Technology, Krakow, Poland

Titanium alloys, like most widely used Ti-6Al-4V, are well known for their high specific strength, biocompatibility and corrosion resistance. However, relatively low wear resistance hinders its eventual application when a direct contact with other ones is required. Thus, a number of methods have been developed with the aim to increase the wear resistance and extend the life-time of the parts produced of such materials. Nitriding has been confirmed as one of the most promising methods of producing a hard and well adhering TiN coating on the top of Ti-based material. Recent reports indicate that nitriding may be even more effective in temperature-time scale if fast diffusion channels are formed by increasing the density of grain boundaries and/or generating a large amount of dislocations in the substrate subsurface area by its plastic deformation. However, understanding the phase transformations taking place at the surface is possible only though the micro- and nanoscale study carried out with the help of the cutting-edge electron microscopes.

Therefore, in this work, the influence of the surface plastic deformation of the Ti-6Al-4V ELI alloy on the formation of TiN coating during gas nitriding was studied. The substrate material was subjected to turning and subsequent low-temperature gas nitriding realized at 540°C for 8, 16 and 24 h. The surface topography was analyzed with Hommel Tester T1000. The microstructure characterization, phase and chemical analysis were carried out with ThermoFisher"s scanning (SEM) and transmission (TEM) electron microscopes i.e. Scios 2 Dual Beam and Themis G2 200 FEG, respectively, both equipped with energy dispersive X-ray spectrometers (EDS). The surface analysis was also done with the scanning Microprobe PHI 5000 Versa Probe II X-ray photoemission spectrometer (XPS). The microhardness of the sample was determined with an FM 7 stand equipped with a Vickers indenter.

The SEM, TEM and XPS characterization of the subsurface area allowed to reveal that the whole surface of the as-turned alloy is coated with un-evenly distributed amorphous tribo-layer acting as an effective nitrogen diffusion barrier preventing formation of titanium nitrides. The growth of TiN layer is also hindered by the presence of continuous a-Al2O3 at the tribo-material/substrate. The thickness of TiN layer after 24h of gas nitriding was measured to be ~100 nm. The results of indentation experiments showed an increase in hardness by ~10% measured for as-machined material and after 24 h of gas nitriding treatment.

Acknowledgment: This work was financially supported by National Science Centre of Poland, grant number UMO-2020/39/D/ST8/02610

MSLB.P010

Post-processing study of focused ion beam and conventional TEM specimens

S. Drev[1], P. Drnovšek[1], M. Koblar[2], M. Čeh[1,3]

[1]Jožef Stefan Institute, Center for Electron Microscopy and Microanalysis, Ljubljana, Slovenia
[2]Jožef Stefan Institute, Electronic ceramics department, Ljubljana, Slovenia
[3]Jožef Stefan International Postgraduate School, school, Ljubljana, Slovenia

Focused ion beam sample preparation and conventional sample preparation have an important role in transmission electron microscopy (TEM). New materials (ceramics, thin films, composites, etc.) that are coming have specific properties and have to be precisely treated and usually post-treated. This poses ever-new challenges, constant adjustments, and improvements in advanced focused ion beam sample preparation, conventional sample preparation, and other TEM preparation techniques.

In this chapter, we compared two nowadays most frequently used TEM sample preparation techniques; focused ion beam sample preparation and conventional sample preparation. Post-processing treatment was performed using NanoMill® (model 1040, Fischione Instruments, Inc.). The study was created for a discussion about different procedures to achieve the best result for the TEM sample.

For the post-processing study of focused ion beam TEM specimens, we study two different approaches. The first TEM sample was pre-thinned using FEI Helios NanoLab NL650 dual-beam Focused Ion Beam (FIB) and cleaned with NanoMill. The second TEM sample was polished using FIB and then thinned and finally cleaned with NanoMill.

For the post-processing study of the conventional TEM sample, we prepared the TEM sample in two different ways. The first TEM sample was ion-milled using PIPS (Precision Ion Polishing System, Gatan Inc.) to achieve perforation and finally post-cleaned with NanoMill. The second TEM sample was dimpled down to transparent thickness (Dimple grinder, Gatan Inc.) and then thinned and finally cleaned using NanoMill.

We want to expose how important these techniques are and how high the quality of the sample that we prepared with this type of sample preparation is. Structural and analytical analysis of TEM samples were investigated on a JEOL ARM 200CF scanning transmission electron microscope with probe Cs corrector.

MSLB.P011

Characterization of Pt-rare-earth nanoparticles by STEM tomography and EDX

M. Hugenschmidt[1], Y. Hu[2], P. Liu[3], S. Bals[1]

[1]University of Antwerp, EMAT, Antwerp, Belgium
[2]Technical University of Denmark, DTU, Department of Energy Conversion and Storage, Kongens Lyngby, Denmark
[3]Technical University of Denmark, DTU, National Centre for Nano Fabrication and Characterization, Kongens Lyngby, Denmark

The search for sustainable energy sources for transport has intensified recently because of the climate crisis. In addition to batteries for electric motors, fuel cells are gaining increasing interest. Platinum-Rare Earth Metal (Pt-RE) alloy nanoparticles (NP) are promising candidates for use in proton-exchange membrane fuel cells (PEMFCs), which are a sustainable alternative to combustion engines in automobiles and buses (*1*). In such PEMFCs, Pt-RE nanoparticles on carbon black can be used as a catalyst for the oxygen reduction reaction and the oxidization of H_2 (Fig. 1) (*1*). They show long-term stability and high catalytic activity, which would be optimized by a strained Pt surface layer over the alloy core, providing optimal reactant binding energies and preventing dealloying (*2*). Recently, a newly developed chemical synthesis route to prepare Pt-RE nanoalloys with tunable alloy phases and particle sizes has been published (*3*). However, preliminary results on Pt_2Gd have shown that after acid leaching to remove byproducts, nanoporous structures with yet unclear 3D distribution of elements are obtained (*2*, *3*).

Here, we present an analysis of the elemental distribution and 3D shape of Pt2Gd nanoalloys. The electron-dispersive X-ray (EDX) map in Figure 2b shows the segregation of Pt and Gd in the particle. The map has been acquired using a Super-X detector at an FEI Osiris S/TEM at 200 kV and a total dose of 3E+6 $e^-/Å^2$ from the particle depicted in Figure 2a. Noise in the elemental maps has been reduced by principal component analysis using the hyperspy toolbox (*4*). A comparison between the HAADF-STEM image and the elemental distribution indicates that darker areas in the STEM image contain more Gd, and appear darker due to the lower atomic number of Gd.

HAADF-STEM tilt series for electron tomography of Pt_2Gd NPs have been acquired using a probe-corrected Titan^3 80-300 equipped with a Fischione photomultiplier STEM detector and operated at 300kV. Figure 2c shows an orthoslice of the volume reconstructed using a workflow based on the ASTRA toolbox (*5*), indicating a porous structure with a denser core. A comparison with Figure 2b however suggests that the darker areas observed in Figures 2a and 2c do not correspond to voids but rather locations in the sample where the Gd might have been segregated.

The investigation of a larger number of particles, ideally in conjunction with EDX tomography is necessary to further clarify this observation beyond doubt. EDX tomography, however, is challenging due to the beam sensitivity of the material.

Fig. 1: Scheme of a proton-exchange membrane fuel cell. Pt-RE nanoparticles on carbon black are used as the yellow-marked anode (left) and cathode (right).

Fig. 2: a) HAADF-STEM image b) Overlay elemental map of Pt (red) and Gd (blue) from the same particle as in (a). c) Orthosclice from STEM Tomography from another nanoparticle.

References

1. M. Shao, Q. Chang, J.-P. Dodelet, R. Chenitz, *Chem. Rev.* **116**, 3594–3657 (2016).
2. Y. Hu *et al.*, *Chem. Mater.* **33**, 535–546 (2021).
3. Y. Hu, J. O. Jensen, L. N. Cleemann, B. A. Brandes, Q. Li, *J. Am. Chem. Soc.* **142**, 953–961 (2020).
4. F. de la Peña *et al.*, hyperspy/hyperspy: Release v1.7.1 (2022), doi:10.5281/zenodo.6659919.
5. W. van Aarle *et al.*, *Ultramicroscopy*. **157**, 35–47 (2015).

Fig. 1

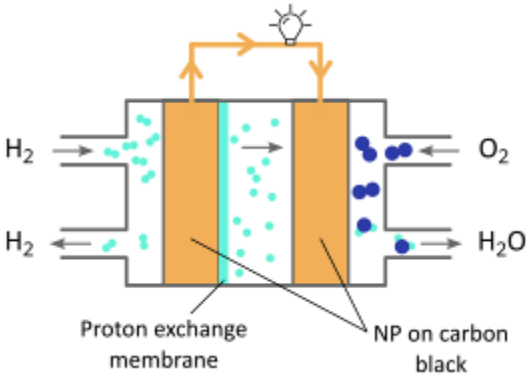
H2
H2
O2
H2O
Proton exchange membrane
NP on carbon black

Fig. 2

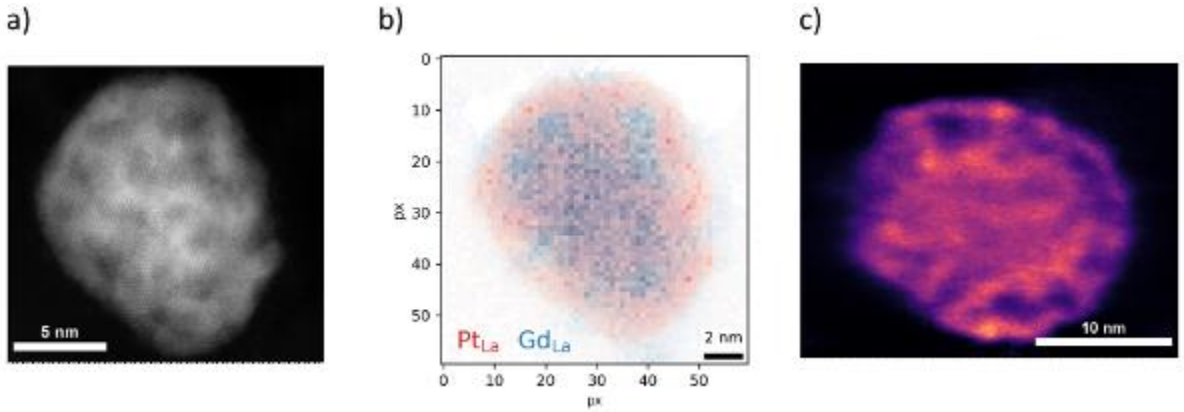
a)
5 nm
b)
PtLa
GdLa
2 nm
px
px
c)
10 nm

MSLB.P012

Direct atomic resolution imaging of superstructure in $LiCoPO_4$ cathode material by simultaneous ADF- and iDPC-STEM modes

M. Meledina[1], A. Meledin[1], E. G. T. Bosch[1], I. Lazić[1], X. Wu[2], U. Simon[2], B. Markus[1], S. Lazar[1], P. Longo[1]

[1]Thermo Fisher Scientific, Eindhoven, Netherlands
[2]RWTH Aachen University, Institute of Inorganic Chemistry, Aachen, Germany

$LiCoPO_4$ is a promising cathode material for the high voltage lithium-ion batteries. However, the moderate cycling stability of the material limits its practical applications. One of the major reasons of the capacity fade of LiCoPO4 is related to its structural degradation: Li and Co site exchange leads to the blocking of the Li+ transport channels[1]. The stabilization of the atomic structure of the material directly depends on the capability to gain knowledge on the degradation mechanisms though advanced characterization.

Cathode materials are obstinate candidates for TEM investigations due to their poor stability under the electron beam. To deal with radiolysis while imaging $LiCoPO_4$ reduced electron dose should be applied. Here, we exploit simultaneous ADF-STEM and iDPC-STEM[2,3] imaging to investigate the $LiCoPO_4$ cathode material down to atomic scale, as iDPC-STEM allows for extremely low dose imaging of beam sensitive materials[4,5]. By combining the experimental and simulation results a superstructure at the surface of the $LiCoPO_4$ nanoparticle is revealed, where every second Li site is partially occupied by Co atoms (Figure 1).

Figure 1. Simultaneously recorded, using HAADF and Panther detectors, high resolution ADF- and iDPC-STEM images (from left to right) of the superstructure at the surface of the $LiCoPO_4$ nanoparticle, viewed along the [001] zone axis, together with the corresponding simulations and proposed surface structure. The probe corrected beam conditions: HT 300kV, Convergence semi-angle 30 mrad, Beam current 15 pA.

[1] X. Wu, M. Meledina, J. Barthel, et. al., *Energy storage materials* **22** (2019) 138

[2] I. Lazić, E.G.T. Bosch and Sorin Lazar, *Ultramicroscopy* **160** (2016) 265

[3] I. Lazić and E.G.T. Bosch, *Advances in Imaging and Electron Physics* **199** (2017) 75

[4] B. Shen, H. Wang, H. Xiong, et al., *Nature* **607** (2022) 703

[5] I. Lazić, M. Wirix, M. L. Leidl et. al., *Nature Methods* **19**, (2022) 1126

Fig. 1

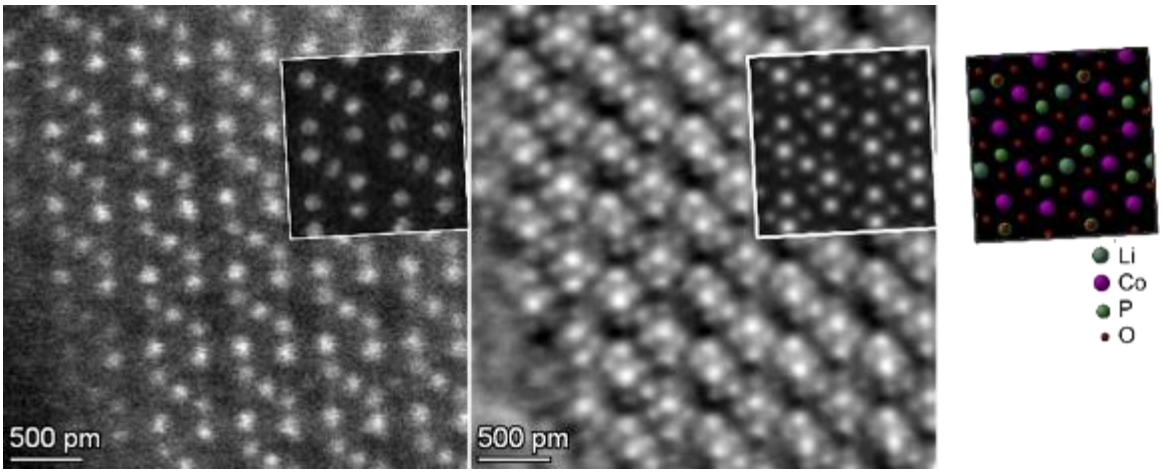

MSLB.P013

Single atom Pt on Pd@Au and Pd shell on AuPt nanowire: application in electrocatalysis

M. Gayen[1], D. Chatterjee[1], S. Shetty[1], P. B.[1], R. Narayanan[1]

[1]Indian Institute of Science, Bengaluru, India

Off late, research in nanoscience emerged as front-runner due to its tremendous industrial applications including application in renewable energy resources. Due to depleting fossil fuel reserves and ever-growing demand for environment friendly renewable energy resources, researchers are trying to develop efficient catalyst for energy conversion. Catalysts based on nanomaterials is one of the focused areas of research. Specifically, one dimensional nanomaterial is widely explored in catalytic applications due to high surface area. Ultrathin Au nanowires have been explored for several applications, but the fragile nature at high temperature, and in polar medium limits its catalytic applications. Instability of these nanowires under the electron beam possess difficulties for its microstructural study. Alloying of Au nanowire with Pd and Pt increases the stability as well as improves electrocatalytic efficiency with faster kinetics due to bifunctional mechanism. In our current investigation, ultrathin single crystalline AuPdPt trimetallic nanowires with different composition have been synthesized using microwave assisted synthesis at liquid-liquid interface. By changing the order of second and third metal reduction on Au nano wire template, single atom Pt on Pd@Au nanowire and Pd shell on AuPt nanowire have been synthesized. Interestingly, these trimetallic nanowires retains single crystalline nature after successive reduction of second and third metal on Au nanowire. Using z-contrast high angle annular dark field imaging (HAADF-STEM), x-ray photoelectron spectroscopy (XPS) and cyclic voltammetry surface atomic distribution as well as chemical environment have been elucidated. Annealing under control atmosphere, e.g., Ar and CO, was performed to modify the surface of these nanowires. Surface atomic distribution has been further visualized and explained using z-contrast HAADF-STEM, and electrocatalysis. Single atom Pt on Pd@Au nanowire showed highest activity with moderate onset potential compared to bimetallic Pd@Au nanowire. After Ar-annealing, alloying improvement led to vanishing Pt single atom rom surface. Whereas CO-annealing caused PdPt segregation on surface leading to improved potential and activity. Ar-annealed Pd shell on AuPt nanowire showed better kinetics than as-synthesized one resulting lower onset potential. CO-annealed Pd shell on AuPt nanowire showed highest activity with higher potential. These nanowires were explored as catalyst for electrocatalytic methanol oxidation. Further, changes in activity with surface atomic distribution has been visualised and explained by electron microscopy.

MSLB.P015

Direct observation of domain-wall-free ferroelectricity in Y-doped HfO_2

K. Song[1], K. J. Go[2], A. Mostaed[3], P. Nellist[3], S. Y. Choi[2]

[1]Korea Institute of Materials Science, Changwon, South Korea
[2]POSTECH, Pohang, South Korea
[3]University of Oxford, Oxford, United Kingdom

Due to the recent discovery of ferroelectricity in doped Hafnium Oxide (HfO_2) film, HfO_2-based materials have significantly attracted lots of attention in the semiconductor industry because of their strong compatibility with Si-based Complementary Metal-Oxide-Semiconductor (CMOS) and thereby their potential for fully integrated ferroelectric devices. The equilibrium phase diagram of bulk HfO_2 consists of non-ferroelectric polymorphs that are the monoclinic ($P2_1/c$, O phase), tetragonal ($P4_2/nmc$, T phase), and cubic ($Fm\text{-}3m$, C phase) phases. The ferroelectric HfO_2 is the metastable, orthorhombic phase ($Pca2_1$), where a unit cell is divided into active cell/inactive cell, in which oxygen atoms can/cannot generate electric dipole. Based on the flat phonon band theory, the inactive cell is predicted to be an inherent spacer between neighboring active cells and therefore inactive cells enable electric dipoles to switch without forming a domain wall [1].The domain-wall-free ferroelectric behavior in HfO_2 has been directly identified by TEM analyses [2,3], but is still challenging due to the polymorphism in doped HfO_2 and pico-metric regime of structural modulation. In this work, we present an atomistic behavior of ferroelectricity in epitaxially grown Yttria-doped HfO_2 (YHO). The crystallographic structure of YHO is quantitatively analyzed by scanning transmission electron microscopy combined with computational techniques via deep machine learning. Furthermore, we apply a 4D-STEM ptychography to visualize the electric field distribution in YHO. Combined experimental results show YHO can hold polarization within a width of to a single unit cell. Boundary cells, inactive cells between the up- and down-polarized cells, are investigated by our first-principle calculation, and our atomistic analysis confirmed that boundary cell possesses the same structure with the inactive cell in bulk YHO, indicative of the absence of the domain wall. This result gives the new insight into the realization of unit cell scale control of ferroelectric materials.

[1] Lee et al., Science 369 (6509), 1343-1347 (2020)

[2] Xu et al., Nature Materials 20, 826–832 (2021)

[3] Kang et al., Science 376 (6594), 731-738 (2022)

MSLB.P016

Multiscale tomography of porous transport electrodes in proton exchange membrane water electrolyzers

M. Bierling[1], D. McLaughlin[1], T. Böhm[1], S. Thiele[1]

[1]Helmholtz-Institut Erlangen-Nürnberg für Erneuerbare Energien, Elektrokatalytische Grenzflächenverfahrenstechnik, Erlangen, Germany

The transition to a carbon-neutral energy sector is linked with the implementation of energy storage solutions. The need for energy storage is due to the fluctuation and intermittency of renewable energy sources. Hydrogen, as an energy carrier produced from electrochemical water splitting, is a promising candidate as a storage solution. Proton exchange membrane water electrolyzers (PEMWEs) are suited to produce hydrogen in a renewable energy-based energy infrastructure due to their flexibility, rapid system response, and scalability.

The membrane electrode assembly of PEMWEs consists either of a catalyst-coated membrane (CCM) or a porous transport electrode (PTE) configuration. In the latter, the catalyst ink is directly coated onto the porous substrate, typically a titanium fiber or sintered titanium powder porous transport layer (PTL) on the anode side.

To date, the CCM configuration is prevalent, but the PTE configuration is a promising alternative concept for PEMWEs.[1] Its different fabrication approach allows the usage of a wider variety of membranes and can reduce the number of processing steps in manufacturing compared to the fabrication of CCMs. However, the PTE design has higher kinetic overpotentials due to a worse connection between catalyst particles and the membrane.[2] The less efficient catalyst utilization originates from the deep infiltration of the catalyst ink into the PTL. We could prove this catalyst distribution and the associated worse catalyst utilization in our recently submitted paper.[3]

Further improvements in PTEs are necessary to make them competitive against CCMs. One essential objective is to understand the whole structure of PTEs to elucidate the transport-activity nexus of these electrodes. Therefore, we used a combination of different tomographic methods to image the structure of the titanium fiber substrate, the IrO_2 catalyst layer, and its catalyst distribution. X-ray tomography and focused ion beam scanning electron microscopy (FIB-SEM) were employed to resolve the whole electrode on the µm- and nm-scale for the first time. Based on the reconstructions, we calculated the structural and transport parameters of the PTE. The analysis revealed the distribution and thickness of the catalyst layer and the grain and pore size distributions on the different length scales. Our correlative microscopy approach revealed that future PTE designs should aim to use a PTL with a porous blocking layer or a micro-porous layer.

[1] M. Bühler, F. Hegge, P. Holzapfel, M. Bierling, M. Suermann, S. Vierrath, S. Thiele, *Journal of Materials Chemistry A* 2019, *7*, 26984.

[2] D. Kulkarni, A. Huynh, P. Satjaritanun, M. O"Brien, S. Shimpalee, D. Parkinson, P. Shevchenko, F. DeCarlo, N. Danilovic, K. E. Ayers, C. Capuano, I. V. Zenyuk, *Applied Catalysis B: Environmental* 2022, *308*, 121213.

[3] M. Bierling, D. McLaughlin, B. Mayerhöfer, S. Thiele, Towards understanding catalyst layer deposition processes and distribution in anodic porous transport electrodes in proton exchange membrane water electrolyzers (submitted).

MSLB.P017

Visualising the spatial distribution of individual molecular dopants of organic semiconductors on the sub-nanometre scale in three dimensions

G. Persson[1], E. Järsvall[2], M. Röding[3,4], R. Kroon[2,5], Y. Zhang[6,7], S. Barlow[6,7], S. Marder[6,7,8,9], C. Müller[2], E. Olsson[1]

[1]Chalmers University of Technology, Department of Physics, Gothenburg, Sweden
[2]Chalmers University of Technology, Department of Chemistry and Chemical Engineering, Gothenburg, Sweden
[3]RISE Research Institutes of Sweden, Biomaterials and Health, Agriculture and Food, Gothenburg, Sweden
[4]Chalmers University of Technology, Department of Mathematical Sciences, Gothenburg, Sweden
[5]Linköping University, Laboratory of Organic Electronics, Norrköping, Sweden
[6]Georgia Institute of Technology, School of Chemistry and Biochemistry and Center for Organic Photonics and Electronics, Atlanta, GA, United States
[7]University of Colorado Boulder, Renewable and Sustainable Energy Institute, Boulder, CO, United States
[8]University of Colorado Boulder, School of Chemical and Biological Engineering, Boulder, CO, United States
[9]University of Colorado Boulder, School of Chemistry, Boulder, CO, United States

Molecular dopants are used to enhance the electronic properties of organic electronics. The three dimensional distribution of the dopants and whether they are present as individual dopants or in clusters determines the electrical properties. In applications, the dopant concentration varies depending on application but it can be up to several molar precents.The dopants are about 1 nm in size and the distance between them is about a few to 10 nm. A detailed information about the spatial distribution is important for the understanding of the conduction mechanisms and how the molecular dopants affect the properties of the surrounding polymer. 1,2

In this study, electron tomography is used to visualize the three-dimensional spatial distribution of individual Mo(tfd-COCF3)3 molecular dopants in the semiconducting polymer p(g42T-T) at the sub-nanometer scale.The thickness of the films is in the range of 13-17 nm and dopant concentrations are 5, 20 and 40 mol%.The acquisition parameters are chosen to obtain sufficient resolution to determine the position of individual dopant molecules in the material. A heterogenous distribution is observed. At dopant concentrations of 5 mol%, the majority of the dopants are positioned individually or in clusters consisting of less than five molecules. At higher concentrations, the dopants form larger sized clusters with increasingly elongated shapes. Despite the larger cluster sizes at higher concentrations, all of the observed dopants remain adjacent to surrounding polymer. This is a crucial aspect for the efficient charge transfer between the dopants and the surrounding polymer. Finally, electrical characterization using a four-point probe setup shows a decrease in thin-film conductivity as larger dopant clusters are formed at high dopant concentrations. 3

1 C.J. Boyle *et al.*, *Nat. Commun.*, 2019, **10**, 1-10

2 A. Fediai *et al.*, *Phys. Chem. Chem. Phys.*, 2020, **22**, 10256-10264

3 G. Persson *et al., Nanoscale,* 2022, **14**, 15404-15413

Fig. 2

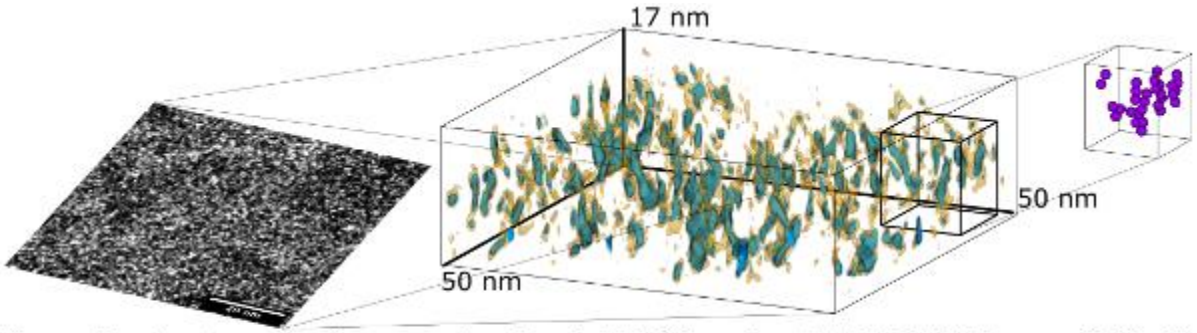

Figure: Electron tomography reconstruction (middle) based on HAADF-STEM images (left) of representative areas in a film doped with 40 mol% Mo(tfd-$COCF_3$)$_3$ dopant species. Blue intensity thresholds in the reconstructions were chosen in order to visualise the position of dopant species. A lower intensity threshold is displayed in yellow. Examples of individual dopant species' positions are seen to the right.

MSLB.P018

Hierarchical self-assembly involving nonclassical and classical steps in organic crystal growth

H. Weissman[1], I. Biran[1], S. Rossene[1], Y. Tsarfati[1], B. Rybtchinski[1], L. Houben[2]

[1]Weizmann Institute of Science, Molecular Chemistry and Material Science, Rehovot, Israel
[2]Weizmann Institute of Science, Department of Chemical Research Support, Rehovot, Israel

Organic crystal nucleation and growth are complex processes that often do not fit into the scope of the existing crystallization theories. We investigated a crystal growth mechanism of an organic dye, perylene diimide, using high-resolution cryogenic transmission electron microscopy and optical spectroscopy. We were able to demonstrate that the evolution of order in our system had a high level of complexity and involved both classical and nonclassical steps. The crystallization mechanism included a series of supramolecular transformations, where each step defined the next one. The crystal growth started from a molecular self-assembly into π-stacks that eventually underwent intermolecular ordering that optimized interactions within the stacks. The latter transformed at the larger scale, by stack interactions, which formed crystalline domains. Finally, the formed faceted crystals gradually grew through oriented attachment of other crystal, and attachment of residual monomeric molecules from solution (Figure 1).

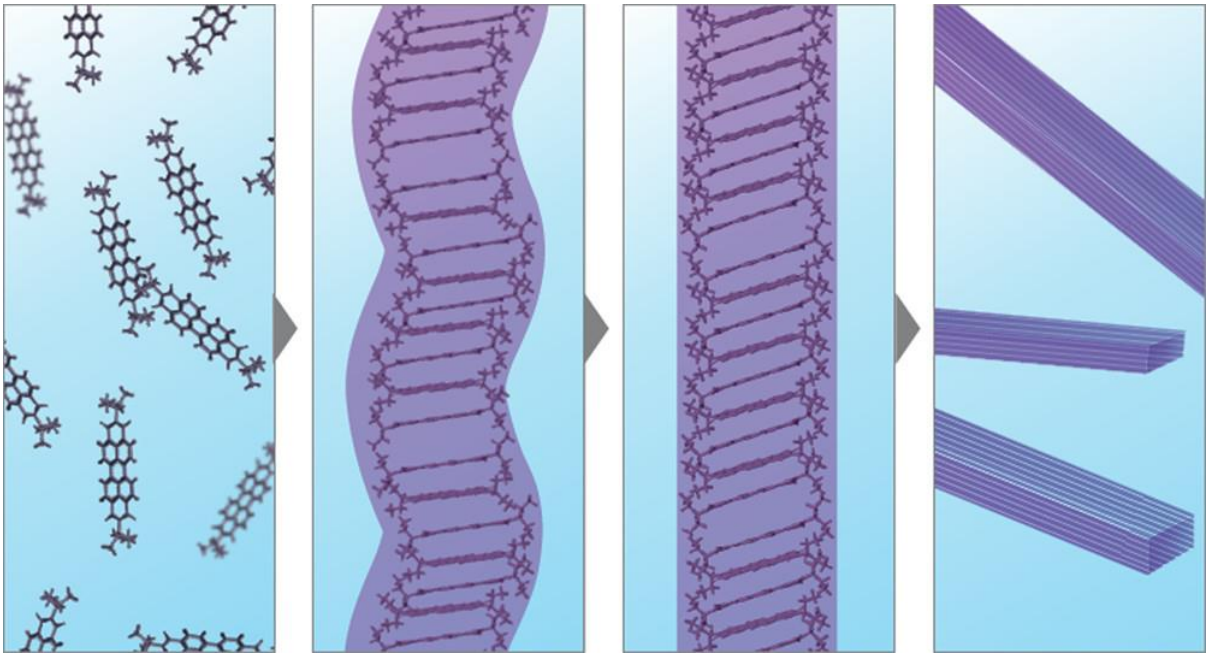

Fig.1 An illusration of order evolution during the crystallization of perylene diimide.

Our findings present a detailed insight into organic crystal growth and reveal that both classical and nonclassical mechanisms can operate within a crystallization process. However, classical/nonclassical dichotomy provides only a partial insight into the crystallization mechanism, which may be described as a sequence of supramolecular events, traversing a vast size scale from the optimization of intermolecular interactions to the oriented attachment of crystals. In summary, our work revealed the inherent nature of supramolecular transformations occurring in organic crystallization, thus advancing conceptually our understanding of order evolution in organic matter.[1]

1. Biran, I.; Rosenne, S.; Weissman, H.; Tsarfati, Y.; Houben, L.; Rybtchinski, B. *Cryst. Growth Des.* **2022**, 22 (11), 6647–6655.

LSLB.P002

Crosshair: semiautomated targeting for electron microscopy

I. Romero Brey[1], H. Fleckenstein[1,2], K. Meechan[1], M. Bernabeu[2], Y. Schwab[1]

[1]EMBL Heidelberg, Cell Biology and Biophysics, Heidelberg, Germany
[2]EMBL Barcelona, Tissue biology and disease modelling, Barcelona, Spain

Volume EM brings new insights on cells and tissues ultrastructure in 3D. However the techniques allowing volume EM are low throughput. Increasing the throughput can be achieved, for instance, via targeting approaches that enable replicates and multiplication of observations.

Here we are presenting a newly developed workflow to target structures of interest within a resin-embedded block. The block has to be first trimmed and subsequently imaged by means of X-rays with a microCT machine. The X-ray tomogram generated is a 3D map, from which we can calculate the location of a specific structures of interest using the Fiji plugin called Crosshair (https://github.com/K-Meech/crosshair). The targeting of the structures of interest is then achieved by the use of a motorized ultramicrotome designed by the EMBL electronic and mechanical workshops that allows precise angular movements.

An example of the application of this workflow to find *Plasmodium falciparum*-infected red blood cells in bioengineered 3D microvessels (that mimic the brain blood barrier) is also shown.

Reference:

Kimberly Meechan, Wei Guan, Alfons Riedinger, Vera Stankova, Azumi Yoshimura, Rosa Pipitone, Arthur Milberger, Helmuth Schaar, Inés Romero-Brey, Rachel Templin, Christopher J Peddie, Nicole L Schieber, Martin L Jones, Lucy Collinson and Yannick Schwab. *Crosshair, semi-automated targeting for electron microscopy with a motorised ultramicrotome.* https://doi.org/10.1101/2022.06.02.491151. Accepted to be published in eLife.

LSLB.P003

A streamlined and ice contamination free cryo-electron tomography workflow to improve throughput and data quality

M. Smeets[1], K. Lau[1], D. Daviran[1]

[1]Delmic B.V., Life Sciences, Delft, Netherlands

Cryo-electron tomography (cryo-ET) is a powerful technique that allows researchers to obtain 3D structures at nanometer resolution in their near-native state. In recent years the technique has gained popularity and a large number of complexes have been resolved. This has improved our understanding of the molecular foundation of viral infections1, skeletal muscles2 and Parkinson"s disease3.

To obtain such a high resolution 3D structure, 1000-2000 copies of a protein complex need to be averaged in a process called subtomogram averaging4,5. This means that a high number of high quality tomograms are needed. Unfortunately the workflow is very error-prone and this has limited the data output6. To acquire high quality tomograms there are two main challenges: keeping the sample ice contamination-free and targeting the region of interest (ROI).

At Delmic we developed two workflow solutions called CERES and METEOR to improve the entire cryo-ET sample preparation workflow. The CERES Ice Defence System is based on the tools developed by Tacke et al7 and consists of multiple innovative tools that are tailored to minimize ice contamination during sample handling (CERES Clean Station), transfer (CERES Vitri-Lock) and FIB milling (CERES Ice Shield). METEOR is an integrated fluorescence light microscope (FLM) that greatly enhances the ROI targeting inside the cryo-FIB/SEM while reducing the number of handling steps required.

We show that these innovative tools can lead to improved cryo-ET data quality and throughput.

1. Klein, S. *et al.* SARS-CoV-2 structure and replication characterized by in situ cryo-electron tomography. *Nature Communications 2020 11:1* **11**, 1–10 (2020).
2. Wang, Z. *et al.* The molecular basis for sarcomere organization in vertebrate skeletal muscle. *Cell* **184**, 2135-2150.e13 (2021).
3. Watanabe, R. *et al.* The In Situ Structure of Parkinson"s Disease-Linked LRRK2. *Cell* **182**, 1508-1518.e16 (2020).
4. Chen, M. *et al.* A complete data processing workflow for cryo-ET and subtomogram averaging. *Nature Methods 2019 16:11* **16**, 1161–1168 (2019).
5. Scaramuzza, S. & Castaño-Díez, D. Step-by-step guide to efficient subtomogram averaging of virus-like particles with Dynamo. *PLoS Biol* **19**, e3001318 (2021).
6. Lau, K., Jonker, C., Liu, J. & Smeets, M. The Undesirable Effects and Impacts of Ice Contamination Experienced in the Cryo-Electron Tomography Workflow and Available Solutions. *Micros Today* **30**, 30–35 (2022).
7. Tacke, S. *et al.* A streamlined workflow for automated cryo focused ion beam milling. *J Struct Biol* **213**, 107743 (2021).

LSLB.P004

Biochemical and structural studies of NAPDH oxidase

V. R. A. Dubach[1], P. San Segundo Acosta[1], B. J. Murphy[1]

[1]Max Planck institure for Biophysics, Murphy group, Frankfurt am Main, Germany

Reactive oxygen species (ROS) are crucial for many cellular processes, from cell to cell signaling to redox regulation. In human cells, the NAPDH oxidase (NOX) membrane proteins are a major source of ROS and play a critical role in the innate immune system and redox regulation processes. Yet, there are large gaps in knowledge on crucial aspects of the function of the NOX proteins, especially with regards to electron transfer pathway and reaction mechanism. Structural and in-depth biochemical studies of human NOX proteins have proven difficult due to complications in heterologous expression and purification of active, stable complexes. Therefore, we have used a bacterial NOX homologue from *Streptococcus pneumonia* (spNOX) to gain insight into the structure and mechanism of NOX proteins. SpNOX is a small membrane of ~47 kDa and can be heterologously expressed in its active state, as confirmed by superoxide dismutase-sensitive cytochrome c reduction. The protein is stable at high concentrations and can be prepared for single particle analysis cryo-EM. Preliminary studies have allowed for the resolving of the low-resolution structure that is consistent with the structure predicted using AlphaFold2.

LSLB.P005

SBFI-SEM and 3D reconstruction of polymer particles in a polymer matrix

D. Benke[1], H. Bargel[2], T. Scheibel[2], M. Retsch[1]

[1]University of Bayreuth, Physical Chemistry I, Bayreuth, Germany
[2]University of Bayreuth, Chair for Biomaterials, Bayreuth, Germany

The aim of the project was to perform a 3-dimensional reconstruction of isotropic and anisotropic polymer particles embedded in polymer films using volume SEM (Serial Blockface Imaging, SBFI). For this purpose, isotropic polystyrene (PS) particles with diameter of 1.4 µm were incorporated in PVA films from aqueous solution. To gain anisotropic ellipsoidal particles, the films were stretched unidirectional at different strain ratios above the glass transition point of PS. [1, 2]. Optimization of the sample preparation method for SBFI SEM included contrasting the PVA films with cesium chloride, and addition of 344 nm silica particles during film production as alignment support for the reconstruction. The particle-film samples were embedded in conductive silver epoxy resin, trimmed and cut using SBFI-SEM (Apreo VS, ThermoScientific/FEI) at 40 nm Z-axis and a total volume thickness of at least 12 µm (min. 300 slices) in low-vac mode to reduce charging artifacts. Image stacks were reconstructed using AMIRA software, utilizing the fiducial silica particles for optimized alignment of the images. Morphometric analysis of the PS particles took place after segmentation, following an optimized image data processing routine. Shrinking of the PVA films due to evaporation of residual water content despite equilibration in low vacuum led to deformation artifacts of the reconstructed PS particles. These could be corrected with an approach based on the geometric data of the silica fiducials. The morphological parameters of thus corrected 3D reconstructed PS particles of all stretching conditions correlated well with measurements of the particles isolated from the films in standard SEM. In summary, we could establish a sufficiently accurate 3D reconstruction and analysis of polymer particle/polymer film-systems using SBFI-REM.

References:

1. Ho C. C., K. A., Odell J. A., Ottewill R. H., Preparation of monodisperse ellipsoidal polystyrene particle. *Colloid and Polymer Science* 1993, 271, 469-479.
2. Champion, J. A.; Katare, Y. K.; Mitragotri, S., Making polymeric micro- and nanoparticles of complex shapes. *Proc Natl Acad Sci U S A* 2007, 104 (29), 11901-11904.

Fig. 1

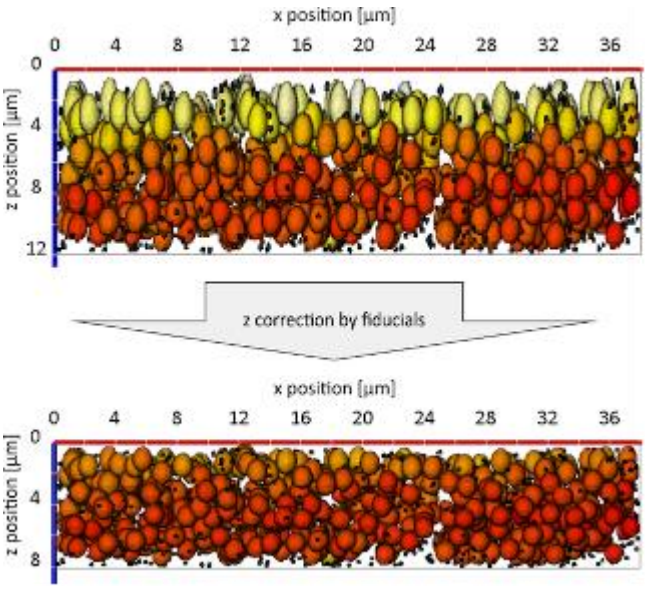

LSLB.P006

Accelerate and deepen our insights into infectious diseases through large-scale 2D and volume electron microscopy combined with artificial intelligence

M. Niessen[1], A. Rus[2], R. Lane[3], M. Schrage[1], K. Lau[1], T. Burgoyne[4]

[1]Delmic, Life science application, Delft, Netherlands
[2]University of Leiden, Leiden, Netherlands
[3]Delft University of Technology, Department of Imaging Physics, Delft, Netherlands
[4]University College London, Institute of Ophthalmology, London, Netherlands

The emergence of new viral variants, which can cause human diseases and pandemics, necessitates a quicker and deeper understanding of the pathogenesis and disease manifestations to develop effective treatments and preventative measures. Viral particles are in the nm range thus their observation requires the nm-resolutions of electron microscopes (EM). EM has been paramount in diagnosing Covid-19 [1] and gaining insights into its disease-causing mechanisms [2]. However, the time-consuming nature and manual operation requirement of conventional EM limit the data throughput, limiting the statistics and understanding over a timespan. Multibeam scanning electron microscope (SEM) technology such as FAST-EM (Delmic B.V., Netherlands) can overcome these bottlenecks. In this work, we apply FAST-EM whole-section imaging to human airway epithelial (HAE) cells 72 hours post-SARS-CoV-2 infection to demonstrate how more profound insights into infectious diseases can be gained faster.

Using FAST-EM, we imaged a whole section of a HAE cell layer spanning an area of 270 x 270 µm2 at a 4 nm pixelsize and at 10 µs/px within only 35 minutes. The same area would take 3.5 hours to image using a single beam SEM with the same pixel size and at 2 µs/px. The EM images revealed the density and the locations of virus-like particles in the HAE cells. At 4 nm resolution hallmarks of SARS-CoV-2 such as electron-dense particles and multilamellar vesicles could be observed (Figure 1).

To perform an accurate examination of the sub-cellular changes caused by different SARS-CoV-2 variants, we analyse the density of the virus-like particles as well as the features that span multiple sections (e.g. multilamellar vesicles, mitochondria, cilia) by performing array tomography and 3D data reconstruction. We employ the available auto-segmentation model empanada MitoNet [3] (Figure 2) and train new segmentation models to extract the rich information present in the FAST-EM data to facilitate downstream quantitative analyses. Our work shows the FAST-EM and artificial intelligence approach as a new and effective way of gaining insights into infectious diseases.

Figure 1 Whole section FAST-EM image of HAE cell layer infected with SARS-CoV-2 enables the study of morphological changes with machine learning. (a) The morphological changes can be studied in the context of the cell layers, 270 x 45 µm², by allowing the identification of different cell types. (b dashed squares) On the cellular level, the impact of the infection is visible once zoomed in. (c, solid squares) The individual mitochondria in the cell layer are identified by employing MitoNet, allowing for quantification of morphological changes in the mitochondria. The scale bar is 20 µm (a) and 5 µm (b-c).

Fig. 1

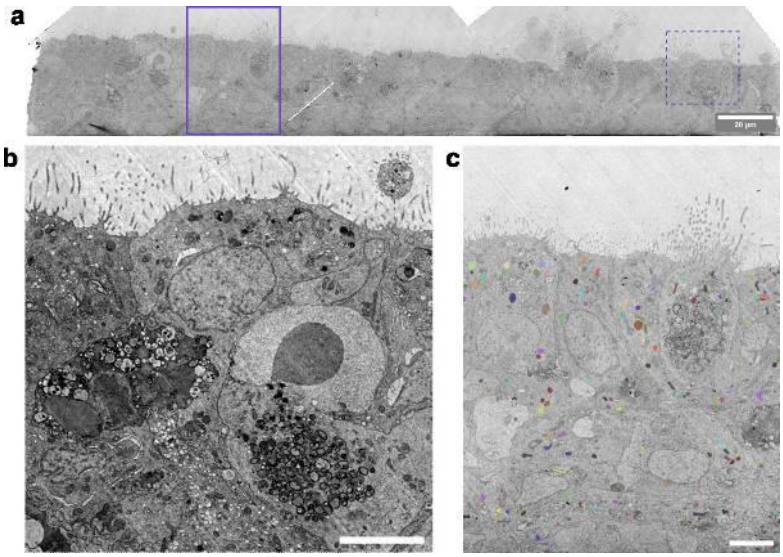

LSLB.P007

Zika virus replication in glioblastoma cells – electron microscopic tomography reveals 3D arrangement of endoplasmic reticulum, replication organelles, and viral ribonucleoproteins

J. G. Wieland[1], U. Rupp[1], R. Groß[2], J. Münch[2], P. Walther[1]

[1]Ulm University, Central Facility for Electron Microscopy, Ulm, Germany
[2]Ulm University, Insitute of Molecular Virology, Ulm, Germany

The ultrastructure of two patient-derived glioblastoma cell lines infected with Zika virus (ZIKV) was investigated using scanning transmission electron microscopy (STEM) tomography of high-pressure frozen, freeze-substituted samples. Formation of viral factories containing largely deranged endoplasmic reticulum was observed. In one cell line, newly formed virions and replication organelles (ROs) consisting of luminal vesicles within the ER were found in close proximity to each other. Reconstruction of STEM tomograms showed many about 100-nm-long filaments in the vicinity of ROs, possibly representing viral ribonucleoprotein complexes (RNPs) consisting of the RNA genome and N protein oligomers of ZIKV. The second cell line showed a different morphology upon ZIKV infection, where the virions were found in ER cisternae at a large distance from replication organelles, possibly indicating a dysfunctional transport of virions or different replication kinetics. This study demonstrates the advantage of EM tomography in the investigation of structures like RNPs, which would be hard to identify in conventional two dimensional TEM. STEM tomography in particular is capable of showing the three dimensional arrangement of multiple larger structures, like the ROs, virions and RNPs encountered in viral factories. The lack of image forming lenses in STEM allows for thick specimen of up to 1 µm to be analyzed. In TEM tomgraphy, sample thickness is limited by inelastic scattering of the beam inside the sample, which leads to chromatic aberration in the image forming lenses. Since a STEM does not use image forming lenses, chromatic aberration does not occur in image acquisition.

Reference: Wieland, J., Frey, S., Rupp, U. *et al.* Zika virus replication in glioblastoma cells: electron microscopic tomography shows 3D arrangement of endoplasmic reticulum, replication organelles, and viral ribonucleoproteins. *Histochem Cell Biol* **156**, 527–538 (2021). https://doi.org/10.1007/s00418-021-02028-2

LSLB.P008

Ultrastructural investigation of the C-terminal region of human cytomegalovirus tegument protein UL71 and its role in secondary envelopment

B. Küß[1,2], A. Metzner[2], L. Cortez Rayas[2], P. Walther[1], C. Read (Villinger)[1,2], J. von Einem[2]

[1]Ulm University, Central Facility for Electron Microscopy, Ulm, Germany
[2]Ulm University Medical Center, Institute of Virology, Ulm, Germany

Human cytomegalovirus (HCMV) is an important human pathogen which can cause serious diseases in immunocompromised patients and complications during pregnancy (Griffith et al., 2015). However, the molecular mechanisms underlying HCMV virion morphogenesis are still not well understood. In this work, an important step of HCMV morphogenesis en route to infectious virions, referred to as secondary envelopment, was investigated by electron microscopy (EM). Understanding the underlying mechanism could lead to the identification of new targets for antiviral therapy. pUL71 is a conserved herpesvirus tegument protein with 361 amino acids and plays an important role in secondary envelopment (Schauflinger et al., 2011). Several functional motifs, mainly localized in the N-terminus of pUL71, have been characterized in detail (Read et al., 2019; Fischer 2012; Metzner, 2022), but the role of the C-terminus of pUL71 is not well studied.

The role of the C-terminus of pUL71 was investigated by generating and characterizing a mutant virus (UL71insHA-299) expressing a truncated version lacking the last 60 amino acids and fused to an HA epitope. A first phenotypic characterization of UL71insHA-299 after infection of human fibroblasts was performed by immunofluorescence microscopy. In contrast to wild-type virus infected cells, virus particles accumulated at the periphery of the cytoplasmic viral assembly complex at large circular structures in UL71insHA-299 infected cells. For direct analysis of secondary envelopment and these capsid accumulations and circular structures, human fibroblasts were again infected and high-pressure frozen at five days post infection, freeze substituted and embedded in epoxy resin. Thereafter the cells were ultrathin sectioned, analyzed by transmission electron microscopy (TEM) and compared with wild-type infected cells.

The ultrastructural phenotype of the UL71insHA-299 mutant was very similar to that of a virus that is unable to express pUL71 (Schauflinger et al., 2011). Thus, our data show that the C-terminus of HCMV pUL71 contains functions that are necessary for sufficient virion morphogenesis and secondary envelopment.

Griffiths P, Baraniak I, Reeves M. The pathogenesis of human cytomegalovirus. J Pathol. 2015 Jan;235(2):288-97. doi: 10.1002/path.4437. PMID: 25205255.

Schauflinger M, Fischer D, Schreiber A, Chevillotte M, Walther P, Mertens T, von Einem J. The tegument protein UL71 of human cytomegalovirus is involved in late envelopment and affects multivesicular bodies. J Virol. 2011 Apr;85(8):3821-32. doi: 10.1128/JVI.01540-10. Epub 2011 Feb 2. PMID: 21289123; PMCID: PMC3126135.

Fischer D, 2012. Dissecting Functional Motifs of the Human Cytomegalovirus Tegument Protein pUL71. Doctoral thesis, Ulm University.

Read C, Schauflinger M, Nikolaenko D, Walther P, von Einem J. Regulation of Human Cytomegalovirus Secondary Envelopment by a C-Terminal Tetralysine Motif in pUL71. J Virol. 2019 Jun 14;93(13):e02244-18. doi: 10.1128/JVI.02244-18. PMID: 30996102; PMCID: PMC6580969.

Annika Metzner. Role of the non-conserved C-terminus of pUL71 for human cytomegalovirus infection. 2022, Bachelor thesis, Ulm University, unpublished.

LSLB.P009

ANTEMA: a neural network-based automated nanoparticle transmission electron micrograph analysis

N. Gumbiowski[1], K. Loza[1], M. Heggen[2], M. Epple[1]

[1]University of Duisburg-Essen, Essen, Germany
[2]Forschungszentrum Jülich GmbH, Ernst Ruska-Centre for Microscopy and Spectroscopy with Electrons, Jülich, Germany

High-resolution transmission electron microscopy (HRTEM) is an important tool for nanoparticle analysis. This is because HRTEM images show information about the size and shape of the particles as well as their inner structure. These are all parameters that influence the physical and chemical properties of the particle and are therefore of importance for all kinds of nanoparticle applications. With high frame rates and increasing capabilities of transmission electron microscopes, large amounts data are generated. However, analysing these micrographs is often done manually which is a tedious and time-consuming process. This is especially important for *in-situ* TEM experiments where hundreds or thousands of frames must be analysed. As a result, only a fraction of the available data is usually quantitively analysed.

To facilitate faster and more in-depth analysis of HRTEM images we have developed an automated image processing module using machine learning techniques. An important step in realizing an automated analysis of the nanoparticles in HRTEM images is to separate the particles from the noisy amorphous background. This is realized by a neural network which was trained on labelled HRTEM images by a supervised learning approach. The segmentation maps that are generated by the network are further processed to exclude particles that cross the image boundary and identify and split overlapping particles. From the resulting binary maps that include all particles in the image, shape and size-related parameters like circularity, equivalent diameter, and Feret diameter are extracted. These steps are all integrated in an automated routine which is able to analyse an HRTEM image within a few seconds. This permits the automated analysis of large quantities of data and gives more insight into nanoparticle structures compared to a manual analysis. It also avoids an operator-induced bias during manual image analysis.

LSLB.P010

Cryo-EM structure of the *E. coli* formate hydrogenlyase complex

R. Steinhilper[1], B. J. Murphy[1]

[1]Max Planck Institute of Biophysics, Redox and Metalloprotein Research Group, Frankfurt am Main, Germany

The prototypical hydrogen producing enzyme, the membrane-bound formate hydrogenlyase (FHL) complex from *Escherichia coli*, catalyzes the conversion of formate to CO_2 and H_2 under anaerobic fermentative conditions. The enzyme is long known to share sequence homology with respiratory complex I, but an energy conserving character of FHL remains elusive.

We aim to get a better understanding of the FHL complex and the role it plays in bacterial bioenergetics by combining high-resolution electron cryo-microscopy (cryo-EM) with complementary biophysical methods.

Our cryo-EM structures reached resolutions of up to 2.6 Å and revealed important differences and similarities between FHL and complex I. We analyzed possible substrate proton pathways to the [NiFe] active site, which may play an important role in the mechanism of the enzyme. Furthermore, we identified an unpredicted metal-ion, which could play a regulatory role in binding the loosely attached formate dehydrogenase component.

Since FHL is an ancestor of respiratory complex I understanding its function on a molecular level sheds light on the evolution of energy conservation from early to modern life.

LSLB.P011

Site-specific and advanced preparation of ultra-thin TEM samples of nanostructured materials

S. Hübner[1], D. Drobek[1], M. Dierner[1], L. Vogl[2], J. Will[1], B. Apeleo Zubiri[1], E. Spiecker[1]

[1]Friedrich-Alexander-Universität Erlangen-Nürnberg, Institute of Micro- and Nanostructure Research, Erlangen, Germany
[2]Eidgenössische Materialprüfungs- und Forschungsanstalt (Empa), Mechanics of Materials & Nanostructures, Thun, Switzerland

Advanced microanalytical investigation techniques allow to characterize the structure as well as the chemical composition of materials down to atomic scale. Especially, nanostructures with their confined length scales require a well-defined and extremely precise sample preparation to elucidate their unique characteristics [1]. Newest dual focused ion beam scanning electron microscopy (FIB-SEM) enables such indispensable site-specific sample preparation with high accuracy and precision on the nm-scale. However, beam sensitive materials and nonconductive substrates increase the challenges of an accurate preparation.

In this work, we illustrate the possibilities and challenges of targeted preparation of nanostructures using the latest FIB-SEM techniques. A selection of investigated nanostructures is presented in Fig. 1. Each unique nanostructure is analyzed precisely in SEM (first column) to identify the desired TEM lamella orientation with respect to the morphology and arrangement of the nanostructure as well as its orientation towards the substrate.

The first sample system are gold bipyramids (Fig. 1a) which exhibit a five-fold-twinned crystal structure with interesting optical properties [2,3,4]. The maximum extent of about ≈65nm limits significantly the position of the lamella and a high accuracy during the preparation is needed. The desired cross section must be perfectly in the center to study the present structure on the atomic scale. The final TEM studies reveal the fivefold twinned atomic structure. The lamella delimits a thin region around the center of the bipyramid, with their surfaces parallel to the central base. In this way, the diameter at the central base can be accurately determined, which shows a rounded geometry compared to the optimal structure.

Fig. 1b shows Au_xNi_{1-x} nanoparticles on a α-Al_2O_3 substrate. In this system, the interface between the ceramic substrate and the metal is of interest due to great scientific and technological importance, with applications in electro-ceramic devices, structural composites and catalysis [5]. Therefore, the nanoparticle orientation with respect to that of the underlying substrate is identified by electron backscatter diffraction (EBSD) measurements. Afterwards, the cross section is prepared in such a way that the center of the particle is located exactly in the center of the lamella (Fig. 1b). Besides the extreme precision, the non-conductive substrate is very challenging. Additionally, advanced STEM methods are needed to image the interface between high and low atomic number materials [5]. For this purpose, lamellae with a thickness of less than 40nm and a very good surface quality are required.

Besides one-dimensional structures, also single nanowires (NW) and the corresponding networks are analyzed. The electrical properties of such networks or NW in contact can be strongly improved by heat treatment to weld the corresponding contact points [6]. The presented example (Fig. 1c) shows two identified and select Ag NW after heat treatment. To investigate the welding zone between both wires, the corresponding cross section has to be precisely prepared. The achieved lamella reveals that the intersecting NW unite with each other and creating a constant internal crystalline microstructure.

[1] 10.1017/S1431927613013780

[2] 10.1021/ac900276n

[3] 10.1021/jacs.6b12143

[4] U. Frank et al. ACS Nano, under review

[5] 10.1038/s41598-018-20377-2

[6] 10.1002/aelm.202100787

Fig. 1

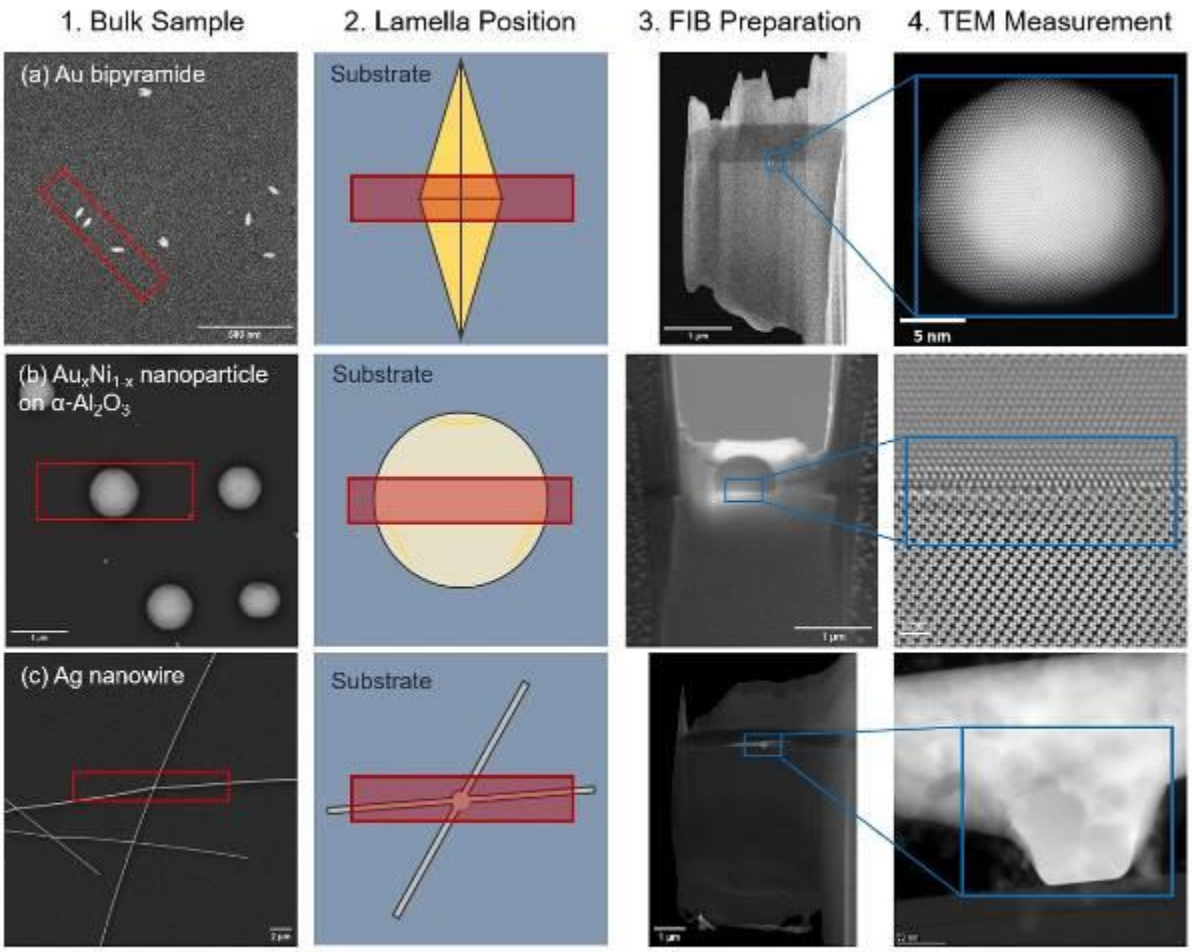

Fig. 1: SEM images of the bulk sample and the finished FIB preparation as well as the corresponding TEM measurements of three different material systems. (a) Gold bipyramides with 60-70 nm length where a cross section was prepared to investigate the fivefold twinned bipyramid base. In (b) a cross section through the middle of an AuNi particle was performed to measure the atomic structure at the interface between particle and substrate and the preparation in (c) reveals the cross section trough two welded Ag nanowires.

LSLB.P012

Ultrastructural rearrangement of the nucleus *in situ* during osmotic stress

P. Hoffmann[1], A. Obarska-Kosińska[1], M. Beck[1]

[1]MPI of Biophysics, Molecular Sociology, Frankfurt am Main, Germany

Osmotic stress causes flux of solvent into or out of cells as a result of changing environmental conditions. On second to minute time scale cells respond by adjusting their volume. How cells cope with the mechanical impact and how this process affects cellular ultrastructure remains underexplored.

We combine fluorescence microscopy and electron cryo-tomography to study the structural rearrangements to the cytosolic and nuclear architecture in *Dictyostelium discoideum* cells during osmotic stress. These cells undergo volume changes that result in changes to the cellular protein concentration, affecting the visibility of protein complexes in the tomogram volume.

We visualize specific changes to nuclear architecture, the organization of regular nuclear filaments upon nuclear shrinkage, as well as changes to the nuclear envelope membrane resulting from osmotic pressure and mechanical forces.

Using subtomogram averaging, we obtain an *in situ* structure of the nuclear pore complex of *D. discoideum* and build a corresponding model from AlphaFold predicted structures of its components. *D. discoideum* nuclear pores have a unique structure compared to other organisms and are subject to dilation and constriction movements under different osmotic stress conditions.

LSLB.P013

Establishing pre-embedding immunogold labelling for the detection of pUL71 in herpesvirus infected cells

J. la Roche[1], J. von Einem[2], L. Cortez Rayas[2], C. Read (Villinger)[1,2], U. Rupp[1]

[1]Ulm University, Central Facility for Electron Microscopy, Ulm, Germany
[2]Ulm University, Institute of Virology, Ulm, Germany

Morphogenesis of human cytomegalovirus (HCMV) is still only partially understood. Previous studies have shown that the HCMV tegument protein pUL71 plays an important role in viral replication and morphogenesis (1). To better understand the function of the protein, pUL71 should be localized in infected cells by pre-embedding immunogold labelling and transmission electron microscopy (TEM). In recent years, EM preparation methods have been published that combine good structural preservation by high-pressure freezing and freeze substitution with subsequent rehydration allowing immunolabeling before resin embedding (e.g., 2,3).

We describe the establishment of this method in our laboratory and its adaptation for HCMV-infected fibroblasts. The major aim is to achieve the best possible ultrastructural preservation while providing sufficient permeabilization for efficient pre-embedding immunogold labeling.

After high-pressure freezing of firoblasts infected with HCMV expressing an HA-tagged variant of pUL71, we tested freeze-substitution (FS) media with different concentrations of glutaraldehyde, osmium tetroxide and uranyl acetate, as well as of the detergents TritonX100 and Digitonin. We then evaluated the ultrastructural preservation of these samples by TEM. Labelling efficiency was then first tested by fluorescence microscopy experiments. Rehydration and permeabilization approaches that provide good labelling efficiency will then be adapted for pre-embedding immunogold labeling of pUL71-HA with anti-HA IgG as primary and Nanogold Fab fragments as secondary antibody.

The most promising tradeoff between ultrastructural preservation, sufficient heavy metal contrast, and antibody penetration was observed with a FS solution containing 0.2% osmium tetroxide, 0.1% uranyl acetate and 5% water in acetone. Fluorescence microscopy showed specific antibody labelling of pUL71-HA after exchanging the FS medium at -20 °C for a medium containing 0.2% glutaraldehyde instead of osmium tetroxide, while it made no difference whether permeabilization was performed with TritonX or Digitonin.

Immunolabeling after FS but before embedding is a promising but complex method, as the fixatives as well as the acetone can interact with the antigens and mask the epitopes. Specifically, the proteolytic effect of osmium tetroxide has a strong effect on antigenicity. However, since this effect is strongly temperature dependent, removal of osmium tetroxide at negative temperatures should have less effect on antigenicity (4,5). The identification of a suitable anti-HA antibody in fluorescence microscopy experiments by using optimized fixation methods enables us to perform immunogold labelling for detection of the antibody by TEM.

1. Schauflinger, M. et al. 2013. Analysis of human cytomegalovirus secondary envelopment by advanced electron microscopy. Cellular Microbiology.

2. Hess, M.W. et al., 2018. Combining high-pressure freezing with pre-embedding immunogold electron microscopy and tomography. Traffic.

3. Tsang, T.K. et al., 2018. High-quality ultrastructural preservation using cryofixation for 3D electron microscopy of genetically labeled tissues. eLife.

4. Flechsler, J. et al., 2020. 2D and 3D immunogold localization on (epoxy) ultrathin sections with and without osmium tetroxide. Microscopy Research and Technique.

5. Koga, D. et al., 2020. Optimizing the reaction temperature to facilitate an efficient osmium maceration procedure. Biomed. Res. 41, 161–168.

LSLB.P014

Acid sphingomyelinase deletion mutant *C. elegans* show formation of electron dense multilamellar bodies, accumulation of various sphingolipid species and increased resistance to *Staphylococcus aureus* infections

V. Perschin[1], M. Rühling[2], A. Prell[3], F. Schumacher[3], M. Fraunholz[2], G. Fazeli[1], B. Kleuser[3], C. Stigloher[1]

[1]University of Würzburg, Imaging Core Facility, Würzburg, Germany
[2]University of Würzburg, Chair of Microbiology, Würzburg, Germany
[3]Freie Universität Berlin, Institute of Pharmacy, Berlin, Germany

Acid sphingomyelinase (ASM; *SMPD1* gene in humans) is a lysosomal enzyme that catalyses the conversion of sphingomyelin to ceramide. Harmful mutations in this gene lead to the lipid storage disease Niemann Pick Disease Types A or B, which are characterized by abnormal accumulation of sphingomyelin and cholesterol in lysosomes of various tissues. Ultrastructural analysis of patient tissues or cell lines shows the lipids arranged as multilamellar structures within the lysosome.

Through its activity, ASM is contributing to lipid homeostasis. Stresses like pathogens or oxidative stress can induce the relocation of ASM from the lysosome to the plasma membrane, where it produces ceramide and thus leads to a rearrangement of ceramide-enriched domains. This process is important in many signalling cascades of the immune system. *C. elegans* has three ASM isoforms, ASM-1, ASM-2 and ASM-3, that are all homologous to the human ASM. Here, we used deletion mutants of the three *asm* genes to characterize ASM in the *C. elegans* sphingolipidome context and investigate their role in *S. aureus* infections. *C. elegans* is susceptible to the human pathogen *S. aureus* and a well-established model to study its pathogenicity.

We fed single, double and triple *asm* mutant worms with *S. aureus* and quantified their survival. None of the control worms, but 40% of the *asm-1* and *asm-3* single or double mutants survived after 72 hours of feeding on *S. aureus*. *asm-2* mutation did not protect the worms against *S. aureus* infection, and even nullified the protective effect of *asm-1* and *asm-3* in double or triple mutants, implying divergent roles of ASM-2 vs. ASM-1 and ASM-3 in the pathogenicity of *S. aureus*.

Ultrastructural analysis of high-pressure frozen specimens revealed excessive lipid accumulation in *asm-1* and *asm-3* mutants, probably in lysosomes, which resemble the multilamellar bodies described in human Niemann-Pick patients. They were rarely observed in controls and *asm-2*.

To confirm that this phenotype is due to a disturbed sphingolipid metabolism, we analysed the sphingolipidome of *C. elegans* using liquid chromatography tandem-mass spectrometry. We found that all ASMs have an impact on the levels of various sphingomyelin and ceramide species. The changes induced by *asm-2* and *asm-3* are very similar to each other, whereas *asm-1* seems to have different roles.

Our findings show that host ASM activities shape the outcome of experimental infection of *C. elegans* with *S. aureus* and that all three *C. elegans* ASMs have an impact on the sphingolipid homeostasis. In the next step, we want to characterize and localize the lipid species contained in the electron dense multilamellar bodies by using a combination of correlative light and electron microscopy and liquid chromatography tandem-mass spectrometry with labelled *C. elegans* specific iso-branched sphingolipids.

LSLB.P015

High resolution imaging of surface dynamics

H. Jafarian[1], T. Juffmann[1]

[1]University of Vienna, Vienna, Austria

ONEM is a new hybrid microscopy technique in which an interface is probed by light in a non-invasive manner, and the structural information is read-out at high spatial resolution using electron optics. To achieve this, an ultra-thin photocathode layer is inserted in the near-field region right after the sample [2], and emitted photo-electrons are collected by the objective lens of an aberration-corrected low-energy electron microscope (LEEM) [3]. The potential applications for ONEM is in life sciences and electrochemical studies.

Electrochemistry studies the processes that occur on the interface of electrodes and electrolytes due to the flow of electrons or ions. This field of study has found widespread applications in nanomanufacturing, developing batteries, hydrogen-based fuels, biosensors and etc [1]. Therefore, measuring the local changes in the formed structures over the whole area of the electrode-electrolyte interface is of great importance.

Despite the significant advances in the development of optical super-resolution and electron microscopes, real-time, damage and label free imaging of dynamics in nm-resolution is yet not achieved. Here, we introduce optical near-field electron microscopy (ONEM) as a noble technique to study electrochemical processes in real time with a few nanometers of spatial resolution. ONEM will be benchmarked with other state of art techniques such as interferometric scattering microscopy (iSCAT) and liquid cell electron microscopy (LC-EM).

ONEM is an ongoing project in collaboration with the Leiden University, Czech academy of sciences, and the Univerity of Vienna.

References:

[1] Beker, Anne France, et al. "In situ electrochemistry inside a TEM with controlled mass transport." Nanoscale 12.43 (2020): 22192-22201.

[2] Marchand, Raphaël, et al. "Optical near-field electron microscopy." Physical Review Applied 16.1 (2021): 014008.

[3] Geelen, D., et al. "Nonuniversal transverse electron mean free path through few-layer graphene." Physical review letters 123.8 (2019): 086802.

Fig. 1

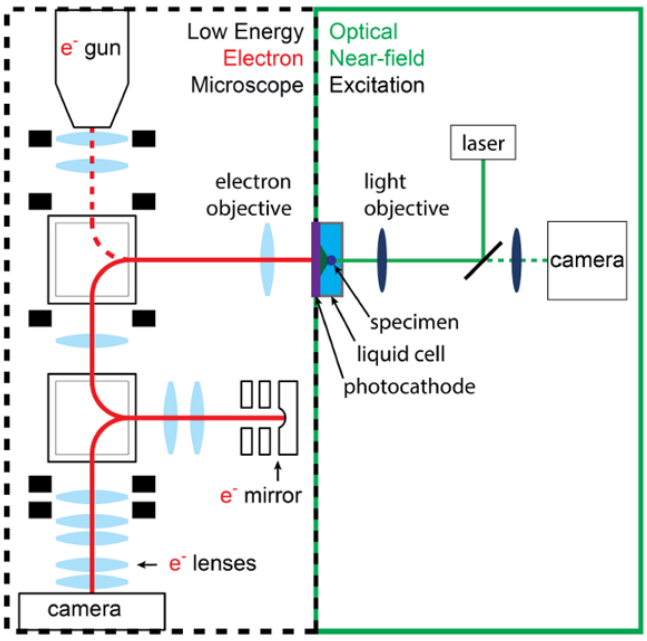

Fig. 2

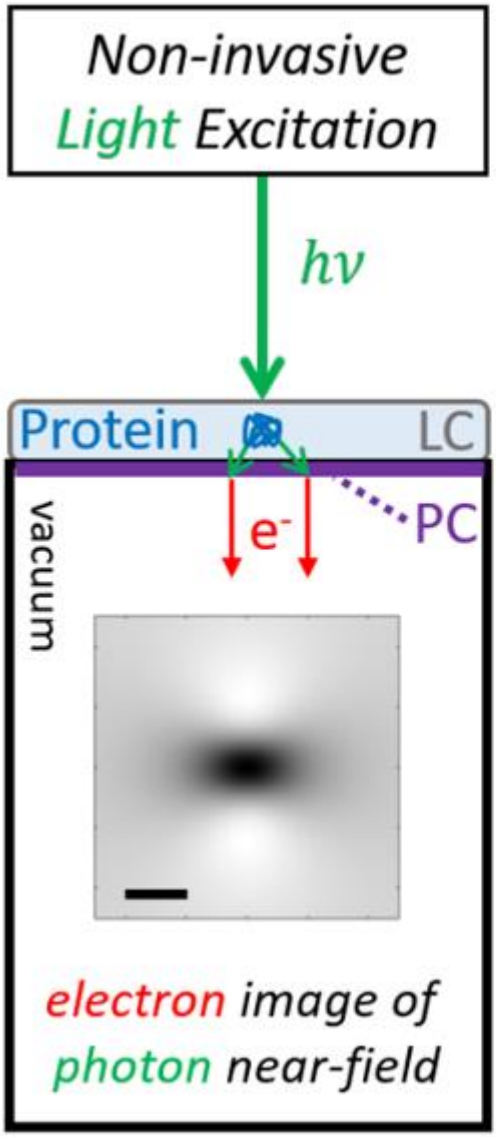
Non-invasive
Light Excitation
hν
Protein
LC
e-
PC
vacuum
electron image of
photon near-field

LSLB.P016

Structural strategies for maximizing bacteriophage capsid capacity

M. Bostina[1]

[1]University of Otago, Dunedin, New Zealand

Tailed bacteriophages use copies of a major capsid protein (MCP) with a common fold to build capsids capable to harbour dsDNA genomes spanning from tens to hundreds of kilobase pairs. Larger capsids are usually constructed by a higher number of MCPs, resulting in a larger triangulation number or in oblongate capsids. However, the continuous evolutionary pressure imposes phage capsids to adapt to various packaging load sizes. For instance, a relatively modest increase in the genome size cannot justify the transition to a novel capsid model, constructed from more MCPs. Instead it calls for strategies that increase the size of the capsid, while maintaining the same triangulation number.

Using cryo-electron microscopy (cryoEM), we solved the architecture of the phiTE phage in several intermediate conformations. The full capsid resolved at 3.4 Å helped us to decipher the structural mechanism by which phiTE capsid is able to accommodate a genome up to 40% larger than that of phages with the same capsid geometry (T=13). The strategy combines three factors: the increase of capsomer surface without an increase in MCP molecular weight, the relative sliding between individual capsomers, and the increase of local capsomer curvature.

Additionally, our cryoEM analysis offers a series of important insights into understanding the general principles of phage architecture. First, we describe two decoration proteins with distinct roles in phage stability and demonstrate that for decoration proteins belonging to the same class, a structure base classification does not mirror the classification based on amino acid alignment. Secondly, we follow the MCP conformations found in the spent empty capsid that displays an expanded geometry. Thirdly, we describe the components of the phiTE tail in the extended and contracted conformations. Finally, we show how the phiTE base plate employs a novel type of conformational change during genome ejection dictated by the reorientation of the tail fibres.

IMLB.P001

New method to characterise Li metal and SEI layer with atomic resolution with inert gas transfer and cryo-FIB

L. Li[1], J. Lin[1], Z. Liu[1], B. van Leer[1]

[1]Thermo Fisher Scientific, Eindhoven, Netherlands

Lithium metal is one of the most promising anode candidate for the next-gen solid state battery. To go through the hurdles for a reliable and cost effective solid state battery, it is crucial to build strong fundamental understandings of different parts of a battery at microscopy level. Techniques such as site-specific DualBeam (FIB-SEM) lamella preparation and subsequent TEM analysis have always been the key steps to unlock atomic resolution for materials science studies. However, due to the air and moisture sensitivity associated with various battery components (Li metal, SEI layer, Solid electrolyte), it used to be a very challenging task to keep sample integrity during the workflow, especially during sample transfer between different instruments.

In the current study, an novel IGST (Inert Gas Sample Transfer) workflow solution was used to enable a DualBeam to TEM workflow by protecting both the bulk sample and the prepared lamella in Ar atmosphere with a inert gas transfer module (CleanConnect).

Using the CleanConnect module, a bulk Li-metal piece was successfully transferred from glovebox to a DualBeam without signs of surface oxidation. Due to the low melting point of lithium, the entire TEM lamella preparation process, including bulk milling, lift out, attach to TEM grid and final thinning were carried out at cryogenic temperature (-178C) with a LN2 cooled cryo-stage and cryo-nano-manipulator. To achieve minimal ion damage to the final lamella, all the ion milling processes were carried out with Ar plasma focused ion beam.

The prepared lamella was then transferred back to glovebox under Ar gas protection using CleanConnect transfer module. Inside the glovebox, the lamella was loaded to a IGST double tilt TEM holder, which allows lamella transfer from glovebox to a CFEG TEM under Ar gas protection.

The lamella was then analyzed in TEM. It is evident that the whole workflow successfully protects the lithium metal lamella from oxidation during transfer between multiple instruments. The lithium metal lamella stays crystalline with minimal signs of surface oxidation. Atomic resolution TEM images from lithium metal were successfully acquired. According to literature survey, this could be the first DualBeam prepared lithium lamella which gives atomic resolution in TEM analysis. EELs maps from the lamella were acquired to quantify the amount of oxidation on the Lithium lamella. It was found that the amount of Oxygen were below 1.8 at%, which validates the results. After the TEM analysis, the lamella were delibrately exposed in atomophere for less than 15 sec, significant oxidation were observed after the exposure, which further proves the necessity of the IGST workflow.

The study successfully shows the capability of the workflow by achieving atomic resolution from Li-metal, which is one of the most challenging samples in terms of air, moisture, and temperature sensitivity. The success of the workflow also enables new methods to study other trending topics in the battery world such as characterization of SEI layer evolution, post-mortem analysis in higher resolution whilst keeping the sample in its original state.

Fig. 1

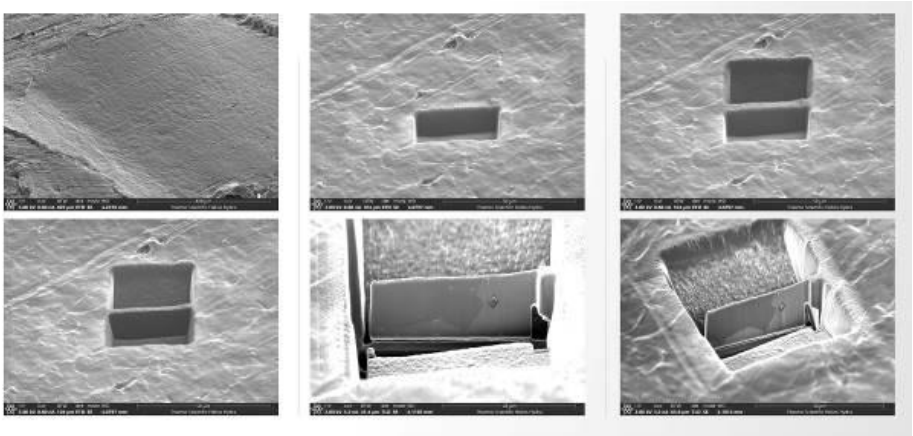

Fig. 2

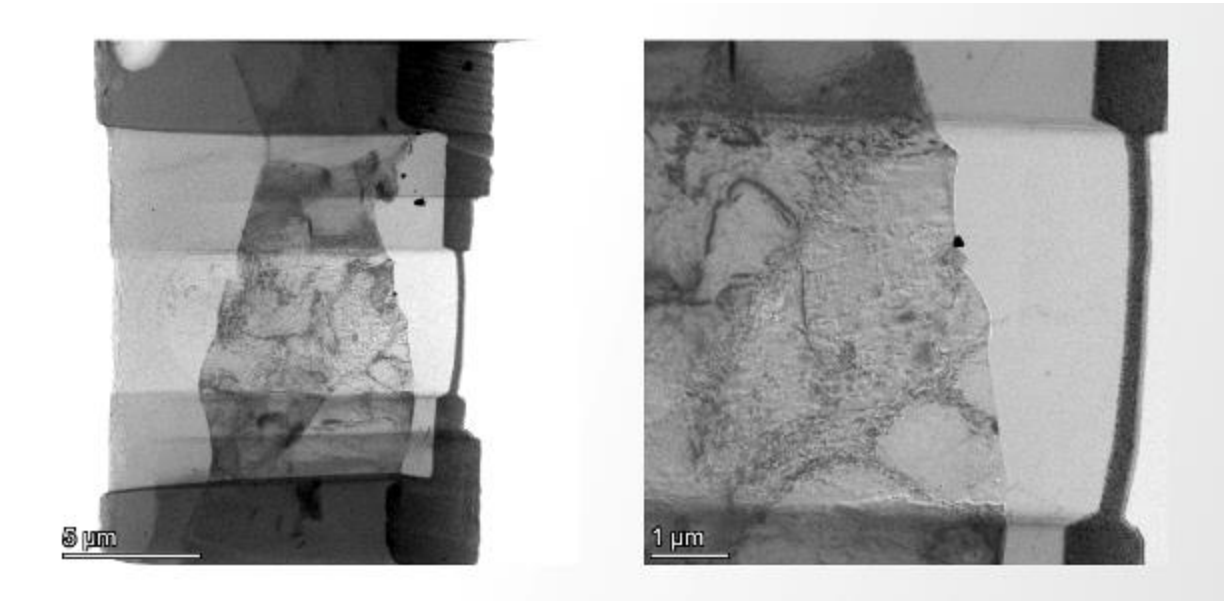

Fig. 3

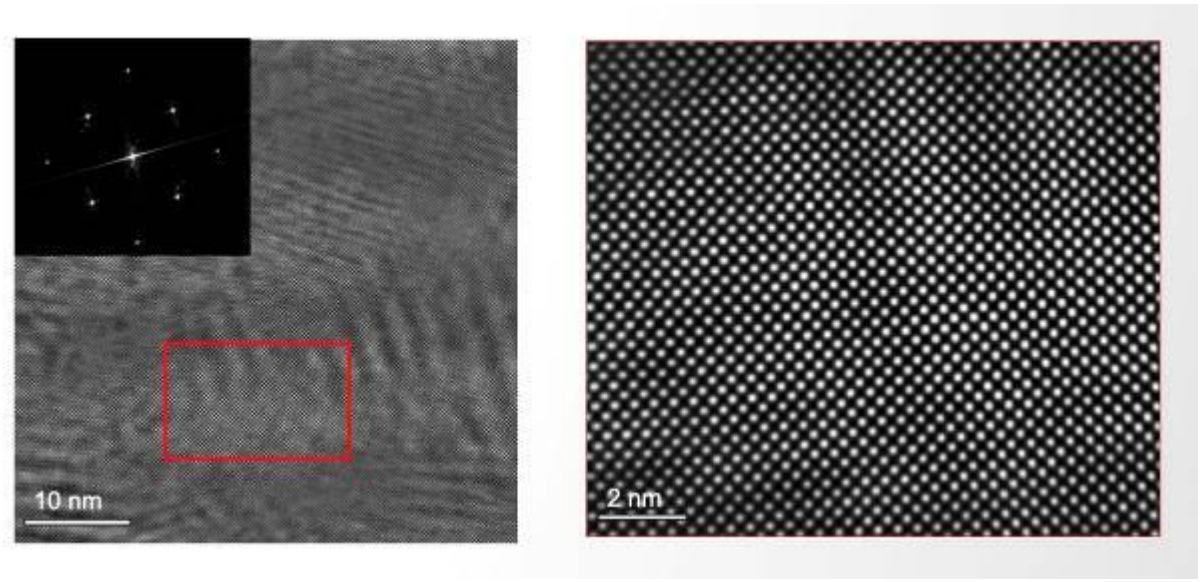

IMLB.P002

Identification of carbides in 28wt.%Cr high chromium cast irons by color etching and electron probe microanalysis

K. Ruangchai[1], R. Tongsri[2], J. T. H. Pearce[3], T. Chairuangsri[3], A. Wiengmoon[1]

[1]Naresuan University, Department of Physics, Faculty of Science, Phitsanulok, Thailand
[2]National Metal and Materials Technology Center, Pathum Thani, Thailand
[3]Chiang Mai University, Department of Industrial Chemistry, Faculty of Science, Chiang Mai, Thailand

Introduction

As-cast microstructures of high-chromium cast irons (HCCIs) with hypoeutectic composition in range of 27-30wt.%Cr and 2-3wt.%Cr irons consist of primary austenite dendrites with eutectic austenite, partially transformed to martensite, and eutectic M7C3 carbides. Normally, the hardness and wear resistance of these irons depend on the type of matrix and carbide formation. Mo can be added to HCCIs to modify the carbide and to increase the volume fraction of the carbide in their microstructures. The aim of this research is to identify the type of carbides and carbide transformation in 28wt.%Cr cast iron containing Mo additions using color etching techniques and electron probe microanalysis.

Materials and methods

Carbides in a 28wt.%Cr (R iron), a 28wt.%Cr-6wt.%Mo (Mo6) and a 28wt.%Cr-10wt.%Mo (Mo10) have been characterized by X-ray diffraction, light microscopy with color etching by Groesbeck"s reagent [1], and an Apreo S Thermo Fisher Scientific field emission scanning electron microscope. The chemical composition of the eutectic carbides was analyzed by electron probe microanalysis (EPMA).

Results

LM and SEM observations shown in Fig. 1 reveal the as-cast microstructures of 28wt.%Cr–2.6wt.%C iron (R iron), and the irons with 6wt.%Mo addition (Mo6) and 10wt.%Mo addition (Mo10). The microstructures consist of primary dendritic austenite (g), eutectic austenite which partly transformed to martensite during cooling and eutectic M7C3 carbides. Mo addition to HCCIs promoted the formation of M6C and M23C6 carbides rather than M7C3 carbides. In the Mo10 iron eutectic M7C3 carbides were not observed and the microstructure contained radiating colonies of M23C6 carbide and lamellar/fish-bone M6C carbide. After color etching, Fig. 1(a-c), M7C3 carbide was colored brown and blue, while austenite matrix remained lighter in contract. The M6C carbide with a lamellar structure/fish-bone had a dark-brown coloration, and the radiating colonies of M23C6 carbide were rainbow colored. At higher magnification, the SEM image in Fig. 1(d) showed that the M23C6 carbide was present as a transition zone between the eutectic M7C3 and M6C in the Mo6 iron, indicating a carbide transition of M7C3 → M23C6 → M6C [2]. SEM-BEI images (Fig. 1(d-f)) revealed that the eutectic M6C carbide in the Mo6 and Mo10 irons had the brightest contrast compared to the M23C6 and M7C3 carbides.Furthermore, Fig. 1(g-i) showing the phase mapping by EPMA, clearly demonstrates that M6C carbide had the highest Mo content, corresponding to the SEM-BEI displaying the brightest contrast due to the high atomic number of Mo. The M7C3 and M23C6 had higher Cr contents. The quantitative elemental analysis can be used to estimate the atomic formulae for M7C3, M23C6 and M6C in the Mo6 iron.

Conclusion

Color etching with Groesbeck"s reagent can be used to distinguish the M7C3, M23C6 and M6C carbides by brown or blue, rainbow, and dark brown coloration respectively. EPMA analysis suggested the stoichiometric formulae of these carbide in the 28wt.%Cr-6wt.%Mo (Mo6) as (Cr4.7Fe1.8Mo0.1)C3, (Cr14.1Fe6.9Mo1.3)C6 and (Cr1.5Fe3.2Mo1.0Si0.1)C, respectively.

References

1. E.C. Groesbeck, Solutions for Carbides, etc., in Alloy Steels, appendix to report of Committee E-4 on Metallography, Proc. ASTM, Vol 26 (Part I), 569 (1926).
2. S. Imurai et al., Effects of Mo on microstructure of as-cast 28 wt.%Cr-2.6 wt.%C-(0-10) wt.% Mo irons. Mater. Charact., Vol. 90, 99-112 (2014).

Fig. 1

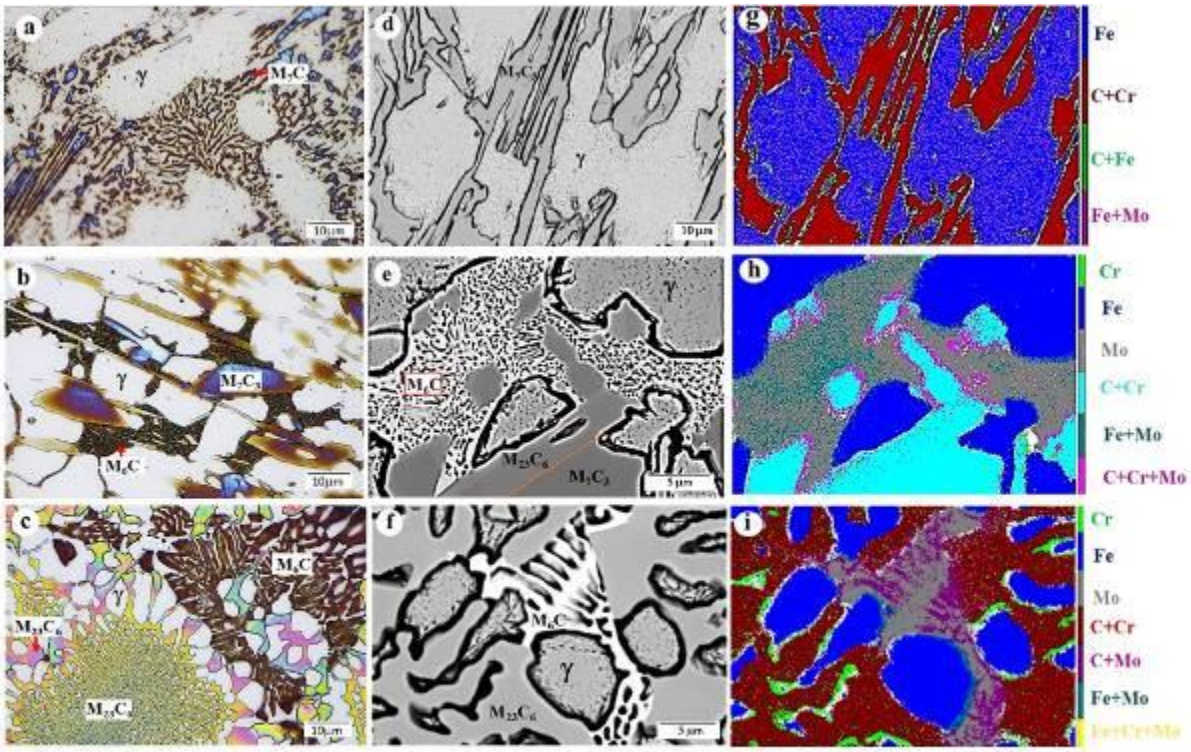

Fig. 1. LM images, SEM-BEI images and EPMA elemental distribution mapping analysis representing the typical microstructures of (a-c) R iron, (d-f) Mo6 iron and (g-i) Mo10 iron.

IMLB.P003

Regularization techniques for 3D surface reconstruction from four quadrant backscattered electron detector images

M. Giardino[1], D. L. Janner[1], D. Meena Narayana Menon[1]

[1]Politecnico di Torino, DISAT, Turin, Italy

In scanning electronic microscopy, four quadrants backscattered electron detectors (FQBSD) allow collecting signals from each quadrant separately and combine them to obtain a tridimensional reconstruction of the surface. The main challenge of this operation consists of the integration of the gradient field obtained as the normalized difference of the signal from each pair of opposite quadrants. Owing to the presence of electronic noise that eventually turns into image noise, a least square integration approach is widely adopted for surface reconstruction.

However, the reconstructed surface could still be affected by distortions due to sensitivity variations amongst the detector quadrants or an imprecise alignment of the FQBSD with the gun axis, which is quite a common occurrence, particularly in systems equipped with manual retractable FQBSD.

In the present work, we demonstrate the possibility of adopting classical regularization techniques to the surface reconstruction from FQBSD images allowing for a substantialimprovement in the 3D surface reconstruction quality. To this purpose, three types of regularization have been explored: background removal by polynomial regression, Dirichlet"s regularization, and Tikhonov"s regularization.

The procedures have been experimentally validated on AISI 316L stainless steel polishedsurfaces with microhardness indentation and on laser-patterned aluminum and silicon samples, showing promising results.

Concerning the indented samples, Dirichlet"s regularization returned the best result, whereas the other two regularization methods introduced some distortions of the indentation mark. On the other hand, for the laser-processed samples, Tikhonov"s regularization allowed the best reconstruction of surface details, whereas Dirichlet"s reconstruction forced the edges of the sample to be flat, thereby strongly altering the surface profile. This points to the need for an application-driven selection of the regularization technique that is easily implementable in commonly available software.

Finally, we will also present paths for further development of the technique to demonstrate the possibility of a quantitative analysis of laser-processed surfaces as an alternative to more expensive and time-consuming optical profilometry and atomic force microscopy.

IMLB.P004

Real-time multi-dimensional spatiotemporal tracking of single anisotropic nanoparticles in live cells by multifunctional light-sheet nanoscopy

Y. Cao[1], S. Lee[1], S. H. Kang[1]

[1]Kyung Hee University, Applied Chemistry, Yongin-si, South Korea

A wavelength-dependent multifunctional light-sheet nanoscopy (MLSN) was developed to simultaneously track spatial movement (*x*, *y*, *z*), rotational dynamics (azimuth and elevation angles) and transport speed (*v*) of anisotropic nanoparticles in single live cells, which are referred to as six dimensions (6D) single-particle tracking (SPT). To obtain more detailed information for cell imaging, differential interference contrast, total internal reflection, epifluorescence, and super-resolution radial fluctuation-stream module were combined with the light-sheet nanoscopy. Because of anisotropic optical property, native gold nanorods (AuNRs; 5 nm diameter × 15 nm length) and surface-functionalized AuNRs were used as imaging probes for 6D SPT. *s*-pol and *p*-pol light sheets induced by optical polarizer could trigger the asymmetric scattering of AuNRs. Therefore, real-time photoswitching images of AuNRs were achieved for super-resolution images and multi-dimensional SPT. Using this technique, the endocytosis and transport processes of AuNRs at the upper and attaching side membrane regions of single live cells were directly observed. The native and surface-functionalized AuNRs showed various motional behaviors on cell membrane, internalization time and intracellular transport processes due to their different surface properties. This MLSN technology is a promising tool to shed new light on the working mechanism of living cells and to decipher super-resolution imaging of living cells with non-fluorescent imaging probes.

Fig. 1

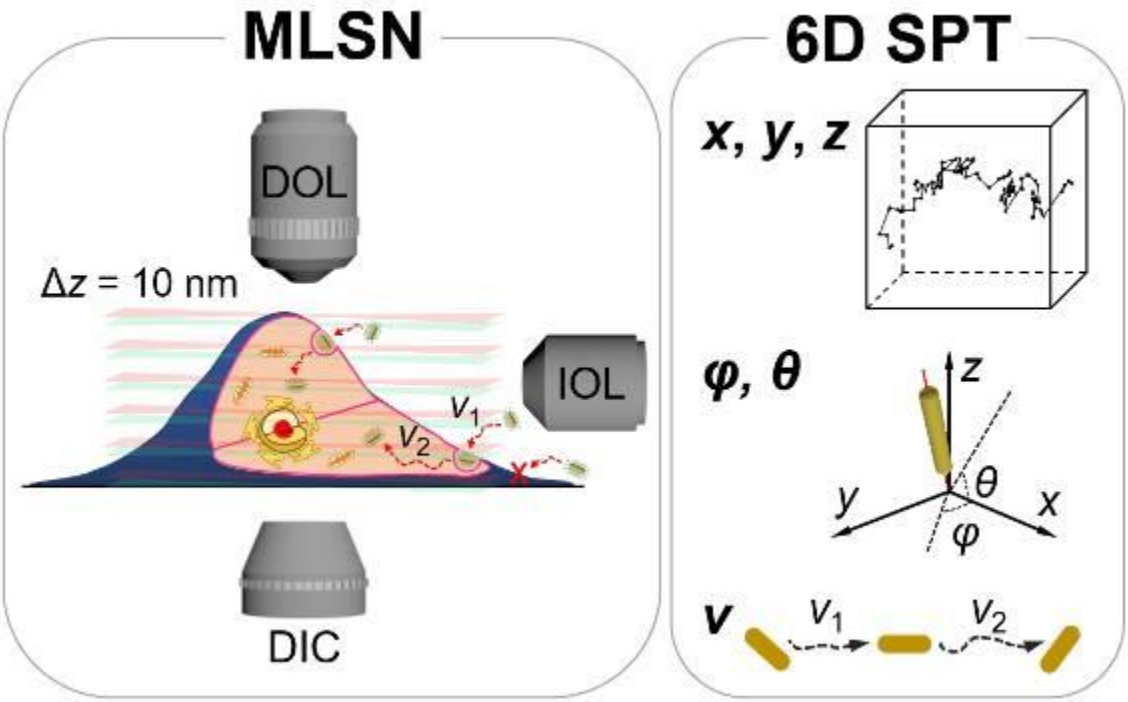

IMLB.P005

Four-dimensional cuboid multiangle illumination-based light-sheet super-resolution microscopy for minimizing optical illusion

S. Lee[1], S. Y. Park[2], S. H. Kang[1]

[1]Kyung Hee University, Applied Chemistry, Yongin-si, South Korea
[2]Seoul National University, Advanced Institute of Convergence Technology, Suwon-si, South Korea

Light-sheet-based super-resolution microscopy (LSRM) is an excellent detection technique for biological samples because light damage is minimized, but uneven light paths resulting from solid-angle illumination result in optical illusions. A three-dimensional (3D) LSRM limitation is uneven optical obstacles because of the inhomogeneous refractive index in orthogonal illumination. In this study, we introduce a four-dimensional (4D) light-sheet super-resolution microscopy (4D LSRM) with a cuboid prism integrated with a total reflection fluorescence and differential interference contrast microscopy to minimize optical illusions. The rotatable cuboid prism simply overcomes the optical illusion by rotating the specimen on the prism to change the direction of light that comes from illumination lens with super-resolution imaging. In addition, a 4D multiangle illumination-based algorithm was created to select the optimal illumination angle by the combining 3D super-resolution image with multiangle observation. Therefore, the 4D cuboid multiangle illumination-based LSM imaging system developed based on multiangle illumination and 3D imaging can provide the advantages of high-quality whole-cell imaging and single-molecule counting by minimizing optical illusions.

IMLB.P006

Specification of electrical properties of pyrolyzed 3D Printed Microstructures

K. Kraft[1,2], Q. Sun[1,2], C. Dolle[1,2], C. Kurpiers[3], R. Schwaiger[4], P. Gumbsch[3,5], Y. M. Eggeler[1,2]

[1]KIT, LEM, Karlsruhe, Germany
[2]KIT, MNM, Karlsruhe, Germany
[3]KIT, IAM, Karlsruhe, Germany
[4]Forschungszentrum Jülich GmbH, Institute of Energy and Climate Research, Jülich, Germany
[5]Fraunhofer Institute, Fraunhofer Institute for Mechanics of Materials IWM, Freiburg, Germany

In the era of miniaturization, increasingly smaller devices are being produced that are mainly made of silicon. Beyond silicon, carbon shows suitable properties for applied micro- and nanostructures, such as electrical conductivity, high mechanical and chemical stability and biocompatibility. These properties are especially suitable for biosensors [1]. To realize small structures, pyrolysis can be employed to shrink by up to 90% [1]. However, the holistic pyrolysis mechanism has not yet been studied in detail. So far there is no work that investigates the property change of pyrolyzed microstructures at different atmospheric pressures. Therefore, the investigation of the properties of pyrolyzed microstructures under different atmospheric influences and different temperatures can provide insights into the pyrolysis process.

In this work, microstructures are printed on Si substrates by two-photon direct laser writing (DLW) with a commercially available photoresist (IP-Dip). These structures (see Figure 1a) are heated under a high vacuum or an inert Ar atmosphere at various pyrolysis temperatures. After pyrolysis, the shrinkage behavior of the microstructures is characterized by SEM [3], which is dependent on the surface-to-volume ratio [1]. Different geometries are considered, with varying cross-sections connecting the microelectrodes (Figure 1b). It is suggested that the electrical conductivity increases with growing pyrolysis temperature since an increasing sp^2 hybridization of the C-C bonds in glassy carbon dominate at higher temperatures [2]. The shrinkage behavior of the microstructures under several temperatures and environments, in correlation to the surface to volume ratio [1], is characterized. For the investigation of electrical properties, *in situ*-SEM nanoprobing with nanomanipulators is used to record voltage-current curves.

In the meantime, we study the influence of different environments on the mass loss. In further work, thermogravimetric analysis will be performed to determine the temperature dependent mass loss. The experimental studies will be accompanied by COMSOL simulations to predict the geometrical shrinkage behavior at other temperatures.

In summary, the study of pyrolyzed carbonaceous microstructures is an area where much research is still possible. With a better understanding of the pyrolysis process, the processes involved and the properties of glassy carbon, new technologies for medicine and industry can be found.

References:

[1] Cardenas-Benitez et. al., Microsyst. Nanoeng. 5,38 (2019).

[2] Tyler et. al., Adv. Eng. Mater. 23, 2001027 (2021).

[3] Sun et. al., Microsc. Microanal. 27 (Suppl 2), 2021.

[4] The authors acknowledge financial funding by the German Research Foundation (DFG) under Germany"s Excellence Strategy (EXC-2082/1–390761711).

Fig. 1

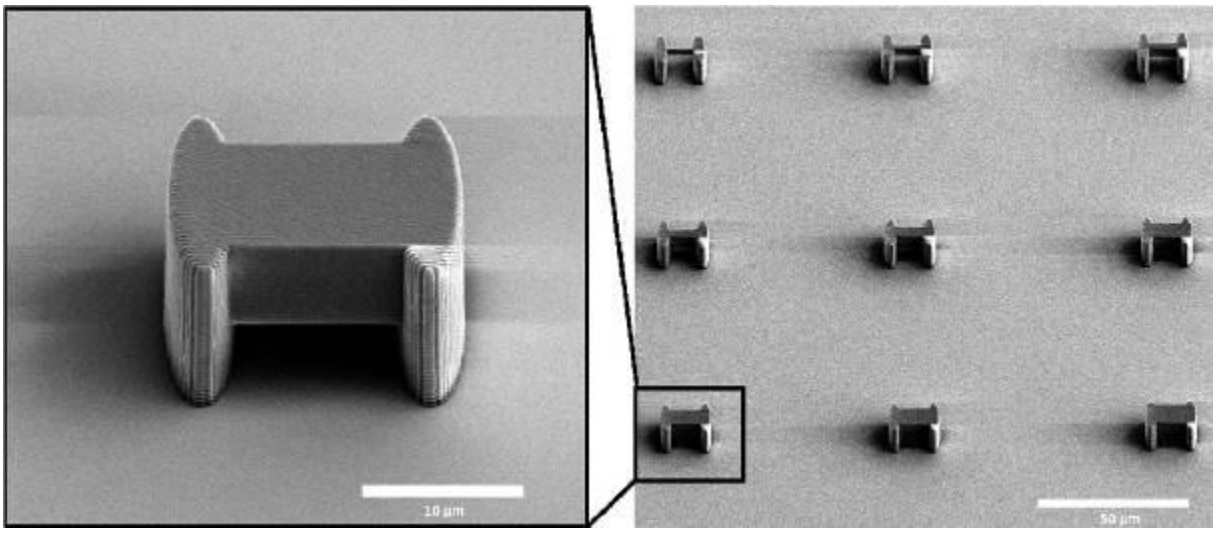

IMLB.P008

Detecting charge transfer in defective 2D WS2 with electron ptychography

C. Hofer[1], J. Madson[2], T. Susi[2], T. J. Pennycook[1]

[1]University of Antwerp, Antwerp, Belgium
[2]University of Vienna, Vienna, Austria

Detecting the electron redistribution in a material is a challenging, but important task as it can reveal fundamental information about chemical bondings. Conventional electron microscopy techniques such as annular dark field scanning transmission electron microscopy (ADF-STEM) are only sensitive to the nuclei rather than the electrons. We demonstrate the use of electron ptychography to detect charge transfer in two-dimensional WS2 at atomic resolution. Compared to other phase contrast imaging methods, it has the advantage of higher dose efficiency, correcting residual aberration after data collection as well as distinguishing heavy and light elements with the additional ADF signal. Importantly for this analysis, we introduce a new method to analyse phases which is robust to different experimental parameters. This is crucial as the changes due to charge transfer are very small.

We investigate the charge transfer of single layer WS2 by comparing structural potentials obtained using the independent atom model (IAM) and density functional theory (DFT). Based on them, we extract the atomic phases using single side band ptychography (SSB) and compare them with the experimentally obtained phases. The phase extraction is performed via an optimization approach where a simplified simulation of the structure is matched to the target image. The simulation is obtained via convolution of a kernel corresponding to the contrast transfer function of SSB with a 2D point phase model. The method is demonstrated to be robust to noise and sample tilt.

We show that charge redistribution can be reliably detected and occurs in the pristine WS2 structure as well as in their defects. While in the pristine structure, Sulphur obtains electrons from Tungsten, S vacancies result in a back transfer of electrons from S to W. Interestingly, the charge transfer is directly related to the density of defects. Our studies open up a new route to analyse charge transfers towards a better understanding of the effects of chemical bonds.

IMLB.P009

Interfacial structure dependent dynamics of Cu/ZnO during the reverse water-gas shift reaction

W. Shi[1,2], Y. Zhou[2], S. Helveg[3], K. Qadir[2], E. Zhan[2], M. Li[2], J. Sehested[4], W. Shen[2]

[1]Forschungszentrum Jülich GmbH, Ernst Ruska-Centre for Microscopy and Spectroscopy with Electrons, Jülich, Germany
[2]Chinese academy of science, Dalian Institute of Chemical Physics, State Key Laboratory of Catalysis, Dalian, China
[3]Technical University of Denmark, Department of Physics Surface Physics and Catalysis, Kongens Lyngby, Denmark
[4]Haldor Topsøe A/S, HaldorTopsøesAllé 1, Lyngby, Denmark

1. Introduction

The active sites for industrial copper/zinc oxide/alumina (Cu/ZnO/Al2O3) catalyzed CO2 transformation have been the subject of intense debate due to the complicated structure together with varied evolution both in activation process and during reaction conditions. Although numerous efforts have been devoted for decades, the precisive identification of desired surface and interface as well as the establishment of dynamic structure-function relationship under catalytic relevant environment still remain a formidable challenge.

2. Objectives

The purpose of this study was to establish the dynamic structure-performance relationship of Cu/ZnO under reaction conditions.

3. Materials & methods

Cu/ZnO, ACTEM, In-situ Holder, ETEM

4. Results

In the current study, the reduction of Cu nanoparticles (NPs) supported on hexagonal ZnO with well-defined nanorod shape (Cu/ZnO) is thoroughly investigated by using the state-of-the-art *in-situ* spherical aberration corrected transmission electron microscopy (ACTEM) on atomic-scale, while the dynamic feature in subsequent circumstance of reverse water-gas shift (RWGS) reaction is further explored *via* a combined microscopic and spectroscopic study at technologically interesting temperature range as well as gas composition. The delicate structural information of successfully synthesized Cu/ZnO catalyst after H2 reduction clearly deciphers a semi-spherical morphology of Cu on nonpolar surface of ZnO, whereas an obvious overgrowth of ZnOx moieties alongside faceted Cu NPs on polar terminations. The observed surface changes on catalyst by environmental TEM (ETEM) through increasing the CO2 content under RWGS conditions are accordant to the distribution of intermediates captured by *in-situ* drift infrared (IR) spectroscopy, which indicates an altered reaction mechanism from "surface-redox" to "formate-Langmuir-Hinshelwood" pathway on the basis of the feed-dependent coverage. In addition, further characterization at low temperature directly elucidates the deactivation of Cu particles on ZnO (10-10) due to the high coverage of accumulated carbon containing species. However, no such poison effect occurs for metallic Cu immobilized on ZnO (0002) and the dynamic behavior derived as the consequence of strong metal-support interaction (SMSI) is verified to play a vital role in facilitating the formation and decomposition of kinetic more favorable metastable species, possible carboxyl on this unique configuration. Hence, the description of dynamic interplay by integrated *in-situ* approaches could provide fundamental insights into the understanding of structure dependent Cu-ZnO catalytic synergy, and pave the way for rational design of low-temperature catalyst with high efficiency.

5. Conclusion

In conclusion, we present an integrated *in-situ* study for fundamentally understanding the structure sensitivity of Cu as well as the promotion mechanism of Cu-ZnO interaction under RGWS reaction conditions. These intuitive and spatially resolved evidences as an important feature elaborates a complex scenario of surface chemical reactions in conjunction with dynamical changes of Cu/ZnO catalyst, which could add a new perspective to the ongoing discussion regarding the structure of active sites associated with steps in Cu surface and the Cu-ZnO interface, mainly including the incorporation of partly reduced Zn atoms into Cu steps for the conversion of CO2 molecule.

Fig. 1

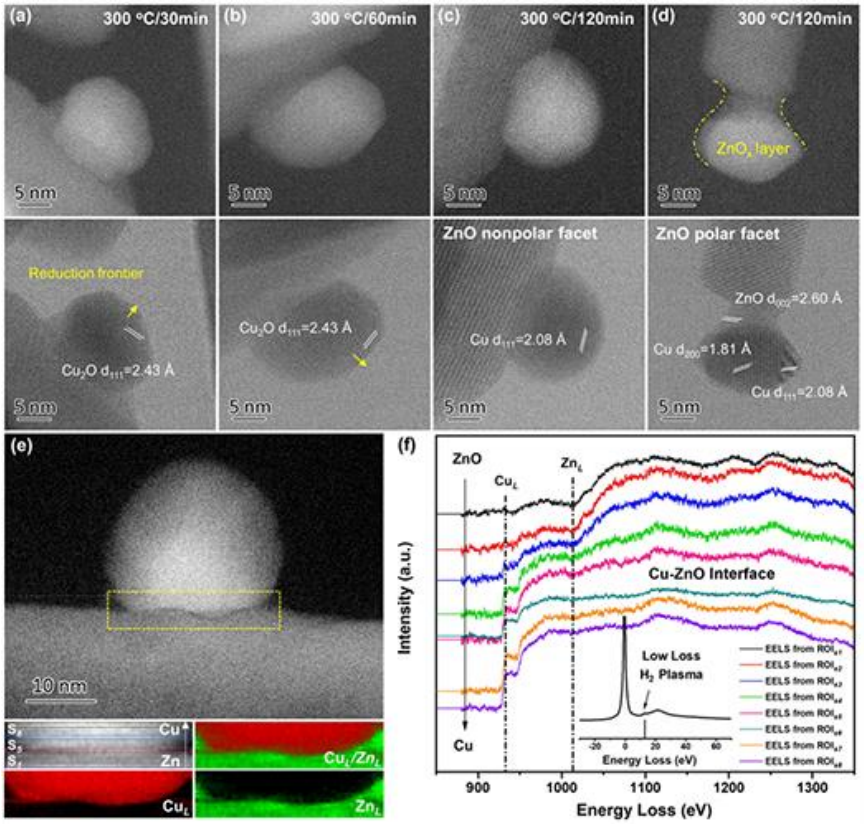

Figure 1. High-resolution HAADF-STEM with the corresponding bright-field (a-d) images of the Cu/ZnO catalyst reduced at 300 °C under 10% H_2/N_2 atmosphere (0.223 ml/min, 850 mbar). EELS-mapping (e) and spectra (f) at the selected area of Cu on ZnO (10-10) interface.

Fig. 2

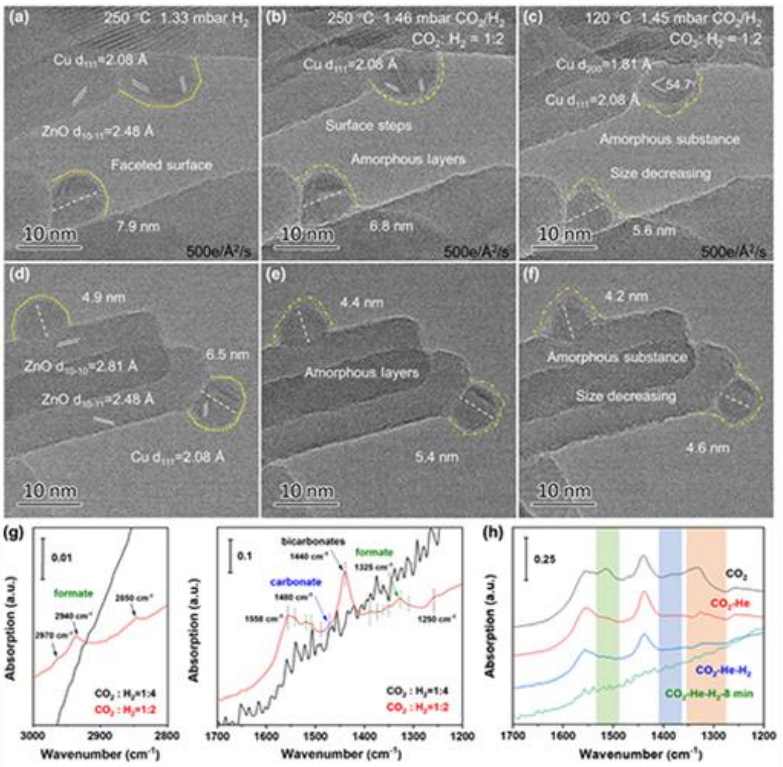

Figure 2. In-situ HRTEM images of Cu particles on nonpolar surface of ZnO during exposing to (a and d) 250 °C, 1.3 mbar H_2; (b and e) 250 °C, 1.46 mbar CO_2/H_2 (CO_2:H_2 = 1:2); (c and f) 120 °C, 1.45 mbar CO_2/H_2 (CO_2:H_2 = 1:2). In-situ IR spectra (g-h) of Cu/ZnO under RWGS reaction conditions at 250 °C.

Fig. 3

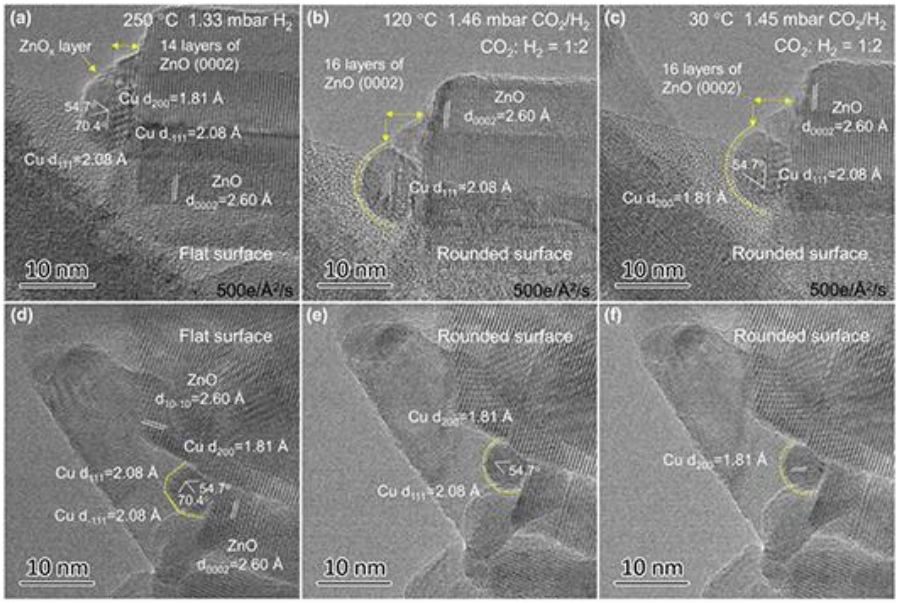

Figure 3. In-situ HRTEM images of Cu particles on polar surface of ZnO during exposing to (a and d) 250 °C, 1.3 mbar H_2; (b and e) 120 °C, 1.46 mbar CO_2/H_2 (CO_2:H_2 = 1:2); (c and f) 30 °C, 1.45 mbar CO_2/H_2 (CO_2:H_2 = 1:2). The images at 120 °C were obtained after maintenance the RWGS reaction at 250 °C for 2 h.

IMLB.P011

Visualizing demulsification of oil-in-water nano-emulsion in LC-TEM

H. Zschiesche[1], A. Baryzewska[1], L. Zeininger[1], N. V. Tarakina[1]

[1]Max Planck Institute of Colloids and Interfaces, Colloid Chemistry, Potsdam, Germany

Nano-emulsions are known as nano-sized dispersions of at least one immiscible liquid in another liquid, kinetically stabilized by emulsifying agent(s), with vast possible applications [1]. One particular interest for probably all application fields is the stability of nano-emulsions, since their stability goes hand in hand with their functionality. However, generally applied procedures are limited to averaging over a bulk volume or are static. Liquid-cell TEM (LC-TEM) is a door opener to reveal local insights to temporally resolved nano-emulsion stability [2].

The here presented work aims direct visualization of kinetically stabilized oil-in-water nano-emulsions using LC-TEM, evaluating their morphology, dynamics and mechanisms of demulsification.

Ultrasonication and homogenization is used to generate droplets with HFE-7500 as the oil dispersed in a Zonyl (surfactant) containing aqueous continuous phase. The average droplet size depends on the applied shear rate and is controlled by dynamic light scattering with a Malvern Panalytical Zetasizer Nano. Protochips" Poseidon LC-TEM holder was used for scanning (S)TEM investigations with Microwell E-chips. (S)TEM studies were performed on a JEOL ARM200F equipped with a cold FEG and Gatan"s Oneview camera.

Nano-droplets of the oil phase (initial average diameter approximately 120 nm, as prepared) are directly visualized in both TEM (homogeneous dose rate of $17 \cdot 10^6$ Gy/s for observation of dynamics) and STEM (averaged dose rate $1 \cdot 10^4$ Gy/s for overview images) mode. The more strongly scattering oil phase appears brighter in annular dark-field STEM excluding a possible confusion with gas bubbles. Moreover, in closely confined regions at the borders of the used LCs, a destabilization of initial nano-droplets towards a formation of larger ones (average diameter 340 nm) is recognized. Surface charges on the LC membranes may locally change the concentration of surfactants that leads to coalescence. In addition to those static observations, in-situ TEM reveals demulsification by coalescence (figure 1) with a rate of $97 \cdot 10^3$ nm^3/s. This determined demulsification rate is orders of magnitude higher than other reported values from indirect determination methods for similar nano-emulsions, where Oswald ripening was assumed to occur [3]. The difference in mechanism and rate might be caused by strong influences of our experimental conditions, such as electron beam damage of surfactants or electric field trap for surfactants at LC membranes, both decreasing the surfactant concentration in the dispersion and therefore destabilizing the nano-droplets leading to coalescence.

Our approach successfully enables studies of oil-in-water nano-emulsions by direct imaging. Demulsification is observed to take place because of a confinement effects in the LC and because of electron beam illuminating effects inducing changes of the surfactant concentration followed by coalescence of nano-droplets. Excluding or reducing those electron beam effects should help to broaden the knowledge on nano-emulsion stabilities and demulsification processes even further. [4]

[1] Anton N et al.; Pharm Res 28 (2011)

[2] Vratsanos, MA et al.; ACS Nano 16 (2022)

[3] Delmas T et al.; Langmuir 27 (2011)

[4] Max Planck Society is acknowledged.

Figure 1: TEM images of nano-emulsion dynamics. Nano-droplets can immediately identified (a) and merge by coalescence during further electron beam exposure (b)-(d).

Fig. 1

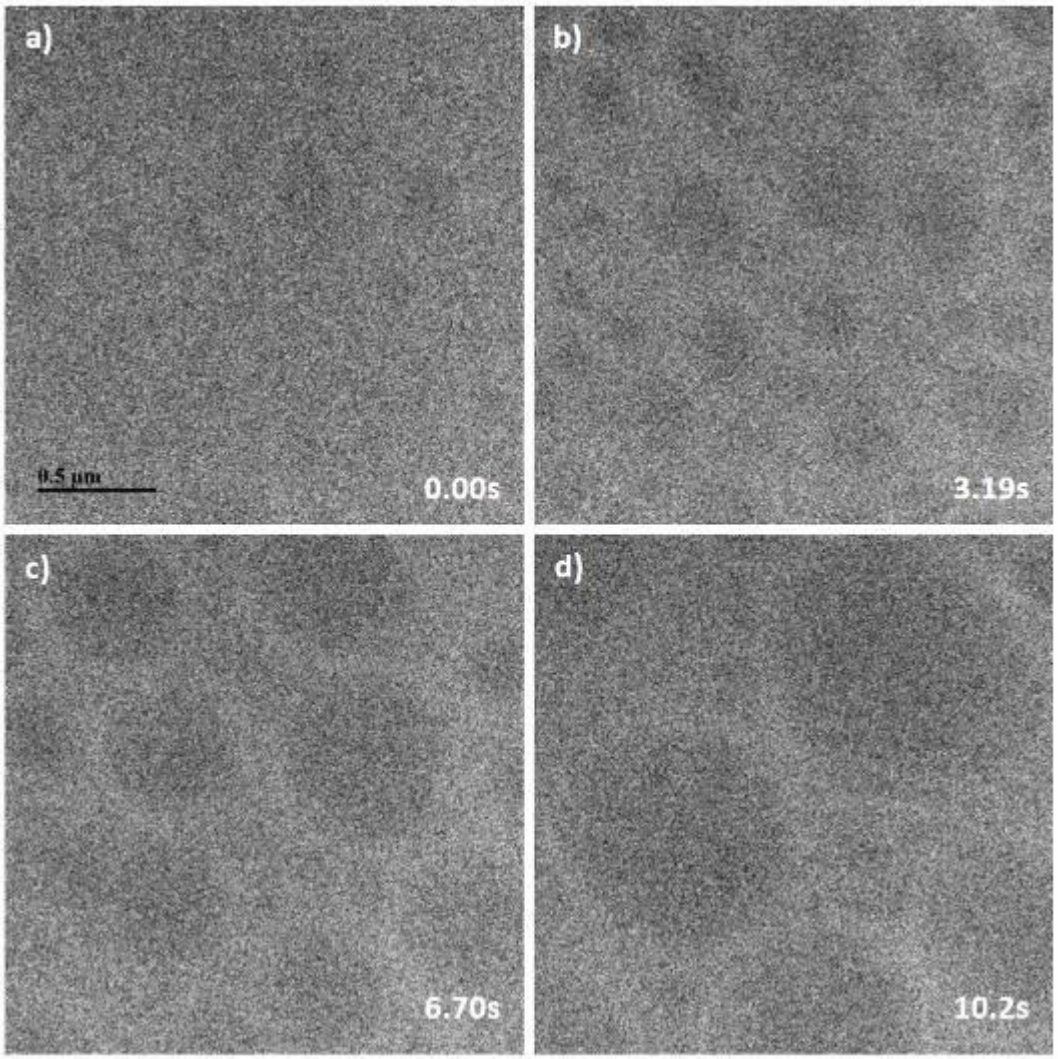

IMLB.P012

Two microscopes are better than one – a unique new Inspection tool for micro/nanostructures by combination of AFM and SEM

H. Frerichs[1], L. Stühn[1], S. Seibert[1], M. Wolff[1], C. Schwalb[1]

[1]Quantum Design Microscopy GmbH, Darmstadt, Germany

Combining different analytical methods into one instrument is of great importance for the simultaneous acquisition of complementary information. Especially the in-situ combination of two of the most powerful microscopy techniques – scanning electron microscopy (SEM) and atomic force microscopy (AFM) – enables completely new insights in the micro and nano-world. [1,2] In this work, we present a unique inspection tool that seamlessly combines SEM and AFM for inspection and process control of Micro- and Nanostructures (see Figure 1). Due to the self-sensing piezoresistive cantilever technology used for the AFM scanner the cantilever deflection signal can be measured completely electrical and allows for simultaneous acquisition of SEM and AFM data directly at the region of interest. We will present a variety of novel case studies to highlight the advantages this new tool for interactive correlative in-situ nanoscale characterization for different materials and nanostructures.

First results will focus on semiconducting BaTiO3-based ceramics with positive temperature coefficient of resistivity (PTCR) that currently gain increased attention due to their application as cabin heater in electrical vehicles. We use electrostatic force microscopy (EFM) in combination with the SEM in order to precisely analyze the grain boundary potential barriers of different BaTiO3-based samples. [3] The grain boundaries were located by backscatter electron detection (BSE) and afterwards measured with in-situ EFM. The barriers were shown to be significantly thinner and more pronounced as the amount of SiO2 was increased from 0 to 5 mol% (see Figure 2). These results can be directly correlated with electron backscatter diffraction (EBSD) measurements to link the AFM and SEM data to the crystallographic microstructure of the different samples.

In addition, we will present first results for the in-situ characterization of magnetic micro- and nanostructures for industrial relevant samples (e.g., duplex steel) by combination of SEM and high-vacuum magnetic force microcopy (MFM). SEM enables to the grain boundaries and position the cantilever directly at the region of interest, whereas in-situ MFM allows for the characterization of 3d topography and magnetic properties with nanometer resolution (see Figure 3).

Based on the broad variety of applications regarding the inspection and process control of different materials and devices, we anticipate that this new inspection tool to be one of the driving characterization tools for correlative SEM and AFM analysis in the future.

Fig. 1

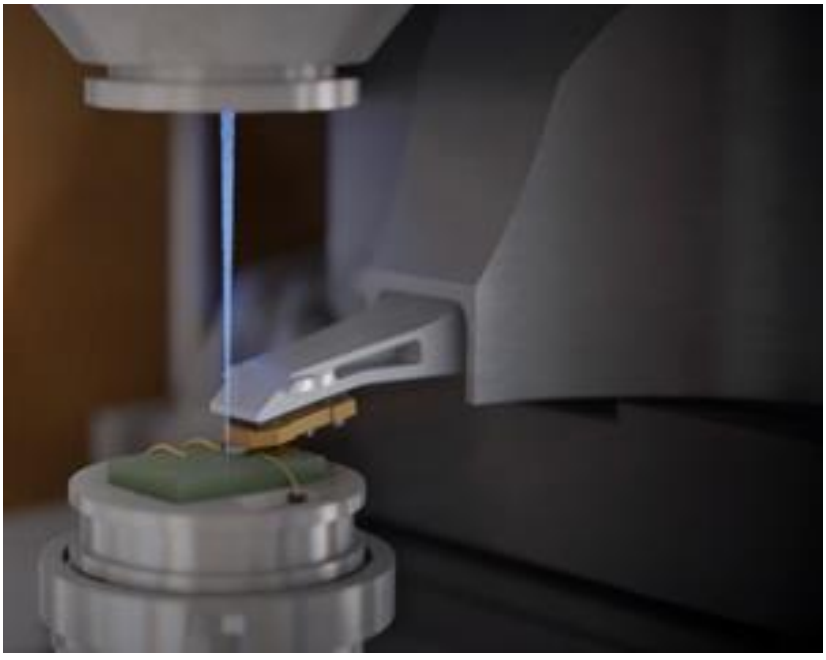

Fig. 2

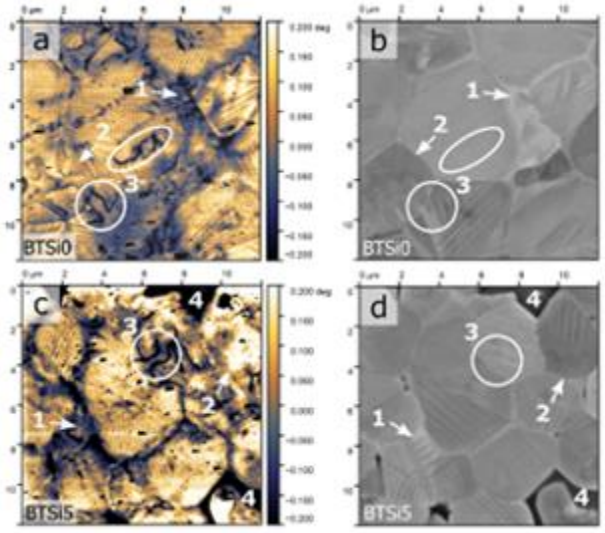

	C–V [μm]	EFM [μm]
BTSi0	0.89 ± 0.04	0.92 ± 0.13
BTSi2	0.47 ± 0.02	0.50 ± 0.06
BTSi5	0.53 ± 0.03	0.52 ± 0.08

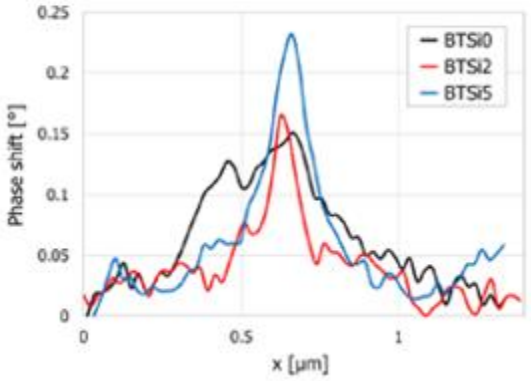

Fig. 3

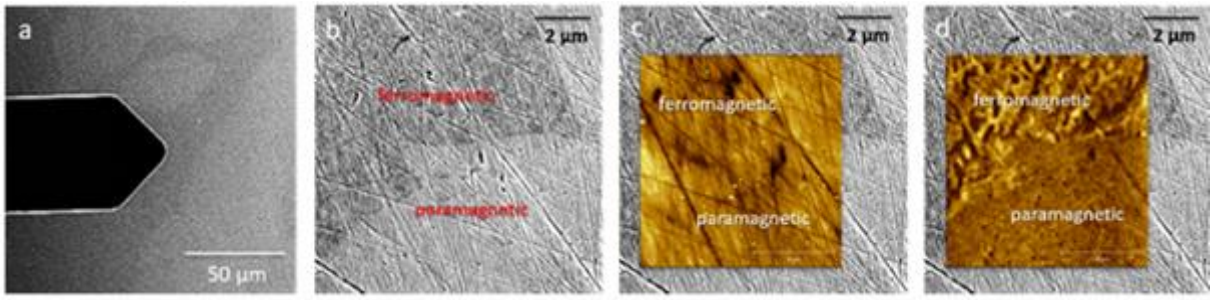

IMLB.P013

Structural evolution of supported ZnPd/ZnO nanoparticle catalysts studied by environmental STEM

A. Meise[1], O. Tiryaki[2], M. Armbrüster[2], R. E. Dunin-Borkowski[1], M. Heggen[1]

[1]Forschungszentrum Jülich, Ernst Ruska-Centre, Jülich, Germany
[2]University of Technology, Institute of Chemistry, Chemnitz, Germany

Methanol Steam Reforming (MSR) is an important reaction converting methanol into hydrogen (CH3OH + H2O à 3 H2 + CO2) holding promise for easy fuel handling in hydrogen based applications like fuel cells. ZnPd/ZnO nanoparticles are promising MSR catalysts due to their high CO2 selectivity, stability and activity.1 It is known that their properties depend strongly on their microstructure and particle size, thus, also on their preparation method.2-5 In order to understand their microstructural evolution during preparation, the calcination of supported Pd(NO3)2 in O2 was studied using in situ high resolution scanning transmission electron microscopy. For additional pre- and post characterisation energy dispersive x-ray spectroscopy and electron energy loss spectroscopy were applied.

References

1. Föttinger, K., Van Bokhoven, et al *J. Phys. Chem. Lett.* **2**, 428–433 (2011).
2. O. Jakdetchai, N. Takayama, T. Nakajima, Kinet. Catal. 46 (2005) 56–64
3. J.-P. Shen, C. Song, Catal. Today 77 (2002) 89–98
4. R.A. Dagle, Y.H. Chin, Y. Wang, Top. Catal. 46 (2007) 358–362
5. Y. Wang, J. Zhang, H. Xu, X. Bai, Chin. J. Catal. 28 (2007) 234–238

IMLB.P014

Twist enables superlubric behavior in bilayer graphene

X. Zhou[1], M. Wu[1], C. Rubach[1], R. Kammel[1], E. Spiecker[1]

[1]Friedrich-Alexander-Universität Erlangen-Nürnberg, Erlangen, Germany

The state of vanishing friction known as superlubricity has important applications for energy saving and increasing the lifetime of micro- or nanomechanical systems with sliding components (1). Superlubric behavior has been found in two-dimensional graphene or graphite because of the weak interlayer van der Waals force and shows a strong dependence on twist angle. Experimentally, M. Dienwiebel et al. recognized two narrow angular regions with a distance of about 61 deg. ± 2 deg. showing high friction, whereas nearly zero friction was observed between these two angular regions. This indicates that the ultralow friction is associated with incommensurability between the rotated graphite layers (2). Theoretically, H. Z. Bai et al. revealed the bilayer graphene (BLG) superlubricity with a coefficient of friction of 0.0003 at a twist angle of 3°, and this coefficient of friction is about 26 times lower than a non-superlubric state (3). Despite the insightful theoretical works, the frictional properties within a small twist angle regime and the dynamic twist process during sliding between atomic layers of graphene have not been directly observed in experiments due to the great challenges of such experiments.

Here, we report the first time direct observation of dislocation activity and twisting in BLG by in situ straining inside a transmission electron microscopy (Fig. 1A). Combining with the 4D STEM technique, strains and twist angles were evaluated at each strain step (Fig. 1A) and their relationship was established to understand the superlubric properties of BLG. In our experiment, a monolayer-bilayer-monolayer graphene configuration was verified (Fig. 2B). As depicted in Fig. 2B-D, the width of the bilayer region decreased as well as the dislocation network changed during straining. With a BLG change of 22 nm (Fig. 2C), dislocation in BLG converted to the Moiré superlattice configuration, indicating the twist between the two monolayers. When it comes to a BLG width change of 121 nm (Fig. 2D), a higher dislocation density is reached, indicating a further increase in twist angle. The analysis on dislocation types revealed that the predominate screw type dislocations with Burgers vectors and remain, while dislocations with Burgers vectors changed from mixed type to mainly screw type (Fig. 2E-G). Meanwhile, the evaluation of twist angle distribution in BLG shows that the twist angle increases along with the continuous sliding, and these results agree well with the twist angle calculated from the Moiré superlattice periodicity (Fig. 2A). Eventually, the relationship between strain and twist angle reveals a clear decreasing tendency in strain with the increasing of twist angle (Fig. 2B), indicating a gradual change towards superlubric behavior in BLG.

In conclusion, we developed an in situ staining method combined with 4D-STEM to realize the direct observation of dislocation activities and investigation of the twist-dependent superlubric behavior in BLG. This method can be taken as a versatile way to study the strain-related physical properties of other 2D materials.

(1) S. Kawai et al. *Science*, , 351, 957 (2016).

(2) M. Dienwiebel, et al. *Phys. Rev. Lett.*, 92, 12 (2004).

(3) H. Z. Bai, et al. *Carbon*, 191, 28 (2002).

(4) X. Zhou, et al. to be published.

Fig. 1 (A) Schematic representation of the straining process and 4D STEM set-up for strain and twist angle evaluation. (B to D) The sequence DF-TEM images taken from the reflection describe the dislocation network and twist in BLG at various strain steps. (E to G) Drawing of the dislocations in the BLG region corresponding to B to D.

Fig. 2 (A) Twist angle distribution at various strain steps. (B) Strain-twist angle correlation, showing a decreasing trend of strain with the increasing of twist angle.

Fig. 1

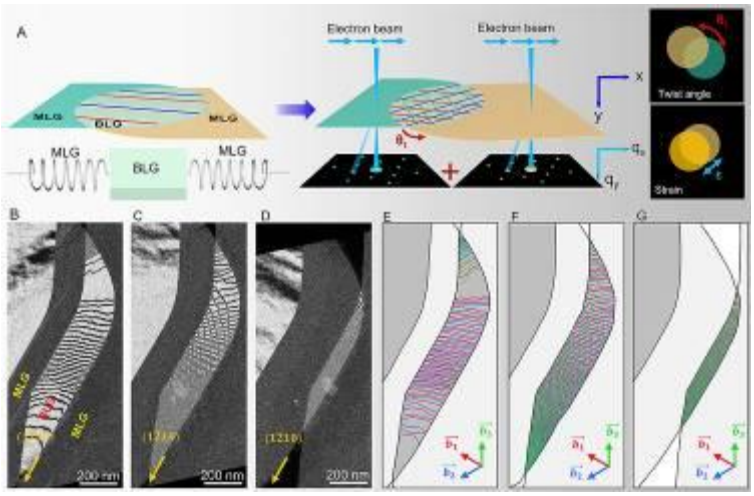
A
Electron beam
Electron beam
MLG
BLG
MLG
MLG
BLG
MLG
Twist angle
Strain
B
C
D
E
F
G
200 nm
200 nm
200 nm

Fig. 2

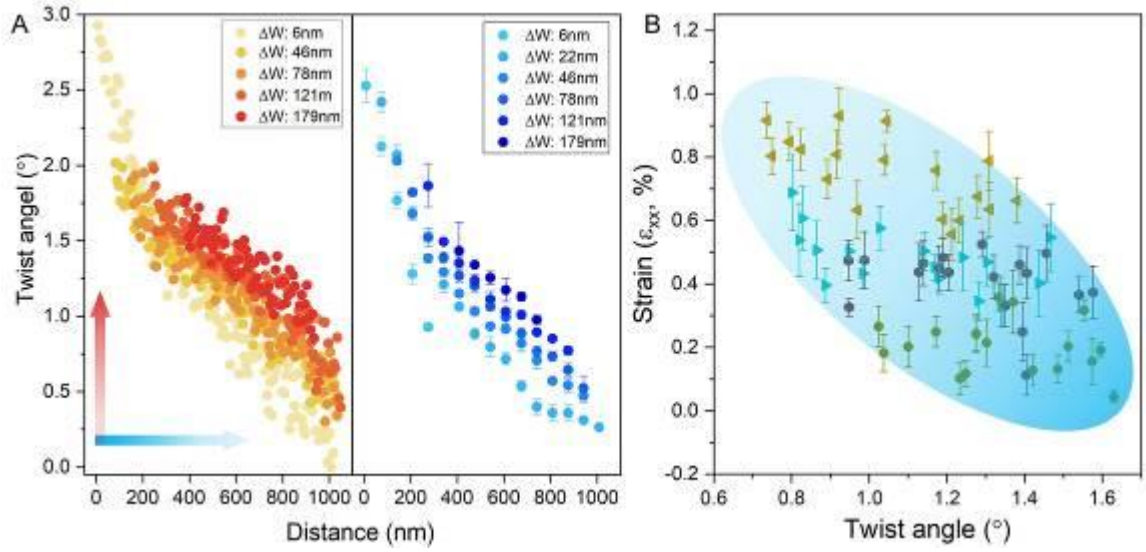
A
ΔW: 6nm
ΔW: 46nm
ΔW: 78nm
ΔW: 121m
ΔW: 179nm
ΔW: 6nm
ΔW: 22nm
ΔW: 46nm
ΔW: 78nm
ΔW: 121nm
ΔW: 179nm
Twist angel (°)
Distance (nm)
B
Strain (εxx, %)
Twist angle (°)

IMLB.P015

EDS nanometric spatial resolution in SEM for bulk material analysis

P. Soni[1], I. Nemeth[1], M. Ben Haj Slama[1]

[1]Bruker Nano, EMA, Berlin, Germany

Reduced-dimensionality materials are increasingly gathering pace and progress in many important fields of life. For instance, they are undergoing rapid development in energy conversion, solid-state lighting, biological sensing, and information technology.

Investigating such nanoscale featured materials became a necessity to achieve better properties and performances. Electron-microscopy chemical mapping is one of the powerful tools to do so. For bulk samples, though, it is very challenging to combine high spatial resolution imaging and spectroscopic analysis at the nanoscale.

In response to this challenge, Bruker launched recently the XFlash® 7 EDS detectors. These new detectors offer high spatial resolution by providing excellent output count rates at low probe currents. This ideal combination is obtained thanks to the best solid angle and highest pulse processing speeds ensuring high sensitivity and the highest collection efficiency.

In the present work, sub-10 nm EDS-spatial resolution is achieved using low and high kVs and are demonstrated through examples of bulk semiconductor and aerospace materials with challenging element combinations.

IMLB.P016

Phase contrast in quantum electron microscopy

S. Loginov[1,2], M. Krielaart[1,2], P. Kruit[1,2]

[1]TU DELFT, Applied Sciences, Netherlands
[2]Delft University of Technology, ImPhys, Delft, Netherlands

Quantum Electron Microscopy technique (QEM) is aimed for improvement of electron dose limited resolution by implementing interaction free measurements [1]. One of the QEM approaches is to build a Mach-Zehnder interferometer for electrons using grated mirrors as electron beam-splitters [2]. Earlier, it was shown that a sample with different transparency levels can be imaged by QEM in interaction free manner [3]. Now we consider the case of phase-only sample which represents a typical cryo-EM situation. We conduct theoretical analysis on the dose limited phase resolution of QEM in order to prove it is worthwhile to build.

Cryo-Electron Microscopy suffers from sensitivity of biological samples to electron damage. Large proteins and protein complexes can be studied in cryo-EM, while for smaller proteins the X-ray diffraction is still the technique of choice. Modern aberration corrected TEMs and STEMs provide atomic resolution in crystalline samples with illumination doses higher than ~10^4 e-/A^2. Protein structure degrades severely already at doses of two orders of magnitude lower. Novel EM techniques aim for higher dose efficiency that will allow new areas for the cryo-EM investigation. One of such techniques is QEM.

In QEM an electron is split into two states, a sample state |S> and reference state |R>, so that initially <S|S> << <R|R>. The sample state is used as a STEM focused probe while the reference state passes through the empty space. The |S>-state experiences phase shift passing through the sample . After the sample plane, the two states are directed back to the beam-splitter where they exchange some of their amplitudes. This cycle is repeated N times and the electron is taken out to the detector plane to collapse in either the |S>-state or in the |R>-state, with probablity depending on the pahse shift in the sample (see Fig. 1)

Phase shift can be tuned such that for a blank sample electrons always arrive in the |S>-state. Then for large the interference on the beam-splitter is inconsistent and probability to find the electron in the |R>-state is overwhelming. The maximal dose is reached at zero phase shift with a value of ≈N/2 representing the fact that electron spends half of the time in the sample arm on average. At large pahse shifts the dose is lower since the |S>-state

Figure 1 Phase dependent behavior of a QEM with N=24 cycles. Phase shift in the sample controls collapse probabilities of electrons. For large phase shifts electrons are mostly locked in the initial reference state (blue). For large phase shifts more electrons are detected in the sample sate (red). Electron dose also depends on the phase (black, right axis), with the receiving maximum dose of ≈N/2 (per electron).

Using a dose-limited phase resolution as a metric we show that the QEM achieves at least twice as good phase contrast as a TEM for a typical cry-EM protein imaging setup (see Fig. 2).

Figure 2 Simulated images (10x10nm^2) of a viral protein (PDB DOI: 10.2210/pdb5I4T/pdb) at 200kV tension for aTEM (left panel) and QEM (right panel).The exaggerted doses applied for image clarity.

Fig. 1

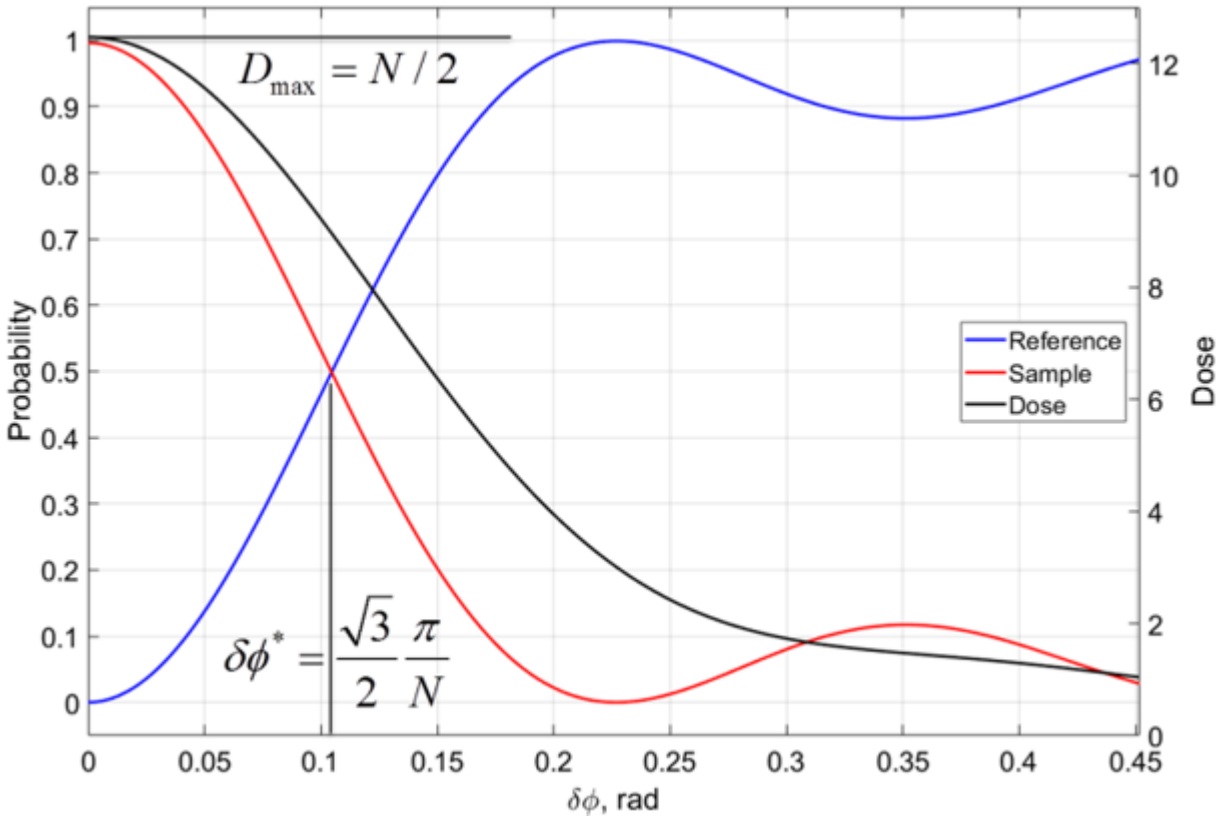
$D_{max} = N/2$
$\delta\phi^* = \frac{\sqrt{3}}{2}\frac{\pi}{N}$
Probability
Dose
Reference
Sample
Dose
$\delta\phi$, rad
0
0.05
0.1
0.15
0.2
0.25
0.3
0.35
0.4
0.45
0
0.1
0.2
0.3
0.4
0.5
0.6
0.7
0.8
0.9
1
0
2
4
6
8
10
12

Fig. 2

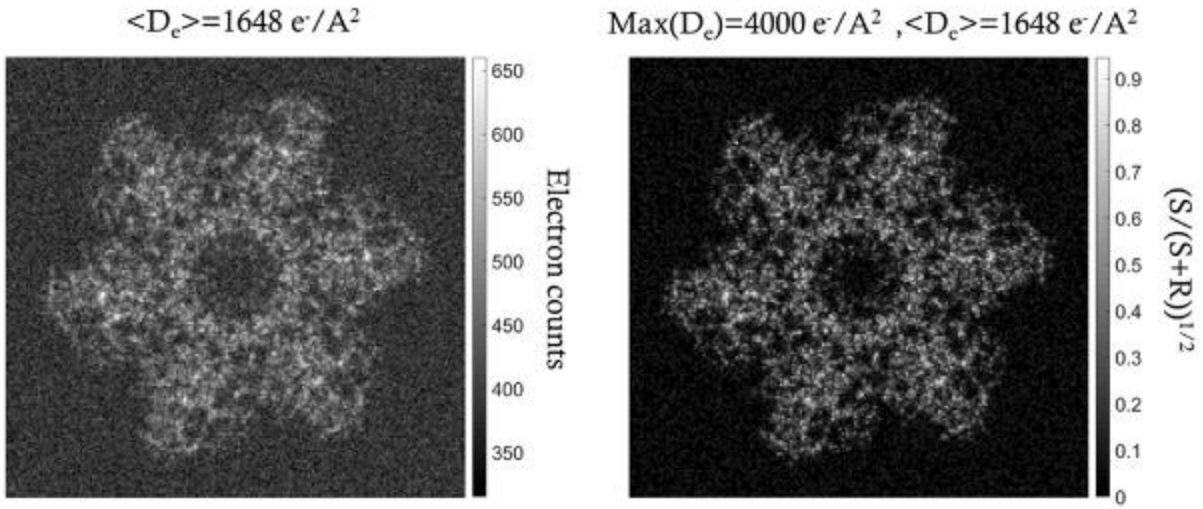
<D_e>=1648 e^-/A^2
Max(D_e)=4000 e^-/A^2 ,<D_e>=1648 e^-/A^2
Electron counts
650
600
550
500
450
400
350
$(S/(S+R))^{1/2}$
0.9
0.8
0.7
0.6
0.5
0.4
0.3
0.2
0.1
0

IMLB.P017

Miniature components for electron optical instruments with two parallel optical axes

D. Maas[1], M. Krielaart[2], L. van Velzen[2], S. Loginov[2], P. Kruit[2]

[1]TU-Delft & TNO, ImPhys, Delft, Netherlands
[2]TU-Delft, ImPhys, Delft, Netherlands

This poster introduces miniature electron-optical components for e.g. a double mirror corrector or quantum electron microscope [1,2]. Krielaart"s QEM design has two *parallel* optical axes; a microscope axis and, shifted by typically a millimetre, a mirror axis. A beam separator pair is needed to tilt the entering beam towards the mirror while the reflected exiting beam passes straight, or vice versa. Electrostatic mirrors are needed to cancel aberrations and diffract the beam in a QEM cavity [2].

The components are designed for electron beam energies up to 5 keV. Experimental data on the performance of a beam separator (EBE unit) and a miniature electron mirror will be presented.

The *EBE unit* is a compact bi-axial beam separator with low higher order deflection aberrations [4]. The EBE unit consists of three dipole layers that are placed spatially along the parallel optical axes. This (di)pole arrangement reduces the inherent hexapole fields. In each layer, a mu-metal pole pair provides for deflection in the two lateral directions by either an electric and/or magnetic field. Experiments at E = 2 keV beam energy show a deflection sensitivity of 0.275 mrad/mA and 1.98 mrad/V for magnetic respectively electric excitation.

Our miniature *mirror unit* design combines classic parts machining (e.g., for the holder frame and the liner tube that guides the beam through the mirror electrode plane) with micro-lithographic technologies as developed by the MEMS industry. The high precision of MEMS manufacturing techniques yields well-defined bur-free free-form flat electrodes. These can be used to build low-cost high-quality electrostatic deflectors, stigmators lenses and mirrors. Here, electrostatic mirrors and lenses are made using metalized silicon elements as electrodes, which are sandwiched in between electrically insulating flat quartz spacers. Typical layer thicknesses are a few hundred micrometres. To avoid electrical fields above the breakdown limit of 10 kV/mm, the beam energy is typically limited to 5 keV. Before fixing their position in the full stack, each electron optical element is accurately aligned to both axes using a dedicated 6-DOF Hexapod stacking tool [5].

The beam is injected into the QEM cavity through a grounded metal liner tube, thus offering electrons a field-free passage through the voltage barrier of the mirror and lens electrodes. The beam is shifted from the microscope axis to the mirror axis by a MEMS electrostatic deflector and vice versa by electro-magnetic deflectors in the EBE unit. To set the focal length and aberrations of the mirror, 3-5 accurately stacked electrodes are energized up to ±5 kV [1-3].

In conclusion, when properly designed, aligned and energized, these new compact electron optical components can together conceive a round-trip cavity as needed to coherently build up the signal in a quantum electron microscope.

References

[1] Dohi, H. and Kruit, P., Ultramicroscopy **189** (2018) 1-23

[2] Krielaart, M.A.R., and Kruit, P., Ultramicroscopy **233** (2022) 113424

[3] M.A.R. Krielaart and P. Kruit, Phys. Rev. A **98** (2018) 063806

[4] Krielaart, M.A.R., Maas, D.J., Loginov, S.V., and Kruit, P., J. Appl. Phys., **127** (2020) 234904

[5] Chapter 5, PhD thesis Zonnevylle, A.C., https://doi.org/10.4233/uuid:23221904-c9c1-4537-af7f-abdbb9df06ed

MK, SL and PK acknowledge funding from the Gordon and Betty Moore Foundation. DM gratefully acknowledges support by Hitachi High Technologies.

Fig. 1

Figure 1. ***Left Panel:*** *Schematic of the electron beam trajectory in Krielaart's QEM cavity [1]. The electron beam enters the QEM cavity on the microscope axis (μA) and is tilted to the mirror axis (MA) by an electrostatic deflector (TD). The EBE units tilt downward beams counter-clockwise (and transmits upward beams). The electrostatic mirrors reflect and refocus the beam on the common cross-over plane (CCP), while generating negative spherical and chromatic aberrations. Using the newly developed miniature components, the total height of the QEM cavity is less than 6 cm.* ***Right panel:*** *Photograph of a 1 cm thick EBE unit [3].*

Fig. 2

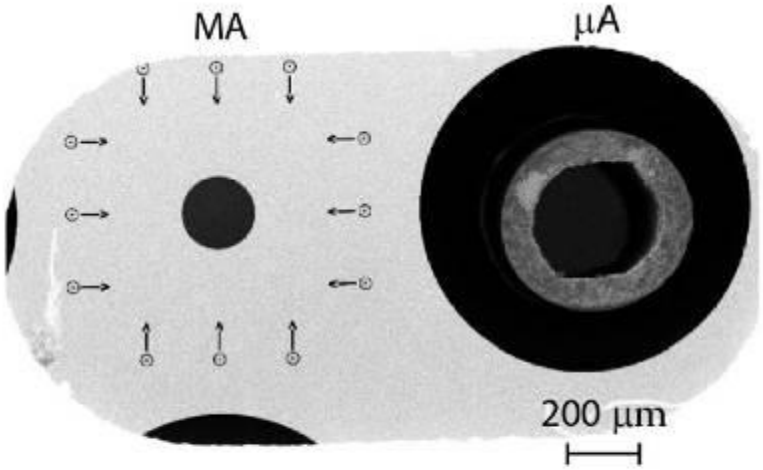

Figure 2. *SEM micrograph image that offers a top-down view on a part of the mirror unit. The large light-grey part is a MEMS mirror electrode. The arrows are alignment marks to accurately position the next MEMS part on top of this MEMS part in the Hexapod stacking tool [5]. The small black hole (at the mirror axis) is the mirror bore with a typical diameter of 200 micron. The metal liner tube (at the microscope axis) in the large black hole shows the characteristic irregularities that classically machined parts have at this length scale.*

IMLB.P018

Event-driven MHz 4D STEM for low dose and *in situ* electron microscopy

P. Lu[1], J. Jo[1], D. Byelov[2], M. Kelder[2], D. Weber[1], A. Clausen[1], T. Yang[1], L. Jin[1], R. E. Dunin-Borkowski[1]

[1]Forschungszentrum Juelich, Ernst Ruska-Centre for Microscopy and Spectroscopy with Electrons and Peter Grünberg Institute, Jülich, Germany
[2]Amsterdam Scientific Instruments, Amsterdam, Netherlands

Four-dimensional scanning transmission electron microscopy (4D STEM) measures 2D reciprocal space diffraction from a focused electron probe scattered at each pixel across a 2D real space area. This high-dimensional dataset allows much richer information to be retrieved than conventional STEM [1]. Particularly the past decade has witnessed the advance of this technique because of the introduction of fast electron-counting detectors [2], which runs at 1-10 *k*Hz continuous readout, while the conventional CCD only works at 1-10 Hz level. However, this "fast" frame rate is still 2-3 orders of magnitude slower than the conventional STEM with single-pixel or segmented detectors. This would prevent at least two kinds of applications which should have been benefited from the versatile 4D STEM measurements. The first is atomic-resolution low-dose phase contrast imaging of sensitive specimens. With a limited amount of dose budget and a fine scanning pixel size (for resolving atomic resolution, unless compressed sensing or ptychography is used), the electron probe current would be impractically low when the diffraction frame rate is only at *k*Hz. As an example, for a total dose of 100 e-/A2 and a pixel size of 0.5 A, the probe current has to reduce to 0.004 pA for 1 *k*Hz detector but can be 4 pA when the detector runs at 1 MHz. Thousandths of pA is either inaccessible in some microscopes or in practice hardly usable in most cases. The second is *in situ* study of dynamic behavior upon external stimuli. Pushing 4D STEM towards conventional STEM speed or beyond would permit time-resolved investigation of dynamic functionalities of the devices from the rich crystallographic and/or phase contrast information.

In contrast to the conventional frame-based detectors, event-driven readout architecture has very recently been applied to electron detection in cryo-EM [3,4], 4D STEM [5,6], as well as coincidence [7,8] and time-resolved [9] spectroscopy. We installed an event-based Timepix3 detector from Amsterdam Scientific Instruments with 2x2 chips (in total 512x512 pixels) on a monochromated and probe-corrected Thermo Fisher Scientific Titan STEM, and tested its performance in 4D STEM experimental setup and applications. Benefiting from its 1.56 ns Time of Arrival (TOA) binning resolution, we can now run 4D STEM measurements at MHz frame rate with reasonable probe current. Digital blanking of detector pixel/area was sometimes used to gain higher probe current within the maximum event rate. We will present three applications that have been tested so far: i) low-dose atomic-resolution phase contrast imaging, ii) large field-of-view crystallography phase mapping, and iii) *in situ* centre of mass analysis of e-beam-induced charging. Further prospects on programmable scanning path to manipulate the e-beam-induced charging or damage as well as near-real-time analysis of event-driven data based on sparse matrix computation will also be discussed during the presentation.

References

[1] C. Ophus, Microsc. Microanal. 25, 563 (2019)
[2] B. D. A. Levin, JPhys Materials 4, 042005 (2021)
[3] J. P van Schayck *et al*., Ultramic. 218, 113091 (2020)
[4] H. Guo *et al*., IUCrJ 7, 860 (2020)
[5] D. Jannis *et al*., Ultramic. 233, 113423 (2022)
[6] P. M. Pelz *et al*., IEEE Signal Process. Mag. 39, 25 (2022)
[7] D. Jannis *et al*., Appl. Phys. Lett. 114, 143101 (2019)
[8] N. Varkentina *et al*., Sci. Adv. 8, eabq4947 (2022)
[9] Y. Auad *et al*., Ultramic. 239, 113539 (2022)

WS1.001-invited

Putting your data into the void

C. Mangler[1], J. Kotakoski[1]

[1]Faculty of Physics/University of Vienna, Physics of Nanostuctured Materials, Vienna, Austria

With rapid advances in detector technology and computing resources, modern microscopes produce massive amounts of data. Additionally, advanced sample preparation techniques often involve various steps utilizing multiple devices each generating additional data. Therefore, data management should be considered a crucial part of today's research infrastructure. This lead to the publication of guiding principles for scientific data-management describing four fundamental cornerstones: Findability, Accessibility, Interoperability and Re-usability (FAIR) [1].

To deal with this, we created a system capable of handling most of the usual data management tasks in an automatic fashion without getting in the way. This is implemented by a file storage infrastructure automatically collecting data from various experimental devices including electron microscopes, optical microscopes, sample preparation devices and mechanical testing systems. Raw research data is considered immutable and is therefore stored read-only on a scalable distributed storage system [2]. The data can be accessed via a front-end server by a secure connection using asymmetric cryptography.

Metadata is handled via an electronic lab book system [3]. This system is accessible via standard web browsers and is used for documenting experimental steps and persons, devices and samples involved in carrying them out. The lab book system is also used for keeping a database of samples. Currently we are testing an automatic sample tracking workflow based on QR-codes and a distributed database populated from the lab book entries.

A complete research data management system also has to cope with data processing. To achieve a reusable and well-documented data processing and analysis workflow, we use GitLab [4] to track development of our analysis tools and manuscripts. The GitLab server also acts as an issue tracker for administration of all the involved hard- and software assets.

To setup a future-proof, independent system and to avoid possible vendor lock-in scenarios, care was taken to only use free and open-source software [5].

In its current state the system is used internally in our work-group. A workflow for publishing data for external use is planned via the Repository for Permanent Hosting, Archiving and Indexing of Digital Resources and Assets (PHAIDRA) at the University of Vienna [6].

References

[1] M. Wilkinson, M. Dumontier, I. Aalbersberg, et al., "The FAIR Guiding Principles for scientific data management and stewardship", Sci Data 3, 160018, 2016, doi:10.1038/sdata.2016.18
[2] S. A. Weil, S. A. Brandt, E. L. Miller, D. D. Long, C. Maltzahn, "Ceph: a scalable, high-performance distributed file system", In Proceedings of the 7th symposium on Operating systems design and implementation (OSDI '06). USENIX Association, USA, 307–320, 2006
[3] N. Carp, A. Minges, M. Piel, "eLabFTW: An open source laboratory notebook for research labs", J. Open Source Softw., 2(12), 146, 2017
[4] P. Choudhury, K.Crowston, L. Dahlander, et al., "GitLab: work where you want, when you want", J. Org. Design 9, 23, 2020, doi:10.1186/s41469-020-00087-8
[5] R. M. Stallman, "GNU's Bulletin, Volume 1 Number 1". https://gnu.org/bulletins/bull1.txt. p. 8. (accessed 2022-07-28)
[6] University of Vienna, https://phaidra.univie.ac.at/ (accessed 2022-07-28)

WS1.002-invited

A community-driven glossary for data interoperability in the electron microscopies

O. Mannix[1], V. Hofmann[2], A. Strupp[2], S. Sandfeld[2]

[1]Helmholtz-Zentrum Berlin für Materialien und Energie, Berlin, Germany
[2]Forshungszentrum Jülich GmbH, Jülich, Germany

Research data has to fulfil a number of requirements for it to be fully exploitable - today and in the future. The FAIR principles [1] – findable, accessible, interoperable, and reusable – provide a conceptual framework to achieve this, but the pathway to implementation is often unclear.

Here we focus on the challenge of implementing the "I" in FAIR. Interoperability is the potential for two independent agents to work on the same data in a coordinated fashion. It is especially relevant for researchers working in interdisciplinary fields, such as electron microscopy, where terminology in adjacent scientific disciplines is unknown, or where identical terms are used with differing meaning, for example, consider a mathematical or biological cell.

The use and adoption of established vocabularies and semantic standards can provide solutions – however these may be infeasible to implement, non-existent, or scientifically unsuitable. This is why a number of initiatives are developing semantic artefacts that aim to describe experimental equipment, workflows, and analysis procedures in electron and ion microscopies. Harmonisation of these efforts to ensure interoperability across the community is required.

To support the long-term semantic interoperability the Helmholtz Metadata Collaboration (HMC) is coordinating a community-wide effort, including over 45 scientists from more than 22 institutions across Switzerland, Austria, and Germany, and including representatives of several NFDI consortia [2], to create a joint resource to harmonize semantics in the field of electron and ion microscopies. In our presentation we will report on this community effort - the EM glossary group [3]. We will describe how we achieve consensus on terms commonly used in electron and ion microscopies via a remote, collaborative workflow based on the platform GitLab. A text-mining approach has been used to evaluate EM image metadata and prioritise terms which are widely used in the community. We will show results, including some of our harmonized definitions, and provide details of our implementation strategy.

The developed resource will provide harmonized and machine actionable semantics to support specific development efforts such as metadata schemas or ontologies in their respective fields. This will benefit experimental scientists by providing clarity when annotating and re-using research data; and by facilitating communication when conducting interdisciplinary studies.

Do you work in electron and/or ion microscopy or related data analysis? Follow us on twitter @helmholtz_hmc or tweet #EMGlossary. You want to get involved in the development and/or join our meetings? Send an email to hmc@fz-juelich.de or hmc-matter@helmholtz-berlin.de

1. Wilkinson, M.D. et al. Scientific Data. http://dx.doi.org/10.1038/sdata.2016.18 (2016)

2. NFDI: Nationale Forschungsdateninfrastruktur. https://www.nfdi.de/

3. EM Glossary GitLab repository: https://codebase.helmholtz.cloud/em_glossary/

Fig. 1


vendors
laboratory
/ ELN schema
EM GLOS SARY
NeXus
large scale
infrastructures
simulation /
analysis

WS1.003-invited

On cloud computing tools for the electron microscopy community and interoperable computational-geometry-based modeling of microstructures

M. Kühbach[1]

[1]Department of Physics, Berlin, Germany

Software is a fundamental tool which is used in virtually all workflows where data of materials characterization experiments with electron microscopes gets transformed into insight and knowledge. The last years have seen an increased interest, awareness, and funding to support the electron microscopy community on a common goal: Namely, data and metadata of electron microscopy experiments should become easier findable, more transparently accessible, and fundamentally more interoperable; so that data can be processed with different tools to improve the reusability and thus value of electron microscopy data [1]. Clear vocabulary, transparently detailed data schemes and software tools are needed to achieve this aim. This is the essential idea behind the FAIR research data stewardship principles [2] and the key reason behind established national funding schemes like the German National Research Data Infrastructure [3], Platform Material Digital [4], and international activities like EOSC [5], and e-DREAM [6].

A large number of workflows are currently developed by scientists using specific software tools locally and running analyses on own computers and high-performance computing resources. Manual data transfer and documentation is still a frequent task. Usually, many file formats and data representations have to be mastered. However, inconsistencies can come with having multiple representations of similar or sometimes even the same type of data. Reference frame conventions or assumptions used are examples which have to be carefully documented and communicated across tools to ensure a correct and valid interpretation of data. For this task, often recent efforts in cloud computing, documenting data via electronic lab notebooks (ELNs), and using research data management systems (RDMS) are expected to support scientists. Clearly, these tools can be useful in that they offer data organization, analysis, and publication services. However, using all these tools without changing culture and and rigorous data documentation, does not necessarily leave us with FAIR data. We will show how we are addressing these topics within the FAIRmat [7] project using NOMAD OASIS as the RDMS [8]. Specifically, this talk pulls focus on two topics relevant for electron microscopy: First, we will show the services which NOMAD offers, usage of ELNs and cloud computing services as examples. We will briefly touch upon the data model that is behind this work [7, 8] and the value of working as a community on interoperable data models [9]. Second, we would like to discuss the specific topic of analyzing diffraction pattern, here with a focus on orientation microscopy. We suggest an approach which can describe the variety of representations of orientation microscopy data. We will show an initial implementation of such an interoperable description using ELNs and NOMAD that can also be used for description of geometrical data like interface network and crystallites.

[1] M. Scheffler et al. Nature 604 (2022) 635
[2] M. Wilkinson et al. Scientific Data 3 (2016) 160018
[3] https://www.nfdi.de
[4] https://www.materialdigital.de
[5] https://eosc-portal.eu
[6] https://e-dream-eu.org
[7] https://fairmat-experimental.github.io/nexus-fairmat-proposal
[8] https://nomad-lab.eu
[9] https://codebase.helmholtz.cloud/em_glossary
[10] https://arxiv.org/abs/2205.13510

The project is funded by the Deutsche Forschungsgemeinschaft (DFG, German Research Foundation) – project 460197019.

WS1.005

Electronic lab notebooks compiling big datasets for machine learning analysis

M. Held[1], C. Eschke[2], F. Kirchner[2], M. Meller[1], S. A. Sahim[2], N. Jung[3], N. Garabedian[4], I. Bagov[4], C. Greiner[4], F. Bock[5], B. Klusemann[5], F. Wieland[2], T. Fried[1], R. C. Aydin[6], F. Isensee[7]

[1]Helmholtz-Zentrum Hereon, Institute of Membrane Research, Geesthacht, Germany
[2]Helmholtz-Zentrum Hereon, Institute of Metallic Biomaterials, Geesthacht, Germany
[3]Karlsruher Institut of Technologie (KIT), Institute of Organic Chemistry, Karlsruhe, Germany
[4]Karlsruher Institut of Technologie (KIT), Institute of Applied Materials, Karlsruhe, Germany
[5]Helmholtz-Zentrum Hereon, Institute of Materials Mechanics, Geesthacht, Germany
[6]Helmholtz-Zentrum Hereon, Institute of Material Systems Modelling, Geesthacht, Germany
[7]German Cancer Research Center, Helmholtz Imaging, Heidelberg, Germany

Electronic lab notebooks (ELNs) serve as means to gather analog metadata, e.g. experimental parameters, that would otherwise be hard to digitalize. Furthermore, they are a key prerequisite to a comprehensive documentation of research processes and the reuse of research data. However, different systems are often used within the same research institution or community, especially when covering a long, interdisciplinary process chain. The use of different systems - each addressing distinct requirements for discipline-specific needs - enables the availability of a broad functionality but results in challenges due to an often missing interoperability of the metadata. We are addressing this lack of interoperability for the two ELNs Herbie and Chemotion with an API-based data exchange. The envisaged reduction of boundaries between the disciplines of chemical synthesis and process engineering in membrane research will enable the creation of large and coherent data sets, including microscopic image data.

Once data management platforms, e.g. ELNs, are in use, the semantic information therein can only be exploited when terms are clearly defined in a glossary. In order to make metadata truly interoperable, glossaries need to be transformed into ontologies, which structure knowledge based on formal logic, reduce ambiguity and offer machine-driven reasoning. We are establishing a glossary and ontology for membrane research, in parallel to a guide that describes the best practices for building these. In combination with existing efforts, e.g. the Helmholtz Electron Microscopy Glossary, our ontology will enable machine-driven interpretation of the linguistic data in our ELNs.

Following the assembly of large datasets in ELNs, we address the ambiguous relationship between pore morphology and fabrication parameters of isoporous block copolymer membranes by machine learning methods. At first, the hexagonality was extracted from 1800 SEM images as a quality descriptor. Analyzing the impact of the fabrication parameters on this descriptor with a neural network revealed that the fraction of the main solvent and the molecular weight have the most pronounced effect on the hexagonal arrangement of pores in the membrane.

In summary, using ELNs in the entire experimental workflow creates holistic, structured datasets that can easily highlight critical parameters when analyzed by machine learning methods. Moreover, enhancing the value of the metadata in ELNs by an ontology creates even more room for digital analyses.

WS1.006

Automation of TEM alignment using python scripting

P. Wachsmuth[1]

[1]JEOL (Germany) GmbH, Freising, Germany

In recent years, image processing technology has been greatly improved and people in various fields have developed automated operations based on image processing technology. In the field of electron microscopy, automated functions and software have been developed that can be used in the fields of materials and biology [1]. Transmission electron microscopes (TEM) of JEOL can be operated using a scripting language with PyJEM, a JEOL made Python module (Python is a trademark or registered trademark of the Python Software Foundation). By using PyJEM, one can read the information on a TEM and send operational commands to it without a direct operation. In addition, the combination of lots of computation and image processing modules enables users to simplify the operation of TEM together with the acquisition of experimental data. Moreover users who are not familiar with microscope operation can perform TEM alignments with the same accuracy as an experienced user in a short time by combining useful functions in Python. In this report, we introduce examples of automated microscope alignments by PyJEM.

[1] M. Schorb. I. Haberbosch. W.J. H. Hagen. Y. Schwab *&* D. N. Mastronarde. Nature Methods 16 (2019). p. 471-477.

WS1.P001

Data processing workflows with nextflow and a ptychography use case

P. Fernandez Robledo[1], T. C. Pekin[1], C. T. Koch[1]

[1]Humboldt-Universität zu Berlin, Department of Physics, Structure Research and Electron Microscopy group, Berlin, Germany

As electron microscopy experimental analysis has become more complex, involving multiple steps (each of which requiring its own analysis code) and large amounts of data, there is a need to organize and scale up this process beyond the personal computer. Ensuring reproducibility from raw data to end results is paramount. Due to the large amounts of data involved, there is a growing trend of moving from personal computers to a server (or cluster), involving interconnected machines. Traditionally, this meant writing specialized code that works on a specific cluster, i.e. the code could not easily be run on a personal computer for testing, or on a different cluster[1]. With the advent of workflow engines, some processing workflows can be implemented in a more hardware independent form[2], with greater ease and usability. This also facilitates the sharing of workflows.

To demonstrate this software paradigm, we implement a ptychographic [3] reconstruction workflow with the workflow engine Nextflow [4], which is infrastructure independent. Within the workflow, processes are described and input/output relations mapped. Thus, possibilities for asynchronous execution are automatically identified and performed. Parallel execution of Nextflow processes is also possible, and done automatically when given multiple inputs that independently traverse the workflow steps. Parallelization within one dataset can also be done via explicit Nextflow constructs. One key advantage of Nextflow is the ability to mix different tools with each other. For example, the output of a Python script can be passed on to be processed by a compiled executable.

Our implemented workflow has as input the raw data files from the microscope as well as a configuration yaml file which describes what settings should be applied for each step. This hierarchical file also controls which processing steps should be executed. As Nextflow does not use a deep hierarchy in its yaml configuration file, but this was desired for our workflow, custom functions were written to extend the functionality of Nextflow to accommodate this.

The workflow itself has the task of preprocessing the raw microscope data and then performing a ptychographic reconstruction. Additional postprocessing steps within the workflow can then follow.

The resulting workflow was developed and executed on a laptop and later executed on a local cluster consisting of one head node and two execution nodes managed by slurm [5]. A shared filesystem between the three machines was also required by Nextflow.

Here, we successfully demonstrate the use of a workflows for electron microscopy data. The use of workflows can ease the transition of code from a personal computer to the cluster, while also emphasizing reproducibility and shareability, helping to manage the complexity in multistep data processing.

[1] C Schiefer et al, (2020), https://doi.org/10.48550/arXiv.2006.03104

[2] F Lehmann, (2021), *Proceedings of the CIKM 2021 Workshops* *http://ceur-ws.org/Vol-3052/short12.pdf*

[3] MJ Humphry et al., Nat. Comm. 3, (2012), p.1. *https://doi.org/10.1038/ncomms1733*

[4] P Di Tommaso et al., Nat. Biotechnol. 35, (2017), p. 316. https://doi.org/10.1038/nbt.3820

[5] Jette, M.; Grondona, M., Proceedings of ClusterWorld Conference and Expo, (June 2003). "SLURM: Simple Linux Utility for Resource Management" (PDF)

WS1.P002

The EM glossary: a community effort to harmonize metadata in the electron microscopies

V. Hofmann[1], O. Mannix[2], A. Strupp[1], S. Sandfeld[1]

[1]Forschungzentrum Jülich, Institute for advanced simulation - Materials Datascience and Informatics (IAS-9), Aachen, Germany
[2]Helmholtzzentrum Berlin, Berlin, Germany

Research data has to fulfil a number of requirements for it to be fully exploitable - today and in the future. The FAIR principles [1] – findable, accessible, interoperable, and reusable – provide a conceptual framework to achieve this, but the pathway to implementation is often unclear. Here we focus on the challenge of implementing the "I" in FAIR.

Interoperability is the potential for two independent agents to work on the same data in a coordinated fashion. It is especially relevant for researchers working in interdisciplinary fields, such as electron microscopy, where terminology in adjacent scientific disciplines is unknown, or where identical terms are used with differing meaning, for example, consider a mathematical or biological cell. The use and adoption of established vocabularies and semantic standards can provide solutions – however these may be infeasible to implement, non-existent, or scientifically unsuitable. This is why a number of initiatives are developing semantic artefacts that aim to describe experimental equipment, workflows, and analysis procedures in electron and ion microscopies. Harmonisation of these efforts to ensure interoperability across the community is required.

To support the long-term semantic interoperability the Helmholtz Metadata Collaboration (HMC) is coordinating a community-wide effort, including over 45 scientists from more than 22 institutions across Switzerland, Austria, and Germany, and including representatives of several NFDI consortia [2], to create a joint resource to harmonize semantics in the field of electron and ion microscopies.

This poster will report on this community effort - the EM glossary group [3]. We will describe how we achieve consensus on terms commonly used in electron and ion microscopies via a remote, collaborative workflow based on the platform GitLab. A text-mining approach has been used to evaluate EM image metadata and prioritise terms which are widely used in the community. We will show results, including some of our harmonized definitions, and provide details of our implementation strategy.

The developed resource will provide harmonized and machine actionable semantics to support specific development efforts such as metadata schemas or ontologies in their respective fields. This will benefit experimental scientists by providing clarity when annotating and re-using research data; and by facilitating communication when conducting interdisciplinary studies.

Do you work in electron and/or ion microscopy or related data analysis? Follow us on twitter @helmholtz_hmc or tweet #EMGlossary. You want to get involved in the development and/or join our meetings? Send an email to hmc@fz-juelich.de or hmc-matter@helmholtz-berlin.de

1. Wilkinson, M.D. et al. Scientific Data. http://dx.doi.org/10.1038/sdata.2016.18 (2016)
2. NFDI: Nationale Forschungsdateninfrastruktur. https://www.nfdi.de/
3. EM Glossary GitLab repository: https://gitlab.hzdr.de/em_glossary

WS2.001-invited

Mesoscale sample preparation by multi-Ion-species-plasma-FIB

J. Reuteler[1]

[1]ETH Zürich, ScopeM, Zurich, Switzerland

Sample preparation for synchrotron X-ray tomography and spectroscopy experiments often requires a target sample size on the order of several tens to hundreds of micrometers. Focused Ion Beam (FIB) based techniques are the most versatile solution: Delicate or brittle materials that are hard to machine mechanically can be dealt with and site-specific preparation is straight forward. Generally Ga-FIB tools can be employed, however, the milling times may be quite long. Here Plasma-FIB instruments offering up to few microamperes of ion current can offer time savings, but also enable to reach dimensions that are simply not manageable by Ga-FIB.
In this talk several sample preparation tasks and their solution will be discussed. The materials range from rock to 3D printed alumina over to embedded polymer electrolyte fuel cells and solid state lithium ion batteries. Different sample geometries (windows, pillars and thick lamellae) are covered, challenges and solutions for in-situ lift-out and mounting are discussed.

Fig. 1. SEM image of 4 uA Ar-PFIB window with an artificial "crack" milled into 3D printed alumina. Sample courtesy of Fabrizio Verga, Inspire /Wegener group, ETH Zürich.

Fig. 1

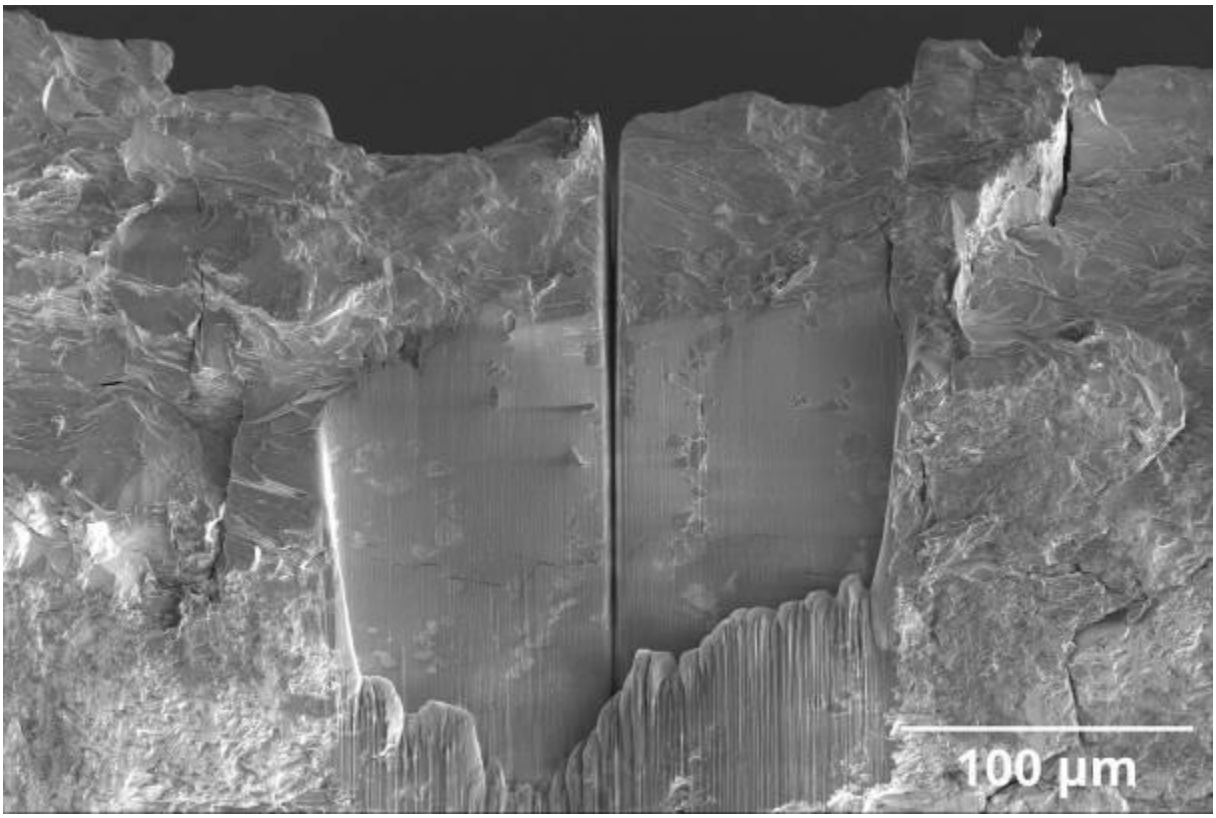

WS2.002-invited

Faster mm-scale defect/failure analysis by combining plasma FIB milling and laser ablation

J. V. Oboňa[1,2], P. Klímek[1], M. Sláma[1]

[1]TESCAN, Brno, Czech Republic
[2]TESCAN, Brno, Czech Republic

The success in materials research is to a certain extent determined by the characterization efficiency. Through faster analysis of materials properties, the performance of engineering materials is improved, better products in the semiconductors and microelectronics industry are developed; and advanced nanomaterials optimize properties of catalysts, coatings, polymers, and many more.

It is obvious, that developing new products and technology is very challenging. One area where laser ablation along with FIB-SEMs plays an important role is Failure Analysis (FA). The goal of FA is to determine the defect"s root cause and provides feedback to maintain feasible time-to-market and product reliability. This must be done as precisely as possible and as fast as possible. Industry-proven plasma FIB technology serving these purposes for nearly a decade. Recently, however, significant increases in both the complexity of the devices and the depth of buried defects, together with pressure on time-to-result may push the plasma FIB speed to its limit. There are different methods how to further enhance sample preparation throughput of a Plasma FIB-SEM without sacrificing the quality of the data—such as the utilization of rocking polishing or mask method—nevertheless, ultimate throughput can be achieved by the smart implementation of the laser ablation technique in some steps of the Failure Analysis workflow. Through the purpose-designed workflow, the plasma FIB sample analysis efficiency is increased, time to the results decreased while new synergies among laser ablation and FIB-SEMs are opened.

In this talk, you will learn about TESCAN Large Volume Workflow. We will guide you through the use cases where wide range of materials and complex devices were investigated for their failures. By the end of the talk, we disclose the method which is used to achieve fast, artifact-free sample preparation while achieving high-quality results proven by UHR SEM imaging.

WS2.003-invited

Next generation sample preparation for cryo-ET – instruments, accessories and workflows

S. Klumpe[1], J. Plitzko[1], O. Schioetz[1], C. Kaiser[1], J. Brenner[1],S. Khavnekar[1]

[1]MPI of Biochemistry, CryoEM Technology, Martinsried, Germany

The recent technological breakthrough in cryo-electron tomography (cryo-ET) opens the possibility of imaging macromolecular complexes in their native cellular context at sub-5Å resolution [1,2]. This technology is the foundation for an emerging field in the life sciences, often termed structural cell biology, capable of revealing how different conformational states of protein complexes are linked to biological functions. However, imaging is highly dependent on sample preparation. This is especially true for transmission electron microscopy (TEM), where samples must be thin enough to provide high-resolution information, homogeneous in thickness for consistent high-quality data, and in their original state, as in cryo-TEM, to preserve the structural features of macromolecules. Sample preparation, while largely underappreciated, is thus a vital part of imaging.
Since its beginnings as a sample-thinning technique for cryoET, cryogenic focused ion beam milling (cryoFIB) using gallium ions has evolved into a procedure that encompasses several different methods. Methods like on-the-grid lamella-preparation of plunge frozen samples, iterative FIB ablation and scanning electron microscopy (SEM) imaging, and most recently lift-out for high-pressure frozen (HPF) multicellular samples [3,4]. The latter is an established method in materials science, but since its introduction for cryo-ET, it has been used rather rarely [5]. The reasons why the lift-out method falls short compared to lamellar preparation on the grid are quite obvious: First, it is very time consuming to mill high-pressure frozen (HPF) samples that are up to 200 microns thick; second, the whole process is often disappointingly inefficient, mainly because of its complexity; third, there is no way to assess ice quality before or during preparation, only after the first TEM image does one know whether the ice is "good" or "bad"; and finally, the "survival rate" of lift-out lamellae is low, either they are lost during manual transfer or they are contaminated beyond recognition.
Yet, there must be ways to streamline this process and make multicellular specimens and small organisms amenable to routine access in a reasonable time frame. PlasmaFIB technology promises to do just that: Higher beam currents and higher ablation rates to make bulky samples easily accessible, hardware automation that frees the user from any manual operation and increases throughput and survival rates, and finally integrated solutions for targeting (correlative fluorescence microscopy, CLEM) and ice quality assessment.
Here we present the latest developments towards full automation for plunge-frozen and high pressure frozen samples, as well as initial results and experiences with a novel plasma cryo-FIB system specifically designed for large scale cryo-FIB milling.

References:
[1] D. Tegunov et al., Nature Methods 18, 186–193 (2021).
[2] S. Khavnekar et al. bioRxiv; DOI: 10.1101/2022.06.16.496417 (2022).
[3] S. Klumpe et al., eLife 2021;10:e70506 (2021).
[4] S. Klumpe et al., Microscopy Today 30(1), 42-47 (2022).
[5] M. Schaffer et al., Nature Methods 16, 757-762 (2019).

WS2.004

State of the art of volume imaging and CLEM of organoids

E. D'Imprima[1], A. M. Steyer[2], P. Ronchi[3], Y. Schwab[3], S. Mattei[2], J. Mahamid[1]

[1]EMBL Heidelberg, SCB, Heidelberg, Germany
[2]EMBL Heidelberg, Heidelberg, Germany
[3]EMBL Heidelberg, Electron Microscopy Core Facility, Heidelberg, Germany

Organoids recapitulate tissue architectures and represent an opportunity to investigate healthy or diseased tissues. Understanding organoid complexity requires the integration of diverse imaging modalities covering different spatial and temporal resolutions. Fluorescence light microscopy allows studying the cellular sociology in living samples. FIB-SEM volume imaging can further probe the multicellular environment at ultrastructural resolution. Cryo-electron tomography (cryoET) bridges the gap with atomic resolution to investigate macromolecular complexes in the cell. Further, deep-learning software is required to correlate and quantitatively analyse these data. Here, we present the state of the art and future direction of light and electron microscopy imaging of organoids both at room temperature and cryogenic regime.

Matrigel-embedded organoids were either cultured directly in HPF carriers1 or multi-well dishes using liquid medium. These carries were used to perform confocal live-cell imaging using cell-permeable fluorescence dyes. After high-pressure freezing, the fluorescence signal guided FIB-SEM volume imaging acquisitions at low temperature. Further, sample thinning for cryo-electron tomography was achieved by lift-out. Alternatively, organoids in HPF carriers were processed by freeze-substitution and resin embedding follow by laser branding to FIB-SEM volume imaging acquisitions2. FIB-SEM was done on a performed on a Zeiss CrossBeam XB550 and on Thermo Fisher Scientific Aquilos. Lastly, correlation of light and electron microscopy data as well as automatic image segmentation was done by ORS Dragonfly.

We show how to make organoid delicate specimens amenable to high-pressure freezing and fluorescence light microscopy both a room temperature and cryogenic regime. We compare the advantages of live dyes versus genetically encoded fluorescent reports and we show the limits of fluorescence light microscopy in imaging large (> 200µm) and deep (> 20µm) biological samples. Then, we illustrate correlative light and electron microscopy approaches for organoid samples. Further, we describe our results of FIB-SEM volume imaging at ultrastructural resolution of organoids at room temperature and the current limits of imaging at low-temperature. To provide a quantitative understanding of the complex and heterogenous multicellular environment of organoids, large FIB-SEM dataset need to be annotated. While manual annotation becomes unfeasible given the large amount of data, deep-learning algorithms offer a workable solution for automating this task. We used trainable convolutional neural networks provided in the software ORS Dragonfly for automatic segmentation of subcellular structures. We focused our attention especially on the interaction between cortical cytoskeleton and cell junctions in the context of patient-derived cancer organoids. Finally, we provide an overview of the actual possibilities to perform lift-out from high-pressure frozen samples for cryoET imaging.

1. Ronchi, P. *et al.* High-precision targeting workflow for volume electron microscopy. *J. Cell Biol.* **220**, (2021).
2. D"Imprima, E. *et al.* Integrated light and electron microscopy continuum resolution imaging of 3D cell cultures. *bioRxiv* 2021.07.02.450855 (2021) doi:10.1101/2021.07.02.450855.

WS2.P001

Improving TEM specimen preparation of oxides with the help of electron backscatter patterns

J. Deuschle[1], T. Heil[1], P. Kopold[1], P. A. van Aken[1]

[1]Max Planck Institute for Solid State Research, Stuttgart Center for Electron Microscopy, Stuttgart, Germany

The quality of the Transmission Electron Microscopy (TEM) specimens is crucial for the quality of results obtainable from a TEM investigation. If Focused Ion Beam (FIB) milling is used for the preparation, the major limitations in specimen quality are due to a damage layer on the specimen surface, which is induced by interactions between the ion beam and the surface atoms. The processes leading to damage are well known for metals and semiconductors, yet, limited studies investigated the interaction mechanisms between ion beams and oxides with more complex lattice structures such as perovskites. Therefore, we aim at a better understanding of FIB-induced damage of oxide surfaces with this investigation and want to use this knowledge for minimizing the damage layer in FIB-prepared samples.

Various ion-beam-milling conditions, that are typically applied during a TEM specimen preparation process in FIB, were used on oxide specimens regarding their surface damaging behavior. To investigate the amount of surface damage, two different methods were applied: Firstly, TEM images of the damage layers were taken after FIB milling with different acceleration voltages, beam currents, and ion incident angles. The damage layer thickness was directly measured from these images. Secondly, individual electron backscatter patterns (EBSP) and electron backscatter diffraction (EBSD) maps were recorded before and after FIB milling to study the effects on the quality of EBSPs, since this a very sensitive measure of surface distortions. Furthermore, the indexing success of EBSD maps has been investigated with respect to the different milling parameters.

The presentation will summarize the results and discuss strategies for obtaining high quality TEM specimen with minimal surface damage.